BSPE-25090-012-12

과거 온난기의 서남극 빙상 후퇴 및 해양 순환 변화 연구

Ice sheet retreat and ocean circulation in West Antarctica during the past warm periods

KOPRI 극지연구소

2026. 2

한 국 해 양 과 학 기 술 원
부 설 극 지 연 구 소

제 출 문

극지연구소장 귀하

본 보고서를 “과거 온난기의 서남극 빙상 후퇴 및 해양 순환 변화 연구”과제의 최종 보고서로 제출합니다.

2026. 02.

연 구 책 임 자 : 유규철
참 여 연 구 원 : 이재일, 이민경
“ : 김성한, 김소영
“ : 문홍수, 김효진
“ : 강명일, 강천윤
“ : 하상범, 박영규

위탁연구기관명 (책임자) : 부산대 (김부근)
연세대 (김진욱)
고려대 (성영배)
전북대 (박영숙)
공주대 (이현희)

KOPRI 극지연구소

보고서 초록

<table>
<tr><td>과제관리번호</td><td>PE25090</td><td>해당단계
연구기간</td><td>2020.01.01
~ 2025.12.31</td><td>단계 구분</td><td>(1+2 단계)</td></tr>
<tr><td rowspan="2"><u>연구사업명</u></td><td>중 사 업 명</td><td colspan="4">기관목적사업</td></tr>
<tr><td>세부사업명</td><td colspan="4">기관기본사업</td></tr>
<tr><td rowspan="2">연구과제명</td><td>중 과 제 명</td><td colspan="4"></td></tr>
<tr><td>세부(단위)과제명</td><td colspan="4">과거 온난기의 서남극 빙상 후퇴 및 해양 순환 변화 연구</td></tr>
<tr><td>연구책임자</td><td>유 규 철</td><td>해당단계
참여연구원수</td><td>총 : 28 명
내부 : 10 명
외부 : 18 명</td><td>해당단계
연구비</td><td>정부: 5,499 백만원
기업: 백만원
계: 5,499 백만원</td></tr>
<tr><td>연구기관명 및 소속부서명</td><td colspan="2">한국해양과학기술원 부설 극지연구소 빙하지권연구본부</td><td colspan="2">참여기업명</td><td></td></tr>
<tr><td>국제공동연구</td><td colspan="5">상대국명 : 뉴질랜드, 미국, 영국, 이태리
상대국연구기관명 : 뉴질랜드 GNS, 뉴질랜드 빅토리아대, 뉴질랜드 오타고대
미국 남플로리다 대학, 휴스톤 대학
영국 BAS
이태리 트리에스테 대학</td></tr>
<tr><td>위 탁 연 구</td><td colspan="5">연구기관명 : 고려대 외 4개 대학 연구책임자 : 성영배 외 4인</td></tr>
<tr><td colspan="4">요약(연구결과를 중심으로 개조식 500자이내)</td><td>보고서 면수</td><td>987</td></tr>
</table>

고환경 연구는 과거의 환경 변화를 이해하고 경향을 파악하여 현재 환경 변화의 원인 이해와 영향 예측에 중요한 역할을 한다. 극지역은 저위도 지역에 비해 기후 변화에 민감하게 반응하여 자연적 기후 변화의 감지에 최적지이며, 특히 서남극은 동남극과 달리 얼음들이 해수면 아래 놓여있어서 현재 온난 위기에 따른 영향을 심각하게 받을 수 있다. 미래 온난 위기에 대한 관심이 어느 때보다도 높으며, 미래 기후 환경이 어떠한 모습인지 예측하는 일은 글로벌 기후 이슈 중 하나로 현재 주요 연구 주제이다. 미래 온난 위기와 상응하는 과거 온난기의 모습이 어떠하였는지 해양 퇴적물을 통해 알 수 있으며, 본 과제는 이 문제에 대한 정보를 과학적으로 제시할 수 있는 연구 사업이다.

본 과제의 최종 목표는 과거 온난기 서남극 빙상의 시공간적 변화 기작 및 영향 규명이며, 1단계 목표는 과거 온난기 (플라이오세 중기, 마지막 간빙기, 홀로세 중기 등)의 서남극 빙상 규모를 복원하고 해양-기반 빙상의 안정성 조절 요인을 규명하는 것이다. 이 목표를 달성하기 위해 제시된 네 가지 성과목표는 (1) 국제공동 시추 프로그램 시료 확보, (2) 서남극 빙상 주변 퇴적물 분포 조사 및 시추 시료 확보, (3) 고기후 지시자 및 연대측정법 개선, (4) 과거 온난기 서남극 해양 순환 및 퇴적 양상 변화 복원 연구이다. 다수의 산학 협동 연구와 국제공동 연구 참여가 이루어졌고, 특히 1단계에서 국내 최초로 국제공동 대륙 시추 프로그램의 일환인 SWAIS 2C 사업 기획에 참여하여 현재 본격적인 드릴링 시추 단계에 접어들었다. 본 보고서에는 2020-2025년의 6년에 걸쳐 연구 지역에 수행된 아라온 기반 탐사 내용과 과제 목표에 따른 연구 성과가 담겨있다.

색 인 어 (각 5개 이상)	한 글	과거 온난기, 서남극, 퇴적물, 고환경, 빙상, 해양 순환
	영 어	past warm periods, West Antarctica, marine sediment, paleoenvironment, ice sheet, ocean circulation

요 약 문

Ⅰ. 제목

과거 온난기의 서남극 빙상 후퇴 및 해양 순환 변화 연구

Ⅱ. 연구개발의 목적 및 필요성

○ 고환경 연구의 필요성

고환경 연구는 환경 변화에 따른 영향을 예측하고 기후 변화의 동인을 이해하는 데 중요한 역할을 한다. 또한 기후 변화를 예측하는 기후 모형의 핵심적 데이터를 제공하며 기후 모형 개선에 결정적 역할을 하고 있다. 최근 급격한 지구 환경 변화가 현실화되면서 기후 변화를 포함한 지구 환경 변화 현상에 대한 과학적 이해의 필요성이 증대되었다.

KOPRI 극지연구소

○ 고환경 연구에서 남극 지역의 중요성

극지역은 기후 변화에 민감하게 반응하여 기후 변화의 영향이 크게 나타나므로 기후 변화 감지의 최적지이다. 그 중 남극은 대기 중의 이산화탄소 농도, 심층수의 형성, 빙상의 증감과 관계가 있어 전지구 기후 및 환경 변화에서 중요한 역할을 한다. 따라서 남극의 과거 환경 변화 연구는 전지구적 규모의 자연적 기후 변화 경향 및 그 영향을 이해하는데 필수적인 정보를 제공한다. 서남극 빙상은 빙상의 바닥과 기반암이 해수면에서 만나는 해양 기반 빙상이다. 해양 기반 빙상의 안정성은 대기 및 해양 온도 변화, 기후 변화로 인한 해수면 변화와 같은 외부 요인에 매우 민감하다. 서남극 빙상이 완전히 사라지면 지구 해수면은 4.8 m 상승할 수 있는데, 이처럼 서남극 빙상의 과거 변동성은 과거 해수면 상승에 관여한 것으로 생각된다. 따라서 서남극 빙상의 과거 증감 기록과 거동을 이해하는 것은 미래 기후변화 예측에 필수적이다. 서남극 빙상의 거동을 포괄적으로 이해하기 위해 웨델해에서 로스해까지 전 해역(웨델해-남극반도-벨링스하우젠해-아문센해-로스해)을 포함하는 서남극 영역의 연구가 필요하다. 남극 대륙 주변부의 해양 및 육상 퇴적물에 대한 과거 기록이 필요한 시점이다.

○ 과거 온난기 고환경 연구의 중요성

기후변화에 관한 정부간 협의체 (IPCC) 5차 보고서가 제시한 미래 기후 예측과 기후 모델과의 비교 연구에서 지구 온난화가 현재대로 진행되면 2030년엔 지구 기후가 3백만 년 전의 플라이오세 중기(현재보다 평균 기온이 2-4도 높음)와 유사해지고, 2150년의 지구 기후는 따뜻하고 빙하가 거의 사라졌던 5천만년 전의 에오세(현재보다 평균 기온이 10-13도 높음)와 비슷해질 것이라고 보고하였다. 미래 지구 온난화와 지구과학적인 측면에서 대조될 수 있는 중요한 과거 온난기는 홀로세 중기(현재보다 약 0.5-1.5도 높음), 지난 간빙기, 플라이오세 중기 등으로 당시 남극의 빙상 안정도와 해양 순환이 어떠하였는지 밝히는 것은 미래 지구 온난화의 모습을 보다 정확하게 예측할 수 있는 단서를 제공할 수 있다. 서남극의 과거 온난기의 환경을 이해할 수 있는 중요한 재료는 시추 빙하와 퇴적물로서 남극 대륙의 과거 대기 환경을 알 수 있는 빙하 시추의 기록과 더불어 시추 퇴적물의 고기후 지시자는 과거 빙상의 전진과 후퇴 및 해양 순환을 이해할 수 있는 열쇠이다. 인류 생존의 부적합한 환경이 될 수 있는 미래 지구 온난화는 인류학적으로 경험해보지 못한 새로운 기후 환경으로 나타날 수 있는데, 과거 온난기 동안 남극해가 어떤 환경이었으며 남극 빙하는 과거 온난화에 어떤 모습을 가지고 있었는지 복원하는 일은 현재의 글로벌 기후 이슈에 대응할 수 있는 중요한 연구이며, 남극 대륙의 빙상과 남극해의 국제공동 퇴적물 시추 프로그램은 과거 온난기 환경의 중요한 정보를 제공할 수 있다.

KOPRI 극지연구소

Ⅲ. 연구개발의 내용 및 범위

○ 최종 목표

과거 온난기 서남극 빙상의 시공간적 변화 기작 및 영향 규명

(1단계) 과거 온난기(플라이오세 중기, 마지막 간빙기, 홀로세 중기 등)의 서남극 빙상 규모를 복원하고 해양-기반 빙상(marine-based ice sheet)의 안정성 조절 요인 규명
(2단계) 과거 온난기의 서남극 빙상 변화 양상 파악 및 해양에 미친 영향 규명

○ 1단계 성과목표 (2020.01.01 ~ 2022.12.31)

- 국제공동 시추 프로그램 시료 확보
- 서남극 빙상 주변 퇴적물 분포 조사 및 시추 시료 확보
- 고기후 지시자 및 연대측정법 개선
- 과거 온난기 서남극 해양 순환 및 퇴적 양상 변화 복원 연구

○ 2단계 성과목표 (2023.01.01. ~ 2025.12.31)

- 국제공동 시추 프로그램 참여

- 국제공동 시추 프로그램 주변 지역 탐사
- 고기후 지시자 및 연대측정법 개선
- 과거 온난기 서남극 빙상 및 해양 환경 변화 규명

○ 1차년도 (2020) 연구목표 및 내용
- 국제공동 IODP 참여 및 시료 확보
- 아문젠해 퇴적물 시추 시료 확보
- 연구선 기반 다중빔 탐사
- 연구선 기반 SBP 탐사
- 빙하운반역 산정 비파괴 X-선 촬영 도입
- 과거 온난기의 퇴적물 내 유기물의 고기후 지시자 분석 도입
- 과거 온난기의 미생물 군집 분석 도입
- 공극수의 고기후 지시자 분석 도입
- 탄산염 안정동위원소 분석법 도입
- Ramped Pyrolysis 연대 측정 적용
- 퇴적물 내 유기물 프록시를 이용하여 중위도 과거 환경 복원
- 홀로세 중기 남극 빙붕 하부에서의 미생물과 점토광물의 반응 및 영향
- 홀로세 중기 크리스탈 사운드 분지의 빙하 후퇴사 연구
- 후기 플라이스토세 동안 로스해의 해양환경 변화
- 스코시아해 엘리펀트 섬 주변의 지난 빙하기 이후의 고환경 변화
- 국제공동 SWAIS 2C 시추 제안서 작성 참여

○ 2차년도 (2021) 연구목표 및 내용
- 로스해 퇴적물 시추 시료 확보
- 연구선 기반 다중빔 탐사
- 연구선 기반 SBP 탐사
- 빙하운반역 산정 비파괴 X-선 촬영 이미지 프로그램 개발
- 과거 온난기의 퇴적물 내 유기물의 고기후 지시자 분석 적용
- 공극수 내 고기후 지시자 분석
- 과거 온난기의 미생물 군집 분석 도입
- 탄산염 안정동위원소 분석법 개선 및 적용
- Ramped Pyrolysis 연대 측정 적용
- 벨링스하우젠해의 지난 빙하기 이후의 해양 순환 변화 연구
- 플라이오세 중기 로스해 해양 순환과 빙권 변화 관계 연구
- 로스해 대륙붕 퇴적물 연구를 통한 해양 기반 빙상의 안정성 연구
- 로스해 빙권 변화에 따른 대륙대 퇴적 양상 변화 연구
- 해빙기의 빙저호 형성 기작 및 빙저호 특성 연구

○ 3차년도 (2022) 연구목표 및 내용

- 아문젠해 퇴적물 시추 시료 확보
- 연구선 기반 다중빔 탐사
- 연구선 기반 SBP 탐사
- 빙하운반역 산정 비파괴 X-선 촬영 이미지 프로그램 적용
- 과거 온난기의 퇴적물 내 유기물의 고기후 지시자 분석 도입
- 공극수 내 고기후 지시자 분석
- 과거 온난기의 미생물 군집 분석 도입
- 유전체 분석를 통한 고환경 해석
- 탄산염 안정동위원소 분석법 적용
- Ramped Pyrolysis 연대 측정 적용
- 홀로세 중기 로스해 해양 순환 변화 연구
- 플라이스토세 기후 변화에 따른 남극 저층수 거동 변화 연구
- 플라이스토세 기후 변화에 따른 남극 표층 생산력 및 해양 환경 변화 연구
- 서남극 빙상의 지역적 후퇴 양상 연구
- 국제공동 SWAIS 2C 사업 참가 협약 MoU 체결

KOPRI 극지연구소

○ 4차년도 (2023) 연구목표 및 내용

- 국제공동 IODP 시추 시료 분석 완료
- 로스해 서부와 중앙 퇴적물 시추 시료 확보
- 연구선 기반 다중빔 탐사
- 연구선 기반 SBP 탐사
- 과거 온난기의 퇴적물 내 유기물의 고기후 지시자 분석 도입
- 과거 온난기의 미생물 군집 분석 도입
- 공극수의 고기후 지시자 분석 도입
- 탄산염 안정동위원소 분석법 도입
- Ramped Pyrolysis 연대 측정 적용
- 퇴적물 내의 대자율 이방성 분석 도입
- 퇴적물 내의 유기오염물질 분석 도입
- 퇴적물 내 와편모조류 시스트 분석 도입
- 홀로세 중기 남극 빙붕 하부에서의 미생물과 점토광물의 반응 및 영향
- 남극반도의 홀로세 중기 온난기의 퇴적물 내 규조 군집 특징 및 표층해양환경 연구
- 해빙기 온난화에 따른 서남극 빙상의 아문젠해 대륙붕 후퇴 특성 연구
- 로스해 대륙대 퇴적물 내의 고지자기 특성 분석을 통한 과거 해양환경 복원 연구
- 13만년 전 지난 간빙기 동안 웨델해의 빙하 흐름 양상

- 벨링스하우젠해의 과거 3 번의 간빙기 동안 퇴적양상 및 해양순환 연구
- 전지구적 기후변화 사건 MBE, MPT 동안 로스해 및 드레이크 해협의 표층해양환경 변화 연구

○ 5차년도 (2024) 연구목표 및 내용

- 국제공동 SWAIS 2C 1차 시추 시료 확보 및 분석
- 국제공동 SWAIS 2C 시추보고서 작성
- 국제공동 SWAIS 2C 추가 분담금 1차 납부
- 국제공동 IODP 시추 시료 분석 완료 및 일부 결과 논문 투고
- 로스해 빙붕 주변 퇴적물 시추 시료 확보
- 연구선 기반 다중빔 탐사
- 연구선 기반 SBP 탐사
- 빙하운반역 산정 비파괴 X-선 촬영 적용
- 과거 온난기의 퇴적물 내 유기물의 고기후 지시자 분석 도입
- 과거 온난기의 미생물 군집 분석 도입
- 공극수의 고기후 지시자 분석 도입
- 탄산염 안정동위원소 분석법 도입
- Ramped Pyrolysis 연대 측정 적용
- 와편모조류 시스트 군집 분석 및 고환경 지시종 적용과 검토
- 남극 퇴적물 내의 유기오염물질 분석을 통한 인류세 기록 복원
- 후기 빙하기-간빙기 빙상 변화에 따른 해양학적 변화 복원 및 특징 연구
- 남극반도의 지난 마지막 빙하기 이후의 표층-저층 해양환경 변화 및 상호작용 연구
- 대륙주변부의 퇴적물 기원지 파악 및 주요 수송 메커니즘 파악 연구
- 빙하기 내 천년 단위의 짧은 온난화 사건에 대한 빙상 반응 연구
- 단일 규조종 골격 내 동위원소를 이용한 홀로세 동안 남극반도 지역 표층해양환경 특성 변화 연구
- 과거 빙하기 이후 스코시아해 표층 수온 복원 연구
- 로스해 대륙붕 퇴적물 연구를 통한 해양 기반 빙상의 안정성 연구
- 로스해 빙권 변화에 따른 대륙대 퇴적 양상 변화 연구

○ 6차년도 (2025) 연구목표 및 내용

- 국제공동 SWAIS 2C 1차 시추 시료 분석
- 국제공동 SWAIS 2C 2차 시추 시료 확보
- 국제공동 SWAIS 2C 추가 분담금 2차 납부
- 국제공동 IODP 시추 시료 분석
- 로스해 빙붕 주변 퇴적물 시추 시료 확보

- 연구선 기반 다중빔 탐사
- 연구선 기반 SBP 탐사
- 빙하운반역 산정 비파괴 X-선 촬영 분석 적용
- 과거 온난기의 퇴적물 내 유기물의 고기후 지시자 분석 도입
- 공극수 내 고기후 지시자 분석
- 과거 온난기의 미생물 군집 분석 도입
- 유전체 분석를 통한 고환경 해석
- 탄산염 안정동위원소 분석법 적용
- Ramped Pyrolysis 연대 측정 적용
- 와편모조류 시스트 군집 변화 기록을 이용한 고환경 해석
- 해저 지형을 이용한 서남극 빙상 후퇴 양상 연구
- 로스해-아문젠해 대륙주변부의 과거 퇴적 양상 변화 및 해양환경 변화 양상 비교 연구
- 로스 빙붕 주변 퇴적물 특성 파악 연구
- 과거 온난화 시기의 서남극 빙상 후퇴 및 해양 순환의 공간적 변화에 대한 보고서 작성 (부록 별도 보고서 참조)

KOPRI 극지연구소

Ⅳ. 연구개발결과

1장 서론에서는 본 연구과제의 내용 및 중요성, 그리고 전반적인 연구목표를 개괄하였고, 2장은 본 연구과제의 가장 중요한 국제공동연구 SWAIS 2C 사업의 전반적인 내용을 제시하였으며, 이후 내용은 남극 현장탐사 결과와 목표별 연구 결과로 구성되어있다. 본 보고서에 포함되어야 할 위탁연구 결과는 별도의 위탁연구 보고서로 제출되었음을 명시한다.

○ 남극 현장 탐사
3장 : 2020년 아라온 아문젠해 탐사
4장 : 2021년 아라온 로스해 탐사
5장 : 2022년 아라온 아문젠해 탐사
6장 : 2023년 아라온 로스해 탐사 (ANA13C)
7장 : 2024년 아라온 로스해 탐사 (ANA14C)
8장 : 2024-25 아라온 로스해 탐사 (ANA15B)

○ 마지막 최대 빙하기 이후 홀로세 중기 온난기와 현재 온난화의 고해양·고기후 연구
9장 : 남극 라슨 C 홀로세 퇴적물의 눈덩이 사건 흔적
10장 : 남극 테라노바 만 소만의 멀티빔 측심과 표층 퇴적물에 대한 점토 광물 분포

11장 : 아문젠해 서부 대륙붕 리글리 만의 해빙 역사 복원

12장 : 마지막 최대 빙하기 이후 스코시아해 퇴적물의 자성 특성: 자성을 조절하는 빙하기의 빙상 방출

13장 : 지난 마지막 빙하기 이후 엘레펀트 섬 인근의 남빙양에서의 고해양 변화: 표층생산성, 영양염 이용률, 저층류, 빙하쇄설성 퇴적물의 연관성

14장 : 지난 마지막 빙하기 이후의 남극반도 동부 분지에서의 고해양적 변화와 그 의미

15장 : 마지막 최대 빙하기 이후의 남극 스코시아해에서의 규조류 골격으로의 멀티 원소 동화

16장 : 마지막 최대 빙하기 이후 로스해 서쪽 드라이갈스키 분지의 빙해양 퇴적물을 이용한 고환경 복원

17장 : 서부 로스해 북 드라이갈스키 트러프의 마지막최대빙하기 빙상 범위

18장 : 남극 로스해 북서부에서 빙상과 해양의 상호작용을 기록한 고해양 자료 탐색

19장 : 남극 로스해 로버트슨 만의 홀로세 고해양 환경 변동: 해양-빙상-기후 상호연결성을 나타내는 해양 퇴적 기록

20장 : 남극 로스해 보퍼트 섬 인근에서 고해양 환경변화 해석을 위한 규조 연구

21장 : 남극 아문젠해에서 규조 군집을 이용한 고환경 변화 기록

○ 지난 간빙기 동안 고해양·고기후 연구

22장 : 로스해에서 플라이스토세 후기 동안의 고해양학적 변화 - 고생산성, 영양염 이용률, 심층수 형성의 빙하기-간빙기 변동

23장 : 벨링스하우젠해에서의 빙상 빙하기-간빙기 변화에 따른 해양환경 변화와 퇴적 작용 변화

○ 고환경 연구에 필수적인 고기후 지시자 및 연대측정법 개선 연구

24장 : 서남극 대륙 주변부 퇴적물로 젊은 탄소를 공급하는 생교란

25장 : 지난 마지막 빙하기 이후 남극 벨링스하우젠해 대륙대에서의 대자율 변동과 육성기원 물질 유입 기작에 관한 의의

26장 : 칠레 푼타 아레나스와 남극 킹조지 섬 해빈 모래의 광물 조성 및 석영 입자의 미세구조를 통한 퇴적사 연구

27장 : 남극 대륙경계부에서 빙하운반역의 동정과 수량화의 방법 비교

28장 : 10Be 동위원소 분석을 통한 고환경 연구

29장 : 중앙 분지 북서 로스해에서의 사례 연구: 재순환된 생물 기원 성분에 의한 고생산성 신호의 오류

30장 : 서남극 주변 해양 표층퇴적물의 와편모조류 시스트 공간 분포 특성에 영향을 미치는 주요 환경요인

○ 플라이스토세 동안 고해양·고기후 연구

31장 : 플라이스토세 동안 로스해의 해양 변동성: 여러 프록시 데이터 비교를 통한 연대 설정 및 과거 환경 분석

32장 : 남극 로스해 대륙대 퇴적물의 대자율 이방성 연구: 고수류 변화 복원에 대한 적용 가능성 평가

33장 : 서남극 아문젠해 대륙사면 퇴적물 내 스멕타이트 광물의 원소 조성을 활용한 제4기 빙기-간빙기 주기 동안 쇄설성 물질의 기원지 규명 연구

34장 : 플라이스토세 로스해 북서부 중앙 분지의 빙해양 엽층 니질퇴적물의 고해양 기록

35장 : 드레이크 해협의 지난 600,000년 동안 빙하기-간빙기 환경 변화

36장 : 로스해 대륙 가장자리에서의 중기-후기 플라이스토세 퇴적환경: 남극 빙상 역학에 대한 시사점

Ⅴ. 연구개발결과의 활용계획

○ 과학 분야: 미래 지구 온난화 문제 해결

- 과거 온난기의 서남극 빙권, 해양 및 기후 환경 복원
- 남극 빙상의 과거 변동 기록 복원을 통해 빙상 안정성 이해
- 미래 지구 온난화에 따른 해수면 변동에 대한 남극 빙상의 기여도 추정
- 고기후 예측 모델의 DB 자료 제공 및 검증

○ 사회/경제적 분야: 지속 가능한 발전 전략 수립

- 기후변화에 따른 환경 재난에 대처하는 사회적인 적응 방안 마련
- 기후변화 영향에 사전 대응하는 농수산/재해 분야의 장기적인 개선 제시

○ 정책 분야: 미래 기후 환경 정책 입안

- 기후 변화 대응책(온실 가스 감축 등)을 위한 국가 환경 정책 마련에 기여

KOPRI 극지연구소

SUMMARY

I. Title

Ice sheet retreat and ocean circulation in West Antarctica during the past warm periods

II. Purpose and Necessity of R&D

○ Significance of paleoenvironmental research

Paleoenvironmental research plays an important role in predicting the impact of environmental change and understanding the drivers of climate change. It also provides key data on climate models that play an important role in predicting climate change and improving climate models. Recent rapid changes in global environmental conditions have increased the need for scientific understanding of global environmental changes, including climate change.

KOPRI 극지연구소

○ paleoenvironmental study in Antarctica

The polar region is the best place to detect climate change because it is sensitive to climate change and shows a great impact of climate change. Antarctica, of course, is associated with atmospheric carbon dioxide concentrations, the formation of deep water, and the increase and decrease of ice sheets, which play an important role in global climate and environmental change. Thus, Antarct ica's past environmental change studies provide essential information for understanding natural climate trends and their impacts on a global scale. The West Antarctic Ice Sheet (WAIS) is an ocean-based ice sheet where the base of the ice sheet and bedrock meet at sea level. The stability of ocean-based ice sheets is very sensitive to external factors such as atmospheric and ocean temperature changes and sea level changes caused by climate change. If the WAIS disappears completely, global sea level could rise by 4.8m, and it is thought that the WAIS was involved in past sea level rise. Therefore,

understanding the historical increase and decrease records and behavior of the WAIS is essential for predicting future climate change. A comprehensive understanding of the behavior of the WAIS can be found in the entire region from the Weddell Sea to the Ross Sea (Weddel Sea-Antarctic Peninsula-Bellingshausen Sea-Amundsen Sea-Ross Sea). Records of marine and terrestrial sediments around Antarctica are needed.

○ Importance of paleoenvironmental research in the past warm periods

According to the 5th report of the Intergovernmental Panel on Climate Change (IPCC), a comparative study of future climate estimates suggests that if global warming proceeds as it is, the global climate in 2030 will follow the mid-Pliocene 3 million years ago (~2 to 4°C higher than present), and the global climate in 2150 will be similar to that of the Eocene (~10 to 13°C higher than present) 50 million years ago when global climate was warm and glaciers were almost gone. From a geological perspective, the past warm periods that can be contrasted with future global warming are the mid-Holocene (~0.5 to 1.5°C higher than present), the last interglacial, and the mid-Pliocene. It can provide clues to more accurately predict future global warming. The important materials for understanding the environment of the past warm periods in West Antarctica are ice and sediment cores. In addition to the record of ice cores that provides information about the past atmospheric environment of Antarctica, the palaeoceanographic records in marine sediments represent the advance and retreat of ice sheets and the ocean circulation change in the past. Future global warming, which can be an unsuitable environment for human survival, can emerge as a new climatic environment that has never been experienced anthropologically. Reconstructing what the Antarctic Ocean was like during the past warm periods and what the Antarctic ice looked like in the past warming is one of the important researches that can respond to current global climate issues, which can provide important information about the past warming environments.

III. Contents and Extent of R&D

○ Research goal

Investigating the mechanisms and effects of temporal and spatial changes in

the West Antarctic Ice Sheet (WAIS) during the past warm periods

(Level 1) To reconstruct vulnerability of the WAIS and identify the stability control factor of the marine-based ice sheet during past warm periods (such as mid-Pleiocene, last interglacial, mid-Holocene, etc.)
(Level 2) To understand the changes in the WAIS during past warm periods and elucidating their impact on the ocean.

○ Performance goal (2020.01.01 ~ 2022.12.31)

- To secure samples from IODP and SWAIS 2C project
- To survey on the distribution of sediment and secure sediment cores around the West Antarctic Ice Sheet
- To implement new paleoclimate proxy/age method and to investigate the principle for climate indicators
- To reconstruct ocean circulation and sedimentary record in West Antarctica during past warm periods

○ Performance goal (2023.01.01 ~ 2025.12.31.)

- To paticipate in IODP and SWAIS 2C projects
- To survey on the areas around SWAIS 2C project sites
- To implement new paleoclimate proxies·dating methods and to investigate the principle for climate indicators
- To reconstruct changes in West Antarctic Ice Sheet and oceanic environment during past warm periods

○ Research contents in 2020

- Participation in IODP and securing samples
- Obtaining samples from sediment cores in the Amundsen Sea
- Research vessel-based multi-beam exploration
- Research vessel-based SBP exploration
- Introduction of non-destructive X-ray imaging for IRDs' estimation
- Introduction of the paleo-proxies analysis of organic matter in marine sediment in the past warm periods
- Introduction of microbial community analysis in the past warm periods
- Introduction of paleo-proxies analysis in pore water
- Introduction of carbonate stable isotope analysis
- Application of ramped pyrolysis dating method

- Reconstruction of mid-latitude paleoenvironments using organic proxies in marine sediments
- Responses and effects of microorganisms and clay minerals beneath sub-ice shelf during the mid-Holocene
- Research on glacial retreat in the Crystal Sound basin during the mid-Holocene
- Paleoceonographic changes of the Ross Sea during the Late Pleistocene
- Paleoenvironmental changes around Elephant Island in the Scotian Sea since the Last Glacial Maximum
- Participation in drafting the international joint SWAIS 2C drilling project

○ Research contents in 2021

- Obtaining samples from sediment cores in the Ross Sea
- Research vessel-based multi-beam exploration
- Research vessel-based SBP exploration
- Non-destructive X-ray imaging application development for IRDs′ estimation
- Applying the paleo-proxies analysis of organic matter to marine sediment in the past warm periods
- Paleo-proxies analysis in pore water
- Introduction of microbial community analysis in the past warm periods
- Applying carbonate stable isotope analysis to marine sediment
- Application of Ramped Pyrolysis dating method
- Oceanic change of Bellingshausen Sea since the Last Glacial Maximum
- Glacial & oceanic change of Ross Sea during the mid-Pliocene
- Stability of marine-based ice sheet by research of shelf sediment in Ross Sea
- Sediment transport to continental rise induced by glacial retreat & advance in Ross Sea
- Marine-based subglacial lake's research during deglaciation

○ Research contents in 2022

- Obtaining samples from sediment cores in the Amundsen Sea
- Research vessel-based multi-beam exploration
- Research vessel-based SBP exploration
- Application of non-destructive X-ray imaging application for IRDs′ estimation
- Applying the paleo-proxies analysis of organic matter to marine sediment in the past warm periods
- Paleo-proxies analysis in pore water
- Introduction of microbial community analysis in the past warm periods

- Paleoenviromental interpretation by microbial community analysis
- Applying carbonate stable isotope analysis to marine sediment
- Application of Ramped Pyrolysis dating method
- Oceanic circulation change of Ross Sea during the mid-Holocene
- Behavier of Antarctic Bottom Water by climatic change during Pleistocene
- Surface productivity and oceanic environmental change during Pleistocene
- Regional glacial retreat trend in WAIS
- Signing of MoU for SWAIS 2C project participation

○ Research contents in 2023

- Analysis of international joint IODP drill samples
- Obtaining drill samples from the western and central Ross Sea
- Research vessel-based multi-beam survey
- Research vessel-based SBP survey
- Introduction of paleoclimate proxies analysis of organic matter in sediments from past warm periods
- Introduction of microbial community analysis from past warm periods
- Introduction of paleoclimate proxies analysis of pore water
- Introduction of carbonate stable isotope analysis
- Application of ramped pyrolysis dating
- Introduction of magnetic anisotropy analysis in marine sediments
- Introduction of organic contaminant analysis in marine sediments
- Introduction of dinoflagellate cyst analysis in marine sediments
- Reactions and influences of microorganisms and clay minerals beneath the mid-Holocene Antarctic Ice Shelf
- Characteristics of diatom communities and surface marine environments during the mid-Holocene Warm Period of the Antarctic Peninsula
- Study of Amundsen Sea continental shelf retreat of the WAIS due to deglacial warming
- Analysis of paleomagnetic characteristics in Ross Sea continental rise
- Glacial fluctuations in the Weddell Sea during the last interglacial (130,000 years ago)
- Sedimentation and ocean circulation during the three interglacials in the Bellingshausen Sea
- Marine environmental changes in the Ross Sea and Drake Passage during the MBE and MPT global climate events

○ Research contents in 2024

- Acquisition and analysis of the first drilling cores of the International joint project (SWAIS 2C)
- Preparation of the International joint project (SWAIS 2C) drilling report
- The first additional contribution to the International joint project (SWAIS 2C)
- Completion of sample analysis from the International Joint IODP and submission of a paper on some of the results
- Acquisition of sediment drilling samples around the Ross Sea ice shelf
- Research vessel-based multi-beam survey
- Research vessel-based SBP survey
- Application of non-destructive X-ray imaging to estimate the glacier transport zone
- Introduction of paleoclimate proxies analysis of organic matter from past warm periods
- Introduction of microbial community analysis from past warm periods
- Introduction of paleoclimate proxies analysis of pore water
- Introduction of carbonate stable isotope analysis
- Application of ramped pyrolysis dating
- Analysis of dinoflagellate cyst communities and application and review of paleoenvironmental proxies
- Reconstruction of the Anthropocene record through analysis of organic contaminants in Antarctic sediments
- Reconstruction and characterization of oceanographic changes following changes in the late glacial and interglacial ice sheets
- Study of surface-bottom marine environmental changes and interactions since the last ice age on the Antarctic Peninsula
- Study of the sources of sediments and major transport mechanisms on the continental margin
- Study of ice sheet responses to short, millennial warming events during glacial periods
- Study of changes in the surface marine environment of the Antarctic Peninsula during the Holocene using isotopes from the skeletal remains of a single diatom species
- Study of post-glacial surface water temperature reconstruction in the Scotia Sea
- Study of the stability of the ocean-based ice sheet through of Ross Sea continental shelf sediments
- Study of changes in continental sedimentation due to changes in the Ross Sea

KOPRI 극지연구소

cryosphere

○ Research contents in 2025

- Analysis of the first drill sample of the International joint project (SWAIS 2C)
- Acquisition of the second drilling sample of the International joint project (SWAIS 2C)
- Payment of the second additional contribution to the International joint project (SWAIS 2C)
- Analysis of the International Joint IODP drilling sample
- Acquisition of sediment drill samples around the Ross Sea Ice Shelf
- Research vessel-based multi-beam survey
- Research vessel-based SBP survey
- Application of non-destructive X-ray imaging analysis to estimate the glacier transport zone
- Analysis of paleoclimate proxies in organic matter of sediments from past warm periods
- Analysis of paleoclimate proxies in pore water
- Analysis of microbial communities from past warm periods
- Paleoenvironmental interpretation through genomic analysis
- Application of carbonate stable isotope analysis
- Application of ramped pyrolysis dating
- Paleoenvironmental interpretation using records of changes in dinoflagellate cyst communities
- Study of WAIS retreat fluctuations using seafloor topography
- Changes in past sedimentary processes and marine environmental changes in the Ross Sea-Amunsen Sea continental margin
- Study on the characteristics of sediments around the Ross Ice Shelf
- Report on the retreat of the WAIS and spatial changes in ocean circulation during past warming periods

IV. R&D Results

In Chapter 1, the introduction outlines the contents, importance, and overall research goals of this research project, and in Chapter 2, the overall contents of the SWAIS 2C project, the most important international joint research project, are presented. The following contents are composed of the results of Antarctic

field exploration and research results in detailed targets. The commissioned research results to be included in this report were submitted as a separate commissioned research report.

○ Antarctic field exploration

Chapter 3 : 2020 Amundsen Sea exploration (ANA10B)

Chapter 4 : 2021 Ross Sea exploration

Chapter 5 : 2022 Amundsen Sea exploration

Chapter 6 : 2023 Ross Sea exploration (ANA13C)

Chapter 7 : 2024 Ross Sea exploration (ANA14C)

Chapter 8 : 2024-25 Ross Sea exploration (ANA15B)

○ Antarctic paleoceanographic and paleoclimatic researches during the mid-Holocene optimum and the recent warming since the Last Glacial Maximum

Chapter 9 : Snowball Earth (the Cryogenian) reincarnated from the Holocene sediments beneath the Larsen C Ice Shelf (Antarctica)

Chapter 10 : Multibeam Bathymetry and Distribution of Clay Minerals on Surface Sediments of a Small Bay in Terra Nova Bay, Antarctica

Chapter 11 : Ice flow reorganization during deglaciation inferred from glacial morphological features mapped in Wrigley Gulf, western Amundsen Sea shelf (West Antarctica)

Chapter 12 : Particle-size dependent magnetic properties of Scotia Sea sediments since the Last Glacial Maximum: Glacial ice-sheet discharge controlling magnetic proxies

Chapter 13 : Paleoceanographic changes in the Southern Ocean off Elephant Island since the last glacial period: links between surface water productivity, nutrient utilization, bottom water currents, and ice-rafted debris

Chapter 14 : Paleoceanographic condition changes in the Eastern Bransfield, Antarctic Peninsula, since the late glacial interval and its implications

Chapter 15 : Incorporation of Multi-elements into Diatom Frustules in the Scotia Sea, Antarctica, Since the Last Glacial Maximum

Chapter 16 : Drygalski Basin of the western Ross Sea since the Last Glacial Maximum

Chapter 17 : Ice sheet range of the northern Drygalski Truff during the Last

Glacial Maximum
Chapter 18 : Hunting paleoceanographic archives of ice sheet-ocean interaction in the northwestern Ross Sea, Antarctica
Chapter 19 : Holocene paleoceanographic variability in Robertson Bay, Ross Sea, Antarctica: A marine record of ocean, ice sheet, and climate connectivity
Chapter 20 : Diatom Research to Interpretation of Paleoenvironmental Changes in Beaufort Island, Ross Sea, Antarctica
Chapter 21 : Recording of paleoenvironmental changes using diatom assemblages from the Amudsen Sea, Antarctica

○ Antarctic paleoceanographic researches during the Last Interglacial
Chapter 22 : Late Pleistocene paleoceanographic changes in the Ross Sea: glacial-interglacial variations in paleoproductivity, nutrient utilization, and deep-water formation
Chapter 23 : Glacial-interglacial changes in oceanic conditions and depositional process in the continental rise in response to ice sheet (shelf) variation in Bellingshausen Sea, Antarctica

○ Improving paleoclimatic proxies and age dating methods essential for paleoenvironmental researches
Chapter 24 : Bioturbation supplying young carbon into West Antarctic continental margin sediment
Chapter 25 : Variation in magnetic susceptibility in the Bellingshausen Sea continental rise since the last glacial period and implications for terrigenous material input mechanisms
Chapter 26 : Petrology and quartz grain microtextures of marine shoreline sands from the Punta Arenas area, southernmost Chile and King George Island, Antarctica and implications for their depositional history
Chapter 27 : A Comparison of Methods for Identifying and Quantifying Ice Rafted Debris on the Antarctic Margin
Chapter 28 : Paleoenvironmental study using 10Be isotope analysis
Chapter 29 : Fallacy of paleoproductivity signals by the recycled biogenic components: case study in the Central Basin of the northwestern Ross Sea
Chapter 30 : Controls on spatial heterogeneity in dinoflagellate cyst distribution in recent sediments off West Antarctica

KOPRI 극지연구소

○ Antarctic paleoceanographic and paleoclimatic researches during the Pleistocene

Chapter 31 : Pleistocene oceanographic variability in the Ross Sea: A multiproxy approach to age model development and paleoenvironmental analyses

Chapter 32 : Anisotropy of magnetic susceptivility of sediments in the Ross Sea continental rise, Antarctica: Evaluation of palecurrent variability reconstruction

Chapter 33 : Elemental composition of smectite minerals in continental rise sediments from the Amundsen Sea, West Antarctica, as a too to identify detrital input from various sources throughout late Quaternary glacial-interglacial cycles

Chapter 34 : Pleistocene glaciomarine laminated muds in the Central Basin of the northwestern Ross Sea and their palaeoceanographic records

Chapter 35 : Glacial-interglacial environmental changes in the Drake Passage over the past 600 kyrs

Chapter 36 : Mid-to-late Peistocene Depositional Environments at the Ross Sea Continental Margin: Implications for Antarctic Ice Sheet Dynamics

KOPRI 극지연구소

V. Application Plans of R&D Results

○ Scientific field: to solve the impacts of global warming in the future from the Antarctic paleoenvironment records during past warm periods

- To construct cryospheric, oceanic and climatic settings in West Antarctica during past warm periods
- To understand ice sheet stability from paleo-records of Antarctic ice sheet changes
- To estimate the contribution of Antarctic ice sheet changes to sea level variations in the future global warming
- To provide the basic DB data to forecast the future climate from GCMs

○ Social/Economical field: To establish the sustainable development strategy

- To provide the social adaptation on the environmental disaster by climate change
- To propose long-term improvements in accordance with impacts of future

climate change in agriculture/fishery and disaster sectors

○ Political field: To plan future climate environment policies

- Contribution to national environmental policies for a countermeasure (such as greenhouse gas reduction) on the future climate changes

KOPRI
극지연구소

목 차

요약문 (국문) ····· i

요약문 (영문) ····· v

제 1 장 서론 ····· 1

1. 연구개발의 배경 및 필요성 ····· 1
2. 국내외 주요 연구 동향 ····· 4
3. 연구개발의 목표 및 내용 ····· 9
참고문헌 ····· 17

제 2 장 기온 2도 온난화에 따른 서남극 빙상 민감도 ····· 23

요약 (영문) ····· 23
1. 서론 ····· 23
2. SWAIS 2C 프로젝트 ····· 26
3. 시추 지역 ····· 26
4. 드릴링 빙저 퇴적물의 새로운 가능성 ····· 28
5. SWAIS 2C 프로젝트의 전략과 도전 ····· 29
요약 (국문) ····· 35
참고문헌 ····· 37

제 3 장 2020년 아라온 아문젠해 탐사 ····· 50

요약 (국문) ····· 50
1. 2020년 입남극 및 출남극 시기 ····· 50
2. 탐사 내용 및 결과 ····· 50
요약 (영문) ····· 53

제 4 장 2021년 아라온 로스해 탐사 ····· 56

요약 (국문) ····· 56
1. 2021년 입남극 및 출남극 시기 ····· 56

KOPRI 극지연구소

2. 탐사 내용 및 결과 ····· 56
요약 (영문) ····· 58

제 5 장 2022년 아라온 아문젠해 탐사 ····· 61
요약 (국문) ····· 61
1. 2022년 입남극 및 출남극 시기 ····· 61
2. 탐사 내용 및 결과 ····· 61
요약 (영문) ····· 63

제 6 장 2023년 아라온 로스해 탐사 (ANA13C) ····· 65
요약 (국문) ····· 65
1. 참여인원 및 일정 ····· 65
2. 연구활동 개요 ····· 65
3. 조사 방법 및 사용 장비 ····· 66
4. 조사 지역 및 시료 리스트 ····· 67
5. 주요 성과내용 ····· 68
요약 (영문) ····· 69

제 7 장 2024년 아라온 로스해 탐사 (ANA14C) ····· 70
요약 (국문) ····· 70
1. 참여인원 및 일정 ····· 70
2. 연구활동 개요 ····· 70
3. 조사 방법 및 사용 장비 ····· 71
4. 조사 지역 및 시료 리스트 ····· 71
5. 주요 성과내용 ····· 73
요약 (영문) ····· 74

제 8 장 2024-25 아라온 로스해 탐사 (ANA15B) ····· 75
요약 (국문) ····· 75
1. 참여인원 및 일정 ····· 75
2. 연구활동 개요 ····· 75
3. 조사 방법 및 사용 장비 ····· 76

KOPRI 극지연구소

4. 조사 지역 및 시료 리스트 ····· 77
5. 주요 성과내용 ····· 78
요약 (영문) ····· 79

제 9 장 남극 라슨 C 홀로세 퇴적물의 눈덩이 사건 흔적 ····· 83
요약 (영문) ····· 83
1. 주요내용 ····· 84
2. 방법 ····· 90
요약 (국문) ····· 93
참고문헌 ····· 94

제 10 장 남극 테라노바 만 소만의 멀티빔 측심과 표층 퇴적물에 대한 점토 광물 분포 ····· 102
요약 (영문) ····· 102
1. 서론 ····· 103
2. 연구지역 ····· 104
3. 시료 및 방법 ····· 104
4. 결과 ····· 106
5. 토의 ····· 107
6. 결론 ····· 110
요약 (국문) ····· 112
참고문헌 ····· 113

제 11 장 아문젠해 서부 대륙붕 리글리 만의 해빙 역사 복원 125
요약 (국문) ····· 125
1. 서언 ····· 125
2. 연구방법 ····· 126
3. 연구결과 ····· 126
4. 토의 ····· 129
5. 결론 ····· 132
요약 (영문) ····· 134
참고문헌 ····· 135

KOPRI 극지연구소

제 12 장 마지막 최대 빙하기 이후 스코시아해 퇴적물의 자성 특성: 자성을 조절하는 빙하기의 빙상 방출 ····· 146

요약 (영문) ····· 146
1. 서론 ····· 147
2. 주상시료 위치 및 지역 환경 ····· 148
3. 분석 방법 ····· 149
4. 연대 모델 ····· 151
5. 결과 ····· 151
6. 토의 ····· 156
7. 결론 ····· 160
요약 (국문) ····· 162
참고문헌 ····· 163

제 13 장 지난 마지막 빙하기 이후 엘레펀트 섬 인근의 남빙양에서의 고해양 변화: 표층생산성, 영양염 이용률, 저층류, 빙하쇄설성 퇴적물의 연관성 ····· 181

요약 (영문) ····· 181
1. 서론 ····· 182
2. 연구지역 ····· 183
3. 시료 및 방법 ····· 184
4. 연대 모델 ····· 186
5. 결과 ····· 186
6. 토의 ····· 188
7. 결론 ····· 195
요약 (국문) ····· 197
참고문헌 ····· 198

제 14 장 지난 마지막 빙하기 이후의 남극반도 동부 분지에서의 고해양적 변화와 그 의미 ····· 215

요약 (영문) ····· 215

1. 서론 ····· 216
2. 연구지역 ····· 217
3. 시료 및 방법 ····· 217
4. 연대 모델 ····· 219
5. 결과 ····· 220
6. 토의 ····· 221
7. 결론 ····· 229
요약 (국문) ····· 231
참고문헌 ····· 232

제 15 장 마지막 최대 빙하기 이후의 남극 스코시아해에서의 규조류 골격으로의 멀티 원소 동화 ····· 250

요약 (영문) ····· 250
1. 서론 ····· 251
2. 시료 및 방법 ····· 252
3. 결과 ····· 253
6. 토의 ····· 254
7. 결론 ····· 263
요약 (국문) ····· 264
참고문헌 ····· 265

제 16 장 마지막 최대 빙하기 이후 로스해 서쪽 드라이갈스키 분지의 빙해양 퇴적물을 이용한 고환경 복원 ····· 280

요약 (영문) ····· 280
1. 서론 ····· 281
2. 연구지역 ····· 283
3. 시료 및 방법 ····· 285
4. 결과 ····· 288
5. 토의 ····· 292
6. 결론 ····· 300
요약 (국문) ····· 301
참고문헌 ····· 302

KOPRI 극지연구소

제 17 장 서부 로스해 북 드라이갈스키 트러프의 마지막최대빙하기 빙상 범위 ····· 320
1. 서론 ····· 320
2. 시료 및 방법 ····· 320
3. 연구결과 ····· 322
4. 토의 ····· 326
5. 결론 ····· 328
6. 참고문헌 ····· 329

제 18 장 남극 로스해 북서부에서 빙상과 해양의 상호작용을 기록한 고해양 자료 탐색 ····· 342
요약 (영문) ····· 342
1. 서론 ····· 343
2. 연구지역 ····· 345
3. 시료 및 방법 ····· 347
4. 결과 ····· 351
5. 해석 및 토의 ····· 356
6. 결론 ····· 364
요약 (국문) ····· 365
참고문헌 ····· 366

제 19 장 남극 로스해 로버트슨 만의 홀로세 고해양 환경 변동: 해양-빙상-기후 상호연결성을 나타내는 해양 퇴적 기록 ····· 392
요약 (영문) ····· 392
1. 서론 ····· 393
2. 시료 및 방법 ····· 394
4. 결과 ····· 397
5. 토의 ····· 402
6. 결론 ····· 410
요약 (국문) ····· 412
참고문헌 ····· 413

KOPRI 극지연구소

제 20 장 남극 로스해 보퍼트 섬 인근에서 고해양 환경변화 해석을 위한 규조 연구 ····· 441

요약 (국문) ····· 441
1. 서론 ····· 441
2. 연구지역 및 연구방법 ····· 442
3. 결과 및 토의 ····· 443
4. 고환경 및 토의 ····· 443
5. 결론 ····· 445
참고문헌 ····· 446
요약 (영문) ····· 449

제 21 장 남극 아문젠해에서 규조 군집을 이용한 고환경 변화 기록 ····· 455

요약 (국문) ····· 455
1. 서론 ····· 455
2. 연구지역 및 연구방법 ····· 456
3. 결과 및 토의 ····· 457
4. 결론 ····· 459
요약 (영문) ····· 460
참고문헌 ····· 461

제 22 장 로스해에서 플라이스토세 후기 동안의 고해양학적 변화 - 고생산성, 영양염 이용률, 심층수 형성의 빙하기-간빙기 변동 ····· 471

요약 (영문) ····· 471
1. 서론 ····· 472
2. 연구지역 ····· 473
3. 시료 및 방법 ····· 474
4. 연대 모델 ····· 476
5. 결과 ····· 477
6. 토의 ····· 478

KOPRI 극지연구소

7. 결론 ····· 482
요약 (국문) ····· 484
참고문헌 ····· 485

제 23 장 벨링스하우젠해에서의 빙상 빙하기-간빙기 변화에 따른 해양환경 변화와 퇴적 작용 변화 ····· 501

요약 (영문) ····· 501
1. 서론 ····· 502
2. 퇴적환경 ····· 503
3. 시료 및 방법 ····· 504
4. 연대 모델 ····· 506
5. 결과 ····· 508
6. 토의 ····· 511
7. 결론 ····· 519
요약 (국문) ····· 521
참고문헌 ····· 522

제 24 장 서남극 대륙 주변부 퇴적물로 젊은 탄소를 공급하는 생교란 ····· 539

요약 (영문) ····· 539
1 서론 ····· 540
2. 시료 및 방법 ····· 541
3. 결과 ····· 542
4. 토의 ····· 543
요약 (국문) ····· 549
참고문헌 ····· 550

제 25 장 지난 마지막 빙하기 이후 남극 벨링스하우젠해 대륙대에서의 대자율 변동과 육성기원 물질 유입 기작에 관한 의의 ····· 563

요약 (영문) ····· 563

KOPRI 극지연구소

1. 서론 ····· 564
2. 연구지역 ····· 565
3. 연대 모델 ····· 566
4. 결과 ····· 568
5. 토의 ····· 569
6. 결론 ····· 574
요약 (국문) ····· 576
참고문헌 ····· 577

제 26 장 칠레 푼타 아레나스와 남극 킹조지 섬 해빈 모래의 광물 조성 및 석영 입자의 미세구조를 통한 퇴적사 연구 ····· 590

요약 (영문) ····· 590
1. 서론 ····· 591
2. 연구지역 ····· 592
3. 방법 및 재료 ····· 595
4. 결과 ····· 596
5. 토의 ····· 599
6. 결론 ····· 603
요약 (국문) ····· 604
참고문헌 ····· 605

제 27 장 남극 대륙경계부에서 빙하운반역의 동정과 수량화의 방법 비교 ····· 623

요약 (영문) ····· 623
1. 서론 ····· 623
2. 빙하운반역 유동량의 결정 방법 ····· 628
3. 재료와 방법 ····· 632
4. 빙하운반역 방법의 비교 ····· 640
5. 토의 ····· 644
6. 빙하운반역 집적률의 결정: 다른 방법들을 사용할 때의 영향 ····· 647
7. 결론 ····· 649

KOPRI 극지연구소

요약 (국문) ····· 651
참고문헌 ····· 652

제 28 장 ^{10}Be 동위원소 분석을 통한 고환경 연구 ····· 669
요약 (국문) ····· 669
1. 육상의 빙하 변화 연구 ····· 669
2. 해양의 해빙 변화 연구 ····· 671
요약 (영문) ····· 673

제 29 장 중앙 분지 북서 로스해에서의 사례 연구: 재순환된 생물기원 성분에 의한 고생산성 신호의 오류 ····· 684
요약 (영문) ····· 684
1. 서론 ····· 685
2. 시료 및 방법 ····· 686
3. 결과 및 토의 ····· 687
4. 결론 ····· 691
요약 (국문) ····· 692
참고문헌 ····· 693

제 30 장 서남극 주변 해양 표층퇴적물의 와편모조류 시스트 공간 분포 특성에 영향을 미치는 주요 환경요인 ····· 702
요약 (영문) ····· 702
1. 서론 ····· 703
2. 연구지역 ····· 705
3. 시료 및 방법 ····· 706
4. 결과 ····· 709
5. 토의 ····· 710
요약 (국문) ····· 719
참고문헌 ····· 720

KOPRI 극지연구소

제 31 장 플라이스토세 동안 로스해의 해양 변동성: 여러 프록시 데이터 비교를 통한 연대 설정 및 과거 환경 분석 ··743
요약 (영문) ····· 743
1. 서론 ····· 744
2. 방법 ····· 747
3. 결과 ····· 751
4. 토의 ····· 753
5. 결론 ····· 763
요약 (국문) ····· 764
참고문헌 ····· 765

제 32 장 남극 로스해 대륙대 퇴적물의 대자율 이방성 연구: 고수류 변화 복원에 대한 적용 가능성 평가 ····· 782
요약 (국문) ····· 782
1. 서론 ····· 782
2. 연구시료 및 방법 ····· 783
3. 결과 ····· 785
4. 토의 ····· 786
5. 결론 ····· 789
참고문헌 ····· 790
요약 (영문) ····· 795

제 33 장 서남극 아문젠해 대륙사면 퇴적물 내 스멕타이트 광물의 원소 조성을 활용한 제4기 빙기-간빙기 주기 동안 쇄설성 물질의 기원지 규명 연구 ····· 802
요약 (영문) ····· 802
1. 서론 ····· 803
2. 연구시료 및 방법 ····· 805
3. 결과 ····· 808
4. 토의 ····· 811
5. 결론 ····· 815
요약 (국문) ····· 817

KOPRI 극지연구소

참고문헌 ····· 818

제 34 장 플라이스토세 로스해 북서부 중앙 분지의 빙해양 엽층 니질퇴적물의 고해양 기록 ····· 836

요약 (영문) ····· 836
1. 서론 ····· 836
2. 연구시료 및 방법 ····· 838
3. 결과 ····· 838
4. 토의 ····· 839
5. 결론 ····· 842
요약 (국문) ····· 843
참고문헌 ····· 844

제 35 장 드레이크 해엽의 지난 600,000년 동안 빙하기-간빙기 환경 변화 ····· 853

요약 (영문) ····· 853
1. 서론 ····· 854
2. 연구지역 ····· 855
3. 연구시료 및 방법 ····· 856
4. 연대 결정 ····· 857
5. 결과 ····· 857
6. 토의 ····· 858
7. 결론 ····· 863
요약 (국문) ····· 865
참고문헌 ····· 866

제 36 장 로스해 대륙 가장자리에서의 중기-후기 플라이스토세 퇴적환경: 남극 빙상 역학에 대한 시사점 ····· 880

요약 (영문) ····· 880
1. 서론 ····· 881
2. 로스해 수괴 및 해양환경 ····· 883
3. 연구시료 및 방법 ····· 884

KOPRI 극지연구소

4. 결과 ····· 887
5. 토의 ····· 889
6. 결론 ····· 901
요약 (국문) ····· 903
참고문헌 ····· 904

KOPRI
극지연구소

Contents

Abstract (in Korean) ····· i

Abstract (in English) ····· vi

Chapter 1. Introduction ····· 1

1. Background and Necessity of Research ····· 1
2. Major Research Trends at Korea and Abroad ····· 4
3. Goals and Contents ····· 9
References ····· 17

Chapter 2. Sensitivity of the West Antarctic Ice Sheet to +2℃ (SWAIS 2C) ····· 23

Abstract (in English) ····· 23
1. Introduction ····· 23
2. SWAIS 2C: testing ice sheet sensitivities to a +2 ○C global warming threshold ····· 26
3. Drill Sites ····· 28
4. New capabilities in drilling subglacial sediment ····· 29
5. The SWAIS 2C Project approach and challenges ····· 35
Abstract (in Korean) ····· 37

Chapter 3. 2020 Amundsen Sea exploration (ANA10B) ····· 50

Abstract (in Korean) ····· 50
1. The cruise information (ANA10B) in 2020 ····· 50
2. Results ····· 50
Abstract (in English) ····· 53

Chapter 4. 2021 Ross Sea exploration ····· 56

KOPRI 극지연구소

Abstract (in Korean) ····· 56
1. The cruise information in 2021 ····· 56
2. Results ····· 56
Abstract (in English) ····· 58

Chapter 5. 2022 Amundsen Sea exploration ····· 61
Abstract (in Korean) ····· 61
1. The cruise information (ANA12C) in 2022 ····· 61
2. Results ····· 61
Abstract (in English) ····· 63

Chapter 6. 2023 Ross Sea exploration (ANA13C) ····· 65
Abstract (in Korean) ····· 65
1. Participants and schedule ····· 65
2. Research activity overview ····· 65
3. Methods and equipment ····· 66
4. Study area and sample lists ····· 67
5. Key results ····· 68
Abstract (in English) ····· 69

Chapter 7. 2024 Ross Sea exploration (ANA14C) ····· 70
Abstract (in Korean) ····· 70
1. Participants and schedule ····· 70
2. Research activity overview ····· 70
3. Methods and equipment ····· 71
4. Study area and sample lists ····· 71
5. Key results ····· 73
Abstract (in English) ····· 74

Chapter 8. 2024-25 Ross Sea exploration (ANA15B) ····· 75
Abstract (in Korean) ····· 75
1. Participants and schedule ····· 75

KOPRI 극지연구소

2. Research activity overview ····· 75
3. Methods and equipment ····· 76
4. Study area and sample lists ····· 77
5. Key results ····· 78
Abstract (in English) ····· 79

Chapter 9. Snowball Earth (the Cryogenian) reincarnated from the Holocene sediments beneath the Larsen C Ice Shelf (Antarctica) ····· 83
Abstract (in English) ····· 83
1. Main ····· 84
2. Methods ····· 90
Abstract (in Korean) ····· 93
References ····· 94

Chapter 10. Multibeam Bathymetry and Distribution of Clay Minerals on Surface Sediments of a Small Bay in Terra Nova Bay, Antarctica ····· 102
Abstract (in English) ····· 102
1. Introduction ····· 103
2. Study area ····· 104
3. Material and Methods ····· 104
4. Results ····· 106
5. Discussion ····· 107
6. Conclusions ····· 110
Abstract (in Korean) ····· 112
References ····· 113

Chapter 11. Ice flow reorganization during deglaciation inferred from glacial morphological features mapped in Wrigley Gulf, western Amundsen Sea shelf (West Antarctica) · 125

Abstract (in Korean) ····· 125
1. Introduction ····· 125
2. Methods ····· 126
3. Results ····· 126
4. Discussion ····· 129
5. Conclusions ····· 132
Abstract (in English) ····· 134
References ····· 135

Chapter 12. Particle-size dependent magnetic properties of Scotia Sea sediments since the Last Glacial Maximum: Glacial ice-sheet discharge controlling magnetic proxies ····· 146
Abstract (in English) ····· 146
1. Introduction ····· 147
2. Core location and regional settings ····· 148
3. Analytical methods ····· 149
4. Age model ····· 151
5. Results ····· 151
6. Discussion ····· 156
7. Conclusions ····· 160
Abstract (in Korean) ····· 162
References ····· 163

Chapter 13. Paleoceanographic changes in the Southern Ocean off Elephant Island since the last glacial period: links between surface water productivity, nutrient utilization, bottom water currents, and ice-rafted debris ····· 181
Abstract (in English) ····· 181
1. Introduction ····· 182

KOPRI 극지연구소

2. Study area ····· 183
3. Material and Methods ····· 184
4. Age model ····· 186
5. Results ····· 186
6. Discussion ····· 188
7. Conclusions ····· 195
Abstract (in Korean) ····· 197
References ····· 198

Chapter 14. Paleoceanographic condition changes in the Eastern Bransfield, Antarctic Peninsula, since the late glacial interval and its implications ····· 215
Abstract (in English) ····· 215
1. Introduction ····· 216
2. Study area ····· 217
3. Material and Methods ····· 217
4. Chronology ····· 219
5. Results ····· 220
6. Discussion ····· 222
7. Conclusions ····· 228
Abstract (in Korean) ····· 230
References ····· 231

Chapter 15. Incorporation of Multi-elements into Diatom Frustules in the Scotia Sea, Antarctica, Since the Last Glacial Maximum ····· 250
Abstract (in English) ····· 250
1. Introduction ····· 251
2. Materials and Methods ····· 252
3. Results ····· 253
4. Discussion ····· 254
5. Conclusions ····· 263

KOPRI 극지연구소

Abstract (in Korean) ····· 264
References ····· 265

Chapter 16. Drygalski Basin of the western Ross Sea since the Last Glacial Maximum ····· 280

Abstract (in English) ····· 280
1. Introduction ····· 281
2. Regional setting ····· 283
3. Materials and Methods ····· 285
4. Results ····· 288
5. Discussion ····· 292
6. Conclusions ····· 300
Abstract (in Korean) ····· 301
References ····· 302

Chapter 17. Ice sheet range of the northern Drygalski Truff during the Last Glacial Maximum ····· 320

1. Introduction ····· 320
2. Materials and Methods ····· 320
3. Results ····· 322
4. Discussion ····· 326
5. Conclusions ····· 328
References ····· 329

Chapter 18. Hunting paleoceanographic archives of ice sheet-ocean interaction in the northwestern Ross Sea, Antarctica ····· 342

Abstract (in English) ····· 342
1. Main ····· 343
2. Regional setting ····· 345
3. Materials and Methods ····· 347

KOPRI 극지연구소

4. Results ····· 351
5. Interpretation and discussion ····· 356
6. Conclusion ····· 364
Abstract (in Korean) ····· 365
References ····· 366

Chapter 19. Holocene paleoceanographic variability in Robertson Bay, Ross Sea, Antarctica: A marine record of ocean, ice sheet, and climate connectivity 392

Abstract (in English) ····· 392
1. Introduction ····· 393
2. Materials and Methods ····· 394
3. Results ····· 397
4. Discussion ····· 402
5. Conclusions ····· 410
Abstract (in Korean) ····· 412
References ····· 413

Chapter 20. Diatom Research to Interpretation of Paleoenvironmental Changes in Beaufort Island, Ross Sea, Antarctica ····· 441

Abstract (in Korean) ····· 441
1. Introduction ····· 441
2. Study area and methods ····· 442
3. Results and discussion ····· 443
4. Paleoenvironmental interpretation ····· 443
5. Conclusions ····· 445
References ····· 446
Abstract (in English) ····· 449

KOPRI 극지연구소

Chapter 21. Recording of paleoenvironmental changes using diatom assemblages from the Amundsen Sea, Antarctica ····· 455
Abstract (in Korean) ····· 455
1. Introduction ····· 455
2. Study area and methods ····· 456
3. Results and discussion ····· 457
4. Conclusion ····· 459
Abstract (in English) ····· 460
References ····· 461

Chapter 22. Late Pleistocene paleoceanographic changes in the Ross Sea: glacial-interglacial variations in paleoproductivity, nutrient utilization, and deep-water formation ····· 471
Abstract (in English) ····· 471
1. Introduction ····· 472
2. Study area ····· 473
3. Material and Methods ····· 474
4. Age model ····· 476
5. Results ····· 477
6. Discussion ····· 478
7. Conclusions ····· 482
Abstract (in Korean) ····· 484
References ····· 485

Chapter 23. Glacial-interglacial changes in oceanic conditions and depositional process in the continental rise in response to ice sheet (shelf) variation in Bellingshausen Sea, Antarctica ····· 501
Abstract (in English) ····· 501

KOPRI 극지연구소

1. Introduction ····· 502
2. Depositional Setting ····· 503
3. Materials and Methods ····· 504
4. Chronology ····· 506
5. Results ····· 508
6. Discussion ····· 511
7. Conclusions ····· 519
Abstract (in Korean) ····· 521
References ····· 522

Chapter 24. Bioturbation supplying young carbon into West Antarctic continental margin sediment ····· 539

Abstract (in English) ····· 539
1. Introduction ····· 540
2. Material and Methods ····· 541
3. Results ····· 542
4. Discussion ····· 543
Abstract (in Korean) ····· 549
References ····· 550

Chapter 25. Variation in magnetic susceptibility in the Bellingshausen Sea continental rise since the last glacial period and implications for terrigenous material input mechanisms ····· 563

Abstract (in English) ····· 563
1. Introduction ····· 564
2. Study area ····· 565
3. Age model ····· 566
4. Results ····· 568
5. Discussion ····· 569
6. Conclusions ····· 574
Abstract (in Korean) ····· 576

KOPRI 극지연구소

References ····· 577

Chapter 26. Petrology and quartz grain microtextures of marine shoreline sands from the Punta Arenas area, southernmost Chile and King George Island, Antarctica and implications for their depositional history ····· 590

Abstract (in English) ····· 590
1. Introduction ····· 591
2. Study areas ····· 592
3. Methods and Materials ····· 595
4. Results ····· 596
5. Discussion ····· 599
6. Conclusions ····· 603
Abstract (in Korean) ····· 604
References ····· 605

Chapter 27. A Comparison of Methods for Identifying and Quantifying Ice Rafted Debris on the Antarctic Margin ····· 623

Abstract (in English) ····· 623
1. Introduction ····· 623
2. Methods of Determining IRD Flux ····· 628
3. Materials and Methods ····· 632
4. Comparison of the IRD Methods ····· 640
5. Discussion ····· 644
6. Determining IRD Mass Accumulation Rates: Implications of Using Different Methodologies ····· 647
7. Conclusions ····· 649
Abstract (in Korean) ····· 651
References ····· 652

KOPRI 극지연구소

Chapter 28. Paleoenvironmental study using ^{10}Be isotope analysis ····· 669
Abstract (in Korean) ····· 669
1. Studies in Ice change on land ····· 669
2. Studies in Sea ice change in marine environment ····· 671
Abstract (in English) ····· 673

Chapter 29. Fallacy of paleoproductivity signals by the recycled biogenic components: case study in the Central Basin of the northwestern Ross Sea ····· 684
Abstract (in English) ····· 684
1. Introduction ····· 685
2. Materials and Methods ····· 686
3. Results and Discussion ····· 687
4. Conclusions ····· 691
Abstract (in Korean) ····· 692
References ····· 693

Chapter 30. Controls on spatial heterogeneity in dinoflagellate cyst distribution in recent sediments off West Antarctica ····· 702
Abstract (in English) ····· 702
1. Introduction ····· 703
2. Study area ····· 705
3. Materials and methods ····· 706
4. Results ····· 709
5. Discussion ····· 710
Abstract (in Korean) ····· 719
References ····· 720

KOPRI 극지연구소

Chapter 31. Pleistocene oceanographic variability in the Ross Sea: A multiproxy approach to age model development and paleoenvironmental analyses ····· 743
Abstract (in English) ····· 743
1. Introduction ····· 744
2. Methods ····· 747
3. Results ····· 751
4. Discussion ····· 753
5. Conclusions ····· 763
Abstract (in Korean) ····· 764
References ····· 765

Chapter 32. Anisotropy of magnetic susceptibility of sediments in the Ross Sea continental rise, Antarctica: Evaluation of paleocurrent variability reconstruction 782
Abstract (in Korean) ····· 782
1. Introduction ····· 782
2. Materials and Methods ····· 783
3. Results ····· 785
4. Discussion ····· 786
5. Conclusions ····· 789
References ····· 790
Abstract (in English) ····· 795

Chapter 33. Elemental composition of smectite minerals in continental rise sediments from the Amundsen Sea, West Antarctica, as a tool to identify detrital input from various sources throughout late Quaternary glacial-interglacial cycles ····· 802
Abstract (in Korean) ····· 802
1. Introduction ····· 803

KOPRI 극지연구소

2. Materials and Methods ····· 805
3. Results ····· 808
4. Discussion ····· 811
5. Conclusions ····· 815
Abstract (in English) ····· 817
References ····· 818

Chapter 34. Peistocene glaciomarine laminated muds in the Central Basin of the northwestern Ross Sea and their palaeoceanographic records ····· 836

Abstract (in English) ····· 836
1. Introduction ····· 836
2. Materials and Methods ····· 838
3. Results ····· 838
4. Discussion ····· 839
5. Conclusions ····· 842
Abstract (in Korean) ····· 843
References ····· 844

Chapter 35. Glacial-interglacial envionmental changes in the Drake Passage over the past 600 kyrs ····· 853

Abstract (in English) ····· 853
1. Introduction ····· 854
2. Study area ····· 855
3. Materials and Methods ····· 856
4. Age determination ····· 857
5. Results ····· 857
6. Discussion ····· 858
7. Conclusions ····· 863
Abstract (in Korean) ····· 865
References ····· 866

KOPRI 극지연구소

Chapter 36. Mid-to-late Pleistocene Depositional Environments at the Ross Sea Continental Margin: Implications for Antarctic Ice Sheet Dynamics ····· 880
Abstract (in English) ····· 880
1. Introduction ····· 881
2. Ross Sea water masses and oceanography ····· 883
4. Materials and Methods ····· 884
5. Results ····· 887
6. Discussion ····· 889
7. Conclusions ····· 901
Abstract (in Korean) ····· 903
References ····· 904

KOPRI
극지연구소

제 1 장

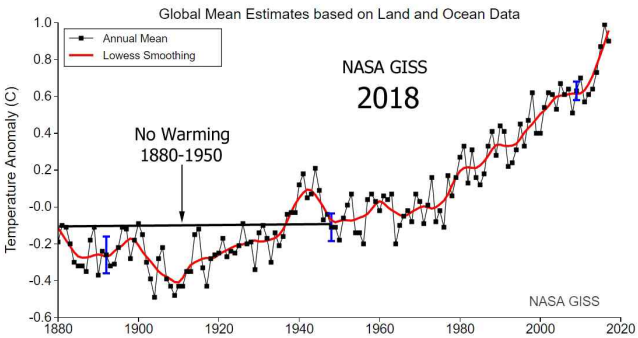
서 론

유규철

한국해양과학기술원 부설 극지연구소

1. 연구개발의 배경 및 필요성

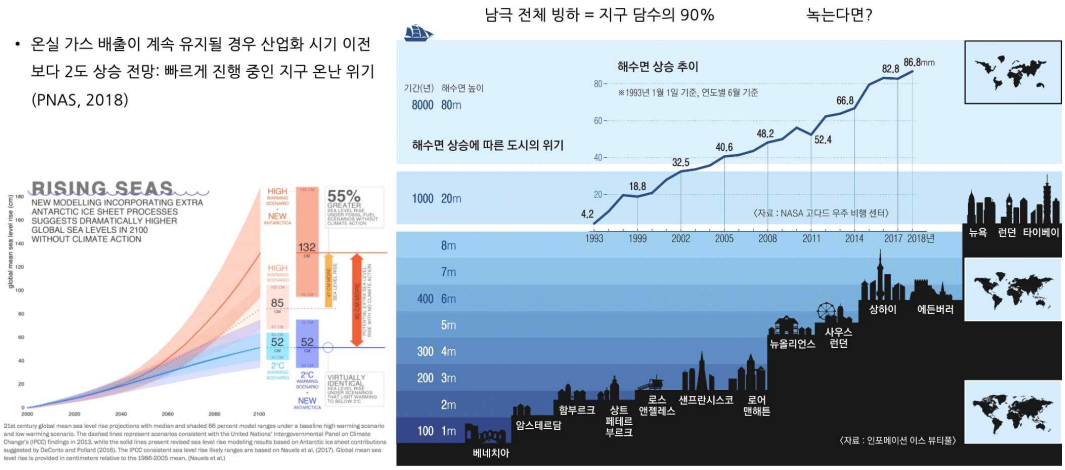
현재 지구 기온이 산업화 이전 대비 약 1도 정도 상승하였고 매 10년마다 0.17도 지속적으로 상승하고 있으며, 이로 인해 미래에 해수면 상승, 기후대/생태계 변화, 사막의 확장, 물 부족, 태풍의 강도 및 빈도 변화 및 집중호우의 강도 변화 등의 문제가 발생할 수 있다. 최근 발생하는 전세계 이상 고온이 지구 온난화의 전조라는 근거는 없지만 지구가 인류 활동에 민감하게 반응할 수 있다는 과학적인 근거는 인정되고 있다. 열대 우림, 영구동토층, 극지 빙하 등 지구 생태계의 순환 시스템이 매년 약 45억 톤의 탄소를 흡수하고 있으나 지구 평균 기온이 산업화 시기 이전에 비해 섭씨 2도 이상 오르면 이 시스템의 균형이 깨져 대기 중 산소 방출로 이어지고 지구는 온난 위기를 맞이할 것으로 예상된다 (Diffenbaugh and Barnes, 2023).



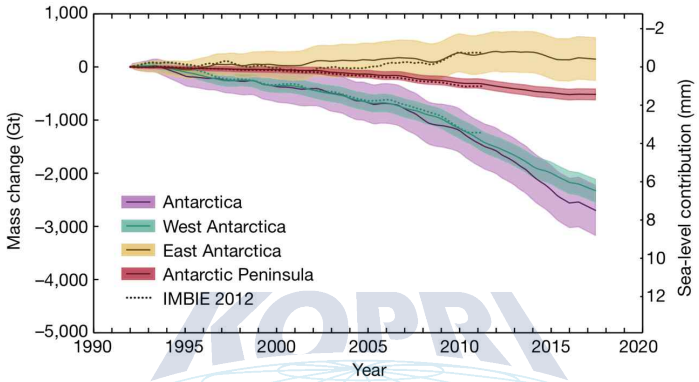
< 산업화 이후 지구 평균 기온 변화>

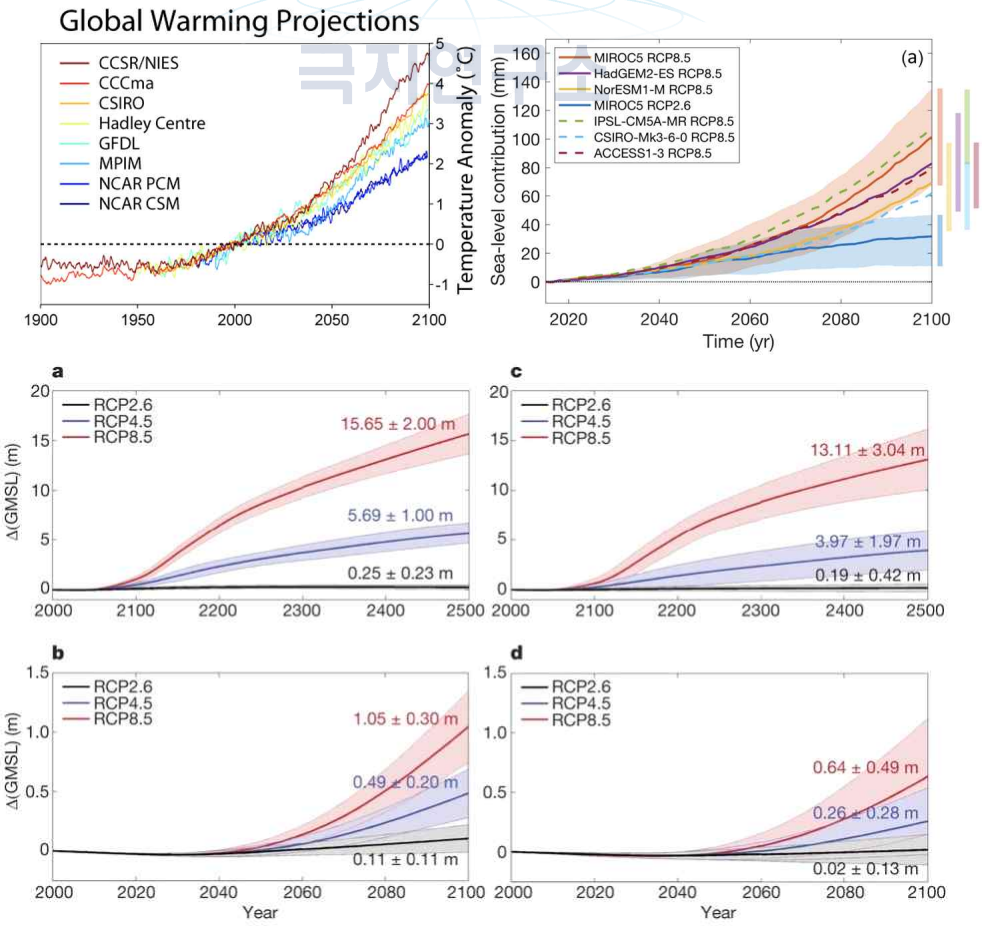
이러한 온난기 지구는 평균 기온이 산업화 시기 이전보다 섭씨 4-5도 빠르게 상승하면서 빙하가 사라지고 해수면은 10-60 m 높아져 인류 생존에 심각한 영향을 줄 것으로 예상된다. 전 지구적인 해수면 변동에 큰 영향을 주는 빙하가 남극(현재 지구 담수의 60%)에 많이 분포하고 있어 지구 온난화에 따른 반응에 과학적인 관심이 지속되었고 빙하 유실에 대한 보고가 꾸준하게 제기되고 있다. 1992년부터 2017년까지 남극의 빙하 유실 분석 결과 최근 속도가 이전보다 3배 더 빨라졌으며 특히 서남극 빙하 유실이 전체의 70%를 차지하고 대부분 붕

괴 직전이라고 보고하였다.



< 남극 빙상의 누적 질량 변화, The IMBIE team (2018) >





< 미래 빙상-기후 모델의 해수면 변동 결과, DeConto and Pollard (2016) >

특히, 미래 빙상-기후 모델 결과에서 남극의 빙하 유실에 따른 해수면 상승은 2100년이면 1 m 이상, 2500년이면 15 m 이상으로 예측하고 있다. 하지만 미래 예측에 대한 과학적 입증이 매우 힘들어 미래 온난기와 대조될 수 있는 과거 온난기에 대한 선행적인 연구가 현재 활발하게 논의되고 있다.

35가지 기후 모델의 의 시나리오
평균 지구 온도(1990-2100년): 약 1.4-5.8℃ 상승 예상

미래 빙상-기후 모델링의 문제점: 모델 예측 확률 약 66%로 신뢰도가 약함



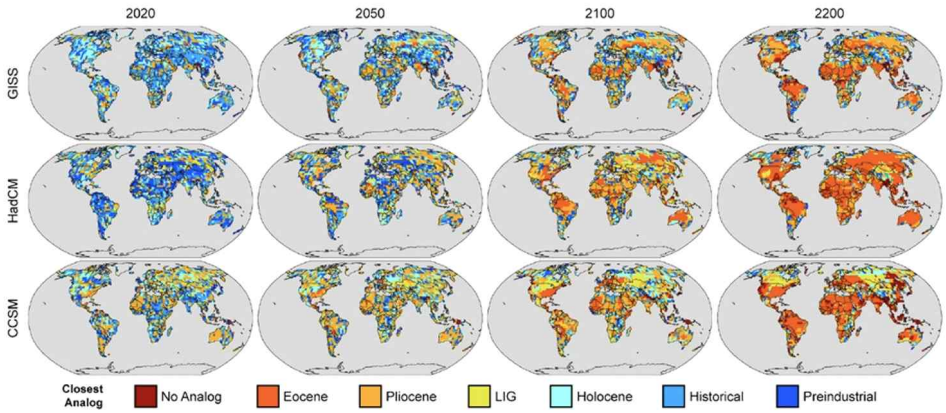
미래 온난기와 대조되는 과거 온난기에 대한 선행 연구 권고 (IPCC)
특히, 남극의 과거 온난기 주목

기후변화에 관한 정부간 협의체 (IPCC) 5차 보고서가 제시한 미래 기후 예측과 기후 모델과의 비교 연구에서 지구 온난화가 현재대로 진행되면 2030년엔 지구 기후가 3백만 년 전의 플라이오세 중기(현재보다 평균 기온이 2-4도 높음)와 유사해지고, 2150년의 지구 기후는 따뜻하고 빙하가 거의 사라졌던 5천만년 전의 에오세(현재보다 평균 기온이 10-13도 높음)와 비슷해질 것이라고 보고하였다 (Burke et al., 2018).

KOPRI 극지연구소

6500만년 전의 주목받는 과거 온난기

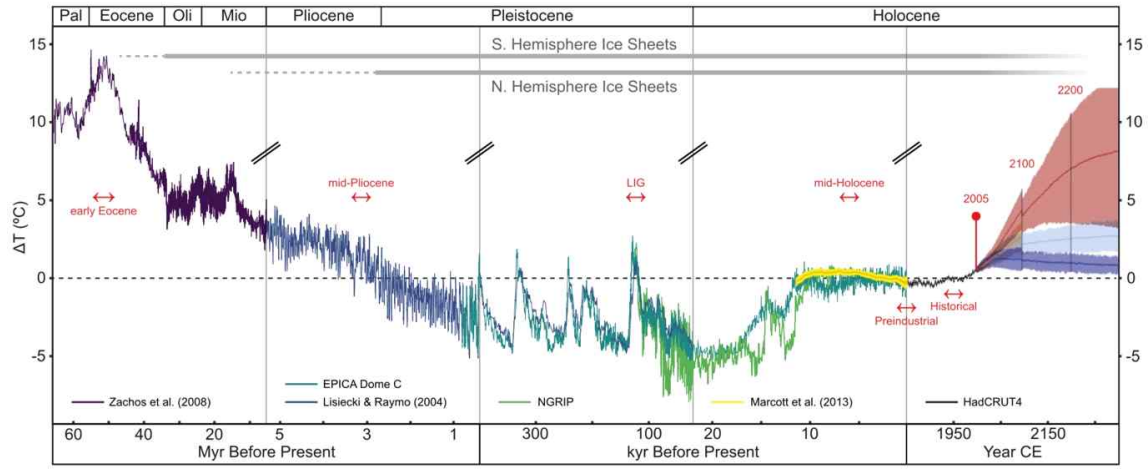
- 기후 예측 모델의 가정: 지구 온난화가 현재대로 진행될 경우
- 2050년: 13만년 전의 지난 간빙기와 홀로세 중기(약 7천년 전, 현재보다 0.5-1.5도 높음)
- 2100년: 약 3백만 년 전의 플라이오세 중기 (현재보다 2-4도 높음)
- 2200년: 빙하가 거의 사라졌던 5천년만 전의 에오세 (현재보다 10-13도 높음)



온실가스 배출 감축 노력을 하지 않을 경우(대표농도경로 RCP 8.5) 기후가 지역별로 어느 시기의 과거와 유사한지를 보여줌. 2100년을 넘어서면 과거 어느 시기에도 경험하지 못한 '새로운' 기후 등장 (PNAS, 2018)

미래 지구 온난화와 지구과학적인 측면에서 대조될 수 있는 중요한 과거 온난기는 홀로세 중기(현재보다 약 0.5-1.5도 높음), 지난 간빙기, 플라이오세 중기 등으로 당시 남극의 빙상 안정도와 해양 순환이 어떠하였는지 밝히는 것은 미래 지구 온난화의 모습을 보다 정확하

게 예측할 수 있는 단서를 제공할 수 있다. 과거 온난기의 환경을 이해할 수 있는 중요한 재료는 시추 빙하와 퇴적물로서 남극 대륙의 과거 대기 환경을 알 수 있는 빙하 시추의 기록과 더불어 시추 퇴적물의 고기후 지시자는 과거 빙상의 전진과 후퇴 및 해양 순환을 이해할 수 있는 열쇠이다.



인류 생존의 부적합한 환경이 될 수 있는 미래 지구 온난화는 인류학적으로 경험해보지 못한 새로운 기후 환경으로 나타날 수 있는데, 과거 온난기 동안 남극해가 어떤 환경이었으며 남극 빙하는 과거 온난화에 어떤 모습을 가지고 있었는지 복원하는 일은 현재의 글로벌 기후 이슈에 대응할 수 있는 중요한 연구이며, 남극 대륙의 빙상과 남극해의 국제공동 퇴적물 시추 프로그램은 과거 온난기 환경의 중요한 정보를 제공할 수 있다.

2. 국내외 주요 연구 동향

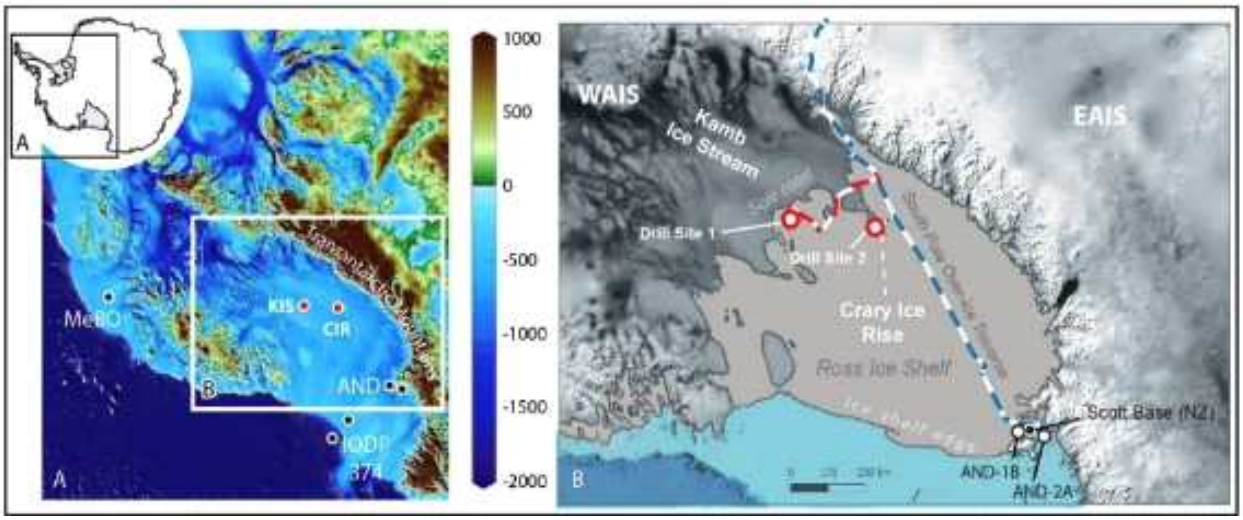
2.1. 국외 주요 이슈

최근의 주요 연구 결과들은 과거 온난기의 남극 환경 복원과 이에 따른 남극 빙상의 안정성 및 해수면 상승과 같은 이슈에 집중하고 있습니다. 현재와 이산화탄소 농도가 비슷했던 플라이오세의 빙상 복원 결과 동남극 빙상이 Wilkes Subglacial Basin 안쪽으로 후퇴했음을 밝히고 있다 (Cook et al., 2013; Patterson et al., 2014; Reinardy et al., 2015). 이에 따른 모델 수정 결과 당시엔 현재보다 해수면 약 17 m 높았을 것으로 계산하였다 (Pollard et al., 2015).

지난 해빙기 중 비교적 먼저 일어났던(약 17 ka) 해수면 상승 현상들은 남극반도 빙상 및 남동 웨델해의 동남극 빙상의 해빙과 관련 있을 수 있다. 스코시아해의 빙하운반 력(ice-drafted debris) 기록에 따르면 서남극 빙상의 후퇴가 Meltwater Pulse 1A의 해수면 상승에 주요한 요인이었음을 지시한다 (Weber et al., 2014). 미래 지구 평균기온이 2℃ 상승할

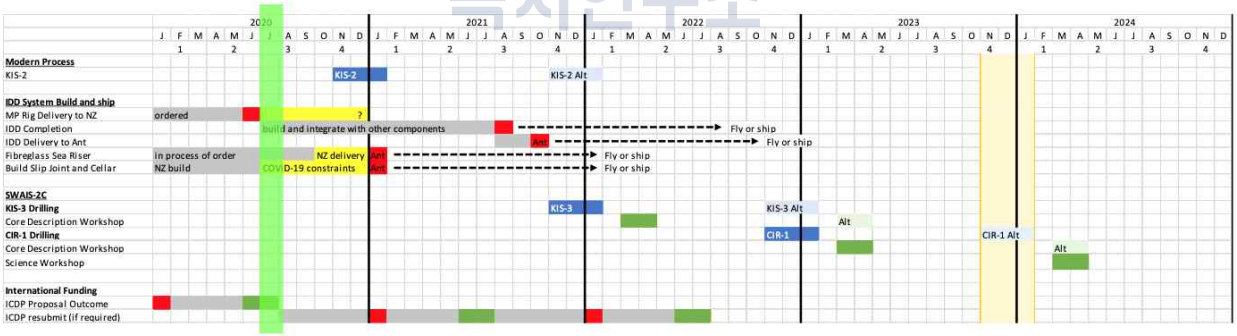
경우, 전 지구적인 영향이 매우 큰 남극 환경이 어떻게 변화할 것인지 국제적인 관심이 집중되고 있으며, 이를 밝히기 위해 과거 온난기 동안에 발생되었던 환경을 추적하기 위한 국제공동 퇴적물 시추 프로그램이 진행되고 있다.

국제공동 SWAIS 2C 시추 프로그램



SWAIS2C

Modified Project Time Line – COVID-19 Impacts

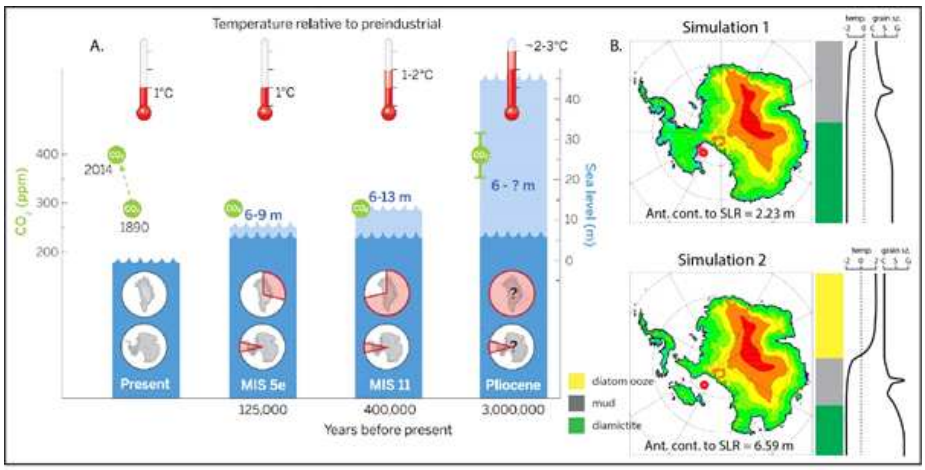


We are here

NZ Programme – no science this season BUT – there will be a traverse

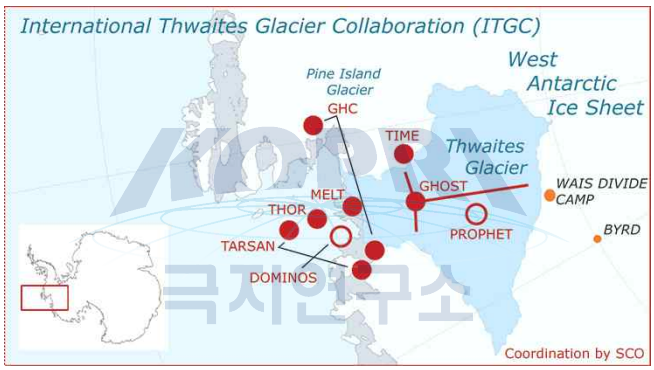
< 프로젝트 타임라인 >

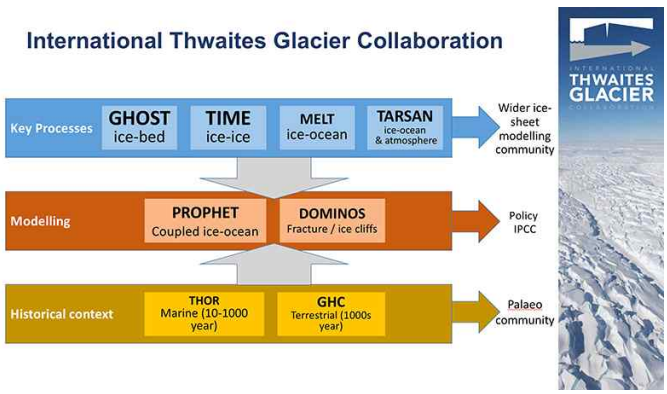
- 사업명: Sensitivity of West Antarctica Ice Sheet to +2 Degrees Celsius (SWAIS 2C)
- 목적: 전 지구 평균 기온 상승에 대한 서남극 빙상의 반응 이해
- 참가국: 뉴질랜드, 미국, 독일, 대한민국, 영국, 일본, 이탈리아, 호주 (현재 8개국 참가)
- 내용: 사이플 코스트의 캠 빙하류(Kamb Ice Stream)과 크레리 아이스라이즈(Crary Ice Rise) 지역에서 빙하 아래의 퇴적물을 시추하여 기후 변동에 대한 과거 서남극 빙상의 변화 복원



국제공동 SWAIS 2C 시추 사업. (A) 전지구 평균 기온 상승에 따른 빙상 축소와 해수면 상승. (B) 현재보다 온난한 간빙기 시기 서남극 빙상 범위에 대한 두 가지 시뮬레이션과 이에 따른 시추 위치에서의 퇴적물 코어 층서 예측. 붉은 점이 제안된 코어 위치.

국제공동 스웨이츠 빙하 연구(ITGC)





- ITGC (International Thwaites Glacier Collaboration)라고 하는 영국 자연 환경 연구 위원회(NERC)와 미국 국립 과학 재단(NSF): 70년 만에 남부 대륙에서 수행된 가장 큰 영-미 공동 프로젝트로 스웨이츠 빙하(Thwaites Glacier)와 인접 해양 지역에 대한 다학제적 연구
- 지난 30년 동안 이 120km 너비의 지역에서 흘러나오는 얼음의 양은 거의 두 배, 2018년부터 앞으로 5년 동안 과학자 팀은 바다와 해양 퇴적물을 탐사하고 깊은 얼음을 향해 흐르는 해류를 측정하며 아래 풍경에서 빙하가 늘어나거나 구부러지고 갈리는 것을 조

사한다.

- 모델링 연구 PROPHET 및 DOMINOS는 주황색으로 열린 원으로 표시
- GHOST는 지진 및 레이더 데이터를 사용하여 얼음과 기반암 특성을 관찰
- GHC는 Thwaites Glacier 양쪽에서 암석 샘플을 수집하여 최근 과거 역사에 대한 단서 추적
- THOR 프로젝트는 해양 퇴적물, 수심 측정 및 해양학 연구
- MELT와 TARSAN은 모두 육지, 얼음, 바다가 만나는 지점에서 빙하와 바다의 상호 작용에 초점을 맞추고 빙하 전면 근처의 얼음이 녹는 속도와 해양 순환 연구
- GHOST, TIME, MELT 및 TARSAN의 4개 프로젝트는 빙하를 후퇴시키거나 기후에 대한 반응을 제어하는 자연적 과정에 초점

- THOR 및 GHC 프로젝트와 다른 사업들은 모델링 연구인 PROPHET과 DOMINOS에 대해 정보 제공

남극 퇴적물 국제공동 해양 시추 프로그램(IODP)

- 서남극 주변에서의 신생대 동안의 빙상 변화, 장기 기후 변화 복원 및 원인 규명을 위한 국제공동 IODP 프로그램 수행한 연구 진행
- Expedition 374: 로스해 (2018.01~2018.03): 로스해 대륙주변부의 신제3기 제4기 퇴적기록을 통한 해양-빙상 상호작용과 서남극 빙상의 취약성 파악. 주요 연구 결과들 및 초기 연구 결과들이 본격적으로 학술지 게재 및 주요 국제학회에서 발표됨
- Expedition 379: 아문젠해 (2019.01~2019.03): 아문젠해의 시추 결과를 통한 서남극 빙상의 발달과 기후 민감도 파악. 주요 연구 결과 및 초기 연구 결과 학술지 게재 및 주요 국제학회에서 발표되기 시작함
- Expedition 382: 스코시아해 (2019.03~2019.05): 남극 대륙의 빙산 유입과 빙권-해양의 역학 변화 파악. 주요 연구 결과 및 초기 연구 결과 학술지 게재 및 주요 국제학회에서 발표되기 시작함
- Expedition 383: 태평양 아남극 해역 (2019.05~2019.07): 태평양에서 남극순환류의 발달 및 변동 연구. 비교적 최근에 수행되어 주요 연구 결과 및 초기 연구 결과가 국제학회에서 발표되기 시작함
- Expedition 378: 남태평양 아남극 해역 (2020.01~2020.03): 고제3기 남극 대륙빙하 발달 및 이에 따른 기후 및 해양 순환 변화 파악. 비교적 최근에 수행되어 주요 연구 결과 및 초기 연구 결과가 국제학회에서 발표되기 시작함

2.2. 남극 고환경 연구 분야 국내 기술 동향

과거 남극 고환경 국내 연구는 주로 마지막 빙하기 이후의 지역적인 고해양 변화 및 퇴적상 해석에 집중하였으나 최근 십여 년 간 많은 발전이 있었다. 국내 남극 고환경 분야 연구는 주로 극지연구소의 연구과제를 통해 이루어졌다. 관련 연구과제로는 "남극권 고해양 및 고기후 연구" (2004.01-2005.12, 연구 책임자 윤호일), "지구온난화 대응책 마련을 위한 극지역 고기후 및 고해양 변화 복원 기술 개발" (2006.1-2010.12, 연구책임자 윤호일, 이재일), "서남극 빙붕 변화 관 측 시스템 구축 및 제4기 해빙사 복원 기술 개발" (2010.1-2016.12, 연구책임자 윤호일, 이재일)이 있었다. 이 중 앞의 두 사업은 남극반도 북단 지역의 마지막 빙하기 이후의 퇴적 환경 변화와 고기후 변화 복원 연구를 중심으로 이루어졌다. "서남극 빙붕 변화 관측 시스템 구축 및 제4기 해빙사 복원 기술 개발" 과제에서는 빙붕 주 변 지역에서 일어나는 변화를 종합적으로 연구하는 과제로서 고환경 연구 뿐 아니 라 지구물리 장비를 활용한 빙붕 관측 및 기타 다학제적 사업으로 수행되었다.

2009년 한국 최초의 쇄빙연구선인 아라온이 건조됨으로써 결빙 해역에 대한 연구가 가능해졌고, 세종기지 주변이 아닌 타 지역의 연구도 가능해졌다. 또한 아라 온 도입과 함께 외국 연구진과의 국제공동연구가 활발해지면서 해양 탐사 자료를 활용한 연구의 질적 향상이 이루어졌다. 2014년에는 장보고 기지가 설립되면서 남극반도 뿐 아니라 로스해 지역까지도 연구 영역이 확대되었다. 현재 극지연구소는 남극반도와 로스해 지역에 과학기지를 운영하고 있고 쇄빙연구선 아라온을 자체적 으로 운영하고 있기 때문에 서남극빙상의 변동을 거시적, 장기적으로 연구할 수 있는 장점이 있다. 또한 남극해에서는 10 m 이상의 긴 퇴적물 코어가 매우 부족한데, 아라온의 롱 코어링 시스템 (Long Coring System)으로 시료를 채취하면 최대 39 m 까지의 퇴적물 시료를 채취할 수 있으므로 보다 긴 기후 기록을 간직한 시료의 획득이 가능해졌다. 이에 따라 본 연구과제 "퇴적물을 활용한 지난 2백만 년간의 남극 빙권 및 해양 변화 복원" (2017.1 - 2019.12, 연구책임자: 이민경, 이재일)에서는 쇄빙선 및 롱코어 시스템, 남극 과학기지 인프라를 활용하여 서남극 빙상 범위를 포함하는 넓은 지역에서 장기 적인 과거 환경을 복원하는 연구를 수행하였다.

2014년 장보고 기지 구축으로 로스해 지역으로 연구 영역이 확대되었으며, 서남극 여러 지역의 자료를 종합적으로 분석하여 지역적 변화가 아닌 거시적인 고환경 해석이 가능해졌다. 특히 서남극 빙상 변화 이슈 대응에 큰 도움이 되어 국제공동연구를 위한 기틀이 마련되었다. 극지연구소 해양 퇴적물 분석을 위한 신규 장비와 분석 기기들이 꾸준히 도입되면서 연대측정 및 퇴적물 프록시 분석 능력이 향상되었다. 최근 남극 주변부에서 수행된 국제공동시추프로그램 (IODP Exp. 374, 379, 382, 383)에 국내 연구진 다수가 참여하였고, 이와 같은 긍정적인 변화들을 통해 SCAR Horizon Scan에서 제기한 세계적인 이슈를 해결할 수 있는 능력이 최근 크게 향상되었다.

3. 연구개발의 목표 및 내용

3.1. 연구개발의 목표

본 연구과제의 최종 목표는 해양 퇴적물과 육상 암석의 고기록으로부터 과거 온난기의 서남극 빙상의 시공간적 변화 기작 및 영향을 규명하는 것이다 (그림 1). 본 과제는 2017 - 2019년 수행되었던 "퇴적물을 활용한 지난 2백만 년간의 남극 빙권 및 해양 변화 복원" 연구과제의 연관되어있지만, 현재 지구환경변화 문제와 직결된 글로벌 아젠다가 포함된 목표를 지향하고 있다. 일단 남극 고환경 연구는 남극과학위원회(SCAR)에서 선정한 80개 주요 해결 과제 (Horizon Scan) 중 6개 주제 (마지막 빙하기 이후 기후 변화, 과거 온난 시기의 기후와 빙상 변화, 해빙 변화, 빙하주기와 빙권-남극해의 관련성, 남극 빙상의 변화 속도, 간빙기 동안 해저 기반 빙상의 안정성)와 관계되어있다. 또한, 2018년 10월 인천 송도에서 기후변화에 관한 정부간 협의체 (IPCC)는 1.5℃ 온난화 특별보고서 (SR15)를 공개하였는데, 이 보고서에서 우리가 계속 지금처럼 온실 기체을 배출한다면 2030-2052년 사이에 전 지구 평균 기온이 산업화 이전보다 1.5℃ 상승(66% 이상의 확률)할 것이라고 예측하였지만, 사실상 전지구적 수치모델링을 통한 감축에 따른 정확한 미래 온난 위기 예측 판단이 아직도 부정확하기 때문에 현재의 인류의 영향과 관계없이 과거 1.5도 내지는 2.0도 높았던 것으로 알려진 온난 시기에 대한 연구가 중요하다고 보고 있다. 미래 기후 온난 상승 시기와 상응하는 과거 온난기 동안 당시 환경이 어떠하였는지가 매우 중요한 지구과학적인 이슈들 중 하나가 되었으며, 특히 전지구적 기후 변화에 민감한 남극대륙 빙상 변화를 복원하고 해양 순환의 귀중한 정보가 미래를 투영할 수 있는 중요한 정보로 대두되었다. 현재 기후 관련 기관이나 협의체에서 고기후학자들에게 이를 잘 제시할 수 있는 과학적인 프로그램을 개발하도록 격려하고 있으며 이에 선진국에서는 선도적으로 과거 온난기 기록에 대한 포괄적인 연구가 진행되고 있다.

본 과제의 1단계 (2020-2022)의 최종 목표는 과거 온난기 (플라이오세 중기, 마지막 간빙기, 홀로세 중기 등)의 서남극 빙상 규모를 복원하고 해양-기반 빙상(marine-based ice sheet)의 안정성 조절 요인에 대한 규명이다. 그리고 성과목표는 (1) 국제공동 시추 프로그램 시료 확보, (2) 서남극 빙상 주변 퇴적물 분포 조사 및 시추 시료 확보, (3) 고기후 지시자 및 연대측정법 개선, (4) 과거 온난기 서남극 해양 순환 및 퇴적 양상 변화 복원 연구이며 (그림 2), 2단계 (2023-2025년) 성과목표는 (1) 국제공동 시추 프로그램 참여, (2) 국제공동 시추 프로그램 주변 지역 탐사, (2) 고기후 지시자 및 연대측정법 개선, (4) 과거 온난기 서남극 빙상 및 해양 환경 변화 규명이다. 본 과제의 성격이 크게는 국제공동연구이며, 시기는 수백만년 전까지의 고기록들 중 특히 미래 온난기와 유사한 환경인 과거 온난기, 연구지역은 서남극의 대륙주변부와 빙상 지역에 초점을 두고 있다 (그림 3과 4). 고환경 지시자 및 연대측정법 개선이 꾸준하게 이루어졌다. 유공충의 붕소 동위원소와 해수의 pH 사이의 연관성에 대한 연구가 발전되면서 (Foster and Rae, 2016; Rae, 2018), 빙하 주기에 따른 심층수의 pH 변화를 복원하는 연구도 수반되어 해양 심층 순환 구조와 대기 이산화탄소 함량 변화 사이의 연관 연구에

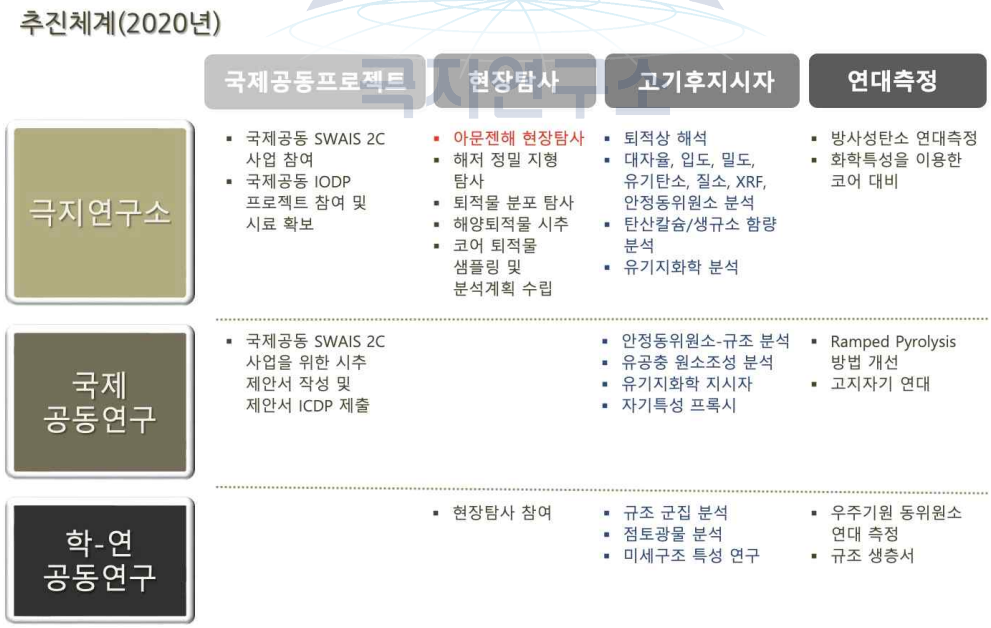
이용될 수 있다 (Chalk et al., 2019). 고환경 지시자인 유공충 연구도 중요한 부분으로 남극 빙상 기저면 인접 지역이거나 빙붕 아래 환경에 있을 때의 유공충 종 조성에 대한 연구도 중시되고 있다 (Majewski et al., 2018). 남극과 같이 쇄설성 유기물 유입이 많은 지역에서 당대의 유기물만을 방사성탄소 연대측정하기 위한 ramped pyrolysis 방법에 대한 적용이 관심받고 있어 본 연구 과제에서도 적용되었다 (Subt et al., 2017).

빙상 아래쪽에 존재하는 호수인 빙저호 혹은 지금은 해양 환경이지만 빙하기 시기 빙저호 환경에서의 퇴적에 대한 연구 결과들(예: Kuhn et al., 2017; Smith et al., 2018)은 이전 과제와 차별적인 본 과제의 연구 목표이며, 서남극 대륙붕의 퇴적물 코어를 분석하여 과거 빙저호 환경에서 퇴적된 것으로 추정되는 퇴적물들이 발견되어 빙저호 환경 퇴적물의 특성이 연구되었다. 로스해 서부에서는 해저 지형 분석은 과거 빙하 하부 융빙수의 수리 시스템과 상류의 빙저호를 인지하고 이들과 빙하 역학간의 연관성이 제시될 수 있다 (Simkins et al., 2017).

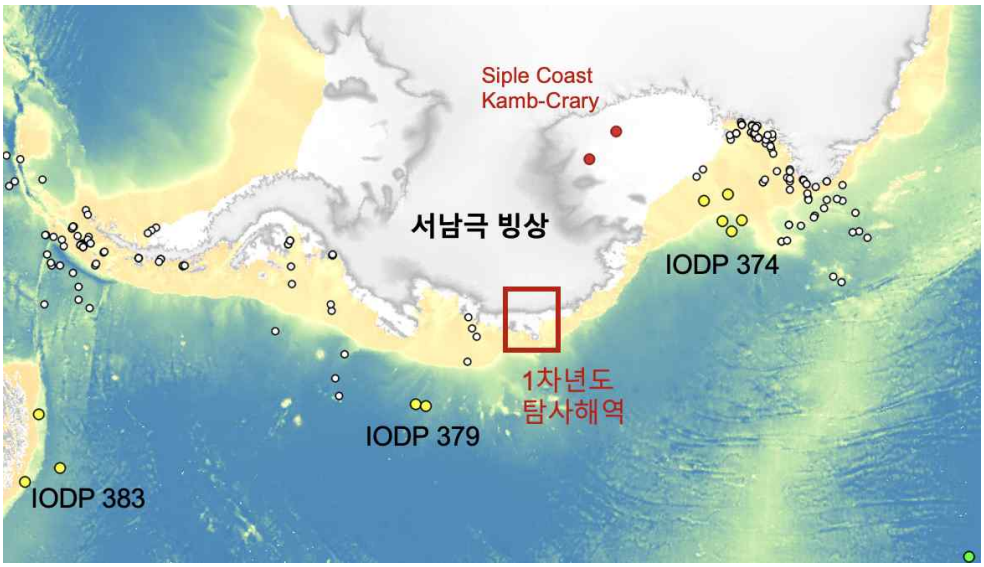
3.2. 연구개발 추진체계 및 수행방법

3.2.1. 1차년도 (2020)

○ 연구계발 추진체계



• 극지연구 인프라 활용: 연구선 기반 남극 탐사(아문젠해 해역) 및 해양퇴적물 코어 채취. 극지연구소에서 주관하며 필요에 따라 공동연구자들과 공동승선연구 수행



○ 연구계발 수행방법

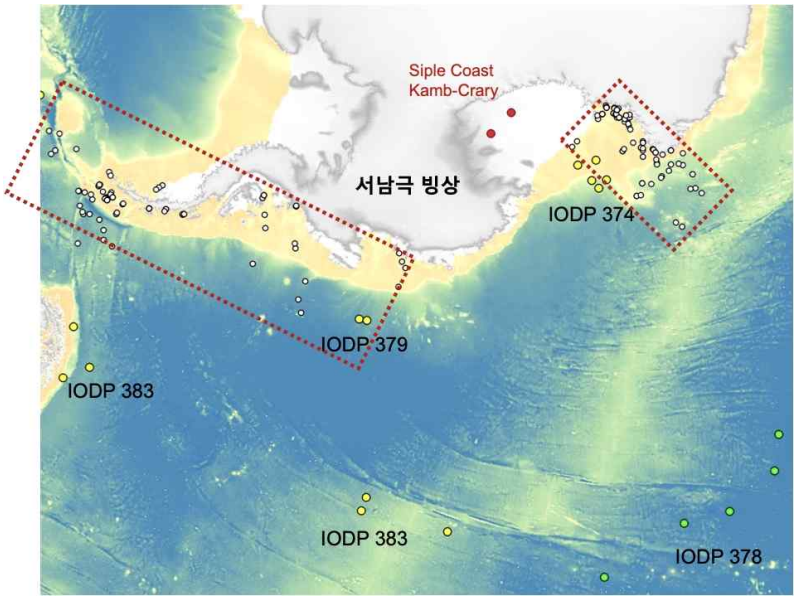
• 고기후 지시자 연구: 최근의 고환경 연구는 인프라 활용 및 프록시 분석을 위해 많은 전문 인력이 필요하며, 극지연구소 인력만으로는 이슈 해결에 어려움이 있으므로 다양한 고기후지시자 분석을 통한 융복합적 고환경 연구를 수행
극지연구소: 퇴적상 해석, 퇴적물 입도 및 밀도 분석, 유기탄소, 질소, XRF 분석, 탄산칼슘 함량 분석, 생규소 함량 분석, 박테리아 군집분석 등을 실시.
뉴질랜드 빅토리아대: 유공충의 안정동위원소 분석
뉴질랜드 오타고대는 퇴적물의 안정동위원소, 규조 종조성
전북대: 규조 종조성 분석
부산대: 퇴적물 미세구조 현미 분석 수행
연세대: 퇴적물 내의 점토광물 조성 및 관련 생지화학적 변이작용 연구

• 분석장비 고도화를 통한 선도적인 실험 환경 조성: 탄소/산소 안정동위원소 분석기 도입

• 연대측정: 퇴적물의 보다 정확한 연대 측정을 위해 극지연구소에서는 퇴적물 및 탄산칼슘 성분에 대한 방사성탄소 연대측정, 고려대와 우주기원 동위원소 연대측정, 전북대와 규조 생층서, 미국 USF와 뉴질랜드 GNS는 Ramped Pyrolysis 방법 개선, 뉴질랜드 오타고대와 고지자기 연대측정에 관한 공동연구를 통해, 각국의 인프라 및 첨단 장비, 자료처리 기술을 공유하고 국내 학연 협력을 통해 고환경 변화 복원을 위한 안정적 연구 협력 시스템 구축

• 기존 확보된 극지연구소 시추 퇴적물 이용: 해양 퇴적물에 나타난 과거 온난기의 고환경 기록과 대비될 수 있는 서남극 빙상의 빙하 시추 자료 확보 및 상호 대비 연구

수행



30년 동안 고해양 연구 그룹이 서남극에서 획득한 시추 퇴적물
(빨간 점선 박스 내 작은 노란색 정점)

- 코로나 위기로 인해 국제공동 시추 프로그램 참여가 쉽지 않아 국제공동 IODP 시추 퇴적물의 플라이오세 중기 기후 변화 시료 확보에 주력
- 기존에 연구선 기반 승선 연구를 통해 획득된 남극해 심해 시추 퇴적물과 1단계 연구선 기반 승선 연구를 통해 얻어진 시추 퇴적물에서 후기 플라이스토세 이후의 온난기에 대한 연구에 집중함

KOPRI 극지연구소

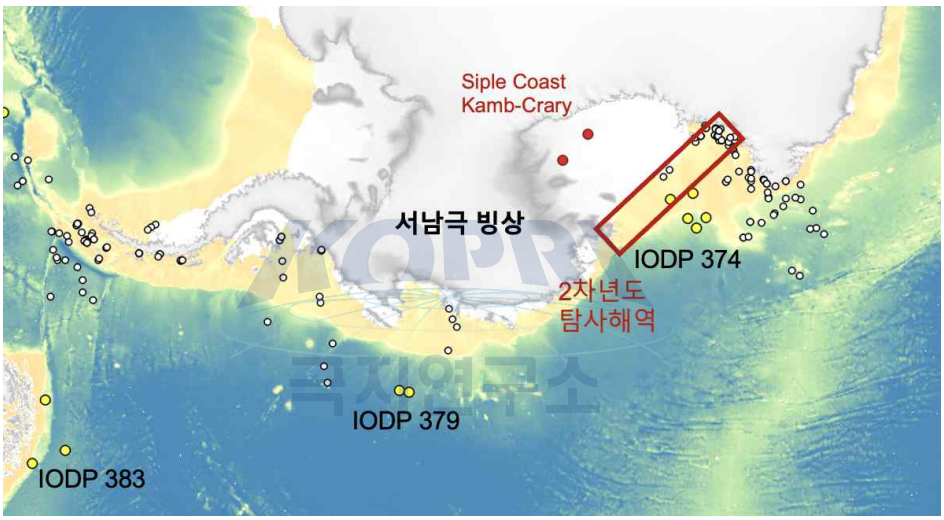
3.2.2. 2차년도 (2021)

○ 연구계발 추진체계

- 극지연구 인프라 활용: 연구선 기반 남극 탐사(로스해 해역) 및 해양퇴적물 코어 채취. 극지연구소에서 주관하며 필요에 따라 공동연구자들과 공동승선연구 수행

추진체계(2021년)

	국제공동프로젝트	현장탐사	고기후지시자	연대측정
극지연구소	▪ 국제공동 SWAIS 2C 사업 참여 ▪ 국제공동 IODP 프로젝트 참여 및 시료 확보	▪ 로스해 현장탐사 ▪ 해저 정밀 지형 탐사 ▪ 퇴적물 분포 탐사 ▪ 해양퇴적물 시추 ▪ 코어 퇴적물 샘플링 및 분석계획 수립	▪ 퇴적상 해석 ▪ 대자율, 입도, 밀도, 유기탄소, 질소, XRF, 안정동위원소 분석 ▪ 탄산칼슘/생규소 함량 분석 ▪ 안정동위원소 분석기 최적화 ▪ 빙하운반역 분석 개발	▪ 방사성탄소 연대측정 ▪ 화학특성을 이용한 코어 대비
국제 공동연구	▪ 국제공동 SWAIS 2C 사업을 위한 시추 제안서 작성 및 제안서 ICDP 다시 제출		▪ 안정동위원소-규조 분석 ▪ 유공충 원소조성 분석 ▪ 유기지화학 지시자 ▪ 자기특성 프록시	▪ Ramped Pyrolysis 방법 개선 ▪ 고지자기 연대
학-연 공동연구		▪ 현장탐사 참여	▪ 규조 군집 분석 ▪ 점토광물 분석 ▪ 미세구조 특성 연구	▪ 우주기원 동위원소 연대 측정 ▪ 규조 생층서



○ 연구계발 수행방법

• 고기후 지시자 연구: 최근의 고환경 연구는 인프라 활용 및 프록시 분석을 위해 많은 전문 인력이 필요하며, 극지연구소 인력만으로는 이슈 해결에 어려움이 있으므로 다양한 고기후지시자 분석을 통한 융복합적 고환경 연구를 수행

극지연구소: 퇴적상 해석, 퇴적물 입도 및 밀도 분석, 유기탄소, 질소, XRF 분석, 탄산칼슘 함량 분석, 생규소 함량 분석, 박테리아 군집분석 등을 실시.

뉴질랜드 빅토리아대: 유공충의 안정동위원소 분석

뉴질랜드 오타고대는 퇴적물의 안정동위원소, 규조 종조성

전북대: 규조 종조성 분석

부산대: 퇴적물 미세구조 현미 분석 수행

연세대: 퇴적물 내의 점토광물 조성 및 관련 생지화학적 변이작용 연구

- 탄소/산소 안정동위원소 분석기 최적화
- 해양 퇴적물 내 X-선 촬영 이미지의 빙하운반역 분석 프로그램 개발
- 해양 퇴적물 내 박테리아 분석 방법 도입

- 연대측정: 퇴적물의 보다 정확한 연대 측정을 위해 극지연구소에서는 퇴적물 및 탄산칼슘 성분에 대한 방사성탄소 연대측정, 고려대와 우주기원 동위원소 연대측정, 전북대와 규조 생층서, 미국 USF와 뉴질랜드 GNS는 Ramped Pyrolysis 방법 개선, 뉴질랜드 오타고대와 고지자기 연대측정에 관한 공동연구를 통해, 각국의 인프라 및 첨단 장비, 자료처리 기술을 공유하고 국내 학연 협력을 통해 고환경 변화 복원을 위한 안정적 연구 협력 시스템 구축

- 기존 확보된 극지연구소 시추 퇴적물 이용: 해양 퇴적물에 나타난 과거 온난기의 고환경 기록과 대비될 수 있는 서남극 빙상의 빙하 시추 자료 확보 및 상호 대비 연구 수행. 코로나 위기에 따른 연구선 기반 남극 탐사의 축소(연구승선일수: 1일)로 인해 기존 로스해에서 획득된 시추 퇴적물을 로스해 고환경 복원에 적극적으로 이용함

- 코로나 위기로 인해 국제공동 시추 프로그램 참여가 쉽지 않아 국제공동 IODP 시추 퇴적물의 플라이오세 중기 기후 변화 시료 확보에 주력
- 기존에 연구선 기반 승선 연구를 통해 획득된 남극해 심해 시추 퇴적물과 1단계 연구선 기반 승선 연구를 통해 얻어진 시추 퇴적물에서 후기 플라이스토세 이후의 온난기에 대한 연구에 집중함

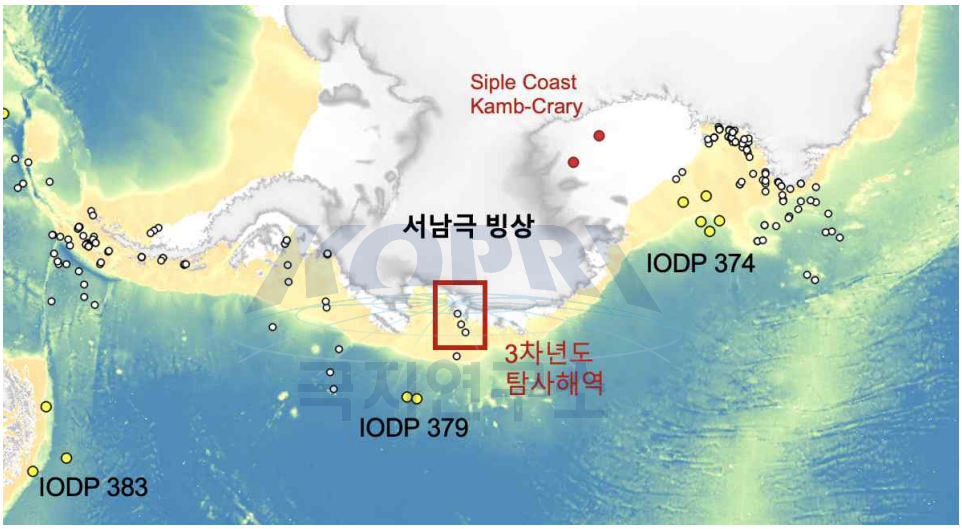
2.2.3. 3차년도 (2022)

○ 연구계발 추진체계

- 극지연구 인프라 활용: 연구선 기반 남극 탐사(아문젠해 해역) 및 해양퇴적물 코어 채취. 극지연구소에서 주관하며 필요에 따라 공동연구자들과 공동승선연구 수행

추진체계(2022년)

	국제공동프로젝트	현장탐사	고기후지시자	연대측정
극지연구소	▪ 국제공동 SWAIS 2C 사업 참여 ▪ 국제공동 IODP 프로젝트 참여 및 시료 확보	▪ 아문젠해 현장탐사 ▪ 해저 정밀 지형 탐사 ▪ 퇴적물 분포 탐사 ▪ 해양퇴적물 시추 ▪ 코어 퇴적물 샘플링 및 분석계획 수립	▪ 퇴적상 해석 ▪ 대자율, 입도, 밀도, 유기탄소, 질소, XRF, 안정동위원소 분석 ▪ 탄산칼슘/생규소 함량 분석 ▪ 안정동위원소 분석기 안정화 ▪ 극미량 분석 방법 개발	▪ 방사성탄소 연대측정 ▪ 화학특성을 이용한 코어 대비
국제 공동연구	▪ 국제공동 SWAIS 2C 사업 수행을 위한 MoU 체결		▪ 안정동위원소-규조 분석 ▪ 유공충 원소조성 분석 ▪ 유기지화학 지시자 ▪ 자기특성 프록시	▪ Ramped Pyrolysis 방법 개선 ▪ 고지자기 연대
학-연 공동연구		▪ 현장탐사 참여	▪ 규조 군집 분석 ▪ 점토광물 분석 ▪ 미세구조 특성 연구 ▪ 유전체 분석	▪ 우주기원 동위원소 연대 측정 ▪ 규조 생층서



○ 연구개발 수행방법

• 고기후 지시자 연구: 최근의 고환경 연구는 인프라 활용 및 프록시 분석을 위해 많은 전문 인력이 필요하며, 극지연구소 인력만으로는 이슈 해결에 어려움이 있으므로 다양한 고기후지시자 분석을 통한 융복합적 고환경 연구를 수행

극지연구소: 퇴적상 해석, 퇴적물 입도 및 밀도 분석, 유기탄소, 질소, XRF 분석, 탄산칼슘 함량 분석, 생규소 함량 분석, 박테리아 군집분석 등을 실시.

뉴질랜드 빅토리아대: 유공충의 안정동위원소 분석

뉴질랜드 오타고대는 퇴적물의 안정동위원소, 규조 종조성

전북대: 규조 종조성 분석

부산대: 퇴적물 미세구조 현미 분석 수행

연세대: 퇴적물 내의 점토광물 조성 및 관련 생지화학적 변이작용 연구

- 탄소/산소 안정동위원소 분석기 최적화
- 해양 퇴적물 내 X-선 촬영 이미지의 빙하운반역 분석 프로그램 적용
- 퇴적물 내 극미량 광물 분석 방법 도입
- 퇴적물 내 와편모조류 시스트 고환경 분석 연구 도입
- 해양 퇴적물 내 유전체 분석 방법 도입

- 연대측정: 퇴적물의 보다 정확한 연대 측정을 위해 극지연구소에서는 퇴적물 및 탄산칼슘 성분에 대한 방사성탄소 연대측정, 고려대와 우주기원 동위원소 연대측정, 전북대와 규조 생층서, 미국 USF와 뉴질랜드 GNS는 Ramped Pyrolysis 방법 개선, 뉴질랜드 오타고대와 고지자기 연대측정에 관한 공동연구를 통해, 각국의 인프라 및 첨단 장비, 자료처리 기술을 공유하고 국내 학연 협력을 통해 고환경 변화 복원을 위한 안정적 연구 협력 시스템 구축

- 2020년 1차년도 아라온 기반 남극 탐사에서 획득된 시추 퇴적물 이용: 해양 퇴적물에 나타난 과거 온난기의 고환경 기록과 대비될 수 있는 서남극 빙상의 빙하 시추 자료 확보 및 상호 대비 연구 수행

- 코로나 위기로 인해 국제공동 시추 프로그램 참여가 쉽지 않아 국제공동 IODP 시추 퇴적물의 플라이오세 중기 기후 변화 시료 확보에 주력. 1단계에서 우선적으로 기존에 확보되어있는 고해양 그룹의 시추 퇴적물과 연구선 기반 승선 연구를 통해 얻어진 시추 퇴적물에서 후기 플라이스토세 이후의 온난기에 대한 연구에 집중함

참고 문헌

Burke, K.D., J.W. Williams, M.A. Chandler, A.M. Haywood, D.J. Lunt, and B.L. Otto-Bliesner, 2018: Pliocene and Eocene provide best analogs for near-future climates. Proc. Natl. Acad. Sci., 115, no. 52, 13288-13293, doi:10.1073/pnas.1809600115.

Chalk, T.B., Foster, G.L., and Wilson, P.A., 2019, Dynamic storage of glacial CO2 in the Atlantic Ocean revealed by boron [CO3 2-] and pH records. Earth and Planetary Science Letters, 510, 1-11.

Cook, C.P. van de Flierdt, T., Williams, T., Hemming, S.R., and others, 2013, Dynamic behaviour of the East Antarctic ice sheet during Pliocene warmth. Nature geoscience, 6, 765-769.

DeConto, R.M. and Pollard, D, 2016. Contribution of Antarctica to past and future sea-level rise. Nature 531(7596), 591-597.

Diffenbaugh, N.S., and Barnes, E.A., 2023. Data-driven predictions of the time remaining until critical global warming thresholds are reached. PNAS 120 (6) e2207183120.

Foster, G.L. and Rae, J.W.B., 2016, Reconstructing ocean pH with Boron isotopes in foraminifera. Annual Review of Earth and Planetary Sciences, 44, 207-237.

Kuhn, G., Hillenbrand, C.-D., Kastern, S., Smith, J.A., Nitsche, F.O., Frederichs, T., Wiers, S., Ehrmann, W., Klages, J.P., and Mogollon, J.M., 2017, Evidence for a palaeo-subglacial lake on the Antarctic continental shelf. Nature communications, 8, 15591.

Majewski, W., Bart, P.J., and McGlannan, A.J., 2018, Foraminiferal assemblages from ice-proximal paleo-settings in the Whales Deep Basin, eastern Ross Sea, Antarctica. Palaeogeography, Palaeoclimatology, Palaeoecology, 493, 64-81.

Patterson, M.O., McKay, R., Naish, T., Escutia, C., Jimenez-Espejo, F.J., Raymo, M.E., Meyers, S.R., Tauxe, L., Brinkhuis, H. and IODP Exp 318 Scientists, 2014. Orbital forcing of the East Antarcic ice sheet during the Pliocene and Early Pleistocene. Nature geoscience, 7, 841-847.

Pollard, D., DeConto R.M., and Alley, R.B., 2015. Potential Antarctic Ice Sheet retreat driven by hydrofracturing and ice cliff failure. Earth and Planetary Science Letters, 412, 112-121.

Rae, J.W.B., Burke, A., Robinson, L.F., Adkins, J.F., Chen, T., Cole, C., Greenop, R., Li, T., Littley, E.F.M., Nita, D.C., Stewart, J.A., and Taylor, B.J., 2018, CO2 storage and release in the deep Southern Ocean on millennial to centennial

KOPRI 극지연구소

timescales, Nature, 562, 569-573.

Reinardy, B.T.I., Escutia, C., Iwai, M., Jimenez-Espejo, F.J., Cook, C., Flierdt, T. van de, Brinkhuis, H., 2015. Repeated advance and retreat of the East Antarctic Ice Sheet on thecontinental shelf during the early Pliocene warm period. Palaeogeography, Palaeoclimatology, Palaeoecology, 422, 65–84.

Simkins, L.M., Anderson, J.B., Greenwood, S.L., Gonnermann, H.M., Prothro, L.O., Halberstadt, A.R.W., Stearns, L.A., Pollard, D., DeConto, R.M., 2017, Anatomy of a meltwater drainage system beneath the ancestral East Antarctic ice sheet. Nature Geoscience, 10, 691-697.

Smith, A.M., Woodward, J., Ross, N., Bentley, M.J., Hodgson, D.A., Siegart, M.J., and King, E.C., 2018, Evidence for the long-term sedimentary environment in an Antarctic subglacial lake. Earth and Planetary Science Letters, 504, 139-151.

Subt, C., Yoon, H.I., Yoo, K.C., Lee, J.I., Leventer, A., Domack, E.W., and Rosenheim, B.E., 2017, Sub-ice shelf sediment geochronology utilizing novel radiocarbon methodology for highly detrital sediments. Geochemmistry, Geophysics, Geosystems, 18, 1404-1418.

The IMBIE team, 2018. Mass Balance of the Antarctic Ice Sheet from 1992 to 2017. Nature, 558(7709), 219–22

Weber, M.E., Clark, P.U., Kuhn, G., Timmermann, A., Sprenk, D., Gladstone, R., Zhang, X., Lohmann, G., Menviel, L., Chikamoto, M.O., Friedrich, T., Ohlwein, C., 2014, M illennial- scale var iabi lity in Antarctic ice-sheet discharge during the last deglaciation. Nature, 510, 134-138.

KOPRI 극지연구소



그림 1. "과거 온난기의 서남극 빙상 후퇴 및 해양 순환 변화 연구"의 총 연구 기간 로드맵. 본 과제는 2020-2022년의 연구과제로서 총 2단계 중 1단계에 해당함.

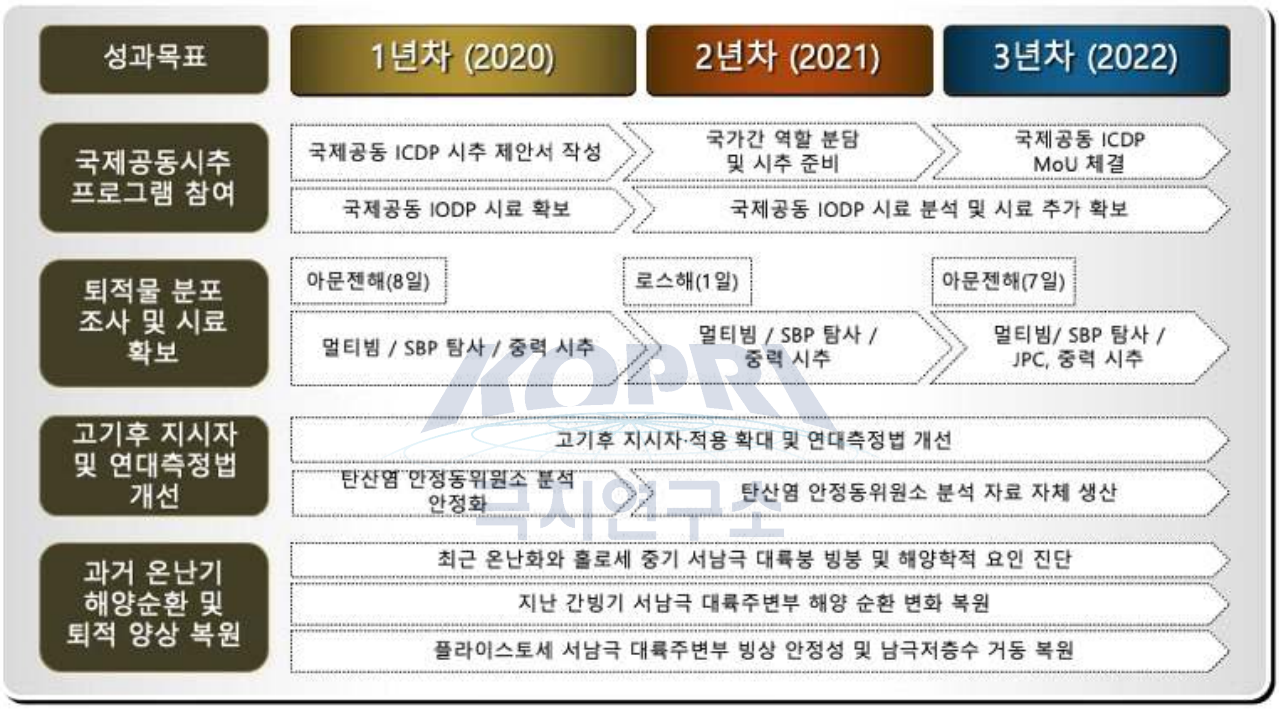


그림 2. 2020-2022년 "과거 온난기의 서남극 빙상 후퇴 및 해양 순환 변화 연구" 로드맵.

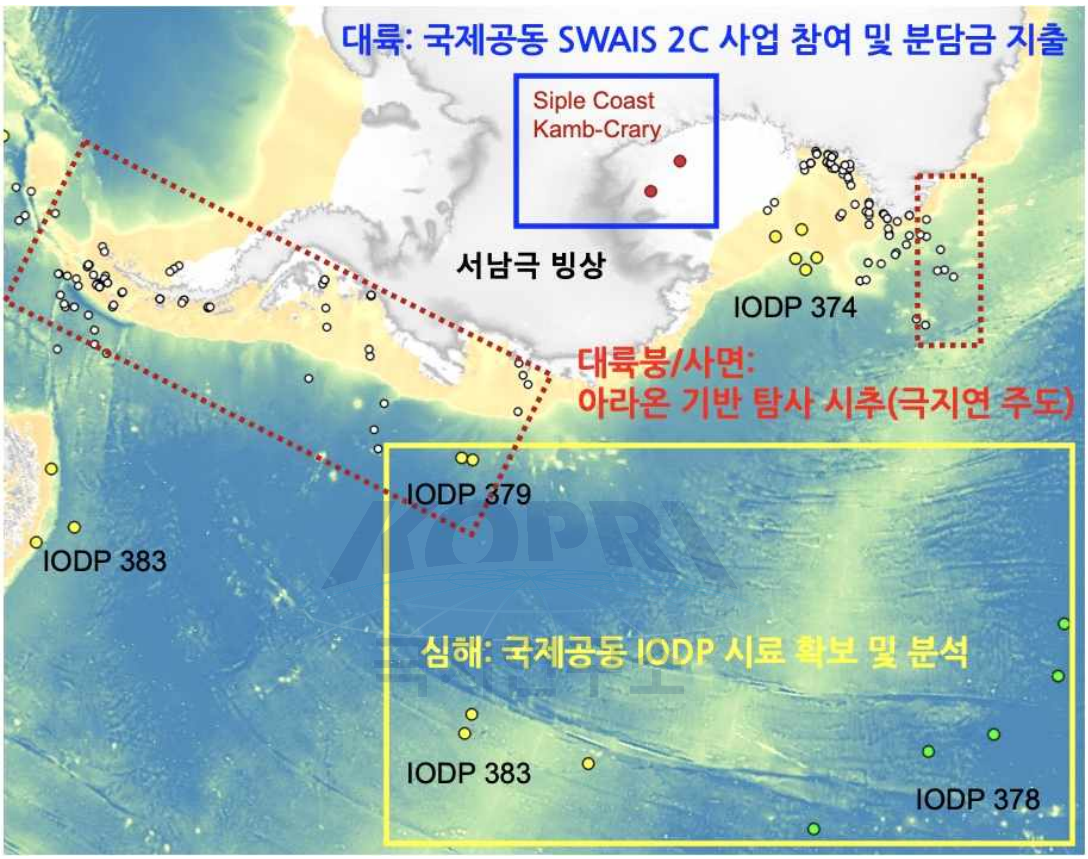


그림 3. 서남극 빙상 주변과 남극해의 퇴적물 시추 위치

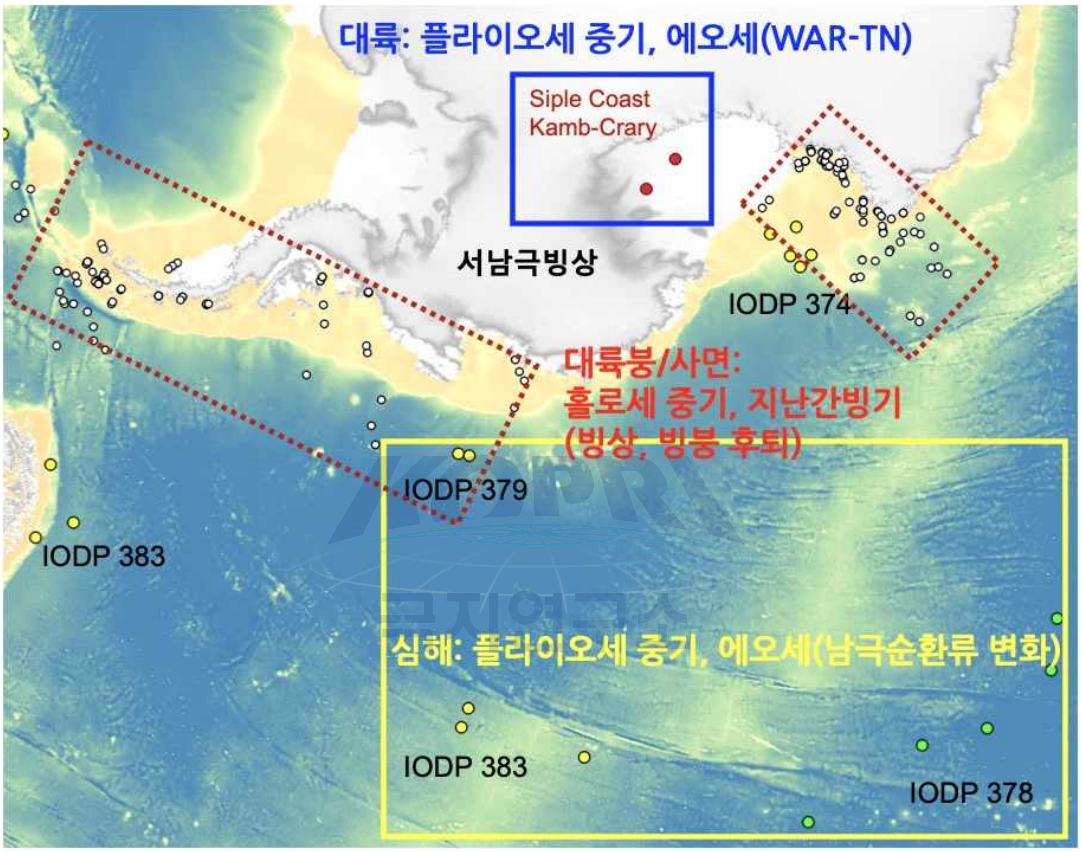


그림 4. 서남극 빙상 주변과 남극해 시추 퇴적물의 중점 연구 및 시기

제 2 장

Sensitivity of the West Antarctic Ice Sheet to +2°C (SWAIS 2C)[1)]

Molly O. Patterson[1], Richard H. Levy[2,3], Denise K. Kulhanek[1,4], Tina van de Flierdt[5], Huw Horgan[3], Gavin B. Dunbar[3], Timothy R. Naish[3], Jeanine Ash[6], Alex Pyne[3], Darcy Mandeno[3], Paul Winberry[7], David M. Harwood[8], Fabio Florindo[9], Francisco J. Jimenez-Espejo[10], Andreas Läufer[11], Kyu-Cheul Yoo[12], Osamu Seki[13,14], Paolo Stocchi[15], Johann P. Klages[16], Jae Il Lee[12], Florence Colleoni[17], Yusuke Suganuma[13], Edward Gasson[18], Christian Ohneiser[19], José-Abel Flores[20], David Try[2], Rachel Kirkman[2], Daleen Koch[2], and the SWAIS 2C Science Team+

[1]Department of Geological Sciences and Environmental Studies, Binghamton University, Binghamton, NY, USA, [2]GNS Science, Lower Hutt, New Zealand, [3]Antarctic Research Centre, Victoria University of Wellington, Wellington, New Zealand, [4]Institute of Geosciences, Christian-Albrecht University of Kiel, Kiel, Germany [5]Department of Earth Science and Engineering, Imperial College London, London, UK, [6]Department of Earth, Environmental and Planetary Sciences, Rice University, Houston, TX, USA, [7]Department of Geological Sciences, Central Washington University, Ellensburg, WA, USA, [8]Department of Earth & Atmospheric Sciences, University of Nebraska-Lincoln, Lincoln, NE, USA, [9]Instituto Nazionale di Geofisica e Vulcanologia, Rome, Italy, [10]Instituto Andaluz de Ciencias de la Tierra, Spanish Research Council (CSIC), Armilla, Spain, [11]Federal Institute for Geosciences and Natural Resources (BGR), Hannover, Germany, [12]Division of Glacial Environment Research, Korea Polar Research Institute, Incheon, Republic of Korea, [13]National Institute of Polar Research, 10-3 Midori-cho, Tachikawa, Tokyo, Japan, [14]Institute of Low Temperature Science, Hokkaido University, Sapporo, Japan, [15]Department of Coastal Systems, NIOZ Royal Netherlands Institute for Sea Research, Den Burg, the Netherlands, [16]Alfred Wegener Institute, Helmholtz Centre for Polar and Marine Research, Bremerhaven, Germany, [17]Istituto Nazionale di Oceanografia e Geofisica Sperimentale, Trieste, Italy, [18]School of Geographical Sciences, University of Bristol, Bristol, UK, [19]Department of Geology, University of Otago, Dunedin, New Zealand

Abstract: The West Antarctic Ice Sheet (WAIS) presently holds enough ice to raise global sea

1) 이 연구 결과는 다음의 논문으로 출판되었음: Patterson, M. et al. (2022). "Sensitivity of the West Antarctic Ice Sheet to +2℃ (SWAIS 2C)." Scientific Drilling 30: 101-112.

level by 4.3 m if completely melted. The unknown response of the WAIS to future warming remains a significant challenge for numerical models in quantifying predictions of future sea level rise. Sea level rise is one of the clearest planetwide signals of human-induced climate change. The Sensitivity of the West Antarctic Ice Sheet to a Warming of 2℃ (SWAIS 2C) Project aims to understand past and current drivers and thresholds of WAIS dynamics to improve projections of the rate and size of ice sheet changes under a range of elevated greenhouse gas levels in the atmosphere as well as the associated average global temperature scenarios to and beyond the +2℃ target of the Paris Climate Agreement. Despite efforts through previous land and ship-based drilling on and along the Antarctic margin, unequivocal evidence of major WAIS retreat or collapse and its causes has remained elusive. To evaluate and plan for the interdisciplinary scientific opportunities and engineering challenges that an International Continental Drilling Program (ICDP) project along the Siple coast near the grounding zone of the WAIS could offer (Fig. 1), researchers, engineers, and logistics providers representing 10 countries held a virtual workshop in October 2020. This international partnership comprised of geologists, glaciologists, oceanographers, geophysicists, microbiologists, climate and ice sheet modelers, and engineers outlined specific research objectives and logistical challenges associated with the recovery of Neogene and Quaternary geological records from the West Antarctic interior adjacent to the Kamb Ice Stream and at Crary Ice Rise. New geophysical surveys at these locations have identified drilling targets in which new drilling technologies will allow for the recovery of up to 200 m of sediments be- neath the ice sheet. Sub-ice-shelf records have so far proven difficult to obtain but are critical to better constrain marine ice sheet sensitivity to past and future increases in global mean surface temperature up to 2℃ above pre-industrial levels. Thus, the scientific and technological advances developed through this program will enable us to test whether WAIS collapsed during past intervals of warmth and determine its sensitivity to a +2℃ global warming threshold (UNFCCC, 2015).

1. Introduction

Human activities are estimated to have caused an increase in average surface temperature of ~1.0℃ above pre-industrial levels (IPCC, 2018, 2021). Global temperature increase is likely to reach +1.5℃ relative to pre-industrial levels between 2030 and 2052 if it continues to rise at the current rate (IPCC, 2018, 2021). Warming of 2℃ could be reached as early as 2039 or as late as the mid-2060s depending on green-house gas emissions pathways (Tebaldi et al., 2021). Global mean sea level (GMSL) has already increased by ~22cm since 1880 (IPCC, 2013). The rate of sea level rise (SLR) has been accelerating over the last several decades due to ocean thermal expansion and increased ice mass loss from Greenland and

Antarctica (Velicogna et al., 2014; Nerem et al., 2018; Shepherd et al., 2018; IMBIE team, 2018) and is currently ~3.6 mm yr^{-1} (Oppenheimer and Alley, 2016). The Intergovernmental Panel on Climate Change (IPCC) has forecast a likely range of SLR between 0.29 and 1.1 m by 2100 (Oppenheimer and Alley, 2016). However, uncertainty in these estimates remains, and multiple new lines of scien- tific evidence indicate a substantially higher GMSL rise is possible due to relatively large contributions from Antarctica's ice sheets (Bamber and Aspinall, 2013; Kopp et al., 2014, 2017; DeConto et al., 2021; Edwards et al., 2021). The range of estimates is partly due to uncertainty regarding glacial processes including marine ice cliff instability (Pollard et al., 2015; DeConto and Pollard, 2016; Edwards et al., 2019; DeConto et al., 2021; Bassis et al., 2021; Golledge and Lowry, 2021; Crawford et al., 2021) and mantle and ice sheet grounding zone dynamics associated with glacial isostatic adjustment (Catania et al., 2012; Gomez et al., 2015; Kingslake et al., 2018; Whitehouse et al., 2019). Efforts to improve our knowledge of glacial processes and dynamics from modern observations and reconstructions of past ice sheet behavior aim to reduce uncertainty in future pro- jections and are a major objective of the Sensitivity of the West Antarctic Ice Sheet to a Warming of 2℃ (SWAIS 2C) Project.

Response of the West Antarctic Ice Sheet (WAIS) to climate warming is the focus of several major national and international science programs including the International Thwaites Glacier Collaboration (https://thwaitesglacier.org/ about/itgc, last access: 10 February 2022), the Subglacial Antarctic Lakes Scientific Access (SALSA) Project (Priscu et al., 2021), and SWAIS 2C. This focus on the WAIS is due, in part, to satellite observations that demonstrate the WAIS is losing mass at an accelerating rate (e.g., Bamber et al., 2018; Shepherd et al., 2018; IMBIE team, 2018), with the potential for future melt to contribute 4.3 m to global sea level (Fretwell et al., 2013). WAIS is considered highly sensitive to future warming because much of it is grounded ~2500 m below sea level, and its associated floating ice shelves are exposed to progressively warming ocean waters.

Quantifying the response of the WAIS to future warming remains a significant challenge. Direct physical evidence of WAIS response in the past, when global mean temperatures were 2℃ warmer than pre-industrial times, offers con straints that will help reduce uncertainty. The international SWAIS 2C Project aims to obtain such records from the West Antarctic interior (Fig. 1) to understand past and current drivers of WAIS dynamics and identify thresholds in the system. Outcomes will improve projections of the rate and size of ice sheet changes under a range of elevated green house gas levels in the atmosphere and associated average global temperature scenarios up to and beyond the 2℃ target of the Paris Climate Agreement (UNFCCC, 2015). The SWAIS 2C Project consists of an interdisciplinary group of engineers, geologists, glaciologist, geophysicists, oceanographers, microbiologists, and climate and ice sheet modelers collaborating to enhance our understanding of (1) WAIS

dynamics during past intervals of warm climate and (2) ice, atmosphere, solid Earth, and ocean interactions and feedbacks at the WAIS grounding zone and the margins of the Ross Ice Shelf cavity through the instrumental period. This information will help determine the likely future response of the WAIS to projected warming and identify environmental implications for the Ross Sea sector and far-field consequences. The international partnership currently comprises 10 nations (Australia, Germany, Italy, Japan, Netherlands, New Zealand, South Korea, Spain, the United Kingdom, and the United States) but is still developing, with participation contingent on successful outcomes from national and inter- national proposals.

2. SWAIS 2C: testing ice sheet sensitivities to a +2℃ global warming threshold

Integral to the SWAIS 2C Project's overall goal is the recov- ery of new Neogene and Quaternary sedimentary archives from beneath the Ross Ice Shelf at the grounding zone of the WAIS (Fig. 1). Because the magnitude of climate warming projected for the next century has not been experienced by Earth during the instrumental period, paleocli- mate reconstructions of WAIS response during time intervals of analogous warmth to what is projected in the future, such as Pleistocene "super-interglacials" and the warmer than present Pliocene and Miocene (e.g., Melles et al., 2012; McKay et al., 2012; Levy et al., 2019), will provide critical insights into its future behavior (Retzlaff et al., 1993; Conway et al., 2002; Joughin and Tulaczyk, 2002; Mitrovica et al., 2009; Joughin et al., 2012; Hay et al., 2014). When integrated with numerical modeling experiments, modern process studies, and biological data, the new drill core data will allow us to examine the influence of climate dynamics and solid Earth processes in driving ice sheet fluctuations. Thus, the SWAIS 2C Project proposes to quantify the Antarctic ice sheet (AIS) contribution to past (with drilling) and future (with modeling) sea level change, through an improved understanding of climate, ocean, cryosphere, biosphere, and solid Earth interactions and feedbacks, so that decision-makers can better anticipate and assess risk associated with SLR and thus make more informed decisions around mitigation pathways. Thus, these unique data archives of late Cenozoic paleoenvironmental history will address the following key question: what can we learn from past "green-house" conditions in Earth's climate to better anticipate future changes in the hydrological and biogeochemical cycle? This is associated with theme 4, Environmental Change, in the International Continental Scientific Drilling Program (ICDP) 2020-2030 Science Plan.

3. Drill sites

The international SWAIS 2C Project plans to drill at two sites: the first adjacent to the grounding zone at Kamb Ice Stream (November 2022) and the second at Crary Ice Rise (November 2023) (Fig. 1). Both sites are to be accessed by overland traverse using the South Pole Over-ice Traverse (SPOT) route and new routes proved by Antarctica New Zealand. Both sites also offer stable drilling platforms as the Kamb Ice Stream has been stagnant for the past ~150 years (e.g., Retzlaff and Bentley, 1993), and Crary Ice Rise stag- nated around ~1 kyr BP (Bindschadler et al., 1990; Catania et al., 2012; Hillebrand et al., 2021).

The Kamb Ice Stream site (KIS-3) is located ~15km seaward of the contemporary grounding line, where sediments are overlain by an ocean cavity and the floating Ross Ice Shelf. KIS-3 provides the opportunity to drill a modern ice stream environment from a stable drilling platform as the grounding line is thought to have migrated past the site since stagnation (Horgan et al., 2017). Three seasons of over- snow geophysics and one sub-ice-shelf direct-access program have provided site survey data, including over 70 km of multichannel seismic data. Over-snow seismic data imaged a thin water column (0-60m) between the ice-shelf base and the seafloor (Fig. 2). Below the seafloor, two units are identified with the upper unit (Unit K-1) characterized by generally homogenous low-amplitude internal reflectivity with occasional high-amplitude horizontal to sub-horizontal internal reflectivity. The unit appears undeformed, and ice sheet modeling experiments suggest negligible glacial erosion at the site. We anticipate that this unit is of Pleistocene age based on the presence of reworked Neogene and Pleistocene diatoms recovered in surface sediments upstream of the drill site. The lower boundary of Unit K-1 is a high-amplitude positive-polarity reflector (Horizon D) at 130-180 m below the seafloor (at 2000 m s^{-1}) and is easily rec- ognized throughout the survey region as well as beneath the adjacent Whillans Ice Stream (Fig. 4) (Horgan et al., 2013; Luthra et al., 2016). Reflectivity within the overlying unit is generally disconformable with Horizon D. The polarity and amplitude of Horizon D suggest the upper sedimentary unit is underlain by more lithified sediment (Unit K-2). Horizon D is likely erosional and may reflect initiation of a more ex- tensive and persistent WAIS, potentially coinciding with the marine isotope stage M2 glaciation event (3.312-3.264 Ma) recorded at AND-1B (McKay et al., 2012).

The Crary Ice Rise site (CIR-1) overlies grounded ice that is frozen at the bed. CIR-1 is downstream of Whillans Ice Stream, adjacent to Kamb Ice Stream, and accounts for over 50% of the buttressing of the Whillans Ice Stream (Retzlaff et al., 1993). Recent geophysical surveying at CIR collected over 15km of seismic data that are interpreted to include a Holocene grounding zone wedge (GZW) deposit (Unit C-1) overlying gently dipping strata (Unit C-2) (Fig. 3). The wedge-shaped sequence (Unit C-1) occurs above a regional disconformity (Horizon H) and is characterized by discontinuous (chaotic) reflectors and velocities estimated at 2200 m s^{-1}. Several hundred meters of stratified and lithified sediment

characterize Unit C−2, and while the age of this unit is unknown, we suggest that the gently dipping layers rep− resent glacial−interglacial cycles comprising glacial till and open marine strata deposited during the Neogene. This hypothesis is based on sediments recovered from Crary Ice Rise during hot−water drilling efforts in the 1980s, where Neogene marine diatoms (Scherer et al., 1988) were recovered, sug− gesting grounding line retreat and open−water conditions as recent as the Pliocene (~3 Ma) (Scherer, 1991). Venturelli et al. (2020) demonstrated that nearby sediments and upstream deposits reflect periods of sub−ice−shelf deposition as recent as the mid−Holocene.

While there is an extensive network of seismic reflection surveys around the Antarctic margin and across the Ross Sea region, these marine data cannot be directly correlated to our proposed sub−glacial drill sites as over−ice/land−based surveys are logistically challenging, and relevant data do not exist. However, we postulate that sedimentary sequences re− covered in the ANDRILL cores (Naish et al., 2009; Levy et al., 2016) and from the central Ross Sea (Hayes et al., 1975a, b; McKay et al., 2019) extend south beneath the Ross Ice Shelf and WAIS (Fig. 4). This hypothesis is based on (1) the character of the seismic sequences we have imaged at the proposed drill sites and, more specifically, the regionally extensive seismic reflector, Horizon D, which likely separates Neogene and Quaternary strata; and (2) reworked late Neogene and Quaternary diatoms recovered in subglacial sediments at CIR, Whillans Ice Stream, and KIS. Recovery of these new interior WAIS stratigraphic records will provide the southern anchor of a drill core transect in the Ross Sea Embayment (McKay et al., 2016), connecting the Ross Sea continental shelf (Naish et al., 2009; Levy et al., 2016; Fielding, 2018; McKay et al., 2019) to the West Antarctic interior, thereby providing a more coherent understanding of the processes regulating WAIS dynamics.

4. New capabilities in drilling subglacial sediment

Engineers from New Zealand's Antarctic Research Centre Science Drilling Office have developed a hot−water/rock drilling system capable of recovering ~200 m of sediment in places where the combined depth of the ice shelf (or sea ice) and water column is <1000m thick. The Antarctic Intermediate Depth Drilling (AIDD) system is housed in a tent that permits all−weather operation (Fig. 5). The new "light−weight" drilling system is designed for long−distance ice traverse. The sediment/rock drill (Multipower Products Ltd MP1000) is an industry−standard wireline system. Soft sediment coring will use two systems: a hydraulic piston corer (HPC) and a punch corer. Hard rock drilling will require diamond−bit rotary coring technology. Thus, cores will be recovered using three different approaches depending on lithology: (1) a hydraulic piston corer inside an NQ−sized drill rod (bit internal diameter, ID

– 57.2 mm, outer tube bit throat ID – 51 mm), the preferred coring tool which will be used until refusal when it will be supplemented with punch coring; (2) rotary coring with NQ2 drill string (bit ID – 50.5 mm); and (3) rotary coring with a BQTK–sized rod (bit ID – 40.7 mm), which may be used in harder lithologies and may be used to cut the NQ drill string if necessary.

The combined rig, drill, and casing package weighs ~30 t, making it feasible to deploy within the constraints of existing Antarctic science support programs, with a much smaller logistical footprint than previous Antarctic drilling programs (i.e., ANDRILL; Falconer et al., 2008). This drill system's small logistical footprint will utilize a 24 h drilling operation to maximize core recovered in the short (~14 d) drilling window.

5. The SWAIS 2C Project approach and challenges

Several international workshops have been held to develop the SWAIS 2C Project and to encourage members of the international science community to join. Most recently in October 2020, researchers, engineers, and logistics providers from partner nations attended a 4h virtual international workshop to further develop the project. Discussions covered project goals, ongoing efforts of site characterization, performance capabilities of the drilling system, logistics, and operational support required to carry out field work, structure and timing of off–ice science workshops, required scientific disciplines for addressing research objectives, potential scheduling and logistical implications due to COVID–19, and numerical modeling experiments. During the workshop, it was acknowledged that areas in which further project development needed to occur centered around downhole logging technologies (e.g., spectral gamma, resistivity, temperature) that are compatible with the new AIDD system and inclusion of research that aims to address outstanding questions in the field of microbiology. In the months following the virtual workshop, science team members carried out detailed discussions with the staff at the ICDP Operational Support Group (OSG) and the Leibniz Institute for Applied Geophysics (LIAG) regarding downhole logging challenges, and additional science team members have been included to address investigations in microbiology. Here we provide an overview of the SWAIS 2C Project goals and approach that were outlined during the virtual workshop but also provide more detail on areas where shortcomings were identified but have since been addressed.

Currently, nearly 40 % of WAIS discharge is through fastflowing ice streams along the Siple coast, in the region of the KIS and CIR (Price et al., 2001). Over decadal, centennial, and millennial timescales, the velocity of these ice streams has been highly variable (Bindschadler et al., 1990; Retzlaff et al., 1993; Joughin et al., 2002; Conway et al., 2002;

Joughin and Tulaczyk, 2002; Hulbe and Fahnestock, 2007; Joughin et al., 2012). Currently there is a major gap in our understanding surrounding the negative feedbacks associated with dynamically relevant topographic features (i.e., pinning points), such as subglacial ice rises and grounding zone deposits, and thus these are poorly represented in ice-sheet models. Therefore, the temporal range of a Last Glacial Maximum (~21 ka) to Recent record (i.e., the last 21 000 years) would provide a wealth of information concerning long-term grounding line dynamics. Paleoenvironmental records from the Pleistocene interglacials would provide evidence of WAIS response to climatic conditions when temperatures were 1-2℃ warmer than pre-industrial times. Analysis of Pliocene and Miocene sediment records will reveal the duration of marine ice sheet cover during previous intervals of time when CO^2 levels were like those projected for the coming decades if we fail to meet greenhouse gas emission targets that aim to keep global average temperatures below 2℃ warming. Proxy-based reconstructions of WAIS response during these past warm times will be integrated with numerical modeling experiments and modern process studies to provide critical insight into WAIS behavior (e.g., Hay et al., 2014). These new paleoenvironmental reconstructions from the Neogene and Quaternary will directly address the following four guiding hypotheses: (1) Ice-solid-Earth feedbacks influenced ice dynamics along the Siple coast on a multi-millennial timescale trajectory dur- ing the Holocene; (2) ocean temperatures and circulation pat- terns are the key governing factor in driving WAIS dynamics during the warmer-than-present late Quaternary super- interglacials; (3) marine-based ice sheets were highly dynamic and periodically expanded and retreated across the Siple coast during the mid-Pliocene to late Pliocene (3.3- 2.6 Ma) but did not advance across the continental shelf dur- ing the early Pliocene (a marine-based WAIS could not grow as climate was too warm prior to the M2 glaciation); and (4) a smaller-than-present terrestrial AIS during the Miocene Climate Optimum (MCO) produced by a combination of high atmospheric CO^2 and tectonic land subsidence resulted in an extensive highly productive shallow marine sea, that sub- sequently drew down CO^2 and culminated in global cooling and Antarctic Ice Sheet expansion during the middle Miocene Climate Transition (MMCT). These new cores will provide the southern end (most proximal to the ice grounding zone) of a transect of recent drill holes in the Ross Embay- ment (e.g., ANDRILL program and International Ocean Discovery Program (IODP) Expedition 374). Furthermore, the new SWAIS 2C sites will serve as a connection to drill sites in the Amundsen Sea sector of West Antarctica (PS104 Expedition "ASE-MeBo", IODP Expedition 379), and the objectives are complementary to the International Thwaites Glacier Project. Ultimately, this land-to-ocean transect across the WAIS will provide a broader understanding of ice sheet history and more accurate predictions of future change.

The small diameter of our new drilling system presents a technical challenge to traditional downhole logging as there are few "off-the-shelf" logging tools slim enough to be

deployed through the drill bit into the open bore-hole. The short drilling/logging window means duration is also an important factor in our logging strategy. Furthermore, the shallow holes (<200 m b.s.f.) and the likely unconsolidated nature of the surrounding sediment mean logging in an open hole heightens the risk of losing logging tools in the hole. Our approach to downhole logging is therefore to use the ICDP Operational Support Group (OSG) "slimhole" Memory Logging tools (sondes) (iMLS) (https://www.icdp-online.org/fileadmin/icdp/services/img/Logging/OSG_Slimhole_Sondes_Specs_pics_2019-05.pdf, last access: 10 February 2022). These are self-contained, and no logging winch is required for deployment. While a new version of the iMLS depth measuring device (DMD) needs to be built, the existing spectral gamma (mSGR) and resistivity (mDIL) tools can be used without modification with an NQ-sized rotary bit. Other memory tools (sonic (mBCS) and magnetic susceptibility (mMS)) are too big to pass through the NQ rotary bit, although the mBCS can be used with the slightly wider NQ-hydraulic piston corer bit in place. Logging occurs as the NQ pipe is pulled from the hole upon a bit change or upon completion of drilling, with the MEMBAT module and mSGR (possibly mBCS) and mDIL tools assembled as a string. This approach saves critical time and will allow us to log the hole without casing. If time and hole conditions permit, it may be also possible to deploy four Leibniz Institute for Applied Geophysics (LIAG) wireline tools: resistivity, magnetic susceptibility, acoustic televiewer, and borehole mud temperature and salinity.

Temperature gradients will be measured in the seafloor at both KIS-3 and CIR-1. These measurements will allow for important geothermal flux and thermal transients to be determined. Heat flow is presently only determined by one shallow (<3 m) probe measurement at Whillans Ice Stream and one at KIS, yet it is an important variable for calculating sub-ice shelf conditions for sliding (or "freeze-on"). At CIR we will also utilize recent advances in fiber optic distributed temperature sensor technology to instrument the borehole throughout the ice thickness and into the sediment after drilling. This technology has been used successfully in the region and is an inexpensive alternative to thermistor strings (Tyler et al., 2013; Fisher et al., 2015). Vertical temperature profiles through the ice will allow the numerical modeling team to validate and refine previous estimates of geothermal heat flux and CIR stagnation time.

Given the desire for a small on-ice project footprint, on-ice science analysis will be limited to X-ray imaging, smear slide analysis, porewater geochemistry, and microbiology sampling. Fast-track samples from core cutter material will be sent off-ice for paleontological assessment prior to off-ice science workshops. Researchers from partner countries will meet in Dunedin, New Zealand, at the Otago Repository for Core Analysis (ORCA) facility, housed at the University of Otago, for initial core characterization and sampling following each drilling season and operate in a similar fashion to a typical IODP expedition and post-cruise

sampling workshop. At the end of initial characterization and sampling, sediment cores will be transported to the Oregon State University Marine and Geology Repository (OSU-MGR) for long-term storage and made available to the scientific community after a 2-year moratorium period. Our research methodology is built around an integrated data-model approach that utilizes paleoclimate data to improve the skill of Antarctic climate and ice sheet models by simulating past Antarctic environmental conditions and the consequences for global sea level (e.g., Naish et al., 2007; Harwood et al., 2008-2009; Pol- lard and DeConto, 2009; Naish et al., 2009; Golledge et al., 2015; DeConto and Pollard, 2016; Gasson et al., 2016; Levy et al., 2016). This integrated data-model approach will improve understanding of climate, ocean, cryosphere, and solid Earth interactions. This knowledge can reduce uncertainty in sea level projections, thereby allowing coastal communities to anticipate and assess hazards and risks associated with sea level rise under different emissions pathways and to evaluate the efficacy of adaption strategies.

There are very few studies on the deep biosphere from beneath Antarctica's ice shelves and at grounded ice rises (e.g., Carr et al., 2013). Recovery of subglacial material along the Siple coast region provides an unprecedented opportunity to extend our knowledge of the deep biosphere and its biogeochemistry across the Ross Sea and will build upon earlier work from ANDRILL (Carr et al., 2013), WISSARD (Christner et al., 2014; Vick-Majors et al., 2020), and ongoing work from IODP Expedition 374 (Ash et al., 2019) and the United States-based SALSA (Subglacial Antarctic Lakes Scientific Access) projects (Hawkings et al., 2020; Priscu et al., 2021). Specifically, determining the taxonomy and activity of both living and inactive microbial populations in sediments will provide insights to modern element cycling and past environmental conditions. Key questions surrounding the discipline of microbiology that could be addressed from the SWAIS 2C Project and extend beyond the geological studies include the following: (1) which organisms characterize the microbial communities and the structure of microbial food webs in the extreme subglacial and sub-ice-shelf environment? (2) What is the functional potential of the microorganisms in these environments, which metabolic pathways do they encode, and how do they contribute to major and trace element cycling and carbon burial? (3) How do microbial communities respond to varying environmental conditions (e.g., temperature) and inputs in organic matter (i.e., open vs. ice-covered conditions, discharge from subglacial lakes) over time? (4) What do inactive members of subsurface communities like cysts, spores, and other inactive cells, as well as extracellular DNA, tell us about past environmental conditions?

Five of the SWAIS 2C partner nations have secured national funding to participate in the project, and the SWAIS 2C Project Team was recently awarded funds to support drilling through the ICDP. Furthermore, several national-level proposals are currently under review. We plan to begin drilling at the KIS site in December 2022. For more information regarding

the SWAIS 2C Project, contact the authors of this article.

Data availability. Seismic data presented in this paper can be accessed through the DMC at IRIS and at http://ds.iris.edu/mda/ 19−016/ (IRIS consortium, 2022) or by directly contacting coauthors Huw Horgan and Paul Winberry for access to our infor− mation regarding seismic data.

Team list. A list of science team members for these projects was assembled following an open call for participation at a PAIS (Past Antarctic Ice Sheet) workshop at the XIII International Symposium on Antarctic Earth Sciences in Incheon, Republic of Korea, in July 2019. We note that this list may not be comprehensive, and additional scientists may join the science team during planning and later stages of each project and as funding from international partners is determined. The current SWAIS 2C science team is as follows (last name alphabetical order): Leanne Armand (Australia National University), Jeanine Ash (Rice University), Jacqueline Austermann (Lamont Doherty Earth Observatory), Catherine Beltran (University of Otago), Mike Bentley (Durham University), Craig Cary (University of Waikato), Jason Coenen (Northern Illinois University), Ester Colizza (University of Trieste), Florence Colleoni (Istituto Nazionale di Oceanografia e di Geofisica Sperimentale), Giuseppe Cortese (GNS Science), Laura Crispini (Università di Genova), Rob DeConto (University of Massachusetts, Amherst), Paola Del Carlo (Istituto Nazional di Geofisica e Vulcanologia), Alessio Di Roberto (Istituto Nazional di Geofisica e Vulcanologia), Justin Dodd (Northern Illinois University), Bella Duncan (Antarctic Research Centre, VUW), Gavin B. Dunbar (Antarctic Research Centre, VUW), Olaf Eisen (Alfred We− gener Institute, Helmholtz Centre for Polar and Marine Research), José−Abel Flores (Universidad de Salamanca), Fabio Florindo (Istituto Nazional di Geofisica e Vulcanologia), Ed Gasson (University of Exeter), Karsten Gohl (Alfred Wegener Institute, Helmholtz Centre for Polar and Marine Research), Nick Golledge (Antarctic Research Centre, VUW), David M. Harwood (University of Nebraska−Lincoln), Huw Horgan (Antarctic Research Centre, VUW), Angelika Humbert (Alfred Wegener Institute, Helmholtz Centre for Polar and Marine Research), Francisco J. Jimenez−Espejo (Instituto Andaluz de Ciencias de la Tierra), Liz Keller (GNS Science), Jung−Hyun Kim (Korean Polar Research Institute), Sunghan Kim (Korean Polar Research Institute), Jonathan Kingslake (Lamont Do− herty Earth Observatory), Johann P. Klages (Alfred Wegener Institute, Helmholtz Centre for Polar and Marine Research), Nikola Koglin (BGR), Jochem Kück (GFZ Potsdam German Research Center for Geosciences), Denise K. Kulhanek (Binghamton University, SUNY; Christian−Albrecht University of Kiel), Andreas Läufer (BGR), Jae Il Lee (Korean Polar Research Institute), Amy Leven− ter (Colgate University), Richard H. Levy (GNS Science/Victoria University of Wellington), Frank Lisker (Universität Bremen), Gerrit Lohmann

(Alfred Wegener Institute, Helmholtz Centre for Polar and Marine Research), Dan Lowry (GNS Science), Rob McKay (Antarctic Research Centre, VUW), Gesine Mollenhauer (Alfred Wegener Institute, Helmholtz Centre for Polar and Marine Re- search), Juliane Müller (Alfred Wegener Institute, Helmholtz Centre for Polar and Marine Research), Tim Naish (Antarctic Research Centre, VUW), Pierre Offre (Royal Netherlands Institute for Sea Research), Christian Ohneiser (University of Otago), Molly O. Patterson (Binghamton University), Joe Prebble (GNS Science), Sonia Sandroni (Museo Nazionale dell'Antartide, Università di Siena), Francesca Sangiorgi (Utrecht University), Osamu Seki (Hokkaido-University), Louise Sime (British Antarctic Survey), James Smith (British Antarctic Survey), Anja Spang (Royal Netherlands Institute for Sea Research), Paolo Stocchi (Royal Netherlands Institute for Sea Research), Yusuke Suganuma (National Institute of Polar Research), Tina van de Flierdt (Imperial College London), Ryan Venturelli (Tulane University), Paul Winberry (Central Washington University), Thomas Wonik (Leibniz Institute for Applied Geophysics), Kiho Yang (Pusan National University), and Kyu-Cheul Yoo (Korean Polar Research Institute).

Author contributions. MOP, RHL, DKK, DT, and RK organized and facilitated the workshop. MOP, RHL, DKK, TvdF, HH, GBD, TRN, PW, DMH, FF, FJJE, AL, KCY, OS, PS, JPK, JIL, FC, YS, EG CO, JAF, and SWAIS 2C Science Team members contributed to developing the scientific objectives of the SWAIS 2C Project presented in the manuscript. GBD and AL contributed to downhole logging. JA contributed to the microbiology project objectives. AP and DM provided the information presented on the drilling system. PW and HH contributed to site survey information. DT, RK, and DK have managed the project and helped facilitate manuscript development. Disclaimer. Publisher's note: Copernicus Publications remains neutral with regard to jurisdictional claims in published maps and institutional affiliations.

Acknowledgements. Richard H. Levy, Timothy R. Naish, Huw Horgan, Gavin B. Dunbar, Alex Pyne, Darcy Mandeno, Christian Ohneiser, David Try, and Rachel Kirkman acknowledge funding support from the New Zealand Ministry of Business and Innovation and Employment through the Antarctic Science Platform contract (ANTA1801) Antarctic Ice Dynamics Project (ASP-021-01). CIR seismic data collection was supported by US NSF grant 1443552 to Paul Winberry, Howard Conway, and Michelle Koutnik. Molly O. Patterson, Denise K. Kulhanek, Jeanine Ash, Paul Winberry, and David M. Harwood acknowledge funding support by US NSF grants 2035035, 2034999, 2035138, and 2034883.

Financial support. This research has been supported by the New Zealand Ministry of Business and Innovation and Employ- ment through the Antarctic Science Platform contract (ANTA1801) Antarctic Ice Dynamics Project (grant no. ASP-021-01) and the US NSF (grant nos. 1443552, 2035035, 2034999, 2035138, and 2034883).

기온 2도 온난화에 따른 서남극 빙상 민감도 (SWAIS 2C)

Molly O. Patterson[1], Richard H. Levy[2,3], Denise K. Kulhanek[1,4], Tina van de Flierdt[5], Huw Horgan[3], Gavin B. Dunbar[3], Timothy R. Naish[3], Jeanine Ash[6], Alex Pyne[3], Darcy Mandeno[3], Paul Winberry[7], David M. Harwood[8], Fabio Florindo[9], Francisco J. Jimenez-Espejo[10], Andreas Läufer[11], Kyu-Cheul Yoo[12], Osamu Seki[13,14], Paolo Stocchi[15], Johann P. Klages[16], Jae Il Lee[12], Florence Colleoni[17], Yusuke Suganuma[13], Edward Gasson[18], Christian Ohneiser[19], José-Abel Flores[20], David Try[2], Rachel Kirkman[2], Daleen Koch[2], and the SWAIS 2C Science Team+

[1]Department of Geological Sciences and Environmental Studies, Binghamton University, Binghamton, NY, USA, [2]GNS Science, Lower Hutt, New Zealand, [3]Antarctic Research Centre, Victoria University of Wellington, Wellington, New Zealand, [4]Institute of Geosciences, Christian-Albrecht University of Kiel, Kiel, Germany [5]Department of Earth Science and Engineering, Imperial College London, London, UK, [6]Department of Earth, Environmental and Planetary Sciences, Rice University, Houston, TX, USA, [7]Department of Geological Sciences, Central Washington University, Ellensburg, WA, USA, [8]Department of Earth & Atmospheric Sciences, University of Nebraska-Lincoln, Lincoln, NE, USA, [9]Instituto Nazionale di Geofisica e Vulcanologia, Rome, Italy, [10]Instituto Andaluz de Ciencias de la Tierra, Spanish Research Council (CSIC), Armilla, Spain, [11]Federal Institute for Geosciences and Natural Resources (BGR), Hannover, Germany, [12]Division of Glacial Environment Research, Korea Polar Research Institute, Incheon, Republic of Korea, [13]National Institute of Polar Research, 10-3 Midori-cho, Tachikawa, Tokyo, Japan, [14]Institute of Low Temperature Science, Hokkaido University, Sapporo, Japan, [15]Department of Coastal Systems, NIOZ Royal Netherlands Institute for Sea Research, Den Burg, the Netherlands, [16]Alfred Wegener Institute, Helmholtz Centre for Polar and Marine Research, Bremerhaven, Germany, [17]Istituto Nazionale di Oceanografia e Geofisica Sperimentale, Trieste, Italy, [18]School of Geographical Sciences, University of Bristol, Bristol, UK, [19]Department of Geology, University of Otago, Dunedin, New Zealand

[20]Department of Geology, University of Salamanca, Salamanca, Spain

요약: 서남극 빙상은 현재 완전히 녹으면 지구 해수면을 4.3m 상승시킬 수 있는 충분한 얼음을 보유하고 있다. 미래 온난화에 대한 서남극 빙상의 알려지지 않은 반응은 미래 해수면 상승 예측을 정량화하는 수치 모델에 중요한 과제로 남아 있다. 해수면 상승은 인간이 유발한 기후 변화의 가장 명확한 전 지구적 신호 중 하나이다. 2℃ 온난화에 대한 서남극 빙상의 민감도(SWAIS 2C) 프로젝트는 서남극 빙상 역학의 과거 및 현재 동인 및 임계값을 이해하여 파리 기후 협약의 +2℃ 목표를

초과하는 관련 평균 지구 온도 시나리오뿐만 아니라 대기 내 상승된 온실 가스 범위에서 빙상 변화의 속도 및 크기 예측을 개선하는 것을 목표로 한다. 이전에 남극 주변부와 주변을 따라 육상 및 선박 기반 시추를 통한 노력에도 불구하고 주요 서남극 빙상 후퇴 또는 붕괴와 그 원인에 대한 명확한 증거는 아직 파악하기 어렵다. 서남극 빙상 지반 기저 근처의 Siple 해안을 따라 ICDP (International Continental Drilling Program) 프로젝트가 제공할 수 있는 학제 간 과학적 기회와 엔지니어링 과제를 평가하고 계획하기 위해서 10개를 대표하는 연구원, 엔지니어 및 물류 제공업체 국가들은 2020년 10월 가상 워크숍을 개최하였다 (그림 1). 지질학자, 빙하학자, 해양학자, 지구물리학자, 미생물학자, 기후 및 빙상 모델학자, 엔지니어로 구성된 이 국제 파트너십은 신생대 및 제4기 지질 기록의 복구와 관련된 특정 연구 목표 및 물적 지원 문제를 설명하였다. Kamb Ice Stream과 Crary Ice Rise에 인접한 서남극 내부에서 새로운 지구물리학적 조사는 새로운 시추 기술을 통해 빙상 아래에서 최대 200m의 퇴적물을 복구할 수 있는 시추 대상을 확인하였다. 빙붕 기록은 지금까지 입수하기 어려운 것으로 입증되었지만 과거와 미래의 지구 평균 표면 온도가 산업화 이전 수준보다 최대 2℃ 상승할 때 해양 빙상 민감도를 더 잘 억제하는 데 중요하다. 따라서 이 프로그램을 통해 개발된 과학 및 기술 발전을 통해 서남극 빙상이 과거 온난 기간 동안 붕괴되었는지 여부를 테스트하고 +2℃ 지구 온난화 임계값에 대한 민감도를 결정할 수 있다 (UNFCCC, 2015).

KOPRI
극지연구소

References

Ash, J. L., Franca, A., Biddle, J., Giovannelli, D., Singh, S. M., Martinez-Mendez, G., Müller, J., Mollenhauer, G., and Hefter, J.: Microbial Sediment Community Changes from the Last Glacial Maximum to Modern beneath the Ross Sea, in: AGU Fall Meeting Abstracts, 5 October 2020, online, vol. 2019, B53L-2573, 2019.

Bamber, J. L. and Aspinall, W. P.: An expert judgement assessment of future sea level rise from the ice sheets, Nat. Clim. Change, 3, 424-427, https://doi.org/10.1038/nclimate1778, 2013.

Bamber, J. L., Westaway, R. M., Marzeion, B., and Wouters, B.: The land ice contribution to sea level during the satellite era, Environ. Res. Lett., 13, 063008, https://doi.org/10.1088/1748- 9326/aac2f0, 2018.

Bassis, J., Berg, B., Crawford, A., and Benn, D.: Transition to marine ice cliff instability controlled by ice thickness gradients and velocity, Science, 372, 1342-1344, 2021.

Bindschadler, R. A., Roberts, E. P., and Iken, A.: Age of Crary Ice Rise, Antarctica, determined from temperature-depth profiles, Ann. Glaciol., 14, 13-16, 1990.

Carr, S. A., Vogel, S. W., Dunbar, R. B., Brandes, J., Spear, J. R., Levy, R., Naish, T. R., Powell, R. D., Wakeham, S. G., and Mandernack, K. W.: Bacterial abundance and composition in marine sediments beneath the Ross Ice Shelf, Antarctica, Geobiology, 11, 377-395, 2013.

Catania, G., Hulbe, C., Conway, H., Scambos, T. A., and Raymond, C. F.: Variability in the mass flux of the Ross ice streams, West Antarctica, over the last millennium, J. Glaciol., 58, 741-752, 2012.

Christner, B. C., Priscu, J. C., Achberger, A. M., Barbante, C., Carter, S. P., Christianson, K., Michaud, A. B., Mikucki, J. A., Mitchell, A. C., and Skidmore, M. L.: A microbial ecosystem beneath the West Antarctic ice sheet, Nature, 512, 310-313, 2014.

Conway, H., Catania, G., Raymond, C. F., Gades, A. M., Scambos, T. A., and Engelhardt, H.: Switch of flow direction in an Antarctic ice stream, Nature, 419, 465-467, 2002.

Crawford, A. J., Benn, D. I., Todd, J., tröm, J. A., Bassis, J. N., and Zwinger, T.: Marine ice-cliff instability modeling shows mixed-mode ice-cliff failure and yields calving rate parameterization, Nat. Commun., 12, 2701, https://doi.org/10.1038/s 41467-021-23070-7, 2021.

DeConto, R. M. and Pollard, D.: Contribution of Antarctica to past and future sea-level rise, Nature, 531, 591-597, https://doi.org/10.1038/nature17145, 2016.

DeConto, R. M., Pollard, D., Alley, R. B., Velicogna, I., Gasson, E., Gomez, N., Sadai, S., Condron, A., Gilford, D. M., Ashe, E. L., Kopp, R. E., Li, D., and Dutton, A.: The

KOPRI 극지연구소

Paris Climate Agreement and future sea-level rise from Antarctica, Nature, 593, 83-89, https://doi.org/10.1038/s41586 -021-03427-0, 2021.

Edwards, T. L., Brandon, M. A., Durand, G., Edwards, N. R., Golledge, N. R., Holden, P. B., Nias, I. J., Payne, A. J., Ritz, C., and Wernecke, A.: Revisiting Antarctic ice loss due to marine ice-cliff instability, Nature, 566, 58-64, 2019.

Edwards, T. L., Nowicki, S., Marzeion, B., Hock, R., Goelzer, H., Seroussi, H., Jourdain, N. C., Slater, D. A., Turner, F. E., Smith, C. J., McKenna, C. M., Simon, E., Abe-Ouchi, A., Gregory, J. M., Larour, E., Lipscomb, W. H., Payne, A. J., Shepherd, A., Agosta, C., Alexander, P., Albrecht, T., Anderson, B., Asay-Davis, X., Aschwanden, A., Barthel, A., Bliss, A., Calov, R., Chambers, C., Champollion, N., Choi, Y., Cullather, R., Cuzzone, J., Dumas, C., Felikson, D., Fettweis, X., Fujita, K., Galton-Fenzi, B. K., Gladstone, R., Golledge, N. R., Greve, R., Hattermann, T., Hoffman, M. J., Humbert, A., Huss, M., Huybrechts, P., Immerzeel, W., Kleiner, T., Kraaijenbrink, P., Le clec'h, S., Lee, V., Leguy, G. R., Little, C. M., Lowry, D. P., Malles, J.-H., Martin, D. F., Maussion, F., Morlighem, M., O'Neill, J. F., Nias, I., Pattyn, F., Pelle, T., Price, S. F., Quiquet, A., Radic´, V., Reese, R., Rounce, D. R., Rückamp, M., Sakai, A., Shafer, C., Schlegel, N.-J., Shannon, S., Smith, R. S., Stra-neo, F., Sun, S., Tarasov, L., Trusel, L. D., Van Breedam, J., van de Wal, R., van den Broeke, M., Winkelmann, R., Zekollari, H., Zhao, C., Zhang, T., and Zwinger, T.: Projected land ice contributions to twenty-first-century sea level rise, Nature, 593, 74-82, https://doi.org/10.1038/s41586-021-03302-y, 2021.

Falconer, T., Pyne, A., Wilson, D., Levy, R., Nielsen, S., and Petrushak, S.: Operations overview for the ANDRILL Southern McMurdo Sound Project, Antarctica, Terra Antarctica, 15, 41-48, 2008.

Fielding, C. R.: Stratigraphic architecture of the Cenozoic succession in the McMurdo Sound region, Antarctica: An archive of polar palaeoenvironmental change in a failed rift setting, Sedimentology, 65, 1-61, https://doi.org/10.1111/sed.12413, 2018.

Fisher, A. T., Mankoff, K. D., Tulaczyk, S. M., Tyler, S. W., Foley, N., and Team, and the W. S.: High geothermal heat flux measured below the West Antarctic Ice Sheet, Sci. Adv., 1, e1500093, https://doi.org/10.1126/sciadv. 1500093, 2015.

Fretwell, P., Pritchard, H. D., Vaughan, D. G., Bamber, J. L., Barrand, N. E., Bell, R., Bianchi, C., Bingham, R. G., Blanken- ship, D. D., Casassa, G., Catania, G., Callens, D., Conway, H., Cook, A. J., Corr, H. F. J., Damaske, D., Damm, V., Ferraccioli, F., Forsberg, R., Fujita, S., Gim, Y., Gogineni, P., Griggs, J. A., Hindmarsh, R. C. A., Holmlund, P., Holt, J. W., Jacobel, R. W., Jenkins, A., Jokat, W., Jordan, T., King, E. C., Kohler, J., Krabill, W., Riger-Kusk, M., Langley, K. A., Leitchenkov, G., Leuschen, C., Luyendyk, B. P., Matsuoka, K., Mouginot, J., Nitsche, F. O., Nogi, Y.,

Nost, O. A., Popov, S. V., Rignot, E., Rippin, D. M., Rivera, A., Roberts, J., Ross, N., Siegert, M. J., Smith, A. M., Steinhage, D., Studinger, M., Sun, B., Tinto, B. K., Welch, B. C., Wilson, D., Young, D. A., Xiangbin, C., and Zirizzotti, A.: Bedmap2: improved ice bed, surface and thickness datasets for Antarctica, The Cryosphere, 7, 375–393, https://doi.org/10.5194/tc-7-375-2013, 2013.

Gasson, E., DeConto, R. M., Pollard, D., and Levy, R. H.: Dynamic Antarctic ice sheet during the early to mid-Miocene, P. Natl. Acad. Sci. USA, 113, 3459–3464, 2016.

Golledge, N. R. and Lowry, D. P.: Is the marine ice cliff hypothesis collapsing?, Science, 372, 1266–1267, 2021.

Golledge, N. R., Kowalewski, D. E., Naish, T. R., Levy, R. H., Fogwill, C. J., and Gasson, E. G.: The multi-millennial Antarctic commitment to future sea-level rise, Nature, 526, 421–425, https://doi.org/10.1038/nature15706, 2015.

Gomez, N., Pollard, D., and Holland, D.: Sea-level feedback lowers projections of future Antarctic Ice-Sheet mass loss, Nat. Commun., 6, 1–8, 2015.

Harwood, D., Florindo, F., Talarico, F., and Levy, R. H.: Studies from the ANDRILL, Southern McMurdo Sound Project, Antarctica, Initial Science Report on AND-2A, in: Terra Antartica, vol. 15, 1–235, ISSN 1122-8628, http://192.167.120.37/Editoria/TAP/volume15.html (last access: 17 February 2022), 2008–2009.

Hawkings, J. R., Skidmore, M. L., Wadham, J. L., Priscu, J. C., Morton, P. L., Hatton, J. E., Gardner, C. B., Kohler, T. J., Stibal, M., and Bagshaw, E. A.: Enhanced trace element mobilization by Earth's ice sheets, P. Natl. Acad. Sci. USA, 117, 31648–31659, 2020.

Hay, C., Mitrovica, J. X., Gomez, N., Creveling, J. R., Austermann, J., and Kopp, R. E.: The sea-level fingerprints of ice-sheet collapse during interglacial periods, Quaternary Sci. Rev., 87, 60– 69, 2014.

Hayes, D. E., Frakes, L. A., Barrett, P. J., Burns, D. A., Chen, P.H., Ford, A. B., Kaneps, A. G., Kemp, E. M., McCollum, D. M., Piper, D. J. W., Wall, R. E., and Webb, P. N.: Sites 270, 271, 272, Initial Reports of the Deep Sea Drilling Project 28, Washington, US Government Printing Office, 211–334, https://doi.org/10.2973/dsdp.proc.28.108.1975, 1975a.

Hayes, D. E., Frakes, L. A., Barrett, P. J., Burns, D. A., Chen, P. H., Ford, A. B., Kaneps, A. G., Kemp, E. M., McCollum, D. M., Piper, D. J. W., Wall, R. E., and Webb, P. N.: Site 273, Initial Reports of the Deep Sea Drilling Project 28, 335–368, https://doi.org/10.2973/dsdp.proc.28.109.1975, 1975b.

Hillebrand, T. R., Conway, H., Koutnik, M., Martín, C., Paden, J., and Winberry, J. P.: Radio-echo sounding and waveform model- ing reveal abundant marine ice in former rifts and basal crevasses within Crary Ice Rise, Antarctica, J. Glaciol., 67, 1–12, 2021.

Horgan, H. J., Alley, R. B., Christianson, K., Jacobel, R. W., Anandakrishnan, S., Muto, A.,

Beem, L. H., and Siegfried, M. R.: Estuaries beneath ice sheets, Geology, 41, 1159–1162, 2013.

Horgan, H. J., Hulbe, C., Alley, R. B., Anandakrishnan, S., Goodsell, B., Taylor–Offord, S., and Vaughan, M. J.: Poststagnation Retreat of Kamb Ice Stream's Grounding Zone, Geophys. Res. Lett., 44, 9815–9822, 2017.

Hulbe, C. and Fahnestock, M.: Century–scale discharge stagnation and reactivation of the Ross ice streams, West Antarctica, J. Geophys. Res. Earth Surf., 112, F03S27, https://doi.org/10.1029/2006JF000603, 2007.

IMBIE team: Mass balance of the Antarctic Ice Sheet from 1992–2017, Nature, 558, 219–222, 2018.

IPCC: Climate Change 2013: The Physical Science Basis. Contribution of Working Group I to the Fifth Assessment Report of the Intergovernmental Panel on Climate Change, edited by: Stocker, T. F., Qin, D., Plattner, G.–K., Tignor, M., Allen, S. K., Boschung, J., Nauels, A., Xia, Y., Bex, V., and Midgley, P. M., Cambridge University Press, Cambridge, United Kingdom and New York, NY, USA, 1535 pp., ISBN 978–1–107–05799–1, 2013.

IPCC: Summary for Policymakers, in: Global Warming of 1.5℃. An IPCC Special Report on the impacts of global warming of 1.5℃ above pre–industrial levels and related global green– house gas emission pathways, in the context of strengthening the global response to the threat of climate change, sustainable development, and efforts to eradicate poverty, edited by: Masson–Delmotte, V., Zhai, P., Pörtner, H.–O., Roberts, D., Skea, J., Shukla, P. R., Pirani, A., Moufouma–Okia, W., Péan, C., Pidcock, R., Connors, S., Matthews, J. B. R., Chen, Y., Zhou, X., Gomis, M. I., Lonnoy, E., Maycock, T., Tignor, M., and Waterfield, T., World Meteorological Organization, Geneva, Switzerland, 32 pp., https://www.ipcc.ch/site/assets/uploads/ sites/2/2019/05/ SR15_SPM_version_report_LR.pdf (last access: 17 February 2022), 2018.

IPCC: Summary for Policymakers, in: Climate Change 2021: The Physical Science Basis. Contribution of Working Group I to the Sixth Assessment Report of the Intergovernmental Panel on Climate Change, edited by: Masson–Delmotte, V., Zhai, P., Pirani, A., Connors, S. L., Péan, C., Berger, S., Caud, N., Chen, Y., Goldfarb, L., Gomis, M. I., Huang, M., Leitzell, K., Lonnoy, E., Matthews, J. B. R., Maycock, T. K., Waterfield, T., Yelekçi, O., Yu, R., and Zhou, B., Cambridge University Press, in press, 2021.

IRIS consortium: Collaborative Research: Grounding Line Dynamics: Crary Ice Rise Revisited [data set], 19–016, 9J 2015, http: //ds.iris.edu/mda/19–016/, last access: 18 February 2022.

Joughin, I. and Tulaczyk, S.: Positive mass balance of the Ross ice streams, West Antarctica,

Science, 295, 476–480, 2002.

Joughin, I., Tulaczyk, S., Bindschadler, R., and Price, S. F.: Changes in west Antarctic ice stream velocities; observation and analysis, J. Geophys. Res. Solid, 107, 2289, https://doi.org/10.1029/2001JB001029, 2002.

Joughin, I., Alley, R. B., and Holland, D. M.: Ice–sheet response to oceanic forcing, Science, 338, 1172–1176, 2012.

Kingslake, J., Scherer, R. P., Albrecht, T., Coenen, J., Powell, R. D., Reese, R., Stansell, N. D., Tulaczyk, S., Wearing, M. G., and Whitehouse, P. L.: Extensive retreat and re–advance of the West Antarctic Ice Sheet during the Holocene, Nature, 558, 430–434, 2018.

Kopp, R. E., Horton, R. M., Little, C. M., Mitrovica, J. X., Oppenheimer, M., Rasmussen, D. J., Strauss, B. H., and Tebaldi, C.: Probabilistic 21st and 22nd century sea–level projections at a global network of tide–gauge sites, Earths Future, 2, 383–406, 2014.

Kopp, R. E., DeConto, R. M., Bader, D. A., Hay, C. C., Horton, R. M., Kulp, S., Oppenheimer, M., Pollard, D., and Strauss, B. H.: Evolving understanding of Antarctic ice–sheet physics and ambiguity in probabilistic sea–level projections, Earths Future, 5, 1217–1233, 2017.

Levy, R., Harwood, D., Florindo, F., Sangiorgi, F., Tripati, R., von Eynatten, H., Gasson, E., Kuhn, G., Tripati, A., DeConto, R., Fielding, C., Field, B., Golledge, N., McKay, R., Naish, T., Olney, M., Pollard, D., Schouten, S., Talarico, F., Warny, S., Willmott, V., Acton, G., Panter, K., Paulsen, T., and Taviani, M.: Antarctic ice sheet sensitivity to atmospheric CO^2 variations in the early to mid–Miocene, P. Natl. Acad. Sci. USA, 113, 3453, https://doi.org/10.1073/pnas.1516030113, 2016.

Levy, R. H., Meyers, S. R., Naish, T. R., Golledge, N. R., McKay, R. M., Crampton, J. S., DeConto, R. M., De Santis, L., Florindo, F., Gasson, E. G. W., Harwood, D. M., Luyendyk, B. P., Powell, R. D., Clowes, C., and Kulhanek, D. K.: Antarctic ice–sheet sensitivity to obliquity forcing enhanced through ocean connections, Nat. Geosci., 12, 132–137, https://doi.org/10.1038/s41561–018– 0284–4, 2019.

Luthra, T., Anandakrishnan, S., Winberry, J. P., Alley, R. B., and Holschuh, N.: Basal characteristics of the main sticky spot on the ice plain of Whillans Ice Stream, Antarctica, Earth Planet. Sci. Lett., 440, 12–19, 2016.

McKay, R., Naish, T., Carter, L., Riesselman, C., Dunbar, R., Sjunneskog, C., Winter, D., Sangiorgi, F., Warren, C., and Pagani, M.: Antarctic and Southern Ocean influences on Late Pliocene global cooling, P. Natl. Acad. Sci. USA, 109, 6423–6428, 2012.

McKay, R. M., Barrett, P. J., Levy, R. S., Naish, T. R., Golledge, N. R., and Pyne, A.: Antarctic Cenozoic climate history from sedimentary records: ANDRILL and beyond, Philos. T. Roy. Soc. A, 374, 1–17, https://doi.org/10.1098/rsta.2014.0301, 2016.

KOPRI 극지연구소

McKay, R. M., De Santis, L., Kulhanek, D. K., and Expedition 374 Scientists (Eds.): Ross Sea West Antarctic Ice Sheet History, International Ocean Discovery Program, https://doi.org/10.14379/iodp.proc.374.2019, 2019.

Melles, M., Brigham-Grette, J., Minyuk, P. S., Nowaczyk, N. R., Wennrich, V., DeConto, R. M., Anderson, P. M., Andreev, A. A., Coletti, A., and Cook, T. L.: 2.8 million years of Arctic climate change from Lake El'gygytgyn, NE Russia, Science, 337, 315- 320, 2012.

Mitrovica, J. X., Gomez, N., and Clark, P. U.: The sea-level fingerprint of West Antarctic collapse, Science, 323, 753-753, 2009. Naish, T., Powell, R., Levy, R., Florindo, F., Harwood, D., Kuhn, G., Niessen, F., Talarico, F., and Wilson, G.: A record of Antarctic climate and ice sheet history recovered, Eos Trans. Am. Geophys. Union, 88, 557-558, 2007.

Naish, T., Powell, R., Levy, R., Wilson, G., Scherer, R., Talarico, F., Krissek, L., Niessen, F., Pompilio, M., Wilson, T., Carter, L., DeConto, R., Huybers, P., McKay, R., Pollard, D., Ross, J., Winter, D., Barrett, P., Browne, G., Cody, R., Cowan, E., Crampton, J., Dunbar, G., Dunbar, N., Florindo, F., Gebhardt, C., Graham, I., Hannah, M., Hansaraj, D., Harwood, D., Helling, D., Henry, S., Hinnov, L., Kuhn, G., Kyle, P., Läufer, A., Mafioli, P., Ma- gens, D., Mandernack, K., McIntosh, W., Millan, C., Morin, R., Ohneiser, C., Paulsen, T., Persico, D., Raine, I., Reed, J., Riesselman, C., Sagnotti, L., Schmitt, D., Sjunneskog, C., Strong, P., Taviani, M., Vogel, S., Wilch, T., and Williams, T.: Obliquity-paced Pliocene West Antarctic ice sheet oscillations, Nature, 458, 322-328, https://doi.org/10.1038/nature 07867, 2009.

Nerem, R. S., Beckley, B. D., Fasullo, J. T., Hamlington, B. D., Masters, D., and Mitchum, G. T.: Climate-change-driven accelerated sea-level rise detected in the altimeter era, P. Natl. Acad. Sci. USA, 115, 2022-2025, https://doi.org/10.1073/pnas.1717312115, 2018.

Oppenheimer, M. and Alley, R. B.: How high will the seas rise?, Science, 354, 1375-1377, 2016.

Pollard, D. and DeConto, R. M.: Modelling West Antarctic ice sheet growth and collapse through the past five million years, Nature, 458, 329-332, https://doi.org/10.1038/nature07809, 2009.

Pollard, D., DeConto, R. M., and Alley, R. B.: Potential Antarctic Ice Sheet retreat driven by hydrofracturing and ice cliff failure, Earth Planet. Sc. Lett., 412, 112-121, https://doi.org/10.1016/j.epsl.2014.12.035, 2015.

Price, S. F., Bindschadler, R. A., Hulbe, C. L., and Joughin, I. R.: Post-stagnation behavior in the upstream regions of Ice Stream C, West Antarctica, J. Glaciol., 47, 283-294, https://doi.org/10.3189/172756501781832232, 2001.

Priscu, J. C., Kalin, J., Winans, J., Campbell, T., Siegfried, M. R., Skidmore, M., Dore, J. E., Leventer, A., Harwood, D. M., Duling, D., Zook, R., Burnett, J., Gibson, D., Krula, E., Mironov, A., McManis, J., Roberts, G., Rosenheim, B., Christner, B. C., Kasic, K., Fricker, H., Lyons, W. B., Barker, J., Bowling, M., Collins, B., Davis, C., Gagnon, A., Gardner, C., Gustafson, C., Kim, O-S., Li, W., Michaud, Al., Patterson, M. O., Tranter, M., Venturelli, R., Vick-Majors, T., Cooper, E., and the SALSA Science Team: Scientific access into Mercer Subglacial Lake: scien- tific objectives, drilling operations and initial observations, Ann. Glaciol., 62, 1-13, 2021.

Retzlaff, R. and Bentley, C. R.: Timing of stagnation of Ice Stream C, West Antarctica, from short-pulse radar stud- ies of buried surface crevasses, J. Glaciol., 39, 553-561, https://doi.org/10.3189/S0022143000016440, 1993.

Retzlaff, R., Lord, N., and Bentley, C. R.: Airborne-radar studies: Ice streams A, B and C, West Antarctica, J. Glaciol., 39, 495- 506, 1993.

Scherer, R. P.: Quaternary and Tertiary microfossils from beneath Ice Stream B: Evidence for a dynamic West Antarc- tic Ice Sheet history, Glob. Planet. Change, 4, 395-412, https://doi.org/10.1016/0921-8181(91)90005-H, 1991.

Scherer, R. P., Harwood, D. M., Ishman, S. E., and Webb, P. N.: Micropaleontological analysis of sediments from the Crary Ice Rise, Ross ice Shelf, Antarctic JUS, 23, 34-36, 1988.

Shepherd, A., Ivins, E., Rignot, E., Smith, B., van den Broeke, M., Velicogna, I., Whitehouse, P., Briggs, K., Joughin, I., Krinner, G., Nowicki, S., Payne, T., Scambos, T., Schlegel, N., A, G., Agosta, C., Ahlstrøm, A., Babonis, G., Barletta, V., Blazquez, A., Bonin, J., Csatho, B., Cullather, R., Felikson, D., Fettweis, X., Forsberg, R., Gallee, H., Gardner, A., Gilbert, L., Groh, A., Gunter, B., Hanna, E., Harig, C., Helm, V., Horvath, A., Horwath, M., Khan, S., Kjeldsen, K. K., Konrad, H., Langen, P., Lecavalier, B., Loomis, B., Luthcke, S., McMillan, M., Melini, D., Mernild, S., Mohajerani, Y., Moore, P., Mouginot, J., Moyano, G., Muir, A., Nagler, T., Nield, G., Nilsson, J., Noel, B., Otosaka, I., Pattle, M. E., Peltier, W. R., Pie, N., Rietbroek, R., Rott, H., Sandberg Sørensen, L., Sasgen, I., Save, H., Scheuchl, B., Schrama, E., Schröder, L., Seo, K.-W., Simonsen, S., Slater, T., Spada, G., Sutterley, T., Talpe, M., Tarasov, L., van de Berg, W. J., van der Wal, W., van Wessem, M., Vishwakarma, B. D., Wiese, D., and Wouters, B.: Mass balance of the Antarctic Ice Sheet from 1992 to 2017, Nature, 558, 219-222, https://doi.org/10.1038/s41586- 018-0179-y, 2018.

Tebaldi, C., Debeire, K., Eyring, V., Fischer, E., Fyfe, J., Friedlingstein, P., Knutti, R., Lowe, J., O'Neill, B., Sanderson, B., van Vuuren, D., Riahi, K., Meinshausen, M., Nicholls, Z., Tokarska, K. B., Hurtt, G., Kriegler, E., Lamarque, J.-F., Meehl, G., Moss, R., Bauer, S. E., Boucher, O., Brovkin, V., Byun, Y.-H., Dix, M., Gualdi, S., Guo, H.,

KOPRI 극지연구소

John, J. G., Kharin, S., Kim, Y., Koshiro, T., Ma, L., Olivié, D., Panickal, S., Qiao, F., Rong, X., Rosen− bloom, N., Schupfner, M., Séférian, R., Sellar, A., Semmler, T., Shi, X., Song, Z., Steger, C., Stouffer, R., Swart, N., Tachiiri, K., Tang, Q., Tatebe, H., Voldoire, A., Volodin, E., Wyser, K., Xin, X., Yang, S., Yu, Y., and Ziehn, T.: Climate model projections from the Scenario Model Intercomparison Project (ScenarioMIP) of CMIP6, Earth Syst. Dynam., 12, 253−293, https://doi.org/10.5194/esd−12−253−2021, 2021.

Tyler, S. W., Holland, D. M., Zagorodnov, V., Stern, A. A., Sladek, C., Kobs, S., White, S., Suárez, F., and Bryenton, J.: Using distributed temperature sensors to monitor an Antarctic ice shelf and sub−ice−shelf cavity, J. Glaciol., 59, 583−591, https://doi.org/10.3189/2013JoG12J207, 2013.

UNFCCC: Adoption of the Paris Agreement, FCCC/CP/2015/10/Add.1, 1−32, Paris, https://www.un.org/en/development/desa/population/migration/generalassembly/docs/globalcompact/FCCC_CP_2015_10_Add.1.pdf (last access: 10 February 2022), 2015.

Velicogna, I., Sutterley, T. C., and van den Broeke, M. R.: Regional acceleration in ice mass loss from Greenland and Antarctica using GRACE time−variable gravity data, Geophys. Res. Lett., 41, 8130−8137, https://doi.org/10.1002/2014gl061052, 2014.

Venturelli, R. A., Siegfried, M. R., Roush, K. A., Li, W., Burnett, J., Zook, R., Fricker, H. A., Priscu, J. C., Leventer, A., and Rosenheim, B. E.: Mid−Holocene Grounding Line Retreat and Readvance at Whillans Ice Stream, West Antarctica, Geophys. Res. Lett., 47, e2020GL088476, https://doi.org/10.1029/2020GL088476, 2020.

Vick−Majors, T. J., Michaud, A. B., Skidmore, M. L., Turetta, C., Barbante, C., Christner, B. C., Dore, J. E., Christian− son, K., Mitchell, A. C., and Achberger, A. M.: Biogeochemical connectivity between freshwater ecosystems beneath the West Antarctic Ice Sheet and the sub−ice marine environment, Glob. Biogeochem. Cy., 34, e2019GB006446, https://doi.org/10.1029/2019GB006446, 2020.

Whitehouse, P. L., Gomez, N., King, M. A., and Wiens, D. A.: Solid Earth change and the evolution of the Antarctic Ice Sheet, Nat. Commun., 10, 1−14, https://doi.org/10.1038/s41467−018−08068− y, 2019.

KOPRI 극지연구소

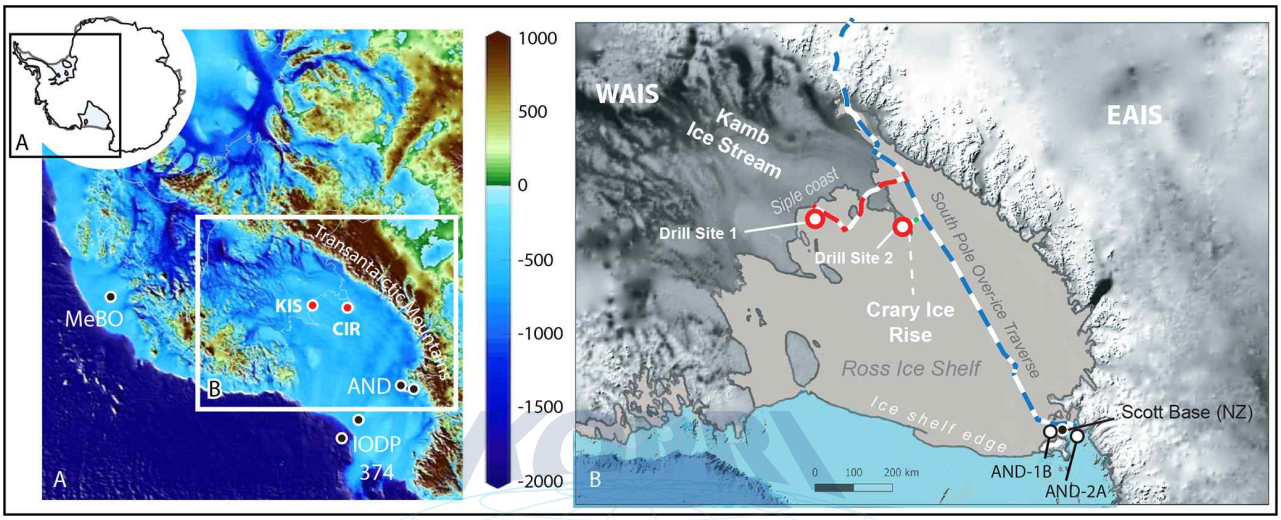


Figure 1. Proposed SWAIS 2C drill sites at Kamb Ice Stream (KIS) and Crary Ice Rise (CIR). (A) Topographic/bathymetric map across West Antarctica (color scale in meters). Other key drill sites include MeBO, ANDRILL (AND-1B and -2A), and IODP Exp. 374 sites (Fretwell et al., 2013). (B) Detail of the Ross Ice Shelf showing the South Pole Over-Ice Traverse and routes to drill sites 1 (KIS) and 2 (CIR). The new sites would anchor the southern end of a drill site transect deeply within West Antarctica.

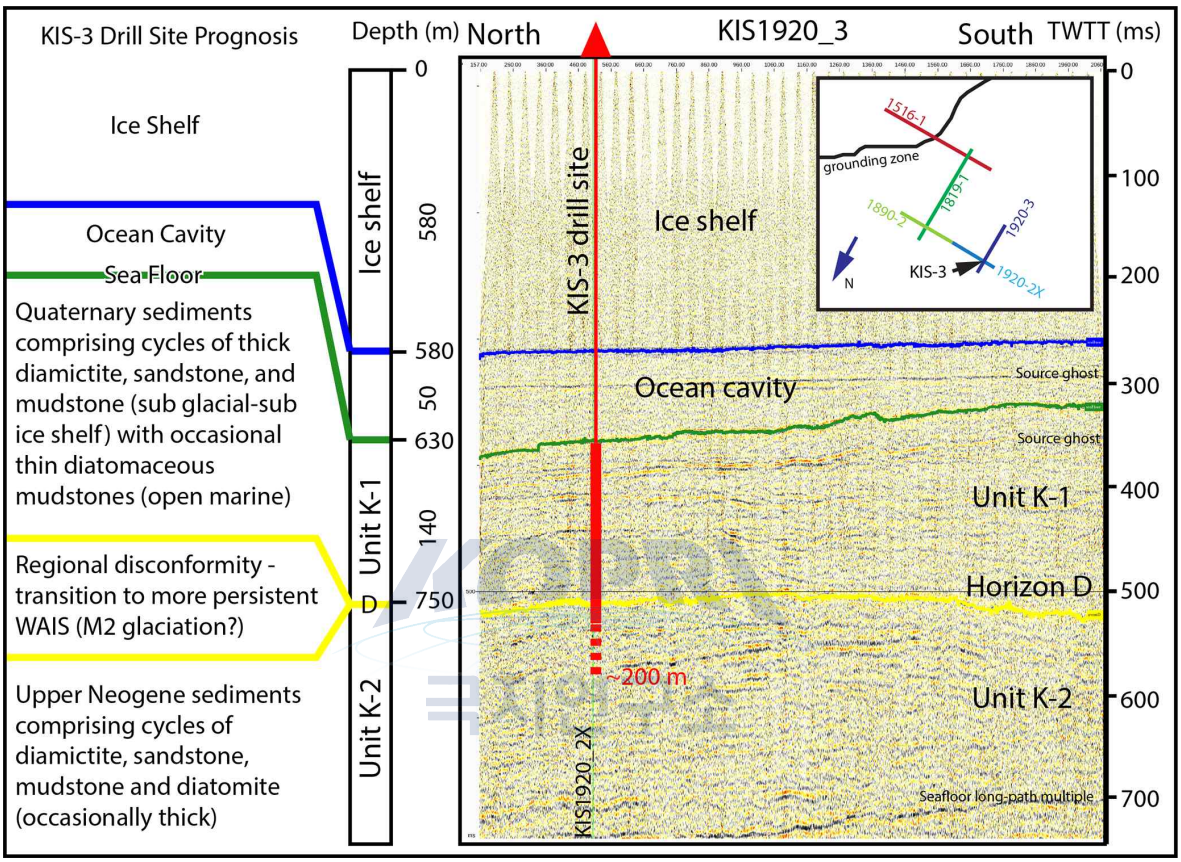


Figure 2. Seismic line KIS 1920_3. The KIS-3 drill site is located on the crossing point with line KIS1920_2X (inset). Drilling prognosis on the left with estimated depths from the surface and a brief description of stratigraphic intervals and horizons. The thick red line shows the 200 m drilling target depth.

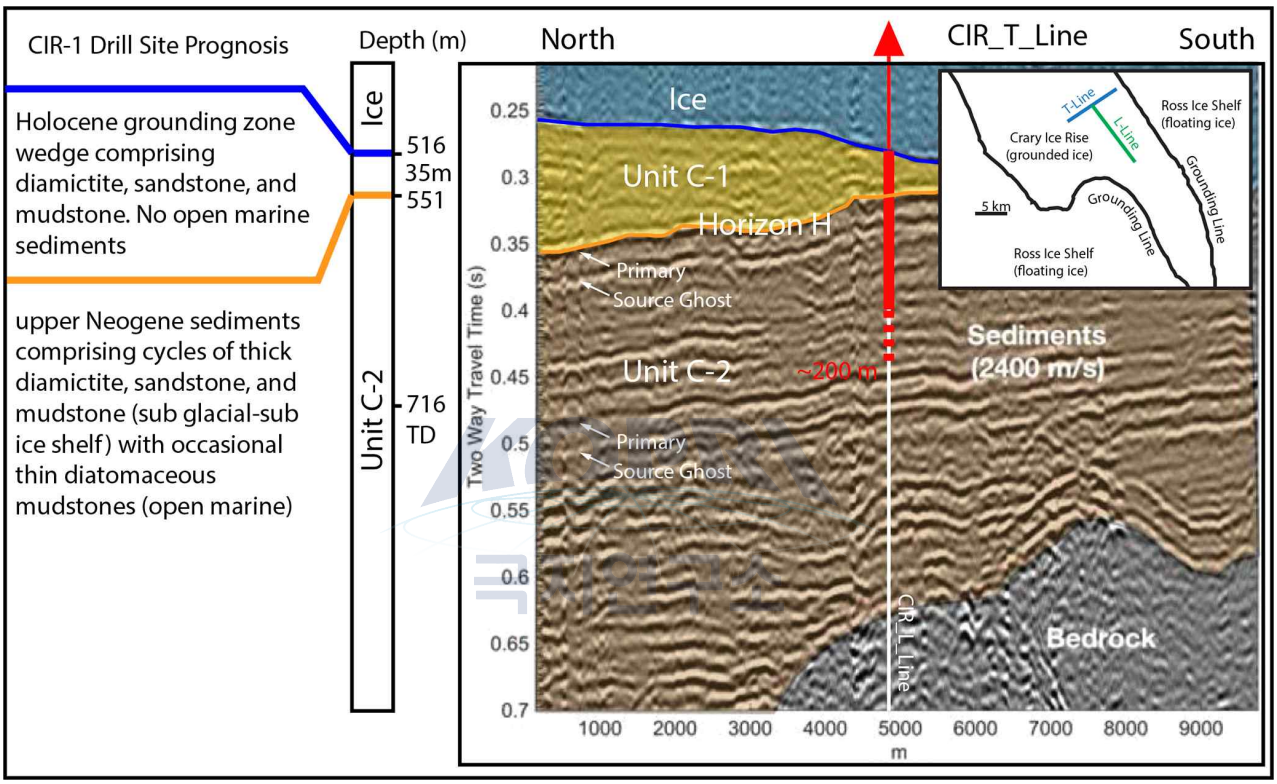


Figure 3. Seismic line CIR_T. The CIR-1 drill site is located on the crossing point with line CIR_L (inset). Drilling prognosis on the left with estimated depths from the surface and a brief description of stratigraphic intervals. The thick red line shows the 200 m drilling target depth.

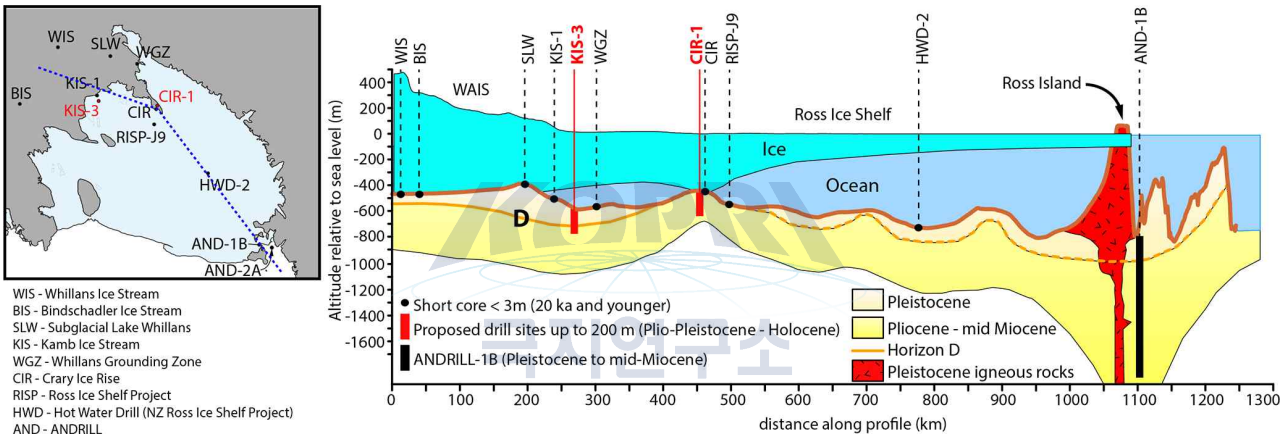


Figure 4. Regional stratigraphic correlation schematic. Dashed blue line is the location of the cross section. D is Horizon D identified at the KIS-3 site.

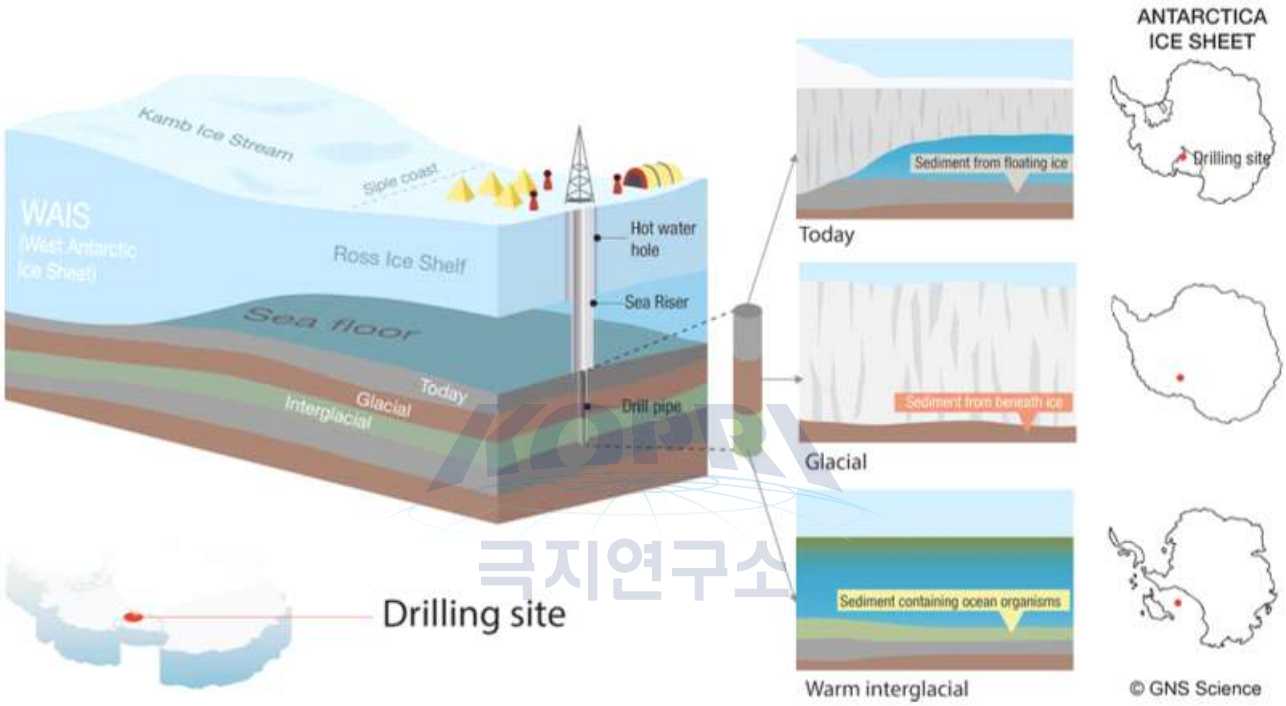


Figure 5. Diagram showing new drilling system sitting on the floating Ross Ice Shelf near the grounding zone at the Kamb Ice Stream site. A drill string up to ~1000 m long will be lowered to the seafloor through a hot-water drilled hole in the ice shelf to core ~200 m into the seafloor to sample sediments deposited in the past.

KOPRI 극지연구소

제 3 장

2020 아라온 아문젠해 탐사

이재일, 김성한, 문흥수, 김주용

극지연구소

요약: 본 연구는 극지연구소의 주요 연구사업의 일환으로, 남극 아문젠해의 플라이스토세 동안 고환경 변화 파악 및 Wrigley Gulf 지역의 지난 마지막 빙하기 이후의 빙상/빙붕 후퇴 및 이와 연관된 고환경 변화를 파악하는 것을 목적으로 수행하였다. 또한, 기존의 연구 결과가 부족한 로스해 동부-아문젠해의 대륙사면 축상을 따라 SBP, 멀티빔 자료를 확보하고자 하였으며, 이를 토대로한 경도별 해양퇴적물을 함께 획득하고자 하였다. 이와 함께, 현재의 해저 생태계 파악을 위한 deep sea camera를 설치하여 현재의 환경을 파악하고자 하였다.

1. 2020년 입남극 및 출남극 시기

1.1. 입남극 : 크라이스트처치 → 아문젠해

일자	인원	이동수단	명 단
2019.12.29.	4	아라온	이재일, 김성한, 문흥수, 김주용

1.2. 출남극 : 아문젠해 → 크라이스트처치

일자	인원	이동수단	명 단
2020.02.27.	4	아라온	이재일, 김성한, 문흥수, 김주용

2. 탐사 내용 및 결과

남극 아문젠해 Wrigley Gulf 안쪽에서 과거 빙상, 빙하의 흐름을 파악하기 위해 SBP, 멀티빔 자료를 확보하였으며, SBP 자료를 토대로 총 6개의 지점에서 박스 코어 및 중력 코어 샘플을 채취하였다. Wrigley Gulf 바깥쪽의 심해의 한 정정에서 박스 코어를 획득하였고, 중력 코어의 경우는 다양한 (9 m, 6 m, 3 m 배럴) 방법으로 시도를 하였으나 시료 획득에 실패하였다 (Fig. 1). 로스해 동부-아문젠해 대륙사면을 따라 SBP, 멀티빔 자료를 확보하였으며, SBP 자료를 토대로 총 5개의 정점에서 경도별 박스 코어, 중력 코어 시료를 확보하였다 (Fig. 1). Wrigley Gulf 안쪽에서 마지막 빙하기 이후 빙상의 거동 파악을 위한 멀티빔 조사를 통해 자세한 해저 지형 자료를 확보

하였다 (Fig. 2). 추후 해양퇴적물 절개 및 분석을 위해, 1.5 m 단위로 절개하여 냉장 보관하였다. 실제 해저생태계 및 오늘날의 환경을 이해하기 위해 deep sea camera를 Wrigley Gulk의 한 사이트의 박스 코어러에 함께 내려 해저면의 영상도 함께 획득하였다 (Fig. 3).

2.1. 시추 코어 정보

드라이갈스크 분지를 따라 획득한 SBP 라인을 토대로 위도별로 해양퇴적물이 분포하는 곳에서 코어 정점을 선정하였다 (Fig. 1).

1) AM20-BC01 (48, 44 cm)
[73° 00.1947' S. 145° 10.4578' W, 4088 m]
2) AMRS20-BC02 (18 cm) & -GC02 (180 cm
[75° 10.0486' S. 179° 04.7294' W, 548 m]
3) AMRS20-BC03 (20, 20 cm) & -GC03 (305 cm)
[75° 09.7062' S. 179° 05.8579' W, 544 m]
4) AMRS20-BC04 (42, 42 cm) & -GC04 (797 cm)
[76° 03.1358' S. 156° 26.7366' W, 3218 m]
5) AMRS20-GC05 (667 cm)
[74° 55.3522' S. 148° 44.2412' W, 3746 m]
6) AM20-BC06 (48, 48 cm) & -GC06 (899 cm)
[74° 00.9419' S. 138° 12.0799' W, 2387 m]
7) AM20-BC07 (29, 30 cm) & -GC07A (296 cm, overspill) & -GC07B (420 cm)
[73° 40.4376' S. 127° 49.4076' W, 806 m]
8) AM20-BC08 (36, 34 cm) & -GC08 (180 cm)
[73° 46.0989' S. 127° 54.8063' W, 726 m]
9) AM20-BC09 (40, 40 cm) & -GC09 (128 cm)
[74° 10.3587' S. 129° 06.7088' W, 873 m]
10) AM20-BC10 (24 cm) & -GC10 (105 cm)
[74° 12.3166' S. 128° 46.8110' W, 803 m]
11) AM20-BC11 (21 cm) & -GC11 (133 cm)
[74° 07.3091' S. 128° 17.1545' W, 598 m]
12) AM20-BC12 (35, 35 cm, deep sea camera)
& -GC12A (295 cm, overspill) & -GC12B (310 cm)
[73° 56.0177' S. 127° 47.9186' W, 792 m]

KOPRI 극지연구소

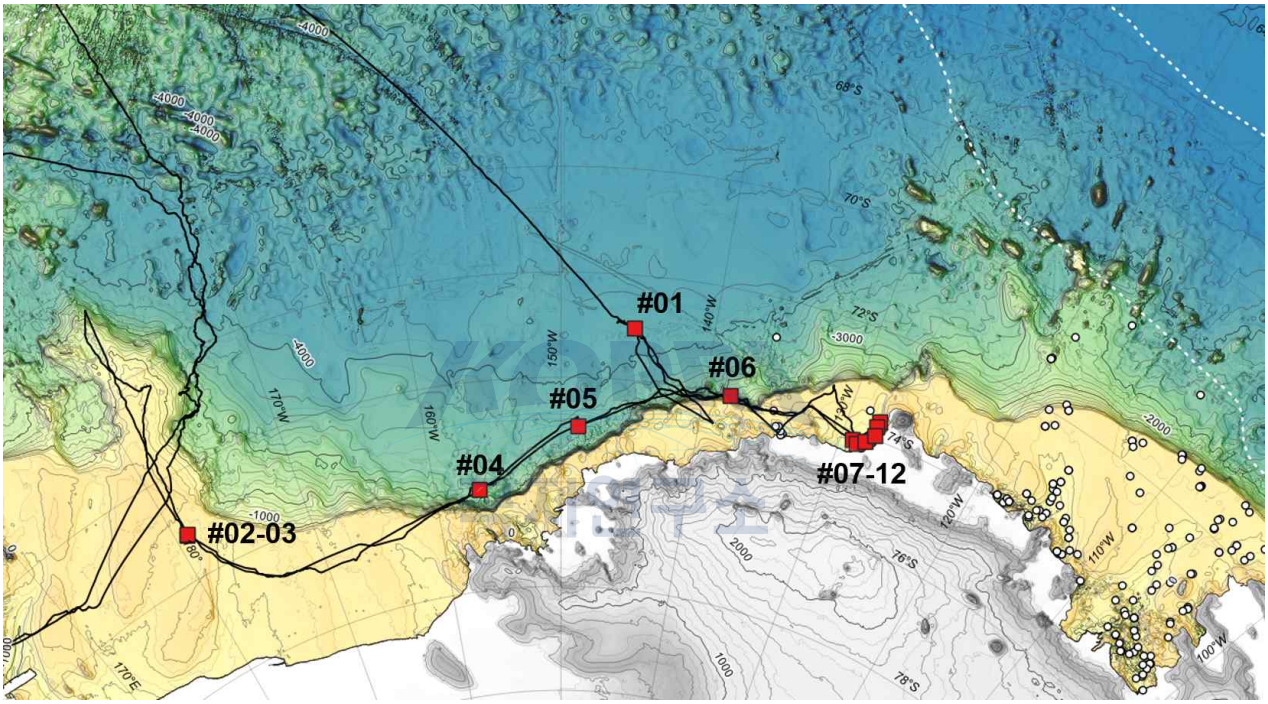


Fig. 1. Locations of all core sites. Box cores were taken together with gravity core site. Gravity core was not taken due to the substrate at core site 1 and deep sea camera was attached to the box corer to take images of bottom environment at core site 12.

2020 Amundsen Sea exploration (ANA10B)

Jae Il Lee, Sunghan Kim, Heung Soo Moon, Joo Yong Kim

Korea Polar Research Institute

Abstract: During 2019/20 summer season (ANA10B Cruise), our research group collected sub-bottom profile (SBP) along the continental slope between central Ross Sea and the Amundsen Sea see the longitudinal distribution of sediments. Based on SBP data, we collected box and gravity cores from six sites along the continental slope between central Ross Sea and the Amundsen Sea. We expect those sediment cores would reveal detailed information on paleoceanographic changes in the Ross Sea and the Amudsen Sea and their interaction changes after physical property, geochemical, sedimentological, and isotopic analysis. The SBP line we obtained during this cruise is the longest contiuous line along the continental slope between the Ross and Amundsen Seas so far, showing longitudinal sedimentation difference which indicates longitudinal ice sheet dynamics were different. Multi-beam data from the Wregley Gulf would provide to reconstruct pale-ice dynamics. In addition, to understand the modern oceanographic environmental changes in the Terra Nova Bay, we deployed two sediment trap systems.

KOPRI 극지연구소

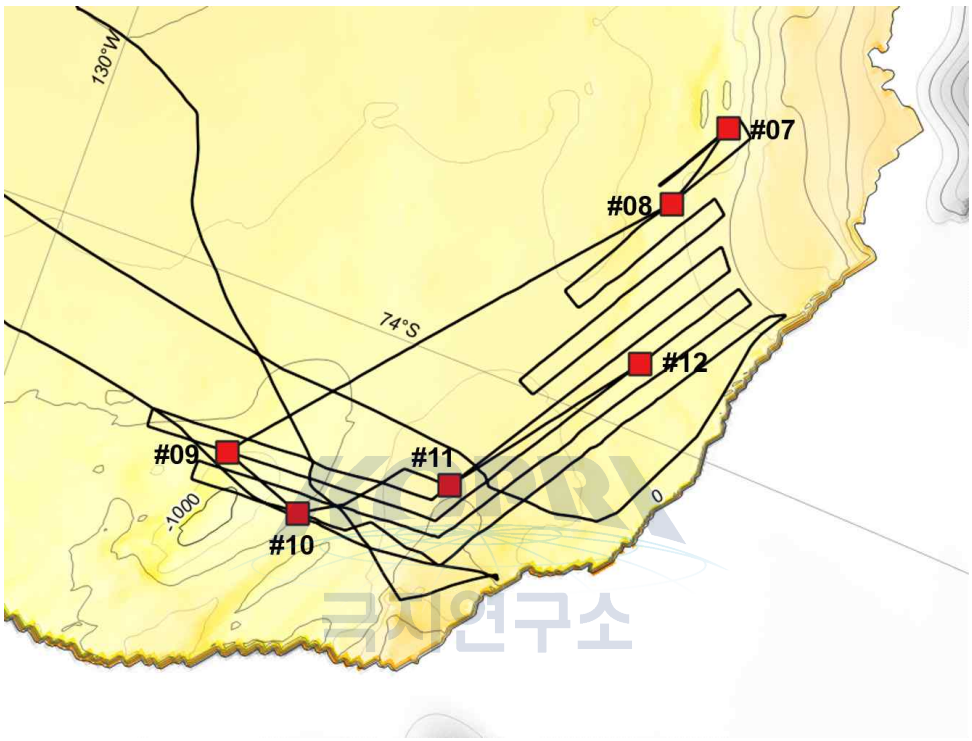


Figure 2. Muli-beam and SBP survey track in the Wrigley Gulf with coring location. Deep-sea camera was attached in the box corer at core site 12.



Fig. 5 Deep sea camera

제 4 장

2021 아라온 로스해 탐사

문흥수

극지연구소

요약: 본 연구는 극지연구소의 주요 연구사업의 일환으로, 남극장보고과학기지 인근해역에서 해양 계류장비를 이용하여 수층의 입자특성과 해양 수층의 물리자료 획득을 통해 해양 환경 변화 관측과 로스해 빙붕 인근의 SBP 자료 획득과 추가적인 해양퇴적물 코어 획득을 통해, 마지막 빙하기 이후 로스해 지역에서의 로스 빙붕의 거동을 파악하였다.

1. 2020년 입남극 및 출남극 시기

1.1. 입남극 : 뉴질랜드 크라이스트처치 → 남극 로스해

일자	인원	이동수단	명 단
2020.11.28.	1	아라온	문흥수

1.2. 출남극 : 세종과학기지 → 푼타 아레나스

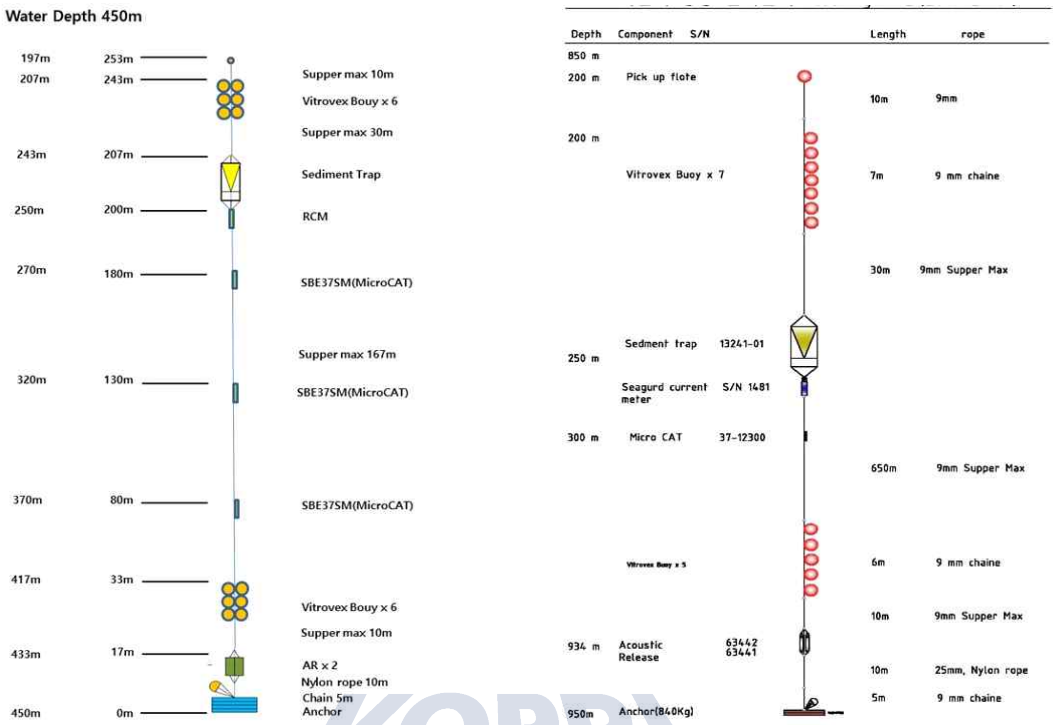
일자	인원	이동수단	명 단
2021.02.02.	1	아라온	문흥수

2. 탐사 내용 및 결과

남극 장보고 과학기지 인근 2개 정점에 수온/전도도 측정기, 퇴적물 입자 포집기 등의 해양 계류장비 설치하였다 (Fig. 1). 남극 로스해(중앙 빙붕) 축을 따라 SBP, 멀티빔 자료를 확보하여, 빙붕 인근 퇴적물의 분포를 확인하여, 박스, 중력 시추기를 이용하여 총 6개의 사이트에서 박스코어 및 중력 코어 시료를 획득하였다 (Fig. 2). 해양퇴적물 분석은 추후 절개 및 분석을 위해, 1.5 m 단위로 절개하여 냉장 보관하였다.

2.1. 장보고 과학기지 인근 해역 2정점의 계류

Sediment Trap System (2set)



M1 : 74° 41.4140'S , 164° 27.904'E X1 : 74° 50.702'S , 166° 15.019'E

2.2. 로스해 중앙 빙붕을 따라 획득된 해양퇴적물 시추 정점 위치

Station	Core Name	Lat(DM)	Lon(DM)	Depth(m)
ANA11A A42	RS21-BC01	77° 00.6315'S	171° 00.0185'E	740m
	RS21-GC01	77° 00.6315'S	171° 00.0185'E	740m
ANA11A A45	RS21-BC02	77° 23.9941'S	176° 17.9590'E	625m
	RS21-GC02	77° 23.9941'S	176° 17.9590'E	625m
ANA11A A59	RS21-BC03	77° 58.4119'S	173° 33.4831'W	535m
	RS21-GC03A	77° 58.4119'S	173° 33.4831'W	535m
	RS21-GC03B	77° 58.4119'S	173° 33.4831'W	535m
ANA11A A60	RS21-BC04	78° 01.5948'S	171° 15.6141'W	517m
	RS21-GC04	78° 01.5948'S	171° 15.6141'W	517m
ANA11A A61	RS21-BC05	78° 17.3683'S	170° 27.4014'W	560m
	RS21-GC05	78° 17.3683'S	170° 27.4014'W	560m
ANA11A A64	RS21-BC06	77° 42.6320'S	161° 51.1843'W	682m
	RS21-GC06	77° 42.6320'S	161° 51.1843'W	682m

KOPRI 극지연구소

2021 Ross Sea exploration

Heung Soo Moon

Korea Polar Research Institute

Abstract: During 2020/21 summer season, our research group collected sub-bottom profile (SBP) along the Ross Ice Shelf to confirm the distribution of sediments. Based on the SBP data, we followed Ross Ice Shelf to collect box cores and gravity cores by six sites. We expect those sediment cores would reveal detailed information on dynamics of the Ross Ice Shelf since the last glacial period after physical property, geochemical, and isotopical analysis. In addition, to understand the modern oceanographic environmental changes in the Terra Nova Bay, we deployed two sediment trap systems.

KOPRI
극지연구소

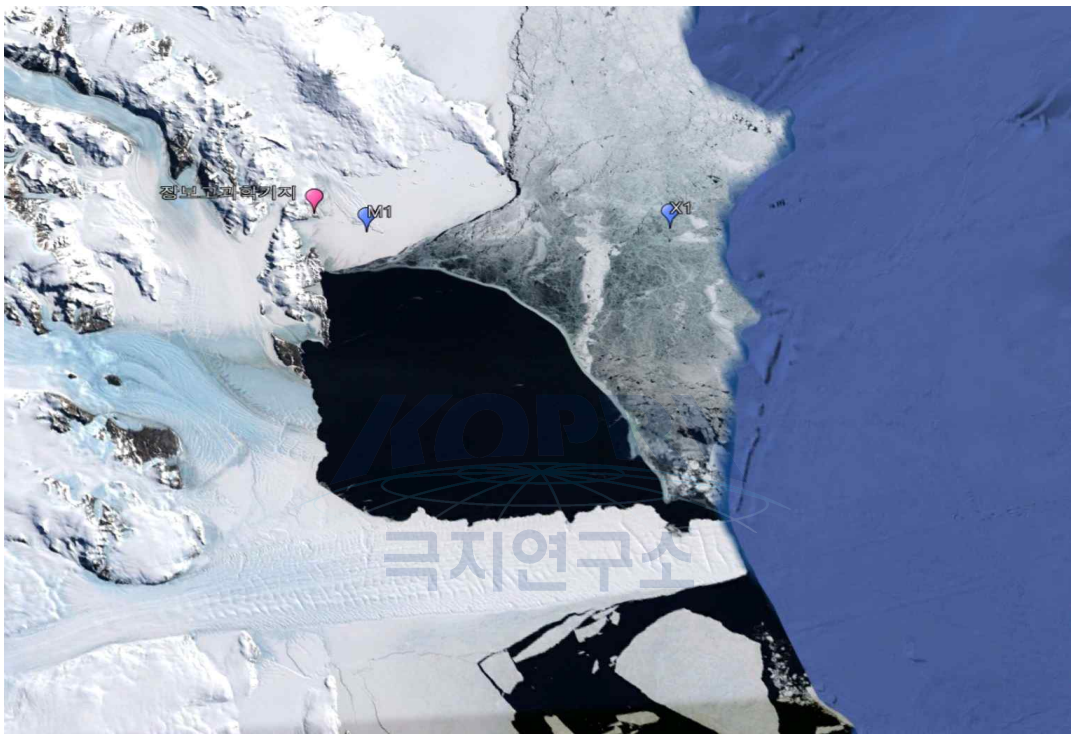


Fig. 1. Locations of sediment mooring (M1 and X1)



Fig. 2. Core sites. (Box cores were taken together with gravity core site.)

제 5 장

2022 아라온 아문젠해 탐사

유규철[1], 이민경[1], 문흥수[1], 강명일[1], 이승준[1], 강인성[2], 이준형[3], 박호진[4]

[1]극지연구소, [2]연세대학교, [3]강릉원주대학교, [4]부경대학교

요약: 본 연구는 극지연구소의 주요 연구사업(PE22090)의 일환으로, 남극 아문젠해 스웨이츠 빙하와 파인 아일랜드 빙하 주변 해역의 해양 퇴적물로부터 마지막 빙하기 이후 홀로세 중기 온난 시기에 대한 환경을 복원하여 미래 기후 2도 상승에 따라 남극의 전지구적 영향력을 추적할 목적으로 수행하였다. 남극 3항차 기간 동안 남극 아문젠해 닷슨과 겟츠A 빙붕 해역을 따라 획득한 지구물리 탐사를 통해 천해 퇴적물 분포와 측심 자료 및 해양 퇴적물을 확보하였다.

1. 2020년 입남극 및 출남극 시기

1.1. 입남극 : 크라이스트처치 → 아문젠해

일자	인원	이동수단	명 단
2022.01.12.	8	아라온	유규철, 이민경, 문흥수, 강명일 이승준, 이준형, 강인성, 박호진

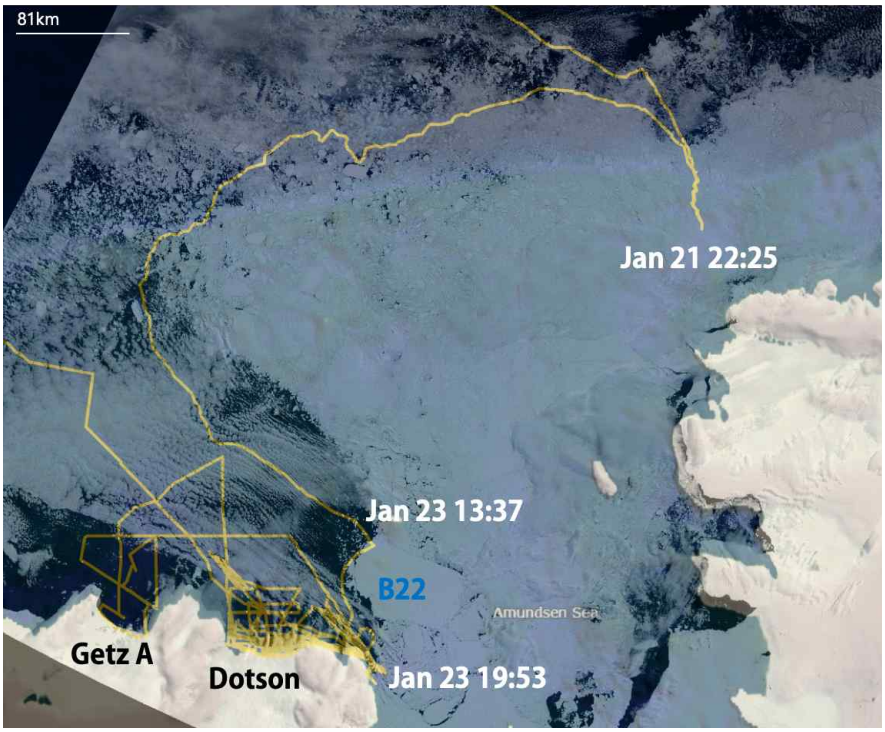
1.2. 출남극 : 아문젠해 → 크라이스트처치

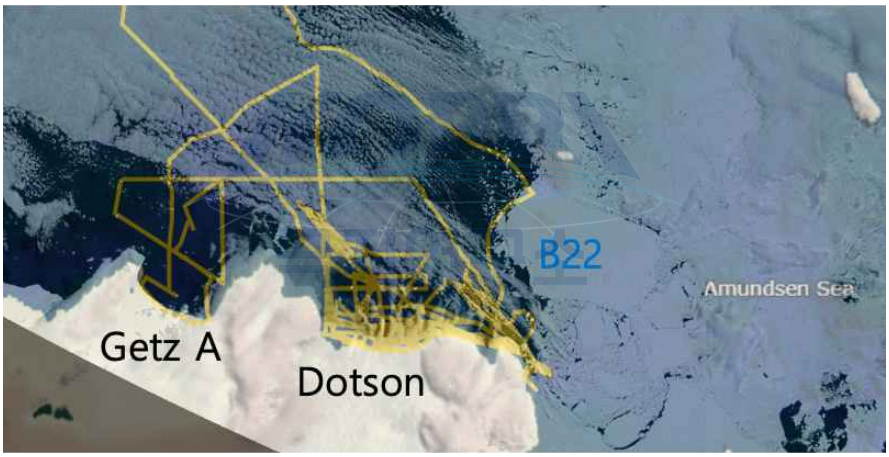
일자	인원	이동수단	명 단
2022.02.19.	8	아라온	유규철, 이민경, 문흥수, 강명일 이승준, 이준형, 강인성, 박호진

2. 탐사 내용 및 결과

남극 아문젠해의 닷슨 빙붕 및 겟츠A 빙붕 앞 해역에서 지형학적 특성 파악을 위해 멀티빔 탐사와 퇴적층 분포 파악을 위해 SBP 탐사를 수행하였다. 닷슨 빙붕 앞 해역에서는 6 정점의 중력 시추 및 2 정점의 박스 시추 시료가 확보되었고, 추가적으로 베어 해령에서 1정점의 중력 시추 시료가 확보되었다.

2.1. 멀티빔 & SBP 탐사 라인





Name	latitude(S)	longitude(W)
Line-1	73° 43.711'S	113° 13.349'W
Line-2	73° 39.581'S	113° 28.116'W
Line-3	73° 37.080'S	113° 42.540'W
Line-4	73° 35.777'S	113° 47.551'W
Line-5	73° 49.90920'S	113° 2.29751'W
Line-4	73° 35.777'S	113° 47.551'W
Line-6	73° 37.9280'S	113° 37.7449'W
Line-7	73° 44.9766'S	113° 9.7990'W
Line-8	73° 45.7094'S	113° 7.7654'W

2022 Amundsen Sea exploration

Kyu-Cheul Yoo[1], Min Kyung Lee[1], Heung Soo Moon[1], Myung Il Kang[1], Jun Seung Lee[1], Sung In Kang[2], Hyung Jun Lee[3], Jin Ho Park[4]

[1]Korea Polar Research Institute, [2]Yonsei University, [3]Gangneung-Wonju Natl' University, [4]Pukyong University

Abstract: During the 2022 summer season, our research group collected sub-bottom profiles (SBP) and multi-beam data to confirm the distribution of sediments and bathymetric characteristics within the Getz A & Dotson ice-shelf embayments. Based on the SBP data, we followed the Getz A & Dotson ice-shelf embayments to collect box cores and gravity cores from a total of 13 sites. We expect those sediment cores would reveal detailed information on the paleoenvironment since the last glacial period after physical property, geochemical, and isotopic analysis.

KOPRI
극지연구소

		Lat	Lon	Length (m)
Dotson	**AM22-GC01**	73° 39.1502'S	113° 37.8846'W	6
	AM22-GC02	73° 46.3271'S	113° 11.3696'W	3.42
	AM22-GC03	73° 57.7007'S	112° 36.0902'W	4.46
	AM22-GC04	74° 3.4457'S	112° 51.1896'W	7.1
	AM22-GC05	74° 7.8340'S	112° 33.0079'W	3.37
	AM22-GC06	74° 7.4386'S	113° 5.2900'W	2.15
Getz A	**AM22-GC07**	73° 30.2968'S	114° 58.1792'W	3.78
	AM22-GC08	73° 40.8901'S	115° 27.3836'W	4.2
	AM22-GC09	73° 49.1534'S	115° 30.3821'W	5.51
	AM22-GC10	73° 58.9701'S	115° 46.1446'W	5.35
Dotson	**AM22-BC11**	74° 13.5203'S	112° 37.1097'W	0.445
	AM22-BC12	74° 13.2516'S	113° 10.3642'W	0.52
Bear Ridge	AM22-GC13	73° 56.860'S	112° 26.0850'W	2.55
				48.855

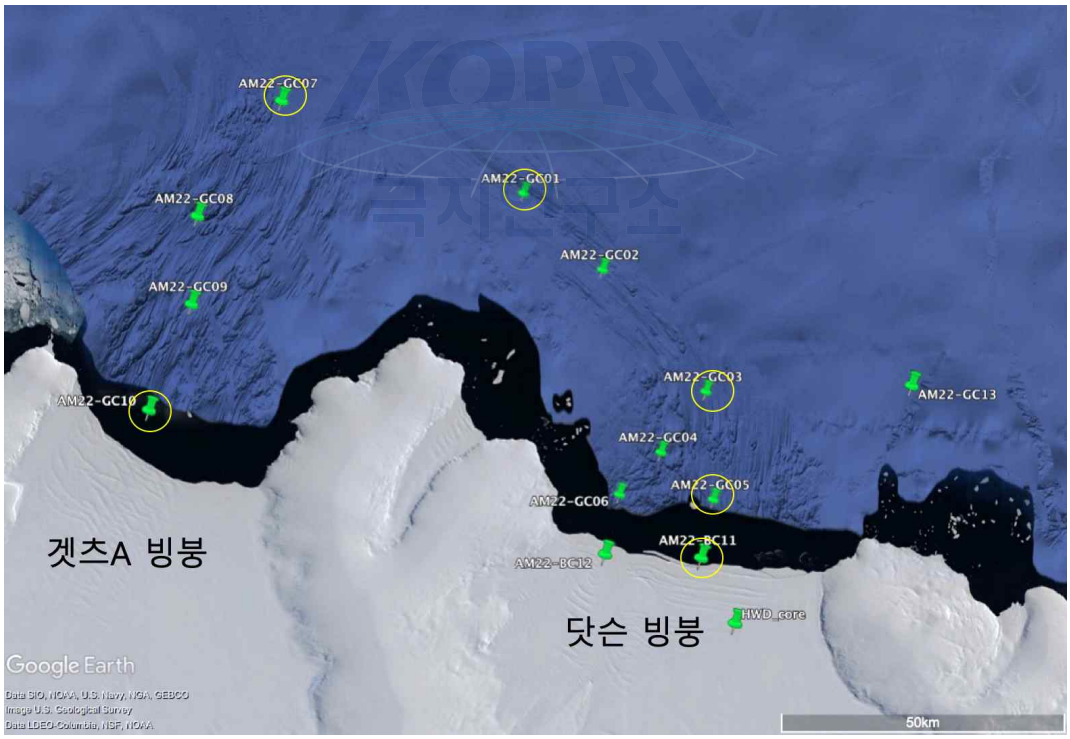


Fig. 1. Study area and sampling locations of gravity/box corings.

제 6 장

2023년 아라온 로스해 탐사 (ANA13C)

이재일, 문흥수, 강명일

한국해양과학기술원 부설 극지연구소

요약: 남극 로스해에서 마지막최대빙하기 이후 홀로세 온난기의 환경을 복원하기 위하여 2023년 3월 극지연구소 3인은 남극 로스해에서 아라온 승선 연구를 통해 지구물리 탐사와 코어 퇴적물 채취 작업을 수행하였다. 대륙붕 지역은 마지막최대빙하기 및 그 이후의 퇴적물 기록이 잘 보존되어 있어 해빙기 환경 변화 및 홀로세 온난기 환경 복원에 적합한 지역이다. 2023년 3월 아라온 탐사 ANA13C에서는 남극 로스해 서부 대륙붕의 콜먼 섬 지역과 조이데스 분지 지역, 로스해 중앙 분지에서 멀티빔 해저 지형 및 천부 지층 탐사를 수행하고 13개 지점에서 해양퇴적물 시료를 채취하였다. 또한 장보고 과학기지 인근 해역 2개 정점에서 해양 계류 장비를 설치하였다.

KOPRI 극지연구소

1. 참여인원 및 일정

가. 참여연구원

성명	소속	활동내용	비고
이재일	극지연구소	현장 조사 책임	
문흥수	극지연구소	해양퇴적물 획득, 퇴적물 트랩 설치	
강명일	극지연구소	해양퇴적물 획득	

나. 입남극, 출남극 일정

일자	인원	경로	이동수단	명단
2023.02.23	3	뉴질랜드 크라이스트처치 → 로스해	아라온	이재일, 문흥수, 강명일
2023.03.29	3	로스해 →뉴질랜드 크라이스트처치	아라온	이재일, 문흥수, 강명일

다. 현장조사기간: 2023.03.03. - 2023.03.22. (19일)

2. 연구활동 개요

○ 로스해 서부 드라이갈스키 분지 2개 정점에서 박스 코어 및 중력 코어 채취

○ 로스해 중앙분지에서 천부지층 탐사 (Sub-bottom profiling; SBP) 및 4개 정점에서 중력 코어 채취

○ 로스해 서부 조이데스 분지에서 멀티빔 해저 지형 탐사 및 SBP 탐사. 7개 정점에서 박스

코어 및 중력 코어 채취

○ 해양 계류 장비 설치: 남극 장보고 과학기지 인근 2개 정점에 수온/전도도 측정기, 퇴적물 입자 포집기 등의 해양 계류 장비 설치

3. 조사 방법 및 사용 장비

가. 지구물리 탐사

(1) SBP 천부 지층 탐사: SBP 탐사를 통하여 해저 천부 지층의 구조와 퇴적물 분포를 파악하고 퇴적물 시료를 채취할 지점을 현장에서 선정하였다. 음향 SBP 탐사는 아라온에 장착된 Konsberg SBP27 시스템을 이용하였다. 주파수 범위는 2-9 kHz, 해상도는 0.2 ms 이다.

(2) 멀티빔 해저지형 탐사: 멀티빔 지형 자료는 아라온에 장착된 Kongsberg EM122 멀티빔 에코사운더를 이용하여 획득하였다.

나. 퇴적물 시료 채취

(1) 표층 퇴적물 채취: 그림과 같은 박스 코어러를 이용하여 표층 해양 퇴적물을 채취하였다. 두 개의 코어 라이너를 이용하여 퇴적물을 확보하였으며, 코어라이너에 든 시료는 코어명과 코어의 상부 하부를 기재하여 냉장 보관하였다.

(2) 해양 퇴적물 주상 시료 채취: 그림과 같은 중력 코어러를 이용하여 해양 퇴적물의 주상시료를 획득하였다. 시료를 추후 해양퇴적물 절개 및 분석을 위해 1.5 m 단위로 절개하여 냉장 보관하였다.



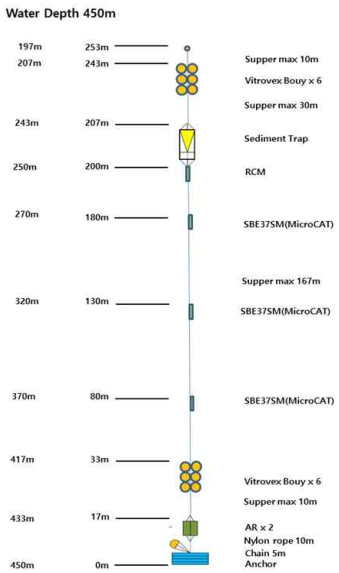
박스 코어러 (Box Corer)

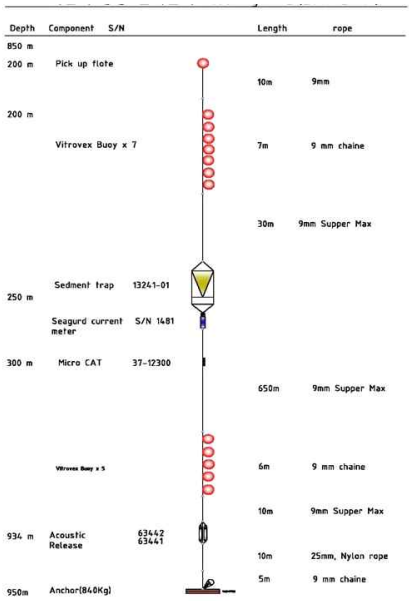


중력 코어러 (Gravity Corer)

다. 해양 계류

수층의 입자 특성과 해양 수층의 물리자료를 획득하기 위하여 그림과 같은 해양 계류장비 (Sediment Trap System)를 장보고 기지 인근 2개 지점에 계류하였다



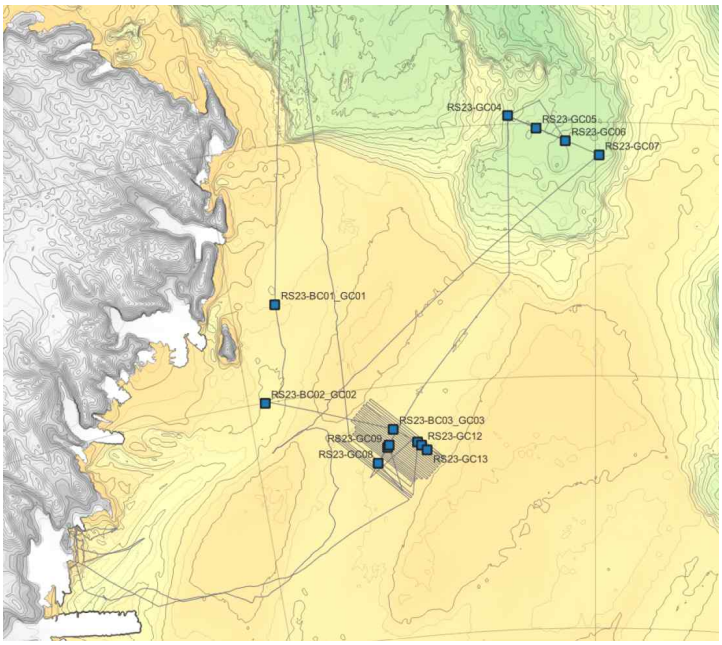


4. 조사 지역 및 시료 리스트

가. 조사지역

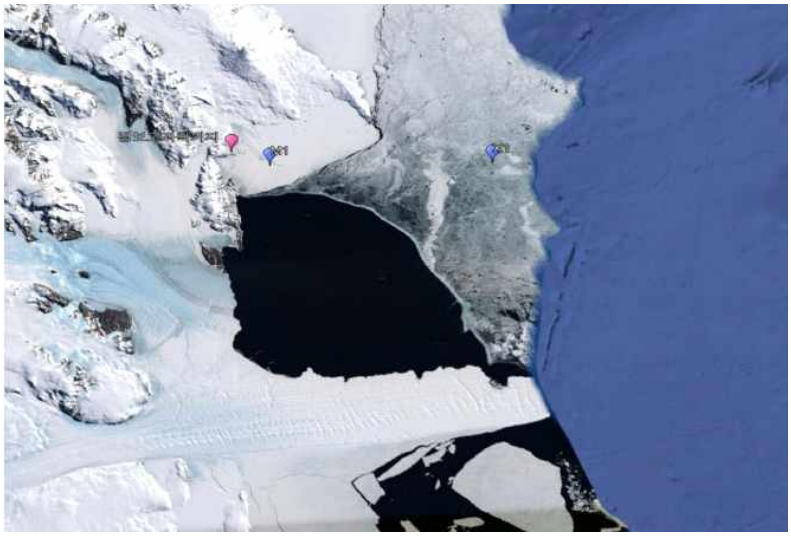
(1) 지구물리 탐사 및 해양퇴적물 채취 지역

정점 간 이동시 멀티빔 해저지형 탐사 및 SBP 탐사를 동시에 수행하였고, 조이데스 분지에서는 마지막최대 빙하기의 빙상접지선 부근에서 집중적인 해저 지형 및 SBP 탐사를 실시하였다 (그림). 해양 퇴적물은 로스해 드라이갈스키 분지 (정점 1-2번), 조이데스 분지 (정점 3번 및 8-13번), 로스해 중앙분지 (정점 4-7번)에서 채취하였다.



(2) 해양 계류 장비 설치 지역

해양 계류장비는 장보고과학기지 (그림의 분홍색 지점) 인근의 두 개 지점 (그림의 하늘색 지점)에 설치하였다. M1은 74° 41.4140′S, 164° 27.904′E, X1은 74° 50.702′S, 166° 15.019′E 이다.



나. 퇴적물 코어 리스트, 위치 및 수심

정점번호	코어명	위도	경도	수심(m)
1	RS23-BC01-GC01	73° 14.4790′S	171° 11.9808′E	525
2	RS23-BC03-GC03	73° 59.9733′S	170° 30.0722′E	641
3	RS23-BC03-GC03	74° 20.4303′S	174° 04.0981′E	577
4	RS23-GC04	71° 56.1179′S	177° 46.1755′E	1,913
5	RS23-GC05	72° 02.3305′S	178° 29.3194′E	2,167
6	RS23-GC06	72° 08.4570′S	179° 13.7445′E	2,183
7	RS23-GC07	72° 15.2948′S	179° 54.5325′E	1,833
8	RS23-GC08	74° 35.5781′S	173° 31.5377′E	519
9	RS23-GC09	74° 28.7403′S	173° 50.1878′E	546
10	RS23-GC10	74° 27.5588′S	173° 53.4123′E	570
11	RS23-GC11	74° 27.5631′S	174° 45.0834′E	541
12	RS23-GC12	74° 29.1847′S	174° 51.2404′E	535
13	RS23-GC13	74° 31.5727′S	175° 0.3979′E	475

5. 주요 성과내용

○ 남극 드라이갈스키 분지, 조이데스 분지, 중앙분지 퇴적물 분포 데이터 및 해양퇴적물 코어 시료 획득

○ 멀티빔 지형조사를 통한 해저 지형 데이터 획득

○ 테라노바 만 해양 물리 연간 데이터 획득

2023 Ross Sea Exploration (ANA13C)

Jae Il Lee, Heung Soo Moon, Myung-Il Kang

Korea Polar Research Institute

To reconstruct the environmental conditions of the Holocene warm period following the Last Glacial Maximum in the Ross Sea, Antarctica, three researchers from the Korea Polar Research Institute conducted onboard research aboard the icebreaker Araon in March 2023. Through this expedition, they carried out geophysical surveys and collected sediment core samples. The continental shelf region preserves well the sedimentary records of the Last Glacial Maximum and subsequent periods, making it an ideal area for investigating deglacial environmental changes and reconstructing Holocene climatic conditions. During the ANA13C expedition of the Araon in March 2023, multibeam bathymetric mapping and shallow sub-bottom profiling were conducted in the Coleman Island area and the Joides Basin on the western continental shelf of the Ross Sea, as well as in the central Ross Sea basin. Marine sediment samples were collected from 13 sites. In addition, oceanographic mooring systems were deployed at two sites in the waters near the Jang Bogo Station.

KOPRI
극지연구소

제 7 장

2024년 아라온 로스해 탐사 (ANA14C)

유규철, 문홍수, 강명일, 하상범

한국해양과학기술원 부설 극지연구소

요약: 본 연구는 극지연구소 주요 연구사업(PE24090)의 일환으로, 2023/24 남극하계 탐사 기간 중 아라온 3항차 동안 남극 로스해 서부 빙붕기저선 주변에서 Subbottom Profiler와 Multi Beam Bathymetry 장비를 사용하여 연구 해역의 천해 퇴적물 분포와 해저 퇴적 구조에 대한 해양 물리 데이터를 획득하였으며, 중력코어러와 박스코어러를 이용하여 해양 퇴적물 코어 시료를 채취하였다. 본 연구사업은 이 지역에서의 과거 해양환경 복원을 통해 서남극 빙붕/빙상/해빙의 변화 추이를 이해하고, 기후 변화 예측 프로그램 개발에 필요한 원천 정보를 제공하고자 한다.

1. 참여인원 및 일정

가. 참여연구원

성명	소속	활동내용	비고
유규철	극지연구소	현장 조사 책임 및 퇴적물 시추	현장 수석연구원
문흥수	극지연구소	해양퇴적물 시추	
강명일	극지연구소	해양퇴적물 시추	
하상범	극지연구소	해양퇴적물 시추	

나. 입남극, 출남극 일정

일자	인원	경로	이동수단	명단
2024.02.17	4	뉴질랜드 크라이스트처치 → 로스해	아라온	유규철, 문흥수, 강명일, 하상범
2024.04.04	4	로스해 →뉴질랜드 크라이스트처치	아라온	유규철, 문흥수, 강명일, 하상범

2. 연구활동 개요

○ 로스해 중서부 빙붕 말단 주변 탐사 (Sub-bottom profiling; SBP) 및 멀티빔 해저 지형 탐사. 7개 정점에서 박스 코어 및 중력 코어 채취

3. 조사 방법 및 사용 장비

가. 지구물리 탐사

(1) SBP 천부 지층 탐사: SBP 탐사를 통하여 해저 천부 지층의 구조와 퇴적물 분포를 파악하고 퇴적물 시료를 채취할 지점을 현장에서 선정하였다. 음향 SBP 탐사는 아라온에 장착된 Konsberg SBP27 시스템을 이용하였다. 주파수 범위는 2-9 kHz, 해상도는 0.2 ms 이다.

(2) 멀티빔 해저지형 탐사: 멀티빔 지형 자료는 아라온에 장착된 Kongsberg EM122 멀티빔 에코사운더를 이용하여 획득하였다.

나. 퇴적물 시료 채취

(1) 표층 퇴적물 채취: 그림과 같은 박스 코어러를 이용하여 표층 해양 퇴적물을 채취하였다. 두 개의 코어 라이너를 이용하여 퇴적물을 확보하였으며, 코어라이너에 든 시료는 코어명과 코어의 상부 하부를 기재하여 냉장 보관하였다.

(2) 해양 퇴적물 주상 시료 채취: 그림과 같은 중력 코어러를 이용하여 해양 퇴적물의 주상시료를 획득하였다. 시료를 추후 해양퇴적물 절개 및 분석을 위해 1.5 m 단위로 절개하여 냉장 보관하였다.



박스 코어러 (Box Corer)

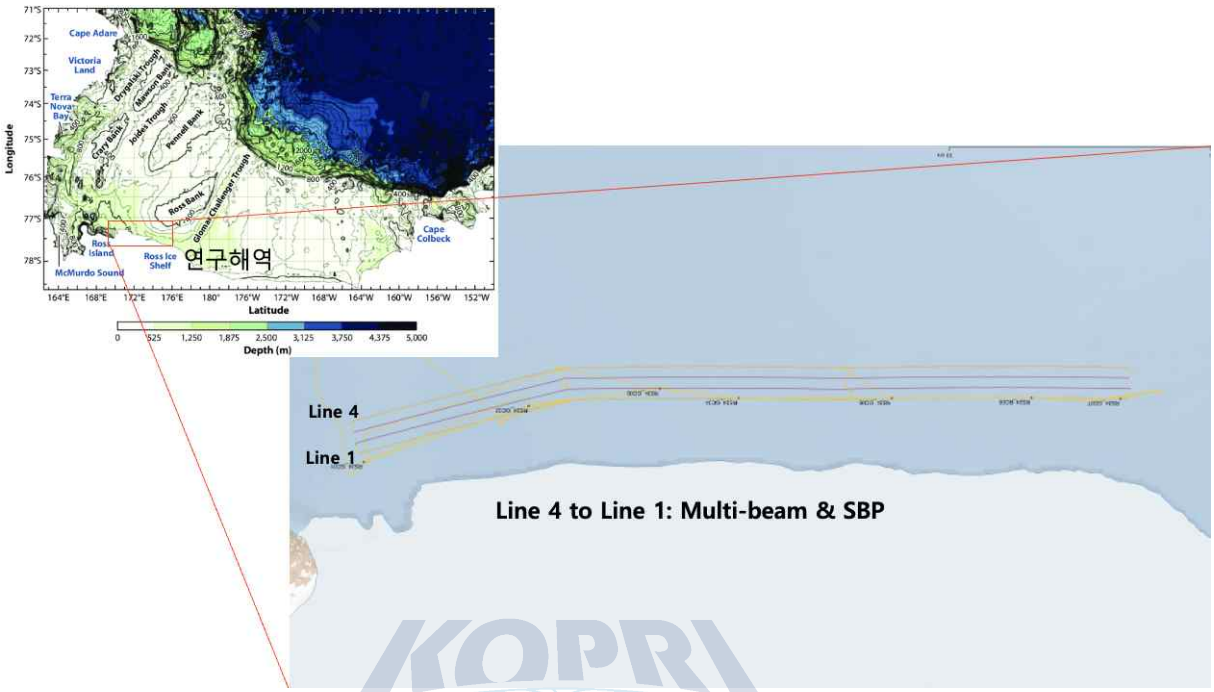


중력 코어러 (Gravity Corer)

4. 조사 지역 및 시료 리스트

가. 조사지역

남극 로스해 서부 빙붕 말단 주변에서 퇴적층 분포 파악 및 지형학적 특성 파악을 위해 SBP 탐사와 멀티빔 탐사를 수행하여 퇴적물 분포 정보 및 해저 퇴적 구조 데이터를 획득하고 해양 퇴적물을 채취하였다.



- 박스/중력 시추 (RS24-GC01, GC02, GC03, GC04, GC05, GC06, GC07)
- Line 1 - Line 5: 멀티빔 및 SBP 탄성파 탐사

나. 퇴적물 코어 리스트, 위치 및 수심

정점번호	코어명	위도	경도	수심(m)
1	RS24-BC01-GC01	-77 21.4422	169 52.9158	755
2	RS24-BC02-GC02	-77 18.6523	171 11.4645	813
3	RS24-BC03-GC03	-77 18.8392	172 11.6210	691
4	RS24-BC04-GC04	-77 20.8099	172 46.5450	655
5	RS24-BC05-GC05	-77 22.5929	173 56.3044	684
6	RS24-BC06	-77 23.8697	174 59.8250	614
7	RS24-BC07-GC07	-77 24.7021	175 40.6493	641

5. 주요 성과내용

○ 로스해 서부 빙붕기저선 주변 퇴적물 분포 데이터 및 해양퇴적물 코어 시료 획득

○ 멀티빔 지형조사를 통한 빙붕 주변 지역 해저 지형 데이터 획득

KOPRI
극지연구소

2024 Ross Sea Exploration (ANA14C)

Kyu-Cheul Yoo, Heung Soo Moon, Myung Il Kang, Sangbeom Ha

.Korea Polar Research Institute

During the 2023/24 austral summer season, our research group conducted an expedition in the western Ross Sea. Marine geophysical data on shallow sediment distribution and seafloor sedimentary structures were acquired around the western Ross Sea ice-shelf grounding line using Subbottom Profiler and Multibeam Bathymetry systems over three Araon research cruises. In addition, marine sediment core samples were collected using a gravity corer and a box corer. Marine sediment samples were collected from 7 sites. In addition, oceanographic mooring systems were deployed at two sites in the waters near the Jang Bogo Station.

KOPRI
극지연구소

제 8 장

2024-25 아라온 로스해 탐사 (ANA15B)

이민경, 강명일, 박영규, 하상범

[1]극지연구소

요약: 본 연구는 극지연구소 주요 연구사업(PE25090)의 일환으로, 2024/25 남극하계 탐사 기간 중 아라온 2항차 동안 남극 로스해 동부 리틀 아메리카 분지 지역에서 Subbottom Profiler와 Multi Beam Bathymetry 장비를 사용하여 연구 해역의 천해 퇴적물 분포와 해저 퇴적 구조에 대한 해양 물리 데이터를 획득하였으며, 중력코어러, 멀티코어러, 박스코어러를 이용하여 해양 퇴적물 코어 시료를 채취하였다. 또한 로스해 서부 테라노바만 해역에서 해양 모니터링 장비 1기의 회수, 데이터 수집, 계류를 진행하였다. 본 연구사업은 이 지역에서의 과거 해양환경 복원을 통해 서남극 빙붕/빙상/해빙의 변화 추이를 이해하고, 기후 변화 예측 프로그램 개발에 필요한 원천 정보를 제공하고자 한다.

1. 참여인원 및 일정

가. 참여연구원

성명	소속	활동내용	비고
이민경	극지연구소	현장 조사 책임 및 퇴적물 시추	
강명일	극지연구소	해양퇴적물 획득, 퇴적물 트랩 설치	
박영규	극지연구소	해양퇴적물 탐사 및 획득	
하상범	극지연구소	해양퇴적물 탐사 및 획득	

나. 입남극, 출남극 일정

일자	인원	경로	이동수단	명단
2024.12.27	4	뉴질랜드 크라이스트처치 → 로스해	아라온	이민경, 강명일, 박영규, 하상범
2025.02.23	4	로스해 →뉴질랜드 크라이스트처치	아라온	이민경, 강명일, 박영규, 하상범

2. 연구활동 개요

○ 로스해 동부 리틀 아메리카 분지 7개 정점에서 천부지층 탐사 (Sub-bottom profiling; SBP) 및 멀티빔 해저 지형 탐사. 7개 정점에서 박스 코어, 멀티 코어 및 중력 코어 채취

○ 해양 계류 장비 설치: 남극 장보고 과학기지 인근 1개 정점에 수온/전도도 측정기, 퇴적물 입자 포집기 등의 해양 계류 장비 설치

3. 조사 방법 및 사용 장비

가. 지구물리 탐사

(1) SBP 천부 지층 탐사: SBP 탐사를 통하여 해저 천부 지층의 구조와 퇴적물 분포를 파악하고 퇴적물 시료를 채취할 지점을 현장에서 선정하였다. 음향 SBP 탐사는 아라온에 장착된 Konsberg SBP27 시스템을 이용하였다. 주파수 범위는 2-9 kHz, 해상도는 0.2 ms 이다.

(2) 멀티빔 해저지형 탐사: 멀티빔 지형 자료는 아라온에 장착된 Kongsberg EM122 멀티빔 에코사운더를 이용하여 획득하였다.

나. 퇴적물 시료 채취

(1) 표층 퇴적물 채취: 그림과 같은 박스 코어러를 이용하여 표층 해양 퇴적물을 채취하였다. 두 개의 코어 라이너를 이용하여 퇴적물을 확보하였으며, 코어라이너에 든 시료는 코어명과 코어의 상부 하부를 기재하여 냉장 보관하였다.

(2) 해양 퇴적물 주상 시료 채취: 그림과 같은 중력 코어러를 이용하여 해양 퇴적물의 주상시료를 획득하였다. 시료를 추후 해양퇴적물 절개 및 분석을 위해 1.5 m 단위로 절개하여 냉장 보관하였다.

KOPRI 극지연구소



박스 코어러 (Box Corer)

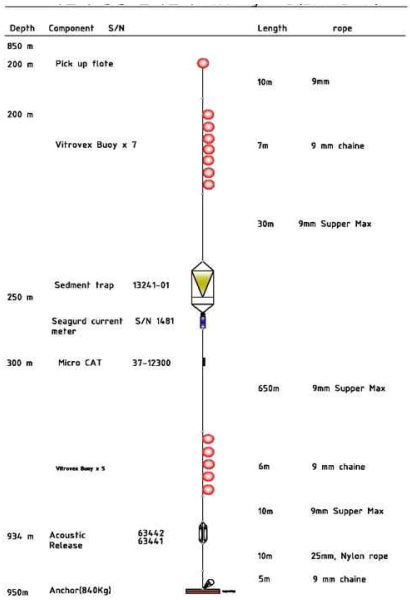


중력 코어러 (Gravity Corer)

다. 해양 계류

수층의 입자 특성과 해양 수층의 물리자료를 획득하기 위하여 그림과 같은 해양 계류장비 (Sediment Trap System)를 장보고 기지 인근 1개 지점에 계류하였다.

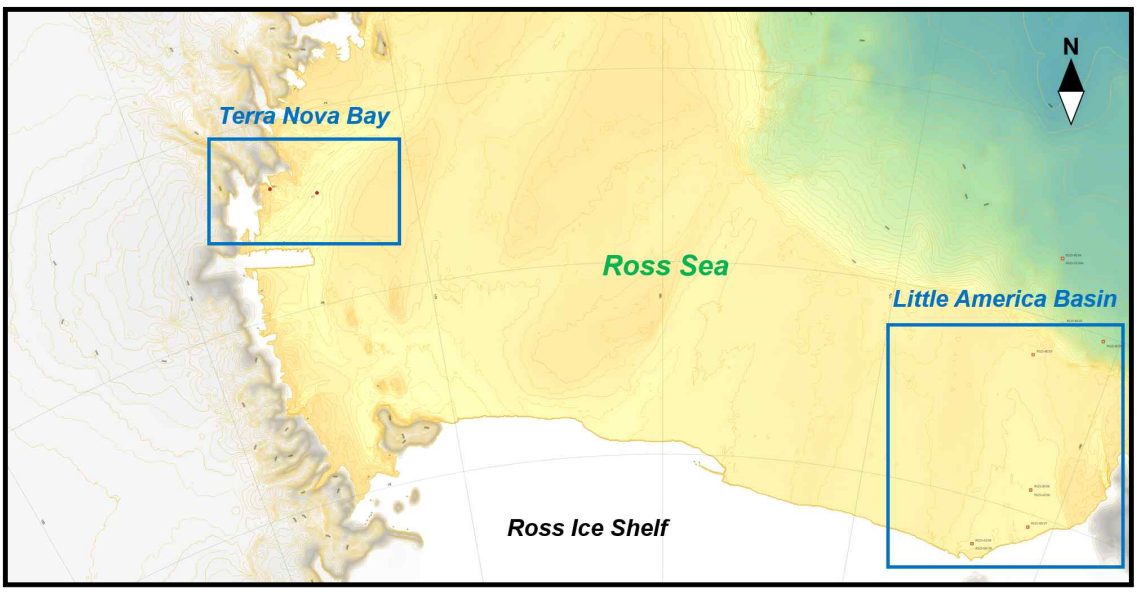




4. 조사 지역 및 시료 리스트

가. 조사지역

남극 로스해 동부 리틀아메리카 분지 대륙붕 및 대륙사면 해역에서 퇴적층 분포 파악 및 지형학적 특성 파악을 위해 SBP 탐사와 멀티빔 탐사를 수행하여 퇴적물 분포 정보 및 해저 퇴적구조 데이터를 획득하고 해양 퇴적물을 채취하였다 (그림 1). 또한 로스해 서부 테라노바만 내 한 정점(X1)의 해양 모니터링 장비를 회수하여 데이터를 수집하고 다시 계류하였다. (그림 2)



나. 퇴적물 코어 리스트, 위치 및 수심

정점번호	코어명	위도	경도	수심(m)
1	RS25-BC03	76°24.4854'S	163°27.2907'W	617
2	RS25-BC04-GC04	75°22.0152'S	163°25.2695'W	3191
3	RS25-BC05	76°1.2099'S	162°35.1847'W	2220
4	RS25-BC06-GC06	77°45.4164'S	161°40.8802'W	670
5	RS25-MC07-GC07	78°7.9043'S	161°13.9423'W	628
6	RS25-MC08-GC08	78°28.3390'S	163°42.3001'W	643
7	RS23-BC07-GC07	76°3.3616'S	160°43.5695'W	2839

다. 테라노바만 해양 모니터링

- 로스해 서부 테라노바만 내 1개 정점(X1)의 해양 모니터링 장비 회수, 계류 및 데이터 수집 (그림 3)

1) X1(74° 51.396’ S, 166° 12.027’ E) 계류 시스템 회수: 1075m 수심의 정점에서 목표 수심에 대해 퇴적물 포집기 1기, 조위계 1기, 수온염분센서 1기가 연결된 계류 시스템을 회수하여 해양 물리 연간 데이터 획득
2) X1(74° 51.329’ S, 166° 12.174’ E) 계류 시스템 재계류: 기존 계류 시스템 회수 후 소모품 교체 및 수온염분센서 1기를 교체하여 당해 해양 물리 데이터 획득을 위해 재계류

5. 주요 성과내용

○ Little America Basin 퇴적물 분포 데이터 및 해양퇴적물 코어 시료 획득
○ 멀티빔 지형조사를 통한 빙붕 주변 지역 해저 지형 데이터 획득
○ 테라노바 만 해양 물리 연간 데이터 획득

2024-25 Ross Sea Exploration (ANA15B)

Min Kyung Lee, Myung Il Kang, Young Kyu Park, Sangbeom Ha

Korea Polar Research Institute

During the 2024/25 summer season, our research group conducted an expedition in Terra Nova Bay in the western Ross Sea and around the Little America Basin in the eastern Ross Sea. In Terra Nova Bay, we recovered one ocean mooring systems that are operated to monitor the present marine environment, retrieved the data, and redeployed the moorings. In the Little America Basin, located in the eastern Ross Sea, we conducted a survey of the seafloor topography and sediment distribution on the continental shelf and continental slope, and collected core sediments by box corer, multi-corer, and gravity corer from a total of 7 sites and surveyed glaciomarine features in front of the ice shelf.

KOPRI
극지연구소

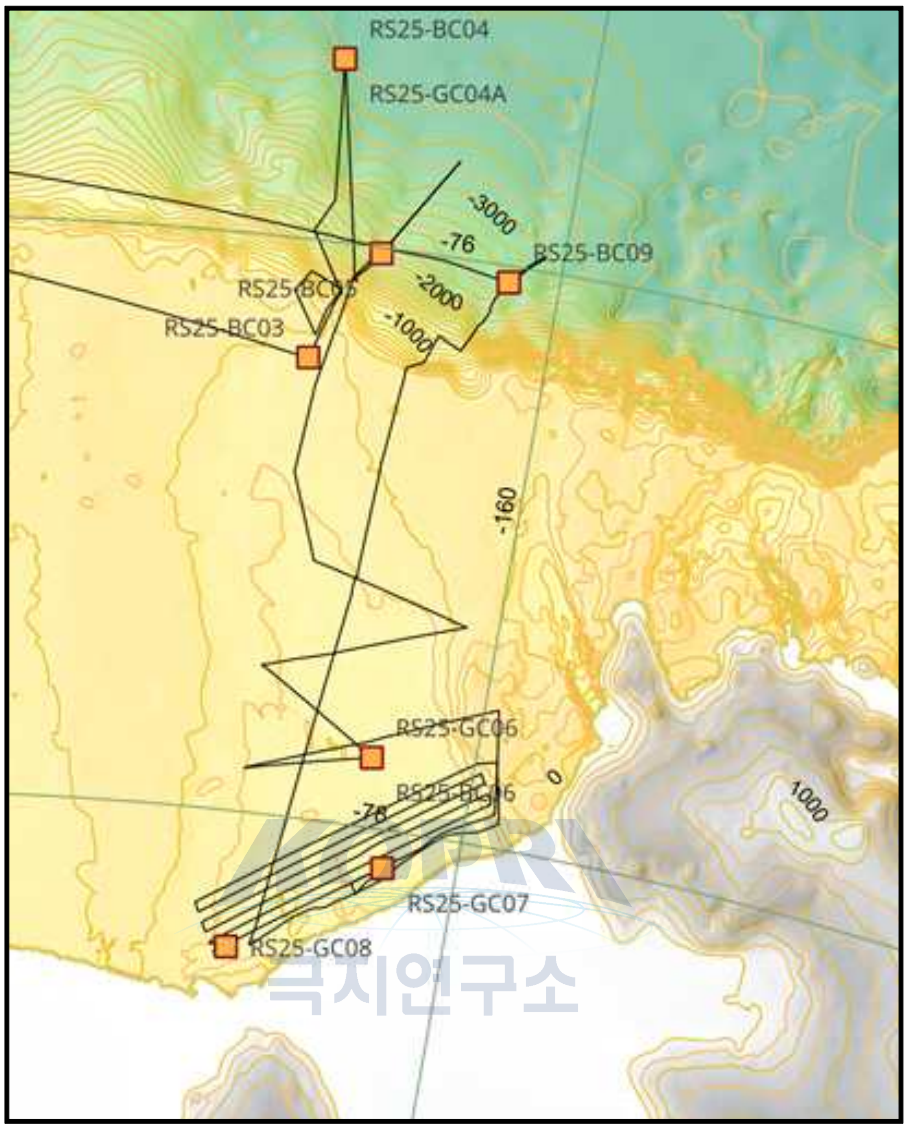


Figure 1. Location of gravity core and box cores (orange squares) from Little America Basin.

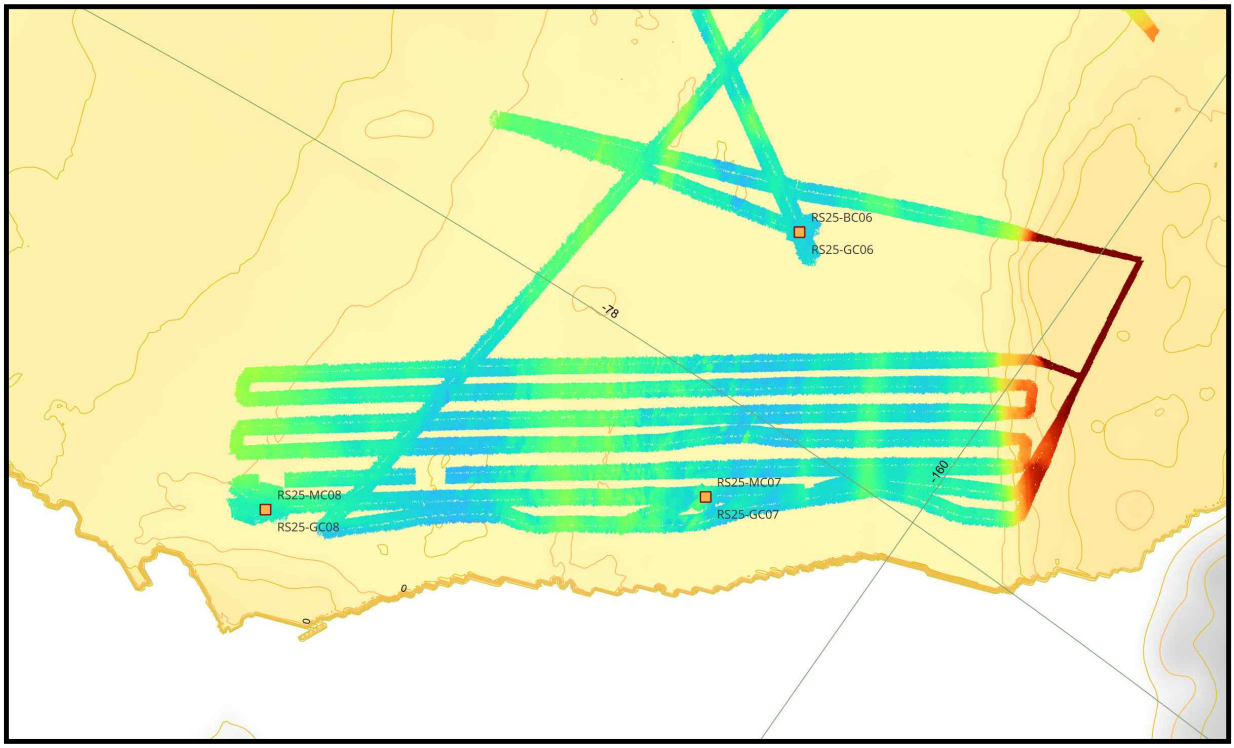


Figure 2. Swath Bathymetry image of the southern portion of Little America Basin showing two sets of mega-scale lineations indicating ice-flowing direction in the western and eastern part respectively.

KOPRI
극지연구소

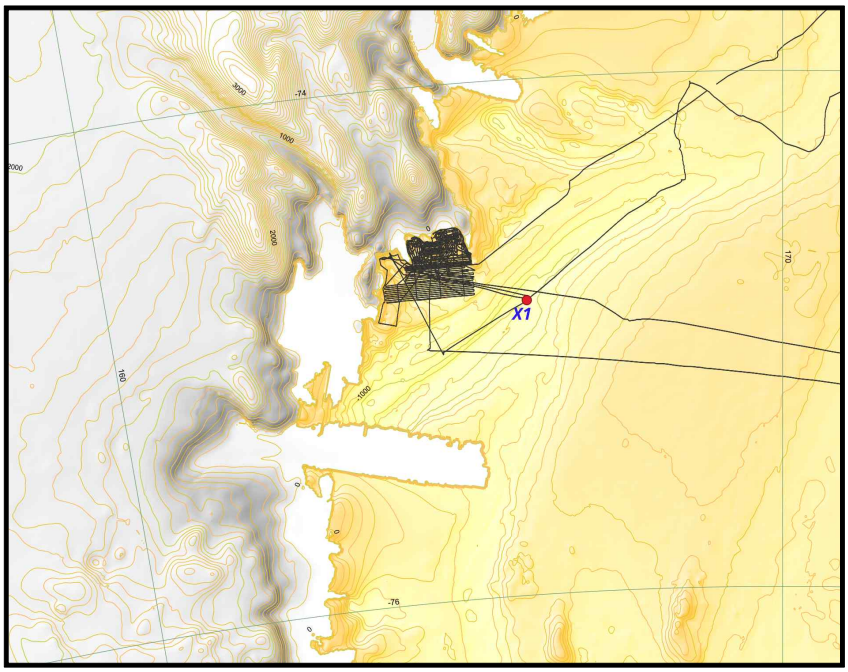


Figure. 3. Location of the ocean mooring systems (X1; blue dot) in Terra Nova Bay.

KOPRI
극지연구소

제 9 장

Snowball Earth (the Cryogenian) reincarnated from the Holocene sediments beneath the Larsen C Ice Shelf (Antarctica)

Kyu-Cheul Yoo[1], Jae Il Lee[1], Min Kyung Lee[1], Sunghan Kim[1], Jaewoo Jung[3], Julia Wellner[4], Cristina Subt[2], Brad Rosenheim[2], Jinwook Kim[6], Amy Leventer[7], Hyun-Hee Rhee[5], Yeong Bae Seong[5], Heung Soo Moon[1], Boo-Keun Khim[8], Jihyun F. Kim[9]

[1]Korea Polar Research Institute, Songdomirae-ro 26, Incheon 21990, Republic of Korea (kcyoo@kopri.re.kr), [2]College of Marine Science, University of South Florida, St Petersburg, Florida, USA, [3]Global Ocean Research Center, Korea Institute of Ocean Science & Technology, Busan 49111, Korea, [4]Department of Earth and Atmospheric Sciences, University of Houston, Houston, TX 77204, USA, [5]Department of Geography, Korea University, Seoul 02841, Republic of Korea, [6]Department of Earth System Sciences, Yonsei University, Seoul 03722, Republic of Korea, [7]Department of Geology, Colgate University, Hamilton, New York, USA, [8]Department of Oceanography, Pusan National University, Busan, 46241, Korea, [9]Department of Systems Biology, Division of Life Sciences, Institute for Life Science and Biotechnology, and Microbiome Initiative, Yonsei University, Seoul, 03722, Korea

KOPRI 극지연구소

Abstract. Larcen C Ice Shelf is facing the crisis of collapse following Larsen A and B Ice Shelves. Sediment core GC16B was collected in Larsen C embayment and) with a unique style of lamination and massive diamicton in core GC16B is the first sedimentary record in Antarctica. Oceanic and glacial changes are reconstructed based upon sedimentological, geochemical, and paleontological data with a chronology based on accelerator mass spectrometry on foraminifera and ramped pyrolysis 14C datings. The paleoceanographic changes since the early Holocene include the transitions from a grounded ice through a floating ice shelf to a consolidated sea-ice condition. The laminated sediments are interpreted to be deposited from sediment-laden meltwater plumes within an ice cavity beneath a floating ice shelf modulated by changes in oceanic forcings. The sedimentological and geochemical records from GC16B, located proximal to the grounding line in Larsen C embayment, are compared to sedimentary rocks featuring dropstone-free, laminated sediments

with massive ice-proximal diamictites during the Sturtian glaciation called "Snowball Earth". These data provide a new analogy for an ice-contact deposition under synglacial environment during the Snowball Earth glaciation.

1. Main

One of the largest recorded icebergs broke off from Larsen C Ice Shelf (LCIS) in the eastern Antarctic Peninsula (EAP) in July 2017 over a decade after 1995 and 2002 collapse of Larsen A and B Ice Shelves (LAIS and LBIS) (Fig. 1a). This event may be a precursor of the future collapse of the whole LCIS in the future warming. The glacial retreat history of LAIS and LBIS was presented previously from the analyses of paleo-records[1,2]. Sediment cores from Larsen B embayment revealed that the LBIS maintained its integrity throughout 11,000 years before present (yrs BP) until recently[2], with the recent LAIS and LBIS breakups associated with local warming in the eastern Antarctic Peninsula (EAP). The first detailed reconstruction of the LCIS also indicates two phases of retreat but without collapse happened since ca. 7,300 yrs BP[3], representing that contemporary ice-shelf loss from the LBIS to the LCIS was unprecedented during the past 11,000 yrs. Thus, the overall LIS of EAP maintained the integrity during the Holocene except for the collapse of the LAIS during the mid-late Holocene[1]. If future warming continues further, the ice-shelf instability is vulnerable to encroaching farther southward along the LCIS. Nevertheless, there have been few direct investigations in the Larsen C embayment. The recent collapses of LISs are attributed to both atmosphere and ocean warming and the paleo-records from marine sediments provide important clues regarding gradual ice-shelf thinning and shrinking during the Holocene. Future warming may impact the LCIS stability. The limited number of paleo-records from the Larsen C embayment[3,4] suggests the need for additional direct investigation of the history of the Larsen C embayment and reconstruction of glacial history and the role of ocean forcing beneath a floating ice-shelf.

With the venture of the icebreaker Araon (Korea Polar Research Institute) a new sedimentary environment was sampled in the Larsen C embayment in April 2013 (Fig. 1). The sediments in core GC16B provide a unique window into sedimentary processes in a setting proximal to the GL adjacent to one of the largest extant ice shelves in Antarctica. Notable features of these sediments include: 1) the occurrence of rhythmic laminations that we suggest may result from oceanic forcing, 2) a lack of any sign of ice-rafted debris (IRD), and 3) an example of sedimentation proximal to

grounding line (GL) adjacent to one of the largest extant ice shelves in Antarctica (Fig. 2). The successive rhythmic laminated facies has rarely been observed under severe glaciation in Antarctica. The unique style of lamination and associated facies context may have direct corollaries with ancient strata found interbedded in rocks of Neoproterozoic age on several continents (laminated siltstones and sandstones devoid of IRD, laminated mudstones with IRD, and large scale interbedding with coarse sandstones and conglomerates). The unusual observations of strata and geochemical associations found in Neoproterozoic stratigraphic successions around the world suggested the Snowball Earth (SE) hypothesis, an extreme glaciation event associated with global glacial cover, restrictions in chemical weathering, and constrictions in the biotic systems of the earth[5]. The hypothesis is controversial because the lithofacies are presumed to require flowing water to transport and deposit sediment from a terrestrial source into the basin of deposition (non-glacial processes). In response, the geologic community has been trying to find evidence of modern examples whereby the sedimentologic associations can be found to be compatible with severe glaciation. Our observed facies context clearly illustrates a direct and close relationship to a large ice-shelf system similar to severe glacial condition, albeit during an interglacial high stand. Here we focus on the paleoceanographic variability in the Larsen C embayment during the Holocene and the possibility of a new analogy compatible with severe glaciation.

Larsen C embayment was accessed in May 2013 when core GC16B was collected (Fig. 1). The regional GL is located within ~25 to 28 km landward of core GC14A (GL distal)6, but the distance between expected GL and core GC16B is within 6 to 8 km, indicating that the core site corresponds to a GL-proximal setting. The glacial geomorphological characteristics in the vicinity of core GC16B include a great number of closely-spaced GL and consistently back-stepped GL features (average distance between each successive grounding zone feature: 740 m)[6]. Core GC14A is a 43-cm in length and consists of a medium sandy facies with some IRDs. Core GC16B was collected from a water depth of 324 m in the ~8.7-km-wide basin is a 236-cm long and consists mostly of laminated sediment (Fig. 2A). An approximately 2.0 m-thick drape sediment observed in sub-bottom profiles corresponds to the entire Holocene sequence (about 1.9 m in thickness) except glacial till (Fig. 1C). Four lithostratigraphic intervals are recognized in core GC16B: a glacial till diamicton (U4, 192-236 cm), a parallel-laminated mud (U3b, 117-192 cm), a cross-laminated mud (U3a, 94-117 cm, 63-90 cm, 34-47 cm, 21-32 cm), a faintly cross-laminated mud (U2, 90-93 cm, 47-63 cm) and a sandy to homogenous mud with IRD (U1, 0-21 cm and 32-34 cm) (Fig. 2). A ramped PyrOx 14C date of 11,577±479 cal. yrs BP on bulk

KOPRI 극지연구소

sediment at the uppermost of U4[7], and the base of U3b provides the timing of the termination of glacial cover on the core site7. All units were compared to the reconstruction of atmospheric temperatures obtained in the James Ross Island (JRI) ice core8 (Fig. 3). The Holocene temperature history from JRI ice core provides important information to infer the Holocene glacial stability along the LIS region. The presence of U3b facies above the glacial till reflects sedimentation during the early Holocene after the core site transitioned from the Last Glacial Maximum to Holocene. The uppermost U1 facies represents the late Holocene and the U3a facies is the mid-Holocene in age[3].

Multy-proxy data document the glacial environment in Larsen C system (Fig. 3). Meteoric 10Be ranges from 0.1 to 9.1×10^{7} atoms g^{-1}, reflecting an ice-shelf open history. The surface ^{10}Be concentrations of the box core are lower than the 10Be concentrations (>5.1×10^{8} atoms g^{-1}) of the upper unit (0~16 cm) recorded at the mid-shelf of Larsen B embayment9. Biogenic opal, a productivity indicator, is between 1.1 and 6.2% (average: 3.2%) in the Holocene sediment, implying limited input of primary production from diatoms. U2 and U3 facies are sedimentologically distinct units of laminated muds (Fig. 2); the characteristics of U2 facies are nearly consistent with sequences of U3a facies. The fine-grained and non-biogenic detritus with no diatoms or foraminifera, and low ^{10}Be concentrations suggest that a floating ice shelf covered to the core site. The high total organic carbon (TOC) and TOC/total Nitrogen (C/N) ratios and the low biogenic opal in U3b unit are interpreted to be due to the input of relict carbons from a sediment-laden meltwater plume beneath a floating ice-shelf. Warm atmospheric and oceanic warm conditions during the mid-Holocene may have allowed the calving line to recede landward, though without collapse[2,3,10]. The increasing ^{10}Be concentrations in the upper facies indicate the proximity of the calving line to the core site. Dispersed IRDs between 32 and 34 cm (~5,200 cal. yrs BP) and between 0 and 21 cm (~4,700 cal. yrs BP to present) were mainly deposited by ice rafting under an open marine condition. However, despite expected primary production in this seasonally open marine setting at this time, the biogenic opal and TOC contents are very low, suggesting a consolidated pack ice environment in Larsen C embayment, limited biological activity. Indeed, sea-ice cover in the Weddell Sea stretches beyond the northern tip of the Antarctic Peninsula into the Drake Passage11. Compact, consolidated pack ice still covers Larsen C embayment in the summer, sometimes with polynyas12. The presence of U3a facies after ~5,200 cal. yrs BP may be due to a sequence of retreat-advance-retreat of the calving line[3]. Nevertheless, there was no abrupt disintegration of the calving line following the neoglacial, irrespective of the recent calving events of LIS since the 1950s[13]. The

factors that enable glacier and ice-shelf retreat include decreasing sea-ice days, intense snowmelt, weakening easterlies, and relative changes in sea surface temperatures[14]. The stability of the calving line likely is associated with the more compact, consolidated pack ice after deglaciation. The persistent pack ice during the late Holocene can suppress iceberg calving and act to stabilize ice shelf to some extent by dampening the external forcings (wind, tide, wave, swell, etc.)[15]. Lake and marine sediments on the north-eastern AP and the JRI ice-core highlight regional Neoglacial onset from ~2,000 to 3,500 cal. yrs BP and the climatic cooling and extensive sea-ice cover persisted to near present[2,16,17]. The glacial history of core GC16B documents the transition from a grounded glacier (glacial till in U4) through a floating ice shelf (mid-Holocene) to a consolidated pack ice (late Holocene). Microbiota profiles also follow a similar environmental trend showing higher microbial diversity and productivity during the late Holocene than during the mid-Holocene (unpublished data)[18]. Most sediments except U1 facies are composed of fine-grained (7.1 to 9.8 phi mean) and non-biogenic detritus without diatom and foraminifera. The fine-grained sediments may be transported from the GL near the core site rather than far open marine. GL-proximal sedimentation is typically achieved by the potential of an ocean cavity and the retreat of GL under a severe glacial environment19. The fine-grained deposition within the GL-proximal zone may result from a sediment-laden plume of an ice cavity, although the presence of an ocean cavity below 300 to 350 m has not been identified. Sub-ice shelf sediment cores collected beneath the floating Pine Island Glacier ice-shelf (the GL located within 30~35 km landward) are also characterized by finely laminated muds in the upper unit and are interpreted to have a sediment-plume source20. The spatial transition from coarse-grained (GL-proximal) to fine-grained sediments (more distal, sub-ice shelf) takes place with increasing distance from the GL3. Suspension settling from sediment-laden meltwater plumes allows sequences of laminated sediments to be deposited distal from the GL to massive muds and sandy mud beneath the sub-ice shelf. However, the fine-grained sediments that characterize core GC16B, collected from a site proximal to the GL, are unlikely to support such a depositional setting with increasing distance from the GL beneath a floating ice shelf. The present GL is very close to the core site (ca. 6 to 8 km). GL retreating rate may have been rapid during deglaciation and the time between the last pinning point of the GL and the onset of sedimentation might be contemporary on the paleoceanographic scale. Therefore, the presence of an ocean cavity that formed post-deglaciation, and the ultimate stable still-stand of the GL may contribute to the fine-grained sedimentation until the mid-Holocene.

U3 facies overlying glacial till sediments, consist of the parallel-laminated (U3b) and cross-laminated facies (U3a) deposited under a low-energy environment. The transition from parallel-laminated (U3b) to cross-laminated facies (U3a) with the stable still-stand of the GL is mainly linked to ocean forcing related to atmospheric change and the retreat of the calving line. The cross-laminated sediments found on the Mac.Robertson Shelf in East Antarctica during the mid-Holocene warm phase are interpreted to form via a signal of episodic strong density currents on the ice shelf such as those associated with High Salinity Shelf Water (HSSW)21. The U3b facies during the mid-Holocene may result from strong density currents inside the core site. Water masses in the Larsen C embayment are HSSW, Ice Shelf Water (ISW), and modified Warm Deep Water (MWDW)22. HSSW is formed during the winter by brine rejection during sea-ice formation and by the wintertime cooling, and salinification of MWDW that has crossed the shelf break locally. The water mass that travels to the deep GLs in the southern LCIS probably is linked to inherent Larsen HSSW that flows beneath the ice front southeast of Kenyon Peninsula (Fig. 4a). It may spawn the ISW that is responsible for the cross-laminated sedimentation to the north of the LCIS. In the contrast, the parallel-laminated facies is likely to be due to the weak density current that flows toward the ocean cavity, implying the weakened ISW flow to the core site due to a more distant sea-ice zone during the early Holocene (Fig. 4b). At the same time, the WDW intrusion was intensified to the inner shelf, resulting in basal melting beneath a floating ice shelf, such that the GL might have retreated during the early Holocene. A cooler condition in the present inner shelf indicates a weakening of warm water intrusions with increasing time to the late Holocene. Indeed, the MWDW is not found in the inner shelf, but in the mid shelf in the present. Thus, the weakening of paleo-ISW to GL along with the intensive intrusion of warm water during the early Holocene likely gave rise to the deposition of parallel-laminated sediments.

The sediment layers defined from 2-D images of the thin-slabs (10×100×4 mm) of the whole Holocene sediment reveal ~1,200 couplets or more of the silt and clay (Fig. 2)[23]. The post-glacial sediments in the Larsen A, B, and C embayment constitute various facies including the homogenous mud, the gravelly mud, the silty sand, and some laminated mud1,2,3. Deposition of laminated sediments can be influenced by the variability and position of GL. On the one hand, successive tidal cycles yield a complex of grounding zone wedges, and sediment deposits on the seafloor exhibit thin drapes[24]. The laminations in core GC16B are composed of the alternation of silt and clay, but there is no evidence of tidal bundles and thickening-thinning patterns. A tidal influence is not largely associated with plume behavior at the ice cavity

through the still-stand GL or a tidal signal can't be revealed from our analysis. Based on an accumulation rate estimated from the core chronology, the average signal of each layer is estimated to reflect multi-year deposition. On decadal timescales, El Niño-Southern Oscillation time scales and forcing might drive the alteration observed in laminated sediments. Cooler waters on the Amundsen shelf in 2012 coincided with La Niña conditions[25]. Warm water incursion to the Weddell Sea with El Niño conditions leads to a looser sea-ice and more open marine conditions, during which the propagation of ocean forcings can have a dynamic influence into the LCIS26. Under these conditions, the coarser particles (silty-sized) from an ice cavity may be deposited.

This is the first report of the occurrence of laminated sediments that were deposited beneath a floating ice shelf during the mid-Holocene. The sequence from glacial till to laminated facies calls attention to the argument specific lithology (diamictite+laminated ironstones), one of the controversial issues of the SE hypothesis[5]. Some laminated ironstone facies are repeatedly interbedded with massive diamictites, yet dropstones and other gravel inputs are nearly absent. The sedimentological features, the diamictite and ironstone, and the location within a paleobathymetric depression[27] are identical to the depositional setting with the glacial till and laminated sediments deposited in a basin beneath the LCIS (Fig. 1C). Today the most severe glacial cover is restricted to Antarctica where extensive continental ice sheets, ice shelves, and large fringes of persistent sea ice lock the southern pole in a severe "ice house" state. In particular, the parallel-laminated U3b sediments in the still-stand GL proximal zone of the inner LCIS during the early Holocene are analogous to the sedimentological facies characteristic of the most severe global scale glaciation in earth's history, SE, which featured low-latitude ice sheets at sea level and widespread marine ice cover. The upper continental crust-normalized patterns of rare earth elements and (La/Yb)n in U3b facies can identify the provenance (Fig. 3) and are consistent to glacial till U4 sediments, suggesting that they have the similar sources with U4 sediments. The lighter values of δ13C in U3b record the very limited productivity in this most ice-covered environment during the mid-Holocene although oceanic organic matter may have been transported to these sediments (abrupt increase of δ15N)[4]. The U3b facies can be compared to Iron Formations (IFs, the finely laminated ironstones) found in Neoproterozoic stratigraphic successions. Eu and Ce anomalies that reflect the contemporaneous water characteristics are a well-established, robust paleoredox proxy[28]. Eu is depleted in general seawater except under hydrothermal conditions, and Ce is depleted in seawater under oxic conditions and preferentially scavenged relative to nonredox sensitive rare earth elements.

Generally, the depleted Eu and Ce anomalies (Eun/Eun* and Cen/Cen* < 1 when normalized to upper continental crust) (Fig. 3) imply that the sediment is deposited under oxygenated conditions without the local hydrothermal vents. More depleted Eu and Ce anomalies in U3b facies indicate oxygenated meltwater near the GL. The increasing oxidation near the ice shelf GL during the early Holocene may be associated with subglacial ablation driven by warm water incursions. Since then, the lower atmospheric temperatures and weaker incursions of warm water occurred, resulting in the lack of Eu anomalies of the less oxygenated meltwater in U3a facies. In the modern ocean, outflow of meltwater-laden fresher water at the inner Thwaites ice shelf was identified via the oceanographic survey by an autonomous underwater vehicle[29]; incursion of warm salty ocean water in the Amundsen Sea becomes colder and fresher, and high levels of dissolved oxygen are found in the meltwater. The melting of meteoric ice typically produces meltwater containing dissolved oxygen from trapped air bubbles. The meltwater supplies GL systems with dissolved oxygen, as seen in modern subglacial lakes that are oxygenated due to inflowing water[30].

The oxygenated condition relative to U3a facies is demonstrated by higher Fe/Ti and Mn/Ti in U3b facies (more glaciated condition) (Fig. 3), supporting the geological analogy to explain the paradox of the IFs during the SE glaciation. The redox-sensitive metals (Fe and Mn) are much enriched in the ice-contact facies IFs deposited under a more oxygenated conditions (depleted Ce anomalies) during glaciation[28]. Sediments proximal to stable GLs within the solid synglacier over the globe preserved the more enriched Fe and Mn signal. In contrast, the similar oxygenated environment in the U3b facies beneath LCIS is much poorer in Fe (1.60 to 1.91% total iron) and Mn (0.16 to 0.17% total manganese). This is attributed to be due to the difference of paleoredox between the oceanic condition during the Sturtian glaciation and the glacio-oceanic environment during the Holocene. The geochemical proxies of these IFs record the relatively high degree of oxygenation in the extensive ice-contact environment within the synglacial oceans and more iron-rich seawater under widespread anoxic ocean far from glaciated margins with a severely inhibited atmospheric exchange. In contrast, in Antarctica, a floating ice-shelf environment during deglaciation is freely connected with the well-oxygenated oceans, resulting in the reductive dissolution of less iron-rich seawater relative to the synglacial redox environment.

2. Methods

Geological location and sediment sampling. Cores and some geophysical data were collected during Antarctic Program (ANA03C Cruise Expedition by the Korea Polar Research Institute) of the Ice breaker R/V Araon in 2013 (Fig. 1). A marine geological expedition conducted in the LIS-C embayment of northwestern Weddell Sea. A whole round core sample (238 cm below the seafloor) of marine sediment (GC16B) was collected on the northwestern part of LIS-C embayment (66° 3.898′ S, 60° 27.692′ W).

Physical properties and geochemical proxies. The MS was measured at 1-cm intervals on split half-core sections using a Bartington MS-2B susceptibility meter. Before splitting the core sections, whole-round magnetic susceptibility values were measured at 1-cm intervals using a core logging sensor (Bartington MS2C). Geochemical proxies were measured from 1- cm-thick samples collected at 2-cm intervals. Biogenic silica (Sibio) concentrations were measured using a continuous flow analyzer (SKALAR SANplus Analyzer) and the wet-alkaline extraction method modified from DeMaster (1981) at the Korea Polar Research Institute. Biogenic opal concentrations were calculated by multiplying biogenic silica concentrations by 2.4, the ratio of biogenic opal (SiO2+nH2O)/Si that was determined by assuming that nH_2O constitutes 10% of biogenic SiO_2 [31]. The relative analytical error of biogenic silica concentration in sediment samples is less than 1%. Total carbon (TC) and Total Nitrogen (TN) concentration was measured using an organic elemental analyzer (FLASH, 2000 NC Analyzer) with an analytical precision of less than ±0.1%. Total inorganic carbon (TIC) concentration was measured using UIC CO2 coulometer (Model CM5240) at the KOPRI. $CaCO_3$ concentrations were calculated by multiplying TIC concentrations by 8.333, the ratio of $CaCO_3$/C. The relative standard deviation for $CaCO_3$ concentration is ±1%. Total organic Carbon (TOC) concentrations were calculated as the difference between TC and TIC.

XRF analysis. Glass beads were prepared using the following methods. The alkali flux used in this study was a lithium tetraborate ($Li_2B_4O_7$). The sample was ignited at 110℃ for 8 h in an oven prior to weighing. Samples were weighed in a ceramic crucible and ignited in a muffle furnace for 20 min/h at 1000℃. Glass beads were prepared by mixing 0.6 g of powdered rock sample, or a mixture of rock sample and a chemical reagent(s), and 6.0 g of the flux (10 times the amount of the standard powder sample). The mixture was put into a Pt crucible (mixed 95% platinum and 5% gold) and 0.05 g of lithium bromide (LiBr) were added as exfoliation agent. Fusing and agitation were carried out with an automated high frequency bead sampler (SPEX, K-2 PRIME); at 300s prefusion (~1050℃), 60 s fusion (~1080℃), during

agitation. The instrument used was a wavelength dispersive XRF (PANalytical Axios Max) at Korea Polar Research institute. The XRF spectrometer was equipped with a Philips 4 kW Rh anode Super Sharp X-ray Tube. The calibration and analysis were automatically performed with the help of a SuperQ software package, which was attached to the XRF spectrometer. The instrumental drift was corrected by measuring synthetic monitor samples (BR-PC3).

KOPRI
극지연구소

남극 라슨 C 홀로세 퇴적물의 눈덩이 사건 흔적

Kyu-Cheul Yoo[1], Jae Il Lee[1], Min Kyung Lee[1], Sunghan Kim[1], Jaewoo Jung[3], Julia Wellner[4], Cristina Subt[2], Brad Rosenheim[2], Jinwook Kim[6], Amy Leventer[7], Hyun-Hee Rhee[5], Yeong Bae Seong[5], Heung Soo Moon[1], Boo-Keun Khim[8], Jihyun F. Kim[9]

[1]Korea Polar Research Institute, Songdomirae-ro 26, Incheon 21990, Republic of Korea (kcyoo@kopri.re.kr), [2]College of Marine Science, University of South Florida, St Petersburg, Florida, USA, [3]Global Ocean Research Center, Korea Institute of Ocean Science & Technology, Busan 49111, Korea, [4]Department of Earth and Atmospheric Sciences, University of Houston, Houston, TX 77204, USA, [5]Department of Geography, Korea University, Seoul 02841, Republic of Korea, [6]Department of Earth System Sciences, Yonsei University, Seoul 03722, Republic of Korea, [7]Department of Geology, Colgate University, Hamilton, New York, USA, [8]Department of Oceanography, Pusan National University, Busan, 46241, Korea, [9]Department of Systems Biology, Division of Life Sciences, Institute for Life Science and Biotechnology, and Microbiome Initiative, Yonsei University, Seoul, 03722, Korea

요약: 라슨 C 빙붕은 라슨 A, B 빙붕에 이어 붕괴 위기에 처해 있다. GC16B 퇴적물 코어는 라슨 C 해역에서 수집되었으며, 코어 GC16B는 남극 대륙 최초의 퇴적 기록인 독특한 엽층리 형태와 밀도 높은 다이아믹톤 (diamicton)을 가지고 있다. 해양 및 빙하 변화는 유공충 및 램프형 열분해 ^{14}C 연대 측정에 대한 가속기 질량 분석법을 기반으로 한 연대기와 함께 퇴적학적, 지구화학적 및 고생물학적 데이터를 기반으로 재구성된다. 초기 홀로세 이후 고해양학적 변화에는 육상 빙하에서 떠다니는 빙붕을 거쳐 해빙 상태로의 전환이 포함된다. 엽층리 퇴적물은 해양 강제력의 변화에 의해 변조된 부유 빙붕 아래의 얼음 공동 내에 퇴적물이 가득한 용융수 유출로 퇴적된 것으로 해석된다. 라슨 C 해역의 빙하 지반선에 근접한 GC16B의 퇴적학적 및 지구화학적 기록은 "눈덩어리 지구 (Snowball Earth)"라고 불리는 스터티안 (Sturtian) 빙하기 동안에 빙하 지반선 근접 기원의 밀도 높은 다이아믹타이트 (diamictites_와 함께 빙하 운반 력 (drop stone)이 없고 엽층리 퇴적물을 특징으로 하는 퇴적암과 비교된다. 이 데이터는 눈덩어리 지구 빙하기 동안의 동시대적인 빙하기 환경에서 빙하 근접 퇴적에 대한 새로운 비교를 제공한다.

References

1. Brachfeld, S., Domak, E., Kissel, C., Laj, C., Leventer, A., Ishman, S., Gilbert, R., Camerlenghi, A. & Eglinton, L.B. Holocene history of the Larsen-A Ice Shelf constrained by geomagnetic paleointensity dating. Geology 31, 749-752 (2003).
2. Domack, E.W., Duran, D., Leventer, A., Ishman, S., Doane, S., McCallum, S., Amblas, D., Ring, J., Gilbert, R. & Prentice, M. Stability of the Larsen B ice shelf on the Antarctic Peninsula during the Holocene epoch. Nature 436, 681-685 (2005).
3. Smith, J.A., Hillenbrand, C.-D., Subt, C., Rosenheim, B.E., Frederichs, T., Ehrmann, W., Andersen, T.J., Wacker, L., Makinson, K., Anker, P., Venables, E.J. & Nicholls, K.W. History of the Larsen C Ice Shelf reconstructed from sub-ice shelf and offshore sediments. Geology 49, 978-982 (2021).
4. Jung, J., Yoo, K.-C., Rosenheim, B.E., Conway, T.M., Lee, J.I., Yoon, H.I., Hwang, C.Y., Yang, K., Subt, C. & Kim, J. Microbial Fe (III) reduction as a potential iron source from Holocene sediments beneath Larsen Ice Shelf. Nat. Comm. 10, 5786 (2019).
5. Hoffman P.F. et al., Snowball Earth climate dynamics and Cryogenian geology-geobiology. Sci. Adv. 3, e1600983 (2017).
6. Campo, J. M., Wellner, J. S., Domack, E., Lavoie, C., Yoo, K.-C. Glacial geomorphology of the northwestern Weddell Sea, eastern Antarctic Peninsula continental shelf: Shifting ice flow patterns during deglaciation. Geomorphology 280, 89-107 (2017).
7. Subt, C., Yoon, H.I., Yoo, K.C., Lee, J.I., Leventer, A., Domack, E.W. & Rosenheim, B.E. Sub-ice shelf sediment geochronology utilizing novel radiocarbon methodology for highly detrital sediments. Geochem. Geophys. Geosyst. 18, doi:10.1002/ 2016GC006578 (2017).
8. Mulvaney, R., Abram, N.J., Hindmarsh, R.C.A., Arrowsmith, C., Fleet, L., Triest, J., Sime, L.C., Alemany, O. & Foord, S. Recent Antarctic Peninsula warming relative to Holocene climate and ice-shelf history. Nature 489, 141-144 (2012).
9. Jeong, A., Lee, J.I., Seong, Y.B., Balco, G., Yoo, K.-C., Yoon, H.I., Domack, E., Rhee, H.H. & Yu, B.Y. Late Quaternary deglacial history across the Larsen B embayment, Antarctica. Quat. Sci. Rev. 189, 134-148 (2018).
10. Minzoni, R.T., Anderson, J.B., Fernandez, R. & Wellner, J.S. Marine record of Holocene climate, ocean, and cryosphere interactions: Herbert Sound, James Ross Island, Antarctica. Quat. Sci. Rev. 129, 239-259 (2015).

KOPRI 극지연구소

11. Anthony, R.E., Aster, R.C. & McGrath D. Links between atmosphere, ocean, and cryosphere from two decades of microseism observations on the Antarctic Peninsula. J. Geophys. Res. Earth Surf. 122, 153-166 (2017).
12. Cape, M. R., Vernet, M., Kahru, M. & Spreen, G. Polynya dynamics drive primary production in the Larsen A and B embayments following ice-shelf collapse, J. Geophys. Res. Oceans 119, 572-594 (2014).
13. Shepherd, A., Fricker, H.A. & Farrell, S.L. Trends and connections across the Antarctic cryosphere. Nature 558, 223-232 (2018).
14. Baumhoer, C.A., Dietz, A.J., Kneisel, C., Paeth, H. & Kuenzer, C. Environmental drivers of circum-Antarctic glacier and ice shelf front retreat over the last two decades. The Cryosphere 15, 2357-2381 (2021).
15. Massom, R.A., Scambos T.A., Bennetts, L.G, Reid, P., Squire, V.A. & Stammerjohn, S.E. Antarctic ice shelf disintegration triggered by sea ice loss and ocean swell. Nature 558, 383-389 (2018).
16. Čejka, T., Nývlt, D., Kopalová, K., Bulínová, M., Kavan, J., Lirio, J.M., Coria, S.H. & Vijver, B.V.D. Timing of the neoglacial onset on the North-Eastern Antarctic Peninsula based on lacustrine archive from Lake Anónima, Vega Island. Global and Planetary Change 184, 103050 (2020)
17. Michalchuk, B.R., Anderson, J.B., Wellner, J.S., Manley, P.L., Majewski, M. & Bohaty, S. Holocene climate and glacial history of the northeastern Antarctic Peninsula: The marine sedimentary record from a long SHALDRIL core. Quat. Sci. Rev. 28(27), 3049-3065 (2009).
18. Yoon, J., Kwak, M.-J., Lee, B., Yoo, K.-C., Song, H.J., Hwang, C.Y., Chung, Y., Kim, K., Kwon, S.-K., Song, J.Y., Yoon, H.S. & Kim, J.F. Biomineralization via iron oxidation beneath the Larsen C Ice Shelf during the Holocene. Submitted. (2022)
19. Smith, J.A., Graham, A.G.C., Post, A.L., Hillenbrand, C.-D., Bart, P.J., and Powell, R.D. The marine geological imprint of Antarctic ice shelves. Nat. Commun. 10, 5635 (2019).
20. Smith, J.A., Andersen, T.J., Shortt, M., Gaffney, A.M., Truffer, M., Stanton, T.P., Bindschadler, R., Dutrieux, P., Jenkins, A., Hillenbrand, C.-D., Ehrmann, W., Corr, H.F., Farley, N., Crowhurst, S. & Vaughan, D.G. Sub-ice-shelf sediments record history of twentieth-century retreat of Pine Island Glacier. Nature 541, 77-80 (2017).
21. Harris, P.T. Ripple cross-laminated sediments on the East Antarctic Shelf: evidence for episodic bottom water production during the Holocene? Mar. Geol. 170, 317-330 (2000).

KOPRI 극지연구소

22. Nicholls, K. W., K. Makinson, & E. J. Venables. Ocean circulation beneath Larsen C Ice Shelf, Antarctica from in situ observations. Geophys. Res. Let. 39, L19608 (2012).
23. Stoney Q.G. & Christopher A.S. Extracting paleoclimate signals from sediment laminae: An automated 2-D image processing method. Computer & Geosciences 52, 345-355 (2013).
24. Dowdeswell, J.A., Batchelor, C.L., Montelli, A., Ottesen, D., Christie, F.D.W., Dowdeswell, E.K. & Evans, J. Delicate seafloor landforms reveal past Antarctic grounding-line retreat of kilometers per year. Science 368, 1020-1024 (2020).
25. Steig, E. J., Ding, Q., Battisti, D. S. & Jenkins, A. Tropical forcing of circumpolar deep water Inflow and outlet glacier thinning in the Amundsen Sea Embayment, West Antarctica. Ann. Glaciol. 53, 19-28 (2012).
26. Etourneau, J., Sgubin, G., Crosta, X., Swingedouw, D., Willmott, V., Barbara, L., Houssais, M-N., Schouten, S., Damsté, J.S.S., Goosse, H., Escutia, C., Crespin, J., Massé, G. & Kim J-H. Ocean temperature impact on ice shelf extent in the eastern Antarctic Peninsula. Nat. Comm. 10, 304 (2019).
27. Lechte M. & Wallace, M. Sub-ice shelf ironstone deposition during the Neoproterozoic Sturtian glaciation. Geology 44(11), G38495.1 (2016).
28. Lechte, M.A., Wallace, M.W., Hood, A.V.S., Li, W., Jiang, G., Halverson, G.P., Asael, D., McColl, S.L. & Planavsky, N.J. Subglacial meltwater supported aerobic marine habitats during Snowball Earth. PNAS 1909165116 (2019).
29. Wåhlin, A. K., A. G. C. Graham, K. A. Hogan, B. Y. Queste, L. Boehme, R. D Larter, E. C. Pettit, J. Wellner & K. J. Heywood. Pathways and modification of warm water flowing beneath Thwaites Ice Shelf, West Antarctica. Sci. Adv. 7(15), eabd7254 (2021).
30. Christner B.C. et al. WISSARD Science Team, A microbial ecosystem beneath the West Antarctic ice sheet. Nature 512, 310-313 (2014).
31. Mortlock, R.A. & Froelich, P.N. A simple method for the rapid determination of biogenic opal in pelagic marine sediment. Deep-Sea Res. 36, 1415-1426 (1989).

KOPRI 극지연구소

Table 1. Sample data for all cores, including AIO ages analyzed at Beta Analytic (modified from Subt et al. 2017).

Core name	Depth (cm)	Type	Age (14C yrs BP)	± (1σ)	Calibrated age (yrs BP)	± (1σ)	Beta No.
GC 16B	0	AIO sediment	12,490	50			
	85	AIO sediment	35,000	1,100			
	85	Isotope Dilution RP1	8,329	424	6,021	429	
	95	Isotope Dilution RP1	10,087	333	8,054	420	
	192	AIO sediment	34,500	1,000			
	192	Isotope Dilution RP1	12,862	417	11,577	479	
	0	Foraminiferal carbonate	4,570	40	1,717	90	
	6	Foraminiferal carbonate	5,160	35	2,518	84	
	10	Foraminiferal carbonate	6,510	30	4,137	79	
	14	Foraminiferal carbonate	6,560	35	4,197	83	
GC 14A	4	AIO sediment	13,740	40			471625
	10	AIO sediment	13,290	40			471626
	20	AIO sediment	14,190	40			471627

KOPRI 극지연구소

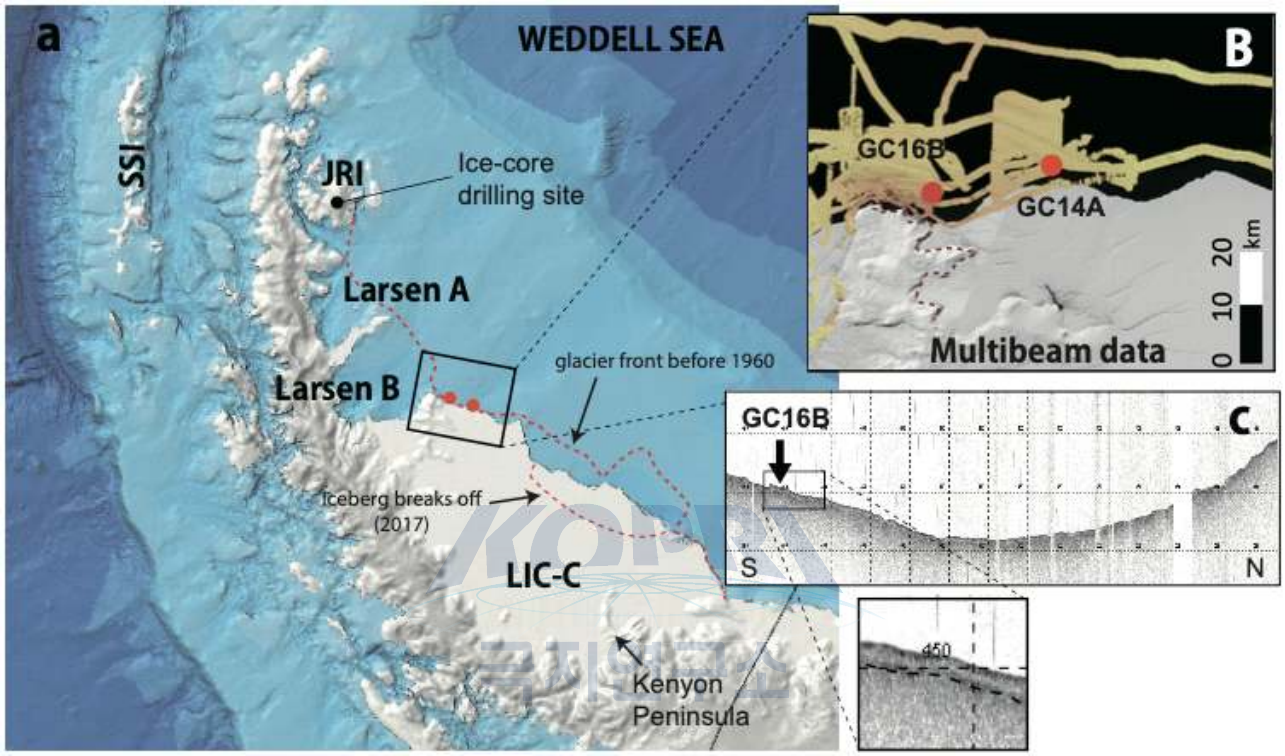


Figure 1. Map and location of coring sites. A) Insect, site map of core GC16B and GC14A (red circles); main map of Antarctic Peninsula, showing the outline of Larsen ice shelves from satellite imagery on the 1950s (a dotted red line)[13] and an ice-core drilling site is indicated by a black circle on the James Ross Island. B) Seabed bathymetry (in metres) of insect map in Larsen C embayment[6] and the evaluated grounding line (a dotted brown line). C) A sea-bottom profile along north to south shown in b. Enlargement of an insect profile shows 2- to 3-m-thick postglacial sediment.

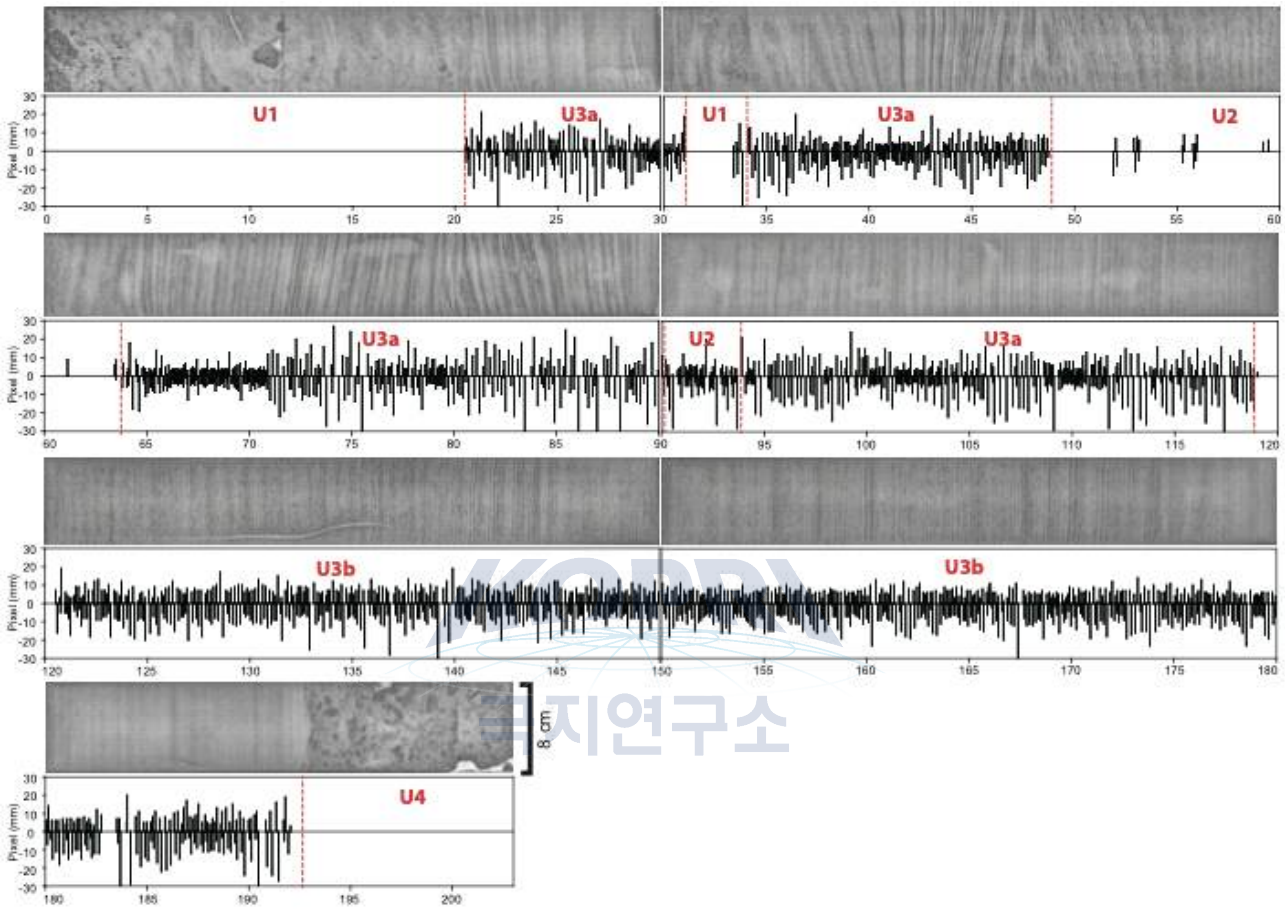


Figure 2. X-radiograph & LA-2D images from core EAP13-GC16B. Dark (+ pixel) and white (- pixel) values obtained from 2-D images of the thin-slabs (10×100×4 mm) indicate each magnitude of one couplet and show about 1,200 couplets of the silt and clay. Features characteristics for grounded glacial lithofacies of U4 (diamictons) and for proximal zone from grounding line lithofacies of U3 (parallel to cross laminations) are best seen in X-radiographs. Parallel (U3b) to cross (U3a) lamination indicates variations of ocean forcings with the retreat of calving lines after deglaciation. A gravelly mud facies with IRDs (U1) demonstrates depositional setting near the glacial front and loose sea-ice.

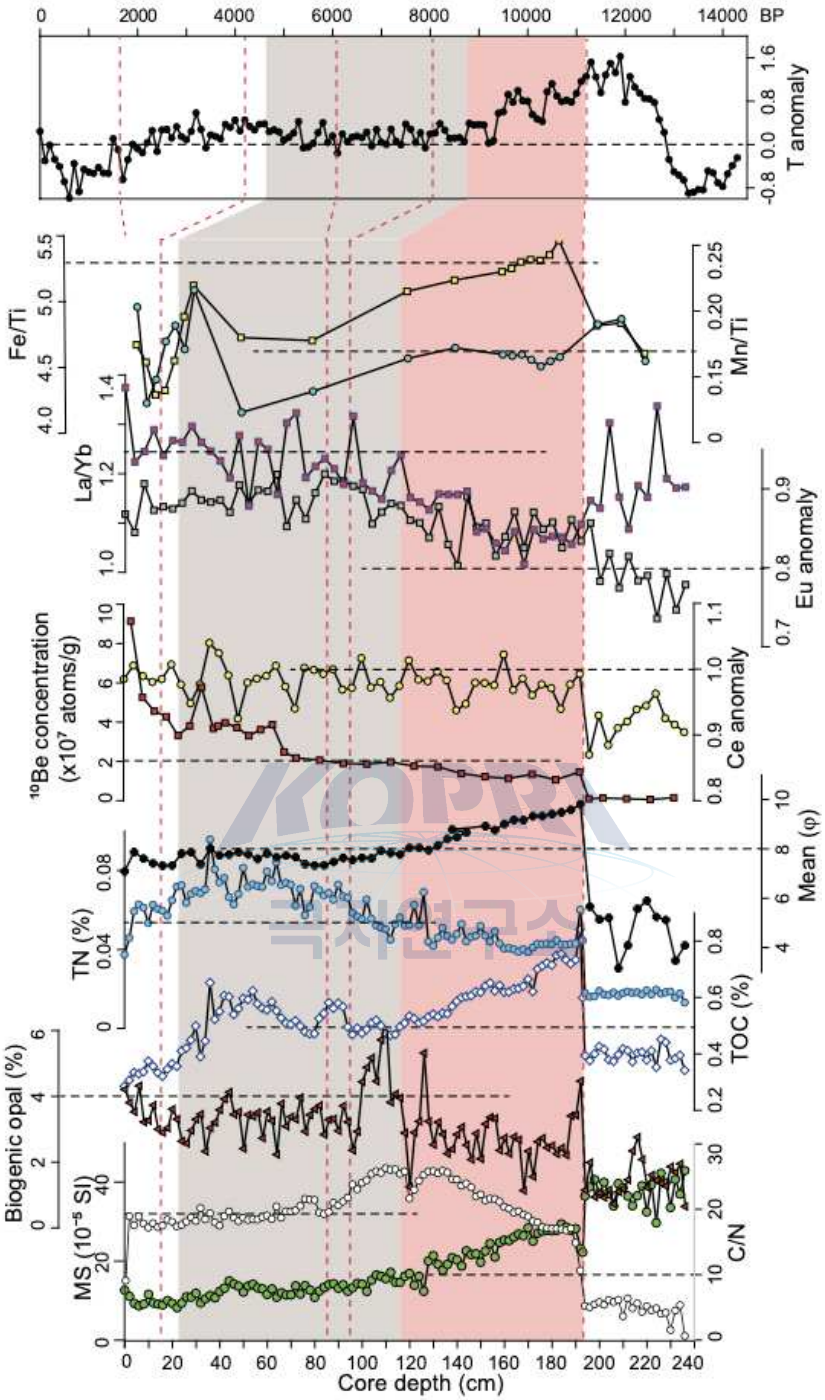


Figure 3. Paleo-environmental proxies in core GC16B. Geochemical parameters and image processing signals: temperature anomaly of ice-core analysis from James Ross Island, Fe/Ti (yellow box), Mn/Ti (sapphire circle), La/Yb (pink box), Eu (gray boxes) and Ce (yellow circle) anomalies, 10Be concentration ($\times 10^7$ atoms/g) (pink box), TOC (total organic carbon) (%) (white rhombus), TN (total nitrogen) (%) (sapphire circle), biogenic opal (%) (pink triangle), MS (magnetic susceptibility) ($\times 10^{-5}$ SI) (white circle) and C/N (carbon/nitrogen) ratios (green circle). The uppermost meteoric ^{10}Be concentration is 9.1×10^7 atoms g^{-1} and corresponds to nearly 6-cm concentration of the box core, implying the loss of coring disturbance. The surface 10Be concentration of undisturbed box core is 0.4 to 2.7×10^8 atoms g^{-1}.

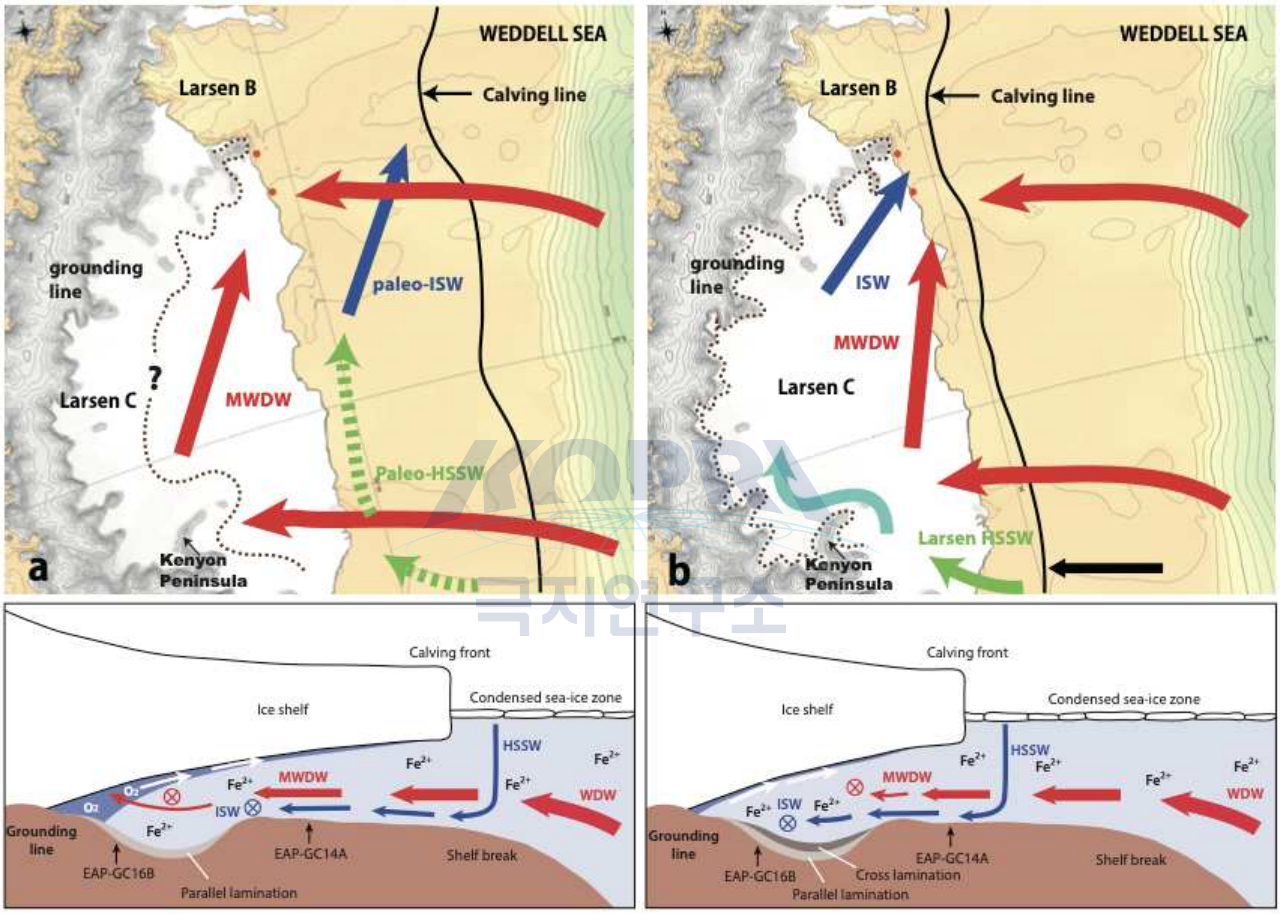


Figure 4. Schematic illustration of the (a) post LGM to (b) modern history of the ice shelf[22] in Larsen C Embayment.

제 10 장

Multibeam Bathymetry and Distribution of Clay Minerals on Surface Sediments of a Small Bay in Terra Nova Bay, Antarctica[2)]

Jaewoo Jung[1], Youngtak Ko[2], Joohan Lee[3], Kiho Yang4, Young Kyu Park[5], Sunghan Kim[6], Heungsoo Moon[6], Hyoung Jun Kim[3], and Kyu-Cheul Yoo[6]

[1]Global Ocean Research Center, Korea Institute of Ocean Science & Technology, Busan, 49111, South Korea; jaewoo@kiost.ac.kr (J.J.), [2]Deep-Sea Mineral Resources Research Center, Korea Institute of Ocean Science & Technology, Busan, 49111, South Korea; ytko@kiost.ac.kr (Y.K.), [3]Department of Future Technology Convergence, Korea Polar Research Institute, Incheon, 21990, South Korea; joohan@kopri.re.kr (J.L.); jun7100@kopri.re.kr (H.J.K.), [4]Department of Oceanography, Pusan National University, Busan, 46241, South Korea; kyang@pusan.ac.kr (K.Y.), [5]Department of Earth System Sciences, Yonsei University, Seoul, 03722, South Korea; pyk125@yonsei.ac.kr (Y.K.P.), [6]Division of Glacial Environment Research, Korea Polar Research Institute, Incheon, 21990, South Korea;

Abstract: The second Antarctic station of South Korea was constructed at Terra Nova Bay, East Antarctica, but local seafloor morphology and clay mineralogical characteristics are still not fully understood. Its small bay is connected with a modern Campbell Glacier, cliffs and raised beaches along coastline. Fourteen sampling sites to collect surface sediments were chosen in the small bay for grain size and clay mineral analyses to study sediment source and sediment-transport process with multibeam bathymetry and sub-bottom profiles. Under the dominant erosional features (streamlined feature and meltwater channel) icebergs are major geological agent for transport and deposition of coarse-sized sediments along the edge of glaciers in summer and thus the study area can reveal the trajectory of transport by icebergs. Glacier meltwater is an important agent to deposit the clay-sized detritus and it results from the dominance of illite content occurring along

2) 이 연구 결과는 다음의 논문으로 출판되었음: Jung, J. et al. (2021). "Multibeam Bathymetry and Distribution of Clay Minerals on Surface Sediments of a Small Bay in Terra Nova Bay, Antarctica." Minerals 11: 72.

the edge of Campbell Glacier Tongue. The high smectite content compared to Antarctic sediments maybe a result by a source of the surrounding volcanic rocks around within the Melbourne Volcanic Province.

1. Introduction

The Ross Sea is adjacent to the Southern Ocean and bounded by the Antarctic continent to the South. Ross ice shelf, the largest ice shelf in Antarctica, is developed and distributed widely along the continental shelf [1]. Grounding line had advanced near to continental shelf edge at the end of the Last Glacial Maximum (LGM, ca. 20 ka) and now is located within the Ross Sea [2,3]. The advance and retreat of ice sheet caused by global climate change has had a significant impact on the depositional condition of continental shelf [4]. Particularly, the Ross Sea is an important area for such study as the largest ice sheet discharge into the embayment [5]. Terra Nova Bay, Ross Sea is a bay which is often ice free, lying from Cape Washington in the north to the Drygalski Ice Tongue in the south [6]. The Terra Nova Bay splits Victoria Land into southern and northern regions: 1) southern Victoria Land, where outlet glaciers and ice streams cross the Transantarctic Mountains and drain the East Antarctic Ice Sheet (EAIS) to the Ross Sea and 2) northern Victoria Land, where a dendritic pattern of glacial valleys has no direct connection to the EAIS, but it is supplied from extensive ice fields [7,8]. Such that, glaciomarine environments in high latitude regions are geologically important in that they contain the sedimentary history trapped by their basin morphology that might preserve a detailed paleoclimate history in Antarctic regions [9]. Acoustic surveys have been performed to understand glacier-influenced continental shelves in Ross Sea, Antarctica [10]. The multibeam bathymetric surveys to map the seafloor morphology of Antarctic regions has been used widely to identify glacial erosion of the seabed and other megascale glacial lineations related to ice sheet movement [11-13]. In order to determine the glaciomarine depositional environments, acoustic seafloor data have been collected from Ross Sea since 1990 [14-16]. The behavior of marine-based ice sheets across continental shelves was mostly reported and interpreted using a regional seafloor bathymetric data [10,17] and satellite-based observations [18]. However, the local seafloor morphology and mineralogical characteristics of Terra Nova Bay have never been reported before, so we provide general geological information including new multibeam bathymetry, sub-bottom profiles (SBP), grain size, clay mineralogy, and illite crystallinity (IC) for the future

KOPRI 극지연구소

study based on the Antarctic station. In the Antarctic region, the mineralogical characteristics of clay minerals in continental shelf sediments have been used successfully to describe the provenance of clay minerals and stratigraphic correlations in catchment areas draining into the Weddell Sea, Bellingshausen Sea, and Amundsen Sea, Antarctica [19-21]. The clay minerals that are common to Antarctic marine sediments include smectite, illite, chlorite, kaolinite, and illite-smectite(I-S) mixed layered clay [22,23]. These clay minerals are generally detrital and their distribution is affected by bedrock composition of source area [24]. Therefore, present study demonstrates a comprehensive understanding through geomorphological data, sedimentary sequences, grain size distributions, and clay mineralogy of surface sediments, where the second Antarctic station of South Korea was constructed. Then, this information contributes to interpreting those sediment-transport processes that influence sedimentation in Antarctic glaciomarine environment for future study.

2. Study area

The study area in Terra Nova Bay of the Ross Sea was located in the offshore within 20 km from Jang Bogo Station (JBS) and Mario Zucchelli Station (MZS) (Figure 1). Seasonal sea ice, approximately 2 to 2.5 m thick, covers the sea surface for 9 to 10 months of the year. The Terra Nova Bay has a winter coastal polynya. The inner bay of the study area is Gerlache Inlet between JBS and MZS. The Tethys bay near MZS is a small cove (1.6 km wide and 3.0 km long), but is very deep (a maximum depth of 280 m) and is surrounded by steep rocks and glaciers. The coastline from MZS to JBS is characterized by rocky cliffs with large boulders forming raised beaches. The raised beaches are present on the coast south of JBS and composed dominantly of angular and sub-angular boulders by wave activity [25]. The Campbell Glacier is located east of the JBS and is approximately 100 km long and approximately 4,000 km2 in the basin area. The Campbell Glacier Tongue (CGT), and approximately 75.5 km2 in surface area, is composed of one main stream (approximately 13.5 km long measured from the grounding line and 4.5 km wide) and another branch stream [26]. Air temperature varies from -30 to 5 ℃ annually, according to the measurement by an Automatic Weather Station installed at JBS.

3. Materials and Methods

KOPRI 극지연구소

3.1. Sampling locations

To understand the surface sediment characteristics in the glacial embayment adjacent JBS in Terra Nova Bay, 14 sampling sites were chosen. However, 11 surface sediments were obtained using a box corer during Ross Sea geological expedition in 2019 by Korea Polar Research Institute (KOPRI) (Figure 1). Any soft sediments at the 3 sampling sites (JBG05, JBG09 and JBG11) weren't acquired and some gravels or failed samples in the box corer indicate that the sites are likely till or rocky bottoms. Water depths at these sites vary between 150 and 523 m (Table 1). The sampling locations are given in Table 1.

3.2. Multibeam bathymetry and sub-bottom profiles

Multibeam swath bathymetry data were collected on geophysical research expedition near JBS aboard the RV/IB Araon. Multibeam soundings were collected in a swath perpendicular to the ship track using a hull-mounted Kongsberg EM122, with a swath of 432 beams, operating at a frequency of 12 KHz. Acquired bathymetry data were processed onboard using CARIS, a specialized bathymetry-processing software, and the results are plotted using Generic Mapping Tools (GMT) software. To understand ice flow activity, we compare the submarine landforms to the seafloor lithology based on sub-bottom profiling results. Shallow sub-bottom profiling data collected in the sampling area using SBP120 Sub-bottom profiler of an optional extension to the highly acclaimed EM122 multibeam echo sounder. The data were logged in the TOPAS raw format and can be saved in SEG-Y format for the postprocessing with a standard seismic package. The data were used to identify seafloor lithology and the thickness of surface sedimentary units (unconsolidated sediments up to 100 m below the seafloor).

3.3. Analysis of grain size and clay mineralogy

Grain size analysis of surface sediments was performed to determine the size fractions of gravel (>2 mm), sand (62.5 mm to 2 mm), silt (2 mm to 62.5 mm), and clay (<2 mm) [27]. The contents of coarse particles larger than 4ϕ (>62.5 mm) were determined by wet sieving and smaller particles than 62.5 탆 was measured using Micrometrics SediGraph III 5120. X-ray diffraction (XRD) analysis was performed using a Rigaku HR-XRD SmartLab with Cu-Kα radiation (20 kV and 10 mA). The XRD profiles over a range of 2Θ angles from 2° to 70° were measured at step sizes of 0.02°

and a scan speed of 1.5°/min. Size fractionated samples (<1 mm) were dispersed in deionized water (0.5 mg/mL) and put in an ultrasonicator bath for 20 seconds to prevent the particle flocculation. The oriented (air-dried) samples were made onto slide glasses for XRD analysis [20]. Then, air-dried samples were treated with ethylene-glycol under a vacuum desiccator for 48 hours [28,29]. Quantitative estimations of clay minerals were measured after the glycolation treatment. The relative percentage of each clay mineral was calculated using weighting factors [29,30]. Search-Match software was used to identify the clay mineralogy [31]. IC and the relative percentage of smectite, chlorite, illite, and kaolinite, were measured and calculated by using OriginPro 2020b [20,28].

4. Results

4.1. Geomorphology

We describe the seafloor landforms identified in the sampling area [32]. Gerlache Inlet (a maximum depth of 350 m) located between JBS and MZS is surrounded by steep bedrocks and glaciers in the western side. Tethys Bay is adjacent to MZS is very deep (about 280 m water depth in the central part). The sampling area is characterized by a rugged seafloor with meltwater channels west of CGT and a large (7.3 km2), deep (520 m water depth) flat-bottomed basin east of MZS (Figure 2). Elongated streamlined features are found west of CGT. In the sub-bottom profiles, the sampling area shows a strong surface with no internal reflectors (Figure 1). The meltwater channels have V-shaped cross-sectional profile cutting through bedrock and flowing between the streamlined features. The reticular channels between streamlined features mainly terminate beneath CGT and the arboriform channels in the offshore of the JBS terminate into the deep basin.

4.2. Granulometric composition

Table 2 shows the results obtained by grain size analysis of the surface sediment samples. The sediments of sampling sites are largely coarse-grained. Sand contents generally exceed 87.5% except at JBG03 and JBG13, while mud (silt+clay) contents do not exceed 9.3% except at JBG13 (27.0%). JBG03 has large amounts of gravel (35.4%), while the gravel contents of other sites are relatively low (<6.2%). The sediment is generally moderately sorted to very poorly sorted (0.7 to 3.2 ϕ). The

mean grain size is generally medium sand (1.7 ϕ) to very fine sand (3.2 ϕ) except at very coarse sand (0.5 ϕ) of JBG03 and at coarse silt of JBG13 (5.1 ϕ). The coarse components more than medium sand, a combination of gravel, coarse sand and medium sand contents, are examined to distinguish coarser fraction from finer fraction of grain size distribution in the surface sediments. The coarser components of JBG02, JBG03 and JBG04 approximately exceed 49.1%, while other sites show low contents below 32.5%.

4.3. Semi-Quantification of clay minerals and illite crystallinity

Oriented and ethylene-glycolated samples were used to determine the clay mineralogy in sediments. In general, the mineralogical assemblages evidenced in surface sediment samples collected at Terra Nova Bay (Figure 1) were: smectite (S), chlorite (Ch), illite (I), kaolinite (K), plagioclase (Pl), and clay-sized quartz (Q). Unfortunately, JBG04 and JBG10 have no results because there were no samples to conduct clay mineral analysis after grain size analysis. Little peak shoulder was observed between 9-10 2-theta degrees, indicating I-S mixed layer. There are no significant mineralogical variations with distance from the coastline. The average clay mineral composition was dominated by illite (53.7- 74.0%, avg. = 64.9%) and chlorite (10.0-16.8%, avg. = 12.8%) with less abundant clay minerals of smectite (6.5-20.1%, avg. = 12.4%) and kaolinite (7.0-13.8%, avg. = 10.0%, Table 3). The relative peak intensity of the minerals showed little difference of intensities through the Terra Nova Bay, but the intensities of quartz peaks increased in JBG08 compared to other sites (Figure 3). In addition, smectite peaks (~17 Å) were very weak at JBG 08 corresponding to lowest concentration of smectite (6.46%). The values of IC in °Δ2Θ show a narrow variation with sampling location ranging 0.40-0.54 and average value is 0.47.

5. Discussion

The investigation of clay mineralogy in surface sediments recorded from the proximal zone of the coastline provides evidences on source areas and transport paths. In a polar setting, physical weathering prevails and chemical weathering is negligible. Detrital clay mineral assemblages in the surface sediments reflect the average rock composition in the surrounding outcrops [23]. In particular, illite and chlorite are typical clay minerals indicating the physical weathering in the soil

environments [24]. The dominance of illite in the sampling area (Figure 4) is likely to reflect the supply of detritus from outcrops of the local sources, because clay mineral assemblages in the surface sediments are formed by the weathering of the outcrops [35]. The narrow variation of IC values (°Δ2Θ = 0.40-0.54, avg.= 0.47) indicates the good crystallinity of illite which is less-altered illite close to the surface. Chemical index of illite (5/10 Å peak area ratio) which are less influenced by sediment dynamic differentiation showed ~0.2 (calculated from Figure 3) indicating that Fe-Mg-rich illite resulting from the physical weathering of bedrocks [23,36], so they may suggest that illite originated in dry and cold environments. Furthermore, clay-size fraction of quartz and plasioclase suggests little chemical weathering of glacially-derived source materials [37]. It may be resulted from the glaciomarine environment of the study area, characterized by a limited moisture supply and short summer season, which do not enhance chemical weathering.

On the other hand, smectite has been derived from hydrothermal alteration of volcanic ash supplied from the surrounding areas or weathering and erosion of exposed volcanic rocks [38]. The content of smectite is relatively high in the quaternary sediments, indicating that sediments originate from basic volcanic rocks in the Ross Sea area [39]. It is consistent with the previous study that the smectite distributed in the Ross Sea is supplied from the McMurdo Volcanic Group in the coast of Victoria Land [40]. The content of smectite in the study area (Table 3) is largely high compared to general Antarctic marine sediments with the relatively low content of smectite. The Melbourne Volcanic Province, one of the McMurdo Volcanic Group, is divided into four subprovinces: Malta Plateau, the Pleiades, Mount Overlord, and Mount Melbourne. The study area is situated about 30 km away from Mount Melbourne that is on the center of Mount Melbourne subprovince adjacent to the CGT and so smectite in the sampling sites may be originated from the outcrops (Figure 2a). Kaolinite is very resistant, reworked kaolinite from older sediments may be found in polar environments [22,41]. Kaolinite might be derived from the paleosol and sedimentary rocks containing kaolinite near the Ross Sea, but it is still not fully understood. In this reason, it is necessary to determine the provenance of clay minerals more clearly through the analysis of rare earth elements (REE) in the sediments.

Surface sediments provide a useful material to reveal how modern environmental conditions are reflected, especially in transportation and depositional processes farther offshore of clastic materials from the surrounding sources. The analysis on the grain size of surface sediments shows that the finer components (silt and clay) of all sampling sites are very low. It indicates that the silt- and clay-sized

components on the surface sediments of all sites occupy the insignificant sedimentary process. The study area is free from sea ice only from the beginning of January to the end of February. In fact, there is no river on the local coast and little turbid onshore meltwater streams entering the ocean since the study area is located in high latitude of polar setting. However, the relative illite abundance is higher at the surface sediments close to CGT, suggesting that illite is derived from the meltwater input of CGT in summer. Strong winds are frequent from the hinterland in winter. They store the rugged surface (e.g., crevasses) of glacier with the physical weathering products in winter, and thus clay fraction may deposit along the edge of CGT through the direct glacier meltwater in summer. The fine-sized detrital components can be transported farther seaward by ocean currents. It turns out that surface sediments on the deep basin (e.g., Drygalski Basin) of Terra Nova Bay predominantly consist of mud. Some fine-sized components are likely to be transported into the study area alongshore by ocean currents. It is reported that a prevailing north-eastward alongshore transport between surface and deep layers from current measurements in Terra Nova Bay [42].

Elongated streamlined features or elongated hills are found near CGT (Figure 2) with no internal, hummocky reflection in the sub-bottom profiles, which indicated till and/or bedrock (Figure 1). Or linear and sinuous meltwater channels are more frequent near CGT. Streamlined features and meltwater channels are erosional seafloor features, which likely indicate till and/or bedrock. Multiple glaciation events are likely to allow actively flowing ice to carve in bedrock [43]. It is reported that some of the proximal areas are modern erosional features when ice recently advances [32]. Some at the proximal bay in front of JBS and the surrounding CGT is likely to be formed during a recent glacial event, the Little Ice Age. On the other hand, a deep basin shows very thin drape overlying a strong reflection in line SL03 (Figure 1). JBG13 has more abundant mud contents than other sites and is a representative deposition site of fine-sized components out of all sampling sites (Table 2).

The coarse components (gravel + sand) are largely supplied from the source rocks (Late Precambrian metamorphic rocks and Late Cenozoic Volcanics) fringing the coast of the sampling area. The dominance of coarse components occurs at all sites except at JBG13. It can be considered that one of the dominant transport media for coarse-sized material into the study area is sediment gravity flow, especially turbidity current [44]. However, the study area has no hydraulic potential to yield the density flow like the continental slope and no sedimentary sequence of density flow in the sub-bottom profiles. Another possible transport medium is the ice-rafted

materials supplied to the ocean by drifting icebergs from the glaciers of the surrounding sources. The coarse components more than medium sand become one of the criteria of ice-rafted transport because Sometimes eolian transport from the surrounding outcrops can be composed by large-sized materials (>4 mm fine sand) [45]. The main source of ice-rafted detritus is from the Campbell Glacier that largely releases small-scale icebergs to the study area with increased temperature (>0 ℃) in summer. The terminus of CGT retreated about 4.4. km between 1984 and 2016 due to the local warming [46]. The dominance of the coarse components more than medium sand along the edge of CGT (Figure 5) maybe resulted from the deposition of ice-rafted detritus in summer. The coarse components of JBG06 and JBG14 sites in front of MZS is likely to be due to the surrounding glaciers, especially in Tethys Bay. It was reported that the seafloor is primarily granitic rock composed of coarse sands or gravels [47].

6. Conclusions

Systematic analysis of the grain size and clay minerals in glaciomarine surface sediments delivered to a small bay of Terra Nova Bay are reviewed with geophysical characteristics from bathymetry and sub-bottom profiles. Our findings suggest the sediment-transport processes of glaciogenic detritus under the influence of recent regional warming. The following conclusions are presented:

(1) The relative abundance of clay minerals in the surface sediments of the study area is largely dominated by illite, reflecting the supply of physical weathering products from the surrounding outcrops. The smectite content is largely high compared to general Antarctic marine sediments, indicative of delivery from products of weathering and erosion of exposed volcanic rocks from the Melbourne Volcanic Province close to the sampling sites.

2) Erosional features (streamlined feature and meltwater channel) are found near CGT with very coarse-sized component more than medium sand on till and/or bedrock except in a deep basin representing a deposition area of fine-sized components in the study area.

3) Clastic materials are mainly transported offshore into the sampling site through two agents: iceberg and glacier meltwater. Icebergs detached from the surrounding glaciers mainly deposit the gravel and medium/coarse sand components (>49.1%) on the rugged bedrocks along the edge of CGT and offshore near the coastline of Tethys Bay. When the study area is free from sea ice for about 2

months in summer, some wind-blown materials (fine sand and silt components) is transported into the sampling sites. Glacier melting occurs in summer and clay-sized component of physical weathering products from the surround land is deposited along the edge of CGT.

KOPRI
극지연구소

남극 테라노바 만 소만의 멀티빔 측심과 표층 퇴적물에 대한 점토 광물 분포

Jaewoo Jung[1], Youngtak Ko[2], Joohan Lee[3], Kiho Yang[4], Young Kyu Park[5], Sunghan Kim[6], Heungsoo Moon[6], Hyoung Jun Kim[3], and Kyu-Cheul Yoo[6]

[1]Global Ocean Research Center, Korea Institute of Ocean Science & Technology, Busan, 49111, South Korea; jaewoo@kiost.ac.kr (J.J.), [2]Deep-Sea Mineral Resources Research Center, Korea Institute of Ocean Science & Technology, Busan, 49111, South Korea; ytko@kiost.ac.kr (Y.K.), [3]Department of Future Technology Convergence, Korea Polar Research Institute, Incheon, 21990, South Korea; joohan@kopri.re.kr (J.L.); jun7100@kopri.re.kr (H.J.K.), [4]Department of Oceanography, Pusan National University, Busan, 46241, South Korea; kyang@pusan.ac.kr (K.Y.), [5]Department of Earth System Sciences, Yonsei University, Seoul, 03722, South Korea; pyk125@yonsei.ac.kr (Y.K.P.), [6]Division of Glacial Environment Research, Korea Polar Research Institute, Incheon, 21990, South Korea;

요약: 한국의 두 번째 남극 기지는 동남극 테라노바만(Terra Nova Bay)에 건설되었지만, 지역 해저 형태와 점토 광물학적 특성은 아직 완전히 이해되지 않고 있다. 그 작은 만은 현재 캠벨 빙하, 절벽 및 해안선을 따라 솟아오른 해변과 연결되어있다. 입자 크기 및 점토 광물 분석을 위해서 표층 퇴적물을 수집하기 위한 14개의 시료 정점이 작은 만에서 선택되었고, 멀티빔 수심 측량 및 하위 바닥 프로필로 퇴적물 기원지 및 퇴적물 수송 과정이 연구되었다. 우세한 침식 지형(유선 지형 및 해빙수로) 하에서 빙산은 여름에 빙하 가장자리를 따라 거친 크기의 퇴적물이 이동 및 퇴적되는 주요 지질학적 작용체이므로 연구 지역은 빙산에 의한 이동 궤적을 밝힐 수 있습니다. 빙하 녹은 물은 점토 크기의 퇴적물을 퇴적시키는 중요한 작용제이며 Campbell Glacier Tongue의 가장자리를 따라 발생하는 일라이트 함량이 우세하기 때문에 발생한다. 남극 퇴적물에 비해 높은 스멕타이트 함량은 아마도 멜버른 화산 지역 내 주변 화산암의 근원에 의한 결과일 것이다.

References

1. Rignot, E.; Jacobs, S.; Mouginot, J.; Scheuchl, B. Ice-shelf melting around Antarctica. Science 2013, 341, 266-270.
2. Howat, I.M.; Domack, E.W. Reconstructions of western Ross Sea palaeo ice stream grounding zones from high resolution acoustic stratigraphy. Boreas 2003, 32, 56-75.
3. Anderson, J.B.; Conway, H.; Bart, P.J.; Witus, A.E.; Greenwood, S.L.; McKay, R.M.; Hall, B.L.; Ackert, R.P.; Licht, K.; Jakobsson, M. Ross Sea paleo-ice sheet drainage and deglacial history during and since the LGM. Quaternary Science Reviews 2014, 100, 31-54.
4. Domack, E.W.; Jacobson, E.A.; Shipp, S.; Anderson, J.B. Late Pleistocene-Holocene retreat of the West Antarctic Ice-Sheet system in the Ross Sea: Part 2-sedimentologic and stratigraphic signature. Geological Society of America Bulletin 1999, 111, 1517-1536.
5. Setti, M.; Marinoni, L.; Lopez-Galindo, A. Mineralogical and geochemical characteristics (major, minor, trace elements and REE) of detrital and authigenic clay minerals in a Cenozoic sequence from Ross Sea, Antarctica. De Gruyter: 2004.
6. Di Nicola, L.; Strasky, S.; Schlüchter, C.; Salvatore, M.C.; Akçar, N.; Kubik, P.W.; Christl, M.; Kasper, H.U.; Wieler, R.; Baroni, C. Multiple cosmogenic nuclides document complex Pleistocene exposure history of glacial drifts in Terra Nova Bay (northern Victoria Land, Antarctica). Quaternary Research 2009, 71, 83-92.
7. Orombelli, G. Terra Nova Bay: a geographic overview. Memorie della Società Geologica Italiana 1987, 33, 69-75.
8. Baroni, C.; Noti, V.; Ciccacci, S.; Righini, G.; Salvatore, M.C. Fluvial origin of the valley system in northern Victoria Land (Antarctica) from quantitative geomorphic analysis. Geological Society of America Bulletin 2005, 117, 212-228.
9. Mosola, A.B.; Anderson, J.B. Expansion and rapid retreat of the West Antarctic Ice Sheet in eastern Ross Sea: possible consequence of over-extended ice streams? Quaternary Science Reviews 2006, 25, 2177-2196.
10. Halberstadt, A.R.W.; Simkins, L.M.; Greenwood, S.L.; Anderson, J.B. Past ice-sheet behaviour: retreat scenarios and changing controls in the Ross Sea, Antarctica. The Cryosphere 2016, 10, 1003-1020.

KOPRI 극지연구소

11. Lee, J.I.; McKay, R.M.; Golledge, N.R.; Yoon, H.I.; Yoo, K.-C.; Kim, H.J.; Hong, J.K. Widespread persistence of expanded East Antarctic glaciers in the southwest Ross Sea during the last deglaciation. Geology 2017, 45, 403-406.
12. Shipp, S.; Anderson, J.B. Drumlin field on the Ross Sea continental shelf, Antarctica. In Glaciated Continental Margins, Springer: 1997; pp. 52-53.
13. Dowdeswell, J.; Ottesen, D.; Evans, J.; Cofaigh, C.; Anderson, J. Submarine glacial landforms and rates of ice-stream collapse. Geology 2008, 36, 819-822.
14. Cooper, A.K.; Barrett, P.J.; Hinz, K.; Traube, V.; Letichenkov, G.; Stagg, H.M. Cenozoic prograding sequences of the Antarctic continental margin: a record of glacio-eustatic and tectonic events. Marine Geology 1991, 102, 175-213.
15. De Santis, L.; Prato, S.; Brancolini, G.; Lovo, M.; Torelli, L. The Eastern Ross Sea continental shelf during the Cenozoic: implications for the West Antarctic ice sheet development. Global and Planetary Change 1999, 23, 173-196.
16. Salvini, F.; Brancolini, G.; Busetti, M.; Storti, F.; Mazzarini, F.; Coren, F. Cenozoic geodynamics of the Ross Sea region, Antarctica: Crustal extension, intraplate strike slip faulting, and tectonic inheritance. Journal of Geophysical Research: Solid Earth 1997, 102, 24669-24696.
17. Greenwood, S.L.; Gyllencreutz, R.; Jakobsson, M.; Anderson, J.B. Ice-flow switching and East/West Antarctic Ice Sheet roles in glaciation of the western Ross Sea. Bulletin 2012, 124, 1736-1749.
18. Brunt, K.M.; Fricker, H.A.; Padman, L.; Scambos, T.A.; O'Neel, S. Mapping the grounding zone of the Ross Ice Shelf, Antarctica, using ICESat laser altimetry. Annals of Glaciology 2010, 51, 71-79.
19. Hillenbrand, C.-D.; Grobe, H.; Diekmann, B.; Kuhn, G.; Fütterer, D.K. Distribution of clay minerals and proxies for productivity in surface sediments of the Bellingshausen and Amundsen seas (West Antarctica)-Relation to modern environmental conditions. Marine Geology 2003, 193, 253-271.
20. Jung, J.; Yoo, K.-c.; Lee, K.-h.; Park, Y.k.; Lee, J.i.; Kim, J. Clay mineralogical characteristics of sediments deposited during the late quaternary in the Larsen ice shelf B embayment, Antarctica. Minerals 2019, 9, 12.
21. Park, Y.K.; Lee, J.I.; Jung, J.; Hillenbrand, C.-D.; Yoo, K.-C.; Kim, J. Elemental compositions of smectites reveal detailed sediment provenance changes during glacial and interglacial periods: The Southern Drake Passage and Bellingshausen Sea, Antarctica. Minerals 2019, 9, 322.
22. Chamley, H. Clay sedimentology; Springer: New York, NY, USA, 2013.
23. Petschick, R.; Kuhn, G.; Gingele, F. Clay mineral distribution in surface sediments of the South Atlantic: sources, transport, and relation to oceanography.

KOPRI 극지연구소

Marine Geology 1996, 130, 203-229.
24. Ehrmann, W.U.; Melles, M.; Kuhn, G.; Grobe, H. Significance of clay mineral assemblages in the Antarctic Ocean. Marine Geology 1992, 107, 249-273.
25. Hong, S.; Lee, M.K.; Seong, Y.B.; Owen, L.A.; Rhee, H.H.; Lee, J.I.; Yoo, K.-C. Holocene sea-level history and tectonic implications derived from luminescence dating of raised beaches in Terra Nova Bay, Antarctica. Geosciences Journal 2020, 1-16.
26. Han, H.; Lee, H. Tide deflection of Campbell Glacier Tongue, Antarctica, analyzed by double-differential SAR interferometry and finite element method. Remote Sensing of Environment 2014, 141, 201-213.
27. Jones, K.; McCave, I.; Patel, D. A computer interfaced sedigraph for modal size analysis of fine grained sediment. Sedimentology 1988, 35, 163-172.
28. Jung, J.; Yoo, K.-C.; Rosenheim, B.E.; Conway, T.M.; Lee, J.I.; Yoon, H.I.; Hwang, C.Y.; Yang, K.; Subt, C.; Kim, J. Microbial Fe (III) reduction as a potential iron source from Holocene sediments beneath Larsen Ice Shelf. Nature communications 2019, 10, 1-10.
29. Biscaye, P.E. Distinction between kaolinite and chlorite in recent sediments by X-ray diffraction. American Mineralogist: Journal of Earth and Planetary Materials 1964, 49, 1281-1289.
30. Biscaye, P.E. Mineralogy and sedimentation of recent deep-sea clay in the Atlantic Ocean and adjacent seas and oceans. Geological Society of America Bulletin 1965, 76, 803-832.
31. Yang, K.; Yoo, K.-C.; Jung, J. Quantitative Analysis of Asbestos-Containing Materials Using Various Test Methods. Minerals 2020, 10, 568.
32. Munoz, Y.P.; Wellner, J.S. Seafloor geomorphology of western Antarctic Peninsula bays: a signature of ice flow behaviour. Cryosphere 2018, 12.
33. Han, H.; Ji, Y.; Lee, H. Estimation of annual variation of ice extent and flow velocity of Campbell Glacier in East Antarctica using COSMO-SkyMed SAR images. Korean Journal of Remote Sensing 2013, 29, 45-55.
34. Guglielmo, L.; Zagami, G.; Saggiomo, V.; Catalano, G.; Granata, A. Copepods in spring annual sea ice at Terra Nova Bay (Ross Sea, Antarctica). Polar Biology 2007, 30, 747-758.
35. Ehrmann, W.; Hillenbrand, C.-D.; Smith, J.A.; Graham, A.G.; Kuhn, G.; Larter, R.D. Provenance changes between recent and glacial-time sediments in the Amundsen Sea embayment, West Antarctica: clay mineral assemblage evidence. Antarctic Science 2011, 23, 471-486.
36. Wang, Q.; Yang, S. Clay mineralogy indicates the Holocene monsoon climate in

KOPRI 극지연구소

the Changjiang (Yangtze River) Catchment, China. Applied Clay Science 2013, 74, 28-36.

37. Sinha, R.; Chatterjee, A. Mineralogy of lacustrine sediments in the Schirmacher range area, eastern Antarctica. Journal of the Geological Society of India 2000, 56, 39-46.
38. Jeong, G.; Yoon, H. The origin of clay minerals in soils of King George Island, South Shetland Islands, West Antarctica, and its implications for the clay-mineral compositions of marine sediments. Journal of Sedimentary Research 2001, 71, 833-842.
39. Jung, J.; Park, Y.; Lee, K.-H.; Hong, J.; Lee, J.; Yoo, K.-C.; Lee, M.; Kim, J. Clay Mineralogical Characteristics and Origin of Sediments Deposited during the Pleistocene in the Ross Sea, Antarctica. Journal of the Mineralogical Society of Korea 2019, 32, 163-172.
40. Salvi, C.; Busetti, M.; Marinoni, L.; Brambati, A. Late Quaternary glacial marine to marine sedimentation in the Pennell Trough (Ross Sea, Antarctica). Palaeogeography, Palaeoclimatology, Palaeoecology 2006, 231, 199-214.
41. Ehrmann, W. Lower Miocene and Quaternary clay mineral assemblages from CRP-1. Terra Antartica 1998, 5, 613-619.
42. Buffoni, G.; Cappelletti, A.; Picco, P. An investigation of thermohaline circulation in Terra Nova Bay polynya. Antarctic Science 2002, 14, 83.
43. Livingstone, S.J.; Cofaigh, C.Ó.; Stokes, C.R.; Hillenbrand, C.-D.; Vieli, A.; Jamieson, S.S. Glacial geomorphology of Marguerite Bay palaeo-ice stream, western Antarctic Peninsula. Journal of Maps 2013, 9, 558-572.
44. Postma, G. Classification for sediment gravity-flow deposits based on flow conditions during sedimentation. Geology 1986, 14, 291-294.
45. Chewings, J.M.; Atkins, C.B.; Dunbar, G.B.; Golledge, N.R. Aeolian sediment transport and deposition in a modern high latitude glacial marine environment. Sedimentology 2014, 61, 1535-1557.
46. Rhee, H.H.; Lee, M.K.; Seong, Y.B.; Hong, S.; Lee, J.I.; Yoo, K.-C.; Yu, B.Y. Timing of the local last glacial maximum in Terra Nova Bay, Antarctica defined by cosmogenic dating. Quaternary Science Reviews 2019, 221, 105897.
47. Pensieri, S.; Bozzano, R.; Schiano, M.E.; Pensieri, L.; Traverso, F.; Trucco, A.; Picco, P.; Bordone, A. Environmental acoustic noise observations in Tethys Bay (Terra Nova Bay, Ross Sea, Antarctica). In Proceedings of 2014 Oceans-St. John's 2014, pp. 1-6.

Table 1. Sampling location and type of samples collected from Terra Nova Bay, Ross Sea, Antarctica

Sampling site	Latitude (S)	Longitude (E)	Water depth (m)	Type of sample
JBG01	74°38.40	164°15.60	150	Sediment
JBG02	74°39.00	164°21.00	390	Sediment
JBG03	74°40.20	164°23.40	225	Sediment
JBG04	74°42.60	164°24.00	523	Sediment
JBG05	74°43.80	164°15.60	328	Rocky bottom
JBG06	74°41.40	164°10.20	386	Sediment
JBG07	74°40.20	164°14.40	390	Sediment
JBG08	74°39.00	164°11.40	255	Sediment
JBG09	74°38.40	164°06.60	230	Rocky bottom
JBG10	74°40.20	164°06.60	235	Sediment
JBG11	74°41.27	164°25.93	280	Rocky bottom
JBG12	74°41.25	164°20.99	270	Sediment
JBG13	74°41.90	164°16.44	515	Sediment
JBG14	74°42.60	164°12.37	388	Sediment

KOPRI
극지연구소

Table 2. Grain size distribution of surface sediments collected from Terra Nova Bay, Ross Sea, Antarctica

Sampling site	Gravel (%)	Sand (%)	Silt (%)	Clay (%)	Gravel + coarse/medium sand (%)	Mean size (φ)	Sorting (φ)
JBG01	0.2	89.9	5.2	4.7	10.1	3.0	1.4
JBG02	6.2	88.1	2.8	2.9	49.1	1.9	1.8
JBG03	35.4	61.0	1.4	2.5	68.3	0.5	2.4
JBG04	0.1	99.5	0.1	0.2	73.6	1.7	0.7
JBG06	3.2	95.0	0.6	1.2	32.5	2.4	1.1
JBG07	0.6	90.1	3.7	5.6	13.3	3.2	1.7
JBG08	0.0	87.5	7.2	5.3	9.6	3.2	1.5
JBG10	0.0	91.9	1.4	6.7	5.3	3.2	1.6
JBG12	0.1	97.2	1.0	1.8	24.5	2.5	0.9
JBG13	0.0	73.0	10.0	17.0	9.3	5.1	3.2
JBG14	0.0	95.9	1.3	2.7	15.8	2.8	0.8

KOPRI
극지연구소

Table 3. Relative abundance of clay minerals and illite crystallinity (IC) of surface sediments collected from Terra Nova Bay, Antarctica

Sampling site	Smectite (%)	Illite (%)	Kaolinite (%)	Chlorite (%)	IC (°Δ2θ)
JBG01	8.6	74.0	7.5	10.0	0.49
JBG02	12.0	67.7	7.8	12.6	0.52
JBG03	11.2	71.3	7.0	10.6	0.49
JBG06	12.7	58.4	13.0	15.9	0.43
JBG07	13.8	65.3	9.3	11.6	0.48
JBG08	6.5	70.3	10.9	12.4	0.41
JBG09	12.9	62.3	11.7	13.2	0.47
JBG12	10.6	69.2	9.1	11.1	0.42
JBG13	15.7	53.7	13.8	16.8	0.40
JBG14	20.1	56.5	9.6	13.8	0.54
Avg.	12.3	64.6	10.0	12.8	0.47

KOPRI
극지연구소

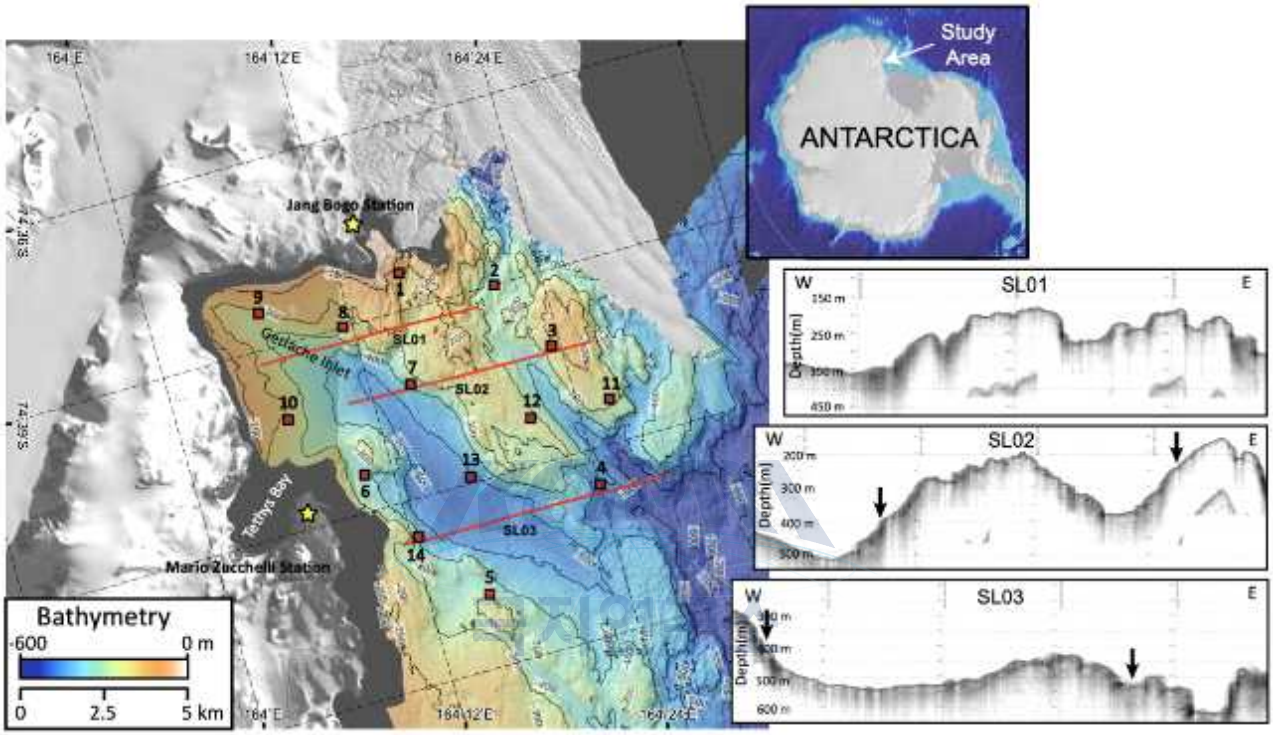


Figure 1. Sampling location, multibeam bathymetry data and sub-bottom profiles of Terra Nova Bay, Antarctica. The arrows on the sub-bottom profiles indicate coring stations.

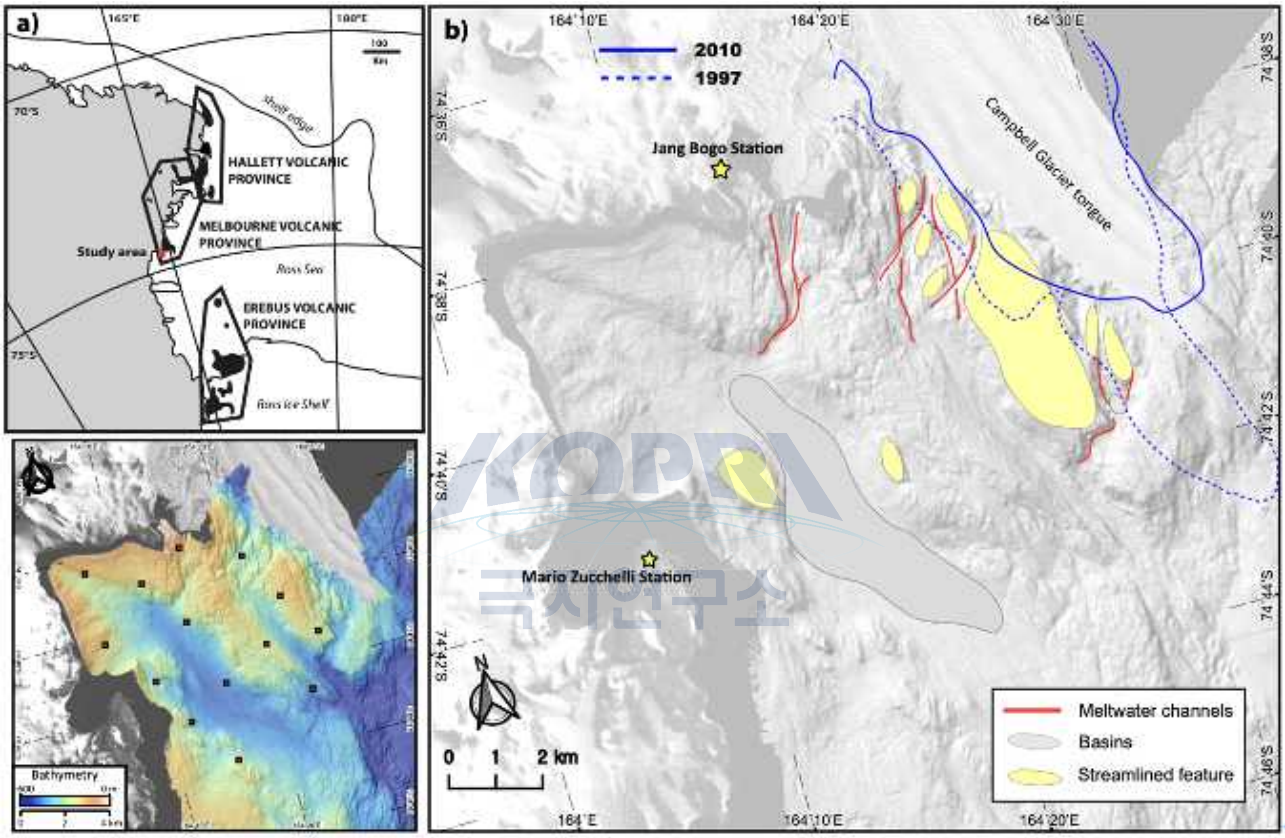


Figure 2. Multibeam swath bathymetry and geomorphology of the study area. a) The study area is included in the Melbourne Volcanic Province. b) The solid line is a boundary of CGT suggested by Han et al. (2013) [51]and the dotted line is suggested by Guglielmo et al. (2007) [52].

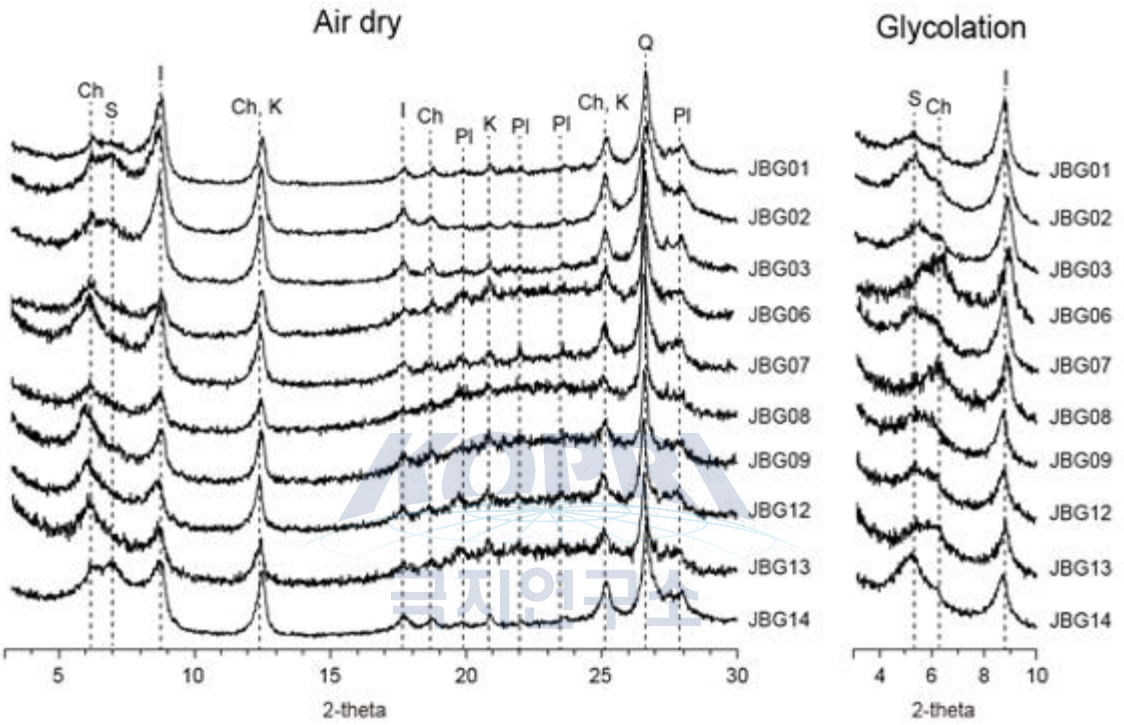


Figure 3. The XRD profiles of air-dried and glycolation treated clay (<1 mm) in surface sediments form Terra Nova Bay (S: smectite, Ch: chlorite, I: illite, K: kaolinite, Pl: plagioclase,Q: quartz)

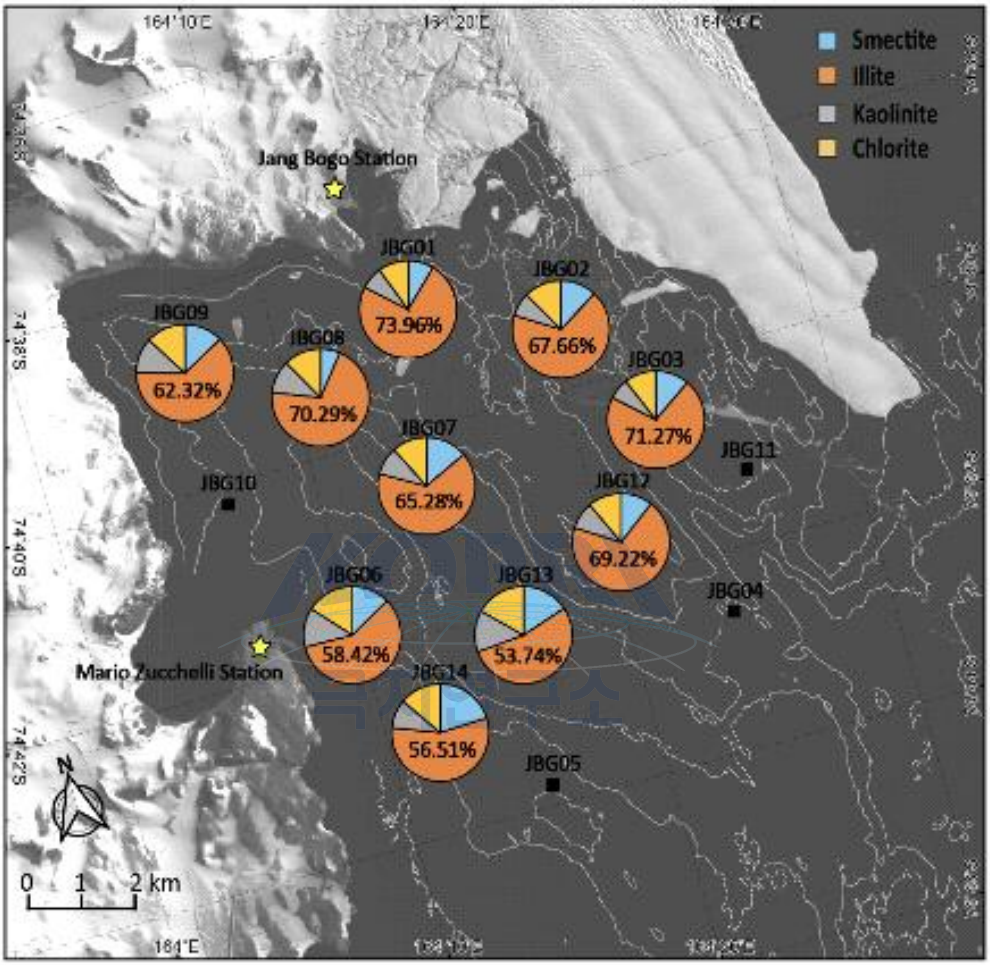


Figure 4. Average clay mineral composition of surface sediments collected from Terra Nova Bay, Antarctica.

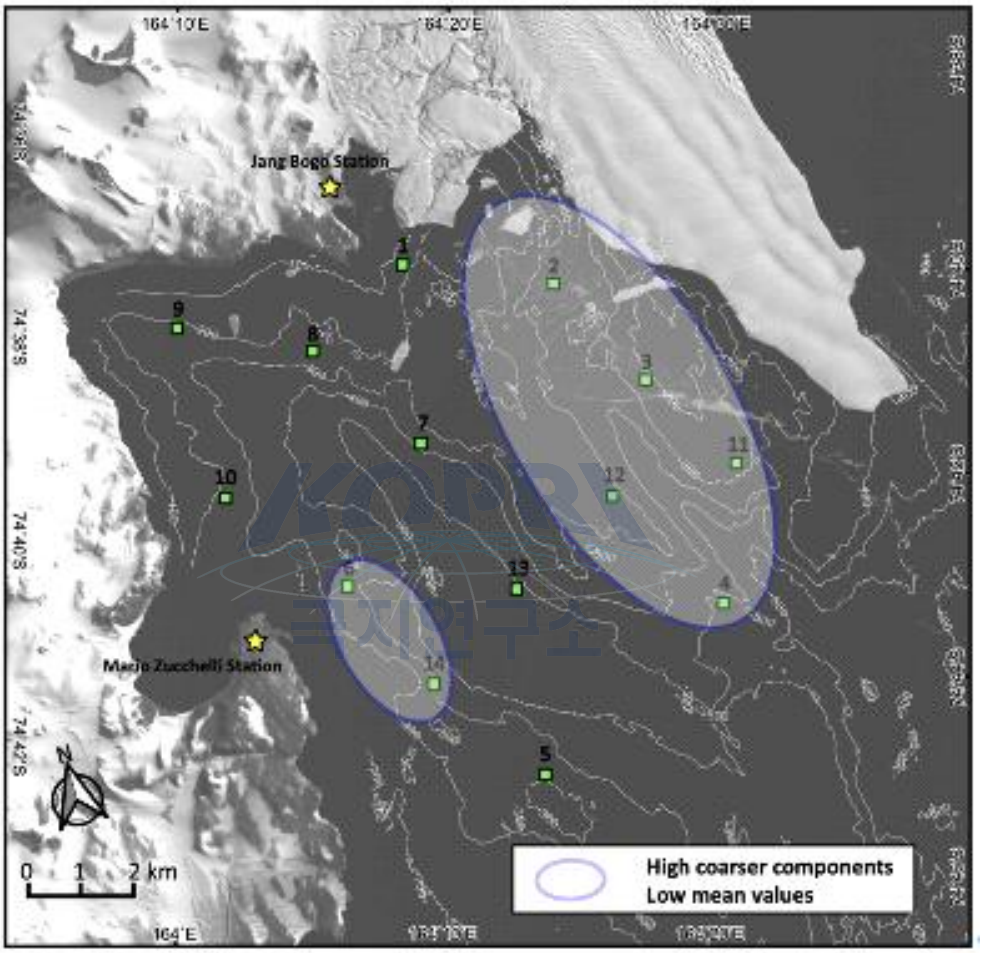


Figure 5. The relative mean size and coarse-sized component of surface sediments.

제 11 장

아문젠해 서부 대륙붕 리글리 만의 해빙 역사 복원

이재일

한국해양과학기술원 부설 극지연구소

요약: 지난 해빙기와 같이 기후가 온난해지는 시기에 해양-기반 빙상이 어떻게 변화했는지 파악하는 것으로부터 외부 자극에 대해 앞으로 빙상이 어떻게 반응할지 예측하는 데 도움을 받을 수 있다. 이 연구에서는 서남극의 아문젠해 서부 대륙붕에 위치한 리글리만에서 획득한 멀티빔 해저수심 자료 및 천부 지층 탐사 자료를 이용하여 빙하에 의해 형성된 지형을 파악하고 지난 빙하기 이후 서남극 빙상의 거동을 복원하였다. 이 지역의 지난 최대 빙하기 동안 서남극 빙상은 리글리 만의 대륙붕 말단까지 확장되었다. 중부-바깥쪽 대륙붕에는 아이스 돔이 위치하였고 이로 인해 서남극 빙상으로부터 흘러나오는 아이스 스트림은 동쪽으로 휘어지게 되었다. 해빙이 시작되면서 아이스 돔은 바깥쪽 대륙붕으로 후퇴하였고 서남극 빙상의 빙하 기저선은 대륙붕 안쪽으로 후퇴하였다. 이후 아이스 돔의 계속된 축소로 인해 빙하 흐름에 큰 규모의 변화가 일어났고 서남극 빙상은 바다 쪽으로 다시 전진하게 되었다. 이 시기 빙상의 전진과 이후 후퇴는 대륙붕 중부-내부에 대규모 빙하 선구조 및 grounding zone wedge들로부터 확인할 수 있다. 이 연구의 해빙 모델은 적절한 지형 조건이 주어지면 해빙 동안 빙하 흐름에 큰 변화가 있어날 수 있음을 지시한다.

1. 서언

게츠 빙붕은 마리버드랜드의 해안을 따라 발달한 트러프 위에 길게 발달한 큰 빙붕으로 서남극빙상 (West Antarctic Ice Sheet)으로부터 기원한 빙하들을 지탱하고 있다 (그림 1; Cochran et al., 2020; Millan et al., 2020; Selley et al., 2021). 게츠 D와 E 빙붕의 전면부에서 빙하의 속도는 연간 600m를 넘어서며 1990년대 이래로 게츠 빙붕 지역에서의 빙하 붕괴는 증가하고 있다 (Selley et al., 2021). 리글리 만은 게츠 D와 E 빙붕 앞쪽에 있는 만으로서 사이플 섬과 그랜트 섬 사이에 위치하고 있다 (그림 1). 게츠 D 빙붕은 베를린, 교토 빙하의 하류에, 게츠 E 빙붕은 드비크, 제네바, 리우 빙하의 하류에 위치한다 (그림 1e).

극지연구소는 2020년 1월에 리글리만에서 멀티빔 해저 지형 조사 및 해저면 천부 음향 탐사 (Sub-bottom profiler; SBP)를 실시하였다 (그림 1c 와 1d). 이 연구에서는 기존 미국 쇄빙선 나타니엘 B. 파머의 멀티빔 자료 (Anderson et al., 2001; Wellner et al., 2001)와 새로 얻은 자료를 종합하여 리글리만에서 마지막 빙하기 이후의 해빙기 동안의 빙상 변화를 복원하고자 하였다. NBP9902 멀티빔 해저 수심 조사에서 리글리만의 트러프가 확인되었고 대륙붕 중앙부에서는 북서 방향의 과거 빙하 흐름을 지시하는 선구조들이 발견되었으나 게츠 E 빙붕 쪽에서는 북쪽이나 북동

방향의 빙하 흐름을 지시하는 선구조들이 발견되었다 (Anderson et al., 2002). 이러한 자료는 리글리 만에 과거 ice stream이 존재하였음을 지시하는 한편 과거에 빙하 흐름의 변화가 있었을 가능성을 시사한다. 하지만 현재까지는 리글리만에서 수심 자료는 매우 제한적이어서 빙하 흐름의 변화와 상대적 시기 등 보다 자세한 정보를 얻을 수 없었다.

아문젠해 내부 대륙붕 지역 중 리글리 만 동쪽의 닷슨-게츠 paleo-ice stream은 닷슨, 게츠 A, 게츠 B 빙붕 지역에서, 서쪽의 Hobbs paleo-ice stream은 Getz F 빙붕 지역에서 멀티빔 해저지형 탐사를 통해 빙하 지형이 자세하게 연구되었다 (Graham et al., 2009; Larter et al., 2009; Klages et al., 2014). 이 지역들의 빙하 지형은 복잡하고 다양한 형태를 보였지만 리글리만에서 보는 바와 같은 빙하 흐름의 변화를 지시하는 형태는 나타나지 않았다. 이 연구에서는 (1) 리글리 만 해저에 보존된 빙하 지형을 보고하고 새로운 수심 자료에 의거하여 과거 빙하 흐름의 변화 양상을 추정하며, (2) 해저면 지형이 어떻게 형성되었는지 복원함으로써 지난 해빙기 동안 서남극 빙상의 거동을 이해하고자 한다.

2. 연구방법

해양 지구물리 자료들은 2020년 1월 쇄빙연구선 아라온을 이용한 ANA10B 탐사 동안 획득되었다. 자세한 멀티빔 해저지형 자료는 아라온에 장착된 kongsberg-Simrad EM122 시스템을 이요하여 획득하였으며 CARIS HIPS and SIPS 소프트웨어 (http://www.caris.com/products/hips-sips/)를 이용하여 20m 그리드로 변환하였다. 미국 쇄빙연구선 나타니엘 B. 파머의 NBP9902, NBP9909, NBP0001, NBP0702, NBP9909, NBP1201의 멀티빔 자료는 Marine Geoscience Data system (http://www.marine-geo.org)에서 획득하였다 (그림 1d; Anderson, 2013; Bengtson, 2013; Jacobs, 2013; Nitsche, 2013; Halanych, 2016). ANA10B 탐사 동안 획득한 SBP 자료는 아라온에 장착된 Kongsberg SBP27 시스템을 이용하여 획득하였다. 운용 주파수는 2-9 kHz, 수직 해상도는 0.2 ms이다. 자료 처리와 이미지화는 Kongberg 소프트웨어 KM SBP 1.4.8을 사용하였다.

3. 연구결과

가. 리글리만 대륙붕의 지형 및 기저 지질

수심 및 기저 지질은 빙상의 흐름 방향을 조정하고 빙하 후퇴 양상을 조절함으로써 빙상의 거동과 빙하 역사에 중요한 역할을 한다 (e.g., Anandakrishnan et al., 1998; Wellner et al., 2001). 이 연구에서는 수심과 해저면의 기복을 기초로 하여 대륙붕을 내부-, 중부, 외부-대륙붕으로 나누었다 (그림 2). 내부와 중부 대륙붕의 경계는 연구지역 서쪽에서는 수심 약 800 m에, 동쪽에서는 수심 약 700 m에 설정하였다. 중부/외부 대륙붕의 경계는 수심 약 600 m 에 해당한다. 멀티빔 수심 자료는 대체로 리를리 만이 깊은 내부 대륙붕과 얕은 대륙붕으로 구성되어 있다는 기존

연구와 일치하지만 자세한 지형은 더 많은 변화가 있다. 내부 대륙붕 중 서부 지역에는 수심 1000 m 이상의 깊은 트러프가 두 개 있는데 (그림 1c의 T1과 T2), T1은 남북 방향으로, T2는 북동-남서 방향으로 발달하고 있다. 딘 섬 북서쪽에는 수심이 얕은 고지 H1이 있어 서쪽과 동쪽의 내부 대륙붕의 경계가 되고 있다 (그림 2). 동쪽의 내부 대륙붕은 800m 보다 얕은 수심으로, 남북 방향의 작고 기복이 적은 골들이 있는 것이 특징적이다. 이들은 30-50 m 깊이, 약 1-3 km 의 폭 (전체로서는 6 km), 약 20 km의 길이를 보인다 (그림 1c의 T3). 북북동-남남서 방향의 좁고 깊은 트러프가 대륙붕과 사이플 섬 서쪽 해안 사이에서 대륙붕 경계까지 길게 발달하고 있으며 이들은 최대 약 800 m 깊이를 보인다 (그림 1c의 T4).

서남극 대륙붕의 해저면은 대개 해저면으로부터 빙하기저부의 부드러운 빙하퇴적물과 후빙기의 빙해양 퇴적물과 같은 미고화 퇴적물, 단단한 빙하퇴적물이나 오래된 퇴적암층과 같은 반고결 퇴적물/퇴적암, 화강암이나 편마암 같은 결정질 암석으로 구성된다. 오래된 퇴적암층과 결정질 암석이 대개 기저 지질을 이루게 된다 (예: Wellner et al., 2001; Graham et al., 2009). 리글리 만의 SBP 자료는 미고결 퇴적물은 드물게 나타나고 두께도 1-2 미터 미만으로 일부 지역에만 한정되어 있음을 보여준다. 탄성파 탐사 결과로는 내부 대륙붕에 결정질 기반암이 있고 바깥쪽 대륙붕에는 퇴적물/퇴적암이 웨지 형태로 이들을 덮고 있는 것으로 보인다 (그림 1c; Anderson et al., 2002). 내부 대륙붕의 해저면의 내부구조는 단단하고 고결된 기질 특성으로 인해 SBP 자료로는 판별할 수 없었다. 하지만 해저면 조성의 차이는 해저면 기복의 변화로 추정할 수 있었다. 서쪽의 내부 대륙붕의 결정질 암석 지역 (Anderson et al., 2002)은 기복이 심한 지형과 SBP 상의 타원형 파형으로 나타나는 반면 퇴적물/퇴적암의 해저면은 보다 부드러운 파형과 완만한 경사로 나타난다 (그림 2와 3). 내부 대륙붕의 결정질 기반암과 중부-외부 대륙붕의 퇴적층은 닷슨-게츠 고 빙하 트러프에서도 발견되는데, 그곳에서는 해저면 기복이 해저면 기질과 밀접하게 연관되어 있음이 보여졌다 (Graham et al., 2009; Larter et al., 2009). 이 관계를 리글리 만에 적용하여 기복으로부터 해저면 기질을 추정하여 보면, 리글리 만의 중부 및 외부 대륙붕은 퇴적층으로 덮여 있는 것으로 보인다 (Wellner et al., 2002; Anderson et al., 2002). 서쪽의 내부 대륙붕과 수심이 얕은 H1 지역은 아마도 주로 결정질 모암으로 구성되고 일부 단단한 퇴적물로 피복되어 있는 것으로 보인다 (그림 3a와 3d의 SBP 참조). 동쪽의 내부 대륙붕은 주로 빙하 퇴적물로 피복되어 있으나 해저면은 중부나 외부 대륙붕 지역보다 기복이 심하다. 동쪽의 경계부 트러프 T4는 아마도 일부 퇴적층으로 덮인 결정질 암석으로 구성된 것으로 보인다 (그림 3e와 3f의 SBP 참조).

나. 해저면에 보존된 빙하 지형

리글리 만의 해저면 지형은 다양한 빙하 지형이 나타나는 것이 특징적이며 이들은 과거의 빙상의 전진과 후퇴 역사를 기록하고 있다 (그림 3). 여기서는 리글리 만의 빙하 지형을 해석하고 그림 4에 종합적으로 도시하였다.

(1) 드럼린 류와 암반 위에 발달한 선형 구조

내부 대륙붕 중 결정질 기반암이 주를 이루는, 수심이 얕은 H1 지역과 깊은 트러프 지역

에서는 길쭉한 그루브-능선 형태의 선형 구조들이 발달하는데 이 선구조의 육지쪽 끝에는 눈물 형태의 머리가 발달하기도 한다 (그림 4). H1 지역에는 대규모의 기반암 그루브와 해자를 두른 눈물 형태의 머리를 지닌 드럼린 류의 구조들이 발달한다. 드럼린 류들에 나타는 해자들은 상류의 해저면에 비해 5-45 m 깊이를 지니며 눈물 형태의 머리는 약 1.5 km의 폭을 보인다 (그림 3a). 이 기반암에 발달한 드럼린들은 약 5 km의 길이를 지니면 하류로는 평행한 선구조로 이어지고 끝으로가면서 가늘어지는 퇴적물은 보이지 않는다. 드럼린 류의 형태는 과거 빙하가 H1을 넘어 북동 방향으로 흘렀음을 보여준다. 트러프 T2의 북서쪽에서는 드럼린 류들과 선형의 그루브들이 나타나는데 (Anderson et al., 2002; 그림 3d), 규모는 H1보다 작아서 폭도 0.3 km 정도로 좁고 길이도 2.5 km 미만으로 나타나지만, 과거 빙하 흐름 방향은 H1과 유사하게 북동 방향의 흐름을 지시한다.

H1의 바로 남서쪽 해저면에서는 상류쪽에 0.3 km 정도 폭의 머리를 보이는 몇몇 길쭉한 능선들이 나타나는데 이들은 4 km 까지 달하는 길고 좁아지는 퇴적물 꼬리를 가지고 있다 (그림 3a의 노란 화살표). 이곳의 해저면은 빙하 선구조이 퇴적층에 나타나는 완만한 해저면 특성을 보인다. 이 구조는 북북동 방향의 과거 빙하 흐름을 지시하고 있다. 가장 서쪽의 내부 대륙붕에 발달하는 트러프 T1의 드럼린 류와 빙하 선구조는 남북 방향으로 발달하고 있어 과거 빙하 방향이 북쪽으로 흘렀음을 보여준다 (그림 3c). 동쪽의 경계부 트러프 T4에서 나타나는 그루브-능선들은 사이플 섬 서쪽에서 북북서 방향의 빙하 흐름에 의해 형성되었다. 따라서 리글리 만의 드럼린류와 기반암에 발달한 선구조들은 과거 북쪽 방향과 북동 방향의 두 방향의 빙하 흐름에 의해 형성된 것으로 볼 수 있다. 이들은 수심 800 m 이상과 600 m 이하 지역에서 주로 나타나며 두 방향의 빙하 흐름은 모든 수심에서 나타난다 (그림 5).

KOPRI 극지연구소

(2) 퇴적암/퇴적물 위에 발달한 선형 구조

서남극 대륙붕에서 퇴적층 기저부 지역에서 대규모 빙하 선구조 (mega-scale glacial lineations; MSGL)을 포함한 빙하 기원의 선형 구조는 흔하게 나타난다 (예: Wellner et al., 2001). 이러한 MSGL과 다른 선형 구조들은 리글리 만에서도 역시 나타나는데 이곳에서는 길고 평행하게 발달한 능선들과 그루브들이 나타나며 길이:폭 비는 대개 15:1보다 크다. 여기서는 결정질 암석 기질 위의 선구조와 구분하기 위하여 MSGL과 퇴적물 기질 위에 발달한 기타 선형구조들을 합쳐서 퇴적물 빙하 선구조로 도시하였다 (그림 4). MSGL은 빠르게 흐르는 빙하 아래에 발달하는 지형으로 길이는 수십 km, 진폭은 수 m, 파장은 수십~수백 m 에 달한다 (예: Clark, 1993; Ó Cofaigh et al., 2005; Bell et al., 2016). 리글리 만에서는 중부-동부 지역의 600-800 m 수심의 해저면에 가장 흔하게 나타난다 (그림 5). 이들은 보존이 잘 되어 있고 빙하에 의해 긁히 자국 외에는 변형이 되지 않아 마지막 빙하기 이후 해빙기의 빙하의 흐름 방향을 지시하는 것으로 보인다. MSGL은 리글리 만에서 지난 해빙기 동안 약 100 km 폭의 북북서 방향의 빙하 스트림이 있었음을 지시한다 (그림 4a, 5b). 연구지역 동쪽에서 MSGL이 지시하는 빙하 흐름 방향은 빙하가 후퇴함에 따라 차츰 서쪽 방향으로 변화하여, 게츠 D 빙붕 앞인 내부 대륙붕 지역에서는 현재 빙붕의 이동 방향과 비슷한 방향이 되었다 (그림 5; Rignot et al., 2017).

(3) 빙하기저선을 지시하는 빙하 지형

리글리 만의 MSGL은 흔히 빙하 기저 쐐기 (grounding zone wedges; GZWs)의 표면에 발달한다 (그림 2e). GZW는 후퇴하는 빙상의 기저선에 램프 형태로 쌓이틀 퇴적체이다. 이들은 보통 비대칭적인 프로파일을 지니며 MSGL은 상류쪽으로 경사진 면 위에 발달하여 빙하 흐름 방향을 지시하게 된다 (예: Batchelor & Dowdeswell, 2015). 동부 리글리만에서 GZW와 MSGL은 북서방향의 빙하 흐름과 남쪽 혹은 남동쪽으로의 빙하기저선 후퇴를 지시한다 (그림 4).

북동-남서 방향으로 선상으로 발달한 빙하 기저선이 서부 지역의 내부 대륙붕에서 발견된다 (그림 3a와 3d의 GL). 기존의 북동-남서 방향으로 길게 발달한 능선 때문에 빙하가 후퇴할 때 일시 안정화를 이루어서 이 지역에 기저선이 발달한 것으로 보인다.

리글리만의 동쪽 지역에서 트러프 T4의 남쪽 경계는 약 5km 폭의, 톱니 형태의 전면부를 보이는 램프로 되어 있다 (그림 3f). 이 램프의 꼭대기는 외해 방향 해저면보다 약 100 m 정도 얕으며 서쪽에 있는 GZW와 연결되어 있어 이 램프가 당시 기저선이었음을 암시하고 있다. 이와 유사한 해저면의 램프는 스웨이츠 빙하 부근의 해저면의 고해상도 멀티빔 자료에서 기저선이 후퇴 당시 일시적으로 멈추었을 때 형성되었음이 보고된 바 있다 (Graham et al., 2022).

(4) 빙하에 의해 긁힌 자국들

특정 방향성을 보이지 않는 빙산에 의해 긁힌 자국들 (iceberg ploughmarks)은 주로 외부 대륙붕의 700 m 보다 얕은 지역에서 많이 발견되며 다른 빙하 구조들을 침식하고 있다 (그림 4). 이들 긁힌 자국들이 이전에 형성된 다른 모든 빙하 지형들을 덮고 있어 지난 빙하기 동안 리글리만 외부 대륙붕에서의 빙상의 범위는 모호해졌다. 하지만 동쪽의 경계부 트러프 T4에서는 MSGL이 거의 남위 73.1 도의 대륙붕 경계부까지 발달하고 있어 과거 기저 빙하가 대륙붕 경계부까지도 전진했음을 지시하고 있다.

(5) 빙하 후퇴에 의해 반복적으로 형성된 소규모의 가로 방향 능선들

육지쪽으로 경사진 서쪽 지역의 중부 대륙붕 지역에는 비교적 작고 촘촘한 북동-남서 방향의 능선들이 수심 650-800 m에 나타난다 (그림 3b; 그림 4의 Transverse ridges). 이 능선들은 MSGL과 빙하에 의해 긁힌 자국이 거의 없는 일부 지역에서만 발견되는데 (그림 4), 이는 이 구조가 나중에 형성된 빙하 구조들에 의해 지워졌으며 과거에는 현재 나타나는 것보다 더 널리 나타났을 가능성을 지시한다. 이 능선들은 약간 휘어진 형태이며 서로 평행한 편이고 높이는 5-20 m, 능선 사이의 거리는 200-500 m 정도 된다. 멀티빔과 SBP 단면상에서 대부분의 능선들은 대부분 대칭적인 형태를 보이지만 적어도 두 개의 능선 (#4와 #10)은 비대칭적이고 급경사 부분이 서북서 방향의 사면에 나타난다 (그림 6b). 이들 능선의 형태와 규모는 얕은 대륙붕 지역에서 흔히 나타나는 빙하 후퇴기의 빙퇴석과 유사한다. 이런 빙퇴석은 기저 빙하가 비교적 천천히 후퇴할 때 빙상의 가장자리에서 규칙적으로 형성된다 (예: Dowdeswell et al., 2008; Simkins et al., 2018). 가로 방향 능선들의 북동쪽 지역은 북서 방향으로 흐른 빙하에 의해 형성된 MSGL로 덮여 있어 (그림 3b) 빙퇴석을 형성한 빙상의 후퇴에 이어 다시 빙상의 전진이 일어 났음을 알 수 있다. 이 지역의 지형 단면을 보면 이 능선들은 비교적 깊은 곳에 형성되어서 빙상이 다시 전진할 때 침식을 피한

것으로 보인다 (그림 6b). 빙퇴석들은 종종 빙상 쪽으로 급경사를, 반대쪽으로는 완만한 경사를 보이므로 (Winkelmann et al., 2010; Klages et al., 2016), 서부 리글리 만에서 기저 빙하는 지난 빙하기의 초기에 서북서 방향, 즉 얕은 외부 대륙붕 쪽으로 후퇴하였고, 후기에 북쪽 방향으로 다시 전진한 것으로 해석하였다.

4. 토의

가. 리글리만에서의 과거 빙하 흐름의 변화

과거 빙하 흐름에 변화가 있었다는 증거는 리글리만 내부 대륙붕에서 발견된다. 가장 뚜렷한 예는 수심이 얕은 H1 지역 부근에서 발견되는데 이곳에서는 모암에 발달한 드럼린과 선형 구조가 이들과는 다른 방향성을 지닌 퇴적물의 빙하 선구조에 의해 덮이거나 (그림 3a의 하얀 삼각형) 깎인 (그림 3a의 검은 삼각형) 형태를 보인다. 모암에 발달한 드럼린과 그루브들은 북동 지난 빙하기의 초기 (빙하 1기)에 북동 방향의 흐름에 의해 형성된 반면, 퇴적물에 발달한 빙하 선구조들은 그보다 나중에 동쪽에서 오는 북서 방향의 흐름과 서쪽에서 오는 북쪽 또는 북동쪽 방향의 흐름이 모여 형성된 것이다 (빙하 2기).

서쪽의 내부 대륙붕 지역에는 초기의 북동 방향의 빙하에 의해 형성된 드럼린류와 그루브/능선들이 이후 북쪽 방향의 빙하에 의해 덮여 있다 (그림 3c와 3d). 트러프 T2의 빙하 구조들은 북동 방향의 빙하가 이 트러프를 채우고 있었으며 따라서 빙하 1기 동안 얼음의 두께는 1000 m 이상이었을 것임을 짐작할 수 있다. 모암에 발달한 선구조와 드럼린류는 트러프 T2의 서쪽 사면에서만 발견된다. 동쪽 사면은 남북 방향의 빙하 흐름을 지시하는 빙하 선구조를 포함한 퇴적층으로 덮여 있다 (그림 3d). 이는 빙하 2기 동안 북동-남서 방향으로 발달한 트러프 위로 북쪽 방향의 기저 빙하가 흘러가면서 트러프의 동쪽 사면에 빙하 퇴적물을 쌓아서 형성된 것으로 해석된다. 빙하 2기 동안 트러프의 가장 깊은 곳의 빙하 구조들은 변형되지 않은 것으로 보아 빙하 2기의 빙상은 빙하 1기의 빙상보다는 두께가 얇았을 것으로 여겨진다. 빙하 2기의 기저 빙하는 빙하 퇴적물이 트러프를 채우거나 빙하 2기에 형성된 지형을 모두 묻어 버리기 전에 육지 쪽으로 후퇴하였던 것으로 보인다. T2 동쪽의 북동-남서 방향의 능선들은 아직도 해저면 지형에서 확인할 수 있다. 서쪽 내부 대륙붕과 비교해 볼 때 동쪽의 내부 대륙붕에서는 빙하 1기의 북동 방향 빙하 흐름을 지시하는 구조는 뚜렷하지 않고 대부분 지역은 북서-남동 방향을 지닌 MSGL로 뒤덮여 있다. 따라서 만약 이전의 빙하 흐름에 의해 형성된 빙하 지형이 있었다고 해도 빙하 2기 동안 그 흔적은 거의 사라진 것으로 보인다. 작은 골짜기 들의 군집인 T3는 이 지역의 MSGL을 형성한 북서 방향의 빙하 흐름에 비스듬하게 발달하고 있다 (그림 3e). T3는 빙하에 의해 형성되었다기 보다는 빙하가 흐르기 이전에 이미 존재하고 있었던 것으로 보이는데, 그 이유는 (1) 골짜기 바닥에서도 MSGL이 발견되므로 MSGL은 골짜기 형성 이후에 만들어진 것이며 (2) MSGL의 방향은 골짜기 주변에서 약간 휘어지는데 이는 골짜기가 MSGL 이후에 형성되었으면 나타나지 않았을 현상이기 때문이다. 골짜기의 서쪽 사면 꼭대기에는 작은 돌출부가 보이는데 (그림 3e의 D-D'프로파일의 검

KOPRI 극지연구소

은 화살표) 이는 빙하가 흐르는 동안 사면 꼭대기에 빙하 퇴적물이 덧붙어 만들어진 것으로 해석된다. 따라서 여기서는 T3가 선형의 골짜기 형태의 모습을 빙하 2기 이전부터 지니고 있었으며 아마도 빙하 1기에 형성된 빙하곡이 이후 빙하 2기에 부분적으로 뒤덮여 현재의 모습을 보이는 것으로 해석하였다.

동쪽 경계부의 트러프 T4는 북북서 방향의 빙하 흐름을 보이며 다른 지역과 달리 빙하 흐름 방향의 변화는 나타나지 않는다. 하지만 여기서도 머리 부분이 평평한 드럼린이 나타나는데 이는 아마도 후기의 빙하에 의한 침식에 의해 형성된 것으로 보인다 (그림 3f의 하얀 삼각형). 따라서 이 지역에서도 서로 다른 시기의 빙하 흐름이 있었던 것으로 해석할 수 있다.

중부-외부 대륙붕에서는 해저면은 대부분 빙하 2기의 흔적들로 덮여 있으며, 북서 방향의 흐름을 보이는 GZW와 MSGL이 나타난다. MSGL들은 외부 대륙붕으로의 기저 빙상의 후퇴를 지시하는 가로 방향 능선들을 덮고 있다 (그림 5b와 6). 과거의 빙하 흐름 방향 분석 결과로는 과거 게츠 E 지역으로부터의 빙하와 게츠 D 지역으로 부터의 빙하가 합쳐져서 중부-외부 대륙붕 지역에서는 100 km 폭의 빙하가 북북서 방향으로 흐르게 되었을 것으로 추정된다 (그림 4c). 육지쪽으로 빙하가 후퇴하면서 이들은 게츠 D 지역에서는 북서 방향의 흐름으로, 게츠 E 지역에서는 북쪽 방향 및 북동 방향의 흐름으로 갈라지게 되었다. H1 남쪽 부분은 이들 두 빙하의 사이에 놓이면서 딘 섬에 의해 침식을 피하게 되어 이전에 형성된 빙하 지형들이 보존된 것으로 보인다 (그림 3a). 현재 빙하의 기저선이 현재의 빙붕 말단 지역 가까이에 있었을 때의 빙하 흐름 방향은 현재 빙붕의 흐름 방향과 유사하였을 것이다 (그림 1e, 5d).

빙하 1기와 빙하 2기의 빙상의 전진 및 후퇴의 방향성은 그림 4b와 4c에 요약되어 있다. 여기서 빙하 1기에 형성된 것으로 해석한 빙하 지형들이 실제로는 여러 번의 빙하기 동안 형성되었을 가능성도 배제할 수는 없다. 하지만 이 시기 빙하 흐름 방향이 연속적이고 여러 번의 빙하기를 지시하는 증거가 없으므로 한 번의 빙하기 동안 형성되었을 것으로 추정하였다.

나. 지난 빙하기 이후 리글리만의 서남극 빙상 변화 복원

(1) 지난 빙하기 동안 빙상의 최대 확장기 (빙하 1기)

이 지역의 마지막 최대 빙하기는 이 연구의 빙하 1기에 해당하며, 이 시기 리글리만의 기저 빙상은 동쪽 경계 트러프의 MSGL 분포로 미루어 볼 때 대륙붕 경계까지 전진했던 것으로 보인다. 이 시기가 전세계적 마지막 최대 빙하기 (19-26.5 ka; Clark et al., 2009)와 일치하는지의 여부는 알 수 없다. 빙하 1기의 빙상은 내부 대륙붕에서 1000 m 이상의 해저면에 닿을 정도로 두꺼웠더다. 서부의 내부 대륙붕의 빙하는 아마도 드비크, 제네바, 리우 빙하의 연장선에 있었을 것으로 동쪽으로 휘어지면서 아마도 T3를 지나 동쪽 경계부 트러프 T4 방향으로 흘러갔을 것이다 (그림 7a). 이 시기 게츠 D 지역으로부터도 빙하가 흘러왔을 것이지만 그 증거는 빙하 2기의 두꺼운 빙하 퇴적물에 덮여 찾을 수 없었다. 빙하 1기 동안 빙하가 동쪽으로 휘어졌다는 것은 북쪽 방향의 흐름이 방해 받았다는 점을 의미하여, 아마도 중부-외부 대륙붕에 발달한 기저 빙하가 아이스 돔을 형성하여 동쪽으로의 휘어짐을 유발한 것으로 보인다 (그림 7a의 리글리 만 아이스 돔). 당시 환경은 마지막 최대 빙하기 동안 남극반도의 중부-외부 대륙붕에 아이스 돔이 발달하고 그

사이사이에 빙하가 발달한 형태와 유사하였을 것으로 보인다 (Domack et al., 2006; Lavoie et al., 2015).

(2) 초기 빙상 후퇴

서쪽의 중부 대륙붕에 있는 빙퇴석 (그림 3b와 4)은 빙하 1기 빙상의 초기 후퇴 시의 기저선의 위치를 표시하는데 이는 빙하 기저선이 내부 대륙붕까지 깊게 후퇴했음을 암시한다. Calving bay reentrant 모델에 따르면 해빙기 동안 빙하의 후퇴는 얕은 뱅크 지역보다 그 사이의 깊은 트러프 지역에서 더 빨리 일어나게 된다 (Domack et al., 2006; Leventer et al., 2006). 리글리 만의 지형에서는 빙하 1기 동안 빙하가 흘렀던 저지대를 따라 해빙이 더 쉽게 일어났을 것이다 (그림 7b). 당시 추정 빙하 기저선을 수심 800, 700, 600 미터 선을 따라 그려보면, 리글리 만 아이스 돔은 외부 대륙붕 방향으로 후퇴하게 된다 (그림 7b). 이 가설은 중부 대륙붕의 빙퇴석의 형태적 분석에 의해서도 지지된다 (그림 6). 이 당시 빙하가 바닥까지 닿지 않았던 지역이 해빙 또는 빙붕으로 덮였었는지 아니면 얼음이 없었는지는 추가적인 고환경 증거가 없이 판단할 수 없다.

(3) 빙하 흐름의 재구성 및 빙상의 전진 (빙하 2기)

리글리 만 아이스 돔이 줄어들면서 빙하 1기의 빙하를 동쪽으로 휘게 만들었던 댐 효과는 줄어들게 되었을 것이다. 해빙기가 진행되면서 외부 대륙붕에서 기저면 깊이가 500 m에서 600m 사이에 도달했을 어느 시점에 리글리 만 아이스 돔은 붕괴하고 더 이상 빙하를 동쪽으로 휘게 만들 수 없게 되었을 것이다. 따라서 빙하 흐름 방향은 재구성되어 빙하 2기의 북북서 방향의 빙하 흐름이 생기게 되었다 (그림 7c). 남쪽으로부터 기저 빙상이 전진함에 따라 직전에 빙하가 바닥에 닿지 않았던 내부 대륙붕 지역도 일부 가장 깊은 곳을 제외하고는 다시 빙상에 의해 뒤덮이게 되었다. 빙하 2기는 트러프 지역에 흐름이 집중되었던 빙하 1기와 달리 넓은 빙하가 중부-외부 대륙붕에 발달하였다는 특징이 있다. 빙하 2기 빙상은 빙하 1기 빙상보다 얇고 중부-외부 대륙붕에는 이를 가로지르는 트러프가 없어서 넓은 빙하가 형성되기 유리한 조건이었던 것으로 보인다.
한 번의 해빙기 동안의 빙하 흐름의 재구성은 여러 원인에 의해 일어날 수 있다. 서부 캐나다 내륙 평원에서 로렌타이드 빙상의 육상 빙하의 궤적은 큰 변화를 보이는데 이는 기저 지질의 시공간적 변화에 기인한 것으로 해석되었다 (Ó Cofaigh et al., 2010). 캐나다의 북극 군도 지역의 빙하의 경우는 상대적 해수면 변동과 연관된 지역적 수심 변화에 따라 큰 변화를 겪게 되었다 (Stokes et al., 2009). 웨델해와 로스해 지역의 서남극 빙상은 홀로세 동안 지각 평형에 의한 반동으로 빙하가 다시 전진한 것으로 제시된 바 있지만 모델 결과 아문젠해 지역에서는 이런 현상이 나타나지는 않은 것으로 보인다 (Kingslake et al., 2018). 리글리 만의 빙하 흐름의 재구성은 서부 로스해 남 빅토리아 랜드 지역에서 동남극 빙상이 홀로세에 다시 전진하는 현상과 유사한 측면이 있는데, 이 지역에서는 해빙기 동안 기저면이 대륙붕 안쪽으로 크게 휘어져 들어오면서 이 지역의 빙하들의 전진을 촉진시킨 바 있다 (Greenwood et al., 2018).

(4) 마지막 해빙기 및 빙하 후퇴 시기

GZW 분포를 보면 마지막 해빙기 동안 빙하 2기의 빙상은 리글리 만 동쪽에서 남동쪽으

로 후퇴하였다 (그림 7d). 서쪽에서는 동쪽보다 기저 빙상이 더 먼저 후퇴하였는데 이는 아마도 서쪽 내부 대륙붕 수심이 더 깊어서 그랬던 것 같다.

CALIB 8.2 프로그램 (Stuiver and Reimer, 1993)과 연대 보정 1300 +/− 70 년 (Berkman and Forman, 1996)을 적용하여 NBP9902 퇴적물 코어의 유기성 탄산염 성분에 대한 방사성탄소 동위원소 연대를 보정하면 NBP9902−26에서는 약 14.5 ka, NBP9902−22에서는 약 13.6 ka 시기가 된다 (그림 1; Anderson et al, 2002). 이는 동쪽 지역에서 기저 빙하의 후퇴가 적어도 1만 4천년 이전에 일어났음을 지시한다 (그림 7). 추가적인 연대 자료가 없이 빙상 후퇴 시기와 속도를 결정하는 것은 어려운 일이다. 연구지역 서쪽의 게츠 F 빙붕 지역의 GZW로부터 채취한 코어의 유기성 탄산염 성분에 대한 방사성탄소 동위원소 연대로는 내부 대륙붕에서 빙상은 21 ka 이전에 후퇴하였고, 가장 안쪽의 대륙붕에서는 13 ka 이전에 후퇴하였다고 한다 (Klages et al., 2014). 게츠 F 연구에서는 또한 이 지역의 마지막 최대 빙하기 빙상의 해빙은 대규모 GZW의 형성에 필요한 시간을 추정해 볼 때 외부 대륙붕에서 24 ka 이전에 시작되었다고 제시하였다 (Klages et al., 2014). 만약 이 연대를 리글리 만의 해빙에 적용해 본다면 빙하 1기 빙상의 초기 해빙과 후퇴는 24 ka 이전에 시작되었고, 빙하 흐름의 재구성은 21 ka 이전에, 내부 대륙붕에서의 빙상 후퇴는 13−14 ka 정도에 일어났을 수 있다. 이러한 추정을 확인하고 해빙기 서남극빙상의 변화를 잘 이해하기 위해서는 리글리 만 대륙붕에서 믿을 만한 연대 자료가 더 많이 필요하다.

5. 결론

KOPRI 극지연구소

서남극 리글리 만 대륙붕의 해저 빙하 지형 조사로부터 서남극 빙상의 해빙 과정에서 기저 빙상 흐름 방향의 재구성이 일어났음이 확인되었다. 이 지역의 마지막 최대 빙하기 동안 서남극 빙상은 대륙붕 가장자리까지 전진하였는데, 얕은 중부−외부 대륙붕 지역에는 아이스 돔이 자리하고 있었고 깊은 트러프 지역에는 빙하가 흐르고 있었다. 중부−외부 대륙붕을 가로지르는 트러프가 없는 상황에서 외해쪽으로 향하던 빙하의 흐름은 아이스 돔에 의해 가로막히고 동쪽으로 휘어지게 되었다. 해빙이 시작되면서 아이스 돔이 작아지고 서남극 빙상의 기저선은 깊은 트러프를 따라 내부 대륙붕 쪽으로 밀려났다. 외부 대륙붕에서 아이스 돔의 축소와 붕괴는 결국 빙하 흐름에서 큰 규모의 변화를 일으키게 되었고 서남극 빙상은 대륙붕을 가로질러 북쪽으로 다시 전진하게 되었다. 리글리 만의 해빙 모델은 적절한 지형적 조건 하에서 해빙 과정 중에 빙하 흐름의 변화가 일어날 수 있음을 보여준다.

Ice flow reorganization during deglaciation inferred from glacial morphological features mapped in Wrigley Gulf, western Amundsen Sea shelf (West Antarctica)

Jae Il Lee

Korea Polar Research Institute

Abstract: Knowledge of the response of marine-based ice sheets during times of climatic warming, such as the last deglaciation, provides important information to understand ice sheet behaviour to external forcing. We used swath bathymetric and acoustic sub-bottom profiler data from Wrigley Gulf on the western Amundsen Sea shelf, West Antarctica, to identify glacial features and reconstruct the changes in the behaviour of the West Antarctic Ice Sheet (WAIS) since the last glaciation. During the local Last Glacial Maximum, the WAIS extended to the shelf edge of Wrigley Gulf. The middle-outer continental shelf was occupied by an ice dome that deflected ice streams draining the WAIS around and converging north of Dean Island eastwards. With the onset of deglaciation, the ice dome retreated onto the outer shelf and the WAIS grounding line retreated further onto the inner shelf via deep trough. The waning of the ice dome steered a large-scale reorganization of the ice flow pattern, with the WAIS re-advancing seaward across the continental shelf. The widespread advance and subsequent retreat of the ice streams draining the WAIS is evidenced by the common occurrence of mega-scale glacial lineations and grounding zone wedges on the middle-inner shelf. This deglaciation model implies that ice flow switching and ice re-advance can occur during deglaciation given appropriate topographic condition.

KOPRI 극지연구소

참고 문헌

Anandakrishnan, S., Blankenship, D. D., Alley, R. B., & Stoffa, P. L. (1998). Influence of subglacial geology on the position of a West Antarctic ice stream from seismic observations. Nature, 394, 62-65.

Anderson, J. (2013). Processed Multibeam Sonar Data (version 2) from the Ross Sea, Amundsen Sea, Bellinghausen Sea, and Antarctic Peninsula acquired during Nathaniel B. Palmer expedition NBP9902 (1999). IEDA. doi:10.1594/IEDA/100355.

Anderson, J. B., Wellner, J. S., Lowe, A. L., Mosola, A. B., & Shipp, S. S. (2001). Footprint of the expanded West Antarctic Ice Sheet: ice stream history and behavior. GSA Today, 11(10), 4-9.

Anderson, J. B., Shipp, S. S., Lower, A. L., Wellner, J. S., and Mosola, A. B. (2002). The Antarctic Ice Sheet during the Last Glacial Maximum and its subsequent retreat history: a review. Quaternary Science Reviews, 21, 49-70.

Arndt, J. E., Schenke, H. W., Jakobsson, M., Nitsche, F. O., Buys, G. et al. (2013). The international bathymetric chart of the Southern Ocean (IBCSO) version 1.0 - a new bathymetric compilation covering circum-Antarctic waters. Geophysical Research Letters, 40, 3111-3117.

Batchelor, C. L. & Dowdeswell, J. A. (2015). Ice-sheet grounding-zone wedges (GZWs) on high-latitude continental margins. Marine Geology, 363, 65-92.

Bell, T., Cooper, A. K., Solheim, A., Todd, B. J., Dowdeswell, J. A., Canals, M., Jakobsson, M., Dowdeswell, E. K., & Hogan, K. A. (2016). Glossary of glaciated continental margins and related geoscience methods. In: Dowdeswell, J. A., Canals, M., Jakobsson, M., Todd, B. J., Dowdeswell, E. K., & Hogan, K. A. (eds.) Atlas of Submarine Glacial Landforms: Modern, Quaternary and Ancient. Geological Society, London, Memoirs, 46, 555-574.

Bengtson, J. (2013). Processed Multibeam Sonar Data (version 1) from the Southern Pacific Ocean acquired during Nathaniel B. Palmer expedition NBP9909 (1999). IEDA. doi:10.1594/IEDA/100362.

Berkman, P. A., & Forman, S. L. (1996) Pre-bomb radiocarbon and the reservoir correction for calcareous marine species in the Southern Ocean. Geophysical Research Letters, 23, 363-366.

Clark, C. D. (1993). Mega-scale glacial lineations and cross-cutting ice-flow landforms. Earth Surface Processes and Landforms, 18 (1), 1-29.

Clark, P. U., Dyke, A. S., Shakun, J. D., Carlson, A. E., Clark, J., Wohlfarth, B., Mitrovica, J. X., Hostetler, S. W., & McCabe, A. M. (2009). The Last Glacial Maximum.

KOPRI 극지연구소

Science, 325, 710−714.

Cochran, J. R., Tinto, K. J., and Bell, R. E. (2020). Detailed bathymetry of the continental shelf beneath the Getz Ice Shelf, West Antarctica. Journal of Geosphysical Research: Earth Surface, 125, e2019JF005493. https://doi.org/ 10.1029/2019JF005493.

Domack, E., Amblas, D., Gilbert, R., Brachfeld, S., Camerlenghi, A., Rebesco, M., Canals, M., & Urgeles, R. (2006) Subglacial morphology and glacial evolution of the Palmer deep outlet system, Antarctic Peninsula. Geomorphology, 75, 125−142.

Dowdeswell, J. A., Ottesen, D., Evans, J., ? Cofaigh, C., & Anderson, J. B. (2008). Submarine glacial landforms and rates of ice−stream collapse. Geology, 36, 819−822.

Graham, A. G. C., Larter, R. D., Gohl, K., Hillenbrand, C.−D., Smith, J. A., & Kuhn, G. (2009) Bedform signature of a West Antarctic palaeo−ice stream reveals a multi−temporal record of flow and substrate control. Quaternary Science Reviews, 28 (25), 2774−2793.

Graham, A. G. C., W?hlin, A., Hogan, K. A., Nitsche, F. O., Heywood, K. J., Totten, R. L., Smith, J. A., Hillenbrand, C.−D., Simkins, L. M., Anderson, J. B., Wellner, J. S., & Larter, R. D. (2022) Rapid retreat of Thwaites Glacier in the pre−satellite era. Nature Geoscience, 15, 706−713.

Greenwood, S. L., Simkins, L. M., Halberstadt, A. R. W., Prothro, L. O., & Anderson, J. B. (2018). Holocene reconfiguration and readvance of the East Antarctic Ice Sheet. Nature Communications, 9, 3176, DOI: 10.1038/s41467−018−05625−3.

Halanych, K., (2016). Raw ship−based Multibeam Sonar Data from the Southern Ocean acquired during R/V Nathaniel B. Palmer expedition NBP1210 (2013). IEDA. doi:10.1594/IEDA/320750.

Hillenbrand, C.−D., Kuhn, G., Smith, J. A., Gohl, K., Graham, A. G. C., Larter, R. D., Klages, J. P., Downey, R., Moreton, S. G., Forwick, M., & Vaughan, D. G. (2013) Grounding−line retreat of the West Antarctic Ice Sheet from inner Pine Island Bay. Geology, 41, 35−38.

Jacobs, S., (2013). Processed Multibeam Sonar Data (version 2) from the Amundsen Sea and Ross Sea acquired during Nathaniel B. Palmer expedition NBP0001. IEDA. doi:10.1594/IEDA/100296.

Kingslake, J., Scherer, R. P., Albrecht, T., Coenen, J., Powell, R. D., Reese, R., Stansell, N. D., Tulaczyk, S., Wearing, M. G., & Whitehouse, P. L. (2018). Extentive retreat and re−advance of the West Antarctic Ice Sheet during the Holocene. Nature, 558, 430−434.

Klages, J. P., Kuhn, G., Hillenbrand, C. D., Graham, A. G. C., Smith, J. A., Larter, R. D., Gohl, K., & Wacker, L. (2014) Retreat of the West Antarctic Ice Sheet from the western Amundsen Sea shelf at a pre− or early LGM stage. Quaternary Science

Reviews, 91, 1-15.

Klages, J. P., Kuhn, G., Hillenbrand, C.-D., Graham, A. G. C., Smith, J. A., Larter, R. D., & Gohl, K. (2016). A glacial landform assemblage from an inter-ice stream setting in the eastern Amundsen Sea Embayment, West Antarctica. In: Dowdeswell, J. A., Canals, M., Jakobsson, M., Todd, B. J., Dowdeswell, E. K., & Hogan, K. A. (eds.) Atlas of Submarine Glacial Landforms: Modern, Quaternary and Ancient. Geological Society, London, Memoirs, 46, 349-352.

Larter, R. D., Graham, A. G. C., Gohl, K., Kuhn, G., Hillenbrad, C.-D., Smith, J. A., Deen, T. J., Livermore, R. A., & Schenke, H.-W. (2009) Subglacial bedforms reveal complex basal regime in a zone of paleo-ice stream convergence, Amundsen Sea embayment, West Antarctica. Geology, 37 (5), 411-414.

Lavoie, C., Domack, E. W., Pettit, E. C., Scambos, T. A., Larter, R. D., Schenke, H. W., Yoo, K. C., Gutt, J., Wellner, J., Canals, M., Anderson, J. B., & Amblas, D. (2015) Configuration of the Northern Antarctic Peninsula Ice Sheet at LGM based on a new synthesis of seabed imagery. The Cryosphere, 9, 613-629.

Leventer, A., Domack, E., Dunbar, R., Pike, J., Stickley, C. E., Maddison, E., Brachfeld, S., Manley, P. L., & McClennen, C. E. (2006) Marine sediment record from the East Antarctic margin reveals dynamics of ice sheet recession. GSA Today, 16(12), 4-10.

McGillicuddy, D. (2016). Raw ship-based Multibeam Sonar Data from the Ross Sea acquired during R/V Nathaniel B. Palmer expedition NBP1201 (2011). IEDA. doi:10.1594/IEDA/319324.

Millan, R., St?Laurent, P., Rignot, E., Morlighem, M., Mouginot, J., & Scheuchl, B. (2020). Constraining an ocean model under Getz Ice Shelf, Antarctica, using a gravity?derived bathymetry. Geophysical Research Letters, 47, e2019GL086522. https://doi.org/10.1029/2019GL086522.

Nitsche, F. O., Jacobs, S. S., Larter, R. D., & Gohl, K. (2007). Bathymetry of the Amundsen Sea continental shelf: Implications for geology, oceanography, and glaciology. Geochemistry Geophysics Geosystems, 8, Q10009, doi:10.1029/2007GC001694.

Nitsche, F.O. (2013). Processed Multibeam Sonar Data (version 2) from the Amundsen Sea acquired during Nathaniel B. Palmer expedition NBP0702 (2007). IEDA. doi:10.1594/IEDA/100372.

Cofaigh, C., Dowdeswell, J. A., Allen, C. S., Hiemstra, J. F., Pudsey, C. J., Evans, J., & Evans, D. J. A. (2005). Flow dynamics and till genesis associated with a marine-based Antarctic palaeo-ice stream. Quaternary Science Reviews, 24, 709-740.

Cofaigh, C., Evans, D. J. A., & Smith, I. R. (2010) Large-scale reorganization and sedimentation of terrestrial ice streams during late Wisconsinan Laurentide Ice Sheet deglaciation. GSA Bulletin, 122, 743-756.

KOPRI 극지연구소

Rignot, E. & Mouginot, J. B. S. (2016). MEaSUREs Antarctic Grounding Line from Differential Satellite Radar Interferometry, Version 2 (NASA National Snow and Ice Data Center Distributed Active Archive Center, Boulder, Colorado, USA) https://doi.org/10.5067/IKBWW4RYHF1Q.

Rignot, E., Mouginot, J., & Scheuchl, B. (2017). MEaSUREs InSAR-Based Antarctica Ice Velocity Map, Version 2. Boulder, Colorado USA. NASA National Snow and Ice Data Center Distributed Active Archive Center. doi: https://doi.org/10.5067/D7GK8F5J8M8R.

Selley, H. L., Hogg, A. E., Cornford, S., Dutrieux, P., Shepherd, A., Wuite, J., Floricioiu, D., Kusk, A., Nagler, T., Gilbert, L., Slater, T., & Kim, T.-W. (2021). Widespread increase in dynamic imbalance in the Getz region of Antarctica from 1994 to 2018. Nature Communications, 12:1133, https://doi.org/10.1038/s41467-021-21321-1.

Simkins, L. M., Greenwood, S. L., & Anderson, J. B. (2018). Diagnosing ice sheet grounding line stability from landform morphology. The Cryosphere, 12 (8), 2707-2726.

Stokes, C. R., Clark, C. D., & Storrar, R. (2009). Major changes in ice stream dynamics during deglaciation of the north-western margin of the Laurentide Ice Sheet. Quaternary Science Reviews, 28, 721-738.

Stuiver, M. & Reimer, P. J. (1993). Extended 14C data base and revised CALIB 3.0 14C age calibration program. Radiocarbon, 35, 215-260.

Wellner, J. S., Lowe, A. L., Shipp, S. S., & Anderson, J. B. (2001). Distribution of glacial geomorphic features on the Antarctic continental shelf and correlation with substrate: implications for ice behaviour. Journal of Glaciology, 47, 397-411.

Winkelmann, D., Jokat, W., Jensen, L., & Schenke, H.-W. (2010). Submarine end moraines on the continental shelf off NE Greenland - Implications for Lateglacial dynamics. Quaternary Science Reviews, 29 (9), 1069-1077.

KOPRI 극지연구소

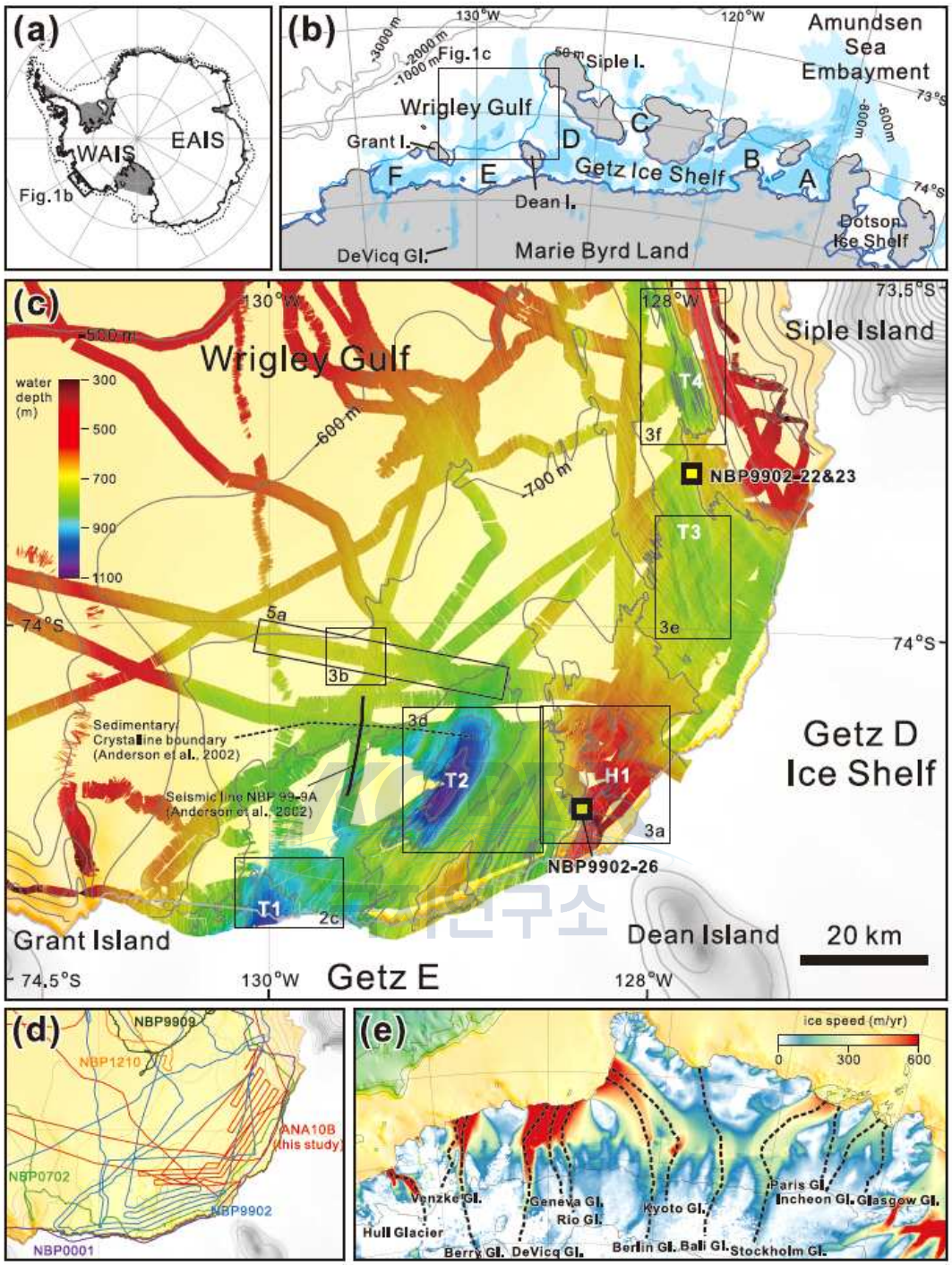


그림 1. 연구지역 지도 (a) 남극 내 연구지역의 위치. WAIS = 서남극빙상 (West Antarctic Ice Sheet), EAIS = 동남극빙상 (East Antarctic Ice Sheet); (b) 게츠 빙붕 지역과 빙붕 아래 수심 (Millan et al., 2020)과 대륙붕 수심 (Arndt et al., 2013), 현재 빙하기저선 (파란 선; Rignot et al., 2016); (c) 멀티빔 수심; (d) 아라온 연구항차 ANA10B 및 파머 연구항차 NBP9902 (Anderson, 2013), NBP9909 (Bengtson, 2013), NBP0001 (Jacobs, 2013), NBP0702 (Nitsche, 2013), NBP 1210 (Halanych, 2016)의 측선; (e) 게츠 빙붕 주변의 빙하들 (Selley et al., 2021)과 현재 빙붕 이동 속도 (Rignot et al., 2017). Getz D와 E 빙붕 명칭은 Hillenbrand 외 (2013)을 따랐으며 (c)의 NBP 위치는 방사성탄소 연대측정 결과가 있는 코어 위치(Anderson et al., 2002)를 지시한다.

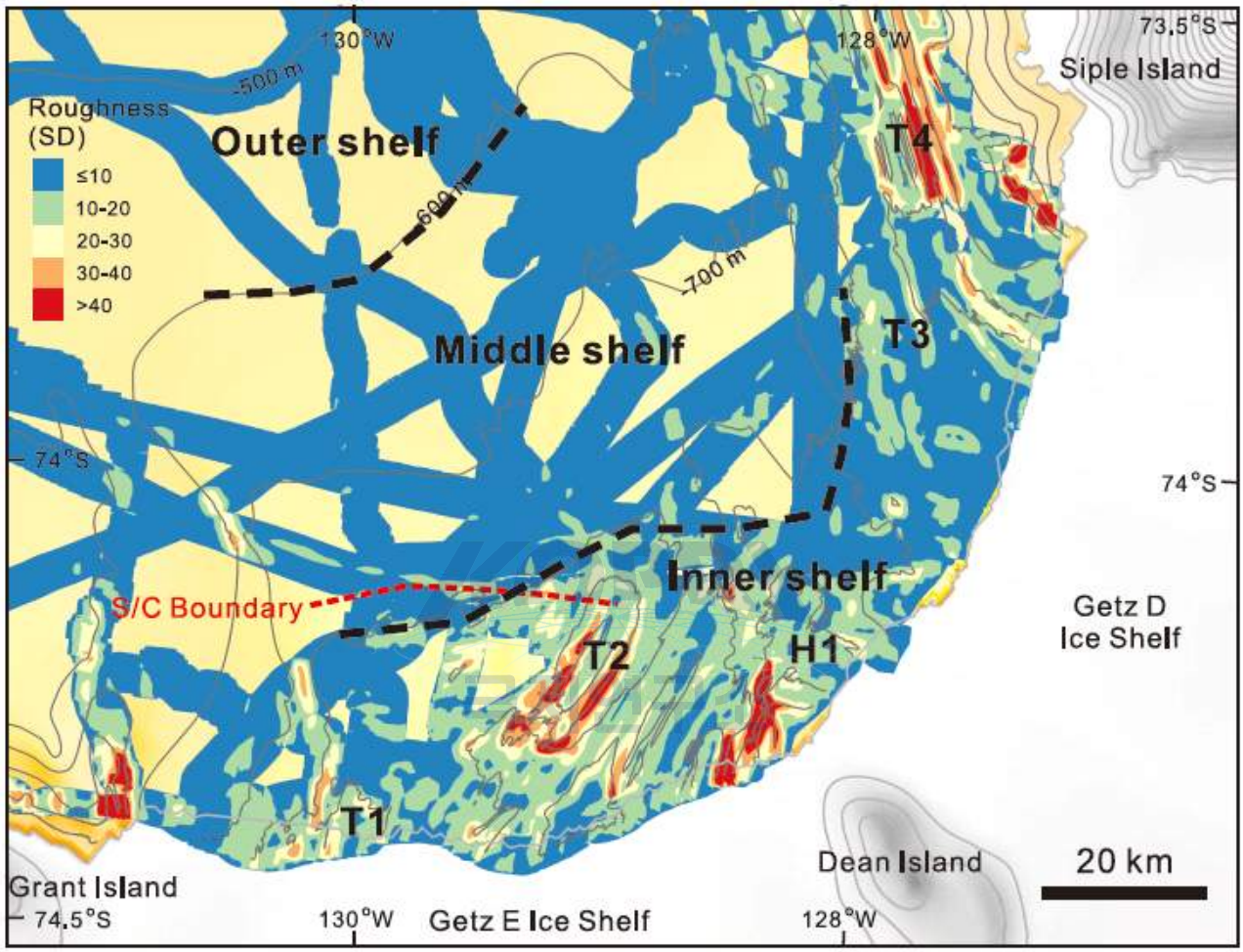


그림 2. 20-m 그리드 100x100 단위의 표준편차 (SD)로부터 계산한 리글리만의 지형 기복. S/C Boundary는 Anderson et al. (2002)의 퇴적물/결정질암 경계를 지시한다.

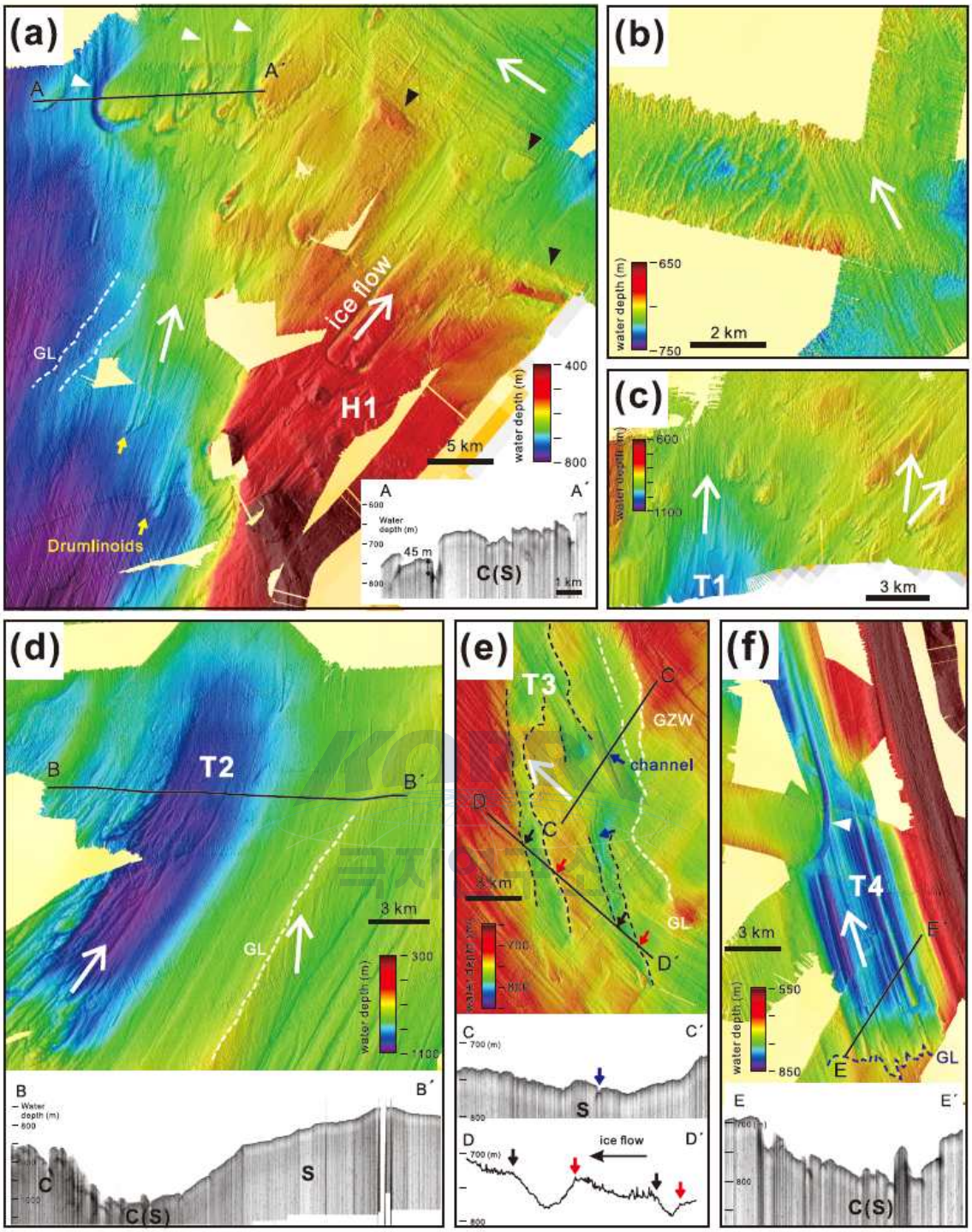


그림 3. 리글리 만의 멀티빔 수심 이미지와 SBP 이미지들. 위치는 그림 1에 표시되어 있다. 하얀 화살표는 과거의 빙하 흐름 방향을 지시한다. (a) H1 지역의 드럼린과 그루브들이 다른 방향을 보이는 빙하 선구조의 아래에 발달한다. (b) 서부 대륙붕에 나타나는 가로 방향 능선들이 빙하 선구조에 의해 덮여 있다. (c) 서쪽 대륙붕 내부의 드럼린 류의 빙하지형과 T1의 빙하 선구조는 북쪽 방향으로 빙하 흐름이 있었음을 지시한다. T1의 동쪽에서는 북동 방향의 빙하 흐름이 북쪽 방향의 흐름보다 먼저 있었음을 알 수 있다. (d) T2 지역의 드럼린 류와 빙하 선구조들은 북동 방향의 빙하 흐름을, 그 동쪽의 퇴적층 위에 발달한 빙하 선구조는 북쪽 방향의 빙하 흐름을 지시한다. (e) T3 지역의 대규모 빙하 선구조, GZW, 채널 구조. (f) T4 지역의 그루브-능선 구조.

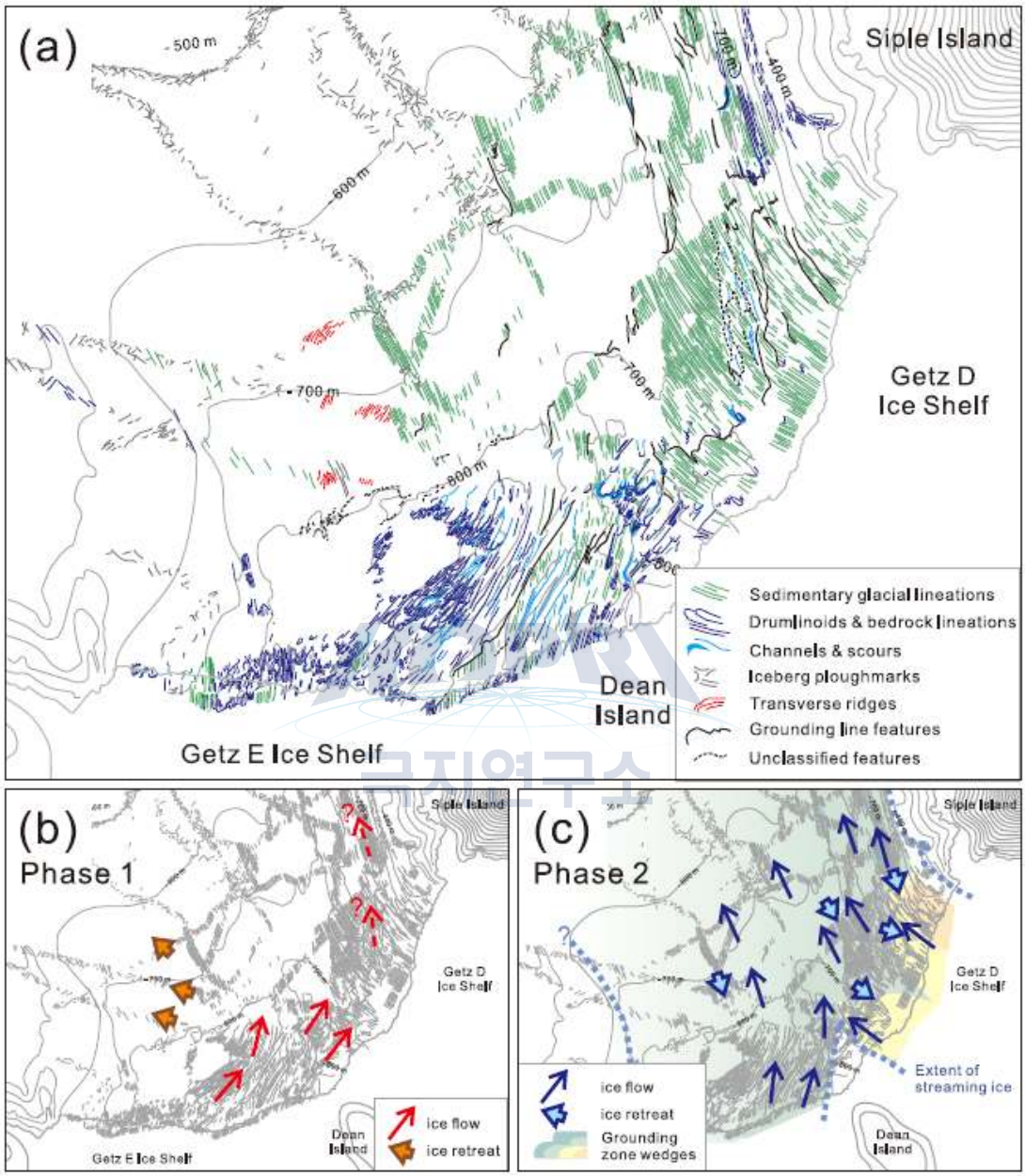


그림 4. 리글리만 해저 지형 분포. (a) 빙하 지형 해석 지도. (b) 빙하 1기 동안의 빙하 흐름과 후퇴 방향. (c) 빙하 2기 동안의 빙하 흐름과 후퇴 방향.

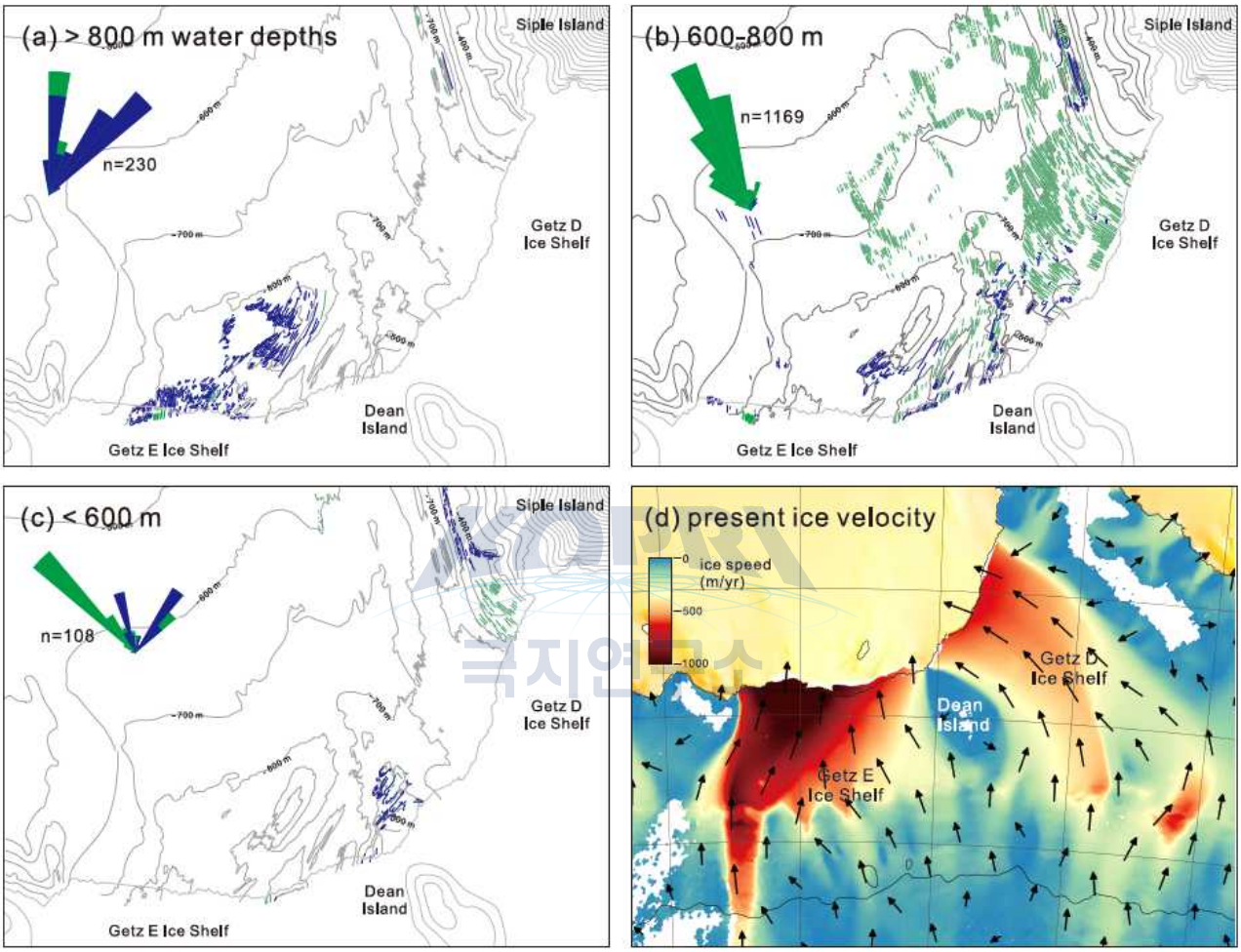


그림 5. (a-c) 수심별 과거 빙하 흐름 방향. 파란색은 드럼린류 및 기반암에 발달한 선구조를, 녹색은 퇴적물 위에 발달한 빙하 선구조를 지시한다. (d) 현재의 빙하 흐름 벡터 (Rignot et al., 2017).

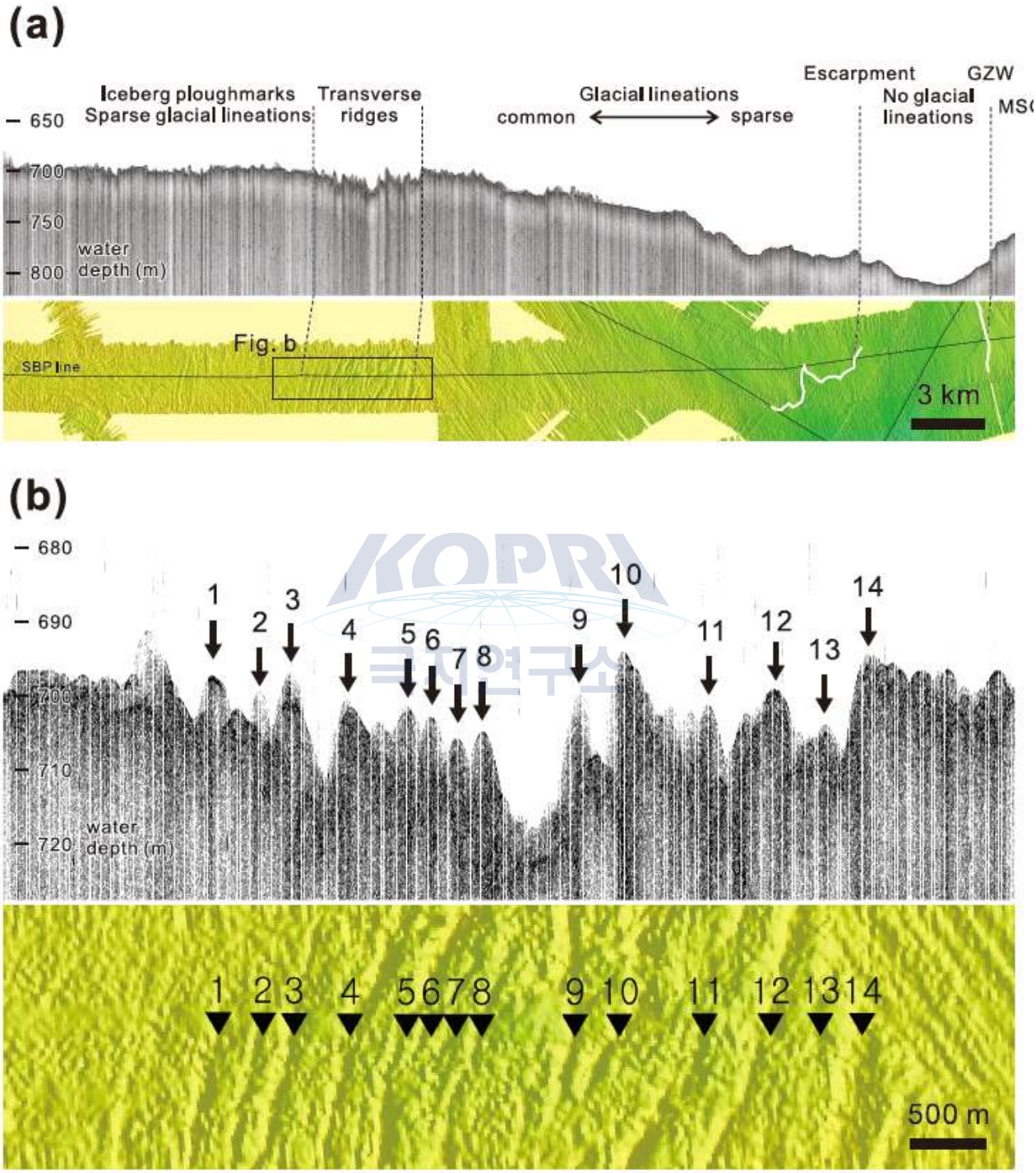


그림 6. 리글리 만 서쪽 대륙붕의 가로 방향 능선 구조의 SBP와 멀티빔 지형 이미지.

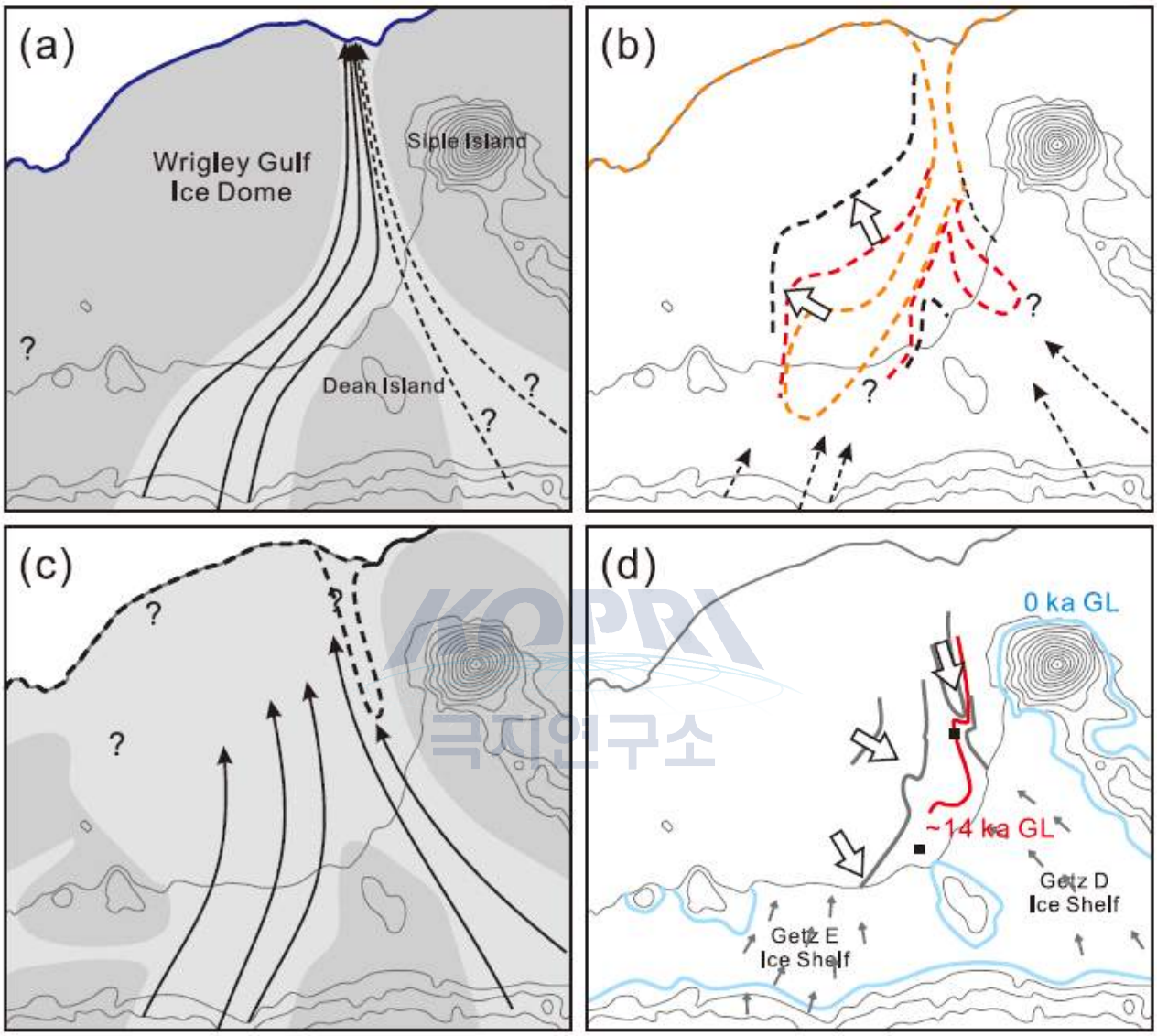


그림 7. 지난 빙하기 이후 리글리 만에서의 서남극 빙상의 해빙 모델. GL=빙하기저선. 두꺼운 실선/점선은 파악된/추정한 빙하기저선을 지시함. 화살표는 빙하 흐름 방향을 지시한다. 하얀 화살표는 빙하 후퇴 방향을 지시한다. 빙하 흐름이 있는 지역은 밝은 회색으로, 아이스 돔 지역은 암회색으로 표시하였다. (a) 이 지역의 최대 빙하기 (빙하 1기)의 빙상 최대 범위. (b) 초기 빙하 후퇴 및 두께 감소 시기. 서부 대륙붕에 빙하 후퇴 모레인 형성. (c) 리글리만 빙하 톰의 붕괴로 인한 빙하 흐름의 재구성 및 빙상의 전진 (빙하 2기). (d) GZW들의 위치로부터 추정한 빙하기저선의 후퇴. 검은 네모 표시는 탄산염 연대 측정이 실시된 NBP 9902 코어의 위치를 지시한다 (Anderson et al., 2002). 작은 화살표는 현재 빙붕의 빙하 흐름 방향을 지시한다 (Rignot et al., 2017).

제 12 장

Particle-size dependent magnetic properties of Scotia Sea sediments since the Last Glacial Maximum: Glacial ice-sheet discharge controlling magnetic proxies[3)]

Ji Young Shin[a,b], Sunghan Kim[b],*, Xiang Zhao[c], Kyu-Cheul Yoo[b], Yongjae Yu[d], Jae Il Lee[b], Min Kyung Lee[b], Ho Il Yoon[b]

[a]Korea Institute of Ocean Science and Technology, [b]Korea Polar Research Institute, [c]Australian National University, [d]Chungnam National University

ABSTRACT: The strong glacial-interglacial similarity between the magnetic susceptibility (MS) of Southern Ocean sediments and Antarctic ice core dust records has often been used to reconstruct Southern Hemisphere atmospheric variability. Although evaluation of various magnetic properties is essential for identifying the magnetic carriers linked to sedimentological variation, detailed magnetic studies are not sufficient in the Scotia Sea. Here we investigate the bulk and particle-size dependent magnetic properties of Scotia Sea sediments over the past ~22 kyr, to determine the main sediment transport mechanism driving bulk magnetic proxies including MS. In bulk sediments, MS is highest during the last glacial period and is accompanied by an increase in the concentration and grain size of ferrimagnetic and antiferromagnetic minerals. For magnetic mineral assemblages, coarse detrital magnetite is dominant. Of three particle-size fractions (> 63, 16-63, and <16 μm), the coarse silt fraction (16-63 μm) is responsible for the magnetic properties of bulk glacial sediments. Such dominant contribution of coarse silts rules out a major input of dust, which is expected as finer silt and clay. The silt fraction exhibits a co-varying magnetic mineral concentration with that of the sand fraction (> 63 μm) throughout the last deglaciation, indicating a close linkage between their input mechanisms. Thus, the sediment particles ranging from sand to coarse silt, which control the bulk glacial magnetic proxies, are most plausibly transported by iceberg-rafted debris (IRD). As hematite is relatively concentrated in the sand fraction, the hematite contribution in the bulk sediment can highlight IRD-related magnetic signals rather than magnetite. The bulk hematite contribution simultaneously varies with the deglacial influx

3) 이 연구 결과는 다음의 논문으로 출판되었음: Shin, J. Y. et al. (2020). "Particle-size dependent magnetic properties of Scotia Sea sediments since the Last Glacial Maximum: Glacial ice-sheet discharge controlling magnetic proxies." Palaeogeography, Palaeoclimatology, Palaeoecology 557: 109906.

of coarse IRD particles (> 1 mm) in Scotia Sea sediments, although their glacial inconsistency possibly suggests a different IRD input mechanism during the advancement and retreat of the ice sheet. Consequently, the glacial increase in the bulk magnetic concentration indicates vigorous iceberg calving activity in the Scotia Sea and further suggests the coupled cryosphere–atmosphere system.

1. Introduction

Terrigenous input to deep–sea sediment environments in the Southern Ocean relies on atmospheric and oceanic circulation patterns which are strongly influenced by climatic variability and Antarctic ice sheet dynamics. As a rapid and simple proxy of the terrigenous fraction, magnetic susceptibility (MS) of Southern Ocean sediments has revealed a close resemblance with Antarctic ice core dust records at the glacial–interglacial, or even, millennial scale (Bareille et al., 1994; Pugh et al., 2009; Weber et al., 2012). This strong resemblance plays a crucial role in relative age reconstruction of carbonate–poor Southern Ocean sediments (e.g., Weber et al., 2012). However, the MS–dust correlation, has not been fully understood in terms of transport mechanisms.

The Scotia Sea, located on the iceberg escape path from Antarctica and on the midway of dust transport from the known major source (Patagonia) to Antarctica (Delmonte et al., 2008), is very sensitive to paleoenvironmental change. MS of Scotia Sea sediments shows distinct glacial highs correlated to ice core dust records, and has been presumed as a proxy of Patagonian dust input (Weber et al., 2012). However, whether aeolian deposition is a major part of terrigenous fraction is a matter of debate, as it is expected to account for only a few percent of sediment accumulation during the last glacial period in the Scotia Sea (Walter et al., 2000; Noble et al., 2012). Apart from aeolian input, the Antarctic Circumpolar Current (ACC) has been suggested as the dominant sediment transporter delivering fine detritus during glacials, on a basis of clay mineralogy and isotopic composition (Diekmann et al., 2000, 2003; Noble et al., 2012; Xiao et al., 2016). On the other hand, Kim et al. (2018b) recently proposed iceberg–rafted debris (IRD) as the main deliver of glacial detrital particles, showing the dominance of coarse sediment fraction (fine sand to coarse silt) from particle–size analysis. These arguments still call for a better understanding of MS through systematic and detailed magnetic study in the Scotia Sea (Weber et al., 2019).

The MS signal is mainly carried by ferrimagnetic minerals, such as magnetite (Mullins, 1977; Maher, 1986), and basically connected to sediment magnetic properties (e.g., concentration, grain size, and composition of magnetic minerals). Since the magnetic properties of bulk sediments are an aggregate of many different components and processes, an evaluation

of these components provides useful information on the bulk signals and sedimentary environments. For instance, Xiao et al. (2016) investigated bulk magnetic properties of Scotia Sea sediments and identified that detrital magnetite is the main magnetic component during glacials, whereas biogenic magnetite is significant during interglacials. With regard to low contribution of highcoercivity minerals, which commonly present in dust, they considered ocean-current transport of fine magnetic minerals as the main detrital input mechanism during glacials. However, detrital magnetic components complicatedly mixed by various processes (e.g., dust, current, and IRD) are not clearly discriminated in bulk magnetic properties in the Scotia Sea.

As an extended approach, magnetic measurements on particle-size fractions enable an isolation of magnetic property depending on particle-size distribution. As a result, the particle-size dependence of magnetic properties has been widely utilized to separate the influences of sediment transport and source in marine sediments (e.g., Razik et al., 2014, 2015; Hatfield et al., 2016, 2017, 2019). In this study, we adopt the particle-size separation approach to isolate detrital magnetic properties in Scotia Sea sediments since the last glacial maximum (LGM). By comparing bulk and particle-size dependent magnetic properties, we identify the major magnetic component and particle-size range carrying bulk signals, and determine the related sediment transport mechanism.

KOPRI 극지연구소

2. Core location and regional settings

An ~890 cm long gravity core GC03-C1 was recovered from the south Scotia Sea, off Elephant Island in the northern Antarctic Peninsula (60°26.57′S, 55°41.98′W; 3774-m water depth; Fig. 1) by R/V Yuzhmorgeologiya during the 2003/2004 Korea Antarctic Research Program expedition. The Scotia Sea is influenced by the input of waters from both the Drake Passage and the Weddell Sea, via the eastward-flowing ACC and northern limb of the Weddell Gyre, respectively (Fig. 1). Particularly, ACC is the dominant oceanic circulation in the Scotia Sea, responding to atmospheric changes, and it lies between the Polar Front and the southern ACC boundary (Anderson et al., 2009). In the Weddell Gyre, many icebergs merge and then escape from Antarctica north into the Scotia Sea along the major pathway named "Iceberg Alley" (Anderson and Andrews, 1999). In addition, the Southern Hemisphere westerlies dominate the atmospheric circulation of the Scotia Sea, delivering aeolian particles from southern Patagonia to proximal and far to distal regions in the Southern Ocean (Weber et al., 2012; Lamy et al., 2014). Thus, the Scotia Sea is sensitive to the terrigenous sediment supply via ocean currents, aeolian input, and ice rafting linked to climate change (Diekmann et al., 2000, 2003; Weber et al., 2014).

3. Analytical methods

3.1. Magnetic measurements and particle-size separation

The core was split into two halves at the Korea Polar Research Institute (KOPRI), and archive halves were used for magnetic measurements. Volume-specific MS (SI unit) data were previously reported by Bak et al. (2010), in which MS was scanned at 1 cm intervals for split half core sections. In this study, a total of 364 discrete samples for bulk sediment were taken with a nearly continuous ~2 cm span using 7 cm3 plastic cubes. All cube samples were measured for mass-specific MS (χ) at dual frequency of 470 Hz and 4700 Hz using a Bartington MS2 magnetometer at KOPRI. The mass normalization was calculated by wet masses; for wet samples, it should be noted that variance in χ can be somewhat different if dilution effect by the water mass is corrected. Hereafter χ in this paper refers to low frequency measurements (χ470Hz). Frequency dependence of MS (χfd%) was defined as 100×(χ470Hz − χ4700Hz) / χ470Hz (Dearing et al., 1996). Anhysteretic remanent magnetization (ARM) was imparted in a direct current (DC) field of 0.05 mT (=39.79 A/m) and a peak alternating field (AF) of 100 mT using a D-Tech D-2000 AF demagnetizer (ASC Scientific). The mass-normalized ARM susceptibility (χARM) was calculated by normalizing the remanence to the DC field. The isothermal remanent magnetization (IRM) was acquired at applied DC fields of 1 T using an ASC Scientific IM-10 impulse magnetizer and is represented as saturation IRM (SIRM). Backfield IRM (BIRM) at 0.3 T was imparted in the direction opposite to that of SIRM. All remanences were measured using a JR6A spinner magnetometer at Chungnam National University, Korea.

χ and SIRM commonly reflect the concentration of ferrimagnetic minerals, such as magnetite. Because χARM is sensitive to fine magnetite grains, χARM/χ was used as a grain size parameter (King et al., 1982). For the concentration of high-coercivity minerals such as hematite, hard IRM (HIRM) was calculated as follows: HIRM=0.5×(SIRM + BIRM). The relative composition of low- and high-coercivity minerals were estimated using S-ratios (Bloemendal et al., 1992): Sratio= 0.5×(1 − BIRM / SIRM). S-ratios close to 1 denote the dominance of low-coercivity minerals.

A total of 32 selected samples were freeze-dried, and hysteresis curves were measured using a Princeton Measurements MicroMag 3900 vibrating sample magnetometer at the Korea Institute of Geoscience and Mineral Resources. From the hysteresis data, the bulk coercive force (Bc), saturation magnetization (Ms), and saturation remanence (Mrs) were obtained by a saturating field of 1 T with field increments of 5 mT. Paramagnetic contribution was

KOPRI 극지연구소

corrected using high-field slope at ≥80% of the peak field. The remanent coercive force (Bcr) values were determined from backfield measurements with a decreasing field step of 4 mT. For the magnetic mineralogy and assemblages, IRM acquisition curves and first-order reversal curves (FORCs) were measured for 18 selected samples. The IRM acquisition curves were obtained up to a DC field of 1.4 T with 120 nonlinear field steps and were fitted by modeled coercivity spectra using an IRM unmixing program from Maxbauer et al. (2016). 134 FORCs were obtained with a field increment of 2 mT up to a maximum applied field of 1 T and were processed in the FORCinel software package (Harrison and Feinberg, 2008) using the VARIFORC built-in function designed by Egli (2013).

In addition, 100 bulk sediment samples were collected from the top 400 cm at 4 cm intervals with a 1 cm span for particle-size separation. The sediments were pretreated with 6% hydrogen peroxide, 0.1M hydrochloric acid, and 1 N sodium hydroxide to remove the non-terrigenous fractions (organic matter, carbonate, and biogenic opal, respectively). Some tested samples revealed no significant magnetization loss after such chemical treatments. This is consistent with previous studies that documented no physical or chemical alteration in magnetic mineral samples by weak to middle (e.g., pH~4) acids (e.g., Hounslow and Maher, 1996; Maher et al., 2003; Strehlau et al., 2014). Based on previous analyses for particle-size distribution in the study area (e.g., Kim et al., 2018b), three main fractions were separated by wet sieving at 63 μm and based on settling velocity: clay to fine silt (< 16 μm), medium to coarse silt (16-63 μm), and sand (> 63 μm). After weighing the dry mass of each fraction to calculate their fractional abundance (wt %), 300 samples (100 samples per fraction) were prepared for magnetic measurements. The sediment fractions were placed into gel capsules through compression to avoid grain rotation and then centered and fixated into 7 cm^3 cubes. The cube samples were subjected to χ measurements using a Kappabridge KLY-2 instrument at 920 Hz and field intensity of 300 A/m. Then, the same magnetic parameters with the bulk cube samples (e.g., ARM and IRM) were obtained. In addition, hysteresis curves and FORCs were measured for some selected samples.

3.2. Radiocarbon dating

Accelerator mass spectrometry (AMS) 14C dates were measured at Rafter Radiocarbon Laboratory, New Zealand (Table 1). Because of the lack of foraminifers or calcareous shell fragments in the sediments, all AMS 14C dating was conducted on acid insoluble organic matter (AIOM) from core GC03-C1. To correct for the core top loss, AIOM AMS 14C dating was additionally conducted from 0 cm of a box core (BC03-C1) from the same location of GC03-C1 (Table 1).

4. Age model

An age model for core GC03-C1 was established by combination of the AIOM AMS 14C dates and correlations among Scotia Sea MS records and the ice core dust record (Fig. 2). For 14C age correction, the possible core top loss of GC03-C1 was estimated by comparing total carbon (TC), total nitrogen (TN), and water content (WC) between BC03-C1 and the top 100 cm of GC03-C1 (Fig. S1). Analytical procedures for TC, TN, and WC followed the common protocol in KOPRI (e.g., Kim et al., 2018a). Based on their inconsistent variations, a length of at least the box core, 32 cm, was thought to be lost during the coring process. As previous studies considered corrected 14C dates after offsetting the surface AMS 14C dates of AIOM, assuming that the old carbon effect was constant with depth (e.g., Domack et al., 1999; Lee et al., 2010), we corrected the AIOM ages of this study using the box core BC03-C1 top 14C age of 4037 yr. This is older than the reservoir age (1300 years) used for the Scotia Sea (e.g., Xiao et al., 2016), indicating that the AIOM ages are influenced by old carbon effect. After offsetting 4037 yr, we obtained calibrated 14C dates of GC03-C1 using CALIB 7.1 software (Stuiver and Reimer, 1993) and the MARINE13 dataset (Reimer et al., 2013) with a standard global reservoir age ($\Delta R=0$), following an approach of Lee et al. (2010) (Table 1). The relatively narrow δ13C range (±0.8□ standard deviation) suggests that the assumption is generally acceptable. Of the calibrated 14C ages, six age points within the deviation range were used to construct the age model for the top 200 cm of GC03- C1 (Table 1 and Fig. 2c, d). The 14C ages below 240 cm were considered as less reliable and disregarded in the age model, because of old carbon effect in the glacial interval (e.g., Kim et al., 2018b).

In the Scotia Sea, the resemblance between MS records and dust record (non-sea-salt Ca2+; nssCa2+) from European Project for Ice Coring in Antarctica Dronning Maud Land (EDML) was used to constrain the age of the Scotia Sea sediment cores (Fischer et al., 2007; Weber et al., 2012). The MS-EDML correlation is particularly useful for the high MS intervals of Scotia Sea cores e.g., Pugh et al., 2009; Weber et al., 2012; Xiao et al., 2016; Kim et al., 2018b). Following the age correlation established by Weber et al. (2012), we assigned seven tie points on volume MS of GC03-C1 (Bak et al., 2010), based on similar peaks and troughs in Scotia Sea MS records (cores MD07-3133 and MD07-3134; Fig. 1) and EDML dust record (Fig. 2 and Table 1). The core top and bottom ages of GC03-C1 were calculated as ~8.5 and ~22.1 ka, respectively, using extrapolation.

5. Results

5.1. Bulk magnetic properties

For the period ~22–8 ka, χ of GC03–C1 exhibits higher values during the LGM and lower values during the early Holocene (Fig. 3a). Water contents show a general opposite trend to χ, varying from ~50% at the upper part to ~30% at the lower part of the core (Table S1). Although correction for the water masses can increase χ values by a factor of ~2 to ~1.7, such dilution effect is not considered to be a critical factor because the trend of χ is analogous. χfd% is generally below 2%, showing relatively low values during the LGM (Fig. 3b). This indicates that contribution of ultrafine superparamagnetic particles is not significant (Dearing et al., 1996), particularly for the glacial increase of χ.

Comparison between χ and other concentration–related magnetic parameters (Ms, SIRM, HIRM, and χARM) shows their consistent temporal variations (Fig. 3), supporting that concentration of magnetic minerals dominate changes in these parameters. Hysteresis loops were closed and Ms was obtained in applied fields between ~350 mT during the LGM and ~270 mT during the early Holocene, indicating the dominance of ferrimagnetic minerals (e.g., magnetite, titanomagnetite, and maghemite). Hence, strong similarity among χ, Ms, and SIRM variations designates ferrimagnetic minerals as the dominant magnetic carrier of χ (Fig. 3a, c, d), although χ includes non–ferrimagnetic (i.e., diamagnetic and paramagnetic) signals. HIRM also varies with SIRM (Fig. 3d, e), indicating that both low– and high–coercivity minerals (e.g., magnetite and hematite, respectively) are closely related to the glacial increase in magnetic concentration. In particular, HIRM shows more distinct fluctuations than in SIRM during the marine isotope stage (MIS) 2, indicating relatively sensitive changes in high–coercivity mineral concentration during the glacial period. Meanwhile, χARM resembles overall glacial–interglacial variations of the other parameters, showing large fluctuations during MIS 1 (Fig. 3f). This implies that fine magnetite concentration varies along with total magnetic concentration and more sensitively changes during the interglacial period. In addition, SIRM, HIRM, and χARM display a common peak at 18.4 ka, which is inconspicuous in χ, indicating a layer of abundant ferrimagnetic minerals.

Generally, low values of the coercivity parameters Bc and Bcr (~8–12 and ~32–36 mT, respectively) suggest that magnetite is the main magnetic carrier (Fig. 4a, d). In particular, low Bc values of ~9 mT during the LGM indicate the dominance of low–coercivity coarse magnetite, such as multidomain (MD) magnetite (Maher, 1988). Other magnetic grain size parameters (Mrs/Ms and χARM/χ) also show similar variations with Bc, indicating that coarser magnetite is dominated during the LGM (Fig. 4b, c). On the other hand, Bcr shows analogous variations with S–ratio (Fig. 4d, e), as Bcr is more sensitive to highcoercivity components than Bc in magnetic mixtures (Roberts et al., 1995). The S–ratios close to 1 (~0.97–0.99) throughout the core indicate the generally low contribution of

high-coercivity minerals (e.g., hematite). However, relatively low S-ratios during MIS 2 indicate their greater contribution during the glacial period. There are some Bcr peaks to ~40 mT concurrent with the S-ratio troughs during MIS 2 (e.g., ~15.9 ka, ~18.4 ka, and ~20.5 ka), supporting the presence of highcoercivity minerals (Fig. 4d, e).

The average magnetite grain size distribution (i.e., hysteresis ratios) for the selected samples is compared with empirical and theoretical data in a Day plot (Day et al., 1977; Fig. 5a). All the samples fall close to the theoretical mixing curves of single-domain (SD) and MD, with relative dominance of MD (Carter-Stiglitz et al., 2001; Dunlop and Carter-Stiglitz, 2006). Compared with empirical data of (unannealed) magnetite (Dunlop, 2002), the average grain size of our samples corresponds to a range from ~9 to>20 μm, with grain size coarsening for the glacial samples. To further identify magnetic mineral assemblages, FORC diagrams were constructed (Fig. 5b). Along with the coarse average grain size, the interglacial sample (~10.2 ka) shows a large triangular vertical spread at low coercivity, indicating the dominance of vortex state detrital magnetite (Roberts et al., 2014, 2017). A typical narrow central ridge along the Bc axis characterizes the presence of non-interacting bacterial SD magnetite (Egli et al., 2010). Meanwhile, the glacial sample (~19.6 ka) is characterized by a stronger vertical spread at low coercivity (Bc <20 mT), which confirms the greater contribution of coarser vortex/MD magnetite during the LGM. For the glacial sample, a high-coercivity component extends beyond 100 mT along the Bu axis. From the IRM unmixing results, the high-coercivity component has a mean coercivity of 201-212 mT (cp3, Fig. 5c), consistent with the coercivity range of hematite (Hyland et al., 2015). The hematite contribution is relatively low (~6-12% of SIRM) but is greater in the glacial sample. In addition, two low-coercivity components (cp1 and cp2) are considered as magnetites of different coercivities (Egli, 2003).

In summary, the magnetic mineral concentration of GC03-C1 is high during the glacial period and low during the interglacial period. The dominant magnetic component is magnetite, showing coarser magnetic grain size during the glacial period. For magnetic mineral assemblages, coarse vortex/MD state detrital magnetite is dominant during the glacial period. During the interglacial period, the contribution of non-interacting biogenic SD magnetite is relatively significant, along with the dominance of vortex detrital magnetite. The hematite contribution is generally low, but relatively high during the glacial period.

5.2. Magnetic concentration of particle-size fractions

For the last ~18 kyr, concentration-related magnetic parameters (χ, Ms, SIRM, χ ARM, and HIRM) for each sized fraction were obtained and compared with their respective bulk values (Fig. 6). The magnetic parameters were calculated as mass-normalized values

(Figs. 6b–f), and then mass–weighted (Figs. 6g–k) by multiplying each fractional mass percent (Fig. 6a) on the mass–normalized values. The mass–normalized values indicate magnetic mineral enrichment in the fractions, while the mass–weighted values reconstruct the fractional contribution to the bulk values, as magnetic concentration properties are linearly additive (e.g., Lascu et al., 2010; Hatfield et al., 2019). The fractional mass distribution shows that the 16–63 μm fraction is predominant (50–70%) (Fig. 6a). Noticeably, the 16–63 μm and > 63 μm relative abundances becomes greater during MIS 2 than during MIS 1, confirming the coarsening of average particle size during the glacial period.

The most abundant fraction, 16–63 μm, generally shows the highest mass–normalized χ values throughout the last ~18 ka (Fig. 6a, b) and, thus, makes the greatest contribution to bulk χ. This is confirmed by the almost identical variations between mass–weighted χ of the 16–63 μm fraction and bulk χ (Fig. 6g). Ms values (after paramagnetic correction) for the three fractions show similar variations with χ (Fig. 6b, c), confirming that the χ variation is mainly controlled by the magnetite concentration. The highest Ms of the 16–63 μm fraction during the glacial period indicates that magnetite is the most–enriched in silts (Fig. 6h), regardless of magnetic grain size (Day et al., 1977; Dunlop, 1986).

Mass–normalized SIRM of each fraction also shows similar temporal variations with χ (Fig. 6b, d); however, the SIRM signals are not the highest for the 16–63 μm fraction. As SIRM is affected by magnetic grain size, coarse magnetites in 16–63 μm can be less respondent to SIRM than χ, owing to their weak magnetic remanence (Maher, 1988). Nevertheless, the strongest SIRM values in the>63 μm fraction during MIS 2 indicates glacial magnetic mineral enrichment with strong magnetic remanence. In particular, SIRM of the three particle–size fractions is comparable throughout the last deglaciation (Fig. 6d), clearly indicating that most of the magnetic minerals are closely linked to the same input mechanism. Owing to its fractional abundance, the 16–63 μm fraction dominantly contributes to bulk SIRM (Fig. 6i).

As χARM is mainly carried by fine magnetite, the finest grain size fraction (< 16 μm) has the highest values (Fig. 6e). The<16 μm fraction consistently shows the highest χARM with severe fluctuation throughout the last ~18 kyr, while the two coarser fractions show similar χARM variations with SIRM (Fig. 6e). The different temporal variations of the<16 μm fraction can be affected by different magnetic sources (e.g., biogenic magnetite) compared to the coarser fractions, particularly during MIS 1. Although bulk χARM is mainly contributed by the<16 μm fraction, the glacial increase of bulk χARM is associated with an increase in the contribution of the 16–63 μm fraction (Fig. 6j).

The highest HIRM values in the>63 μm fraction reveal that hematite is the most concentrated in the coarse sand fraction (Fig. 6f). The 16–63 μm fraction has markedly low HIRM (Fig. 6f) but dominantly contributes to bulk HIRM (Fig. 6k), owing to its high

fractional abundance. The HIRM variations between 16 and 63 μm and>63 μm are very similar during MIS 2 (Fig. 6f, k), indicating the same input source of hematite. Moreover, such HIRM variations are analogous to those of all other parameters (Figs. 6b–k), suggesting that the concentration of magnetite and hematite is mostly linked to the same input of sediment, ranging from sand to coarse silt.

5.3. Magnetic mineralogy and grain size of particle–size fractions

The bulk and size–fractionated samples were selected at ~17.7 ka and constructed FORC diagrams to confirm their magnetic assemblages (solid symbols in Fig. 7a). FORC diagrams of the bulk and 16–63 μm fraction resemble each other, showing the dominant feature of coarse vortex/MD magnetite (i.e., triangular–shaped contour with large vertical spread). The<16 and>63 μm fractions are dominated by finer vortex state magnetite. For the<16 μm fraction, the central ridge signal remains. This indicates a good preservation of biogenic magnetite during the glacial period, although its contribution is largely diluted in the bulk glacial samples (Figs. 7a and 5b). For>63 μm, the SD–like isolated peak with vortex magnetic feature ensures the presence of fine magnetic inclusions (Roberts et al., 2014, 2017). In addition, a large contribution of hematite with higher coercivity (> 100 mT) is distinctively observed in this fraction (Fig. 7a).

For each fraction, 11 samples were selected for hysteresis analyses, and their magnetic grain sizes were viewed on a Day plot (Fig. 7b). Note, the magnetic grain size is based on magnetic properties (i.e., domain state), which should not be confused with physical particle size (Hatfield et al., 2017). Hysteresis ratios of the<16 μm (blue symbols in Fig. 7b) and 16–63 μm (red symbols in Fig. 7b) fractions are well clustered and comparable to ratios of 3–6 μm and>14 μm magnetite grains, respectively (Dunlop, 2002). The<16 and 16–63 μm fractions also fall on the theoretical SD–MD mixing line (Carter–Stiglitz et al., 2001; Dunlop and Carter–Stiglitz, 2006), with greater MD contribution in the 16–63 μm fraction. Meanwhile, the>63 μm fraction displays a wide distribution of hysteresis ratios that fall between those of the<16 and 16–63 μm fractions (yellow symbols in Fig. 7b). The ratios are also dominantly distributed close to those of the<16 μm fraction, corresponding to 6–9 μm magnetite grains (Dunlop, 2002). This decoupling of physical and magnetic grain sizes indicates that magnetic minerals in the sand fraction are dominantly present as inclusions in other minerals, such as silicates (e.g., Feinberg et al., 2005; Chang et al., 2016), rather than as discrete magnetite grains.

Compared with bulk hysteresis ratios at the same ages (magenta symbols in Fig. 7b), the ratios of the 16–63 μm fraction show a large overlap with those of coarser glacial bulk samples. This indicates that the silt fraction is the predominant magnetic carrier during the

glacial period, which is also supported by the resemblance of FORC diagrams between the bulk sample and the 16–63 μm fraction (Fig. 7a). Hence, the coarsening of bulk magnetic grain size in the glacial period is resulted from the increased contribution of coarse vortex/MD magnetic minerals in silts.

6. Discussion

6.1. Comparison of Scotia Sea rock–magnetic properties with dust records

Long–range dust transport from Patagonia to East Antarctica during the Pleistocene is traced by a dust proxy (nssCa2+) from the EDML ice cores (e.g., Fischer et al., 2007, Fig. 8a). The glacial increase in Antarctic dust concentration indicates enhanced Patagonian dust production related to various factors, such as exposure of the source area and evolution of the southern westerly wind belt (Lamy et al., 2010; Lambert et al., 2012). As previously reported in the Scotia Sea, MS variations of core GC03–C1 and Scotia Sea cores (Weber et al., 2012; Xiao et al., 2016) are very similar to EDML nssCa2+ (Figs. 8a–d); volume MS records were used for comparison among cores. This visual resemblance between MS and Antarctic dust records seems to reflect the sink of Patagonian dust into the Scotia Sea and Antarctica (e.g., Weber et al., 2012). However, the particle–size range of 16–63 μm, suggested as the main contributor to the MS signal of GC03–C1, is coarser than fine aerosol particles of<10 μm which are generally expected to be long–range transported (Maher et al., 2010; Muhs, 2013).

As a proximal record of Patagonian dust from the source, MS of a sediment core from the PASADO site 2 at Laguna Potrok Aike in Patagonia (Lisé–Pronovost et al., 2015) is also compared. The lacustrine sediments reflect the deposition of short–term suspended dust particles of tens to hundreds of kilometers in the distance. Lisé–Pronovost et al. (2015) presented that the Patagonian lake sediments show glacial–interglacial MS variations covariant with the dust record of the Antarctic ice core (Fig. 8a, e), although there is an inconsistency in the millennial scale. They suggested that the glacial increase in the two records reflects a common response to the aeolian flux from the source area; the higher magnetic concentration is associated with the greater aeolian supply. The millennial inconsistency was suggested as grain size effect on MS, because the glacial high MS of the lake sediments is also correlated to higher coercivity of ferrimagnetic grains (i.e., increase in median destructive field of IRM; Fig. 8e), reflecting a fining of magnetic grain size due to weakening of the Southern Hemisphere westerly winds (Kohfeld et al., 2013; Lisé–Pronovost et al., 2015). For long–range transported dust to the Scotia Sea and Antarctica, the particle–size is independent

of the change in wind intensity (Muhs, 2013), but it should be generally smaller than the Patagonian lake sediments. Lisé-Pronovost et al. (2015) identified that medium and coarse silts (~10-30 μm) mainly carry the magnetic information of the lake sediments, suggesting that dust transport to the Scotia Sea would involve finer particles, such as fine silt and clay. This implies that glacial sediments of GC03-C1 are unlikely transported primarily by Patagonian dust, as the high magnetic concentration is mostly carried by medium to coarse silts (16-63 μm).

In the south Scotia Sea, the particle-size distribution with the dominance of medium to coarse silt in glacial sediment was consistently reported from four nearby cores (GC03-C2, GC03-C4, GC04-G03, and GC02-SS02; Fig. 1), based on particle-size analysis (Kim et al., 2018b). For magnetic grain size, LGM sediments of GC03-C1 dominated by coarse vortex/MD magnetite have similar hysteresis ratio distribution with the central Scotia Sea sediments (PS67/219-1 and PS67/197-1; Fig. 1) during glacials (Xiao et al., 2016; Fig. S2). This coarse magnetic grain size distribution of the glacial Scotia Sea sediments is also comparable with that of the Laguna Potrok Aike sediments (Lisé-Pronovost et al., 2015), which were deposited by short-term transport during the last glacial period (Fig. S2). Altogether, these results show general agreement in the coarse physical and magnetic grain size of the glacial sediments in the Scotia Sea and rule out dust input as the main sediment transport mechanism during the glacial period.

Interestingly, the<16 μm fraction of GC03-C1 has a very low hematite concentration (Figs. 6f and 7a), although it is expected to primarily contain the aeolian dust fraction. Rather, the hematite contribution in the glacial bulk sediments is associated with the coarser sand and silt fractions (Fig. 6k). Therefore, the bulk hematite concentration should not be considered as an indication of dust input, because of its low contribution in the Scotia Sea, although aeolian dust generally involves high-coercivity minerals such as hematite (e.g., Bloemendal et al., 1992; Xiao et al., 2016).

6.2. Contribution of biogenic magnetite in Scotia Sea sediments

Biogenic magnetite has been suggested as a dominant contributor to the MS signal in the sub-Antarctic Indian Ocean, where low detrital input occurs; it could be associated with iron fertilization caused by increased dust input during glacials (Yamazaki and Ikehara, 2012). However, the relative proportion of biogenic magnetite to detrital magnetite in bulk sediments of GC03-C1 decreases during the glacial period (Fig. 5b), as consistently shown in the central Scotia Sea sediments (Xiao et al., 2016). Although biogenic magnetite is not the main magnetic carrier during the glacial period, the glacial<16 μm sample displays a significant contribution of biogenic magnetite compared to the bulk sample largely diluted by coarse

detrital magnetite (Fig. 7a). The glacial increase in biogenic magnetite is not noticeable, but the presence of biogenic magnetite implies a suitable environment for its production and/or preservation during the glacial period.

6.3. Implications for possible sediment transport environments

The particle-size dependent magnetic properties of core GC03-C1 indicate that coarse sediments (sands and silts) are mainly transported by the same mechanism during the glacial period, with strong magnetic remanence in sands (Fig. 6d, f). The glacial dominance of sediment particles ranging from fine sand to medium silt is consistently reported from the nearby cores in the south Scotia Sea (Kim et al., 2018b). These results indicate that the main terrigenous supply mechanism during the glacial period dominantly delivers coarse detrital particles in the range of sand to silt to the Scotia Sea.

Several studies have suggested that ocean currents play an important role in sediment transport during glacials in the Scotia Sea (e.g., Diekmann et al., 2000, 2003; Noble et al., 2012; Xiao et al., 2016). In the Scotia Sea, ACC carries suspended terrigenous materials from the Antarctic Peninsula and Patagonia and disperses continental detritus through the Drake Passage (Diekmann et al., 2000; Hemming et al., 2007). During glacials, enhanced current erosion in extended terrigenous source areas at low sea level stands could provide more detrital materials to the sea (Noble et al., 2012; Xiao et al., 2016). However, sediment supply by current erosion is generally expected to deliver finegrained detritus (e.g., silt and clay) to deep-sea environments (e.g., Diekmann et al., 2000; Noble et al., 2012), as the lateral transport of>63 μm particles requires turbulence of higher velocities than is often available in the deep sea. Therefore, current transport of the dominant sand- to medium-silt-sized fractions in the glacial sediments should be accompanied by enhanced ACC intensity; however, ACC intensity was reportedly weaker during the glacial period than during the Holocene in the Scotia Sea and the Drake Passage (McCave et al., 2014; Lamy et al., 2015; Jouve et al., 2017). For instance, the fine sand fraction in sediments from the southernmost continental margin of South America significantly decreased during the glacial period, reflecting weak ACC intensity (Lamy et al., 2015). This implies that the glacial ACC was not strong enough to deliver sands from South America continents to the Scotia Sea. Thus, current transport would not be the main transport mechanism for increasing coarse particles ranging from sand to coarse silt in the Scotia Sea, although it could result in a quantitative increase in fine-grained detritus input during the glacial period.

Mass flow such as turbidites can entrain coarse sand; however, turbidite deposition was not observed in the glacial intervals in GC03-C1 and nearby cores (Fig. 1; Kim et al., 2018b). Furthermore, the possibility of significant sediment redistribution (e.g., winnowing

effect) by the bottom current was ruled out for south Scotia Sea sediments during the glacial period (Kim et al., 2018b). Sea ice extension or an advance of the ice-sheet grounding zone can deliver fine-grained detritus by trapping and resuspension, respectively; nevertheless, they would also fail to be the main transport mechanisms of coarser silts and sands (Weber et al., 2012; Kim et al., 2018b).

In this study, IRD is considered as the most plausible transport mechanism capable of delivering sand- to silt-sized sediments during the glacial period. Kim et al. (2018b) suggested iceberg calving activity as the main contributor to the high MS of glacial sediments in the south Scotia Sea, because the particle-size distribution of the dominant silt mode is very similar to that of IRD modeled from the subarctic icebergs (Jonkers et al., 2015). For GC03-C1, the dominance of silt-sized (16-63 μm) sediments carrying glacial MS can support the large input of silts by IRD influx. Of course, the IRD-related magnetic signals in silts can be diluted by other source of finer materials, such as current and/or dust. Thus, the sand fraction with enriched magnetic minerals (SIRM; Fig. 6f) can be considered to retain strong IRD-related magnetic signals, despite its low fractional abundance. In particular, the sand fraction retains relatively concentrated hematite than finer fractions (HIRM; Fig. 6f), which characterizes IRD-derived sediments containing hematite. Such hematite contribution could highlight IRD-related signals in bulk sediment, compared to magnetite influenced by various origins.

Bulk HIRM of GC03-C1 is compared with the IRD flux previously reported for the Scotia Sea for the last ~22 kyr (Fig. 9); Weber et al. (2014) proposed a high-resolution IRD flux, based on counts of grains coarser than 1mm from sediment cores in the central Scotia Sea (IRD >1mm flux; Fig. 9d). The IRD >1mm flux is strikingly high during the deglacial period (~17-9 ka), consistent with the timing of the iceberg retreat related to deglacial warming. This deglacial fluctuation of the IRD >1mm flux is very similar to that of bulk HIRM of GC03-C1 (Fig. 9b), which is more highlighted in the magnetic mineral enrichment in the sand fraction (SIRM of>63 μm fraction; Fig. 9c). This strongly indicates a simultaneous IRD influx into widespread Scotia Sea sediments, while also supporting that IRD influx results in the enrichment of magnetic minerals, both magnetite and hematite. Such abundant magnetic minerals of IRD could be related to potential source rock property in Antarctica (e.g., Pirrung et al., 2002; Brachfeld et al., 2013). In previous petrographic/mineralogical studies, origin of IRD clasts in Scotia Sea sediments was inferred as magmatic and metasedimentary rocks in the Antarctic Peninsula (Conolly and Ewing, 1965; Diekmann et al., 2000). However, a simulated model of Antarctic iceloss reveals that the IRD (> 1 mm) input time series in the Scotia Sea can be influenced from various sectors of ice-sheet discharge (e.g., the Weddell and Ross Seas), as icebergs merge together through the Iceberg Alley (Weber et al., 2014; Golledge et al., 2014).

Weber et al. (2014) suggested weak iceberg discharge during the last glacial period, as the flux of grains>1mm is very low (Fig. 9d). Although IRD input generally has been estimated by the number of grains coarser than 1mm or 2mm in the Scotia Sea (e.g., Diekmann et al., 2000; Weber et al., 2014), such method biased toward coarser gravel cannot fully evaluate the entire IRD contribution with various particle sizes. Alternatively, magnetic concentration, such as the bulk hematite contribution, could reflect relative contribution of the IRDderived grains distributed in all sizes. Indeed, common peaks of SIRM, HIRM, and χ ARM found in the bulk sediments during the last deglaciation is associated with magnetic peaks in the sand and silt fraction (Figs. 3 and 6d–k), indicating an IRD–related peak. Therefore, the glacial increase in magnetic concentration reflects that highly introduced fine IRD grains (fine sand to coarse silt) into sediments. The inconsistency between the low input of coarse (> 1 mm) grains and high input of finer IRD grains during the glacial period requires a more comprehensive understanding of the IRD input mechanism related to climate change. For instance, Kim et al. (2018b) suggested a different IRD input mechanism between the time of ice–sheet advance and retreat, which could supply vigorous finer IRD input at the margin of the ice shelf during glacial ice–sheet advances. To confirm such an unknown mechanism, various sedimentological and mineralogical studies would be needed; IRD provenance discrimination using geochemical indices will also be useful. Nevertheless, our results based on bulk and particlesize dependent magnetic properties clearly show that the higher concentration of magnetic minerals (e.g., high MS and HIRM values) during the glacial period is mainly caused by IRD input, implying active glacial iceberg discharge in the Scotia Sea. In addition, this further suggests cryosphere–atmosphere interactions, as shown by synchronization between MS and dust records.

7. Conclusions

Magnetic properties of bulk sediments and three particle–size fractions (> 63, 16–63, and<16 μm) of Scotia Sea sediments were investigated over the past 22 kyr. In bulk sediments, concentration–related magnetic parameters (χ, Ms, SIRM, HIRM, and χARM) show similar variations with distinct glacial highs and interglacial lows, indicating a glacial increase in both the magnetite and hematite concentrations. Both magnetic mineral assemblages and grain size analyses indicate the dominance of coarse vortex/MD detrital magnetite in bulk and coarse silt (16–63 μm) sediments during the glacial period. The glacial increase in bulk magnetic concentration is mainly contributed by the silt fraction, but it is also associated with the significant enrichment of magnetic minerals in the sand (> 63 μm) fraction. Moreover, magnetic concentration between silts and sands covaries throughout the last deglaciation,

indicating the same sediment transport mechanisms. As the most plausible mechanism capable of transporting sediment particles ranging from sand to coarse silt, IRD input is considered. As hematite is relatively concentrated in the sand fraction (i.e., high HIRM values) during the glacial period, HIRM of bulk sediment can highlight IRD-related signal. The bulk HIRM variation could reflect the IRD contribution in various sediment particle-size, and thus its glacial increase suggests a considerable IRD input by active iceberg calving, resulting in high magnetic concentration.

KOPRI
극지연구소

마지막 최대 빙하기 이후 스코시아해 퇴적물의 자성 특성: 자성을 조절하는 빙하기의 빙상 방출

신지영[a,b], 김성한[b,*], Xiang Zhao[c], 유규철[b], 유용재[d], 이재일[b], 이민경[b], 윤호일[b]

[a]한국해양과학기술원, [b]극지연구소, [c]Australian National University, [d]충남대학교

요약: 남빙양 퇴적물의 대자율과 남극 빙하 코어의 먼지 기록의 강한 빙하기-간빙기 유사성은 종종 남반구의 대기 순환을 복원하는데 사용된다. 퇴적학적 변동과 연결되어 자성을 띄는 물질을 규명하는 것은 다양한 지자기적 특성을 평가하는데 매우 중요함에도 불구하고, 남극 스코시아해에서 자세한 지자기 연구는 충분히 이루어지지 않았다. 여기서 우리는 지난 약 22천년의 기록을 가지는 스코시아해 해양퇴적물에서 벌크와 사이즈 별 지자기 특성을 파악하여 대자율을 포함하는 벌크 자기 프록시를 조절하는 주요 퇴적물 운송 기작을 이해하고자 하였다. 벌크 퇴적물에서 대자율 값은 마지막 빙하기 동안 가장 높게 나타났고 이 것은 ferrimagnetic과 antiferromagnetic 광물의 함량과 입도 증가와 함께 연동되어 나타났다. 자성광물 군집에서 조립한 쇄설성 마그네타이트가 가장 우세하게 나타났다. 세개의 입도 구간중에서 조립질 실트 구간이 빙하기 벌크 퇴적물의 지자기 특성을 가장 잘 반영하고 있었다. 이러한 조립질 실트의 우세도는 이러한 우세 입도 광물질들이 세립질 실트나 점토 사이즈 등과 같이 바람에 의해 운송되어져 온 것이 아니라는 결론을 내릴 수 있다. 실트 사이즈는 사질 입자의 지자기 특성과 지난 마지막 후빙기 이후 동일한 변동 패턴을 보여왔고, 이것은 서로의 유입 기작이 연결되어 있다는 것을 의미한다. 따라서 빙하기 동안의 벌크 지자기 특성을 조절하는 사질에서 조립질 실트에 이르는 퇴적물은 빙하쇄설성 퇴적물의 형태로 운송되어 온 것으로 해석된다. 적철석은 상대적으로 사질 입자에 농축되어 있고 적철석의 농도는 스코시아해 퇴적물의 1 mm 이상의 조립한 빙하쇄설성 입자들의 유입과 후빙기 이후 함께 변동됨에도, 빙하기의 불일치는 빙상의 전진과 후퇴에 따라서 이들의 관계가 다르다는 것을 의미한다. 결과적으로, 빙하기 동안의 벌크 지자기 함량 증가는 스코시아해에서 광범위한 빙산 쪼개짐이 일어났음을 의미하고 이것은 나아가 빙권과 대기권의 변동 사이에 강한 연결이 있음을 의미한다.

참고 문헌

Anderson, J.B., Andrews, J.T., 1999. Radiocarbon constraints on ice sheet advance and retreat in the Weddell Sea, Antarctica. Geology, 27 (2), 179−182. https://doi.org/10.1130/0091−7613(1999)027<0179:RCOISA>2.3.CO;2.

Anderson, R.F., Ali, S., Bradtmiller, L.I., Nielsen, S.H.H., Fleisher, M.Q., Anderson, B.E., Burckle, L.H., 2009. Wind−driven upwelling in the Southern Ocean and the deglacial rise in atmospheric CO2. Science 323, 1443−1448. https://doi.org/10.1126/science.1167441.

Bak, Y., Lee, J., Yoon, H.I., Yoo, K., Lee, S., 2010. Holocene paleoclimate change in the area around Elephant Island, Antarctica: Evidence from the diatom record. J. Geol. Soc. Korea 46, 111−117.

Bareille, G., Grousset, F.E., Labracherie, M., Labeyrie, L.D., Petit, J.−R., 1994. Origin of detrital fluxes in the southeast Indian Ocean during the last climatic cycles. Paleoceanography 9, 799−819. https://doi.org/10.1029/ 94PA01946.

Bloemendal, J., King, J.W., Hall, F.R., Doh, S.−J., 1992. Rock magnetism of Late Neogene and Pleistocene deep−sea sediments: relationship to sediment source, diagenetic processes, and sediment lithology. J. Geophys. Res. 97, 4361−4375. https://doi.org/10.1029/91JB03068.

Brachfeld, S., Pinzon, J., Darley, J., Sagnotti, L., Kuhn, G., Florindo, F., Wilson, G., Ohneiser, C., Monien, D., Joseph, L., 2013. Iron oxide tracers of ice sheet extent and sediment provenance in the ANDRILL AND−1B drill core, Ross Sea, Antarctica. Glob. Planet. Change 110, 420−433. https://doi.org/10.1016/j.gloplacha.2013.09.015.

Carter−Stiglitz, B., Moskowitz, B., Jackson, M., 2001. Unmixing magnetic assemblages and the magnetic behavior of bimodal mixtures. J. Geophys. Res. Solid Earth 106, 26397−26411. https://doi.org/10.1029/ 2001JB000417.

Chang, L., Roberts, A.P., Heslop, D., Hayashida, A., Li, J., Zhao, X., Tian, W., Huang, Q., 2016. Widespread occurrence of silicate−hosted magnetic mineral inclusions in marine sediments and their contribution to paleomagnetic recording. J. Geophys. Res. Solid Earth 121, 8415−8431. https://doi.org/10.1002/2016JB013109.

Conolly, J.R., Ewing, M., 1965. Ice−rafted detritus as a climatic indicator in Antarctic deep−sea cores. Science 150 (80), 1822−1824. https://doi.org/10.1126/science.150.3705.1822.

Day, R., Fuller, M., Schmidt, V.A., 1977. Hysteresis properties of titanomagnetites: Grainsize and compositional dependence. Phys. Earth Planet. Inter. 13, 260−267. https://doi.org/10.1016/0031−9201(77)90108−X.

KOPRI 극지연구소

Dearing, J.A., Dann, R.J.L., Hay, K., Lees, J.A., Loveland, P.J., Maher, B.A., O'Grady, K., 1996. Frequency-dependent susceptibility measurements of environmental materials. Geophys. J. Int. 124, 228-240. https://doi.org/10.1111/j.1365-246X.1996.tb06366.x.

Delmonte, B., Andersson, P.S., Hansson, M., Schöberg, H., Petit, J.R., Basile-Doelsch, I., Maggi, V., 2008. Aeolian dust in East Antarctica (EPICA-Dome C and Vostok): Provenance during glacial ages over the last 800 kyr. Geophys. Res. Lett. 35, 256-264. https://doi.org/10.1029/2008GL033382.

Diekmann, B., Kuhn, G., Rachold, V., Abelmann, A., Brathauer, U., Fütterer, D.K., Gersonde, R., Grobe, H., 2000. Terrigenous sediment supply in the Scotia Sea (Southern Ocean): response to Late Quaternary ice dynamics in Patagonia and on the Antarctic Peninsula. Palaeogeogr. Palaeoclimatol. Palaeoecol. 162, 357-387. https://doi.org/10.1016/S0031-0182(00)00138-3.

Diekmann, B., Fütterer, D.K., Grobe, H., Hillenbrand, C.D., Kuhn, G., Michels, K., Petschick, R., Pirrung, M., 2003. Terrigenous sediment supply in the polar to Temperate South Atlantic: Land-ocean links of environmental changes during the Late Quaternary. In: The South Atlantic in the Late Quaternary. Springer Berlin Heidelberg, Berlin, Heidelberg, pp. 375-399. https://doi.org/10.1007/978-3-642-18917-3_18.

Domack, E.W., Jacobson, E.A., Shipp, S., Anderson, J.B., 1999. Late Pleistocene-Holocene retreat of the West Antarctic Ice-Sheet system in the Ross Sea: Part 2 - Sedimentologic and stratigraphic signature. Bull. Geol. Soc. Am. 111, 1517-1536. https://doi.org/10.1130/0016-7606(1999)111 <1517:LPHROT>2.3.CO;2.

Dunlop, D.J., 1986. Coercive forces and coercivity spectra of submicron magnetites. Earth Planet. Sci. Lett. 78, 288-295. https://doi.org/10.1016/ 0012-821X(86)90068-3.

Dunlop, D.J., 2002. Theory and application of the Day plot (Mrs/Ms versus Hcr/Hc) 1. Theoretical curves and tests using titanomagnetite data. J. Geophys. Res. 107. https://doi.org/10.1029/2001JB000486.

Dunlop, D.J., Carter-Stiglitz, B., 2006. Day plots of mixtures of superparamagnetic, singledomain, pseudosingle-domain, and multidomain magnetites. J. Geophys. Res. Solid Earth 111, B12S09. https://doi.org/10.1029/ 2006JB004499.

Egli, R., 2003. Analysis of the field dependence of remanent magnetization curves. J. Geophys. Res. Solid Earth 108, 1-25. https://doi.org/10.1029/ 2002JB002023.

Egli, R., 2013. VARIFORC: An optimized protocol for calculating non-regular first-order reversal curve (FORC) diagrams. Glob. Planet. Change 110, 302-320. https://doi.org/10.1016/j.gloplacha.2013.08.003.

Egli, R., Chen, A.P., Winklhofer, M., Kodama, K.P., Horng, C.-S., 2010. Detection of noninteracting single domain particles using first-order reversal curve diagrams. Geochem. Geophys. Geosyst. 11, Q01Z11. https://doi.org/ 10.1029/2009GC002916.

Feinberg, J.M., Scott, G.R., Renne, P.R., Wenk, H.-R., 2005. Exsolved magnetite inclusions in silicates: Features determining their remanence behavior. Geology 33, 513-516. https://doi.org/10.1130/G21290.1.

Fischer, H., Fundel, F., Ruth, U., Twarloh, B., Wegner, A., Udisti, R., Becagli, S., Castellano, E., Morganti, A., Severi, M., Wolff, E., Littot, G., Röthlisberger, R., Mulvaney, R., Hutterli, M.A., Kaufmann, P., Federer, U., Lambert, F., Bigler, M., Hansson, M., Jonsell, U., de Angelis, M., Boutron, C., Siggaard-Andersen, M.-L., Steffensen, J.P., Barbante, C., Gaspari, V., Gabrielli, P., Wagenbach, D., 2007. Reconstruction of millennial changes in dust emission, transport and regional sea ice coverage using the deep EPICA ice cores from the Atlantic and Indian Ocean sector of Antarctica. Earth Planet. Sci. Lett. 260, 340-354. https://doi.org/10.1016/j.epsl.2007.06.014.

Gersonde, R., Crosta, X., Abelmann, A., Armand, L., 2005. Sea-surface temperature and sea ice distribution of the Southern Ocean at the EPILOG Last Glacial Maximum-a circum-Antarctic view based on siliceous microfossil records. Quat. Sci. Rev. 24, 869-896. https://doi.org/10.1016/j.quascirev.2004.07.015.

Golledge, N.R., Menviel, L., Carter, L., Fogwill, C.J., England, M.H., Cortese, G., Levy, R.H., 2014. Antarctic contribution to meltwater pulse 1A from reduced Southern Ocean overturning. Nat. Commun. 5, 5107. https://doi.org/10.1038/ncomms6107.

Harrison, R.J., Feinberg, J.M., 2008. FORCinel: An improved algorithm for calculating first-order reversal curve distributions using locally weighted regression smoothing. Geochem. Geophys. Geosyst. 9, Q05016. https://doi.org/10.1029/2008GC001987.

Hatfield, R.G., Reyes, A.V., Stoner, J.S., Carlson, A.E., Beard, B.L., Winsor, K., Welke, B., 2016. Interglacial responses of the southern Greenland ice sheet over the last 430,000 years determined using particle-size specific magnetic and isotopic tracers. Earth Planet. Sci. Lett. 454, 225-236. https://doi.org/10.1016/j.epsl.2016.09.014.

Hatfield, R.G., Stoner, J.S., Reilly, B.T., Tepley, F.J., Wheeler, B.H., Housen, B.A., 2017. Grain size dependent magnetic discrimination of Iceland and South Greenland terrestrial sediments in the northern North Atlantic sediment record. Earth Planet. Sci. Lett. 474, 474-489. https://doi.org/10.1016/ j.epsl.2017.06.042.

Hatfield, R.G., Wheeler, B.H., Reilly, B.T., Stoner, J.S., Housen, B.A., 2019. Particle size specific magnetic properties across the Norwegian-Greenland Seas: Insights into the influence of sediment source and texture on bulk magnetic records. Geochem. Geophys. Geosyst. 20, 1004-1025. https://doi.org/10.1029/2018GC007894.

Hemming, S.R., van de Flierdt, T., Goldstein, S.L., Franzese, A.M., Roy, M., Gastineau, G., Landrot, G., 2007. Strontium isotope tracing of terrigenous sediment dispersal in the Antarctic circumpolar current: implications for constraining frontal positions. Geochem. Geophys. Geosyst. 8, Q06N13. https://doi.org/10.1029/2006GC001441.

Hounslow, M.W., Maher, B.A., 1996. Quantitative extraction and analysis of carriers of magnetization in sediments. Geophys. J. Int. 124, 57–74. https://doi.org/10.1111/j.1365–246X.1996.tb06352.x.

Hyland, E.G., Sheldon, N.D., Van der Voo, R., Badgley, C., Abrajevitch, A., 2015. A new paleoprecipitation proxy based on soil magnetic properties: implications for expanding paleoclimate reconstructions. Geol. Soc. Am. Bull. 127, B31207.1. https://doi.org/10.1130/B31207.1.

Jonkers, L., Barker, S., Hall, I.R., Prins, M.A., 2015. Correcting for the influence of icerafted detritus on grain size–based paleocurrent speed estimates. Paleoceanography 30, 1347–1357. https://doi.org/10.1002/2015PA002830.

Jouve, G., Lisé–Pronovost, A., Francus, P., De Coninck, A.S., 2017. Climatic influence of the latest Antarctic isotope maximum of the last glacial period (AIM4) on Southern Patagonia. Palaeogeogr. Palaeoclimatol. Palaeoecol. 472, 33–50. https://doi.org/10.1016/j.palaeo.2017.02.020.

Kim, S., Yoo, K.–C., Lee, J.I., Khim, B.–K., Bak, Y.–S., Lee, M.K., Lee, J., Domack, E.W., Christ, A.J., Yoon, H.I., 2018a. Holocene paleoceanography of Bigo Bay, west Antarctic Peninsula: Connections between surface water productivity and nutrient utilization and its implication for surface–deep water mass exchange. Quat. Sci. Rev. 192, 59–70. https://doi.org/10.1016/j.quascirev.2018.05.028.

Kim, S., Yoo, K.–C., Lee, J.I., Lee, M.K., Kim, K., Yoon, H.I., Moon, H.S., 2018b. Relationship between magnetic susceptibility and sediment grain size since the last glacial period in the Southern Ocean off the northern Antarctic Peninsula – Linkages between the cryosphere and atmospheric circulation. Palaeogeogr. Palaeoclimatol. Palaeoecol. 505, 359–370. https://doi.org/10.1016/j.palaeo.2018.06.016.

King, J., Banerjee, S.K., Marvin, J., Özdemir, Ö., 1982. A comparison of different magnetic methods for determining the relative grain size of magnetite in natural materials: Some results from lake sediments. Earth Planet. Sci. Lett. 59, 404–419. https://doi.org/10.1016/0012–821X(82)90142–X.

Kohfeld, K.E., Graham, R.M., De Boer, A.M., Sime, L.C., Wolff, E.W., Le Quéré, C., Bopp, L., 2013. Southern Hemisphere westerly wind changes during the Last Glacial Maximum: Paleo–data synthesis. Quat. Sci. Rev. 68, 76–95.

Lambert, F., Bigler, M., Steffensen, J.P., Hutterli, M., Fischer, H., 2012. Centennial mineral dust variability in high–resolution ice core data from Dome C, Antarctica. Clim. Past 8, 609–623. https://doi.org/10.5194/ cp–8–609–2012.

Lamy, F., Kilian, R., Arz, H.W., Francois, J.–P., Kaiser, J., Prange, M., Steinke, T., 2010. Holocene changes in the position and intensity of the southern westerly wind belt. Nat. Geosci. 3, 695–699. https://doi.org/10.1038/ ngeo959.

Lamy, F., Gersonde, R., Winckler, G., Esper, O., Jaeschke, A., Kuhn, G., Ullermann, J., Martinez-Garcia, A., Lambert, F., Kilian, R., 2014. Increased dust deposition in the Pacific Southern Ocean during Glacial periods. Science 343 (80), 403-407. https://doi.org/10.1126/ science.1245424.

Lamy, F., Arz, H.W., Kilian, R., Lange, C.B., Lembke-Jene, L., Wengler, M., Kaiser, J., Baeza-Urrea, O., Hall, I.R., Harada, N., Tiedemann, R., 2015. Glacial reduction and millennial-scale variations in Drake Passage throughflow. Proc. Natl. Acad. Sci. 112, 13496-13501. https://doi.org/ 10.1073/pnas.1509203112.

Lascu, I., Banerjee, S.K., Berquó, T.S., 2010. Quantifying the concentration of ferrimagnetic particles in sediments using rock magnetic methods. Geochem. Geophys. Geosyst. 11. https://doi.org/10.1029/2010GC003182.

Lee, J.I., Bak, Y.-S., Yoo, K.-C., Lim, H.S., Yoon, H.I., Yoon, H.S., 2010. Climate changes in the South Orkney Plateau during the last 8600 years. The Holocene 20, 395-404. https://doi.org/10.1177/0959683609353430.

Lisé-Pronovost, A., St-Onge, G., Gogorza, C., Haberzettl, T., Jouve, G., Francus, P., Ohlendorf, C., Gebhardt, C., Zolitschka, B., 2015. Rock-magnetic proxies of wind intensity and dust since 51,200 cal BP from lacustrine sediments of Laguna Potrok Aike, southeastern Patagonia. Earth Planet. Sci. Lett. 411, 72-86. https://doi.org/10.1016/j.epsl.2014.11.007.

Maher, B.A., 1986. Characterisation of soils by mineral magnetic measurements. Phys. Earth Planet. Inter. 42, 76-92. https://doi.org/10.1016/ S0031-9201(86)80010-3.

Maher, B.A., 1988. Magnetic properties of some synthetic sub-micron magnetites. Geophys. J. Int. 94, 83-96. https://doi.org/10.1111/ j.1365-246X.1988.tb03429.x.

Maher, B.A., Alekseev, A., Alekseeva, T., 2003. Magnetic mineralogy of soils across the Russian Steppe: climatic dependence of pedogenic magnetite formation. Palaeogeogr. Palaeoclimatol. Palaeoecol. 201, 321-341. https://doi.org/10.1016/S0031-0182(03)00618-7.

Maher, B.A., Prospero, J.M., Mackie, D., Gaiero, D., Hesse, P.P., Balkanski, Y., 2010. Global connections between aeolian dust, climate and ocean biogeochemistry at the present day and at the last glacial maximum. Earth-Sci. Rev. 99, 61-97. https://doi.org/10.1016/j.earscirev.2009.12.001.

Maxbauer, D.P., Feinberg, J.M., Fox, D.L., 2016. MAX UnMix: A web application for unmixing magnetic coercivity distributions. Comput. Geosci. 95, 140-145. https://doi.org/10.1016/j.cageo.2016.07.009.

McCave, I.N., Crowhurst, S.J., Kuhn, G., Hillenbrand, C.-D., Meredith, M.P., 2014. Minimal change in Antarctic Circumpolar Current flow speed between the last glacial and Holocene. Nat. Geosci. 7, 113-116. https://doi.org/10.1038/ngeo2037.

KOPRI 극지연구소

Muhs, D.R., 2013. The geologic records of dust in the Quaternary. Aeolian Res. 9, 3–48. https://doi.org/10.1016/j.aeolia.2012.08.001.

Mullins, C.E., 1977. Magnetic susceptibility of the soil and its significance in soil science – A review. J. Soil Sci. 28, 223–246. https://doi.org/10.1111/ j.1365–2389.1977.tb02232.x.

Noble, T.L., Piotrowski, A.M., Robinson, L.F., McManus, J.F., Hillenbrand, C.–D., Bory, A.J.M., 2012. Greater supply of Patagonian–sourced detritus and transport by the ACC to the Atlantic sector of the Southern Ocean during the last glacial period. Earth Planet. Sci. Lett. 317–318, 374–385. https://doi.org/10.1016/j.epsl.2011.10.007.

Orsi, A.H., Whitworth, T., Nowlin, W.D., 1995. On the meridional extent and fronts of the Antarctic Circumpolar Current. Deep Sea Res. Part I Oceanogr. Res. Pap. 42, 641–673. https://doi.org/10.1016/0967–0637 (95)00021–W.

Pirrung, M., Hillenbrand, C.D., Diekmann, B., Fütterer, D., Grobe, H., Kuhn, G., 2002. Magnetic susceptibility and ice–rafted debris in surface sediments of the Atlantic sector of the Southern Ocean. Geo–Marine Lett. 22, 170–180. https://doi.org/10.1007/s00367–002–0109–7.

Pugh, R.S., McCave, I.N., Hillenbrand, C.–D., Kuhn, G., 2009. Circum–Antarctic age modelling of Quaternary marine cores under the Antarctic Circumpolar Current: icecore dust–magnetic correlation. Earth Planet. Sci. Lett. 284, 113–123. https://doi.org/10.1016/j.epsl.2009.04.016.

Razik, S., Dekkers, M.J., von Dobeneck, T., 2014. How environmental magnetism can enhance the interpretational value of grain–size analysis: A time–slice study on sediment export to the NW African margin in Heinrich Stadial 1 and Mid Holocene. Palaeogeogr. Palaeoclimatol. Palaeoecol. 406, 33–48. https://doi.org/10.1016/ j.palaeo.2014.04.009.

Razik, S., Govin, A., Chiessi, C.M., von Dobeneck, T., 2015. Depositional provinces, dispersal, and origin of terrigenous sediments along the SE South American continental margin. Mar. Geol. 363, 261–272. https://doi.org/10.1016/j.margeo.2015.03.001.

Reimer, P.J., Bard, E., Bayliss, A., Beck, J.W., Blackwell, P.G., Ramsey, C.B., Buck, C.E., Cheng, H., Edwards, R.L., Friedrich, M., Grootes, P.M., Guilderson, T.P., Haflidason, H., Hajdas, I., Hatté, C., Heaton, T.J., Hoffmann, D.L., Hogg, A.G., Hughen, K.A., Kaiser, K.F., Kromer, B., Manning, S.W., Niu, M., Reimer, R.W., Richards, D.A., Scott, E.M., Southon, J.R., Staff, R.A, Turney, C.S.M., van der Plicht, J., 2013. IntCal13 and Marine13 radiocarbon age calibration curves 0–50,000 years cal BP. Radiocarbon 55, 1869–1887.

Roberts, A.P., Cui, Y., Verosub, K.L., 1995. Wasp–waisted hysteresis loops: Mineral magnetic characteristics and discrimination of components in mixed magnetic systems. J. Geophys. Res. Solid Earth 100, 17909–17924. https://doi.org/10.1029/95JB00672.

KOPRI 극지연구소

Roberts, A.P., Heslop, D., Zhao, X., Pike, C.R., 2014. Understanding fine magnetic particle systems through use of first-order reversal curve diagrams. Rev. Geophys. 52, 557-602. https://doi.org/10.1002/2014RG000462.

Roberts, A.P., Almeida, T.P., Church, N.S., Harrison, R.J., Heslop, D., Li, Y., Li, J., Muxworthy, A.R., Williams, W., Zhao, X., 2017. Resolving the origin of pseudo-single domain magnetic behavior. J. Geophys. Res. Solid Earth 122, 9534-9558. https://doi.org/10.1002/2017JB014860.

Strehlau, J.H., Hegner, L.A., Strauss, B.E., Feinberg, J.M., Penn, R.L., 2014. Simple and efficient separation of magnetic minerals from speleothems and other carbonates. J. Sediment. Res. 84, 1096-1106. https://doi.org/10.2110/ jsr.2014.89.

Stuiver, M., Reimer, P.J., 1993. Extended 14C database and revised CALIB radiocarbon calibration program. Radiocarbon 35, 215-230.

Walter, H., Hegner, E., Diekmann, B., Kuhn, G., Rutgers van der loeff, M., 2000. Provenance and transport of terrigenous sediment in the south Atlantic Ocean and their relations to glacial and interglacial cycles: Nd and Sr isotopic evidence. Geochim. Cosmochim. Acta 64, 3813-3827. https://doi.org/10.1016/S0016-7037(00)00476-2.

Weber, M.E., Kuhn, G., Sprenk, D., Rolf, C., Ohlwein, C., Ricken, W., 2012. Dust transport from Patagonia to Antarctica - a new stratigraphic approach from the Scotia Sea and its implications for the last glacial cycle. Quat. Sci. Rev. 36, 177-188. https://doi.org/10.1016/ j.quascirev.2012.01.016.

Weber, M.E., Clark, P.U., Kuhn, G., Timmermann, A., Sprenk, D., Gladstone, R., Zhang, X., Lohmann, G., Menviel, L., Chikamoto, M.O., Friedrich, T., Ohlwein, C., 2014. Millennial-scale variability in Antarctic ice-sheet discharge during the last deglaciation. Nature 510, 134-138. https://doi.org/10.1038/nature13397.

Weber, M.E., Raymo, M.E., Peck, V.L., Williams, T., 2019. Expedition 382 Preliminary Report: Iceberg Alley and Subantarctic Ice and Ocean Dynamics, International Ocean Discovery Program Preliminary Report. International Ocean Discovery Program. https://doi.org/10.14379/ iodp.pr.382.2019.

Xiao, W., Frederichs, T., Gersonde, R., Kuhn, G., Esper, O., Zhang, X., 2016. Constraining the dating of late Quaternary marine sediment records from the Scotia Sea (Southern Ocean). Quat. Geochronol. 31, 97-118. https://doi.org/10.1016/j.quageo.2015.11.003.

Yamazaki, T., Ikehara, M., 2012. Origin of magnetic mineral concentration variation in the Southern Ocean. Paleoceanography 27, PA2206. https://doi.org/10.1029/ 2011PA002271.

KOPRI 극지연구소

Table 1. Acid insoluble organic matter radiocarbon dates from cores GC03−C1 and BC03−C1 and correlation points between GC03−C1 MS and EDML nss−Ca2+ records.e*Ages used as tie points for the age model in this study. Corrected and calibrated ages are obtained using CALIB 7.1 software (Stuiver and Reimer, 1993) and the MARINE13 dataset (Reimer et al., 2013) with a standard global reservoir age (ΔR=0) after subtracting the BC03−C1 top age of 4037 yr, following the approach in Lee et al. (2010). **Out−of−range ages.

Depth (cm)	Lab code	^{14}C age (yr BP)	Error (yr)	δ^{13}C (‰)	Corrected and calibrated age (2 σ) (cal. yr BP)	MS–EDML age (cal. yr BP)
GC03-C1						
10*	NZA-21383	12,290	± 45	−24.9	8790	
30*	NZA-21384	12,788	± 45	−25.8	9427	
50**	NZA-21466	16,169	± 65	−25	13,581	
60*	NZA-21385	13,338	± 50	−25.4	10,143	
100	NZA-21467	13,209	± 50	−25.6	9970	
120*	NZA-21386	13,749	± 50	−26.4	10,613	
150*	NZA-21387	14,091	± 50	−25.9	11,060	
181*						12,802
200*	NZA-21388	16,290	± 60	−24.9	13,713	
240**	NZA-21468	18,519	± 80	−26.9	17,118	
250*						14,797
311*						16,488
340*						17,628
350**	NZA-21469	21,900	± 110	−27.4	21,085	
450**	NZA-21470	22,050	± 120	−27.1	21,288	
478*						18,390
550**	NZA-21471	22,200	± 120	−25.4	21,499	
650**	NZA-21472	23,470	± 130	−25.3	22,908	
683*						20,046
750**	NZA-21549	21,430	± 120	−24.9	20,487	
839*						21,617
BC03-C1						
0	NZA-21382	4037	± 30	−25.9	0	

KOPRI
극지연구소

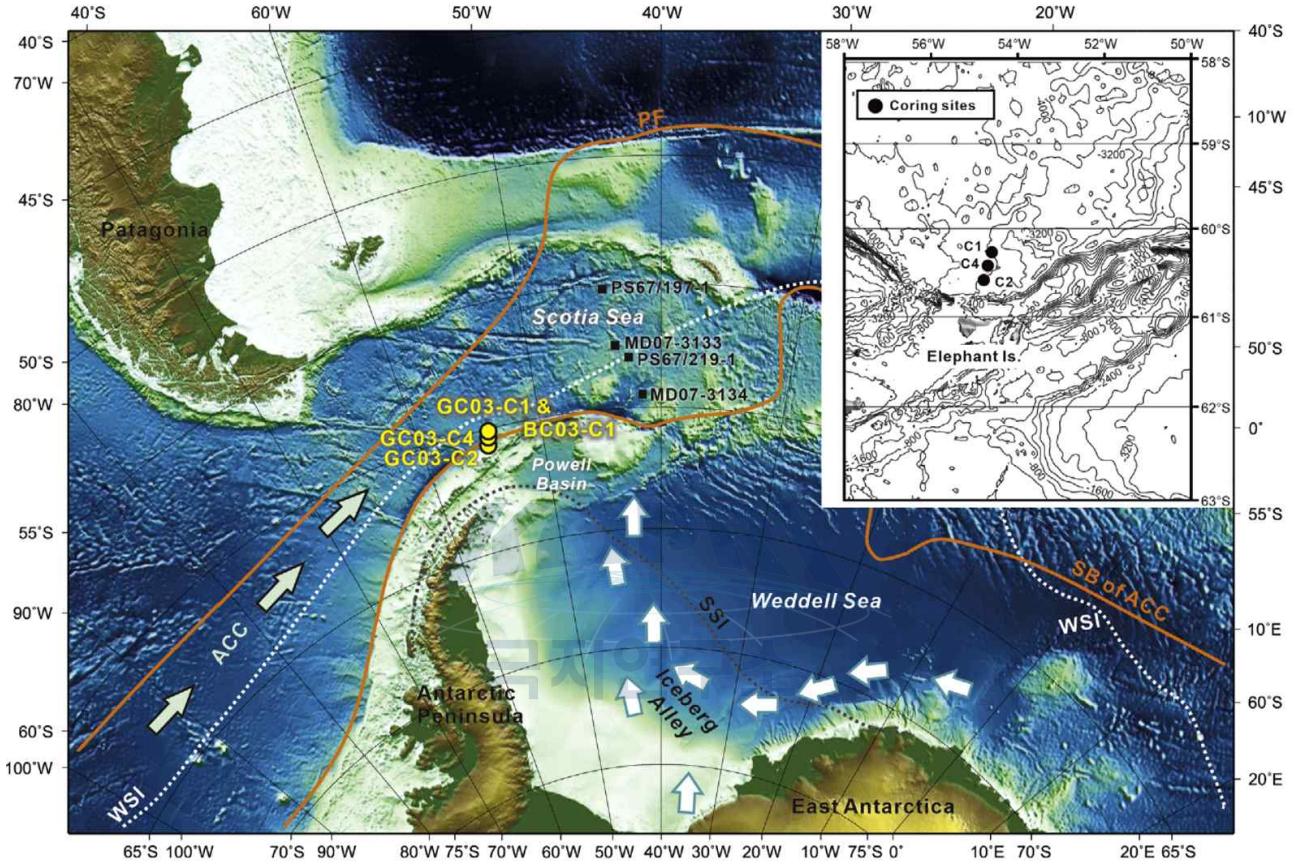


Figure 1. (a) Map of the study region indicating the locations of the sediment cores examined in this study as well as in previous investigations. The white open arrows indicate the location of iceberg alley (from Anderson and Andrew, 1999); the orange lines indicate the Polar Front (PF) and the Southern Boundary of the Antarctic Circumpolar Current (SBACC; Orsi et al., 1995); the dark gray and white dashed lines indicate the summer (SSI) and winter (WSI) sea ice extent, respectively (Gersonde et al., 2005); and the light green arrows indicate the ACC.

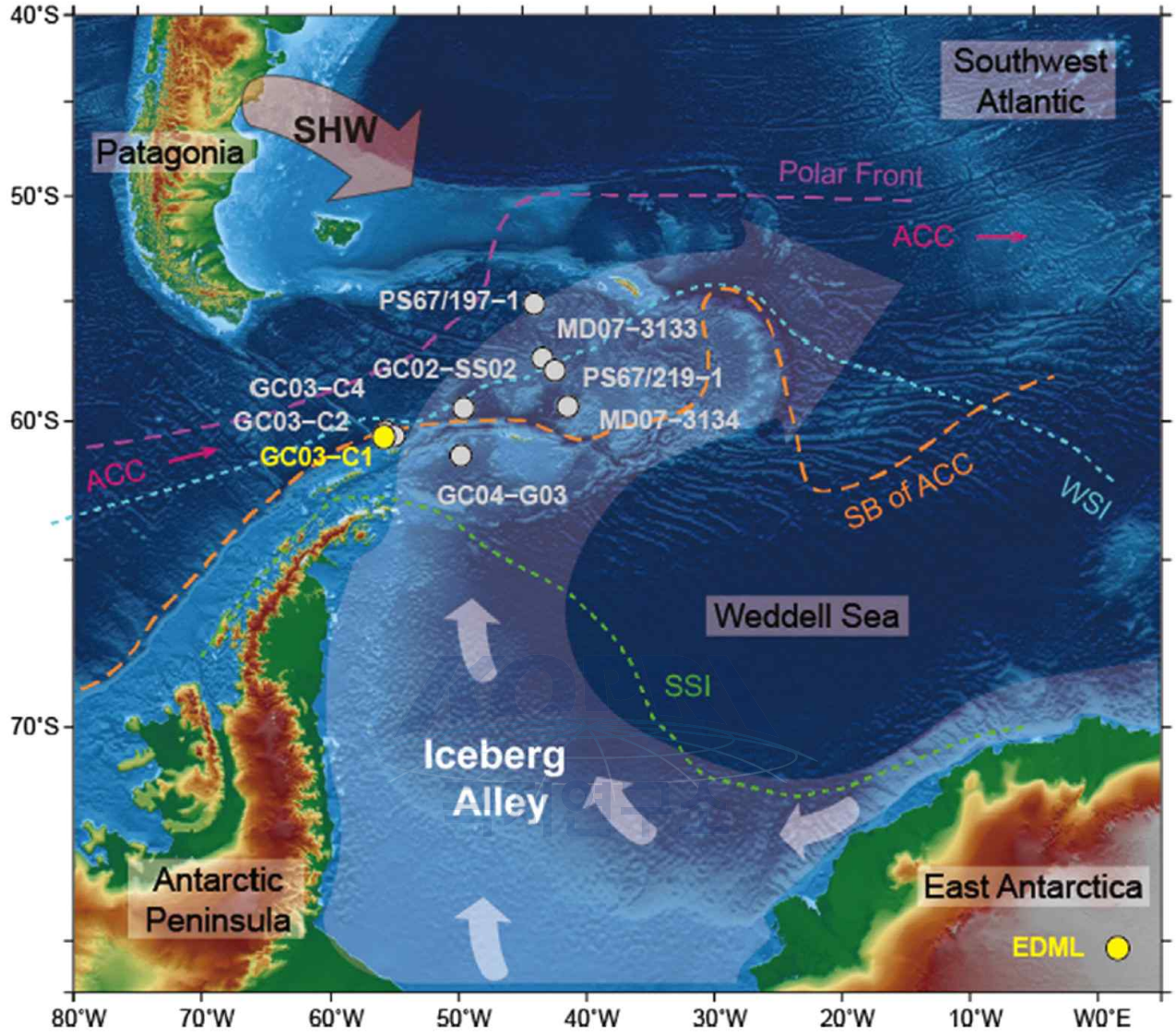


Figure 1. Site location map for the studied core GC03-C1 (yellow dot) and reference sites (gray dots). Reference sites: GC03-C2, GC03-C4, GC04-G03, and GC02-SS02 from Kim et al. (2018b), MD07-3133 and MD07-3134 from Weber et al. (2012), and PS67/219-1 and PS67/197-1 from Xiao et al. (2016). Iceberg Alley from Anderson and Andrews (1999) is illustrated by white shaded arrows. The main wind direction of the Southern Hemisphere westerlies (SHW) is indicated by a red shaded arrow. Green and light blue dotted lines indicate the summer sea ice (SSI) and winter sea ice (WSI) sea-ice extent, respectively (Gersonde et al., 2005). The purple dotted line is the polar front, and orange dotted line is southern boundary of the Antarctic Circumpolar Current (SB of ACC; Orsi et al., 1995). ACC is shown by magenta arrows. (For interpretation of the references to colour in this figure legend, the reader is referred to the web version of this article.)

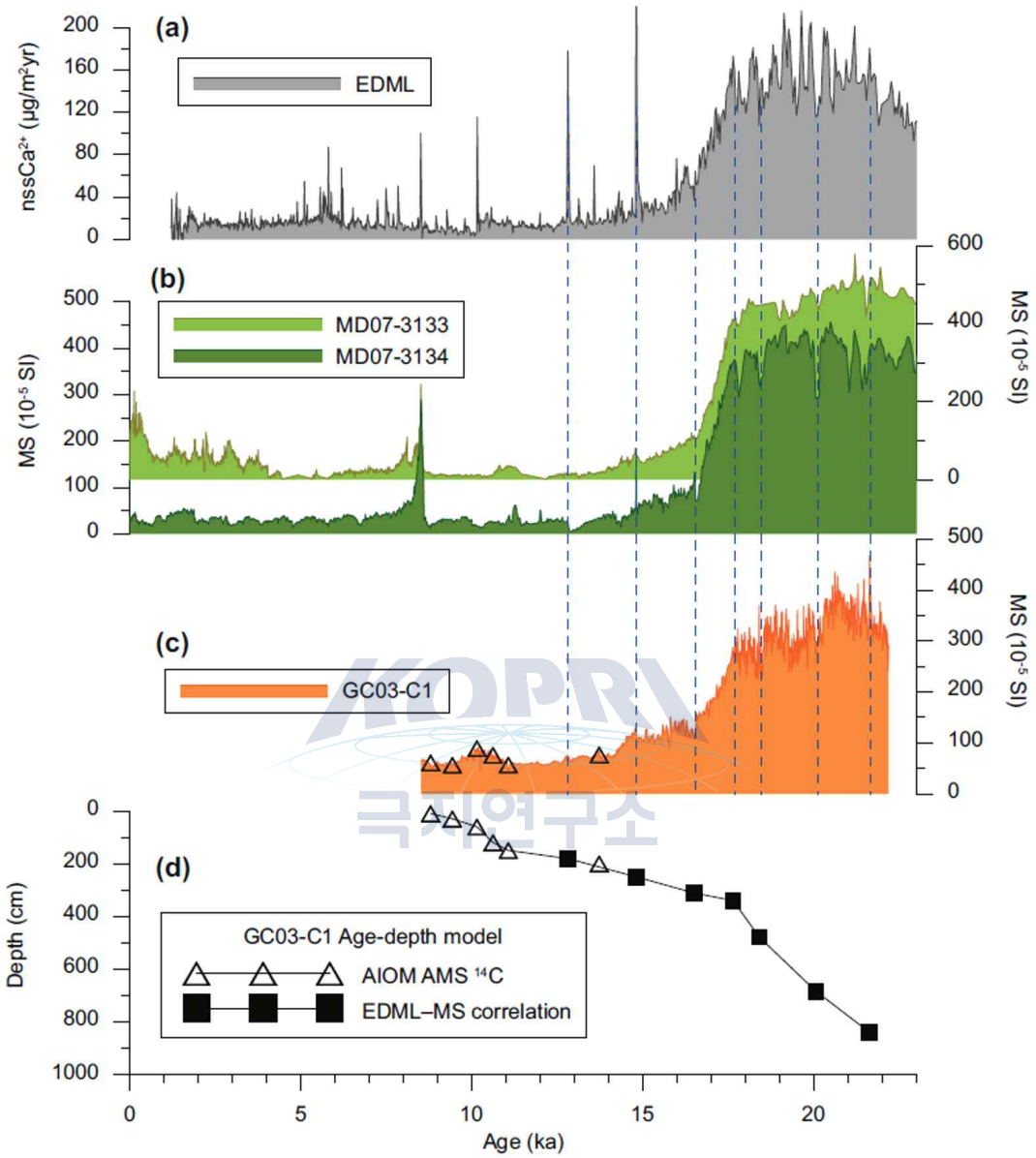


Figure 2. Age control for core GC03-C1. (a) EDML ice core non-sea-salt Ca2+ (nssCa2+) flux, dust record (Fischer et al., 2007); (b) magnetic susceptibility (MS) of cores MD07-3133 and MD07-3134 (Weber et al., 2012); (c) MS of GC03-C1 (Bak et al., 2010); and (d) final age-depth model of GC03-C1 based on the EDML-MS correlations combined with 14C dates for the top 200 cm. The 14C dates are marked as open triangles and the correlation tie points are shown as closed squares.

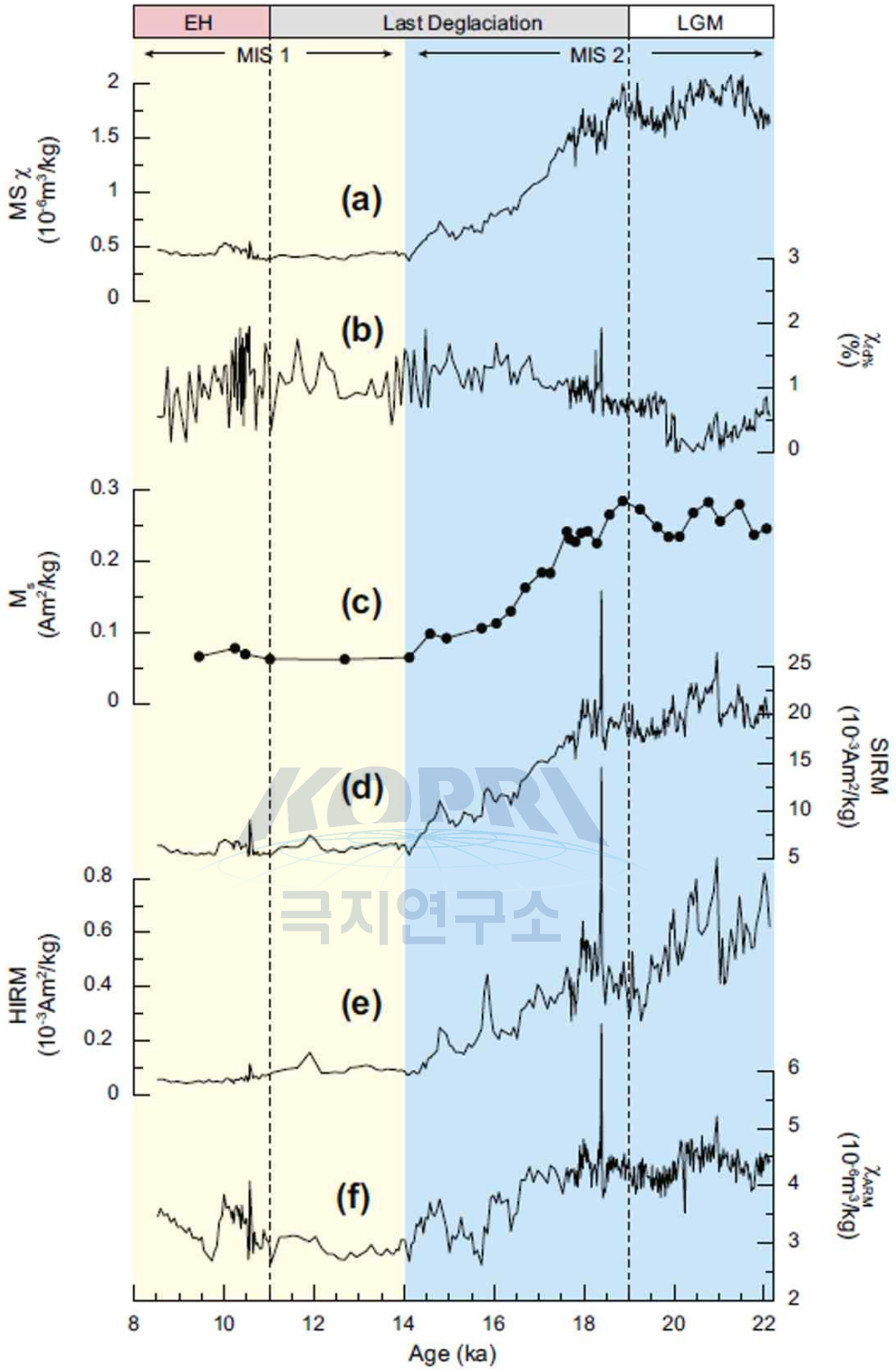


Figure 3. Temporal variations of magnetic concentration parameters for GC03-C1. (a) Mass-specific MS (χ); (b) frequency-dependent χ (χfd%); (c) saturation magnetization (Ms); (d) saturation isothermal remanent magnetization (SIRM); (e) hard IRM (HIRM); and (f) susceptibility of anhysteretic remanent magnetization (χARM). Yellow and blue bars indicate MIS 1 and 2, respectively. Three paleoclimatic events (the Early Holocene (EH), the Last Deglaciation, and the LGM) are labeled at the top. (For interpretation of the references to colour in this figure legend, the reader is referred to the web version of this article.)

KOPRI 극지연구소

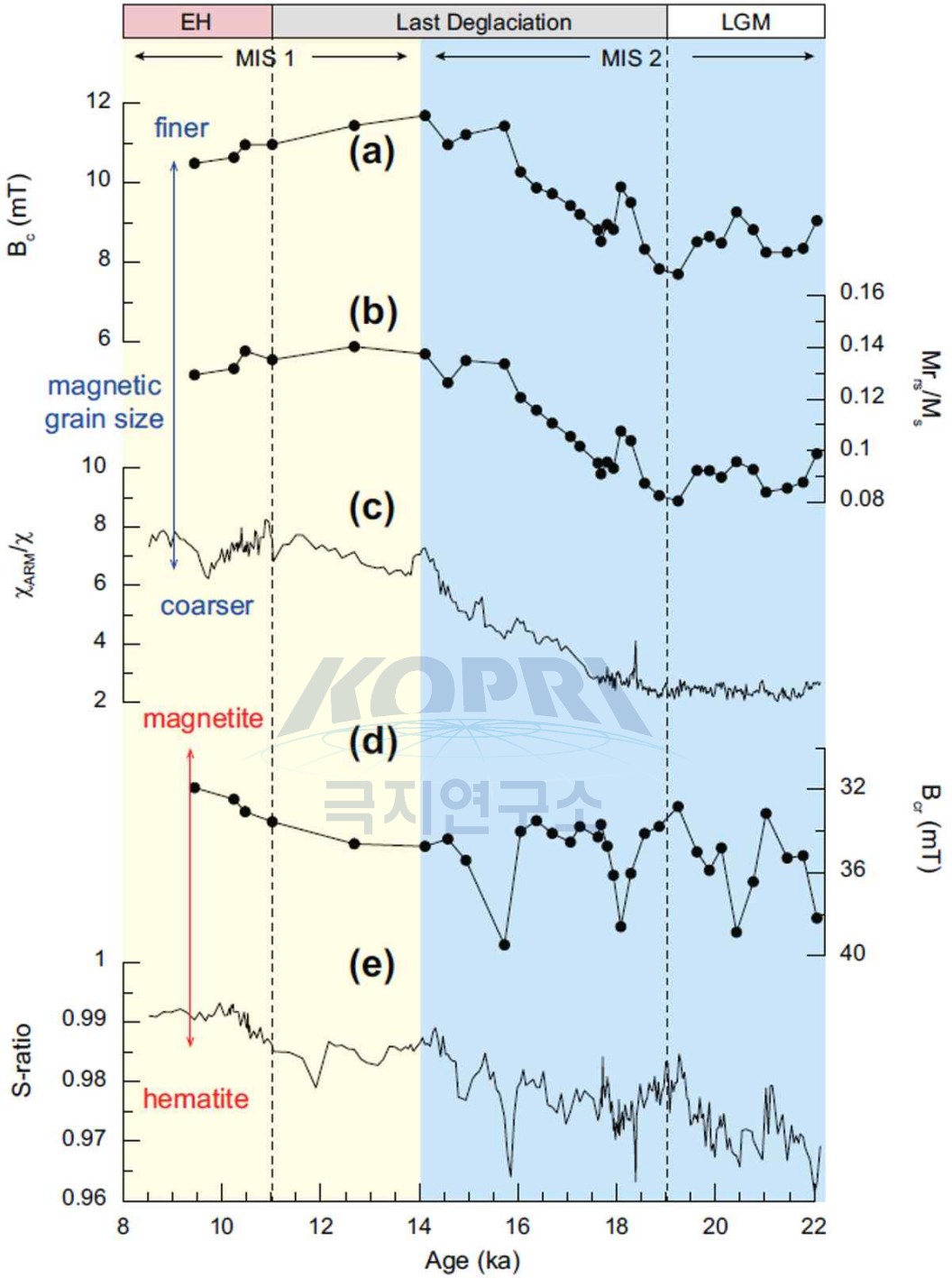


Figure 4. Temporal variations of magnetic composition and grain size parameters. (a) Coercive force (Bc), (b) saturation remanence (Mrs) relative to Ms, and (c) χARM/χ indicate magnetic grain size variations. (d) Remanent coercivity (Bcr) and (e) S-ratio reflect the relative compositions of magnetite and hematite.

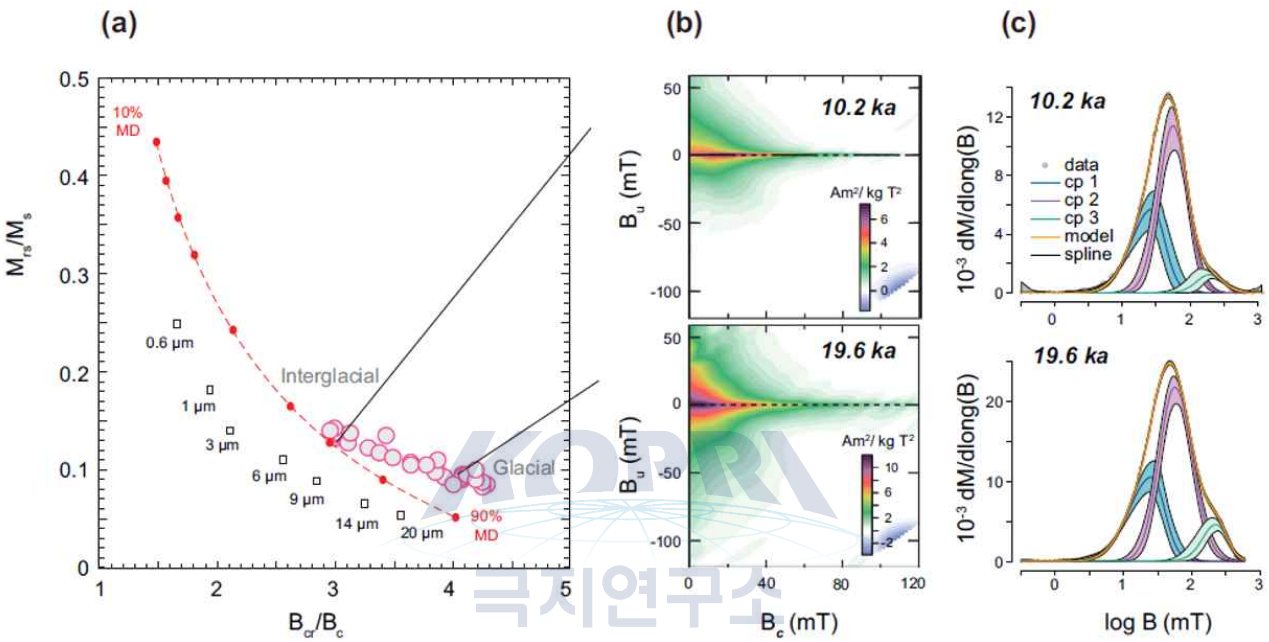


Figure 5. Magnetic grain size and magnetic mineral assemblages for selected bulk sediment samples. Hysteresis ratios (magenta circles) are plotted in the (a) Day plot (Day et al., 1977). The sample ages for hysteresis ratios are the same in Fig. 4b. Red dotted line is a theoretical mixing line of single-domain (SD) and multidomain (MD) magnetite (Carter-Stiglitz et al., 2001; Dunlop and Carter-Stiglitz, 2006). Open squares are hysteresis ratios from unannealed natural-sized titanomagnetite (Dunlop, 2002). For representative interglacial (10.2 ka) and glacial (19.6 ka) samples, (b) FORC diagrams are plotted as Bc versus interaction field (Bu), and (c) IRM coercivity spectra were modeled using three components (cp 1 in blue, cp 2 in purple, and cp 3 in green in order of magnitude). Gray symbols are our data, and the black line is the spline fit. Shaded envelopes represent 95% confidence intervals. (For interpretation of the references to colour in this figure legend, the reader is referred to the web version of this article.)

KOPRI 극지연구소

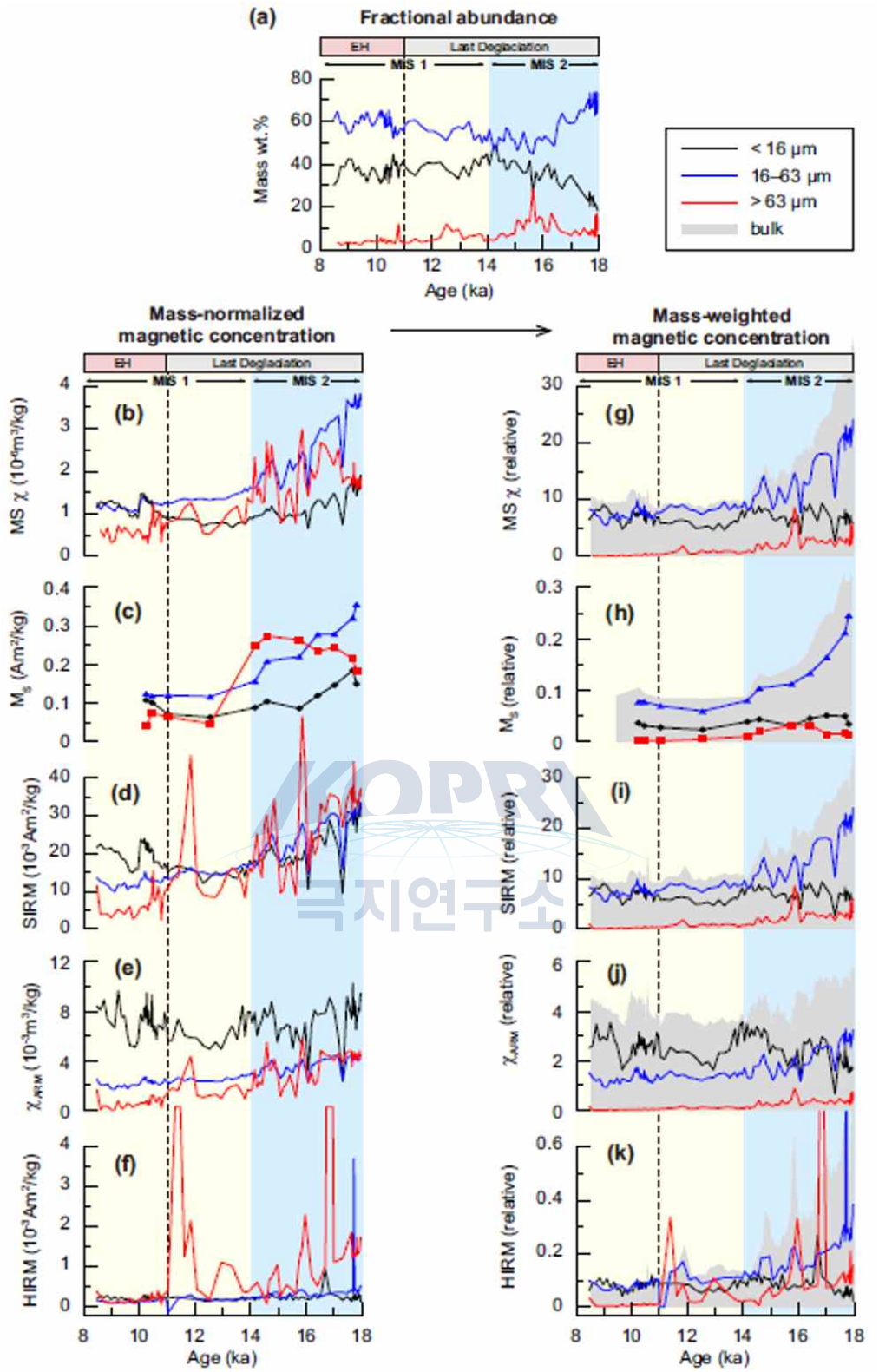


Figure 6. Fractional abundance and magnetic concentration parameters (χ, Ms, SIRM, χARM, and HIRM) of sediment particle-size fractions for the last ~18 kyr. (a) Drymass weight percent (wt%) for three sized fractions (< 16 μm in black, 16-63 μm in blue, and>63 μm in red) indicates the fractional abundance. For each fraction, variations of (b-f) mass-normalized and (g-k) mass-weighted magnetic concentration parameters are presented. The same parameters for bulk sediment are shown as gray shaded in the right panel for comparison. (For interpretation of the references to colour in this figure legend, the reader is referred to the web version of this

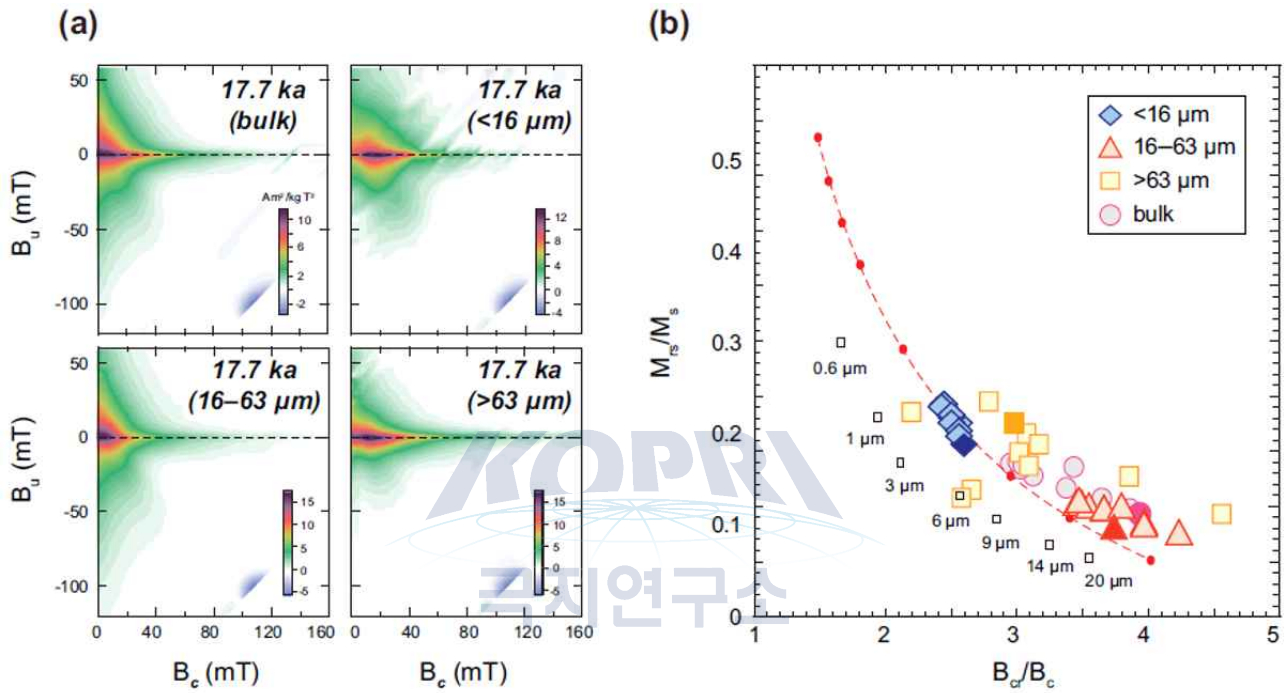


Figure 7. Magnetic mineral assemblages and grain sizes for selected bulk sediment samples and their particle−size fractions. (a) FORC diagrams for bulk and sizefractionated samples at ~17.7 ka are presented. (b) In the Day plot, hysteresis ratios of three fractions (< 16 μm, 16−63 μm, and>63 μm) are marked in blue diamonds, red triangles, and yellow squares, respectively. The sediment ages of 11 samples for each fraction correspond to ~10−18 ka, as the same in Fig. 6c. The bulk hysteresis ratios at the same ages are shown as magenta circles for comparison, and closed symbols corresponds to 17.7 ka samples for the FORC diagrams. See caption of Fig. 5 for the description of the Day plot and FORC diagrams. (For interpretation of the references to colour in this figure legend, the reader is referred to the web version of this article.)

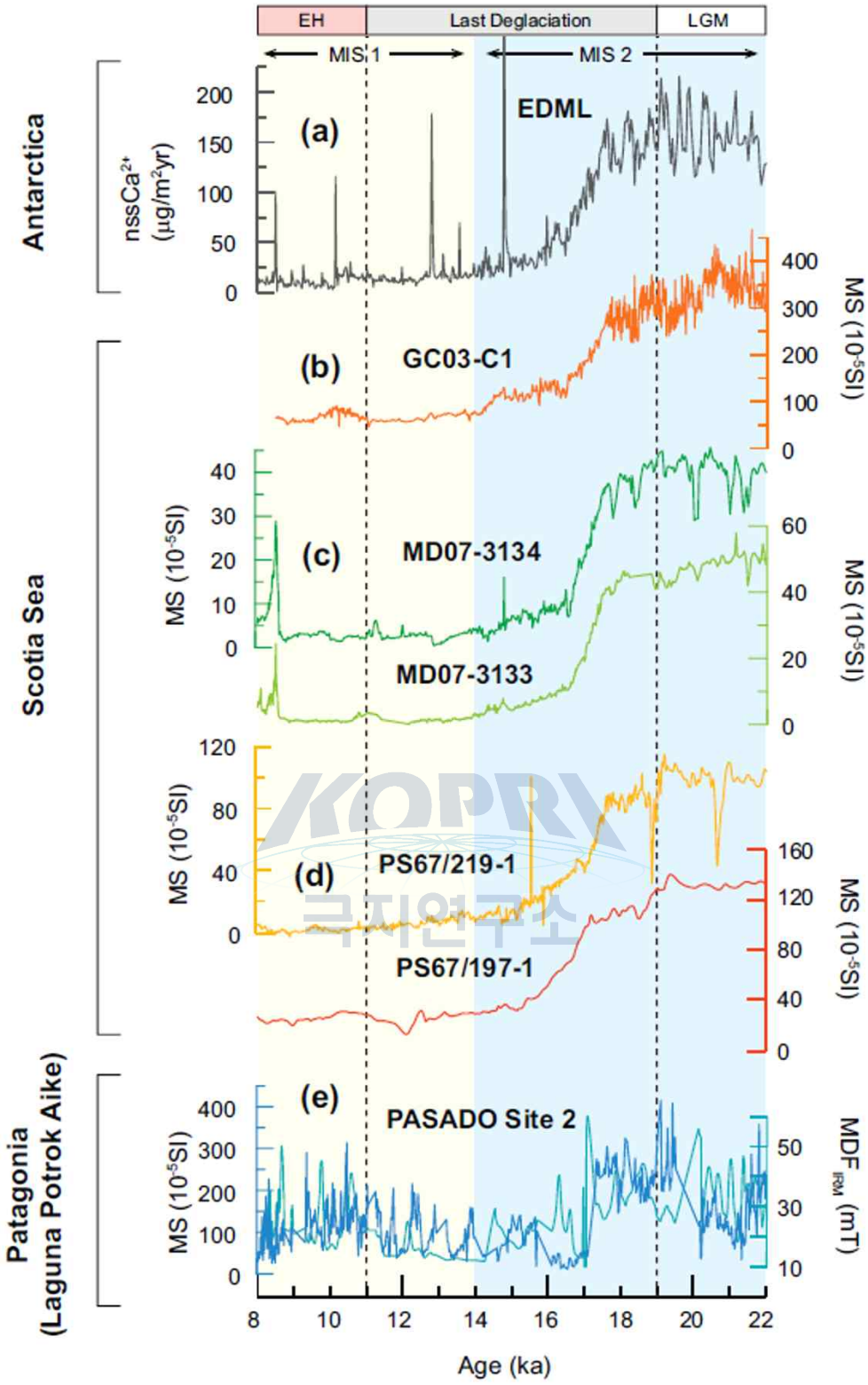


Figure 8. Comparison among Antarctic ice core dust record and MS records in the Scotia Sea and Patagonia. (a) Non-sea-salt Ca2+ (nssCa2+) flux of EDML ice core from Antarctica (Fischer et al., 2007); MS records of (b) GC03-C1 (Bak et al., 2010), (c) MD07-3134 and MD07-3133 (Weber et al., 2012), (d) PS67/219-1 and PS67/197-1 (Xiao et al., 2016) from the Scotia Sea; and (e) MS (dark blue) and median destructive field of IRM (MDFIRM; light blue) from PASADO Site 2 from Laguna Potrok Aike in Patagonia (Lisé-Pronovost et al., 2015). (For interpretation of the references to colour in this figure legend, the reader is referred to the web version of this article.)

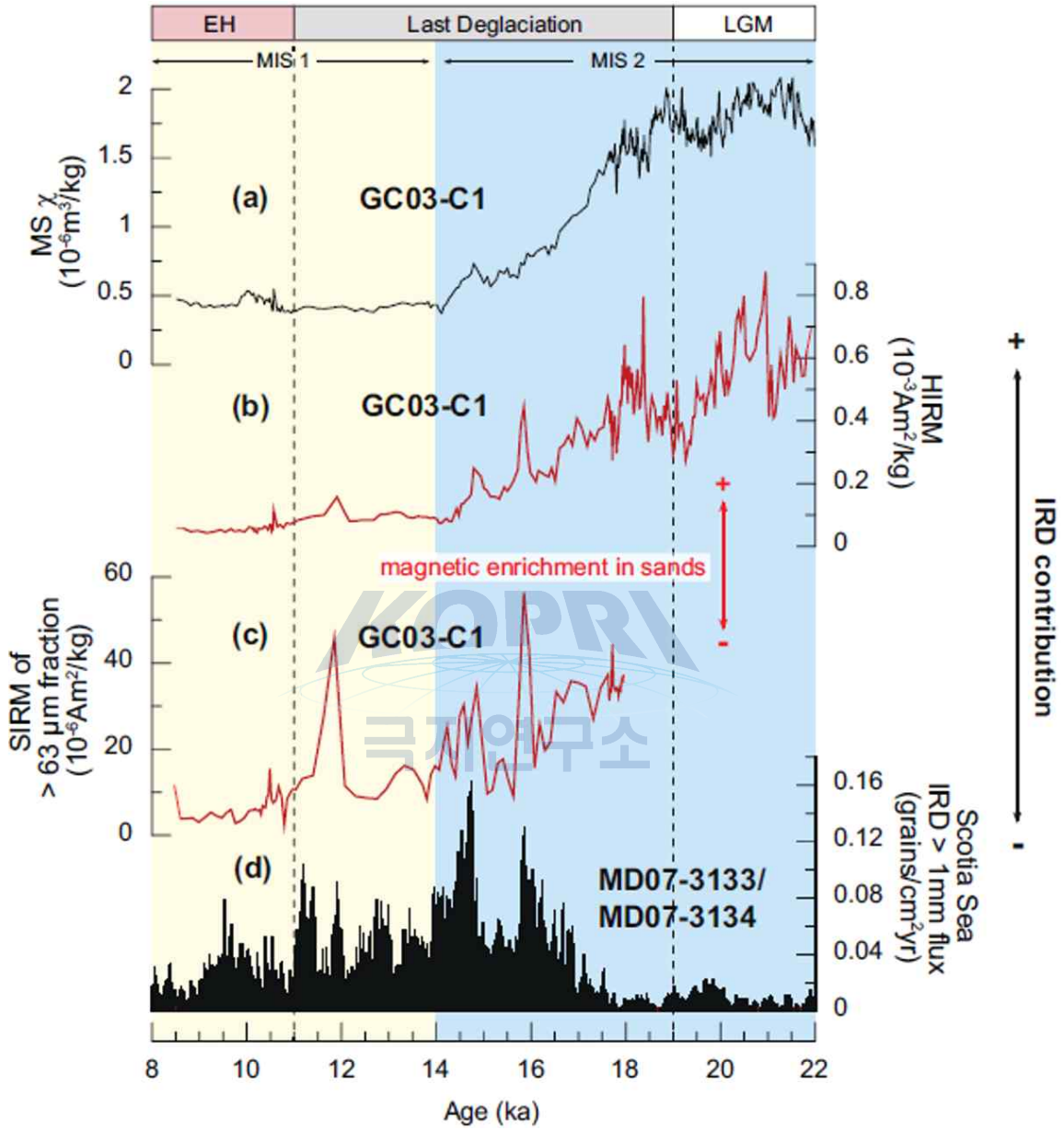


Fig. 9. Comparison between magnetic concentration parameters for core GC03-C1 and Scotia Sea iceberg rafted debris (IRD) flux from Weber et al. (2014). (a) χ and (b) HIRM for GC03-C1 bulk sediments; (c) SIRM of the>63 μm fraction of GC03-C1; and (d) integrated flux of IRD coarser than 1mm (IRD >1mm flux) for cores MD07-3133 and MD07-3134 (Weber et al., 2014).

제 13 장

Paleoceanographic changes in the Southern Ocean off Elephant Island since the last glacial period: links between surface water productivity, nutrient utilization, bottom water currents, and ice-rafted debris[4)]

Sunghan Kim[a], Kyu-Cheul Yoo[a,*], Jae Il Lee[a], Youn Ho Roh[a,b], Young-Suk Bak[c], In-Kwon Um[d], Min Kyung Lee[a], Ho Il Yoon[a]

[a]Korea Polar Research Institute, [b]University of Science and Technology, [c]Jeonbuk National University, [d]Korea Institute of Geoscience and Mineral Resources

Abstract: To understand past changes in ocean-cryosphere interactions in the Southern Ocean off the Antarctic Peninsula, multi-proxy analyses of three sediment cores located off Elephant Island were used to reconstruct changes in paleoproductivity, nutrient utilization, bottom current intensity, and iceberg calving since the last glacial period. The glacial period was characterized by low surface water productivity with high nutrient utilization, indicating surface water stratification. During the deglaciation, surface water productivity increased with decreasing nutrient utilization, implying that the increase is associated with increased nutrient supply from the subsurface water by enhancing Antarctic Circumpolar Current (ACC) influence as fronts migrate southward with warming. Abundant occurrence of grains >1 mm during the deglacial period indicates rapid ice sheet retreat with large-scale melting and calving. During the glacial period, however, coarse silt-fine sand-sized fraction represented ice-rafted debris (IRD). The different IRD grain size characteristics are thought to be related to the IRD source material characteristics. Regardless of IRD input, the running downcore correlation (5 to 9-point) between sortable silt mean grain size and percentage showed that sediments are well sorted by bottom current. However, the cross plot of them showed different temporal relationships. Sediments were sorted by the ACC and southwestward flowing bottom current. Along with southward migration of fronts and the ACC, southwestward flowing bottom current influence diminished, whereas the ACC influence

4) 이 연구 결과는 다음의 논문으로 출판되었음: Kim, S. et al. (2020). "Paleoceanographic changes in the Southern Ocean off Elephant Island since the last glacial period: Links between surface water productivity, nutrient utilization, bottom water currents, and ice-rafted debris." Quaternary Science Reviews 249: 106563.

increased particularly from 7 ka. Our results indicate that the sedimentary processes in the Scotia Sea largely depend on the regional interactions between the ocean and the cryosphere.

1. Introduction

The Southern Ocean is divided into the Antarctic Zone (AZ), Polar Front Zone (PFZ), and Subantarctic Zone (SAZ) (Tréguer and Jacques, 1992; Orsi et al., 1995). Sediment traps and surface sediments along a latitudinal transect showed a close link between Southern Ocean zonation and the total mass flux and composition of sediments (e.g., Honjo et al., 2000; Cárdenas et al., 2019). The position of each zone varies with the latitudinal displacement of the Southern Ocean fronts, which migrate equatorward during cold periods and poleward during warm periods (Gersonde et al., 2005; Kemp et al., 2010; Manoj and Thamban, 2015; Roberts et al. 2017). These frontal migrations can alter the surface oceanography and influence surface water productivity. The latitudinal difference between the Polar Front (PF) and the southern boundary of the Antarctic Circumpolar Current (SBACC) narrows toward the Drake Passage. In addition, the SBACC is related to the extent of the winter sea-ice field (Orsi et al., 1995). Therefore, the northern end of the Antarctic Peninsula is an ideal location to assess changes in surface water conditions in response to frontal/sea-ice variability since the last glacial period.

The estimates of biogenic opal productivity since the last glacial period from the Scotia Sea implied a dominance of open-ocean species (e.g., Fragilariopsis kerguelensis) during high opal productivity and a dominance of Eucampia Antarctica (a dominant glacial species) during low productivity (Burckle and Burak, 1988; Bak et al., 2010, 2014; Xiao et al., 2016). Export production was found to be relatively low during the last glacial maximum (LGM) in the southern Scotia Sea (e.g., Yoon et al., 2007). Sedimentary records from the south Orkney Plateau covering the last 8600 years showed a weakened correlation between biogenic opal and total organic carbon (TOC) after 5 ka (Lee et al., 2010). However, the coupling of biogenic opal and export production since the last glacial period in the Scotia Sea remains inconclusive due to the absence of TOC records. Despite the high biogenic opal production in the Scotia Sea (e.g., Bak et al., 2010; Sprenk et al., 2013; Xiao et al., 2016), the relationship between nutrient utilization and primary production since the last glacial period is unknown. As a result, surface-subsurface water mass exchanges and the controlling mechanisms on surface water productivity since the last glacial remains unclear.

Diatom records from Scotia Sea sediment cores imply an expansion of sea ice during glacial periods (Gersonde et al., 2005; Bak et al., 2010, 2014; Collins et al., 2012; Xiao et al., 2016). Bentley et al. (2014) showed that the grounding line advanced to the continental

shelf break in the northern Antarctic Peninsula at ca. 20 ka, which subsequently retreated in conjunction with increasing global sea level. The sequential sedimentological changes in response to the glacial retreat are likely to be recorded in Scotia Sea sediments. Previously, only the presence of coarse grains (>1 or 2 mm) (e.g., Diekmann et al., 2000; Weber et al., 2012) were interpreted as ice-rafted debris (IRD) in sediment records of the Scotia Sea; however, a recent study shed new light on the grain size distribution of IRD in sediments that coarse silt-fine sand fractions are dominant (Kim et al., 2018a). Analysis of the sedimentary IRD footprint can highlight the depositional processes of IRD in response to oceanographic changes. Moreover, past cryospheric changes in Antarctica likely influenced bottom water conditions due to the presence of numerous deep/bottom water currents in the Scotia Sea (Orsi et al., 1995; Hernández-Molina et al., 2006).

In this study, we present downcore records of surface water productivity (biogenic opal and TOC concentrations), nutrient utilization (δ15N), sedimentology (grain size and abundance of >1 mm), physical property (magnetic susceptibility (MS), and water content (WC)) from three sediment cores off Elephant Island in the Southern Ocean. They are also supported by the diatom assemblage. We aim to reconstruct and assess the relationships between 1) surface water productivity, 2) nutrient utilization, 3) bottom current intensity, and 4) iceberg calving since the last glacial period.

KOPRI 극지연구소

2. Study area

The eastward flowing Antarctic Circumpolar Current (ACC) dominates oceanic circulation in the Scotia Sea, which is located in the Atlantic sector of the Southern Ocean (Fig. 1). The ACC is the world's largest current (Donohue et al., 2016) and consists of various surface and bottom water masses with a total transport volume of >173.3 Sverdrup (1 Sv = 106 m^3S^{-1}).

The occurrence of phytoplankton blooms and begins starts in early spring as the surface water column stabilizes in response to melting ice (Fryxell and Kendrick, 1988). The spatial distribution of phytoplankton is strongly influenced by frontal systems, the sea ice edge, and grazing pressure (Tréguer et al., 1991; Socal et al., 1997). The Antarctic PF and the northern limit of seasonal sea ice are characterized by high biosiliceous production rates (Geibert et al., 2005; Diekmann, 2007), and the SBACC is related to the limit of the winter sea ice field (Xiao et al., 2016).

The Scotia Sea receives terrestrial sediments by ice rafting, oceanic currents, and eolian input (Diekmann et al., 2000; Ó Cofaigh et al., 2001; Weber et al., 2014; Kim et al., 2018a). The Scotia Sea is located at the extension of Iceberg Alley (Anderson and Andrew, 1999)-a

zone of highest iceberg transport from the Weddell Sea. In addition, the Scotia Sea is the most likely location for detecting icebergs based on ALTIBERG database observations (Tournadre et al., 2015) and modeling results (Merino et al., 2016). The Scotia Sea is influenced by the Weddell Sea Deep Water (WSDW) and ACC, consequently the bottom water transport of sediment is important. Various contourite drifts in the Scotia Sea and northwestern Weddell Sea have been reported from Holocene sediments (e.g., Gilbert et al., 1998; Maldonado et al., 2003; Yoon et al., 2007).

3. Material and methods

Sediment cores GC03-C1, BC03-C1 (60°27′S, 55°42′W, 3774 m depth, 892 cm length for GC03-C1 and 32 cm length for BC03-C1), GC03-C2 (60°34′S, 55°55′W, 3750 m depth, 834 cm length), and GC03-C4 (60°33′S, 55°52′W, 3778 m depth, 840 cm length) were collected from the southern Scotia Sea off Elephant Island onboard the R/V Yuzhmorgeologiya during the 2003/2004 Korea Antarctic Research Program (Fig. 1). All cores were opened, described, and sub-sampled at the Korea Polar Research Institute (KOPRI), South Korea.

KOPRI
극지연구소

3.1. Physical properties (MS and WC)

The MS values for all cores were measured at 1 cm intervals on split half core sections using a Bartington MS-2B susceptibility meter at KOPRI. The MS values for GC03-C1 and GC03-C2 were reported in Bak et al. (2010) and Bak et al. (2014), respectively. The MS values for GC03-C4 were reported in Kim et al. (2018a). WC for all cores was measured at 4 cm intervals on 1 cm thick sub-samples. WC was calculated using the following equation. (%) = (mass of wet sediment − (mass of dry sediment + mass of salt)) / mass of wet sediment × 100

3.2. Geochemical proxies (biogenic opal, TOC, and CaCO3 concentrations)

The geochemical proxies for all cores were measured at 2 cm intervals on 1 cm thick sub-samples; however, biogenic opal for cores GC03-C2 and GC03-C4 was measured at 4 cm intervals. Biogenic silica concentrations were measured using a Continuous Flow Analyzer (SKALAR SANplus Analyzer) by the wet-alkaline extraction method modified from DeMaster (1981) at KOPRI (Kim et al., 2018b). Biogenic opal concentrations were calculated by multiplying biogenic silica concentrations by 2.4 (Mortlock and Froelich, 1989), and the

relative error of biogenic silica concentrations was <1%. Total inorganic carbon (TIC) concentrations were measured using a UIC CO2 coulometer (Model CM5240) at KOPRI, and the relative standard deviation was ±0.1%. CaCO3 concentrations were calculated by multiplying TIC concentrations by 8.333, and the relative standard deviation was ±1%. Total carbon (TC) concentrations were measured by an Organic Elemental Analyzer (FLASH 2000 NC Analyzer) with an analytical precision of less than ±0.1%. TOC concentration was calculated as the difference between TC and TIC.

3.3. δ15N values

δ15N (δ15Nacid) values for GC03-C1 were measured at 4 cm intervals following sediment treatment with 20% HCl. To compare δ15Nacid and bulk δ15N, we measured bulk δ15N values from 27 horizons covering a range (low to high) of δ15Nacid values.

Bulk δ15N values for GC03-C2 were measured at 4 cm intervals. All δ15N values were measured using an EA-IRMS (Europa Scientific RoboPrep-CN elemental analyzer & Europa Scientific 20-20 mass spectrometer) at Iso-Analytical Ltd., UK. Nitrogen isotope ratios are expressed in the conventional delta notation, which is the per mil deviation from atmospheric nitrogen. The precision for nitrogen isotopes was approximately ±0.2□.

KOPRI 극지연구소

3.4. Grain size analysis and count of grains >1 mm

We removed all biogenic components-including biogenic opal, organic matter, and CaCO3-from the bulk sediments using sodium hydroxide, hydrogen peroxide, and hydrochloric acid, respectively. The grain size was then analyzed at 8 cm intervals for all cores using a laser diffraction particle analyzer (Microtrac S3500) at the Korea Institute of Geoscience and Mineral Resources. We classified the sediments following the scheme by Folk and Ward (1957). The mean grain size (MGS) within the range of 10-63 μm was calculated for sortable silt (SS: 10-63 μm). The volume percentages for 10 and 63 μm were calculated by interpolation of the two nearest values, as suggested in McCave and Andrews (2019).

We took X-radiographs of center slices (1 cm thick x 5 cm width x 30 cm length) removed from each core section. Finally, grains >1 mm in diameter were manually counted every 1 cm on the X-radiographs.

3.5. Diatom assemblage

Diatom assemblages for GC03-C1 are reported in Bak et al. (2010); assemblages were analyzed at 4 cm intervals in the above 316 cm interval which has low MS values and were

analyzed at 12 cm intervals in the below 316 cm interval which has high MS values. Up to 200 diatom valves were counted per sample; Chaetoceros resting spores were excluded in the specimen count. Diatom assemblages in GC03-C2 are reported in Bak et al. (2014). To understand the general changes in the surface water environment since the LGM, the dominant diatom species that appeared in GC03-C1 were counted in GC03-C2 (Bak et al., 2014). As Chaetoceros resting spores in GC03-C2 were not counted and not presented in Bak et al. (2014), we counted the Chaetoceros resting spores for GC03-C2 in this study using the same diatom slides. The total diatom abundance of GC03-C1 and GC03-C2 is Chaetoceros-free.

4. Age model

The age model for cores GC03-C1 was established by combination of AMS 14C dates of acid insoluble organic matter (AIOM) and MS correlation with the European Project for Ice Coring in Antarctica (EPICA) Dronning Maud Land (EDML) ice core nssCa2+ record (Shin et al., 2020). AIOM AMS 14C dates were corrected by the box core top age and calibrated with no local reservoir age ($\Delta R=0$) using CALIB 7.1 software (Stuiver and Reimer, 1993) with the MARINE13 dataset (Reimer et al., 2013) following Lee et al. (2010). Six AIOM AMS 14C dates were used as tie points from the interval of <15 ka. From the high MS interval of >12.5 ka, seven tie points were set by the MS-EDML dust record correlations together with comparisons to the MS values of MD07-3133 and MD07-3134 in the Scotia Sea (Weber et al., 2012). The two cores are highly correlated to the EDML dust record and have very high sedimentation rates.

The age model for GC03-C2 was also established by combination of AMS 14C dates of AIOM and MS correlation with the EDML ice core nssCa2+ record (Kim et al., 2018a). The age model for GC03-C4 was established by MS correlation with GC03-C2 (Kim et al., 2018a).

5. Results

5.1. Geochemical and physical proxies and bulk δ15N

We observed high MS values for all cores prior to 17.6 ka at >200 10-6 x CGS; this decreased to <100 x 10-6 CGS after 15 ka (Fig. 2). Trends in biogenic opal, TOC concentrations, and WC co-varied and showed opposite trends to the MS variability, with lower values before 17.6 ka and increasing values across the transition period corresponding

to the deglacial period (17.6 to 10 ka) (Fig. 2). We identified no significant differences in TOC concentrations between the three cores; however, biogenic opal concentrations of GC03-C1 were generally 10% higher than those of cores GC03-C2 and GC03-C4 (Fig. 2). Biogenic opal concentrations in cores GC03-C2 and GC03-C4 gradually decreased from 7 ka (Fig. 2). TOC concentrations reached a maximum at 15 ka; this was followed by a decrease until 7 ka, after which the values remained constant (<0.5%) (Fig. 2). The C/N ratios of the three cores showed similar variability to MS, with high values (>10) before 17.6 ka and a decreasing trend (to <10) thereafter 17.6 ka, though some values were out-ranged (Fig. 2). The C/N ratios from GC03-C1 after 15 ka is generally lower than those of cores GC03-C2 and GC03-C4 (Fig. 2). We observed higher (>6□) bulk δ15N values before 17.6 ka in GC03-C2, which was followed by a gradual decrease to 3□ (Fig. 2). δ15Nacid values for GC03-C1 are ~ 1□ lower than those of GC03-C2; however, both cores showed a similar variation pattern, with higher values (4-5□) before 17.6 ka and a gradual decrease to 2□ thereafter (Fig. 2). We observed a significant correlation between bulk δ15N and δ15Nacid for GC03-C1 (r2 = 0.94, n=27). The results are provided in Supplementary information 1.

5.2. Grain size and abundance of grain >1 mm

Grain size analysis showed coarser MGS (>30 μm) before 17.6 ka in all three cores; this was followed by a decrease to 15 μm until 15 ka. MGS then gradually coarsened toward the core top (up to 20 μm) and was accompanied by an increasing proportion of silt (Fig. 3). The sand fraction for all three cores co-varied and was comparable to the MS trend, with higher values (>20%) before 17.6 ka followed by a subsequent decrease to <10% until 15 ka (Fig. 3). The silt fraction for all cores was lower before 17.6 ka, which then increased with decreasing MS and sand fraction until 15 ka; this continued to increase to almost 80% (Fig. 3). The clay fraction was low (<6%) before 17.6 ka, and sharply increased to 15% at 17.6 ka; this was followed by a gradual decrease to <6% (Fig. 3). SS MGS decreased from >30 μm during the glacial period to 23 μm at 7 ka; it then increased up-core to 27 μm. Grains >1 mm occurred throughout the records in all three cores, but were most abundant from 17.6 ka to 9 ka (Fig. 3). The results are provided in Supplementary information 1.

5.3. Diatom assemblage

Diatom assemblage of GC03-C1 was reported in Bak et al. (2010). Total diatom valves were low (<4 x107/g) in the high MS interval before 17.6 ka, whereas were high (>10 x107/g) in the low MS interval after 15 ka (Fig. 4). High MS intervals are characterized by

low relative abundance of F. kerguelensis (20%) and high relative abundances of Actinocyclus actinochilus (15%) and E. antarctica var. recta (20%), whereas low MS intervals are characterized by high relative abundance of F. kerguelensis (80%) and low relative abundances of A. actinochilus (<5%) and E. antarctica var. recta (<5%). Chaetoceros resting spores showed high abundances (up to 80 x106 valves/g) during 15 to 10 ka (Fig. 4).

Diatom assemblage of GC03-C2 was reported in Bak et al. (2014). Like GC03-C1, total diatom valves were low (<2 x107/g) in the high MS interval before 17.6 ka, whereas were high (>6 x107/g) in the low MS interval after 17.6 ka (Fig. 4). The high MS interval is characterized by low relative abundance of F. kerguelensis and high relative abundance of A. actinochilus, whereas the low MS interval is characterized by the opposite (Fig. 4). Trace amounts of Chaetoceros resting spores were observed in GC03-C2 before 17.6 ka; they reached a maximum abundance (25 x106 valves/g) at 11 ka and began to decrease from 7 ka (Fig. 4). We observed similar variations in Chaetoceros resting spore abundance for both GC03-C2 and GC03-C1, but Chaetoceros resting spores are much higher in GC03-C1. The diatom data shown in this study are provided in Supplementary information 1.

6. Discussion

KOPRI
극지연구소

6.1. Variability in surface water productivity and nutrient utilization

As biogenic opal concentrations showed similar variability to total diatom abundance (r^2=0.67, n=127, $p<0.05$ for GC03-C1 and r^2=0.47, n=41, $p<0.05$ for GC03-C2) (Fig. 5), we assume that changes in biogenic opal concentrations reflect changes in diatom productivity change, which is consistent with previous studies (Xiao et al., 2016). Relatively lower r^2 value with a lower regression slope for GC03-C2 than GC03-C1 can be thought to be due to underestimation of total diatom counts (Fig. 5). The total diatom counts could be underestimated by not including Chaetoceros resting spores in this study. Because the correlation does not become significantly better by including Chaetoceros resting spores to total diatom counts, it is considered not the main reason. In addition, the abundance of total diatom values and Chaetoceros resting spores in both cores are consistent with previously reported values from the same region (Crosta et al., 1997). Because diatom preservation status is often related to diatom abundance and/or biogenic opal concentration, the lower total diatom counts and Chaetoceros resting spores of GC03-C2 are considered to be related to lower biogenic opal concentrations. Considering different methods for both biogenic opal concentration and diatom assemblage analysis, r^2 of 0.47 is considered as a good correlation.

There was a good correlation between biogenic opal and TOC concentrations in all

three cores (r=0.90, n=447 for GC03-C1, r=0.74, n=201 for GC03-C2, and r=0.65, n=210 for GC03-C4 with $p<0.05$ for all cores), indicating that diatom production had dominated the total primary production in the southern Scotia Sea since the last glacial period (Fig. 2). As F. kerguelensis was reported as an important contributor to carbon transfer to depth (Grigorov et al., 2014), F. kerguelensis-dominant diatom assemblage of all cores can cause good correlations between biogenic opal and TOC. This is in agreement with previous studies that have identified high diatom production in the Southern Ocean south of the PF (Honjo et al., 2000). As C/N ratios are lower in marine organic matter relative to terrestrial organic matter (Lamb et al., 2006 and references therein), the lower C/N ratios after 17.6 ka may be indicative of high diatom organic matter (Fig. 2).

The biogenic opal and diatom abundance records indicate lower surface water productivity during the glacial period (before 17.6 ka) relative to the Holocene (Figs. 2 and 4). The deglacial period is characterized by decreases in sea ice diatoms (A. actinochilus; Armand et al., 2005) and the glacial dominant species (E. antarctica var. recta) and increases in both open ocean species (F. kerguelensis) and Chaetoceros resting spores, and total diatom valves (Bak et al., 2010, 2014, Fig. 4). The sea ice diatom F. curta did not show a clear change during the deglacial period; however, the decreased abundances of sea ice species A. actinochilus and cold water mass species E. antarctica var. recta (Leventer et al., 2002) imply reduced sea ice during the deglaciation. These findings indicate increased surface water productivity in response to sea ice retreat and an increased influence of the ACC in the Scotia Sea. The dominance of F. kerguelensis in other sediment cores PS67/197-1 and PS67/219-1 in the Scotia Sea also suggests increased interglacial opal production under open ocean conditions (Xiao et al., 2016). Thus, it has been suggested that an increase in surface water productivity during interglacial periods is related to retreat of sea ice which inhibits light availability.

As the SBACC is related to the winter sea ice extent (Xiao et al., 2016 and references therein), the sea ice retreat during the deglaciation is likely accompanied by the increasing influence of the ACC on the core site (Roberts et al., 2017). However, despite the importance of the ACC on surface water production, past changes in the influence of the ACC in the Scotia Sea have not yet been considered in terms of surface water productivity. Bulk $\delta^{15}N$ has been used as a nitrate utilization proxy (Francois et al., 1992; Altabet and Francois, 1994), including in the western Antarctic Peninsula (Kim et al., 2018b). As Schubert and Calvert (2001) reported the presence of inorganic nitrogen (IN) in the polar region (Arctic), we compared the $\delta^{15}N_{acid}$ and the bulk $\delta^{15}N$ trend to determine the isotopic influence of IN in GC03-C1 (e.g., Nie et al., 2014). Since the trends are almost identical with r^2 of 0.94 (Fig. 2), we conclude that the influence of IN is negligible; consequently, $\delta^{15}N_{acid}$ in GC03-C1 and bulk $\delta^{15}N$ in GC03-C2 can be compared without any analytical offset.

Despite the ~1□ difference between δ15Nacid in GC03-C1 (lower) and bulk δ15N in GC03-C2 (higher), the two records indicate higher nutrient utilization during the last glacial period relative to the Holocene (Fig. 2). If surface water productivity is predominantly controlled by changes in sea ice extent, we expect to observe enhanced nutrient utilization at the core sites due to increased light availability in response to sea ice retreat. However, nitrate utilization decreased despite increased surface water productivity and reduced sea ice influence (Fig. 2). To explain increased export and diatom production in the surface water with decreased nutrient utilization, the total amount of nutrient supplied should be increased. Since this is typical of a place characterized by enhanced nutrient supply from sub-surface water (e.g., Brzezinski et al., 2002; Brunelle et al., 2010; Studer et al., 2015; Kim et al., 2018b), increased surface water productivity in the Scotia Sea since the deglaciation is likely related to increased sub-surface nutrient supply by a strengthening ACC in response to sea ice retreat. This is consistent that a southward shift of all fronts during deglacial period occurred with enhancing ACC in the Drake Passage (Roberts et al., 2017). Thus, our results suggest that nutrient availability associated with the ACC-sea ice balance was the dominant control on surface water productivity in the Scotia Sea during the deglaciation.

Bulk δ15N values-and therefore nutrient utilization-continued to decrease until the late Holocene (Fig. 2). According to the trends in biogenic opal and diatom abundance, diatom production at cores GC03-C2 and GC03-C4 began to decrease gradually after 7 ka (Figs. 2 and 4); this suggests a change in the relationship between diatom production and nutrient utilization after 7 ka (Figs. 2 and 6). We observed a negative and positive relationship between biogenic opal production and nutrient utilization before and after 7 ka, respectively (Fig. 6). The positive relationship after 7 ka may be due to a deepening of the mixed layer depth (MLD) and/or increasing sea ice extent. The diatom assemblage record for GC03-C2 after 7 ka showed low/insignificant variability of sea ice species (including F. curta) and an increasing abundance of the cold water species E. antarctica var. recta (Fig. 4). McCave et al. (2014) reported a faster ACC during the Holocene relative to the glacial period in the sea ice zone south of 56캳. A strengthened ACC at the core site would have caused a deepening of the MLD (i.e., cooling in the surface ocean). A deepening MLD is also supported by the decreased abundance of Chaetoceros resting spores in GC03-C2 since 7 ka (Fig. 4), which are indicative of high production and melt water stratification (Leventer 1991; Leventer et al., 1996; Crosta et al., 2004). The lower export production per diatom production after 7 ka also supports a deepening of the MLD (Fig. 6a).

TOC concentrations are similar between all cores, but biogenic opal concentrations are significantly higher in GC03-C1 (Fig. 2). Diatom Si/NO3- uptake ratios are dependent on Fe availability, with high (low) ratios coinciding with low (high) Fe concentrations (Hutchins and Bruland, 1998; Hutchins et al., 2002). Fe concentrations decrease with increasing distance

from the Antarctic continent in the western Antarctic Peninsula (De Jong et al., 2015). The geomorphology of our study region causes the fronts to merge at our core sites, our results therefore show that the small latitudinal differences between the core sites can result in significant differences in Fe concentrations. However, due to the wide frontal distribution in the central to eastern Scotia Sea, core records located in this region showed no decreasing trends in biogenic opal (e.g., Sprenk et al., 2013; Xiao et al., 2016).

Bulk δ15N is influenced by both nutrient utilization and changes in diatom assemblage (Needoba et al., 2003; Horn et al., 2011). It is difficult to identify strong correlations between diatom assemblage and bulk δ15N (or δ15Nacid) variability in cores GC03-C1 and GC03-C2 (Bak et al., 2010, 2014) (Fig. 2); this suggests that bulk δ15N values more likely reflect changes in diatom nutrient utilization in Scotia Sea surface water. Despite minor offsets, the δ15N values of pennate, central, and total diatoms were found to co-vary (Studer et al., 2015). In addition, bulk δ15N was found to reflect as nutrient utilization in the west Antarctic Peninsula (Kim et al., 2018b). Sedimentary records of diatom assemblages reflect the diatoms that are preserved rather than diatoms that lived in the surface water (Crosta and Koç, 2007); therefore, it is more likely that δ15N values reflect the total nutrient utilization of phytoplankton-dominated by diatom production-in the surface water.

KOPRI 극지연구소

6.2. Iceberg calving activity since the last glacial period

Down-core coarse-grain abundances have been used as an indicator for IRD in the Southern Ocean (Diekmann et al., 2000; Weber et al., 2012, 2014). Weber et al. (2014) reported that increased IRD during the last deglacial period in the Scotia Sea is indicative of large-scale iceberg calving during ice sheet/shelf retreat. Grains >1 mm were observed throughout all cores; however, higher abundance was observed during the last deglaciation (17.6-9 ka) in the southern Scotia Sea (Fig. 3). This suggests continued iceberg calving since the last glacial period in the southern Scotia Sea, with highest activity during the deglaciation. The high abundance of Chaetoceros resting spores-indicative of high productivity and melt water stratification (Leventer 1991; Leventer et al., 1996; Crosta et al., 2004)-also indicates large-scale ice melting and the rapid retreat of the Antarctic Peninsula and/or Weddell Sea ice sheets in response to deglacial warming (Fig. 4). We observed highest abundance of grains >1 mm in all three cores from 16-14.5 ka and 11.1-9 ka coinciding with increases in the relative abundance of open ocean diatoms such as F. kerguelensis at GC03-C1 (Figs. 3 and 4). These time periods correspond to previously reported intervals of high IRD flux to the Scotia Sea (Weber et al., 2014), indicating the potential contribution of ice sheet/shelf melting to global sea level rise. Because clay fraction of GC03-C2 and GC03-C4 showed relatively high values (ca. 15%) between 17.6 and 12.5 ka (Fig. 3), it can be interpreted that clay

supply increased during ice sheet/shelf melting and retreating. Therefore, our results indicate rapid reduction of ice sheets/shelves in the Weddell Sea and the west Antarctic Peninsula in response to oceanic forcing from sea ice retreat and atmospheric warming (Fig. 3i; Jouzel et al., 2007).

A wide range of grain size—including coarse grains (> 1mm)—can act as an indicator for IRD (Andrews, 2000; Jonkers et al., 2012, 2015; McCave and Andrews, 2019). For example, analysis of sediment grain size distribution in Svalbard icebergs showed that the grains were predominantly ranged from coarse silt to fine sand (Jonkers et al., 2015). Studies have identified strong correlations between sediment core MS records in the Scotia Sea and the EDML ice core dust record (e.g., Pugh et al., 2009; Weber et al., 2012; Xiao et al., 2016; Kim et al., 2018a; Shin et al., 2020). However, proposed mechanisms were different. Kim et al. (2018a) found good correlations between the MS values and grain size (particularly with coarse silt to fine sand—sized grains of 16 – 250 μm) from southern Scotia Sea cores including GC03—C2 and GC03—C4, and they interpreted that the coarse silt to fine sand—sized grains having high MS values were delivered as IRD during the glacial period. Although biogenic magnetite was suggested to control MS values in the sub—Antarctic Indian Ocean which is far from the Scotia Sea (Yamazaki and Ikehara, 2012), Shin et al. (2020) reported that coarse silt to fine sand grains having high MS values were delivered as IRD during the glacial period based on magnetic properties. The strong correlations between MS, MGS, and the sand fraction in all cores suggest that high MS values during glacial periods are related to grain size, particularly the coarse silt to fine sand fraction (Figs. 3 and 7). Thus, the high MS variation of all cores implies that the iceberg calving was more active during the glacial period and decreased from 17.6 ka.

Intriguingly, grain size distribution of IRD in sediments are different; with coarse silt to fine sand dominant size during the glacial period vs with more grains >1 mm during the deglacial period (Fig. 3). If IRD source material is assumed same including grain size distribution and provenance between two different time intervals, the discrepancy must be related to depositional process. A high flow speed can cause reduced deposition rate of fine fraction, but sand sized grains are considered difficult to be moved. MS values/g and magnetic properties of sand and coarse silt fractions vary between the glacial and deglacial period in GC03—C1 (Shin et al. 2020). The relative abundance of sand and coarse silt fractions can vary, but similar values are expected if IRD source material is same. Thus, the different characteristics of IRD between the glacial and deglacial period indicate that IRD source characteristics are different.

Because the study area is located at the extension of Iceberg Alley (Fig. 1), the study area receives a mixture of icebergs from all around the Antarctica. This means that it is difficult to identify the IRD provenance in our cores. There is a possibility that the study site

received IRDs originating from the western part of Antarctic Peninsula Ice sheet/shelf during the glacial period when ice sheet/shelf reached close to the shelf break (Bentley et al., 2014). Nevertheless, it is difficult to confine its source region in this study due to lack of detailed information on properties of potential source regions. Of note is that the size characteristics of IRD during glacial and deglacial periods are different in the Scotia Sea. Thus, the IRD estimation by the coarse fraction can lead to underestimation of iceberg calving particularly during glacial periods in response to ice-sheet expansion in the Scotia Sea (Jonkers et al., 2015 and Kim et al., 2018a). Although smaller sizes (125 or 150 μm) were applied for determining IRD in other regions of the Antarctica (e.g., Passchier, 2011; Patterson et al., 2014), our results still suggest potential underestimation of iceberg calving during glacial periods. To fully understand iceberg calving history in the Antarctica, further studies are required.

6.3. Bottom current intensity changes in the Scotia Sea

The SS MGS is commonly used to reconstruct bottom current intensity (McCave et al., 1995, 2017; McCave and Andrews, 2019) and bottom current speed (e.g., Bianchi and McCave, 1999; Boessenkool et al., 2007; Jonkers et al., 2015; Wu et al., 2018). IRD deposition has the potential to influence the SS MGS (Jonkers et al., 2015), as IRD is not only limited to the coarse-grain size fraction (e.g., Dowdeswell and Dowdeswell, 1989; Andrews, 2000; Jonkers et al., 2012, 2015; Kim et al., 2018a). IRD input can influence MGS of SS such that it does not reflect flow speed (Jonkers et al., 2015). If sediments are predominantly current-sorted, McCave and Andrews (2019) argue that SS MGS records can provide reliable paleo-current data, despite the input of IRD. Thus, it is necessary to be assessed if the SS MGS during the glacial period can be used as an indicator for paleo current intensity.

Well sorted surface sediments by the bottom current showed a good correlation between the SS MGS and SS% (McCave and Andrews, 2019). Although the running downcore correlations (5 to 9-point) in GC03-C4 showed <0.5 before 12.5 ka, they were generally >0.5 in GC03-C1 and GC03-C2, except for some short intervals (Fig. 7). According to McCave and Andrews (2019), this indicates that the SS MGS can be used as a paleo-current speed indicator in this study regardless of IRD influence.

All three cores are divided into three intervals; the glacial period with high MS values, deglacial period, and the Holocene with low MS values, thus linear regressions were calculated by each period (Fig. 8). The relationship between the SS MGS and SS% at GC03-C1 clearly suggests that SS is well current-sorted for all time intervals, but with different slopes (Fig. 8a). In contrast, the relationships at GC03-C2 and GC03-C4 showed

relatively high to low correlations for the glacial and deglacial periods (Fig. 8). Nevertheless, the relationships in all cores for the Holocene showed strong correlations (Fig. 8). This is probably related to characteristics of input sediments and this clearly suggests that changes in SS MGS needs to be discussed by the different time periods.

Based on the SS MGS changes between the Holocene and the last glacial period, the ACC bottom current (i.e., the intensity of the ACC) was studied in the Drake Passage and the Scotia Sea (McCave et al., 2014). SS MGS is coarser during the glacial period than the Holocene (Fig. 3). Coarser SS MGS during the LGM was also found from the eastern Scotia Sea core located near the SBACC (McCave et al., 2014). If the influencing bottom current was the ACC during the glacial period, it means that the ACC was enhanced during the glacial period under more extensive sea ice and northward migrated fronts. Thus, the bottom current during the glacial period in the study area was not related to the ACC. Drift sediments are well developed in the Antarctic Peninsula margin in association with southwestward flowing bottom current (Barker and Camerlenghi, 2002), and Lucchi et al. (2002) and Lucchi and Rebesco (2007) reported contourite deposition during glacial periods indicating the presence of southwestward flowing bottom current. Considering the direction of the bottom current and the location of our cores, the study site was most likely influenced by the southwestward flowing bottom current during the glacial period under more extensive sea ice and northward migrated fronts conditions accompanying with weakened ACC influence on the site. As the relationships between the SS MGS and SS% are different between the Holocene and the glacial period (Fig. 8), paleo-current intensity comparison between the Holocene and the glacial period by SS MGS need a caution. Nevertheless, ~10 μm difference suggests that the bottom current speed was faster during the glacial period.

All cores showed a continuous decrease in the SS MGS during the deglacial period (Fig. 3) and good correlations between the SS MGS and SS% are found in GC03-C1 and GC03-C2 during the deglacial period (Fig. 8). This indicates that the bottom current intensity continuously decreased with climate warming accompanying with southward migration of fronts. Thus, the southwestward flowing bottom current is thought to be weakened probably due to southward migration.

The SS MGS started to increase from 7 ka in GC03-C2 and GC03-C4 (Fig. 3). This implies a strengthening bottom current from the early to the late Holocene in the southern Scotia Sea. Since our core site is close to the SBACC in modern days (Orsi et al., 1995), the dominant bottom current must be the ACC during the Holocene. The deepening of the MLD after 7 ka also supports increased influence of the ACC. Thus, the increasing SS MGS from 7 ka suggests a strengthening ACC. In addition, the enhancing ACC at our sites indicates is related to ongoing southward migration.

6.4. Ocean–cryosphere interactions in the Scotia Sea since the last glacial period

The schematic environmental model for the last glacial period was presented in Figure 9a. The last glacial period was characterized by extensive sea ice and an advanced ice shelf (Gersonde et al., 2005; Bak et al., 2010, 2014; Collins et al., 2012; Bentley et al., 2014; Xiao et al., 2016). All fronts including the SBACC therefore shifted northward during the last glacial period, which reduced the influence of the ACC in the study site. The diatom production decreased accompanying with enhanced nutrient utilization, indicating increased surface water stratification (Figs. 2 and 4). Iceberg calving was active and coarse silt to fine sand grains were dominantly supplied as IRD with less grains > 1 mm. Good correlations between the SS MGS and SS% in GC03–C1 and GC03–C2 indicate that the sediments are sorted by the southwestward flowing bottom current. Southwestward flowing bottom current was enhanced under weakened ACC influence contemporaneously with northward migration of fronts.

The schematic environmental model for the deglacial period was presented in Figure 9b. Sea ice retreat after 17.6 ka created open ocean conditions in the southern Scotia Sea (Bak et al., 2010, 2014; Xiao et al., 2016); this caused an increase in surface water productivity. Because nutrient utilization was not increased accompanying with increased light penetration, more nutrients were supplied from the subsurface water in response to the southward migration of fronts including the SBACC during the deglaciation. Iceberg calving also occurred during the deglaciation contemporaneously with rapid ice shelf/sheet break; however, grains >1 mm were abundantly deposited (Fig. 9b). Good correlations between the SS MGS and SS% in GC03–C1 and GC03–C2 indicate that the sediments are sorted by the southwestward flowing bottom current. The southwestward flowing bottom current became weak contemporaneously with climate warming.

The schematic environmental model for the Holocene was presented in Figure 9c. Surface water production started to decrease at 7 ka with a shift of the relationship between surface water production and nutrient utilization from being negative to positive. Decreases in surface water production and nutrient utilization and an increase in cold water diatom species after 7 ka indicate further deepening of the MLD, deeper than euphotic zone, associated with the enhanced ACC. High correlations between the SS MGS and SS% indicate that the SS is sorted by bottom current. The SS MGS continued to increase after 7 ka, indicating the increased ACC bottom current. This means that southward migration of the ACC and other fronts persisted from 7 ka.

7. Conclusions

We reconstructed the past variability of surface water productivity, nutrient utilization, bottom current intensity, and iceberg calving since the last glacial period using three sediment cores (GC03-C1, -C2, and -C4) in the Southern Ocean off Elephant Island. During the last deglaciation, surface water productivity increased with decreased nutrient utilization as sea ice retreats, indicating enhanced subsurface nutrient supply in response to an intensified surface current. Diatom production decreased along with decreased nutrient utilization from 7 ka due to deeper MLD than euphotic zone derived by enhancing ACC with further southward migration.

Running downcore correlations of the SS MGS and SS% of all cores indicate that sediments are sorted by bottom currents regardless of IRD influence. However, the slopes were different among different time intervals. Bottom current speed decreased during the deglacial period with southward migration of the ACC and fronts, implying that the dominant bottom current was most likely southwestward flowing bottom current. The influence of the ACC started to increase from 7 ka with further southward migration of the ACC and fronts.

Coarse silt to fine sand sized grains with sparse grains >1 mm were the dominant IRD grain size in sediments of the glacial period. In contrast, during the deglacial period, grains >1 mm occurred abundantly, which indicates large-scale ice melting and the rapid retreat of ice sheets during the deglaciation. Although the source IRD regions for the glacial and deglacial periods are know sure, the different grain size characteristics of IRD in sediments are thought to reflect different IRD source characteristics. Our multi-proxy records show that the sedimentary processes in the Southern Ocean off Elephant Island were significantly linked to the dynamics of the ocean-cryosphere system.

KOPRI 극지연구소

지난 마지막 빙하기 이후 엘레펀트 섬 인근의 남빙양에서의 고해양 변화: 표층생산성, 영양염 이용률, 저층류, 빙하쇄설성 퇴적물의 연관성

김성한[a], 유규철[a,*], 이재일[a], 노연호[a,b], 박영숙[c], 엄인권[d], 이민경[a], 윤호일[a]

[a]극지연구소, [b]UST과학기술연합대학원대학, [c]전북대학교, [d]한국지질자원연구원

요약: 남극반도 인근의 남빙양에서 해양과 빙권의 상호작용의 과거 변화를 이해하기 위해, 엘리펀트섬 인근에서 획득된 3개의 퇴적물 코어에서 멀티 프록시 분석을 통해 지난 마지막 빙히기 이후의 고생산성, 영양염 이용률, 저층해류속도, 빙하쪼개짐을 복원하였다. 빙하기는 낮은 표층생산성과 높은 영양염 이용률이 나타났고, 이는 표층해수가 성층화 되어 있었다는 것을 의미한다. 후빙기 동안 표층생산성은 낮아진 영양염 이용률과 함께 증가하였다. 이 것은 남극순환류의 남쪽으로의 이동에 의한 남극순환류의 강화에 의해서 표층으로 저층에서 영양염의 공급이 증가하였기 때문인 것으로 보인다. >1 mm 입자들의 경우 후빙기부터 많이 나타나는 것이 확인되었고, 이 것은 후빙기 동안 큰 규모의 융빙과 빙붕쪼개짐이 있었다는 것을 의미한다. 하지만, 빙하기 동안에는 조립질 실트에서 세립 사의 구간에서의 퇴적물이 빙하쇄설성 퇴적물로 유입되는 것을 확인하였다. 다른 빙하쇄설성 퇴적물 입자 크기가 나타나는 것은 빙하쇄설성 퇴적물의 유입 기원지의 차이에 의한 것으로 보여진다. 그리고 빙하쇄설성 퇴적물의 유입과 상관없이 5-9 point 이동평균 값은 sortable silt가 저층류에 의한 분급이 잘 이루어져, 저층해류의 속도 변화를 잘 나타낼 수 있다는 것을 의미한다. 퇴적물은 남극순환류와 남서쪽으로 흐르는 저층류에 의해 분급이 나타나는 것으로 보인다. 남극 순환류의 남쪽으로의 이동과 함께 남서쪽으로 흐르는 해류의 영향은 감소하는 반면, 남극순환류의 영향이 7 천년 전 부터 강하게 나타나는 것을 확인하였다. 이러한 결과들은 스코시아해에서의 퇴적작용이 해양과 빙권의 지역적인 상호작용에 크게 의존한다는 것을 의미한다.

KOPRI 극지연구소

참고 문헌

Allen, C.S., Pike, J., Pudsey, C.J., 2011. Last glacial-interglacial sea-ice cover in the SW Atlantic and its potential role in global deglaciation. Quat. Sci. Rev. 30, 2446-2458.

Altabet, M.A., Francois, R., 1994. Sedimentary nitrogen isotopic ratio as a recorder for surface ocean nitrate utilization. Global Biogeochem. Cy. 8, 103-116.

Anderson, J.B., Andrew, J.T., 1999. Radiocarbon constraints on ice sheet advance and retreat in the Weddell Sea, Antarctica. Geology 27, 179-182.

Andrews, J., 2000. Icebergs and iceberg rafted detritus (IRD) in the North Atlantic: Facts and assumptions. Oceangraphy 13, 100-108.

Bak, Y.S., Lee, J.D., Yoon, H.I., Yoo, K.C., Lee, S.J., 2010. Holocene paleo-climate change in the area around Elephant Island, Antarctica: evidence from the diatom record. J. Geol. Soc. Korea 46, 111-117 (in Korean with English abstract).

Bak, Y.S., Yoo, K.C., Yoon, H.I., 2014. Late Quaternary climate changes around the Elephant Islands, Antarctic Peninsula. Geosci. J. 18, 495-501, doi:10.1007/s12303-014-0011-0.

Barker, P.F., Camerlenghi, A., 2002. Glacial history of the Antarctic Peninsula from Pacific margin sediments. In: Barker, P.F., Camerlenghi, A., Acton, G.D., Ramsay, A.T.S. (Eds.), Proc. ODP, Sci. Results 178 [Online], http://www-odp.tamu.edu/publications/178_SR/synth/synth.htm>.

Bentley, M.J., Cofaigh, C.Ó., Anderson, J.B., Conway, H., Davies, B., Graham, A.G.C., Hillenbrand, C.-D., Hodgson, D.A., Jamieson, S.S.R., Larter, R.D., Mackintosh, A., Smith, J.A., Verleyen, E., Ackert, R.P., Bart, P.J., Berg, S., Brunstein, D., Canals, M., Colhoun, E.A., Crosta, X., Dickens, W.A., Domack, E., Dowdeswell, J.A., Dunbar, R., Ehrmann, W., Evans, J., Favier, V., Fink, D., Fogwill, C.J., Glasser, N.F., Gohl, K., Golledge, N.R., Goodwin, I., Gore, D.B., Greenwood, S.L., Hall, B.L., Hall, K., Hedding, D.W., Hein, A.S., Hocking, E.P., Jakobsson, M., Johnson, J.S., Jomelli, V., Jones, R.S., Klages, J.P., Kristoffersen, Y., Kuhn, G., Leventer, A., Licht, K., Lilly, K., Lindow, J., Livingstone, S.J., Massé, G., McGlone, M.S., McKay, R.M., Melles, M., Miura, H., Mulvaney, R., Nel, W., Nitsche, F.O., O'Brien, P.E., Post, A.L., Roberts, S.J., Saunders, K.M., Selkirk, P.M., Simms, A.R., Spiegel, C., Stolldorf, T.D., Sugden, D.E., van der Putten, N., van Ommen, T., Verfaillie, D., Vyverman, W., Wagner, B., White, D.A., Witus, A.E., Zwartz, D., the RAISED Consortium, 2014. A community-based geological reconstruction of Antarctic Ice Sheet deglaciation since the Last Glacial Maximum. Quat. Sci. Rev. 100, 1-9, doi:10.1016/j.quascirev.2014.06.025.

Bianchi, G.G., McCave, I.N., 1999. Holocene periodicity in North Atlantic climate and

KOPRI 극지연구소

deep-ocean flow south of Iceland, Nature 397, 515-517.

Boessenkool, K.P., Hall, I.R., Elderfield, H., Yashayaev, I., 2007. North Atlantic climate and deep- ocean flow speed changes during the last 230 years. Geophys. Res. Lett. L13614, doi:10.1029/2007GL030285.

Brambati, A., Melis, R., Quaia, T., Salvi, G., 2002. Late Quaternary climatic changes in the Ross Sea area, Antarctica. In: Gamble, J.A., Skinner, D.N.B., Henrys, S. (Eds.), Antarctica at the close of a millennium. Proceedings Volume 8th International Symposium on Antarctic Earth Sciences, Royal Society of New Zealand Bulletin 35, 359-364.

Brunelle, B.G., Sigman, D.M., Jaccard, S.L., Keigwin, L.D., Plessen, B., Schettler, G., Cook, M.S., Haug, G.H., 2010. Glacial/interglacial changes in nutrient supply and stratification in the western subarctic North Pacific since the penultimate glacial maximum. Quat. Sci. Rev. 29, 2579- 2590.

Brzezinski, M.A., Pride, C.J., Franck, V.M., Sigman, D.M., Sarmiento, J.L., Matsumoto, K., Gruber, N., Rau, G.H., Coale, K.H., 2002. A switch from Si(OH)4 to NO3- depletion in the glacial Southern Ocean. Geophys. Res. Lett. 29, 5-1-5-4, doi:10.1029/2001GL014349.

Burckle, L.H., Burak, R.W., 1988. Fluctuations in Late Quaternary diatom abundances: stratigraphic and paleoclimatic implications from subantarctic deep sea cores. Palaeogeogr. Palaeoclimatol. Palaeoecol. 67, 147-156.

Cárdenas, P., Lange, C.B., Vernet, M., Esper, O., Srain, B., Vorrath, M.E., Ehrhardt, S., Müller, J., Kuhn, G., Arz, H.W., Lembke-Jene, L., Lamy, F., 2019. Biogeochemical proxies and diatoms in surface sediemnts across the Drake Passage reflect oceanic domains and frontal systems in the region. Prog. Oceanogr. 174, 72-88, doi:10.1016/j.pocean.2018.10.004.

Chough, S.K., Lee, G.H., Park, B.K., Kim, S.W., 1984. Fine structures of turbidite and associated muds in the Ulleung (Tsushima) Basin, East (Sea of Japan). J. Sediment. Petrol. 54, 1212-1220.

Collins, L.G., Pike, J., Allen, C.S., Hodgson, D.A., 2012. High-resolution reconstruction of southwest Atlantic sea-ice and its role in the carbon cycle during marine isotope stages 3 and 2. Paleoceanography 27, PA3217.

Crosta, X., Koç, N., 2007. Chapter Eight Diatoms: From Micropaleontology to Isotope Geochemistry. Developments in Marine Geology 1, 327-369, doi:10.1016/S1572-5480(07)01013-5.

Crosta, X., Pichon, J.J., Labracherie, M., 1997. Distribution of Chaetoceros resting spores in modern peri-Antarctic sediments. Mar. Micropaleontol. 29, 283-299.

Crosta, X., Sturm, A., Armand, L., Pichon, J.J., 2004. Late Quaternary sea ice history in the

Indian sector of the Southern Ocean as recorded by diatom assemblages. Mar. Micropaleontol. 50, 209-223, doi:10.1016/S0377-8398(03)00072-0.

De Jong, J.T.M., Stammerjohn, S.E., Ackley, S.F., Tison, J.L., Mattielli, N., Schoemann, V., 2015. Sources and fluxes of dissolved iron in the Bellingshausen Sea (West Antarctica): The importance of sea ice, icebergs and the continental margin. Mar. Chem. 177, 518-535, doi:10.1016/j.marchem.2015.08.004.

DeMaster, D.J., 1981. The supply and accumulation of silica in the marine environment. Geochim. Cosmochim. Acta 5, 1715-1732.

Diekmann, B., 2007. Sedimentary patterns in the late Quaternary Southern Ocean. Deep-Sea Res. II 54, 2350-2366.

Diekmann, B., Kuhn, G., Rachold, V., Abelmann, A., Brathauer, U., Fütterer, D.K., Gersonde, R., Grobe, H., 2000. Terrigenous sediment supply in the Scotia Sea (Southern Ocean): response to Late Quaternary ice dynamics in Patagonia and on the Antarctic Peninsula. Palaeogeogr. Palaeoclimatol. Palaeoecol. 162, 357-387.

Donohue, K., Tracey, K., Watts, D., Chidichimo, M., Chereskin, T., 2016. Mean Antarctic Circumpolar Current transport measured in Drake Passage. Geophys. Res. Lett. 43, 11760-11767, doi:10.1002/2016GL070319.

Dowdeswell, J.A., Dowdeswell, E.K., 1989. Debris in icebergs and rates of glaci-marine sedimentation-Observations from Spitsbergen and a simple model. J. Geol. 97, 221-231.

Fahrbach, E., Peterson, R.G., Rohardt, G., Schlosser, P., Bayer, R., 1994. Suppression of bottom water formation in the southeastern Weddell Sea. Deep-Sea Res. I 41, 389-411, doi:10.1016/0967-0637(94)90010-8.

Folk, R.L., Ward, W.C., 1957. Brazos River bar [Texas]; a study in the significance of grain size parameters. J. Sediment. Res. 27, 3-26.

Francois, R., Altabet, M.A., Burckle, L.H., 1992. Glacial-interglacial changes in surface nitrate utilization in the Indian sector of the Southern Ocean as recorded by sediment δ 15N. Paleoceanography 7, 589-606.

Fryxell, G.A., Kendrick, G.A., 1988. Austral spring microalgae across the Weddell Sea ice edge: spatial relationships found along a northward transect during AMERIEZ 83. Deep-Sea Res. 35, 1-20.

Gersonde, R., Crosta, X., Abelmann, A., Armand, L., 2005. Sea-surface temperature and sea ice distribution of the Southern Ocean at the EPILOG Last Glacial Maximum-a circum- Antarctic view based on siliceous microfossil records. Quat. Sci. Rev. 24, 869-896.

Geibert, W., Rutgers van der Loeff, M.M., Usbeck, R., Gersonde, R., Kuhn, G., Seeberg-Elverfeldt, J., 2005. Quantifying the opal belt in the Atlantic and southeast

KOPRI 극지연구소

Pacific sector of the Southern Ocean by means of 230Th normalization. Glob. Biogeochem. Cycles 19, GB4001, doi:10.1029/2005GB002465.

Gilbert, I.M., Pudsey, C.J., Murray, J.W., 1998. A sediment record of cyclic bottom-current variability from the northwest Weddell Sea. Sediment. Geol. 115, 185-214.

Grigorov, I., Rigual-Hernandez, A.S., Honjo, S., Kemp, A.E.S., Armand, L.K., 2014. Settling fluxes of diatoms to the interior of the Antarctic circumpolar current along 170갊. Deep-Sea Res. I 93, 1-13, doi:10.1016/j.dsr.2014.07.008.

Hernández-Molina, F.J., Larter, R.D., Rebesco, M., Maldonado, A., 2006. Miocene reversal of bottom water flow along the Pacific Margin of the Antarctic Peninsula: stratigraphic evidence from a contourite sedimentary tail. Mar. Geol. 228, 93-116.

Honjo, S., Francois, R., Manganini, S., Dymond, J., Collier, R., 2000. Particle fluxes to the interior of the Southern Ocean in the Western Pacific sector along 170갊. Deep-Sea Res. II 47, 3521- 3548.

Horn, M.G., Robinson, R.S., Rynearson, T.A., Sigman, D.M., 2011. Nitrogen isotopic relationship between diatom-bound and bulk organic matter of cultured polar diatoms. Paleoceanography 26, PA3208, doi:10.1029/2010PA002080.

Hutchins, D.A., Bruland, K.W., 1998. Iron-limited diatom growth and Si:N uptake ratios in a coastal upwelling regime. Nature 393, 561-564.

Hutchins, D.A., Hare, C.E., Weaver, R.S., Zhang, Y., Firme, G.F., DiTullio, G.R., Alm, M.B., Riseman, S.F., Maucher, J.M., Geesey, M.E., Trick, C.G., Smith, G.J., Rue, E.L., Conn, J., Bruland, K.W., 2002. Phytoplankton iron limitation in the Humboldt Current and Peru Upwelling. Limnol. Oceanogr. 47, 997-1011.

Jonkers, L., Prins, M.A., Moros, M., Weltje, G.J., Troelstra, S.R., Brummer, G.-J.A., 2012. Temporal offsets between surface temperature, ice-rafting and bottom flow speed proxies in the glacial (MIS 3) northern North Atlantic. Quat. Sci. Rev. 48, 43-53.

Jonkers, L., Barker, S., Hall, I.R., Prins, M.A., 2015. Correcting for the influence of ice-rafted detritus on grain size-based paleocurrent speed estimates. Paleoceanography 30, 1347-1357, doi:10.1002/2015PA002830.

Jouzel, J., Masson-Delmotte, V., Cattani, O., Dreyfus, G., Falourd, S., Hoffmann, G., Minster, B., Nouet, J., Barnoloa, J.M., Chappellaz, J., Fischer, H., Gallet, J.C., Johnsen, S., Leuenberger, M., Loulergue, L., Luethi, D., Oerter, H., Parrenin, F., Raisbeck, G., Raynaud, D., Schilt, A., Schwander, J., Selmo, E., Souchez, R., Spahni, R., Stauffer, B., Steffensen, J.P., Stenni, B., Stocker, T.F., Tison, J.L., Werner, M., Wolff, E.W., 2007. Orbital and millennial Antarctic climate variability over the past 800,000 years. Science 317, 793-796.

Kanfoush, S.I., Hodell, D.A., Charles, C.D., Guilderson, T.P., Mortyn, P.G., Ninnemann, U. S., 2000. Millennial-scale instability of the Antarctic Ice Sheet during the Last

Glaciation. Science 288, 1815-1818.

Kemp, A.E.S., Grigorov, I., Pearce, R.B., Naveira Garabato, A.C., 2010. Migration of the Antarctic Polar Front through the mid-Pleistocene transition: evidence and climatic implications. Quat. Sci. Rev. 29, 1993-2009.

Kim, S., Yoo, K.C., Lee, J.I., Lee, M.K., Kim, K., Yoon, H.I., 2018a. Relationship between magnetic susceptibility and sediment grain size since the last glacial period in the Southern Ocean off the northern Antarctic Peninsula-Linkages between the cryosphere and atmospheric circulation. Palaeogeogr. Palaeoclimatol. Palaeoecol. 505, 359-370, doi:10.1016/J.palaeo.2018.06.016.

Kim, S., Yoo, K.C., Lee, J.I., Khim, B.K., Bak, Y.S., Lee, M.K., Lee, J., Domack, E.W., Christ, A.J., Yoon, H.I., 2018b. Holocene paleoceanography of Bigo Bay, west Antarctic Peninsula: Connections between surface water productivity and nutrient utilization and its implication for surface- deep water mass exchange. Quat. Sci. Rev. 192, 59-70, doi:10.1016/j.quascirev.2018.05.028.

Lee, J.I., Bak, Y.S., Yoo, K.C., Lim, H.S., Yoon, H.I., Yoon, S.H. 2010. Climate changes in the South Orkney Plateau during the last 8600 years. The Holocene 20(30), 395-404.

Lee, J.I., Yoon, H.I., Yoo, K.-C., Lim, H.S., Lee, Y.I., Kim, D., Bak, Y.S., Itaki, T., 2012. Late Quaternary glacial-interglacial variations in sediment supply in the southern Drake Passage. Quat. Res. 78, 119-129, doi:10.1016/j.yqres.2012.03.010.

Leventer, A., 1991. Sediment trap diatom assemblages from the northern Antarctic Peninsula region. Deep Sea Res. 38, 1127-1143.

Leventer, A., Domack, E.W., Ishman, S.E., Brachfeld, S., McClennen, C.E., Manley, P.L., 1996. Productivity cycles of 200-300 years in the Antarctic Peninsula region: Understanding linkages among the sun, atmosphere, oceans, sea ice, and biota. Geol. So. Am. Bull. 108, 1626-1644, doi:10.1130/0016-7606(1996)108<1626:PCOYIT>2.3.CO;2.

Lucchi, R.G., Rebesco, M., 2007. Glacial contourites on the Antarctic Peninsula margin: insight for palaeoenvironmental and palaeoclimatic conditions. In: Viana, A.R., Rebesco, M. (Eds.), Economic and Palaeoceanographic Significance of Contourite Deposits. Geological Society, London, Special Publications 276, 111-127.

Lucchi, R.G., Rebesco, M., Camerlenghi, A., Busetti, M., Tomadin, L. ,Villa, G., Persico, D., Morigi, C., Bonci, M.C., Giorgetti, G., 2002. Mid-late Pleistocene glacimarine sedimentary processes of a high-latitude, deep-sea sediment drift (Antarctic Peninsula Pacific margin). Mar. Geol. 189, 343-370.

Maldonado, A., Barnolas, A., Bohoyo, F., Galindo-Zaldívar, Hernández-Molina, J., Lobo, F., Rodríguez-Fernández, Somoza, L., Vázquez, J.T., 2003. Contourite deposits in the central Scotia Sea: the importance of the Antarctic Circumpolar Current and the

Weddell Gyre flows. Palaeogeogr. Palaeoclimatol. Palaeoecol. 198, 187–221.

Manoj, M.C., Thamban, M., 2015. Shifting frontal regimes and its influence on bioproductivity variations during the Late Quaternary in the Indian sector of Southern Ocean. Deep–Sea Res. II 118, 261–274, doi:10.1016/j.dsr2.2015.03.011.

McCave, I.N., Andrews, J.T., 2019. Distinguishing current effects in sediments delivered to the ocean by ice, I. Principles, methods and examples. Quat. Sci. Rev. 212, 92–107, doi:10.1016/j.quascirev.2019.03.031.

McCave, I.N., Crowhurst, S.J., Kuhn, G., Hillenbrand, C.–D., Meredith, M.P., 2014. Minimal change in

Antarctic Circumpolar Current flow speed between the last glacial and Holocene. Nat. Geosci. 7, 113–116, doi: 10.1038/ngeo2037.

McCave, I.N., Manighetti, B., Robinson, S.G., 1995. Sortable silt and fine sediment size composition slicing–parameters for paleocurrent speed and paleoceanography. Paleoceanography 10, 593–610, doi:10.1029/94PA03039.

McCave, I.N., Thornalley, D.J.R., Hall, I.R., 2017. Relation of sortable silt grain size to deep–sea current speeds: Calibration of the 'Mud Current Meter.' Deep–Sea Res. I 127, 1–12, doi: 10.1016/j.dsr.2017.07.003.

Merino, N., Le Sommer, J., Durand, G., Jourdain, N.C., Madec, G., Mathiot, P., Tournadre, J., 2016. Antarctic icebergs melt over the Southern Ocean: Climatology and impact on sea ice. Ocean Model. 104, 99–110, doi:10.1016/j.ocemod.2016.05.001.

Mortlock, R.A., Froelich, P.N., 1989. A simple method for the rapid determination of opal in pelagic marine sediments. Deep–Sea Res. 36, 1415–1426.

Needoba, J.A., Waser, N.A., Harrison, P.J., Calvert, S.E., 2003. Nitrogen isotope fractionation in 12 species of marine phytoplankton during growth on nitrate. Mar. Ecol. Prog. Ser. 255, 81–91.

Nie, Y., Liu, X., Wen, T., Sun, L., Emslie, S.D., 2014. Environmental implication of nitrogen isotopic composition in ornithogenic sediments from the Ross Sea region, East Antarctica: Δ15N as a new proxy for avian influence. Chem. Geol. 363, 91–100, doi:10.1016/j.chemgeo.2013.10.031.

Ó Cofaigh, C.O., Dowdeswell, J.A., Pudsey, C.J., 2001. Late Quaternary iceberg rafting along the Antarctic Peninsula continental rise and in the Weddell and Scotia Seas. Quaternary Research 56, 308–321.

Orsi, A.H., Johnson, G.C., Bullister, J.L., 1999. Circulation, mixing, and production of Antarctic Bottom Water. Prog. Oceanogr. 43, 55–109.

Orsi, A.H., Whitworth, T., Nowlini Jr., W. D., 1995. On the meridional extent and fronts of the Antarctic circumpolar current. Deep Sea Res. I 42(5), 641–673.

Passchier, S., 2011. Linkages between East Antarctic Ice Sheet extent and Southern Ocean

temperatures based on a Pliocene high-resolution record of ice-rafted debris off Prydz Bay, East Antarctica. Paleoceanography 26, PA4204, doi:10.1029/2010PA002061.

Patterson, M.O., McKay, R., Naish, T., Escutia, C., Jimenez-Espejo, F.J., Raymo, M.E., Meyers, S.R., Tauxe, L., Brinkhuis, H., IODP Expedition 318 Scientists, 2014. Orbital forcing of the East Antarctic ice sheet during the Pliocene and Early Pleistocene. Nat. Geosci. 7, 841-847, doi:10.1038/NGEO2273.

Pugh, R.S., MaCave, I.N., Hillenbrand, C.-D., Kuhn, G., 2009. Circum-Antarctic age modeling of Quaternary marine cores under the Antarctic Circumpolar Current: ice-core dust-magnetic correlation. Earth Planet. Sci. Lett. 284, 113-123.

Roberts, J., McCave, I.N., McClymont, E.L., Kender, S., Hillenbrand, C.D., Matano, R., Hodell, D.A., Peck, V.L., 2017. Earth Planet. Sci. Lett. 474, 397-408, doi:10.1016/j.epsl.2017.07.004.

Shin, J.Y., Kim, S., Zhao, X., Yoo, K.C., Yu, Y., Lee, J.I., Lee, M.K., Yoon, H.I., 2020. Particle-size dependent magnetic properties of Scotia Sea sediments since the Last Glacial Maximum: Glacial ice-sheet discharge controlling magnetic proxeis. Palaeogeogr. Palaeoclimatol. Palaeoecol. 557, 109906, doi:10.1016/j.palaeo.2020.109906.

Socal, G., Noethig, E.M., Bianchi, F., Boldrin, A., Mathot, S., Rabitti, S., 1997. Phytoplankton and particulate matter at the Weddell/Scotia Confluence (47갊) in summer 1989, as a final step of a temporal succession (EPOS project). Polar Biol. 18, 1-9.

Sprenk, D., Weber, M.E., Kuhn, G., Rosén, P., Frank, M., Molina-Kescher, M., Liebetrau, V., Röhling, H.G., 2013. Southern Ocean bioproductivity during the last glacial cycle-new detection method and decadal-scale insight from the Scotia Sea. Geol. Soc. London. Spec. Publ. 381, 245-261, doi:10.1144/SP381.17.

Stanley, D.J., Maldonado, A., 1981. Depositional models for fine-grained sediments in the western Hellenic Trench, Eastern Mediterranean. Sedimentology 28, 273-290.

Stow, D.A.V., Piper, D.J.W., 1984. Deep-water fine-grained sediments: facies models, 1984. Geol. Soc. London Spec. Publ. 15, 611-646, doi:10.1144/GSL.SP.1984.015.01.38..

Studer, A.S., Sigman, D.M., Martínez-García, A., Benz, V., Winckler, G., Kuhn, G., Esper, O., Lamy, F., Jaccard, S.L., Wacker, L., Oleynik, S., Gersonde, R., Haug, G.H., 2015. Antarctic Zone nutrient conditions during the last two glacial cycles. Paleoceanography 30, 845-862, doi:10.1002/2014PA002745.

Tournadre, J., Bouhier, N., Girard-Ardhuin, F., Rmy, F., 2015. Large icebergs characteristics from altimeter waveforms analysis. J. Geophys. Res. 120, 1954-1974, doi:10.1002/2014JC010502.

Tréguer, P., Linder, L., van Bennekon, A.J., et al., 1991. Production of biogenic silica in the

KOPRI 극지연구소

Weddell- Scotia Seas measured by using 32Si. Limnol. Oceanogr. 36, 1217-1227.

Tréguer, P., Jacques, G., 1992. Dynamics of nutrients and phytoplankton, and fluxes of carbon, nitrogen and silicon in the Antarctic Ocean. Polar Biol. 12, 149-162.

Weber, M.E., Kuhn, G., Sprenk, D., Rolf, C., Ohlwein, C., Ricken, W., 2012. Dust transport from Patagonia to Antarctica-a new stratigraphic approach from the Scotia Sea and its implications for the last glacial cycle. Quat. Sci. Rev. 36, 177-188.

Weber, M.E., Clark, P.U., Kuhn, G., Timmermann, A., Sprenk, D., Gladstone, R., Zhang, X., Lohmann, G., Menviel, L., Chikamoto, M.O., Friedrich, T., Ohlwein, C., 2014. Millennial-scale variability in Antarctic ice-sheet discharge during the last deglaciation. Nature 510, 134-138.

Wu, L., Wang, R., Xiao, W., Krijgsman, W., Li, Q., Ge, S., Ma, T., 2018. Late Quaternary deep stratification-climate coupling in the Southern Ocean: implications for changes in abyssal carbon storage. Geochem. Geophys. Geosyst. 19, doi:10.1002/2017GC007250.

Xiao, W., Frederichs, T., Gersonde, R., Kuhn, G., Esper, O., Zhang, X., 2016. Constraining the dating of late Quaternary marine sediment records from the Scotia Sea (Southern Ocean). Quat. Geochronol. 31, 97-118, doi:10.1016/j.quageo.2015.11.003.

Yabuki, T., Suga, T., Hanawa, K., Matsuoka, K., Kiwada, H., Watanabe, T., 2006. Possible source of the Antarctic bottom water in the Prydz Bay region. J. Oceanogr. 62, 649-655, doi:10.1007/s10872-006-0083-1.

Yamazaki, T., Ikehara, M., 2012. Origin of magnetic mineral concentration variation in the Southern Ocean. Paleoceanography 27, PA2206, doi:10.1029/2011PA002271.

Yoon, H.I., Khim, B.K., Yoo, K.-C., Bak, Y.S., Lee, J.I., 2007. Late glacial to Holocene climatic and oceanographic record of sediment facies from the South Scotia Sea off the northern Antarctic Peninsula. Deep-Sea Res. II 54, 2367-2387.

KOPRI 극지연구소

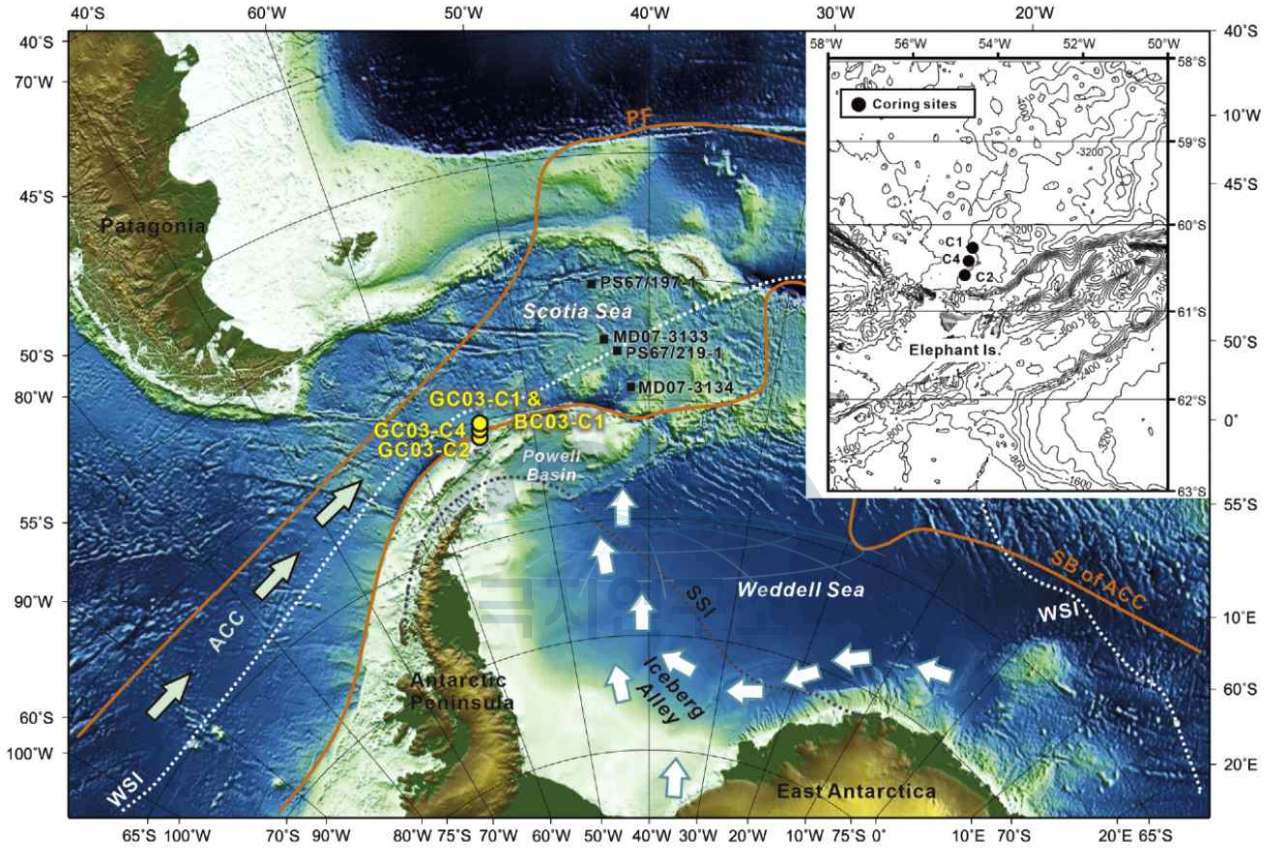


Figure 1. (a) Map of the study region indicating the locations of the sediment cores examined in this study as well as in previous investigations. The white open arrows indicate the location of iceberg alley (from Anderson and Andrew, 1999); the orange lines indicate the Polar Front (PF) and the Southern Boundary of the Antarctic Circumpolar Current (SBACC; Orsi et al., 1995); the dark gray and white dashed lines indicate the summer (SSI) and winter (WSI) sea ice extent, respectively (Gersonde et al., 2005); and the light green arrows indicate the ACC.

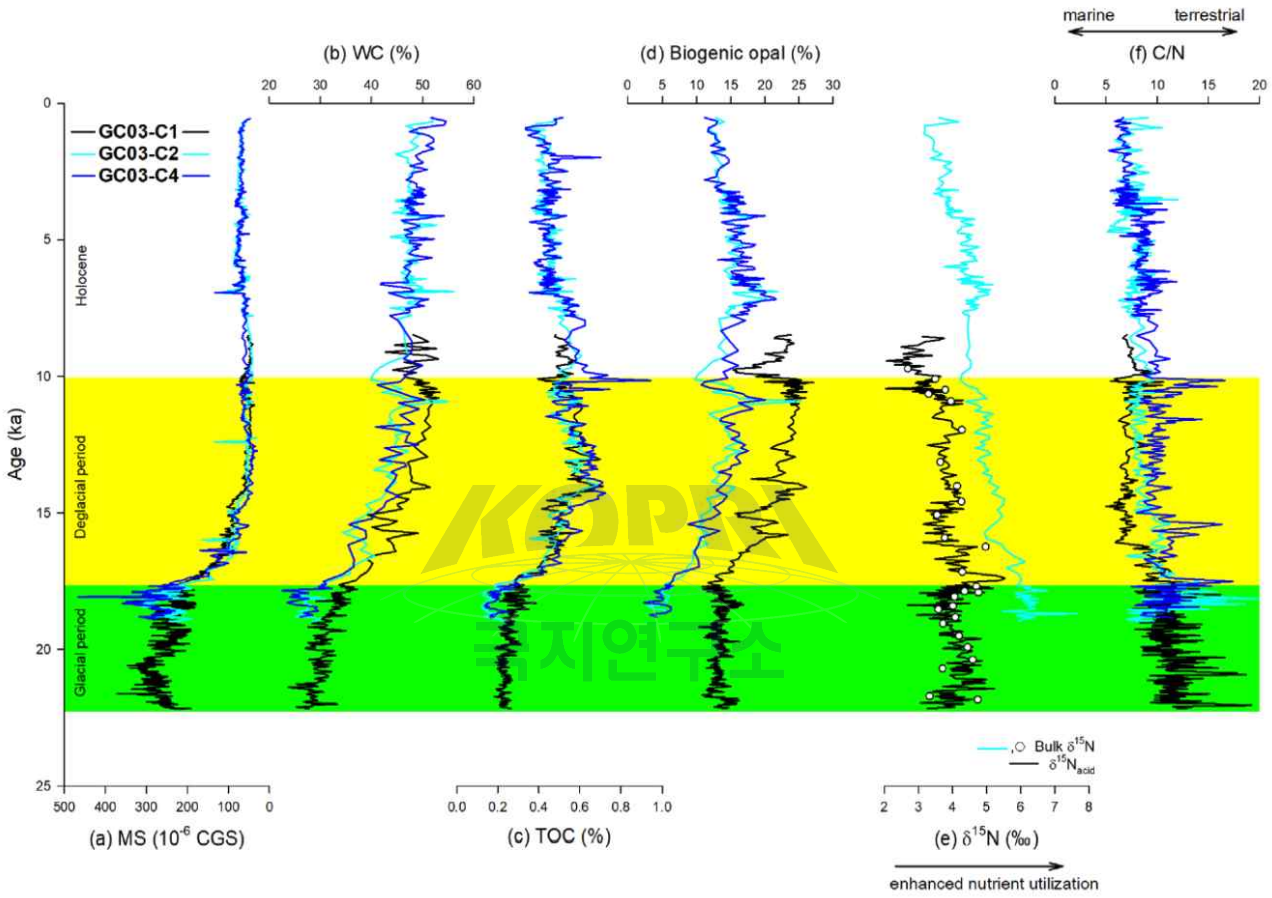


Figure 2. Downcore profiles of (a) MS, (b) WC, (c) TOC concentration, (d) biogenic opal concentration, (d) δ15N, and (e) C/N ratios of cores GC03-C1 (black), -C2 (cyan), and -C4 (blue).

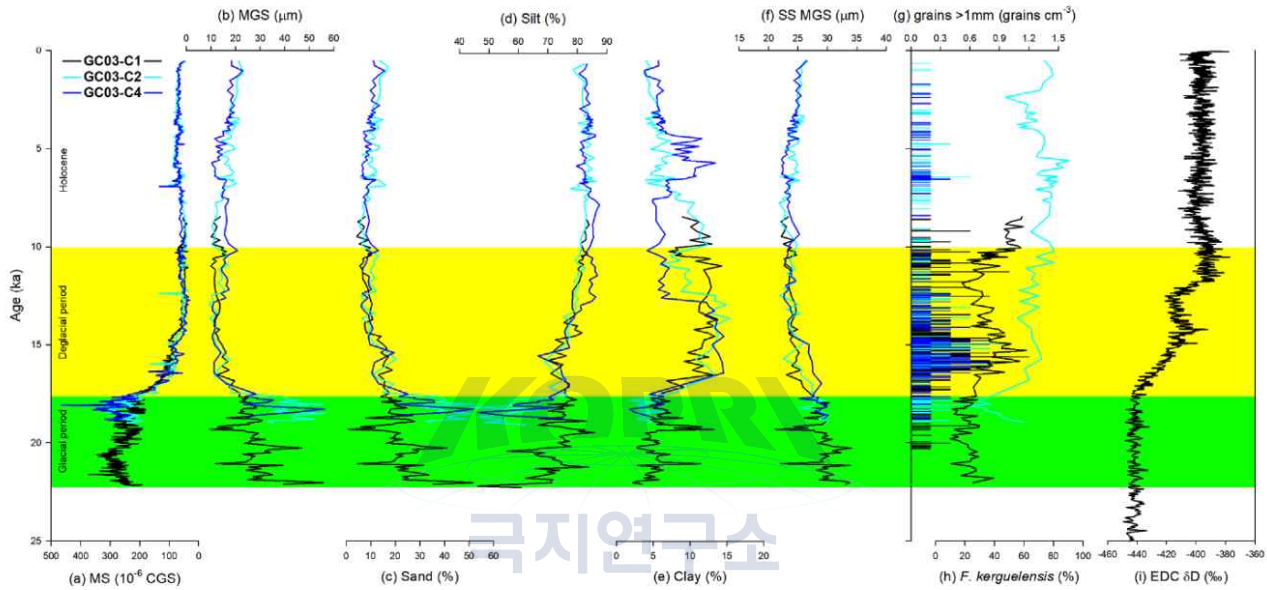


Figure 3. Downcore profiles of (a) MS, (b) mean grain size (MGS), (c) sand proportion, (d) silt proportion, (e) clay proportion, (f) sortable silt MGS, and (g) abundance of grains >1 mm per cm3 of cores GC03−C1 (black), −C2 (cyan), and −C4 (blue); (h) the relative abundance of open ocean diatom F. kerguelensis in GC03−C1 (Bak et al., 2010) and GC03−C2 (Bak et al., 2014); and (i) the EDC δD ice core record (Jouzel et al., 2007).

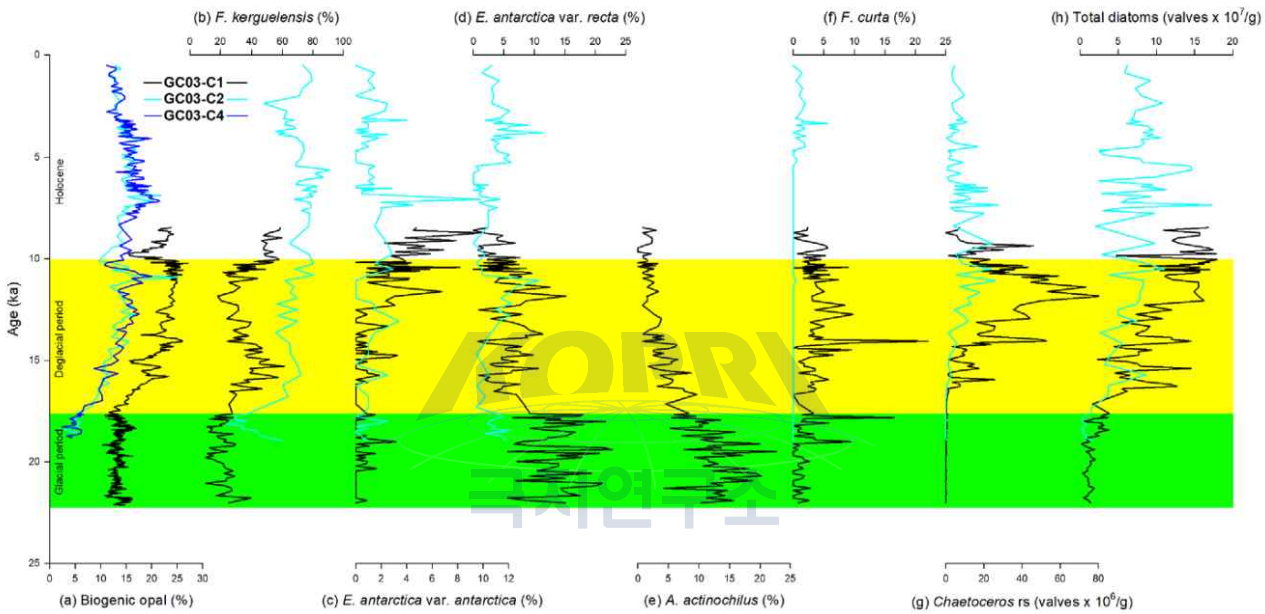


Figure 4. Downcore profiles of (a) biogenic opal concentration, relative abundance of (b) F. kerguelensis, (c) E. antarctica var. antarctica, (d) E. antarctica var. recta, (e) A. actinochilus, and (f) F. curta, (g) Chaetoceros resting spores, and (h) total diatoms of cores GC03-C1 (black), -C2 (cyan), and -C4 (blue). Diatom records for GC03-C1 are from Bak et al. (2010) and for GC03-C2 are from Bak et al. (2014), except for Chaetoceros resting spores in GC03-C2 (this study).

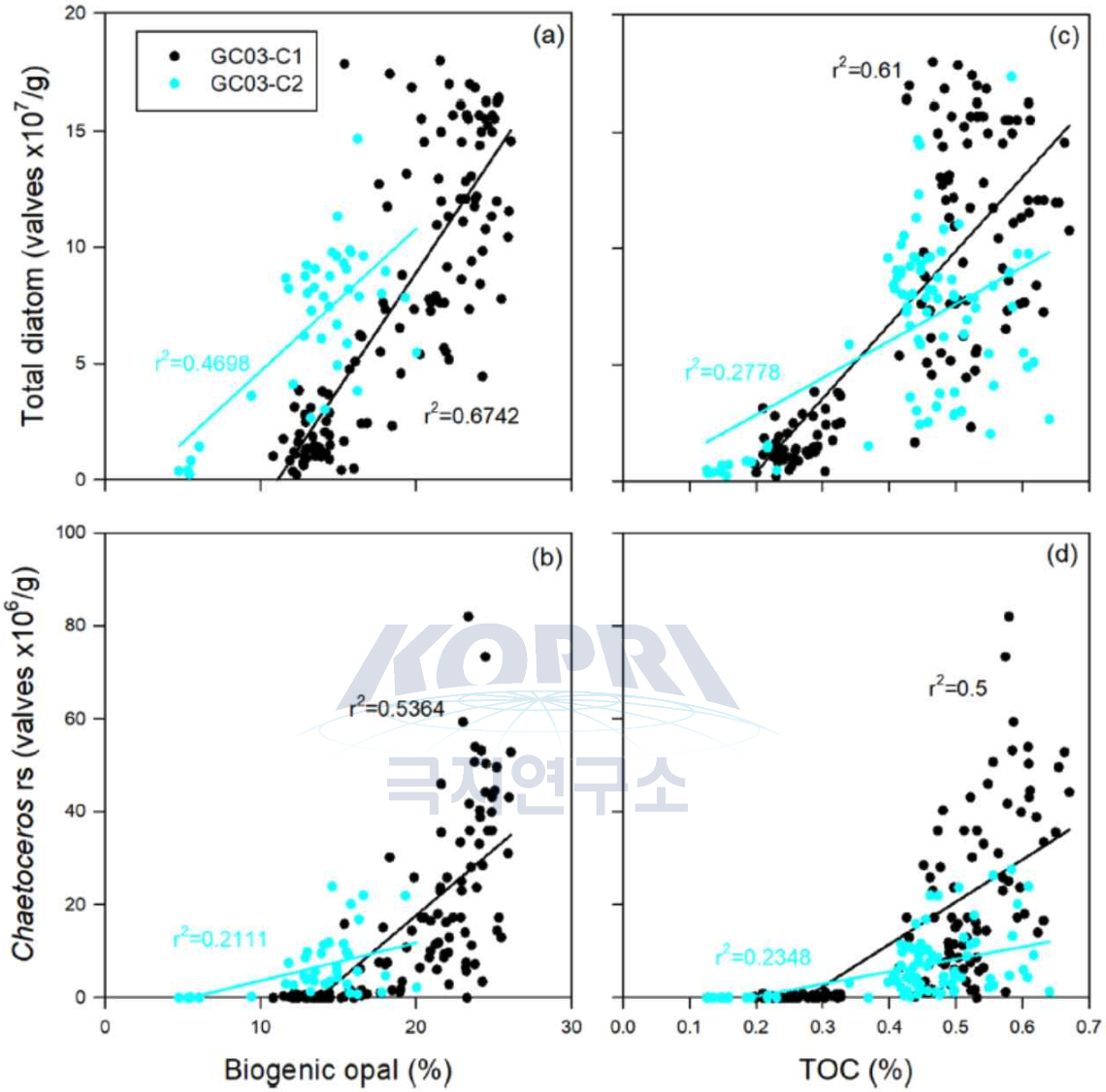


Figure 5. Correlations of biogenic opal concentration with (a) total diatom abundance and (b) Chaetoceros resting spores and of TOC concentration with (c) total diatom abundance and (d) Chaetoceros resting spores for GC03-C1 (black) and GC03-C2 (cyan).

KOPRI 극지연구소

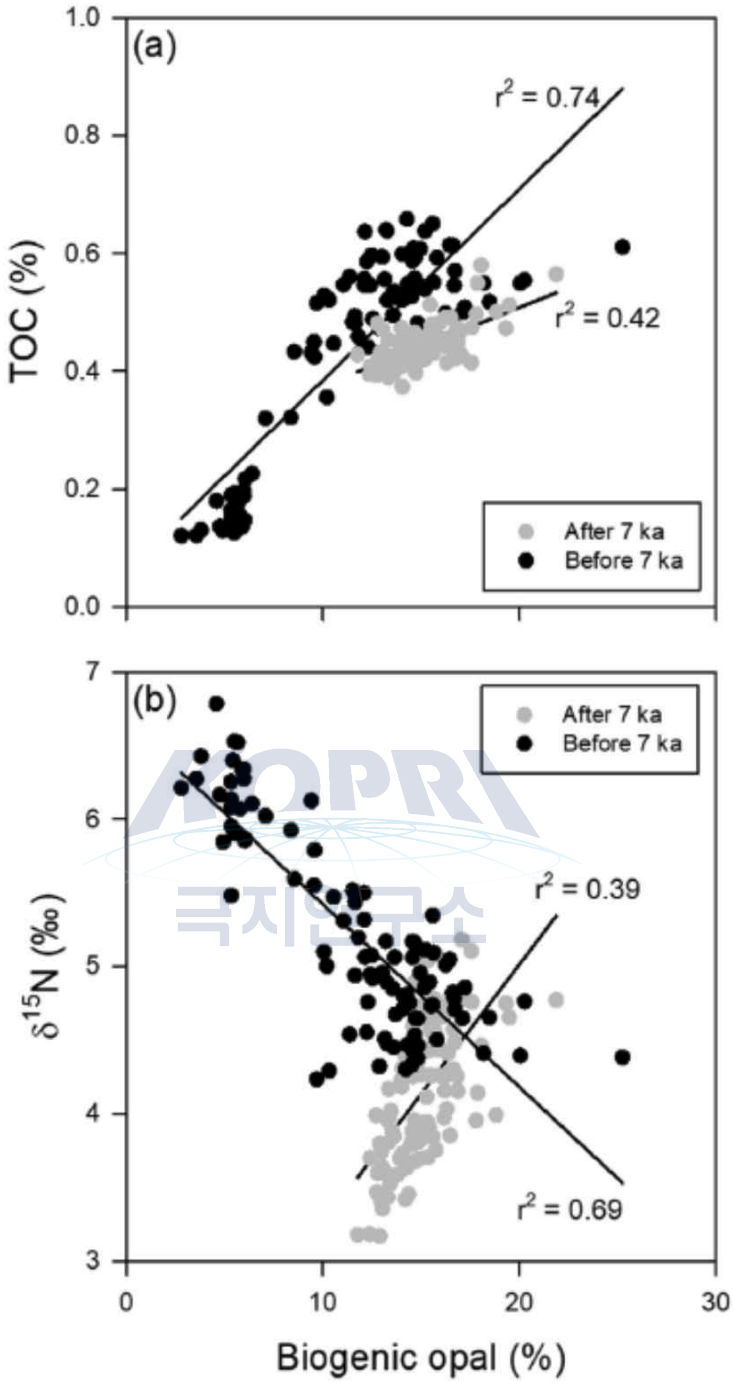


Figure 6. Correlations of biogenic opal concentration with (a) TOC concentration and (b) bulk δ15N from core GC03-C2 before (black) and after 7 ka (gray).

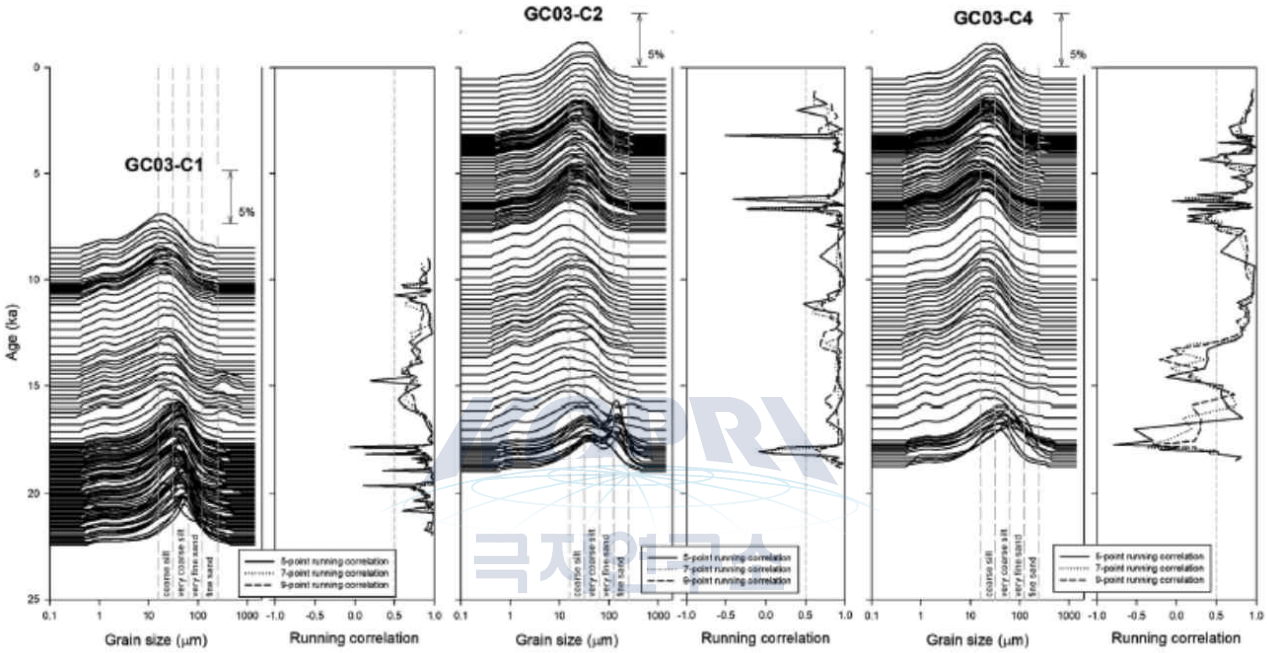


Figure 7. Downcore profiles of grain size distribution and the running 5−, 7−, and 9−point correlation between the SS MGS and SS% for GC03−C1, −C2, and −C4. (Very) coarse silt and (very) fine sand sizes are shown by long dashed lines. R value of 0.5 is shown as short dashed lines.

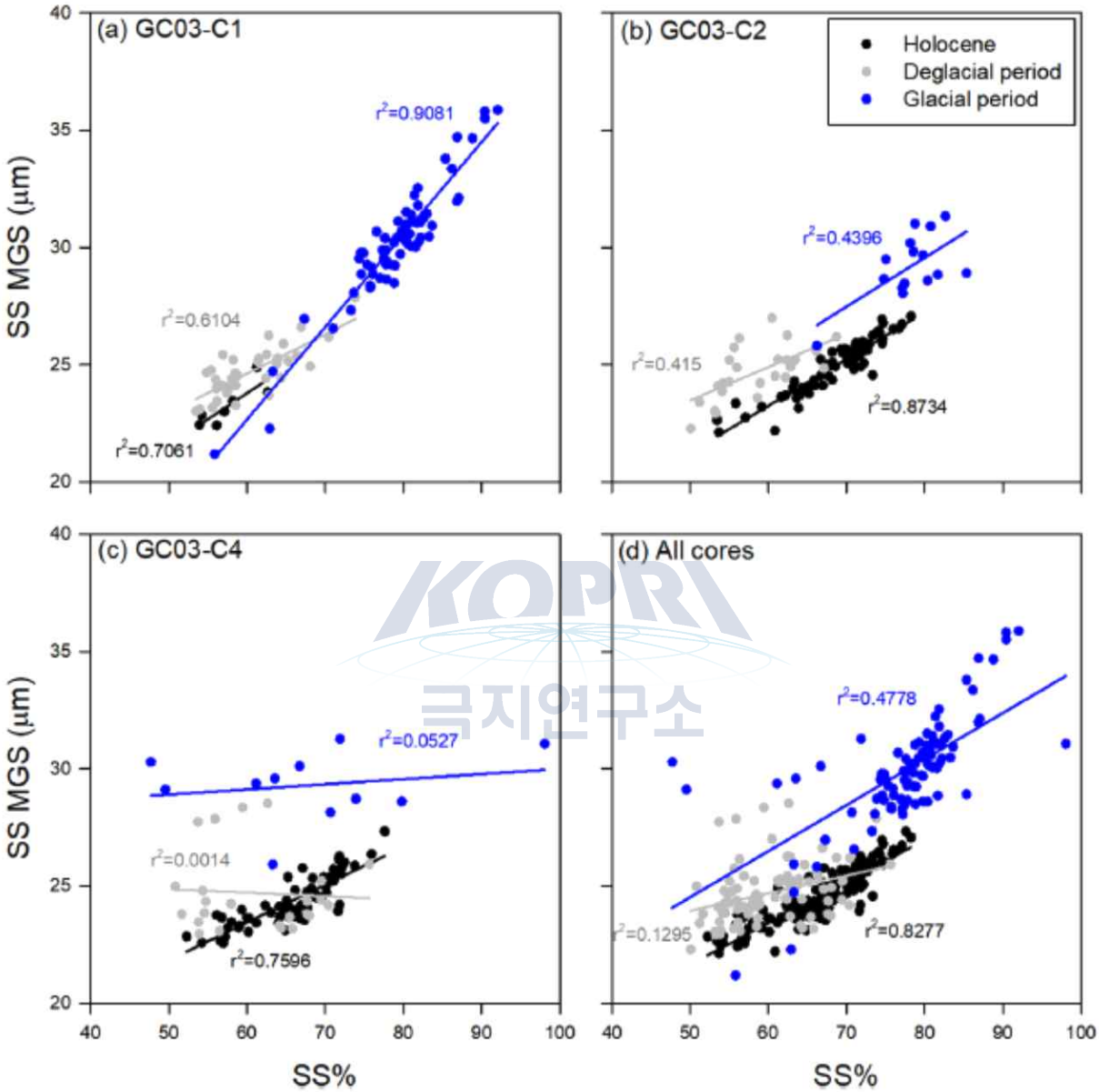


Figure 8. Correlations of the SS MGS and SS% for (a) GC03-C1, (b) GC03-C2, (c) GC03-C4, (d) and all three cores for the last glacial period (blue), the deglacial period (gray), and the Holocene (black).

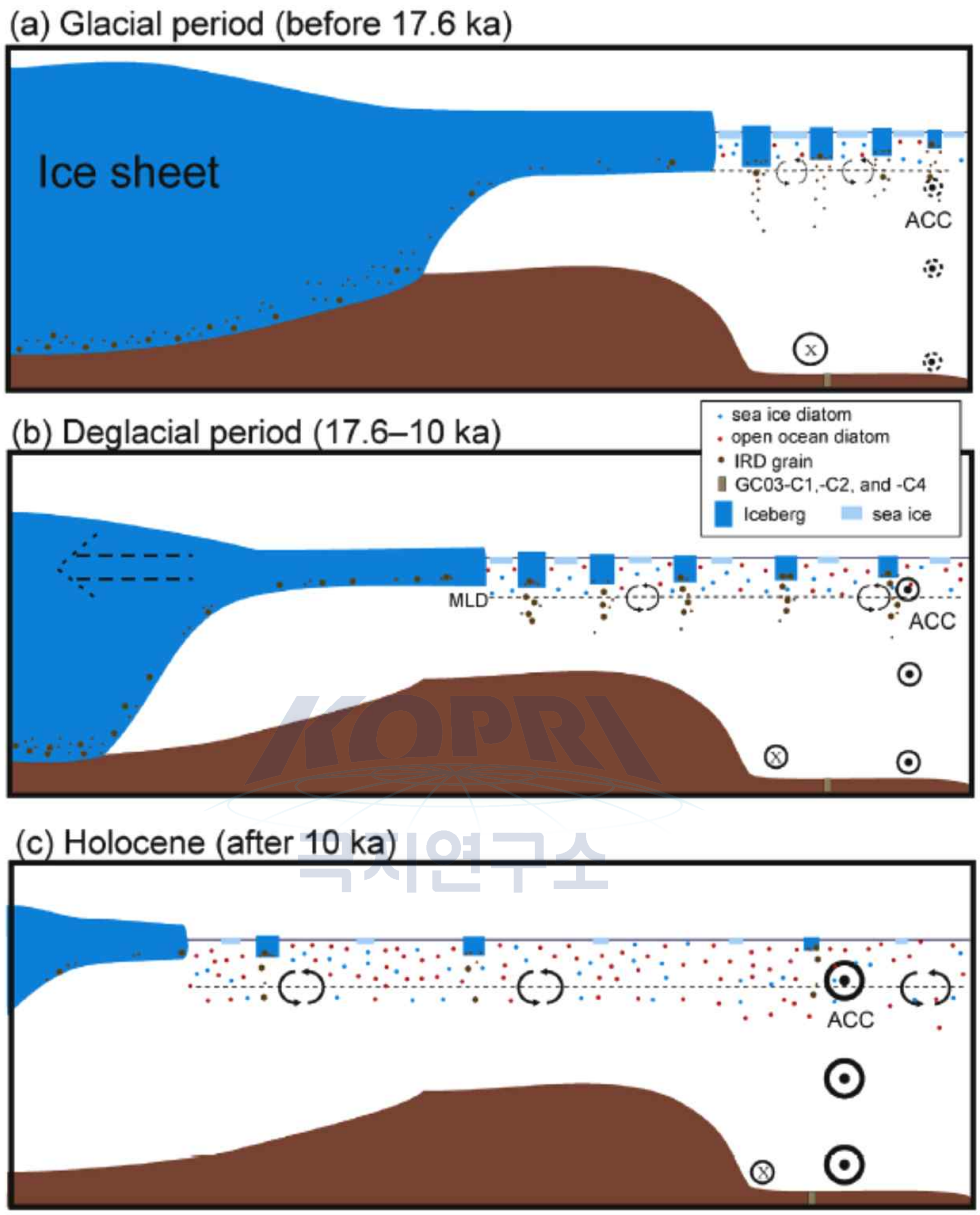


Figure 9. Paleoceanographic models of (a) the glacial period (before 17.6 ka), (b) the deglacial period (17.6–10 ka), and (c) the Holocene (after 10 ka) in the Southern Ocean off Elephant Island. MLD is the mixed layer depth.

제 14 장

Paleoceanographic condition changes in the Eastern Bransfield Basin, Antarctic Peninsula, since the late glacial interval and its implications[5)]

Sunghan Kim[a,b,*], Young-Suk Bak[c,+], Kyu-Cheul Yoo[a], Min Kyung Lee[a], Jae Il Lee[a], Sookwan Kim[d], Jinku Park[a], So-Young Kim[a], Heung Soo Moon[a], Myung-Il Kang[a], Hyo Jin Kim[a]

[a]Korea Polar Research Institute, Incheon 21990, Republic of Korea
[b]Department of Polar Sciences, University of Science and Technology (UST), Incheon 21990, Republic of Korea
[c]Department of Earth and Environmental Sciences, Jeonbuk National University, Jeonju, 54896, Republic of Korea
[d]Korea Institute of Ocean Science and Technology, Busan 49111, Republic of Korea

KOPRI 극지연구소

Abstract: Antarctic Peninsula is the most northerly area in the Antarctica, thus it is vulnerable to warming climate. Although it is well known that relatively warm water mass input onto the Antarctic shelf region facilitates ice shelf retreat, when and how the water mass exchange between the deep Southern Ocean and the Antarctic shelf regions is not well known in ice proximal areas due to sea ice dynamics on the continental shelf region. Here, we document the diatom assemblage record of a sediment core with high sedimentation rates since the late glacial interval from 34.6 ka to address surface environmental changes in the Eastern Bransfield Basin (EBB). We found that the EBB was covered by extensive sea ice showing millennial-scale variations during the late glacial interval. The sea ice started to decrease during the deglacial interval (19–11 ka) with slight increases of open ocean influence. In addition, meltwater input was significant during 14.7–11.3 ka which corresponds to Antarctic Ice Sheet Discharge events reported in the Scotia Sea including Meltwater pulse 1A and 1B. During the Holocene after 9 ka, relatively warm water mass input distinctively increased into the EBB contemporaneous with a remarkable decrease in sea ice influence indicating the strong relationship between sea ice and warm

5) 이 연구 결과는 다음의 논문으로 출판되었음: Kim, S. et al. (2025). "Paleoceanographic condition changes in the Eastern Bransfield Basin, Antarctic Peninsula, since the late glacial interval and its implications" Palaeogeography Palaeoclimatology, Palaeoecology 669: 112934.

water mass input. In addition, meltwater input at 9 ka was also distinctive in the EBB, but there was no corresponding Antarctic Ice Sheet Discharge event in the Scotia Sea. Our results show how well surface environmental changes in the EBB correspond to the global climate change and the regional climatic characteristics at the same time.

1. Introduction

Many studies have been conducted in the Antarctic Peninsula (AP) region to reconstruct paleoceanographic changes in response to ice shelf/sheet retreat (e.g., Domack et al., 2001; Pudsey and Evans, 2001; Taylor et al., 2001; Domack, 2002; Taylor and Sjunneskog, 2002; Domack et al., 2003; Ingolfsson et al., 2003; Pudsey et al., 2006; Heroy et al., 2008; Michalchuk et al., 2009; Milliken et al., 2009; Bentley et al., 2009; Allen et al., 2011; Majewski et al., 2012; Barnard et al., 2014; Kim et al., 2018; Vorrath et al., 2023). However, most studies covered only some part of the Holocene, not back to the late glacial interval because mixing of sediments in glacial deposits makes proxies unsuitable for paleoenvironmental records. As a result, a glacial to interglacial sedimentological succession record, which is found in the continental slope and rise, lacks in the ice proximal locations. That is, there is no information on how and when water mass changes between the deep Southern Ocean and the shallow shelf region occurred and how they are related to changing surface environments as ice sheet/shelf retreat from glacial to deglacial intervals.

The Eastern Bransfield Basin (EBB) is located in between Joinville Island and Elephant Island in the northern Antarctic Peninsula. Due to its geomorphologic character and scarcity of adjacent land, the EBB was likely not filled with grounded ice during the late glacial interval. As such, the EBB is being able to provide continuous sedimentary records from the late glacial interval to the Holocene. Diatoms are the main phytoplankton to dominate primary production in Antarctica (Tréguer et al., 1995). The distribution of diatoms in sediments of the Southern Ocean is dependent on primary production and other parameters including nutrients (Burckle et al., 1987), grazing effect (Bodungen et al., 1985), sea surface temperature (Neori and Holm-Hansen, 1982), sea ice cover (Ablmann and Gersonde, 1991; Armand et al., 2005), and stability of the water column (Leventer, 1991). As a result, diatom assemblage data are often used to reconstruct paleo-environmental changes in the western Antarctic Peninsula shelf regions (e.g., Leventer et al., 1996, 2002; Taylor et al., 2001; Taylor and Sjunneskog, 2002; Heroy et al., 2008; Allen et al., 2010).

In this study, we documented diatom assemblage data in the EBB sediments to reconstruct changes in surface water environments and water mass exchange between the Southern Ocean and the Antarctic Peninsula continental shelf since the late glacial interval.

KOPRI 극지연구소

2. Study area

The Bransfield Strait is a semi-closed ocean basin which separates the South Shetland Islands (SSI) and the Antarctic Peninsula (Fig. 1; López et al., 1999; Kerr et al., 2018). The narrow (100–150 km wide and ~450 km long) Bransfield Strait is morphologically divided into three deep basins (Western, Central, and Eastern Bransfield Basins) by the highs of Deception and Bridgeman Islands (Jeffers and Anderson, 1991). Bransfield Strait opened as a rift basin after the cessation of the spreading of the Phoenix-Antarctic Ridge at ~4 Ma (Jeffers and Anderson, 1991; Galindo-Zaldivar et al., 2004).

There are two primary sources for surface circulation in the Bransfield Basins; (1) warmer, lower salinity waters entering from the Bellingshausen Sea and (2) colder, saltier waters from the Weddell Sea (García et al., 2002). The Bransfield Basins receive modified Circumpolar Deep Water (m-CDW) originating from the Antarctic Circumpolar Current through the seaways between the South Shetlands Island including King George, Elephant, Snow, Smith, and Low Islands and Antarctic Peninsula (Niiler et al., 1991; Hofmann et al., 1996; Dotto et al., 2016). Dense Shelf Water is advected from the Weddell Sea into the Bransfield Basins by the Antarctic Coastal Current (Heywood et al., 2014; Sangrà et al., 2017). The denser water from the Weddell Sea sinks to form a deeper layer of the Bransfield Basins while mixing with ambient waters (e.g., Whitworth et al., 1994; Gordon et al., 2000). The modern Bransfield Basins are covered by a mean winter sea ice concentration of ~50% but spring and summer sea ice decreases to between 18% and less than 2% coverage (Fig. 1, Vorrath et al., 2019).

3. Materials and Methods

A 29.1 m long sediment core AP18-LC08 (62°7.4960´S, 56°7.8605´W, 1324 m water depth) was collected using a 36 m long jumbo piston corer from the southwestern part of the EBB by IBR/V Araon during ANA08D Cruise. Additionally, a 54 cm long box core, AP18-BC08, was collected from this location. Neither core displays any evidence of core disturbance. AP18-LC08 is composed of moderately bioturbated diatomaceous mud with occasional sandy mud/sand layers from 0 to 21 m. The interval below 21 m is characterized by sandy mud with sand lenses, patches, and dispersed clasts. This general lithology change of AP18-LC08 is similar to that of an adjacent core that shows a transition from pebbly sandy stratified mud to diatomaceous mud, as reported in the Central

Bransfield Basin (Heroy et al., 2008).A 29.1 m long sediment core AP18-LC08 (62°7.4960´S, 56°7.8605´W, 1324 m water depth) was collected using a 36 m long jumbo piston corer from the southwestern part of the EBB by IBR/V Araon during ANA08D Cruise. Additionally, a 54 cm long box core, AP18-BC08, was collected from this location. Neither core displays any evidence of core disturbance. AP18-LC08 is composed of moderately bioturbated diatomaceous mud with occasional sandy mud/sand layers from 0 to 21 m. The interval below 21 m is characterized by sandy mud with sand lenses, patches, and dispersed clasts. This general lithology change of AP18-LC08 is similar to that of an adjacent core that shows a transition from pebbly sandy stratified mud to diatomaceous mud, as reported in the Central Bransfield Basin (Heroy et al., 2008).

3.1. Physical Properties

Magnetic susceptibility (MS) values were measured at 1 cm intervals on split half core sections using a Bartington MS-2B susceptibility meter at Korea Polar Research Institute (KOPRI). Water content (WC) was measured at 1 cm intervals on 1 cm thick sub-samples. The WC was calculated by the following equation:

WC (%) = (Masswet – (Massdry + Masssalt))/ Masswet × 100

where Masswet, Massdry, and Masssalt, are the mass of the original sample, dried sample, and salt content assuming 35 psu, respectively.

KOPRI 극지연구소

3.2. Diatom assemblage

Diatom assemblages were analyzed in 98 sampling intervals with ~30 cm intervals (~350 years). The sample preparation and diatom counting methods followed Bak et al. (2007). 2 g of dried sediment was used. Permanent slides were made from the deposits in 60 ml bottles. Approximately 250 μl of agitated suspension with 50 ml distilled water was settled and dried on a coverslip. All counts were completed on a light microscope at 400–1000x magnification. 400 diatom specimens were counted for each sample where possible. 400 viewfields were scanned for samples in which diatoms were rare. The quantitative analysis of the diatom slides followed the procedures described in Scherer (1994). Absolute abundance was calculated using the following equation: abundance = ((A x B)/(C x D))/E, where A is the number of specimens counted, B is the area of the settling chamber, C is the number of microscope fields of view, D is the area of the field of view, and E is the sample mass. Chaetoceros resting spores (CRS) were separately counted while 400 total non-CRS diatom specimens were counted. CRS were not included in the specimen count because its statistical dominance would mask trends in other taxa.

4. Chronology

Twenty-one accelerator mass spectrometry (AMS) 14C dates were measured at Beta Analytic, USA (Table 1). We analyzed seventeen horizons for acid insoluble organic matter (AIOM) and four horizons for foraminifers (the mixture of planktonic and benthic foraminifera for 1284 cm and 1924 cm and planktonic foraminifera for 2406 cm and 2666 cm). The core top 14C age was calculated as 3870 years, which is older than the local reservoir age of 1300 years reported from the adjacent areas (Xiao et al., 2016; Kim et al., 2018). This older age of the core top is likely attributed to reworked old carbon influence (e.g., Gordon and Harkness, 1992). Thus, the core-top age was subtracted from measured AIOM 14C dates as a correction for the reservoir effect and possible old carbon input following Lee et al. (2010). To obtain core top age of AP18-LC08 site and potential core top loss of AP18-LC08, two AMS 14C dates (0 and 50 cm) of AIOM were measured from a box core AP18-BC08 in the same location (Table 1). In addition, the top age of the box core AP18-BC08 was subtracted from measured AIOM 14C dates as a correction for the reservoir effect and possible old carbon input of AP18-LC08. The calibrated ages of the top of AP18-LC08 corresponds to 645 cal. yr BP, indicating some sediment loss in AP18-LC08.

Four AMS 14C dates of foraminifera were calibrated using CALIB 8.2 (Stuiver and Riemer, 2020) with the MARINE20 dataset (Heaton et al., 2020) using a constant marine reservoir effect of 1300 years, consistent with previous Southern Ocean and Western Antarctic Peninsula studies (e.g., Domack et al., 2001; Anderson et al., 2002; Pugh et al., 2009; Kilfeather et al., 2011; Xiao et al., 2016; Kim et al., 2018). Although marine reservoir ages are variable through time as a result of changes in oceanic circulation and ventilation (Sikes et al., 2000; Skinner et al., 2010), we used a constant reservoir age in this study because it is not well studied on temporal reservoir age change in the study area and because previous studies mentioned above also used a constant reservoir age. Although two samples are composed of only planktonic foraminifera and the other two are composed of planktonic and benthic foraminifera because of insufficient number of planktonic foraminifera, we treated them both the same in this study.

Calibrated AMS 14C dates of AIOM during the Holocene commonly showed continuous down core increase without significant age reversals in the Antarctic continental margins, which implies their reliability (e.g., Lee et al., 2010; Kim et al., 2018; Shin et al., 2020). Before the Holocene, however, calibrated AMS 14C dates of AIOM often showed age reversals indicating their unreliability. δ13C values were also ~1‰ higher than those above 1500 cm (Table 1). In addition, calibrated AMS 14C dates of AIOM below 1500 cm were

older than calibrated AMS 14C dates of foraminifera, which are believed more robust (Fig. 2). Thus, we determined not to use calibrated AMS 14C dates of AIOM below 1500 cm to establish an age-depth model for AP18-LC08 (Fig. 2). In addition, two outliers (1200 cm and 1292 cm) were excluded in the age model (Fig. 2). Ages were obtained based on simple linear interpolation of 11 accepted dates. Since there was no significant difference between ages obtained by simple linear interpolation and those obtained by polynomial regressions, we applied ages obtained by simple linear interpolation in this study. Based on the linear extrapolation of the last two age-depth information, the bottom of AP18-LC08 corresponds to 34.6 ka.

5. Results

AP18-LC08 is composed of bioturbated sandy mud with dispersed clasts during the late glacial interval, diatom-rich to diatom-bearing bioturbated mud during the Holocene, and a transitional facies during the deglacial interval. We define the deglacial interval as the period between the end of the Last Glacial Maximum and the early Holocene (19–11 ka) following Clark et al. (2011). MS values vary from 20 to 350 throughout the core (Fig. 3). MS values are generally high with large amplitudes (225 ±48) during the late glacial interval, drop during the deglacial (106 ±52) to values below 100 from ~15–11 ka before increasing to >200 at ~9 ka then vary between 20 and 200 for the rest of the Holocene (114 ±35) (Fig. 3). WC shows the opposite pattern; low (31 ±3%) during the late glacial interval and high (58±6%) during the Holocene through the deglacial interval (42±8%) (Fig. 3). There were some excursions both in MS and WC, but we consider them as outliers if the excursions are not found in both records. Excursions at ~4.2 ka and ~8.0 ka correspond to muddy sand to sand layers with a sharp bottom contact. Sedimentation rates (SR) are low at ~40 cm/kyr during the late glacial interval and increase over the deglacial interval to >140 cm/kyr during the Holocene (Fig. 3). Highest Holocene SRs occur during ~7.3 to ~8.4 ka (~220 cm/kyr) and after ~1.6 ka (~300 cm/kyr), whereas relatively low values occur during ~3.4 to 6.4 ka (Fig. 3).

We identify 63 diatom species belonging to 27 genera in AP18-LC08. Diatom concentrations are low (~0.2±0.2 x107 v/dgs) with an average occurrence of five species during the late glacial interval (34.6–19 ka) (Fig. 3). Diatoms increase from 4 to 58 x107 v/dgs during the deglacial interval. Average number of species is twenty-three during the deglacial and twenty-six during the Holocene. Diatom preservation status is generally poor during the late glacial interval compared to that during the Holocene. This increase is contemporaneous with the increase in WC and decrease in MS values (Fig. 3). The

variation pattern of CRS mostly resembles that of total diatom concentration, but CRS absolute abundance started to increase from 18.4 ka which was a lag of 600 years (Fig. 3). Major species in AP18-LC08 are displayed on Figure 4 according to their averaged relative abundance (≥1.5%).

During the late glacial interval, most species (including Corethron criophilum, Eucampia antarctica var. antarctica, Fragilariopsis obliquecostata, Odontella weissflogii, Proboscia inermis) are not present, with other taxa displaying rare or sporadic increases, including abundances up to or exceeding 20% (e.g., Actinocyclus actinochilus, E. antarctica var. recta, F. curta, F. kerguelensis, F. linearis, F. rhombica, F. ritscheri, R. styliformis, Thalassiosira antarctica, and Shionodiscus. gracilis) (Fig. 4). Of note is the absolute diatom abundance is substantially low and the number of species is very low during the late glacial interval, thus the glacial variation should be neglected when comparing with the deglacial interval or the Holocene. C. criophilum, F. curta, F. linearis, F. obliquecostata, F. rhombica, F. ritscheri, O. weissflogii, P. inermis, T. antarctica, and S. gracilis started to increase mostly at the beginning of the deglaciation (17.5 to 19.2 ka) showing continuous occurrences (Fig. 4). F. obliquecostata showed an early deglacial maximum (Fig. 4). Nonetheless, the general pattern during the deglacial interval is species specific. For example, C. criophilum showed its maximum at the end of the deglacial interval, but F. obliquecostata showed its maximum at the beginning of the deglacial interval (Fig. 4). E. anatarctica var. antarctica started to increase much later at 12.8 ka, reached its maximum at 7.3 ka, and then sharply decreased and remained low (Fig. 4e). F. kerguelensis and R. styliformis started to increase from 8.9 ka during the Holocene (Fig. 4). F. curta, F. linearis, F. obliquecostata, F. ritscheri, and T. antarctica show higher relative abundance during the deglacial interval than the Holocene (Fig. 4).

6. Discussion

Although the variation patterns of F. curta, F. linearis, F. obliquecostata, F. rhombica, F. ritscheri, and T. antarctica are somewhat different from each other, they are all related to sea ice (Armand et al., 2005). However, T. antarctica is usually associated with sea ice formation rather than sea ice melt (Pike et al., 2008). Thus, we grouped them as sea ice diatom except for T. antarctica in this study. Among minor species, F. cylindrus, F. separanda, F. sublinearis, Porosira glacialis, Stellarima microtrias, were also components for the sea ice group (Armand et al., 2005). It was suggested that F. linearis is a synonym for F. curta (Cefaelli et al., 2010). In addition, F. linearis was not reported from previous studies in the Bransfield Strait and adjacent areas (e.g., Barcena et al., 1998, 2002, 2006;

Heroy et al., 2008; Vorraths et al., 2023). As both species are grouped into sea ice diatom, treating them separately or together as F. curta does not alter the interpretation. However, as there is disagreement in the literature and they showed subtle differences, we treated them separately in this study.

Likewise, we considered the sum of F. kerguelensis and S. gracilis, Rhizosolenia spp, E. antarctica var. antarctica as open ocean diatoms (Leventer et al., 2002; Crosta et al., 2005). Thalassiosira lentiginosa, T. oliverana, Thalassiothrix longissima, and Thalassionema nitzchioides belong to the open ocean diatom group as minor species (Crosta et al., 2005). Although relative abundance of some species during the late glacial interval looks abundant (>20%), absolute diatom valves are significantly lower during the late glacial interval than the Holocene and the deglacial interval (Fig. 4). Indeed, occurrence of sea ice diatoms and open ocean diatom calculated by relative abundance times total valve number showed very low occurrence despite their high relative abundance during the late glacial interval (Fig. 5). Thus, we assumed high relative diatom abundance during the late glacial interval is less meaningful and biased by limited occurrence numbers when we discuss temporal variation using relative abundance changes.

6.1. The late glacial interval (34.6 – 19 ka)

The glacial sediments of AP18-LC08 are characterized by high MS values, very low diatom concentrations, very low CRS abundance, low WC and low SR that indicate diatom productivity was severely limited under more glacial/terrestrial influence. MS values are high during the late glacial interval in the Antarctic Peninsula region (e.g., Sprenk et al., 2013; Weber et al., 2014, 2022; Xiao et al., 2016; Kim et al., 2018, 2020; Shin et al., 2020). MS values are controlled primarily by dilution of ferromagnetic phases with biogenic material (Leventer et al., 1996), and glaciogenic process must have been dominant during the glacial interval. Thus, high MS values indicate a combination of higher terrestrial inputs under advanced glacial conditions and less dilution by biogenic material. If the EBB was covered by perennial sea ice, open ocean species would be largely excluded in the EBB. However, the open ocean species, F. kerguelensis, was found during the late glacial interval together with sea ice diatoms (Fig. 4). Sea ice diatom abundance is very low under perennial sea ice condition (Allen et al., 2011; Müller et al., 2011). In addition, sea ice diatoms are not detected under >11 months/year and >50% of February sea ice concentration in the Southern Ocean (Armand et al., 2005). Thus, these data suggest that during the late glacial interval the EBB was covered by extensive sea ice which was mostly perennial but occasionally allowed water mass exchange with the Southern Ocean. As diatom preservation was poor during the glacial intervals, glacial diatom assemblages might

have been affected by preservation bias. However, because the species, F. kerguelensis or sea ice diatoms are not robust, glacial diatom assemblages are thought not to be affected by it.

Based on the age model, these intermittent exchanges are considered to have occurred at a millennial time scale. The combination of Millennial-scale variations in the MS and diatom records likely reflects the intermittent millennial-scale climate changes. Millennial-scale climatic changes during the glacial interval are observed in ice cores of both the Northern (North Greenland Ice Core Project members, 2004) and Southern Hemisphere (Jouzel et al., 2007) (Fig. 6). In addition, millennial-scale climate fluctuations during the last glacial interval have also been reported from sea-salt Na+ flux, a sea ice proxy, (Fischer et al., 2007), CO2 record of Byrd ice core (Ahn and Brook, 2008), radiolarian-based summer sea surface temperature at ODP 1089 (Cortese and Abelmann, 2002), and biogenic opal concentrations of MD07-3133 and MD07-3134 in the Scotia Sea. We believe our millennial-scale variation during the late glacial interval is likely related to those millennial-scale climatic events, but at this moment due to relatively low sampling resolution it is a bit difficult to draw such conclusions.

According to time slice reconstruction of the Antarctic Ice Sheet (Bentley et al., 2014), during the Last Glacial Maximum the South Shetlands Islands were occupied by grounded ice, but none of the three Bransfield Basins were grounded. As the m-CDW intruded onto the continental shelf from the deep Southern Ocean in the post-LGM period, millennial-scale climate changes may indicate that passages between SSI and AP were not covered by the grounded ice or the ice on that area was unstable, showing millennial-variation.

6.2. The deglacial interval (19 – 11 ka)

From 19 ka diatom abundance shows a gradual increase to >50 x107 v/dgs by 11 ka indicating a rise in diatom productivity (Fig. 3). As diatom productivity increases, relative abundance of sea ice diatoms shows a modest decrease from 80% to 60% between ~18 and 11 ka, whereas open ocean diatoms started to increase from ~13 ka. Thus, sea ice coverage in the EBB started to decrease during the deglacial interval in line with regional retreat of grounded ice and global warming toward the Holocene. Reported deglaciation initiation in the Antarctic Peninsula regions varies from 17.5 ka to 15.7 ka to 14.1 ka in the various locations including the SSI, northern AP, Anvers Margin, Bransfield Strait, Gerlache Strait, and Maxwell Bay (Heroy and Anderson, 2007; Ó Cofaigh et al., 2014; Roseby et al., 2022). Although our deglaciation age seems to be a bit earlier than those reported previously, our deglacial age is based on AMS 14C dates of foraminifera. In addition, the

wide and deep area of the EBB may help record deglacial histories well.

Among sea ice species, F. obliquecostata reached its maximum during the early deglacial interval, presumably reflecting heavier sea ice conditions. This is because February sea surface temperature at maximum relative abundance of F. obliquecostata is -1 to 0, which is the coldest among sea ice diatoms (Armand et al., 2005). By the end of the deglacial interval, the dominant species were still sea ice diatoms despite their decreasing relative abundance and increasing open ocean species. F. lineata showed an overall high relative abundance together with T. antarctica during the deglacial interval (Fig. 3). SR also increased showing a similar pattern to that of diatom absolute abundance, implying that the SR increase was ascribed to increased diatom productivity (Fig. 4). CRS, indicative of surface water stratification in association with a receding ice edge (i.e., ice melting) and high primary productivity (Leventer et al., 1996, 2006; Crosta et al., 1997, 2004, 2008; Sjunneskog and Taylor, 2002), increased at 15.3 ka, indicating that deglacial warming was enhanced from 15.3 ka in the EBB. Other species, C. criophilum, O. weisflogii, and P. inermis, also increased from 15.3 ka (Fig. 4). Due to deglacial warming, early sea ice break-up and ice sheet/shelf meltwater likely enhanced surface water stratification, which may have enhanced surface water warming favoring open ocean species (e.g., Crosta et al., 2008; Shevenell et al., 2011). This is why often high primary productivity co-occurs with CRS (e.g., Leventer et al., 1996; 2006). F. obliquecostata showed a sharp increase during the early deglacial interval indicating relatively heavy sea ice condition during the early deglacial interval. Diatom production was increasing towards the Holocene as sea ice retreated in the EBB. As the sea ice is one important factor for controlling the surface diatom production (Ablmann and Gersonde, 1991; Armand et al., 2005; Chase et al., 2015), sea ice variation itself is also considered important for diatom production changes.

Although a distinctive increase in diatom abundance did not occur at 14.8 ka, a marked decrease in MS values and increase in WC at 14.8 ka are noted in the record (Fig. 3). There were two periods of rapid post-glacial global sea level rise; Meltwater Pulse 1A (MWP1A) during 14.7–13.5 ka (Blanchon, 2011; Hanabuth et al., 2000; Hanebuth and Stattegger, 2003) and MWP1B during 11.5–11.2 ka (Edwards et al., 1993; Bard et al., 1996). MWP1A co-occurred with the Bølling-Allerød warm period, which was found in the North GRIP ice core at 14.7 ka (Steffensen et al., 2008). However, the meltwater source for the sea level rise is controversial whether from the Antarctic Ice Sheet (Deschamps et al., 2012), the Laurentide Ice Sheet (Gregoire et al., 2012), or the Fennoscandian and Barents Sea Ice Sheets (Brendryen et al., 2020). According to modeling or calculation based on geological data, MWP1A received a significant contribution from the Antarctic Ice Sheet (e.g., Clark et al., 1996, 2002; Bassett et al., 2005; Carlson and Clark, 2012; Golledge et al., 2014). However, atmospheric and oceanic cooling event, Antarctic Cold Reversal, occurred in the southern

high latitude between 14.7 and 13 ka (Pedro et al., 2016). Unfortunately, no record from the Antarctic Peninsula was included in Pedro et al. (2016). In addition, biogenic opal accumulation (i.e., diatom production) in the Scotia Sea specifically shows a general increasing trend during the deglacial interval indicating general warming without cooling excursions (e.g., Sprenk et al., 2013; Kim et al., 2020).

As a source of the MWP1B, it was proposed that Antarctic Ice Sheet retreat may have supplied meltwater from the Prydz Bay region in East Antarctica (Leventer et al., 2006) and from the Ross Sea (McKay et al., 2008). Weber et al. (2014) reported several centennial- to millennial-scale ice rafted debris events indicating Antarctic Ice Sheet discharge (AID) in the Scotia Sea including the MWP1A and MPW1B. This implies that Antarctic deglaciation occurred contemporaneously with MWP1A and MWP1B. Thus, the high occurrence of CRS during 15.4–12.1 ka in the EBB may relate to a significant amount of meltwater input which is most likely related to the Antarctic Ice Sheet deglaciation. According to IRD records (Weber et al., 2014; Jasper et al., 2024), there were five centennial- to millennial-scale deglaciation events recorded in Scotia Sea sediment core during 14.7–11.2 ka (Fig. 6). Thus, high CRS with fluctuations observed during 15.4–12.1 ka in AP18-LC08 may be related to the centennial- to millennial-scale deglaciation events recorded in the Scotia Sea. Our result suggests that distinctive meltwater input occurred at the beginning of MWP1A and the Bølling-Allerød despite IRD events occurred in the Scotia Sea earlier at 20–19 ka (AID8) and 17–16 ka (AID7) (Weber et al., 2014). CRS started to modestly increase at 17.5 ka which is the recession timing from the Bransfield Basin (Ó Cofaigh et al., 2014) (Fig. 3). In addition, there is no sign of CRS increase during 20–19 ka in our core. Interestingly, however, CRS was low during 11.8–9.7 ka including the MWP1B (Fig. 6), suggesting different responses in EBB and the Scotia Sea. If we assume that EBB records are associated with Antarctic Peninsula Ice Sheet and Scotia Sea records are more associated with West Antarctic Ice Sheet, Antarctic Peninsula Ice Sheet retreats resemble those of West Antarctic Ice Sheet during the deglacial intervals, but differ in important detail of deglacial events.

6.3. The Holocene (after 11 ka)

SRs of AP18-LC08 in the Holocene are generally high (>140 cm/kyr) compared to the late glacial interval (Fig. 2). The increased SR during the Holocene is also found in the adjacent core collected from the Central BB (Heroy et al., 2008). Although AP18-LC08 shows much higher SR (>140 cm/kyr) than the SR of ~60 cm/kyr in the Central BB, this is likely due to regional environment differences. These consistently show that SR increased during the Holocene. CRS abundance was high throughout the interval 9–6.4 ka. Holocene

Climate Optimum (HCO) is the warmest period during the Holocene from 9.5–5.5 ka (Marcott et al., 2013) and many previous studies reported the HCO in the west AP (e.g., Taylor et al., 2001; Leventer et al., 2002; Taylor and Sjunneskog, 2002; Allen et al., 2010). The CRS peak during 9–6.4 ka is likely related to HCO in the EBB and indicates that rapid warming occurred resulting in massive amount of meltwater into the EBB. E. antarctica var. antarctica showed its maximum occurrence during 9–6.7 ka in the Palmer Deep (Leventer et al., 2002). Thus, the occurrence of E. antarctica var. antarctica can be used for HCO in the study area and the AP. It is of note that E. antarctica var. antarctica started to increase from 12.8 ka. This implies that southward incursion of warmer water started before the HCO. From 9 ka, the indicator of ACC influence F. kerguelensis (Crosta et al., 2005), increased considerably (Fig. 4) reflecting a southward incursion of warmer water from the Southern Ocean. Sea ice forming related species T. antarctica showed a distinct decrease at 9 ka and remained low throughout the Holocene (Fig. 5), suggesting that sea ice formation decreased contemporaneously with warm water mass intrusions to the EBB. This means either that decreased sea ice allowed incursions of warmer waters or that the increase in warmer waters caused sea ice decrease at 9 ka. As Shevenell et al. (2011) reported higher sea surface temperature in association with meltwater stratification during 11.8–9 ka in the in the west of the Antarctic Peninsula, warmer sea surface temperature may have facilitated sea ice retreat in the EBB. This is supported by increased T. antarctica relative abundance, which is related to sea ice formation (Pike et al., 2008), during 12.6–9 ka. In either case, the conditions indicate the strong coupling between sea ice and warm water mass intrusion into the EBB. Thus, the massive meltwater discharge during the HCO in the EBB was triggered by the input of a relatively warmer water mass through straits in SSI, although this event is not recorded as an IRD event in the Scotia Sea (Weber et al., 2014). According to timeslice reconstructions for Antarctic Ice Sheet, ice on the SSI and on the northern AP significantly retreated from 10 ka to 5 ka (Bentley et al., 2014). Thus, the meltwater source is considered from those areas during the HCO. SR also increased at 9 ka indicating that diatom production was likely elevated (Fig. 3).

Diatom production was low during 6.5–3.7 ka with a decreased CRS and decreased total number of sea ice and open ocean species, but with increased relative abundance of sea ice species (Figs. 5 and 6). Thus, this period is characterized by increasing sea ice and decreased warmer water mass intrusion, implying a cold period in the EBB.

Diatom concentrations increased slightly after 3.4 ka with brief episode of higher CRS and sea ice diatoms (Fig. 6). Thus, the productivity increase at 3–2 ka is related to sea ice diatom production. The period after 2.2 ka is characterized by decreasing sea ice diatoms, increased open ocean diatoms, decreasing CRS, and high SR (Fig. 5). This may

indicate the EBB received an increase in warmer water that supported higher production of open ocean species in the EBB. According to Antarctic grounded ice limits reported in Bentley et al. (2014), further retreat occurred from 5 ka to today. Thus, we believe that high CRS during the Holocene (8.5–6 ka) is ascribed to meltwater input driven by retreating Antarctic Peninsula Ice sheet.

C. criophilum, O. weissflogii, P. inerimis, and R. styliformis showed a general increase in relative abundance during the Holocene (Fig. 4). C. criophilum started to increase from the deglacial interval and showed its minimum during 10–7.4 ka when E. antarctica var. antarctica showed increased relative abundance (Fig. 4). P. inerimis and R. styliformis showed their minimum during 7.1–4.1 ka when overall diatom production decreased (Fig. 4). Those species increased during the late Holocene; C. criophilum at 2.6 ka, O. weissflogii at 4.4 ka, P. inerimis at 3.7 ka, and R. styliformis at 3.7 ka (Fig. 4). However, not much is known about those species in the Antarctic Ocean and what environmental change occurred in association with those diatom assemblage changes needs to be further studied in the future.

6.4 Implications

Paleoenvironmental condition changes in the Antarctic Peninsula during the Holocene showed regionally different patterns (e.g., Domack et al., 2001; Pudsey and Evans, 2001; Taylor et al., 2001; Domack, 2002; Taylor and Sjunneskog, 2002; Domack et al., 2003; Ingolfsson et al., 2003; Pudsey et al., 2006; Heroy et al., 2008; Michalchuk et al., 2009; Milliken et al., 2009; Bentley et al., 2009; Allen et al., 2011; Majewski et al., 2012; Barnard et al., 2014; Kim et al., 2018; Vorrath et al., 2023). Post-glacial climate along the East Antarctic coastal margins based on shallow marine and coastal terrestrial records also showed regionally different results (e.g., Verleyen et al., 2011 and references there in). This suggests that regionally different responses are ascribed to regional settings in Antarctica, thus comparison with adjacent regions is essential to resolve the patterns and scales of regional variability. However, this paper focuses on the climatic changes since the late glacial interval, thus detailed regional comparison is not dealt in this study.

Vorrath et al. (2023) reported deglacial and Holocene sea ice and climate dynamics in the BB; increased open ocean species at 8.3 ka and decreasing sea ice until 14–8.3 ka, which is consistent with our result. In addition, the SR of the late glacial interval in this study is ~40 cm/kyr, which is very high, although diatom occurrence is low. Thus, our record plays an important role in understanding surface environmental changes in response to ice dynamics since the late glacial interval.

Decreasing MS values and increasing diatom production at AP18-LC08 indicate

increasing marine influence and decreasing glacial/terrestrial influence during the deglacial interval in the EBB. However, glacial diatom data showing high relative abundance of open ocean species in AP18-LC08 (Fig. 4) do not fit to the environmental characteristics of the late glacial interval reported from the previous studies (e.g., Bak et al., 2007; Xiao et al., 2016). As explained earlier, this is due to bias effect caused by very low diatom abundance in this interval.

In the Scotia Sea, open ocean species F. kerguelensis reached its maximum at ~12 ka (Xiao et al., 2016). F. kerguelensis in AP18-LC08 sharply increased at 9 ka (Fig. 4). This delayed increase in AP18-LC08 is likely related to its position located in the south and the sea ice barrier effect in the EBB which hinders incursions of warmer waters into the EBB (Fig. 6). As increased marine influence in connection with rising global sea level and retreat of ice shelf/sheet until 8 ka was reported in Maxwell Bay, in Antarctica, initiation of warmer water mass intrusion into the EBB is also related to rising global sea level. Since the EBB is connected to the open Southern Ocean through m-CDW and is one of the widest basins in West Antarctica, EBB records are considered to reflect global climate change.

The Southern Annular Mode (SAM) describes the latitudinal movement of the Southern Westerly Winds, an important wind belt encircling in the Southern Ocean (Toggweiler, 2009; Moreno et al., 2018), over a timescale of decades to centuries. The SAM is a key climatic factor to influence glacier dynamics in response to climate change (Darvill et al., 2016; Davies et al., 2020). As centennial timescale SAM-like changes were reported in southern Patagonia (Merino et al., 2018), we cannot exclude the possibility that our millennial-scale variations might be related to the SAM variation. Yet, further studies are required to unveil the possibility.

7. Conclusions

Using diatom assemblage data and physical properties, we reconstructed surface environmental changes in the EBB in response to ice dynamics from the late glacial interval to the Holocene to understand how surface environments changed as ice retreats and timing of relatively warm water mass intrusion into the EBB. Diatom assemblage data and physical properties of AP18-LC08 showed a consistent variation pattern with global climate change from the late glacial interval to the Holocene and the local variabilities as well.

High MS values and very low diatom abundance, but with some occurrences of open ocean and sea ice diatom species during the late glacial interval (34.6 – 19 ka) indicate that the EBB likely was largely covered by extensive sea ice during that interval. However,

millennial-scale variations are demonstrated. Sea ice diatoms started to decrease at 19 ka coincident with the beginning of the global deglaciation, with increasing open ocean species and decreasing MS values indicating ongoing sea ice decrease during the deglaciation. Increased CRS during 14.7–11.3 ka is related to global deglacial warming events; MWP1A and 1B and to AID events reported in the Scotia Sea, implying massive amount of meltwater input. During the HCO CRS also showed its maximum indicating early Holocene Antarctic Ice Sheet retreat resulting in massive amount of meltwater discharge. Water mass exchange between the Southern Ocean and the EBB intensified at 9 ka showing distinctive an increase (decrease) in open ocean (sea ice) species. This indicates that sea ice is strongly related to warm water mass input from the Southern Ocean. These findings highlight the close linkage between regional and global climatic events, emphasizing the role of warm water mass intrusions on the surface environments of the EBB. More detailed research using various proxies is needed in the future to comprehensively understand paleoceanographic changes and the relationship between the EBB and the Southern Ocean.

KOPRI
극지연구소

지난 마지막 빙하기 이후의 남극반도 동부 분지에서의 고해양학적 변화와 그 의미[6)]

Sunghan Kim[a,b,*], Young-Suk Bak[c,+], Kyu-Cheul Yoo[a], Min Kyung Lee[a], Jae Il Lee[a], Sookwan Kim[d], Jinku Park[a], So-Young Kim[a], Heung Soo Moon[a], Myung-Il Kang[a], Hyo Jin Kim[a]

[a]Korea Polar Research Institute, Incheon 21990, Republic of Korea
[b]Department of Polar Sciences, University of Science and Technology (UST), Incheon 21990, Republic of Korea
[c]Department of Earth and Environmental Sciences, Jeonbuk National University, Jeonju, 54896, Republic of Korea
[d]Korea Institute of Ocean Science and Technology, Busan 49111, Republic of Korea

요약: 남극반도는 남극 대륙에서 가장 북쪽에 위치한 지역으로 기후 온난화에 특히 취약하며, 비교적 따뜻한 수괴가 남극 대륙붕으로 유입될 경우 빙붕 후퇴를 촉진한다는 점은 잘 알려져 있으나, 대륙붕에서의 해빙 역학으로 인해 빙하 인접 지역에서 남빙양 심층수와 대륙붕 사이의 수괴 교환이 언제, 어떻게 이루어지는지는 여전히 명확하지 않다. 본 연구는 동부 브랜스필드 분지(EBB)에서 채취한 고퇴적률 퇴적물 코어를 이용하여 약 3만 4,600년 전 이후 후기 빙기부터 현재까지의 규조 군집 기록을 분석함으로써 표층 환경 변화를 규명하였다. 그 결과 후기 빙기 동안 EBB는 밀레니엄 규모의 변동성을 보이는 광범위한 해빙으로 덮여 있었으며, 빙기–간빙기 전이기(19–11 ka) 동안 해빙이 점차 감소하고 개방 해양 환경의 영향이 소폭 증가하였다. 특히 14.7–11.3 ka 동안에는 융빙수 유입이 두드러지게 증가하여 스코샤해에서 보고된 남극 빙상 방출 사건과, 즉 융빙수 펄스 1A 및 1B 시기와 일치하였다. 홀로세, 특히 9 ka 이후에는 상대적으로 따뜻한 수괴의 유입이 현저히 증가하고 해빙의 영향이 크게 감소하여 해빙과 따뜻한 수괴 유입 간의 밀접한 연관성이 확인되었으며, 이 시기 EBB에서 나타난 융빙수 유입은 스코샤해에서 보고된 빙상 방출 사건과는 직접적으로 대응되지 않았다. 이러한 결과는 동부 브랜스필드 분지의 표층 환경 변화가 전 지구적 기후 변화와 지역적 기후 특성을 동시에 반영하고 있음을 보여준다.

6) 이 연구 결과는 다음의 논문으로 출판되었음: Kim, S. et al. (2025). "Paleoceanographic condition changes in the Eastern Bransfield Basin, Antarctic Peninsula, since the late glacial interval and its implications" Palaeogeography Palaeoclimatology, Palaeoecology 669: 112934.

References

Abelmann, A., Gersonde, R., 1991. Biosiliceous particle flux in the Southern Ocean. Mar. Chem. 35, 503–536.

Ahn, J., Brook, E., 2008. Atmospheric CO2 and climate on millennial time scales during the last glacial period. Science 332, 83–85, doi:10.1126/science.1160832.

Allen, C.S., Oakes-Fretwell, L., Anderson, J.B., Hodgson, A., 2010. A record of Holocene glacial and oceanographic variability in Neny Fjord, Antarctic Peninsula. The Holocene 20, 551–564, doi:10.1177/0959683609356581.

Allen, C.S., Pike, J., Pudsey, C.J., 2011. Last glacial-interglacial sea-ice cover in the SW Atlantic and its potential role in global deglaciation. Quat. Sci. Rev. 30, 2446–2458.

Anderson, J.B., Shipp, S.S., Lowe, A.L., Wellner, J.S., Mosola, A.B., 2002. The Antarctic Ice Sheet during the Last Glacial Maximum and its subsequent retreat history: A review. Quat. Sci. Rev. 21(1–3), 49–70, doi:10.1016/S0277-3791(01)00083-X.

Armand, L.K., Cornet-Barthaux, V., Mosseri, J., Quéguiner, B., 2008. Late summer diatom biomass and community structure on and around the naturally iron-fertilised Kerguelen Plateau in the Southern Ocean. Deep-Sea Res. II 55, 653–676.

Bak, Y.S., Yoo, K.C., Yoon, H.I., Lee, J.D., Yun, H., 2007. Diatom evidence for Holocene paleoclimatic change in the South Scotia Sea, west Antarctica. Geosci. J. 11, 11–22.

Bárcena, M.A., Gersonde, R., Ledesma, S., Fabrés, J., Calafat, A.M., Canals, M., Sierro, F.J., Flores, J.A., 1998. Record of Holocene glacial oscillations in Bransfield Basin as revealed by siliceous microfossil assemblages, Antarct. Sci., 10, 269–285, doi:10.1017/S0954102098000364.

Bárcena, M.A., Fabrés, J., Isla, E., Flores, J.A., Sierro, F.J., Canals, M., Palanques, A., 2006. Holocene neoglacial events in the Bransfield Strait (Antarctica). Palaeocenographic and palaeoclimatic significance. Scientia Marina 70, 607–619.

Isla, E., Plaza, A., Flores, J.A., Sierro, F.J., Masqué, P., Sanchez-Cabeza, J.A., Palanques, A., 2002. Bioaccumulation record and paleoclimatic significance in the Western Bransfield Strait. The last 200 years. Deep-Sep Res. II 49, 935–950.

Bárcena, M.A., Isla, E., Plaza, A., Flores, J.A., Sierro, F.J., Masqué, P., Sanchez-Cabeza, J.A., Palanques, A., 2002. Bioaccumulation record and paleoclimatic significance in the Western Bransfield Strait. The last 200 years. Deep-Sep Res. II 49, 935–950.

Bard, E. et al., 1996. Deglacial sea-level record from Tahiti corals and the timing of global meltwater discharge. Nature, 382, 241–244.

Barnard, A., Wellner, J.S., Anderson, J.B., 2014. Late Holocene climate change recorded in proxy records from a Bransfield Basin sediment core, Antarctic Peninsula. Polar

KOPRI 극지연구소

Res. 33, 17236, doi:10.3402/polar.v33.17236.

Bassett, S. E., Milne, G.A., Mitrovica, J.X., Clark, P.U., 2005. Ice sheet and solid earth influences on far-field sea-level histories. Science 309, 925–928, doi:10.1126/science.1111575.

Bentley, M.J., Cofaigh, C.Ó., Anderson, J.B., Conway, H., Davies, B., Graham, A.G.C., Hillenbrand, C.-D., Hodgson, D.A., Jamieson, S.S.R., Larter, R.D., Mackintosh, A., Smith, J.A., Verleyen, E., Ackert, R.P., Bart, P.J., Berg, S., Brunstein, D., Canals, M., Colhoun, E.A., Crosta, X., Dickens, W.A., Domack, E., Dowdeswell, J.A., Dunbar, R., Ehrmann, W., Evans, J., Favier, V., Fink, D., Fogwill, C.J., Glasser, N.F., Gohl, K., Golledge, N.R., Goodwin, I., Gore, D.B., Greenwood, S.L., Hall, B.L., Hall, K., Hedding, D.W., Hein, A.S., Hocking, E.P., Jakobsson, M., Johnson, J.S., Jomelli, V., Jones, R.S., Klages, J.P., Kristoffersen, Y., Kuhn, G., Leventer, A., Licht, K., Lilly, K., Lindow, J., Livingstone, S.J., Massé, G., McGlone, M.S., McKay, R.M., Melles, M., Miura, H., Mulvaney, R., Nel, W., Nitsche, F.O., O'Brien, P.E., Post, A.L., Roberts, S.J., Saunders, K.M., Selkirk, P.M., Simms, A.R., Spiegel, C., Stolldorf, T.D., Sugden, D.E., van der Putten, N., van Ommen, T., Verfaillie, D., Vyverman, W., Wagner, B., White, D.A., Witus, A.E., Zwartz, D., 2014. A community-based geological reconstruction of Antarctic Ice Sheet deglaciation since the Last Glacial Maximum. Quat. Sci. Rev. 100, 1–9, doi:10.1016/j.quascirev.2014.06.025.

Bentley, M.J., Hodgson, D.A., Smith, J.A., Ó Cofaigh, C., Domack, E.W., Larter, R.D., Roberts, S.J., Brachfeld, S., Leventer, A., Hjort, C., Hillenbrand, C.D., Evans, J., 2009. Mechanisms of Holocene palaeo-environmental change in the Antarctic Peninsula region. The Holocene 19, 51–69, doi:10.1177/0959683608096603.

Blanchon, P., 2011. Meltwater Pulses. In: Hopley, D. (Ed.) Encyclopedia of Modern Coral Reefs: structure, form and process. Springer-Verlag Earth Science Series, Springer Science, New York, 683–690.

Bodungen, B.V., Smetacek, V.S., Tilzer, M.M., Zeitzschel, B., 1985. Primary production and sedimentation during spring in the Antarctic Peninsula region. Deep-Sea Research 33, 177–194.

Brendryen, J., Haflidason, H., Yokoyama, Y., Haaga, K.A., Hannisdal, B., 2020. Eurasian Ice Sheet collapse was a major source of Meltwater Pulse 1A 14,600 years ago. Nature Geoscience 13, 363–368.

Burckle, L.H., Jacob, S.S., McLaughlin, R.B., 1987. Late austral spring diatom distribution between New Zealand and the Ross Ice Shelf, Antarctica: hydrography and sediment correlations. Micropaleontology 33 (1), 74–81.

Carlson, A.E., Clark, P.U., 2012. Ice sheet sources of sea level rise and freshwater discharge during the last deglaciation. Rev. Geophys. 50, RG4007, doi:10.1029/2011RG000371.

Cefarelli, A.O., Ferrario, M.E., Almandoz, G.O., Atencio, A.G., Akselman, R., Vernet, M., 2010. Diversity of the diatom genus Fragilariopsis in the Argentine Sea and Antarctic waters: morphology, distribution and abundance. Polar Biol. 33, 1463–1484, doi:10.1007/s00300-010-0794-z.

Clark, P.U., Alley, R.B., Keigwin, L.D., Licciardi, J.M., Johnsen, S.J., Wang, H., 1996. Origin of the global meltwater pulse following the last glacial maximum. Paleoceanography, 11(5), 563–577, doi:10.1029/96PA01419.

Clark, P.U., Shakun, J.D., Baker, P.A., Bartlein, P.J., Brewer, S., Brook, E., Carlson, A.E., Cheng, H., Kaufman, D.S., Liu, Z., Marchitto, T.M., Mix, A.C., Morrill, C., Otto-Bliesner, B.L., Pahnke, J., Russell, J.M., Whitlock, C., Adkins, J.F., Blois, J.L., Clark, J., Colman, S.M., Curry, W.B., Flower, B.P., He, F., Johnson, T.C., Lynch-Stieglitz, J., Markgraf, V., McManus, J., Mitrovica, J.X., Moreno, P.I. Williams, J.W., 2011. Global climate evolution during the last deglaciation. Proceedings of the National Academy of Sciences 13, E1134–E1142, doi:10.1073/pnas.1116619109.

Clark, P.U., Mitrovica, J.X., Milne, G.A., Tamisiea, M.E., 2002. Sea-level fingerprinting as a direct test for the source of global meltwater pulse 1A. Science 295, 2438–2441.

Cortese, G., Abelmann, A., 2002. Radiolarian-based paleotemperatures during the last 160 kyr at ODP Site 1089 (Southern Ocean, Atlantic Sector). Palaeogeogr., Palaeoclimatol., Palaeoecol. 182, 259–286.

Crosta, X., Pichon, J.J., Labracherie, M., 1997. Distribution of Chaetoceros resting spores in modern peri-Antarctic sediments. Mar. Micropaleontol. 29, 283–299.

Crosta, X., Sturm, A., Armand, L., Pichon, J.J., 2004. Late Quaternary sea ice history in the Indian sector of the Southern Ocean as recorded by diatom assemblages. Mar. Micropaleontol. 50, 209–223, doi:10.1016/S0377-8398(03)00072-0.

Crosta, X., Denis, D., Ther, O., 2008: Sea-ice seasonality during the Holocene, Adélie Land, East Antarctica. Mar. Micropaleontol. 66, 222–32.

Crosta, X., Romero, O., Armand, L.K., Pichon, J.-J., 2005: The biogeography of major diatom taxa in Southern Ocean sediments: 2. Open ocean related species. Palaeogeography, Palaeoclimatology, Palaeoecology 223, 66–92.

Darvill, C.M., Bentely, M.J., Stokes, C.R., Shulmeister, J., 2016. The timing and cause of glacial advances in the southern mid-latitudes during the last glacial cycle based on a synthesis of exposure ages from Patagonia and New Zealand. Quat. Sci. Rev. 149, 200–214.

Davies, B.J., Darvill, C.M., Lovell, H., Bendle, J.M., Dowdeswell, J.A., Fabel, D., García, J.L., Geiger, A., Glasser, N.F., Gheorghiu, D.M., Harrison, S., Hein, A.S., Kaplan, M.R., Martin, J.R.V., Mendelova, M., Palmer, A., Pelto, M., Rodés, Á., Sagredo, E.A., Smedley, R.K., Thorndycraft, V.R., 2020. The evolution of the Patagonian Ice Sheet

from 35 ka to the present day (PATICE). Earth-Science Rev. 204, 103152.

Deschamps, P., Durand, N., Bard, E., Hamelin, B., Camoin, G., Thomas, A.L., Henderson, G.M., Okuno, J., Yokoyama, Y., 2012. Ice-sheet collapse and sea-level rise at the Bolling warming 14,600 years ago. Nature 483(7391), 559–564, doi:10.1038/nature10902.

Domack, E.W., Leventer, A., Dunbar, R., Taylor, F., Brachfeld, S., Sjunneskog, C., Cowan, E., Daniels, J.W., Escutia, C., Evans, A., Eyles, N., Guyodo, Y., Ioio, M., Iwai, M., Kyte, F., Lauer, C., Maldonado, A., Morez, T., Osterman, L., Pudsey, C., Schuffert, J., Vigar, K., Weinheimer, A., Williams, T., Winter, D., Wolf-Welling, T.C.W., 2001. Chronology of the Palmer Deep site, Antarctic Peninsula: A Holocene palaeoenvironmental reference for the circum-Antarctic. The Holocene 11, 1–9, doi:10.1191/095968301673881493.

Domack, E.W., Leventer, A., Root, S., Ring, J., Williams, E., Carlson, D., Hirshorn, E., Wright, W., Gilbert, R., Burr, G., 2003. Marine sedimentary record of natural environmental variability and recent warming in the Antarctic Peninsula. In: Domack, E., Leventer, A., Burnett, A., Bindschadler, R., Convey, P, Kirby, M. (Eds.), Antarctic Peninsula Climate Variability: Historial and Paleoenvironmental Perspectives. American Geophysical Union Antarctic Research Series 79, 205–224.

Domack, E. 2002: A synthesis for Site 1098: Palmer Deep. In Barker, P.F., Camerlenghi, A., Acton, G.D. and Ramsay, A.T.S., editors, Proceedings of the Ocean Drilling Program, scientific results volume 178. Texas A&M University: Ocean Drilling Program.

Dotto, T.S., Kerr, R., Mata, M.M., Garcia, C.A., 2016. Multidecadal freshening and lightening in the deep waters of the bransfield strait, antarctica. J. Geophys. Res.: Oceans 121, 3741–3756.

Edwards, R.L., Beck, J.W., Burr, G.S., Donahue, D.J., Chappell, J.M., Bloom, A.L., Druffel, E.R., Taylor, F.W., 1993. A large drop in atmospheric C-14/C-12 and reduced meltingin the Younger Dryas, documented with Th-230 ages of corals. Science 260, 962–968.

Fischer, H., Fundel, F., Ruth, U., Twarloh, B., Wegner, A., Udisti, R., Becagli, S., Castellano, E., Morganti, A., Severi, M., Wolff, E., Littot, G., Röthlisberger, R., Mulvaney, R., Hutterli, M.A., Kaufmann, P., Federer, U., Lambert, F., Bigler, M., Hansson, M., Jonsell, U., de Angelis, M., Boutron, C., Siggaard-Andersen, M.-L., Steffensen, J. P., Barbante, C., Gaspari, V., Gabrielli, P., Wagenbach, D., 2007. Reconstruction of millennial changes in dust emission, transport and regional sea ice coverage using the deep EPICA ice cores from the Atlantic and Indian Ocean sector of Antarctica, Earth Planet. Sc. Lett., 260, 340–354, doi:10.1016/j.epsl.2007.06.014.

Galindo-Zaldivar, J., Gamboa, L., Maldonado, A. Nakao, S., Bochu, Y., 2004. Tectonic development of the Bransfield basin and its prolongation to the South Scotia Ridge, northern Antarctic Peninsula. Mar. Geol. 206, 267–282.

García, M.A., Castro, C.G., Ríos, A.F., Doval, M.D., Rosón, G., Gomis, D., López, O., 2002. Water masses and distribution of physico-chemical properties in the Western Branfield Strait and Gerlache Strait during austral summer 1995/96. Deep-Sea Res. II 49, 585–602.

Golledge, N.R., Menviel, L., Carter, L., Fogwill, C.J., England, M.H., Cortese, G., Levy, R.H., 2014. Antarctic contribution to meltwater pulse 1A from reduced Southern Ocean overturning. Nature Comm. 5, 5107, doi:10.1038/ncomms6107.

Gordon, J.E., Harkness, D.D., 1992. Magnitude and geographic variation of the radiocarbon content in Antarctic marine life: Implications for reservoir corrections in radiocarbon dating. Quat. Sci. Rev. 11, 697–708, doi:10.1016/0277-3791(92)90078-M.

Gordon, A.L., Mensch, M., Zhaoqian, D., Smethie, W.M., de Bettencourt, J., 2000. Deep and bottom water of the bransfield strait eastern and central basins. J. Geophys. Res.: Oceans 105, 11337–11346.

Gregoire, L.J., Payne, A.J., Valdes P.J., 2012. Deglacial rapid sea level rises caused by ice-sheet saddle collapses. Nature 487, 219–222.

Hanebuth, T., Stattegger, K., and Grootes, P. M., 2000. Rapid flooding of the Sunda Shelf: a late-glacial sea-level record. Science, 288, 1033–1035.

Hanebuth, T.J.J., Stattegger, K., 2003. The stratigraphic evolution of the Sunda Shelf during the past fifty thousand years. In: Sedi, F.H., Nummedal, D., Posamentier, H.W., Darman, H., Imbet, P. (Eds.), Deltas of Southeast Asia and Vicinity – Sedimentology, Stratigraphy, and Petroleum Geology. SEPM Spec. Publ. 76, 189–200.

Heaton, T.J., Köhler, P., Butzin, M., Bard, E., Reimer, R.W., Austin, W.E.N., Ramsey, C.B., Grootes, P.M., Hughen, K.A., Kromer, B., Reimer, P.J., Adkins, J., Burke, A., Cook, M. S., Olsen, J., Skinner, L., 2020. MARINE20 – the marine radiocarbon age calibration curve (0–55,000 cal BP). Radiocarbon 62, 779–820.

Heroy, D.C., Anderson, J.B., 2007. Radiocarbon constraints on Antarctic Peninsula Ice Sheet retreat following the Last Glacial Maximum (LGM). Quat. Sci. Rev. 26, 3286–3297.

Heroy, D.C., Sjunneskog, C., Anderson, J.B., 2008: Holocene climate change in the Bransfield Basin, Antarctic Peninsula: evidence from sediment and diatom analysis. Antarct. Sci. 20, 69–87.

Heywood, K.J., et al., 2014. Ocean processes at the Antarctic continental slope. Philos. Trans. R. Soc. A-Math. Phys. Eng. Sci. 372, 20130047. https://doi.org/10.1098/rsta.2013.0047.

Hofmann, E.E., Klinck, J.M., Lascara, C.M., Smith, D.A., 1996. Water mass distribution and circulation west of the Antarctic Peninsula and including Bransfield Strait. In: Ross, R.M., Hofmann, E.E., Quetin, L.B. (Eds.), Antarctic Research Series, 70, pp. 61–80. https://doi.org/10.1029/AR070p0061.

Ingólfsson, Ó., Hjort, C., Humlum, O., 2003: Glacial and climate history of the Antarctic Peninsula since the Last Glacial Maximum. Arct. Antarct. Alp. Res. 35, 175–86.

Jasper, C.E., Dyer, B., Reilly, B.T., Williams, T., Hemming, S., Raymo, M.E., 2024. A 3.3-million-year record of Antarctic iceberg rafted debris and ice sheet evolution quantified by machine learning. Paleoceanography and Paleoclimatology 39, e2024PA004897. https://doi.org/10.1029/2024PA004897.

Jeffers, J.D., Anderson, J.B., 1991. Sequence Stratigraphy of the Bransfield Basin, Antarctica: implications for tectonic history and hydrocarbon potential. In: Antarctica as an Exploration Frontier: Hydrocarbon Potential, Geology and Hazards (Ed. By B. St John), AAPG. Stud. In Geol., 31, 13–29.

Jouzel, J., Masson-Delmotte, V., Cattani, O., Dreyfus, G., Falourd, S., Hoffmann, G., Minster, B., Nouet, J., Barnoloa, J.M., Chappellaz, J., Fischer, H., Gallet, J.C., Johnsen, S., Leuenberger, M., Loulergue, L., Luethi, D., Oerter, H., Parrenin, F., Raisbeck, G., Raynaud, D., Schilt, A., Schwander, J., Selmo, E., Souchez, R., Spahni, R., Stauffer, B., Steffensen, J.P., Stenni, B., Stocker, T.F., Tison, J.L., Werner, M., Wolff, E.W., 2007. Orbital and millennial Antarctic climate variability over the past 800,000 years. Science 317, 793–796.

Kerr, R., Mata, M.M., Mendes, C.R.B., Secchi, E.R., 2018. Northern Antarctic Peninsula: a marine climate hotspot of rapid changes on ecosystems and ocean dynamics. Deep Sea Res. Part II Top. Stud. Oceanogr. 149, 4–9. https://doi.org/10.1016/j.dsr2.2018.05.006.

Kilfeather, A.A., Ó Cofaigh, C., Lloyd, J.M., Dowdswell, J.A., Xu, S., Moreton, S.G., 2011. Ice-stream retreat and ice-shelf history in Marguerite Trough, Antarctic Peninsula: Sedimentological and foraminiferal signatures, Geol. Soc. Am. Bull., 123, 997–1015.

Kim, S., Yoo, K.C., Lee, J.I., Lee, M.K., Kim, K., Yoon, H.I., 2018. Relationship between magnetic susceptibility and sediment grain size since the last glacial period in the Southern Ocean off the northern Antarctic Peninsula—Linkages between the cryosphere and atmospheric circulation. Palaeogeogr. Palaeoclimatol. Palaeoecol. 505, 359–370, doi:10.1016/J.palaeo.2018.06.016.

Kim, S., Yoo, K.C., Lee, J.I., Roh, Y.H., Bak, Y.S., Um, I.K., Lee, M.K., Yoon, H.I., 2020. Paleoceanographic changes in the Southern Ocean off Elephant Island since the last glacial period: Links between surface water productivity, nutrient utilization, bottom water currents, and ice-rafted debris. Quat. Sci. Rev. 249, 106563.

KOPRI 극지연구소

Lee, J.I., Bak, Y.S., Yoo, K.C., Lim, H.S., Yoon, H.I., Yoon, S.H. 2010. Climate changes in the South Orkney Plateau during the last 8600 years. The Holocene 20(30), 395–404.

Leventer, A., Domack, E.W., Ishman, S.E., Brachfeld, S., McClennen, C.E., Manley, P., 1996. Productivity cycles of 200–300 years in the Antarctic Peninsula region: Understanding linkages among the sun, atmosphere, oceans, sea ice, and biota. Geol. Soc. Am. Bull. 108, 1626–1644, doi:10.1130/0016-7606(1996)108<1626:PCOYIT>2.3.CO;2.

Leventer, A., Domack, E., Dunbar, R., Pike, J., Stickley, C., Maddison, E., Brachfeld, S., Manley, P., McClennen, C., 2006. Marine sediment record from the East Antarctic margin reveals dynamics of ice sheet recession. GSA Today, 16, 4–10.

Leventer, A., Domack, E., Barkoukis, A., McAndrews, B., Murray, J., 2002. Laminations from the Palmer Deep: a diatom-based interpretation. Paleoceanography 17, PAL 3-1–PAL 3-15.

Leventer, A., 1991. Sediment trap diatom assemblages from the northern Antarctic Peninsula region. Deep-Sea Res. 38, 1127–1143.

Lisiecki, L.E., Raymo, M.E., 2005. A Pliocene-Pleistocene stack of 57 globally distributed benthic δ18O records. Paleoceanography 20, PA1003, doi:1029/2004PA001071.

López, O., García, M.A., Gomis, D., Rojas, P., Sospedra, J., Sánchez-Arcilla, A., 1999. Hydrographic and hydrodynamic characteristics of the eastern basin of the Bransfield Strait (Antarctica). Deep-Sea Res. I, 46, 1755–1778.

Majewski, W., Wellner, J.S., Szczuciński, W., Anderson, J.B., 2012. Holocene oceanographic and glacial changes recorded in Maxwell Bay, West Antarctica. Mar. Geol. 326–328, 67–79.

Marcott, S.A., Shakun, J.D., Clark, P.U., Mix, A.C., 2013. A reconstruction of regional and global temperature for the past 11,300 years. Science 339, 1198–1201.

McKay, R.M., Dunbar, G.B., Naish, T.R., Barrett, P.J., Carter, L., Harper, M., 2008. Retreat history of the Ross Sea Ice Sheet (Shelf) since the Last Glacial Maximum from deep-basin sediment cores around Ross Island. Palaeogeogr. Palaeoclimatol. Palaeoecol. 260, 245–261.

Meier, W.N., Fetterer, F., Windnagel, A.K., Stewart, J.S., 2001. NOAA/NSIDC Climate Data Record of Passive Microwave Sea Ice Concentration. (G02202, Version4). [Data Set]. Boulder, Colorado USA. National Snow and Ice Data Center. https://doi.org/10.7265/efmz-2t65. Data Accessed 01-08-2024.

Michalchuk B.R., Anderson J.B., Wellner J.S., Manley P.L., Majewski W., Bohaty S., 2009. Holocene climate and glacial history of the northeastern Antarctic Peninsula: the marine sedimentary record from a long SHALDRIL core. Quat. Sci. Rev. 28, 3049–

3065.

Milliken, K.T., Anderson, J.B., Wellner, J.S., Bohaty, S.M., Manley, P.L., 2009. High-resolution Holocene climate record from Maxwell Bay, South Shetland Islands, Antarctica. Geol. Soc. Am. Bull. 121, 1711–1725, doi:10.1130/B26478.1.

Moreno, P.I., Vilanova, I., Villa-Martínez, R., Dunbar, R.B., Mucciarone, D.A., Kaplan, M.R., Garreaud, R.D., Rojas, M., Moy, C.M., De Pol-Holz, R., Lambert, F., 2018. Onset and evolution of Southern Annular Mode-like changes at centennial timescale. Scientific Reports 8, 3458, doi:10.1038/s41598-018-21836-6.

Müller, J., Wagner, A., Fahl, K., Stein, R., Prange, M., Lohmann, G., 2011. Towards quantitative sea ice reconstructions in the northern North Atlantic: A combined biomarker and numerical modelling approach, Earth Planet. Sc. Lett., 306, 137–148, doi:10.1016/J.EPSL.2011.04.011.

Neori, A., Holm-Hansen, O., 1982. Effect of temperature on rate of photosynthesis in Antarctic phytoplankton. Polar Biol. 1, 33–38.

Niiler, P.P., Amos, A., Hu, J.-H., 1991. Water masses and 200 m relative geostrophic circulation in the western Bransfield Strait region. Deep-Sea Res., Part I 38, 943–959, doi:10.1016/0198–0149(91)90091–S.

North Greenland Ice Core Project members, 2004. High-resolution record of Northern Hemisphere climate extending into the last interglacial period. Nature 431, 147–151.

Ó Cofaigh, C., Davies, B.J., Livingstone, S.J., Smith, J.A., Johnson, J.S., Hocking, E.P., Hodgson, D.A., Anderson, J.B., Bentely, M.J., Canals, M., Domack, E., Dowdeswell, J.A., Evans, J., Hlasser, N.F., Hillenbrand, C.D. Larter, R.D., Roberts, S.J., Simms, A.R., 2014. Reconstruction of ice-sheet changes in the Antarctic Peninsula since the Last Glacial Maximum. Quat. Sci. Rev. 100, 87–110, doi:10.1016/j.quascirev.2014.06.023.

Pedro, J.B., Bostock, H.C., Bitz, C.M., He, F., Vandergoes, M.J., Steig, E.J., Chase, B.M., Krause, C.E., Rasmussen, S.O., Markle, B.R., Cortese, G., 2016. The spatial extent and dynamics of the Antarctic Cold Reversal. Nat. Geosci. 9, 51–55, doi:10.1038/ngeo2580.

Pike, J., Allen, C.S., Leventer, A., Stickley, C.E., Pudsey, C.J., 2008. Comparison of contemporary and fossil diatom assemblages from the western Antarctic Peninsula shelf. Mar. Micropaleontol. 67, 274–287.

Pudsey, C.J., Evans, J., 2001. First survey of Antarctic sub-ice shelf sediments reveals mid-Holocene ice shelf retreat. Geology, 29: 787–790.

Pudsey, C.J., Murray, J.W., Appleby, P., Evans, J., 2006. Ice shelf history from petrographic and foraminiferal evidence, northeast Antarctic Peninsula. Quat. Sci. Rev. 25,

KOPRI 극지연구소

2357e2379.

Pugh, R.S., MaCave, I.N., Hillenbrand, C.‐D., Kuhn, G., 2009. Circum-Antarctic age modeling of Quaternary marine cores under the Antarctic Circumpolar Current: ice-core dust-magnetic correlation. Earth Planet. Sci. Lett. 284, 113‐123.

Roseby, Z.A., Smith, J.A., Hillenbrand, C.D., Cartigny, M.J.B., Rosenheim, B.E., Hogan, K.A., Allen, C.S., Leventer, A., Kuhn, G., Ehrmann, W., Larter, R.D., 2022. History of Anvers-Hugo Trough, western Antarctic Peninsula shelf, since the Last Glacial Maximum. Part I: Deglacial history based on new sedimentological and chronological data. Quat. Sci. Rev. 291, 107590, doi:10.1016/j.quascirev.2022.107590.

Sangrà, P., Stegner, A., Hernández-Arencibia, M., Marrero-Díaz, Á., Salinas, C., Aguiar-González, B., Henríquez-Pastene, C., Mouriño-Carballido, B., 2017. The Bransfield Gravity Current, Deep-Sea Res. Pt. I, 119, 1‐15, doi:10.1016/j.dsr.2016.11.003.

Scherer, R.P., 1994. A new method for the determination of absolute abundance of diatoms and other silt-sized sedimentary particles. J. Paleolimn. 12, 171‐180.

Shevenell, A.E., Ingalls, A.E., Domack, E.W., Kelly, C., 2011. Holocene Southern Ocean surface temperature variability west of the Antarctic Peninsula. Nature 470, 250‐254, doi:10.1038/nature09751.

Shin, J.Y., Kim, S., Zhao, X., Yoo, K.C., Yu, Y., Lee, J.I., Lee, M.K., Yoon, H.I., 2020. Particle-size dependent magnetic properties of Scotia Sea sediments since the Last Glacial Maximum: Glacial ice-sheet discharge controlling magnetic proxeis. Palaeogeogr. Palaeoclimatol. Palaeoecol. 557, 109906, doi:10.1016/j.palaeo.2020.109906.

Sikes, E.L., Samson, C.R., Guilderson, T.P., Howard, W.R., 2000. Old radiocarbon ages in the southwest Pacific Ocean during the last glacial period and deglaciation. Nature 405, 555e559.

Skinner, L.C., Fallon, S., Waelbroeck, C., Michel, E., Barker, S., 2010. Ventilation of the deep Southern Ocean and deglacial CO2 rise. Science 328, 1147e1151.Sjunneskog, C., Taylor, F., 2002. Postglacial marine record of the Palmer Deep, Antarctic Peninsula (ODP Leg 178, Site 1098): 1. Total diatom abundance. Paleoceanography 17, PAL 4-1‐PAL 4-8, doi:10.1029/2000PA00563.

Sprenk, D., Weber, M.E., Kuhn, G., Rosén, P., Frank, M., Molina-Kescher, M., Liebetrau, V., Röhling, H.G., 2013. Southern Ocean bioproductivity during the last glacial cycle—new detection method and decadal-scale insight from the Scotia Sea. Geol. Soc. London. Spec. Publ. 381, 245‐261, doi:10.1144/SP381.17.

Steffensen, J.P., Anderson, K.K., Bigler, M., Clausen, H.B., Dahl-Jensen, D., Fischer, H., Goto-Azuma, K., Hansson, M., Johnsen, S.J., Jouzel, J., Masson-Delmotte, V., Popp, T., Rasmussen, S.O., Röthlisberger, R., Ruth, U., Stauffer, B., Siggaard-Andersen, M.,

Sveinbjörnsdóttir, Á.E., Svensson, A., White, J.W., 2008. High-resolution Greenland Ice Core Data show abrupt climate change happens in few years. Science 321, 680–684.

Stuiver, M., Reimer, P.J., Reimer, R.W., 2020. CALIB 8.2 [www program] at http://calib.org.

Taylor, F. and Sjunneskog, C. 2002: Postglacial marine diatom record of the Palmer Deep, Antarctic Peninsula (ODP Leg 178, Site 1098) 2. Diatom assemblages. Paleoceanography 17, doi:10.1029/2000PA000564.

Taylor, F., Whitehead, J., Domack, E., 2001. Holocene paleoclimate change in the Antarctic Peninsula: evidence from the diatom sedimentary and geochemical record. Mar. Micropaleontol. 41, 25–43.

Toggweiler, J.R., 2009. Shifting Westerlies. Science 323, 1434–1435.

Tréguer, P., Nelson, D.M., van Bennekom, A.J., DeMaster, D.J., Leynaert, A., Que´guiner, B., 1995. The silica balance in the world ocean: a reestimate. Science 268, 375–379.

Verleyen, E., Hodgson, D.A., Sabbe, K., Cremer, H., Emslie, S.D., Gibson, J., Hall, B., Imura, S., Kudoh, S., Marshall, G.J., McMinn, A., Melles, M., Newman, L., Roberts, D., Roberts, S.J., Singh, S.M., Sterken, M., Tavernier, I., Verkulich, S., Van de Vyver, E., Van Nieuwenhuyze, W., Wagner, B., Vyverman, W., 2011. Post-glacial regional climate variability along the East Antarctic coastal margin–Evidence from shallow marine and coastal terrestrial records. Earth-Sci. Rev. 104, 199–212.

Vorrath, M.E., Müller, J., Cárdenas, P., Opel, T., Mieruch, S., Esper, O., Jene-Lembke, L., Etourneau, J., Vieth-Hillebrand, A., Lahajnar, N., Lange, C.B., Leventer, A., Evangelinos, D., Escutia, C., Mollenhauer, G., 2023. Deglacial and Holocene sea-ice and climate dynamics in the Bransfield Strait, northern Antarctic Peninsula. Clim. Past 19, 1061–1079. doi:10.5194/cp-19-1061-2023.

Vorrath, M.E., Müller, J., Esper, O., Mollenhauer, G., Haas, C., Schefuβ, E., Fahl, K., 2019. Highly branched isoprenoids for Southern Ocean sea ice reconstructions: a pilot study from the Western Antartic Peninsula. Biogeosciences 16, 2961–2981, doi:10.5194/bg-16-2961-2019.

Weber, M.E., Clark, P.U., Kuhn, G., Timmermann, A., Sprenk, D., Gladstone, R., Zhang, X., Lohmann, G., Menviel, L., Chikamoto, M.O., Friedrich, T., Ohlwein, C., 2014. Millennial-scale variability in Antarctic ice-sheet discharge during the last deglaciation. Nature 510, 134–138.

Weber, M.E., Bailey, I., Hemming, S. R., Martos, Y. M., Reily, B. T., Ronge, T.A., Brachfeld, S., Williams, T., Raymo, M., Belt, S.T., Smik, L., Vogel, H., Peck, V.L., Armbrecht, L., Cage, A., Cardillo, F.G., Du, Z., Fauth, G., Fogwill, C.J., Garcia, M., Garnsworthy, M., Glüder, A., Guitard, M., Gutjahr, M., Hernández-Almeida, I., Hoem, F.S., Hwang, J.H., Iizuka, M., Kato, Y., Kenlee, B., OConnell, S., Pérez, L.F.,

Seki, O., Stevens, L., Tauxe, L., Tripathi, S., Warnock, J., Zheng, X., 2022. Antiphased dust deposition and productivity in the Antarctic Zone over 1.5 million years. Nature Comm. 13, 2044, doi:10.1038/s41467-022-29642-5.

Whitworth, T., Nowlin, W., Orsi, A., Locarnini, R., Smith, S., 1994. Weddell sea shelf water in the bransfield strait and weddell-scotia confluence. Deep-Sea Res. Part I: Oceanogr. Res. Pap. 41, 629–641.

Xiao, W., Frederichs, T., Gersonde, R., Kuhn, G., Esper, O., Zhang, X., 2016. Constraining the dating of late Quaternary marine sediment records from the Scotia Sea (Southern Ocean). Quat. Geochronol. 31, 97–118, doi:10.1016/j.quageo.2015.11.003.

KOPRI
극지연구소

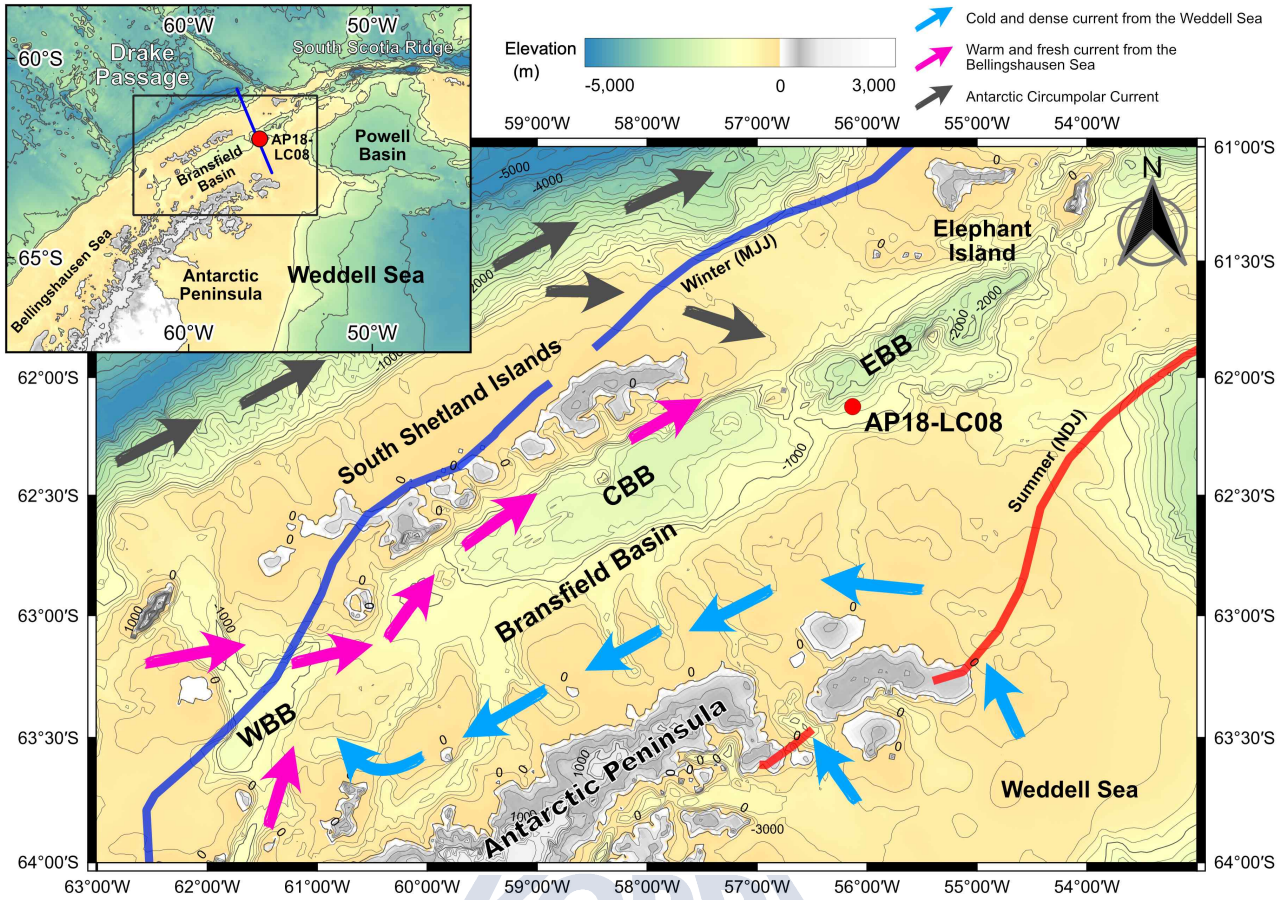


Figure 1. Location map of core AP18-LC08. Winter sea ice (blue line) and summer sea ice (red line) extent are shown. The 15% sea ice concentration defines the sea ice limits. The data source is the NOAA/NSIDC Climate Data Record of Passive Microwave Sea Ice Concentration, Version 4 (Meier et al., 2001). Arrows indicate the different surface water masses and flow directions referred from Barcena et al. (1998). WBB, CBB, and EBB for Western, Central, and Eastern Bransfield Basin, respectively. The blue line is the axis for schematic model Figure #+6.

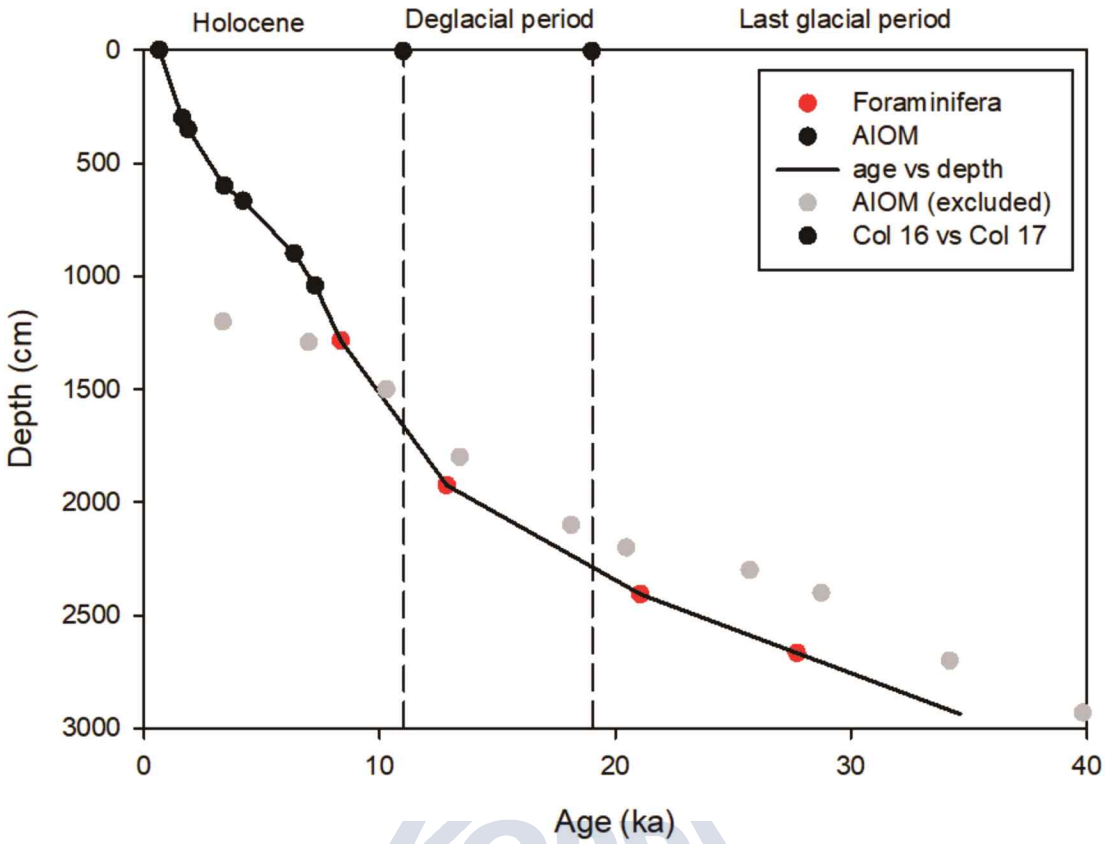


Figure 2. Age-depth model for core AP18-LC08 including AMS 14C dates using foraminifera (red circles) and acid insoluble organic matter (back circles). Gray circles are excluded ages using acid insoluble organic matter in this study.

KOPRI 극지연구소

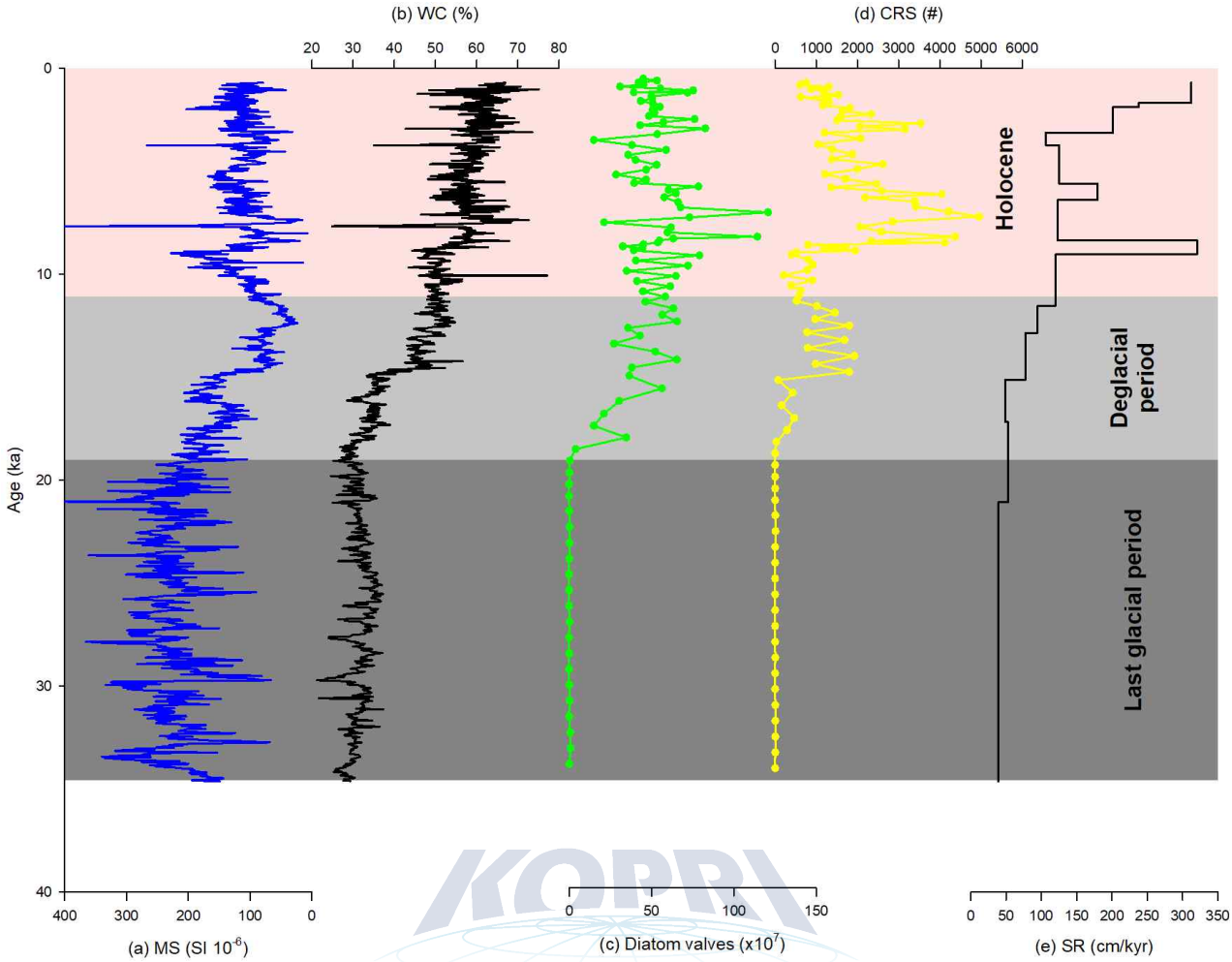


Figure 3. downcore profiles of (a) magnetic susceptibility, (b) water content, (c) total diatom valves, (d) Chaetoceros resting spores, and (e) sedimentation rates of core AP18-LC08. Darker colors in (a) and (b) are 11 point running mean of magnetic susceptibility and water content, respectively.

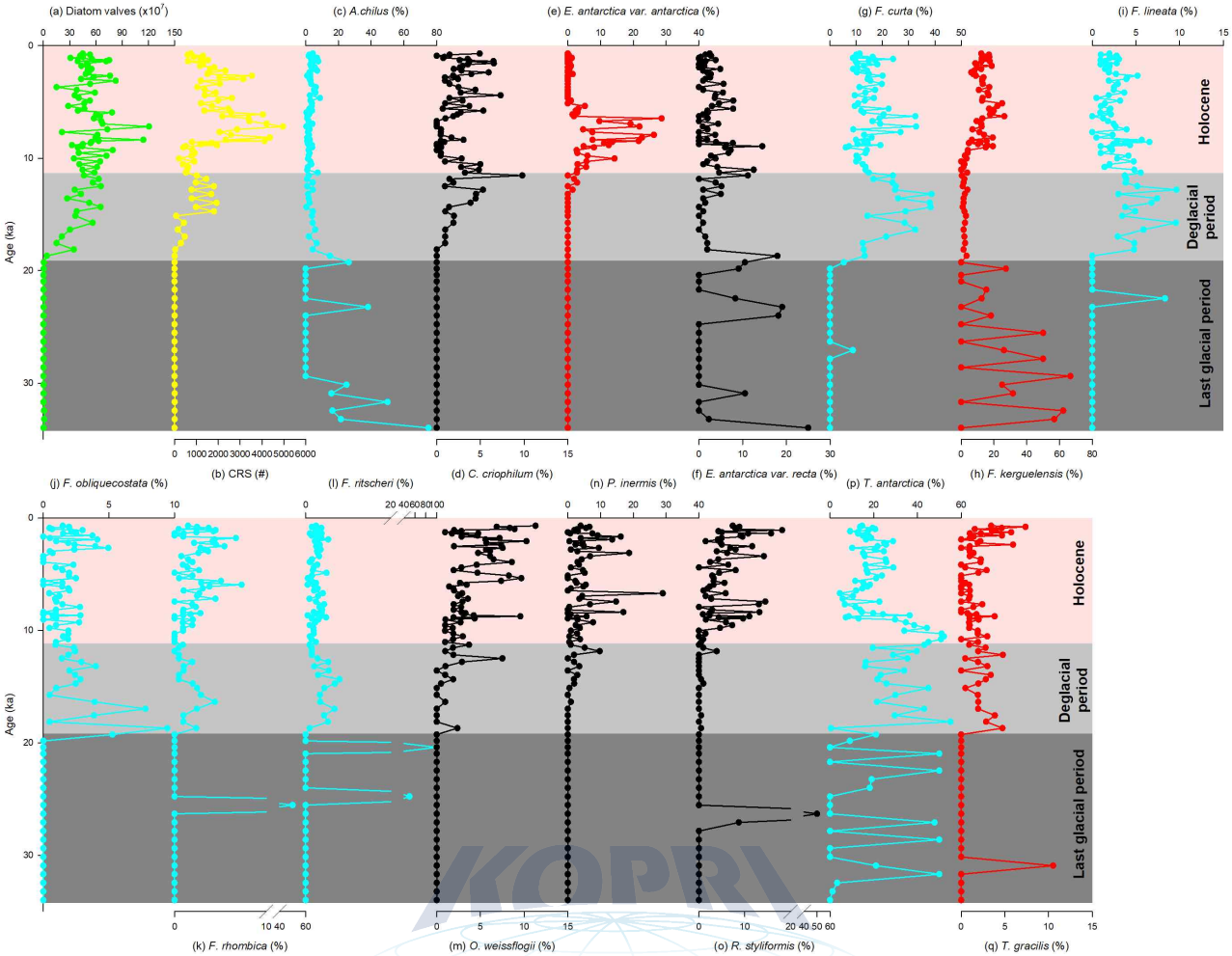


Figure 4. downcore profiles of diatoms in core AP18-LC08; (a) total diatom valves, (b) Chaetoceros resting spores, and relative abundances of (c) A. actinochilus, (d) C. criophilum, (e) E. antarctica var. antarctica, (f) E. antarctica var. recta, (g) F. curta, (h) F. kerguelensis, (i) F. linearis, (j) F. obliquecostata, (k) F. rhombica, (l) F. ritscheri, (m) O. weissflogii, (n) P. inermis, (o) R. stylifomis, (p) T. antarctica, and (q) S. gracilis. Sea ice (melting) and open ocean species are displayed in cyan and red, respectively. Blue color indicates sea ice forming related species. Black colors indicate others.

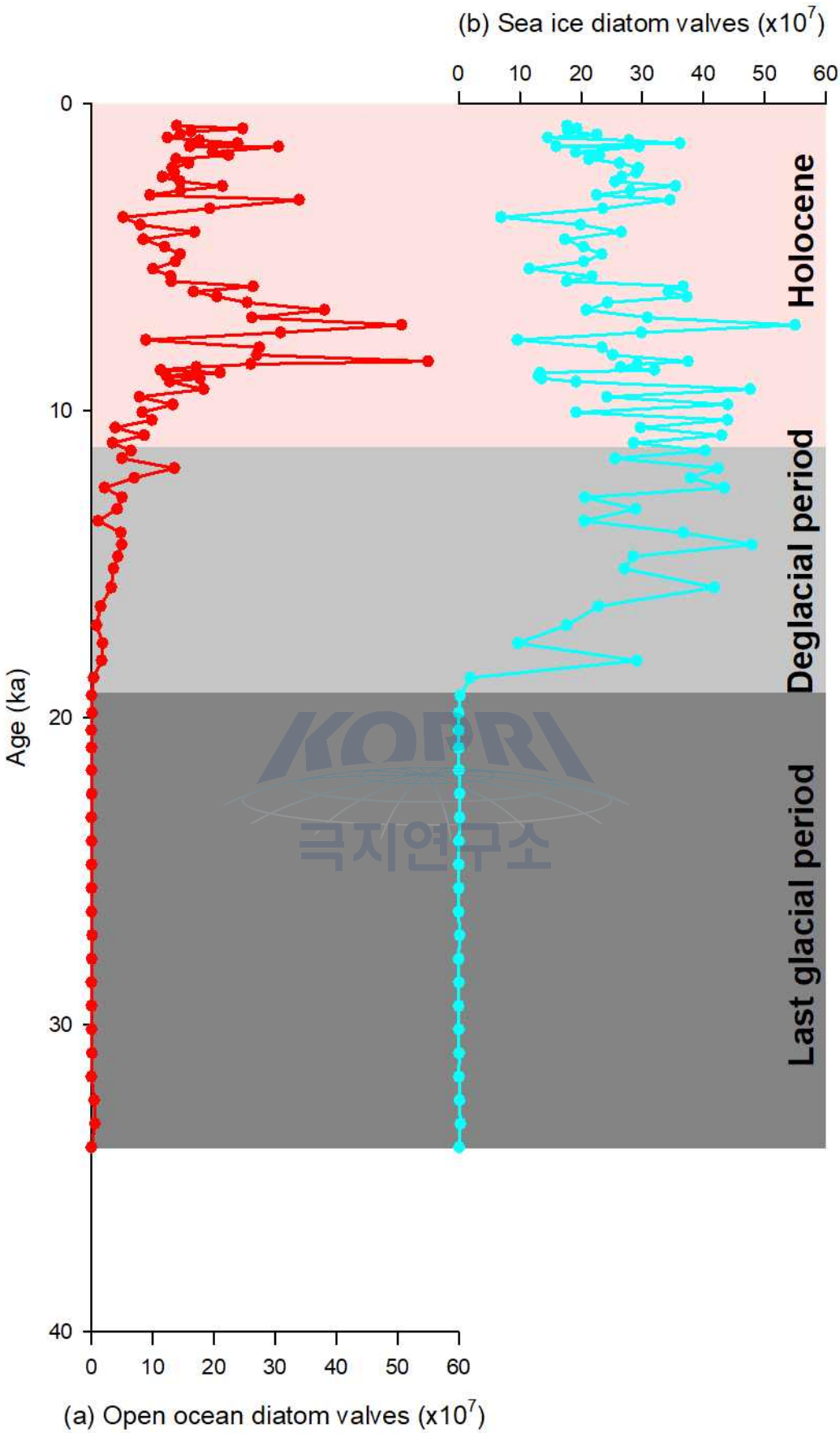


Figure 5. downcore profiles of total occurrence valves for (a) open ocean species (the sum of F. kerguelensis, S. gracilis, Rhizosolenia spp, and E. antarctica var. antarctica) and (b) sea ice species (F. curta, F. linearis, F. obliquecostata, F. rhombica, F. ritscheri, F. cylindrus, F. separanda, F. sublinearis, P. glacials, and S. microtrias) in AP18-LC08.

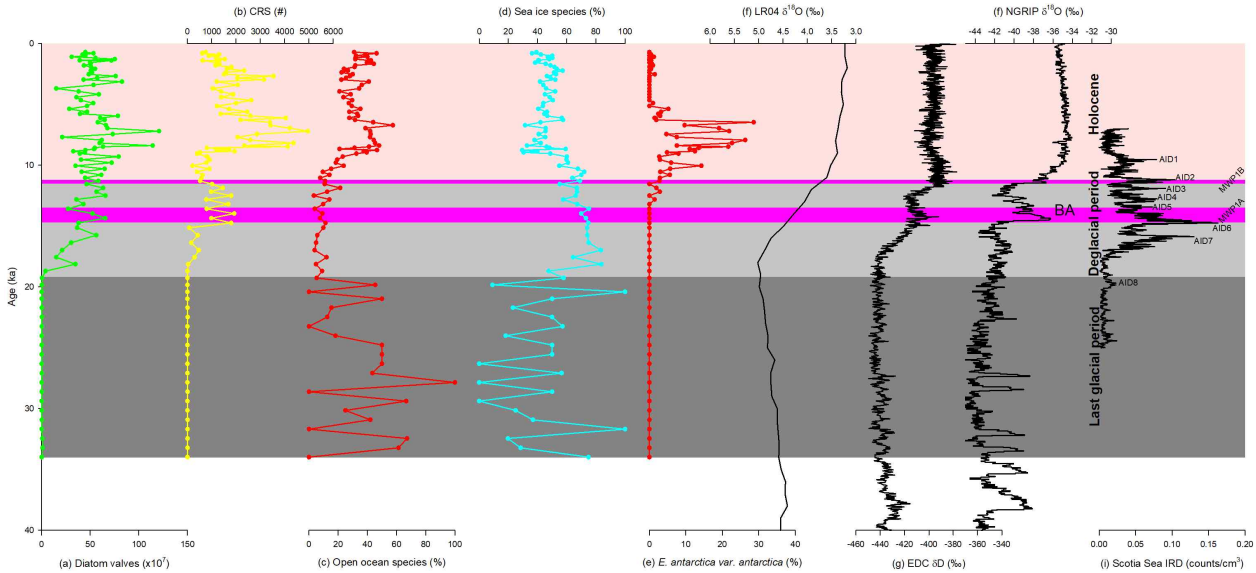
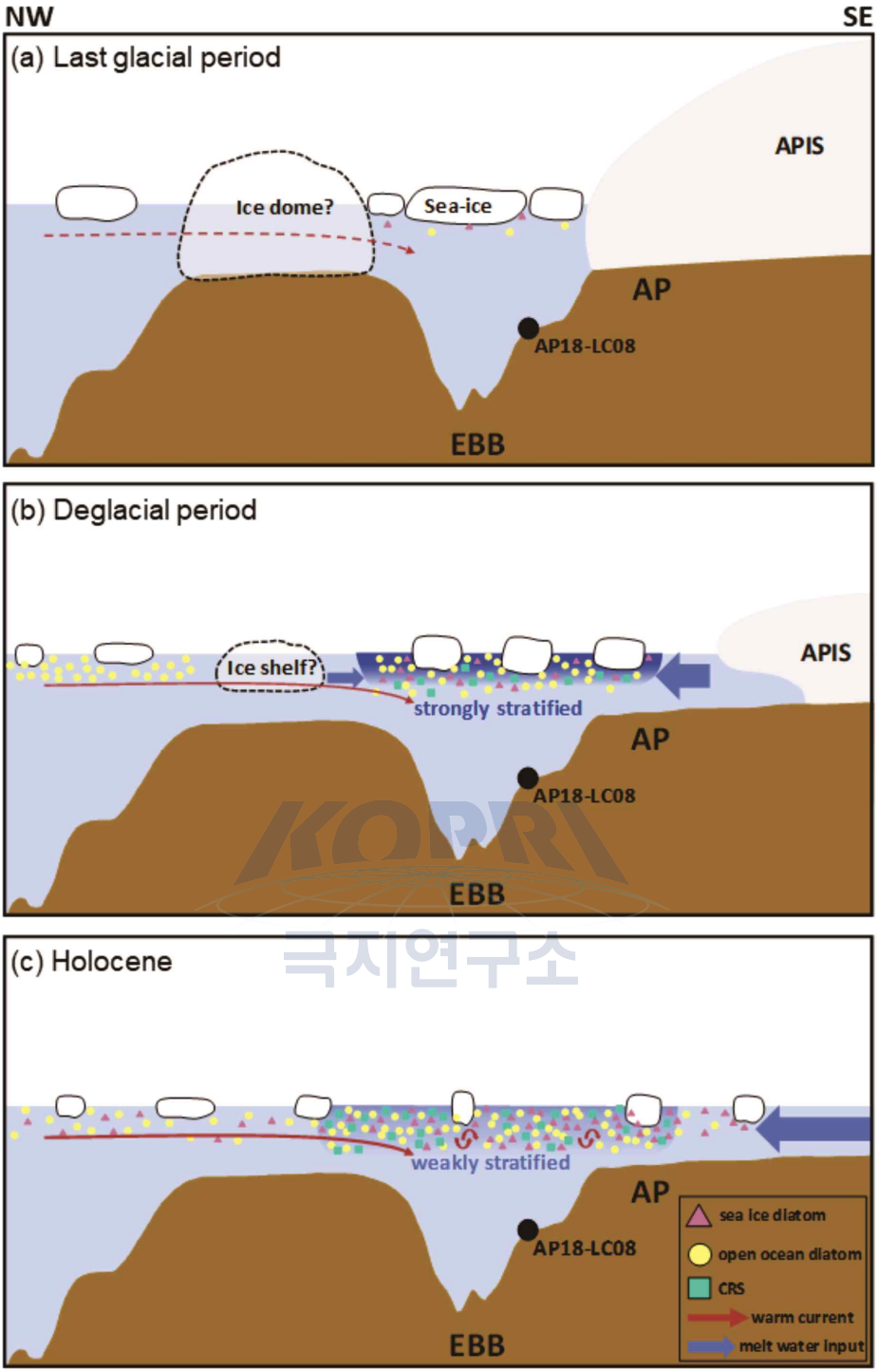


Figure 6. downcore profiles of (a) total diatom valves, (b) Chaetoceros resting spores, relative abundance for (c) open ocean species, (d) sea ice species, and (e) E. antarctica var. antarctica of AP18-LC08, (f) T. antarctica, (g) LR04 δ18O (Lisiecki and Raymo, 2005), (h) NGRIP δ18O (North Greenland Ice Core Project members, 2004), (i) EDC δD (Jouzel et al., 2007), and (j) Scotia Sea IRD record (Weber et al., 2014). MWP1A and MWP1B (purple bars): Meltwater Pulse 1A and 1B, respectively. BA: Bølling-Allerød. AID: Antarctic Ice Sheet Discharge event. HCO: Holocene Climate Optimum.

KOPRI
극지연구소



KOPRI
극지연구소

Figure 7. Schematic models for (a) the late glacial interval, (b) the deglacial interval, and (c) the Holocene in the EBB. During the late glacial interval (a), the EBB is marked by an extensive sea ice cover and occasional water mass exchanges by intrusion of relatively warm m-CDW (red dashed arrow). This would limit overall diatom productivity (pink triangle), except

for sporadic occurrences of open ocean species (yellow circle). In the deglacial interval (b), diatom productivity begins to increase due to the warming-induced sea ice loss and glacial meltwater input (blue arrows) from retreating ice sheet/shelf. The diatom assemblages are still dominated by sea ice species, together with an increase of open ocean species facilitated by enhanced intrusion of the m-CDW (red arrow). During the Holocene (c), a rapid climate warming leads to not only substantial sea ice loss, but also massive amounts of meltwater inputs from continuously retreating ice sheet/shelf (blue arrow). This promotes a distinct decrease of sea ice species and a sharp increase of CRS abundance (green square). The transect is shown in Figure 1 as a blue line. APIS: Antarctic Peninsula Ice Sheet, EBB: Eastern Bransfield Basin, and CRS: Chaetoceros resting spore.

KOPRI
극지연구소

제 15 장

Incorporation of Multi-elements into Diatom Frustules in the Scotia Sea, Antarctica, Since the Last Glacial Maximum[7)]

Sunghan Kim[1,2*], Bo Kyung Kim[3], Kyu-Cheul Yoo[1], Min Kyung Lee[1], Jae Il Lee[1], Sookwan Kim[4], Young-Suk Bak[5]

[1]Korea Polar Research Institute, Incheon, 21990, South Korea.
[2]Department of Polar Sciences, University of Science and Technology (UST), Incheon 21990, South Korea
[3]Department of Marine Sciences and Convergent Engineering, Hanyang University, Ansan 15588, South Korea.
[4]Korea Institute of Ocean Science and Technology, Busan 49111, South Korea.
[5]Department of Earth and Environmental Sciences, Jeonbuk National University, Jeonju 54896, South Korea

KOPRI 극지연구소

Abstract: The glacial-interglacial cycle of elements and the linkage with biological production is very important. Nonetheless, records on incorportation of elements into diatom frustules are very poor in the Southern Ocean where diatom productivity is very high. As a result, there is a big gap in our understanding of elemental cycles in association with biological production and the controlling mechanisms. Here, we documented concentrations of major, trace, and rare earth elements of diatom frustules in two cores collected from the Southern Ocean since the Last Glacial Maximum to understand changes of incorporation of these elements into diatom frustules and to investigate mechanisms for changing incorportation. We found that there are three types of glacial-interglacial variation patterns. Most elements showed increased (decreased) concentrations during the glacial period (interglacial) with decreased (increased) diatom production in the surface water following the variation pattern of magnetic susceptibility, whereas P, Ge, and Sb showed

7) 이 연구 결과는 다음의 논문으로 출판되었음: Kim, S. et al. (2024). "Incorporation of Multi-elements into Diatom Frustules in the Scotia Sea, Antarctica, Since the Last Glacial Maximum" Paleoceanography and Paleoclimatology 39: e2023PA004790.

the opposite trend following the variation pattern of biogenic opal. Li, Ni, Ag, W, U, and I showed no clear glacial-interglacial variation pattern. These different variation patterns imply that elemental incorporation into diatom frustules are also different according to elements. Our results revealed that biologically-mediated removal of most elements from surface water to deep-sea is comparable between glacial (low diatom production with high elements assimilation) and interglacial (high diatom production with low elements assimilation) periods in the Southern Ocean. However, more removal of P, Sb, and Ge in the surface water by diatoms occurs during interglacial periods in the Southern Ocean.

1. Introduction

Phytoplankton are a very important component in the ocean system and play a crucial role in elemental cycles in the ocean (Morel et al., 2003; Twining & Baines, 2013; Lobus et al., 2021). Among them, diatoms are a key player because they are widely distributed in the world, particularly high nutrient regions, where surface water production is very high, such as the Southern Ocean, North Pacific high latitudes, and the eastern Equatorial Pacific (Nelson et al., 1995; Malviya et al., 2016). The Southern Ocean is the widest area of all and is the most environmentally dynamic region in the world. Thus, it is important to understand the role of diatoms in elemental cycles in the Southern Ocean.
Phytoplankton remove dissolved forms of chemical elements in the surface water through adsorption, desorption, and biological absorption into the deep ocean and sediment (Martin & Knauer, 1973; Li, 1991). Although it is important to analyze the multi-element composition of phytoplankton for assessing environmental changes in changing climatic conditions (Twining & Baines, 2013; Moreno & Martiny, 2018; Morel et al., 2020), chemical composition of total diatom frustules is scarce (Martin and Knauer, 1973; Masuzawa et al., 1999; Ho et al., 2003; Xiong et al., 2012; Lobus et al., 2021). In addition, records of temporal variation of multi-element composition in phytoplankton are rare.

Surface productivity, mainly contributed by diatoms, repeated increase during interglacial periods and decrease during glacial periods in largely response to glacial-interglacial variations of sea ice and/or degree of nutrient supply associated with stratification variation in the Scotia Sea (Sprenk et al., 2013; Xiao et al., 2016; Kim et al., 2020). This means that diatoms' role in elemental cycles in the ocean can be variable on glacial-interglacial time scale. However, there have been little studies on glacial-interglacial variations of diatoms' contribution to elemental cycle. Meanwhile, there is an issue whether the cleaned diatom frustules are free from post-mortem element incorporation or not (e.g., Sigman et al., 1999; Dixit et al., 2001; Crosta & Shemesh, 2002; Morley et al., 2004;

Robinson et al., 2005; Koning et al., 2007; Ren et al., 2013; Kim & Khim, 2017).

In this study, we documented concentrations of major (Na, Mg, Al, Si, P, S, K, Ca, and Fe), trace (Li, Be, B, Ti, V, Cr, Mn, Co, Ni, Cu, Zn, Ga, As, Se, Rb, Sr, Mo, Ag, Cd, Sn, Sb, Cs, Ba, Hg, Tl, Pb, Bi, Th, and U), and rare earth (Sc, Y, La, Ce, Pr, Nd, Sm, Eu, Gd, Tb, Dy, Ho, Er, Tm, Yb, and Lu) elements within diatom frustules from two sediment cores collected in the South Scotia Sea off Elephant Island, Antarctica since the LGM in order 1) to report variations of concentrations of multi-elements in diatom frustules, 2) to understand changes of incorporation of those elements into diatom frustules in response to climate change and/or post depositional diagenesis since the LGM. In addition, we would like to investigate the controlling mechanisms for the changing incorporation since the LGM.

2. Materials and Methods

Cores GC03-C1 (60°27´S, 55°42´W, 3774 m water depth, and 892 cm long) and GC03-C2 (60°34´S, 55°55´W, 3750 m water depth, and 834 cm long) were collected from the South Scotia Sea off Elephant Island onboard the R/V Yuzhmorgeologiya during the 2003/2004 Korea Antarctic Research Program (Figure 1). The clockwise-flowing Antarctic Circumpolar Current dominates oceanic circulation in the study area (Orsi et al., 1995). Weddell Sea Deep Water and Warm Deep Water from the Weddell Sea flows anti-clockwise along the slope and upper rise (Hernández-Molina et al., 2006).

2.1 Diatom treatment

Organic matter and carbonate were removed from a few grams of bulk sediment according to the method reported by Morley et al. (2004). Diatoms were then separated physically from the residual sediments based on the method reported by Sigman et al. (1999). However, we skipped a 10 μm sieving step to remove clays, but we repeated settling steps for clay removal (even up to more than 40 times) to collect small sized diatom frustules following Studer et al. (2012). After chemical cleaning procedures (Robinson et al., 2005), the purified diatom frustules were visually checked by a scanning electron microscope (SEM) to confirm its purity. During chemical cleaning procedures, we placed samples in a tempered glass pot with boiling water to raise the chemical reaction efficiency by raising boilling temperature. The glass pot is big and high enough to contain samples.

2.2 Measurement of elemental concentrations

The analysis of chemical elements was carried out at ALS Scandinavia, Sweden. The concentrations of major, trace, and rare earth elements in solutions obtained after digestion of the purified diatom frustules were determined by multi-collector inductively coupled plasma mass spectrometry (NEPTUNE PLUS). The analysis was conducted on ~30 cm (~500 years) intervals for GC03-C1 and on ~21 cm (~500 years) intervals for GC03-C2.

2.3 Age model

We used previously reported age-depth models for GC03-C1 (Shin et al., 2020) and GC03-C2 (Kim et al., 2018). The age-depth models for both cores were constrained by acid insoluble organic matter accelerator mass spectrometry 14C dates and correlation tie points between sediment magnetic susceptibility (MS) values and dust record (non-sea salt Ca2+; nssCa2+) from European Project for Ice Coring in Antarctica Dronning Maud Land (EDML) ice core (Fischer et al., 2007). The graphical correlation of core MS values with ice core dust record have been applied to constrain age-depth models for Scotia Sea cores (e.g., Kim et al., 2018; Shin et al., 2020).

3. Results

Downcore variations of elements inside diatom frustule in two sediment core samples are presented in Figures 2–4 with detection limit of each element. In this study, elements are divided into three; major (Na, Mg, Al, Si, P, S, K, Ca, and Fe), trace (Be, B, Na, Ti, V, Cr, Mn, Co, Ni, Cu, Zn, Ga, Ge, As, Se, Rb, Sr, Zr, Nb, Mo, Ag, Cd, Sn, Sb, Cs, Ba, Hf, W, Hg, Tl, Pb, Th, and U), and rare earth elements (Sc, Y, I, La, Ce, Pr, Nd, Sm, Eu, Gd, Dy, Ho, Er, Yb, and Lu). Fourteen elements (Br, Ru, Rh, Pd, Te, Tb, Tm, Ta, Re, Os, Ir, Pt, Au, and Bi) in samples had values below detection limits, thus data for these elements were excluded from the results. Downcore variations of all elements of the two cores including elements below detection limits are shown in supplementary Figures 1–3 for major, trace, and rare earth elements, respectively.

3.1 Major elements

Downcore variations of major elements showed a good consistence between two cores. Na, Mg, Al, S, K, Ca, and Fe showed high concentrations during the LGM (before 17.6 ka), decreasing during deglaciation (17.6–10 ka), and low concentrations during the Holocene (after 10 ka) (Figure 2). However, P showed the opposite variation pattern having low concentrations during the LGM, increasing during deglaciation, and high concentrations during the Holocene (Figure 2). Si showed relatively constant values (± 3.5% and 3% of

standard deviation for GC03-C1 and GC03-C2, respectively) throughout the core (Figure 2). Interestingly, S concentrations of GC03-C1 were constantly higher than those of GC03-C2 (Figure 2).

3.2 Trace elements

Downcore variations of trace elements showed also a good consistence between two cores, except for Li, Cr, Ni, Mo, Sn, and W (Figure 3). Concentrations of Be, B, Ti, V, Cr, Mn, Co, Cu, Zn, Ga, As, Rb, Sr, Nb, Mo, Sn, Cs, Ba, Hf, Ti, Pb, and Th showed high during the LGM and low values during the Holocene, having a transition period during the deglaciation (Figure 3). Intriguingly, Ge and Sb showed the opposite variation pattern having low concentrations during the LGM, increasing during deglaciation, and high concentrations during the Holocene (Figure 3). However, there were no clear variation patterns in Li, Ni, Ag, W, and U of GC03-C1 and GC03-C2 (Figure 3).

3.3 Rare earth elements

Downcore variations of rare earth elements showed also a good consistence between two cores, except for I (Figure 4). Concentrations of Y, La, Ce, Pr, Nd, Sm, Gd, Dy, Ho, Er, Yb, and Lu showed high during the LGM and low values during the Holocene, having a transition period during the deglaciation (Figure 4). There were no elements showing the opposite pattern found in major or trace elements. An element, I, showed no clear variation patterns at GC03-C1 and GC03-C2 (Figure 4).

4. Discussion

Since the procedures remove clays, adhering organic matter, and other contaminants, the purified frustules in this study mean silica wall and protected/preserved intrinsic organic matter. Diatom-bound nitrogen isotope was used for a nitrate utilization indicator (e.g., Sigman et al., 1999; Robinson et al., 2005; Brunelle et al., 2007, 2010). In addition, silicon isotope of diatom frustules was used for a silicic acid utilization indicator (e.g., Hendry & Brzezinski; Xiong et al., 2015). Using purified diatoms oxygen isotopes were also measured (e.g., Swann et al., 2007; Meister et al., 2023). These isotopes are very vulnerable to impurities such as remained clay particles or external organic matter. Thus, we assume that elemental concentration in the frustules is representative of elemental concentration in the diatom.

The purity of diatom frustules treated in a similar way has been confirmed in the previous studies (Sigman et al., 1999; Crosta & Shemesh, 2002; Morley et al., 2004; Robinson et al., 2005; Kim & Khim, 2017) and this study (Figure 5). Although the detailed method of this study is somewhat different from previously reported study of Ellwood and Hunter (1999), purified diatom frustules are not considered to be significantly different enough to cause different results. However, other studies reported post-mortem Al incorporation into diatom frustules (Dixit et al., 2001; Koning et al., 2007; Ren et al., 2013). Thus, the issue about the purity of diatom frustules in this study needs to be discussed more and discussed in the following sections.

Although it is not reported for all elements discussed in this study, Zn and Fe taken by diatoms are incorporated into diatom frustules (Ellwood and Hunter, 2000). However, Cu, Co, and Mn were not detected in frustules of diatom species Thalassiosira pseudonana in the previous study (Ellwood and Hunter, 2000). Except for some elements under detection limits, however, we were able to detect all elements in diatom frustules and their downcore variations were in tandem (Figures 2–4). Thus, we believe that those elements are assimilated into diatom frustules as well. However, due to lack of culture experiments, the following is not clear so far; 1) partial dissolution of frustules affects elemental concentrations, 2) incorporation is a passive or active process, 3) where exactly in the frustules are these elements, and 4) whether elemental uptake varies with the rate of silicification or species. de Jong et al. (2010) showed three-dimensional distributions of the elements (Si, P, Cl, K, Ca, Mn, Fe, Cu, and Zn) in freshwater diatom, Cyclotella meneghiniana, with 400-nm resolution. The result shows elemental-specific ditribution patterns within the frustule. According to nanoSIMS imaging, organic matter within the frustule is present throughout the frustule but shows higher concentrations at the pore walls (Akse et al., 2021). However, since these results are based on limited number of diatom species, elemental and organic matter distribution for many species should be studied to understand where incorporated elements are stored in frustules. Because the distribution pattern of elements within frustule is different among elements (de Jong et al., 2010), we assumed that elemental uptake is an active process in this study. In spite of these uncertainties, this study provides very important information able to understand incorporation processes of multi-elements into diatom frustules because this study provides information on glacial-interglacial concentrations of multi-elements within total diatom frustules in the Southern Ocean.

Because major elements (Na, Mg, Al, S, K, Ca, and Fe), trace elements (Be, B, Ti, V, Cr, Mn, Co, Cu, Zn, Ga, As, Rb, Sr, Nb, Mo, Sn, Cs, Ba, Hf, Ti, Pb, and Th), and rare earth elements (Y, La, Ce, Pr, Nd, Sm, Gd, Dy, Ho, Er, Yb, and Lu) showed the same variation pattern as that of MS, we grouped them as MS-type in this study. Since there are

too many elements in MS-type, we used Al, Ti, and La as representatives for MS-type. There is no specific reason for selection of representatives, except for simplification. The results are consistent regardless of representative element selection. Because major element P and trace elements Ge and Sb showed the same variation pattern as that of biogenic opal, we grouped them as biogenic opal-type in this study.

4.1 Variation of multi-elements incorportation into diatom frustules since the LGM

4.1.1 MS-type elemements

MS-type elements, represented by Al, Ti, and La, of GC03-C1 and GC03-C2 showed high concentrations during the LGM and low concentrations during the Holocene with a transition during the deglacial period like MS values (Figure 6). Because the elemental concentrations are within diatom frustules, they indicate how much of them is incorporated into diatom frustules. That is, during glacial periods more incorporation into diatom frustules occurred in the Southern Ocean. During deglacial periods, MS-type elements incorporation into diatoms were decreasing. During the Holocene less incorporation into diatom frustules occurred. Although Si concentrations within diatom frustules varies slightly, the elemental concentrations were normalized to Si concentrations (Figure 7). The normalized values showed identical variation pattern with concentrations (Figures 6 and 7). Higher assimilations of MS-type elements occurred with decreased diatom production and increased terrestrial input during the glacial period (Kim et al., 2020; Shin et al., 2020), implying that assimilations of those elements are negatively correlated with diatom production and positively correlated with terrestrial materials. As soluble and particulate metals from ice melt are the main source of trace elements in the Southern Ocean (Lannuzel et al., 2011; Death et al., 2014; Hawkings et al., 2014, 2018; Herraiz-Borreguero et al., 2016), most elements are terrestrial origin. The amount of elements in the surface water likely increased during glacial periods due to increased terrestrial input either by increased IRD and dust (Weber et al., 2012; Kim et al., 2020; Shin et al., 2020). As ice core dust record also increased during glacial periods (Fischer et al., 2007), increased terrestrial material in GC03-C1 and GC03-C2 is related to increased IRD and dust rather than the dilution signal for low diatom production. As a result, more elements could have been assimilated into diatoms frustules during glacial periods. In addition, low diatom production implies that competition to use elements in the ambient water among individual diatoms was low resulting in higher assimilation of each element. In summary, elemental assimilation into diatom frustules is thought to be controlled by degree of terrestrial input and diatom productivity, which is related to concentration of the elements in the surface

water and biological competition, respectively.

During the deglacial period, MS values decreased and diatom production increased in the study area (e.g., Sprenk et al., 2013; Xiao et al., 2016; Kim et al., 2020). As a result, concentrations of MS-type elements decreased with decreasing terrestrial influence and increasing diatom productivity.

During the Holocene, diatom production increased with decreased terrestrial influence under open ocean condition (Sprenk et al., 2013; Xiao et al., 2016; Kim et al., 2020). The amounts of elements were likely decreased in the surface water due to decreased terrestrial inputs, resulting in decreased assimilation by diatoms. In addition, based on high surface water productivity, species competition in the surface water was likely severe leading to decreased assimilation of those elements. Thus, elements concentrations in the ambient water and biological competition within the ambient water are important factors for the glacial-interglacial incorporation of MS-type elements into diatom frustules in the Southern Ocean.

Ren et al. (2013) reported high Al/Si ratios from diatom frustules extracted from sediment in the Bering Sea and suggested that sedimentary clays are the main source of Al by early diagenesis. In addition, rapid post-mortem incorporation of Al in diatom frustules were observed in a series of laboratory experiemnts (Koning et al., 2007). Thus, the pattern of MS-type elements including Al might be related to the early diagenesis rather than incorporation in the surface water; increased elemental concentrations with increased precipitation of dissolved elements from increased terrestrial materials during glaical periods and decreasing concentrations with decreasing terrestrial material input toward Holocene.

A shift in pore structure towards smaller pores due to structual association of Al and Si in biogenic silica were observed (Koning et al., 2007). Indeed, the precipitation of new mineral on the surface and inside the pores of diatom frustules were observed in cleaned diatom samples (Ren et al., 2013). However, there seems no visual sign of reduced pores by precipitation and precipitation of new mineral on the surface in the SEM image (Figure 5). Al/Si ratios for smaples of surface water and sediments vary from place to place (Ren et al., 2013 and references therein). Al/Si ratio of surface sediment in the Scotia Sea ranges 0.035 to 0.08 for uncleaned biogenic silica (Rickert et al., 2002). After cleaning they decreased to ~0.02. Al/Si ratios of GC03-C1 and GC03-C2 range from 0.0024 to 0.0189. In addition, the average value of glacial periods is ~0.013. As a result, the influence of dissolved element adsorption on the diatom frustule is thought to be less. Considering Al/Si ratio of diatom frustules collected from coastal Antarctic Sediment trap in Marguerite Bay (0.000021 – 0.0003; Hendry et al., 2010) and that from coastal Antarctic surface sediment in Marguerite Bay (0.0021 – 0.028; Hendry and Rickaby, 2008), however, Al/Si ratios of diatom frustules extracted from sediment are much high indicating precipitation of Al in

the sediment. As Fe, Ca, and Mg also showed similar vairation pattern with Al (Ren et al., 2013), all MS-type elements in this study might be a result of precipitation of dissolved elements from clays (i.e., terrigeneous materials) which means the incorporated elements reflect the degree of diagenetic effect rather than the degree of assimilation in the surface water. Furthermore, this could indicate visually clean status of diatom frustules does not garentee absence of post-depositional alteration.

Gehlen et al. (2002) reported that structural insertion of tetrahedral Al inside the frustule is incorporated by diatom during biosynthesis. In addition, Al/Si ratio of opal collected by the sediment traps, which is considered post-depositional Al incorporation free, showed a monthly variation which indicates that surface Al uptake varies with surface environmental condition changes (Hendry et al., 2010). Although Al and Zn belong to MS-type elements in this study, Zn/Si ratio of diatom frustules in the surface sediment is lower than that collected by sediment traps in coastal Antarctic Marguerite Bay (Hendry and Rickaby, 2008). Furthermore, Zn/Si ratio of opal in core top shows a good correlation with chlorophyll a and mixed layer salinity, suggesting Zn/Si ratio in the sediment reflects surface biological process (Hendry and Rickaby, 2008). This suggests that the same variation pattern does not necessarily mean the same incorporation mechanism. Al/Si ratio of diatom frustule collected from North Sea surface water shows 0.0083 which is a higher ratio than Al/Si ratios of core GC03-C1 and GC03-C2 (Gehlen et al., 2002). It seems clear that our cleaned diatom samples have some post-depositional diagenesis influence, but is not easy to quantify how much is related to the diageneic effect due to lack of Al/Si ratio of diagenetic free diatom frustules in the study area.

According to diatom assemblages of GC01-C1 (Bak et al., 2010), relative abundance variation pattern of Fragilariopsis kerguelensis (Eucampia antarctica var. recta and Actinocyclus actinochilus) was similar to the variation pattern of biogenic opal (MS) (Figure 7). This means that diatom composition, silicification, and diatom growth rate, which are considered as important factors for elemental incorporation, are temporally different. Thus, the MS-type elemental variation pattern could be related to diatom assemblage changes involving those factors. However, there are no records to enable to give information on those processes so far. It is not known if incorporation of elements and incorporation by diagenetic process are species specific.

Therefore, we conclude that MS-type element variation is controlled by a combination of surface uptake and post-depositional incorporation with a potential of diatom assemblage change; high (low) incorporation both in the surface water and sediment in association with increased (decreased) terrestrial materials during glacial (inerglacial) periods. However, the degree of element incorporation by diatoms with different element concentration in the ambient water and how they are reflected in the diatom frustules

sould be tested by culture experiments. In addition, post-depositional process for other elements should be studied in the future. Since glacial periods in the high latitude of both norhtern and southern hemisphere are characterized by dominant terrestrial material and decreased diatom production (e.g., Kim et al., 2011, 2018, 2020; Xiao et al., 2016), records from the Subantarctic Zone, where biogenic components are predominant and diatom production increases during glacial periods (e.g., Charles et al., 1991), might be helpful to understand the dynamics of element variation and its controlling factor. More importanly, diatom frustule purity issue should be resolved with further methodological improvement. Then, what controls MS-type element variations would be clear.

4.1.2 biogenic opal-type elements

Biogenic opal-type elements, P, Ge, and Sb, of GC03-C1 and GC03-C2 showed low concentrations during the LGM and high concentrations during the Holocene with a transition during the deglacial period like biogenic opal concentrations (Figure 6). Although Si concentrations within diatom frustules varies slightly, the elemental concentrations were normalized to Si concentrations (Figure 7). The normalized values showed identical variation pattern with concentrations (Figures 6 and 7).

Higher assimilations of biogenic opal-type elements occurred with increased diatom production and decreased terrestrial input during the Holocene, implying that assimilations of those elements are positively correlated with diatom production and negatively correlated with terrestrial materials. This means that the variation of biogenic opal-type elements is not related to controlling factors for MS-type elements including post-depositional effect. Previous records of Ge/Si ratios from South Atlantic cores showed the same variation pattern as that of biogenic opal-type elements; high during the Holocene and low during the LGM (Mortlock et al., 1991; Ellwood and Hunter, 1999). Ge is an indicator of clay contamination (Mortlock and Froelich, 1989). However, Ge/Si of diatom frustule was similar to Ge/Si ratio of seawater, indicating Ge was not related to clay contamination (Shemesh et al., 1988; Froelich et al., 1992). The Holocene interval of GC03-C1 and GC03-C2 is characterized by less terrestrial material and Figure 5 shows purity of diatom frustules. Thus, Ge is not related to clay contamination in this study. Sun et al. (2020) reported Ge/Si ratio is related to continental weathering, early diagenesis, or biological productivity. The similarity between biogenic opal and Ge and/or Ge/Si of GC03-C1 and GC03-C2 indicates that Ge is likely related to diatom productivity in the Southern Ocean. Indeed, Ge has similar chemical properties to Si and follows analogous geochemical pathways (Froelich et al., 1985). Low Ge/Si ratios during glacial periods were associated with low biosiliceous productivity and incomplete Si consumption, causing a discrimination of Ge against Si in

the surface water (Mortlock et al., 1991).

Because, however, there has been not much information about glacial-interglacial variation of P (or P/Si) or Sb (or Sb/Si) within diatom frustules, little is known about those two elements variation. Our study showed that their variation patterns are similar to Ge in the Southen Ocean (Figure 6). Although B, As, Ge, and Sb are in the same group of periodic table as metalloid, B and As belong to MS-type elements. Thus, we cannot conclude that their variations are controlled as similar to Ge, but at least we can confirm that they show the same pattern in this study.

The limited information of all element cycles in association with diatom productivity restricts our understanding of biogeochemical cycles of those elements presented in this study. Although discrimination of Ge against Si was proposed for low Ge/Si of diatom frustules during glacial periods in the Southern Ocean, why only two other elements P and Sb of all show the same pattern remains unclear. We do not know if diatoms preferentially assimilated those three elements under open ocean conditions. Nonetheless, it is proven that P, Ge, and Sb were more (less) assimilated into diatoms under open ocean (more sea ice) conditions when diatom productivity was high (low) with less (more) terrestrial input. Our results suggest that culture or field studies for multi-elements rather than a few number of elements are required in the future.

The relationship between light intensity and P uptake of freshwater diatoms was studied and it revealed a positive correlation between P uptake and photosyntheic activity (Shi et al., 2015). According to previous studies in the study area, surface environment changed from more sea ice cover and duration during the glacial period to more open ocean condition during interglacial periods through a transitional deglacial period (Bak et al., 2010, 2014; Weber et al., 2012; Xiao et al., 2016; Kim et al., 2018, 2020). If the elements ratio to Si of diatom frustules reflect elements uptake by diatom, at least P variation pattern is explained.

Si/N(C) uptake ratios of diatoms are reported dependent on Fe concentration; high under Fe depleted conditions and low under Fe enriched conditions (Hutchins & Bruland, 1998; Takeda, 1998; Firme et al., 2003). Interglacial periods in the Scotia Sea are characterized by low MS and dominance of open water species (F. kerguelensis) (Weber et al., 2012; Bak et al., 2014; Xiao et al., 2016; Kim et al., 2018, 2020). In addition, ice core dust record showed decreased dust input into the Antarctica (Fischer et al., 2007). Thus, more Si and/or less N-C uptake would occur during interglacial periods under Fe depleted conditions. In contrast, glacial periods in the Scotia Sea are characterized by high MS and dominance of sea ice and/or cold environment indicative species (Bak et al., 2010, 2014; Weber et al., 2012; Xiao et al., 2016; Kim et al., 2018, 2020). Ice core dust record showed increased dust input into the Antarctica (Fischer et al., 2007). Thus, less Si and/or more

N-C uptake would occur during glacial periods under Fe depleted conditions. This glacial-interglacial Si/N(C) uptake ratio changes in accordance to Fe concentration changes were reported from the Southern Ocean (e.g., Horn et al., 2011; Studer et al., 2015) and from the northern high latitudes (Brunelle et al., 2007, 2010; Kim & Khim, 2017).

However, the uptake ratios in the previous studies are based on the amount of each element consumed by entire diatoms, not the ratio within the diatom frustules. Thus, our P/Si in diatom frustules can provide an important message about C/Si or N/Si within diatom frustules. Although there is no record for P/Si uptake ratio according to Fe availability, we can assume P uptake is similar to N-C uptake in response to Fe availability becuase the soft parts of diatoms are composed of C, N, and P. However, our result shows that P does not follow the uptake behavior of N or C, which implies that P has a different behavior from N and/or C despite that they all consist the soft parts of the diatoms. As it is not confirmed that C-N/Si within diatom frustules follows the behavior of C-N/Si uptake ratio by diatoms according to Fe availability, no further comparison of P with N and/or C is available. Nevertheless, it should be further tested in the future to understand relationships between diatom and key nutrients.

It may be possible that biogenic opal-type elements behave like Si; high (low) assimilation with low (high) Fe availability. To make sure the mechanism for P, Ge, and Sb uptake by diatoms, laboratory experiments on how diatom uptake changes according to light intensity and Fe availability are required in the future. At least we can propose that biogenic opal-type elements are mainly controlled by biological process in this study.

Relative abundance variation pattern of F. kerguelensis is similar to the variation pattern of biogenic opal and biogenic opal-type elements (Figures 6 and 7). Thus, biogenic opal-type elements are possibly related to F. kerguelensis, but again, due to lack of studies on species specific elemental uptake, it needs to be confirmed by future studies. E. antarctica var. recta, which shows the opposition pattern to biogenic opal-type element variations (Figure 7), is heaviliy silicified, so silicification may be involved as well. However, it is not clear whether variation of silicification is related to species composition changes or related to the variation of the degree of silicification for each species at this moment.

4.1.3 patternless type elements

Patternless type elements (Li, Ni, Ag, W, U, and I) of GC03-C1 and GC03-C2 showed no clear variation pattern between glacial and interglacial periods (Figures 3 and 4). If the element/Si ratios are determined simply by the ratio and/or concentration in the seawater, no variation pattern of these elements is difficult to explain because most

elements have the same terrestrial origin. In addition, no variation pattern means that post-depositional precipitation did not occur for patternless type elements indicating that they are not related to concentrations in the pore water.

Thus, the three different variation patterns in incorporation of elements into diatom frustules in the Southern Ocean suggest that diatoms assimilate elements differently according to their characteristics which need to be further investigated in the future. Further, this indicates that diatoms uptake some elements actively (possibly selectively) and that differences in behavior point to different modes of incorporation.

4.2 Glacial-interglacial biogeochemical cycle of elements in the Southern Ocean

MS-type elements showed higher incorporation during the glacial period than during the Holocene (Figures 2–4). Terrestrial material input in the Scotia Sea shows a clear glacial-interglacial cycle; high during glacial periods under advanced ice sheet/shelf conditions and low during interglacial periods under more open ocean conditions (Diekmann et al., 2000; Weber et al., 2012; Xiao et al., 2016; Kim et al., 2018, 2020). Thus, the input of those elements in the study area likely increased (decreased) under increased (decreased) terrestrial influence during glacial (interglacial) periods. As a result, post-depositional precipitation of MS-type elements also likely increased (decrased) during glacial (interglacial) periods due to increased (decreased) terrestrial materials. However, the diatom production in the surface water and biogenic opal content in the sediment are the opposite; high (low) during the Holocene (the glacial period) (Sprenk et al., 2013; Xiao et al., 2016; Kim et al., 2020). Considering the elemental concentrations in diatom frustules between the glacial and the Holocene, biologically-mediated elemental removal was likely balanced between glacial and interglacial periods; high (low) elemental assimilation with low (high) diatom production under more (less) terrestrial input and less (more) competition for glacial (interglacial) periods (Figure 8). Diatom associated elemental removal in the sediment by post-depositional incorporation was also likely balanced between glacial and interglacial periods; high (low) post-depositional element incorporation with low (high) diatom content in the sediment due to more (less) terrestrial input during glacial (interglacial) periods (Figure 8).

However, the cycles of biogenic opal-type elements showed an imbalanced glacial-interglacial pattern; high (low) removal effect during interglacial (glacial) periods due to both high (low) elemental assimilation and diatom production. Thus, the assimilation of P, Ge, and Sb by diatoms leads to imbalanced glacial-interglacial elemental cycles: increased (decreased) during interglacial (glacial) periods. As a result, understanding of why imbalanced glacial-interglacial cycles of opal-type elements occurs is important and more

studies are necessary in the future. Because incorportation of patternless type elements does not have a clear glacial-interglacial contrast, their glacial-interglacial cycle is also imbalanced as well.

5. Conclusions

We have documented major, trace, and rare earth elements concentration within diatom frustules of sediment cores GC03-C1 and GC03-C2 collected from the Southern Ocean since the LGM. There were three types of element variation: 1) MS-type, 2) biogenic opal-type elements, and 3) patternless type elements. Most elements (Na, Mg, Al, S, K, Ca, Fe, Be, B, Ti, V, Cr, Mn, Co, Cu, Zn, Ga, As, Rb, Sr, Nb, Mo, Sn, Cs, Ba, Hf, Ti, Pb, Th, Y, La, Ce, Pr, Nd, Sm, Gd, Dy, Ho, Er, Yb, and Lu) in diatom frustules belong to the MS-type which shows high concentration during the LGM and low concentration during the Holocene. This implies that incorporation into diatoms in the surface water and/or post-depositional precipitation of dessolved elements were higher (lower) during glacial (interglacial) periods due to increased (decreased) terrestrial supply and decreased (increased) competition among individual species. As a result, glacial-interglacial removals of these elements from the surface water to deep water by diatom production and by incorporation by diagenetic process in the surface sediment are balanced in the Southern Ocean.

P, Ge, and Sb belongs to the biogenic opal type which shows a contemporaneous pattern with biogenic opal; high during the Holocene and low during the last glacial period. This opposite variation pattern to other elements implies that assimilations of P, Ge, and Sb by diatoms are controlled by different mechanisms. We propose that P, Ge, and Sb incorporation into diatom frustules is likely controlled by light intensity and/or Fe availability which regulates uptake affinity of P, Ge, and Sb; high during interglacial periods with low Fe availability under open ocean condition and low during glacial periods with high Fe availability under more sea ice condition together with increased terrestrial influence. As a result, more (less) removal of these elements occurred during interglacial (glacial) periods for P, Ge, and Sb in the Southern Ocean.

Li, Ni, Ag, W, U, and I showed no clear variation pattern. As a result, more (less) removal of these elements occurred during interglacial (glacial) periods in the Southern Ocean. Although we documented variation patterns and their potential controls of mult-elements, why there are three different types of elemental incorporation into diatom frustules in the Southern Ocean needs to be further investigated in the future.

KOPRI 극지연구소

마지막 최대 빙하기 이후 남극 스코시아해에서의 규조류 골격으로의 멀티 원소 동화[8)]

Sunghan Kim[1,2*], Bo Kyung Kim[3], Kyu-Cheul Yoo[1], Min Kyung Lee[1], Jae Il Lee[1], Sookwan Kim[4], Young-Suk Bak[5]

[1]Korea Polar Research Institute, Incheon, 21990, South Korea.
[2]Department of Polar Sciences, University of Science and Technology (UST), Incheon 21990, South Korea
[3]Department of Marine Sciences and Convergent Engineering, Hanyang University, Ansan 15588, South Korea.
[4]Korea Institute of Ocean Science and Technology, Busan 49111, South Korea.
[5]Department of Earth and Environmental Sciences, Jeonbuk National University, Jeonju 54896, South Korea

요약: 빙기-간빙기 동안 원소 순환과 생물학적 생산성 간의 연관성은 매우 중요하다. 그럼에도 불구하고 규조 생산성이 매우 높은 남빙양에서는 규조 껍질로의 원소 편입에 대한 기록이 매우 제한적이다. 그 결과, 생물학적 생산과 연관된 원소 순환 및 이를 제어하는 메커니즘에 대한 이해에는 큰 공백이 존재한다. 본 연구에서는 남빙양에서 최종빙기최대기 이후에 퇴적된 두 개의 코어를 대상으로 규조 껍질 내 주요 원소, 미량 원소, 희토류 원소의 농도를 분석하여, 이들 원소의 규조 껍질로의 편입 변화와 그 조절 메커니즘을 규명하고자 하였다. 그 결과, 빙기-간빙기 변화 양상은 세 가지 유형으로 구분되었다. 대부분의 원소는 표층 규조 생산성이 감소한 빙기 동안 농도가 증가하고, 규조 생산성이 증가한 간빙기 동안 농도가 감소하는 경향을 보였으며, 이는 자기감수율 변화 양상과 유사하다. 반면 인, 게르마늄, 안티몬은 생물기원 오팔의 변화 양상과 유사하게 빙기에는 감소하고 간빙기에는 증가하는 반대 경향을 나타냈다. 리튬, 니켈, 은, 텅스텐, 우라늄, 요오드는 뚜렷한 빙기-간빙기 변화 양상을 보이지 않았다. 이러한 상이한 변화 유형은 원소별로 규조 껍질로의 편입 메커니즘이 서로 다름을 시사한다. 본 연구 결과에 따르면, 남빙양에서는 빙기(낮은 규조 생산성과 높은 원소 동화)와 간빙기(높은 규조 생산성과 낮은 원소 동화) 모두에서 대부분의 원소가 표층수에서 심해로 생물학적으로 제거되는 총량은 유사한 수준을 보인다. 그러나 인, 안티몬, 게르마늄의 경우에는 간빙기 동안 규조에 의해 표층수에서 더 많이 제거되는 것으로 나타났다.

8) 이 연구 결과는 다음의 논문으로 출판되었음: Kim, S. et al. (2024). "Incorporation of Multi-elements into Diatom Frustules in the Scotia Sea, Antarctica, Since the Last Glacial Maximum" Paleoceanography and Paleoclimatology 39: e2023PA004790.

References

Akse, S. P., Das, G., Agustí, S., Pichevin, L., Polerecky, L., & Middelburg, J. J. (2021). Imaging of organic signals in individual fossil diatom frustules with nanoSIMS and Raman spectroscopy. Marine Chemistry, 228, 103906.

Bak, Y. S., Lee, J. D., Yoon, H. I., Yoo, K. C., & Lee, S. J. (2010). Holocene paleoclimate change in the area around Elephant Island, Antarctica: evidence from the diatom record. Journal of the Geological Society of Korea, 46, 111-117. (In Korean with English abstract)

Bak, Y. S., Yoo, K. C., & Yoon, H. I. (2014). Late Quaternary climate changes around the Elephant Islands, Antarctic Peninsula. Geosciences Journal, 18, 495-501. https://doi.org/10.1007/s12303-014-0011-0

Brunelle, B. G., Sigman, D. M., Cook, M. S., Keigwin, L. D., Haug, G. H., Plessen, B., Schettler, G., & Jaccard, S. L. (2007). Evidence from diatom-bound nitrogen isotopes for subarctic Pacific stratification during the last ice age and a link to North Pacific denitrification changes. Paleoceanography, 22, PA1215. https://doi.org/10.1029/2005PA001205

Brunelle, B. G., Sigman, D. M., Jaccard, S. L., Keigwin, L. D,. Plessen, B., Schettler, G., et al. (2010). Glacial/inerglacial changes in nutrient supply and stratification in the western subarctic North Pacific since the penultimate glacial maximum. Quaternary Science Reviews, 29, 2527-2590. https://doi.org/10.1016/j.quascirev.2010.03.010

Charles, C. D., Froelich, P., N., Zibello, M. A., Mortlock, R. A., & Morley, J. J. (1991). Biogenic opal in Southern Ocean sediments over the last 450,000 years: Implications for surface water chemistry and circulation. Paleoceanography, 6, 697-728.

Crosta, X., & Shemesh, A. (2002). Reconciling down core anticorrelation of diatom carbon and nitrogen isotopic ratios from the Southern Ocean. Paleoceanography, 17, 1010. https://doi.org/10.1029/2000PA000565

Death, R., Wadham, J. L., Monteiro, F., Le Brocq, A. M., Tranter, M., Ridgwell, A., Dutkiewiez, S., & Raiswell, R. (2014). Antarctic ice sheet fertilises the Southern Ocean. Biogeosciences, 11, 2635-2644.

de Jong, M. D., Holzner, C., Baines, S. B., Twining, B. S., Ignatyev, K., Diaz, J., Howard, D. L., Legnini, D., Miceli, A., McNulty, I., Jacobsen, C. J., & Vogt, S. (2010). Quantitative 3D elemental microtomography of Cyclotella meneghiniana at 400-nm resolution. Proceedings of the National Academy of Sciences of the United States of America, 107, 15676-15680.

Diekmann, B., Kuhn, G., Rachold, V., Abelmann, A., Brathauer, U., Fütterer, D. K., et al. (2000). Terrigenous sediment supply in the Scotia Sea (Southern Ocean): response to late quaternary ice dynamics in Patagonia and on the Antarctic Peninsula. Palaeogeography, Palaeoclimatology, Palaeoecology, 162, 357-387. https://doi.org/10.1016/S0031-0182(00)00138-3

Dixit, S., van Cappellen, P., & van Bennekom, A. J. (2001). Processes controlling solubility of biogenic silica and pore water build-up of silicic acid in marine sediments. Marine Chemistry, 73, 333-352.

Ellwood, M. J., & Hunter, K.A. (1999). Determination of the Zn/Si ratio in diatom opal: a method for the separation, cleaning and dissolution of diatoms. Marine Chemistry, 66, 149-160.

Ellwood, M. J., & Hunter, K.A. (2000). The incorporation of zinc and iron into the frustule of the marine diatom Thalassiosira pseudonana. Limnology and Oceanography, 45, 1517-1524.

Firme, G. F., Rue, E. L., Weeks, D. A., Bruland, K. W., & Hutchins D. A. (2003). Spatial and temporal variability in phytoplankton iron limitation along the California coast and consequences for Si, N, and C biogeochemistry, Global Biogeochemical Cycles, 17(1), 1016. https://doi.org/10.1029/2001GB001824

Fischer, H., Fundel, F., Ruth, U., Twarloh, B., Wegner, A., Udisti, R., et al. (2007). Reconstruction of millennial changes in dust emission, transport and regional sea ice coverage using the deep EPICA ice cores from the Atlantic and Indian Ocean sector of Antarctica. Earth Planetary Science Letters, 260, 340-354.

Froelich, P. N., Hambrick, G. A., Andreae, M. O., Mortlock, R. A., & Edmond, J. M. (1985). The geochemistry of inorganic germanium in natural waters. Journal of Geophysical Research: Oceans, 90, 1133-1141.

Froelich, P. N., Blanc, V., Mortlock, R. A., Chillrud, S. N., Dunstan, W., Udomkit, A., & Peng, T. H. (1992). River fluxes of dissolved silica to the ocean were higher during glacials: Ge/Si in diatoms, rivers and oceans. Paleoceanography, 7, 739-767.

Gehlen, M., Beck, L., Calas, G., Flank, A. -M., Van Bennekom, A. J., & Van Beusekom, J. E. E. (2002). Unraveling the atomic structure of biogenic silica: Evidence of the structural association of Al and Si in diatom frustules. Geochemica et Cosmochemica Acta, 66, 1601-1609.

Hawkings, J. R., Wadham, J. L., Tranter, M., Raiswell, R., Benning, L. G., Statham, A. T., Nienow, P., Lee, K., & Telling, J. (2014). Ice sheets as a significant source of highly reactive nanoparticulate iron to the oceans. Nature Communications, 5, 3929. https://doi.org/10.1038/ncomms4929

Hawkings, J. R., Benning, L. G., Ridgwell, A., Kaulich, B., Araki, T., Abyaneh, M., Stockdale, A., Koch-Mueller, M., Wadham, J. L., & Tranter, M. (2018). Biolabile ferrous iron bearing nanoparticles in glacial sediments. Earth and Planetary Science Letters, 493, 92-101.

Hendry, K. R., & Brzezinski, M. A. (2014). Using silicon isotopes to understand the role of the Southern Ocean in modern and ancient biogeochemistry and climate. Quaternary Science Reviews, 89, 13-26.

Hendry, K. R., Meredith, M. P., Measures, C. I., Carson, D. S., & Rickaby, R. E. M. (2010). The role of sea ice formation in cycling of aluminium in northern Marguerite Bay,

Antarctica. Estuarine, Coastal and Shelf Science, 87, 103-112.

Hendry, K. R. & Rickaby, R. E. M. (2008). Opal (Zn/Si) ratios as a nearshore geochemical proxy in coastal Antarctica. Paleoceanography, 23, PA2218. http://doi.org/10.1029/2007PA001576

Hernández-Molina, F. J., Larter, R. D., Rebesco, M., & Maldonado, A. (2006).

Herraiz-Borreguero, L., Lannuzel, D., van der Merwe, P., Treverrow, A., & Pedro, J. B. (2016). Large flux of iron from the Amery Ice Shelf marine ice to Prydz Bay, East Antarctica. Journal of Geophysical Research: Oceans, 121, 6009-6020.

Ho, T. Y., Quigg, A., Finkel, Z. V., Milligan, A. J., Wyman, K., Falkowski, P. G., & Morel, F. M. M. (2003). The elemental composition of some marine phytoplankton. Journal of Phycology, 39, 1145-1159.

Horn, M. G., Beucher, C. P., Robinson, R. S., & Brzezinski, M. A. (2011). Southern ocean nitrogen and silicon dynamics during the last deglaciation. Earth and Planetary Science Letters, 310, 334-339. https://doi.org/10.1016/j.epsl.2011.08.016

Hutchins, D. A., & Bruland, K. W. (1998). Iron-limited diatom growth and Si:N uptake ratios in a coastal upwelling regime. Nature, 393, 561-564. https://doi.org/10.1038/31203

Kim, S., Kim, B. K., Yoo, K.-C., Lee, M. K., Lee, J. I., Kim, S., & Bak, Y.-S. (2024a). Downcore element concentration for GC03-C1 [Dataset]. Korea Polar Data Center. https://dx.doi.org/doi:10.22663/KOPRI-KPDC-00002447.1

Kim, S., Kim, B. K., Yoo, K.-C., Lee, M. K., Lee, J. I., Kim, S., & Bak, Y.-S. (2024b). Downcore element concentration for GC03-C2 [Dataset]. Korea Polar Data Center. https://dx.doi.org/doi:10.22663/KOPRI-KPDC-00002448.1

Kim, S., & Khim, B. K. (2017). Estimate of glacial silicic acid reduction over the last 600 ka in the Bering Sea using δ30Si of diatom frustules. Geochemical Journal, 51, 347-357, https://doi.org/10.2343/geochemj.2.0474

Kim, S., Khim, B. K., Uchida, M., Itaki, T., & Tada, R. (2011). Millennial-scale paleoceanographic events and implication for the intermediate-water ventiliation in the northern slope area of the Bering Sea during the last 71 kyrs. Global and Planetary Change, 79, 89-98.

Kim, S., Yoo, K-C., Lee, J. I., Lee, M. K., Kim, K., Yoon, H. I., et al. (2018). Relationship between magnetic susceptibility and sediment grain size since the last glacial period in the Southern Ocean off the northern Antarctic Peninsula- Linkages between the cryosphere and atmospheric circulation. Palaeogeography, Palaeoclimatology, Palaeoecology, 505, 359-370. https://doi.org/10.1016/j.palaeo.2018.06.016

Kim, S., Yoo, K-C., Lee, J. L., Roh, Y. H., Bak, Y-S., Um, I-K., et al. (2020). Paleoceanographic changes in the Southern Ocean off Elephant Island since the last glacial period: Links between surface water productivity, nutrient utilization, bottom water currents, and ice-rafted debris. Quaternary Science Reviews, 249, 106563. https://doi.org/10.1016/j.quascirev.2020.106563

Koning, E., Gehlen, M., Flank, A. -M., Galas, G., & Epping, E. (2007). Rapid post-mortem

incorporation of aluminum in diatom frustules: Evidence from chemical and structural analyses. Marine Chemistry, 106, 208-222.

Lannuzel, D., Bowie, A. R., van der Merwe, P. C., Townsend, A. T., & Schoenmann, V. (2011). Distribution of dissolved and particulate metals in Antarctic sea ice. Marine Chemistry, 124, 134-146.

Li, Y. H. (1991). Distribution patterns of the elements in the ocean: A synthesis. Geochimica et Cosmochimica Acta, 55, 3223-3240.

Lobus, N. V., Kulikovskiy, M. S., & Maltsev, Y. I. (2021). Multi-Element Composition of Diatom Chaetoceros spp. from Natural Phytoplankton Assemblages of the Russian Arctic Seas. Biology, 10, 1009. https://doi.org/10.3390/biology10101009

Malviya, S., Scalco, E., Audic, S., Vincent, F., Veluchamy, A., Poulain, J., et al. (2016). Proceedings of the National Academy of Sciences, 113, E1516-E152. https://doi.org/10.1073/pnas.1509523113

Martin, J. H., & Knauer, G. A. (1973). The elemental composition of plankton. Geochimica et Cosmochimica Acta, 37, 1639-1653. https://doi.org/10.1016/0016-7037(73)90154-3

Masuzawa, T., Suzuki, T., Seki, K., Kosugi, T., Hibi, Y., Yamamoto, M., Takada, J., Matsushita, R., & Yanada, M. (1999). Multielement compositions of marine phytoplankton samples from coastal areas of japan by instrumental neutron activation analysis. Biological Trace Element Research, 71, 331-342.

Meister, P., Alexandre, A., Bailey, H., Barker, P., Biskaborn, B. K., Broadman, E., et al. (2023). A global compilation of diatom silica oxygen isotope records from lake sediment - trends and implications for climate reconstruction. Climate of the Past, 20, 363-392. https://doi.org/10.5194/cp-20-363-2024

Morel, F. M. M., Lam, P. J., & Saito, M. A. (2020). Trace metal substitution in marine phytoplankton. Annual Review of Marine Science, 48, 491-517.

Morel, F. M. M., Milligan, A. J., & Saito, M. A. (2003). The role of trace metals in the oceanic cycles of major nutrients. In: Holland, H. D., & Turekian, K. K. (Eds.), Treatise on Geochemistry, Elsevier, Amsterdam, Volume 6, pp 113-143.

Moreno, A. R., & Martiny, A. C. (2018). Ecological stoichiometr of ocean plankton. Annual Review of Marine Science, 10, 43-69.

Morley, D. W., Leng, M. J., Mackay, A. W., Sloane, H. J., Rioual, P., & Battarbee, R. W. (2004). Cleaning of lake sediment samples for diatom oxygen isotope analysis. Journal of Paleolimnology, 31, 391-401. https://doi.org/10.1023/B:JOPL.0000021854.70714.6b

Mortlock, R. A., & Froelich, P. N. (1989). A simple method for the rapid determination of biogenic opal in pelagic marine sediments. Deep-Sea Research, 36, 1415-1426.

Mortlock, R. A., Charles, C. D., Froelich, P. N., Zibello, M. A., Saltzman, J., Hays, J. D., & Burckle, L. H. (1991). Evidence for lower productivity in the Antarctic Ocean during the last glaciation. Nature, 351, 220-223.

Nelson, D. M., Treguer, P., Brzezinski, M. A., Leynaert, A., & Queguiner, B. (1995). Production and dissolution of biogenic silica in the ocean: revised global estimates, comparison

with regional data and relationship to biogenic sedimentation. Global Biogeochemcal Cycles, 9, 359-372. https://doi.org/10.1029/95GB01070

Ren, H., Brunelle, B. G., Sigman, D. M., & Robinson, R. S. (2013). Diagenetic aluminum uptake into diatom frustules and the preservation of diatom-bound organic nitrogen. Marine Chemistry, 155, 92-101.

Rickert, D., Schlüter, M., & Wallmann, K. (2022). Dissolution kinetics of biogenic silica from the water column to the sediments. Geochimica et Cosmochimica Acta, 66, 439-455.

Robinson, R. S., Sigman, D. M., DiFiore, P. J., Rohde, M. M., Mashiotta, T. A., & Lea, D. W. (2005). Diatom-bound 15N/14N: New support for enhanced nutrient consumption in the ice age subanatarctic. Paleoceanography, 20, PA3003. https://doi.org/10.1029/2004PA001114

Shemesh, A., Mortlock, R. A., Smith, R. J., & Froelich, P. N., 1988. Determination of Ge/Si in marine siliceous microfossils: separation, cleaning and dissolution of diatoms and radiolarian. Marine Chemistry, 25, 305-323.

Shi, P., Shen, H., Wang, W., Chen, W., & Xie, P. (2015). The relationship between light intensity and nutrient uptake kinetics in six freshwater diatoms. Journal of Environmental Sciences, 34, 28-36.

Shin, J. P., Kim, S., Zhao, X., Yoo, K-C., Yu, Y., Lee, J. I., et al. (2020). Particle-size dependent magnetic properties of Scotia Sea sediments since the Last Glacial Maximum: Glacial ice-sheet discharge controlling magnetic proxies. Palaeogeography, Palaeoclimatology, Palaeoecology, 557, 109906. https://doi.org/10.1016/j.palaeo.2020.109906

Sigman, D. M., Altabet, M. A., Francois, R., McCorkle, D. C., & Gaillard, J. -F. (1999). The isotopic composition of diatom-bound nitrogen in Southern Ocean sediments. Paleoceanography, 14, 118-134.

Sprenk, D., Weber, M. E., Kuhn, G., Rosén, P., Frank, M., Molina-Kescher, M., et al. (2013). Southern Ocean bioproductivity during the last glacial cycle- new detection menthod and decadal-scale insight from the Scotia Sea. Geological Society, London, Special publications, 381, 245-261. https://doi.org/10.1144/SP381.17.

Studer, A. S., Martínez-Garcia, A., Jaccard, S. L., Girault, F. E., Sigman, D. M., & Haug. G. H. (2012). Enhanced stratification and seasonality in the Subarctic Pacific upon Northern Hemisphere Glaciation-New evidence from diatom-bound nitrogen isotopes, alkenones and archaeal tetraethers. Earth and Planetary Science Letters, 351-352, 84-94.

Studer, A. S., Sigman, D.M., Martínez-García, A., Benz, V., Winckler, G., Kuhn, G., et al. (2015). Antarctic Zone nutrient conditions during the last two glacial cycles. Paleoceanography, 30, 845-862. https://doi.org/10.1002/2014PA002745

Sun, W. P., Hu, C. Y., Han, Z. B., Shen, C., Zhang, W. Y., Zhu, J. H., Yu, P. S., Zhang, H. F., & Pan, J. M. (2020). Variations of diatom opal Ge/Si in Prydz Bay, East Antarctica. Marine Chemistry, 227, 103879. https://doi.org/10.1016/j.marchem.2020.103879

Swann, G. E. A., Leng, M. J., Sloane, H. J., Maslin, M. A., & Onodera, J. (2007). Diatom oxygen

KOPRI 극지연구소

isotopes: Evidence of a species effect in the sediment record. Geochemistry Geophysics Geosystems, 8, Q06012. https://doi.org/10.1029/2006GC001535

Takeda, S. (1998). Influence of iron availability on nutrient consumption ratio of diatoms in oceanic waters. Nature, 393, 774-777. https://doi.org/10.1038/31674

Twining, B. S., & Baines, S. B. (2013). The trace metal composition of marine phytoplankton. Annual Review of Marine Science, 5, 191-215.

Weber, M. E., Kuhn, G., Sprenk, D., Rolf, C., Ohlwein, C., & Ricken, W. (2012). Dust transport from Patagonia to Antarctica - a new stratigraphic approach from the Scotia Sea and its implications for the last glacial cycle. Quaternary Science Reviews, 36, 177-188.

Xiao, W., Frederichs, T., Gersonde, R., Kuhn, G., Esper, O., & Zhang, X. (2016). Constraining the dating of late quaternary marine sediment records from the Scotia Sea (Southern Ocean). Quaternary Geochronology, 31, 97-118. https://doi.org/10.1016/j.quageo.2015.11.003

Xiong, Z., Li, T., Algeo, T., Chang, F., Yin, X., & Xu, Z. (2012). Rare earth element geochemistry of laminated diatom mats from tropical West Pacific: Evidence for more reducing bottomwaters and higher primary productivity during the Last Glacial Maximum. Chemical Geology, 296-297, 103-118. https://doi.org/10.1016/j.chemgeo.2011.12.012

Xiong, Z., Li, T., Algeo, T., Doering, K., Frank, M., Brzezinski, M. A., Chang, F., et al. (2015). The silicon isotope composition of Ethmodiscus rex laminated diatom mats from the tropical West Pacific: Implications for silicate cycling during the Last Glacial Maximum. Paleoceanography, 30, 803-823. https://doi.org/10.1002/2015PA002793

KOPRI 극지연구소

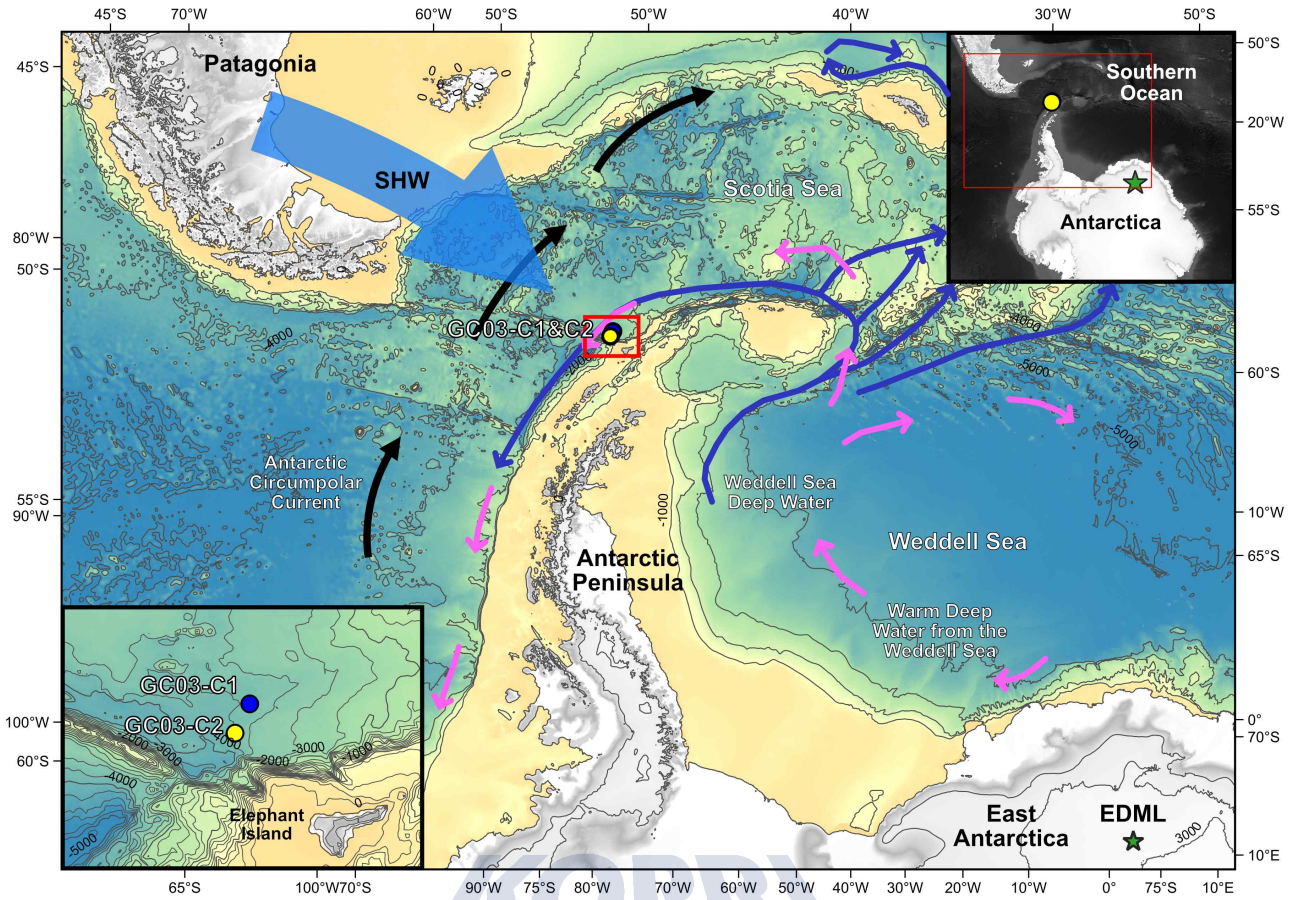


Figure #. Map of the study area, showing the location of studied sediment cores GC03-C1 (blue circles) and GC03-C2 (yellow circles). The green star indicates the location of the EDML ice core. The large blue arrow represents the Southern Hemisphere westerly winds (SHW). Weddell Sea Deep Water and Warm Deep Water from the Weddell Sea paths are from Hernández-Molina et al. (2006).

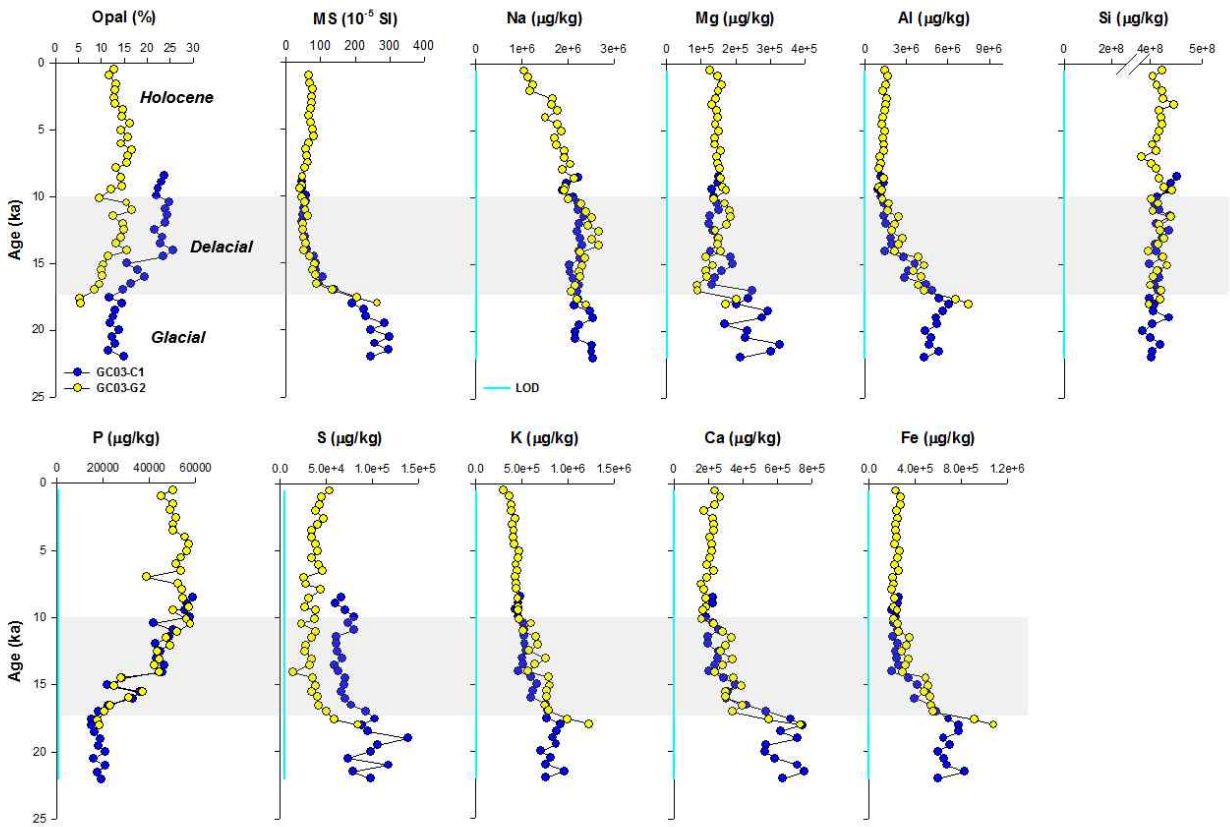


Figure #. Downcore variation of major geochemical elements at GC03-C1 (blue) and GC03-C2 (yellow) over the past 23 ka with biogenic opal concentration and MS values. The light blue lines represent the limit of detection (LOD) of the analytical method for each element. Biogenic opal and MS values for the two cores were reported in Kim et al. (2020).

KOPRI 극지연구소

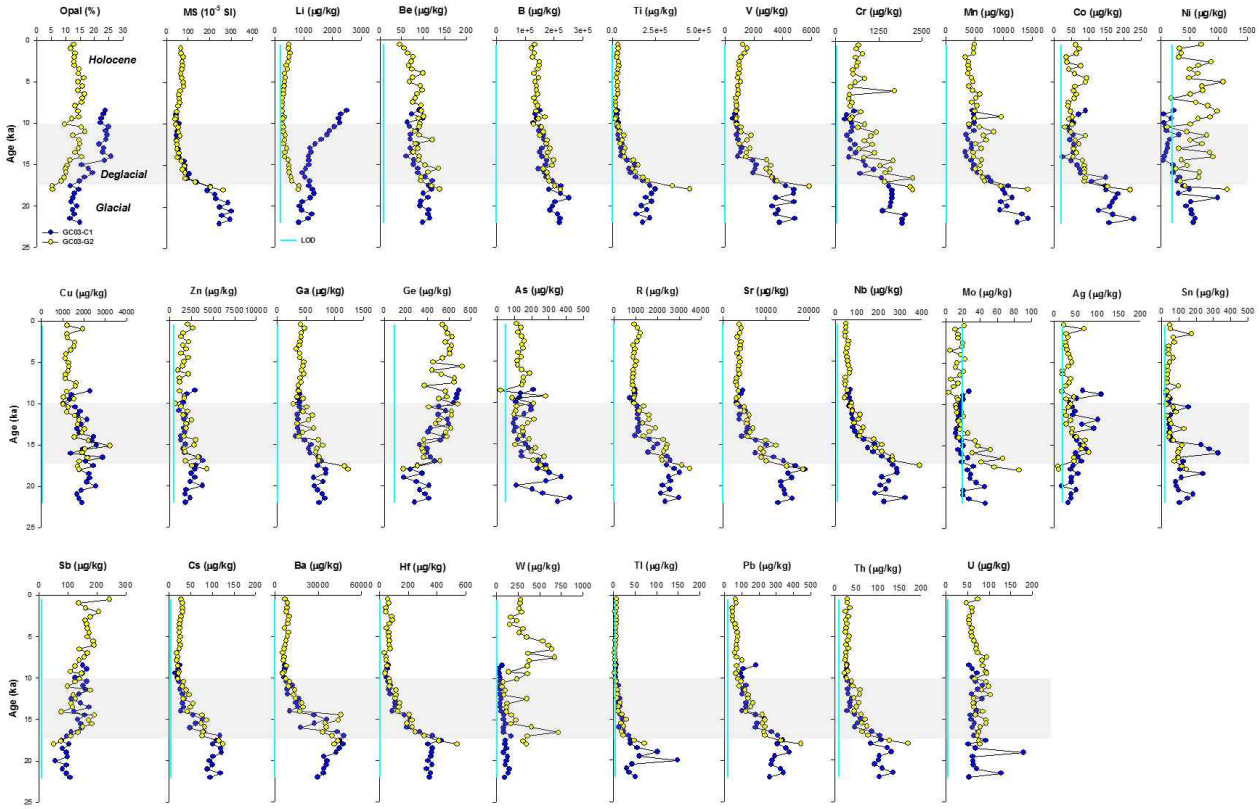


Figure #. Downcore variation of trace geochemical elements at GC03-C1 (blue) and GC03-C2 (yellow) over the past 23 ka with biogenic opal concentration and MS values. The light blue lines represent the limit of detection (LOD) of the analytical method for each element. Biogenic opal and MS values for the two cores were reported in Kim et al. (2020).

극지연구소

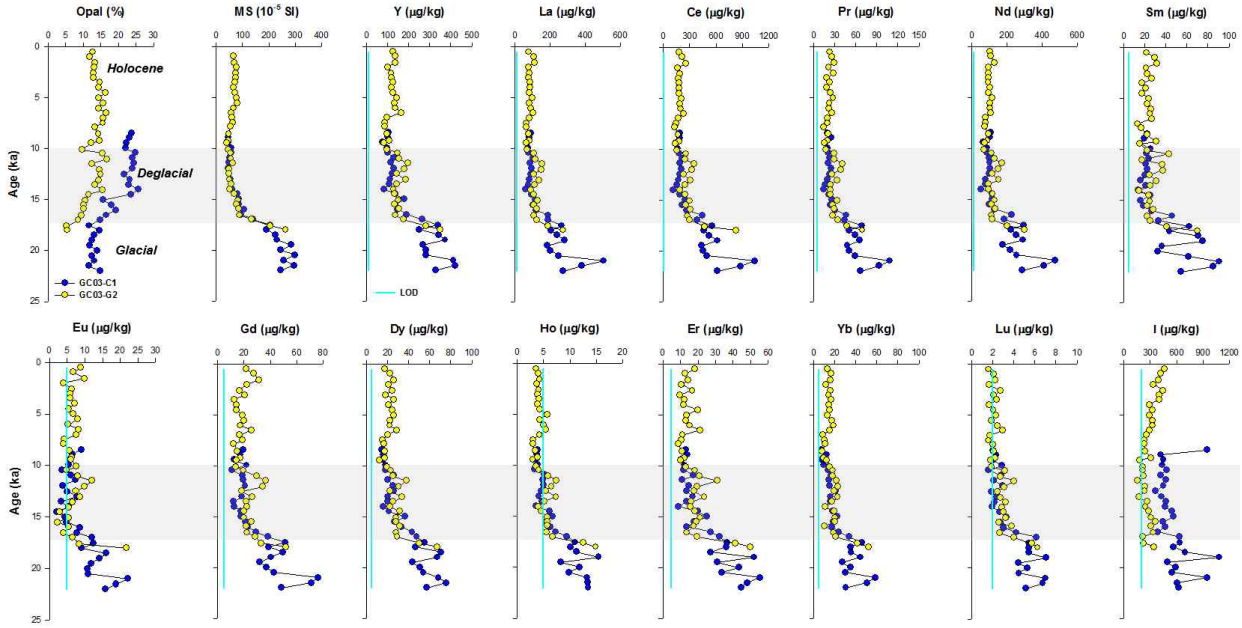


Figure #. Downcore variation of rare earth geochemical elements at GC03-C1 (blue) and GC03-C2 (yellow) over the past 23 ka with biogenic opal concentration and MS values. The light blue lines represent the limit of detection (LOD) of the analytical method for each element. Biogenic opal and MS values for the two cores were reported in Kim et al. (2020).

KOPRI
극지연구소

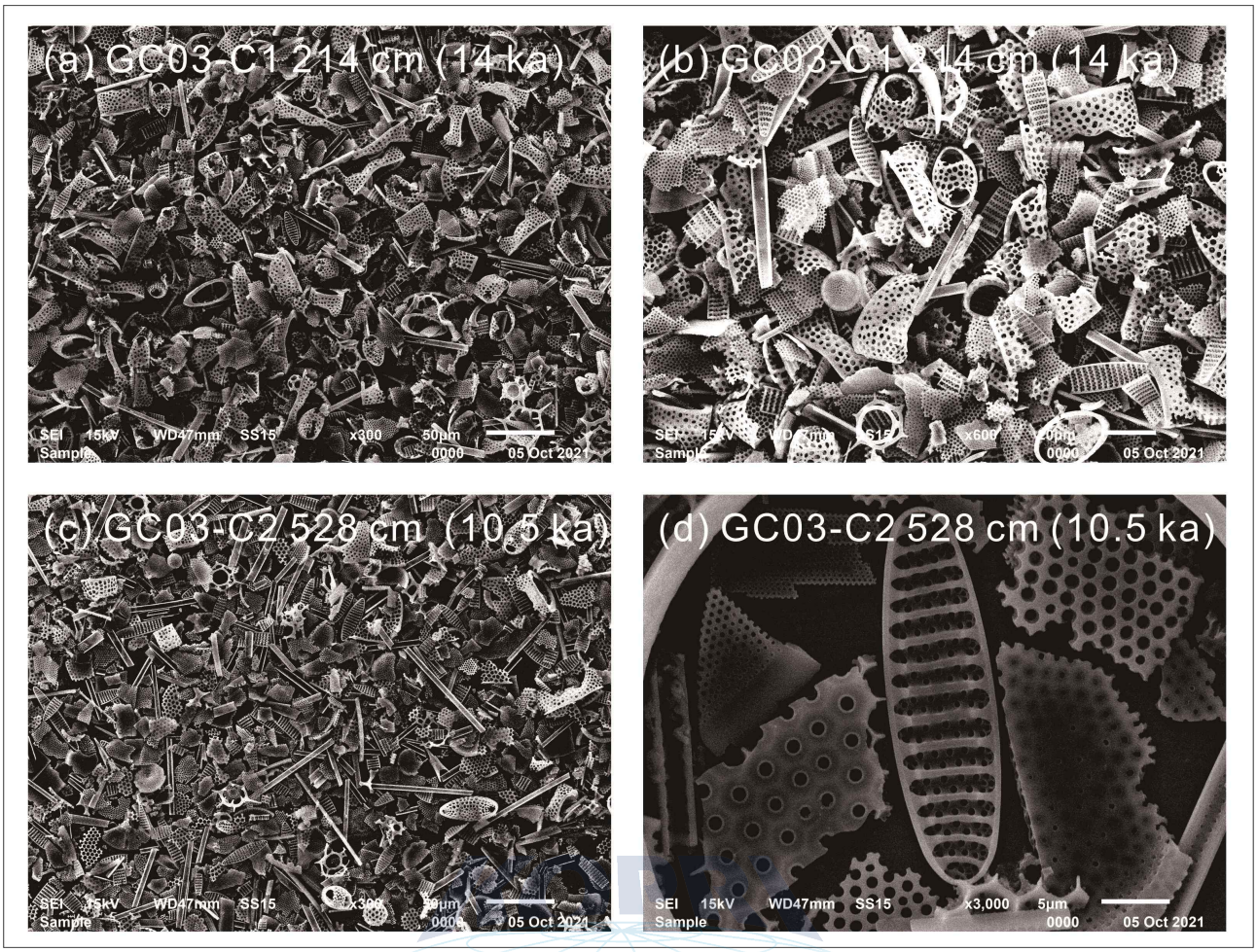


Figure #. Scanning electron microscopic images of purified diatom frustules at GC03-C1 214 cm (~14 ka) (a) with ×300 magnetude and (b) with ×600 magnetude, and at GC03-C2 528 cm (10.5 ka) (c) with ×300 magnetude and (d) with ×3,000 magnetude showing purity of diatom frustules after all treatments.

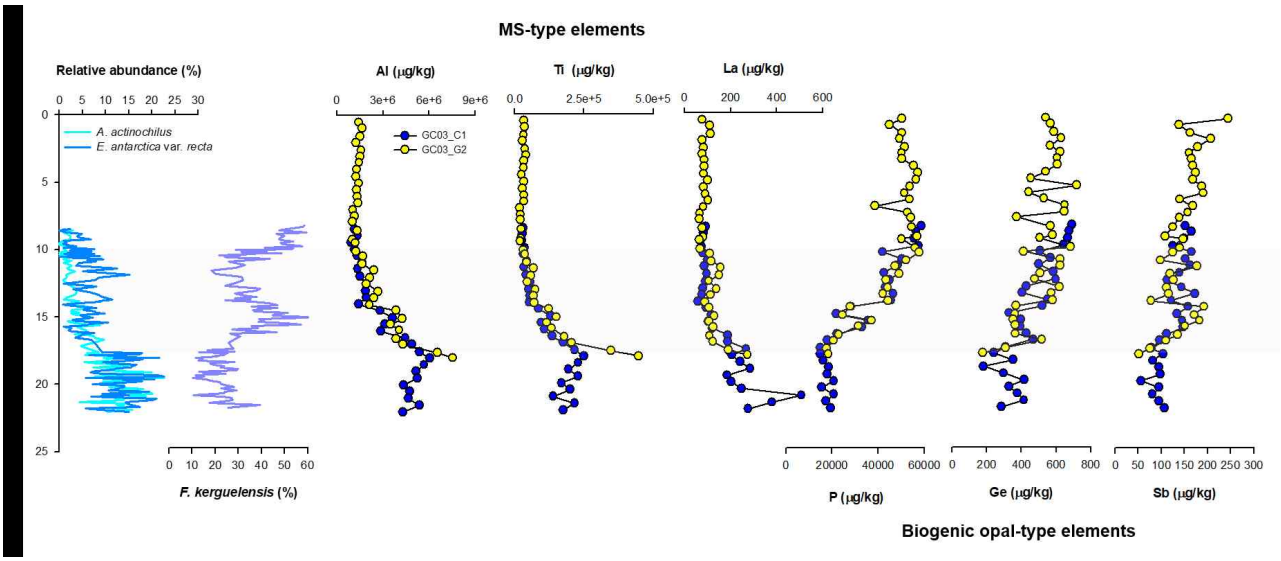


Figure #. Downcore variation of Al, Ti, and La, representative of MS-type and P, Ge, and Sb, representative of biogenic opal-type at GC03-C1 (blue) and GC03-C2 (yellow) over the past 23 ka with dominant diatoms. Diatom data for GC03-C1 were reported in Bak et al. (2010).

KOPRI
극지연구소

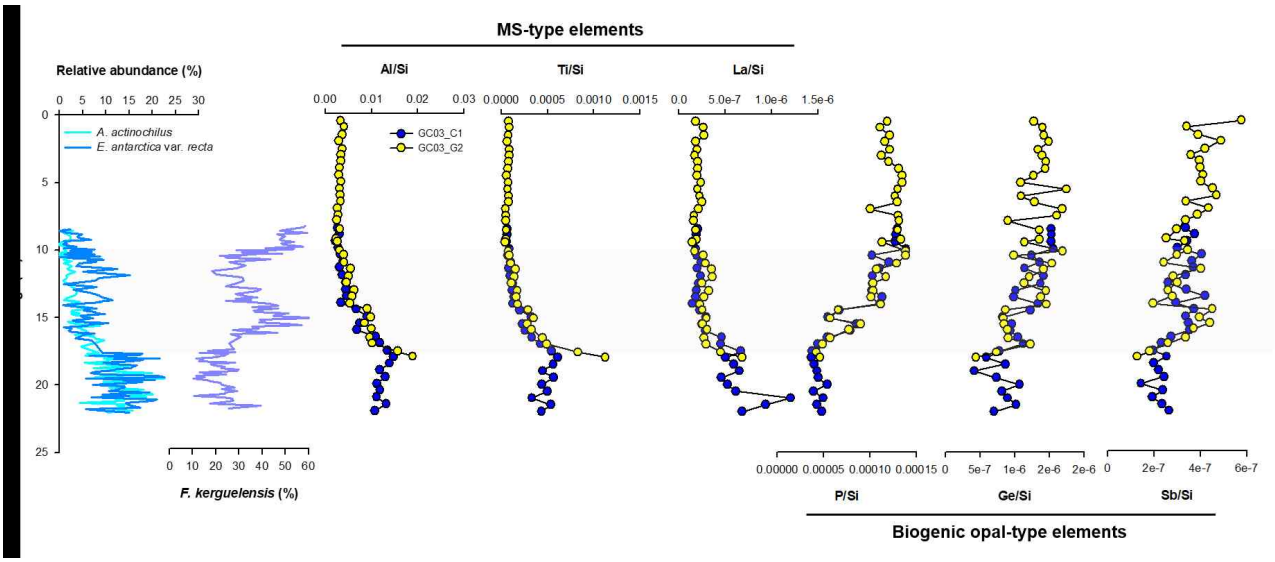


Figure #. Downcore variation of Al/Si, Ti/Si, and La/Si, representative of MS-type and P/Si, Ge/Si, and Sb/Si, representative of biogenic opal-type at GC03-C1 (blue) and GC03-C2 (yellow) over the past 23 ka with dominant diatoms. Diatom data for GC03-C1 were reported in Bak et al. (2010).

KOPRI
극지연구소

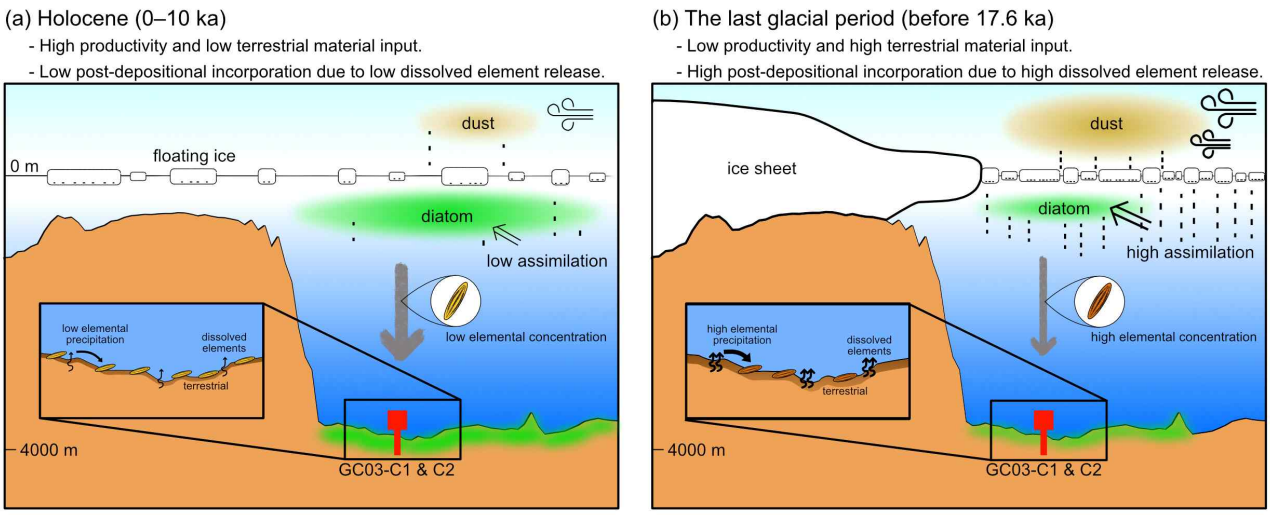


Figure #. Schematic models of MS-type elemental removal by diatoms in the surface water and in the surface sediment (a) during the Holocene showing low assimilation due to low element concentration in the ambient water and high species competition in the surface water and low post-depositional incorporation due to low terrestrial materials and (b) during the last glacial periods showing high assimilation due to high element concentration in the ambient water and low species competition and high post-depositional incorporation due to high terrestrial materials.

KOPRI
극지연구소

KOPRI
극지연구소

제 16 장

Drygalski Basin of the western Ross Sea since the Last Glacial Maximum[9)]

Sangbeom Ha[a,b,*], Jae Il Lee[b], Young-Suk Bak[c], Kyu-Cheul Yoo[a], Boo-Keun Khim[a,d*]

[a]Department of Oceanography, Pusan National University, Busan 46241, Republic of Korea
[b]Division of Glacial Environment Research, Korea Polar Research Institute, Incheon 21990, Republic of Korea
[c]Earth Environmental System Research Center, Jeonbuk National University, Jeonju 54896, Republic of Korea
[d]Marine Research Institute, Pusan National University, Busan 46241, Republic of Korea

Abstract: The repeated growth and reduction of the ice sheet have controlled the striking variation of the continental shelf environment in the Ross Sea. Particularly, glaciomarine shelf sedimentation is closely related to the ice sheet dynamics and ice shelf development since the Last Glacial Maximum (LGM). Using the four gravity (and box) cores obtained from the northern Drygalski Basin in the western Ross Sea, multi-proxies including sediment properties, geochemical proxies, carbon isotopic values of organic matter, clay mineral compositions of fine-grained sediments, and diatom assemblage were analyzed with AMS 14C dating from bulk organic matters. Based on the core description, X-radiograph observation, and results of grain size distribution, the core sediments were classified into the seven sediment facies: clast-rich muddy diamicton, clast-rich sandy diamicton, massive mud, laminated mud, bioturbated mud, massive sandy mud, and bioturbated sandy mud. The association of these sediment facies defines the four lithologic units in terms of the depositional evolution. Lithologic unit 1 represents diamicton deposited proximal to the grounding line. When the ice sheet and ice shelf retreated since the LGM, the unsorted sediment mass was deposited proximal to the grounding line. Lithologic unit 2 consists of the massive mud deposited under the sub-ice shelf condition. During the ice sheet retreat, the fine-grained particles were transported by the meltwater plume to the sub-ice shelf floor. The biogenic materials were also transported from the seasonal open marine area to

9) 이 연구 결과는 다음의 논문으로 출판되었음: Ha, et al. (2023). "Glacial-interglacial environmental changes in the Drake Passage over the past 600 kyrs" Palaeogeography Palaeoclimatology, Palaeoecology 631: 111835.

the sub-ice shelf by the currents. Lithologic unit 3 was composed of sandy mud and mud with abundant dropstones that might have been deposited at the calving line. As the calving line passed the Drygalski Basin, a large amount of the coarse fractions was deposited due to ice shelf breakup. The terrestrial sediments from the Victoria Land coast were transported from the grounding line of the remained local ice sheet, when the calving line passed the north side of Drygalski Ice Tongue. Lithologic unit 4 comprises the bioturbated mud and sandy mud that were deposited under the seasonal open marine condition. The biological productivity increased significantly during the late Holocene, while the terrestrial sedimentation decreased under seasonal open marine conditions. The diatom assemblage and δ13C values of sediment organic matter indicate the mid-Holocene warm climate with more sea ice melting. Since the LGM, the paleoenvironmental change and glaciomarine depositional evolution on the northern Drygalski Basin were closely linked with the ice sheet dynamics and ice shelf activity, in addition to the climate change during the Holocene.

1. Introduction

In the Ross Sea, the bathymetry and topography such as the northnorthwest oriented deep and narrow basins (e.g., Glomar-Challenger Basin, Joides Basin, and Drygalski Basin) and shallow banks (e.g., Ross Bank, Pennell Bank, and Crary Bank) have been generated by the advanced ice sheet during the glacial periods (Fig. 1). The Drygalski Basin is located in the western Ross Sea and includes the deepest area on the Ross Sea continental shelf. Numerous outlet glaciers along the coastline of the western Ross Sea originated from the ice domes (Dome C (Charlie), Taylor dome, and Talos dome) on the Victoria Land (Giovinetto and Bentley, 1985; Frezzotti et al., 2000). After the LGM, the outlet glaciers on Northern Victoria Land retreated as the global sea level rose, whereas those on Southern Victoria Land retreated after Meltwater Pulse 1A (~14 ka) (Goehring et al., 2019; Christ and Bierman, 2020). The David Glacier, which is the largest, forms the Drygalski Ice Tongue (DIT) that protrudes into Terra Nova Bay (Fig. 1). The deposition of biogenic particles in the Drygalski Basin is locally high, because Terra Nova Bay is the major polynya formed by the persistent katabatic wind from the Nansen Ice Shelf and characterized by the high spring diatom blooms leading to the increased primary productivity in the surface water (Arrigo et al., 2000, 2003). The study on the paleoenvironmental reconstruction of the Drygalski Basin could provide the retreating history of the ice sheet and ice shelf related to the global sea level change and climate warming since the Last Glacial Maximum (LGM).

KOPRI 극지연구소

During the LGM, the ice sheet advanced to reach the continental shelf edge at the eastern side of the Ross Sea, but did not reach the shelf edge at the western side (Anderson et al., 2014; Halberstadt et al., 2016; Bart et al., 2018; Prothro et al., 2020). The retreat history of the grounded ice sheet after the LGM was reported by several studies using the sediment cores and seismic surveys in many areas of the Ross Sea (e.g. Conway et al., 1999; Domack et al., 1999; McKay et al., 2008; Prothro et al., 2020). Although the precise timing of the ice sheet retreat could not be determined due to the uncertainty of age dating, the ice sheet retreated from ~16 ka to ~8 ka in the northern Drygalski Basin (McKay et al., 2008; Prothro et al., 2020), and continued retreating toward the present-day position after ~8 ka (Conway et al., 1999; McKay et al., 2008; Lowry et al., 2019). The ice shelf in the Ross Sea also moved to the outer continental shelf and shelf edge with the ice sheet expansion during the LGM. Previous studies summarized glaciomarine sedimentation related to the retreating ice shelf during the deglacial period (e.g. McGlannan et al., 2017; Prothro et al., 2018; Smith et al., 2019). Although the retreat timing of the ice shelf in the northern Drygalski Basin is still unclear, the retreat of the ice shelf was later than that of the ice sheet (Prothro et al., 2020).

The types of sediment facies in the Antarctic continental shelf depend mainly on the distance from the grounding line, the position of the calving line, and the open marine condition. These are closely related to the variation of the ice sheet and ice shelf between the glacial and interglacial periods (Domack et al., 1999; McKay et al., 2008; Tolotti et al., 2013; Prothro et al., 2018; Smith et al., 2019). In addition, the hydrographic conditions such as sea ice, meltwater, water masses, and currents affect sediment deposition on the Antarctic continental shelf (Grobe and Mackensen, 1992; Gilbert et al., 1998; Anderson, 1999; Ehrmann et al., 2011). Smith et al. (2019) differentiated the depositional sequences in relation to changes in the ice sheet in the Antarctic continental shelf: the stiff diamicton beneath the ice sheet and the diatom-bearing mud or diatomaceous mud under the seasonal open marine conditions. In particular, under ice shelf conditions, the sediment grain size decreased as the distance from the grounding line increased. Far from the grounding line and near the calving line of the ice shelf, the coarse-grained particles as ice-rafted debris (IRD) and the biogenic particles increase to deposit under the seasonal open marine conditions. In the Drygalski Basin, change in the sediment facies from diamicton during the glacial period to open marine sediment deposit during the interglacial period was also reported (Brambati et al., 1997; Frignani et al., 1998; Domack et al., 1999; Licht et al., 1999; Prothro et al., 2018).

Hillenbrand et al. (2009) reported that the source of sediments changed by the shift of the ice flow direction in the Bellingshausen Sea. In the Bellingshausen Sea, the main provenance of the sediments supplied by the advanced ice sheet was the English Coast

located at the southeastern side of the continental shelf during the LGM. On the other hand, the main provenance was shifted to the Beethoven Peninsula, located at the eastern side of the continental shelf, with the ice sheet retreat during the Holocene. Later, McGlannan et al. (2017) established the glaciomarine sedimentation variation related to the retreating ice sheet and ice shelf based on the sediment properties and geochemical proxies on the Wales Deep Basin located at the eastern continental shelf of the Ross Sea since the LGM. In this basin, the transported sediments by the ice sheet and meltwater decreased and biogenic materials from the open mains increased, following the retreating ice sheet.

In the Drygalski Basin, based on the grounding zone wedge and moraines on the seafloor, the ice flow directions were southward and westward during the deglacial period (Greenwood et al., 2018; Prothro et al., 2020; Rhee et al., 2020). These previous studies suggest glaciomarine sedimentation in the Drygalski Basin could be affected by the sediment transport of the ice flow since the LGM. For example, based on the 10Be contents of sediments, Yokoyama et al. (2016) reported that the local ice shelf was pinned on the shallow bank or inner shelf in the western Ross Sea, which affected the glaciomarine sedimentation after the retreat of the grounded ice sheet. Nevertheless, the study on the ice flow using gravity cores has not been conducted at the northern part of the DIT in the Drygalski Basin.

This study aims at reconstructing the paleoenvironments of glaciomarine sediment deposition since the LGM and determining the effect of the ice flow direction from the local glacier at the north of the DIT using sediment properties, geochemical proxies, clay mineral compositions of fine-grained sediments, and diatom assemblage along with the accelerator mass spectrometry (AMS) 14C age dating of the gravity (and box) cores.

2. Regional setting

Many paleoenvironmental and sedimentological studies on the advance and retreat of the ice sheet have been conducted in the continental shelves of the Ross Sea (Anderson et al., 1984; Domack et al., 1999; Salvi et al., 2006; Mosola and Anderson, 2006; McKay et al., 2008; McGlannan et al., 2017; Majewski et al., 2020). The advanced ice sheet during the glacial periods formed mega-scale glacial lineations and large-scale erosion on the seafloor of the continental shelf (e.g., Shipp et al., 1999). Above mega-scale glacial lineations, the remolding and deformation of the redeposited sediments formed subglacial diamictons during the last glacial period from 26.5 to 19.5 ka (Anderson et al., 1992; Domack et al.,

1999; Bart et al., 2000). The retreat of the grounding line and calving line since ~11 ka formed diverse sediment facies such as stratified diamicton by debris flow or turbidity cur rents at the front of the grounding line, laminated or massive mud by the meltwater plume from the grounding line, and massive mud with abundant IRD under the calving line (Domack et al., 1999; McKay et al., 2008; Smith et al., 2019; Prothro et al., 2020). Following the retreat of the calving line, the seasonal open marine condition began to control the diatom bloom, resulting in the deposition of mainly diatom-bearing or diatomaceous mud on the continental shelf in the Ross Sea (Melis and Salvi, 2009; Smith et al., 2011; McGlannan et al., 2017).

Diamicton deposition during the LGM indicated that the Drygalski Basin was covered with an advanced ice sheet (Brambati et al., 1997; Domack et al., 1999; Melis and Salvi, 2009; Prothro et al., 2020). After the LGM, the advanced ice sheet retreated rapidly along with the ice shelf (McKay et al., 2008; Prothro et al., 2020). In general, a complete sequence of sediment deposits indicating ice sheet or ice shelf retreat is rarely observed due to the relatively short duration of the sediment deposition (Smith et al., 2019). In the northern Drygalski Basin, Domack et al. (1999) reported the complete sequence of the sediment facies since the LGM from even only one sediment core that differentiates diamicton, fining-upward sediments related to the retreat of the grounding line, null zone, calving line deposit, and siliceous sediments under the seasonal open marine condition. In contrast, other core sediments from the central part of the Drygalski Basin generally preserve the diamicton, short glaciomarine sediments, and Holocene biogenic sediments (e.g. Brambati et al., 1997; Frignani et al., 1998; Licht et al., 1999; McKay et al., 2008). Based on the depositional sediment sequence, Prothro et al. (2020) reported that a seasonal open marine environment began to develop at ~8 ka in the Drygalski Basin.

The geochemical properties (TOC, TN, biogenic opal, CaCO3, and C/N ratio) and δ 13CSOM values represent the degree of biological productivity in the surface water of the continental shelf in the Ross Sea (e.g. Dunbar et al., 1998; Frignani et al., 1998; Villinski et al., 2000; Salvi et al., 2004; Salvi et al., 2006; McGlannan et al., 2017). These geochemical properties exhibit distinct difference between the glacial condition due to the wide coverage of the ice sheet on the continental shelf and the interglacial condition characterized by the retreat of the ice sheet and more influence of the seasonal open marine condition in the Ross Sea (Domack et al., 1999; Salvi et al., 2006; McKay et al., 2008; McGlannan et al., 2017). The δ13CSOM values are controlled by various factors such as primary production in surface water, temperature and CO2 concentration of seawater, terrestrial organic carbon, and heterotrophy (Rau et al., 1982; Villinski et al., 2000; Crosta et al., 2005; Henley et al., 2012; Berg et al., 2013; Tesi et al., 2020), among which δ13CSOM values of the Ross Sea continental sediments are mainly determined by the biogenic fractionation and productivity

within the water column (Villinski et al., 2000; Tesi et al., 2020).

The provenance of clay minerals in the Ross Sea embayment has been still poorly investigated mainly owing to the thick ice sheet on the bedrock of the continent. Nevertheless, previous studies reported the possible provenance of clay minerals in the Ross Sea (e.g. Kyle, 1990; Ehrmann, 1998; Smellie and Hole, 1998; Ehrmann et al., 2005; Giorgetti et al., 2009; Franke and Ehrmann, 2010). Illite is thought to originate from the erosion of the Beacon Super Group or crystalline rock of the Transantarctic Mountains under the ice sheet, whereas smectite is supplied from the McMurdo Volcanic Group (Erebus, Melbourne, and Hallett volcanic province). The source of chlorite was estimated as the bedrock or sedimentary rock of the Transantarctic Mountains. Despite unidentified, the source of kaolinite was estimated as paleosoils or sedimentary rock containing kaolinite around the Ross Sea. For example, Salvi et al. (2006) reported that the clay mineral compositions changed as the ice sheet retreated or advanced since the LGM on the JOIDES Basin of the Ross Sea. During the deglaciation, the retreating ice sheet supplied a large amount of smectite that originated from the McMurdo Volcanic Group at the Victoria Land coast. Nevertheless, the sediments at the front of the grounding zone and the Holocene sediments contain high levels of illite and chlorite, which might have been transported from the rocks in the East Antarctic interior.

The diatom assemblage of the continental shelf sediments in the Ross Sea was used to interpret the environmental condition of the surface water, such as sea ice extent or open marine conditions, despite the caution on reworking species (Cunningham and Leventer, 1998; Crosta et al., 2004, 2005; Armand et al., 2005; Tolotti et al., 2013; Tesi et al., 2020). Chaetoceros resting spores are linked to the seasonal stratified meltwater from sea ice melting in spring. Thalassiosira antarctica (cold type), E. antarctica var. recta, F. curta, and F. obliquecostata indicate seasonal sea ice condition. In the Ross Sea continental shelf, Tolotti et al. (2013) reported that the diatom assemblage was changed by the depositional condition since the LGM. They emphasized that the diatom abundance increased with the formation of the seasonal open marine condition. On the other hand, P. sulcata has been used as an indicator of the reworking deposition. For example, McGlannan et al. (2017) reported that the dominant diatom assemblage was shifted from the reworked species to the modern species at an increasing distance from the grounding line related to the retreating ice sheet.

3. Materials and Methods

A Gravity cores (GC01, GC02, and GC04) were collected each at three sites

(DG12-01, DG12-02, and DG12-04) along the central floor of the Drygalski Basin and another gravity core (GC05) was collected at site DG12-05 on the southwestern flank of the Crary Bank (Fig. 1). At each site, box cores (BC01, BC02, BC04, and BC05) were also collected (Table 1). These cores were split, visually described, and X-ray photographed at the Korea Polar Research Institute (KOPRI).

The magnetic susceptibility (MS), water content (WC), grain size, total carbon (TC), total nitrogen (TN), total organic carbon (TOC), and CaCO3 were measured at KOPRI. The MS was measured at 1 cm intervals using a Bartington MS-2B susceptibility meter. The WC was also measured at 1 cm intervals using 1 cm thick subsamples by calculating the following equation with an assumption of 35 psu for the salinity of seawater:

$$WC(\%) = \frac{mass\,of\,wet\,sediment - (mass\,of\,dry\,sediment + mass\,of\,salt)}{mass\,of\,wet\,sediment \times 100}$$

The grain size was measured at 4 cm intervals. After removing organic matter using 10 % H2O2 and biogenic silica using 2 N NaOH, the coarse fraction (>63 μm) was analyzed using 1 phi interval sieves. In contrast, the fine fraction (<63 μm) was analyzed using Micrometrics Sedigraph III 5120. The grain size classification followed the scheme of Folk and Ward (1957). The TC and TN contents were analyzed using an elemental analyzer (FLASH 2000 NC Analyzer) with an analytical precision of <0.1 %. Total inorganic carbon (TIC) was measured using a UIC CO2 coulometer (Model CM5240). CaCO3 concentration was calculated by multiplying TIC content by 8.333 (i.e., the ratio of CaCO3 and carbon). TOC content was calculated as the difference between TC and TIC contents.

Biogenic silica concentration was measured at 8 cm intervals (GC01, GC04, and GC05) and 4 cm intervals (GC02) using the wet alkaline sequential extraction method using 1 N NaOH solution at 85 °C modified from DeMaster (1981) at Pusan National University. Biogenic opal content was calculated by multiplying biogenic silica concentrations by 2.4 (i.e., the ratio of biogenic opal and Si) (Mortlock and Froelich, 1989). The analytical precision for the biogenic opal measurement was ±1 %.

The carbon isotope composition (δ13CSOM) of the sediment organic matter was measured for selected sediment samples at 10 cm intervals from GC01 and at 8 or 16 cm intervals from GC02, 04, and 05 using elemental analysis-isotope ratio mass spectrometry (EA-IRMS: Europa Scientific 20-20 isotope ratio mass spectrometer) at IsoAnalytical Ltd. (UK). The δ13CSOM values were expressed in conventional delta notation, which is the per mil deviation from the V-PDB standard. The analytical precision for δ13CSOM was approximately ±0.08 ‰.

The samples for clay mineral compositions were collected from GC01 and GC04 at

10 or 20 cm intervals. The organic matter was removed using 10 % H2O2, and the fine fraction (<63 μm) was separated using a sieve. The fraction under 2 μm was extracted using Stokes' law, smeared on the slide, and air-dried following Stokke and Carson (1973). An air-dried slide was treated with ethylene-glycol for 24 h. X-ray diffraction (XRD) was performed using a Siemens/Brucker D5005 at Gyeongsang National University with Cu-Kα radiation (40 kV, 35 mA). The clay mineral composition was identified based on the basal reflections recorded in the XRD patterns, following the methods of Brown and Brindley (1980) and Moore and Reynolds Jr (1989). The four major clay minerals (illite, smectite, chlorite, and kaolinite) were estimated by semiquantitative calculation using the method of Biscaye (1965). The analytical precision for the clay mineral composition was approximately ±5 %.

The samples for diatom assemblage were selected at nine horizons from GC01 and GC04, respectively. The sediment treatment, slide preparation, and diatom counting were carried out at Jeonbuk National University. The quantitative analysis of the diatom slides was performed according to the procedure described in Scherer (1994). The absolute abundance was calculated as follows:

$$Abundance = \left(\frac{number\ of\ specimens\ counted \times area\ of\ the\ settling\ chamber}{number\ of\ microscope\ fields\ of\ view \times area\ of\ the\ field\ of\ view} \right) \div sample\ mass$$

KOPRI 극지연구소

Chaetoceros resting spores were not included in specimen counting.

AMS 14C dating was conducted at the core-top (0-1 cm) of BC01 and BC04, two horizons of GC01, and three horizons of GC04 (Table 2). The 14C activity was measured using the acid-insoluble organic matter (AIOM) of the bulk sediments at Beta Analytic (USA) due to the scarcity of foraminifera in the core sediments. The AMS 14C ages obtained by AIOM of bulk sediments are generally biased by old carbon in the Antarctic seawater, reworking of sediments, and glacial erosion of old sediments (e.g., Andrews et al., 1999; Pudsey et al., 2006; Mezgec et al., 2017; Tesi et al., 2020; Ha et al., 2022). As a result, these ages incorporate the regional marine reservoir effect (MRE) as well as the local contamination offset (LCO) by dead carbon. The LCO should be corrected before calibrating AMS 14C ages, assuming that the MRE and LCO are not different between the glacial periods and the Holocene (Hall et al., 2010; Hillenbrand et al., 2010). The MRE near Terra Nova Bay was estimated to be about 1.2 ka by Hall et al. (2010). The AMS 14C ages of AIOM were dated 3.7 ka and 4.1 ka at the core-top of BC01 and BC04, respectively (Table 2). Similar old ages of the surface sediments are normally found on the Antarctic continental shelf (e.g. Licht et al., 1996; Andrews et al., 1999; Hall et al., 2010; Anderson et al., 2014). Consequently, the LCO at BC01 (2510 yrs) and BC04 (2890 yrs) was judged by subtracting

the MRE (1.2 ka) from the core-top AMS 14C age. This LCO was then applied to GC01 and GC04 for the reliable age correction. The LCO-corrected ages were subsequently converted to the calibrated AMS 14C ages using Calib 8.2 with calibration curve MARINE 20 (Heaton et al., 2020; Stuiver et al., 2021).

4. Results

Based on the core description, X-ray photographs, and grain size results, seven sediment facies are defined (Figs. 2 and 3): (a) clast-rich muddy diamicton, (b) clast-rich sandy diamicton, (c) massive mud, (d) laminated mud, (e) bioturbated mud, (f) massive sandy mud, and (g) bioturbated sandy mud. The clast-rich sandy or muddy diamicton contained large amounts (average ~75 % and ~35 %, respectively) of coarse grains in a fine sand or mud matrix and the mean grain sizes are 5.3ø and 6.6ø, respectively. They were observed at the lower part of GC01, GC04, and GC05 (Fig. 3). The massive mud is structureless fine-grained sediment (>90 % of silt and clay) with a mean grain size of 10.3ø, whereas the laminated mud shows thin laminations with a similar mean grain size of 10.4ø (Fig. 2). These two sediment facies are intercalated in the middle part (~2 m thick) of GC04 with a thin (~2 cm) sandy mud at 147 cm (Fig. 3). The bioturbated mud is the fine-grained sediment (>8.7ø of mean grain size) showing a mixture by biogenic activity and containing scattered ice-rafted debris (IRD) (Fig. 2). This material was observed mostly at the upper part of the core (GC01, GC02, and GC05) (Fig. 3). However, the bioturbated sandy mud (7.8ø of mean grain size) with IRD was observed at the upper part of GC04 (Fig. 3). The massive sandy mud (30-40 % sand fraction) characterized by a mean grain size of ~7ø lacks primary sedimentary structure (Fig. 2). The intercalation of massive sandy mud and bioturbated sandy mud was also observed at GC02 and GC04 (Fig. 3). Finally, based on the association of sediment facies, four lithologic units (Units 1 to 4 from core-bottom to core-top) were determined (Fig. 3).

4.1. Lithologic unit 1

Lithologic unit 1 consisted of clast-rich sandy diamicton (GC01 and GC04) or clast-rich muddy diamicton (GC05), characterized by generally high MS (up to 200 at GC01 and GC04, ~130 at GC05) and low WC (~25 %) (Fig. 4). The geochemical and isotope properties of this unit are characterized by very low TN (mostly below detection limit), TOC (~0.25 %), and biogenic opal (<7 %), CaCO3 (<0.8 % except for GC01), and high C/N ratio (>15) (Fig. 5). The δ13CSOM values of Unit 1 are mostly constant ranging between ~-24 ‰ and

~-26 ‰ (Fig. 5). The clay mineral compositions of Unit 1 are characterized by relatively high smectite (10-23 %) and chlorite (14-22 %) and low illite (48-67 %) content (Fig. 6). The preservation of the diatom in this unit is very poor and only Paralia sulcata appeared at GC04 (Fig. 7). The calibrated AMS 14C ages above the unit boundary date 13.3 ka at GC01 and 22.9 ka at GC04, respectively (Fig. 4).

Unit 1 was observed at the bottom part of GC01, GC04 and GC05. The sediments of Unit 1 were characterized by sorted or unsorted granulometry with a large amount of coarse sand or mud matrix (Figs. 2 and 3). The sediment properties of Unit 1 are characterized by relatively high and low WC (Fig. 4). The advanced ice sheet during the last glacial period eroded the underlying bedrock and sediments, forming massive unconsolidated diamictons on the continental shelf in the Ross Sea (Licht et al., 1999). The diamictons are characterized by commonly high shear strength and MS intensity, poorly sorted granulometry, large amount of coarse fraction, low WC, and absent or little biogenic materials (Domack et al., 1999; Licht et al., 1999; Smith et al., 2019). These geochemical properties are related to the transported old biogenic fragments and lithogenic materials by the advanced ice sheet (Sjunneskog and Scherer, 2005; McGlannan et al., 2017; Smith et al., 2017; Smith et al., 2019). The geochemical proxies of Unit 1 indicate very low biogenic productivity due to the wide coverage of the ice sheet and, particularly, high C/N ratios might be attributed to eroded terrestrial sediments (Anderson et al., 1984; Domack et al., 1999; Salvi et al., 2006; McGlannan et al., 2017; Prothro et al., 2018; Smith et al., 2019).

KOPRI 극지연구소

4.2. Lithologic unit 2

Lithologic unit 2 consists of the thick massive mud intercalated with thin laminated mud occurring only at the middle part of GC04 (Fig. 3), which is characterized by low MS (~30) and high WC (~70 %) (Fig. 4). The geochemical and isotope properties of Unit 2 are mostly consistent with tiny fluctuations, showing TN (~0.03 %), TOC (~0.5 %), C/N ratio (~18), CaCO3 (~0.02 %), biogenic opal (~2 %), and δ13CSOM (-24.5 ‰) (Fig. 5). The clay mineral composition of this unit is similar to that of Unit 1 such as relatively high smectite (9-26 %) and chlorite (13-18 %) and low illite (53-67 %) content (Fig. 6). The occurrence of diatom is barren similar to Unit 1, except for the appearance of Fragilariopsis curta and F. kergulensis at the middle of Unit 2 (Fig. 7).

Unit 2 was observed only at the middle part of GC04, consisting of massive mud intercalated with laminated mud, although a sand layer (2 cm thick) intervened at 148 cm (Fig. 3). Based on X-ray photographs, the sand layer seems to be deposited accidentally by lateral transport from the topographic high of the inner bay at the western side of the basin rather than the deposition of IRD. The sediment properties of Unit 2 are

characterized by a thick massive mud layer with homogeneous MS and high WC and without pebbles (Fig. 4). Similar sediment properties were reported in the massive or faint laminated mud in the Ross Sea and Amundsen Sea (McGlannan et al., 2017; Simkins et al., 2017; Smith et al., 2019). The old AMS 14C ages in Unit 2 are, without doubt, due to the incorporation of old organic matters. The geochemical proxies of Unit 2 are characterized by a slight increase in TOC, TN, and δ13CSOM values and a decrease in C/N ratios and biogenic opal and CaCO3 contents (Fig. 5). Domack et al. (1999) reported that the finegrained sediments deposited by meltwater plume from the grounding line contained more biogenic materials than the diamicton. The increasing biogenic materials are not generated in the surface water under the ice shelf condition, but transported to deposit farther by the currents from the calving line which is located under the seasonally open marine condition (Prothro et al., 2018; Smith et al., 2019). The geochemical proxies of Unit 2 indicate that the fine sediment was transported by the meltwater plume from the grounding line with little amount of biogenic material from the open marine area farther from the DIT.

4.3. Lithologic unit 3

Lithologic unit 3 consists of alternating sandy mud and massive mud at the lower part of GC02 and at the upper part of GC04 (Fig. 3), showing the fluctuation of MS (50-200) and WC (20-74 %) (Fig. 4). The geochemical and isotope properties (TN: ~0.02 %, TOC: ~0.4 %, C/N: ~16, CaCO3: ~0.05 %, biogenic opal: ~2 %, and δ13CSOM: ~-24.6 ‰) of Unit 3 are similar to those of Unit 2, despite the slight fluctuations (Fig. 5). The clay mineral composition of this unit falls between Units 2 and 4 (Fig. 6). The occurrence of diatom in Unit 3 is also similar to that of Unit 2, with only the appearance of F. curta and F. kergulensis and mostly absence (Fig. 7).

Unit 3, observed at cores GC02 and GC04, is characterized by the alternation of mud and sandy mud layers with rich pebbles, gravels, and sand fractions (Fig. 4). Despite the uncertainty of the precise timing, while the retreating position of the ice shelf edge is unclear, the grounding line located at the coast of the Victoria Land and DIT until about 4 ka (Prothro et al., 2020). When the ice shelf was broken up, many dropstones from the icebergs were deposited on the seafloor. However, it is difficult to find the sediment layer indicating the deposition at the calving line due to its unstable position and the random supply of dropstones (Smith et al., 2019; Prothro et al., 2020). Nonetheless, the sediment layer deposited at the calving line was reported by previous studies on the Ross Sea, Antarctic Peninsula and Prydz Bay (Domack and Harris, 1998; Domack et al., 1998; Kilfeather et al., 2011; McGlannan et al., 2017). The geochemical proxies of Unit 3 are

similar to those of Unit 2 as relatively low TN, TOC, and biogenic opal content with high C/N ratios and δ13CSOM values (Fig. 5). Previous studies reported the different geochemical characteristics at the calving line showing the increasing biogenic materials due to the seasonal open marine condition or similar properties to the diamicton proximal at the grounding line such as a large amount of sediments by the meltwater discharge (Domack et al., 1999; McGlannan et al., 2017).

The geochemical proxies of Unit 3 indicate that the sediments contained the transported sediments from the inner shelf or Antarctic continent similar to Unit 2.

4.4. Lithologic unit 4

Lithologic unit 4 occupies the upper part of all cores as the bioturbated mud (GC01, GC02, and GC05) and bioturbated sandy mud (GC04) containing scattered IRD (Fig. 3). In general, the MS is low (20-60) and the WC is high (~60 %) in this unit, but the MS depends on the IRD and sand fraction (Fig. 4). The geochemical properties of Unit 4 are characterized by a gradual increasing trend (TN: from 0.02 % to 0.15 %, TOC: from 0.2 % to 1.0 %, and biogenic opal: from 2 % to 35 %) with constantly low C/N ratios (~8) (Fig. 5). CaCO3 content is also mostly low (<0.02 %) and all core-tops mark the minimum (Fig. 5). The δ 13CSOM values range between -27.1 and -23.8 ‰, particularly showing the lowest value (~-27 ‰) at the middle part of Unit 4 (Fig. 5). The clay mineral composition of this unit is characterized by high illite (64-88 %) and low smectite (0-14 %) and chlorite (8-15 %, except for 21 % in GC04) (Fig. 6). Unit 4 preserves a high number (>7 × 10^{-1}/g) of diatom valves consisting of diverse species (Fig. 7). The calibrated AMS 14C ages in Unit 4 are 4.6 ka at the middle part of GC01 and 20.6 ka and 7.7 ka at the bottom and middle parts of GC04 (Fig. 4).

Unit 4 is observed at the top of all gravity cores and consists of bioturbated mud or sandy mud with dispersed IRD (Figs. 2 and 3). The AMS 14C ages at the middle of Unit 4 in GC01 confirmed that the sediments were deposited during the Holocene, although the ages at the bottom were relatively old due to the inclusion of old carbon. While the sediments transported from the subglacial ice and Antarctic continent decreased dramatically, the biogenic materials originating from the surface water increased to deposit on the continental shelf under the seasonal open marine conditions after the retreat of the ice sheet and ice shelf on the continental shelf (e.g. Smith et al., 2011; Hillenbrand et al., 2014; Larter et al., 2014; O Cofaigh et al., 2014; McGlannan et al., 2017). The geochemical proxies of Unit 4 are characterized by the gradual increase in TOC, TN, and biogenic opal contents and a decrease in C/N ratios (Fig. 5). The CaCO3 contents of Unit 4 are mostly

very low. Generally, these geochemical proxies indicate that the biogenic productivity in the surface water increased after the onset of the seasonal open marine system in the continental shelf of the Ross Sea (Domack et al., 1999; Mosola and Anderson, 2006; Salvi et al., 2006; McGlannan et al., 2017; Prothro et al., 2018). The geochemical proxies of Unit 4 indicate that the biogenic productivity in the surface water increases under the seasonal open marine condition after the retreat of the ice shelf on the northern Drygalski Basin.

5. Discussion

5.1. Paleoenvironmental reconstruction of Unit 1 in the Drygalski Basin

Prothro et al. (2018) divided the types of the diamicton in the Ross Sea: subglacial diamicton as till on the topset of the grounding zone wedge, proglacial diamicton on the foreset of the grounding zone wedge, and proglacial diamicton near the grounding zone. The subglacial diamicton which is deposited under the advanced ice sheet is characterized by constantly high MS, low sand content, constant pebble abundance, and low WC (Anderson et al., 1980; Cunningham et al., 1999; Licht et al., 1999; Prothro et al., 2018; Smith et al., 2019). The proglacial diamicton deposited mostly by debris flow is characterized by a sandy silt matrix, constant pebble abundance, constantly high MS, and relatively low WC, whereas proglacial (or pelletized) diamicton near the grounding zone deposited by basal debris melt-out is characterized by the sandy silt matrix, variable MS and pebble abundance, and relatively high WC (Anderson et al., 1980; Cunningham et al., 1999; Licht et al., 1999; McKay et al., 2012; Prothro et al., 2018). The sediment properties (MS, granulometry, and WC) of Unit 1 in GC01 fluctuated, while those in GC04 and GC05 were mostly constant (Fig. 4). The sediment properties of Unit 1 in GC01 correspond to the diamicton deposited by the basal debris melt-out under the glaciomarine environment at the front of the grounding line during the retreating of the ice sheet. On the other hand, Unit 1 in GC04 and GC05 is the diamicton deposited by the debris flow proximal to the grounding line.

The poor relationship among geochemical proxies in Unit 1 confirms that in situ surface water productivity was not their main source (Fig. 8). Almost barren diatoms in Unit 1, except for the upper boundary (Fig. 7), also confirm that the biogenic fragments were recycled. These results are supported by previous studies reporting the absence of diatoms or the presence of reworked species in the glaciomarine diamicton on the Ross Sea continental shelf (Licht et al., 1996; McKay et al., 2008; Tolotti et al., 2013; McKay et al., 2016). The appearance of the reworked and sea ice taxa at the top of Unit 1 may suggest

the lift-off of the retreating ice sheet and the intrusion of seawater in the study area.

The CaCO3 content of the diamicton is generally low, except for the supply of old reworked foraminifera fragments (Cunningham et al., 1999; Melis and Salvi, 2009; Kilfeather et al., 2011). Melis and Salvi (2009) found out the reworked foraminifera fragments from the diamicton on the JOIDES Basin, where the diamicton consisted of the old inner shelf sediments eroded by the WAIS. On the other hand, the foraminifera are completely barren in the diamicton formed directly in the Drygalski Basin. The slightly high CaCO3 content (~2 %) of Unit 1 in GC05 is due to the reworked foraminifera from the inner shelf. The δ 13CSOM values of Unit 1 are almost constant (about -25 to -26 ‰) (Fig. 5). Ohkouchi and Eglinton (2006) reported that the δ13CSOM values of the terrestrial sediments from the Antarctic continent are -24 ‰ to -32 ‰. Because of the diamicton components, the δ 13CSOM values are mainly affected by the old organic matters transported by the ice sheet rather than the fresh organic matters generated in the surface water. In addition, the invariant δ13CSOM values of Unit 1 indicate that the sediment source of diamicton was not changed during deposition.

The smectite content of the shelf sediments in the Ross Sea is locally different up to 80 % at the McMurdo Sound (Ehrmann, 1998; Salvi et al., 2006; Franke and Ehrmann, 2010; Jung et al., 2021). The supply of smectite from the McMurdo Volcanic Group changed, depending on the advanced ice sheet and surface currents in the continental shelf (Brambati et al., 1997; Salvi et al., 2006; Ha et al., 2022). On the Pennell Trough, more smectites were supplied from the McMurdo Sound during the LGM (Salvi et al., 2006). The smectite content of Unit 1 is high (10-24 %) during the last glacial and deglacial period (Fig. 6). The smectite provenances are known as the Erebus volcanic province (>60 %) near the McMurdo Sound and the Melbourne volcanic province (~12
%) near Terra Nova Bay (Ehrmann et al., 2005; Jung et al., 2021). The advanced ice sheet from the Erebus volcanic province supplied smectiterich sediments to the Drygalski Basin whereas the ice sheet from the Melbourne volcanic province transported smectite-poor and illite-rich sediments to the northern part of Drygalski Ice Tongue. Thus, the smectite-rich sediments of Unit 1 were deposited during the retreat of the grounding line of the advanced ice sheet.

5.2. Paleoenvironmental reconstruction of Unit 2 in the Drygalski Basin

The grounded ice sheet retreated to the western and southern sides of the Drygalski Basin during the deglacial period (Greenwood et al., 2018; Rhee et al., 2020). Although the ice shelf and grounding line in the Drygalski Basin retreated continuously during about 11-8 ka to the Victoria Land coast, the retreat of the ice shelf is much slower

than that of the grounding line (Halberstadt et al., 2016; Prothro et al., 2020; Rhee et al., 2020). The northern basin of the DIT could be located under the ice shelf environment. The fine-grained sediments can be transported by meltwater plume from the grounding line farther by 250 km along the continental shelf under the ice shelf (Domack et al., 1999; Simkins et al., 2017; Smith et al., 2019). In addition, the current from the open marine area transported the open marine diatom and fine sediment to the sub-ice shelf (Domack and Harris, 1998). Domack et al. (1999) already reported that, during the retreat of the ice shelf on the Ross Sea, the structureless silty clay interval was deposited at the northern part of the Drygalski Basin. Based on our results, the massive and laminated mud layer of Unit 2 could be deposited until 8 ka by continuous or temporal supply of the fine-grained particles by the meltwater from the grounding line during the ice sheet retreat (e.g. Simkins et al., 2017; Smith et al., 2019).

The poor relationship among the geochemical proxies also indicates that the biogenic materials are not produced by the surface water productivity, similar to Unit 1 (Fig. 8). The increasing TOC and TN contents were attributed to more transport of fine-grained sediments containing biogenic materials by the currents from the ice-uncovered areas. In contrast, the decreasing C/N ratios are due to the decreasing meltwater plume from the grounding line. Cunningham et al. (1999) reported that the biogenic silica in the massive mud facies of the Drygalski Basin was a mixture of the transport from the grounding line and supply by in situ diatom production. Although the diatom valves appeared nearly barren, the sea ice diatom taxa were observed at the middle part of Unit 2 (Fig. 7). However, the biogenic opal content of Unit 2 is almost minimum (Fig. 5). It implies that the distance of GC04 from the grounding line and the seasonal open marine area might be too far to transport the reworked and in situ produced diatoms.

The CaCO3 content of Unit 2 is lower than that of Unit 1. The CaCO3 content consists mainly of the benthic or planktonic foraminifera in the continental shelf on the Ross Sea (Anderson et al., 1984; Capotondi et al., 2018). The intrusion of Circumpolar Deep Water (CDW) into the continental shelf could dissolve CaCO3 on the surface sediments (Anderson, 1975; Kim et al., 2020). The very low CaCO3 content of Unit 2 resulted from the limited carbonate production due to the subglacial ice shelf environment. Furthermore, CaCO3 might be dissolved by the modfified CDW from the outer continental shelf. The constant δ13CSOM values (about -25 ‰) of Unit 2 are higher than those of Unit 1 (Fig. 5). While the retreat of the grounding line ceased temporally in the Drygalski Basin, Unit 2 indicates that the sediment is delivered mainly by the meltwater plume under the ice shelf from the grounding line with the sediment transported by the currents from the seasonally open areas.

The clay mineral compositions of Unit 2 are similar to those of Unit 1, characterized by

relatively high smectite and low illite (Fig. 6). The relatively high smectite content is interpreted as the transport of eroded sediment from the McMurdo volcanic province located at the south of Drygalski Basin. The clay mineral composition of Unit 2 indicates that the sediments were still supplied by the meltwater plume from the grounding line at the southern side of the Drygalski Basin to the northern side under the subglacial ice shelf system.

5.3. Paleoenvironmental reconstruction of Unit 3 in the Drygalski Basin

Following the retreat of the ice shelf, the calving line retreated landward. The MS and WC of Unit 3 fluctuated with the coarse fraction (Fig. 4). McGlannan et al. (2017) reported the ice shelf breakup facies in the outer continental shelf of the Whales Deep Basin in the eastern Ross Sea. This sediment facies is characterized by the massive sandy silt to mud matrix with large IRD and variable MS and WC. The sediment properties of Unit 3 are similar to those of sediments deposited under the calving line. In addition, the alternation of the sandy mud and mud layer in Unit 3 might form by the temporal meltwater plume under the remaining local ice shelf near Terra Nova Bay. The sorting of transported sediments is controlled by the amount of meltwater discharge and the current velocity under the ice shelf (Kirshner et al., 2012; Simkins et al., 2017). Yokoyama et al. (2016) suggested the possibility of the remaining local ice shelf at the western coast of the Ross Sea, although the ice shelf had already retreated to the southern side of the Drygalski Basin. Hence, the sediments of Unit 3 were deposited by the meltwater plume beneath the local ice shelf from the grounding line with many IRD at the calving line.

The geochemical proxies characterized by the low biogenic productivity and high C/N ratio might reflect a little increase of the biogenic production in the surface water. However, the correlation among the geochemical proxies is relatively stronger than Unit 2 (Fig. 8). The better relationship reflects that more biogenic materials of in situ production in the surface water were deposited under the calving line.

Despite a slight increase in CaCO3 content of Unit 3, carbonate productivity by the planktonic or benthic foraminifera did not increase at the calving line due to the very low values (<0.1 %) (Fig. 5). The foraminifera community observed at the inner and outer sides of the calving line in the Ross Sea was controlled by the position of the calving line, multi-year sea ice, water mass, or katabatic wind (Pawlowski et al., 2005; Majewski et al., 2018). However, the skeleton of the dead foraminifera on the surface water could be easily dissolved by the corrosive water mass (Majewski and Anderson, 2009; Melis and Salvi, 2009; Majewski et al., 2016). The very low CaCO3 values of Unit 3 seem to be affected by the intrusion of the corrosive water mass, despite the presence of foraminifera community.

The δ13CSOM values of Unit 3 were also similar to those of Unit 2 (Fig. 5). Based on the results of the geochemical proxies of Unit 3, the increased biogenic particles by in situ production could change the δ13CSOM values. However, the sediments of Unit 3 were still affected strongly by the meltwater plume from the grounding line based on the sediment properties. The constant δ13CSOM values of Unit 3 compared to Unit 2 were affected by the meltwater plume more than the biogenic productivity under the calving line.

The appearance of diatom is not abundant, but diatom assemblage (Chaetoceros resting spore, F. kerguelensis, and F. curta) indicates a seasonal sea ice environment and biogenic productivity in the surface water during the Holocene (Fig. 7). Sjunneskog and Scherer (2005) reported that the diatom assemblage was a mixture of reworked and modern taxa at the calving line sediments in the central Ross Sea. The low diatom abundance and low diatom assemblage are a result of winnowing and transport by the current (Cunningham et al., 1999; Taylor et al., 2001; Sjunneskog and Scherer, 2005). The presence of modern diatom taxa suggests in situ biogenic productivity in the surface water, but the low diatom abundance might indicate low productivity in the surface water or poor preservation of the diatom frustule under the calving line.

The clay mineral composition of Unit 3 is characterized by relatively high smectite and low illite contents with an upward decreasing smectite toward Unit 4. Furthermore, kaolinite and chlorite contents are relatively high at several intervals. As explained, the main source of the smectite is restricted in the Ross Sea. The transport by the current, iceberg, wind, and meltwater in the continental shelf controlled the clay mineral compositions (Hillenbrand et al., 2003; Ehrmann et al., 2011). The decreasing smectite content indicates that the supply from the source area is limited by the weakening of erosion and/or transport. Lee et al. (2017) suggested the eastern and east-western ice flow from the southern Victoria Land to the southern part of the DIT during the deglacial period. This ice flow could block sediment transportation from the southern to the northern Drygalski Basin. The source area of kaolinite and chlorite is not clear, but its basement rock was distributed at the Transantarctic Mountains on Victoria Land (Cooper and Davey, 1985). The decreasing smectite and increasing kaolinite and chlorite indicate that the sediment supply declined from the southern Drygalski Basin and increased from the bedrock in the local coastal area.

5.4. Paleoenvironmental reconstruction of Unit 4 in the Drygalski Basin

The sediments of Unit 4 are characterized by the lower MS and higher WC due to the less coarse fractions, compared to Unit 1 diamicton (Fig. 4). The low MS intensity of the Holocene sediments is generally attributed to the lower number of IRD transported by

the ice-bergs or sea ice during the warm climate conditions (Hillenbrand et al., 2010; Weber et al., 2014; Shin et al., 2020; Ha et al., 2022). The coarse particles of the Holocene sediments on the continental shelf of the Ross Sea are generally transported by IRD or gravity flow or otherwise they were the remanent sediments winnowed by the strong bottom current (Anderson et al., 1984; Langone et al., 1998; Salvi et al., 2006; McKay et al., 2008). The northern side of the DIT has experienced seasonal open marine conditions since 8 ka, resulting in increased biogenic productivity in the surface water (Hall et al., 2004; McKay et al., 2008; Yokoyama et al., 2016; Prothro et al., 2020). Based on the results, Unit 4 reflects the seasonal open marine condition after the complete retreat of the ice shelf during the Holocene.

The biogenic materials from the surface water increase during the middle to late Holocene on the Ross Sea (Prothro et al., 2018; Tesi et al., 2020). The variation of the geochemical proxies of Unit 4 is similar to the result of previous studies reporting that biogenic materials by the surface productivity increased under the seasonal open marine condition and carbonate was dissolved by the corrosive water on the continental shelf. Additionally, the relationship among the geochemical proxies indicates that the biogenic materials in Unit 4 originated from in situ production in the surface water (Fig. 8).

The variation of δ13CSOM values, showing the upward decrease and increase with the lowest value at the middle part, is different from that of TOC and biogenic opal contents, showing a continuous increase without a peak in GC01 (Fig. 5). The decrease in δ 13CSOM values is generally affected by the terrestrial organic matter under the sub-ice sheet or ice shelf environment. However, more deposition of terrestrial organic matter is difficult after the complete retreat of the grounding line, and the δ13CSOM values are strongly influenced by the primary production under the seasonal open marine condition in the Ross Sea (Villinski et al., 2000; Tesi et al., 2020). The degree of the primary production is controlled by the duration of the open water, sea ice formation, diatom taxa and nutrient utilization, etc. (Fischer, 1991; Leventer et al., 1993; Cunningham et al., 1999; Arrigo et al., 2000, 2003; Smith Jr et al., 2014; Alderkamp et al., 2019). The diatom assemblage and sea ice formation at the western coast of the Ross Sea during the warmer middle Holocene were different from the modern condition (Mezgec et al., 2017; Jones et al., 2021; Hall et al., 2023). Tesi et al. (2020) reported that the relationship between the low δ13CSOM values and the long duration of the open marine environment was characterized by the dominant diatom species (Corethron pennatum) during the middle to late Holocene in the northwestern Ross Sea. The decrease in δ13CSOM values at the middle part of Unit 4 may be attributed to the different diatom species under the gradual increase of primary productivity during the warm Holocene, although other additional factors cannot be ruled out.

The diatom assemblage at the middle part of Unit 4 is also characteristic (Fig. 7). At the lower part of Unit 4, the reworking diatom (P. sulcata) is dominant, but C. criophilum accounts for up to 17 % with the highest at 129 cm in GC01. This open marine species indicating the spring melting season in the continental shelf is distributed widely in the Antarctic Ocean (Gersonde and Wefer, 1987; Leventer et al., 1993; Crawford, 1995). The absence of C. criophilum in GC04 might be due to poor preservation. At the upper part, F. curta, F. kereguelensis, T. antarctica, and E. antarctica var. recta, indicating the seasonal sea ice formation, are dominant. The deposition of Unit 4 reflects the seasonal open marine environmental conditions after the complete retreat of the ice shelf during the Holocene. Mezgec et al. (2017) reported that the diatom species during the middle Holocene (5.8-3.6 ka) at the Victoria Land coast was different, characterizing the early sea ice retreat and a long ice-free season. During the middle Holocene, the warm climate leads to the bloom of C. criophilum and the appearance of open marine species F. obliquecostata (Fig. 7). During the late Holocene, the neoglacial climate cooling maintains the long duration of sea ice characterized by dominant sea ice species in the northern Drygalski Basin. Fischer (1991) reported the different relationship between the low δ13CSOM values and dominant C. criophilum and between high δ13CSOM values and dominant Thalassiosira spp. around the Antarctic continental margin. The diatom assemblage and δ13CSOM values in Unit 4 were related to the climate change during the middle to late Holocene.

The clay mineral composition of Unit 4 is characterized by relatively lower smectite and higher illite contents (Fig. 6). Under the seasonal open marine system, the clay mineral composition of the fine-grained sediments on the continental shelf is controlled by the current rather than ice flow (Hillenbrand et al., 2003, 2009). Salvi et al. (2006) reported the significant decrease of smectite content during the late Holocene which was caused by a decline in the glacial transport of sediment from the inner shelf. The decreasing smectite content in Unit 4 is caused by the reduction of the eroded and transported sediments from the McMurdo Sound by the glacial ice. The other clay minerals are still supplied from the basement rocks on Victoria Land underneath the glacier to the Drygalski Basin. Although the smectite could be supplied from the Melbourne Volcanic province near Terra Nova Bay, its content was not comparable to that from the McMurdo Sound province (Franke and Ehrmann, 2010; Jung et al., 2021). The clay mineral composition of Unit 4 indicates that the sediment supply from the southern side of the Drygalski Basin decreased while that from the local source area was continuous to the northern Drygalski Basin.

5.5. Paleoenvironmental evolution in the Drygalski Basin since the Last Glacial Maximum

Although AMS 14C ages could not provide the exact timing on the retreat of the

ice sheet and ice shelf presumably due to the incorporation of old carbons, the variation of sediment deposition suggests the successive change of the glaciomarine depositional environment in the northern Drygalski Basin of the Ross Sea.

The subglacial circumstance at the northern part of the DIT maintained until at least 11 ka and the grounding line retreated southward between 11 and 10 ka (Licht and Andrews, 2002; Halberstadt et al., 2016). Unit 1 is characterized by unsorted granulometry, high MS, low WC, high smectite content, low δ13CSOM values, and less biogenic materials with almost barren diatom and reworked diatom taxa. The depositional process of Unit 1 in the Drygalski Basin was strongly affected by the advanced ice sheet from the western and southern sides of the Drygalski Basin under the proximal to the grounding line condition (Fig. 9a).

The grounding line in the Drygalski Basin retreated to the present DIT position at about 8 ka and the ice shelf covering its northern part was pinned to stop retreating by the Crary Bank and the Terra Nova Bay (Halberstadt et al., 2016; Greenwood et al., 2018; Prothro et al., 2020; Rhee et al., 2020). Unit 2 consists exclusively of the massive mud characterized by relatively low MS, a slight increase of biogenic materials, slightly high δ 13CSOM values, a decrease of C/N ratio, high smectite content, and a barren diatom with the appearance of sea ice taxa. The sediments of Unit 2 were supplied continuously by the meltwater plume during the sub-ice shelf condition from the near local ice shelf to the northern part of the DIT (Fig. 9b). In addition, the sediments from the seasonally open marine areas were transported to deposit by the currents under the ice shelf. On the other hand, the debris flow proximal to the grounding line could not influence the study area.

After the retreat of the grounding line ceased at the DIT, the calving line retreated continuously toward the DIT and the small bay at the Victoria Land coast. Unit 3 is characterized by the alternating sandy mud and mud with many coarse fractions and fluctuating MS and WC. The geochemical proxies and δ13CSOM values are similar to those of Unit 2. The breakup of the ice shelf supplies a large amount of IRD and the meltwater plume from the grounding line transports the mud or sandy mud to the northern Drygalski Basin. In addition, the seasonal open marine condition developed by the breakup of the ice shelf and the biogenic materials were deposited at the north side of DIT (Fig. 9c). Although biogenic production in the surface water began around the calving line, the influence of the meltwater plume from the nearby grounding line was stronger at the northern part of the DIT.

The northern Drygalski Basin retained the seasonal open marine condition after the complete retreat of the ice shelf (Yokoyama et al., 2016; Prothro et al., 2020; Rhee et al., 2020). Unit 4 consists of the bioturbated sediment facies, which is characterized by relatively low MS, C/N ratio and smectite content, a distinct increase of biogenic materials,

and an upward decrease and increase of δ13CSOM values with abundant diatoms and diverse diatom taxa. The biogenic components of the Holocene sediments increased by the enhanced biogenic productivity in the surface water, while the sediments transported by the ice and meltwater decreased dramatically (Fig. 9d). The variation of sea ice duration by the climate change during the middle Holocene strongly affected the diatom assemblage and δ 13CSOM values. In addition, the detrital fine-grained sediments were delivered mainly from near the Victoria Land coast.

6. Conclusions

Gravity and box core sediments were analyzed in terms of the sediment and geochemical properties, carbon isotopic values of sediment organic matter, clay mineral compositions of fine-grained sediments, and diatom assemblage along with AMS 14C dating of bulk sediments. These results determine the paleoenvironmental change and depositional evolution in the glaciomarine sediments related to the retreat of the ice sheet and ice shelf in the northern Drygalski Basin since the LGM. The relatively old AMS 14C ages of the bulk sediments are generally due to the incorporation of old and reworked carbons on the continental shelf, as dated by 3.7 and 4.1 ka at the core-top sediments. Nevertheless, AMS 14C ages distinguished pre-Holocene, early to middle Holocene, and late Holocene sediments. Based on the analytical results, the sediments were classified into seven sediment facies (clast-rich muddy or sandy diamicton, massive or laminated or bioturbated mud, and massive or bioturbated sandy mud), which were used to delineate four lithologic units on the basis of depositional evolution since the LGM.

KOPRI 극지연구소

마지막 최대 빙하기 이후 로스해 서쪽 드라이갈스키 분지의 빙해양 퇴적물을 이용한 고환경 복원

Sangbeom Ha[a,b,*], Jae Il Lee[b], Young-Suk Bak[c], Kyu-Cheul Yoo[a], Boo-Keun Khim[a,d*]

[a]Department of Oceanography, Pusan National University, Busan 46241, Republic of Korea
[b]Division of Glacial Environment Research, Korea Polar Research Institute, Incheon 21990, Republic of Korea
[c]Earth Environmental System Research Center, Jeonbuk National University, Jeonju 54896, Republic of Korea
[d]Marine Research Institute, Pusan National University, Busan 46241, Republic of Korea

요약: 로스해에서는 빙상의 반복적인 성장과 쇠퇴가 대륙붕 환경의 현저한 변화를 지배해 왔다. 특히 빙하해성 대륙붕 퇴적작용은 최종빙기최대기(LGM) 이후 빙상 역학과 빙붕 발달과 밀접하게 연관되어 있다. 본 연구에서는 로스해 서부의 드라이갈스키 북부 분지에서 획득한 4개의 중력 코어(및 박스 코어)를 이용하여, 퇴적물 물성, 지화학적 지시자, 유기물의 탄소 동위원소 값, 세립질 퇴적물의 점토광물 조성, 규조류 군집 등 다중 지시자를 분석하였으며, 벌크 유기물에 대한 AMS 14C 연대측정을 수행하였다. 코어 기술, X-선 영상 관찰, 그리고 입도 분포 분석 결과를 바탕으로, 코어 퇴적물은 쇄설물이 풍부한 이질성 이질암, 쇄설물이 풍부한 사질 이질암, 괴상 이질, 층리질 이질, 생물교란된 이질, 괴상 사질 이질, 그리고 생물교란된 사질 이질의 7개 퇴적상으로 구분되었다. 이러한 퇴적상의 조합은 퇴적 진화에 따른 4개의 암상 단위를 규정한다. 암상 단위 1은 접지선에 인접한 환경에서 퇴적된 이질암을 나타낸다. LGM 이후 빙상과 빙붕이 후퇴함에 따라, 분급되지 않은 퇴적물 덩어리가 접지선 인근에 퇴적되었다. 암상 단위 2는 빙붕 하부 환경에서 퇴적된 괴상 이질로 구성된다. 빙상이 후퇴하는 동안, 세립질 입자들은 용융수 플룸에 의해 빙붕 하부 바닥으로 운반되었으며, 생물기원 물질 또한 계절적 개방 해양 영역에서 해류를 통해 빙붕 하부로 이동되었다. 암상 단위 3은 풍부한 드롭스톤을 포함하는 사질 이질과 이질로 이루어져 있으며, 이는 분리선(calving line) 부근에서 퇴적된 것으로 해석된다. 분리선이 드라이갈스키 분지를 통과하면서 빙붕 붕괴로 인해 다량의 조립질 성분이 퇴적되었다. 분리선이 드라이갈스키 빙설설의 북측을 지날 때, 빅토리아 랜드 연안에서 유래한 육상 기원 퇴적물이 잔존한 국지 빙상의 접지선으로부터 운반되었다. 암상 단위 4는 계절적 개방 해양 조건하에서 퇴적된 생물교란된 이질과 사질 이질로 구성된다. 후기 홀로세 동안 생물 생산성은 현저히 증가한 반면, 계절적 개방 해양 조건하에서 육상 기원 퇴적물의 공급은 감소하였다. 규조류 군집과 퇴적물 유기물의 δ13C 값은 중기 홀로세의 온난한 기후와 해빙 증가를 지시한다. LGM 이후 드라이갈스키 북부 분지에서의 고환경 변화와 빙하해성 퇴적 진화는 홀로세 동안의 기후 변화뿐만 아니라 빙상 역학과 빙붕 활동과도 밀접하게 연관되어 있었다.

References

Alderkamp, A.C., van Dijken, G.L., Lowry, K.E., Lewis, K.M., Joy-Warren, H.L., van de Poll, W., Laan, P., Gerringa, L., Delmont, T.O., Jenkins, B.D., Arrigo, K.R., 2019. Effects of iron and light availability on phytoplankton photosynthetic properties in the Ross Sea. Marine Ecology Progress Series 621, 33-50.

Anderson, J.B., 1975. Factors controlling CaCO3 dissolution in the Weddell Sea from foraminiferal distribution patterns. Marine Geology 19, 315-332.

Anderson, J.B., 1999. Antarctic Marine Geology. Cambridge University Press, p. 289.

Anderson, J.B., Kurtz, D.D., Domack, E.W., Balshaw, K.M., 1980. Glacial and glacial marine sediments of the Antarctic continental shelf. The Journal of Geology 88, 399-414.

Anderson, J.B., Brake, C.F., Myers, N.C., 1984. Sedimentation on the Ross Sea continental shelf, Antarctica. Marine Geology 57, 295-333.

Anderson, J.B., Shipp, S.S., Bartek, L.R., Reid, D.E., 1992. Evidence for a grounded ice sheet on the Ross Sea continental shelf during the late Pleistocene and preliminary paleodrainage reconstruction. In: Elliot, D.H. (Ed.), Contributions to Antarctic Research III. vol. 57. American Geophysical Union, pp. 39-62.

Anderson, J.B., Conway, H., Bart, P.J., Witus, A.E., Greenwood, S.L., McKay, R.M., Hall, B.L., Ackert, R.B., Licht, K., Jakobsson, M., Stone, J.O., 2014. Ross Sea paleo-ice sheet drainage and deglacial history during and since the LGM. Quaternary Science Reviews 100, 31-54.

Andrews, J.T., Domack, E.W., Cunningham, W.L., Leventer, A., Licht, K.J., Jull, A.T., DeMaster, D.J., Jennings, A.E., 1999. Problems and possible solutions concerning radiocarbon dating of surface marine sediments, Ross Sea, Antarctica. Quaternary Research 52, 206-216.

Armand, L.K., Crosta, X., Romero, O., Pichon, J.J., 2005. The biogeography of major diatom taxa in Southern Ocean sediments: 1. Sea ice related species. Palaeogeography, Palaeoclimatology, Palaeoecology 223, 93-126.

Arrigo, K.R., DiTullio, G.R., Dunbar, R.B., Robinson, D.H., VanWoert, M., Worthen, D.L., Lizotte, M.P., 2000. Phytoplankton taxonomic variability in nutrient utilization and primary production in the Ross Sea. Journal of Geophysical Research, Oceans 105, 8827-8846.

Arrigo, K.R., Robinson, D.H., Dunbar, R.B., Leventer, A.R., Lizotte, M.P., 2003. Physical control of chlorophyll a, POC, and TPN distributions in the pack ice of the Ross Sea, Antarctica. Journal of Geophysical Research, Oceans 108, 3316.

Bart, P.J., Anderson, J.B., Trincardi, F., Shipp, S.S., 2000. Seismic data from the Northern basin, Ross Sea, record extreme expansions of the East Antarctic Ice Sheet during the late Neogene. Marine Geology 166, 31-50.

Bart, P.J., DeCesare, M., Rosenheim, B.E., Majewski, W., McGlannan, A., 2018. A centurieslong delay between a paleo-ice-shelf collapse and grounding-line retreat in the Whales

KOPRI 극지연구소

Deep Basin, eastern Ross Sea, Antarctica. Scientific Reports 8, 12392.

Berg, S., Leng, M.J., Kendrick, C.P., Cremer, H., Wagner, B., 2013. Bulk sediment and diatom silica carbon isotope composition from coastal marine sediments off East Antarctica. Silicon 5, 19-34.

Biscaye, P.E., 1965. Mineralogy and sedimentation of recent deep-sea clay in the Atlantic Ocean and adjacent seas and oceans. Geological Society of America Bulletin 76, 803-832. Brambati, A., Fanzutti, G.P., Finocchiaro, F., Melis, R., Frignani, M., Ravaioli, M., Setti, M., 1997. Paleoenvironmental record in Core Anta91-30 (Drygalski Basin, Ross Sea, Antarctica). Geology and Seismic Stratigraphy of the Antarctic Margin 2 (71), 137-151.

Brown, G.T., Brindley, G.W., 1980. X-ray diffraction procedures for clay mineral identification. In: Brindley, G.W., Brown, G. (Eds.), Crystal Structure of Clay Minerals and Their X-ray Identification. Mineralogical Society of London, pp. 305-359.

Capotondi, L., Bergami, C., Giglio, F., Langone, L., Ravaioli, M., 2018. Benthic foraminifera distribution in the Ross Sea (Antarctica) and its relationship to oceanography. Bollettino della Societa Paleontologica Italiana 57, 187-202.

Christ, A.J., Bierman, P.R., 2020. The local last glacial maximum in McMurdo Sound, Antarctica: implications for ice-sheet behavior in the ross sea embayment. Geological Society of America Bulletin 132, 31-47.

Conway, H., Hall, B.L., Denton, G.H., Gades, A.M., Waddington, E.D., 1999. Past and future grounding-line retreat of the West Antarctic Ice Sheet. Science 286, 280-283.

Cooper, A.K., Davey, F.J., 1985. Marine geological and geophysical investigations in the Ross Sea, Antarctica. Antarctic Journal of the United States 19, 80-82.

Crawford, R.M., 1995. The role of sex in the sedimentation of a marine diatom bloom. Limnology and Oceanography 40, 200-204.

Crosta, X., Sturm, A., Armand, L., Pichon, J.J., 2004. Late Quaternary sea ice history in the Indian sector of the Southern Ocean as recorded by diatom assemblages. Marine Micropaleontology 50, 209-223.

Crosta, X., Crespin, J., Billy, I., Ther, O., 2005. Major factors controlling Holocene δ13Corg changes in a seasonal sea-ice environment, Adelie Land, East Antarctica. Global Biogeochemical Cycles 19, GB4029.

Cunningham, W.L., Leventer, A., 1998. Diatom assemblages in surface sediments of the Ross Sea: relationship to present oceanographic conditions. Antarctic Science 10, 134-146.

Cunningham, W.L., Leventer, A., Andrews, J.T., Jennings, A.E., Licht, K.J., 1999. Late Pleistocene-Holocene marine conditions in the Ross Sea, Antarctica: evidence from the diatom record. The Holocene 9, 129-139.

DeMaster, D.J., 1981. The supply and accumulation of silica in the marine environment. Geochimica et Cosmochimica Acta 45, 1715-1732.

Domack, E.W., Harris, P.T., 1998. A new depositional model for ice shelves, based upon sediment cores from the Ross Sea and the Mac. Robertson shelf, Antarctica. Annals

KOPRI 극지연구소

of Glaciology 27, 281-284.

Domack, E.W., O'Brien, P., Harris, P., Taylor, F., Quilty, P.G., De Santis, L., Raker, B., 1998. Late Quaternary sediment facies in Prydz Bay, East Antarctica and their relationship to glacial advance onto the continental shelf. Antarctic Science 10, 236-246.

Domack, E.W., Jacobson, E.A., Shipp, S., Anderson, J.B., 1999. Late Pleistocene-Holocene retreat of the West Antarctic Ice-Sheet system in the Ross Sea: part 2-sedimentologic and stratigraphic signature. Geological Society of America Bulletin 111, 1517-1536.

Dunbar, R.B., Leventer, A.R., Mucciarone, D.A., 1998. Water column sediment fluxes in the Ross Sea, Antarctica: atmospheric and sea ice forcing. Journal of Geophysical Research, Oceans 103, 30741-30759.

Ehrmann, W., 1998. Implications of late Eocene to early Miocene clay mineral assemblages in McMurdo Sound (Ross Sea, Antarctica) on paleoclimate and ice dynamics. Palaeogeography, Palaeoclimatology, Palaeoecology 139, 213-231.

Ehrmann, W., Setti, M., Marinoni, L., 2005. Clay minerals in Cenozoic sediments off Cape Roberts (McMurdo Sound, Antarctica) reveal palaeoclimatic history. Palaeogeography, Palaeoclimatology, Palaeoecology 229, 187-211.

Ehrmann, W., Hillenbrand, C.D., Smith, J.A., Graham, A.G., Kuhn, G., Larter, R.D., 2011. Provenance changes between recent and glacial-time sediments in the Amundsen Sea embayment, West Antarctica: clay mineral assemblage evidence. Antarctic Science 23, 471-486.

Fischer, G., 1991. Stable carbon isotope ratios of plankton carbon and sinking organic matter from the Atlantic sector of the Southern Ocean. Marine Chemistry 35, 581-596.

Folk, R.L., Ward, W.C., 1957. Brazos River bar [Texas]: a study in the significance of grain size parameters. Journal of Sedimentary Research 27, 3-26.

Franke, D., Ehrmann, W., 2010. Neogene clay mineral assemblages in the AND-2A drill core (McMurdo Sound, Antarctica) and their implications for environmental change. Palaeogeography, Palaeoclimatology, Palaeoecology 286, 55-65.

Frezzotti, M., Tabacco, I.E., Zirizzotti, A., 2000. Ice discharge of eastern Dome C drainage area, Antarctica, determined from airborne radar survey and satellite image analysis. Journal of Glaciology 46, 253-264.

Frignani, M., Giglio, F., Langone, L., Ravaioli, M., Mangini, A., 1998. Late PleistoceneHolocene sedimentary fluxes of organic carbon and biogenic silica in the northwestern Ross Sea, Antarctica. Annals of Glaciology 27, 697-703.

Gersonde, R., Wefer, G., 1987. Sedimentation of biogenic siliceous particles in Antarctic waters from the Atlantic sector. Marine Micropaleontology 11, 311-332.

Gilbert, I.M., Pudsey, C.J., Murray, J.W., 1998. A sediment record of cyclic bottom-current variability from the northwest Weddell Sea. Sedimentary Geology 115, 185-214.

Giorgetti, G., Talarico, F., Sandroni, S., Zeoli, A., 2009. Provenance of Pleistocene sediments in the ANDRILL AND-1B drillcore: clay and heavy mineral data. Global and Planetary Change 69, 94-102.

Giovinetto, M.B., Bentley, C.R., 1985. Surface balance in ice drainage of Antarctica, Antarct. JUS 20, 6-13.

Goehring, B.M., Balco, G., Todd, C., Moening-Swanson, I., Nichols, K., 2019. Late-glacial grounding line retreat in the northern Ross Sea, Antarctica. Geology 47, 291-294.

Greenwood, S.L., Simkins, L.M., Halberstadt, A.R.W., Prothro, L.O., Anderson, J.B., 2018. Holocene reconfiguration and readvance of the East Antarctic Ice Sheet. Nature Communications 9, 3176.

Grobe, H., Mackensen, A., 1992. Late Quaternary climatic cycles as recorded in sediments from the Antarctic continental margin. In: Kennett, J.P., Warnke, D.A. (Eds.), The Antarctic Paleoenvironment: A Perspective on Global Change. American Geophysical Union, pp. 349-376.

Ha, S., Colizza, E., Torricella, F., Langone, L., Giglio, F., Kuhn, G., Macri, P., Khim, B.K., 2022. Glaciomarine sediment deposition on the continental slope and rise of the central Ross Sea since the Last Glacial Maximum. Marine Geology 445, 106752.

Halberstadt, A.R.W., Simkins, L.M., Greenwood, S.L., Anderson, J.B., 2016. Past ice-sheet behaviour: retreat scenarios and changing controls in the Ross Sea, Antarctica. The Cryosphere 103, 1003-1020.

Hall, B.L., Baroni, C., Denton, G.H., 2004. Holocene relative sea-level history of the Southern Victoria Land Coast, Antarctica. Global and Planetary Change 42, 241-263.

Hall, B.L., Henderson, G.M., Baroni, C., Kellogg, T.B., 2010. Constant Holocene Southern-Ocean 14C reservoir ages and ice-shelf flow rates. Earth and Planetary Science Letters 296, 115-123.

Hall, B.L., Koch, P.L., Baroni, C., Salvatore, M.C., Hoelzel, A.R., de Bruyn, M., Welch, A.J., 2023. Widespread southern elephant seal occupation of the Victoria land coast implies a warmer-than-present Ross Sea in the mid-to-late Holocene. Quaternary Science Reviews 303, 107991.

Heaton, T.J., Kohler, P., Butzin, M., Bard, E., Reimer, R.W., Austin, W.E., Ramsey, C.B., Grootes, P.M., Hughen, K.A., Kromer, B., Reimer, P.J., Adkins, J., Burke, A., Cook, M.S., Olsen, J., Skinner, L.C., 2020. Marine20-the marine radiocarbon age calibration curve (0-55,000 cal BP). Radiocarbon 62, 779-820.

Henley, S.F., Annett, A.L., Ganeshram, R.S., Carson, D.S., Weston, K., Crosta, X., Tait, A., Dougans, J., Fallick, A.E., Clarke, A., 2012. Factors influencing the stable carbon isotopic composition of suspended and sinking organic matter in the coastal Antarctic sea ice environment. Biogeosciences 9, 1137-1157.

Hillenbrand, C.D., Grobe, H., Diekmann, B., Kuhn, G., Futterer, D.K., 2003. Distribution of clay minerals and proxies for productivity in surface sediments of the Bellingshausen and Amundsen seas (West Antarctica)-relation to modern environmental conditions. Marine Geology 193, 253-271.

Hillenbrand, C.D., Kuhn, G., Frederichs, T., 2009. Record of a Mid-Pleistocene depositional anomaly in West Antarctic continental margin sediments: an indicator for ice-sheet

KOPRI 극지연구소

collapse? Quaternary Science Reviews 28, 1147-1159.

Hillenbrand, C.D., Smith, J.A., Kuhn, G., Esper, O., Gersonde, R., Larter, R.D., Maher, B., Moreton, S.G., Shimmield, T.M., Korte, M., 2010. Age assignment of a diatomaceous ooze deposited in the western Amundsen Sea Embayment after the Last Glacial Maximum. Journal of Quaternary Science 25, 280-295.

Hillenbrand, C.D., Bentley, M.J., Stolldorf, T.D., Hein, A.S., Kuhn, G., Graham, A.G., Fogwill, C.J., Kristofferson, Y., Smith, J.A., Anderson, J.B., Larter, R.D., Melles, M., Hodgson, D.A., Mulvanet, R., Sugden, D.E., 2014. Reconstruction of changes in the Weddell Sea sector of the Antarctic Ice Sheet since the Last Glacial Maximum. Quaternary Science Reviews 100, 111-136.

Jones, R.S., Whitmore, R.J., Mackintosh, A.N., Norton, K.P., Eaves, S.R., Stutz, J., Christl, M., 2021. Regional-scale abrupt Mid-Holocene ice sheet thinning in the western Ross Sea, Antarctica. Geology 49, 278-282.

Jung, J., Ko, Y., Lee, J., Yang, K., Park, Y.K., Kim, S., Moon, H., Kim, H.J., Yoo, K.C., 2021. Multibeam bathymetry and distribution of clay minerals on surface sediments of a small bay in Terra Nova Bay, Antarctica. Minerals 11, 72.

Kilfeather, A.A., O Cofaigh, C., Lloyd, J.M., Dowdeswell, J.A., Xu, S., Moreton, S.G., 2011. Icestream retreat and ice-shelf history in Marguerite Trough, Antarctic Peninsula: sedimentological and foraminiferal signatures. Geological Society of America Bulletin 123, 997-1015.

Kim, S., Lee, J.I., McKay, R.M., Yoo, K.C., Bak, Y.S., Lee, M.K., Roh, Y.H., Yoon, H.I., Moon, H., Hyun, C.U., 2020. Late pleistocene paleoceanographic changes in the Ross Seaglacial-interglacial variations in paleoproductivity, nutrient utilization, and deepwater formation. Quaternary Science Reviews 239, 106356.

Kirshner, A.E., Anderson, J.B., Jakobsson, M., O'Regan, M., Majewski, W., Nitsche, F.O., 2012. Post-LGM deglaciation in Pine island Bay, west Antarctica. Quaternary Science Reviews 38, 11-26.

Kyle, P.R., 1990. A. McMurdo volcanic group western Ross embayment. Volcanoes of the Antarctic Plate and Southern Oceans 48, 18-145.

Langone, L., Frignani, M., Labbrozzi, L., Ravaioli, M., 1998. Present-day biosiliceous sedimentation in the northwestern Ross Sea, Antarctica. Journal of Marine Systems 17, 459-470.

Larter, R.D., Anderson, J.B., Graham, A.G., Gohl, K., Hillenbrand, C.D., Jakobsson, M., Johnson, J.S., Kuhn, G., Nitsche, F.O., Smith, J.A., Witus, A.E., Bentley, M.J., Dowdeswell, J.A., Ehrmann, W., Klages, J.P., Lindow, J., O Cofaigh, C., Spiegel, C., 2014. Reconstruction of changes in the Amundsen Sea and Bellingshausen sea sector of the West Antarctic ice sheet since the last glacial maximum. Quaternary Science Reviews 100, 55-86.

Lee, J.I., McKay, R.M., Golledge, N.R., Yoon, H.I., Yoo, K.C., Kim, H.J., Hong, J.K., 2017. Wide spread persistence of expanded East Antarctic glaciers in the southwest Ross Sea during the last deglaciation. Geology 45, 403-406.

Leventer, A., Dunbar, R.B., DeMaster, D.J., 1993. Diatom evidence for late Holocene climatic events in Granite Harbor, Antarctica. Paleoceanography 8, 373-386.

Licht, K.J., Andrews, J.T., 2002. The 14C record of Late Pleistocene ice advance and retreat in the central Ross Sea, Antarctica. Arctic, Antarctic, and Alpine Research 34, 324-333.

Licht, K.J., Jennings, A.E., Andrews, J.T., Williams, K.M., 1996. Chronology of late Wisconsin ice retreat from the western Ross Sea, Antarctica. Geology 24, 223-226.

Licht, K.J., Dunbar, N.W., Andrews, J.T., Jennings, A.E., 1999. Distinguishing subglacial till and glacial marine diamictons in the western Ross Sea, Antarctica: implications for a last glacial maximum grounding line. Geological Society of America Bulletin 111, 91-103.

Lowry, D.P., Golledge, N.R., Bertler, N.A., Jones, R.S., McKay, R., 2019. Deglacial groundingline retreat in the Ross Embayment, Antarctica, controlled by ocean and atmosphere forcing. Science Advances 58, eaav8754.

Majewski, W., Anderson, J.B., 2009. Holocene foraminiferal assemblages from Firth of Tay, Antarctic Peninsula: paleoclimate implications. Marine Micropaleontology 73, 135-147.

Majewski, W., Wellner, J.S., Anderson, J.B., 2016. Environmental connotations of benthic foraminiferal assemblages from coastal West Antarctica. Marine Micropaleontology 124, 1-15.

Majewski, W., Bart, P.J., McGlannan, A.J., 2018. Foraminiferal assemblages from iceproximal paleo-settings in the Whales Deep Basin, eastern Ross Sea, Antarctica. Palaeogeography, Palaeoclimatology, Palaeoecology 493, 64-81.

Majewski, W., Prothro, L.O., Simkins, L.M., Demianiuk, E.J., Anderson, J.B., 2020. Foraminiferal patterns in deglacial sediment in the western Ross Sea, Antarctica: life near grounding lines. Paleoceanography and Paleoclimatology 35, e2019PA003716.

McGlannan, A.J., Bart, P.J., Chow, J.M., DeCesare, M., 2017. On the influence of post-LGM ice shelf loss and grounding zone sedimentation on West Antarctic ice sheet stability. Marine Geology 392, 151-169.

McKay, R.M., Dunbar, G.B., Naish, T.R., Barrett, P.J., Carter, L., Harper, M., 2008. Retreat history of the Ross Ice Sheet (Shelf) since the Last Glacial Maximum from deep-basin sediment cores around Ross Island. Palaeogeography, Palaeoclimatology, Palaeoecology 260, 245-261.

McKay, R., Naish, T., Powell, R., Barrett, P., Scherer, R., Talarico, F., Kyle, P., Monien, D., Kuhn, G., Jackolski, C., Williams, T., 2012. Pleistocene variability of Antarctic ice sheet extent in the Ross embayment. Quaternary Science Reviews 34, 93-112.

McKay, R., Golledge, N.R., Maas, S., Naish, T., Levy, R., Dunbar, G., Kuhn, G., 2016. Antarctic marine ice-sheet retreat in the Ross Sea during the early Holocene. Geology 44, 7-10.

Melis, R., Salvi, G., 2009. Late Quaternary foraminiferal assemblages from western Ross Sea (Antarctica) in relation to the main glacial and marine lithofacies. Marine Micropaleontology 70, 39-53.

Mezgec, K., Stenni, B., Crosta, X., Masson-Delmotte, V., Baroni, C., Braida, M., Ciardini, V., Colizza, E., Melis, R., Salvatore, M.C., Severi, M., Scarchilli, C., Traversi, R., Udisti,

KOPRI 극지연구소

R., Frezzotti, M., 2017. Holocene sea ice variability driven by wind and polynya efficiency in the Ross Sea. Nature Communications 8, 1334.

Moore, D.M., Reynolds Jr., R.C., 1989. X-ray Diffraction and the Identification and Analysis of Clay Minerals. Oxford University Press.

Mortlock, R.A., Froelich, P.N., 1989. A simple method for the rapid determination of biogenic opal in pelagic marine sediments. Deep Sea Research Part A 36, 1415-1426.

Mosola, A.B., Anderson, J.B., 2006. Expansion and rapid retreat of the West Antarctic Ice Sheet in eastern Ross Sea: possible consequence of over-extended ice streams? Quaternary Science Reviews 25, 2177-2196.

O Cofaigh, C., Davies, B.J., Livingstone, S.J., Smith, J.A., Johnson, J.S., Hocking, E.P., Hodgson, D.A., Anderson, J.B., Bentley, M.J., Canals, M., Comack, E., Dowdeswell, J.A., Evnas, J., Glasse, N.F., Hillenbrand, C.D., Larter, R.D., Roberts, S.J., Simms, A.R., 2014. Reconstruction of ice-sheet changes in the Antarctic Peninsula since the Last Glacial Maximum. Quaternary Science Reviews 100, 87-110.

Ohkouchi, N., Eglinton, T.I., 2006. Radiocarbon constraint on relict organic carbon contributions to Ross Sea sediments. Geochemistry, Geophysics, Geosystems 7, Q04012.

Orsi, A.H., Wiederwohl, C.L., 2009. A recount of Ross Sea waters. Deep Sea Research, Part II 56, 778-795.

Pawlowski, J., Fahrni, J.F., Guiard, J., Conlan, K., Hardecker, J., Habura, A., Bowser, S.S., 2005. Allogromiid foraminifera and gromiids from under the Ross Ice Shelf: morphological and molecular diversity. Polar Biology 28, 514-522.

Prothro, L.O., Simkins, L.M., Majewski, W., Anderson, J.B., 2018. Glacial retreat patterns and processes determined from integrated sedimentology and geomorphology records. Marine Geology 395, 104-119.

Prothro, L.O., Majewski, W., Yokoyama, Y., Simkins, L.M., Anderson, J.B., Yamane, M., Miyairi, Y., Ohkouchi, N., 2020. Timing and pathways of east Antarctic ice sheet retreat. Quaternary Science Reviews 230, 106166.

Pudsey, C.J., Murray, J.W., Appleby, P., Evans, J., 2006. Ice shelf history from petrographic and foraminiferal evidence, Northeast Antarctic Peninsula. Quaternary Science Reviews 25, 2357-2379.

Rau, G.H., Sweeney, R.E., Kaplan, I.R., 1982. Plankton 13C:12C ratio changes with latitude: differences between northern and southern oceans. Deep Sea Research Part A 29, 1035-1039.

Rhee, H.H., Lee, M.K., Seong, Y.B., Lee, J.I., Yoo, K.C., Yu, B.Y., 2020. Post-LGM dynamic deglaciation along the Victoria Land coast, Antarctica. Quaternary Science Reviews 247, 106595.

Salvi, C., Salvi, G., Stenni, B., Brambati, A., 2004. Palaeoproductivity in the Ross Sea, Antarctica, during the last 15 kyr BP and its link with ice-core temperature proxies. Annals of Glaciology 39, 445-451.

KOPRI 극지연구소

Salvi, C., Busetti, M., Marinoni, L., Brambati, A., 2006. Late Quaternary glacial marine to marine sedimentation in the Pennell Trough (Ross Sea, Antarctica). Palaeogeography, Palaeoclimatology, Palaeoecology 231, 199-214.

Scherer, R.P., 1994. Other silt-sized sedimentary particles. Journal of Paleolimnology 12, 171-179.

Shin, J.Y., Kim, S., Zhao, X., Yoo, K.C., Yu, Y., Lee, J.I., Lee, M.K., Yoon, H.I., 2020. Particle-size dependent magnetic properties of Scotia Sea sediments since the Last Glacial Maximum: glacial ice-sheet discharge controlling magnetic proxies. Palaeogeography, Palaeoclimatology, Palaeoecology 557, 109906.

Shipp, S., Anderson, J.B., Domack, E.W., 1999. Late Pleistocene-Holocene retreat of the West Antarctic Ice-Sheet system in the Ross Sea: part 1-geophysical results. Geological Society of America Bulletin 111, 1486-1516.

Simkins, L.M., Anderson, J.B., Greenwood, S.L., Gonnermann, H.M., Prothro, L.O., Halberstadt, A.R.W., Strarns, L.A., Pollard, D., DeConto, R.M., 2017. Anatomy of a meltwater drainage system beneath the ancestral East Antarctic ice sheet. Nature Geoscience 10, 691-697.

Sjunneskog, C., Scherer, R.P., 2005. Mixed diatom assemblages in glacigenic sediment from the central Ross Sea, Antarctica. Palaeogeography, Palaeoclimatology, Palaeoecology 218, 287-300.

Smellie, J.L., Hole, M.J., 1998. Products and processes in Pliocene-Recent, sub-aqueous to emergent volcanism in the Antarctic Peninsula: examples of englacial Surtseyan volcano construction. Bulletin of Volcanology 58, 628-646.

Smith Jr., W.O., Ainley, D.G., Arrigo, K.R., Dinniman, M.S., 2014. The oceanography and ecology of the Ross Sea. Annual Review of Marine Science 6, 469-487.

Smith, J.A., Hillenbrand, C.D., Kuhn, G., Larter, R.D., Graham, A.G., Ehrmann, W., Moreton, S.G., Forwick, M., 2011. Deglacial history of the West Antarctic Ice Sheet in the western Amundsen Sea embayment. Quaternary Science Reviews 30, 488-505.

Smith, J.A., Andersen, T.J., Shortt, M., Gaffney, A.M., Truffer, M., Stanton, T.P., Binschadler, R., Dutrieux, P., Jenkins, A., Hillenbrand, C.D., Ehrmann, W., Corr, H.F.J., Farley, N., Crowhurst, S., Vaughan, D.G., 2017. Sub-ice-shelf sediments record history of twentieth-century retreat of Pine Island Glacier. Nature 541, 77-80.

Smith, J.A., Graham, A.G., Post, A.L., Hillenbrand, C.D., Bart, P.J., Powell, R.D., 2019. The marine geological imprint of Antarctic ice shelves. Nature Communications 101, 5635.

Stokke, P.R., Carson, B., 1973. Variation in clay mineral X-ray diffraction results with the quantity of sample mounted. Journal of Sedimentary Research 43, 957-964.

Stuiver, M., Reimer, P.J., Reimer, R.W., 2021. CALIB 8.2. CALIB Radiocarbon Calibration. URL: http://calib.org/calib/calib.html.

Taylor, F., Whitehead, J., Domack, E., 2001. Holocene paleoclimate change in the Antarctic Peninsula: evidence from the diatom, sedimentary and geochemical record. Marine Micropaleontology 41, 25-43.

KOPRI 극지연구소

Tesi, T., Belt, S.T., Gariboldi, K., Muschitiello, F., Smik, L., Finocchiaro, F., Giglio, F., Colizza, E., Gazzurra, G., Giordano, P., Morigi, C., Capotondi, L., Nogarotto, A., Koseoglu, D., Di Roberto, A., Gallerani, A., Langone, L., 2020. Resolving sea ice dynamics in the north-western Ross Sea during the last 2.6 ka: from seasonal to millennial timescales. Quaternary Science Reviews 237, 106299.

Tolotti, R., Salvi, C., Salvi, G., Bonci, M.C., 2013. Late Quaternary climate variability as recorded by micropalaeontological diatom data and geochemical data in the western Ross Sea, Antarctica. Antarctic Science 25, 804-820.

Villinski, J.C., Dunbar, R.B., Mucciarone, D.A., 2000. Carbon 13/carbon 12 ratios of sedimentary organic matter from the Ross Sea, Antarctica: a record of phytoplankton bloom dynamics. Journal of Geophysical Research, Oceans 105, 14163-14172.

Weber, M.E., Clark, P.U., Kuhn, G., Timmermann, A., Sprenk, D., Gladstone, R., Zhang, X., Lohmann, G., Menviel, L., Chikamoto, M.O., Friedrich, T., Ohlwein, C., 2014. Millennial-scale variability in Antarctic ice-sheet discharge during the last deglaciation. Nature 510, 134-138.

Yokoyama, Y., Anderson, J.B., Yamane, M., Simkins, L.M., Miyairi, Y., Yamazaki, T., Koizumi, M., Suga, H., Kusahara, K., Prothro, L.O., Hasumi, H., Southon, J.R., Ohkouchi, N., 2016. Widespread collapse of the Ross Ice Shelf during the late Holocene. Proceedings of the National Academy of Sciences 1139, 2354-2359.

KOPRI
극지연구소

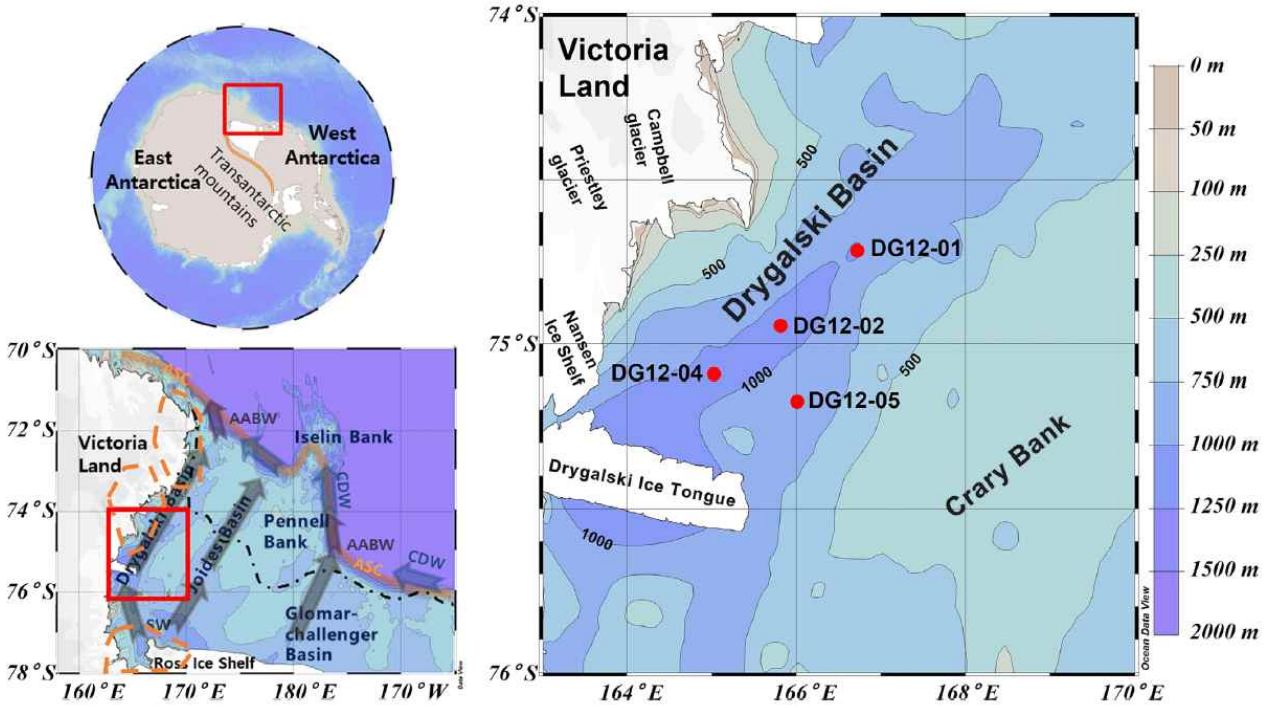


Figure #. Study area (red rectangle in the Antarctic continent and the western Ross Sea) showing the Drygalski Basin. Coring sites (DG12-01, DG12-02, DG12-04, and DG12-05) were located in the northern Drygalski Basin. The orange dotted line marks the source area of smectite (the Hallett, Melbourne, and Erebus volcanic provinces from north to south). CDW: Circumpolar Deep Water, ASC: Antarctic Slope Current, AABW: Antarctic bottom water, SW: shelf water (Orsi and Wiederwohl, 2009).

KOPRI 극지연구소

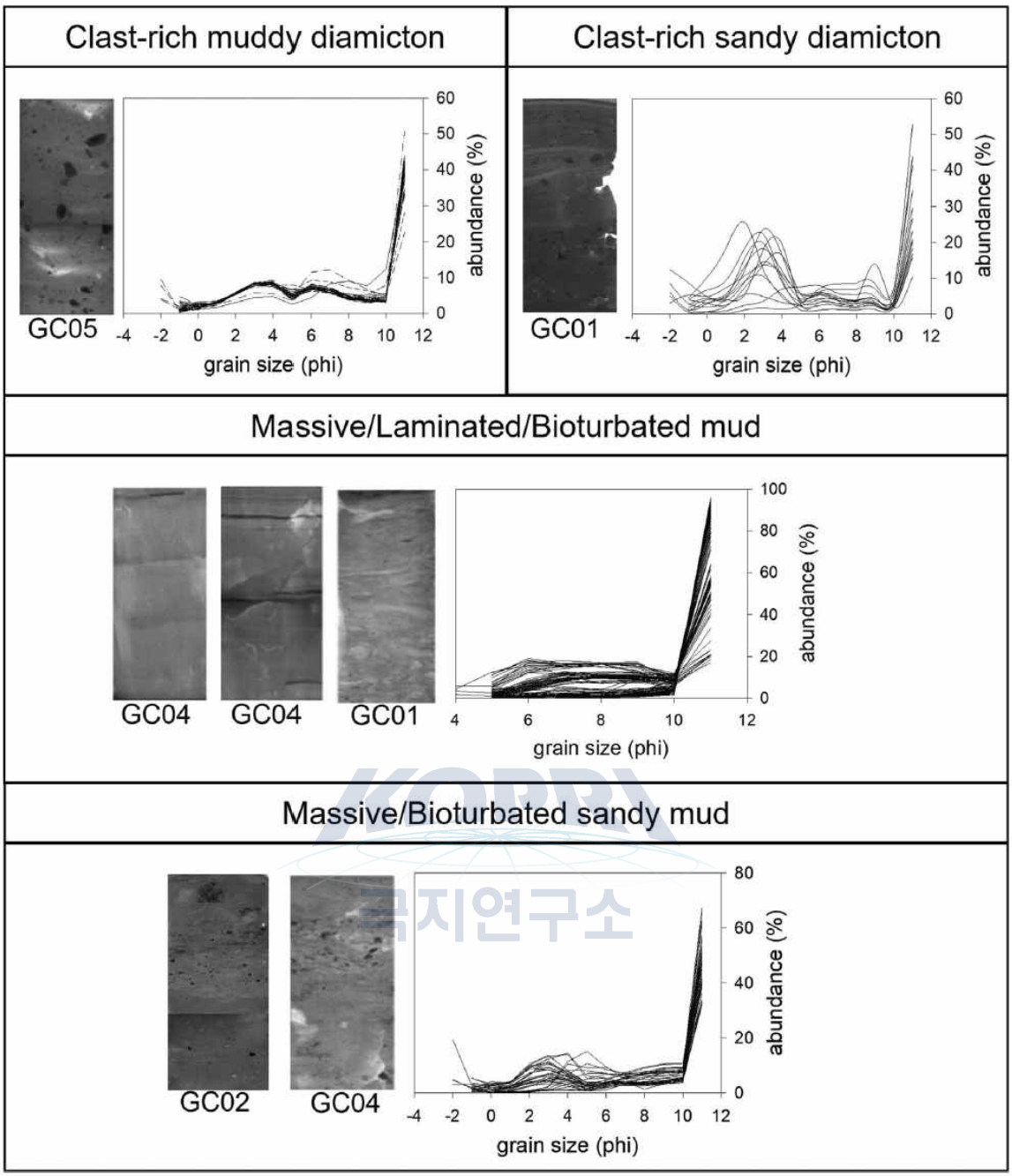


Figure #. Classification of seven sediment facies based on the X-ray photographs and grain size distribution of four gravity cores (DG12-GC01, DG12-GC02, DG12-GC04, and DG12-GC05).

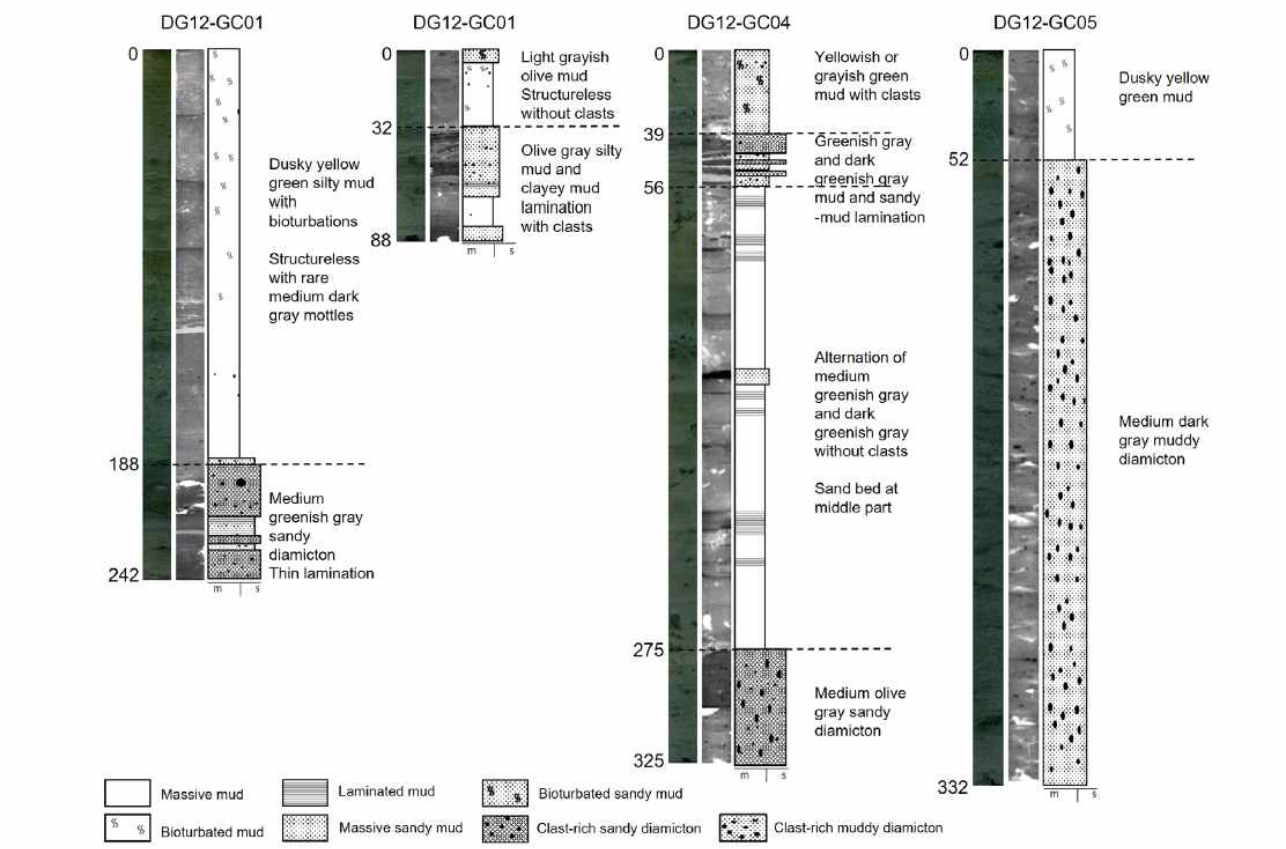


Figure #. Core descriptions with photograph, X-ray radiograph, and sediment facies of four gravity cores (DG12-GC01, DG12-GC02, DG12-GC04, and DG12-GC05).

KOPRI
극지연구소

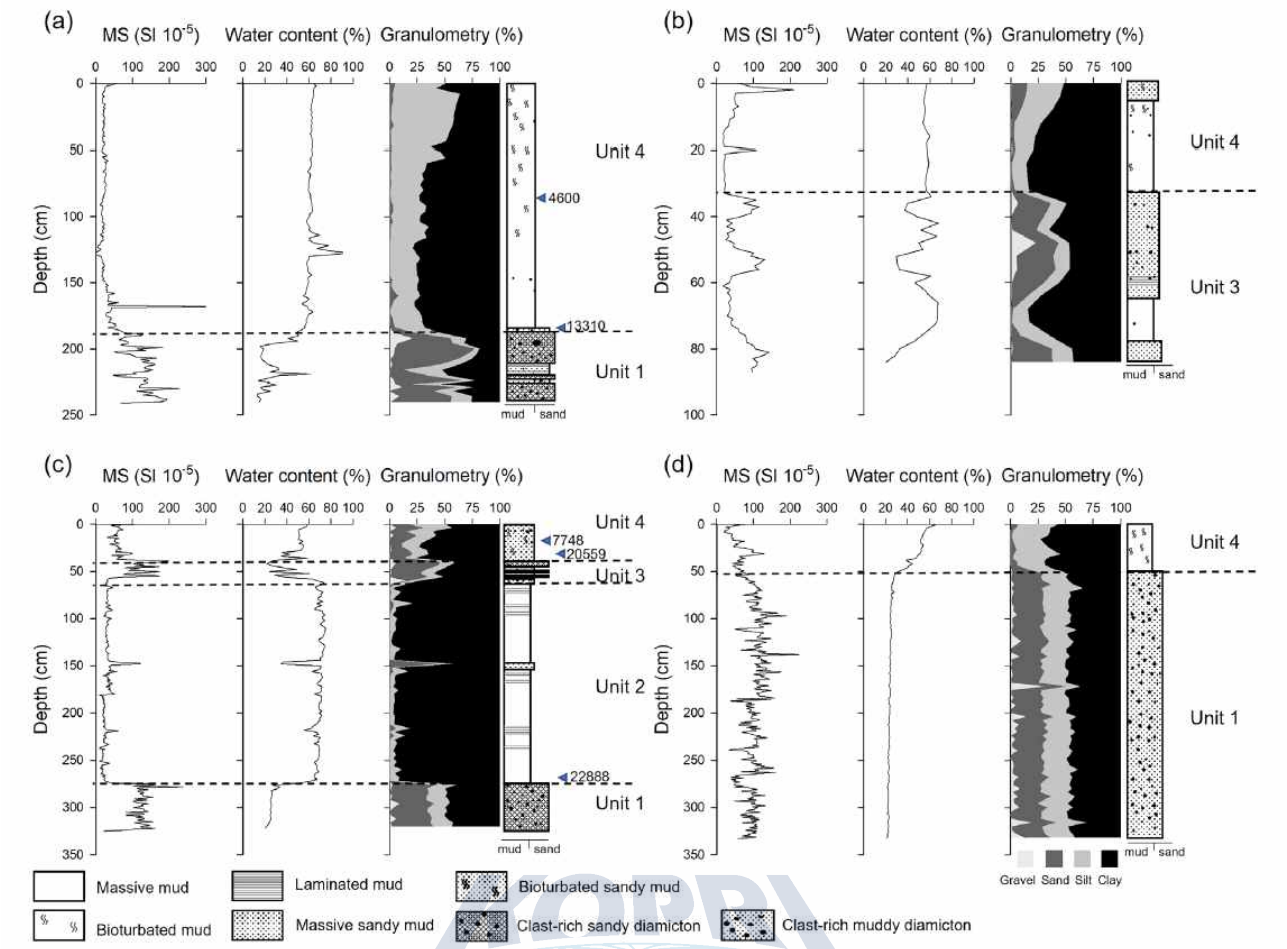


Figure #. Downcore variation of sediment properties (magnetic susceptibility (MS), water content, and granulometry) with sediment facies. (a) GC01, (b) GC02, (c) GC04, and (d) GC05. Lithologic units (1, 2, 3, and 4) are divided by the dotted lines and calibrated ages are shown.

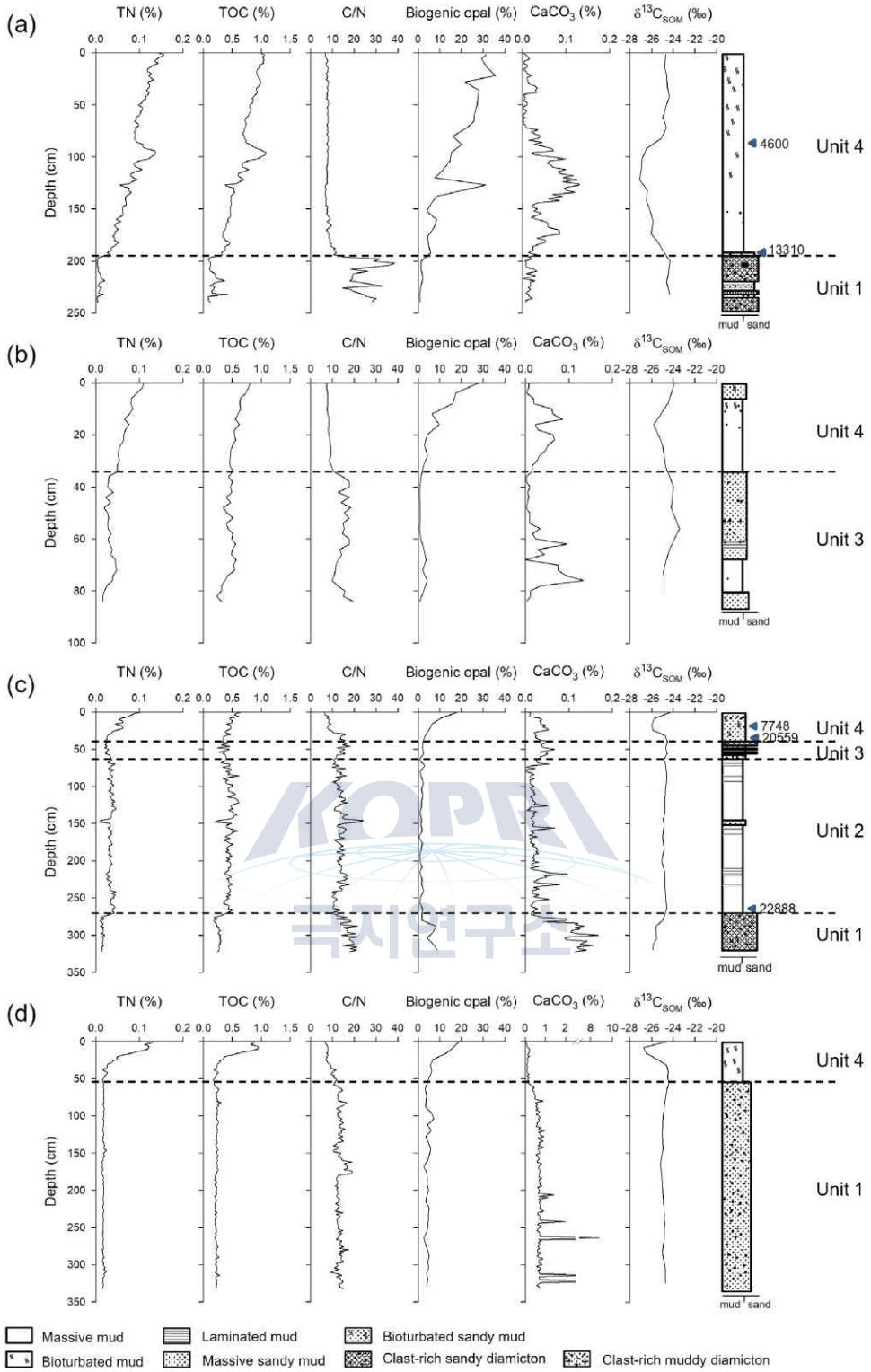


Figure #. Downcore variation of geochemical proxies (total nitrogen (TN), total organic carbon (TOC), TOC/TN (C/N), biogenic opal, and CaCO3) and δ13C values of sediment organic matter with the columnar section of sediment facies. (a) GC01, (b) GC02, (c) GC04, and (d) GC05. Lithologic units (1, 2, 3, and 4) are divided by the dotted lines, and calibrated ages are shown

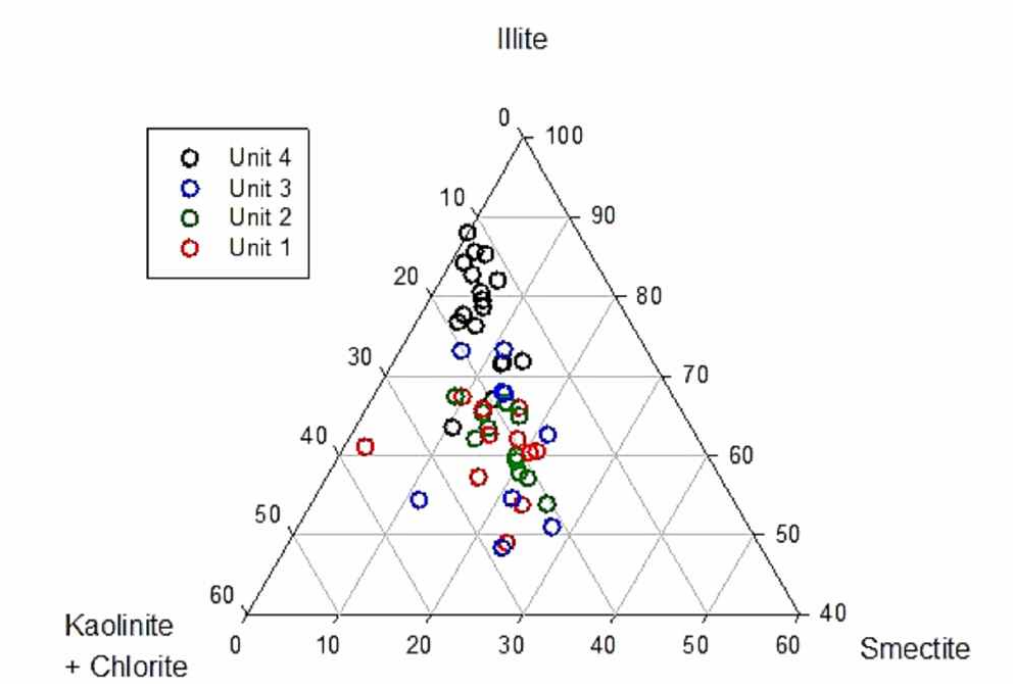


Figure #. Ternary diagram of fine-grained clay mineral compositions of the lithologic unit at cores GC01 and GC04.

KOPRI
극지연구소

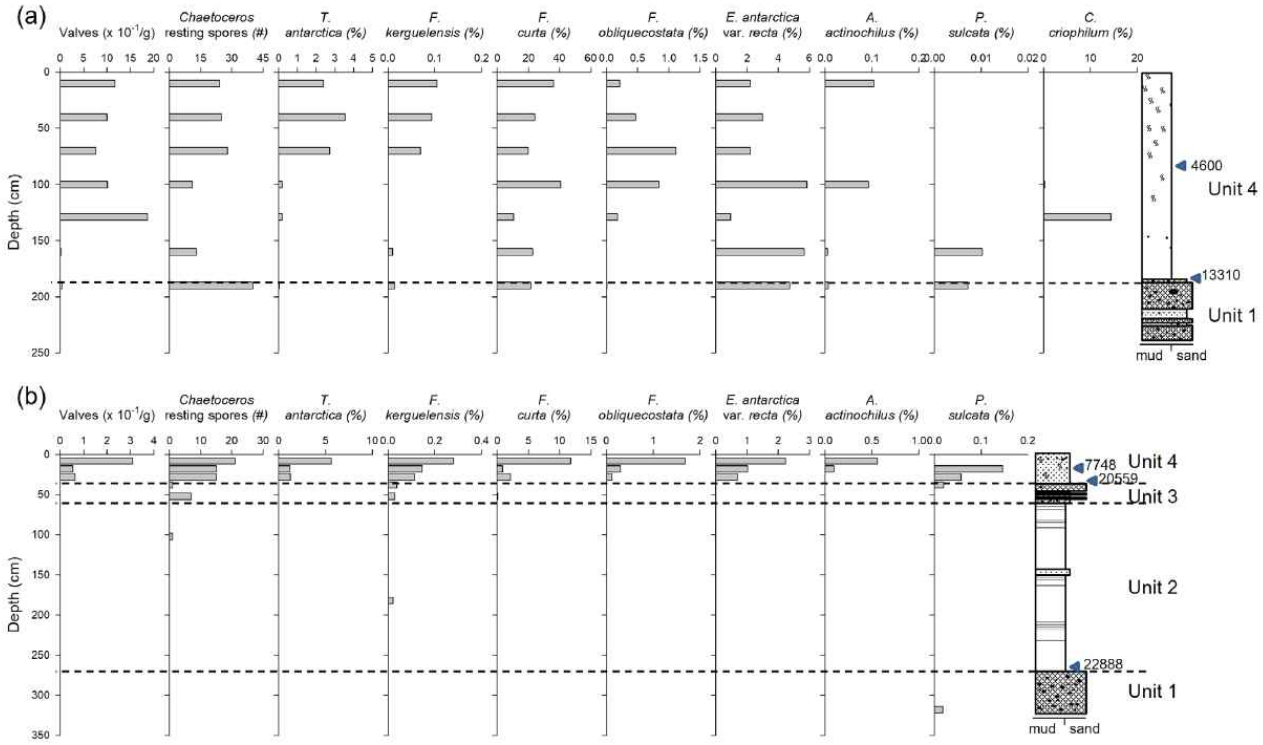


Figure #. Downcore variation of diatom assemblage with the columnar section of sediment facies. (a) GC01, (b) GC04. Lithologic units (1, 2, 3, and 4) are divided by the dotted lines, and calibrated ages are shown.

KOPRI
극지연구소

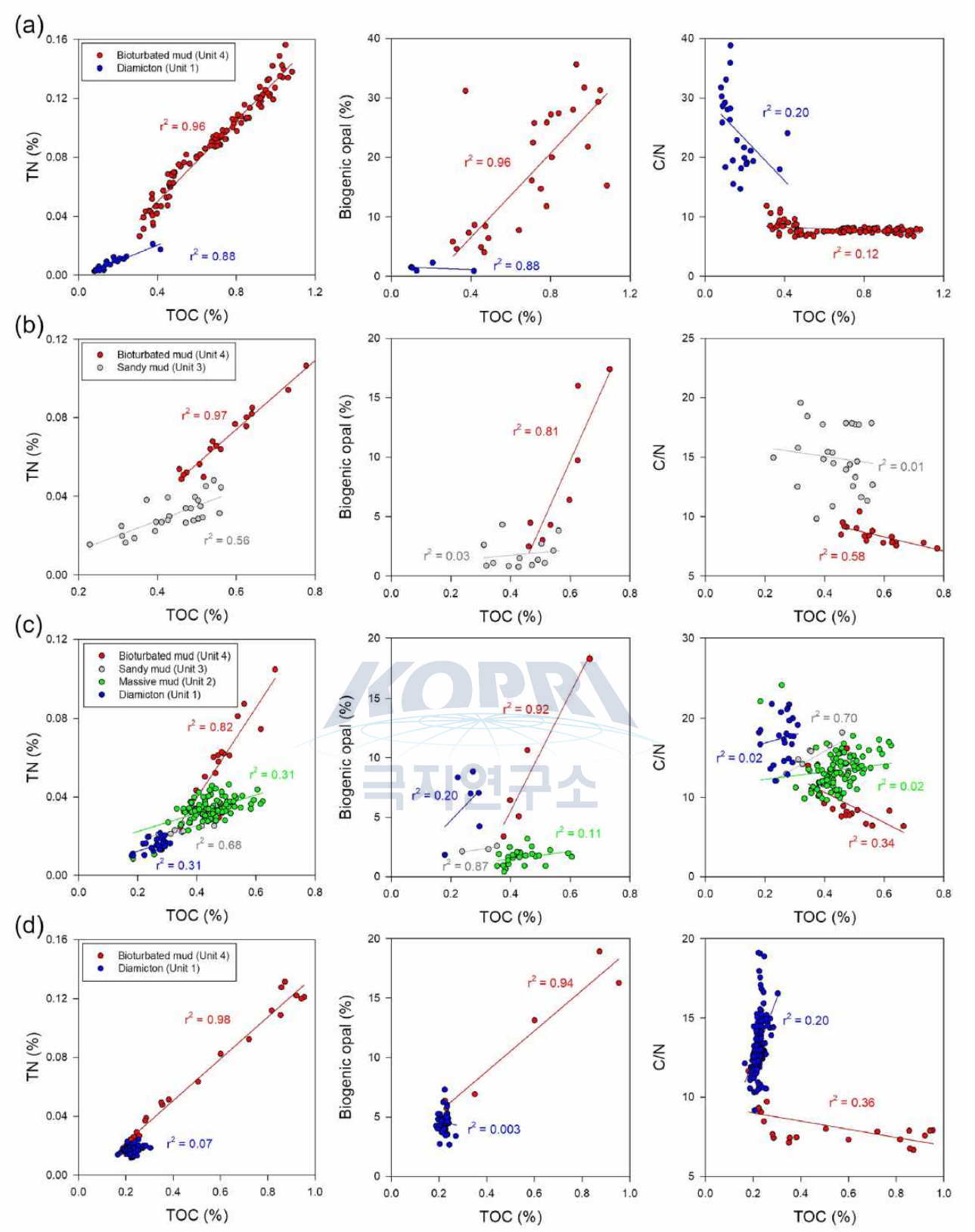


Figure #. Correlation between TOC and TN, between TOC and biogenic opal, and between TOC and C/N ratio of the lithologic unit. (a) GC01, (b) GC02, (c) GC04, and (d) GC05.

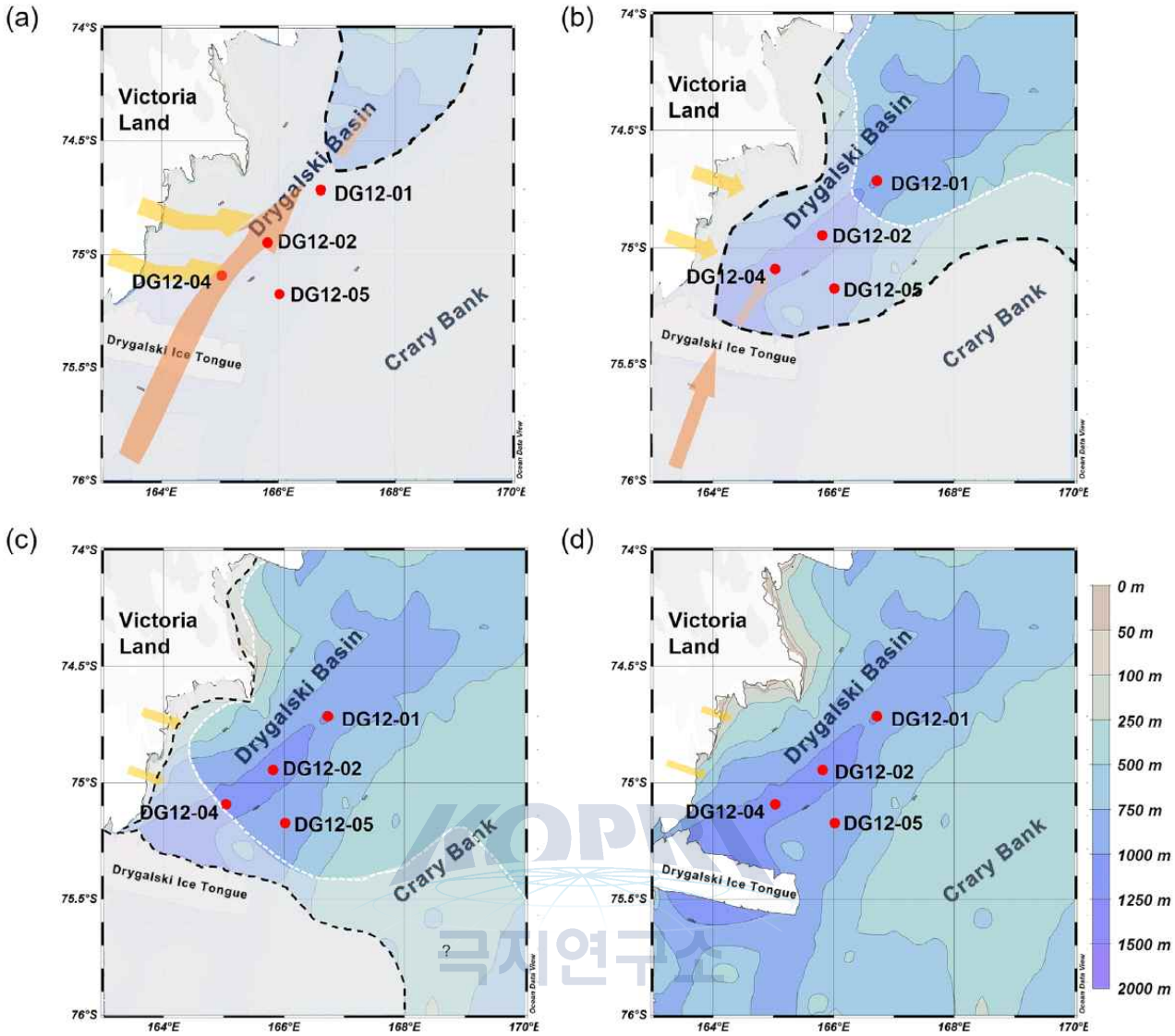


Figure #. Schematic model showing the evolution of northern Drygalski Basin characterized by the sediment transport during the retreat of the ice sheet and ice shelf. The dotted black line and white line represent the grounding line and calving line, respectively. Orange and yellow arrows represent the sediment transport from the southern Drygalski Basin and the Victoria Land coast, respectively. The retreat of the grounding and calving lines was modified from Rhee et al. (2020) and Prothro et al. (2020).

KOPRI 극지연구소

제 17 장

서부 로스해 북 드라이갈스키 트러프의 마지막최대빙하기 빙상 범위[10)]

이재일

한국해양과학기술원 부설 극지연구소

1. 서론

남극 빙상 (Antarctic Ice Sheet, AIS)의 시간적 범위 변화 연구는 빙상 모델 및 해수면 변화에 대한 AIS의 기여도를 평가하고, 서남극의 수심이 깊은 대륙붕에서 해양 기반 빙상 불안정성의 임계 조건을 이해하는 데 매우 중요하다. 마지막최대빙하기 (Last Glacial Maximum, LGM) 동안 해양 기반 빙상은 로스해 지역에 널리 분포하고 있었다 (Anderson et al., 2014). 동부 로스해에서는 빙상 접지선이 대륙붕 경계까지 발달하고 있었었으나, 서부 로스해에서는 그만큼 전진하지 않았다 (Halberstadt et al., 2016).

서부 로스해에서 LGM 시기 동안의 빙상 접지선은 콜먼 섬 Grounding Zone Wedge (GZW)로 알려진, 콜먼 섬 북쪽에 발달하는 GZW의 경계까지 발달했던 것으로 추정되어 왔다 (Shipp et al., 1999; GZW B in Figs. 1 & 2). 한편, GZW B 남쪽 코어에서 산출된 생물기원 탄산염의 방사성탄소 연대 (25 - 30 14C kyr BP)에 따르면 LGM 빙상 범위는 이보다 좁았을 것으로 볼 수 있다 (Licht et al., 1996; Df87-32 and Df80-177 in Fig. 1a). 그러나 탄소 연대는 오래된 탄산염이 재퇴적되었을 가능성이 있고 콜먼 섬 남쪽에는 뚜렷한 접지 지형이 부족하기 때문에, 일반적으로는 GZW B가 LGM 시기의 최대 범위를 지시하는 것으로로 간주되어 왔다 (Shipp et al., 1999; Mosola and Anderson, 2006; Halberstadt et al., 2016).

이 연구에서는 서부 로스해 Northern Drygalski Trough (NDT)에서 해양 지질 및 지구물리 자료를 이용하여 지난 약 4만 년 동안의 빙하 전진 및 후퇴 시기를 규명하고자 한다. 이 지역은 마지막 해빙기 동안 AIS가 상당한 질량을 상실했던 지역으로서 (Anderson et al., 2014), LGM 전후 및 LGM 동안 해양 기반 빙상의 경계부가 환경 변화에 어떻게 반응했는지를 복원할 수 있다는 데 중요성이 있다.

2. 연구 자료 및 방법

10) 이 연구 결과는 2026년 2월 학술지 Quaternary Science Reviews에 투고되었음.

가. Sub-bottom profile 자료

음향 Sub-bottom profile (SBP) 자료는 쇄빙선 Araon의 2013_JBG-NZ (2014), ANA05B (2015), ANA09B (2019), ANA09C (2019), ANA10C (2020) 항해에서 획득하였다. 2014 - 2019년 항해에서는 Kongsberg SBP120 시스템을, 2020년 항해에서는 SBP27 시스템을 사용하였다. 주파수 및 해상도는 SBP120은 2.5 - 7 kHz와 0.3 ms이며, SBP27은 2 - 9 kHz와 0.2 ms이다. 자료 처리와 시각화에는 Kongsberg 소프트웨어 KM SBP v1.4.8을 사용하였다.

나. 방사성탄소 연대측정

산불용성 유기물(AIO)과 생물 기원의 탄산염 성분에 대하여 Beta Analytic에서 AMS 방사성탄소 연대를 측정하였다(Table 1). 방사성탄소 연대는 CALIB 8.2 프로그램 (http://calib.org/calib/calib.html) 과 MARINE20 보정 곡선을 이용하여 보정하였다 (Heaton et al., 2020; Stuiver et al., 2021). 지역적 방사성탄소 보정값 ΔR은 622 ± 172년을 사용하였으며, 이 값은 서부 로스해의 12개 ΔR 자료의 가중 평균으로부터 산정되었다 (Stuiver et al., 1981; Mabin, 1985; Whitehouse et al., 1988; Hall et al., 2010) .

로스해의 ΔR은 지난 6,000년 동안 비교적 안정적이었으나 (Hall et al., 2010), 빙기 동안에는 극지역에서 지역적으로 방사성 탄소의 고갈 발생했을 가능성이 있다 (Heaton et al., 2023a, 2023b). 따라서 11.5 ka보다 오래된 시료에 대해서는 최대 고갈 시나리오와 최소 고갈 시나리오를 각각 적용하여 보정하였다 (Table 1). Table 1의 연령 범위는 두 시나리오에서 도출된 보정 연령의 전체 범위를 지시한다.

AIO 시료의 방사성탄소 연대는 보정 전에 지역 오염 보정값 (local contamination offset, LCO)을 적용하였다 (Hillenbrand et al., 2010). LCO는 퇴적물 내에 있는 오래된 유기물로부터 기인하며, 이 연구에서는 박스 코어 최상부 연대에로부터 산정하여 전체적으로 1172년을 차감하였다. 과거 LCO 변화에 대한 정보가 부족한 상황에서 코어 전체에서 LCO 값이 일정하다고 가정하였으나, 실제로는 퇴적 환경에 따라 변동하였을 가능성이 높다.

다. 퇴적물 코어 채취 및 코어 분석

중력 코어 RS19-GC04 (73° 57.4102′ S, 170° 34.0365′ E, 수심 648 m, 코어길이 454 cm) 와 RS19-GC05B(73° 14.2519′ S, 170° 58.6333′ E, 수심 518 m, 코어길이 273 cm) 는 2019년 ANA09B 항해 중 NDT에서 채취되었다. 박스 코어 RS19-BC04는 GC04와, 박스코어 RS19-BC05는 GC05B와 동일 위치에서 채취하였다. 중력 코어 RS23-GC02 (73° 59.9733′ S, 170° 30.0722′ E, 수심 641 m, 코어길이 324 cm)는 2023년 ANA13C 항해에서 채취되었다.

Be 동위원소를 제외한 대부분의 고환경 분석은 한국극지연구소(KOPRI)에서 수행되었다. 1 cm 두께의 퇴적 슬랩에 대해 Softrex M-100W X-선 촬영을 수행하고 NTB EZ-320 디지털 스캐

너로 이미지를 획득하여 iX-Pect EZ 소프트웨어를 이용하여 X-선 이미지를 획득하였다. 대자율(MS)은 Bartington MS-2B 기기를 사용하여 1 cm 간격으로 측정하였다. 입자 밀도는 AccuPyc II 1340 가스 피크노미터를 이용하여 4 cm 간격으로 측정하였다. 함수율은 퇴적물 채취 시의 중량과 건조 중량 차이를 이용하여 1 cm 간격으로 계산하였다. 입도 분석은 유기물을 제거한 실트 및 점토에 대해 Sedigraph III 5120을 사용하여 4 cm 간격으로 실시하였다. 모래 및 자갈 크기 입자는 체질 후 1 파이 간격으로 무게를 측정하였다. 탄산칼슘 함량은 총무기탄소(TIC)에 8.333을 곱해 계산하는데, TIC는 2 cm 간격으로 CO_2 Coulometer CM5240을 이용해 측정하였다. 코어 절단면에서 ITRAX XRF 코어 스캐너를 이용해 Mo X-ray 튜브, 1-mm 스텝 간격, 노출시간 5초, 30 kV, 30mA 조건으로 Ca 계수를 측정하였다. 총유기탄소(TOC)는 총탄소에서 TIC를 차감하여 계산하였다. 총탄소 및 총질소는 FLASH2000 원소 분석기로 측정하였다. 생물기원 규소 농도는 DeMaster (1981)의 습식 알칼리 추출법을 사용하여 KOPRI에서 Continuous Flow Analyzer (SKALAR SANplus Analyzer를 이용하여 분석하였으며 (Kim et al., 2018), 이를 2.4배 하여 생물기원 오팔 농도로 환산하였다 (Mortlock and Froelich, 1989). 상대 오차는 1% 미만이다. Meteoric (자생) Be 분석을 위한 시료 준비는 Jeong et al. (2018)의 방법을 따랐다. ^{9}Be 농도와 $^{10}Be/^{9}Be$ 비는 한국과학기술원에서 ICP-MS와 가속기 질량분석기로 측정하였다.

3. 연구결과

KOPRI 극지연구소

가. 수심 단면과 빙하 지형학적 특징

NDT 축을 따라 약 490 km에 걸쳐 취득한 Sub-bottom profile (SBP) 자료는 빙하 지형 및 음향 퇴적상 분포를 잘 보여준다 (Fig. 2a). 수심은 Terra Nova Bay(TNB) 방향인 남서쪽으로 갈수록 깊어지는 역경사를 보이는데, 군데군데 수 m에서 수십 cm 규모의 높은 지대가 존재한다.

GZW A는 대륙붕 경계로부터 남서쪽으로 약 25 km 떨어진 곳에서 관찰된다(Figs. 1b, 2b). 아래쪽 경계면은 확인되지 않고 내부 구조도 모호하지만 쐐기형 형태를 보이는 점에서 Grounding Zone Wedge (GZW)로 해석된다(Bart et al., 2000). GZW B는 NDT 내에서 가장 발달한 GZW로, 약 100 m의 기복을 보이며(Figs. 2b, 3a), 기존 연구에서 마지막 최대 빙하기(LGM)의 접지선을 표시하는 지형으로 인식되어 왔다(Shipp et al., 1999; Mosola and Anderson, 2006; Halberstadt et al., 2016). GZW C는 콜먼 섬 남쪽, 약 남위 74° 부근에서 관찰된다(Figs. 1b, 2b). GZW A 및 B와 비교할 때 GZW C는 상대적으로 낮은 기복(~20 m)과 완만한 경사를 가지며, 쐐기형 형태가 덜 발달되어 있다(Figs. 2, 3b). GZW C의 lee side에는 괴상의 쐐기형 퇴적체가 관찰되며(Fig. 3b), GZW C 북쪽에 나타나는 층리가 있는 퇴적물은 thrust와 유사한 변형 구조을 보인다.

콜먼 섬 인근의 NDT 해저면은 iceberg furrow에 의해 심하게 교란되어 SBP 이미지에서 매우 굴곡이 많은 해저면으로 나타난다 (Fig. 3). 남쪽으로는 NDT 축을 따라 잘 발달한 mega-scale

glacial lineations (MSGLs)이 관찰된다(Fig. 4a). MSGL 분포 지역과 iceberg furrow 지역의 경계는 약 남위 74.3°, 수심 약 680 m 지점에서 나타난다 (Fig. 4a).

GZW C와 TNB 사이에서는 광범위한 MSGL 지형이 나타나며, 간헐적으로 소규모 (<10 m 기복)의 비대칭적인 GZW들이 나타난다 (Figs. 4b, c). MSGL은 빙하 활동에 의해 더 이상 교란되지 않았으므로, 가장 최근에 있었던 빙하 전진 시기에 NDT 축을 따라 흐르던 ice steram 하부에서 형성된 것으로 해석된다 (Anderson et al., 2014; Livingstone et al., 2012). MSGL과 GZW는 음향학적으로 투명하게 나타나는 얇은 층에 의해 피복되어 있다. Drygalski Ice Tongue 인근의 NDT 최남단·최심부에서는 둔덕 형의 고지들이 관찰되며, 이는 접지선 관련 지형으로 해석된다. 이들 지형은 TNB 지역에서 GZW로 보고된 지형에 속한다 (Stutz et al., 2021). 이 둔덕형 고지 북쪽으로는 수 km에 걸쳐 층리를 보이는 퇴적물이 분포한다 (Figs. 4d, e).

나. NDT의 음향 퇴적상(AF)과 퇴적물 분포

SBP 자료를 바탕으로 NDT의 퇴적층을 형태, 내부 구조, 공간적 분포에 따라 다섯 개의 음향 퇴적상(acoustic facies, AF)으로 구분하였다(Table 2). AF A는 얇고 음향적으로 투명하며, 측방 연속성이 좋은 드레이프형 퇴적물로 NDT 전반에서 최상부층을 이룬다. 수심 800 m 이상에서만 뚜렷하게 확인 가능하다. 층서적 위치와 지형 피복 특성으로 보아, AF A는 가장 최근의 suspension settling에 의해 형성된 퇴적물로 해석된다. 이는 여름철에 해빙이 없는 해양 환경을 반영하는 로스해 전형적인 표층 퇴적물, 즉 생교란된 규조질 머드와 간헐적인 빙하운반쇄설물(IRD)로 구성된 퇴적물에 해당한다(Shipp et al., 1999). NDT의 천부에서는 저층 해류에 의한 퇴적물의 재동 등으로 인해 AF A가 매우 얇거나 삭박된 것으로 보인다.

AF A는 GZW C와 TNB 사이 대부분의 지역에서 기반암을 직접 피복한다. 그러나 Drygalski Ice Tongue 인근 NDT 축의 일부 기반암 위에는 층리가 있는 퇴적물(AF B)이 존재한다. AF B는 Drygalski Ice Tongue 인근에서 장축 수 km 규모의 북동-남서 방향으로 연장된 분지 내에 제한적으로 분포한다(Figs. 4d, e). AF B는 수 m 두께를 가지며, 약 20 m 기복의 둔덕형 고지 북쪽에서 관찰된다. 이 둔덕형 고지는 AF B의 퇴적과 연관된 지형으로, 빙하 후퇴 과정 중 일시적인 정체기에 형성된 접지선 지형으로 해석된다. 이는 남서부 로스해에서 보고된 후퇴성 모레인(recessional moraine)과는 달리 규모가 더 크고 간격이 넓다 (예: Simkins et al., 2017). 또한 이들은 비대칭적인 형태를 보이는 전형적인 GZW와도 차이가 있다. AF B는 길게 연장된 쐐기형(Fig. 4d) 또는 측방으로 긴 분지 충전형(Fig. 4e) 단면을 보이며, 평행 또는 준평행 층리를 특징으로 한다. 이는 접지선 인접 환경에서 중력류와 현탁 침강이 복합적으로 작용하여 퇴적된 퇴적상으로 해석된다.

AF C는 남위 약 74° 이북에서 NDT 서측 경계를 따라 분포하는 층리화된 드레이프형 퇴적물이다. GZW B 상부에서는 거의 관찰되지 않아 남쪽과 북쪽의 AF C가 GZW B에 의해 분리된 것처럼 보이지만, 실제로는 AF C가 GZW B를 향해 점진적으로 박층화되어 소멸되기 때문이다. GZW B 북쪽의 AF C는 GZW B 하부 사면을 따라 온랩(onlap) 구조를 보이며(Fig. 3a), 이는 AF C가 GZW B 형성 이후에 퇴적되었음을 의미한다. 이 퇴적물은 Shipp et al.(1999)이

보고한 ponded deposits과 대응되는데, JOIDES와 Pennell Trough에서 ponded deposit은 빙하 전면 또는 빙붕 하부 환경에서 형성된 퇴적층으로 해석된 바 있다. GZW B 남쪽에서 나타나는 AF C는 NDT의 서쪽 경계를 따라 나타나면 GZW C가 남쪽 경계를 이룬다 (Fig. 3b).

AF D는 GZW C의 lee side에 분포하는 높이 약 18 m의 괴상의 쐐기형 퇴적체이다 (Fig. 3b). 분포 양상과 형태로 보아, GZW 전면 사면에서 발생한 사면 붕괴(slump)에 의해 형성된 중력류 퇴적물로 해석된다. 이와 유사한 퇴적상이 JOIDES Trough에서 보고되었다 (Simkins et al., 2018). AF D는 층리가 있는 퇴적층인 AF C를 피복하며 (Fig. 3b), GZW C 인접부의 AF C에서는 thrust 변형 구조가 관찰된다. 이는 GZW C가 AF C 퇴적 이후에 형성되었음을 시사한다.

다. 코어 퇴적물 특성과 퇴적 환경

(1). 코어 RS19-GC04

코어 RS19-GC04는 GZW B와 GZW C 사이에 분포하는 층리가 발달한 퇴적물 (AF C)에서 채취되었으며, GZW B 형성 이후부터 GZW C 형성 이전까지의 퇴적 기록을 확보하기 위해 전략적으로 선정된 지점에서 채취되었다 (Figs. 2, 3b). 본 코어는 퇴적상, 고기후 지시자 분석 자료, 퇴적 연대를 기반으로 세 개의 단위로 구분되었다(Fig. 5, Table 3). 본문에서 언급되는 모든 연대는 보정 연대(calibrated age, ka BP)이다.

최하부 단위인 Unit 3 (376 - 452 cm)는 주로 생물교란된 사질 머드로 구성되며, 오팔 및 $CaCO_3$ 함량 변동성이 크고 높은 $^{10}Be/^{9}Be$ 비를 보인다 (Table 3). 특히 최대 24 wt.%에 이르는 높은 $CaCO_3$ 함량은 생물기원 탄산염의 존재와 관련된다. 421 - 424 cm와 438 - 439 cm 깊이에서 산출된 저서성 유공충의 보정 연대는 각각 36.5 ka와 36.2 ka로, Marine Isotope Stage (MIS) 3에 해당한다 (Table 1).

Unit 3의 하부 (447 - 452 cm)는 테프라가 풍부한 자갈질 사질층으로 구성되며, 높은 모래 함량, 매우 높은 대자율, 매우 낮은 TOC 값이 특징적이다. 멜버른 화산의 화산재층에서 $^{40}Ar/^{39}Ar$ 연대를 측정한 결과 50±70 ka, 35±22 ka가 나온바 있다 (Giordano et al., 2012). 하지만 이 테프라층이 멜버른 화산 활동과 직접 관련이 있는지는 연대만으로는 판단하기 어렵다. 테프라가 많은 층은 분출 당시 직접 퇴적된 화산재 층일 수도 있고, 이전 분출 물질이 지연 퇴적된 결과일 수도 있기 때문이다. 해빙기에 빙붕 또는 다년빙이 붕괴하면서 그 위에 오랜 기간 동안 쌓인 풍성 기원 물질이 퇴적되면 높은 테프라 함량을 보일 수 있다 (예: Lee et al., 2007). 정확한 기원 규명을 위해서는 추가적인 테프라 조성 및 연대 연구가 필요하다.

Unit 3의 생물기원 탄산염·오팔 생산과 높은 $^{10}Be/^{9}Be$ 비는 퇴적 당시 코어 지점이 빙상 접지 상태가 아니었으며, 개방 해양 환경이었음을 시사한다. 높은 MS 값은 조립 쇄설물 유입과 연관되며 $CaCO_3$ 함량과 반비례한다. 이는 테프라를 포함한 조립 쇄설물 유입이 탄산염 생성을 억제했음을 의미할 수 있다. GC04의 Unit 3은 MS 패턴과 연대 모델을 기반으로 GC05의 Unit 3 상부와 대비된다.

Unit 2 (238 - 376 cm)는 다양한 퇴적상으로 구성되며, Unit 3에 비해 낮은 $CaCO_3$ 함량과 낮은 $^{10}Be/^{9}Be$ 비를 보인다 (Table 3). 217 - 224 cm와 254 - 257 cm에서 측정된 유공충 연대는

각각 22.2 ka와 26.2 ka이다(Table 1). 본 단위는 암상에 따라 세 개의 하위 단위로 세분되었다. Unit 2C (238 – 376 cm)는 Unit 3을 명확한 경계로 덮으며, 평행층리 구조를 가지는 머드/모래 교호층과 엽리가 있는 머드 층으로 구성된다. 입도와 C/N 비 변동이 크고, TOC·오팔 함량 및 $^{10}Be/^{9}Be$ 비는 상대적으로 낮다. 상부로 갈수록 오팔과 $^{10}Be/^{9}Be$ 비가 증가한다. Unit 2B (199 – 238 cm)는 규조질 머드가 자갈질 모래-머드층 위에 놓인 구조로, 높은 오팔 함량과 높은 $^{10}Be/^{9}Be$ 비를 보인다. 이 층은 Unit 2A의 머드질 다이아믹트에 의해 명확한 경계로 피복된다. Unit 2A(167 – 199 cm)의 다이아믹튼은 함수율·TOC·오팔·$^{10}Be/^{9}Be$ 비가 모두 낮은 특징이 있다.

Unit 2는 MIS 2 동안 빙붕 하부 환경에서 빙상접지선 부근의 퇴적작용을 지시하며, 중간에 일시적인 개방 해양 시기가 포함된다. Unit 2C와 2B는 빙붕 하부 환경과 개방 해양 환경을 각각 지시하며, Unit 2A는 빙상의 재전진을 지시한다. Unit 2C의 낮은 $^{10}Be/^{9}Be$ 비와 낮은 오팔 함량은 연중 얼음에 의해 덮여 있었던 환경과 낮은 규조 생산성을 시사한다. 상부에서의 이 값들이 증가하는 경향은 빙붕 붕괴 및 외해로부터의 유입 증가를 의미한다. 오팔 함량은 TOC보다 환경 변화에 더 민감한 지표로 작용한다. Unit 2B 하부의 자갈질 모래층은 빙붕 말단에서 빙산 집결로 인한 IRD 증가와 평균 입도 증가로 특징지어지는 빙붕 말단 환경을 반영한다. 이를 덮는 생물교란 규조질 머드는 계절적 개방 해양 퇴적을 지시한다. 퇴적 속도를 일정하다고 가정하면, 빙붕 붕괴 시점은 약 24 ka로 추정된다. Unit 2A는 내부구조가 없는 머드질 다이아믹튼으로 구성되며 침식 기저를 가진다. 두께와 구조로 볼 때 빙상접지선과 인접한 빙해성 퇴적물로 해석된다.

Unit 1 (0 – 167 cm)은 규조를 포함한 모래질 머드로 구성되며 높은 TOC, 오팔, $^{10}Be/^{9}Be$ 비를 보인다. 하부는 마지막 해빙 이후의 해빙기 환경을 반영하고 상부는 계절적 개방 해양 환경의 특징을 보여준다.

(2). 코어 RS19-GC05B

GC05B는 얇은 퇴적 드레이프가 기반암을 피복하고 있는 GZW B 전면 사면에서 채취되었다 (Figs. 2, 3a). 이 퇴적층은 SBP 상에서 전형적인 AF A처럼 내부 구조가 투명하게 보이지 않고 북쪽으로 가면서 점차 두꺼워져 층리상 퇴적상 AF C로 변한다. 이 코어는 네 개의 단위로 구분된다.

가장 오래된 Unit 4 (176 – 273 cm)는 낮은 함수율, 높은 입자 밀도, 낮은 TOC·오팔·$^{10}Be/^{9}Be$ 비를 보이는 전형적 빙하 다이아믹튼이다. GZW 상 코어의 위치로 볼 때 이는 GZW 전면 사면에서 형성된 중력류 퇴적물로 해석된다.

Unit 3 (76 – 176 cm)은 탄산염 함유 머드로, 낮은 MS, 높은 TOC, 높은 $^{10}Be/^{9}Be$ 비를 보인다. 탄산염 함량은 변동이 크지만 최대 41 wt.%까지 높게 나타나며 오팔 함량과는 반비례하는 관계를 보인다. 저서성 유공충에 대한 방사성탄소 연대측정 결과로는 MIS 3 시기의 퇴적물인 것으로 보인다 (Table 1). MS 값으로 볼 때 GC05B의 상부가 GC04의 Unit 3에 대비된다. 높은 TOC, 높은 탄산염, 높은 오팔 등으로 볼 때 개방 해양 환경의 퇴적물로 해석된다.

Unit 2 (24 – 76 cm)에서는 MS가 증가하고 조립화 경향이 보이며 탄산염과 Be 비는 감소한다.

규조를 포함한 약간 자갈질인 이질 모래가 Unit 2의 탄산염을 포함한 머드 층을 경사진 경계면 위로 덮고 있다. 약 10 cm 두께의 규조를 포함한 머드 층 (48-58 cm)이 자갈을 포함한 사질 머드 사이에 끼어 있다. GC05B의 Unit 2는 GC04에 비해 훨씬 얇게 나타나지만 퇴적학적으로는 비슷한 특성을 보인다. 빙상접지선에 가까운 빙해성 퇴적이 우세하며 중간에 개방 해양 퇴적이 잠시 일어났던 것으로 해석된다.

Unit 1(0 - 24 cm)은 전형적 로스해 홀로세 퇴적과 달리 탄산염을 10-26 wt.% 포함한다 (Table 3). 하부 13-24 cm에는 규조질 머드가, 0-13 cm에는 탄산염을 포함한 머드가 나타난다. 탄산염 연대는 약 0.6 - 6 ka 연대를 보인다. 이 unit은 홀로세 개방 해양 환경을 반영한다. 초기에는 규조 생산이 우세했으나 약 6 ka 이후 탄산염 생산이 지배적으로 전환되었다.

(3). 코어 RS23-GC02

GC02는 GZW C 전면 사면에서 채취되었다 (Figs. 2 & 3b). 코어 위치에서 음향학적 기반암은 층리가 있는 퇴적층 AF C,와 그 위를 덮는 괴상의 웨지형 퇴적체 AF D에 의해 덮여 있고 최상부에 얇은 퇴적 드레이프 AF A가 있다 (Fig. 3b). 코어는 AF C까지는 도달하지 못하였고 AF A와 AF D에 해당하는 Unit 1과 Unit 2로 구성된다.

Unit 2 (7 - 324 cm)는 자갈질 함량이 낮은 이질 다이아믹튼으로 구성된다. 낮은 함수율, 높은 입자 밀도, 낮은 TOC를 보인다 (Table 3). AF D는 GZW C 사면 붕괴에 의한 중력류 퇴적물로 해석되었는데 Unit 2의 퇴적학적 특성은 이러한 환경 해석과 일치한다.

Unit 1 (0 - 7 cm)은 얇은 규조 함유 자갈질 이질 사층으로, 개방 해양 조건에서의 현탁 퇴적을 반영한다. 일반적인 로스해의 홀로세 규질 머드보다 조립질 성분이 많은데 지역적인 winnowing 현상이 있었을 것으로 추정된다.

4. 토의

가. MIS 4 이후 NDT의 빙하 환경 변화

지구물리 자료와 퇴적 기록 분석에 따르면, MIS 2와 MIS 4 동안 빙상은 코어 채취 지점 근처까지 전진했고, MIS 1과 MIS 3 동안에는 후퇴하였다 (Fig. 6). MIS 4 시기에는 빙상이 콜먼섬 북쪽까지 확장되어 GZW B를 형성하였다 (Unit 4). 이후 MIS 3 동안 빙상은 후퇴하였고, 북부 NDT에서는 생물기원 탄산염을 포함한 빙해양성 퇴적물이 개방 해양 환경에서 퇴적되었다 (Unit 3). MIS 3 개방 해양 환경은 남서부 로스해에서도 펭귄 화석의 방사성탄소 연대를 통해 제시된 바 있으며 (Emslie et al., 2007), 이는 MIS 3 동안 서부 로스해 전반이 개방 해양 상태였을 가능성을 시사한다.

빙상은 MIS 3 후기 - MIS 2 초기 동안 다시 확장하였으며, 약 24 ka까지 NDT 서측 연안 뱅크를 따라 빙붕 환경이 형성되었다. 이 시기의 빙상은 가장 최근에 있었던 후기 MIS 2 빙상보다 얇았던 것으로 해석되는데, MIS 3 후기 - MIS 2 초기에는 GC04 지점에서 부빙 상태였던 반면, 후기 MIS 2에는 동일 지역에서 빙상이 접지된 상태였기 때문이다. 약 24 ka에 빙붕이

붕괴되었고, 이후 약 3천 년 동안 개방 해양 조건이 지속되었다. 이 시기 접지선은 GZW C 남쪽에 위치했을 것으로 해석된다. 더 남쪽 McMurdo Ice Shelf 지역에서는 24.6 ka 및 23.1 ka 보정 연대를 가진 따개비 화석이 보고되었으며 (Kellogg et al., 1990), 이는 NDT가 개방 해양 상태였던 시기 남부 McMurdo Sound에도 빙상이 존재하지 않았음을 의미한다. 이는 GZW B 위치에서 남쪽으로 약 550 km에 이르는 대규모 접지선 후퇴가 있었을 가능성을 암시한다. 하지만 AIM 2 온난 사건 당시 NDT 전역에 빙상이 없었는지, 빙붕은 얼마나 얇아졌는지를 알기 위해서는 추가 연구가 필요하다. 이후 후기 MIS 2에 빙상이 다시 확장하여 GC04 지점에 빙상 접지선 인접한 다이아믹튼을 퇴적시켰고, 이 전진의 최대 범위는 GZW C의 위치일 것으로 해석된다. 방사성탄소 연대에 따르면 GC04 지점에서 빙하 후퇴는 약 19.7 ka에 시작하였다.

나. LGM 동안 빙상 범위

빙하 지형과 퇴적 구조를 종합하면, NDT에서 가장 큰 범위의 빙상 확장은 LGM 이전에 발생했으며, LGM 동안의 빙상은 콜먼 섬 남쪽(GZW C)까지 후퇴한 상태였음을 시사한다. 기존 연구에서는 DIT와 콜먼 섬 사이의 MSGL 분포를 근거로 GZW B를 LGM 최대 범위로 해석했다 (Halberstadt et al., 2016). 그러나 본 연구에서는 MSGL이 GZW B까지 연장되지 않고, 그보다 남쪽에서 빙산에 의해 침식된 지형으로 전이되는 것을 확인하였다 (Fig. 4a). 이에 더해 MSGL과 GZW B 사이에 GZW C가 존재하는 점을 고려한다면, NDT의 MSGL이 GZW B와 동일 시기에 형성되었다고 단정할 수 없다. GC04에서 MIS 2와 MIS 3 퇴적물이 보존되어 있다는 사실은 GZW C 북쪽 지역이 가장 최근의 빙기 동안 빙상 접지되지 않았음을 의미한다. GZW B의 경사면에서 채취한 GC05B에서 MIS 3 탄산염 퇴적이 확인되는 점 역시 GZW B가 MIS 2 이전에 형성되었음을 지지한다. GC05B 기저 다이아믹튼은 MIS 4 퇴적으로 해석되며, GZW B 역시 MIS 4에 형성되었을 가능성이 높다. 더 북쪽의 GZW A는 MIS 6 또는 그 이전의 더 큰 빙하기에 형성된 것으로 추정된다.

남위 약 74°의 GZW C는 MIS 3 - 초기 MIS 2 층리 퇴적물을 덮고 있으며, NDT에서 LGM 빙상의 접지선 경계을 나타내는 지형으로 해석된다. 이는 기존 지형 기반 추정보다 약 75 km 남쪽에 위치하며 (Mosola and Anderson, 2006; Halberstadt et al., 2016), 탄산염 연대 기반 해석과는 일치한다 (Licht et al., 1996). 또한 이 연구 결과는 기존의 빙상 범위에 의해 계산했던 LGM 빙상 체적 추정 (e.g., Danielson and Bart, 2024)은 수정될 필요가 있음을 시사한다.

콜먼 섬 북서쪽의 작은 곡에 나타나는 빙하구조들에서 보듯이 LGM 동안 NDT 서측 연안에서는 GZW C보다 북쪽까지 빙상이 존재했다 (Shipp et al, 1999; Anderson et al., 2014). SBP 자료에 따르면 콜먼 섬 동쪽에서 수심 500 m 이상인 수심 지역에는 LGM 이전 빙붕 하부-공해 환경 퇴적물(AF C)이 보존되어 있지만, 이 퇴적물은 콜먼 섬 남쪽 연안과 GZW B 위에서는 관찰되지 않고 이 지역에서는 거친 표면의 쐐기형 둔덕들이 분포한다 (Fig. 7). SBP 상에서 볼 때 이는 LGM GZW로 해석된다. 이러한 자료를 종합하여 본 연구에서는 수정된 LGM 접지선 위치를 제안한다 (Fig. 8).

GZW 위치를 근거로 볼 때 빙상 범위는 MIS 6(또는 그 이전) > MIS 4 > MIS 2 순으로 점진적으로 축소되었다. 테라노바 만 인근 육상 노출 연대 연구 역시 MIS 6 이후 지속적으로 빙

상 두께가 얇아졌음을 지시한다 (Di Nicola et al., 2009; Straski et al., 2009; Rhee et al., 2019). 종합해서 볼 때 북 빅토리아 랜드와 서부 로스해에서는 MIS 6 이후 빙상이 범위와 두께 모두 축소되어 왔음을 지시한다. 이는 또한 서부 로스해 빙상이 MIS 2 해수면 저하에 기여한 정도가 이전 빙하기보다 작았을 것임을 의미한다.

다. 해양 기반 빙상의 환경 민감성에 대한 시사점

이 지역에서 약 24 ka에 개방 해양 환경으로의 전환은 AIM 2 온난 사건 (23-24 ka 시기에 천년 간 지속된 온난기, WAIS Divide Project Members, 2013)과 동시기에 일어났으며, 이는 빙상이 수천 년 규모 기후 변동에 매우 빠르게 반응했음을 의미한다 (Fig. 6). AIM 2는 서남극 WAIS Divide 빙하 코어 및 동남극 EPICA Dronning Maud Land 빙하 코어 기록에서는 확인되지만, 다른 동남극 빙하 코어 기록에서는 명확하지 않다(EPICA Community Members, 2006; Stenni et al., 2011; WAIS Divide Project Members, 2013, 2015). MIS 3 시기의 AIM 기록들은 남극해 표층 온도 기록에서 확인된 바 있으나 (Anderson et al., 2021), 남극 대륙붕 해양 지역에서 이와 관련된 빙하접지선 변동 기록이 보고된 바는 없었다. 이 연구는 서부 로스해에서 AIM 2 온난화가 상당 규모의 빙하 후퇴를 유발하였으며 천년 단위 대기의 온난화가 빙기 동안에도 빙붕의 후퇴를 불러올 수 있음을 보여준다. 이 연구의 기록에 따르면 개방 해양 조건은 약 3천 년간 지속되었는데, 이는 AIM 2 온난 기간(~1천 년)보다 길다. 이는 냉각에 대한 빙상의 반응이 온난화에 대한 반응보다 지연되었을 가능성을 시사한다. 다만 연대 모델 단순화로 인한 불확실성이 존재한다.

NDT에서의 빙상 후퇴 시작 시점은 약 19.7 ka로 (Fig. 6), 기존에 해양 퇴적물 코어로부터 제시된 8–13 ka보다 훨씬 이르고 (Licht et al., 1996; Domack et al., 1999; Baroni and Hall, 2004), 터커 빙하의 초기 후퇴 시기로 추정된 약 17 ka (Goehring et al., 2019)보다도 더 이르다. 19.7 ka 연대는 WAIS Divide 빙하 코어에 기록된 대기 온도 상승과 남극해 표층 수온 상승과 일치하며 (Fig. 6), 웨델해에서 빙상의 후퇴 시작 시기와도 일치한다 (Weber et al., 2011). 이는 해양 기반 빙상이 기후 온난화 초기 단계의 해양 및 대기 온도 상승에 매우 민감했음을 의미한다. 또한 최근 4만 년간 NDT 빙상 변동은 동남극보다 서남극 온도 기록과 더 잘 맞아떨어지는 경향이 있다.

해양 빙상 불안정성 가설에 따르면 역경사 지형에서는 접지선이 빠르게 후퇴해야 한다 (Schoof. 2007). 따라서 GZW C와 DIT 사이의 역경사에서는 빠른 빙상 후퇴가 예상되었다. 그러나 실제로는 19.7 ka에 시작한 빙상 후퇴가 홀로세 중기까지 단계적으로 지속된 것으로 보인다. 이는 해구 폭 변화, 인접 빙체와의 상호작용, 국지 지형 효과 등이 안정성을 제공했기 때문으로 해석되며 유사한 사례들이 극지역 대륙 연변부에서 보고된 바 있다 (Gudmundsson et al., 2012; Jamieson et al., 2012; Greenwood et al., 2021; Stutz et al., 2021).

5. 결론

본 연구에서는 NDT 축을 따라 수심 단면을 제시하고, LGM 동안 빙상의 접지선 위치를 남위

약 74°로 제시하였다. 이는 LGM 빙상 범위가 기존에 콜먼 섬 GZW를 기준으로 추정되었던 범위보다 더 좁았음을 의미한다. 콜먼 섬 GZW는 MIS 3 퇴적물이 그 위와 남쪽에 보존되어 있다는 점에서 MIS 4 동안의 더 큰 빙상 전진기에 형성된 것으로 해석된다. 또한 약 24 ka와 약 19.7 ka에 발생한 빙상 후퇴가 대기 및 해양 온도 상승과 연관되어 있음을 보여주었으며, 이는 해양 기반 빙상 가장자리가 기후 강제력에 대해 매우 취약하다는 점을 지지한다. 본 연구는 NDT에서 마지막 해빙기의 초기 후퇴 시점을 제시하였지만, NDT 전반의 빙하 후퇴 역사를 보다 정밀하게 복원하기 위해서는 추가적인 연대 자료가 필요하다.

6. 참고문헌

Anderson, H.J., Pedro, J.B., Bostock, H.C., Chase, Z., Noble, T. L. 2021. Compiled Southern Ocean sea surface temperatures correlate with Antarctic Isotope Maxima. Quat. Sci. Rev. 255, 106821.https://doi.org/10.1016/j.quascirev.2021.106821.

Anderson, J.B., Conway, H., Bart, P.J., Witus, A.E., Greenwood, S.L., McKay, R.M., Hall, B.L., Ackert, R.P., Licht, K., Jakobsson, M., Stone, J.O., 2014. Ross Sea paleo-ice sheet drainage and deglacial history during and since the LGM. Quat. Sci. Rev. 100, 31-54. http://doi.org/10.1016/j.quascirev.2013.08.020.

Arndt, J.E., Schenke, H.W., Jakobsson, M., Nitsche, F.O., Buys, G., Goleby, B., Rebesco, M., Bohoyo, F., Hong, J., Black, J., Greku, R., Udintsev, G., Barrios, F., Reynoso-Peralta, W., Taisei, M., Wigley, R., 2013. The international bathymetric chart of the Southern Ocean (IBCSO) version 1.0 - a new bathymetric compilation covering circum-Antarctic waters. Geophys. Res. Lett. 40, 3111-3117. https://doi.org/10.1002/grl.50413.

Baroni, C., Hall, B.L., 2004. A new Holocene relative sea-level curve for Terra Nova Bay, Victoria Land, Antarctica. J. Quat. Sci. 19, 377-396.https://doi.org/10.1002/jqs.825.

Bart, P.J., Anderson, J.B., Trincardic, F., Shipp, S.S., 2000. Seismic data from the Northern basin, Ross Sea, record extreme expansions of the East Antarctic Ice Sheet during the late Neogene. Mar. Geol. 166, 31 - 50. https://doi.org/10.1016/S0025-3227(00)00006-2.

Chandler, D., Langebroek, P., 2021. Southern Ocean sea surface temperature synthesis: Part 2. Penultimate glacial and last interglacial. Quat. Sci. Rev. 271, 107190. https://doi.org/10.1016/j.quascirev.2021.107190.

Cuffey, K.M., Clow, G.D., Steig, E.J., Buizert, C., Fudge, T.J., Koutnik, M., Waddington, E.D., Alley, R.B., Severinghaus, J.P., 2016. Deglacial temperature history of West Antarctica. Proc. Nat. Ac. Sci. 113, 14249-14254. https://doi.org/10.1073/pnas.1609132113.

Danielson, M.A., Bart, P.J., 2024. The staggered retreat of grounded ice in the Ross Sea,

Antarctica, since the Last Glacial Maximum (LGM). The Cryosphere 18, 1125-1138. https://doi.org/10.5194/tc-18-1125-2024.

DeMaster, D.J., 1981. The supply and accumulation of silica in the marine environment. Geochem. Cosmochim. Acta 5, 1715-1732. https://doi.org/10.1016/0016-7037(81)90006-5.

Di Nicola, L., Strasky, S., Schlüchter, C., Salvatore, M.C., Akcar, N., Kubik, P.W., Christl, M., Kasper, H.U., Wieler, R., Baroni, C., 2009.Multiple cosmogenic nuclides document complex Pleistocene exposure history of glacial drifts in Terra Nova Bay (northern Victoria Land, Antarctica). Quat. Res. 71, 83-92. https://doi.org/10.1016/j.yqres.2008.07.004.

Domack, E.W., Jacobson, E.A., Shipp, S., Anderson, J.B., 1999. Late Paleistocene-Holocene retreat of the West Antarctic Ice-Sheet system in the Ross Sea: part 2-Sedimentologic and stratigraphic signature. GSA Bull. 111, 1517-1536. https://doi.org/10.1130/0016-7606(1999)111%3C1517:LPHROT%3E2.3.CO;2.

Emslie, S.D., Coats, l., Licht, K., 2007. A 45,000 yr record of Adélie penguins and climate change in the Ross Sea, Antarctica. Geology 34, 61-64. https://doi.org/10.1130/G23011A.1.

EPICA Community Members, 2006. One-to-one coupling of glacial climate variability in Greenland and Antarctica. Nature 444, 195-198. https://doi.org/10.1038/nature05301.

Frank, T.D., James, N.P., Bone, Y., Malcom, I., Bobak, L.E., 2014. Late Quaternary carbonate deposition at the bottom of the world. Sed. Geol. 305, 1-16. http://dx.doi.org/10.1016/j.sedgeo.2014.02.008.

Giordano, G., Lucci, F., Phillips, D., Cozzupoli, D., Runci, V., 2012. Stratigraphy, geochronology and evolution of the Mt. Melbourne volcanic field (North Victoria Land, Antarctica). Bull. Volcanol. 74, 1985-2005. http://dx.doi.org/10.1007/s00445-012-0643-8.

Goehring, B.M., Balco, G., Todd, C., Moening-Swanson, I., Nichols, K., 2019. Late-glacial grounding line retreat in the northern Ross Sea, Antarctica. Geology 47, 291-294. https://doi.org/10.1130/G45413.1.

Greenwood, S.L., Simkins, L.M., Winsborrow, M.C.M., Bjarnadóttir, L.R., 2021. Exceptions to bed-controlled ice sheet flow and retreat from glaciated continental margins worldwide. Science Advances 7, eabb6291. https://doi.org/10.1126/sciadv.abb6291.

Gudmundsson, G.H., Krug, J., Durand, G., Favier, L., Gagliardini, O., 2012. The stability of grounding lines on retrograde slopes. The Cryosphere 6, 1497-1505. https://doi.org/10.5194/tc-6-1497-2012.

Halberstadt, A.R.W., Simkins, L.M., Greenwood, S.L., Anderson, J.B., 2016. Past ice-sheet behaviour: retreat scenarios and changing controls in the Ross Sea, Antarctica. The

Cryosphere 10, 1004-1020. https://doi.org/10.5194/tc-10-1003-2016.

Hall, B., Henderson, G.M., Baroni, C., Kellogg, T.B., 2010. Constant Holocene Southern-Ocean ^{14}Creservoirages and ice-shelf flow rates. Earth and Planetary Science letters 296, 115-123. https://doi:10.1016/j.epsl.2010.04.054.

Heaton, T.J., Köhler, P., Butzin, M., Bard, E., Reimer, R.W., Austin, W.E.N., Bronk Ramsey, C., Hughen, K.A., Kromer, B., Reimer, P.J., Adkins, J., Burke, A., Cook, M.S., Olsen, J., Skinner, L.C., 2020. Marine20-the marine radiocarbon age calibration curve (0-55,000 cal BP). Radiocarbon 62, doi: 10.1017/RDC.2020.68.

Heaton, T.J., Bard, E., Ramsay, C.B., Butzin, M., Hatté, C., Hughen, K.A., Köhler, P., Reimer, P.J., 2023a. A response to community questions on the Marine20 radiocarbon age calibration curve: marine reservoir aged and the calibration of ^{14}C samples from the oceans. Radiocarbon 65, 247-273. https://doi.org/10.1017/RDC.2022.66.

Heaton, T.J., Butzin, M., Bard, E., Bronk Ramsey, C., Hughen, K.A., Köhler, P., Reimer, P.J., 2023b. Marine radiocarbon calibration in polar regions: a simple approximate approach using Marine20. Radiocarbon 65, 848-875. https://doi.org/10.11017/RDC.2023.42.

Hillenbrand, C.-D., Smith, J.A., Kuhn, G., Esper, O., Gersonde, R., Larter, R.D., Maher, B., Moreton, S.G., Shimmield, T.M., Korte, M., 2010. Age assignment of a diatomaceous ooze deposited in the western Amundsen Sea Embayment after the Last Glacial Maximum. Journal of Quaternary Science 25, 280-295. https://doi.org/10.1002/jqs.1308.

Jamieson, S.S.R., Vieli, A., Livingstone, S.J., Ó Cofaigh, C., Stokes, C., Hilenbrand, C.-D., Dowdeswell, J.A., 2012. Ice-stream stability on a reverse bed slope. Nature Geoscience 5, 799-802. https://doi.org/10.1038/ngeo1600.

Jeong, A., Lee, J.I., Seong, Y.B., Balco, G., Yoo, K.-C., Yoon, H.I., Domack, E., Rhee, H.H., Yu, B.Y., 2018, Late Quaternary deglacial history across the Larsen B embayment, Antarctica. Quat. Sci. Rev. 189, 134-148. https://doi.org/10.1016/j.quascirev.2018.04.011.

Jouzel, J., Masson-Delmotte, V., Cattani, O., Dreyfus, G., Falourd, S., Hoffmann, G., Minster, B., Nouet, J., Barnola, J.M., Chappellaz, J., Fischer, H., Gallet, J.C., Johnsen, S., Leuenberger, M., Loulergue, L., Luethi, D., Oerter, H., Parrenin, F., Raisbeck, G., Raynaud, D., Schilt, A., Schwander, J., Selmo, E., Souchez, R., Spahni, R., Stauffer, B., Steffensen, J.P, Stenni, B., Stocker, T.F., Tison, J.L., Werver, M., Wolff, E.W., 2007. Orbital and millennial Antarctic climate variability over the past 800,000 years. Science 317, 793-796. https://doi.org/10.1126/science.1141038.

Kellogg, T.B., Kellogg, D.E., Stuiver, M. 1990. Late Quaternary history of the southwestern

Ross Sea: Evidence from debris bands on the McMurdo Ice Shelf, Antarctica. Contributions to Antarctic Research Ⅰ, Antarctic Research Series 50, 25-56. https://doi.org/10.1029/AR050p0025.

Kim, S., Yoo, K.-C., Lee, J.I., Khim, B.-K., Bak, Y.-S., Lee, M.K., Lee, J., Domack, E.W., Christ, A.J., Yoon, H.I., 2018. Holocene paleoceanography of Bigo Bay, west Antarctic Peninsula: Connections between surface water productivity and nutrient utilization and its implication for surface-deep water mass exchange. Quat. Sci. Rev. 192, 59-70. https://doi.org/10.1016/j.quascirev.2018.05.028.

Lee, Y.I., Lim, H.S., Yoon, H.I., Tatur, A., 2007. Characteristics of tephra in Holocene lake sediments on King George Island, West Antarctica: implications for deglaciation and paleoenvironment. Quat. Sci. Rev. 26, 3167-3178. https://doi.org/10.1016/j.quascirev.2007.09.007.

Licht, K.J., Jennings, A.E., Andrews, J.T., Williams, K.M., 1996. Chronology of late Wisconsin ice retreat from the western Ross Sea, Antarctica. Geology 24, 223-226. https://doi.org/10.1130/0091-7613(1996)024%3C0223:COLWIR%3E2.3.CO;2.

Lisiecki, L.E., Raymo, M.E., 2005. A Pliocene-Pleistocene stack of 57 globally distributed benthic d18O records. Paleoceanography 20, PA1003. https://doi.org/10.1029/2004PA001071.

Livingstone, S.J., Ó Cofaigh, C., Stokes, C.R., Hillenbrand, C.-D., Vieli, A., Jamieson, S.S.R., 2012. Antarctic palaeo-ice streams. Earth-Science Rev. 111, 90 - 128. https://doi.org/10.1016/j.earscirev.2011.10.003.

Mabin, M.C.G., 1985. ^{14}Cagesfor′heroicera′penguinandsealbonesfromInexpressibleIsland,TerraNovaBay,North VictoriaLand.NewZealandAntarcticRecord6,24-25.

Mortlock, R.A. and Froelich, P.N., 1989. A simple method for the rapid determination of opal in pelagic marine sediments. Deep-Sea Res. 36, 1415-1426. https://doi.org/10.1016/0198-0149(89)90092-7.

Mosola, A.B., Anderson, J.B., 2006. Expansion and rapid retreat of the West Antarctic Ice Sheet in eastern-Ross Sea: possible consequence of over-extended ice streams? Quat. Sci. Rev. 25, 2177-2196. https://doi.org/10.1016/j.quascirev.2005.12.013.

Prothro, L.O., Simkins, L.M., Majewski, W., Anderson, J.B., 2018. Glacial retreat patterns and processes determined from integrated sedimentology and geomorphology records. Mar. Geol. 309, 104-119. http://dx.doi.org/10.1016/j.margeo.2017.09.012.

Rhee, H.H., Lee, M.K., Seong, Y.B., Hong, S., Lee, J.I., Yoo, K.-C., Yu, B.Y., 2019. Timing of the local glacial maximum in Terra Nova Bay, Antarctica defined by cosmogenic dating. Quat. Sci. Rev. 221, 105897. https://doi.org/10.1016/j.quascirev.2019.105897.

Rhee, H.H., Lee, M.K., Seong, Y.B., Lee, J.I., Yoo, K.-C., Yu, B.Y., 2020. Post-LGM

KOPRI 극지연구소

dynamic deglaciation along the Victoria Land coast, Antarctica. Quat. Sci. Rev. 247, 106595. https://doi.org/10.1016/j.quascirev.2020.106595.

Schoof, C., 2007. Ice sheet grounding line dynamics: Steady states, stability, and hysteresis. J. Geophys. Res. 112, F03S28. https://doi.org/10.1029/2006JF000664.

Shipp, S., Anderson, A., Domack, E., 1999. Late Pleistocene-Holocene retreat of the West Antarctic Ice-Sheet system in the Ross Sea: Part 1-Geophysical results. GSA Bulletin 111, 1486-1516. https://doi.org/10.1130/0016-7606(1999)111%3C1486:LPHROT%3E2.3.CO;2.

Simkins, L.M., Anderson, J.B., Greenwood, S.L., Gonnermann, H.M., Prothro, L.O., Halberstadt, A.R.W., Stearns, L.A., Pollard, D., DeConto, R.M., 2017. Anatomy of a meltwater drainage system beneath the ancestral East Antarctic ice sheet. Nat. Geosci. 10, 691-697. https://doi.org/10.1038/ngeo3012.

Simkins, L.M., Greenwood, S.L., Anderson, J.B., 2018. Diagnosing ice sheet grounding line stability from landform morphology. The Cryosphere 12, 2707-2726. https://doi.org/10.5194/tc-12-2707-2018.

Smith, J.A., Graham, A.G.C., Post, A.L., Hillenbrand, C.-D., Bart, P.J., Powell, R.D., 2019. The marine geological imprint of Antarctic ice shelves. Nat. Comm. 10, 5635. https://doi.org/10.1038/s41467-019-13496-5.

Stenni, B., Buiron, D., Frezzotti, M., Albani, S., Barbante, C., Bard, E., Barnola, J.M., Baroni, M., Baumgartner, M., Bonazza, M., Capron, E., Castellano, E., Chappellaz, J., Delmonte, B., Falourd, S., Genoni, L., Iacumin, P., Jouzel, J., Kipfstuhl, S., Landais, A., Lemieux-Dudon, B., Maggi, V., Masson-Delmotte, V., Mazzola, C., Minster, B., Montagnat, M., Mulvaney, R., Narcisi, B., Oerter, H., Parrenin, F., Petit, J.R., Ritz, C., Scarchilli, C., Schilt, A., Schüpbach, S., Schwander, J., Selmo, E., Severi, M., Stocker, T.F., Udisti, R., 2011. Expression of the bipolar see-saw in Antarctic climate records during the last deglaciation. Nature Geosci. 4, 46-49. https://doi.org/10.1038/ngeo1026.

Strasky, S., Di Nicola, L., Baroni, C., Salvatore, M.C., Baur, H., Kubik, P.W.,Schlüchter, C., Wieler, R., 2009.Surface exposure ages imply multiple low-amplitude Pleistocene variations in East Antarctic ice sheet, Ricker Hills, Victoria Land. Antarctic Science 21, 59-69. https://doi.org/10.1017/S0954102008001478.

Stuiver, M., Denton, G.H., Hughes, T. J., Fastook, J.L., 1981. History of last glaciation: A working hypothesis. In: Denton, G.H., Hughes, T.J., eds., The Last Great Ice Sheets. New York, John Wiley & Sons, p 319-440.

Stuiver, M., Reimer, P.J., Reimer, R.W., 2021. CALIB 8.2 at http://calib.org.

Stutz, J., Mackintosh, A., Norton, K., Whitmore, R., Baroni, C., Jamieson, S.S.R., Jones, R.S., Balco, G., Salvatore, M.C., Casale, S., Lee, J.I., Seong, Y.B., McKay, R., Vargo,

L.J., Lowry, D., Spector, P., Christl, M., Ochs, S.I., Di Nicola, L., Iarossi, M., Stuart, F., Woodruff, T., 2021. Mid-Holocene thinning of David Glacier, Antarctica: Chronology and Controls. The Cryosphere 15, 5447-5471. https://doi.org/10.5194/tc-15-5447-2021.

Taviani, M., Reid, D.E., Anderson, J.B., 1993. Skeletal and isotopic composition and paleoclimatic significance of Late Pleistocene carbonates, Ross Sea, Antarctica. J. Sed. Petrol. 63, 84-90. https://doi.org/10.1306/D4267A96-2B26-11D7-8648000102C1865D.

WAIS Divide Project Members, 2013. Onset of deglacial warming in West Antarctica driven by local orbital forcing. Nature 500, 440-444. https://doi.org/10.1038/nature12376.

WAIS Divide Project Members, 2015. Precise interpolar phasing of abrupt climate change during the last ice age. Nature 520, 661-665. https://doi.org/10.1038/nature14401.

Weber, M.E., Clark, P.U., Ricken, W., Mitrovica, J.X., Hostetler, S.W., Kuhn, G., 2011. Interhemispheric ice-sheet synchronicity during the Last Glacial Maximum. Science 334, 1265-1269. https://doi.org/10.1126/science.1209299.

Whitehouse, I.E., Chinn, T.J.H., von Hofle, H.C., McSaveney, M.J., 1988. Radiocarbon contaminated penguin bones from Terra Nova Bay, Antarctica. New Zealand Antarctic Record 8, 11-23.

KOPRI 극지연구소

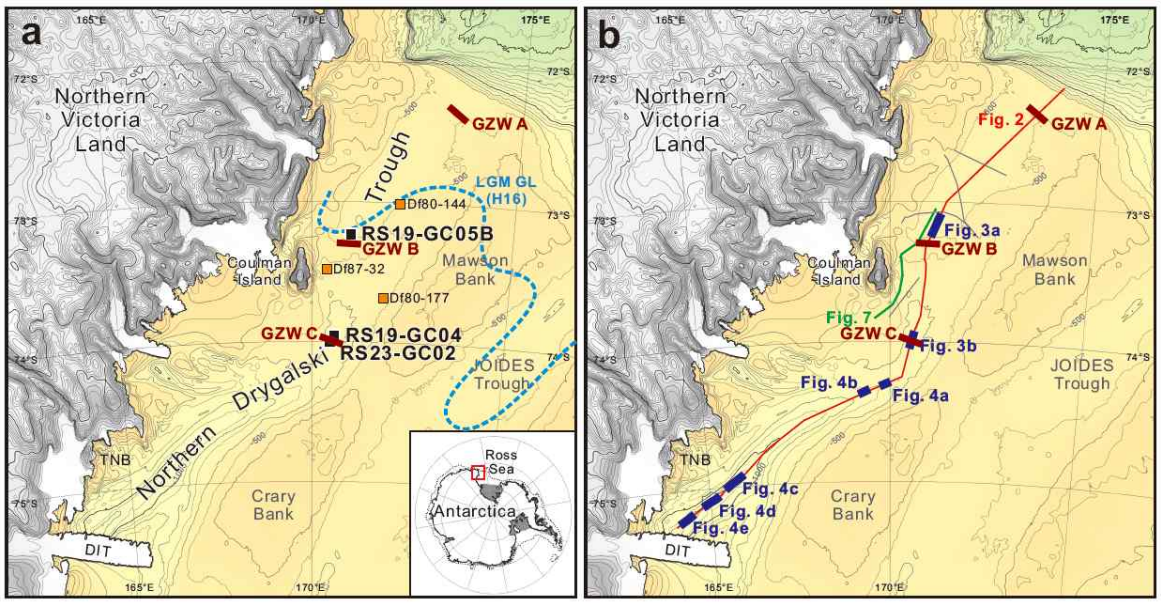


Fig. 1. a) Location map of sediment cores RS19-GC04, RS19-GC05B, and RS23-GC02. Also shown are Last Glacial Maximum grounding line (LGM GL) H16 by Halberstadt et al. (2016), grounding zone wedges (GZWs) discussed in the text, and location of sediment cores with previously reported carbonate ages (Df cores). Bathymetric data from Arndt et al. (2013). DIT=Drygalski Ice Tongue, TNB=Terra Nova Bay. b) Sub-bottom profile (SBP) track lines in Figs. 2-4 and 7 and other SBP track lines used in this study (dark gray solid lines).

KOPRI 극지연구소

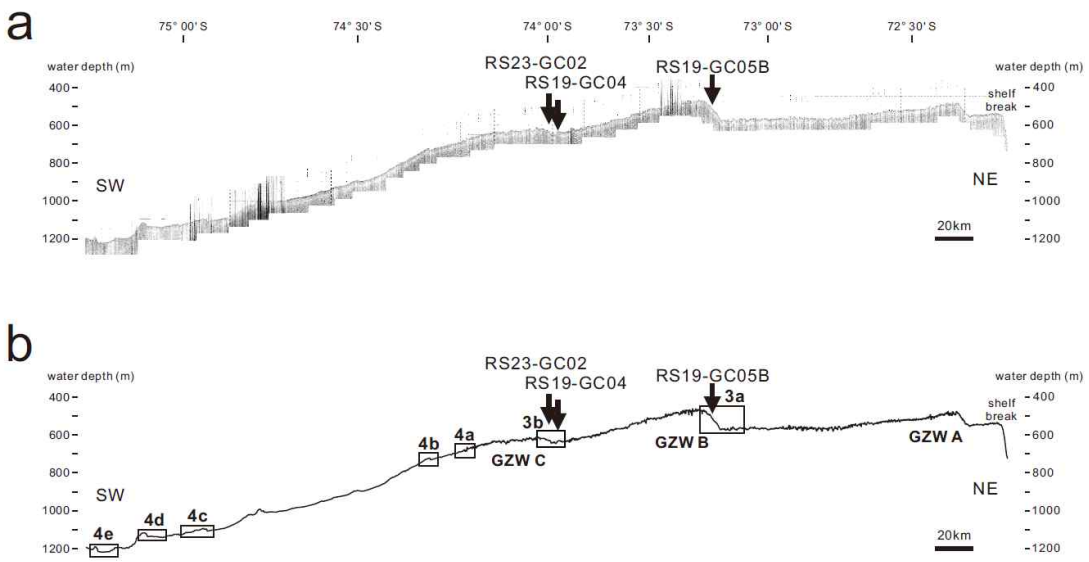


Fig. 2. a) Compiled SBP images and b) bathymetric profile along the axis of the northern Drygalski Trough with locations of sediment cores.

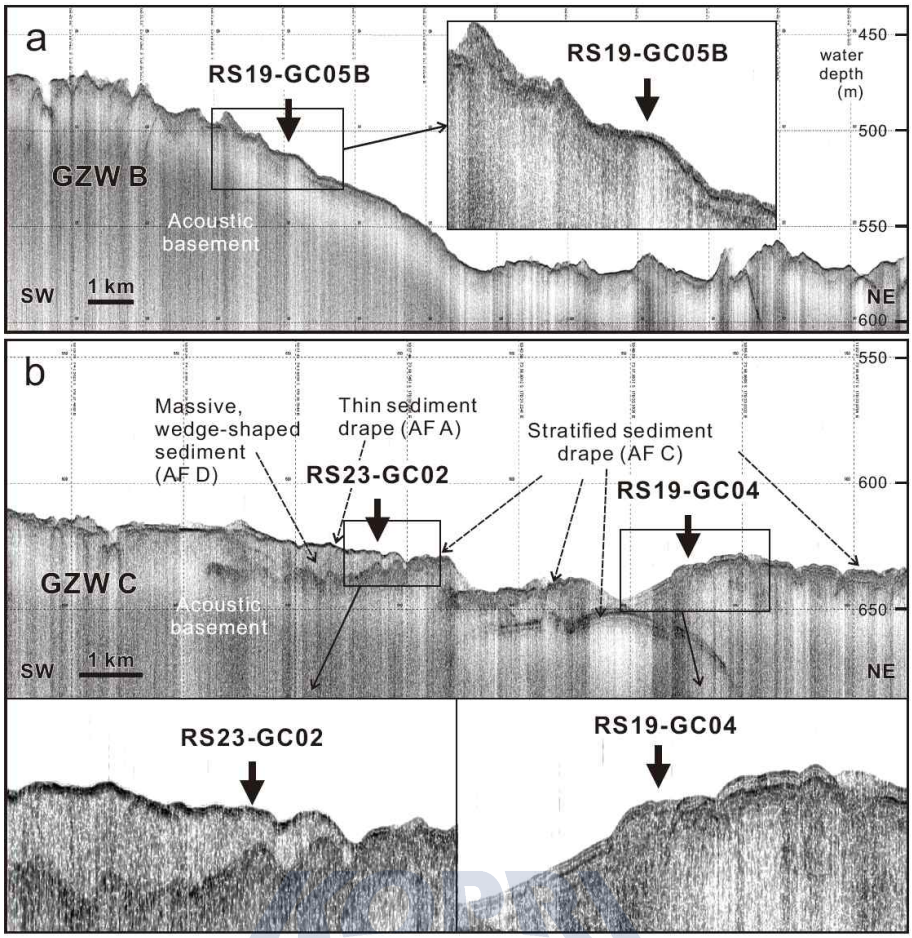


Fig. 3. SBP images around a) GZW B and b) GZW C.

극지연구소

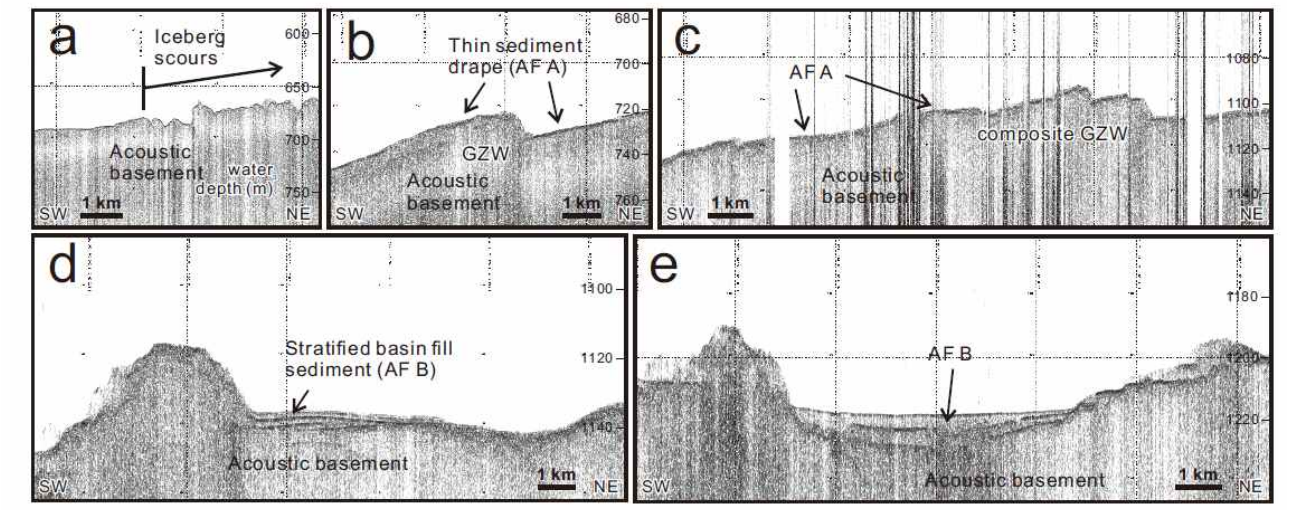


Fig. 4. Selected SBP images showing notable geomorphological and depositional features along the axis of the northern Drygalski Trough. a) Transition from smooth seafloor to iceberg furrow field. b-c) Small GZWs in south of GZW C. d-e) Transect of small-scale elongated basins with stratified sediments.

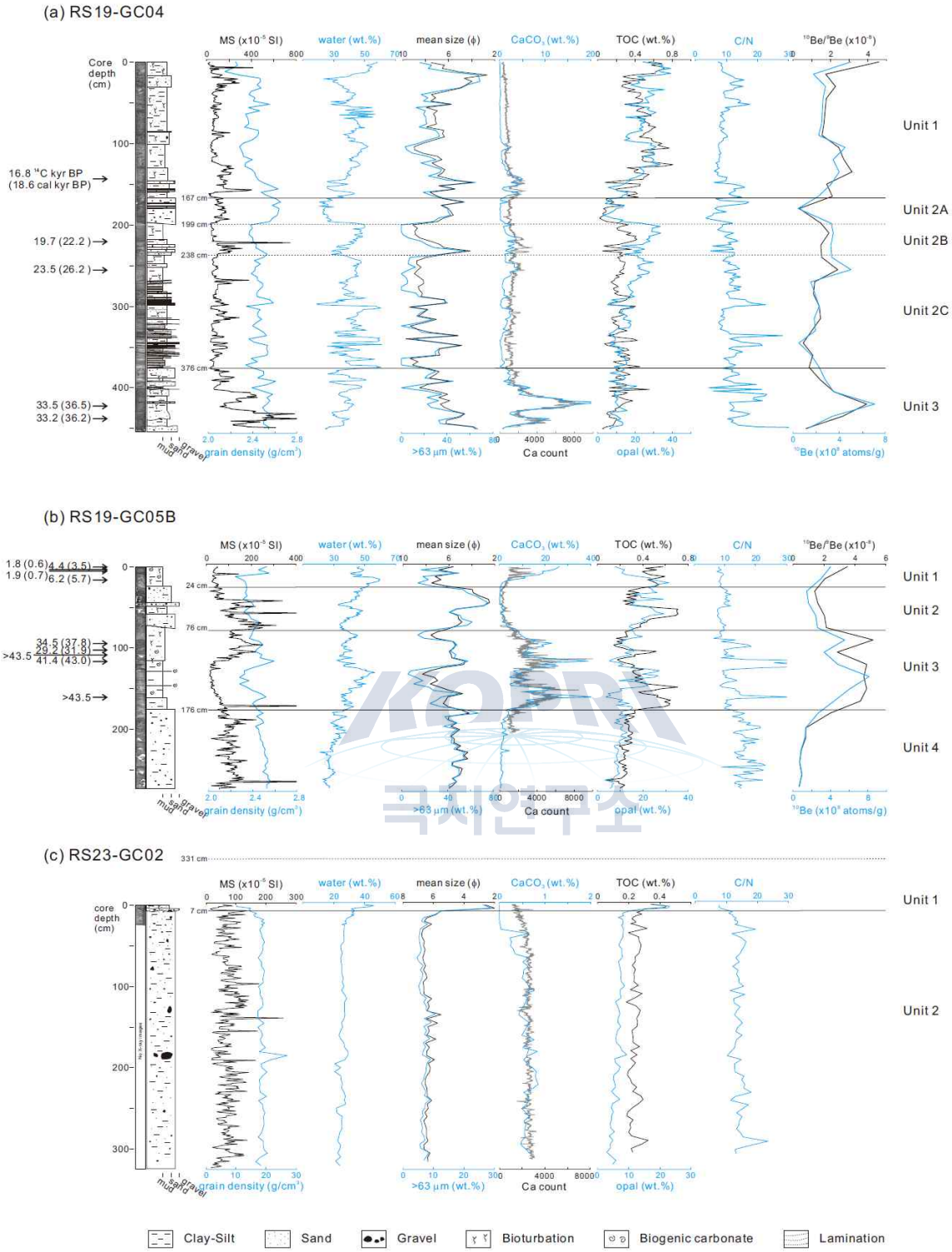


Fig. 5. Down-core variations in magnetic susceptibility (MS), grain density, water content, mean grain size, sand and gravel content (>63 m), carbonate content (CaCO3), XRF core scan Ca count, total organic carbon (TOC) content, opal content, TOC/total nitrogen ratio (C/N), 10Be/9Be ratio, and 10Be concentration of cores (a) RS19-GC04, (b) RS19-GC05B and (c) RS23-GC02, with X-radiograph images and core log. Shown in the left are conventional radiocarbon ages (and calibrated ages) for foraminifera samples.

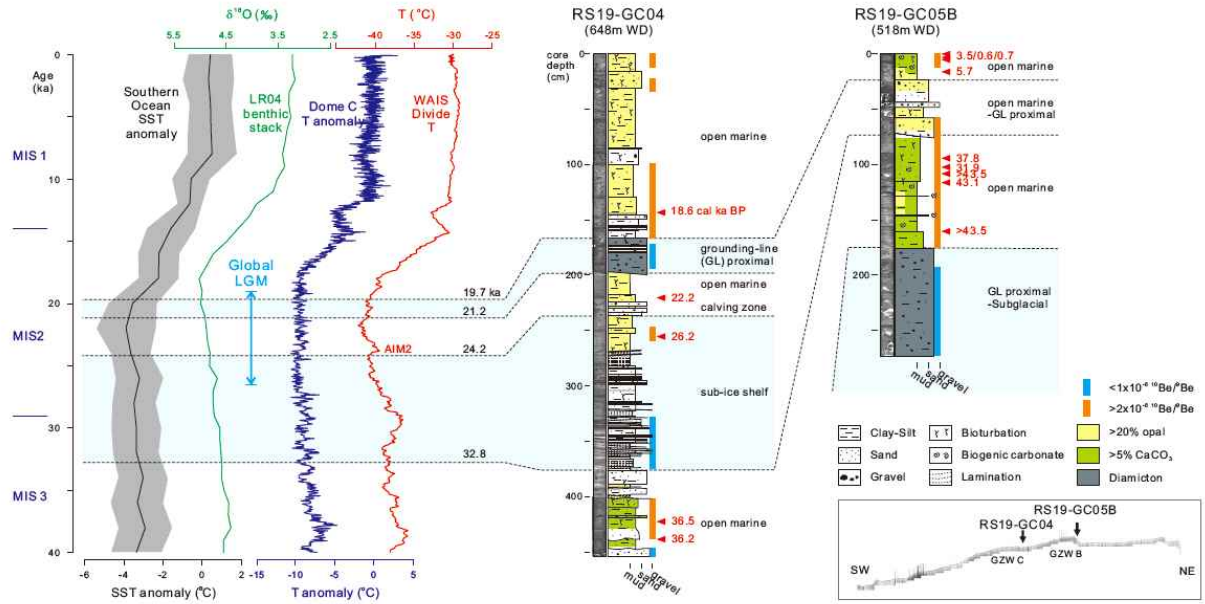


Fig. 6. Correlation of cores RS19-GC04 and RS19-GC05 with Southern Ocean mean annual sea surface temperature (95% confidence interval in gray shade, Chandler and Langebroek, 2021), LR04 benthic stack (Lisiecki and Raymo, 2005), Dome C temperature anomaly (Jouzel et al., 2007), and WAIS Divide surface temperature (Reconstruction Eq. 2 of Cuffey et al., 2016). Global LGM range from Clark et al. (2009). Depositional rates between dated depths of RS19-GC04 were assumed to be linear.

KOPRI 극지연구소

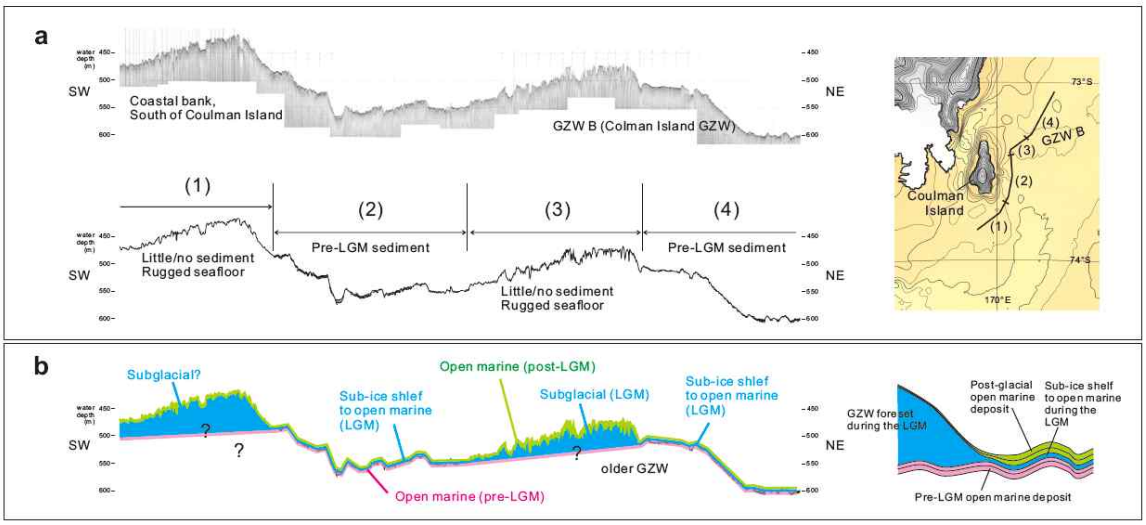


Fig. 7. (a) SBP image showing the NE-SW bathymetric profile and distribution of pre-LGM sediment in the east of Coulman Island. (b) Interpretation diagram of the SBP record showing sediment distribution and depositional environments since the penultimate glaciation.

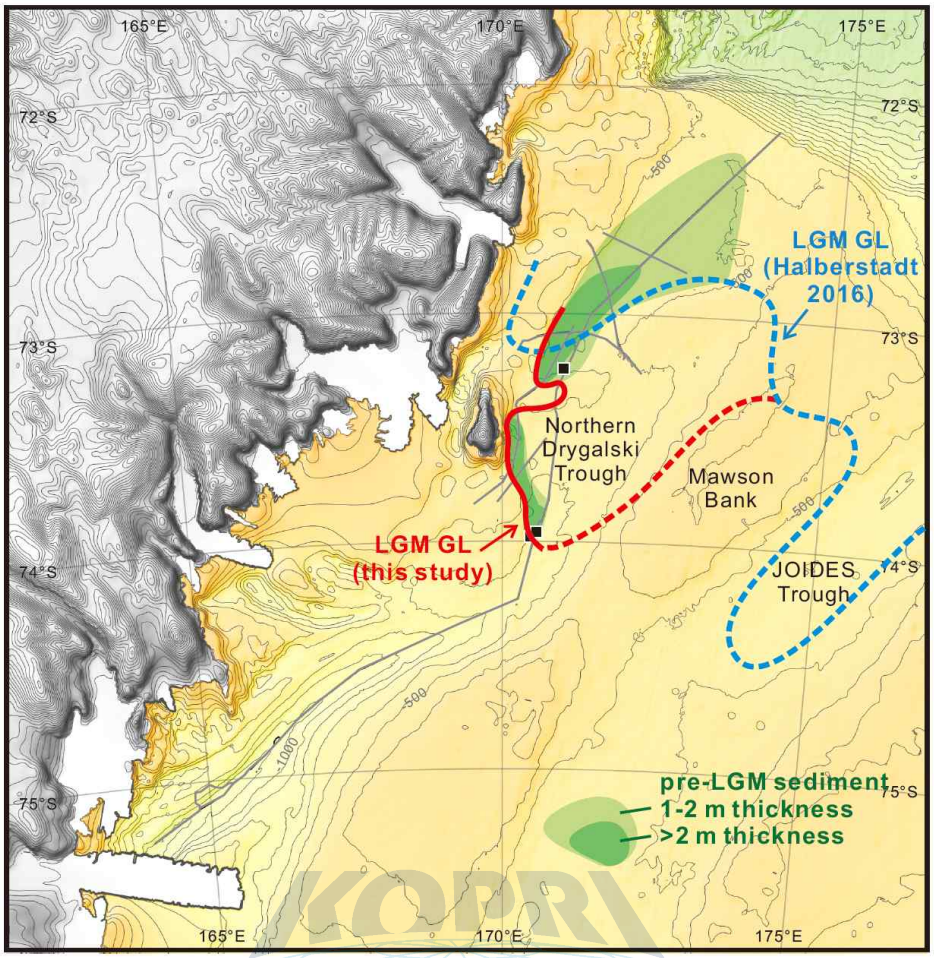
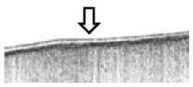
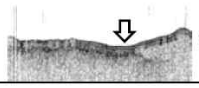
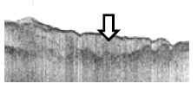


Fig. 8. Distribution of pre-LGM stratified sediment in the northern Drygalski Trough and suggested grounding line position in the NW Ross Sea during the LGM. Filled squares indicate the location of sediment cores.

Table 1. Conventional radiocarbon, corrected and calibrated ages analyzed on carbonate and acid-insoluble organic matter (AIO) samples from the northern Drygalski Trough. Stable isotopic ratios, local contamination offset (LCO), and R are also shown. R for glacial high depletion scenario (GS) (RGS) were determined by a calculation suggested by Heaton et al. (2023).

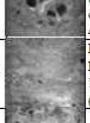
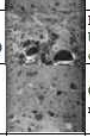
Core ID and sample depth	Dating material	Conventional radiocarbon age (^{14}C yr BP, 1σ)	δ^{13}C (‰)	δ^{18}O (‰)	LCO (yr)	LCO-corrected age (^{14}C yr BP)	ΔR (yr)	Calibrated age, median probability (cal yr BP)	Calibrated age interval (cal yr BP, 95.4%)	ΔR^{GS} (yr)	Calibrated age for GS, median probability (cal yr BP)	Calibrated age interval for GS (cal yr BP, 95.4%)	Calibrated age interval, combined (cal yr BP)	Lab number
RS19-BC04 (box core), 0-1 cm	AIO	2910 ± 30	-24.5	-	1738	1172	622 ± 172	-	-	-	-	-	-	Beta-535615
RS19-GC04, 40-41 cm	AIO	17950 ± 60	-25.2	-	1738	16212	622 ± 172	18039	[17546, 18555]	-	-	-	[17546, 18555]	Beta-581956
RS19-GC04, 80-81cm	AIO	17700 ± 50	-24.9	-	1738	15962	622 ± 172	17747	[17270, 18197]	-	-	-	[17270, 18197]	Beta-581957
RS19-GC04, 121-122 cm	AIO	16850 ± 50	-25.8	-	1738	15112	622 ± 172	16705	[16202, 17188]	-	-	-	[16202, 17188]	Beta-581958
RS19-GC04, 142-145 cm	Benthic foraminifera	16780 ± 50	0.5	5.2	-	-	622 ± 172	18648	[18207, 19069]	-	-	-	[18207, 19069]	Beta-587255
RS19-GC04, 200-201 cm	AIO	26100 ±110	-24.3	-	1738	24362	622 ± 172	27128	[26643, 27580]	1082 ± 172	26665	[26181, 27137]	[26181, 27580]	Beta-581959
RS19-GC04, 217-224 cm	Benthic foraminifera	19730 ± 60	-2.7	3.6	-	-	622 ± 172	22185	[21726, 22649]	1082 ± 172	21654	[21110, 22140]	[21110, 22649]	Beta-592505
RS19-GC04, 220-221 cm	AIO	24800 ±100	-24.5	-	1738	23062	622 ± 172	25808	[25361, 26263]	1082 ± 172	25372	[24912, 25801]	[24912, 26263]	Beta-581960
RS19-GC04, 254-257 cm	Benthic foraminifera	23480 ± 80	-2.8	3.4	-	-	622 ± 172	26203	[25801, 26742]	1082 ± 172	25768	[25307, 26214]	[25307, 26742]	Beta-592506
RS19-GC04, 421-424 cm	Benthic foraminifera	33480 ± 220	-0.8	4.5	-	-	622 ± 172	36510	[35908, 37192]	1082 ± 172	36012	[35375, 36628]	[35375, 37192]	Beta-587256
RS19-GC04, 438-439 cm	Foraminifera *Globocassidulina* sp.	33180 ± 200	-0.7	5.1	-	-	622 ± 172	36187	[35580, 36803]	1082 ± 172	35716	[35175, 36246]	[35175, 36803]	Beta-581961
RS19-BC05 (box core), 0-1 cm	AIO	3270 ± 30	-25.2	-	2098	1172	622 ± 172	-	-	-	-	-	-	Beta-535616
RS19-GC05B, 0-1 cm	Mixed foraminifera	4370 ± 30	1.5	3.0	-	-	622 ± 172	3519	[3052, 3984]	-	-	-	[3052, 3984]	Beta-564903
RS19-GC05B, 3-4 cm	Bivalvia	1830 ± 30	3.1	4.4	-	-	622 ± 172	625	[282, 969]	-	-	-	[282, 969]	Beta-535624
RS19-GC05B, 5-6 cm	Barnacle *Bathylasma corolliforme*	1870 ± 30	1.7	4.5	-	-	622 ± 172	662	[312, 1010]	-	-	-	[312, 1010]	Beta-535625
RS19-GC05B, 16-17 cm	Mixed foraminifera	6170 ± 30	1.1	3.6	-	-	622 ± 172	5741	[5340, 6153]	-	-	-	[5340, 6153]	Beta-568909
RS19-GC05B, 94-95 cm	Mixed foraminifera, mostly *Globocassidulina* sp.	34490 ± 220	0.1	4.6	-	-	622 ± 172	37838	[37006, 38735]	1084 ± 172	37162	[36394, 38047]	[36394, 38735]	Beta-564905
RS19-GC05B, 102-103 cm	Barnacle *Bathylasma corolliforme*	29230 ± 140	-1.1	4.0	-	-	622 ± 172	31850	[31273, 32637]	1084 ± 172	31356	[30972, 31808]	[30972, 32637]	Beta-535626
RS19-GC05B, 108-109 cm	Shell fragment	> 43500	-4.9	3.5	-	-	622 ± 172	-	-	-	-	-	-	Beta-535627
RS19-GC05B, 116-117 cm	Mixed foraminifera, mostly *Globocassidulina* sp.	41350 ± 520	0.1	4.3	-	-	622 ± 172	43071	[42393, 43985]	1084 ± 172	42751	[42154,43645]	[42154, 43985]	Beta-564906
RS19-GC05B, 160-161 cm	Mixed foraminifera, mostly *Globocassidulina* sp.	> 43500	-0.6	4.4	-	-	622 ± 172	-	-	-	-	-	-	Beta-568910

Table 2. Acoustic facies of the northern Drygalski Trough sediments and their characteristics.

Acoustic facies (AF) ID	Acoustic profile	Thickness	Internal characteristics	Outer geometry	Occurrence	Interpretation
AF A		0-3 m	Structureless (transparent), or too thin to identify internal structure	Continuous sheet drape.	Uppermost strata (surface sediment). Common along the axis of the NDT. Thicker at deeper depths (>800 m). Bearly identifiable at shallower depths.	Holocene suspension-settling deposit
AF B		0-15 m	Stratified, parallel to sub-parallel	Elongated tapering wedge (Fig. 4d) or laterally elongated basin fill (Fig. 4e).	North of mound-shaped highs. Along the NDT axis, close to the Drygalski Ice Tongue.	Mixture of gravity flow and suspension-settling deposit under grounding line proximal environment
AF C		0-4 m	Stratified, parallel to sub-parallel	Parallel to convergent sheet drape.	Along the western part of the northern Drygalski Trough, latitude between 72.5 and 74 °S.	Suspension-settling deposit under grounding line proximal to distal, sub-ice shelf condition
AF D		0-18 m	Massive	Wedge (maximum depth ~18 m, width ~3 km), pinching out northward	Drygalski Trough at ~74 °S (north of GZW C) Overlying acoustic facies C, underlain by acoustic facies A	Grounding line proximal gravity flow deposit
Acoustic basement			Massive, chaotic	High amplitude boundaries. Showing a variety of boundary shapes, e.g., smooth and even, wedge-shaped, mound-shaped, and furrowed.	Acoustic basement	Probably composed of subglacial tills. Bounday shape reflecting submarine glacial landforms, e.g., glacially-eroded surface, grounding zone wedges, moraine ridges, and iceberg ploghmarks.

KOPRI 극지연구소

Table 3. Lithological units of cores RS19-GC04, RS19-GC05, and RS23-GC02, and their sedimentological characteristics, proxy data, and depositional environments.

Core name	Unit	Core depth (cmbsf)	Representative sedimentary facies	X-ray image (width=8 cm)	Sedimentological properties: lithology, sediment characteristics, and mean content (range) of gravel(G)- and sand(S)-sized particles in wt.%.	Physical properties, mean values (range): magnetic susceptibility (MS, SI 10^{-6}), water content (WC, wt.%), grain density (g/cm^3)	Biogeochemial properties, mean values (range): TOC (wt.%), TOC/TN (C/N), $CaCO_3$ (wt.%), opal (wt.%), $^{10}Be/^{9}Be$ (Be, x10^{-8})	Sedimentary environment and depositional process
RS19-GC04	1	0-146	dM (diatomaceous mud)		Diatom-bearing to diatom-rich, (slightly gravelly) sandy mud. Diatom-bearing gravelly muddy sand at 15-31 cm. Bioturbated. Light olive gray to grayish green. G 3 (0-27), S 26 (3-65)	MS 96 (13-416), WC 44 (22-61), density 2.37 (2.15-2.55)	TOC 0.51 (0.26-0.81), C/N 9 (6-18), CaCO3 0.6 (0.0-5.1), opal 26 (15-39), Be 2.4 (1.5-4.6)	Open marine. Suspension settling of biogenic and terrigenous particles, including ice-rafted materials.
		146-167	gsM/dM (Interbedded gravelly sandy mud/diatomaceous mud)		Interbedded gravelly sandy mud/diatom-bearing sandy mud. Crudely-stratified. Layering disturbed by bioturbation. Grayish green. G 3 (0-8), S 35 (19-57)	MS 146 (19-404), WC 33 (24-45), density 2.54 (2.48-2.63)	TOC 0.32 (0.08-0.45), C/N 12 (6-16), $CaCO_3$ 2.5 (0.6-4.3), opal 13 (6-17), Be 1.9 (1.8-2.0)	Transitional from GL-proximal to open marine with ice retreat. Rainout of debris and suspension settling.
	2A	167-199	D (diamicton)		Clast-poor muddy diamicton. Massive to crudely-stratified. Grayish green. G 3 (1-5), S 36 (25-51)	MS 123 (42-207), WC 25 (19-44), density 2.61 (2.58-2.65)	TOC 0.11 (0.02-0.28), C/N 9 (3-17), $CaCO_3$ 0.4 (0.1-1.9), opal 10 (4-23), Be 0.9 (0.3-1.5)	GL-proximal. Glacigenic debris flow, rainout of debris
	2B	199-223	dM (diatomaceous mud)		Diatom-rich mud and sandy mud. Bioturbated. Grayish green. G 1 (0-5), S 3 (0-13)	MS 52 (32-93), WC 48 (40-52), density 2.39 (2.37-2.41)	TOC 0.32 (0.21-0.42), C/N 10 (7-14), $CaCO_3$ 2.1 (0.8-3.7), opal 29 (26-34), Be 1.9	Open marine. Suspension settling of biogenic and terrigenous particles, including ice-rafted materials.
		223-238	gmS/gsM (Interbedded gravelly muddy sand-gravelly sandy mud)		Gravelly muddy sand interbedded by slightly gravelly sandy mud. Crudely stratified. Diatom-bearing. Grayish green. G 7 (1-11), S 32 (20-45)	MS 193 (90-746), WC 35 (28-43), density 2.47 (2.43-2.53)	TOC 0.20 (0.05-0.36), C/N 10 (5-13), $CaCO_3$ 2.2 (1.1-3.2), opal 20 (13-25), Be 1.5	Calving line. Rainout of debris and suspension settling.
	2C	238-267	dM (diatomaceous mud)		Diatom-bearing to diatom-rich mud and clay. Bioturbated. Grayish green. G 0 (0-0), S 6 (0-12)	MS 71 (48-103), WC 45 (38-49), density 2.44 (2.39-2.50)	TOC 0.25 (0.18-0.29), C/N 12 (9-15), $CaCO_3$ 2.3 (1.2-4.1), opal 24 (21-30), Be 2.0 (1.5-2.4)	Sub-ice shelf, close to calving line. Suspension settling of biogenic and terrigenous particles.
		267-283	lM (laminated mud)		Parallel-laminated mud. Grayish Green. G 0 (0-0), S 3 (0-5)	MS 128 (73-378), WC 38 (33-41), density 2.47 (2.45-2.49)	TOC 0.18 (0.14-0.22), C/N 12 (11-15), $CaCO_3$ 0.8 (0.6-1.0), opal 18 (16-21)	Sub-ice shelf. GL distal. Suspension settling from sediment plumes originating from the GL.
		283-322	gsM/C (Interstratified gravelly sandy mud-clay)		Interstratified slightly gravelly sandy mud and clay layers. Parallel bedding/lamination. Diatom-bearing. Grayish Green. G 1 (0-4), S 20 (7-39)	MS 110 (38-293), WC 43 (17-64), density 2.46 (2.34-2.59)	TOC 0.24 (0.13-0.41), C/N 11 (7-23), $CaCO_3$ 1.3 (0.2-2.5), opal 14 (6-20), Be 1.3 (1.1-1.4)	
		322-331	lC (laminated clay/mud)		Parallel-laminated clay and sandy mud. Grayish green. G 1 (0-1), S 6 (0-12)	MS 50 (44-66), WC 46 (40-53), density 2.43 (2.40-2.45)	TOC 0.24 (0.19-0.31), C/N 9 (8-10), $CaCO_3$ 1.3 (0.8-1.8), opal 15 (10-18), Be 1.0	
		331-362	gsM/mS/C (Interstratified gravelly sandy mud-muddy sand-clay)		Interstratified slightly gravelly sandy mud, slightly gravelly muddy sand, and clay layers. Parallel to low-angle cross bedding. G 1 (0-3), S 30 (10-49)	MS 98 (35-189), WC 42 (25-64), density 2.49 (2.37-2.54)	TOC 0.24 (0.07-0.43), C/N 15 (11-28), $CaCO_3$ 0.4 (0.0-0.9), opal 10 (6-14), Be 0.8 (0.4-1.0)	
		362-376	lC (laminated clay/mud)		Interstratified dark olive clay and greenish gray mud layers. Lack of sand- and gravel-sized particles. Parallel to low-angle cross-stratification. Low bioturbation at 364.5-366.5 cm. Micro-faulted (normal). G 0 (0-0), S 0 (0-0)	MS 60 (32-87), WC 48 (38-64), density 2.39 (2.34-2.44)	TOC 0.30 (0.17-0.45), C/N 11 (9-13), $CaCO_3$ 0.7 (0.1-1.1), opal 14 (9-16), Be 0.8	
	3	376-398	(g)sM (slightly gravelly sandy mud)		Slightly gravelly sandy mud and intercalated mud. Bioturbated. G 1 (0-4), S 25 (16-45)	MS 128 (34-250), WC 38 (25-53), density 2.50 (2.41-2.61)	TOC 0.24 (0.92-0.34), C/N 12 (9-20), $CaCO_3$ 1.9 (0.9-2.6), opal 12 (6-15), Be 1.4	Transition from open marine to sub-ice shelf
		398-402	dlC (diatomaceous laminated clay)		Trough cross-laminated clay. Diatom-bearing to diatom-rich. G 0, S 0	MS 76 (65-91), WC 49 (46-50), density 2.39	TOC 0.21 (0.12-0.30), C/N 8 (4-11), $CaCO_3$ 6.0 (5-8), opal 20 (18-21)	Open marine. Suspension settling
		402-447	cM (carbonate-bearing mud)		dm-scale bioturbated sandy mud to muddy sand layers. Dark greenish gray to dark gray. Containing biogenic carbonates. Gravel-layer at 417-419 cm. Fining-upward bed with erosional base at 419-440 cm. G 1 (0-5), S 33 (21-51)	MS 354 (69-880), WC 37 (28-44), density 2.53 (2.50-2.58)	TOC 0.22 (0.10-0.56), C/N 15 (6-23), $CaCO_3$ 8.5 (2.2-23.7), opal 11 (7-16), Be 2.9 (2.3-3.9)	Open marine. Biogenic carbonate production, suspension settling of detritus including IRD, reworking by bottom current
		447-452	(g)mS (slightly gravelly muddy sand)		Slightly gravelly muddy sand to sandy mud. Tephra-rich. Drak gray. G 3 (0-5), S 63 (59-68)	MS 441 (336-618), WC 25 (23-26), density 2.55 (2.54-2.55)	TOC 0.08 (0.05-0.09), C/N 33 (20-51), $CaCO_3$ 1.1 (0.7-1.4), opal 8 (7-9), Be 0.7	High input of volcanogenic material
RS15-GC05B	1	0-13	cM (carbonate-bearing mud)		Biogenic carbonate- and diatom-bearing sandy mud. Bioturbated. Light olive brown. G 1 (0-2), S 31 (17-50)	MS 46 (27-144), WC 46 (41-49), density 2.44 (2.24-2.55)	TOC 0.49 (0.40-0.59), C/N 9 (8-10), $CaCO_3$ 20.1 (10.4-26.1), opal 12 (8-18), Be 3.5	Open marine. Biogenic carbonate production, suspension settling.
		13-24	dM (diatomaceous mud)		Diatom-rich slightly gravelly sandy mud. Bioturbated. Light olive brown. G 5 (1-9), S 16 (13-14)	MS 37 (25-55), WC 56 (51-60), density 2.33 (2.32-2.34)	TOC 0.50 (0.44-0.54), C/N 9 (8-9), $CaCO_3$ 4.4 (0.9-11.3), opal 26 (23-31), Be 2.1	Open marine. Suspension settling of biogenic and terrigenous particles, including ice-rafted materials.
	2	24-48	gsM/gmS (Interbedded gravelly sandy mud-gravelly muddy sand)		Diatom-bearing gravelly mud to gravelly muddy sand. Crudely stratified. Light olive. G 12 (7-20), S 46 (21-61)	MS 89 (16-340), WC 44 (33-52), density 2.35 (2.31-2.39)	TOC 0.32 (0.22-0.51), C/N 10 (8-12), $CaCO_3$ 0.2 (0.0-0.6), opal 21 (15-29), Be 1.5 (1.4-1.6)	Open marine. Suspension settling.
		48-58	dM (diatomaceous mud)		Diatom-bearing slightly gravelly sandy mud. Bioturbated. Light olive. G 4 (0-8), S 50 (41-64)	MS 153 (63-441), WC 44 (37-49), density 2.36 (2.32-2.41)	TOC 0.59 (0.36-0.71), C/N 9 (8-12), $CaCO_3$ 1.4 (0.8-1.8), opal 23 (16-26)	Open marine. Suspension settling of biogenic and terrigenous particles, including ice-rafted materials.
		58-76	gmS (gravelly muddy sand)		Diatom-bearing slightly gravelly muddy sand (modified diamicton?). Bioturbated at 58-66 cm. Massive at 66-76 cm. Light olive. G 2 (1-4), S 53 (47-59)	MS 171 (83-312), WC 38 (34-47), density 2.42 (2.37-2.46)	TOC 0.50 (0.38-0.71), C/N 9 (8-10), $CaCO_3$ 2.1 (0.5-4.3), opal 20 (14-29), Be 2.1 (2.0-2.2)	Open marine-GL proximal
	3	76-176	cM (carbonate-bearing mud)		Biogenic carbonate-bearing sandy mud. Bioturbated. Carbonate sand layers at 129 and 146 cm. Grayish blue green to light olive. G 1 (0-5), S 30 (5-56)	MS 86 (14-517), WC 41 (32-57), density 2.42 (2.28-2.59)	TOC 0.37 (0.14-0.71), C/N 14 (6-53), $CaCO_3$ 14.6 (4.4-40.7), opal 14 (4-27), Be 4.4 (2.9-5.2)	Open marine. Biogenic carbonate production, suspension settling of detritus including IRD, some reworking by bottom current
	4	176-183	gmS (gravelly muddy sand)		Gravelly muddy sand. Crudely stratified. Greenish gray. G 4 (1-6), S 58 (55-61)	MS 79 (48-102), WC 32 (29-37), density 2.47 (2.45-2.49)	TOC 0.31 (0.24-0.33), C/N 14 (13-17), $CaCO_3$ 3.6 (2.5-4.0), opal 11 (9-14), Be 2.4	Transitional from GL-proximal to open marine
		183-273	D (Diamicton)		Muddy diamicton. Greenish gray. Massive. G 6 (1-13), S 40 (28-47)	MS 111 (22-546), WC 29 (21-38), density 2.50 (2.43-2.56)	TOC 0.24 (0.08-0.32), C/N 17 (9-23), $CaCO_3$ 1.3 (0.2-4.4), opal 9 (3-13), Be 0.6 (0.4-0.8)	GL-proximal to subglacial
RS23-GC02	1	0-7	dS (diatomaceous sand)		Diatom-bearing gravelly muddy sand, bioturbated, light olive gray. Gravels at 3-7 cm. G 18 (17-18), S 57 (55-59)	MS 41 (13-89), WC 38 (31-46), density 2.50 (2.50-2.50)	TOC 0.38 (0.30-0.44), C/N 8 (8-10), $CaCO_3$ 0.0 (0.0-0.0), opal 19 (13-23)	Open marine. Suspension settling of biogenic and terrigenous particles, including ice-rafted materials.
	2	7-324	D (diamicton)		Clast-poor muddy diamicton. Massive; medium gray. G 2 (0-12), S 32 (27-40)	MS 72 (17-259), WC 26 (21-34), density 2.59 (2.55-2.67)	TOC 0.24 (0.19-0.33), C/N 14 (10-23), $CaCO_3$ 0.5 (0.0-0.9) opal 7 (3-10)	Proglacial GL proximal. Gravity flow deposit.

제 18 장

Hunting paleoceanographic archives of ice sheet–ocean interaction in the northwestern Ross Sea, Antarctica[11)]

Sookwan Kim[1*], Laura De Santis[2], Jong Kuk Hong[3], Ester Colizza[4], Sunghan Kim[3], Andrea Bergamasco[5], Sang-Hoon Lee[1], Seung-Goo Kang[3], Min Kyung Lee[3], Hyoungjun Kim[3], Yeonjin Choi[3], Andrea Geniram[4], Hyoung Gyu Choi[3], Jae Il Lee[3], Kyu-Cheul Yoo[3] and Yongcheol Park[3]

[1]Korea Institute of Ocean Science and Technology, Busan, Republic of Korea,
[2]National Institute of Oceanography and Applied Geophysics-OGS, Trieste, Italy,
[3]Korea Polar Research Institute, Incheon, Republic of Korea,
[4]Department of Mathematics and Geosciences, University of Trieste, Trieste, Italy,
[5]Institute of Marine Sciences-National Research Council, Venice, Italy

KOPRI 극지연구소

Abstract. The analysis of sedimentary deposits influenced by bottom currents in glaciated continental margins provides crucial insights into paleo-depositional and oceanographic conditions. These reconstructions enable the assessment of interactions between advance and retreat of grounded ice sheets and past ocean circulation patterns. However, questions regarding these interactions and their specific mechanisms remain largely unanswered due to a lack of data in this remote area. In this study, we conducted a comprehensive analysis by integrating marine geophysical data, surficial sediment cores, oceanographic measurements, and ocean circulation models. Our aim was to understand spatial and temporal variations in sedimentary and oceanographic conditions during the past glacial and interglacial periods in combination with the longterm stratigraphic evolution. By integrating and cross-referencing diverse datasets, we were able to infer how bottom-current-controlled deposits (i.e., contourites) developed along the western bathymetric high of the Central Basin in the northwestern Ross Sea margin, Antarctica. Contouritic deposits lying over and along the flanks of bathymetric highs were identified through their

11) 이 연구 결과는 다음의 논문으로 출판되었음: Khim, S. et al. (2023). "Hunting paleoceanographic archives of ice sheet-ocean interaction in the northwestern Ross Sea, Antarctica" Frontiers in Earth Science 11:1234347.

mound-shaped external geometry and acoustically stratified facies, characterized by reflectors pinching toward the moat. Acoustic facies and multi-beam backscatter results, in conjunction with sedimentary core data, revealed contrasting patterns. Bathymetric highs exhibited thin (<10m thick) coarsergrained sedimentary layers with higher backscatter, while the lower slope and rise displayed thick (>10m thick), finer-grained stratified sediments with lower backscatter. These findings indicate that seabed winnowing occurred by stronbottom current during past glacial periods as supported by sedimentological analysis. The pathways of the westward-deflected dense shelf water outflow and the westward-flowing along-slope current, as simulated by oceanographic models, explain the distinctive development of contourites influenced by bottomcurrent processes. Moreover, the large accumulations of sediment in the contourites, resulting from bathymetric barriers in the north of the Central Basin, may contribute to submarine slope failures.

1. Main

The glaciated continental margins display geomorphic and sedimentary features that contain invaluable records, shedding light on variations in intensity and shifts in the locations of ocean bottom currents influenced by ice sheet dynamics (Rebesco et al., 1996; Dowdeswell et al., 2006; Uenzelmann-Neben, 2006; 2018; Pérez et al., 2015; Lasabuda et al., 2018; Le Heron et al., 2019; Rydningen et al., 2020; Mosher and Boggild, 2021; Bjordal-Olsen et al., 2023). Among these regions, the Ross Sea continental margin, positioned between East and West Antarctica, has evolved stratigraphically and geomorphologically over a long duration, shaped by the Antarctic Ice Sheet since the earliest Oligocene (Brancolini et al., 1995; De Santis et al., 1995; 1999; Bart and De Santis, 2012; Anderson et al., 2014; Halberstadt et al., 2016; McKay et al., 2016; Bart et al., 2017). The Ross Sea plays a significant role in global ocean circulation by contributing cold and dense shelf water (DSW) through its outflow (Jacobs et al., 1970; Bergamasco et al., 2002; Budillon et al., 2002; 2011; Rivaro et al., 2003; Orsi and Wiederwohl, 2009). Additionally, the influx of warm Circumpolar Deep Water (CDW) and the westward-flowing Antarctic Slope Current (ASC) have been observed at the outer Ross Sea continental margin (Gordon et al., 2009; 2015; Smith et al., 2012; Carter et al., 2022) (Figure 1). Given the close association between cryospheric and paleoceanographic changes in polar continental margins (Kennett, 1977; Uenzelmann-Neben and Gohl, 2012; Huang et al., 2014; Hochmuth et al., 2020; Kim et al., 2020), the outer continental margin of the Ross Sea is a key area for reconstructing the evolution of oceanographic and depositional conditions during the late Cenozoic, characterized by repeated ice-sheet advances and retreats. Despite the Ross Sea having a

crucial influence on global ocean circulation through ocean–cryosphere interactions, our understanding of bottom-current-controlled sedimentary deposits (i.e., contourites) and the associated environmental conditions remains insufficient due to data limitations. Previous seismostratigraphic studies in the Ross Sea embayment revealed the acoustic basement structure and stratal geometry affected by subglacial processes of grounded ice sheets, using single and multi-channel seismic (SCS and MCS) reflection profiles (Anderson and Bartek, 1992; Brancolini et al., 1995; De Santis et al., 1995; 1999; Bart and De Santis, 2012). However, recent acquisitions of SCS/MCS data and scientific drilling results (Granot et al., 2010; Gordon et al., 2015; Bart et al., 2017; Kim et al., 2018; McKay et al., 2019; Conte et al., 2021; Gales et al., 2021; King et al., 2022) have expanded our seismic coverage to the outer continental shelf, slope, and rise, enabling a better understanding of variations in depositional and oceanographic settings through continuous sedimentary records. Recent sedimentological studies in the northwestern Ross Sea have suggested that sedimentation on the continental slope is controlled by bottom-current activity coupled with DSW export and glacial meltwater pulses (Khim et al., 2021; Torricella et al., 2021; Bollen et al., 2022). Furthermore, strong bottom-current activity during glacial periods has been suggested through coarser sediment recovered from the Iselin Bank, which is an eastern boundary of the Central Basin (Kim et al., 2020). Combining geomorphic and seismostratigraphic mapping results with sediment core data offers valuable insights into spatial variations in modern depositional and oceanographic environments, contourite development, and the reconstruction of past environmental settings (e.g., López-Quirós et al., 2020; Mosher and Boggild, 2021; Rodrigues et al., 2022). Bottom-currentcontrolled sedimentary processes along the continental slope can significantly impact sedimentation rates and slope stability, potentially leading to submarine landslides (Laberg and Camerlenghi, 2008; Miramontes et al., 2018). Therefore, understanding how bottom currents are influenced by climate change is crucial for assessing the potential risk of submarine geohazards (e.g., Gales et al., 2023).

This study focused on the Central Basin in the northwestern Ross Sea and mainly used seismic profiles and morpho-bathymetric data to identify bottom-current-controlled deposits. The primary objective was to understand the sedimentary and geomorphic processes that occurred in the Central Basin during previous glacial-interglacial periods. This investigation included the identification and mapping of acoustic facies of surficial sediments and seafloor morphology within the basin floor and surrounding bathymetric highs. The results of seabed mapping were compared with grain-size and water-content data extracted from sediment cores to validate the geophysical interpretations. Physical oceanographic measurements and ocean circulation models were used to assess the distributions of bottom-current features, the pathway and velocity of DSW cascading, and alongslope bottom currents under recent oceanographic conditions (e.g., Thran et al., 2018). This

research can contribute to our comprehensive understanding of the environmental conditions influencing the interplay between bottom currents and ice sheets in both modern and Quaternary periods, bridging the gap between paleoclimatic, paleo-oceanographic interpretations, and sparsely distributed sediment cores (McKay et al., 2019; Conte et al., 2021; King et al., 2022).

2. Regional setting

2.1 Geological and morphological setting

The Ross Sea continental shelf, which lies between ~70°S and ~78°S latitude and ~160°E and ~150°W longitude (Figure 1), consists of rift basins and half-grabens formed by the West Antarctic Rift System since the Early-mid Cretaceous (Lawver et al., 1992; Davey and Brancolini, 1995). The Joint Oceanographic Institutions for Deep Earth Sampling (JOIDES) Trough and Central Basin in the western Ross Sea were formed by a rifting episode that involved a NE–SW extension of ~100 km, occurring from ~61 to 53 Ma (Cande et al., 2000; Cande and Stock, 2004; Wilson and Luyendyk, 2009). A recent preliminary crustal model by marine gravity and seismic data suggests that the Central Basin was formed by the same extension episode with the JOIDES Trough (Davey et al., 2021). The Central Basin was actively infilled by sediments transported under a temperate climate in the early phase and wet-based glaciers since ~34 Ma (Brancolini et al., 1995). In this study, the target sedimentary units are positioned above the Ross Sea Unconformity (RSU) 4 (middle Miocene, ~14.7 Ma) (Savage and Ciesielski, 1983; Pérez et al., 2021) can be considered as post-rift sedimentary deposits and they developed in a relatively stable tectonic setting according to the tectonic history and stratigraphic evolution of the northwestern Ross Sea (Brancolini et al., 1995; Davey et al., 2021).

The JOIDES Trough, characterized by water depths of 500–600 m in the outer shelf and 600–800 m in the inner shelf, exhibits gently over-deepened (landward dipping) seafloor morphology (Figure 1). The JOIDES Trough is believed to have been one of the main drainage pathways of the East Antarctic Ice Sheet sourced ice feeding into the Ross Sea during the Last Glacial Maximum (LGM) (Anderson and Bartek, 1992; Shipp et al., 1999; Livingstone et al., 2012; Anderson et al., 2014; Harris et al., 2014; Halberstadt et al., 2016) and most of the glaciogenic sediment delivered to the Central Basin (Brancolini et al., 1995; Bart et al., 2000; Kim et al., 2018).

The Central Basin, located beyond the JOIDES Trough, is bounded to the east by the Iselin Bank, to the west by the Hallett Ridge, and to the north by the eastern branch

of the Hallett Ridge named as Bank B (Kim et al., 2018) (Figure 2A). The regional bathymetry data show that a relatively gentle slope extending beyond the western part of JOIDES Trough mouth, characterized by an inclination of ~1.2° within the water depth range of 500–1,400 m. Subsequently, the middle to lower slope exhibits a lesser inclination of ~0.7° within the depth range of 1,400–2000 m. Finally, the Central Basin floor demonstrates a nearly flat topography, with a slight inclination of ~0.2° from 2000 to 2,200 m, representing the lower slope transitioning to the basin floor (Figure 2A). In contrast, the eastern continental slope beyond the JOIDES Trough features a bounding bathymetric high named as Bank A (Kim et al., 2018), which is associated with a steeper gradient ranging ~ 4.1°–6.7° between 1,000 and 1,600 m (Figure 2A). Unlike the deeply incised submarine canyons observed at the Pennell and Glomar Challenger Trough mouths in the eastern Ross Sea (Hillary Canyon) and the western Ross Sea (Bowers Canyon), respectively, the gently sloping area beyond the mouth of the JOIDES Trough does not have any deeply incised submarine canyon (Figures 1, 2A). The Central Basin is connected to the deeper and smaller basin through a narrow gateway, ~30 km wide, referred to informally as the Scott Canyon Basin and the northeastern gap (NE Gap), respectively (Figure 2A). According to the International Bathymetric Chart of the Southern Ocean Version 2 (IBCSO v2; Dorschel et al., 2022), the average water depth reveals a relatively shallow bathymetry in the NE Gap. This area is ~180 m higher than the adjacent Central Basin floor (upper left inset of Figure 2). The Scott Canyon, a deeply incised submarine canyon, extends from the NE Gap to the continental rise in the Scott Canyon Basin floor (Davey, 2004). In contrast to the Bowers and Hillary Canyons, which originate from the shelf edge and upper slope, respectively, the Scott Canyon exhibits unique characteristics in its distinctive positioning within the deeper environment of the continental rise.

2.2 Oceanographic setting

The Antarctic Circumpolar Current (ACC), which is the most prominent oceanographic feature in the Southern Ocean, flows eastward around Antarctica (Whitworth, 1988; Cunningham et al., 2003; Carter et al., 2022) (upper right inset of Figure 1). Located south of the ACC, the Ross Gyre is a clockwise circulation element influenced by the advance and retreat of the Antarctic ice sheets (Kennedy et al., 2015; Carter et al., 2022). The Ross Gyre can entrain the CDW to the Ross Sea outer continental margin (Orsi and Wiederwohl, 2009). The CDW transports heat and salt to the Ross Sea continental margin (Jacobs et al., 2002; Jacobs, 2004). In the Ross Sea, ASC is a bottom water current that is located further south of Ross Gyre. The ASC flows westward along the Antarctic margin slope, driven by the easterly polar winds (Chavanne et al., 2010; Armitage et al., 2018;

Carter et al., 2022).

DSW forms on the continental shelf through brine rejection in the Drygalski and JOIDES Troughs in the western Ross Sea (Jacobs et al., 1985; Budillon et al., 2002; Gordon et al., 2009; 2015; Orsi and Wiederwohl, 2009; Budillon et al., 2011). DSW is also generated by heat loss in the eastern Ross Sea (Bergamasco et al., 2002; Rivaro et al., 2003) (Figure 1). This dense water mixes with surrounding waters and subsequently sinks to the bottom of the ocean, forming Antarctic Bottom Water (AABW) (Orsi and Wiederwohl, 2009).

3. Materials and methods

3.1 Reflection seismic data

A total of 5,400 L-km of sub-bottom profiler (SBP) data were acquired in the Central Basin region using the Kongsberg SBP120 system during three separate R/V Araon Antarctic Expeditions – ANA03B, ANA05B, and ANA09C – conducted in the years 2013, 2015, and 2019, respectively (Figure 2B). The SBP data were simultaneously recorded together with MCS surveys and during transits at variable ship speeds from 5 to 12 knots. The SBP data have a lateral sampling interval of ~2.6 m when the ship was travelling at 5 knots and with a ping rate of 1 s. A chirp pulse with a linearly swept frequency was used, with a frequency range of 2.5–7.0 kHz and a pulse length of 20 ms. This configuration allowed for a maximum vertical resolution of about 0.3 ms, equivalent to ~ 23 cm at a sound speed of 1,500 m/s. The depth of penetration of SBP signal varies depending on the subsurface characteristics, such as lithology and physical properties. In most cases, it ranges from tens of meters to less than 100 m.

The original data recorded in the Topas Raw format were converted to the SEG-Y format to enable conventional seismic data processing. This processing included gain correction, delay time-shifting, and signal enveloping. These tasks were performed using the Seismic Unix software (https://wiki.seismic-unix.org).

During the ANA09C expedition in 2019, a basin-crossing MCS profile, ANA09C-MCS-01, was acquired to fill a gap in the existing MCS grid in the Central Basin (Figure 2B). The MCS data were acquired using eight airguns, specifically the Sercel G-Gun II, which had a combined volume of 1,200 in3 and operated at a working pressure of 2000 psi. To ensure appropriate data coverage, the shot point interval was set at 50 m. A 1.5 km-long 120-channel solid-type streamer (Sercel Sentinel) was towed at a depth of 6 m below sea level during the MCS data acquisition. The MCS data were recorded with a length of 10 s and a sampling rate of 1 ms. Considering the shot interval and streamer geometry, each common mid-point (CMP) gather in the dataset provided a 15-fold coverage

and featured a CMP spacing of 6.25 m.

The ANA09C MCS data underwent a standard seismic data processing workflow, using Schlumberger OMEGA 2017 software, which included deconvolution, trace editing, multiple attenuations, velocity analysis, and Kirchhoff pre-stack time migration. The resulting processed seismic profiles from ANA09C were combined with the existing MCS datasets (KSL12 in 2013 and KSL14 in 2015) sourced from the Korea Polar Data Center (KPDC, https://kpdc.kopri.re.kr) of the Korea Polar Research Institute (KOPRI) and legacy seismic data from the Antarctic Seismic Data Library System (SDLS, https://sdls.ogs.trieste.it). This compilation of the seismic dataset allowed the extension of previous seismic stratigraphic interpretations in the northwestern Ross Sea outer continental margin (Brancolini et al., 1995; Granot et al., 2010; Kim et al., 2018) into the ANA09C MCS data in the Central Basin region.

The processed SBP and MCS data were imported into Schlumberger Petrel software for seismic stratigraphic interpretation and seismic facies mapping. The acoustic facies of the subsurface sediments, as delineated by the SBP data, were classified into two distinct types (Table 1): acoustically stratified (Facies S) and acoustically transparent (Facies T). This classification was based on an analysis of their internal configuration, external geometry, stacking patterns, and stratigraphic relationships (Veeken and van Moerkerken, 2013). The thickness of Facies S and Facies T for creating the isopach map was determined based on the penetration depth of the SBP data, which is influenced by the seabed morphology and geological conditions. Facies S can be further subdivided into two sub-types, namely, Facies Sh and Sw, based on the resolvable thickness, as outlined in Table 1. The resolvable depth of the SBP data provide a crucial information about the physical characteristics of the seafloor and the subsurface sedimentary layers, such as seafloor roughness (smooth vs. undulated), grain-size composition (finer vs. coarser), and sediment compaction (soft vs. hard) (e.g., Neto et al., 2013; Kim et al., 2021). Therefore, the thickness and distribution of these facies were mapped to show their spatial variability within the Central Basin and along the surrounding bathymetric highs.

3.1.1 Seismic stratigraphic framework

The seismostratigraphic unit boundaries of RSU4 (~14.7 Ma), RSU3-CB (~5.5–8.5 or ~10.5 Ma), and RSU2 (~2.8–4.0 or ~2.0 Ma) delineated in previous seismic stratigraphy and sediment core studies conducted on the western Ross Sea continental margin (Savage and Ciesielski, 1983; Brancolini et al., 1995; Granot et al., 2010; Bart et al., 2011; Kim et al., 2018; McKay et al., 2019; Pérez et al., 2021) were extended to the ANA09C-MCS-01 profile (Figure 3A). RSU1-CB (~0.7 Ma) cannot be correlated with deeper

sedimentary layers due to its termination and merging with the seafloor reflection at the upper-mid slope beyond the JOIDES Trough mouth (Kim et al., 2018). However, establishing accurate correlations between the basin and bathymetric highs proved challenging. Therefore, the major unit boundaries were tentatively determined in the sedimentary deposits on the basement highs of the Hallett Ridge and western Iselin Bank, with consideration given to recent drilling results and seismostratigraphic findings from the eastern flank of the Iselin Bank (McKay et al., 2019; Conte et al., 2021).

3.2 Multibeam echosounder data

Simultaneous recording of multi-beam echosounder (MBES) bathymetry and backscatter data was conducted during the SBP and MCS surveys aboard the R/V Araon. The MBES data were processed using Caris HIPS and SIPS software and subsequently gridded at a lateral cell spacing of 50 m × 50 m using the nearneighbor module in GMT 6.3 software. The recently acquired MBES grid was then integrated with existing datasets from the IT17RS expedition by the RV OGS Explora in 2017 and the Global Multi-Resolution Topography synthesis (GMRT; Ryan et al., 2009). The GMRT data provides a maximum lateral resolution of ~61 m. The compilation of MBES bathymetry data encompasses ~40% of the Central Basin and its surrounding banks (Figure 2B). To address data gaps, the IBCSO v2 regional bathymetric data (Dorschel et al., 2022), with a resolution of 500 m × 500 m, were incorporated to fill in data gaps.

The MBES backscatter data encompass the seafloor extending from the outer shelf and slope beyond the JOIDES Trough to the Central Basin and the surrounding bathymetric highs. To ensure accuracy, selections of the MBES backscatter data exhibiting poor quality (e.g., over the northern Iselin Bank and eastern Central Basin) were excluded.

3.3 Sediment core data

During the ANA03B and ANA05B expeditions, sediment core samples were retrieved from the northern part of the Central Basin (KI13-BC2, KI13-C1, and RS15-LC42), the northeastern flank of Hallett Ridge (KI13-BC3 and KI13-C2), the lower slope beyond the JOIDES Trough (KI13-BC4), and the northern tip of the Iselin Bank (RS15-GC40 and RS15GC41) (Figure 2B; Table 2). Additionally, as part of the Italian Antarctic Research Program (PNRA) expedition in 2016, a 240-cm-long piston core (HLF16-3PC) and two 27-cm-long box cores (HLF16-4BC and HLF16-5BC) were recovered from the crest and upper slope of Hallett Ridge. To encompass a wide range of depositional environments, four legacy sediment cores (ANTA91-4C, ANTA95-98C, ANTA95-99C1, and ANTA99-23C)

collected during previous PNRA programs were also re-analyzed. Details regarding the sediment cores used in this study, such as location and recovered length, can be found in Table 2 and are further described in relevant studies (Tolotti et al., 2013; Ohneiser et al., 2019; Kim et al., 2020; Khim et al., 2021; Melis et al., 2021; Torricella et al., 2021; Bollen et al., 2022; McKay et al., 2022), as well as the Museo Nazionale dell'Antartide (http://www.mna.it) and the Italian Antarctic Data Center (https://iandc.pnra.aq).

Sediment grain sizes were derived using a laser diffraction instrument (Malvern Mastersizer) at multiple institutions: RS15-GC40 and RS15-GC41 were analyzed at KOPRI, RS15-LC40 at Victoria University of Wellington, and HLF16, ANTA91, ANTA95, ANTA99, and KI13 cores at the University of Trieste. Sediments with grain sizes larger than 2 mm were removed through sieving. For particles smaller than 2 mm, laser particle size analysis was conducted at intervals of 1 cm (KI13-BC2, KI13-BC3, KI13-BC4, and HLF16-5BC) or 2 cm (HLF16-4BC) for box core samples, at intervals of 2, 4, 6, or 8 cm for gravity core samples (KI13-C1, KI13-C2, HLF16-3PC, ANTA95-98C, ANTA95-99C1, RS15-GC40, RS15-GC41), at 10 cm intervals for a jumbo gravity core (RS15-LC42), and ~20 or 30 cm intervals for the legacy cores (ANTA91-4C and ANTA99-23C). The sand (>63 μm), silt (63–2 μm), and clay (<2 μm) fractions were determined using the grain-size classification of Friedman and Sanders (1978) and Blott and Pye (2001).

The water content (WC) was calculated using the following equation, assuming a seawater salinity of 0.035 (Kim et al., 2020):

WC (%) = (mass of wet sediment − mass of dry sediment + mass of salt)/mass of wet sediment × 100

Water content values of the RS15 cores were calculated at KOPRI, while all other cores were analyzed at the University of Trieste. Water content data for KI13-C2 is unavailable due to a poor state of preservation (Table 2).

3.4 General ocean circulation model and oceanographic measurements

The Regional Ocean Modeling System (ROMS; Shchepetkin and McWilliams, 2005) was used to simulate bottom current conditions in the northwestern Ross Sea, specifically the Central Basin, for two distinct periods: 15-year periods of Austral winter spanning from 1999 to 2013 and 15-year periods of Austral summer spanning from 2000 to 2014. The model's lateral resolution is 5 km by 5 km, while the vertical resolution varies according to water depth, with a vertical grid comprising 32 cells uniformly distributed across all depths (e.g., 50-m vertical resolution at 1,600 m water depth). In this study, the lowest layer of the

model was used to depict the speed and direction of bottom currents, which play a significant role in influencing sedimentary processes.

The expandable conductivity-temperature-depth (XCTD) data collected during the ANA05B expedition in 2015 were used to produce potential temperature-salinity (Θ/S) diagrams using the Seawater 3.3 package in Python. These oceanographic measurements serve as valuable inputs to represent the contemporary thermohaline structure of the Central Basin region in this study.

4. Results

4.1 Seismic stratigraphic analysis

4.1.1 MCS data

The basin-crossing MCS profile reveals that the Central Basin has infilled with sediment layers reaching a thickness of ~2–3 km (Figure 3A). On the crest of the Hallett Ridge, there is a mounded sedimentary deposit with continuous internal reflections, ranging in thickness from 200 to 350 m (CMP No. 5500–9,500 in Figure 3A). Contrasting the eastern basement of the Hallett Ridge, which exhibits a series of tilted blocks, the western side of the Iselin Bank features a broad bathymetric bench spanning ~23 km. This bathymetric bench is covered by sheet-like, stratified sediments without distinct mounded stacking patterns (CMP No. 25000–29000 in Figure 3A).

The deposition of small patches of sediments was initiated above RSU4 on the eastern slope of Hallett Ridge (CMP 10000–12000 in Figure 3A), and the undulated sedimentary deposits developed until the time of RSU2. Above RSU2, the subparallel internal reflections of the undulating sediments are more laterally continuous, and have distinctive trough and mound features on the slope. The crests of the small mound features exhibit a migration pattern towards higher elevations along the mid-lower slope of the Hallett Ridge (lower left inset of Figure 3A). Additionally, the seismostratigraphic unit above RSU2 is characterized by higher thickness than the underlying unit located between RSU2 and RSU3-CB, both on the lower slope of the northern Hallett Ridge and within the western part of the Central Basin (CMP 12000–17000 in Figure 3A).

Irregular-shaped sediment body, characterized by indistinct internal reflections, is evident in the shallow subsurface strata on the lower slope of the Hallett Ridge and in the northwestern portion of the Central Basin (CMP 12000–18000 in Figure 3A). The base of this sediment body truncates the underlying wavy, stratified sedimentary succession (lower right inset of Figure 3A).

4.1.2 SBP data

The acoustically stratified facies (Facies S) is distinguished by its subparallel internal reflections, which align with the lower strata in a conformable manner. Within Facies S, a relatively thin sedimentary deposit (Facies Sw) exhibits a strong seafloor reflection and faint subparallel internal layers, less than 10 m in thickness at a sound speed of 1,500 m/s (Figure 3B; Table 1). On the other hand, a thicker deposit of Facies S (Facies Sh), surpassing 10 m in thickness, displays a weaker seafloor reflection and greater penetration depth (Figures 3C, D; Table 1). In contrast to Facies S, the acoustically transparent facies (Facies T) is identified by its poorly defined internal reflections and a lens-shaped or irregular external geometry (Table 1). Acoustically transparent subunits of Facies T exhibit lower boundaries that truncate the underlying strata, while their upper boundaries align subparallel to the internal reflections of the overlying stratified subunits (Figure 3D).

Isopach maps derived from the SBP data provide the spatial distribution and depocenters of Facies S and T (Figures 4A, B). Facies Sh, characterized by relatively thick and stratified subunits, mainly developed along the mid-lower slope of the eastern flank of Hallett Ridge, the northeastern sector of the Central Basin floor, as well as the Scott Canyon Basin floor (orange to yellow areas in Figure 4A). Smaller patches of Facies Sh are observed on the lower slope of the southwestern part of the Central Basin facing the eastern slope of Hallett Ridge (red line labeled X – X′ in Figure 4C). In contrast, the thinner stratified subunits of Facies Sw are primarily distributed along the crests and upper slopes of both the Hallett Ridge and Iselin Bank (Figures 3B, C, purple to navy-blue areas in Figure 4A). Additionally, Facies Sw can be found on the lower slope extending beyond the JOIDES Trough mouth and within the southern region of the Central Basin floor (Figure 4A).

Facies T occurs on the outer continental shelf and the gentle slope, extending beyond the JOIDES Trough mouth (Figure 4B). A notable occurrence within the northwestern sector of the Central Basin is the presence of a considerable deposit of Facies T, distinguished by its thickness surpassing 10 m (Figure 4B). This deposit has an estimated volume of ~9.7 km^3.

4.2 Multibeam bathymetry and backscatter intensity analyses

The MBES bathymetry grid obtained from the southwestern part of the Central Basin shows the presence of undulations oriented parallel to the lower slope of southern Hallett Ridge in deeper waters ranging from ~1700 to 1900 m. These undulations deviate

the slope by crest amplitudes of ~45 and ~78 m (upper right inset of Figure 5A). The southern crest of Hallett Ridge near the JOIDES Trough mouth is asymmetric, with a slope gradient of ~2.1° towards the west and ~4.0° towards the east, extending from the crest at 1,000 m to the upper slope at 1,150 m (upper right inset of Figure 5B). On the crest of the Hallett Ridge, high backscatter intensities are observed, while the elongated mounds parallel to the slope exhibit varying intensities ranging from moderate to high (Figure 5B). The low backscatter stripes observed near the undulations (Figure 5B) exhibit a notable association with the 40-m-deep trough and mound features (Figures 4A, C).

Furthermore, the MBES data acquired from the northeastern Hallett Ridge region show a trapezoid-shaped bathymetric depression with an area of >220 km2 on the middle to lower slope (Figure 6). The depression is almost flat and is bounded by scarps measuring ~12 km in length towards the southwest and ~18 km in length towards the northeast (Figure 6B). These scarps displayed a relief ranging from ~40 to 50 m (Figure 4D). The backscatter intensity within this depression generally remains at a low to moderate level compared to the crest and upper slope of the Hallett Ridge (Figure 6B). At the downslope end of the northeastern scarp, wrinkled or hummocky seafloor features are observed, exhibiting moderate to high backscatter intensities in comparison to the low backscatter levels observed in the surrounding flat morphology (purple dashed ellipses in the right inset of Figure 6B).

The southern part of Hallett Ridge is asymmetric (Figure 5), becoming more symmetric towards the northern part (Figures 3A, B, 6A). The slope gradient in this region measures ~2.9° towards the west and ~2.4° towards the east, extending from the crest to the upper slope. Higher backscatter intensities are observed on the northern crest of the Hallett Ridge, while the northwestern Central Basin floor displays relatively lower intensities (Figure 6B).

Similar to the southwestern portion of the Central Basin, the northern part of the eastern flank of the Hallett Ridge displays slope-parallel elongated seafloor undulations at ~1,300–1850 m (Figure 6A). Additionally, the subsurface stratal patterns of these undulations can be observed in the MCS (Figure 3A) and SBP data (Figure 3C). The northward-elongated undulations with a crest amplitude of ~130 m (lower left inset of Figure 3A) exhibit moderate to low backscatter intensities (Figure 6B).

The Scott Canyon, developed north of Bank B, exhibits deep incisions exceeding 100 m in depth, initiating at ~2,200 m from the NE Gap of the Central Basin (Figure 7). This canyon features a sinuous thalweg that extends in a northwestward direction, characterized by side-scarps. However, the thalweg becomes unclear at ~3,300 m in the northern region of the Scott Canyon Basin (Figure 7A). The northeastern levee of the Scott Canyon shows a relatively smooth seafloor (upper right inset of Figure 7A) characterized by low backscatter

intensity (Figure 7B). In contrast, the southwestern part of the levee displays a relatively steeper morphology, facing the northern slope of Bank B (Figure 7A). Bank B stands over 1,500 m higher than the northern Central Basin floor, is separated from the western side of the Iselin Bank by the NE Gap (Figures 2, 7). Small conical-shaped mounds are observed around the 1500-m-high mount (purple dashed ellipses in Figure 7B). The bathymetric high located between the Hallett Ridge and Bank B displays linear seafloor features trending in a SE–NW or SSE–NNW direction (Figure 7A) with moderate to high backscatter intensity (Figure 7B).

The southeastern region of the Central Basin is bounded by a relatively steep slope of Bank A and the southwestern side of the Iselin Bank (Figure 8). Small conical-shaped mounds can be observed in front of the steep slopes of Bank A and the western slope of the Iselin Bank, exhibiting small-scale slope failures similar to those found along the fringe of Bank B. Additionally, distinctive downslope incisions are apparent on the southwestern slope of Iselin Bank (Figure 8A). Moderate intensities are present over the stacked acoustically transparent lenses (Facies T) and stratified surficial sedimentary layer (Facies Sw) located on the southern portion of the Central Basin floor (lower right inset of Figures 8A, B). There is no distinctive difference in backscatter intensity between the top of Facies T and Facies Sw. Meanwhile, higher backscatter intensities are observed on the bathymetric high of Bank A and on the top of small conical mounds (purple dashed ellipses in Figure 8B).

KOPRI 극지연구소

4.3 Grain-size and water-content analyses of surficial sediments

Sediment cores were acquired from the crest and upper slope of bounding bathymetric highs, as well as the middle to lower slope and the Central Basin floor (Figure 9; Table 2). Longer sediment cores were collected in the lower slope and basin floor regions than in the upper slope and crests of bathymetric highs (Figure 9; Table 2).

Box core HLF16-5BC was retrieved from the crest of Hallett Ridge, measuring 26 cm in length. This core has an average sand content of 49.9%. Another box core, HLF16-4BC, also 26 cm in length and collected from Hallett Ridge, exhibits an average sand content of 41.0%. Additionally, a piston core, HLF16-3PC, extending to a length of 240 cm on Hallett Ridge, displays a sand content 44.3% (Table 2). Core RS15-GC40 on the northern shallow region of the Iselin Bank exhibits an average sand content of 65.2%. On the outer shelf of the JOIDES Trough, core ANTA95-99C1, measuring 71 cm in length, shows an average sand content of 29.5%. This core is characterized by a relatively shallow penetration depth, distinguishing it from other piston or gravity cores. The mean water contents of HLF16-3PC, HLF16-4BC, HLF16-5BC, RS15-GC40, and ANTA95-99C1 range from

21.5% to 25.8% (Table 2).

In contrast, sediment cores collected from deeper areas generally exhibit lower average sand content values. The 35-cm-long box core, KI13-BC3 and the 232-cm-long gravity core, KI13-C2, exhibit lower average sand contents of 19.6% and 31.2%, respectively. Similarly, the 1186-cm-long gravity core, RS15-LC42, displays a low average sand content of 16.1%. Core ANTA99-23C shows an average sand content of 13.4% over its 548 cm length. On the mid-slope and small basin of the northern Iselin Bank, core RS15-GC41, displays an average sand content of 30.2%. The remaining cores, obtained at greater depths, exhibit average sand content ranging from 11.4% to 17.8% (KI13-BC4: 14.1%, KI13-C1: 16.7%, KI13-BC2: 17.8%, ANTA91-4C: 13.3%, and ANTA95-98C: 11.4%). Regarding water content, the majority of sediment cores retrieved from the mid-lower slope and basin floor exhibit high average water contents, surpassing 30%, with some cores even exceeding 40% (KI13-BC3 and KI13-BC4). However, two cores, ANTA95-98C (27.7%) and KI13-C1 (29.5%), deviate slightly with relatively lower water content less than 30%. Nevertheless, these two cores still exhibit higher water content in comparison to the sediment cores obtained from shallower depths.

4.4 Oceanographic measurements and circulation model

The 15-year mean of ROMS ocean circulation models for austral winters (1999–2013) and summers (2000–2014) shows a clockwise circulation of bottom current flow in the Central Basin (Figures 10A, B). The model predictions suggest both flow speed and direction were similar for austral winters and summers, with slightly higher speeds observed during the austral summer. However, the difference in speed between the two seasons is relatively small.

On the upper slope, seaward of the JOIDES Trough mouth, a faster westward-flowing bottom current stream is observed parallel to the shelf edge at water depths ranging from 400 to 800 m, with an average speed of 15 cm/s. Certain areas within it exhibit velocities exceeding 20 cm/s (Figures 10A, B). The eastern flank of southern Hallett Ridge, at water depths of ~1,300–1900 m, is characterized by a northward branch of the bottom current stream, with speeds ranging from 15 to 20 cm/s. The northward flow along the northeastern flank of Hallett Ridge and the southern slope of Bank B slows down to speeds of 8–15 cm/s. As the current flows around Bank B to the west of the NE Gap, its velocity increases to ~20 cm/s. In contrast, the bottom along the western flank of Iselin Bank is characterized by a contour-parallel southward flow with speeds ranging from 8 to 15 cm/s, and in some areas exceeding 15 cm/s. This southward flow contributes to a clockwise circulation within the Central Basin. On the other hand, the crests of the

northern Hallett Ridge and Iselin Bank exhibit very slow bottom current speeds, estimated to be less than 5 cm/s based on the circulation models.

The annual variabilities of bottom current speed of austral winter and summer are generally pronounced along the slopes of the surrounding bathymetric highs as indicated by the standard deviation (Figures 10C, D). In contrast, it is comparatively lower in the central section of the basin, the shallow region of the south Iselin Bank, and the northern crest of Hallett Ridge. The distribution of high standard deviation values (>2 cm/s) of the bottom current speeds shows a similar trend to the distribution of moderate to fast-flowing (>8 cm/s) along-slope currents. Significant levels of variability (>5 cm/s) are observed along the southeastern slope of the Hallett Ridge, especially during the austral winter (Figure 10C).

The analysis of XCTD data reveals the presence of three distinct water masses within the Central Basin (Figures 11A – F). These water masses comprise the cold and fresh surface water (Antarctic Surface Water: AASW), the less cold and salty deep water (CDW), and the cold and dense bottom water (DSW). This is evident from the temperature-salinity-density profiles obtained by obliquely crossing the mid-slope to the outer shelf beyond the JOIDES Trough mouth (Figure 11G). Additionally, the XCTD data collected in the deeper water depths along the southern and northern slopes of Hallett Ridge demonstrate the extension of cold and dense bottom water further northward (Figures 11E, F, H).

KOPRI 극지연구소

5. Interpretation and discussion

5.1 Bottom-current-controlled sedimentary architecture in MCS data

The large mound deposit developed on the crest of Hallett Ridge (Figure 3A) can be interpreted as a detached-type of elongated, mounded contourite influenced by along-slope bottom currents based on its geometric and acoustic characteristics (Rebesco et al., 2014; Rodrigues et al., 2022). The presence of the similar scale sedimentary deposit, as reported in a previous study on the southern Hallett Ridge (Kim et al., 2018) (KSL14-08 in Figure 12), indicates that the mound likely extends along the Hallett Ridge. The asymmetric stacking pattern of the mound on the southern Hallett Ridge, characterized by a thinner stratified unit above RSU2 on its steeper eastern flank, can be attributed to the influence of fast-flowing bottom currents (Figure 12). Moreover, the relatively low topography of a saddle-like feature (Figure 2A) serves as a preferred pathway for the along-slope bottom current, allowing it to flow towards the Adare Basin when encountering the bathymetric barrier presented by the crest of Hallett Ridge. The concentrated and fast-flowing bottom

current passing through the saddle of the southern Hallett Ridge contributes to an asymmetric stacking pattern and external morphology. The contouritic mound in the northern sector of Hallett Ridge displays a more symmetrical, aggradational stacking pattern in comparison with the one in the southern sector (Figures 3A, 12). This implies that the along-slope current weakens farther north, creating a less energetic and more uniform environment on both flanks of Hallett Ridge, consistent with the model of modern bottom current circulation (Figures 10A, B).

The elongated and parallel undulating sedimentary features along the northeastern slope contour of Hallett Ridge (Figures 3A, C, 6A) are interpreted as a multi-crested mound-and-moat system. This interpretation is consistent with previous work in this region (Kim et al., 2018) (Figure 5A) and is supported by analogies drawn from similar features observed in other regions (Howe et al., 2002; Lu et al., 2003; Verdicchio and Trincardi, 2008; Martorelli et al., 2011; García et al., 2016; Miramontes et al., 2016). We interpret the long-term development of these elongated features as suggesting that the currents have persisted throughout their development with similar magnitudes to today. The migration pattern of internal reflectors (lower left inset of Figure 3A), which show an up-slope migration and onlap onto older reflectors within the multi-crested mound, further supports the influence of slope-parallel bottom currents in the formation of these features. This migration pattern distinguishes them from deformations caused by soft-sediment mechanisms such as creep folds, which lack true lateral migration (e.g., up-slope or up-current movement) and exhibit broader crests and narrower troughs (Wynn and Stow, 2002 and references therein).

The thicker development of the multi-crested mounds since the middle to late Pliocene (above RSU2), which formed over a shorter period (~4.0 Myr) compared to the underlying depositional layers between RSU4 to RSU2 (lower left inset of Figure 3A), indicates a higher influx of sediment towards the north than the previous period during the middle Miocene to middle Pliocene (~10.0 Myr). This interpretation, based on a single 2-D seismic profile, is consistent with previous regional sediment thickness mapping results in the Central Basin (Kim et al., 2018), which revealed a distinct depocenter along the northeastern lower slope of Hallett Ridge above RSU2, deviating from the trend observed in the underlying units between RSU4 to RSU2.

5.2 Acoustic facies in the SBP data

The acoustically stratified character of Facies S in the SBP data can be attributed to the presence of alternating intervals characterized by higher acoustic impedance, consisting of coarse-grained material, and intervals with lower acoustic impedance, comprising

fine-grained sediment (Neto et al., 2013). The coarse-grained intervals within Facies S are likely the result of iceberg rafting (Joe et al., 2020) and/or winnowing by bottom currents (Kim et al., 2020) commonly found in glaciated continental margins. In contrast, the fine-grained intervals are likely formed by hemipelagic settling (hemipelagic drape), turbid meltwater plumes (post-glacial mud), or sedimentation influenced by bottom currents (contourites), as documented in previously studies conducted in glaciated continental margins (Anderson et al., 1979; Taylor et al., 2002; Ó Cofaigh et al., 2003; Matthiessen et al., 2010; Lucchi et al., 2013). These depositional processes have been occurred on the lower slope and in the northern part of the Central Basin for an extended period, spanning multiple glacial-interglacial cycles over at least the past 1.34 million years, as inferred from the analysis of core RS15-LC42 (Bollen et al., 2022).

As described in Section 3.1, Facies S can be subdivided into two sub-types based on its resolvable thickness in the SBP data. The presence of large thicknesses of Facies Sh and moderate to low backscatter intensities from MBES data suggests the deposition of less compacted sediment and hence a smaller acoustic impedance contrast at the seabed, allowing deeper penetration (e.g., Fransner et al., 2018; Huang et al., 2018). This interpretation is supported by the sediment cores recovered from Facies Sh, which exhibit relatively low average sand contents with high water contents (KI13-BC3, KI13-C2, RS15-LC42, and ANTA99-23C in Figures 9, 12; Table 1). In contrast to Facies Sh, the weakly stratified nature of Facies Sw is relatively thin (<10 m), suggesting a shallower penetration into the seafloor. We attribute this observation to the presence of a denser and/or coarser sediment layer within Facies Sw. Supporting this interpretation, we note the high backscatter intensity observed in the seafloor's MBES data, as well as the high sand contents and low water contents found in cores HLF16-3PC, HLF16-4BC, and HLF16-5BC (Figures 9, 12).

The absence of internal structure, coupled with the irregular external geometry and truncation of underlying strata exhibited by Facies T can be related with rapid deposition, internal deformation, and basal erosion (Veeken and van Moerkerken, 2013). In the glaciated continental margins, these characteristics of Facies T are consistent with the presence of subglacial tills on the continental shelf (Ó Cofaigh et al., 2005; Dove et al., 2014; Halberstadt et al., 2016; Bart et al., 2017; Kim et al., 2021), as well as mass transport deposits formed by submarine slides, slumps, or glaciogenic debris flows on slopes (Vorren and Laberg, 1997; Ó Cofaigh et al., 2003; Donda et al., 2008; Joe et al., 2020; Kim et al., 2021). The gravity-driven downslope sedimentary processes that form these massive deposits are significantly influenced by the advance and retreat of grounded ice masses.

5.3 Surficial sedimentary and geomorphic features

The surficial sediments on the elongated contourite mound along the Hallett Ridge (Figures 3B, 5B) exhibit distinctive characteristics, including the presence of Facies Sw (Figure 4A), high backscatter intensity (Figures 5B, 6B), and high sand contents (Figures 9, 12; Table 1). Furthermore, the significantly high sand content (65.2%) observed in core RS15-GC40, obtained from shallow depth of the northern part of the Iselin Bank, in conjunction with the formation of a thinly developed sedimentary layer, provides support for the hypothesis that the bathymetric highs surrounding the Central Basin were subjected to winnowing effects caused by the fast-flowing along-slope bottom currents. However, the modeled present-day current speed in this region indicates relatively low, with values below 5 cm/s (Figures 10A, B) and low variabilities (Figures 10C, D). This suggests that the present-day open marine or ice distal oceanographic condition differs from the past ice marginal or glaciomarine environments which experienced significant influence from vigorous bottom current-induced winnowing of fine-grained sediments (e.g., Conte et al., 2021). One potential explanation for the high sand content observed on the crest of Hallett Ridge is that the preferential deposition of fine-grained sediments on the lower slope, rather than on the shallow ridge crest, can be attributed to the downslope sediment-gravity flows (such as debris flows and turbidity currents) and meltwater discharge from the advanced ice sheet during the past glacial periods. This may occur due to the presence of the bathymetric high, which acts as a barrier and restricts the flow of relatively dense sediment-laden bottom currents over the Hallett Ridge. Consequently, the crest of the Hallett Ridge exhibits a relatively high sand content due to the scarcity of fine-grained sediments in comparison to the lower slope, where a significant accumulation of fine-grained sediment occurs in a low-energy deep-sea depositional environment. Another possibility is that winnowing may have occurred, supported by the intensified along-slope bottom currents (i.e., ASC in Figure 1) during the windier glacial period (Thompson et al., 2018; Kim et al., 2020). The wind-driven ASC likely played a significant role in these winnowing processes. Furthermore, in conjunction with the advancement of ice sheets during that time, there would have been an increased supply of coarser fractions (e.g., McKay et al., 2019; Conte et al., 2021; Gales et al., 2023). These combined processes likely contributed to the current low proportion of fine-grained sediments and the thin unconsolidated deposits found in the upper sections of Hallett Ridge and Iselin Bank.

The contrasting thickness of Facies S on the multi-crested mound and moat system on the northeastern and southeastern part of Hallett ridge indicate that the accumulation of fine-grained sediment is highly affected by bottom currents (McCave and Swift, 1976; McCave and Hall, 2006) in the northern part than southern part. The spatial distribution of Facies Sh (Figure 4A) generally corresponds to regions characterized by moderately-flowing bottom currents (~8–15 cm/s) along the lower slope of the northern Hallett Ridge and

Bank B (Figures 4A, 10A, B). These bottom currents possess the capacity to entrain, transport, and selectively release fine-grained sediments on the seafloor, aligning with the bedform-velocity matrix for deep-water bottom-current systems (Rebesco et al., 2014). These environmental conditions create favorable circumstances for the accumulation of fine-grained sediment, as evident in the recorded characteristics of Facies Sh. Whereas, the southeastern flank of the Hallett Ridge, characterized by Facies Sw and higher backscatter intensity, is influenced by the northward flowing fast bottom current (>15 cm/s) with higher fluctuation as shown in the ROMS model (Figure 10). Based on the findings from geophysical, sedimentological, and oceanographic analyses, it can be inferred that Facies Sh originated within a moderate to low energy conditions. This environment is situated in a deep-water slope setting. This trend is consistent with long-term development of multi-crested mounds depicted in the MCS data (Figure 12). In addition, the amplitude of undulation also increased northward, indicating that the active sedimentation of the mound increases the relief from the moat to the crest of the mound.

The presence of isolated sediment bodies characterized as Facies T in the northwestern region of the Central Basin (Figures 3D, 4B) can be interpreted as mass transport deposit resulting from slope failures. The absence of internal structure, erosional basal boundary, and irregular-shaped external geometry observed in both MCS and SBP data indicate this mass transport deposit were formed by short-lived sedimentary processes. This interpretation can be supported by the identification of side scarps associated with slope failures in the MBES bathymetric data (Figure 6A), as well as similar seismic and geomorphic characteristics of mass transport deposits from previous studies conducted in the eastern Ross Sea margin and Arctic Ocean (e.g., Conte et al., 2021; Schlager et al., 2021; Gales et al., 2023). Westward thickening of the seismostratigraphic unit above RSU2 in the MCS profile (Figure 3A) is partly attributed by this mass transport deposit on the lower slope of Hallett Ridge.

The estimated volume of the mass transport deposit, derived from sparse seismic grids, is ~9.7 km3. This volume falls within the simply calculated range of ~8.8–11 km3, which is determined based on the area of the trapezoid-shaped depression (~220 km2) and the relief of the side scarps (~40–50 m) (Figures 3D, 4D, 6). Based on this observation, we can infer that the mass transport deposit originated from the failure of the slope of the well-developed multi-crested mound. In addition, moderate to low backscatter intensity in the area of the trapezoid-shaped depression (Figure 6B) consistent with occurrence of Facies Sh (Figure 4D), indicate that fine-grained sediment accumulation within the depression was continued after the major slope failure occurred. The presence of wrinkled or hummocky seafloor features with moderate backscatter intensity observed in proximity to the side scarps (right inset of Figure 6B) can be considered to be indicative of sedimentary blocks

generated by mass transport processes. Furthermore, similar seafloor features, such as a group of small conical mounds around the steep slopes of Bank A, Bank B, and the western slope of Iselin Bank (Figures 7, 8), are also likely associated with mass wasting by smaller scale slope failures. These rough seafloor features and inhomogeneous subsurface sedimentary deposits tend to increase the backscatter intensity (Jackson et al., 1986; Mitchell, 1993).

The widespread Facies T deposits near the JOIDES Trough mouth (Figure 4B) suggests their origin from subglacial or ice-marginal sedimentation during the advancement of the grounded ice sheet near the paleo-shelf break (Ó Cofaigh et al., 2003; e.g.; Batchelor and Dowdeswell, 2014). These deposits exhibit distinct characteristics compared to the slope failure deposits found on the lower slope of northeastern Hallett Ridge. On the lower slope and the southern Central Basin floor, stacked debris flow deposits with moderated backscatter intensity can be observed (Figures 4C, 5B, 8A, B). However, the stacked debris flow deposits observed on the upper slope and the grounding zone wedge on the outer shelf show higher backscatter intensity (Figures 4B, E, 9), which can be attributed to the roughness of seafloor and inhomogeneities of subsurface sediments (Jackson et al., 1986; Mitchell, 1993). According to the ROMS model (Figures 10A, B), we identified vigorous, fast-flowing bottom currents (>20 cm/s) traversing the outer shelf and upper slope beyond the JOIDES Trough mouth and the southeastern flank of the Hallett Ridge. These areas with elevated current speeds correspond to the regions displaying Facies T (Figure 4B) and relatively high MBES backscatter intensity (Figure 9). The unusually short penetration depth observed in the nearest gravity core ANTA95-99C1 (~71 cm, Table 2; Figure 9) suggests the presence of relatively coarser sediments that hinders deep sampling. Based on these results, we infer the glaciogenic sedimentary deposits on the outer shelf and upper slope beyond the JOIDES Trough mouth as mainly composed of coarse-grained sediment, contrasting with the stacked debris flow deposits on the lower slope. These deposits are largely influenced by the winnowing process induced by fast-flowing bottom currents, which hinders the accumulation of fine-grained particles within the surface sediment layer (Stow, 2002; Conte et al., 2021; Bollen et al., 2022).

The elongated stripes of low backscatter intensities, observed near the undulations of the southern Hallett Ridge (Figure 5B), coincide with the presence of ~15–17 m thick deposits of Facies Sh, which are separated by a sediment-starved trough (Figure 4C). These features, characterized by their northward elongation as observed in the 7.5 km-width MBES bathymetry and backscatter grids, along with well-developed sediment accumulation on both sides of the trough, suggest the presence of a submarine channel-levee system (e.g., Fransner et al., 2018; Boggild and Mosher, 2021). Unlike larger-scale, deeply incised submarine canyons such as the Hillary Canyon and Bowers Canyon beyond the Pennell

Trough and Drygalski Trough, this submarine channel exhibits smaller dimensions and lacks distinct side scarps. This indicates that the gravity flows responsible for forming the submarine channel in the JOIDES Trough and Central Basin region were less erosive than those occurring in the Hillary and Bowers Canyons. The westward-deflected outflow of DSW along the eastern flank of Hallett Ridge, influenced by the Coriolis effect, may encounter reduced overall speeds due to the semi-closed geometry of the Central Basin, attributed to bathymetric obstacles and narrow gateways (Figures 10A, B). This is evident from the confined path of DSW spreading widely in the northern part of the basin as shown in a recently published modeling result, which demonstrated the presence of dense shelf water exceeding 200 m in thickness in the Central Basin (Morrison et al., 2020) (Figure 2A). The existence of Bank B and the narrow gateway of the NE Gap (Figure 2A), serves as an effective obstruction that blocks the northward flow of DSW from the northern Central Basin toward the Scott Canyon Basin. These bathymetric barriers functions in a manner similar to a low dam or weir, impeding the northward movement of water. As a result, the denser water accumulated in the northern part of the Central Basin can be reaccelerated at the NE Gap due to the steep gradient, leading to the erosion of underlying strata and the subsequent formation of the Scott Canyon, characterized by its deeply incised nature. The distinctive bathymetric features of the Central Basin provide an explanation for the presence of smaller-scale channel-levee systems on the lower slope beyond the JOIDES Trough, as well as the initiation of the Scott Canyon in deeper environments.

KOPRI 극지연구소

5.4 Influence of ice sheet dynamics and ocean circulation on contourite development

Previous studies have documented multiple advances of a grounded ice sheet in the vicinity of the JOIDES Trough near the continental shelf edge during Quaternary glacial cycles (Brancolini et al., 1995; Bart et al., 2011; Kim et al., 2018; Bollen et al., 2022). Based on the seismostratigraphic interpretation in the Central Basin (Kim et al., 2018), the contourites developed simultaneously with the formation of the topset-truncated trough-mouth fan beyond the mouth of the JOIDES Trough since the time of RSU2 (the mid–late Pliocene or early Pleistocene). The sediments deposited beyond the shelf edge by grounded ice during glacial maxima were influenced by down-slope debris and turbidity flows during deglacial and interglacial periods, together with the sediment-starved submarine channel thalweg and the formation of levee systems in the southwestern Central Basin (Figures 4C, 12). We propose that the suspended fine-grained components of such flows, remobilized by bottom currents, have contributed to the formation of contourites on the crest and flanks of Hallett Ridge after the time of formation of RSU2. RSU2 marks the major transition to the modern cold dry-based Antarctic ice sheet (Rebesco et al., 2006;

McKay et al., 2012), and the observed northward thickening of the multi-crested mounds in the MCS data (above RSU2, Figures 3A, 12) can be explained by an advanced grounding line further north. This interpretation aligns with previous studies suggesting active sedimentation controlled by bottom currents on the middle to lower slope of northern Hallett Ridge (Khim et al., 2021; Torricella et al., 2021; Bollen et al., 2022).

As the interpretation of Facies S in Section 5.2, the subparallel internal reflections observed in the stratified sedimentary deposits are indicative of changes in the sedimentary processes, which may be attributed to variations in bottom current strength, potentially influenced by processes such as DSW export during glacial and interglacial periods. As the grounded ice sheet approached the shelf break, it is likely that DSW cascading diminished or ceased due to the absence of factors that promote the production of dense water, such as large ice shelves, coastal polynyas, and large cross-shelf depressions (Amblas and Dowdeswell, 2018; Bollen et al., 2022). In contrast, DSW export was most vigorous during interglacial periods (Bollen et al., 2022; Kim et al., 2023), creating an oceanographic setting conductive to the formation of contourites (Thran et al., 2018). During the LGM, the grounding line of the ice sheet at the JOIDES Trough mouth is believed to have been located more than 100 km landward of the shelf break (Anderson et al., 2014; Halberstadt et al., 2016; Prothro et al., 2020). A recent investigation of sediment core RS15-LC42 has suggested that partial advances of grounded ice in the JOIDES Trough may have occurred during “mild” glacial periods within the past 0.3 Myr and during 1.4–1.2 Ma (Bollen et al., 2022). In addition, the partial advances of the grounded ice can explain the lack of the deep incisions (e.g., submarine canyon and gullies) on the gentle upper slope beyond the JOIDES Trough mouth similar to the Pennell Trough mouth in the eastern Ross Sea (e.g., Gales et al., 2021). If the well-developed contourites along the Hallett Ridge above RSU2 primarily formed due to active bottom-current processes intensified by DSW export, it can be inferred that DSW export sustained by the partial advance of the ice sheet during mild glaciations and the over-deepened morphology of the outer shelf (Figure 2A) significantly contributed to the development of the contourites. Pleo-circulation modelling and deep drilling is needed to verify this hypothesis.

The occurrence of slope failures on the eastern flank of northern Hallett Ridge can be attributed to the high accumulation of sediment caused by the advancement of the grounded ice sheet near the shelf break, as indicated by previous studies (e.g., Lucchi et al., 2002; McKay et al., 2019; Conte et al., 2021). The preferential deposition of fine-grained sediments on the northern Hallett Ridge, due to the slowed northward-flowing DSW caused by the semi-closed geometry of the Central Basin, may have resulted in an elevation of pore pressure within the weak, water-rich interglacial sediments interbedded with low permeable glaciogenic sediments (e.g., Gales et al., 2023). This increase in pore pressure

likely contributes to slope instability and serves as a causal factor for the observed slope failures (e.g., Long et al., 2003; Laberg and Camerlenghi, 2008; Miramontes et al., 2018). Glacio-isostatic rebound associated with the retreat of the grounded ice sheet could have triggered slope failure in inherently vulnerable contourite deposits (Kaufmann et al., 2005; Whitehouse et al., 2019; Gales et al., 2023), as observed in the northwestern part of the Central Basin.

6. Conclusion

The mutually reinforcing evidence of the geophysical, sedimentological, and oceanographic analyses presented in this study lead to a reliable inference of past and modern sedimentary and geomorphic processes in the northwestern Ross Sea margin. The combined results indicate that the westward-deflected DSW cascading in the northwestern Ross Sea margin likely contributed to the formation of the well-developed contourite deposits lying on and along the Hallett Ridge. The northward thickening of multi-crested mounds above RSU2 and of the stratified surficial sediments of Facies S reflects a progressive northward shift of the sediment source from the advanced grounded ice sheet since Late Pliocene global cooling. Active bottom-current processes enhanced by DSW export during interglacial periods and mild glaciations with partial advance of the grounded ice sheet may have contributed substantially to the development of contourites on and along Hallett Ridge. The preferential accumulation of fine-grained sediments on northern Hallett Ridge as a result of slowed DSW due to the semi-closed basin geometry may have increased slope instability and caused slope failures. This study demonstrates the high potential for multidisciplinary studies to find geological archives that are critical to ice sheet and circulation reconstructions.

KOPRI 극지연구소

남극 로스해 북서부에서 빙상과 해양의 상호작용을 기록한 고해양 자료 탐색

김수관[1*], Laura De Santis[2], 홍종국[3], Ester Colizza[4], 김성한[3], Andrea Bergamasco[5], 이상훈[1], 강승구[3], 이민경[3], 김형준[3], 최연진[3], Andrea Geniram[4], 최형규[3], 이재일[3], 유규철[3], 박용철[3]

[1]한국해양과학기술원

[2]National Institute of Oceanography and Applied Geophysics-OGS, Trieste, Italy

[3]극지연구소

[4]Department of Mathematics and Geosciences, University of Trieste, Trieste, Italy,

[5]Institute of Marine Sciences-National Research Council, Venice, Italy

초록: 빙하가 발달한 대륙 주변부에서 저층류의 영향을 받은 퇴적층을 분석하는 것은 과거 퇴적 환경과 해양학적 조건을 이해하는 데 중요한 단서를 제공한다. 이러한 복원은 접지된 빙상의 전진과 후퇴 과정이 과거 해양 순환 패턴과 어떻게 상호작용했는지를 평가할 수 있게 한다. 그러나 이 외딴 지역에서는 자료가 부족하기 때문에 이러한 상호작용과 구체적인 메커니즘에 대한 질문들이 여전히 대부분 해결되지 않은 상태로 남아 있다. 본 연구에서는 해양 지구물리 자료, 표층 퇴적 코어, 해양 관측 자료, 그리고 해양 순환 모델을 통합하여 종합적인 분석을 수행하였다. 연구의 목적은 장기적인 층서 발달과 함께 과거 빙기 및 간빙기 동안의 퇴적 및 해양학적 조건이 시간적·공간적으로 어떻게 변화했는지를 이해하는 것이었다. 다양한 자료를 통합하고 상호 비교함으로써, 우리는 남극 북서부 로스해 주변 중앙 분지의 서쪽 해저 지형 고지를 따라 저층류에 의해 조절되는 퇴적체가 어떻게 발달했는지를 추론할 수 있었다. 해저 지형 고지 위와 사면을 따라 분포하는 콘투라이트 퇴적층은 둔덕 형태의 외부 기하와 음향적으로 층리화된 상을 통해 확인되었으며, 이는 반사면이 해구 방향으로 점차 얇아지는 특징을 보였다. 음향상 분석과 다중빔 후방산란 결과는 퇴적 코어 자료와 함께 상반된 패턴을 보여주었다. 해저 고지에서는 두께가 얇은(<10m) 조립질 퇴적층과 높은 후방산란 값이 나타난 반면, 하부 사면 및 해저 융기부에서는 두께가 두꺼운(>10m) 세립질 층리 퇴적층과 낮은 후방산란 값이 관찰되었다. 이러한 결과는 과거 빙기 동안 강한 저층류에 의해 해저 표층 퇴적물이 제거되는 와류 작용이 발생했음을 시사하며, 이는 퇴적학적 분석을 통해서도 뒷받침된다. 또한 해양 순환 모델에서 모의된 서쪽으로 편향된 고밀도 대륙붕수의 유출 경로와 사면을 따라 서쪽으로 흐르는 저층류는, 저층류 과정에 의해 영향을 받은 콘투라이트의 독특한 발달 양상을 설명해준다. 더 나아가 중앙 분지 북쪽의 해저 지형 장벽에 의해 형성된 대규모 콘투라이트 퇴적물 축적은 해저 사면 붕괴에 기여할 가능성도 있다.

KOPRI 극지연구소

References

Amblas, D., and Dowdeswell, J. A. (2018). Physiographic influences on dense shelf-water cascading down the Antarctic continental slope. Earth-Science Rev. 185, 887–900. doi:10.1016/j.earscirev.2018.07.014

Anderson, J. B., and Bartek, L. R. (1992). "Cenozoic glacial history of the Ross Sea revealed by intermediate resolution seismic reflection data combined with drill site information," in Contributions to antarctic research III antarctic research series. Editor D. H. Elliot (Washington, D.C., United States: American Geophysical Union), 231–263.

Anderson, J. B., Conway, H., Bart, P. J., Witus, A. E., Greenwood, S. L., McKay, R. M., et al. (2014). Ross Sea paleo-ice sheet drainage and deglacial history during and since the LGM. Quat. Sci. Rev. 100, 31–54. doi:10.1016/j.quascirev.2013.08.020

Anderson, J. B., Kurtz, D., and Weaver, F. M. (1979). "Sedimentation on the Antarctic continental slope," in Geology of continental slopes special publication. Editors L. J. Doyle, and O. Pilkey (Tulsa: SEPM), 265–283.

Armitage, T. W. K., Kwok, R., Thompson, A. F., and Cunningham, G. (2018). Dynamic topography and sea level anomalies of the Southern Ocean: variability and teleconnections. J. Geophys. Res. Oceans 123, 613–630. doi:10.1002/2017JC013534

Bart, P., Anderson, J., Trincardi, F., and Shipp, S. (2000). Seismic data from the northern basin, Ross Sea, record extreme expansions of the East antarctic ice sheet during the late neogene. Mar. Geol. 166, 31–50. doi:10.1016/s0025-3227(00)00006-2

Bart, P. J., Anderson, J. B., and Nitsche, F. (2017). Post-LGM grounding-line positions of the bindschadler paleo ice stream in the Ross Sea embayment, Antarctica. J. Geophys. Res. Earth Surf. 122, 1827–1844. doi:10.1002/2017jf004259

Bart, P. J., and De Santis, L. (2012). Glacial intensification during the neogene: a review of seismic stratigraphic evidence from the Ross Sea, Antarctica, continental shelf. Oceanography 25, 166–183. doi:10.5670/oceanog.2012.92

Bart, P. J., Sjunneskog, C., and Chow, J. M. (2011). Piston-core based biostratigraphic constraints on Pleistocene oscillations of the West antarctic ice sheet in western Ross Sea between north Basin and AND-1B drill site. Mar. Geol. 289, 86–99. doi:10.1016/j.margeo.2011.09.005

Batchelor, C. L., and Dowdeswell, J. A. (2014). The physiography of High Arctic cross-shelf troughs. Quat. Sci. Rev. 92, 68–96. doi:10.1016/j.quascirev.2013.05.025

Bergamasco, A., Defendi, V., Zambianchi, E., and Spezie, G. (2002). Evidence of dense water overflow on the Ross Sea shelf-break. Antarct. Sci. 14, 271–277.

KOPRI 극지연구소

doi:10.1017/s0954102002000068

Bjordal-Olsen, S., Rydningen, T. A., Laberg, J. S., Lasabuda, A. P. E., and Knutsen, S.-M. (2023). Contrasting neogene–quaternary continental margin evolution offshore mid-north Norway: implications for source-to-sink systems. Mar. Geol. 456, 106974. doi:10.1016/j.margeo.2022.106974

Blott, S. J., and Pye, K. (2001). GRADISTAT: a grain size distribution and statistics package for the analysis of unconsolidated sediments. Earth Surf. Process. Landforms 26, 1237–1248. doi:10.1002/esp.261

Boggild, K., and Mosher, D. C. (2021). Turbidity currents at polar latitudes: a case study of NP-28 channel in the amundsen basin, Arctic Ocean. Mar. Geol. 440, 106571. doi:10.1016/j.margeo.2021.106571

Bollen, M., Riesselman, C. R., Ohneiser, C., Albot, O., McKay, R., Lee, M. K., et al. (2022). Pleistocene oceanographic variability in the Ross Sea: a multiproxy approach to age model development and paleoenvironmental analyses. Glob. Planet. Change 216, 103901. doi:10.1016/j.gloplacha.2022.103901

Brancolini, G., Cooper, A. K., and Coren, F. (1995). "Seismic facies and glacial history in the western Ross Sea (Antarctica)," in Geology and seismic Stratigraphy of the antarctic margin antarctic research series. Editors A. K. Cooper, P. F. Barker, and G. Brancolini (United States: Wiley Online Library), 209–233.

Budillon, G., Castagno, P., Aliani, S., Spezie, G., and Padman, L. (2011). Thermohaline variability and Antarctic bottom water formation at the Ross Sea shelf break. Deep Sea Res. Part I Oceanogr. Res. Pap. 58, 1002–1018. doi:10.1016/j.dsr.2011.07.002

Budillon, G., Cordero, S. G., and Salusti, E. (2002). On the dense water spreading off the Ross Sea shelf (Southern Ocean). J. Mar. Syst. 35, 207–227. doi:10.1016/S0924-7963(02)00082-9

Cande, S. C., and Stock, J. M. (2004). "Constraints on late cretaceous and cenozoic extension in the Ross Sea from the southwest pacific plate circuit," in Eos transactions American geophysical union (New Jersey, United States: Wiley).

Cande, S. C., Stock, J. M., Müller, R. D., and Ishihara, T. (2000). Cenozoic motion between east and west Antarctica. Nature 404, 145–150. doi:10.1038/35004501

Carter, L., Bostock-Lyman, H., and Bowen, M. (2022). "Chapter 4 - water masses, circulation and change in the modern Southern Ocean," in Antarctic climate evolution. Editors F. Florindo, M. Siegert, L. D. Santis, and T. Naish (Amsterdam: Elsevier), 165–197. doi:10.1016/B978-0-12-819109-5.00003-7

Chavanne, C. P., Heywood, K. J., Nicholls, K. W., and Fer, I. (2010). Observations of the antarctic slope undercurrent in the southeastern weddell sea. Geophys. Res. Lett. 37. doi:10.1029/2010GL043603

Conte, R., Rebesco, M., Santis, L. D., Colleoni, F., Bensi, M., Kovacevic, V., et al. (2021). Bottom current control on sediment deposition between the Iselin Bank and the hillary canyon (Antarctica) since the late Miocene: an integrated seismic-oceanographic approach. Deep-Sea Res. Part I 176, 103606. doi:10.1016/j.dsr.2021.103606

Cunningham, S. A., Alderson, S. G., King, B. A., and Brandon, M. A. (2003). Transport and variability of the antarctic circumpolar current in drake passage. J. Geophys. Res. Oceans 108, 1978–2012. doi:10.1029/2001JC001147

Davey, F., and Brancolini, G. (1995). "The late mesozoic and cenozoic structural setting of the Ross Sea region," in Geology and seismic Stratigraphy of the antarctic margin antarctic research series. Editors A. K. Cooper, P. F. Barker, and G. Brancolini (Washington, D.C., United States: American Geophysical Union), 167–182.

Davey, F. J., Cande, S., and Stock, J. (2021). Cenozoic continental rifting in the north-western Ross Sea. null 65, 389–396. doi:10.1080/00288306.2021.1891942

Davey, F. J. (2004). Ross Sea bathymetry. Lower Hutt, New Zealand: Institute of Geological and Nuclear Science Limited.

De Santis, L., Anderson, J. B., Brancolini, G., and Zayatz, I. (1995). "Seismic record of late Oligocene through Miocene glaciation on the central and eastern continental shelf of the Ross Sea," in Geology and seismic Stratigraphy of the antarctic margin antarctic research series. Editors A. K. Cooper, P. F. Barker, and G. Brancolini (Washington, D.C., United States: American Geophysical Union), 235–260.

De Santis, L., Prato, S., Brancolini, G., Lovo, M., and Torelli, L. (1999). The eastern Ross Sea continental shelf during the cenozoic: implications for the West antarctic ice sheet development. Glob. Planet. Change 23, 173–196. doi:10.1016/s0921-8181(99)00056-9

Donda, F., O'Brien, P., De Santis, L., Rebesco, M., and Brancolini, G. (2008). Mass wasting processes in the western wilkes land margin: possible implications for East Antarctic glacial history. Palaeogeogr. Palaeoclimatol. Palaeoecol. 260, 77–91. doi:10.1016/j.palaeo.2007.08.008

Dorschel, B., Hehemann, L., Viquerat, S., Warnke, F., Dreutter, S., Tenberge, Y. S., et al. (2022). The international bathymetric chart of the Southern Ocean Version 2. Sci. Data 9, 275. doi:10.1038/s41597-022-01366-7

Dove, D., Polyak, L., and Coakley, B. J. (2014). Widespread, multi-source glacial erosion on the Chukchi margin, Arctic Ocean. Quat. Sci. Rev. 92, 112–122. doi:10.1016/j.quascirev.2013.07.016

Dowdeswell, J. A., Evans, J., Ó Cofaigh, C., and Anderson, J. B. (2006). Morphology and sedimentary processes on the continental slope off pine island bay, amundsen sea, west Antarctica. GSA Bull. 118, 606–619. doi:10.1130/B25791.1

Fransner, O., Noormets, R., Flink, A. E., Hogan, K. A., and Dowdeswell, J. A. (2018).

Sedimentary processes on the continental slope off Kvitøya and Albertini troughs north of Nordaustlandet, Svalbard – the importance of structural-geological setting in trough-mouth fan development. Mar. Geol. 402, 194–208. doi:10.1016/j.margeo.2017.10.008

Friedman, G. M., and Sanders, J. E. (1978). Principles of sedimentology. New Jersey, United States: John Wiley and Sons.

Gales, J. A., McKay, R. M., De Santis, L., Rebesco, M., Laberg, J. S., Shevenell, A. E., et al. (2023). Climate-controlled submarine landslides on the Antarctic continental margin. Nat. Commun. 14, 2714. doi:10.1038/s41467-023-38240-y

Gales, J. A., Rebesco, M., De Santis, L., Bergamasco, A., Colleoni, F., Kim, S., et al. (2021). Role of dense shelf water in the development of Antarctic submarine canyon morphology. Geomorphology 372, 107453. doi:10.1016/j.geomorph.2020.107453

García, M., Hernández-Molina, F. J., Alonso, B., Vázquez, J. T., Ercilla, G., Llave, E., et al. (2016). Erosive sub-circular depressions on the guadalquivir bank (gulf of cadiz): interaction between bottom current, mass-wasting and tectonic processes. Mar. Geol. 378, 5–19. doi:10.1016/j.margeo.2015.10.004

Gordon, A. L., Huber, B. A., and Busecke, J. (2015). Bottom water export from the western Ross Sea, 2007 through 2010. Geophys. Res. Lett. 42, 5387–5394. doi:10.1002/2015gl064457

Gordon, A. L., Orsi, A. H., Muench, R., Huber, B. A., Zambianchi, E., and Visbeck, M. (2009). Western Ross Sea continental slope gravity currents. Deep Sea Res. Part II Top. Stud. Oceanogr. 56, 796–817. doi:10.1016/j.dsr2.2008.10.037

Granot, R., Cande, S., Stock, J., Davey, F., and Clayton, R. (2010). Postspreading rifting in the Adare Basin, Antarctica: regional tectonic consequences. Geochem. Geophys. Geosystems 11. doi:10.1029/2010gc003105

Halberstadt, A. R. W., Simkins, L. M., Greenwood, S. L., and Anderson, J. B. (2016). Past ice-sheet behaviour: retreat scenarios and changing controls in the Ross Sea, Antarctica. Cryosphere 10, 1003–1020. doi:10.5194/tc-10-1003-2016

Harris, P. T., Macmillan-Lawler, M., Rupp, J., and Baker, E. K. (2014). Geomorphology of the oceans. Mar. Geol. 352, 4–24. doi:10.1016/j.margeo.2014.01.011

Hochmuth, K., Gohl, K., Leitchenkov, G., Sauermilch, I., Whittaker, J. M., Uenzelmann-Neben, G., et al. (2020). The evolving paleobathymetry of the circum-antarctic Southern Ocean since 34 Ma – A key to understanding past cryosphere-ocean developments. Geochem. Geophys. Geosystems 21, e2020GC009122. doi:10.1029/2020GC009122

Howe, J. A., Stoker, M. S., Stow, D. A. V., and Akhurst, M. C. (2002). “Sediment drifts and contourite sedimentation in the northeastern rockall Trough and faroe-shetland

KOPRI 극지연구소

channel, north atlantic ocean," in Deep-water contourite systems: modern drifts and ancient series, seismic and sedimentary characteristics geological society, London, memoirs. Editors D. A. V. Stow, C. J. Pudsey, J. A. Howe, J.-C. Faugeres, and A. R. Viana (United Kingdom: The Geological Society of London), 65–72.

Huang, X., Gohl, K., and Jokat, W. (2014). Variability in Cenozoic sedimentation and paleo-water depths of the Weddell Sea basin related to pre-glacial and glacial conditions of Antarctica. Glob. Planet. Change 118, 25–41. doi:10.1016/j.gloplacha.2014.03.010

Huang, Z., Siwabessy, J., Cheng, H., and Nichol, S. (2018). Using multibeam backscatter data to investigate sediment-acoustic relationships. J. Geophys. Res. Oceans 123, 4649–4665. doi:10.1029/2017JC013638

Jackson, D. R., Winebrenner, D. P., and Ishimaru, A. (1986). Application of the composite roughness model to high-frequency bottom backscattering. J. Acoust. Soc. Am. 79, 1410–1422. doi:10.1121/1.393669

Jacobs, S. S., Amos, A. F., and Bruchhausen, P. M. (1970). Ross sea oceanography and antarctic bottom water formation. Deep Sea Res. Oceanogr. Abstr. 17, 935–962. doi:10.1016/0011-7471(70)90046-x

Jacobs, S. S. (2004). Bottom water production and its links with the thermohaline circulation. Antarct. Sci. 16, 427–437. doi:10.1017/s095410200400224x

Jacobs, S. S., Fairbanks, R. G., and Horibe, Y. (1985). "Origin and evolution of water masses near the antarctic continental margin: evidence from H218O/H216O ratios in seawater," in Oceanology of the antarctic continental shelf (Washington, D.C., United States: American Geophysical Union), 59–85. doi:10.1029/AR043p0059

Jacobs, S. S., Giulivi, C. F., and Mele, P. A. (2002). Freshening of the Ross Sea during the late 20th century. Science 297, 386–389. doi:10.1126/science.1069574

Joe, Y. J., Polyak, L., Schreck, M., Niessen, F., Yoon, S. H., Kong, G. S., et al. (2020). Late quaternary depositional and glacial history of the arliss plateau off the East siberian margin in the western Arctic Ocean. Quat. Sci. Rev. 228, 106099. doi:10.1016/j.quascirev.2019.106099

Kaufmann, G., Wu, P., and Ivins, E. R. (2005). Lateral viscosity variations beneath Antarctica and their implications on regional rebound motions and seismotectonics. J. Geodyn. 39, 165–181. doi:10.1016/j.jog.2004.08.009

Kennedy, A. T., Farnsworth, A., Lunt, D. J., Lear, C. H., and Markwick, P. J. (2015). Atmospheric and oceanic impacts of Antarctic glaciation across the Eocene–Oligocene transition. Philosophical Trans. R. Soc. Lond. A Math. Phys. Eng. Sci. 373, 20140419. doi:10.1098/rsta.2014.0419

Kennett, J. P. (1977). Cenozoic evolution of Antarctic glaciation, the circum-Antarctic Ocean,

and their impact on global paleoceanography. J. Geophys. Res. 82, 3843–3860. doi:10.1029/jc082i027p03843

Khim, B.-K., Colizza, E., Lee, J. I., Giglio, F., Ha, S., and Bak, Y.-S. (2021). Biological productivity and glaciomarine sedimentation in the Central Basin of the northwestern Ross Sea since the last glacial maximum. Polar Sci. 28, 100682. doi:10.1016/j.polar.2021.100682

Kim, S., Bak, Y.-S., Prebble, J. G., Kang, M.-I., Kim, S., Park, J., et al. (2023). Glacial-interglacial changes in oceanic conditions and depositional process in the continental rise in response to ice sheet (shelf) variation in Bellingshausen Sea, Antarctica. Front. Mar. Sci. 10. doi:10.3389/fmars.2023.1183516

Kim, S., De Santis, L., Hong, J. K., Cottlerle, D., Petronio, L., Colizza, E., et al. (2018). Seismic stratigraphy of the Central Basin in northwestern Ross Sea slope and rise, Antarctica: clues to the late cenozoic ice-sheet dynamics and bottom-current activity. Mar. Geol. 395, 363–379. doi:10.1016/j.margeo.2017.10.013

Kim, S., Lee, J. I., McKay, R. M., Yoo, K.-C., Bak, Y.-S., Lee, M. K., et al. (2020). Late Pleistocene paleoceanographic changes in the Ross Sea - Glacial-interglacial variations in paleoproductivity, nutrient utilization, and deep-water formation. Quat. Sci. Rev. 239, 106356. doi:10.1016/j.quascirev.2020.106356

Kim, S., Polyak, L., Joe, Y. J., Niessen, F., Kim, H. J., Choi, Y., et al. (2021). Seismostratigraphic and geomorphic evidence for the glacial history of the northwestern chukchi margin, Arctic Ocean. J. Geophys. Res. Earth Surf. 126, e2020JF006030. doi:10.1029/2020jf006030

King, M. V., Gales, J. A., Laberg, J. S., McKay, R. M., De Santis, L., Kulhanek, D. K., et al. (2022). Pleistocene depositional environments and links to cryosphere-ocean interactions on the eastern Ross Sea continental slope, Antarctica (IODP Hole U1525A). Mar. Geol. 443, 106674. doi:10.1016/j.margeo.2021.106674

Laberg, J. S., and Camerlenghi, A. (2008). "The significance of contourites for submarine slope stability," in Contourites developments in sedimentology. Editors M. Rebesco, and A. Camerlenghi (Amsterdam, Netherlands: Elsevier), 537–556. doi:10.1016/S0070-4571(08)10025-5

Lasabuda, A., Geissler, W. H., Laberg, J. S., Knutsen, S., Rydningen, T. A., and Berglar, K. (2018). Late cenozoic erosion estimates for the northern barents sea: quantifying glacial sediment input to the Arctic Ocean. Geochem. Geophys. Geosystems 19, 4876–4903. doi:10.1029/2018gc007882

Lawver, L. A., Gahagan, L. M., and Coffin, M. F. (1992). "The development of paleoseaways around Antarctica," in The antarctic palaeoenvironment: a perspective on global change antarctic research series. Editors J. P. Kennett, and D. A. Warnke

(Washington, DC): AGU), 7 – 30.

Le Heron, D. P., Hogan, K. A., Phillips, E. R., Huuse, M., Busfield, M. E., and Graham, A. G. C. (2019). in Glaciated margins--the sedimentary and geophysical archive. Editors D. P. Le Heron, K. A. Hogan, E. R. Phillips, M. Huuse, M. E. Busfield, and A. G. C. Graham (Washington, D.C., United States: Geological Society London).

Livingstone, S. J., Cofaigh, C., Stokes, C. R., Hillenbrand, C.-D., Vieli, A., and Jamieson, S. S. (2012). Antarctic palaeo-ice streams. Earth-Science Rev. 111, 90 – 128. doi:10.1016/j.earscirev.2011.10.003, Ó

Long, D., Stevenson, A. G., Wilson, C. K., and Bulat, J. (2003). "Slope failures in the faroe-shetland channel," in Submarine mass Movements and their consequences: 1st international symposium advances in natural and technological hazards research series. Editors J. Locat, and J. Mienert (Netherlands: Kluwer Academic Publishers), 281 – 289.

López-Quirós, A., Lobo, F. J., Escutia, C., García, M., Hernández-Molina, F. J., Pérez, L. F., et al. (2020). Geomorphology of ona basin, southwestern scotia sea (Antarctica): decoding the spatial variability of bottom-current pathways. Mar. Geol. 422, 106113. doi:10.1016/j.margeo.2020.106113

Lu, H., Fulthorpe, C. S., and Mann, P. (2003). Three-dimensional architecture of shelf-building sediment drifts in the offshore Canterbury Basin, New Zealand. Mar. Geol. 193, 19 – 47. doi:10.1016/S0025-3227(02)00612-6

Lucchi, R. G., Camerlenghi, A., Rebesco, M., Colmenero-Hidalgo, E., Sierro, F. J., Sagnotti, L., et al. (2013). Postglacial sedimentary processes on the storfjorden and kveithola Trough mouth fans: significance of extreme glacimarine sedimentation. Glob. Planet. Change 111, 309 – 326. doi:10.1016/j.gloplacha.2013.10.008

Lucchi, R. G., Rebesco, M., Camerlenghi, A., Busetti, M., Tomadin, L., Villa, G., et al. (2002). Mid-late Pleistocene glacimarine sedimentary processes of a high-latitude, deep-sea sediment drift (Antarctic Peninsula Pacific margin). Mar. Geol. 189, 343 – 370. doi:10.1016/S0025-3227(02)00470-X

Martorelli, E., Petroni, G., Chiocci, F. L., Party, , and the, P. S. (2011). Contourites offshore Pantelleria island (sicily channel, mediterranean sea): depositional, erosional and biogenic elements. Geo-Marine Lett. 31, 481 – 493. doi:10.1007/s00367-011-0244-0

Matthiessen, J., Niessen, F., Stein, R., and Naafs, B. D. A. (2010). Pleistocene glacial marine sedimentary environments at the eastern Mendeleev Ridge, Arctic Ocean. Polarforschung 79, 123 – 137.

McCave, I. N., and Hall, I. R. (2006). Size sorting in marine muds: processes, pitfalls, and prospects for paleoflow-speed proxies. Geochem. Geophys. Geosystems 7. doi:10.1029/2006gc001284

McCave, I. N., and Swift, S. A. (1976). A physical model for the rate of deposition of

fine-grained sediments in the deep sea. GSA Bull. 87, 541–546. doi:10.1130/0016-7606(1976)87<541:apmftr>2.0.co;2

McKay, R. M., Albot, O., Dunbar, G. B., Lee, J. I., Lee, M. K., Yoo, K.-C., et al. (2022). A comparison of methods for identifying and quantifying Ice Rafted Debris on the Antarctic margin. Paleoceanogr. Paleoclimatology 37, e2021PA004404. doi:10.1029/2021pa004404

McKay, R. M., Barrett, P. J., Levy, R. S., Naish, T. R., Golledge, N. R., and Pyne, A. (2016). Antarctic cenozoic climate history from sedimentary records: aNDRILL and beyond. Philosophical Trans. R. Soc. Lond. A Math. Phys. Eng. Sci. 374, 20140301. doi:10.1098/rsta.2014.0301

McKay, R. M., De Santis, L., and Kulhanek, D. K. (2019). "Expedition 374 scientists," in Proceedings of the International Ocean Discovery Program, Lautoka, Fiji, to Papeete, 3 January–6 February 2020.

McKay, R. M., Naish, T., Carter, L., Riesselman, C., Dunbar, R., Sjunneskog, C., et al. (2012). Antarctic and Southern Ocean influences on late Pliocene global cooling. Proc. Natl. Acad. Sci. 109, 6423–6428. doi:10.1073/pnas.1112248109

Melis, R., Capotondi, L., Torricella, F., Ferretti, P., Geniram, A., Hong, J. K., et al. (2021). Last glacial maximum to holocene paleoceanography of the northwestern Ross Sea inferred from sediment core geochemistry and micropaleontology at Hallett Ridge. J. Micropalaeontology 40, 15–35. doi:10.5194/jm-40-15-2021

Miramontes, E., Cattaneo, A., Jouet, G., Théreau, E., Thomas, Y., Rovere, M., et al. (2016). The pianosa contourite depositional system (northern tyrrhenian sea): drift morphology and plio-quaternary stratigraphic evolution. Mar. Geol. 378, 20–42. doi:10.1016/j.margeo.2015.11.004

Miramontes, E., Garziglia, S., Sultan, N., Jouet, G., and Cattaneo, A. (2018). Morphological control of slope instability in contourites: a geotechnical approach. Landslides 15, 1085. doi:10.1007/s10346-018-0956-6

Mitchell, N. C. (1993). A model for attenuation of backscatter due to sediment accumulations and its application to determine sediment thicknesses with GLORIA sidescan sonar. J. Geophys. Res. Solid Earth 98, 22477–22493. doi:10.1029/93jb02217

Morrison, A. K., Hogg, A. McC., England, M. H., and Spence, P. (2020). Warm Circumpolar Deep Water transport toward Antarctica driven by local dense water export in canyons. Sci. Adv. 6, eaav2516. doi:10.1126/sciadv.aav2516

Mosher, D. C., and Boggild, K. (2021). Impact of bottom currents on deep water sedimentary processes of Canada Basin, Arctic Ocean. Earth Planet. Sci. Lett. 569, 117067. doi:10.1016/j.epsl.2021.117067

Neto, A. A., Mendes, J. de N. T., Souzade, J. M. G. M. R., Pontes, R. L. B., and Leandro

Bastos Pontes, R. (2013). Geotechnical influence on the acoustic properties of marine sediments of the santos basin, Brazil. Mar. Georesources Geotechnol. 31, 125–136. doi:10.1080/1064119x.2012.669815

Ó Cofaigh, C., Dowdeswell, J. A., Allen, C. S., Hiemstra, J. F., Pudsey, C. J., Evans, J., et al. (2005). Flow dynamics and till genesis associated with a marine-based Antarctic palaeo-ice stream. Quat. Sci. Rev. 24, 709–740. doi:10.1016/j.quascirev.2004.10.006

Ó Cofaigh, C., Taylor, J., Dowdeswell, J. A., and Pudsey, C. J. (2003). Palaeo-ice streams, trough mouth fans and high-latitude continental slope sedimentation. Boreas 32, 37–55. doi:10.1080/03009480310001858

Ohneiser, C., Yoo, K.-C., Albot, O. B., Cortese, G., Riesselman, C., Lee, J. I., et al. (2019). Magneto-biostratigraphic age models for Pleistocene sedimentary records from the Ross Sea. Glob. Planet. Change 176, 36–49. doi:10.1016/j.gloplacha.2019.02.013

Orsi, A. H., and Wiederwohl, C. L. (2009). A recount of Ross Sea waters. Deep Sea Res. Part II Top. Stud. Oceanogr. 56, 778–795. doi:10.1016/j.dsr2.2008.10.033

Pérez, L. F., De Santis, L., McKay, R. M., Larter, R. D., Ash, J., Bart, P. J., et al. (2021). Early and middle Miocene ice sheet dynamics in the Ross Sea: results from integrated core-log-seismic interpretation. GSA Bull. 134, 348–370. doi:10.1130/B35814.1

Pérez, L. F., Hernández-Molina, F. J., Esteban, F. D., Tassone, A., Piola, A. R., Maldonado, A., et al. (2015). Erosional and depositional contourite features at the transition between the western scotia Sea and southern south atlantic ocean: links with regional water-mass circulation since the middle Miocene. Geo-Marine Lett. 35, 271–288. doi:10.1007/s00367-015-0406-6

Prothro, L. O., Majewski, W., Yokoyama, Y., Simkins, L. M., Anderson, J. B., Yamane, M., et al. (2020). Timing and pathways of East Antarctic ice sheet retreat. Quat. Sci. Rev. 230, 106166. doi:10.1016/j.quascirev.2020.106166

Rebesco, M., Camerlenghi, A., Geletti, R., and Canals, M. (2006). Margin architecture reveals the transition to the modern Antarctic ice sheet ca. 3 Ma. Geology 34, 301–304. doi:10.1130/g22000.1

Rebesco, M., Hernández-Molina, F. J., Van Rooij, D., and W\aahlin, A. (2014). Contourites and associated sediments controlled by deep-water circulation processes: state-of-the-art and future considerations. Mar. Geol. 352, 111–154. doi:10.1016/j.margeo.2014.03.011

Rebesco, M., Larter, R. D., Camerlenghi, A., and Barker, P. F. (1996). Giant sediment drifts on the continental rise west of the Antarctic Peninsula. Geo-Marine Lett. 16, 65–75. doi:10.1007/bf02202600

Rivaro, P., Frache, R., Bergamasco, A., and Hohmann, R. (2003). Dissolved oxygen, NO and PO as tracers for Ross Sea ice shelf water overflow. Antarct. Sci. 15, 399–404. doi:10.1017/s095410200300141x

KOPRI 극지연구소

Rodrigues, S., Hernández-Molina, F. J., Fonnesu, M., Miramontes, E., Rebesco, M., and Campbell, D. C. (2022). A new classification system for mixed (turbidite-contourite) depositional systems: examples, conceptual models and diagnostic criteria for modern and ancient records. Earth-Science Rev. 230, 104030. doi:10.1016/j.earscirev.2022.104030

Ryan, W. B., Carbotte, S. M., Coplan, J. O., O'Hara, S., Melkonian, A., Arko, R., et al. (2009). Global multi-resolution topography synthesis. Geochem. Geophys. Geosystems 10. doi:10.1029/2008gc002332

Rydningen, T. A., Høgseth, G. V., Lasabuda, A. P. E., Laberg, J. S., Safronova, P. A., and Forwick, M. (2020). An early neogene–early quaternary contourite drift system on the SW barents Sea continental margin, Norwegian arctic. Geochem. Geophys. Geosystems 21, e2020GC009142. doi:10.1029/2020gc009142

Savage, M., and Ciesielski, P. (1983). A revised history of glacial sedimentation in the Ross Sea region. Aust. Acad. Sci. Adel. 1983 555–559.

Schlager, U., Jokat, W., Weigelt, E., and Gebhardt, C. (2021). Submarine landslides along the siberian termination of the lomonosov ridge, Arctic Ocean. Geomorphology 382, 107679. doi:10.1016/j.geomorph.2021.107679

Shchepetkin, A. F., and McWilliams, J. C. (2005). The regional oceanic modeling system (ROMS): a split-explicit, free-surface, topography-following-coordinate oceanic model. Ocean. Model. 9, 347–404. doi:10.1016/j.ocemod.2004.08.002

Shipp, S. S., Anderson, J., and Domack, E. (1999). Late pleistocene–holocene retreat of the West antarctic ice-sheet system in the Ross Sea: part 1—geophysical results. Geol. Soc. Am. Bull. 111, 1486–1516. doi:10.1130/0016-7606(1999)111<1486:lphrot>2.3.co;2

Smith, W. O., Sedwick, P. N., Arrigo, K. R., Ainley, D. G., and Orsi, A. H. (2012). The Ross Sea in a sea of change. Oceanography 25, 90–103. doi:10.5670/oceanog.2012.80

Stow, D. A. (2002). Deep-water contourite systems: modern drifts and ancient series, seismic and sedimentary characteristics. England: Geological Society of London.

Taylor, J., Dowdeswell, J. A., and Siegert, M. J. (2002). Late Weichselian depositional processes, fluxes, and sediment volumes on the margins of the Norwegian Sea (62–75oN). Mar. Geol. 188, 61–77. doi:10.1016/s0025-3227(02)00275-x

Thompson, A. F., Stewart, A. L., Spence, P., and Heywood, K. J. (2018). The antarctic slope current in a changing climate. Rev. Geophys. 56, 741–770. doi:10.1029/2018rg000624

Thran, A. C., Dutkiewicz, A., Spence, P., and Müller, R. D. (2018). Controls on the global distribution of contourite drifts: insights from an eddy-resolving ocean model. Earth Planet. Sci. Lett. 489, 228–240. doi:10.1016/j.epsl.2018.02.044

Tolotti, R., Salvi, C., Salvi, G., and Bonci, M. C. (2013). Late Quaternary climate variability as recorded by micropalaeontological diatom data and geochemical data in the western Ross Sea, Antarctica. Antarct. Sci. 25, 804–820. doi:10.1017/S0954102013000199

Torricella, F., Melis, R., Malinverno, E., Fontolan, G., Bussi, M., Capotondi, L., et al. (2021). Environmental and oceanographic conditions at the continental margin of the Central Basin, northwestern Ross Sea (Antarctica) since the last glacial maximum. Geosciences 11, 155. doi:10.3390/geosciences11040155

Uenzelmann-Neben, G. (2006). Depositional patterns at drift 7, antarctic peninsula: along-slope versus down-slope sediment transport as indicators for oceanic currents and climatic conditions. Mar. Geol. 233, 49–62. doi:10.1016/j.margeo.2006.08.008

Uenzelmann-Neben, G., and Gohl, K. (2012). Amundsen Sea sediment drifts: archives of modifications in oceanographic and climatic conditions. Mar. Geol. 299, 51–62. doi:10.1016/j.margeo.2011.12.007

Uenzelmann-Neben, G. (2018). Variations in ice-sheet dynamics along the amundsen Sea and bellingshausen sea West Antarctic ice sheet margin. GSA Bull. 131, 479–498. Available at. doi:10.1130/B31744.1

Veeken, P. C. H., and van Moerkerken, B. (2013). Seismic stratigraphy and depositional facies models. Thousand Oaks, California: EAGE publications.

Verdicchio, G., and Trincardi, F. (2008). Mediterranean shelf-edge muddy contourites: examples from the gela and south adriatic basins. Geo-Marine Lett. 28, 137–151. doi:10.1007/s00367-007-0096-9

Vorren, T. O., and Laberg, J. S. (1997). Trough mouth fans—Palaeoclimate and ice-sheet monitors. Quat. Sci. Rev. 16, 865–881. doi:10.1016/s0277-3791(97)00003-6

Whitehouse, P. L., Gomez, N., King, M. A., and Wiens, D. A. (2019). Solid Earth change and the evolution of the antarctic ice sheet. Nat. Commun. 10, 503. doi:10.1038/s41467-018-08068-y

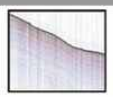
Whitworth, T. (1988). The Antarctic circumpolar current. Oceanus 31, 53–58.

Wilson, D. S., and Luyendyk, B. P. (2009). West Antarctic paleotopography estimated at the Eocene-Oligocene climate transition. Geophys. Res. Lett. 36, L16302. doi:10.1029/2009gl039297

Wynn, R. B., and Stow, D. A. (2002). Classification and characterisation of deep-water sediment waves. Mar. Geol. 192, 7–22. doi:10.1016/s0025-3227(02)00547-9

KOPRI 극지연구소

Table 1. Classification of acoustic facies of the surficial sedimentary strata in the sub-bottom profiler (SBP) data..

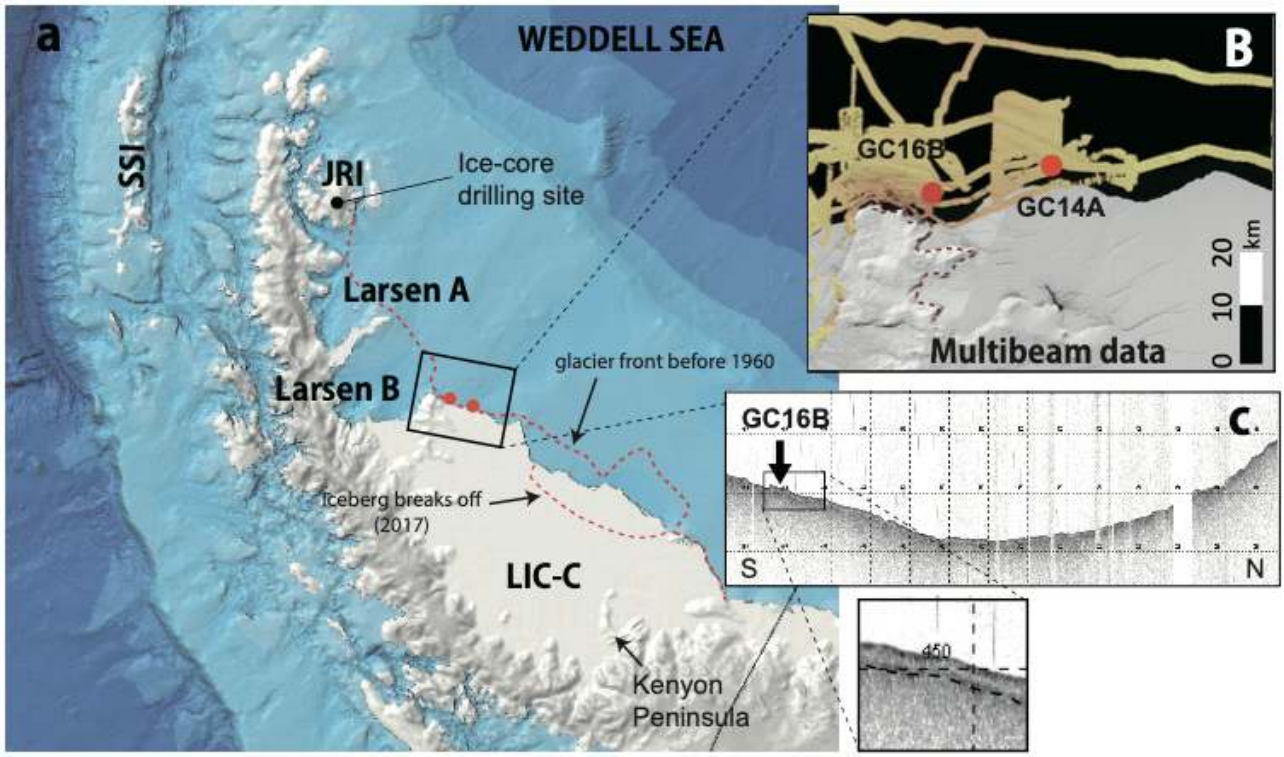
Seismic facies		Description	Interpretation	Occurrence
Facies S		Thick (>10 m), highly stratified units with laterally continuous, low-to-medium amplitude subparallel internal reflections; weak-to-moderate amplitude seafloor reflection	Contourite deposits affected by relatively slow-flowing downslope and along-slope bottom-current processes in deep water settings; hemipelagic settling or suspension settling from turbid meltwater plumes in the ice-distal environments	Mid-lower slope of western Hallett Ridge, northern and eastern part of the Central Basin, on the Scott Canyon Basin, southwestern part of the Central Basin
	Facies Sh			
		Thin (<10 m), weakly stratified units composed of most internal reflections with low amplitude and a few high-amplitude reflections; high amplitude seafloor reflection	Contourite deposits affected by bottom current winnowing processes in shallow water settings	Crests and upper slopes of the Hallett Ridge, northern and eastern slope of Iselin Bank
	Facies Sw			
Facies T		acoustically transparent unit with erosional lower boundary and irregular- or lens-shaped external geometry	Subglacial till or glaciogenic debris flow deposits in the subglacial or ice-proximal settings; mass transport deposits in the deep water and ice-distal settings	Outer shelf and slope beyond the JOIDES Trough, eastern lower slope of the Hallett Ridge

KOPRI
극지연구소

Table 2. Sediment cores retrieved in the northwestern Ross Sea margin.

Expedition	Core name	Gear type	Year	Water depth (m)	Latitude	Longitude	Recovery (cm)	Average sand/ silt/clay content (%)	Average water content (%)
ANA03B	KI13-BC2	Box	2013	2,246	71°52′S	179°30′E	37	17.8/76.3/5.9	37.3
ANA03B	KI13-C1	Gravity	2013	2,256	71°52′S	179°30′E	326	16.7/73.3/10.0	29.5
ANA03B	KI13-BC3	Box	2013	1,800	71°52′S	177°48′E	35	19.6/73.5/6.9	41.1
ANA03B	KI13-C2	Gravity	2013	1,797	71°52′S	177°48′E	232	31.2/62.3/6.5	-
ANA03B	KI13-BC4	Box	2013	1,772	72°34′S	177°33′E	44	14.1/79.2/6.7	41.1
ANA05B	RS15-GC40	Gravity	2015	1,083	71°37′S	178°17′W	257	65.2/32.9/1.8	23.9
ANA05B	RS15-GC41	Gravity	2015	1,557	71°23′S	178°59′W	540	30.2/64.9/5.0	34.4
ANA05B	RS15-LC42	Gravity	2015	2,084	71°49′S	178°35′E	1,186	16.3/79.8/3.9	36.3
PNRA	ANTA91-4C	Gravity	1991	2,815	71°10′S	178°28′E	630	13.3/75.2/11.5	36.6
PNRA	ANTA95-98C	Gravity	1995	1,788	72°33′S	177°34′E	376	11.4/75.5/13.1	27.7
PNRA	ANTA95-99C1	Gravity	1995	532	73°22′S	177°02′E	71	29.5/64.3/6.2	21.5
PNRA	ANTA99-23C	Gravity	1999	2,158	72°05′S	179°04′E	548	13.4/62.3/11.0	36.9
PNRA	HLF16-3PC	Piston	2016	1,320	71°50′S	177°26′E	240	44.3/51.3/4.4	25.5
PNRA	HLF16-4BC	Box	2016	1,320	71°50′S	177°26′E	26	41.0/52.3/6.7	23.6
PNRA	HLF16-5BC	Box	2016	800	71°50′S	177°03′E	26	49.9/46.0/4.1	25.8

KOPRI 극지연구소


a
WEDDELL SEA
SSI
JRI
Ice-core
drilling site
Larsen A
Larsen B
glacier front before 1960
Iceberg breaks off
(2017)
LIC-C
Kenyon
Peninsula
B
GC16B
GC14A
0 10 20 km
Multibeam data
GC16B
C
S
N
450

KOPRI
극지연구소

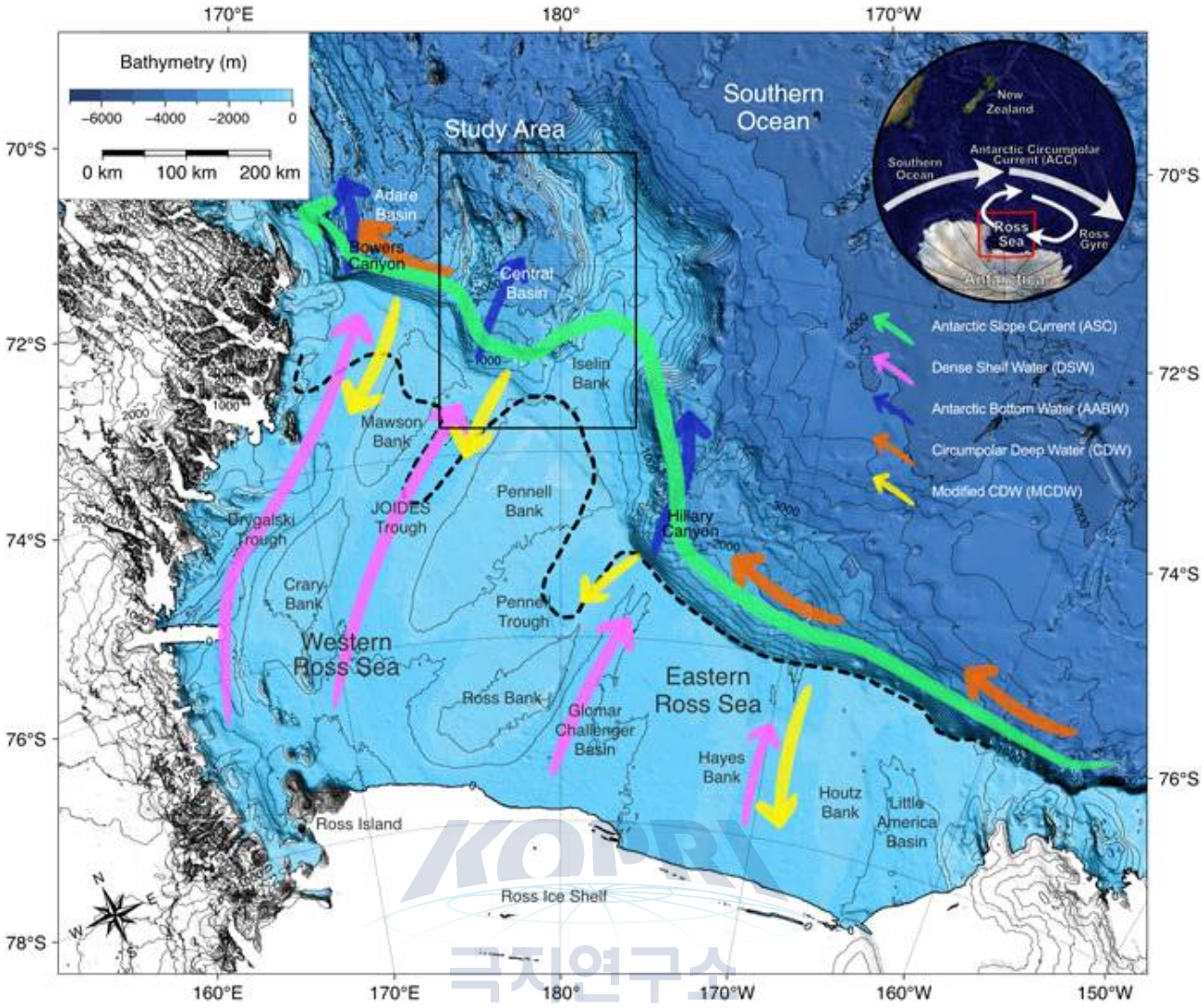


Figure 1. The regional bathymetry and elevation extracted from the International Bathymetric Chart of the Southern Ocean Version 2 (IBCSO v2; Dorschel et al., 2022) and oceanographic setting (modified from Smith et al., 2012) of Ross Sea region in Antarctica. The red rectangle in the upper right inset locates the Ross Sea in the Antarctica. In the upper right inset figure, the white thick and thin arrows represent the flow direction of the Antarctic Circumpolar Current (ACC) and the circulation of Ross Gyre, respectively. The black rectangle in the main figure locates the Central Basin. The main water masses in the Ross Sea are indicated by color-coded arrows, with labels and abbreviations provided in the upper right. The black dashed line is the reconstructed grounding line at the Last Glacial Maximum (Halberstadt et al., 2016).

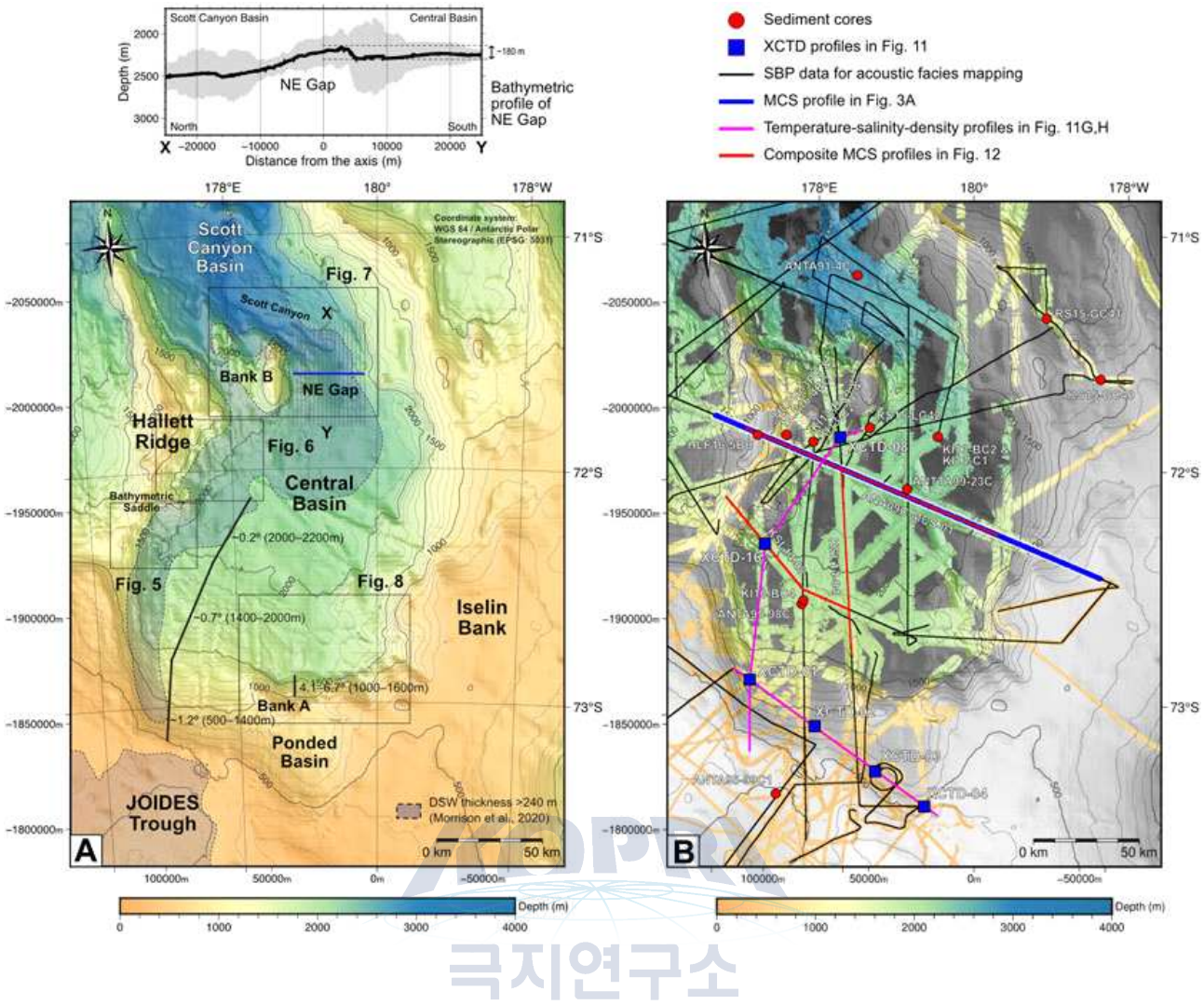


Figure 2. (A) Bathymetric map of the Central Basin extracted from IBCSO v2 (Dorschel et al., 2022). The thick black solid line with numbers represents the measured slope gradient beyond the JOIDES Trough. Blue translucent areas with dashed outlines indicate the distribution of dense shelf water (DSW) outflow thicker than 240 m, as given in the oceanographic modeling of Morrison et al. (2020). Black rectangles locate enlarged MBES bathymetry and backscatter images (Figures 5–8). The upper left inset is a median stacked bathymetric profile at the northeastern gap (NE Gap) of the Central Basin. The black solid line shows a stacked bathymetric profile and the gray area representing the 2σ confidence bounds on the stacked median profile. (B) Map showing locations of sub-bottom profiler (SBP) and multi-channel seismic (MCS) data, multi-beam echosounder (MBES) bathymetry, sediment core sites, and expandable conductivity-temperature-depth (XCTD) data in the Central Basin and over its surrounding bathymetric highs. The MBES bathymetry data (color-coded grid) is superimposed on the regional bathymetry of IBCSO v2 (gray-color grid).

KOPRI 극지연구소

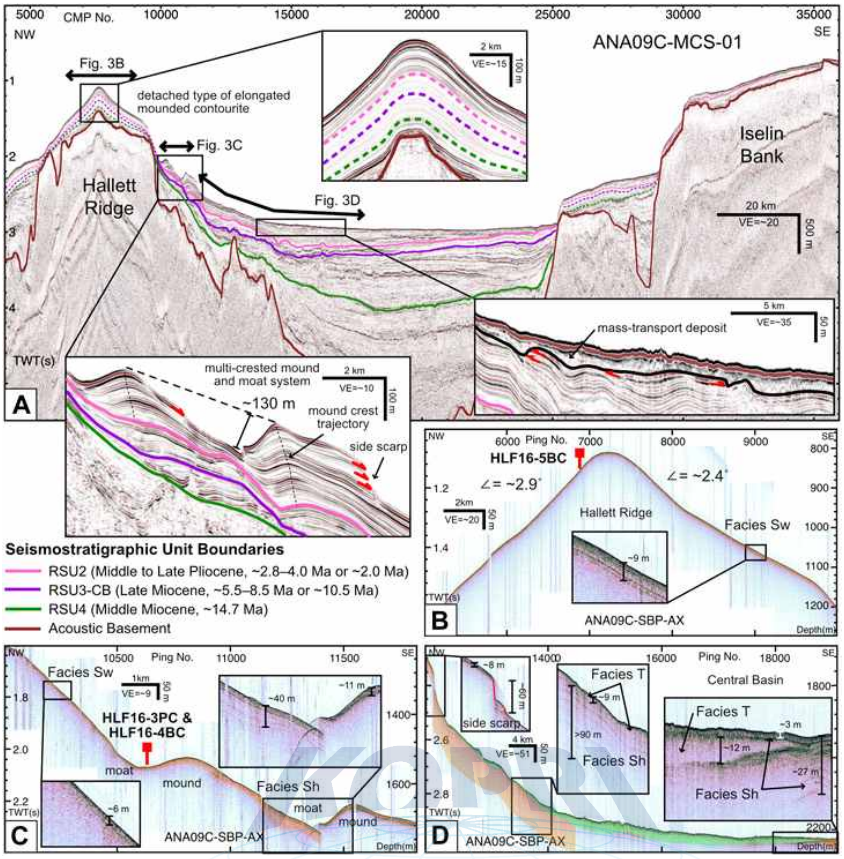


Figure 3. (A) The cross-basin multi-channel seismic (MCS) profile ANA09C-MCS-01, showing the acoustic basement structure and seismic stratigraphic setting in the Central Basin, Hallett Ridge, and Iselin Bank. Color-coded lines in the MCS profile indicate seismostratigraphic boundaries. Dashed lines in the sedimentary deposits on the basement highs of the Hallett Ridge and western Iselin Bank are tentatively identified seismostratigraphic boundaries. Black double arrows represent the locations of corresponding sub-bottom profiler (SBP) images shown in (B – D). Red arrows mark the termination of internal reflections against scarps, suggesting slope failures or erosional surfaces. (B) SBP image shows thin (<10 m) stratified sedimentary layer of Facies Sw (orange-shaded area) on the crest of Hallett Ridge. The red icon pointing down indicates a location of sediment core. (C) Thin stratified sedimentary layer on the upper slope and moats, thickening in the down-slope direction. (D) Thick stratified sedimentary layer of Facies Sh (orange-shaded area) on the lower slope of the western Central Basin, overlain by an irregular-shaped sediment body of Facies T (green-shaded area) in the northwestern part of the Central Basin.

극지연구소

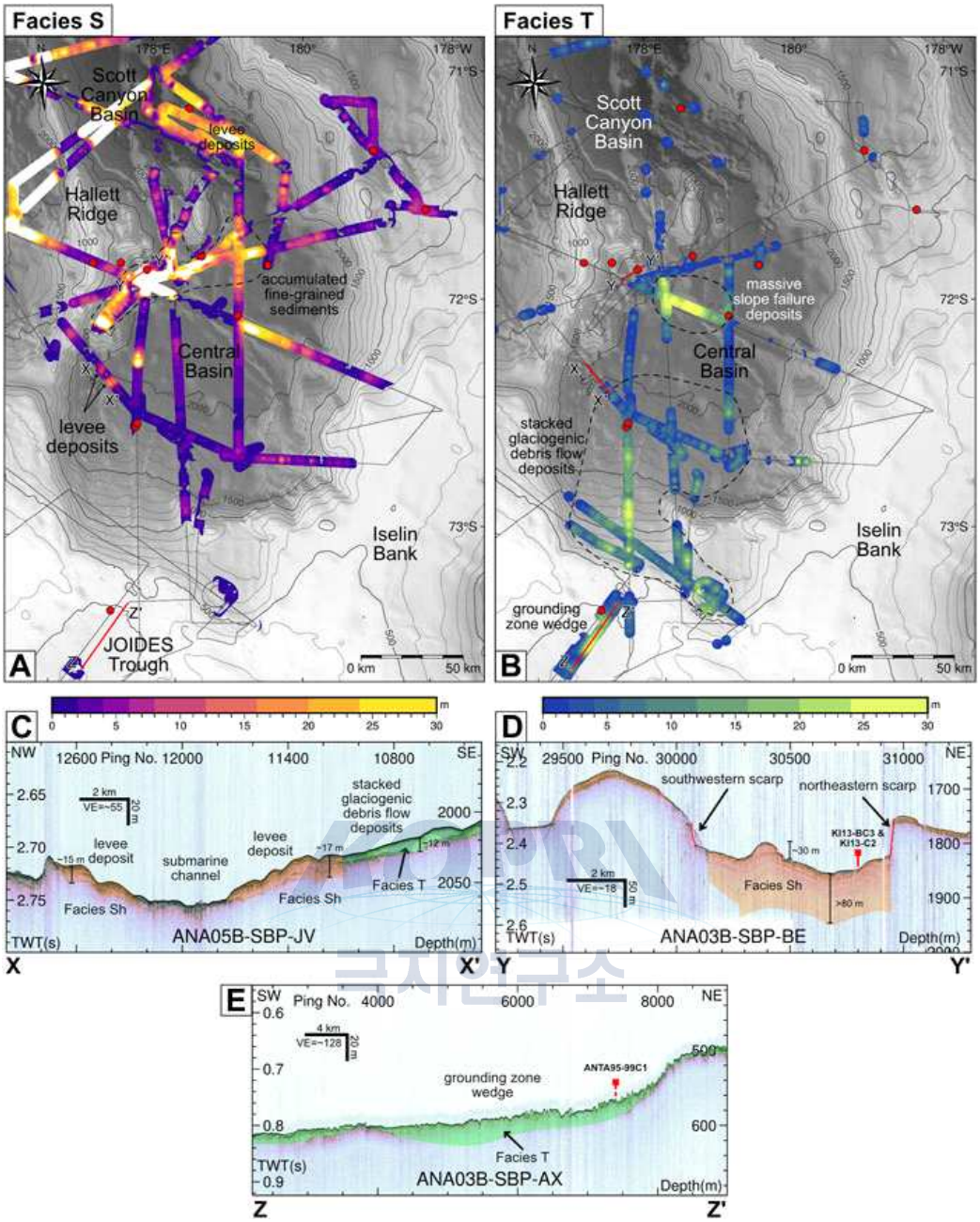


Figure 4. (A) Sediment thickness map showing acoustically stratified facies (Facies S) resolved from SBP data in the study area. Thin black lines represent the SBP data used for acoustic facies mapping. The red lines locate SBP profiles shown in (C, D). The red dots represent the locations of sediment cores used in this study (Figures 2, 9; Table 2). (B) Sediment thickness map showing acoustically transparent facies (Facies T). (C) The SBP profile imaging the presence of a submarine channel-levee feature in the southwestern part of the Central Basin. (D) The SBP profile displaying the side scarps of slope failures on the lower slope of northeastern Hallett Ridge. The red icon pointing down indicates a location of sediment core. (E) The SBP profile showing the grounding zone wedge on the outer shelf of the JOIDES Trough. The dashed red icon pointing down indicates a projected location of sediment core.

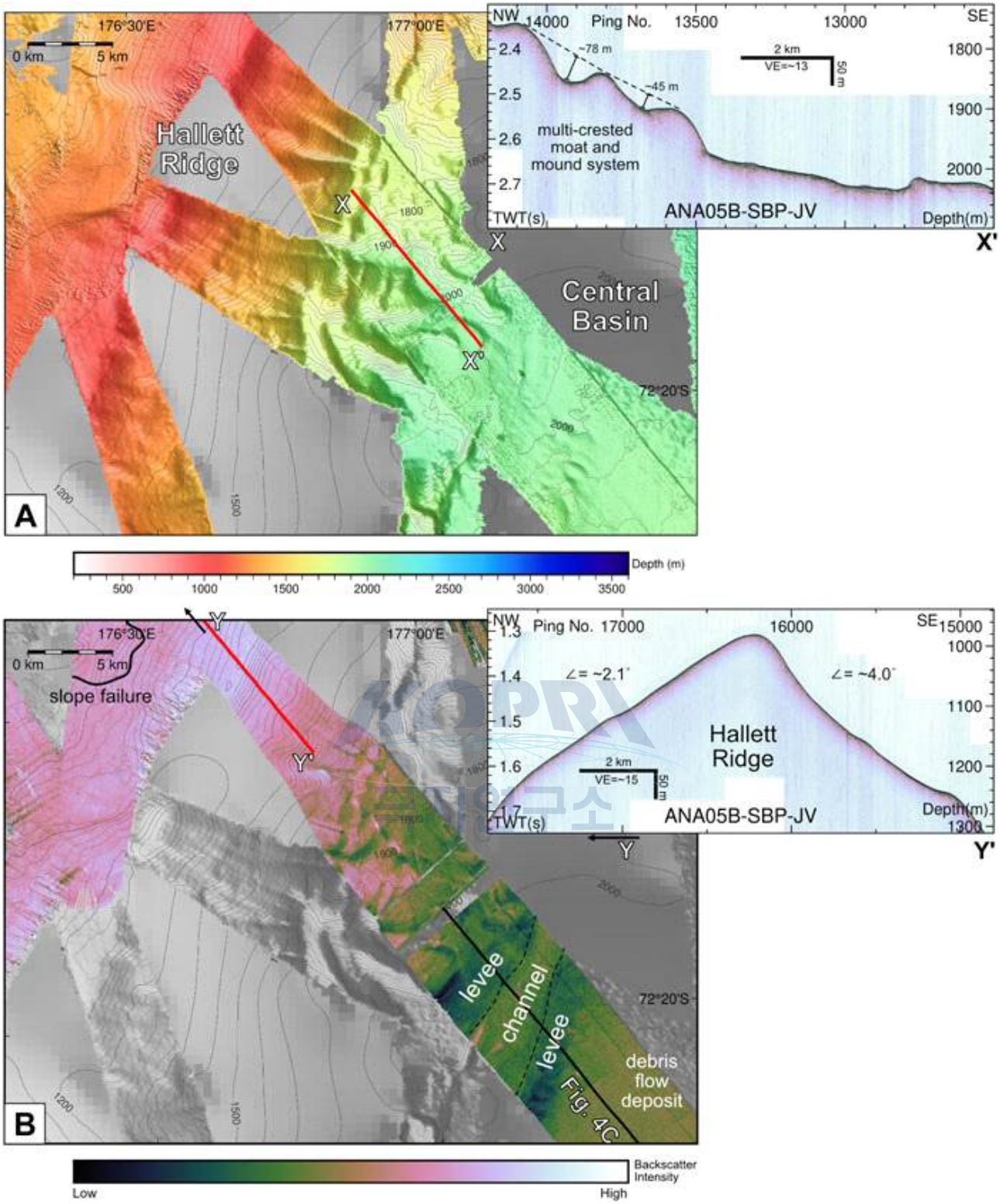


Figure 5. (A) Detailed submarine morphology of the southeastern Hallett Ridge and the western part of the Central Basin captured in an enlarged mosaic of MBES bathymetric data. The red line locates of the SBP data shown in the upper right inset. (B) MBES backscatter data illustrating high and low backscatter intensities depicted in bright and dark green colors, respectively.

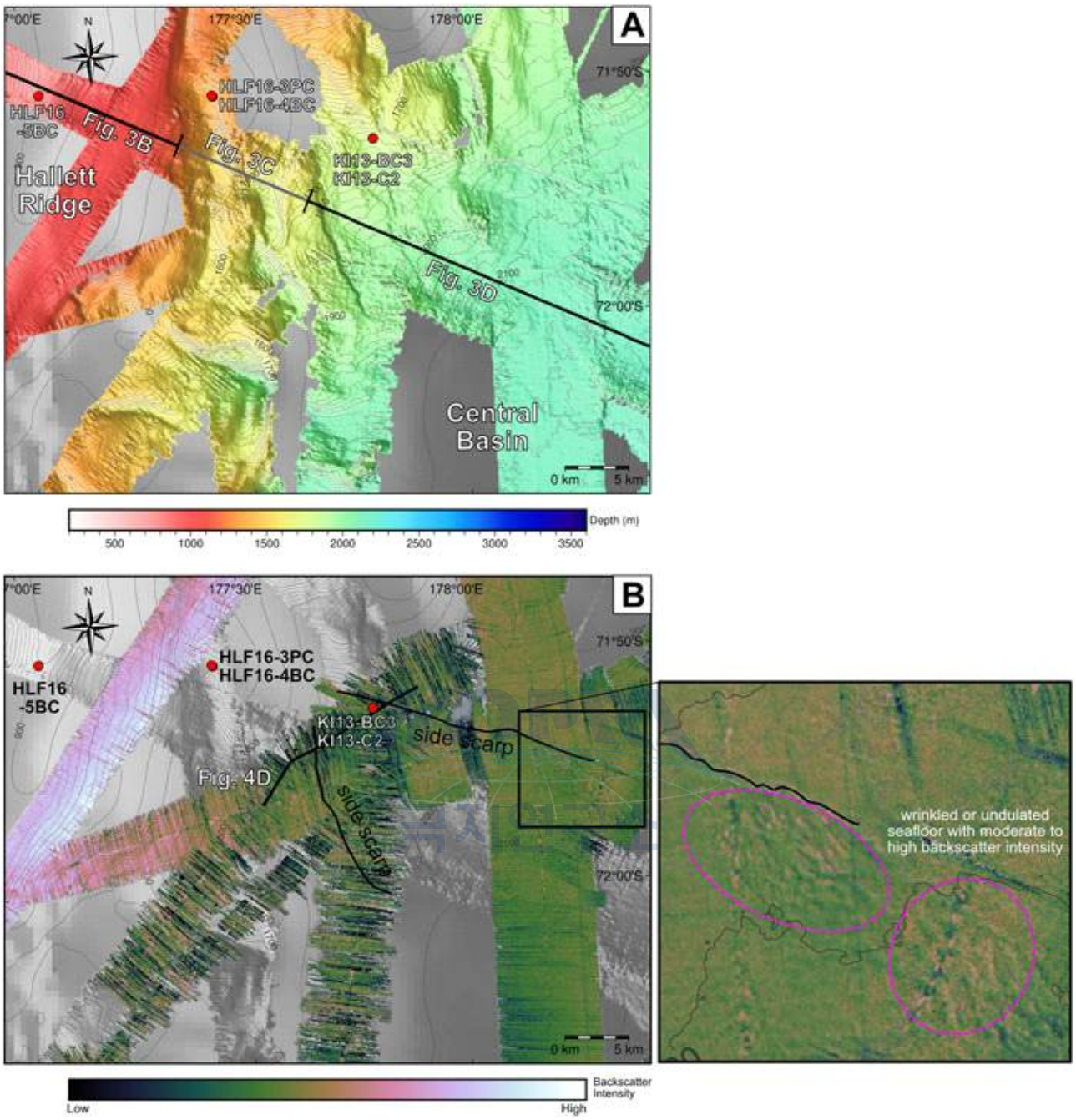


Figure 6. (A) Enlarged mosaic of the MBES bathymetry showing the northwestern sector of the Central Basin. Black and gray lines locate the SBP data crossing eastern slope of Hallett Ridge and northwestern part of Central Basin (Figures 3B – D). The red dots represent the locations of sediment cores. (B) MBES backscatter data of the northwestern sector of the Central Basin. Relatively moderate to high backscatter intensities observed on the wrinkled or undulated seafloor features in front of northern side scarp of the slope failure feature. The black line locates the SBP data crossing the slope failure feature (Figure 4D).

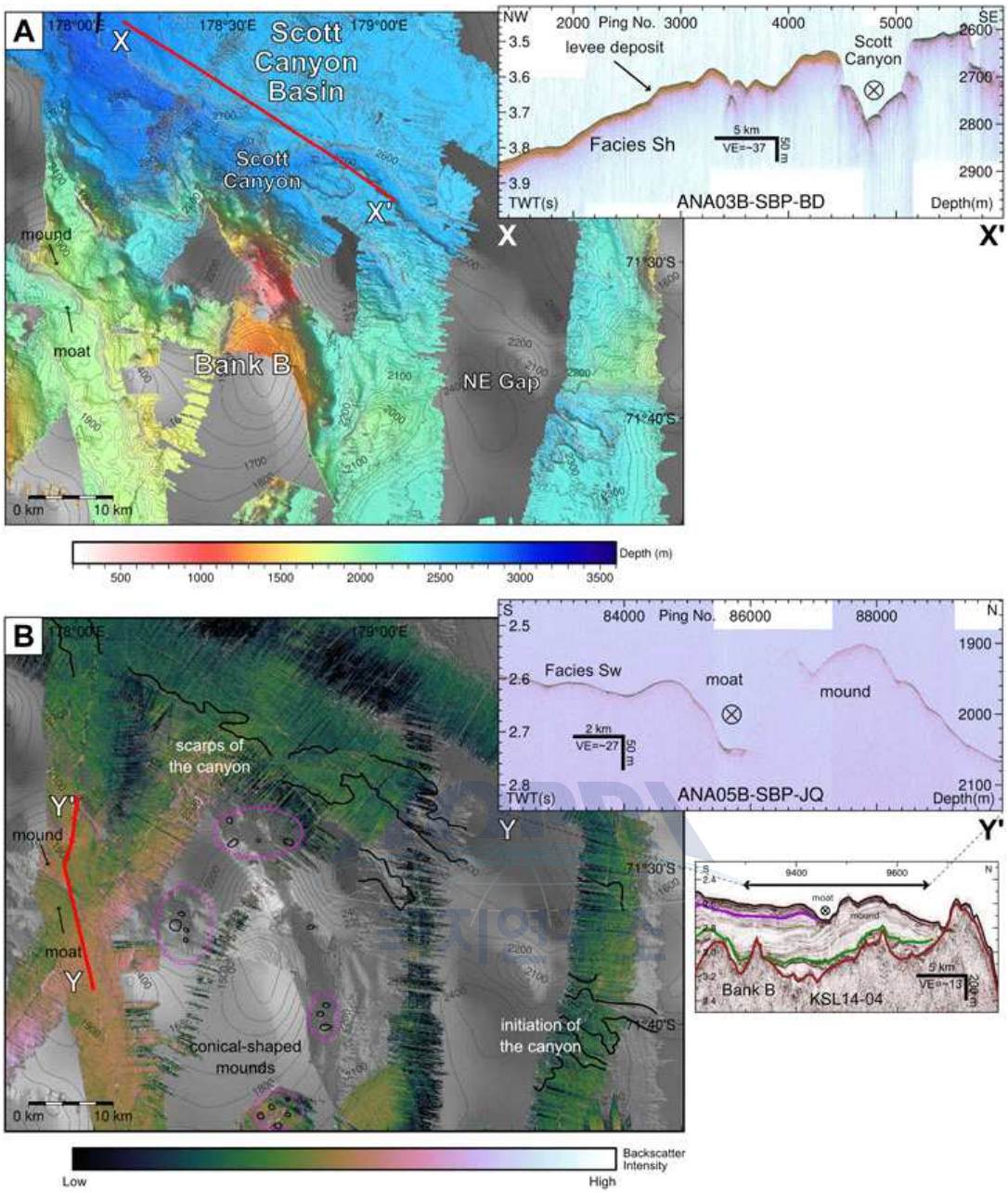


Figure 7. (A) Enlarged mosaic of the MBES bathymetry showing the northern sector of the Central Basin including Bank B, northeastern gap, and Scott Canyon Basin. The red line indicates the locations of the SBP data shown in the upper right inset. (B) Corresponding MBES backscatter data. The purple dashed ellipses indicate groups of small conical-shaped mounds. The SBP profile, depicted in the upper right inset, illustrates the shallow subsurface strata of contourites on Bank B. The MCS profile, corresponding to the SBP data (black double arrow in the right inset), illustrates the subsurface seismostratigraphic units and acoustic basement of Bank B (modified from Kim et al., 2018).

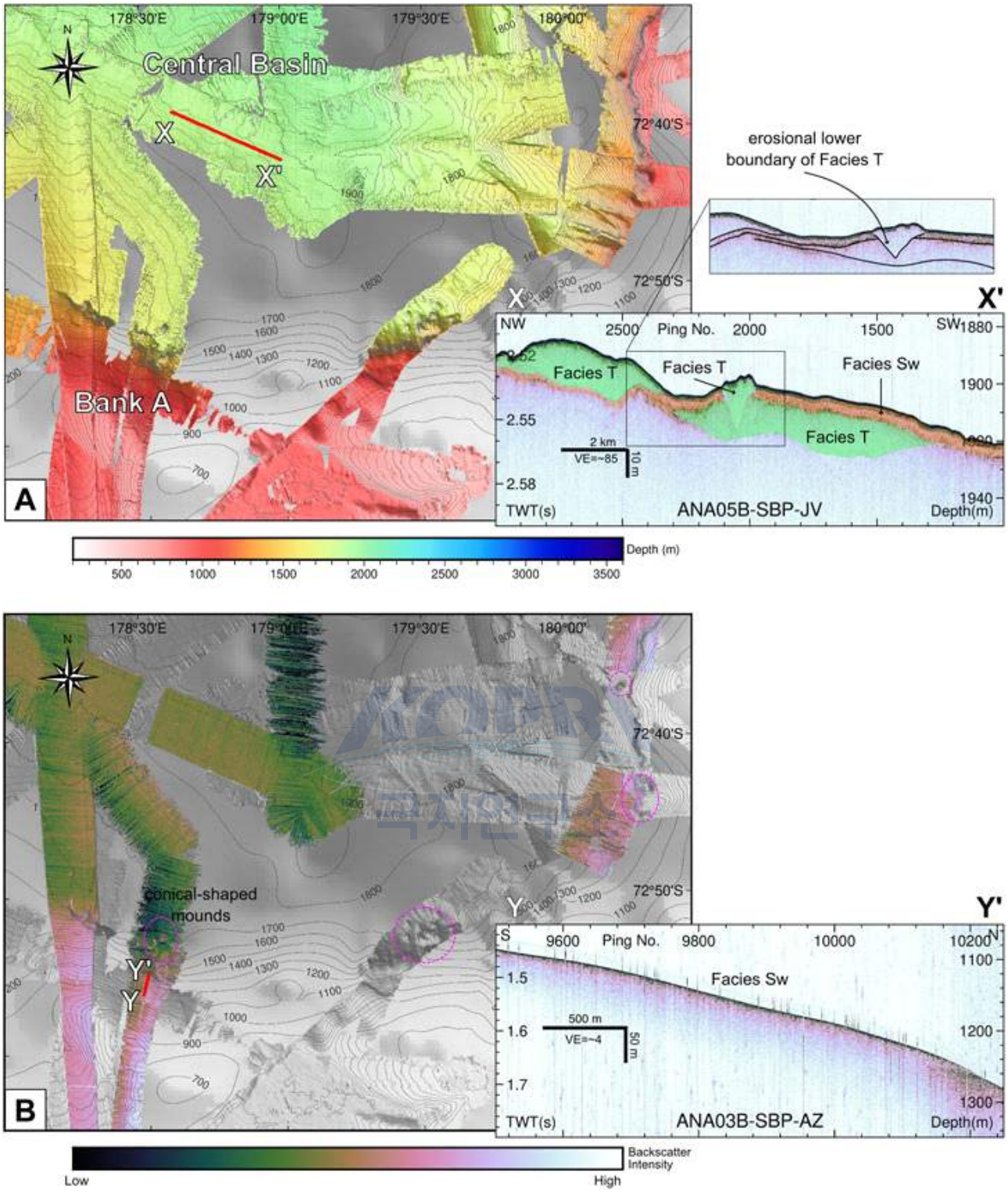


Figure 8. (A) Enlarged mosaic of the MBES bathymetry showing the southeastern sector of the Central Basin. The red line indicates the locations of the SBP data shown in the lower right inset. (B) Corresponding MBES backscatter data.

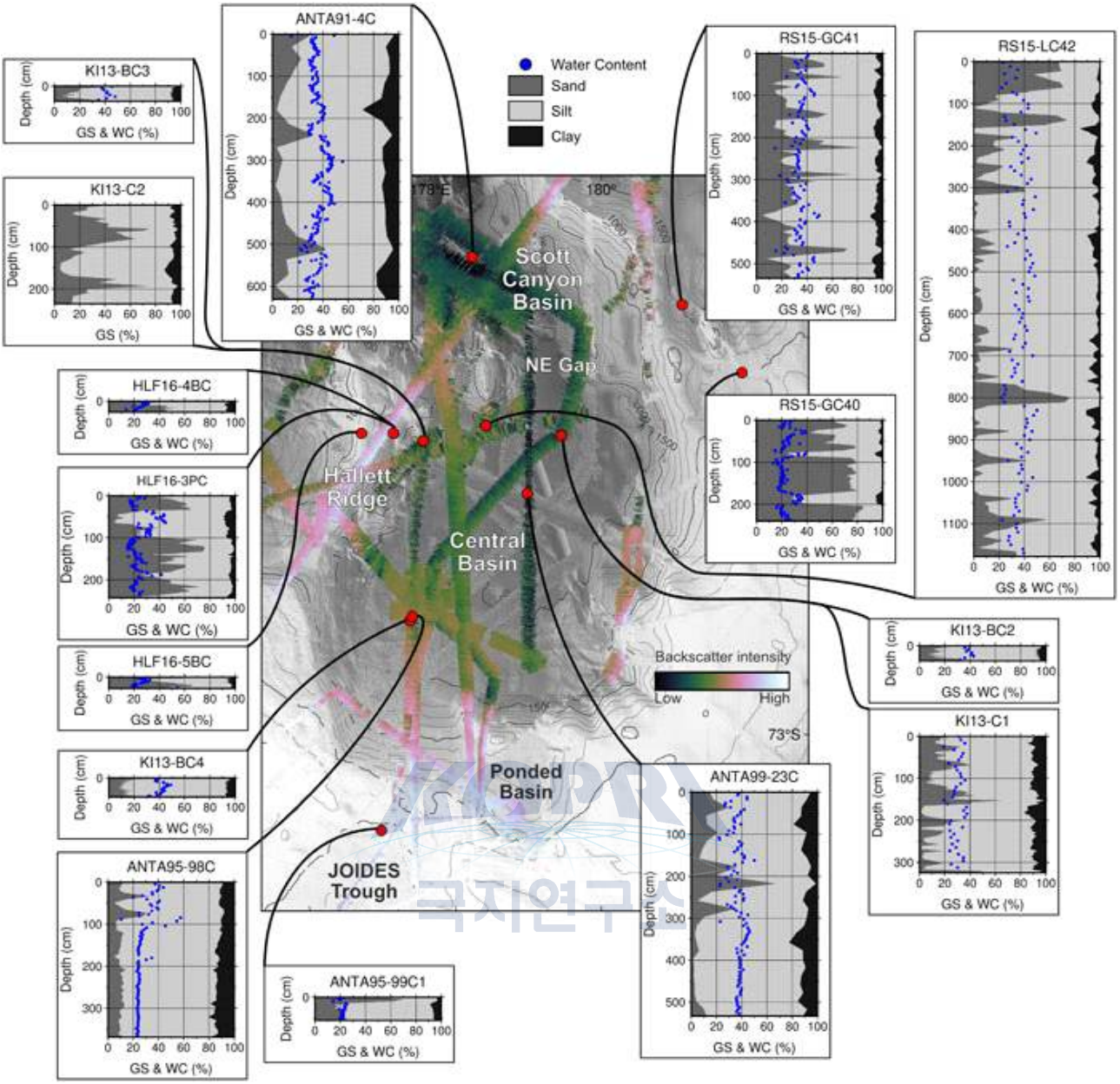


Figure 9. Grain size (GS) and water content (WC) analysis of all sediment cores in the Central Basin. Dark gray, light gray, and black indicate sand, silt, and clay contents of the surficial sediments, respectively. Blue dots are water content values in the sediment cores. The color-coded grid indicates MBES backscatter intensity. Red dots are the locations of the sediment cores.

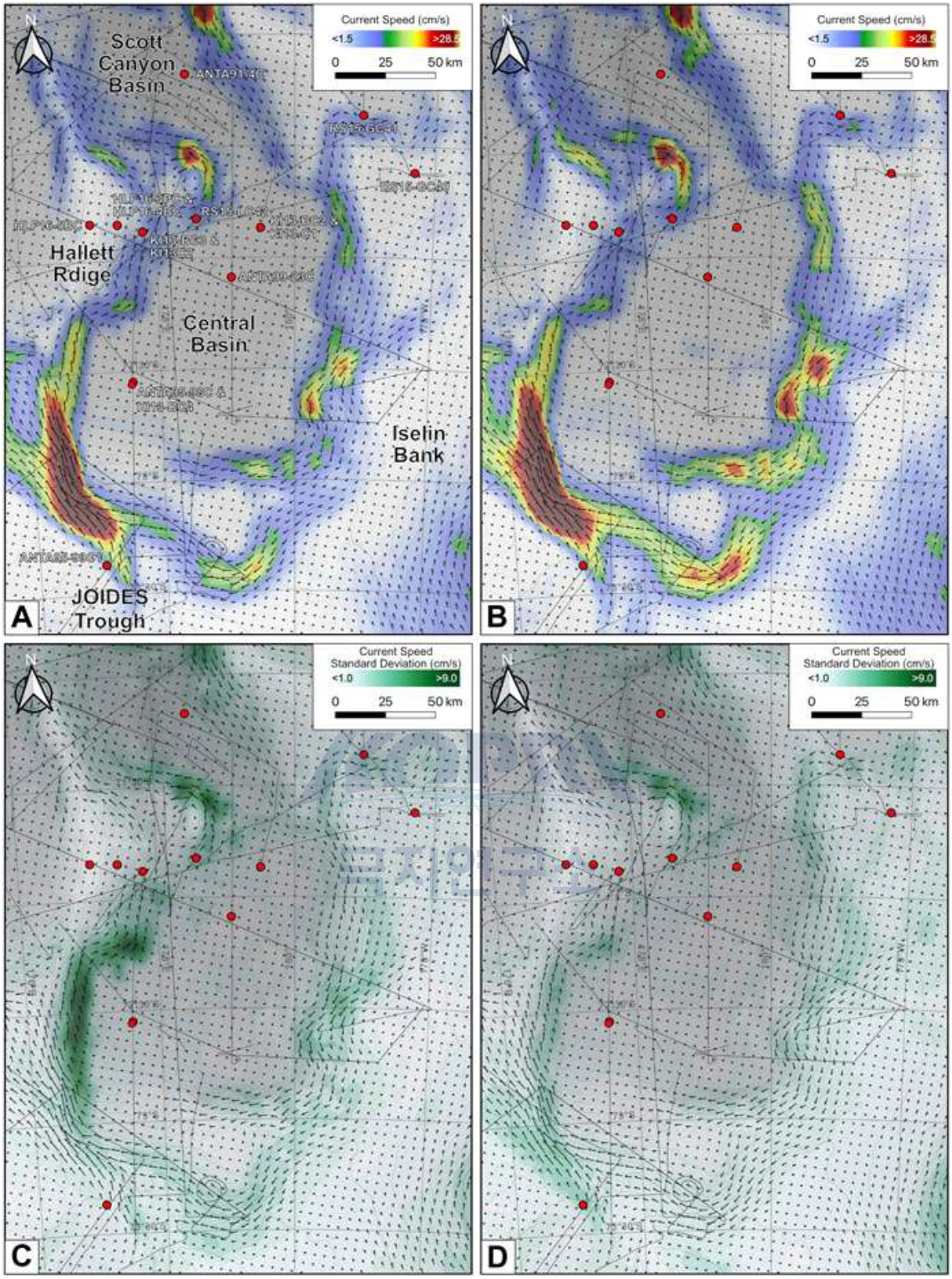


Figure 10. (A) Average austral winter bottom current speed and direction (1999–2013) obtained from the ocean circulation model. Arrows represent direction, and colors indicate velocity magnitude. Red dots indicate sediment core locations. (B) Average austral summer bottom current speed and direction (2000–2014). (C) Standard deviation of bottom current speed during austral winter (1999–2013). (D) Standard deviation of bottom current speed during austral summer (1999–2014).

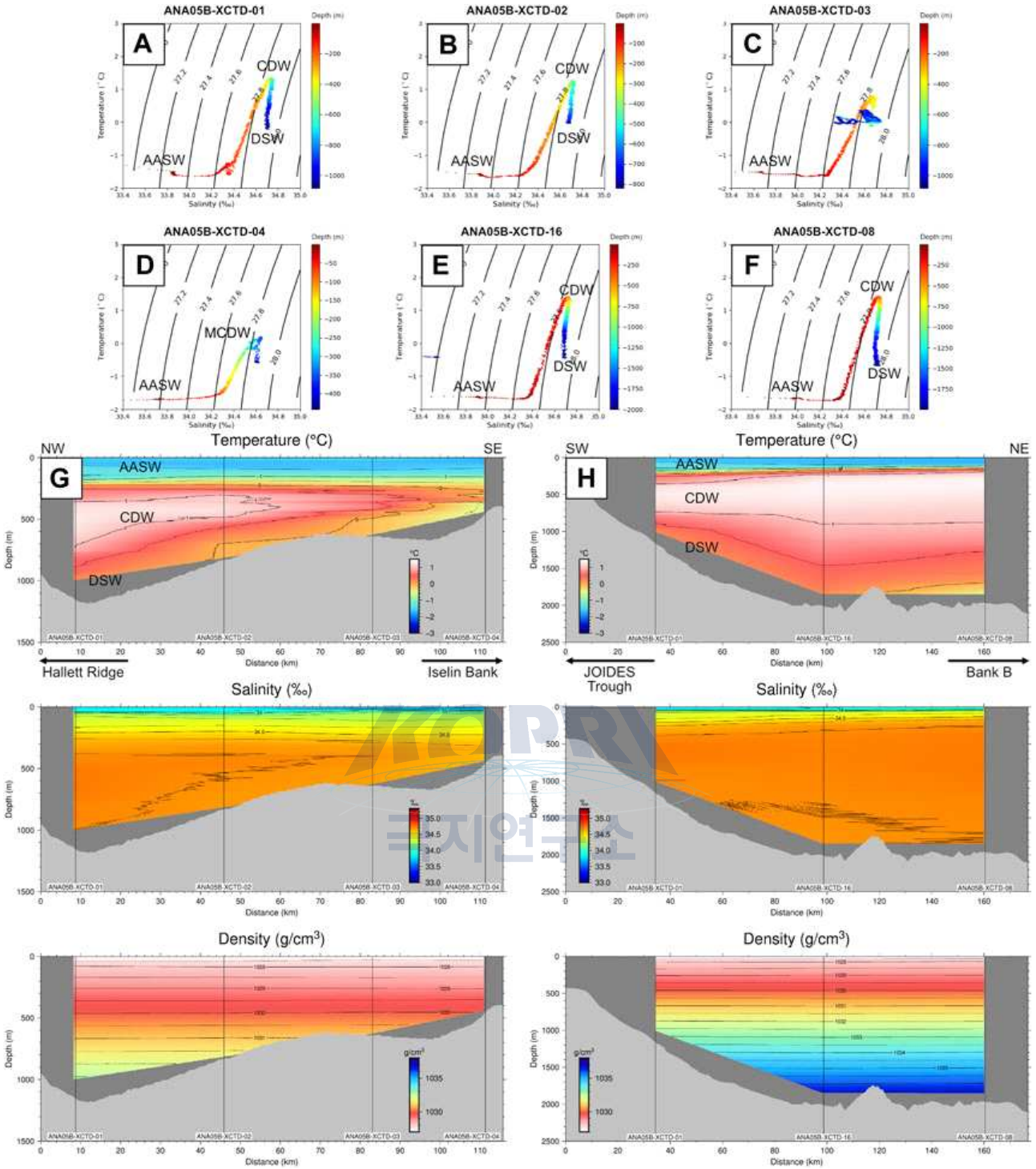


Figure 11. (A–F) Expandable conductivity-temperature-depth (XCTD) profiles acquired in February 2015 illustrating the cascading of DSW into the Central Basin along the eastern slope of Hallett Ridge. XCTD locations are represented by blue squares in Figure 2B. (G) Temperature-salinity-density structures obliquely crossing from the mid-slope to the outer shelf beyond the JOIDES Trough mouth using the ANA05B-XCTD-01 to 04 (A–D). (H) Temperature-salinity-density structures from the outer shelf of the JOIDES Trough to Bank B in the northern Central Basin using the ANA05B-XCTD-01, −16, and −08 (A,E,F).

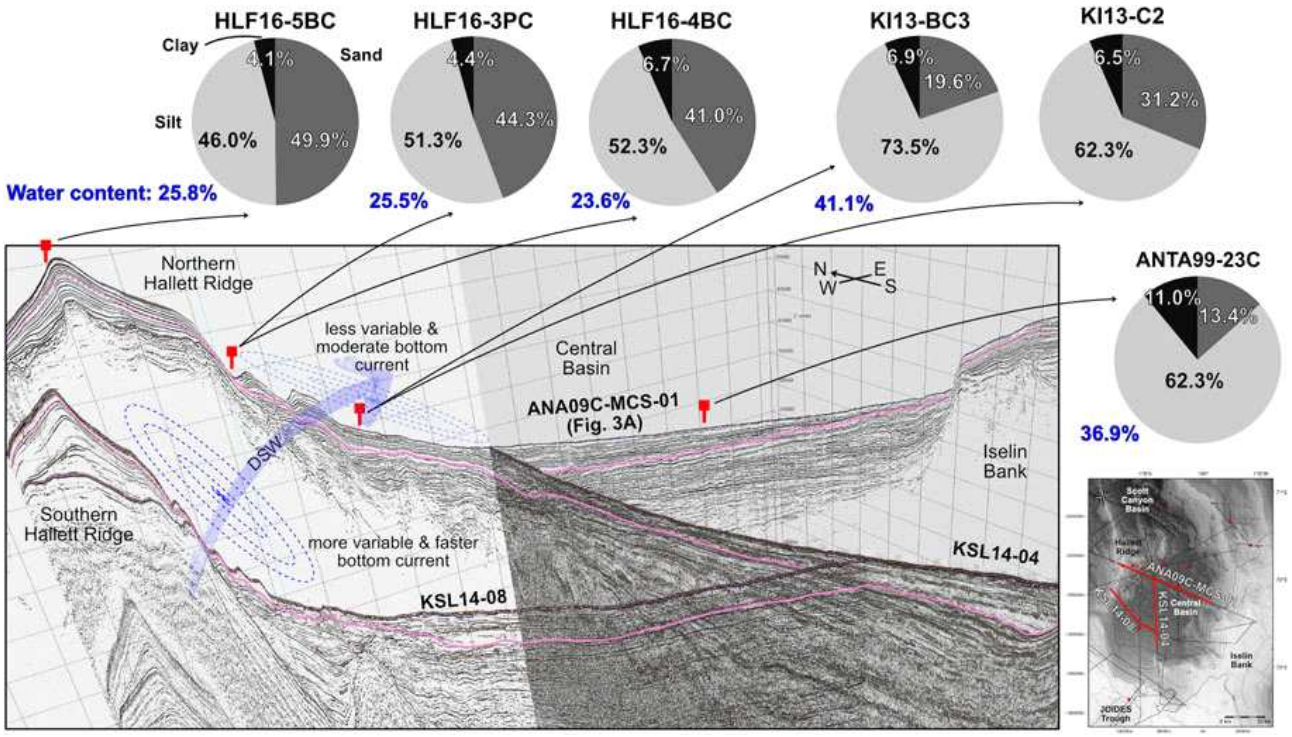


FIGURE 12. Fence diagram of three MCS lines showing the multi-crested mound-and-moat system along the middle to lower slope of Hallett Ridge. Seismic line locations are represented by red lines in the lower right inset and Figure 2B. Pink line indicates the mid-late Pliocene or early Pleistocene boundary, RSU2. Red icons indicate the projected locations of sediment cores. Dark gray, light gray, and black on the pie charts indicate the mean sand, silt, and clay contents of the sediment cores, respectively. Blue numbers near the pie charts are the mean water contents of the sediment cores (Table 2).

제 19 장

Holocene paleoceanographic variability in Robertson Bay, Ross Sea, Antarctica: A marine record of ocean, ice sheet, and climate connectivity[12)]

Olivia J. Truax[1,2,*], Christina R. Riesselman[1,2], Gary S. Wilson[2,3], Craig L. Stevens[4,5], Rebecca L. Parker[1], Jae Il Lee[6], Robert M. McKay[7], Brad E. Rosenheim[8], Catherine E. Ginnane[9], Jocelyn C. Turnbull[9,10]j, Heung Soo Moon[6], Min Kyung Lee[6], Bob Dagg[1,2], Kyu-Cheul Yoo[6]

[1]Department of Geology, University of Otago, New Zealand
[2]Department of Marine Science, University of Otago, New Zealand
[3]University of Waikato, New Zealand
[4]National Institute of Water and Atmospheric Research, New Zealand
[5]Department of Physics, University of Auckland, New Zealand
[6]Korea Polar Research Institute, South Korea
[7]Antarctic Research Centre, Victoria University of Wellington, New Zealand
[8]University of South Florida College of Marine Science, USA
[9]Rafter Radiocarbon Laboratory, GNS Science, New Zealand
[10]CIRES, University of Colorado at Boulder, USA

Abstract: Accelerating ocean-driven basal melting of Antarctic ice shelves in recent decades has implications for sea level rise and global overturning circulation. Here, we reconstruct oceanographic conditions at the confluence of the Ross Sea and the Southern Ocean by analyzing a multi-proxy Holocene marine sedimentary record collected from Robertson Bay. A ramped pyrolysis oxidation radiocarbon age-depth model provides a timeline for glacial behavior and oceanographic changes over the last 6700 years. The diatom assemblage, magnetic susceptibility, grain size, total organic carbon and nitrogen, trace elements, and bulk δ13C are used as proxies for changing ocean and glacial conditions, which we interpret in the context of modern oceanographic measurements.

Our record shows evidence of persistent ice cover in the northwestern Ross Sea during the

12) 이 연구 결과는 다음의 논문으로 출판되었음: Truax et al. (2024). "Holocene paleoceanographic variability in Robertson Bay, Ross Sea, Antarctica: A marine record of ocean, ice sheet, and climate connectivity." Quaternary Science Reviews 332: 108635.

Antarctic mid-Holocene climate optimum (ca. 5 cal kyr BP). Based on this observation, we suggest that meltwater and iceberg discharge associated with ice sheet retreat in the Ross Sea region altered local oceanography during the mid-Holocene. The onset of modern style oceanographic conditions in Robertson Bay occurred at ca. 4 cal kyr BP. Stable late Holocene conditions in are punctuated by a period of enhanced polynya activity and upwelling of nutrient rich Circumpolar Deep Water ca. 0.8 cal kyr BP and an increase in the seasonal duration of sea ice after 0.7 cal kyr BP, during the Little Ice Age. The response of the marine environment in Robertson Bay to mid-Holocene ice sheet retreat and natural climate variability during the last millennium underscores the sensitivity of the Antarctic ice-ocean interface to projected changes in coming decades.

1. Introduction

Ice-ocean interactions play a key role in governing the stability of Antarctic ice sheets at their marine margins (Pritchard et al., 2012). Today, the incursion of relatively warm (>0 °C) Circumpolar Deep Water (CDW) onto the continental shelf drives basal melt of the outlet glaciers at the northern margins of the East and West Antarctica ice sheets in response to a poleward contraction of the Southern Hemisphere Westerly Winds (Rignot et al., 2019; Spence et al., 2014). A number of observational and modeling studies show that meltwater discharge may further warm subsurface waters on the continental shelf, initiating a positive feedback with consequences for both the future stability of the ice sheet and ocean overturning circulation (Bronselaer et al., 2018; Li et al., 2023; Miles et al., 2016; Silvano et al., 2018). However, our understanding of how changes in global mean climate state will affect the interplay between CDW upwelling and ice sheet stability is limited by sparse observations, present modeling capability, and the short duration of the instrumental period. The current generation of coupled global climate models are too coarse (i.e., approximately 1°) to capture the fine-scale processes such as local bathymetry, eddies, and polynyas that drive large regional differences in water mass circulation on the Antarctic continental shelf (Thompson et al., 2018). Further, the ~40 yr observational period routinely used to develop and evaluate predictive models is not long enough to characterize oceanographic variability on multi-centennial timescales (Jones et al., 2016; Thompson et al., 2018).

Paleoceanographic reconstructions from the Holocene (11,500 years ago to present) extend modern instrumental datasets and provide a unique opportunity to investigate the processes and feedbacks that drive the Antarctic ice-ocean system on multi-centennial to millennial timescales and during past intervals of ice sheet retreat. The Holocene was a

dynamic period in the Antarctic. The East and West Antarctic ice sheets underwent rapid periods of retreat in the Ross Embayment, the continent's largest ice drainage basin, between 8 and 3.5 cal kyr BP (Halberstadt et al., 2016; Jones et al., 2020; McKay et al., 2016; Rhee et al., 2020; Siegert et al., 2019; Spector et al., 2017). Recent work shows that retreat was followed by a period of readvance and the ice sheets reached their modern configurations during the late Holocene (Neuhaus et al., 2021, Venturelli et al., 2020). Evidence of readvance is consistent with marine sediment cores, which record a baseline shift from a stable mid-Holocene climate optimum to a cooler, more variable, "Neoglacial" between 4.5 and 3 cal kyr BP (Ashley et al., 2021; Crosta et al., 2007; Denis et al., 2010; Domack et al., 2001; Johnson et al., 2021; Kim et al., 2018; Leventer et al., 1996; Peck et al., 2015). After the ice sheets stabilized, marine sediment and ice core records record multi-centennial variability in coastal sea ice, Antarctic Bottom Water (AABW) production, and CDW upwelling (Mezgec et al., 2017; Shevenell et al., 2011; Tesi et al., 2020; Xu et al., 2021).

We examine mid-to-late Holocene paleoceanographic variability at the confluence of the Ross Sea and the Southern Ocean by analyzing a 6700 year multi-proxy record from Robertson Bay in the context of modern instrumental data. Our Robertson Bay record presents a unique opportunity to reconstruct the impact of mid-Holocene ice sheet retreat (Halberstadt et al., 2016; Jones et al., 2020; Siegert et al., 2019; Spector et al., 2017) on a downstream region of the East Antarctic margin and assess the impact of orbital trends and large-scale modes of atmospheric variability (i.e. the Southern Annular Mode and El Niño-Southern Oscillation) on late Holocene sea ice dynamics and water mass exchange.

KOPRI 극지연구소

2. Materials and methods

2.1. Instrumental data

A salinity and temperature profile (CTD cast) was collected from Robertson Bay in early November of 2015 through a borehole in the sea ice (71°32.2672′S 170 °03.5386′E) (Fig. 1; Fig. 2). Salinity and temperature of the water column were measured to a depth of 470 m using a Sea-Bird SBE 19 CTD with a Sea-Bird SBE 43 dissolved oxygen sensor and a Wetlabs Wetstar WS3S fluorometer on the downcast. Two Sea-Bird SBE 37-SMP-ODO CTDs mounted on hydrographic moorings were deployed in the interior of the Bay at depths of 45 m, 53 m, and 302 m ("shallow" and "deep" respectively, Fig. 1) in January 2015 during KOPRI cruise ANA05B and recovered in January of 2017 (Fig. 3). Salinity, potential temperature, and dissolved oxygen measurements from the CTD cast are corrected

using the mooring data (Supplementary Data). A weather station measuring wind direction, wind speed, and air temperature was also installed on the Cape Adare ridge and we present one year of continuous measurement starting in November 2015. Modern sea ice dynamics (2003–2022) were examined using satellite data from Terra MODIS and Aqua MODIS and accessed via NASA Worldview images (Fig. 3) (NASA Worldview; https://worldview.earthdata.nasa.gov/).

2.2. Sampling and subsampling

Gravity core RS15-GC57 was collected from Robertson Bay by the R/V Araon during the ANA05B Cruise in 2015 (71°32.27′S, 170°03.54′E; 344 m water depth), recovering 570 cm of sediment. Shipboard observations indicate intact recovery of the core top. The core was split, imaged, X-rayed, and described at the Korea Polar Research Institute (KOPRI) in August of 2015. U-channels were collected and sub-samples for geochemical and quantitative diatom analysis were taken at 5 cm increments to enable high-resolution paleoenvironmental reconstruction. All subsamples were frozen and freeze-dried before analysis.

KOPRI 극지연구소

2.3. Proxy analysis

Samples were homogenized using an agate mortar and pestle for geochemical analysis. Biogenic silica (wt% BSi) was measured at the University of Otago using an alkaline extraction spectrophotometric method modified from Strickland and Parsons, 1972 and Mortlock and Froelich (1989). Replicates were measured after every 10th sample, and one blank and one internal standard were analyzed with every analytical run. The average standard deviation of the 31 replicates is 0.25%.

Sample preparation for total organic carbon (TOC) and δ13C analysis of bulk decalcified sediment was completed at the University of Otago. Thirty milligrams of sediment was weighed into silver capsules. The sediment was acidified progressively with four additions of 6% sulphurous acid (H2SO3) (40 ml x1; 60 µL × 2; 80 µL × 1) to remove carbonate and analyzed using a Carlo Erba NA1500 Series 2 Elemental Analyzer interfaced with a DeltaPlus isotope ratio mass spectrometer via a ConFlo II interface at the Stanford University Stable Isotope Laboratory. The average standard deviation across 35 replicates is 0.20‰ for δ13C and 0.03% for TOC. Total nitrogen (TN) concentrations were measured with an Organic Elemental Analyzer (FLASH, 2000 NC Analyzer) at KOPRI. Volume-normalized magnetic susceptibility was measured at 1 cm increments on a u-channel using a 30 mm Barrington loop sensor (MS2C) on the University of Otago's Geotek multi-sensor core

logger.

Grain size data were analyzed at 5 cm intervals at KOPRI on samples treated with H2O2 and HCl to remove organic matter and CaCO3, respectively. Coarse fractions (>63 μm) were analyzed with a set of sieves to determine the distribution of gravel to very fine sand grain sizes. Grain size distribution of finer fractions (<63 μm) were analyzed using a Micrometric Sedigraph III 5120. The grain size statistics follows the methods of Folk and Ward (1957) and lithological classification scheme follows that of McKay et al. (2019). Diatomaceous opal in the core is relatively low (8–15%; Section 3.3) compared to other Holocene Antarctic sediments (e.g. 30–60%, Ashley et al., 2021), and therefore biogenic opal will only represent a subordinate signal within the grainsize distributions, with the greatest influence in the fine silt size range (McKay et al., 2022; Warner and Domack, 2002). Bromine (Br), titanium (Ti), magnesium (Mn), and iron (Fe) counts were measured on split core using ITRAX XRF Core Scanner with Mo X-ray tube, 1-mm step size, and 5-s exposure time at 30 kV and 30 mA at KOPRI.

Settled slides for quantitative diatom analysis were prepared at the University of Otago using the method of Warnock and Scherer (2015). Diatom census counts were carried out using an Olympus BX41 microscope using a 63 x objective and 10x eyepiece; a minimum of 300 valves per sample were counted to reach a statistically representative census. Pennate diatoms and Eucampia antarctica were counted as 'one half' for each apex or elevation identified, and the total count was divided by two. Each centric valve was counted as 'one' if the margin and central area were present. The relative abundance of each diatom species was determined as a percentage of total diatom valves counted for each sample. Absolute diatom abundance was calculated following Warnock and Scherer (2015).

Environmental inferences from proxy archives are made according to the literature summarized in Table 1.

2.4. Statistical analysis

Principal components analysis (PCA), was carried out on proxy archives using the Scikit-learn Python module (Pedregosa et al., 2011). Data were resampled to 5 cm binned averages prior to PCA analysis and linear correlations between records were calculated using the pandas Python module (Reback et al., 2020).

2.5. Age model

The age model of core RS15 – GC57 is based on accelerator mass spectrometry (AMS) radiocarbon measurements from eight core depths. Three horizons yielded sufficient

carbonate from foraminifera and a shell fragment for radiocarbon measurement and six horizons were radiocarbon dated using the ramped pyrolysis oxidation (RPO) method (Rosenheim et al., 2008). Radiocarbon preparation by RPO reduces contamination from ancient detrital sources by exploiting the thermochemical stability differences between the fresh autochthonous, acid-insoluble organic (AIO) material and the diagenetically stabilized allochthonous AIO material (Rosenheim et al., 2013b; Subt et al., 2016). During RPO, a pretreated sediment sample is gradually heated at 5 °C/min up to 1000 °C under a stream of helium, pyrolyzing organic material according to its thermochemical stability. The resultant volatile compounds are oxidized to CO2 over Pt, Ni, and Cu wires with ultra-high purity oxygen gas and fractions are cryogenically collected according to the temperature at which the volatiles were evolved. The separation of samples into several fractions (termed splits) for radiocarbon dating produces a spectrum of ages. Generally, the least thermochemically stable material, evolved at lowest pyrolysis temperature, is youngest, while the most thermochemically stable material, evolved at highest pyrolysis temperature, is oldest (Rosenheim et al., 2013b; Subt et al., 2016).

Samples from four depths (0, 180, 455, and 560 cm) were pretreated for RPO at the University of Otago following Rosenheim et al. (2008). Samples were acidified for 24 h in 1N HCl to remove any carbonate material present, dried at 60 °C, and stored in pre-combusted vials until analysis. RPO and CO2 fraction collection was performed at the College of Marine Science, University of South Florida (USF), United States of America. RPO pretreatment and CO2 fraction collection were performed on two additional samples (380 and 505 cm) at the Rafter Radiocarbon Lab (RRL) AMS facility at GNS Science, New Zealand. These samples were acidified in 1N HCl for 18 h to remove any carbonate material present, dried at 50 °C, and stored in pre-combusted vials until analysis. RPO and CO2 fraction collection at RRL was carried out using protocols adapted from Rosenheim Laboratory at the USF (Rosenheim et al., 2013b; Ginnane et al., 2024). All radiocarbon measurements were performed at the RRL AMS facility following standard graphitization and AMS measurement protocols (Turnbull et al., 2015; Zondervan et al., 2015), corrected for blank contamination by the procedures outlined in Fernandez et al. (2014), and modified for the systems at USF and RRL during the time of analysis (Supplementary Data).

3. Results

3.1. Modern environment

Robertson Bay is a protected embayment close to the shelf break at the western confluence of the Ross Sea and the Southern Ocean (Fig. 1). Outlet glaciers from the

Transantarctic Mountains terminate into the bay. Robertson Bay has a sill at approximately 200 m, and the inner bay is divided into inner and outer basins.

A CTD cast taken through a hole in the sea ice in November 2015 provides a snapshot of the complex water column structure in Robertson Bay (Fig. 2). From the surface, potential temperature (Θ) and oxygen decrease and salinity increases. Oxygen concentration reaches a minimum of 8.2 mg/L ca. 135 m and increases with depth. A colder water mass (<-1.8 °C) between 50 and 300 m overlies warmer waters (>-1.8 °C), and the salinity gradient sustains water column stability.

Robertson Bay has typically been sea ice-free from mid-January to mid-March during the satellite era (Fig. 3) (NASA Worldview; https://worldview.earthdata.nasa.gov/). Surface waters in the embayment warn, freshen, and become more oxygenated over the course of the summer open water season. Sea ice advances from the north towards the coast in late March, and pack ice is typically present in the bay by the end of March. Sea ice coverage in the bay can change rapidly due to wind. Strong southeasterly winds form a polynya at the head of Robertson Bay in April of most years (Fig. 3). Shallow (45 and 53 m) and deep (302 m) moorings show that the cold, oxygenated water mass formed by brine rejection broke down the salinity gradient in the embayment in April of 2015, ventilating the inner basin (Fig. 3). The water mass produced during wintertime convection in Robertson Bay in 2016 is close to the surface freezing point (~ −1.8 °C) and fresher than Dense Shelf Waters formed in the Ross Sea, which have a salinity of less than 34.5 psμ (Orsi and Wiederwohl, 2009). When polynya activity ceased and fast ice conditions were established in early May 2015 warmer CDW upwelling along the East Antarctic margin intruded over the sill (cf. Williams et al., 2010). This warmer, saltier, oxygen-depleted water mass was modified by the colder, fresher, and more oxygenated waters within the embayment (Fig. 3).

We synthesize our interpretation of the mooring, satellite data, and CTD cast data to characterize three endmembers of Antarctic Surface Water in Robertson Bay (Orsi and Wiederwohl, 2009). The upper water column consists of warmer (>-1.8 °C) and fresher (<34.0 psμ) surface waters. This water mass warms throughout the summer season and freshens due to melt from sea ice and East Antarctic outlet glaciers, which terminate into the embayment (Fig. 1; Fig. 2; Fig. 3). Saltier (>34.0 psμ) and colder (<-1.8 °C) waters occupy mid-depths and are likely a remnant of the water mass formed during autumn sea ice production (cf. Silvano et al., 2017). This remnant winter water overlies a warmer (>-1.8 °C) and saltier (>34.1 psμ) water mass produced by mixing between the cold oxygenated water mass produced within Robertson Bay during autumn polynya activity and warmer, saltier mCDW located off the continental shelf in the Cape Adare region (Gordon et al., 2015).

3.2. Sedimentary chronology

The age model of core RS15-GC57 is based on AMS radiocarbon dates for eight stratigraphic horizons (Table 2). In core RS15-GC57, the ages of the second measured RPO CO2 fraction (split 2, varying temperature ranges but typically 300–350 °C) are younger than the first measured fraction (split 1, typically up to ~300 °C) and exhibit age differences between 130 and 810 14C yrs (Table 2; Supplementary Data). The second split is also found to trend slightly younger than the first split in other diatom-rich Holocene sediment cores collected from the western Ross Sea (Ginnane et al., 2024; Parker, 2017). Younger radiocarbon age trends in the second split imply that older, potentially translocated or naturally degraded, labile material volatilized at low temperatures is contaminating the lowest temperature split (Ginnane et al., 2024). This behavior appears to be unique to Ross Sea sediments; generally, older organic matter has been associated with higher temperature splits in Antarctic margin sediments (Rosenheim et al., 2008, 2013b; Subt et al., 2016, 2017; Venturelli et al., 2020) and elsewhere in the world (Bianchi et al., 2015; Gaglioti et al., 2014; Rosenheim et al., 2013a; Rosenheim and Galy, 2012; Schreiner et al., 2014; Vetter et al., 2017; Williams et al., 2015; Zhang et al., 2017). The only other examples of older samples volatilizing at lower temperatures using this method come from sediment contaminated with petroleum from Miocene-aged source rock (Adhikari et al., 2016; Pendergraft et al., 2013; Pendergraft and Rosenheim, 2014). The second RPO split at 180 cm (collected between 316 and 382 °C) is more consistent with the carbonate dates at 180 cm (2770 ± 65 and 2642 ± 26 14C yrs BP respectively; Supplementary Data) than the first split, which contained carbon volatilized below 316 °C. Better agreement between the second RPO split at 560 cm and a carbonate date at 567 cm (7320 ± 100 and 6914 ± 152 14C yrs respectively) provides further indication that split 2 provides a more robust age constraint, supporting the conclusion that a higher proportion of pre-aged organic matter is volatilizing in the lowest temperature interval (Supplementary Data).

The final age-depth model for core RS15-GC57 was built on eight dated horizons (Fig. 4). Calibration of 14C dates to calendar years before present (cal yr BP) was performed using the Bchron R package (Haslett and Parnell, 2008) and the Marine20 calibration curve, which includes a time-varying global reservoir age of ~600 years, R(t) (Heaton et al., 2020). The core top RPO radiocarbon age of 1310 14C year BP (1375 years before core collection 2015 CE) is adopted as the most robust estimate of the local ocean reservoir effect (ΔR) and any remaining contamination by detrital carbon (DC) in RPO dates. We adopt an uncertainty of ±150 years to account for the error in the core top radiocarbon date (±65 years, Table 2) combined in quadrature with Holocene reservoir

variability in the Ross Sea region (±137 years, Gao et al., 2022; Hall et al., 2010). We also adopt a global marine reservoir, R(t), of 603 years, the most recent available estimate from the Marine20 calibration curve, which yields a total local radiocarbon correction (ΔR + DC) of 772 years (Heaton et al., 2020).

We employ a constant local radiocarbon correction with the caveat that variable upwelling of mCDW in the northern Ross Sea during the Holocene (e.g. Xu et al., 2021) likely drives substantial radiocarbon reservoir variability because mCDW is depleted in 14C relative to the global marine radiocarbon reservoir (Heaton et al., 2020, Heaton et al., 2023; King et al., 2018). Though precise calibrations that account for polar ΔR variability are not yet available, future efforts to develop and validate high latitude curves will be essential to constrain the timing of Antarctic paleoceanographic change during the Holocene (Heaton et al., 2023).

A local radiocarbon reservior age of 1375 ± 150 years in Robertson Bay is consistent with the Holocene radiocarbon reservoir age of 1000 – 1300 years in the Southwestern Ross Sea calculated from the difference between U/Th and 14C in corals (Hall et al., 2010) and measurements from other regions of the Antarctic margin (Ó Cofaigh et al., 2014 and references therein). We adopt our locally calculated radiocarbon offset (ΔR + DC) of 772 ± 150 years to generate our age model, noting that it is statistically indistinguishable from the weighted average ΔR for the Ross Sea region 609 ± 137 (Gao et al., 2021). Agreement between the locally calculated reservoir off set for core GC57 and the regional average Ross Sea ΔR provides further evidence that the core top was recovered intact and RPO mitigates contamination from ancient detrital sources, which influence bulk radiocarbon dates from coastal sediment cores in the Ross Sea (e.g. Mezgec et al., 2017; Tesi et al., 2020).

3.3. Multi-proxy marine archive

Principal component analysis (PCA) was used to determine the relationship between proxy indicators of primary production, glaciomarine sedimentation, and ocean conditions in core RS15-GC57 (Fig. 5). The first two axes of the PCA account for 26% and 11% of the variance in the proxy records respectively. Magnetic susceptibility (MS), weight percent biogenic silica (wt% BSi), Br/Ti ratio, TN, and δ13C are strongly correlated (R > ± 0.57, Supplementary Data) in core RS15-GC57 and dominate the variance captured by axis 1 of the PCA. Axis 2 of the PCA reflects the inverse relationship between the relative abundance of the diatom Fragilariopsis curta and both the ratio of vegetative frustules of the diatom genus Chaetoceros to Chaetoceros resting spores (CRS) and the Mn/Fe elemental ratio. Changes in the PCA were used to identify four stratigraphic intervals: Unit 1 (0 – 105 cm), Unit 2 (105 – 215 cm), Unit 3 (215 – 460) and Unit 4 (460 – 570) (Fig. 5). Two

lithofacies are identified in the core: pervasively bioturbated biosilica-bearing muds (0 – 403 cm) and laminated sandy mud (403 – 570 cm) (Table 3).

The uppermost unit of core RS15-GC57, Unit 1 (0 – 105 cm), is characterized by F. curta relative abundance greater than 50% and lowest down core abundances of Fragilariopsis sublinearis (<5%) and Thalassiosira antarctica (0 – 2%) (Fig. 6; Supplementary Data). The CRS relative abundance, Br/Ti ratio, TOC, and ADA are higher in the upper section of Unit 1, Unit 1a, and lower in Unit 1b and 1c (Fig. 7). Fragilariopsis curta abundance is higher (>65%) in Unit 1b than Unit 1c (50%). δ13C also shifts from more positive values in Unit 1b to more negative values at the top of Unit 2.

The relative abundance of F. curta drops below 50% in Unit 2 (105 – 215 cm) and the diatom assemblage is further characterized by the highest down core abundances of Fragilariopsis sublinearis (Fig. 7; Supplementary Data). The upper section, Unit 2a, is distinguished from the lower Unit 2b by a higher ratio of Chaetoceros spp. to CRS and the highest Mn/Fe values measured in RS15-GC57. ADA, Br/Ti, TOC, TN, and wt% BSi are lower in Unit 2b and δ13C and MS are higher; this inverse relationship is captured by axis 1 of the PCA. Sedimentary accumulation in Unit 2b lower (~1 mm/yr) than Unit 2a and Unit 1 (>1.5 mm/yr) (Supplementary Data).

Unit 3 (215 – 455 cm) is defined by a return to higher F. curta abundance (>50%). Wt% BSi and Br/Ti shift toward higher values between 170 cm and 305 cm and are more variable between 305 cm and the base of Unit 3, 455 cm. Although F. curta abundance is generally above 50% throughout the unit, a transient interval of lower in F. curta relative abundance (40%), lower wt% BSi, ADA, TOC, and Br/Ti, and elevated MS and δ13C is evident ca. 380 cm. A transient increase in the relative abundance of CRS is also evident at 380 cm (Fig. 7). The transition from pervasively bioturbated diatom-bearing mud to laminated sandy mud occurs within Unit 3 at 403 cm (Table 3); laminae are particularly pronounced between 405 and 420 cm. A stepwise shift toward higher Br/Ti, ADA, wt% BSi, and TOC and lower MS, sand abundance, and δ13C marks the boundary between Unit 3 and Unit 4 (460 cm). Average sedimentary accumulation rate is higher (1.3 mm/yr) in the upper section of Unit 3 and lower (<1 mm/yr) between 380 and 455 cm (Supplementary Data). Higher abundance of Fragilariopsis kerguelensis persists across the transition between Unit 3 and Unit 4 (Fig. 7).

Unit 4a (460 – 550 cm) is characterized by peak MS, sand abundance, and δ13C, and relatively low wt% BSi, ADA, TOC, Br/Ti ratio and accumulation rate. Sand abundance, MS, and δ13C trend towards lower values between 460 cm and 570 cm while TOC, Br/Ti, and wt% BSi increase. The diatom assemblage is characterized by low relative abundance of F. curta and highest relative abundance of F. obliquecostata (Fig. 7). Transient elevated wt% BSi and TOC values at 485 and 505 cm correspond to lower MS and sand

concentration. Unit 4a (460 – 550 cm) is distinguished from Unit 4b (550 – 570 cm) by a trend towards a higher proportion of fine sand, a more coarse-skewed grain size assemblage, higher relative abundance of T. antarctica, reduced clay content, and lower sedimentary accumulation (<0.5 mm/yr) (Supplementary Data). Proxy values in Unit 4b resemble those in units 1, 2 and 3.

4. Discussion

Combining a multi-proxy marine sedimentary dataset with modern observations allows us to characterize the Holocene paleoenvironmental history of inner Robertson Bay from the mid-Holocene (6.7 cal kyr BP) to the present (Table 4; Fig. 8; Fig. 9). Instrumental measurements and satellite data provide a snapshot of modern Robertson Bay oceanography (Fig. 2; Fig. 3), which serves as a basis for our interpretation of past changes in primary productivity, sea ice dynamics, polynya activity, and mCDW intrusion within the embayment.

The most prominent feature in the reconstruction is a transition in paleoenvironmental conditions during the mid-to late-Holocene after 4.0 cal kyr BP (3.5 – 4.7 cal kyr BP, 95% confidence interval). This shift is most evident in proxy indicators for the relative contributions of terrigenous sedimentation (MS) and primary production (wt% BSi, Br/Ti ratio, δ13C) which dominate the variance in axis 1 of the PCA (Table 1; Fig. 5). Higher values of PCA axis 1 reflect a greater proportion of terrigenous sedimentation whereas lower values indicate greater biogenic flux. The sedimentary accumulation rate also increases from <0.5 mm/yr to >1.0 mm/yr after 4.0 cal yr BP. Transitions ca. 1500 cal yr BP and 700 cal yr BP are inferred from shifts in proxies for the seasonal duration of sea ice (F. curta relative abundance) and water mass circulation/stratification (Mn/Fe ratio, δ 13C, and Chaetoceros ratio) captured by axis 2 of the PCA. High values of PCA axis 2 are associated with sedimentary proxies for nutrient-rich, mixed surface waters and lower abundance of the diatom F. curta, which thrives in melt-stratified conditions at the sea ice edge in regions where seasonal sea-ice duration averages 9 – 11 months a year (Armand et al., 2005).

4.1. Mid-Holocene [6.7 – 4.0 cal kyr BP; Unit 4]

We interpret low sediment accumulation (0.4 mm/yr) and proxy indicators of low primary production (TOC, ADA, wt% BSi) during the mid-Holocene as evidence for sedimentary deposition beneath multi-year sea ice or a small ice shelf, particularly after 6.2

cal kyr BP (Fig. 8) (Minzoni et al., 2015, Smith et al., 2019). Sorted, fine sand/coarse silt laminae with coarse-skewed grain size assemblages suggest that moderately strong bottom currents winnowed the seabed or prevented the suspension settling of muds (Supplementary Data; Table 3) (Hemer and Harris, 2003). Highest down-core abundance of Fragilariopsis obliquecostata, characteristic of regions covered year-round by sea ice (Armand et al., 2005; Gersonde and Zielinski, 2000), provides further evidence of ice-capped conditions within the embayment (Fig. 7). Declining biogenic influence and sedimentation rate indicate an increase in the spatial extent of perennial ice cover in inner Robertson Bay between 6.2 cal kyr BP and 4.0 cal kyr BP. We interpret transient increases in biogenic flux approaching late Holocene values as brief recurrences of seasonally open marine conditions associated with ice shelf retreat or the breakup of perennial sea ice.

Relatively higher δ13C values (>-24 ‰) from 6.2 to 4.0 cal kyr BP also support the interpretation of either diatom growth within perennial sea ice or increased influence from terrestrial organic matter within an under-ice shelf depositional environment. Changes in the bulk δ13C of marine sediment are the result of the interplay between biological productivity, water mass circulation, and terrestrial sources. Primary production enriches the dissolved inorganic carbon pool of surface waters in 13C because photosynthesis preferentially removes 12C during the production of biomass, which therefore contains a greater proportion 12C. Increased biological fractionation will increase the δ13C of surface waters if the carbon pool is not replenished (such as in a semi-stratified sea ice environment) and primary producers record this signature (Geilfus et al., 2015; Gibson et al., 1999; Henley et al., 2012; Tesi et al., 2020). In Antarctic environments, δ13C can be interpreted as a proxy for total primary production because the fractionation effect of increased primary production on δ13C of surface waters is thought to dominate the effects of oceanographic change (stratification) and species-specific fractionation processes (Berg et al., 2013; Panizzo et al., 2014; Stoll et al., 2017; Villinski et al., 2000). Furthermore, because diatoms thrive in a stratified environment (Leventer and Dunbar, 1996), periods of high primary productivity typically co-occur with increases in stratification, such that both processes operate simultaneously to increase the δ13C of surface waters. However, in Robertson Bay, δ13C and indicators of primary production (wt% BSi, Br/Ti, TOC) are anticorrelated ($r < -0.80$, $p < 0.001$) and positively correlated with proxies for the relative contribution of terrigenous sediment (MS, sand percentage). This correlation indicates that the combined influence of reduced biogenic flux under nutrient limited, stratified surface conditions (such as within sea ice) and an increase in the relative proportion of terrestrial organic matter exerts primary control on bulk δ13C (Fig. 6; Fig. 7; Supplementary Data).

The inferred northward expansion of persistent ice cover in Robertson Bay between 6.2 and 4.0 cal kyr BP coincides with the final phase of glacial and ice sheet retreat in the

Ross Embayment between 7 and 3.5 cal kyr BP (Ashley et al., 2021; Jones et al., 2020; Spector et al., 2017) (Fig. 8). This period is also associated with freshened surface waters, inhibited dense water formation, and the absence of CDW on the continental shelf in other regions of the East Antarctic coastal margin (Ashley et al., 2021; Crosta et al., 2018; Denis et al., 2009a; Kim et al., 2012). Based on these observations, we propose that the influence of Antarctic ice sheet in the Ross Embayment and glacial retreat in Robertson Bay during the mid-Holocene may have altered the local oceanographic regime (Ashley et al., 2021), supporting the expansion of multi-year sea ice cover or an expanded ice shelf during the mid-Holocene Hypsithermal climate optimum (Allen et al., 2010; Christ et al., 2015; Crosta et al., 2007; Kim et al., 2018; Leventer et al., 1996; Minzoni et al., 2015; Panizzo et al., 2014; Peck et al., 2015; Pike et al., 2009; Totten et al., 2022).

4.2. Onset of the Neoglacial [ca. 4.0 cal kyr BP, Unit 3–4 transition]

A step-change in TOC, wt% BSi, and MS values and sedimentation rate ca. 4.0 cal kyr BP is consistent with the establishment of seasonally open marine conditions in Robertson Bay (Smith et al., 2019). After 4.0 cal kyr BP, δ13C values of less than −24‰ are within the range of modern values for seasonally open marine conditions in Robertson Bay and other regions of the Ross Sea (Villinski et al., 2000). Higher abundances of F. kerguelensis, a diatom species associated with SSTs >1 °C (Armand et al., 2005; Crosta et al., 2005) occur during the inferred breakup of ice-covered conditions ca. 4.0 cal kyr BP, indicating that warmer ocean temperatures may have played a role in establishing open water conditions within the inner basin of Robertson Bay.

The curvate and blocky nature of deformation in the laminated sandy muds persists in core RS15-GC57 from the base of the core at 6.7 cal kyr BP until ca. 3.2 cal kyr BP (2.7–3.7 cal kyr BP, 95% CI), consistent with the ongoing influence of local ice-shelf breakup after open-water conditions were established over the core site. In contrast, such deformation is absent after 3.2 cal kyr BP, suggesting that deep-draft icebergs occupied Robertson Bay after open marine conditions were established over the core site ca. 4.0 cal kyr BP but were absent during the late Holocene. Enhanced discharge of icebergs derived from thickened ice sheets that were previously buttressed by an ice shelf or multi-year fast ice would be anticipated following the collapse of the ice shelf (Wise et al., 2017). Iceberg keel depth would also reduce after thinning of the inland ice sheet had occurred, explaining a lack of scouring after 3.2 cal kyr BP.

Oceanographic feedbacks linked to the stabilization of the Antarctic ice sheets in the Ross Embayment and outlet glaciers along the Victoria Land coast provide a potential mechanism for the onset of seasonally open marine conditions and higher rates of primary

production in Robertson Bay ca. 4.0 cal kyr BP (cf. Ashley et al., 2021). This transition occurs against the backdrop of more gradual trends in seasonal insolation (Fig. 8). Colder temperatures during summer and autumn linked to changes in seasonal insolation south of 60°S may have also supported more consolidated, multi-year sea ice or an expanded ice shelf in Robertson Bay during the mid-Holocene (cf. Crosta et al., 2018; Pike et al., 2009). However, the inferred expansion of multi-year ice cover after 6.2 cal kyr BP and break-up ca. 4.0 cal kyr BP is inconsistent with a monotonic trend in seasonal insolation during the late Holocene (Fig. 8). Additionally, evidence of ice covered conditions in Robertson Bay is at odds with marine records of an Antarctic mid-Holocene Hypsithermal climatic optimum characterized by higher rates of primary productivity, warmer conditions in spring and early summer, and a longer ice free season along the Adélie land margin and the Antarctic Peninsula relative to the late Holocene (Allen et al., 2010; Christ et al., 2015; Crosta et al., 2007; Kim et al., 2018; Leventer et al., 1996; Minzoni et al., 2015; Panizzo et al., 2014; Peck et al., 2015; Pike et al., 2009; Totten et al., 2022). We invoke local influence and feedbacks relating to glacier and ice sheet retreat and meltwater discharge as a mechanism to reconcile our inference of persistent ice cover in Robertson Bay between 6.2 and 4.0 cal kyr BP and low sedimentation rates and other coastal western Ross Sea sediment cores (Mezgec et al., 2017) with marine records of a mid-Holocene climatic optimum in other regions.

Marine sediment cores from both the Antarctic Peninsula and East Antarctic margin also show a base-line shift in coastal sea ice between 4.5 and 2.5 cal kyr BP, which characterizes the transition from the mid-Holocene conditions to colder, more variable, late Holocene Neoglacial conditions (Ashley et al., 2021; Domack et al., 2001; Johnson et al., 2021; Peck et al., 2015; Totten et al., 2022). Following Ashley et al. (2021), we emphasize the potential influence of regionally specific ice-ocean feedbacks in driving this transition, which is characterized by the inferred breakup of perennial ice cover in Robertson Bay and an increase in the seasonal duration of sea ice in other regions of the Antarctic margin (Crosta et al., 2007; Taylor et al., 2001; Totten et al., 2022). The mid-to-late Holocene transition occurs ~1000 years earlier in Antarctic marine records from the Ross Sea and Adélie Land (ca. 3.5–4.5 kyr BP) than the Antarctic Peninsula (ca. 2.5–3.5 kyr BP) (Bentley et al., 2009; Johnson et al., 2021; Mezgec et al., 2017; Totten et al., 2022). This discrepancy may be related to the timing of ice sheet retreat and differing oceanographic regimes and ice-ocean feedbacks in East and West Antarctica.

4.3. Late Holocene Neoglacial [4.0–1.5 cal kyr BP, Unit 3]

Following the establishment of open-marine conditions in Robertson Bay ca. 4.0 kyr BP, the relative abundance of the diatom F. curta can be used to infer changes in the

seasonal duration of sea ice (Armand et al., 2005). Higher abundances of F. curta in Robertson Bay and farther south in Cape Hallett and Woods Bay (Mezgec et al., 2017) during the late Holocene are characteristic of a similar-to-modern duration of the summer open water season (1–3 months) and persistent sea ice meltwater stratification in spring (Fig. 8). Fragilariopsis curta is seeded by melting pack/fast ice and dominates the meltwater-stratified ice edge of the Ross Sea during the austral spring and early summer (Cunningham and Leventer, 1998). The relative abundance of F. curta in core RS15-GC57 is negatively correlated with indicators of a more nutrient rich, mixed surface layer (Chaetoceros ratio) and oxygenated conditions in the deep basin of Robertson Bay (Mn/Fe), which we interpret as a signature of enhanced polynya activity (Table 1; Fig. 5). This inverse relationship, represented by axis 2 of the PCA, aligns with F. curta's preference for the spring sea ice meltwater-stratified environment, which is sustained by northerly winds along the East Antarctic margin (Campagne et al., 2016; Leventer and Dunbar, 1996). However, we also note the significant influence of seasonality on these proxies; F. curta is primarily associated with spring sea ice conditions, whereas open polynya conditions in Robertson Bay occur in April (austral autumn) during the satellite period (Fig. 3).

Fragilariopsis curta relative abundance is generally higher between 4.0 cal kyr BP and 1.5 cal kyr BP (40–50%). A transient decrease to 35% is consistent with a short term (~500 year) reestablishment of multi-year ice cover ca. 2.9 cal kyr BP (2.5–3.3 cal kyr BP, 95% CI) (Fig. 9). This interpretation is supported by grainsize analysis, which is also more characteristic of mid-Holocene conditions (Supplementary Data) and a decline in biogenic sedimentation (Fig. 9). The spike in CRS relative abundance following this interval may be associated with meltwater stratification in the surface layer following perennial ice breakup (e.g. Hillenbrand et al., 2010), possibly due to the influence of warmer ocean temperatures.

4.4. Last millennium environmental variability [1.5–0.7 cal kyr BP, Unit 2]

Fluctuations in F. curta abundance and proxies for biogenic sedimentation in Robertson Bay and along the Victoria Land margin indicate shifts in sea ice dynamics and nutrient availability during the period between 1.5 and 0.7 cal kyr BP (Mezgec et al., 2017). Lower F. curta abundance in Robertson Bay (<40%) is characteristic of a reduction in spring sea ice concentration and a longer summer open water season (Armand et al., 2005). Reduced spring sea ice concentrations in Robertson Bay between 1.5 and 0.7 cal kyr BP is broadly consistent with regional records from the Victoria Land coastal margin (Mezgec et al., 2017; Tesi et al., 2020). A longer open-water season in the embayment may have supported the expansion of the Cape Adare Adélie penguin colony, which reached its maximum size ca. 1.2 cal kyr BP (Emslie et al., 2018). Marine records located farther south

along the Victoria Land coast (Mezgec et al., 2017) and Adélie Land (Johnson et al., 2021), are also consistent with a decrease in coastal sea ice after 1.5 cal kyr BP. Proxies for biogenic sedimentation (axis 1 of the PCA) indicate reduced primary production in Robertson Bay until 1.0 cal kyr BP despite a longer ice free season (Table 4; Fig. 9), perhaps due to nutrient limitation within the surface layer. A greater relative abundance of CRS relative to Chaetoceros spp. supports the interpretation of reduced primary productivity under nutrient-limited conditions because Chaetoceros spp. form resting spores under nutrient-depleted conditions (Leventer et al., 1996).

Our interpretation of nutrient-limited conditions in Robertson Bay during the period from 1.5 cal kyr BP to 1.0 cal kyr BP contrasts with evidence of intensified upwelling of nutrient-rich mCDW and enhanced productivity along both the East and West Antarctic margins (Fig. 7; Fig. 8) (Johnson et al., 2021; Kim et al., 2012; Shevenell et al., 2011). This offset may be an artifact of radiocarbon dating uncertainty, which is greater than 300 years in the upper section of our reconstruction. However, we also note that this discrepancy is consistent with the oceanographic regime along the Victoria Land coastal margin. In the modern environment, brine rejection during sea ice production in autumn breaks down the salinity gradient in the water column, oxygenating the inner basin of Robertson Bay and driving cross-shelf exchange of warmer, nutrient rich, waters, present off the shelf at Cape Adare (Gordon et al., 2015) (Fig. 3). We hypothesize that a longer and warmer summer season inferred from terrestrial records ca 1.4 cal kyr BP (Jin et al., 2021; Mezgec et al., 2017; Stenni et al., 2017) may have restricted polynya formation in Robertson Bay and other regions of the Victoria Land coastal margin, thereby reducing associated transport of nutrient rich CDW into the surface layer (Mezgec et al., 2017; Morrison et al., 2020; Xu et al., 2021). The breakdown of spring meltwater stratification and a destabilized water column, which transports diatoms below the pycnocline (Höfer et al., 2019), could have further acted to limit primary production in Robertson Bay during a period of reduced spring sea ice concentrations.

A higher ratio of Chaetoceros spp. to CRS and more negative δ13C during the early part of the last millennium (ca. 0.8 cal kyr BP) is consistent with a period of more nutrient-rich, mixed surface waters in Robertson Bay, which supported increased biogenic flux (Fig. 9). Peak Mn/Fe ratio indicates a period of more oxygen-rich conditions in the deep basin of Robertson Bay. Taken together, we interpret the proxy records to indicate active polynya formation and production of denser-than-modern waters within the embayment. In the modern environment, the cold, oxygenated water mass produced in Robertson Bay's autumn polynya is displaced by warmer, less oxygenated mCDW (Fig. 3). We propose that enhanced polynya efficiency ca. 0.8 cal kyr BP could have produced a cold and oxygenated water mass of sufficient density to displace the warmer, saltier, less

oxygenated water mass which occupies the deep basin in the modern day (Fig. 2; Fig. 3), while outflow of dense waters drove enhanced compensatory inflow of CDW into the embayment at intermediate depths.

Nutrient-replete conditions in the surface layer of Robertson Bay ca. 0.8 cal kyr BP are consistent with an increase in nutrient availably further south in the Terra Nova Bay region, which has been linked to greater on-shelf presence of mCDW between 1.0 and 0.6 cal kyr BP (Fig. 9) (Xu et al., 2021). The delayed onset of peak mCDW influence and primary productivity in the Ross Sea relative to the Antarctic Peninsula, where warmer subsurface temperatures are observed after 1.6 cal kyr BP (Shevenell et al., 2011), is consistent with the differing oceanographic regimes. Modified Circumpolar Deep Water flows directly onto the shelf on the Antarctic Peninsula (Thompson et al., 2018). By contrast, mCDW intrusion into Robertson Bay and the wider Ross Sea region is modulated by dense water production and export (Morrison et al., 2020; Thompson et al., 2018) and may have been inhibited by warmer climate conditions and suppressed polynya along the Victoria Land Coast before 1.0 cal kyr BP (An et al., 2021; Mezgec et al., 2017).

Our interpretation of enhanced polynya activity in Robertson Bay ca. 0.8 cal kyr BP is broadly consistent with previous research which identifies mean state changes in the Southern Annular Mode (SAM) and the El Niño/Southern Oscillation (ENSO) as a dominant control on last millennium Ross Sea climate (Bertler et al., 2018; Koffman et al., 2023; Lüning et al., 2019). Increased upwelling of CDW along the margin the Antarctic Peninsula (Shevenell et al., 2011) and a strengthening of atmospheric circulation along the Siple Coast (Koffman et al., 2023) has been linked to intensified Southern Hemisphere Westerly Winds associated with a multi-centennial trend towards a positive phase of the SAM during the early part of the last millennium (Dätwyler et al., 2018; Goodwin et al., 2014; Hinojosa et al., 2017; Koffman et al., 2014; Perren et al., 2020). A sustained positive phase of the SAM and an increased prevalence of the La Niña phase of ENSO ca. 0.8 cal kyr BP (Goodwin et al., 2014; Hinojosa et al., 2017) may have acted to enhance southerly and katabatic winds in the coastal Ross Sea (Stammerjohn et al., 2008). Stronger southerly winds promote dense water production, compensatory inflow of mCDW, and earlier sea ice breakout during the summer ice-free season in the Ross Sea (Morrison et al., 2020; Schine et al., 2016).

Considered together, Ross Sea paleoclimate records are consistent with a role for large scale modes of climate variability in driving an increase in CDW upwelling, primary productivity, and polynya activity along the Victoria Land margin during the first part of the last millennium (ca. 0.8 cal kyr BP), a period that has been characterized as Antarctic manifestation of the MCA (Lüning et al., 2019 and references therein). However, we note that evidence of baseline shifts in SAM and ENSO dynamics during the early part of the

last millennium remain equivocal (Henke et al., 2017; King et al., 2023), and further work is required to conclusively link late Holocene Antarctic climate evolution to multi-centennial trends in dynamic modes of climate variability (Johnson et al., 2021; Truax et al., 2022).

4.5. Little Ice Age [0.7 cal kyr BP – present; Unit 1]

Reconstructions from Robertson Bay and other coastal sediment cores from the western Ross Sea indicate an increase in the seasonal duration of sea ice between 0.7 cal kyr BP and the present, consistent with ice core temperature reconstructions of cooling atmospheric temperatures (Fig. 9) (Bertler et al., 2011; Orsi et al., 2012; Rhodes et al., 2012; Stenni et al., 2017; Tesi et al., 2020). This shift towards more consolidated last millennium sea ice conditions in the Cape Hallet region, located less than 100 km south of Robertson Bay, has been dated to ca. 0.7 cal kyr BP using tephrochronology (Di Roberto et al., 2019; Mezgec et al., 2017; Tesi et al., 2020). The onset of icier spring conditions in Robertson Bay, inferred from the relative abundances of F. curta and T. antarctica also occurs at 0. 7 cal kyr BP, which provides confidence in the accuracy of the core's radiocarbon-based chronology. We interpret a lower Mn/Fe ratio after 0.7 cal kyr BP as a decrease in bottom water oxygenation within the inner basin of Robertson Bay (Fig. 9). Proxies for nutrient-rich, mixed surface waters (Chaetoceros ratio and δ13C) decline after 0.7 cal kyr BP, consistent with a reduction in nutrient-rich mCDW in the upper water column (cf. Xu et al., 2021). Indicators of primary productivity in Robertson Bay (axis 2 of the PCA) remained elevated relative to the Holocene baseline, perhaps due to alternative sources of nutrients such as iron fertilization from dust sourced from the nearby McMurdo Volcanic Group (Kyle, 1990; Winton et al., 2014) and favorable conditions for diatom growth in a sea ice meltwater-stratified surface layer (Leventer and Dunbar, 1996).

Icier spring conditions and a sea-ice meltwater stratified surface layer in Robertson Bay, particularly after 0.5 cal kyr BP, are consistent with marine and terrestrial records of an Antarctic Little Ice Age (LIA) (Orsi et al., 2012; Rhodes et al., 2012; Simms et al., 2021; Totten et al., 2022). The interplay between an externally forced last millennium cooling trend (Neukom et al., 2019; Otto-Bliesner et al., 2015; Truax et al., 2022) and a multi-centennial shift towards the negative phase of the SAM after 0.6 cal kyr BP (Abram et al., 2014; Dätwyler et al., 2018; Goodwin et al., 2014; Perren et al., 2020) could have supported more consolidated sea ice conditions in the western Ross Sea. However, the increase in spring sea ice concentrations persisted along the Victoria Land coastal margin after the mean state of the SAM became more positive ca. 0.3 cal kyr BP (Abram et al., 2014; Dätwyler et al., 2018; Sadai et al., 2020), which suggests that atmospheric cooling over the Victoria Land region may have exerted primary control over sea ice conditions in the

Ross Sea during the LIA (Mezgec et al., 2017; Rhodes et al., 2012; Stenni et al., 2017; Tesi et al., 2020). We speculate that the persistence of consolidated coastal sea ice conditions along the Victoria Land coastal margin to the present day (Tesi et al., 2020), despite warming atmospheric temperatures after 1850 CE (Rhodes et al., 2012; Stenni et al., 2017), and a positive trend in the SAM since 1950 CE (Marshall, 2003), may be associated with the modern influence of West Antarctic Ice Sheet melt. Increasing mass loss from the WAIS has freshened surface waters in the Ross Sea since the 1950s (Jacobs et al., 2022), and freshened surface waters could support more consolidated sea ice conditions despite atmospheric forcing (e.g. Bintanja et al., 2013).

5. Conclusions

Our multi-proxy record of changing ocean conditions at the intersection between the Ross Sea and the Southern Ocean provides new perspective on the influence of ice sheet and glacial retreat on mid-Holocene oceanographic conditions. We interpret indicators of persistent ice cover in Robertson Bay between 6.2 and 4.0 cal kyr BP as a local response to AIS retreat during the mid-Holocene. We propose that meltwater discharge associated with the formation of the modern Ross Ice Shelf and glacial retreat along the Victoria Land coastal margin altered the structure of the continental shelf-break frontal system, freshening surface waters and isolating downstream regions of the East Antarctic margin from upwelling mCDW. Both regional processes and the local retreat of glaciers within the embayment could have supported the expansion of multi-year sea ice or a small-cavity ice shelf in inner Robertson Bay during a period characterized by warmer spring conditions and increased primary production in other regions of Antarctica. We suggest that ice sheet retreat was an important, perhaps dominant, driver of contrasting mid-Holocene environmental conditions around the Antarctic margin. The formation of modern ice shelf cavities and the onset of modern-style water mass transformation is a plausible mechanism for rapid environmental change against the backdrop of more gradual trends in seasonal insolation (cf. Ashley et al., 2021). This result underscores that the mid-to-late Holocene transition, recorded in Antarctic marine sediment cores (ca. 4 cal kyr BP), is a valuable target for coupled ice sheet-ocean modeling studies which seek to understand the regional impact of Antarctic ice sheet retreat and the ice-ocean feedbacks that support ice sheet readvance (cf. Venturelli et al., 2020).

Greater influence of global modes of atmospheric variability and climate evolution (SAM, ENSO, insolation changes, volcanic eruptions) on late Holocene Ross Sea oceanography is consistent with the termination of regional forcing associated with Antarctic

KOPRI 극지연구소

ice sheet retreat. Variability in F. curta relative abundance and other indicators of sea ice and oceanographic dynamics in Robertson Bay and other regions of the Victoria Land costal margin indicate relatively large environmental shifts during the late Holocene, despite subtle changes in external forcings. We identify a period associated with a shorter seasonal duration of sea ice, reduced polynya activity, and nutrient limitation in Robertson Bay between 1.5 and 1.0 cal kyr BP. A subsequent increase in productivity and bottom water oxygenation ca. 0.8 cal kyr BP is consistent with enhanced polynya activity, a greater presence of mCDW in the surface layer, and displacement of oxygen-poor mCDW from the deep basin of Robertson Bay. These conditions coincide with the core period of an Antarctic MCA. After 0.7 cal kyr BP, more consolidated sea ice conditions in Robertson Bay persist during the Little Ice Age, a period of colder atmospheric temperatures in Ross Sea linked to orbital, volcanic and solar forcing, and a sustained negative trend in the SAM. In contrast to the mid-to-late Holocene, last millennium climate transitions were more regionally consistent, and the Little Ice Age recorded in terrestrial and marine records from West and East Antarctica (onset 700-400 cal yr BP) is more synchronous than any prior event.

Holocene marine paleoclimate records from Robertson Bay and across the Antarctic margin record the oceanographic response to mid-Holocene glacial retreat, as well as natural variability in SAM and ENSO dynamics and global mean temperatures during the last millennium. These findings highlight the likely sensitivity of the Antarctic ice-ocean interface to projected changes in AIS meltwater discharge, global mean temperatures, SAM, and ENSO in the coming decades. Furthermore, the regionally specific impact of mid-Holocene ice sheet retreat underlines the critical need to integrate and accurately represent feedback mechanisms between Antarctic oceanography and ice sheet dynamics in projections of future changes.

KOPRI 극지연구소

남극 로스해 로버트슨 만의 홀로세 고해양 환경 변동: 해양–빙상–기후 상호연결성을 나타내는 해양 퇴적 기록

Olivia J. Truax[1,2,*], Christina R. Riesselman[1,2], Gary S. Wilson[2,3], Craig L. Stevens[4,5], Rebecca L. Parker[1], 이재일[6], Robert M. McKay[7], Brad E. Rosenheim[8], Catherine E. Ginnane[9], Jocelyn C. Turnbull[9,10]j, 문홍수[6], 이민경[6], Bob Dagg[1,2], 유규철[6]

[1]Department of Geology, University of Otago, New Zealand
[2]Department of Marine Science, University of Otago, New Zealand
[3]University of Waikato, New Zealand
[4]National Institute of Water and Atmospheric Research, New Zealand
[5]Department of Physics, University of Auckland, New Zealand
[6]극지연구소
[7]Antarctic Research Centre, Victoria University of Wellington, New Zealand
[8]University of South Florida College of Marine Science, USA
[9]Rafter Radiocarbon Laboratory, GNS Science, New Zealand
[10]CIRES, University of Colorado at Boulder, USA

요약: 최근 수십 년 동안 남극 빙붕의 해양 기인 저면 융해가 가속화되면서, 이는 해수면 상승과 전 지구적 열염순환에 중요한 영향을 미치고 있다. 본 연구에서는 로스해와 남극해가 만나는 지점에서의 해양학적 조건을 복원하기 위해, 로버트슨 만에서 채취한 홀로세 다중지표 해양 퇴적 기록을 분석하였다. 가속 열분해 산화 방식을 적용한 방사성탄소 연대-심도 모델을 통해, 지난 6,700년 동안의 빙하 거동과 해양학적 변화에 대한 시간 틀을 구축하였다. 규조류 군집, 자기 감수율, 입도, 총 유기탄소 및 질소, 미량 원소, 그리고 탄소 동위원소 값은 해양 및 빙하 조건 변화의 대리지표로 활용되었으며, 이는 현대 해양 관측 자료의 맥락에서 해석되었다. 우리의 기록은 약 5,000년 전 중기 홀로세 기후 최적기 동안 로스해 북서부 지역에 지속적인 해빙이 존재했음을 보여준다. 이러한 관측을 바탕으로, 로스해 지역에서 빙상이 후퇴하면서 발생한 용융수와 빙산 방출이 중기 홀로세 동안 지역 해양 환경을 변화시켰음을 제안한다. 로버트슨 만에서 현대적 양상의 해양학적 조건이 시작된 시기는 약 4,000년 전으로 나타났다. 후기 홀로세 동안 비교적 안정적인 조건이 유지되었으나, 약 800년 전에는 폴리냐 활동이 강화되고 영양염이 풍부한 심층수의 용승이 증가한 시기가 확인된다. 또한 소빙기 동안인 약 700년 전 이후에는 계절적 해빙 지속 기간이 증가한 것으로 나타났다. 로버트슨 만 해양 환경이 중기 홀로세 빙상 후퇴와 지난 천 년간의 자연 기후 변동성에 반응한 양상은, 향후 수십 년 동안 예상되는 변화에 대해 남극의 빙상 - 해양 경계면이 매우 민감하게 반응할 수 있음을 강조한다.

References

N.J. Abram, R. Mulvaney, F. Vimeux, S.J. Phipps, J. Turner, M.H. England. Evolution of the Southern Annular Mode during the past millennium. Nat. Clim. Change, 4 (2014), pp. 564-569, 10.1038/nclimate2235

P.L. Adhikari, K. Maiti, E.B. Overton, B.E. Rosenheim, B.D. Marx. Distributions and accumulation rates of polycyclic aromatic hydrocarbons in the northern Gulf of Mexico sediments. Environ. Pollut. Barking Essex, 212 (1987) (2016), pp. 413-423, 10.1016/j.envpol.2016.01.064

R. Agnihotri, M.A. Altabet, T.D. Herbert, J.E. Tierney. Subdecadally resolved paleoceanography of the Peru margin during the last two millennia. Geochem. Geophys. Geosystems, 9 (2008), 10.1029/2007GC001744

C.S. Allen, L. Oakes-Fretwell, J.B. Anderson, D.A. Hodgson. A record of Holocene glacial and oceanographic variability in Neny Fjord, Antarctic Peninsula. Holocene, 20 (2010), pp. 551-564, 10.1177/0959683609356581

C. An, S. Hou, S. Jiang, Y. Li, T. Ma, M.A.J. Curran, H. Pang, Z. Zhang, W. Zhang, J. Yu, K. Liu, G. Shi, H. Ma, B. Sun. The Long-Term Cooling Trend in East Antarctic Plateau Over the Past 2000 Years Is Only Robust Between 550 and 1550 CE. Geophys. Res. Lett., 48 (2021), Article e2021GL092923, 10.1029/2021GL092923

L.K. Armand, X. Crosta, O. Romero, J.-J. Pichon. The biogeography of major diatom taxa in Southern Ocean sediments: 1. Sea ice related species. Palaeogeogr. Palaeoclimatol. Palaeoecol., 223 (2005), pp. 93-126, 10.1016/j.palaeo.2005.02.015

K.E. Ashley, R. McKay, J. Etourneau, F.J. Jimenez-Espejo, A. Condron, A. Albot, X. Crosta, C. Riesselman, O. Seki, G. Massé, N.R. Golledge, E. Gasson, D.P. Lowry, N.E. Barrand, K. Johnson, N. Bertler, C. Escutia, R. Dunbar, J.A. Bendle. Mid-Holocene Antarctic sea-ice increase driven by marine ice sheet retreat. Climate of the Past, 17 (2021), pp. 1-19. https://doi.org/10.5194/cp-17-1-2021

C. Beans, J.H. Hecq, P. Koubbi, C. Vallet, S. Wright, A. Goffart. A study of the diatom-dominated microplankton summer assemblages in coastal waters from Terre Adélie to the Mertz Glacier, East Antarctica (139°E – 145°E). Polar Biol., 31 (2008), pp. 1101-1117, 10.1007/s00300-008-0452-x.

M.J. Bentley, D.A. Hodgson, J.A. Smith, C. ó Cofaigh, E.W. Domack, R.D. Larter, S.J. Roberts, S. Brachfeld, A. Leventer, C. Hjort, C.-D. Hillenbrand, J. Evans. Mechanisms of Holocene palaeoenvironmental change in the Antarctic Peninsula region. Holocene, 19 (2009), pp. 51-69, 10.1177/0959683608096603.

S. Berg, M.J. Leng, C.P. Kendrick, H. Cremer, B. Wagner. Bulk sediment and diatom silica

KOPRI 극지연구소

carbon isotope composition from coastal marine sediments off East Antarctica. Silicon, 5 (2013), pp. 19-34, 10.1007/s12633-012-9113-3.

N.A.N. Bertler, H. Conway, D. Dahl-Jensen, D.B. Emanuelsson, M. Winstrup, P.T. Vallelonga, J.E. Lee, E.J. Brook, J.P. Severinghaus, T.J. Fudge, E.D. Keller, W.T. Baisden, R.C.A. Hindmarsh, P.D. Neff, T. Blunier, R. Edwards, P.A. Mayewski, S. Kipfstuhl, C. Buizert, S. Canessa, R. Dadic, H.A. Kjær, A. Kurbatov, D. Zhang, E.D. Waddington, G. Baccolo, T. Beers, H.J. Brightley, L. Carter, D. Clemens-Sewall, V.G. Ciobanu, B. Delmonte, L. Eling, A. Ellis, S. Ganesh, N.R. Golledge, S. Haines, M. Handley, R.L. Hawley, C.M. Hogan, K.M. Johnson, E. Korotkikh, D.P. Lowry, D. Mandeno, R.M. McKay, J.A. Menking, T.R. Naish, C. Noerling, A. Ollive, A. Orsi, B.C. Proemse, A.R. Pyne, R.L. Pyne, J. Renwick, R.P. Scherer, S. Semper, M. Simonsen, S.B. Sneed, E.J. Steig, A. Tuohy, A.U. Venugopal, F. Valero-Delgado, J. Venkatesh, F. Wang, S. Wang, D.A. Winski, V.H.L. Winton, A. Whiteford, C. Xiao, J. Yang, X. Zhang. The Ross Sea Dipole – temperature, snow accumulation and sea ice variability in the Ross Sea region, Antarctica, over the past 2700 years. Clim. Past, 14 (2018), pp. 193-214, 10.5194/cp-14-193-2018.

N.A.N. Bertler, P.A. Mayewski, L. Carter. Cold conditions in Antarctica during the Little Ice Age – implications for abrupt climate change mechanisms. Earth Planet Sci. Lett., 308 (2011), pp. 41-51, 10.1016/j.epsl.2011.05.021.

T.S. Bianchi, V. Galy, B.E. Rosenheim, M. Shields, X. Cui, P. Van Metre. Paleoreconstruction of organic carbon inputs to an oxbow lake in the Mississippi River watershed: effects of dam construction and land use change on regional inputs. Geophys. Res. Lett., 42 (2015), pp. 7983-7991, 10.1002/2015GL065595.

R. Bintanja, G.J. Van Oldenborgh, S.S. Drijfhout, B. Wouters, C.A. Katsman. Important role for ocean warming and increased ice-shelf melt in Antarctic sea-ice expansion. Nature Geosci, 6 (2013), pp. 376-379. https://doi.org/10.1038/ngeo1767

M.M. Bowen, D. Fernandez, A. Forcen-Vazquez, A.L. Gordon, B. Huber, P. Castagno, P. Falco. The role of tides in bottom water export from the western Ross Sea. Sci. Rep., 11 (2021), p. 2246, 10.1038/s41598-021-81793-5.

S.A. Brachfeld, S.K. Banerjee. Rock-magnetic carriers of century-scale susceptibility cycles in glacial–marine sediments from the Palmer Deep, Antarctic Peninsula. Earth Planet Sci. Lett., 176 (2000), pp. 443-455, 10.1016/S0012-821X(00)00008-X.

B. Bronselaer, M. Winton, S.M. Griffies, W.J. Hurlin, K.B. Rodgers, O.V. Sergienko, R.J. Stouffer, J.L. Russell. Change in future climate due to Antarctic meltwater. Nature (2018), 10.1038/s41586-018-0712-z.

P. Campagne, X. Crosta, S. Schmidt, M. Noëlle Houssais, O. Ther, G. Massé. Sedimentary response to sea ice and atmospheric variability over the instrumental period off

Adélie Land, East Antarctica. Biogeosciences, 13 (2016), pp. 4205-4218, 10.5194/bg-13-4205-2016.

A.J. Christ, M. Talaia-Murray, N. Elking, E.W. Domack, A. Leventer, C. Lavoie, S. Brachfeld, K.-C. Yoo, R. Gilbert, S.-M. Jeong, S. Petrushak, J. Wellner, the LARISSA Group. Late Holocene glacial advance and ice shelf growth in Barilari Bay, Graham Land, West Antarctic Peninsula. Geol. Soc. Am. Bull., 127 (2015), pp. 297-315, 10.1130/B31035.1.

X. Crosta, J. Crespin, D. Swingedouw, O. Marti, V. Masson-Delmotte, J. Etourneau, H. Goosse, P. Braconnot, R. Yam, I. Brailovski, A. Shemesh. Ocean as the main driver of Antarctic ice sheet retreat during the Holocene. Glob. Planet. Change, 166 (2018), pp. 62-74, 10.1016/j.gloplacha.2018.04.007.

X. Crosta, M. Debret, D. Denis, M.A. Courty, O. Ther. Holocene long- and short-term climate changes off Adélie Land, East Antarctica. Geochem. Geophys. Geosystems, 8 (2007), 10.1029/2007GC001718.

X. Crosta, D. Denis, O. Ther. Sea ice seasonality during the Holocene, Adélie Land, East Antarctica. Marine Micropaleontology, 66 (2008), pp. 222-232. https://doi.org/10.1016/j.marmicro.2007.10.001

X. Crosta, O. Romero, L. Armand, J.-J. Pichon. The biogeography of major diatom taxa in Southern Ocean sediments: 2. Open ocean related species. Palaeogeogr. Palaeoclimatol. Palaeoecol., 223 (2005), 10.1016/j.palaeo.2005.03.028.

W.L. Cunningham, A. Leventer. Diatom assemblages in surface sediments of the Ross Sea: relationship to present oceanographic conditions. Antarct. Sci., 10 (1998), pp. 134-146, 10.1017/S0954102098000182.

C. Dätwyler, R. Neukom, N.J. Abram, A.J.E. Gallant, M. Grosjean, M. Jacques-Coper, D.J. Karoly, R. Villalba. Teleconnection stationarity, variability and trends of the Southern Annular Mode (SAM) during the last millennium. Clim. Dyn., 51 (2018), pp. 2321-2339, 10.1007/s00382-017-4015-0.

D.J. DeMaster, O. Ragueneau, C.A. Nittrouer. Preservation efficiencies and accumulation rates for biogenic silica and organic C, N, and P in high-latitude sediments: the Ross Sea

J. Geophys. Res. Oceans, 101 (1996), pp. 18501-18518, 10.1029/96JC01634.

D. Denis, X. Crosta, L. Barbara, G. Massé, H. Renssen, O. Ther, J. Giraudeau. Sea ice and wind variability during the Holocene in East Antarctica: insight on middle‐high latitude coupling. Quat. Sci. Rev., 29 (2010), pp. 3709-3719, 10.1016/j.quascirev.2010.08.007.

D. Denis, X. Crosta, S. Schmidt, D.S. Carson, R.S. Ganeshram, H. Renssen, V. Bout-Roumazeilles, S. Zaragosi, B. Martin, M. Cremer. Holocene glacier and deep water dynamics, Adélie Land region, East Antarctica. Quaternary Science Reviews, 28

(2009), pp. 1291-1303. https://doi.org/10.1016/j.quascirev.2008.12.024

A. Di Roberto, E. Colizza, P. Del Carlo, M. Petrelli, F. Finocchiaro, G. Kuhn. First marine cryptotephra in Antarctica found in sediments of the western Ross Sea correlates with englacial tephras and climate records. Sci. Rep., 9 (2019), Article 10628, 10.1038/s41598-019-47188-3.

E. Domack, A. Leventer, R. Dunbar, F. Taylor, S. Brachfeld, C. Sjunneskog, Odp Chronology of the Palmer Deep site, Antarctic Peninsula: a Holocene palaeoenvironmental reference for the circum-antarctic. Holocene, 11 (2001), pp. 1-9, 10.1191/095968301673881493.

E.W. Domack, E.A. Jacobson, S. Shipp, J.B. Anderson. Late Pleistocene–Holocene retreat of the West Antarctic ice-sheet system in the Ross Sea: Part 2—sedimentologic and stratigraphic signature. GSA Bull, 111 (1999), pp. 1517-1536, 10.1130/0016-7606(1999)111<1517:LPHROT>2.3.CO;2.

S.D. Emslie, A. McKenzie, W.P. Patterson. The rise and fall of an ancient Adélie penguin 'supercolony' at Cape Adare, Antarctica. R. Soc. Open Sci., 5 (2018), Article 172032, 10.1098/rsos.172032.

Domack and Ishman, 1993. E.W. Domack, S. Ishman. Oceanographic and physiographic controls on modern sedimentation within Antarctic fjords. GSA Bulletin, 105 (1993), pp. 1175-1189, 10.1130/0016-7606(1993)105<1175:OAPCOM>2.3.CO;2.

D.J.A. Evans, D.I. Benn. A Practical Guide to the Study of Glacial Sediments. Routledge (2014).

A. Fernandez, G.M. Santos, E.K. Williams, M.A. Pendergraft, L. Vetter, B.E. Rosenheim. Blank corrections for ramped pyrolysis radiocarbon dating of sedimentary and soil organic carbon. Anal. Chem., 86 (2014), pp. 12085-12092, 10.1021/ac502874j

R.L. Folk, W.C. Ward. Brazos River bar [Texas]; a study in the significance of grain size parameters. J. Sediment. Res., 27 (1957), pp. 3-26, 10.1306/74D70646-2B21-11D7-8648000102C1865D.

B.V. Gaglioti, D.H. Mann, B.M. Jones, J.W. Pohlman, M.L. Kunz, M.J. Wooller. Radiocarbon age-offsets in an arctic lake reveal the long-term response of permafrost carbon to climate change. J. Geophys. Res. Biogeosciences, 119 (2014), pp. 1630-1651, 10.1002/2014JG002688.

M. Gao, S.-J. Kim, J. Yang, J. Liu, T. Jiang, B. Su, Y. Wang, J. Huang. Historical fidelity and future change of Amundsen Sea Low under 1.5°C–4 °C global warming in CMIP6. Atmos. Res. (2021), Article 105533, 10.1016/j.atmosres.2021.105533.

Y. Gao, M.C. Salvatore, Q. Xu, L. Yang, L. Sun, Z. Xie, C. Baroni. The occupation history of the longest-dwelling Adélie penguin colony reflects Holocene climatic and environmental changes in the Ross Sea, Antarctica. Quat. Sci. Rev., 284 (2022), Article

107494, 10.1016/j.quascirev.2022.107494.

N.-X. Geilfus, R.J. Galley, O. Crabeck, T. Papakyriakou, J. Landy, J.-L. Tison, S. Rysgaard. Inorganic carbon dynamics of melt-pond-covered first-year sea ice in the Canadian Arctic Biogeosciences, 12 (2015), pp. 2047-2061, 10.5194/bg-12-2047-2015.

R. Gersonde, U. Zielinski. The reconstruction of late Quaternary Antarctic sea-ice distribution－the use of diatoms as a proxy for sea-ice. Palaeogeogr. Palaeoclimatol. Palaeoecol., 162 (2000), pp. 263-286, 10.1016/S0031-0182(00)00131-0.

J.A.E. Gibson, T. Trull, P.D. Nichols, R.E. Summons, A. McMinn. Sedimentation of 13C-rich organic matter from Antarctic sea-ice algae: a potential indicator of past sea-ice extent. Geology, 27 (1999), p. 331, 10.1130/0091-7613(1999)027<0331:SOCROM>2.3.CO;2.

C.E. Ginnane, J.C. Turnbull, S. Naeher, B.E. Rosenheim, R.A. Venturelli, A.M. Phillips, S. Reeve, J. Parry-Thompson, A. Zondervan, R.H. Levy, K.-C. Yoo, G. Dunbar, T. Calkin, C. Escutia, J.G. Pastor. Advancing Antarctic sediment chronology through combined ramped pyrolysis oxidation and pyrolysis-GC-MS. Radiocarbon (2024), pp. 1-20, 10.1017/RDC.2023.116.

I. Goodwin, S. Browning, A. Lorrey, P. A. Mayewski, S. J. Phipps, N. Bertler, R. Edwards, T. Cohen, T. Van Ommen, M. Curran, C. Barr, J. Stager. A reconstruction of extratropical Indo-Pacific sea-level pressure patterns during the Medieval Climate Anomaly. Clim. Dyn., 43 (2014), pp. 1197-1219, 10.1007/s00382-013-1899-1.

A.L. Gordon, B.A. Huber, J. Busecke. Bottom water export from the western Ross Sea, 2007 through 2010. Geophys. Res. Lett., 42 (2015), pp. 5387-5394, 10.1002/2015GL064457.

A.R.W. Halberstadt, L.M. Simkins, S.L. Greenwood, J.B. Anderson. Past ice-sheet behaviour: retreat scenarios and changing controls in the Ross Sea, Antarctica. Cryosphere, 10 (2016), pp. 1003-1020, 10.5194/tc-10-1003-2016.

B.L. Hall, G.M. Henderson, C. Baroni, T.B. Kellogg. Constant Holocene Southern-Ocean 14C reservoir ages and ice-shelf flow rates. Earth Planet Sci. Lett., 296 (2010), pp. 115-123, 10.1016/j.epsl.2010.04.054.

J. Haslett, A. Parnell. A simple monotone process with application to radiocarbon-dated depth chronologies. J. R. Stat. Soc. Ser. C Appl. Stat., 57 (2008), pp. 399-418.

TJ Heaton, M Butzin, E Bard, et al. Marine Radiocarbon Calibration in Polar Regions: A Simple Approximate Approach using Marine2. Radiocarbon, 65 (4) (2023), pp. 848-875, 10.1017/RDC.2023.42.

T.J. Heaton, P. Köhler, M. Butzin, E. Bard, R.W. Reimer, W.E.N. Austin, C.B. Ramsey, P.M. Grootes, K.A. Hughen, B. Kromer, P.J. Reimer, J. Adkins, A. Burke, M.S. Cook, J. Olsen, L.C. Skinner. Marine20－the marine radiocarbon age calibration curve (0－55,000 cal BP). Radiocarbon, 62 (2020), pp. 779-820, 10.1017/RDC.2020.68.

M.A. Hemer, P.T. Harris. Sediment core from beneath the Amery Ice Shelf, East Antarctica,

suggests mid-Holocene ice-shelf retreat. Geology, 31 (2003), pp. 127-130, 10.1130/0091-7613(2003)031<0127:SCFBTA>2.0.CO;2.

L.M.K. Henke, F.H. Lambert, D.J. Charman. Was the Little Ice Age more or less El Niño-like than the Medieval Climate Anomaly? Evidence from hydrological and temperature proxy data. Clim. Past, 13 (2017), pp. 267-301, 10.5194/cp-13-267-2017.

S.F. Henley, A.L. Annett, R.S. Ganeshram, D.S. Carson, K. Weston, X. Crosta, A. Tait, J. Dougans, A.E. Fallick, A. Clarke. Factors influencing the stable carbon isotopic composition of suspended and sinking organic matter in the coastal Antarctic sea ice environment. Biogeosciences, 9 (2012), pp. 1137-1157, 10.5194/bg-9-1137-2012.

C.-D. Hillenbrand, M.J. Bentley, T.D. Stolldorf, A.S. Hein, G. Kuhn, A.G.C. Graham, C.J. Fogwill, Y. Kristoffersen, JamesA. Smith, J.B. Anderson, R.D. Larter, M. Melles, D.A. Hodgson, R. Mulvaney, D.E. Sugden. Reconstruction of changes in the Weddell Sea sector of the Antarctic Ice Sheet since the Last Glacial Maximum. Quat. Sci. Rev., Reconstruction of Antarctic Ice Sheet Deglaciation (RAISED), 100 (2014), pp. 111-136, 10.1016/j.quascirev.2013.07.020.

C.-D. Hillenbrand, J.A. Smith, G. Kuhn, O. Esper, R. Gersonde, R.D. Larter, B. Maher, S.G. Moreton, T.M. Shimmield, M. Korte. Age assignment of a diatomaceous ooze deposited in the western Amundsen Sea Embayment after the Last Glacial Maximum. J. Quat. Sci., 25 (2010), pp. 280-295, 10.1002/jqs.1308.

J.L. Hinojosa, C.M. Moy, C.H. Stirling, G.S. Wilson, T.I. Eglinton. A New Zealand perspective on centennial-scale Southern Hemisphere westerly wind shifts during the last two millennia. Quat. Sci. Rev., 172 (2017), pp. 32-43, 10.1016/j.quascirev.2017.07.016.

J. Höfer, R. Giesecke, M.J. Hopwood, V. Carrera, E. Alarcón, H.E. González. The role of water column stability and wind mixing in the production/export dynamics of two bays in the Western Antarctic Peninsula. Prog. Oceanogr., Subantarctic and Antarctic Marine Ecosystems: outlining patterns and processes in a changing ocean, 174 (2019), pp. 105-116, 10.1016/j.pocean.2019.01.005.

S.S. Jacobs, C.F. Giulivi, P. Dutrieux. Persistent Ross Sea freshening from imbalance West Antarctic ice shelf melting. J. Geophys. Res. Oceans, 127 (2022), Article e2021JC017808, 10.1029/2021JC017808.

J. Jin, X. Chen, L. Xu, Y. Nie, X. Wang, H. Huang, S.D. Emslie, X. Liu. Chronology and paleoclimatic implications of lacustrine sediments at Inexpressible Island, Ross Sea, Antarctica. Palaeogeogr. Palaeoclimatol. Palaeoecol., 576 (2021), Article 110497, 10.1016/j.palaeo.2021.110497.

K.M. Johnson, R.M. McKay, J. Etourneau, F.J. Jiménez-Espejo, A. Albot, C.R. Riesselman, N.A.N. Bertler, H.J. Horgan, X. Crosta, J. Bendle, K.E. Ashley, M. Yamane, Y.

Yokoyama, S.F. Pekar, C. Escutia, R.B. Dunbar. Sensitivity of Holocene East Antarctic productivity to subdecadal variability set by sea ice. Nat. Geosci. (2021), 10.1038/s41561-021-00816-y.

J.M. Jones, S.T. Gille, H. Goosse, N.J. Abram, P.O. Canziani, D.J. Charman, K.R. Clem, X. Crosta, C. de Lavergne, I. Eisenman, M.H. England, R.L. Fogt, L.M. Frankcombe, G.J. Marshall, V. Masson-Delmotte, A.K. Morrison, A.J. Orsi, M.N. Raphael, J.A. Renwick, D.P. Schneider, G.R. Simpkins, E.J. Steig, B. Stenni, D. Swingedouw, T.R. Vance. Assessing recent trends in high-latitude Southern Hemisphere surface climate. Nat. Clim. Change, 6 (2016), pp. 917-926, 10.1038/nclimate3103.

R.S. Jones, R.J. Whitmore, A.N. Mackintosh, K.P. Norton, S.R. Eaves, J. Stutz, M. Christl. Regional-scale abrupt Mid-Holocene ice sheet thinning in the western Ross Sea, Antarctica. Geology, 49 (2020), pp. 278-282, 10.1130/G48347.1.

J.-H. Kim, X. Crosta, V. Willmott, H. Renssen, J. Bonnin, P. Helmke, S. Schouten, J.S. Sinninghe Damsté. Holocene subsurface temperature variability in the eastern Antarctic continental margin. Geophys. Res. Lett., 39 (2012), 10.1029/2012GL051157.

S. Kim, K.-C. Yoo, J.I. Lee, B.-K. Khim, Y.-S. Bak, M.K. Lee, J. Lee, E.W. Domack, A.J. Christ, H.I. Yoon. Holocene paleoceanography of Bigo Bay, West Antarctic Peninsula: connections between surface water productivity and nutrient utilization and its implication for surface-deep water mass exchange. Quat. Sci. Rev., 192 (2018), pp. 59-70, 10.1016/j.quascirev.2018.05.028.

J. King, K.J. Anchukaitis, K. Allen, T. Vance, A. Hessl. Trends and variability in the Southern Annular Mode over the Common Era. Nat. Commun., 14 (2023), p. 2324, 10.1038/s41467-023-37643-1.

T.M. King, B.E. Rosenheim, A.L. Post, T. Gabris, T. Burt, E.W. Domack. Large scale intrusion of Circumpolar Deep Water on Antarctic margin recorded by stylasterid corals. Paleoceanogr. Paleoclimatol., 33 (2018), pp. 1306-1321, 10.1029/2018PA003439.

B.G. Koffman, S.L. Goldstein, G. Winckler, M.R. Kaplan, L. Bolge, P. Biscaye. Abrupt changes in atmospheric circulation during the Medieval Climate Anomaly and Little Ice Age recorded by Sr-Nd isotopes in the Siple Dome ice core, Antarctica. Paleoceanogr. Paleoclimatol., 38 (2023), Article e2022PA004543, 10.1029/2022PA004543.

B.G. Koffman, K.J. Kreutz, D.J. Breton, E.J. Kane, D.A. Winski, S.D. Birkel, A.V. Kurbatov, M.J. Handley. Centennial-scale variability of the Southern Hemisphere westerly wind belt in the eastern Pacific over the past two millennia. Clim. Past, 10 (2014), pp. 1125-1144, 10.5194/cp-10-1125-2014.

P.r. Kyle. A. McMurdo volcanic Group western Ross Embayment. Volcanoes of the Antarctic Plate and Southern Oceans, American Geophysical Union (AGU) (1990), pp. 18-145, 10.1029/AR048p0018.

KOPRI 극지연구소

A. Leventer. Modern distribution of diatoms in sediments from the George V Coast, Antarctica. Mar. Micropaleontol., 19 (1992), pp. 315-332, 10.1016/0377-8398(92)90036-J.

J. Laskar, P. Robutel, F. Joutel, M. Gastineau, A.C.M. Correia, B. Levrard. A long-term numerical solution for the insolation quantities of the Earth. A&A, 428 (2004), pp. 261-285, 10.1051/0004-6361:20041335.

A. Leventer, E.W. Domack, S.E. Ishman, S. Brachfeld, C.E. McClennen, P. Manley. Productivity cycles of 200–300 years in the Antarctic Peninsula region: understanding linkages among the sun, atmosphere, oceans, sea ice, and biota. GSA Bull, 108 (1996), pp. 1626-1644, 10.1130/0016-7606(1996)108<1626:PCOYIT>2.3.CO;2.

A. Leventer, R.B. Dunbar. Factors influencing the distribution of diatoms and other algae in the Ross Sea. J. Geophys. Res. Oceans, 101 (1996), pp. 18489-18500, 10.1029/96JC00204.

Q. Li, M.H. England, A.M. Hogg, S.R. Rintoul, A.K. Morrison. Abyssal ocean overturning slowdown and warming driven by Antarctic meltwater. Nature, 615 (2023), pp. 841-847, 10.1038/s41586-023-05762-w.

S. Lüning, M. Gałka, F. Vahrenholt. The Medieval Climate Anomaly in Antarctica. Palaeogeogr. Palaeoclimatol. Palaeoecol., 532 (2019), Article 109251, 10.1016/j.palaeo.2019.109251.

G. Marshall. Trends in the Southern Annular Mode from observations and reanalyses. J. Clim., 16 (003), pp. 4134-4143, 10.1175/1520-0442(2003)016<4134:TITSAM>2.0.CO;2.

R. McKay, O. Albot, G.B. Dunbar, J.I. Lee, M.K. Lee, K. Yoo, S. Kim, N. Turton, D. Kulhanek, M. Patterson, R. Levy. A comparison of methods for identifying and quantifying ice rafted debris on the Antarctic margin. Paleoceanogr. Paleoclimatol., 37 (2022), 10.1029/2021PA004404.

R. McKay, N.R. Golledge, S. Maas, T. Naish, R. Levy, G. Dunbar, G. Kuhn. Antarctic marine ice-sheet retreat in the Ross Sea during the early Holocene. Geology, 44 (2016), pp. 7-10, 10.1130/G37315.1.

R.M. McKay, L. De Santis, D.K. Kulhanek. Ross Sea West Antarctic ice sheet history. Proceedings of the International Ocean Discovery Program. International Ocean Discovery Program (2019), 10.14379/iodp.proc.374.2019.

R.M. McKay, G.B. Dunbar, T.R. Naish, P.J. Barrett, L. Carter, M. Harper. Retreat history of the Ross Ice Sheet (Shelf) since the Last Glacial Maximum from deep-basin sediment cores around Ross Island. Palaeogeogr. Palaeoclimatol. Palaeoecol., 260 (2008), pp. 245-261, 10.1016/j.palaeo.2007.08.015.

Mezgec et al., 2017. K. Mezgec, B. Stenni, X. Crosta, V. Masson-Delmotte, C. Baroni, M. Braida, V. Ciardini, E. Colizza, R. Melis, M.C. Salvatore, M. Severi, C. Scarchilli, R. Traversi, R. Udisti, M. Frezzotti. Holocene sea ice variability driven by wind and polynya efficiency in the Ross Sea. Nat. Commun., 8 (2017), p. 1334,

KOPRI 극지연구소

10.1038/s41467-017-01455-x.

B.W.J. Miles, C.R. Stokes, S.S.R. Jamieson. Pan‐ice-sheet glacier terminus change in East Antarctica reveals sensitivity of Wilkes Land to sea-ice changes. Sci. Adv., 2 (2016), Article e1501350, 10.1126/sciadv.1501350.

R.T. Minzoni, J.B. Anderson, R. Fernandez, J.S. Wellner. Marine record of Holocene climate, ocean, and cryosphere interactions: Herbert Sound, James Ross Island, Antarctica. Quat. Sci. Rev., 129 (2015), pp. 239-259, 10.1016/j.quascirev.2015.09.009.

A.K. Morrison, A.M. Hogg, M.H. England, P. Spence. Warm Circumpolar Deep Water transport toward Antarctica driven by local dense water export in canyons. Sci. Adv., 6 (2020), Article eaav2516, 10.1126/sciadv.aav2516.

R.A. Mortlock, P.N. Froelich. A simple method for the rapid determination of biogenic opal in pelagic marine sediments. Deep-Sea Res. Part A Oceanogr. Res. Pap., 36 (1989), pp. 1415-1426, 10.1016/0198-0149(89)90092-7.

R. Mulvaney, N.J. Abram, R.C.A. Hindmarsh, C. Arrowsmith, L. Fleet, J. Triest, L.C. Sime, O. Alemany, S. Foord. Recent Antarctic Peninsula warming relative to Holocene climate and ice-shelf history. Nature, 489 (2012), pp. 141-144, 10.1038/nature11391.

S. Naeher, A. Gilli, R.P. North, Y. Hamann, C.J. Schubert. Tracing bottom water oxygenation with sedimentary Mn/Fe ratios in Lake Zurich, Switzerland. Chem. Geol., 9 (2013).

S.U. Neuhaus, S.M. Tulaczyk, N.D. Stansell, J.J. Coenen, R.P. Scherer, J.A. Mikucki, R.D. Powell. Did Holocene climate changes drive West Antarctic grounding line retreat and readvance? Cryosphere, 15 (2021), pp. 4655-4673, 10.5194/tc-15-4655-2021.

R. Neukom, L.A. Barboza, M.P. Erb, F. Shi, J. Emile-Geay, M.N. Evans, J. Franke, D.S. Kaufman, L. Lücke, K. Rehfeld, A. Schurer, F. Zhu, S. Brönnimann, G.J. Hakim, B.J. Henley, F.C. Ljungqvist, N. McKay, V. Valler, L. von Gunten, 2k Consortium Pages. Consistent multidecadal variability in global temperature reconstructions and simulations over the Common Era. Nat. Geosci., 12 (2019), pp. 643-649, 10.1038/s41561-019-0400-0.

C. Ó Cofaigh, B.J. Davies, S.J. Livingstone, J.A. Smith, J.S. Johnson, E.P. Hocking, D.A. Hodgson, J.B. Anderson, M.J. Bentley, M. Canals, E. Domack, J.A. Dowdeswell, J. Evans, N.F. Glasser, C.-D. Hillenbrand, R.D. Larter, S.J. Roberts, A.R. Simms. Reconstruction of ice-sheet changes in the Antarctic Peninsula since the Last Glacial Maximum. Quat. Sci. Rev., Reconstruction of Antarctic Ice Sheet Deglaciation (RAISED), 100 (2014), pp. 87-110, 10.1016/j.quascirev.2014.06.023.

A.J. Orsi, B.D. Cornuelle, J.P. Severinghaus. Little Ice Age cold interval in West Antarctica: evidence from borehole temperature at the West Antarctic Ice Sheet (WAIS) divide. Geophys. Res. Lett., 39 (2012), 10.1029/2012GL051260.

KOPRI 극지연구소

A.H. Orsi, C.L. Wiederwohl. A recount of Ross Sea waters. Deep Sea Research Part II. Topical Studies in Oceanography, Southern Ocean Shelf Slope Exchange, 56 (2009), pp. 778-795.

B.L. Otto-Bliesner, E.C. Brady, J. Fasullo, A. Jahn, L. Landrum, S. Stevenson, N. Rosenbloom, A. Mai, G. Strand. Climate variability and change since 850 CE: an ensemble approach with the Community Earth System Model. Bull. Am. Meteorol. Soc., 97 (2015), pp. 735-754, 10.1175/BAMS-D-14-00233.1.

V. Panizzo, J. Crespin, X. Crosta, A. Shemesh, G. Massé, R. Yam, N. Mattielli, D. Cardinal

Sea ice diatom contributions to Holocene nutrient utilization in East Antarctica. Paleoceanography, 29 (2014), pp. 328-343, 10.1002/2014PA002609.

Parker, R.L. 2017. Sea ice extent and diatom primary production within the SW Ross Sea, Antarctica: the response to post-glacial warming. [Master's thesis, University of Otago].

V.L. Peck, C.S. Allen, S. Kender, E.L. McClymont, D.A. Hodgson. Oceanographic variability on the West Antarctic Peninsula during the Holocene and the influence of upper circumpolar deep water. Quat. Sci. Rev., 119 (2015), pp. 54-65, 10.1016/j.quascirev.2015.04.002.

F. Pedregosa, G. Varoquaux, A. Gramfort, V. Michel, B. Thirion, O. Grisel, M. Blondel, P. Prettenhofer, R. Weiss, V. Dubourg, J. Vanderplas. Scikit-learn: Machine learning in Python

the Journal of machine Learning research, 12 (2011), pp. 2825-2830.

M.A. Pendergraft, Z. Dincer, J.L. Sericano, T.L. Wade, J. Kolasinski, B.E. Rosenheim. Linking ramped pyrolysis isotope data to oil content through PAH analysis. Environ. Res. Lett., 8 (2013), Article 044038, 10.1088/1748-9326/8/4/044038.

M.A. Pendergraft, B.E. Rosenheim. Varying relative degradation rates of oil in different forms and environments revealed by ramped pyrolysis. Environ. Sci. Technol., 48 (2014), pp. 10966-10974, 10.1021/es501354c.

B.B. Perren, D.A. Hodgson, S.J. Roberts, L. Sime, W. Van Nieuwenhuyze, E. Verleyen, W. Vyverman. Southward migration of the Southern Hemisphere westerly winds corresponds with warming climate over centennial timescales. Commun. Earth Environ., 1 (2020), pp. 1-8, 10.1038/s43247-020-00059-6.

J. Pike, X. Crosta, E.J. Maddison, C.E. Stickley, D. Denis, L. Barbara, H. Renssen. Observations on the relationship between the Antarctic coastal diatoms Thalassiosira antarctica Comber and Porosira glacialis (Grunow) Jørgensen and sea ice concentrations during the late Quaternary. Mar. Micropaleontol., 73 (2009), pp. 14-25, 10.1016/j.marmicro.2009.06.005.

H.D. Pritchard, S.R.M. Ligtenberg, H.A. Fricker, D.G. Vaughan, M.R. van den Broeke, L.

KOPRI 극지연구소

Padman. Antarctic ice-sheet loss driven by basal melting of ice shelves. Nature, 484 (2012), pp. 502-505, 10.1038/nature10968.

J. Reback, McKinney W.Jbrockmendel, J.V.D. Bossche, T. Augspurger, P. Cloud, Sinhrks Gfyoung, A. Klein, M. Roeschke, S. Hawkins, J. Tratner, C. She, W. Ayd, Petersen Terji, M. Garcia, J. Schendel, Hayden A.MomIsBestFriend, V. Jancauskas, P. Battiston, Skipper SeaboldChris-B, H. Vetinari, S. Hoyer, W. Overmeire, Kaiqi Dong Alimcmaster, C. Whelan, Mehyar Mortada. pandas-dev/pandas: pandas 1.0.3. https://doi.org/10.5281/ZENODO.3715232 (2020)

H.H. Rhee, M.K. Lee, Y.B. Seong, J.I. Lee, K.-C. Yoo, B.Y. Yu. Post-LGM dynamic deglaciation along the Victoria Land coast, Antarctica. Quat. Sci. Rev., 247 (2020), Article 106595, 10.1016/j.quascirev.2020.106595.

R.H. Rhodes, N.A.N. Bertler, J.A. Baker, H.C. Steen-Larsen, S.B. Sneed, U. Morgenstern, S.J. Johnsen. Little Ice Age climate and oceanic conditions of the Ross Sea, Antarctica from a coastal ice core record. Clim. Past, 8 (2012), pp. 1223-1238, 10.5194/cp-8-1223-2012.

E. Rignot, J. Mouginot, B. Scheuchl, M. van den Broeke, M.J. van Wessem, M. Morlighem

Four decades of Antarctic Ice Sheet mass balance from 1979–2017. Proc. Natl. Acad. Sci., 116 (2019), pp. 1095-1103, 10.1073/pnas.1812883116.

B.E. Rosenheim, M.B. Day, E. Domack, H. Schrum, A. Benthien, J.M. Hayes. Antarctic sediment chronology by programmed-temperature pyrolysis: methodology and data treatment. Geochem. Geophys. Geosystems, 9 (2008), 10.1029/2007GC001816.

B.E. Rosenheim, V. Galy. Direct measurement of riverine particulate organic carbon age structure. Geophys. Res. Lett., 39 (2012), 10.1029/2012GL052883.

B.E. Rosenheim, K.M. Roe, B.J. Roberts, A.S. Kolker, M.A. Allison, K.H. Johannesson. River discharge influences on particulate organic carbon age structure in the Mississippi/Atchafalaya River System. Glob. Biogeochem. Cycles, 27 (2013), pp. 154-166, 10.1002/gbc.20018.

B.E. Rosenheim, J.A. Santoro, M. Gunter, E.W. Domack. Improving Antarctic Sediment 14C Dating Using Ramped Pyrolysis: An Example from the Hugo Island Trough. Radiocarbon, 55 (2013), pp. 115-126.

S. Sadai, A. Condron, R. DeConto, D. Pollard. Future climate response to Antarctic Ice Sheet melt caused by anthropogenic warming. Science Advances, 6 (2020), p. eaaz1169. https://doi.org/10.1126/sciadv.aaz1169

C.M.S. Schine, G. van Dijken, K.R. Arrigo. Spatial analysis of trends in primary production and relationship with large-scale climate variability in the Ross Sea, Antarctica (1997–2013)

J. Geophys. Res. Oceans, 121 (2016), pp. 368-386, 10.1002/2015JC011014.

K.M. Schreiner, T.S. Bianchi, B.E. Rosenheim. Evidence for permafrost thaw and transport from an Alaskan North Slope watershed. Geophys. Res. Lett., 41 (2014), pp. 3117-3126, 10.1002/2014GL059514.

A.E. Shevenell, A.E. Ingalls, E.W. Domack, C. Kelly. Holocene Southern Ocean surface temperature variability west of the Antarctic Peninsula. Nature, 470 (2011), pp. 250-254, 10.1038/nature09751.

M.J. Siegert, J. Kingslake, N. Ross, P.L. Whitehouse, J. Woodward, S.S.R. Jamieson, M.J. Bentley, K. Winter, M. Wearing, A.S. Hein, H. Jeofry, D.E. Sugden. Major ice sheet change in the Weddell sea sector of West Antarctica over the last 5,000 years. Rev. Geophys., 57 (2019), pp. 1197-1223, 10.1029/2019RG000651.

A. Silvano, S.R. Rintoul, B. Peña-Molino, G.D. Williams. Distribution of water masses and meltwater on the continental shelf near the Totten and Moscow University ice shelves. J. Geophys. Res.: Oceans, 122 (2017), pp. 2050-2068, 10.1002/2016JC012115.

A. Silvano, S.R. Rintoul, B. Peña-Molino, W.R. Hobbs, E. van Wijk, S. Aoki, T. Tamura, G.D. Williams. Freshening by glacial meltwater enhances melting of ice shelves and reduces formation of Antarctic Bottom Water. Sci. Adv., 4 (2018), Article eaap9467, 10.1126/sciadv.aap9467.

A.R. Simms, M.J. Bentley, L.M. Simkins, J. Zurbuchen, L.C. Reynolds, R. DeWitt, E.R. Thomas. Evidence for a “Little Ice Age” glacial advance within the Antarctic Peninsula – examples from glacially-overrun raised beaches. Quat. Sci. Rev., 271 (2021), Article 107195, 10.1016/j.quascirev.2021.107195.

J.A. Smith, A.G.C. Graham, A.L. Post, C.-D. Hillenbrand, P.J. Bart, R.D. Powell. The marine geological imprint of Antarctic ice shelves. Nat. Commun., 10 (2019), pp. 1-16, 10.1038/s41467-019-13496-5.

P. Spector, J. Stone, S.G. Cowdery, B. Hall, H. Conway, G. Bromley. Rapid early-Holocene deglaciation in the Ross Sea, Antarctica: early-Holocene Ross Sea deglaciation. Geophys. Res. Lett., 44 (2017), pp. 7817-7825, 10.1002/2017GL074216.

P. Spence, S.M. Griffies, M.H. England, A.McC. Hogg, O.A. Saenko, N.C. Jourdain. Rapid subsurface warming and circulation changes of Antarctic coastal waters by poleward shifting winds: Antarctic subsurface ocean warming. Geophys. Res. Lett., 41 (2014), pp. 4601-4610, 10.1002/2014GL060613.

S.E. Stammerjohn, D.G. Martinson, R.C. Smith, X. Yuan, D. Rind. Trends in Antarctic annual sea ice retreat and advance and their relation to El Niño–Southern oscillation and Southern Annular Mode variability. J. Geophys. Res. Oceans, 113 (2008), 10.1029/2007JC004269.

B. Stenni, M.A.J. Curran, N.J. Abram, A. Orsi, S. Goursaud, V. Masson-Delmotte, R. Neukom, H. Goosse, D. Divine, T. van Ommen, E.J. Steig, D.A. Dixon, E.R. Thomas,

N.A.N. Bertler, E. Isaksson, A. Ekaykin, M. Werner, M. Frezzotti. Antarctic climate variability on regional and continental scales over the last 2000 years. Clim. Past, 13 (2017), pp. 1609-1634, 10.5194/cp-13-1609-2017.

H.M. Stoll, A. Mendez-Vicente, L. Abrevaya, R.F. Anderson, A.S. Rigual-Hernández, S. Gonzalez-Lemos. Growth rate and size effect on carbon isotopic fractionation in diatom-bound organic matter in recent Southern Ocean sediments. Earth Planet Sci. Lett., 457 (2017), pp. 87-99, 10.1016/j.epsl.2016.09.028.

J.D.H. Strickland, T.R. Parsons. A Practical Handbook of Seawater Analysis (2nd edition) (1972). https://doi.org/10.25607/OBP-1791

C. Subt, K.A. Fangman, J.S. Wellner, B.E. Rosenheim. Sediment chronology in Antarctic deglacial sediments: reconciling organic carbon 14C ages to carbonate 14C ages using Ramped PyrOx. Holocene, 26 (2016), pp. 265-273, 10.1177/0959683615608688.

C. Subt, H. I. Yoon, K.-C. Yoo, J.I. Lee, A. Leventer, E. Domack, B. Rosenheim. Sub-ice shelf sediment geochronology utilizing novel radiocarbon methodology for detrital-rich sediments. Geochem. Geophys. Geosystems (2017), 10.1002/2016GC006578.

F. Taylor, J. Whitehead, E. Domack. Holocene paleoclimate change in the Antarctic Peninsula: evidence from the diatom, sedimentary and geochemical record. Mar. Micropaleontol., 41 (2001), pp. 25-43, 10.1016/S0377-8398(00)00049-9.

T. Tesi, S.T. Belt, K. Gariboldi, F. Muschitiello, L. Smik, F. Finocchiaro, F. Giglio, E. Colizza, G. Gazzurra, P. Giordano, C. Morigi, L. Capotondi, A. Nogarotto, D. Köseoğlu, A. Di Roberto, A. Gallerani, L. Langone. Resolving sea ice dynamics in the north-western Ross Sea during the last 2.6 ka: from seasonal to millennial timescales. Quat. Sci. Rev., 237 (2020), Article 106299, 10.1016/j.quascirev.2020.106299.

A.F. Thompson, A.L. Stewart, P. Spence, K.J. Heywood. The Antarctic Slope current in a changing climate. Rev. Geophys., 56 (2018), pp. 741-770, 10.1029/2018RG000624.

R.L. Totten, A.N.R. Fonseca, J.S. Wellner, Y.P. Munoz, J.B. Anderson, T.S. Tobin, A.A. Lehrmann. Oceanographic and climatic influences on Trooz Glacier, Antarctica during the Holocene. Quat. Sci. Rev., 276 (2022), Article 107279, 10.1016/j.quascirev.2021.107279

O.J. Truax, B.L. Otto-Bliesner, E.C. Brady, C.L. Stevens, G.S. Wilson, C.R. Riesselman. Drivers of last millennium Antarctic climate evolution in an ensemble of Community Earth System Model simulations. Geosciences, 12 (2022), p. 299, 10.3390/geosciences12080299.

J.C. Turnbull, A. Zondervan, J. Kaiser, M. Norris, J. Dahl, T. Baisden, S. Lehman. High-precision atmospheric 14CO 2 measurement at the Rafter Radiocarbon Laboratory Radiocarbon, 57 (2015), pp. 377-388, 10.2458/azu_rc.57.18390.

R.A. Venturelli, M.R. Siegfried, K.A. Roush, W. Li, J. Burnett, R. Zook, H.A. Fricker, J.C.

Priscu, A. Leventer, B.E. Rosenheim. Mid-Holocene grounding line retreat and readvance at whillans ice stream, west Antarctica. Geophys. Res. Lett., 47 (2020), Article e2020GL088476, 10.1029/2020GL088476.

L. Vetter, B.E. Rosenheim, A. Fernandez, T.E. Törnqvist. Short organic carbon turnover time and narrow 14C age spectra in early Holocene wetland paleosols. Geochem. Geophys. Geosystems, 18 (2017), pp. 142-155, 10.1002/2016GC006526.

J. Villinski, R. B. Dunbar, D. Mucciarone. Carbon 13/Carbon 12 ratios of sedimentary organic matter from the Ross Sea, Antarctica: a record of phytoplankton bloom dynamics. J. Geophys. Res., 105 (2000), pp. 14163-14172, 10.1029/1999JC000309.

N.R. Warner, E.W. Domack. Millennial- to decadal-scale paleoenvironmental change during the Holocene in the Palmer Deep, Antarctica, as recorded by particle size analysis. Paleoceanography, 17 (2002), 10.1029/2000PA000602. 5-1-PAL 5-14

J. Warnock, R. Scherer. A revised method for determining the absolute abundance of diatoms. J. Paleolimnol., 53 (2015), pp. 157-163, 10.1007/s10933-014-9808-0.

E.K. Williams, B.E. Rosenheim, M. Allison, A.P. McNichol, L. Xu. Quantification of refractory organic material in Amazon mudbanks of the French Guiana Coast. Mar. Geol., 363 (2015), pp. 93-101, 10.1016/j.margeo.2015.02.009.

G.D. Williams, S. Aoki, S.S. Jacobs, S.R. Rintoul, T. Tamura, N.L. Bindoff. Antarctic bottom water from the Adélie and George V Land coast, East Antarctica (140–149°E). J. Geophys. Res. Oceans, 115 (2010), 10.1029/2009JC005812.

V.H.L. Winton, G.B. Dunbar, N.a.N. Bertler, M.-A. Millet, B. Delmonte, C.B. Atkins, J.M. Chewings, P. Andersson. The contribution of aeolian sand and dust to iron fertilization of phytoplankton blooms in southwestern Ross Sea, Antarctica. Glob. Biogeochem. Cycles, 28 (2014), pp. 423-436, 10.1002/2013GB004574.

M.G. Wise, J.A. Dowdeswell, M. Jakobsson, R.D. Larter. Evidence of marine ice-cliff instability in Pine Island Bay from iceberg-keel plough marks. Nature, 550 (2017), pp. 506-510, 10.1038/nature24458.

Q.B. Xu, L.J. Yang, Y.S. Gao, L.G. Sun, Z.Q. Xie. 6,000-Year reconstruction of Modified Circumpolar Deep Water intrusion and its effects on sea ice and penguin in the Ross Sea. Geophys. Res. Lett., 48 (2021), Article e2021GL094545, 10.1029/2021GL094545.

X. Yuan. ENSO-related impacts on Antarctic sea ice: a synthesis of phenomenon and mechanisms. Antarct. Sci., 16 (2004), pp. 415-425, 10.1017/S0954102004002238.

X. Zhang, T.S. Bianchi, X. Cui, B.E. Rosenheim, C.-L. Ping, A.J.M. Hanna, M. Kanevskiy, K.M. Schreiner, M.A. Allison. Permafrost organic carbon Mobilization from the watershed to the Colville river Delta: evidence from 14C ramped pyrolysis and lignin biomarkers. Geophys. Res. Lett., 44 (11) (2017), 10.1002/2017GL075543 491-11,500

M. Ziegler, T. Jilbert, G.J. de Lange, L.J. Lourens, G.-J. Reichart. Bromine counts from XRF

scanning as an estimate of the marine organic carbon content of sediment cores. Geochem. Geophys. Geosystems, 9 (2008). https://doi.org/10.1029/2007GC001932

A. Zondervan, T.M. Hauser, J. Kaiser, R.L. Kitchen, J.C. Turnbull, J.G. West. XCAMS: the compact 14C accelerator mass spectrometer extended for 10Be and 26Al at GNS Science, New Zealand. Nucl. Instrum. Methods Phys. Res. Sect. B Beam Interact. Mater. At., 361 (2015), pp. 25-33, 10.1016/j.nimb.2015.03.013.

KOPRI
극지연구소

Table 1. Summary of the relationships between sedimentary proxies and environmental conditions.

Proxy	Proxy interpretation
Magnetic susceptibility (MS)	The relative contribution of terrigenous input and siliceous diatom productivity (Brachfeld and Banerjee, 2000).
Weight percent biogenic silica (wt% BSi)	The relative contribution of terrigenous input and siliceous diatom productivity (DeMaster et al., 1996)
Total organic carbon (TOC)	Primary productivity and/or anoxia (Domack and Ishman, 1993)
Total nitrogen (TN)	Primary productivity (e.g. Kim et al., 2018)
Absolute diatom abundance (ADA)	Siliceous diatom primary productivity (Leventer, 1992).
The ratio of bromine to titanium (Br/Ti)	Primary production (Agnihotri et al., 2008; Ziegler et al., 2008).
Grain size	The grainsize of fine sands and muds are a function of current strength and settling velocity (Johnson et al., 2021)
$\delta^{13}C$	Biologic productivity and water mass circulation (Gibson et al., 1999; Villinski et al., 2000)
The ratio of Chaetoceros spp. *to Chaetoceros resting spores (CRS)*	Nutrient-rich, mixed, surface waters, mCDW influence (Beans et al., 2008; Leventer et al., 1996)
The relative abundance of Fragilariopsis curta	Persistent spring sea ice; sea ice melt-water stabilized upper water column (Cunningham and Leventer, 1998; Leventer and Dunbar, 1996)
The ratio of manganese to iron (Mn/Fe)	Sediment redox conditions (high Mn/Fe ratios indicate oxic conditions) (Naeher et al., 2013)

KOPRI
극지연구소

Table 2. Dated horizons in core RS15-GC57. Dates included in the final calibrated age model highlighted in bold. Room temperature is abbreviated to RT.

Depth (cmbsf)	Type of date	Temp. range (C)	RPO lab	NZA #	Conventional Radiocarbon Age (^{14}C yr BP)	Calibrated age range (95% CI, cal yr BP)	
						Min	Max
0–1	RPO split 1	RT - 297	USF	62683	1440 ± 80		
	RPO split 2	**297–341**	**USF**	**62684**	**1310 ± 60**	**−71**	**49**
180–181	RPO split 1	RT - 316	USF	62685	3360 ± 140		
	RPO split 2	316–382	USF	62686	2770 ± 85		
	Carbonate (shell fragment)	-	-	**61835**	**2642 ± 26**	**824**	**1430**
220–222	**Carbonate (shell fragment)**	-	-	**61836**	**2885 ± 26**	**1771**	**1894**
380–381	**RPO split 2**	**300–380**	**RRL**	**72390**	**4012 ± 88**	**2416**	**3292**
455–456	RPO split 1	RT -328	USF	62696	4910 ± 120		
	RPO split 2	**328–403**	**USF**	**62697**	**4650 ± 110**	**3373**	**4884**
505–506	RPO split 2	270–370	RRL	72389	5888 ± 44	4823	5518
560–561	RPO split 1	RT- 284	USF	62691	8130 ± 170		
	RPO split 2	**284–327**	**USF**	**62692**	**7320 ± 100**	**5809**	**6733**
567–568	**Carbonate (benthic and planktic foraminifera)**	-	-	**61894**	**6914 ± 152**	**6169**	**7049**

KOPRI
극지연구소

Table 3. Table 3. Sedimentary facies descriptions and interpretations.

Facies	Core Depth (cmbsf)	X-radiograph	Lithology and Sedimentary features	Interpretation
M_{BSi}	0–403		Pervasively bioturbated biosilica-bearing muds with dispersed clasts (DO). Moderately high wt% biogenic silica (10–14%), TOC content (>0.5%)	Pelagic sedimentation with hemipelagic suspension settling (Domack et al., 1999; Smith et al., 2019). Occasional ice rafted debris. Diatom assemblage is consistent with seasonal fast ice overlying the site, but with sea ice breakout in summer (this study; section 3.1).
SM_L	403–570		Laminated sandy mud, physically intermixed with bioturbated mud containing dispersed clasts (wt% biogenic silica <10%). Deformed mm-scale fine sands to coarse silts laminae, that commonly have sharp upper and lower contacts. Intermixing characterised by discrete "blocks" of the differing lithologies, with curvate, cross-cutting lower contacts.	Hemipelagic suspension settling. Lower biogenic silica content likely represents increase ice cover (perennial sea ice or small cavity ice shelf) over site (reduced productivity) (Domack et al., 1999; Hemer and Harris, 2003). Outsized clasts are present, but rare - indicative of depostion beneath sea ice or a small cavity ice shelf containing basal debris proximal to grounding line (Domack et al., 1999; Hemer and Harris, 2003; McKay et al., 2008). Sorted, fine sand/coarse silt laminae suggest presence of moderately-strong bottom current to winnow/prevent suspension settling of muds (Mckay et al., 2008; Smith et al., 2019; Johnson et al., 2021). Intermixing is consistent with post-depositional scouring/turbation by icebergs (Hillenbrand et al., 2014), or glaciotectonic deformation in a proglacial setting (Evans and Benn, 2014).

KOPRI
극지연구소

Table 4. Summary of the proxy characteristics and environmental interpretation for each unit.

Unit		Proxy characteristics and environmental interpretation
Little Ice Age	Unit 1a	↑ TOC → preservation of a modern core top
	Unit 1b <0.5 cal kyr BP	↑ ↑ *F. curta* → onset the modern sea ice cycle (9–11 months of sea ice cover)
	Unit 1c 0.7–01.5 cal kyr BP	↑ $\delta^{13}C$ and ↓ *Chaetoceros* spp.: CRS ratio → stable, nutrient-limited, surface layer ↑ *F. curta* → longer duration of sea ice
Early last millennium	Unit 2a 1.0–0.7 cal kyr BP	↓ $\delta^{13}C$ and ↑ *Chaetoceros* spp.: CRS ratio → mixed, nutrient-rich, surface waters ↑ Mn/Fe ratio → enhanced polynya activity ↑ Sedimentary accumulation → deposition of biogenic and terrigenous sediment
	Unit 2b 1.5–1 cal kyr BP	↑ MS and sand → higher proportion of terrigenous sediment ↓Wt% BSi, TOC, Br/TI, ADA → reduced primary productivity and export ↓*F. curta* → shorter seasonal duration of sea ice
Neoglacial	Unit 3 4.0–1.5 cal kyr BP	↓ $\delta^{13}C$ → nutrient rich, mixed, surface waters ↓ MS and sand % → lower proportion of terrigenous sediment ↑ Wt% BSi, TOC, Br/TI, ADA → primary productivity and export ↑ *F. curta* → longer seasonal duration of sea ice
Mid-Holocene	Unit 4a 6.2–4.0 cal kyr BP	↓ PCA axis 1 → greater proportion of terrigenous sediment ↓ sedimentary accumulation → reduced primary productivity and export ↑ $\delta^{13}C$ → stratification and primary production within sea ice ↑ *F. obliquecostata* → year-round sea ice cover ↑ coarse skewed grainsize assemblage → winnowing of sediment by bottom currents
	Unit 4b 6.7–6.2 cal kyr BP	Multi-proxy record (PCA axes 1 and 2, grain size assemblage) and individual proxies (e.g. wt% BSi) resemble Unit 3 → seasonally open marine conditions

KOPRI
극지연구소

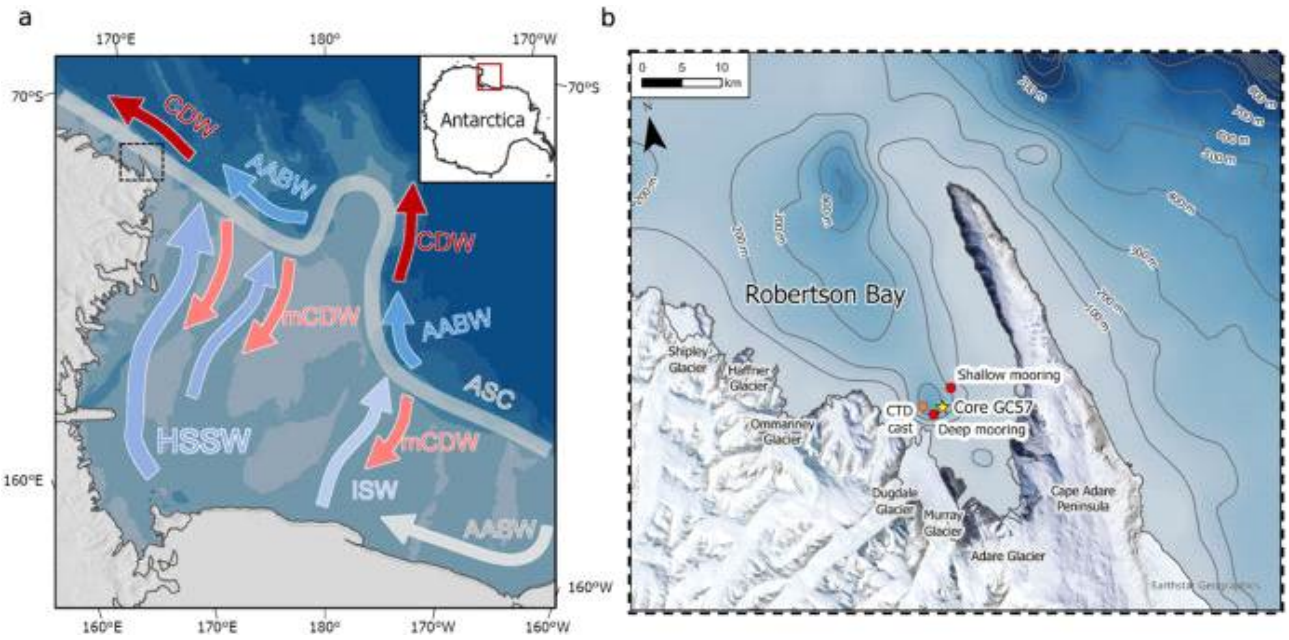


Figure 1. Maps of a) the Ross Sea continental shelf highlighting major circulation features including Antarctic Surface Water, AASW (light blue); Circumpolar Deep Water, CDW (red); Modified Circumpolar Deep Water, mCDW (pink); Antarctic Bottom Water, AABW (dark blue), High Salinity Shelf Water (HSSW); and Ice Shelf Water (ISW). Grey line indicates the easterly flow of the Antarctic Slope Current (ASC). Dashed box shows the location of Robertson Bay with specific features highlighted in b) including the location of the RS15-GC57 core site (yellow), the location of the CTD cast (orange), and the shallow and deep moorings (red).

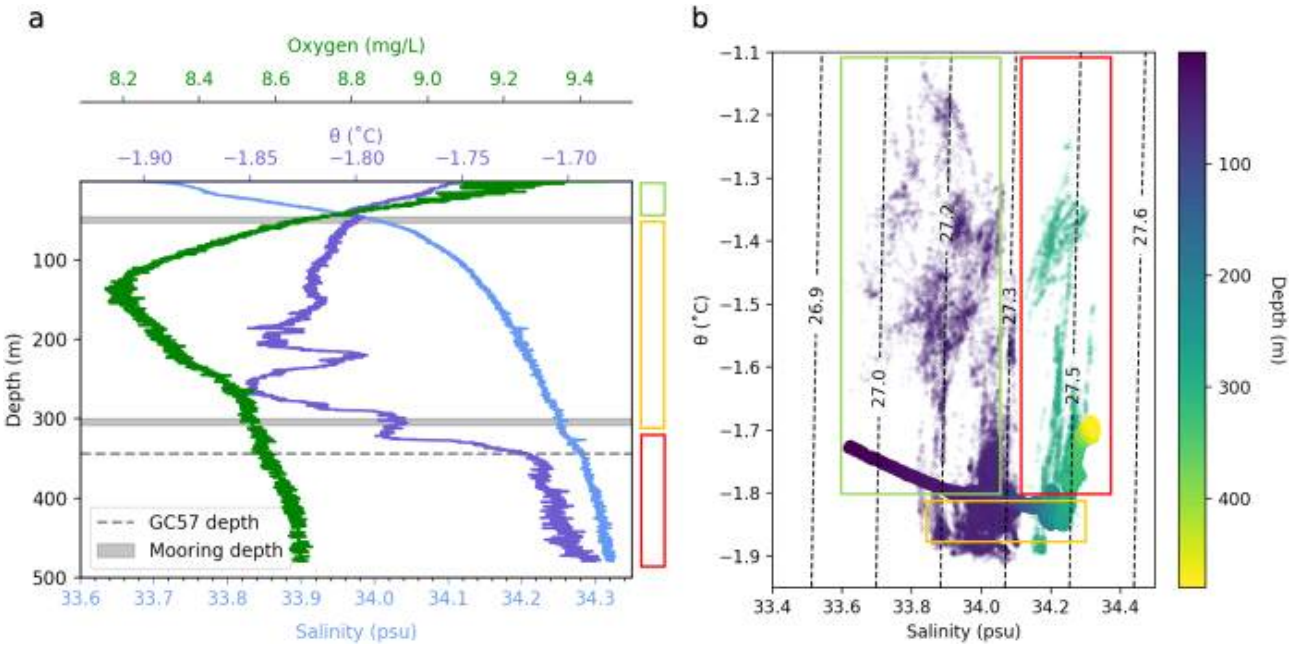


Figure 2. Characteristics of water masses in Robertson Bay; a) vertical profile from the CTD cast taken in November of 2015 showing oxygen concentration (green), potential temperature (Θ; purple), and salinity (blue); grey bars indicate the depths of the shallow and deep moorings, dashed line shows depth of the GC57 core site. Colored boxes indicate warmer and fresher Antarctic Surface Waters (pale green), colder remnant Winter Water (orange), and warmer heavily modified Circumpolar Deep Water present at depth (red); and b) Potential temperature (Θ) versus salinity from the CTD cast (November 2015) and moorings (February 2015 to February 2016). Dashed lines show lines of neutral density; colored boxes indicate water masses identified in the main text.

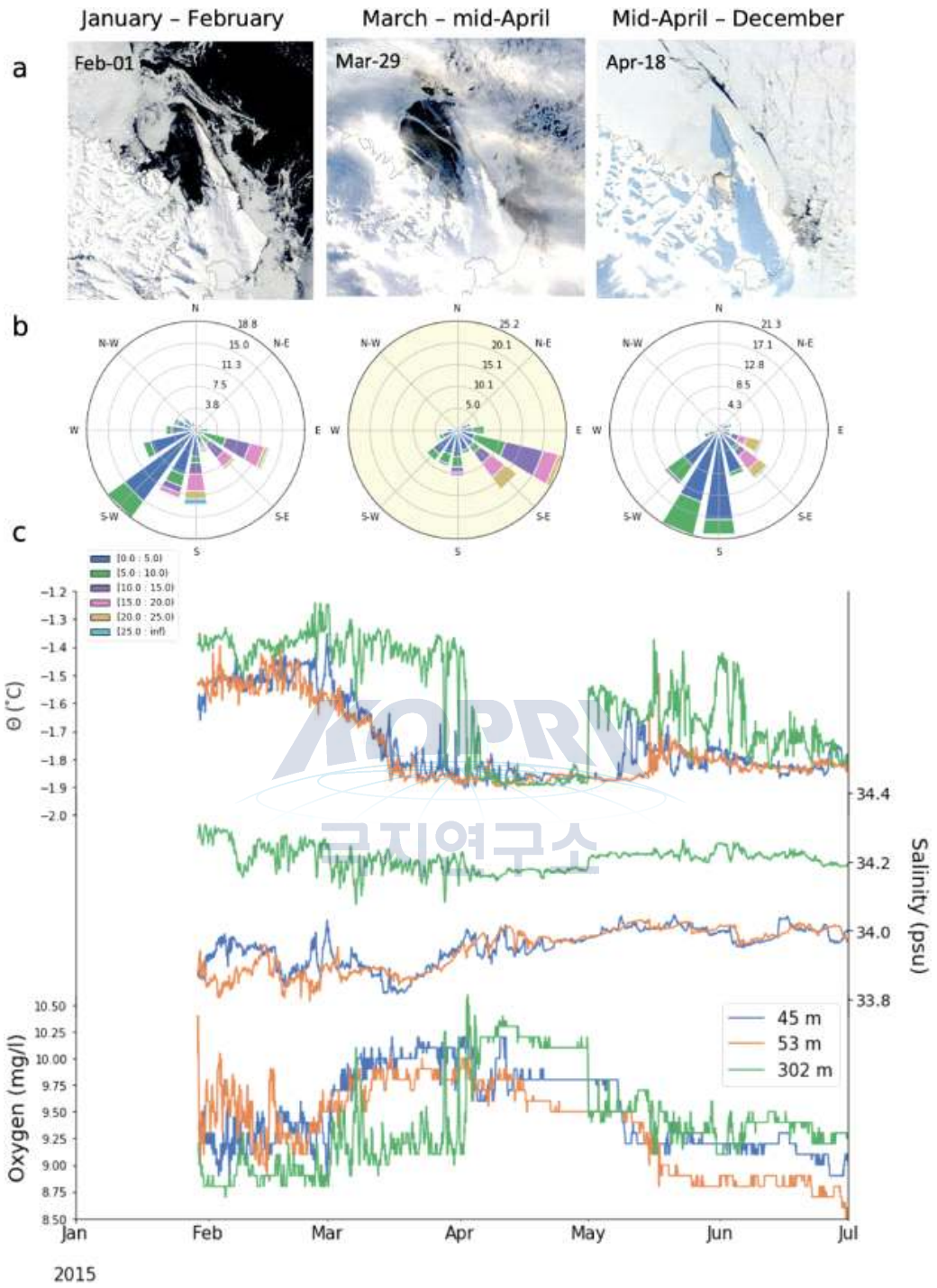


Figure 3. Synthesis of modern conditions in Robertson Bay; a) satellite photos of Robertson Bay sea ice dynamics in austral summer, autumn, and early winter of 2015 (NASA Worldview; https://worldview.earthdata.nasa.gov/); b) prevailing winds (January and February, March to April 15th, and April 15th through December) by direction, strength (meters per second), and frequency along the Cape Adare Ridge in 2016 (see also Supplementary Data); c) oceanographic data from Sea-Bird SBE 37-SMP-ODO CTDs deployed on shallow (45 and 53 m) and deep (302) hydrographic moorings.

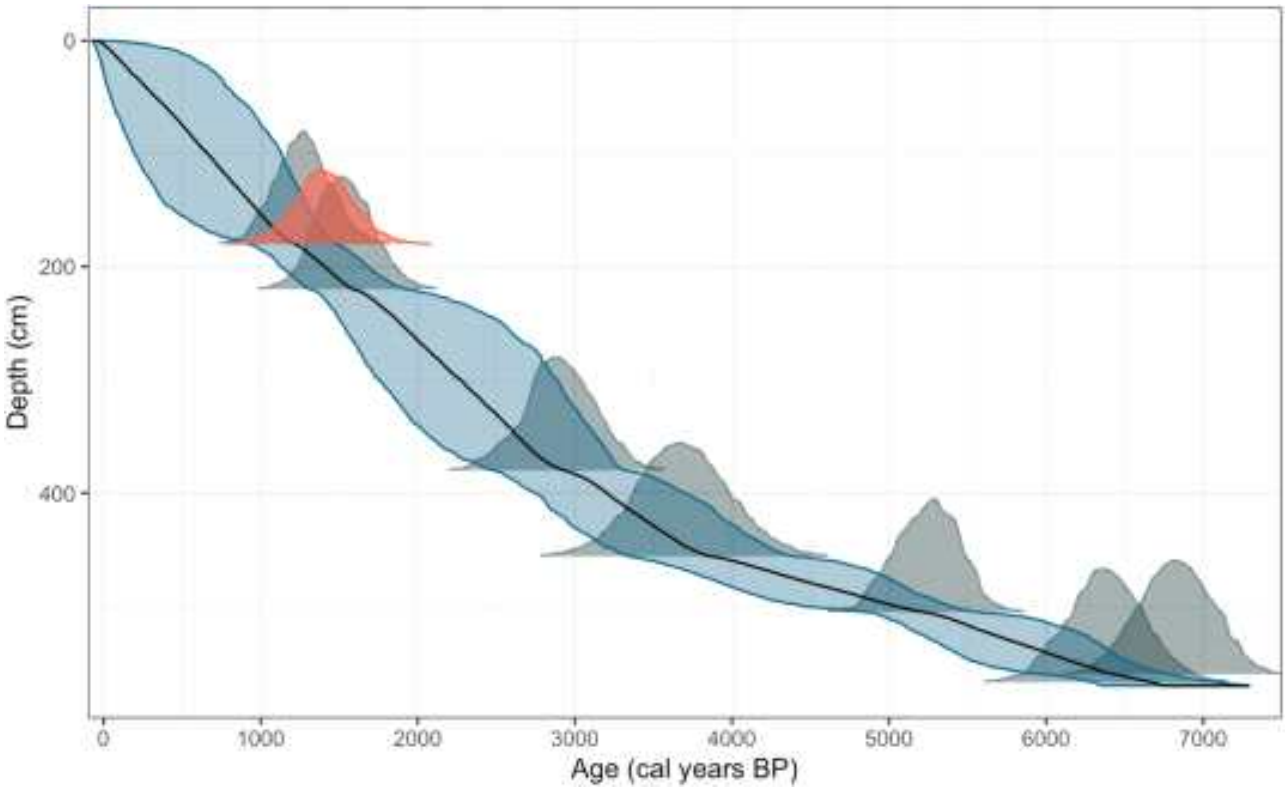


Figure 4. Calibrated age model for core RS15-GC57. Median age–depth relationship is in black, with 95th percentile range shaded in blue. Calibrated radiocarbon dates included in the age model are shown in grey. The date at 180 cm excluded from the final age-depth model is highlighted in red.

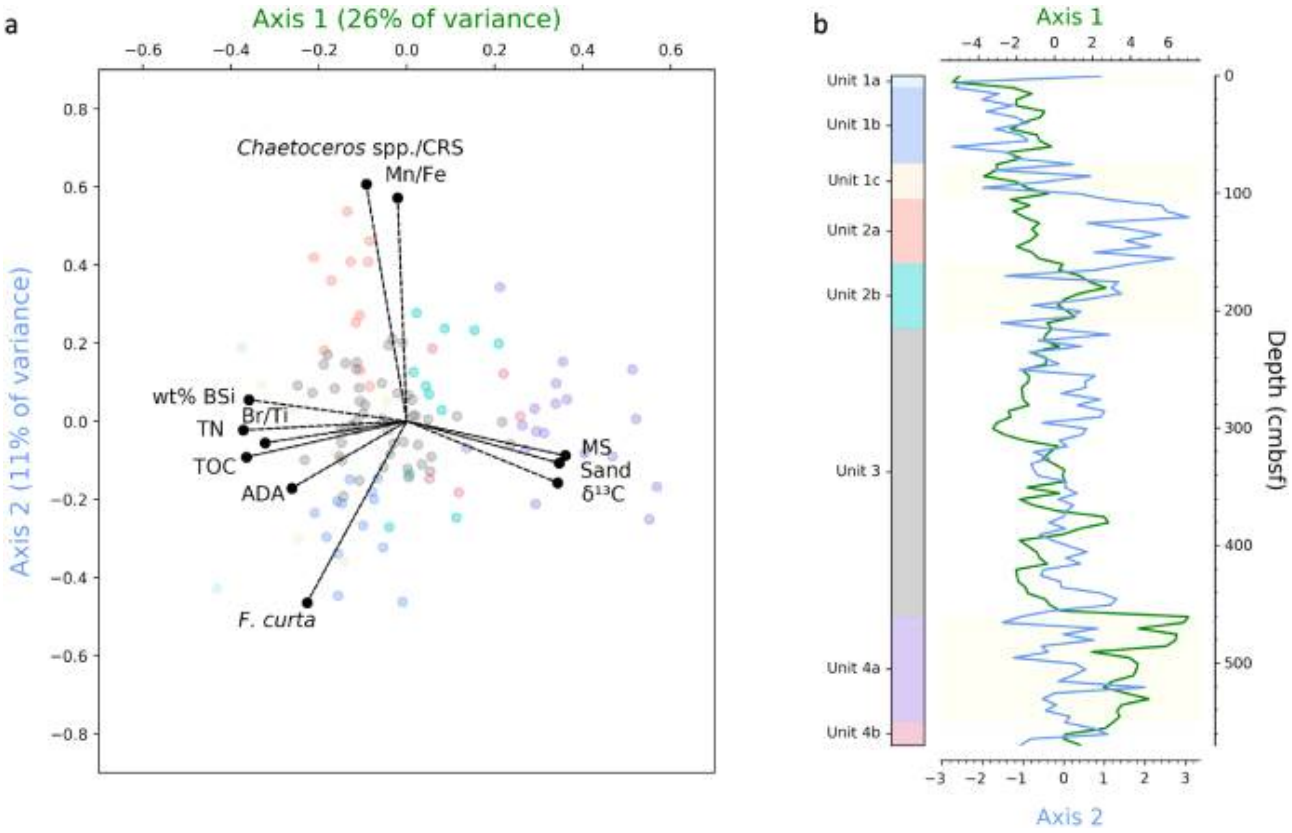


Figure 5. Principal Component Analysis (PCA) results from Robertson Bay environmental proxies. Axis 1 is dominated by proxies for terrigenous versus biogenic sedimentation, and axis 2 is dominated by proxies for sea ice, nutrient concentration, and polynya activity (see details in Table 4). a) Ordination bi-plot of variable loadings for the first two axes of the PCA; b) stratigraphic plot of component scores for Axes 1 and 2.

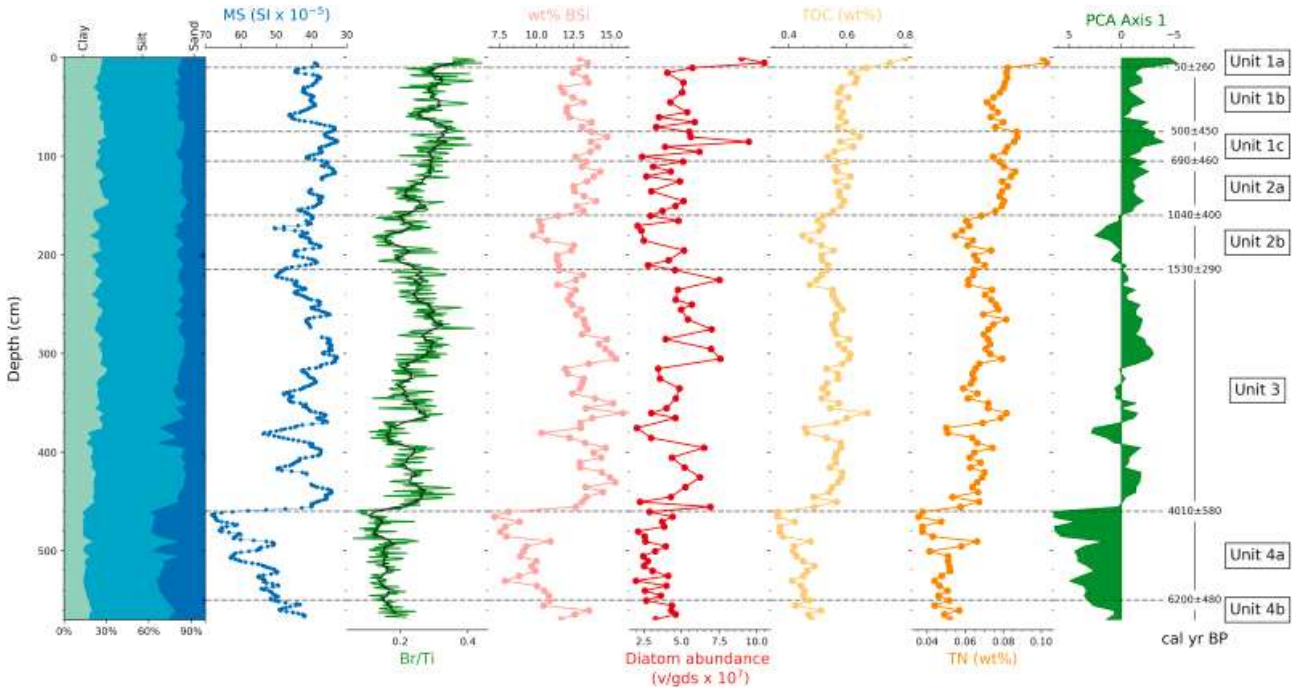


Figure 6. RS15-GC57 downcore profiles of proxies for terrigenous and biogenic sedimentation including grain size; magnetic susceptibility (MS; SI); bromine to titanium ratio (Br/Ti), weight percent biogenic silica (wt% BSi), absolute diatom abundance (ADA; valves per gram dry sediment), total organic carbon (TOC; %), total nitrogen (TN; %), and axis 1 of the PCA, which is dominated by variance in these proxies (Fig. 5). Dashed lines show boundaries between units and subunits identified based on the PCA with calibrated ages and uncertainties from the age-depth model.

KOPRI
극지연구소

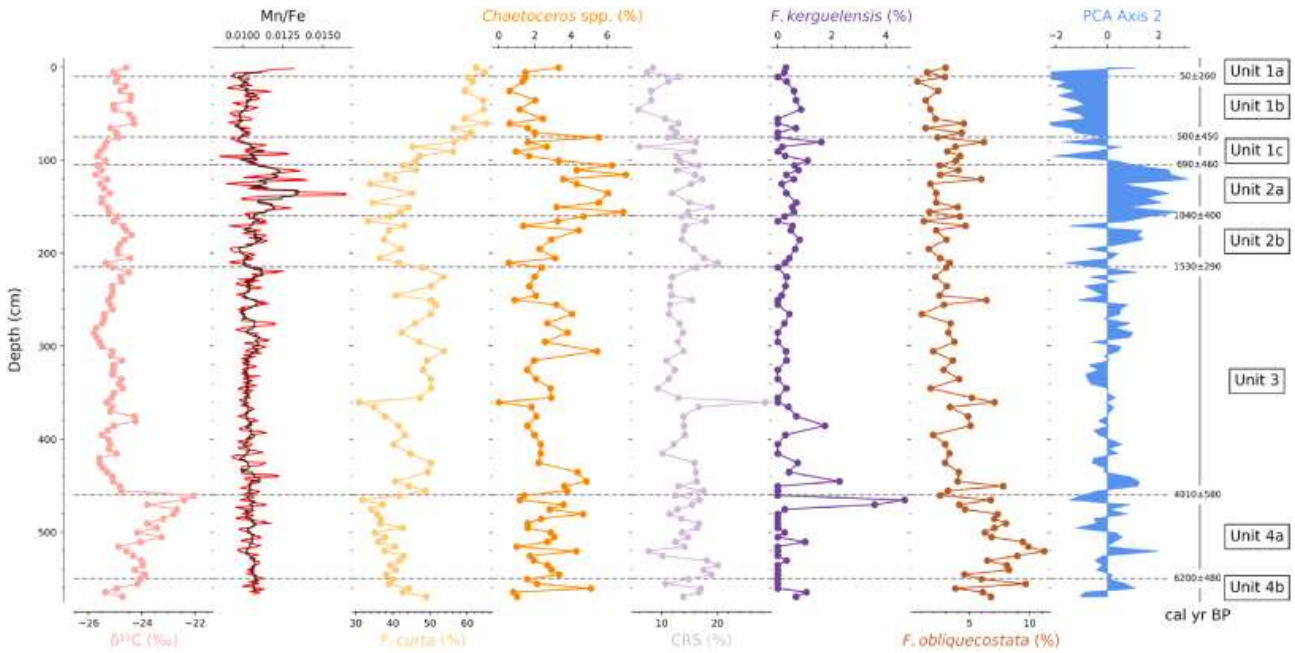


Figure. 7. RS15-GC57 downcore profiles of proxies for oceanographic and sea ice dynamics including stable isotopes of carbon (δ13C), manganese to iron ratio (Mn/Fe), the relative abundances of F. curta, Chaetoceros spp., Chaetoceros resting spores (CRS), F. kerguelensis, and F. obliquecostata, and axis 2 of the PCA, which is dominated by variance in F. curta, Chaetoceros spp., and CRS abundance and Mn/Fe ratio. Dashed lines show boundaries between units and subunits identified based on the PCA with calibrated ages and uncertainties from the age-depth model.

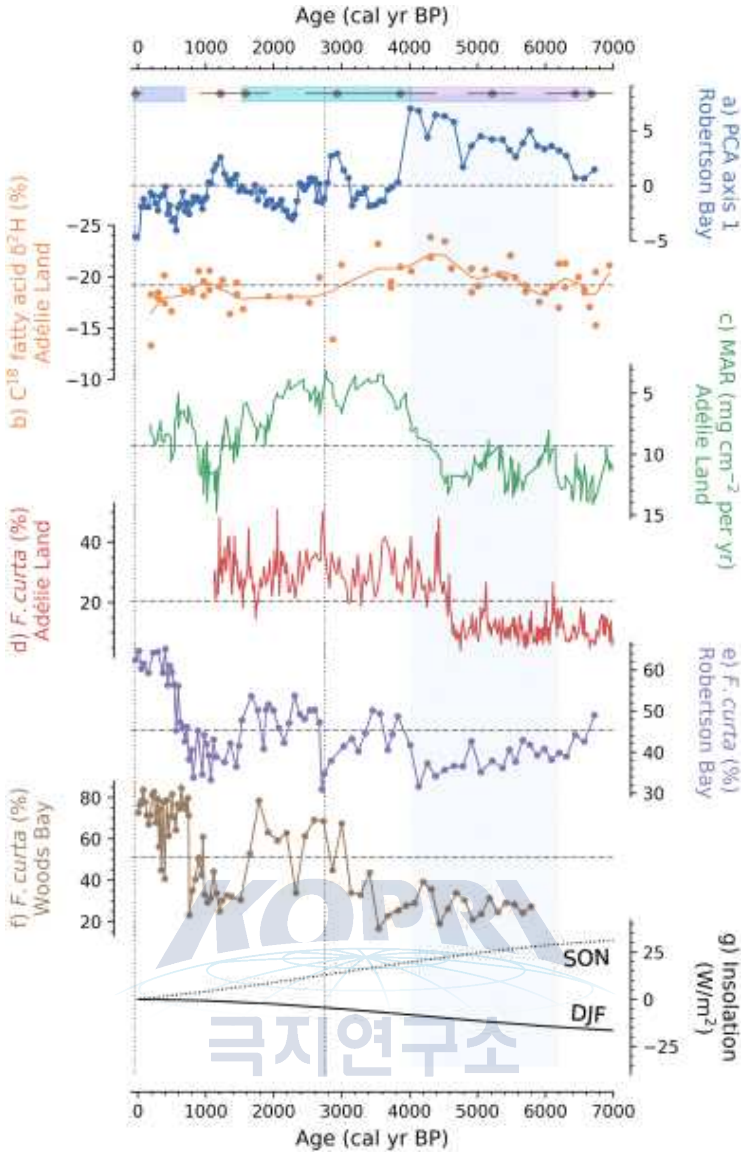


Figure. 8. Millennial-scale Holocene variability. Top circles show dated horizons in core RS15-GC57. Colored bars indicate the sedimentary units discussed in text (Unit 1 = blue; Unit 2 = beige; Unit 3 = teal; Unit 4 = purple). Dashed line indicates the Holocene average for the record. Inferred ice-capped conditions in inner Robertson Bay highlighted by the shaded blue bar between 6200 and 4000 cal yr BP; (a) PCA axis 1 (this study); (b) δ2H C18 fatty acid with locally weighted smoothing at Site U1357 in Adélie Land, East Antarctica (Ashley et al., 2021); (c) mass accumulation rates of biogenic material at Site U1357 in Adélie Land (Ashley et al., 2021); (d) relative abundance of F. curta from core MD03-2601 interpreted as a proxy for sea ice extent and duration in Adélie Land (Crosta et al., 2008; age model adapted in Ashley et al., 2021); (e) F. curta relative abundance from Robertson Bay (this study); (f) Relative abundance of F. curta from core WRS_WB interpreted as a proxy for sea ice extent and duration in the northwest Ross Sea (Mezgec et al., 2017). (g) insolation anomaly from 2000 CE at 71° S for September, October, and November (SON) and December, January, and Feburary (DJF) (Laskar et al., 2004). Dotted lines show time period highlighted in Fig. 9.

KOPRI 극지연구소

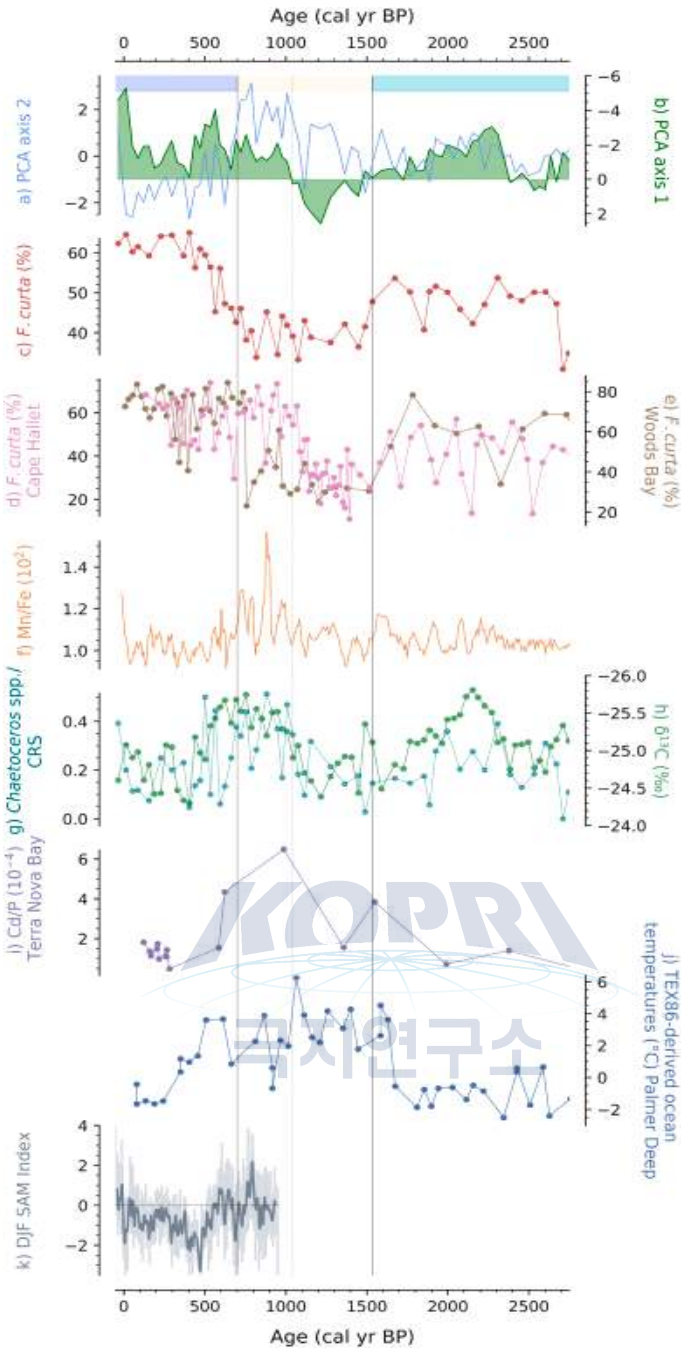


Figure. 9. Climate evolution during the late Holocene. Colored bars highlight the sedimentary units discussed in text (Unit 1 = blue; Unit 2 = beige; Unit 3 = teal). Dashed line shows Unit 2a and Unit 2b boundary. (a) PCA axis 1 (this study); (b) PCA axis 2 (this study); (c) F. curta relative abundance (this study); (d) F. curta relative abundance near Cape Hallet (Mezgec et al., 2017); (e) F. curta relative abundance in Woods Bay (Mezgec et al., 2017); (f) Mn/Fe ratio (this study); (g) Chaetoceros spp./CRS ratio (this study); (h) δ13C in Robertson Bay (this study); (i) Cd/P ratio in Terra Nova Bay, interpreted as increased nutrient supply and CDW upwelling (Xu et al., 2021); (j) TEX-86 derived ocean temperatures in the Palmer Deep, Antarctic Peninsula (Shevenell et al., 2011); and (k) reconstructed summer (DJF) SAM Index with 30-yr loess smoothing (dark grey), horizontal line shows average across the record (Dätwyler et al., 2018).

제 20 장

남극 로스해 보퍼트 섬 인근에서 고해양 환경변화 해석을 위한 규조 연구[13)]

박영숙[1], 이재일[2], 유규철[2], 김성한[2], 이민경[2]

[1]전북대학교

[2]한국해양과학기술원 부설 극지연구소

요약: 남극 로스해 보퍼트 섬 인근에서 획득한 코어퇴적물로부터 고환경변화를 복원하기위해 규조를 분석하였다. RS19-GC09코어로부터 총 27속 57종의 규조를 감정하였으며, 규조의 생산성을 나타내는 개체수 농도는 0.01-28.75×107/g 범위에 해당하였다. 규조의 수직분포 변화를 토대로 4개의 군집대를 설정하였다. 해빙종(Sea-ice species: TC); Fragilariopsis curta, Fragilariopsis linearis, Fragilariopsis obliquecostata, Fragilariopsis ritscheri와 Pseudo-nitzschia turgiduloides)와 공해종(Open water species: TW); Fragilariopsis kerguelensis, Thalassiosira lentiginosa, Thalassiosira antarctica와 Rhizosolenia styliformis)의 산출을 대자율(Magnetic Susceptibility; MS)과 총유기탄소(Total organic carbone; TOC)값과 비교하였다. 군집대 I은 낮은 TC, TW와 TOC를 보이고, 반대로 높은 MS 곡선을 나타내어 두꺼운 해빙 또는 빙붕 하부 환경에 해당하였다. 군집대 II는 높은 TC, 증가하는 TW와 TOC, 반대로 낮아지는 대자율을 나타내어 계절적인 해빙의 지속기간이 길고 분포가 확장되었다. 군집대 III은 감소된 TC, 높은 TW과 TOC, 가장 낮은 곡선의 MS를 보이는 구간으로 공해환경의 지속기간이 길었던 시기이다. 군집대 IV에서는 TC의 증가와 반대로 TW가 감소하며, TOC 값은 유의미한 변화를 보이지 않고, MS가 약간 상승하는 시기로서 다시 해빙의 지속기간이 길어졌음을 나타낸다.

1. 서론

남극 대륙은 지구 및 지역 순환, 기후, 해수면 조절에 근본적인 역할을 하며, 현재의 빙하 상태에서 남극 대륙은 남반구에서 위도에 따른 온도 구배를 증폭시켜 대기 순환을 향상시키고(Lemke et al., 1980; Flohn, 1984; Raphael, 2003), 강하고 차가운 바람을 생성하여 표면 수를 냉각하고 해빙 생산을 유지함으로써 남극 저층수의 형성에 기여하고 있다(Gordon, 2009; Riesselman and Dunbar, 2013). 남극 로스 빙붕은 세계에서 가장 큰 빙붕으로, 2000년에 북쪽 가장자리에서 30 km 너비의 빙하가 갈라졌음에도 불구하고, 로스 빙붕은 현재 평균 여름 기온이 약 -8℃이기 때문에 비교적 안정적인 상태를 유지하고 있다. 남극에서 빙하의 감소가 급속하게 나타나는 것은 대기와 해양의 순환이 변화하기 때문이며 남극 반도와 벨링스하우젠해, 아문젠해와 로스해 부근에서 온난화의 경향이 뚜렷하게 나타난다. 로스해는 대규모의 저층수가 형성되는 지역이기 때문에 로스 해 지역의 해빙의 분포 변화 및 해양학적 특성의 변화를

13) 이 연구 결과는 다음의 논문으로 출판되었음: 박영숙 외 (2025). "남극 로스해 보퍼트 섬 인근에서 고해양 환경변화 해석을 위한 규조 연구." 한국지구과학회지 46권 제2호, pp. 107-114.

연구하는 것이 전지구적 기후 변화에 대비하는데 있어 매우 중요한 데이터가 된다. 로스해는 전 지구적 기후 변화의 결과로 심층수의 형성 속도가 달라져 염분농도가 감소하고 있으며(Jacobs et al., 2002), 이는 서남극 빙상의 융빙과 해수 순환에 영향을 미치는 것으로 생각된다. 서부 로스 만은 이 지역의 지반선이 LGM 이후 약 1300 km 후퇴했기 때문에 해양 기반 서남극 빙상의 민감성을 이해하는 데 중요한 위치이며, 이 후퇴는 홀로세 내내 비교적 지속되었고 아직도 진행 중이다(Conway et al., 1999). 서남극반도에서 규조 군집은 s ea-ice, 영양염류 공급, 성층화 및 ice-mass의 변화를 알려 주기 때문에 종 조성에 대한 연구는 과거 온난기에 대한 기록을 가장 반영하고 있다. 따라서, 본 연구는 규조의 기록을 체계적으로 연구하여 로스 빙붕 인근 퇴적물에서 기후변화에 따른 해빙 및 빙상의 분포 변화를 파악하는 데 목적이 있다.

2. 연구 지역 및 연구 방법

2.1. 연구 지역

보퍼트 섬(Beaufort Island; 76° 57' S, 166° 55' E)은 로스해에 있는 거의 얼음과 눈으로 덮인 섬으로, 길이가 약 5 km, 너비가 2.5 km이고 가장 높은 지점 771m이다 (Seppelt et al., 1999; Fig. 1). 연구지역인 로스해의 해저 퇴적물은 생물학적 실리카와 인접 대륙으로부터 운반된 육지기원의 점토, 유빙에 의해 운반된 자갈 등이 섞여 있다. 로스해의 높은 생산성은 지역적인 대기-해양순환과 상호작용에 의해 유지되며, 특히 저위도에서 온 따뜻하고 영양분이 풍부한 남극순환류(Antarctic Circumpolar Current)가 로스 환류에 의해 순환심층수(Circumpolar Deep water)와 변형 순환심층수(Modified Circumpolar Deep Water)를 유입시켜 열과 영양분을 재공급 해준다(Zheng et al., 2023). 연구지역의 바깥쪽에 존재하는 로스 환류는 남극 순환류를 따라 이동하는 해수를 로스해 연안으로 전달하고 반대로 로스해 대륙붕 해양의 해수를 외해로 전달하는 역할을 하기 때문에 로스해 연안의 빙붕의 용융과 해수면 변동에 중요한 역할을 한다(Rignot et al., 2013; Rye et al., 2014; Yoon, 2022).

2.2. 연구방법

보퍼트 섬 인근에서 채취한 RS19-GC09 코어 퇴적물 (76° 57.7422′ S, 166° 23.0916′ E; water depth: 840 m, total core length: 3.39 m)로부터 규조 연구를 위해 10 cm 간격으로 총 34개의 시료를 분석하였다. 규조를 추출을 위한 실내 실험은 Bak and Lee (2017) 처리 방법을 사용하였으며, 규조의 정량분석을 위해서는 Scherer (1994)의 실험과 계산방법을 이용하였다. 각 층준으로 부터 건조 시료 2 g씩을 비이커에 담은후 묽은 염산(10%) 25 mL와 과산화수소수 25mL를 첨가한다. Hotplate 위에서 1시간 이상 가열한 후, 묽은 염산과 과산화수소수를 추가하여 끓인 후 24시간 동안 놓아 둔다. 증류수를 이용하여 세척한 침전물로부터 부표본을 채취하여 슬라이드가 장착된 침전장치에 넣고 50℃의 건조기 안에서 건조 시킨다. 건조된 슬라이드에 접착제를 이용하여 커버 글라스를 덮어 관찰 슬라이드를 완성한다. 규조의 관찰과 종감정을 위해서 Z eis s광 학현미경을 이용하여 200개 이상의 규조각을 산정하였으며, 개체수가 매우 빈약한 층준에서는 viewfield를 200개 이상 관찰하여 산정하였다. 중심 규조목은 중심부를 포함한 규조각의 2/3 이상이 보존되어 있을 경우 1개체로, 우상 규조목은 규조각이 1/2이상 남아있고 정축부가 나타나 감정이 가능하면 1개체로 산정하였다. 규조 절대 개체수 계산 방법은 다음과 같다.

Abundance=((A×B)/(C×D))/E (A= number of specimens counted; B=area of settling chamber; C=number of field of view in microscope; D=area o f field of v iew; E =mas s of s ample).

3. 결과 및 토의

RS19-GC09코어 퇴적물 총 34개로부터 규조를 감정한 결과 27속 57종이 감정되었으며, 정량분석의 결과 절대 개체수 농도가 0.01-28.75×10^7/g 범위로 나타났다, Fragilariopsis curta (32.3%)가 상대적으로 우세하게 산출되었으며, Thalassiosira antarctica (16.2%), Eucampia antarctica var. recta (8.4%), Fragilariopsis obliquecostata (6.7%)와 Fragilariopsis sublineata (5.7%) 등이 비교적 다량 산출되었다. 연구지역에서 재이동 규조라 할 수 있는 Stephanopxis turris는 180-200 cm, Paralia sulcata는 190 cm 이하 층준에서 산출된다.

3.1. 규조 군집대

연구 코어 RS19-GC09로부터 산출된 규조 종의 군집 분포 양상에 따라 4개의 군집대를 설정하였다 (Fig. 2).

3.1.1. 규조 군집대 I (330-190 cm)

규조 개체수 농도가 매우 낮은 구간으로 0.01-0.32×10^7/g에 해당된다. E. antarctica var. recta가 상대적으로 많이 나타나지만 전체적인 산출량이 매우 적다. A. actinochilus의 산출이 시작이 되며, F. curta, F. obliquecostata와 F. sublinearis도 나타난다.

3.1.2. 규조 군집대 II (190-130 cm)

규조 개체수 농도는 3.11-13.25×10^7/g에 해당되며, 군집대 I에서 보다 증가한다. F. curta, F. obliquecostata, F. sublinearis와 Pseudonitzschia turgiduloides의 산출이 증가하고, T. antarctica cold type의 산출도 증가한다. 이와 더불어, Chaetoceros RS의 산출도 증가한다.

3.1.3. 규조 군집대 III (130-70 cm)

규조 개체수 농도는 10.94-22.43×10^7/g에 해당되며, 군집대 II에서 보다 증가하는 경향을 보인다. 해빙종인 F. curta, F. obliquecostata, F. sublinearis와 P. turgiduloides의 산출이 약간 감소하며, T. antarctica (냉수종)의 산출은 군집대 II에서 보다 급증한다.

3.1.4. 규조 군집대 IV (70-0 cm)

규조 개체수 농도는 16.32-28.75×10^7/g로 전기간에 걸쳐 가장 높은 구간이다 F. kerguelensis의 산출이 가장 높게 나타나며, F. curta의 산출이 다시 증가하고 A. actinochilus와 E. antarctica var. recta의 산출도 증가한다. 군집대 III에서 풍부하게 나타났던 T. antarctica (냉수종)의 산출은 감소한다.

4. 고환경 및 토의

RS19-GC09코어 퇴적물의 퇴적상은 317-330 cm 구간에서는 olive gray mud, 251-317 cm에

서는 이질 다이아믹톤(muddy diamicton), 208-251 cm에서는 다시 olive gray mud, 204-208 cm에서 gravelly sand, 197-204 cm에서는 생교란 니질퇴적체(bioturbated mud), 180-197 cm에서 bluish gray mud, 180 cm 이상의 층준에서는 생교란 규질 점토(bioturbated diatom mud) 로 구성되어 있다. RS19-GC09에서 산출되는 시대 지시종으로는 Proboscia barboi (LAD: 1.6-1.73Ma), Thalassiosira vulnifica (LAD: 2.15-2.19 Ma), Thalassiosira inura (LAD: 2.53-2.55Ma)와 Denticulopsis lauta (LAD: 12.46-13.73 Ma) 등이 산출되었으며(Cody et al., 2008), 이들의 산출은 190 cm 이하의 층준에서 나타났다 (Fig. 3). 앞에서 언급된 바와 같이, 190 cm 이하의 층준은 이질 다이아믹톤(muddy diamicton)과 gravelly sand층준을 포함하여 전반적으로 gray mud로 구성되어 있고 이러한 퇴적물에서의 규조 산출은 미약하다.

군집대 I (330-190 cm)에서 시대 지시종의 대부분이 산출 되고 있으며, 이들의 시기가 Miocene에서 Pleistocene에 해당되는 것으로 연구지역의 퇴적 시기를 반영하는 것으로 볼 수 없다. 왜냐하면, 이 시기는 규조의 산출이 매우 적고, 대자율(MS)값이 높게 나타나는 것으로 보아 일차생산성이 낮으면서, 후퇴하는 grounded ice로부터 육원성 퇴적물들이 공급된 것으로 보이며 생물학적 파편들도 희석된 것으로 생각된다. 또한, 과거에 연안 및 내대륙붕에서 퇴적된 Paralia sulcata의 산출도 이때 유입된 것으로 생각된다(Fig. 3). 퇴적물에서 Paralia sulcata의 높은 생산성은 약 3℃ 이상의 간빙기와 관련이 있으며(Krzywinski and Stabell, 1984; Roelofs, 1984; Zong, 1997), Marian Cove지역에서는 빙하의 후퇴를 지시하는 것으로 알려져 있다(Ha et al., 2019). 각이 단단하여 쉽게 가라앉고 용해에 비교적 강하여 빙하 운반에서도 보존이 용이하기 때문에 Ross Sea에서는제3기 지층으로부터 재이동 되었음을 지시해준다(Sjunneskog and Scherer, 2005). 따라서, 시대 지시종들은 재이동 되었음이 확실하며, 이와 더불어 이 시기에 공해종(TW)과 해빙종(TC)의 산출, 총유기탄소 (TOC)및 규조 개체수 농도가 매우 낮기 때문에 군집대 I이 퇴적될 당시 연구지역이 빙상의 지면(grounded ice sheet)와 근접해 두꺼운 얼음(해빙 또는 빙붕)으로 덮여 있었던 환경이었음을 나타낸다(Fig. 4).

군집대 II (190-130 cm)에서는 대자율 값이 서서히 감소하고, 총유기탄소값이 증가하기 시작한다(Fig. 4). 규조의 공해종과 해빙종의 산출 및 규조 개체수 농도가 증가하는 경향을 보이며, 이러한 자료는 군집대 I에서 나타났던 빙하 환경에서 빙하 융빙수(Ice melt water)가 수반된 계절적인 해빙 환경으로 변화하였음을 나타낸다. 또한, 이시기에 산출되기 시작하는 P. inermis는 따뜻하고 빈영양수의 유입(Stickley et al. 2005)과 계절적인 해빙대(Maddison et al. 2006)와 관계된 종이다. 따라서, 이 시기는 따뜻한 해수가 유입이 되는 계절적인 해빙환경으로 나타난다.

Terra Nova Bay 지역에서는 7-12.1 ka 사이에 deglaciation이 일어났다고 제안되었으며(Baroni and Orombelli, 1991; 1994), Licht et al. (1996)의 연구에 의하면 규조의 개체수 농도가 급격히 증가하고 총유기탄소 비율도 증가하는 것은 상관관계가 있으며, 이러한 생물 기원 생산의 변화는 빙하 하부 다이아믹톤에서 해양 점토로 변화하는 것과도 관계가 있다고 하였다. 로스섬 근처 코어에서 해양 점토에 대한 연대 측정한 결과는 빙상이 약 7 ka 전에 현재의 위치로 후퇴했다고 보고 되었다.

아문젠 해와 Wilkes Land 지역에 분포하는 빙상의 지면 경계(grounding line)은 홀로세가 시작될 무렵부터 자리 잡았지만(Hillenbrand et al., 2013; Mackintosh et al., 2014), Ross Sea에서는 빙하의 후퇴가 계속되는 것으로 보이며 8.6Ka BP전에 R os s Is land 근처에서 처음으로 open marine의 증거가 나타났다고 보고되어 있다(Mckay et al., 2015). 따라서, 규조 개체수 농도와 총유기탄소의 양이 급증하는 군집대 II의 시작 시기를 기존 연구결과와 대비해 볼 때 최소한 8.6 Ka BP전에 퇴적이 시작된 것으로 볼 수 있다. 그러나, 정확한 퇴적시기를 알기 위해서는 연대측정을 위한 연구가 수행되어야 한다.

군집대 III (130-70 cm)에서는 대자율값(MS)이 군 집대 II에서 보다 아주 약간 감소하는 경향을

보이며, 총 유기탄소값(TOC)은 좀 더 증가하는 경향을 보인다(Fig. 4). 해빙종 (TC)의 산출이 군집대 II에서 보다 감소하는 반면 공해종(TW)의 산출은 증가한다. 규조 개체수의 농도도 군집대 II에서보다 증가하는 경향을 나타낸다. 연간 해빙 면적이 9-11m/년이면서 여름철 해수 온도가 -1.3-2.5℃ 인 지역에서 풍부하게 나타나는 F. curta (Armand et al., 2005)가 감소하다가 증가하는 경향을 보이고, 긴 광주기 환경(Long photoperiod environment)의 천해(shallow water)에 분포한 얼음 가장자리(ice-edge)근처에서 풍부한 P. turgiduloides (Almandoz et al., 2008)의 산출이 감소하면서 차가운 해수가 있는 해빙의 가장자리 근처에 공해 환경이 존재 한다는 것을 지시해주는 종인 T.antarctica (Barbara et al., 2016) 의 냉수종의 산출이 증가한다. 따라서, 이 시기는 군집대 II 시기보다 좀 더 온난한 환경으로, 계절적인 해빙(Sea-ice) 환경에 놓여 있었으며 이전 시기에 비해 공해(open water) 환경의 지속 기간이 더 길어진 것으로 보인다.

군집대 IV (70-0cm)에서는 대자율(MS)값이 상부로 갈수록 약간 증가하는 경향을 보이고 총유기탄소 (TOC) 값은 군집대 III와 비슷하지만 대자율 값과 마찬가지로 상부에서 미약한 증가를 보인다(Fig. 4). 해빙종의 산출은 군집대 III에서 보다 증가하여 군집대 II와 비슷하게 나타나며, 이와 반대로 공해종의 경우는 군집대 III에서 보다 감소하여 군집대 II와 비슷하게 나타나나 상부에서는 약간 감소한다. 규조의 절대 개체수는 상대적으로 가장 높은 구간이다. 따라서, 이시기는 군집대 III시기보다는 더 추운 환경이었음을 나타낸다.

5. 결 론

로스해 보퍼트 섬(Beaufort island) 인근에서 채취한 RS19-GC09 퇴적물로부터 규조를 분석하여 퇴적 시기동안의 해빙의 분포 변화 기록을 획득하였다. 규조의 일차 생산성은 0.01-28.75×10^7/g의 범위로 군집대 I에서의 생산성이 매우 낮고 군집대 IV의 생산성이 높아 폭이 매우 넓다. 코어 퇴적물 총 34개로부터 감정된 규조 27속 57종 중에서 해빙과 밀접한 관계가 있는 Fragilariopsis curta, F. obliquecostata, F. sublineata와 Pseudo-nitzschia turgiduloides, 공해환경을 지시해 주는 F. kerguelensis, Proboscia inermis와 Thalassiosira antarctica등을 이용하여 4개의 군집대를 설정하였다(Armand et al., 2005; Crosta et al.,2005). 군집대 I은 grounded ice sheet와 인접한 두꺼운 해빙환경 또는 빙붕 하부 환경에서 퇴적되었으며, 군집대 II는 군집대 I보다 따뜻한 시기이지만 해빙의 분포와 지속기간이 공해환경 지속기간보다 더 길게 나타나는 시기이다. 군집대 III은 퇴적 기간 중 가장 온난하여 공해환경의 지속기간이 길어진 시기였고, 군집대 IV는 다시 해빙이 확장하는 시기였던 것으로 나타났다. 이들의 정확한 퇴적시기를 알기 위해서는 연대 측정이 필수 적이나, Ross Sea에서 빙상 후퇴의 연구 결과(Mckay et al., 2015)와 비교해 볼 때 약 8.6 cal. Kyr B.P.전까지는 빙상으로 덮혀 있었을 것 으로 생각된다.

참고문헌

Almandoz, G., Ferreyra, G., Schloss, I.R., Dogliotti, A.I., Rupolo, V., Paparazzo, F.E., Esteves, J.L. and Ferrario, M.E., 2008, Distribution and ecology of Pseudonitzschia species (Bacillariophyceae) in surface waters of the Weddell Sea (Antarctica). Polar Biology, 31, 429-442.

Armand, L.K., Crosta, X., Romero, O., and Pichon, J.J., 2005, The biogeography of major diatom taxa in Southern Ocean sediments: 1. Sea ice related species. Palaeogeography Palaeoclimatology Palaeoecology, 223, 93-126.

Bak, Y.S. and Lee, Y.U., 2017, Late Quaternary Paleoclimatic change in the Ulleung Basin, East Sea, Korea. Acta Geologica Sinica, 91, 263-269.

Barbara, L., Crosta, X., Leventer, A., Schmidt, S., Etourneau, J., Domack, E. and Massé, G., 2016, Environmental responses of the Northeast Antarctic Peninsula to the Holocene climate variability. Paleoceanography, 31, 131-147.

Baroni, C. and Orombelli, G., 1991, Holocene raised beaches at Terra Nova Bay, Victoria Land, Antarctica. Quaternary Research, 36, 157-177.

Baroni, C. and Orombelli, G., 1994, Holocene glacier variations in the Terra Nova Bay area (Victoria Land, Antarctica). Antarctic Science, 6(4), 497-505.

Crosta, X., Romero, O., Armand, L.K., and Pichon, J.-J., 2005, The biogeography of major diatom taxa in Southern Ocean sediments: 2. Open-ocean related species. Palaeogeography Palaeoclimatology Palaeoecology, 223, 66-92.

Cody, R.D., Levy, R.H., Harwood, D.M., and Sadler, P.M., 2008, Thinking outside the zone: high-resolution quantitative biochronology for the Antarctic Neogene. Palaeogeography Palaeoclimatology Palaeoecology, 260, 92-121.

Conway, H., B.L. Hall, G.H. Denton, A.M. Gades and E.D. Waddington, 1999, Past and future grounding-line retreat of the West Antarctic Ice Sheet. Science, 286, 280-283.

Flohn, H., 1984, Climate evolution in the Southern hemisphere and the equatorial region during the late Cenozoic. In: Vogel, J.C. (Ed.), Late Cainozoic Paleoclimates of the Southern Hemisphere, pp. 5-20.

Gordon, A., 2009. Bottom water formation. In: Steele, J.H., Thorpe, S.A., Turekian, K.K. (Eds.), Ocean Currents: a Derivative of the Encyclopedia of Ocean Sciences. Academic Press, pp. 263-269

Ha, S.-Y., Ahn, I.-Y., Moon, H.-W., Choi, B., and Shin, K.-H., 2019, Tight trophic association between benthic diatom blooms and shallow-water megabenthic communities in a rapidly deglaciated Antarctic fjord. Estuarine, Coastal and Shelf Science, 218, 258-267.

Hillenbrand, C.-D., et al., 2013, Grounding-line retreat of the West Antarctic Ice Sheet from inner Pine Island Bay: Geology, v. 41, p. 35-38, doi:10.1130 /G33469.1.

Jacobs, S.S., Giulivi, C.F., and Mele, P.A., 2002, Freshening of the Ross Sea during the late 20th century. Science, 297(5580), 386-389.

Krzywinski, K. and Stabell, B., 1984, Late Weichselian sea level changes at Sotra, Hordaland,

western Norway. Boreas, 13, 159-202.

Lemke, P.E., Trinki, E.W. and Hasselman, K., 1980, Stochastic dynamic analysis of polar sea ice variability. Journal of Physical Oceanography, 97, 2100-2120.

Licht, K.J., Jennings, A.E., Andrews, J.T., and Williams, K.M., 1996, Chronology of late Wisconsin ice retreat from the western Ross Sea, Antarctica. Geology, 24(3), 223-26.

Maddison, E.J., Pike, J., Leventer, A., Dunbar, R.,Brachfeld, S., Domack, E.W., Manley, P. and McClennen, C., 2006, Post-glacial seasonal diatom record of the Mertz Glacier Polynya, East Antarctica. Marine Micropaleontology, 60, 66-88.

Mackintosh, A.N., et al., 2014, Retreat history of the East Antarctic Ice Sheet since the Last Glacial Maximum: Quaternary Science Reviews, 100, 10-30, doi: 10.1016/ j.quascirev.2013.07.024.

McKay, R., Golledge1, N.R., Maas, S., Naish, T., Levy, R., Dunbar, G. and Kuhn, G. 2015, Antarctic marine icesheet retreat in the Ross Sea during the early Holocene. Geology, doi: 10.1130/G37315.1.

Raphael, M.N., 2003, Impact of observed sea-ice concentration on the Southern Hemisphere extratropical atmospheric circulation in summer. Journal of Geophysical Research 108 (D22), ACL1.1-ACL1.11.

Riesselman C.R. and Dunbar, R.B., 2013, Diatom evidence for the onset of Pliocene cooling from AND-1B, McMurdo Sound, Antarctica. Palaeogeography, Palaeoclimatology, Palaeoecology, 369, 136-153.

Rignot, E., Jacobs, S.S., Mouginot, J. and Scheuchl, B., 2013, Ice-shelf melting around Antarctica. Science, 341(6143), 266-270.

Roelofs, A.K., 1984, Distributional patterns and variation of valve diameter of Paralia sulcata in surface sediments of southern British Columbia InletsEstuarine, Coastal and Shelf Science, 18, 165-176.

Rye, C.D., Naveira Garabato, A.C., Holland, P.R., Meredith, M.P., Nurser, A.J.G., Hughes, C.W., Coward, A.C. and Webb, D.J., 2014, Rapid sea-level rise along the Antarctic margins in response to increased glacial discharge. Nature Geoscience, 7(10), 732-735.

Scherer, R.P., 1994, A new method for the determination of absolute abundance of diatoms and other silt-sized sedimentary particles. Journal of Paleolimnology, 12, 171-179.

Sjunneskog C.M. and Scherer R.P., 2005, Mixed Diatom Assemblages in Ross Sea (Antarctica) Glacigenic Facies. Palaeogeography Palaeoclimate Palaeoecology, 218, 287-300.

Sppelt, R.D., Green, T.G.A. and Skotnicki, M., 1999, Notes on the Flora, Vertebrate Fauna and Biological Significance of Beaufort Island, Ross Sea, Antarctica. Polarforschung, 66 (1/2), 53-59.

Stickley, C.E., Pike, J., Leventer, A., Dunbar, R., Domack, E.W., Brachfeld, S., Manley, P. and McClennan, C., 2005, Deglacial ocean and climate seasonality in laminated diatom sediments, Mac.Robertson Shelf, Antarctica. Palaeogeography Palaeoclimatology Palaeoecology,

227, 290-310.

KOPRI 극지연구소

Yoon, S.-T., 2022, Responses of the Ross Sea to the Climate Change: Importance of observations in the Ross Sea, Antarctica. Ocean and Polar Research, 44(1), 69-82.

Yoon, S.T., 2022, Responses of the Ross Sea to the Climate Change: Importance of observations in the Ross Sea, Antarctica. Ocean and Polar Research, 44(1), 69-82.

Zheng, Z., Jin, J., Nie, Y., Hao, J., Xue, Y., Liu, C., Chen, Y., Emslie, S.D. and Liu, X., 2023, Historical population changes of Ad´elie penguins in the Ross Sea region, Antarctica, and its climatic forcings. Quaternary Science Reviews ,318, 108308.

Zong, Y., 1997, Implications of Paralia sulcata abundance in Scottish isolation basins. Diatom Research, 12, 125- 150.

KOPRI
극지연구소

Diatom Research to Interpretation of Paleoenvironmental Changes in Beaufort Island, Ross Sea, Antarctica

Young-Suk Bag[1], Jae Il Lee[2], Kyu-Cheul Yoo[2], Sunghan Kim[2], Min Kyung Lee[2]

[1]Jeonbuk National University

[2]Korea Polar Research Institute

Abstract: Diatoms were analyzed to determine paleoenvironmental changes in core sediments obtained near Beaufort Island in the Ross Sea. A total of 57 species belonging to 27 genera were identified from the RS19-GC09, and the number of diatom valve abundance ranged from 0.01 to 28.75×107/g. Four assemblage zones were established based on the vertical distribution curves of diatom. The occurrence of sea ice species (TC; Fragilariopsis curta, F. linearis, F. obliquecostata, F. ritscheri, and Pseudo-nitzschia turgiduloides) and open water species (TW; F. kerguelensis, Thalassiosira lentiginosa, T. antarctica, and Rhizosolenia styliformis) was compared with magnetic susceptibility (MS) and total organic carbon (TOC) values. Diatom assemblage zone I showed a high MS curve, contrary to low TC, TW, and TOC corresponding to heavy sea-ice or sub-ice shelf conditions. Diatom assemblage zone II showed high TC, increasing TW and TOC values, and conversely, decreasing MS values indicating a long duration of seasonal sea-ice and an expanded distribution. Diatom assemblage zone III showed decreased TC, high TW and TOC, and the lowest MS curve, indicating a long period in an open water environment. Diatom assemblage zone IV showed a period of decreasing TW, conversely increasing TC, no noticeable change in TOC, and slightly increasing MS, again indicating a period of long sea-ice duration.

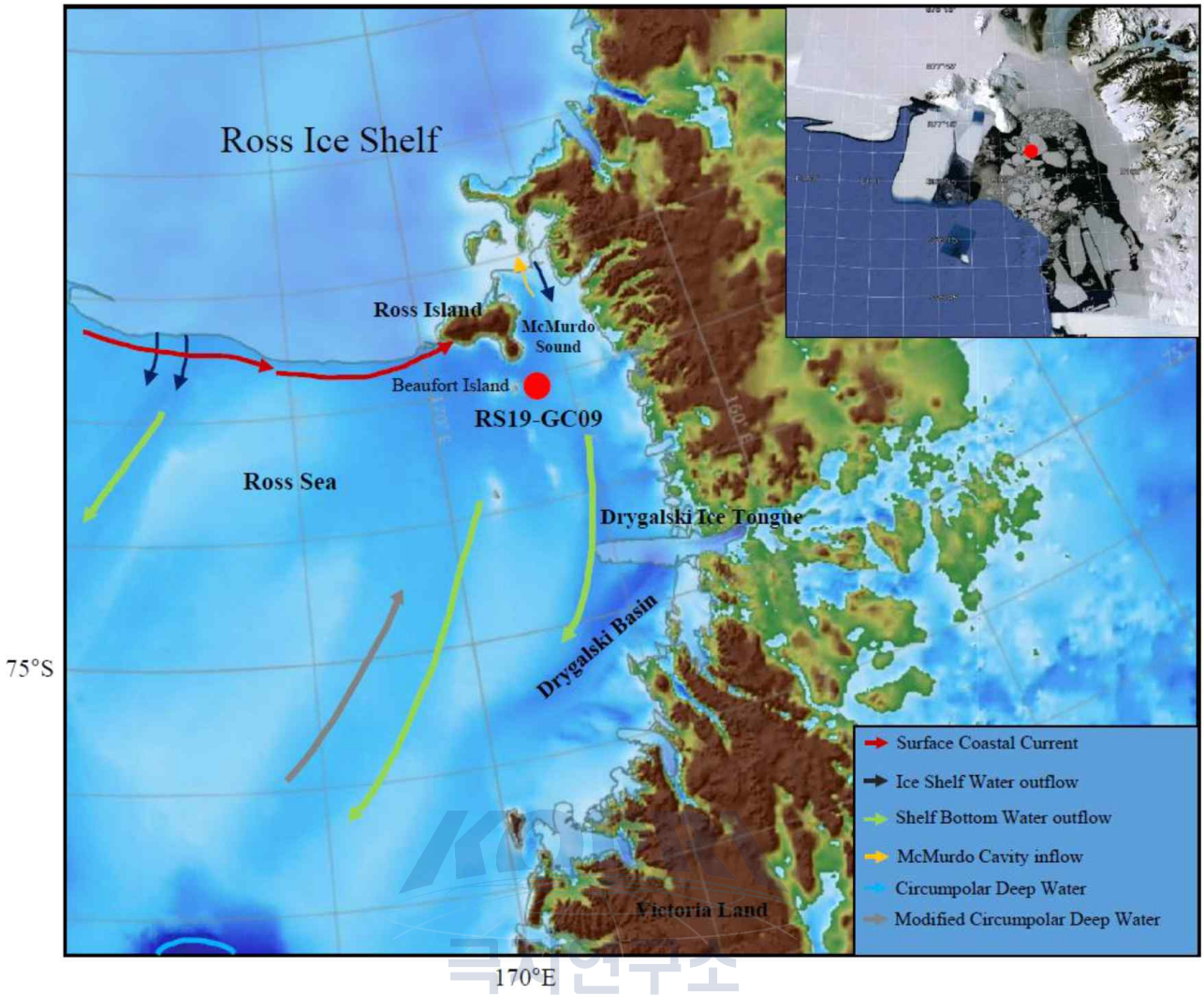


Figure 1. Location map of RS19-GC09 sediments with schematic ocean circulation (modified from Zheng et al., 2023).

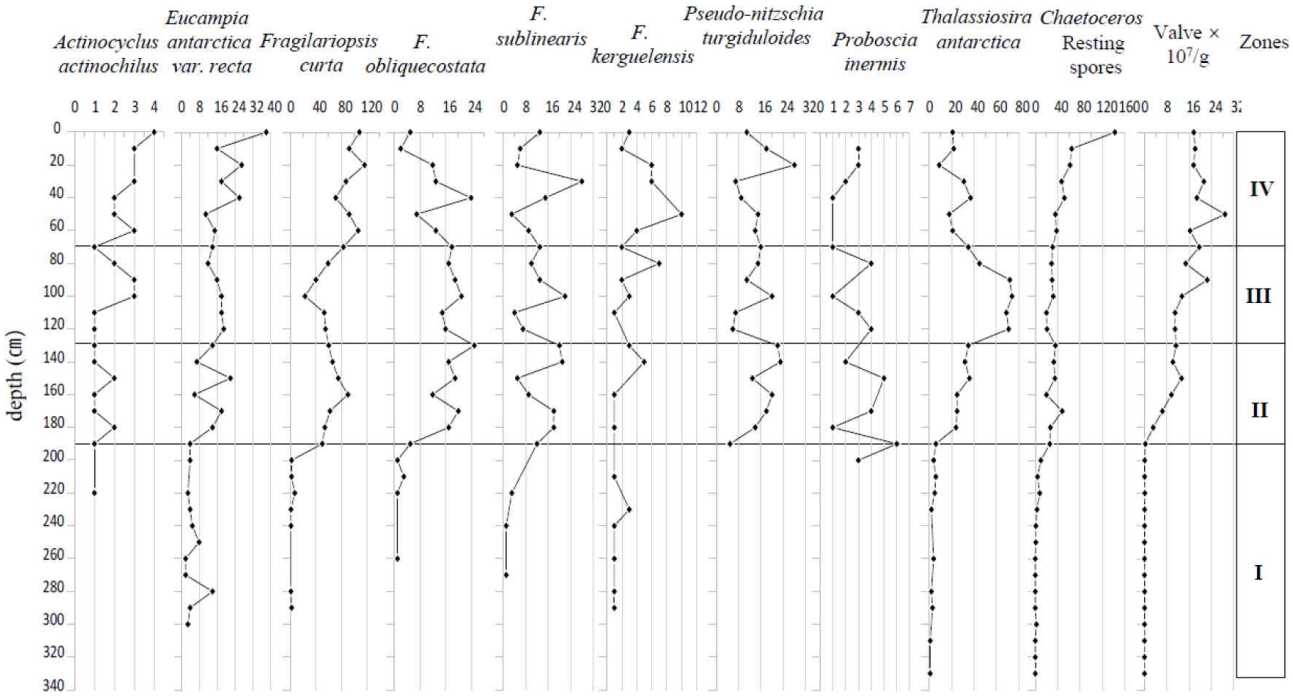


Figure 2. Down-core variations of relative abundance of the selected species and diatom assemblage zones from RS19-GC09.

KOPRI
극지연구소

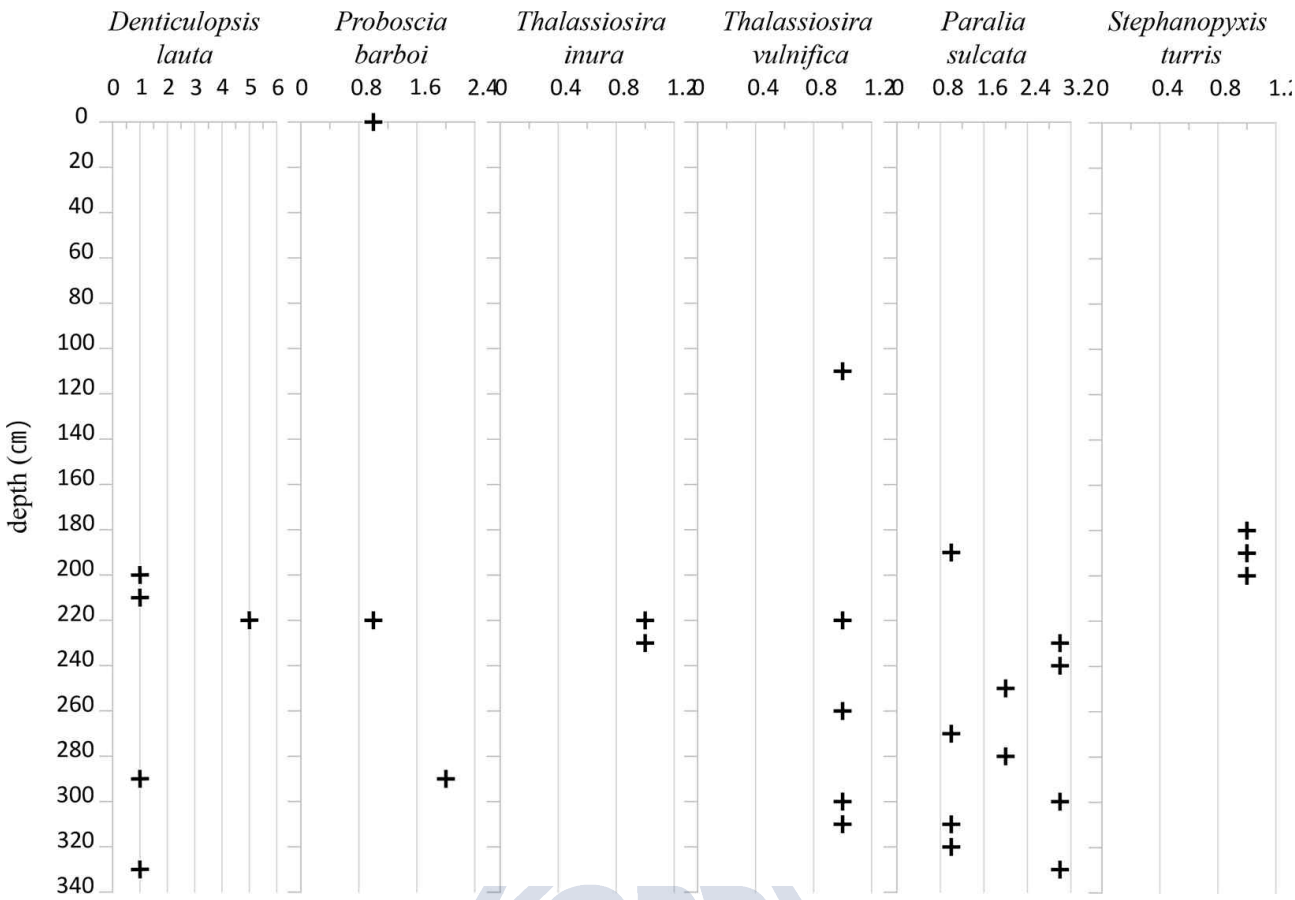


Figure 3. Distribution of reworked species from RS19-GC09.

KOPRI
극지연구소

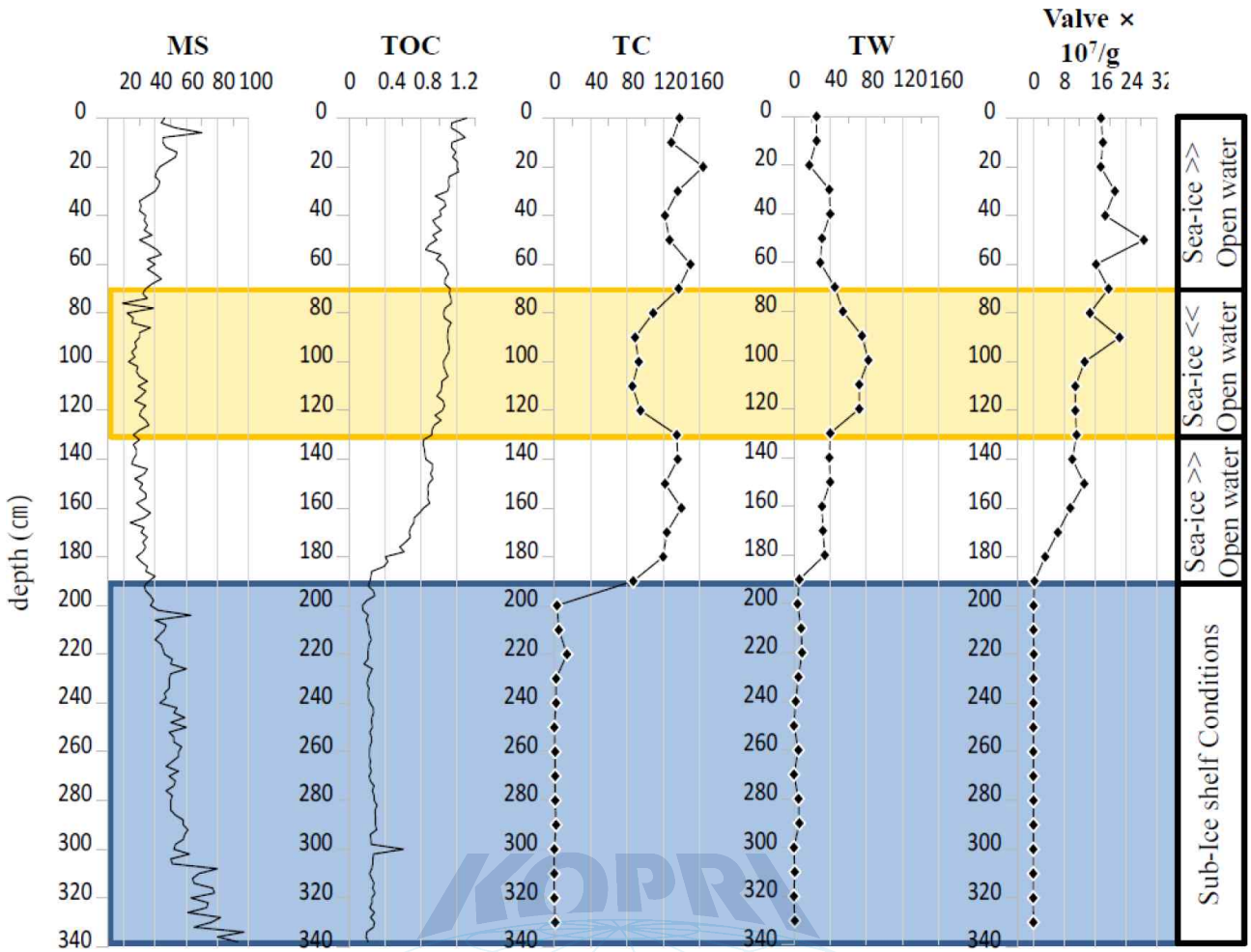


Figure 4. RS19-GC09 downcore curves of Magnetic susceptibility, TOC concentration, TC (Sea-ice species), TW (open water species) and total diatom abundance (X10^7/g).

KOPRI
극지연구소

제 21 장

남극 아문젠해에서 규조 군집을 이용한 고환경 변화 기록

14)

박영숙[1], 김성한[2], 유규철[2], 이재일[2], 이민경[2], 하상범[2]

[1]전북대학교

[2]한국해양과학기술원 부설 극지연구소

초록: 남극 아문젠해 만내 Getz ‘A’ Ice Shelf 인근에서 획득한 AM22-GC10B로부터 과거 빙붕의 분포 변화를 알아보기 위해 규조를 분석하였다. 총 22속 50종의 규조가 동정되었으며, 규조 개체수 농도는 0.5~8.3×107/g의 범위에 해당하였다. 규조 군집의 해빙종과 공해종의 분포 양상, 대자율값을 분석하여 총 3개의 군집대를 설정하였고, 이는 과거 환경 변화를 뚜렷하게 보여준다. 군집대 I 은 규조 산출이 거의 없고 대자율 값이 높게 나타나는 특징을 보이며, 이는 빙하하부에서 형성된 환경을 지시한다. 군집대 II는 규조류 개체수가 증가하고 대자율 값이 감소하는 경향을 나타내며, 이는 빙하하부 환경에서 벗어나 계절적으로 해빙이 없는 해양 환경으로 전이되는 빙해양 환경을 지시한다. 군집대 III에서는 개체수와 휴면포자(Chaetoceros resting spores)의 수가 뚜렷하게 증가하고 해빙종의 산출이 감소하는 반면 공해종의 산출이 증가하는 양상을 보이는 것은 계절적으로 해빙이 사라진 환경에서 퇴적된 것으로 해석된다.

1. 서론

아문젠해 만(ASE: Amundsen Sea Embayment)은 서남극 빙상의 약 35%를 배수하며 남극 빙상/빙붕 중 가장 빠르게 감소하는 지역 중 하나이며, 지난 20년 동안 아문젠해 만(예: 파인 아일랜드(Pine Island)와 스웨이츠(Thwaites)) 의 빙하 표면 고도가 3.5~5.5 ma-1만큼 감소했다(Shepherd et al., 2004; Scott et al., 2009). 서남극 빙상은 최대 3.3 m의 잠재적 해수면 상승의 가능성을 가지고 있으며(Bamber et al., 2009), 남극 주변에서 가장 빠르게 얇아지는 빙붕을 포함하고 있다(Pritchard et al., 2012). 이러한 얇아짐과 관련된 빙하 융빙수(glacial meltwater; MW)의 가장 큰 공급원 중 하나는 아문젠해 만(ASE)이다. 1996년부터 2006년 사이에 서남극에서 아문젠해와 벨링스하우젠해(Bellingshausen Sea)의 연안을 따라 얼음 질량(ice mass)의 손실이 59% 정도 증가하였으며(Rignot et al., 2008), 아문젠해 지역에서 감소된 ice mass의 총량은 81±17 km3/년으로 나타났다(Rignot et al., 2004). 빙하가 얇아지고 후퇴의 속도는 가속되었으며, 서남극빙상(West Antarctic Ice Sheet, WAIS)의 안정성에 중요한 변화를 일으키고 있다(Joughin and Alley, 2011;Konfirst et al., 2012). 이러한 현상은 따뜻한 환극 심층수(Circumpolar Deep Water)에 의한 기저빙하 용융에 많은 영향을 미친다. 이 지역에 분포하는 파인 아일

14) 이 연구 결과는 다음의 논문으로 출판되었음: 박영숙 외 (2025). "남극 아문젠해에서 규조 군집을 이용한 고환경 변화 기록." 지질학회지 61권 제3호, pp. 263-270.

랜드 빙상은 서남극빙상의 유출을 억제하는 버팀목 역할을 해주고 있으나 현재의 유출 속도를 볼 때, 약 100년 이내에 안정성을 잃고 해수면을 3.3-5 m 상승시키게 할 수 있다고 보고되었다 (Vaughan, 2008; Bamber et al., 2009). Pattyn과 Morlighem (2020)의 연구에서는 남극 빙상의 일부 지역은 빙하 기후 시스템의 강력한 긍정 피드백(positive feedbacks)으로 인해 현재 관측되는 것보다 더 빠른 해수면 상승으로 이어질 가능성이 있다고 하였다. Hillenbrand et al. (2010)은 아문젠해 만에서 채취한 5개의 코어퇴적물을 연구 한 결과, 빙하 하부의 접지선에 인접한(grounding-line proximal facies) 퇴적상 위에서 순수한 규조연니층을 발견하였고, 상대적 고강도(relative paleointensity; RPI)연대 측정 결과 내대륙 붕(inner shelf)에 12,000-12,700 cal yr BP이전에는 얼음이 없었다고 제시하였다. 아문젠해는 남극 주변을 돌고 있는 순환심층수가 유입되어 빙붕이 빠르게 녹아내리고 있는 지역으로 빙붕의 융빙에 의해 봄철과 여름철에 식물 플랑크톤의 번성이 활발하기 때문에 규조 군집변화를 이용한 퇴적기록을 이용하기에 좋은 지역이다. 국내에서의 아문젠 해 산출 규조에 대한 연구는 아문젠해 폴리냐(polynya)의 가운데 지역에서의 결과로 10.5 cal. ka BP에 계절적 개방 수역(seasonal open water)에 놓이기 시작했음이 보고 되었다 (Kim et al., 2023). 본 연구는 아문젠해 폴리냐의 내부에 위치한 Getz ‘A’ Ice Shelf의 인접 부근에서 채취한 코어퇴적물의 규조 군집변화를 통해, 이지역의 과거 환경변화를 파악하는데 목적이 있다.

2. 연구 지역 및 연구 방법

2.1. 연구 지역

Getz 빙붕의 면적은 33,200 km2, 길이가 505 km로 지난 20년 동안 극적으로 얇아졌으며, 1992년에서 2001년 사이에는 1년에 -36 ± 2 cm의 고도 변화가 기록되었다(Shepherd et al., 2004). 아문젠해에 영향을 미치는 주요한 세 개의 수괴가 존재하며, 300~600 m 깊이에 변환환극심층수(mCDW; modified Circumpolar Deep Water; 1.13~1.55℃), 상부 50~100 m에 남극표층수(AASW; Antarctic Surface water; -1.5℃), 이들 두 수괴 사이에 겨울수괴 (Winter Water, WW; -1.14~-1.67℃)가 존재한다(Dutrieux et al., 2014). 환극심층수(Circumpolar Deep Water; >2℃)는 Dotson-Getz Trough를 통해 서쪽 아문젠해 만 대륙붕을 가로질러 흐르고 대륙붕수 및 빙하 융빙수와 혼합되어 변환환극심층수를 형성한다. 남극표층수는 남극 여름에 관찰되며 태양 복사를 통해 가열되고 해빙에 의해 영향을 받는다. 겨울수괴층은 변환환극심층수위에 더 차갑고 신선하며, 산소가 많이 함유된 수괴로 계절적으로 존재한다 (Biddle et al., 2017).

2.2. 연구 방법

Getz ‘A’ 빙붕 부근에서 규조를 연구하기 위해 AM22-GC10B (73°98.2853'S, 115°76.9077'W)코어를 채취하였고, 수심 1249 m에서 시추한 퇴적물의 코어 총길이는 5.35 m 이다(그림 1). AM22-GC10B 코어는 단면에 대한 면밀한 육안 관찰과 X-선 사진의 분석 결과, 하부로부터 diamicton (260~500 cm), sandy mud (260~160 cm)과 bioturbated mud (0~160 cm)로 이루어져 있으며, 규조의 연구를 위하여 0~260 cm 구간에서는 10 cm 간격, 270~500 cm 구간에서는 ~80 cm 간격으로 총 31개의 시료를 분석하였다(그림 2). 규조 추출 및 관찰을 위하여 Bak and Lee (2017)의 실험 방법을 수행하였으며, 규조 정량분석을 위한 실험과 계산은 Scherer (1994)의 방법을 수정하여 사용하였다. 각 층준으로부터 채취한 건조시료 2 g에 묽은 염산(10%) 25 ml와 과산화수소수(35%) 15 ml를 첨가한 후 가열판(hot plate)위에서

1시간 이상 가열한다. 2차로 묽은 염산과 과산화수소수 15 ml를 첨가하여 끓여 준 후 24시간 정도 반응시킨다. 1차 증류수 세척 과정을 3번 이상 반복하여 산이나 부유성 물질들을 모두 제거한다. 침전물 중 부표본을 취하여 슬라이드글라스가 장치된 settling container에 넣고 저온의 건조기(약 50℃) 안에서 건조 시킨다. 접착제를 이용하여 커버글라스를 고정시킨 후, Zeiss Axioscope 5 광학현미경을 이용하여 400-1000배로 각 층준에서 300개체 이상을 동정하였으며, 개체수가 매우 적은 구간에서는 view field를 300개 이상 관찰하였다. 절개되지 않은 코어에서 대자율(magnetic susceptibility, MS) 값은 1 cm 간격으로 Bartington MS2C 센서를 이용하여 극지연구소에서 측정하였다.

3. 결과 및 토의

3.1. 규조 분석

AM22-GC10B의 각 층준으로부터 총 22속 50종의 규조가 동정되었으며, 정량 분석의 결과로 규조 개체수 농도가 0.5~8.3 ×107/g 범위로 나타났다. 산출된 규조 군집에서 가장 다량으로 산출된 종은 Fragilariopsis curta (34.2%) 이며, Eucampia antarctica var. recta (18.4%), Shionodiscus gracilis (4.5%), Fragilariopsis ritscheri (4.4%), Fragilariopsis vanheurckii (4%)순으로 산출되었고 나머지 종들의 산출률은 매우 적고 보존 상태가 불량하였다. 대자율 값은 100~1600 ×105 SI의 범위로 나타났으며, 규조 종의 산출이 많은 0~260 cm에서는 전반적으로 낮은 값을 보였으며, 반대로 산출이 거의 되지 않는 260~500 cm 까지는 높은 값(>800 ×105 SI)을 보였다(그림 2). 대자율 값은 빙하가 전진하는 시기에는 육지퇴적물의 유입으로 인해 높은 값이 나타나고, 빙하가 후퇴하거나 안정되는 시기에는 표층 생산력이 상대적으로 증가하기 때문에 낮은 값이 나타나는 경향이 있다(Jovane et al., 2019).

3.1.1. 규조 군집대

연구 코어 AM22-GC10B로부터 산출된 주요 종들의 산출 분포를 근거로 3개의 군집대를 설정하였다(그림 3).

규조군집대 I: 260~500 cm
규조 군집대 I은 산출이 거의 없는 구간으로서 규조의 생존 및 보존이 어려운 기저빙하의 영향이 우세한 환경조건을 지시한다.

규조군집대 II: 160~260 cm
이 구간에서는 해빙종인 F. curta, F. vanheurckii, Fragil-ariopsis obliquecostata, F. ritscheri, Fragilariopsis turgiduloides 및 Stellarima microtria의 산출이 상대적으로 풍부하게 나타난다. 또한, 공해종으로서 Fragilariopsis kerguelensis, Odontella weissflogii의 산출도 상대적으로 높게 나타나는 구간이다(그림 3). 해빙종이 공해종보다 풍부하게 나타나는 혼합 규조 조성을 보여준다.

규조군집대 III: 0~160 cm
규조 군집대 II에서 풍부하게 나타났던 해빙종인 F. vanheurckii의 산출이 점진적으로 줄어들며, F.

obliquecostata, F. ritscheri의 산출도 감소하는 경향을 보인다(그림 3). 이와 대조적으로 해빙의 가장자리에서 번성하는 것으로 알려진 E. antarctica var. rercta와 함께 공해종인 Thalassiosira antarctica와 Shionodiscus gracilis의 산출이 규조 군집대 II에 비하여 상대적으로 증가하는 양상을 보인다(그림 3).

3.2. 고환경 및 토의

AM22-GC10B코어 퇴적물에서는 시대 지시종 및 재이동 규조각의 산출이 거의 나타나지 않는다. 군집대 I에서는 규조의 산출이 거의 없고, 대자율 값이 높게 나타나는 것으로 보아 규조의 일차 생산성이 매우 낮은 환경으로 생각된다(그림 4). Smith et al. (2011)은 본 연구코어와 인접한 곳에서 획득한 VC415에서 해저에 접지된 기저 빙상(grounded ice sheet) 환경으로부터 해빙이 없는 환경(open marine)으로 전이되기까지 빙하하부(facies 3; subglacial), 근위 접지선(facies 2; proximal grounding line), 계절적으로 개방된 해양(facies 1; seasonal open marine)에서 퇴적된 세가지 퇴적상을 식별하였다. 따라서, 군집대 I은 규조가 거의 산출되지 않는 것으로 보아 빙상으로 덮여 있었던 빙하하부 환경에서 퇴적된 것으로 해석된다. 군집대 II는 규조의 절대 개체수는 0.5~3.2 ×107/g 범위에 해당하고, 대자율 값이 급감하는 구간이다(그림 4). 이 구간에서는 해빙종(F. curta, F. vanheurckii, F. obliquecostata, F. ritscheri, F. turgiduloides 및 S. microtria)과, 공해종인 F. kerguelensis와 O. weissflogii의 산출이 높게 나타난다(그림 3). 또한, 휴면 포자(Chaetoceros RS)의 산출이 증가한다(그림 4). 이러한 군집 변화를 고려하면 군집대 I에서 나타났던 빙하하부에서 퇴적된 환경에서 계절적으로 개방된 해양환경으로 변화하는 전이구간으로 빙해양(glaciomarine)환경으로 생각된다. 이 시기에 산출되기 시작하는 F. ritscheri는 해수면 온도가 0-3℃일 때 가장 풍부하게 관찰되며, 해빙(sea-ice) 지속 기간이 연간 9개월일 때 가장 풍부하게 나타난다. 또한, 해빙에서 채취한 표본보다 인접한 수층에서 더 풍부하게 발견되는 것은 융빙수 환경을 선호할 가능성을 시사한다 (Armand et al., 2005). 군집대 II 내에서는 하부에서 가장 풍부하게 산출되며 상부로 갈수록 감소하는 경향을 보인다. F. kerguelensis는 현재 남극해 퇴적물에서 우세하게 산출되는 구성요소이며(Burckle and Cirilli, 1987), 특히 해빙대의 북쪽에서 발견되는 퇴적물에서 두드러지게 산출된다(Esper et al., 2010). 그러나, 퇴적물에서의 상대적인 풍부성은 미세한 규질각의 선택적 용해에 의해 종종 과대평가 될 수 있다는 점을 고려해야 한다. 현재 표층수에서 F. kerguelensis은 남반구의 봄철 동안 풍부하게 관찰된다(Cortese and Gersonde, 2007). Thoma et al. (2008)에 의해 개발된 아문젠해 해양학 모델에 의하면 늦겨울부터 봄철까지 아문젠해 저기압이 남서쪽으로 이동하면서 대륙붕으로의 순환 심층수(Circumpolar Deep Water, CDW)의 용승이 증가하는 것으로 나타난다. 따라서, 군집대 II 하부에서 F. kerguelensis의 산출이 증가하는 것은 이러한 CDW 용승의 영향으로 해석될 수 있다.

빙하가 후퇴한 이후, 동남극과 서남극 대륙붕에 육성기원 퇴적층과 함께 혼합 규조 군집을 포함하는 휴면포자가 풍부한 퇴적층이 쌓였다(Hillenbrand et al., 2010). Leventer et al. (2006)은 동남극 대륙붕에서는 철이 풍부한 융빙수가 유입되면서 성층화된 표층수내에서 봄철에 대규모 번성이 일어나 휴면포자가 풍부하게 나타난다고 설명하였다. 또한, 규조류는 염분 부족이나 질소의 결핍에 의해서 해빙경계(sea-ice edge) 부근에서 휴면포자를 형성하게 된다(Leventer, 1991, 1992; Crosta et al., 1997). 이러한 관점에서 규조 군집대 II를 살펴보면 휴면포자의 산출이 상부로 갈수록 증가하는 경향을 나타낸다.

아문젠해 만 중심부에 위치한 헌트 블러프(Hunt Bluff)의 마지막 빙하기는 아마도 마지막 빙하기 극대기(21.1 ±5.8 ka)에 시작되어 대륙붕에서 빙상이 완전히 후퇴한 시기인 9.6 ± 0.9 ka에 끝난 것으로 보고 되었다(Johnson et al., 2017). 또한 Smith et al. (2011)은 Dotson 빙붕과 Getz 빙붕 연구를 통해 서부 아문젠해 만의 빙하 후퇴는 현재로부터 22.4 ka에 이미 시작되었음을 밝혔다. 이 빙하는 13.8 ka

에 중간 대륙붕에 도달했고, 12.6에서 10.1 ka사이에는 내륙 대륙붕이 현재 빙붕 전선에서 약 10～12 km 떨어진 지 점까지 후퇴했다고 보고하였다. VC415과 AM22-GC10B 코어의 위치가 매우 가깝게 분포하고 있어 연대 측정이 되어 있는 VC415코어의 대자율 값과 비교해 본 결과, 규조 군집대 II는 빙하후퇴의 전이구간으로, 빙하가 현재 빙붕 전선에 가까운 위치까지 녹은 시점은 10.1 ka에 대비될 수 있다(Smith et al., 2011)(그림 2). 그러나, 정확한 빙상 후 퇴시기를 파악하기 위해서는 동위 원소 분석에 의한 연대 측정이 필요하다. 군집대 III의 규조 개체수는 1.4～8.3 ×107/g 범위이며, 대자율 값은 군집대 II에 비해 약간 감소한다. 이 군집대에서는 휴면포자 산출이 풍부하게 나타난다(그림 4). F. curta는 정착빙(fast ice)과 유빙(pack ice)에서 풍부하게 산출되며 성층화된 해역에서 융빙수 공급의 지시자로서도 매우 유용하다(Garrison et al., 1987; Leventer and Dunbar 1987, 1988, 1996; Cunningham and Leventer, 1998). 군집대 III에서는 이러한 F. curta가 매우 풍부하게 산출된다. T. antarctica는 공해종으로 알려져 있으나 대륙주변부 해빙단(marginal ice edge) 환경에서도 일차 생산자로서 중요한 역할을 하며(Leventer and Dunbar, 1987, 1988, 1996; Fryxell and Kendrick, 1988; Leventer, 1992; Leventer et al., 1993; Taylor et al., 1997), 연안 해빙과 떠다니는 판상 얼음(platelet ice)들이 있는 환경에서도 산출된다(Hasle and Heimdal, 1968; Villareal and Fryxell, 1983; Smetacek et al., 1992; Gleitz et al., 1996). T. antarctica와 S. gracilis는 냉수역 (Cold Open Water)에 분포하며, 차가운 해수면 온도를 가진 해빙 가장자리 근처에 개방 수역 조건이 존재함을 나타낸다(Barbara et al., 2013). 군집대 III의 T. antarctica는 하부에서 가장 풍부하게 나타나지만 상부로 갈수록 감소하는 경향을 보이며, S. gracilis는 60 cm 층준 상부에서 감소하는 경향을 보인다.

군집대 III에서 상대적으로 풍부하게 나타나는 Cocconeis spp.은 10 m 이상의 수심에서 서식하며(Whitehead and McMinn, 1997), 해안의 조하대에서 봄/여름에 대규모 번성을 일으킨다. 이 종은 빙하가 없는 기간 동안 수층의 강한 난류를 지시하는 것으로 알려져 있다(Heil, 2006; Barbara et al., 2013). 따라서, 군집대 III는 계절적인 공해 환경에서 퇴적되었음을 알 수 있다.

4. 결 론

남극 아문젠해 만내 Getz ‘A’ Ice Shelf (빙붕) 인근에서 채취한 코어 퇴적물 AM22-GC10B를 분석하여 총 22속 50종의 규조를 동정하였으며, 이를 바탕으로 퇴적 시기 동안 빙붕의 분포 변화를 파악하였다. 규조 개체수 농도는 건조 중량 1 g당 0.5～8.3×107의 범위로 일차 생산성이 높지 않으며, 군집대 I에서는 거의 산출되지 않는다. 규조 군집의 해빙종과 공해종의 산출 분포 양상 및 대자율값에 의하여 3개의 군집대를 설정하였다. 군집대 I (260～500 cm)은 규조가 살기 어려운 빙하하부(subglacial) 환경에서 퇴적된 시기에 해당되며, 군집대 II (160～260 cm)는 군집대 I보다 온난한 시기이나 해빙종들의 산출이 우세하게 나타나는 것으로 보아 빙하하부 환경의 영향 아래에 서 계절적으로 해빙이 줄어드는 빙해양(glaciomarine) 환경에서 형성된 것으로 해석된다. 군집대 III (0～160 cm)는 해빙종의 산출이 줄어들고 공해종의 산출이 증가하며, 휴면포자의 산출이 풍부한 것으로 보아 계절적으로 개방된 해양(open marine) 환경에서 퇴적되었다. 정확한 빙상 후퇴의 시기를 알기 위해서는 연대 측정이 필요하나 현대 빙붕 전선에 가까운 위치로 빙하가 녹은 시점은 기존의 연구 결과(Smith et al., 2011)와 대비해 볼 때 10.1 ka에 해당된다.

Recording of paleoenvironmental changes using diatom assemblages from the Amundsen Sea, Antarctica

Young-Suk Bak[1], Sunghan Kim[2], Kyu-Cheul Yoo[2], Jae Il Lee[2], Min Kyung Lee[2], Sangbeom Ha[2]

[1]Jeonbuk National University

[2]Korea Polar Research Institute

Abstract: To reconstruct past ice shelf behavior, diatoms were analyzed from core sediments obtained near the Getz 'A' Ice Shelf in the Amundsen Sea embayment of Antarctica. A total of 50 diatom species representing 22 genera were identified from AM22-GC10B, with abundances varying from 0.5 to 8.3×107/g. By examining the patterns of sea ice, open ocean species, and magnetic susceptibility (MS) values, three assemblage zones were established. These zones reveal significant changes in the paleoenvironment: Diatom assemblage zone I corresponds to subglacial condition, characterized by low diatoms and high magnetic susceptibility values. Diatom assemblage zone II represents the glacialmarine, showing a shift from subglacial to seasonal open marine conditions, with increasing diatom abundance and decreasing magnetic susceptibility. Diatom assemblage zone III indicates a seasonal open marine period, characterized by high diatom abundance, increasing Chaetoceros resting spores, decreasing sea ice species, and increasing open ocean species.

KOPRI 극지연구소

참고 문헌

Armand, L.K., Crosta, X., Romero, O. and Pichon, J.-J., 2005, The biogeography of major diatom taxa in Southern Ocean sediments: 1. Sea ice related species, Palaeogeography, Palaeoclimatology, Palaeoecology, 223, 93-126.

Arndt, J.E., Schenke, H.W., Jakobsson, M., Nitsche, F.O., Buys, G., Goleby, B., Rebesco, M., Bohoyo, F., Hong, J., Black, J., Greku, R., Udintsev, G., Barrios, F., Reynoso-Peralta, W., Taisei, M. and Wigley, R., 2013, The International Bathymetric Chart of the Southern Ocean (IBCSO) Version 1.0-A new bathymetric compilation covering circum-Antarctic waters. Geophysical Research Letters, 40, 3111-3117, doi:10.1002/grl.50413.

Bak, Y.S. and Lee, Y.U., 2017, Late Quaternary Paleoclimatic change in the Ulleung Basin, East Sea, Korea. Acta Geologica Sinica, 91, 263-269.

Bamber, J.L., Riva, R.E., Vermeersen, B.L. and LeBrocq, A.M., 2009, Reassessment of the potential of the West Antarctic icesheet. Science, 324, 901-903, doi:10.1126/science.1169335.

Barbara, B., Crosta, X., Schmidt, S. and Massé, G., 2013, Diatoms and biomarkers evidence for major changes in sea ice conditions prior the instrumental period in Antarctic Peninsula. Quaternary Science Reviews, 79, 99-110.

Biddle, L.C., Heywood, K.J. and Kaiser, J., 2017, Glacial Meltwater Identification in the Amundsen Sea. Journal of Physical Oceanography, 47, 933-954.

Burckle, L.H. and Cirilli, J., 1987, Origin of diatom ooze belt in the Southern Ocean: implications for late Quaternary paleoceanography. Micropaleontology, 33, 82-86.

Cortese, G. and Gersonde, R., 2007, Morphometric variability in the diatom Fragilariopsis kerguelensis: Implications for Southern Ocean paleoceanography. Earth and Planetary Science Letters, 257, 526-544.

Crosta, X., Pichon, J.-J. and Labracherie, M., 1997, Distribution of Chaetoceros resting spores in modern peri-Antarctic sediments. Marine Micropaleontology, 29, 283-299.

Cunningham, W.L. and Leventer, A., 1998, Diatom assemblages in surface sediments of the Ross Sea: relationship to present oceanographic conditions. Antarctic Science, 10, 134-146.

Dutrieux, P., De Rydt, J., Jenkins, A., Holland, P.R., Ha, H.K., Lee, S.H., Steig, E.J., Ding, Q., Abrahamsen, E.P. and Schröder, M., 2014, Strong sensitivity of Pine Island ice-shelf melting to climatic variability. Science, 343, 174-178, doi:10.1126/science. 1244341.

Esper, O., Gersonde, R. and Kadagies, N., 2010, Diatom distribution in southeastern Pacific surface sediments and their relationship to modern environmental variables. Palaeogeography, Palaeoclimatology, Palaeoecology, 287, 1-27.

Fryxell, G.A. and Kendrick, G.A., 1988, Austral spring microalgae across the Weddell Sea ice edge: spatial relationships found along a northward transect during AMERIEZ 83. Deep Sea

Research Part A. Oceanographic Research Papers, 35, 1-20.

Garrison, D.L., Buck, K.R. and Fryxell, G.A., 1987, Algal ice edge assemblages in Antarctic pack ice and in ice-edge plankton. Journal of Phycology, 23, 564-572.

Gleitz, M., Grossmann, S., Scharek, R. and Smetacek, V., 1996, Ecology of diatomand bacterial assemblages in water associated with melting summer sea ice in the Weddell Sea, Antarctica.

Antarctic Science, 8, 135-146.

Hasle, G.R. and Heimdal, B.R., 1968, Morphology and distribution of the marine centric diatom Thalassiosira antarctica Comber. Journal of the Royal Microscopical Society, 88, 357-369.

Heil, P., 2006, Atmospheric conditions and fast ice at Davis, East Antarctica: A case study. Journal of Geophysical Research: Oceans, 111, C05009, doi:10.1029/2005JC002904.

Hillenbrand, C.-D., Smith, J.A., Kuhn, G., Esper, O., Gersonde, R., Larter, R.D., Maher, B.A., Moreton, S.G., Shimmield, T.M. and Korte, M., 2010, Age assignment of a diatomaceous ooze deposited in the western Amundsen Sea Embayment after the last glacial maximum. Journal of Quaternary Science, 25, 280-295.

Johnson, J.S., Smith, J.A., Schaefer, J.M., Young, N.E., Goehring, B.M., Hillenbrand, C.-D., Lamp, J.L., Finkel, R.C. and Gohl, K., 2017, The last glaciation of Bear Peninsula, central Amundsen Sea Embayment of Antarctica: Constraints on timing and duration revealed by in situ cosmogenic 14C and 10Be dating. Quaternary Science Reviews, 178, 77-88.

Joughin, I. and Alley, R.B., 2011, Stability of the West Antarctic ice sheet in a warming world. Nature Geoscience, 4, 506-513.

Jovane, L., Florindo, F., Acton, G., Ohneiser, C., Sagnotti, L., Strada, E., Verosub, K.L., Wilson, G.S., Iacoviello, F., Levy, R.H. and Passchier, S., 2019, Miocene Glacial Dynamics Recorded by Variations in Magnetic Properties in the ANDRILL-2A Drill Core. Journal of Geophysical Research: Solid Earth, 124, 2297-2312.

Kim, M., Lee, J.I., Bak, Y.-S., Hillenbrand, C.-D., Yang, E.J., Montlucon, D.B., Haghipour, N., Eglinton, T.I. and Hwang, J., 2023, Holocene Palaeoenvironmental and Palaeoproductivity Changes in the Western Amundsen Sea Embayment of Antarctica. Journal of Geophysical Research: Oceans, 128, e2023JC019797, doi:10.1029/2023JC019797.

Konfirst, M.A., Scherer, R.P., Hillenbrand, C.-D. and Kuhn, G., 2012, A marine diatom record from the Amundsen Sea Insights into oceanographic andclimatic response to the Mid-Pleistocene Transition in the West Antarctic sector of the Southern Ocean. Marine Micropaleontology, 92-93, 40-51.

Leventer, A., 1991, Sediment trap diatom assemblages from the northern Antarctica Peninsula region. Deep Sea Research Part A. Oceanographic Research Papers, 38, 1127-1143.

Leventer, A., 1992, Modern distribution of diatoms in sediments from the George V Coast, Antarctica. Marine Micropaleontology, 19, 315-332.

Leventer, A., Domack, E., Dunbar, R., Pike, J., Stickley, C., Maddison, E., Brachfeld, S., Manley, P. and McClennen, C., 2006, Marine sediment record from the East Antarctic margin reveals dynamics of ice sheet reces-sion. GSA Today, 16, 4-10.

Leventer, A. and Dunbar, R., 1987, Diatom flux in McMurdo Sound, Antarctica. Marine

Micropaleontology, 12, 49-64.

Leventer, A. and Dunbar, R., 1988, Recent diatom record of McMurdo Sound, Antarctica: implications for history of sea ice extent. Paleoceanography, 3, 259-274.

Leventer, A. and Dunbar, R., 1996, Factors influencing the distribution of diatoms and other algae in the Ross Sea. Journal of Geophysical Research, 101, 18489-18500.

Leventer, A., Dunbar, R. and DeMaster, D.J., 1993, Diatom evidence for Late Holocene climatic events in Granite Harbor, Antarctica. Paleoceanography, 8930, 373-386.

Pattyn, F. and Morlighem, M., 2020, The uncertain future of the Antarctic Ice Sheet. Science, 367, 1331-1335.

Pritchard, H.D., Ligtenberg, S.R.M., Fricker, H.A., Vaughan, D.G., van den Broeke, M.R. and Padman, L., 2012, Antarctic ice-sheet loss driven by basal melting of ice shelves. Nature, 484, 502-505, doi:10.1038/nature10968.

Rignot, E., Thomas, R.H., Kanagaratnam, P., Casassa, G., Frederick, E., Gogineni, S., Krabill, W., Rivera, A., Russell, R., Sonntag, J., Swift, R. and Yungel, J., 2004, Improved estimation of the mass balance of glaciers draining into the Amundsen Sea sector of West Antarctica from the CECS/NASA 2002 campaign. Annals of Glaciology, 39, 231-237.

Rignot, E., Bamber, J.L., Van der Broeke, M.R., Davis, C., Li, Y., Van der Berg, W.J. and Van Meijgaard, E., 2008, Recent Antarctic ice mass loss from radar interferometry and regional climate modeling. Nature Geosciences, 1, 106-110.

Scherer, R.P., 1994, A new method for determination of absolute abundance of diatoms and other siltsized sedimentary particles. Journal of Paleolimnology, 12, 171-179.

Scott, J.B.T., Gudmundsson, G.H., Smith, A.M., Bingham, R.G., Pritchard, H.D. and Vaughan, D.G., 2009, Increased rate of acceleration on Pine Island Glacier strongly coupled to changes

in gravitational driving stress. The Cryosphere, 3, 125-131.

Shepherd, A., Wingham, D. and Rignot, E., 2004, Warm ocean is eroding West Antarctic ice sheet. Geophysical Research Letters, 31, doi:10.1029/2004GL021284.

Smetacek, V., Scharek, R., Gordon, L.I., Eicken, H., Fuhtbach, E., Rohardt, G. and Moore, S., 1992, Early spring phytoplankton blooms in ice platelet layers of the southern Weddell Sea, Antarctica. Deep Sea Research Part A. Oceanographic Research Papers, 39, 153-168.

Smith, J.A., Hillenbrand, C.-D., Kuhn, G., Larter, R.D., Graham, A.G.C., Ehrmann, W., Moreton, S.G. and Forwick, M., 2011, Deglacial history of the West Antarctic Ice Sheet in the western

Amundsen Sea Embayment. Quaternary Science Reviews, 30, 488-505.

Taylor, F., McMinn, A. and Franklin, D., 1997, Distribution of diatoms in surface sediments of Prydz Bay, Antarctica. Marine Micropaleontology, 32, 209-229.

Thoma, M., Jenkins, A., Holland, D. and Jacobs, S., 2008, Modeling Circumpolar Deep Water intrusions on the Amundsen Sea continental shelf, Antarctica. Geophysical Research Letters, 35, L18602, doi:10.1029/2008GL034939.

KOPRI 극지연구소

Vaughan, D., 2008, West Antarctic Ice Sheet collapse - the fall and rise of a paradigm. Climatic Change, 91, 65-79.

Villareal, T.A. and Fryxell, G.A., 1983, Temperature effects on the valve structure of the bipolar diatoms Thalassiosira antarctica and Porosira glacialis. Polar Biology, 2, 163-169.

Whitehead, J.M. and McMinn, A., 1997, Paleodepth determination from Antarctic benthic diatom assemblages. Marine Micropaleontology, 29, 301-318.

KOPRI
극지연구소

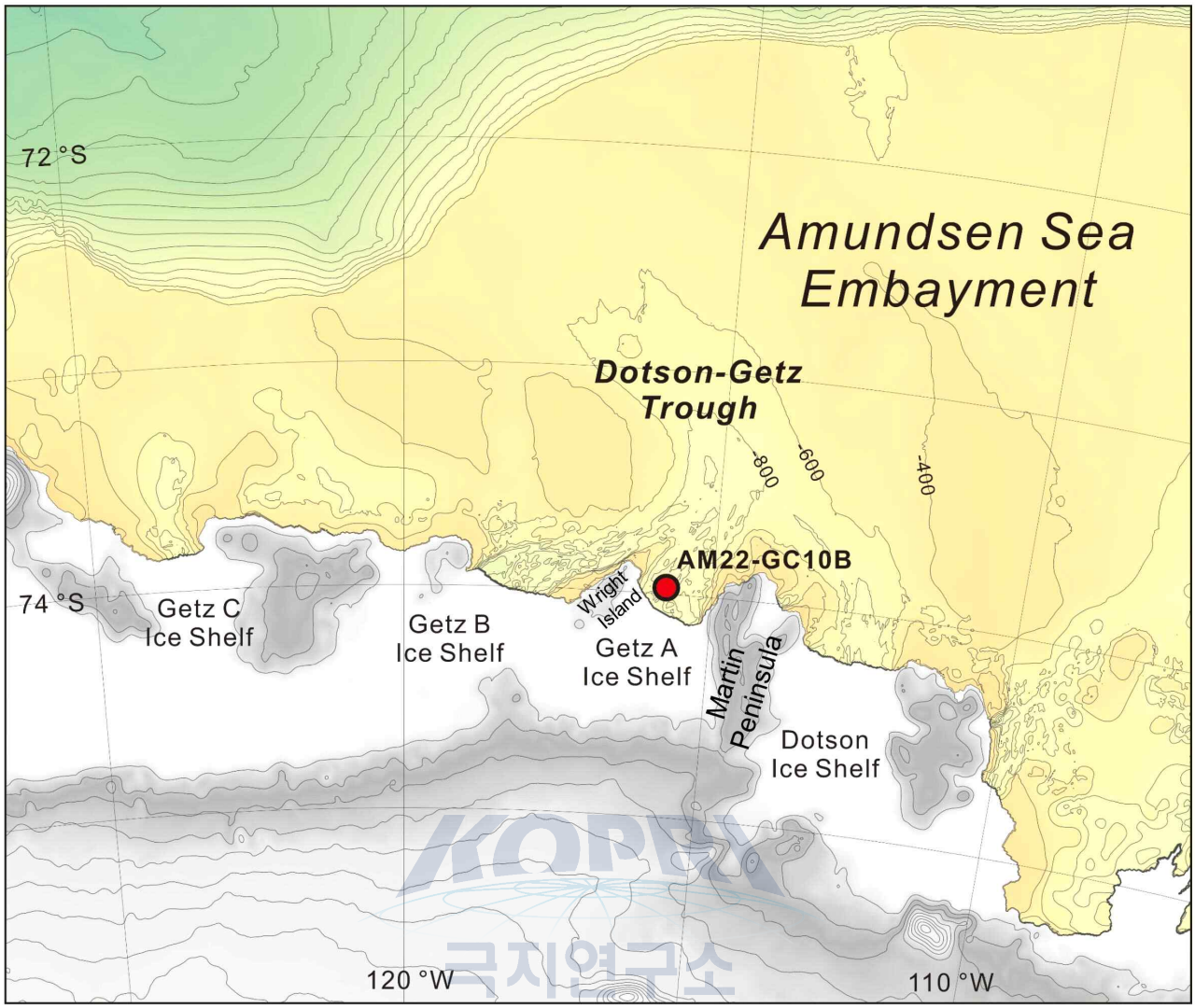
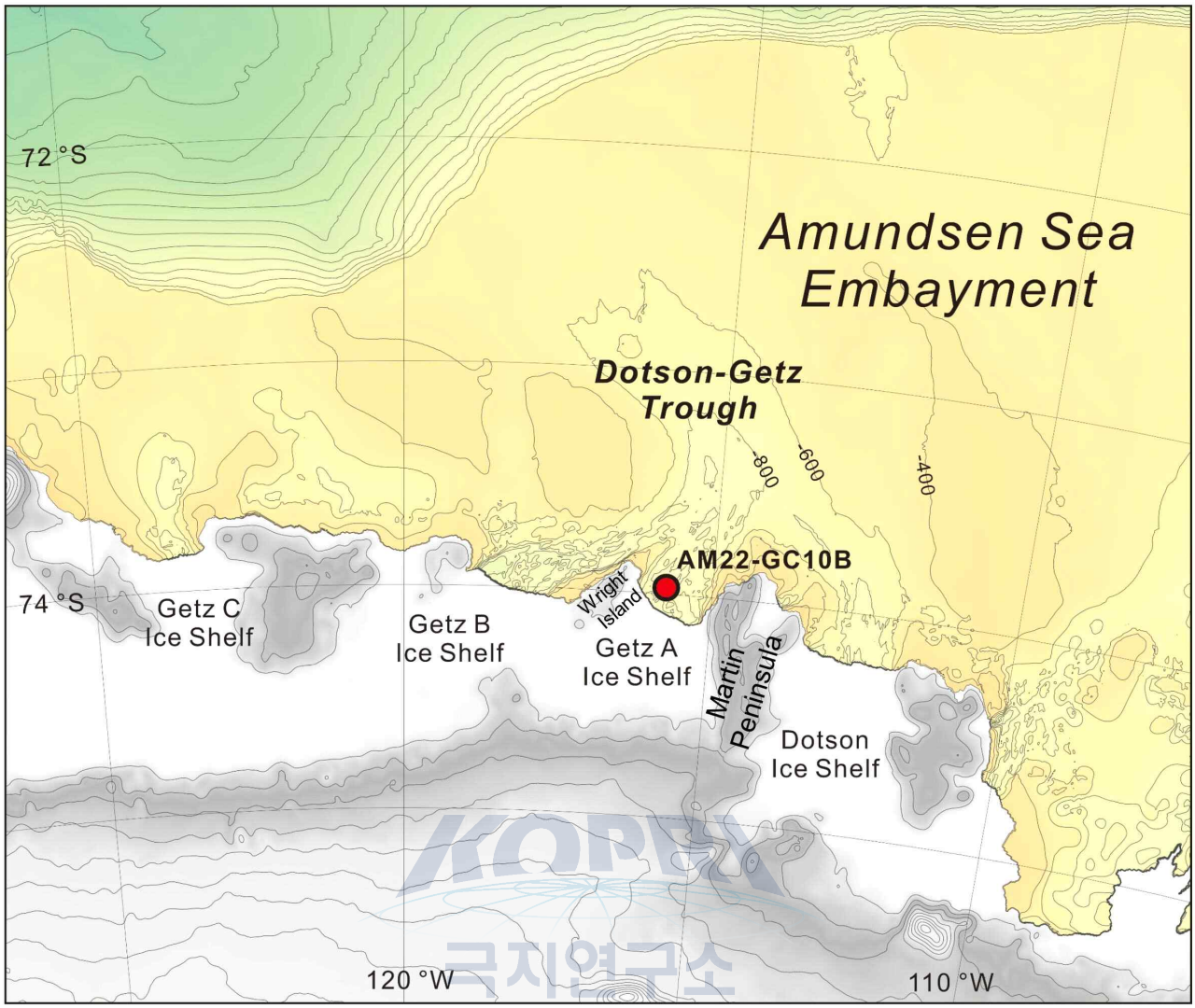
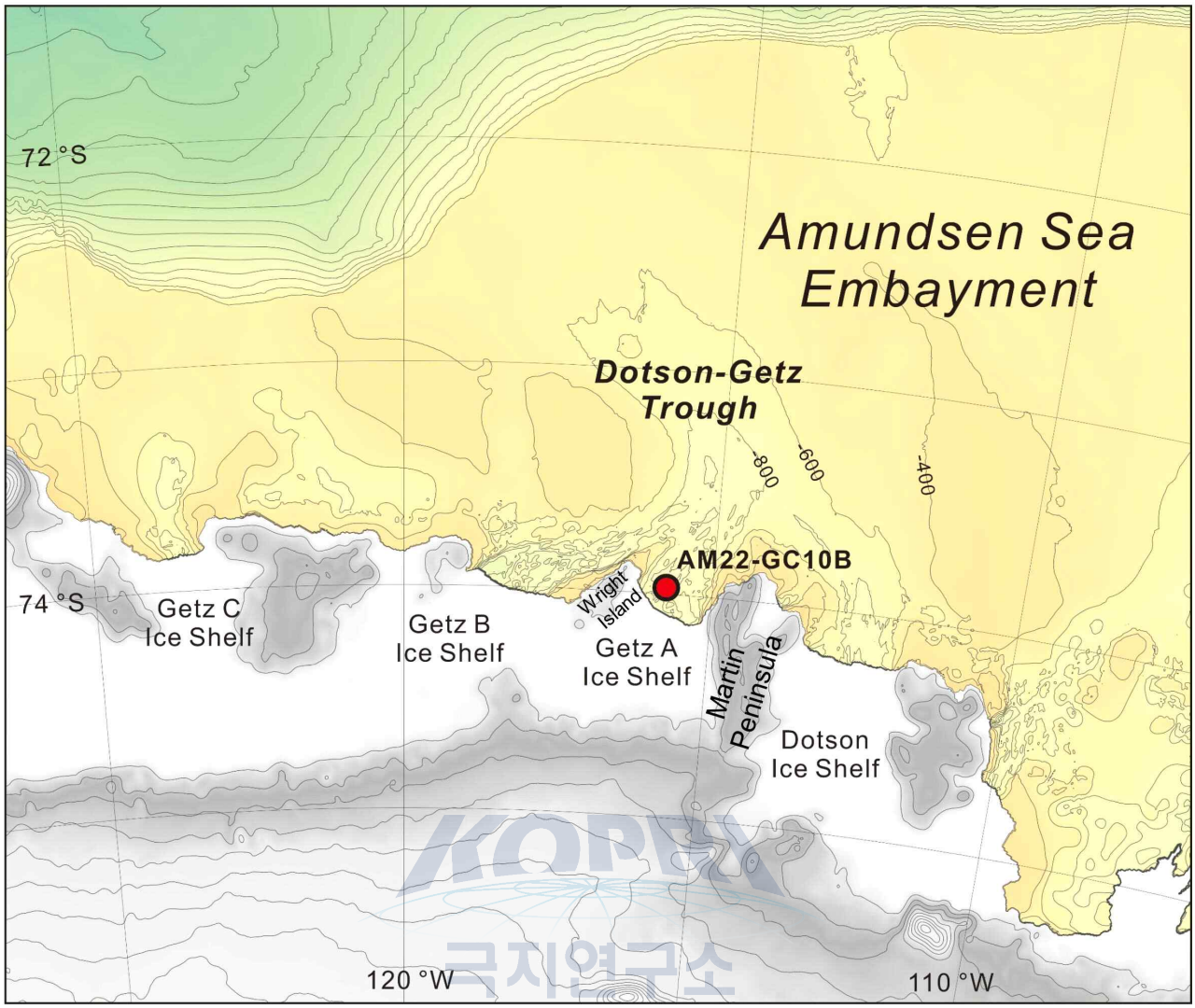


Fig. 1. Location map of core AM22-GC10B in Antarctica Bottom depth (colored, negative) and ice shelf draft (adapted from Arndt et al., 2013).


72 °S
Amundsen Sea
Embayment
Dotson-Getz
Trough
-800
-600
-400
AM22-GC10B
Wright
Island
74 °S
Getz C
Ice Shelf
Getz B
Ice Shelf
Getz A
Ice Shelf
Martin
Peninsula
Dotson
Ice Shelf
120 °W
110 °W

KOPRI
극지연구소


72 °S
Amundsen Sea
Embayment
Dotson-Getz
Trough
-800
-600
-400
AM22-GC10B
74 °S
Getz C
Ice Shelf
Getz B
Ice Shelf
Wright
Island
Getz A
Ice Shelf
Martin
Peninsula
Dotson
Ice Shelf
120 °W
110 °W

KOPRI
극지연구소

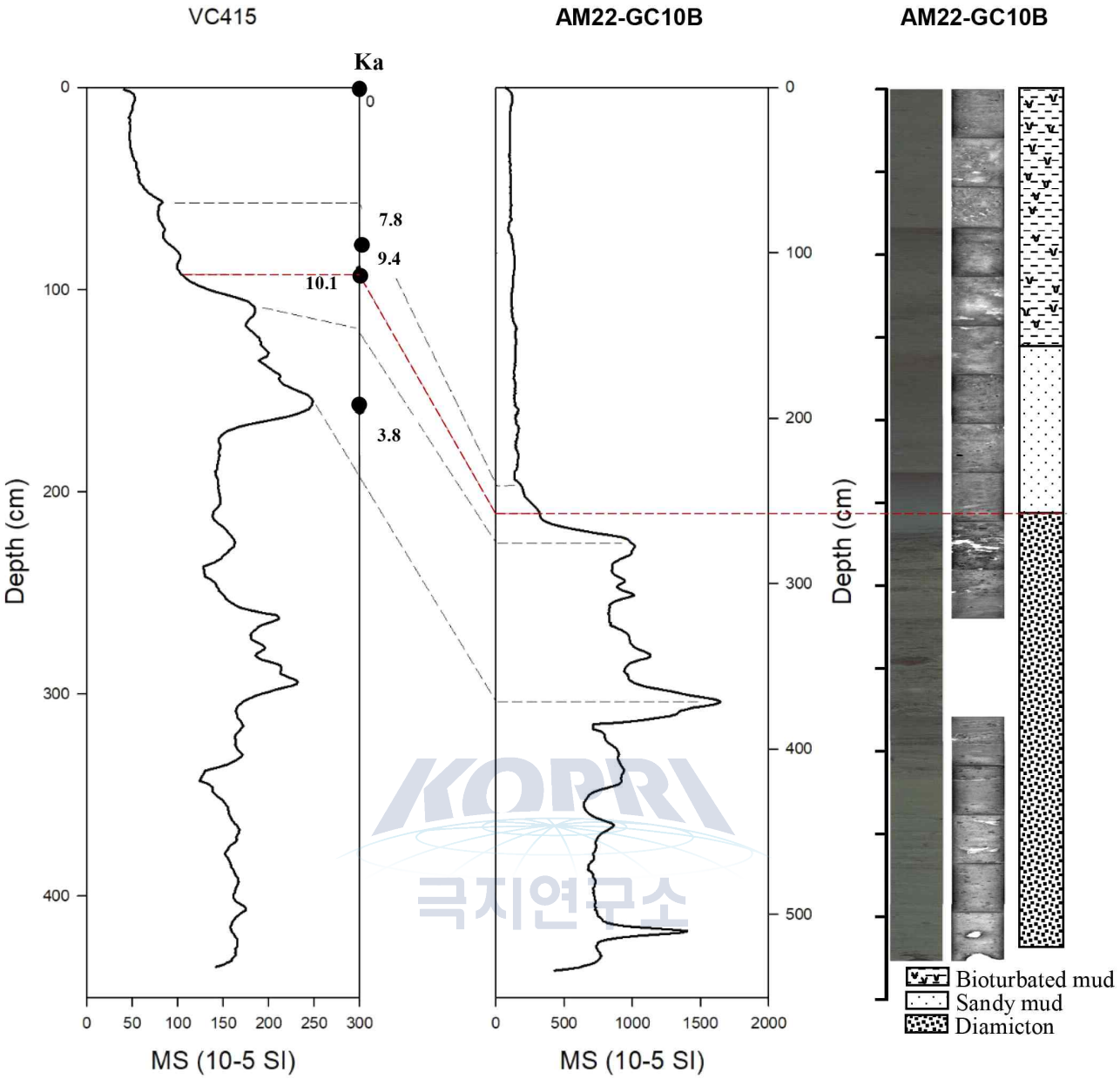


Fig. 2. Age of deglaciation based on the magnetic susceptibility values of the VC415 (Smith et al., 2011) and AM22-GC10 cores (this study) and sediment core log for AM22-GC10B.

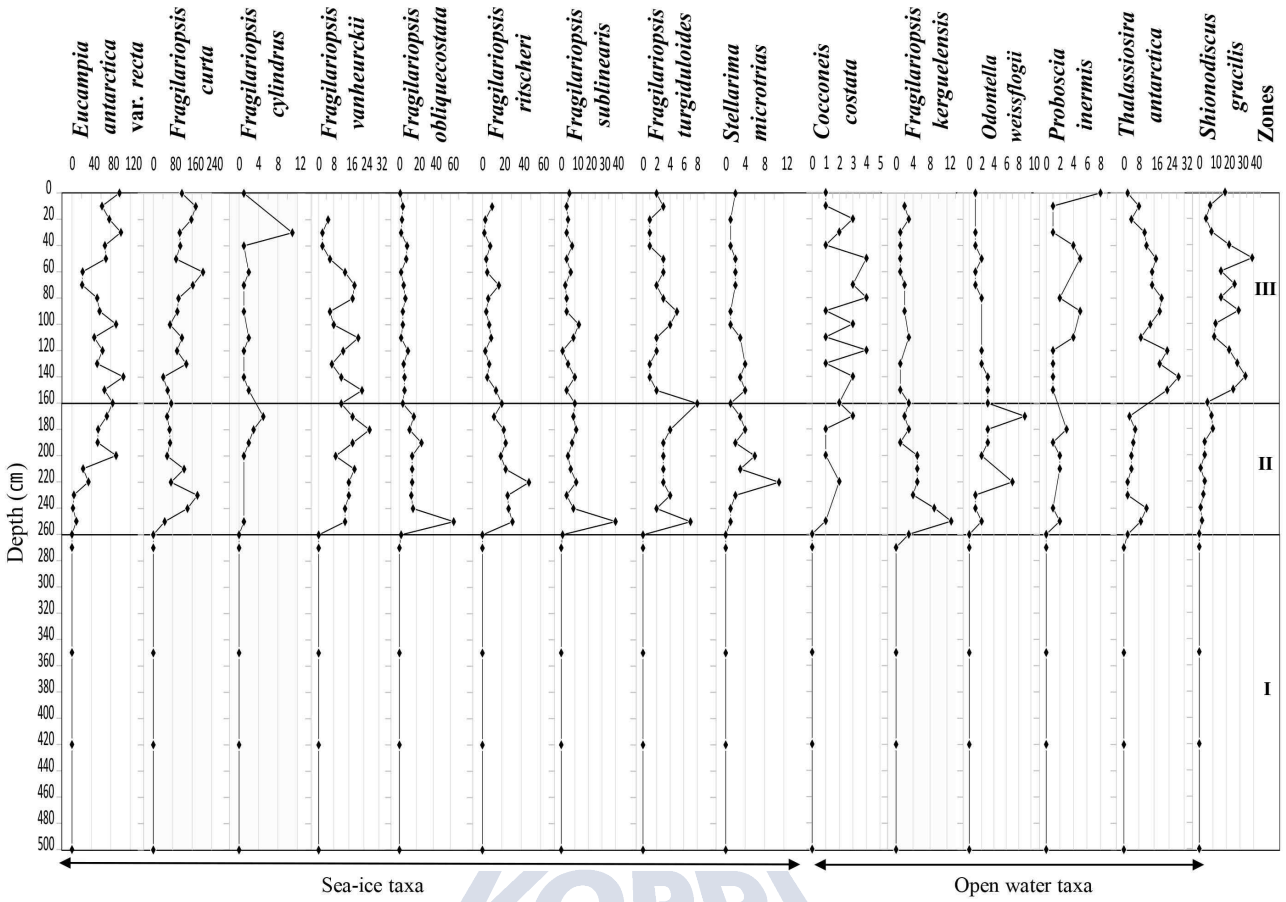


Fig. 3. Down-core variations of abundance of the sea ice and open water species, and diatom assemblage zones from AM22-GC10B.

KOPRI 극지연구소

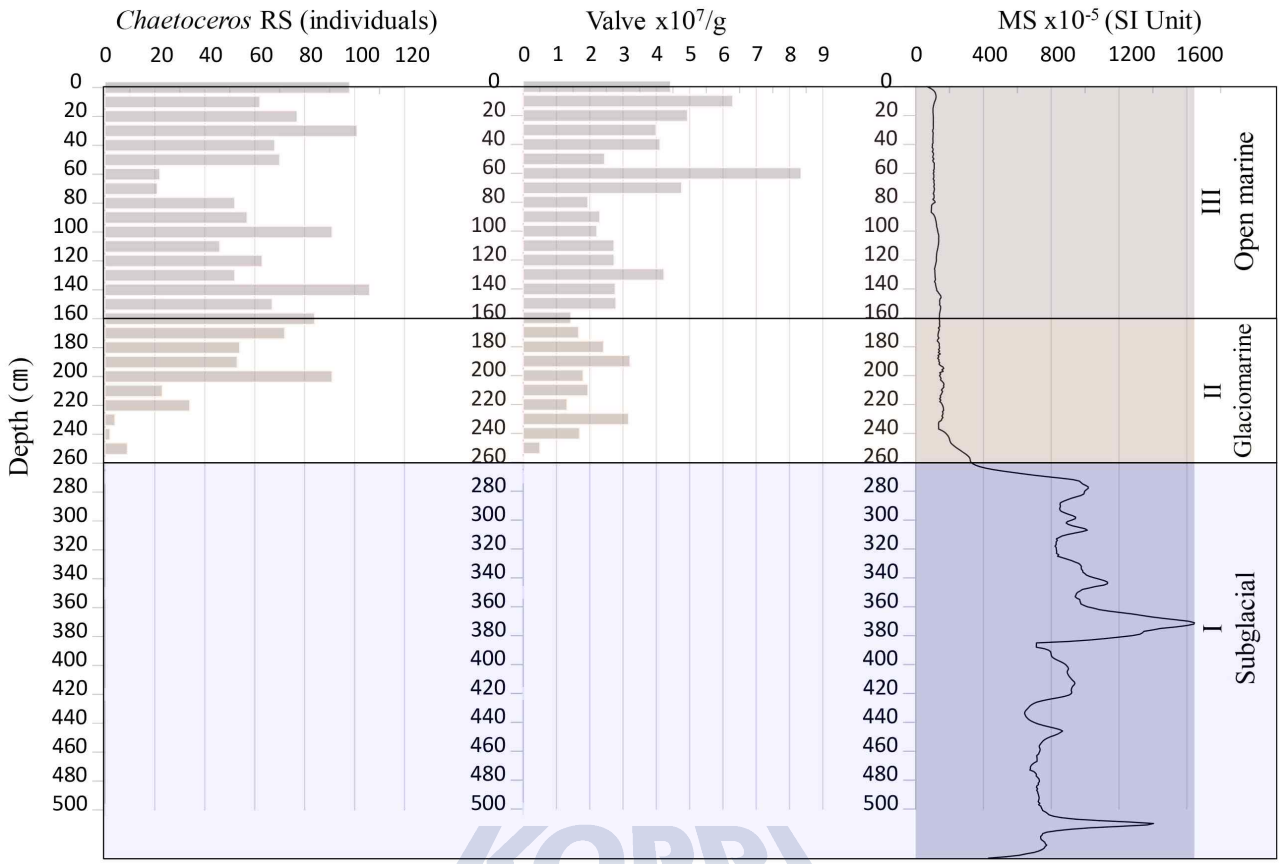


Fig. 4. Down-core variations of Chaetoceros RS, valve abundance (×107/g) and whole-round MS (×10-5) from AM22-GC

KOPRI 극지연구소

제 22 장

Late Pleistocene paleoceanographic changes in the Ross Sea – glacial–interglacial variations in paleoproductivity, nutrient utilization, and deep–water formation[15)]

Sunghan Kim[a,*], Jae Il Lee[a], Robert M. McKay[b], Kyu–Cheul Yoo[a], Young–Suk Bak[c], Min Kyung Lee[a], Youn Ho Roh[a,d], Ho Il Yoon[a], Heung Soo Moon[a], Chang–Uk Hyun[a]

[a]Korea Polar Research Institute, [b]Victoria University of Wellington, [c]Chonbuk National University, [d]University of Science and Technology

Abstract: The outer Ross Sea continental shelf has experienced large variations in ice sheet extent over the Pleistocene that are theorized to be largely driven by changes in the westward–flowing Antarctic Slope Current (ASC) at the continental shelf break. This current regulates southward incursions of warm modified Circumpolar Water, and it is thought to have triggered past marine ice sheet retreat. Additionally, expansions of grounded ice sheets on the continental shelf have fundamentally altered the Ross Sea water mass formation processes, influencing surface water salinity, sea ice cover, nutrient utilization, deep–water ventilation, and primary productivity. Here, we report the geochemical, physical properties, grain size, bulk δ15N, and diatom records during the late Pleistocene from two sediment cores from the Iselin Bank on the outermost continental shelf in the Ross Sea. These core sites were not overridden by grounded ice sheets during the late Pleistocene glacial–interglacial cycles, allowing for a continuous archive of glacimarine environments that were influenced by the ASC. Interglacial periods are typically characterized by high surface water productivity and nutrient utilization, with Chaetoceros resting spores indicating nutrient limitation under open ocean conditions, and glacial periods are typically characterized by low surface water productivity and nutrient utilization, with sea ice diatoms and planktonic foraminifers indicating light limitation under extensive sea ice/ice margin proximal conditions. A grain size analysis indicates coarse–skewed distributions and winnowing in the Iselin Bank region during cold periods. The winnowing may be related to enhanced ASC flow instead of density driven shelf water outflow.

15) 이 연구 결과는 다음의 논문으로 출판되었음: Kim, S. et al. (2020). "Late Pleistocene paleoceanographic changes in the Ross Sea - glacial-interglacial variations in paleoproductivity, nutrient utilization, and deep-water formation." Quaternary Science Reviews 239: 106356.

1. Introduction

The modern Ross Sea is characterized by the Ross Ice Shelf which is fed by ice from both the East Antarctic Ice Sheet (EAIS) and West Antarctic Ice Sheet (WAIS). During past glacial expansions these ice masses were grounded over much of the outer continental shelf edge in the Ross Sea (Anderson et al., 2014). The ANDRILL AND-1B cores collected beneath the Ross Ice Shelf showed that changes in Ross Sea shelf sedimentary facies correspond to up to 28 expansion and retreat cycles between 5-1 Ma, but they contained numerous hiatuses due to periods of glacial erosion (Naish et al., 2009). However, although the evidence for WAIS collapse after 1 Ma remains equivocal, the sedimental facies and deformational features of AND-1B suggest that shifts between grounded ice sheet and floating ice shelf conditions have occurred in the past 1 Ma at frequencies consistent with those of orbital pacing (McKay et al., 2012). Although the exact timing of these events in AND-1B remains difficult to constrain, seismic surveys in the Northern Basin of the Ross Sea also indicate that there were shelf-wide advancements and retreats during the Plio-Pleistocene (Bart et al., 2011; Anderson et al. 2019). Given that the Ross Sea experienced large shifts in ice sheet coverage during the Plio-Pleistocene ice age cycles and is currently a key area for Antarctic Bottom Water (AABW) formation and sea ice production (Smith et al., 2012), the outer continental shelf in the Ross Sea is an ideal region for investigating oceanic changes through past glacial-interglacial changes.

The last four glacial-interglacial cycles are characterized by large glacial-interglacial variations in ice volume, temperature, sea-level, and pCO2 (Bintanja et al., 2005; Lisiecki and Raymo, 2005; Jouzel et al., 2007; Lüthi et al., 2008; Siddall et al., 2010). However, Ross Shelf sediment records are largely restricted to the last glacial period due to difficulties in obtaining sediment core that can penetrate the Last Glacial Maximum glacial sediments (e.g., Cuningham et al., 1999; Domack et al., 1999; Licht et al., 1999; Anderson et al., 2014; McKay et al., 2016), and more continuous sedimentary records from Ross Sea continental slope/rise are sparse (e.g., Ceccarori et al., 1998). Although five sites at the Ross Sea shelf and slope were drilled during International Ocean Discovery Program Expedition 374 in 2018 (McKay et al., 2019), the detailed scientific analyses are ongoing. Thus, a large gap remains in our understanding of ice shelf and ice sheet changes and their oceanic impacts on the Ross Sea during the late Pleistocene. Furthermore, it is undetermined whether changes in the Ross Sea are synchronous with those in other Antarctic regions, the Southern Ocean (Hillenbrand et al., 2009), and global paleoceanographic records on AABW formation (Hodell and Venz-Curtis, 2006; Elderfield et al., 2012).

KOPRI 극지연구소

Sedimentary facies on the Antarctic continental shelf, including the Ross Sea, are commonly associated with the position of the ice shelf grounding and calving line, but they can also be influenced by the meltwater or mass flow processes (e.g., Domack et al., 1999; McKay et al., 2009, 2012; McGlannan et al., 2017; Simkins et al., 2017; Prothro et al., 2018). Although sediment trap studies in the Ross Sea showed significant fluxes in CaCO3 toward the seafloor (Collier et al., 2000), sediment cores containing CaCO3 in the Ross Sea are extremely limited due to their poor preservation of corrosive bottom water mass (Kennett, 1968; Anderson, 1975; Anderson et al., 2014). Some sediment cores in the outer shelf regions with Circumpolar Deep Water (CDW) influence exhibit high CaCO3 concentrations, but the major constituents are benthic carbonates (e.g., Taviani et al., 1993; Licht et al., 1996; Frank et al., 2014). Due to the limited number of studies on CaCO3 enriched deposits in this setting, there is a lack understanding of 1) the dynamics of surface water CaCO3 changes through time despite significant production in modern surface water and 2) how shifting bottom water properties over time may influence carbonate preservation.

In this study, we developed a multi-proxy record using geochemical (biogenic opal, CaCO3, and total organic carbon (TOC) concentrations), bulk δ15N, physical properties (magnetic susceptibility (MS), water content (WC), and grain density), grain size, and diatom assemblages from two sediment cores in the outermost Ross Sea. These multiproxy records allow for the novel reconstruction of glacial-interglacial changes in surface water productivity, nutrient utilization, current speed, ice rafting, and bottom water mass during the last four glacial-interglacial cycles. We also infer how these paleooceanographic changes may relate to changes in ice sheet and ice shelf coverage on the Ross Sea continental shelf during this time period.

2. Study area

The Iselin Bank is a submarine bank located in the northern edge of the Ross Sea continental shelf break (Fig. 1), and it was not covered by a grounded ice sheet during the last glacial period (Anderson et al., 2002; The RAISED Consortium et al., 2014). Because the Iselin Bank forms a bathymetric high, the bottom water/current in the shelf region flows into adjacent troughs (Dinniman et al., 2011; Smith et al., 2012), and the sedimentation in this region is therefore not significantly influenced by density currents. However, the Iselin Bank is located in the path of Antarctic Slope Current (ASC) which flows westward along the continental slope (Smith et al., 2012). The ASC is characterized by a subsurface front that separates Antarctic Surface Water on the shelf from the CDW on the lower continental slope (Orsi and Weiderwohl, 2009). Because this front serves as a barrier to prevent the transfer of

CDW to the Ross Sea continental shelf (Ainley and Jacobs, 1981; Thompson et al., 2018), ASC vigor may have regulated the intrusion of CDW into the Ross Sea continental shelf and influenced the marine ice sheet variance over past Plio–Pleistocene glacial–interglacial (Naish et al., 2009). Because of the Iselin Bank's relatively shallower water depths, CaCO3 is better preserved in sediments in the Iselin Bank than in deeper water continental slope/rise; however, it is more likely to contain a complete record than that of the glacially–eroded Ross Sea continental shelf. Nevertheless, no detailed sedimentary studies of late Pleistocene records have been conducted from the Iselin Bank.

Although the sea ice coverage in the Ross Sea exhibits large annual variations, an open water polynya typically forms across much of the Ross Sea from December to February (NSIDC, 1998). The average surface chlorophyll and carbon concentrations of the Ross Sea water column are high between November and March, when the seasonal sea ice retreats (Arrigo and van Dijken, 2004). However, major surge of biogenic opal export occurs during the fall sea ice regrowth phase (Collier et al., 2000). The mismatch in surface water production observed in satellite data versus sediment traps is likely the consequence of recycling of phytoplankton blooms in the upper Ross Sea–water column (Collier et al., 2000).

3. Materials and methods

KOPRI 극지연구소

Two sediment cores were collected from the western flank of the Iselin Bank by the IBR/V Araon during the ANA05B cruise in 2015, the 2.57–m–long RS15–GC40 (71°37.004 4′S, 178°17.4630′W, 1083 m in depth) and the 5.4–m–long RS15–GC41 (71°23.0785′S, 178°59.2588′W, 1557 m in depth). Both gravity cores were opened, described, sampled, and analyzed at the Korea Polar Research Institute (KOPRI), South Korea.

3.1. Physical properties (MS, WC, and grain density)

The MS of the two cores were measured at 1–cm intervals on split half–core sections using a Bartington MS–2B susceptibility meter. Before splitting the core sections, whole–round MS values were measured at 1–cm intervals using a core logging sensor (Bartington MS2C). The WC of the two cores was measured at 1–cm intervals on 1–cm–thick sub–samples and was calculated using the following equation with an assumption of 35 psu for seawater:(%) = (mass of wet sediment − (mass of dry sediment + mass of salt))/ mass of wet sediment × 100grain density was measured at 2 cm intervals for RS15–GC40 and 5 cm intervals for RS15–GC41 on 1 cm thick sub–samples using a gas pycnometer (AccuPyc II 1340).

3.2. Geochemical proxies (biogenic opal, TOC, and $CaCO_3$ concentrations)

Geochemical proxies for the two cores were measured from 1-cm-thick samples collected at 5-cm intervals. Biogenic silica (SiBIO) concentrations were measured using a continuous flow analyzer (SKALAR SANplus Analyzer) and the wet-alkaline extraction method modified from DeMaster (1981) at the KOPRI (Kim et al., 2018). Biogenic opal concentrations were calculated by multiplying biogenic silica concentrations by 2.4, the ratio of biogenic opal (SiO_2+nH_2O)/Si that was determined by assuming that nH_2O constitutes 10% of biogenic SiO_2 (Mortlock and Froelich, 1989). The relative analytical error of biogenic silica concentration in sediment samples is less than 1%. Total inorganic carbon (TIC) concentration was measured using UIC CO_2 coulometer (Model CM5240) at the KOPRI. $CaCO_3$ concentrations were calculated by multiplying TIC concentrations by 8.333, the ratio of $CaCO_3$/C. The relative standard deviation for $CaCO_3$ concentration is ±1%. Total carbon (TC) concentration was measured using an organic elemental analyzer (FLASH 2000 NC Analyzer) with an analytical precision of less than ±0.1%. TOC concentrations were calculated as the difference between TC and TIC.

3.3. Bulk $\delta^{15}N$ values

Bulk δ15N values for the two cores were measured at 5-cm intervals using Europa Scientific RoboPrep-CN elemental analyzer and Europa Scientific 20-20 isotopic ratio mass spectrometer from Iso-Analytical Ltd., UK. Nitrogen isotope ratios were expressed in the conventional delta notation, which is the per mil deviation from atmospheric nitrogen. The precision for nitrogen isotopes was approximately ±0.2□.

3.4. Grain size analysis

After removing the organic matter and biogenic silica from the bulk sediments using 10% H2O2 and 2N NaOH, respectively, grain size was analyzed at-4 cm intervals for the two cores. Coarser fractions (> 63 um) were weighed at 1-phi intervals using sieves, while finer fractions (< 63 um) were analyzed using a Micrometrics Sedigraph III 5120 at the KOPRI. The classification of sediments follows that of Folk and Ward (1957).

3.5. Diatom assemblage analysis

Thirty-two diatom assemblage samples for RS15-GC41 containing either a high or low biogenic opal concentration were analyzed at approximately 15-cm intervals. Due to the

low abundances in many samples, up to 200 diatom specimens were counted. For samples with extremely low diatom abundances, 200 microscope fields of view were observed and counted. The sample preparation and diatom counting methods followed those described in Bak et al. (2007). The quantitative analysis of the diatom slides followed the procedures described in Scherer (1994). Absolute abundance was calculated using the following equation: abundance = ((A × B)/(C × D))/E, where A is the number of specimens counted, B is the area of the settling chamber, C is the number of microscope fields of view, D is the area of the field of view, and E is the sample mass. Chaetoceros resting spores were not included in the specimen count.

3.6. Radiocarbon dating

Accelerator mass spectrometry (AMS) 14C dates were either measured using the planktonic foraminifer Neogloboqudria pachyderma (sin.) or using a mixture of planktonic and benthic foraminifers. Four intervals in RS15-GC40 and two intervals in RS15-GC41 were dated at Beta Analytic, USA or Rafter Radiocarbon, New Zealand (Table 1). Beta Analytic also provided the $\delta^{18}O$ values of the carbonate materials (Fig. 2).

KOPRI
극지연구소

4. Age model

The radiocarbon age results were calibrated using CALIB 7.1 (Stuiver et al. 1993) and the MARINE dataset (Reimer et al., 2013). Although there is a large variation in ΔR from 480 yr to 990 yr in the Antarctic regions (e.g, Domack 1992; Domack et al., 2001; Wu et al., 2017; Christ et al., 2015; Hillenbrand et al., 2010; Kim et al., 2018), we used a ΔR of 900 years. Regardless of which reservoir ages are used, the chronological framework for the two cores is nearly the same considering the time scales for the two cores. We used planktonic foraminifer AMS 14C dates as the tie points for the uppermost sediments which constrain the timing of the Last Glacial Maximum to 26.5 ka to 19 ka (Clark et al., 2009) for both cores (Fig. 2). The ages of 19.5 ka at 3 cm and 24.5 ka at 5 cm in RS15-GC40 (Table 1) may be related to potential disturbance of the core top during the coring process and suggests potential core top loss, particularly for the Holocene section of RS15-GC40. The $\delta^{18}O$ values of planktonic foraminifers used for age dating correspond to the LR-04 variations (Fig. 2), and the planktonic foraminifer AMS 14C ages appear to be reliable.

Because of the lack of continuous $\delta^{18}O$ stratigraphy in the Southern Ocean, previous studies covering the late Quaternary in Antarctica have constrained ages by using correlations between surface water productivity proxies such as biogenic opal/silica and Ba concentration,

either measured directly or scanned using X-ray fluorescence, with an assumption that surface water productivity is high during warm periods with less sea ice (e.g., Ceccareni et al., 1998; Hillenbrand et al., 2009; Wu et al., 2017). The MS is typically negatively correlated with biogenic components in Southern Ocean sediments (e.g., Ceccaroni et al., 1998; Hillenbrand et al., 2009; Yoon et al., 2009; Sprenk et al., 2013). RS15-GC40 and RS15-GC41 also demonstrate negative correlations with biogenic components (Fig. S1). As a result, high MS values typically occur during glacial periods (e.g., Ceccaroni et al., 1998; Hillenbrand et al., 2009). Therefore, we graphically correlate whole-round MS values with the LR04 δ18O stack using Analyseries software (Paillard et al., 1996) (Fig. 2 and Table 2). As gravel-sized grains are dispersed randomly throughout the two cores, whole-round MS values are thought to be more representative of the bulk sediment than point MS values which can be biased toward single large grains. Although the LR04 δ18O stack does not directly reflect Antarctic climate changes, the variation pattern is nearly identical to that of the EPICA Dome C (EDC) ice core δD record (Jouzel et al., 2007) (Fig. 2). The age model tie points are not a unique solution, and the visual tuning approach broad minima ties in MS occurr approximately every 1.2 m to the last four full interglacial periods in the LR04 stack and in the δD record from the EDC ice core (Fig. 2). We minimize the number of these ties and focus our interpretations of these cores on the differences in oceanographic conditions between the last four glacial-interglacial cycles since marine isotope stage (MIS) 11. The assumption that a high MS corresponds to glacial periods is further assessed, though comparisons to geochemical proxies and diatom assemblages (Figs. 3 and 4).

KOPRI 극지연구소

5. Results

The MS values of RS15-GC40 and RS15-GC41 are generally high (>100 10-5 SI) during glacial periods and low (<100 10-5 SI) during interglacial periods (Fig. 3). In contrast, WC, biogenic opal, and TOC concentrations display the opposite pattern, with high values during interglacial periods and low values during glacial periods (Fig. 3). Interglacial biogenic opal concentration peaks gradually decrease after MIS 11 in both cores (Fig. 3). TOC concentrations are generally lower than 0.2%, except for those in the core top (Fig. 3). MS values are higher for RS15-GC40 than RS15-GC41 (Fig. 3), and they display an inverse relationship with WC, suggesting that grain size (and the associated porosity) is a primary control on MS values. This inference is supported the sand percent values, where high sand percentages are related to higher MS values (Fig. 2). $CaCO_3$ concentration at the two cores is generally low (or absent) during interglacial periods and high (>5%) during glacial periods (Fig. 3). RS15-GC41 exhibits sparse $CaCO_3$ peaks at 21 ka, 298 ka, 342 ka, and 363 ka,

whereas RS15-GC40 shows broader and more frequent $CaCO_3$ peaks during glacial periods and some interglacial intervals with low biogenic opal concentrations (Fig. 3). The total diatom valve abundance of RS15-GC41 is inconsistent with biogenic opal concentration (Fig. 3). The diatom preservation status was generally poor, and the sea ice diatoms Fragilariopsis curta and F. cylindrus (Sjunneskog and Taylor, 2002; Armand et al., 2005) were not observed. However, other Antarctic sea ice related diatoms, F. ritscheri, Actinocyclus actinochilus, and F. sublinearis (Armand et al., 2005), were observed for RS15-GC41. In general, these sea ice diatoms were rare during high biogenic opal and TOC intervals, but were abundant during low biogenic opal and TOC intervals, and they are associated with a concomitant increase in Eucampia antarctica var. recta, a cold-water species (Leventer et al., 2002) (Fig. 4). Sea ice-related species and E. antarctica var. recta occur in higher abundances following MIS 8 (Fig. 4). The abundances of Chaetoceros resting spores vary and are typically low, and they are only found during intervals of high biogenic opal and TOC (Fig. 4). F. kerguelensis is typically absent until MIS 7 and begins to appear more abundantly during interglacial periods (Fig. 4).

RS15-GC40 is characterized by a coarser mean grain size (MGS) than that of RS15-GC41 due to its greater abundance of coarse grains (sand and gravel) (Fig. 2). The high gravel and sand contents in both cores coincide with high MS values, coarser MGSs, and coarse-skewed grain size distributions, whereas the mud content increases with lower MS intervals characterized by high biogenic opal and TOC concentrations (Figs. 2 and 3).

Bulk δ15N values of the two cores vary from 3□ to 6□ (Fig. 3). Bulk δ15N values increased during interglacial periods, particularly for high biogenic opal and TOC concentration intervals (Fig. 3). In contrast, the C/N ratios of the two cores demonstrated the opposite pattern; they were low during interglacial periods and high during glacial periods, although the C/N ratio of RS15-GC40 is higher than that of RS15-GC41 (Fig. 3).

Variations in biogenic opal, TOC, and $CaCO_3$ MARs are similar to the variations in their concentrations (Figs. 3 and 4). LSRs are high during interglacial periods and low during glacial periods. The highest LSRs occur during intervals of high biogenic opal and TOC concentrations (Figs. 3 and 4).

6. Discussion

RS15-GC40 is mainly composed of clast-rich muddy sand with well-preserved planktonic foraminifers and gradational lower contacts passing into diatom-bearing mud. RS15-GC41 is composed of interbedded clast-common/rich sandy mud to muddy sand and diatom-bearing mud. We interpret that both sites experienced alternations between interglacial

open marine (diatom-bearing mud) and glacial ice proximal/extensive sea ice conditions with ice-rafting (clast-rich/common sandy mud to muddy sand). However, although these gravel grains were likely delivered by icebergs, increases in gravel are unlikely to directly relate to the dynamic ice processes, as the coarser grain concentrations may result from the winnowing processes. The occurrence of winnowing is supported by low proportions of very fine sand to coarse grains (>63 um) (Fig. 5). The co-variation in MS and grain size indicates that the MS variation is primarily controlled by grain size, which likely relates to the presence of mafic lithologies in the sand fraction (Fig. 2). Because coarse-skewed grain size distributions in the Ross Sea outer shelf indicates the winnowing of fine materials (Prothro et al., 2018), increased skewness during intervals of high MS and gravel concentrations in the two cores indicates stronger bottom currents during glacial periods that winnowed or prevented the settling of finer-grained material at the site (Fig. 2). Despite these stronger currents, the glacial intervals of the two cores are characterized by depositions of well-preserved planktonic foraminifers, sea ice related diatoms, and E. antarctica var. recta. Consequently, the two core records are considered to reflect both surface and bottom paleoceanographic changes in the Ross Sea over the last 400 kyrs. However, increased skewness is found within the interglacial periods, such as MIS 11, 7, and 5, implying that the Ross Sea paleoceanographic changes are controlled by not only 100-kyr cycles but also by shorter 41-kyr cycles.

KOPRI 극지연구소

6.1. Glacial-interglacial surface water productivity changes and associated nutrient utilization changes

The co-variations of biogenic opal and TOC at the two core sites suggest that TOC is mainly controlled by surface water diatom production (Figs. 3 and S1). Thus, lower C/N ratios during interglacial periods indicate that high biogenic opal and TOC concentrations during interglacial periods are related to increased surface water productivity in the study area because marine organic matter has a lower C/N ratio than that of terrestrial organic matter (Lamb et al., 2006 and references therein). Although terrestrial organic matter is likely to be very low in the Antarctic, the Ross Sea sediment trap record (Mooring MS-6) exhibited a seasonally lower C/N ratio during the open ocean period than that during the sea ice covered period (Collier et al., 2000), implying that a low C/N ratio is attributed to marine organic matter. In Antarctic shelf regions, surface water productivity increases as the ice shelf/sea ice retreats, particularly under open ocean conditions (Leventer and Dunbar 1988; Cunningham et al., 1999; Domack et al., 1999; Collier et al., 2000; McKay et al., 2008; Naish et al., 2009; Prothro et al., 2018). A low MS and grain density, fine MGS, and high WC are exhibited during interglacial periods (Fig. 3), with low MS values being the consequence of increasing biogenic inputs and increased mud content. Biogenic components have lower densities than

those of lithic grains, and WC increases with an increase in mud content and/or biogenic opal concentration in the sediment (e.g., Domack et al., 1999; McKay et al., 2016, Fig. S1). Thus, the characteristics of physical properties during interglacial periods imply that higher surface water productivity occurred under more open ocean conditions in the Iselin Bank region. Although decreased current speed can increase settling of biogenic material, an open ocean during interglacial periods is also supported by the increased relative abundance of the open ocean diatom species F. kerguelensis (Crosta et al., 2005) (Fig. 4).

Bulk $\delta^{15}N$ values in the two cores and surface water production increased during interglacial periods (Fig. 4). Because bulk δ15N is used as a nutrient utilization proxy, increased $\delta^{15}N$ values indicate enhanced nitrate utilization in the Ross Sea during interglacial periods due to increased surface water production (e.g., Robinson et al., 2014; Kim et al., 2018 and references therein). Chaetoceros resting spores predominantly occur in high biogenic opal and TOC intervals (Fig. 4) and are commonly interpreted as indicating high primary production resulting from surface water stratification due to melt water (Leventer, 1991; Stockwell, 1991; Leventer et al., 1996; Sjunneskog and Taylor, 2002; Crosta et al., 2005). Thus, the high surface water productivity and nutrient limitation during interglacial periods occurs under a more stratified open ocean. This is presented as a schematic paleoceanographic model for interglacial periods (Fig. 6).

Glacial periods are characterized by low biogenic opal concentration, low TOC concentration, low WC, low bulk $\delta^{15}N$, high MS, high grain density, and high C/N ratio, and coarse MGS with abundant coarse grains (Fig. 3). The glacial characteristics indicate 1) low surface water productivity with low nitrate utilization; and 2) siliclastic influence derived from a glacimarine source. The dominant diatom species during glacial periods are sea ice related species and cold-water species, including E. antarctica var. recta (Fig. 4). Prothro et al. (2018) reported that calcareous foraminifera specimens dominate in an ice-proximal environment, which is consistent with previous observations that the abundance of N. pachyderma (sin.) in Antarctic continental shelves can be used as a proxy for ice shelf calving and the melting of ice masses close to ice marginal zones (Kellogg and Kellogg, 1988; Anderson et al., 1991). Previous studies found that a high abundance of N. pachyderma (sin.) occurred during the Last Glacial Maximum, and they linked this finding to the increased presence of sea ice (Bonaccori and Mellis, 2001). In addition, Asioli and Langone (1997) suggested that the occurrence of N. pacyderma (sin.) is related to annual sea ice conditions, and abundant living N. pacyderma (sin.) were found in sea ice in the Ross and Weddell Seas (Sprindler and Diekman, 1986; Dieckmann et al., 1991; Quaia and Cespuglio, 2000). Thus, glacial sediments in the Iselin Bank area are deposited under cold and extensive sea ice conditions in close proximity to ice shelves or grounded ice sheet margins providing meltwater. Chase et al. (2015) reported that biogenic opal concentration and nutrient

utilization decreases southward from the Antarctic Polar Front as sea ice duration increases. This is due to the light limitation resulting from the extensive sea ice cover, which restricts surface water productivity and decreases nitrate utilization during glacial periods in the Iselin Bank region. This result is supported by our observation of a high relative abundance of sea ice-related diatoms coinciding with low surface water productivity (Fig. 4).

In addition, higher C/N ratios indicate the relative increase in terrestrial input, which can decrease marine productivity and potentially increase glacimarine influence (and thus reworked terrestrial organic matter) due to the existence of more proximal ice masses. Abundant gravel grains, coarser MGS, skewness in grain size distributions, and coarse grain sizes indicate stronger bottom currents during glacial periods that restricted the deposition of fine grain clay. Given that this site is currently predominately influenced by zonal wind-driven ASC flows (Smith et al., 2012), stronger currents may have occurred during glacial periods in these locations (Thompson et al., 2018 and references therein). This theory is also supported by previous observations that calcareous foraminifera specimens dominate in higher-energy current settings in the Ross Sea continental margin (Prothro et al., 2018). The glacial paleoceanographic conditions are presented in a schematic model (Fig. 6).

6.2. Variation in $CaCO_3$ in the Ross Sea and its implication for bottom water mass change during the late Pleistocene

KOPRI 극지연구소

$CaCO_3$ peaks, mostly planktonic foraminifers, in RS15-GC40 and RS15-GC41 occurred mostly during glacial periods, and $CaCO_3$ was better preserved in RS15-GC40 (1083 m in water depth) than in RS15-GC41 (1557 m in water depth) due to the shallower water depth of RS15-GC40 (Fig. 3). This indicates that the water column in the Ross Sea became less corrosive during glacial periods, which was potentially due to the accumulation of siliceous detritus on the sea floor that facilitated the decay of organic matter and dissolution of calcareous foraminifers (Kennett, 1968). Conversely, strong bottom currents during glacial periods for RS15-GC40 and RS15-GC41 raised the $CaCO_3$ preservation by restrictig fine material deposition (Taviani et al., 1993; Anderson, 1999; Frank et al., 2014). This is supported by the fact that $CaCO_3$ increases only occur during intervals of low biogenic opal and TOC concentrations and with coarse MGSs (Fig. S1).

6.3. Implications of Antarctic Slope Currents variations during the late Pleistocene

Intrusions of CDW into the Ross Sea continental shelf area are largely regulated by current speed at the continental shelf edge, providing heat and salinity which have implications for marine ice sheet mass balance and the formation of dense waters on the

continental shelf (Jacobs 1970; Orsi and Weiderwohl, 2009; Gordon, 2009; Jacobs et al., 2011; Pritchard et al., 2012). The continental shelf exposure to open ocean and floating ice shelves, is important for dense water formation in the Antarctic continental shelf (Yabuki et al., 2016). However, as the marine-based Antarctic ice sheet terminated near the continental shelf break in the Ross Sea, the size of the Ross ice shelf cavity was also greatly reduced during the last glacial period (Anderson et al., 2002; Halberstadt et al., 2016), and this likely resulted in less continental shelf dense water formation. Thus, the enhanced bottom current at the Iselin Bank is unlikely to be directly related to the cascading density flows of super-cooled, saline shelf waters. Carbonate organisms are often found with benthic carbonates in outer shelf regions where there is enriched nutrient delivery by impinging CDW (Elverhoi and Roaldset, 1983; Taviani et al., 1993; Anderson, 1999). However, because the dominant component of CaCO3 in RS15-GC40 and RS15-GC41 is planktonic foraminifer, either surface water conditions allowed for the increased productivity of foraminifera, or there was less CDW influence. Because the ASC currently flows along the Iselin Bank (Smith et al., 2012, Fig. 1) and is wind-driven (Thopson et al., 2018), the winnowing is most likely related to the enhanced ASC strength under windier glacial conditions, which is evidenced by the EDC ice core dust record (Fig. 5; Jouzel et al., 2007). Thus, it is revealed that winnowing mechanisms are regulated by shifts in wind speeds that govern ASC flow in the Iselin Bank during glacial periods.

The Weddell Sea has a wide shelf area and is a major contributor to AABW formation, which plays an important role in the deposition of $CaCO_3$ (Berger, 1970). Anderson (1975) reported that $CaCO_3$ dissolution in the Weddell Sea is related to water mass, particularly saline shelf water. Considering the similarities between the Ross Sea and the Weddell Sea, dense shelf water in the Ross Sea is considered to be undersaturated with respect to $CaCO_3$. Thus, the improved preservation of $CaCO_3$ can be attributed to the weakened formation of dense shelf water in the Ross Sea. CDW intrusion was weakened due to 1) the reduced shelf dense water formation in the Ross Sea and 2) a strong ASC acting as a hydrographic barrier to prevent CDW intrusion. Great $CaCO_3$ preservation can occur due to reduced CO2-rich CDW. Thus, we propose that the improved preservation of CaCO3 in the Iselin Bank is due to a combination of the restriction of fine siliceous detritus inputs and reduced influence of both CDW and shelf dense water during glacial periods. The glacial-interglacial $CaCO_3$ variation is shown in the schematic model (Fig. 6). However, because of the complicated bathymetry in the Ross Sea, there are likely to regional oceanographic differences; thus, to understand the entire temporal $CaCO_3$ variation system of the Ross Sea, additional studies are required.

7. Conclusions

In this study, the concentrations of biogenic opal, $CaCO_3$, and TOC, and bulk nitrogen isotopes, physical properties, and diatom assemblages of RS15-GC40 and RS15-GC41 were measured to reconstruct glacial-interglacial paleoceanographic changes during the late Quaternary period in the Ross Sea, including changes in surface water productivity, nutrient utilization, and bottom water mass ventilation. The main findings of this study are as follows:

1. The sedimentation rates and sedimentary compositions of the two cores are strongly correlated with both surface and bottom oceanographic changes associated with ice sheet/shelf dynamics. In addition, paleoceanographic records in the Iselin Bank display cyclic variations consistent with orbital-scale variations observed in ice core and deep sea benthic isotope records.

2. High surface water productivity with enhanced nutrient utilization occurred under open marine conditions during interglacial periods. The co-occurrence of Chaetoceros resting pores indicates nutrient limitation under stratified surface water conditions.

3. Low surface water productivity with incomplete nutrient utilization occurred under extensive sea ice/ice proximal conditions during glacial periods, implying that there was light limitation due to the sea ice.

4. Grain size and $CaCO_3$ records indicate strong bottom currents during glacial periods that prevented the deposition of fine sediment and diatom frustules (winnowing). The intensified bottom currents during glacial periods were interpreted to be induced by wind-driven ASC.

5. $CaCO_3$ (mainly planktonic foraminifers) preservation in the Iselin Bank improved during glacial periods due to 1) the strong bottom current causing less organic matter decomposition by sweeping away fine materials and 2) the influence of grounded ice sheets on the continental shelf restricting the formation of corrosive dense shelf water that was undersaturated with respect to $CaCO_3$.

KOPRI 극지연구소

로스해에서 플라이스토세 후기 동안의 고해양학적 변화 – 고생산성, 영양염 이용률, 심층수 형성의 빙하기–간빙기 변동

김성한[a,*], 이재일[a], Robert M. McKay[b], 유규철a, 박영숙[c], 이민경[a], 노연호[a,d], 윤호일[a], 문흥수[a], 현창욱[a]

[a]극지연구소, [b]Victoria University of Wellington, [c]전북대학교, [d]UST과학기술연합대학원대학교

요약: 로스해 외대륙붕은 플라이스토세 동안 광범위한 빙상의 변동을 겪었다. 이러한 변동은 대륙붕단에서 서쪽으로 흐르는 남극사면해류의 변화에 의해 크게 조절된다. 이 해류는 남쪽으로 들어와 빙붕의 하부를 녹이는 비교적 따뜻한 남극환류의 유입을 조절한다. 그리고 대륙붕에서 기저면에 닿아있는 빙상의 확장은 로스해의 수괴 형성 과정을 변화 시키고, 이는 표층해수 염분, 해빙 분포, 영양염 이용률, 심층순환과 표층생산성에 영향을 미친다. 여기서 우리는 플라이스토세 후기의 기록을 지화학, 물성자료, 입도, 안정질소동위원소, 규조 기록을 로스해 대륙붕 가장 바깥쪽에 위치한 이셀린 퇴에서 획득된 두 코어 정점에서 복원하였다. 이들 코어 사이트는 플라이스토세 후기 동안의 빙하기–간빙기 순환에서 빙상에 의해 덮이지 않았던 곳이라, 연속적인 빙해양환경의 기록을 잘 가지고 있을 것으로 생각된다. 간빙기 동안에는 높은 표층생산성과 높은 영양영 이용률이 나타났고, Chaetoceros resting spore가 함께 나타났고 이것은 공해환경에서 영양염의 제한이 일어났다는 것을 의미한다. 그리고 빙하기 동안에는 낮은 표층생산성과 함께 낮은 영양염 이용률이 나타났으며, 해빙환경에서 서식하는 규조류가 발견되었으며, 부유성 유공충이 함께 나타났다. 이러한 환경은 해빙이 광범위하게 발달하고, 얼음의 마진에서 빛에 의한 제한이 일어났음을 의미한다. 입도 분석의 결과 추운 빙하기 동안 조립한 부분으로 치우친 첨도 분포와 위노잉잉 일어났다는 것을 확인해 준다.이러한 winnowing은 대륙붕에서 심해로 흘러가는 대륙붕고밀도수 보다는 남극 사면해류와 관련이 되는 것으로 보인다.

참고 문헌

Ainley, D.G., Jacobs, S.S., 1981. Sea-bird affinities for ocean and ice boundaries in the Antarctic. Deep Sea Res. Part Oceanogr. Res. Pap. 28, 1173-1185, doi:10.1016/0198-0149(81)90054-6.

Anderson, J.B., 1975. Factors controlling CaCO3 dissolution in the Weddell Sea from foraminiferal distribution patterns. Mar. Geol. 19, 315-332.

Anderson, J.B., 1999. Antarctic Marine Geology. Cambridge University Press, Cambridge.

Anderson, J.B., Conway, H., Bart, P.J., Witus, A.E., Greenwood, S.L., McKay, R.M., Hall, B.L., Ackert, R.P., Licht, K., Jakobsson, M., Stone, J.O., 2014. Ross Sea paleo-ice sheet drainage and deglacial history during and since the LGM. Quat. Sci. Rev. 100, 31-54.

Anderson, J.B., Kennedy, D.S., Smith, M.J., Domack, E.W., 1991. Sedimentary facies associated with Antarctica's floating ice masses. In: Anderson, J.B., Ashlye, G.M., (Eds.), Glacial Marine Sedimentation; Paleoclimatic significance. Boulder, Colorado, GSA Special Paper 261.

Anderson, J.B., Shipp, S.S., Lowe, A.L., Wellner, J.S., Mosola, A.B., 2002. The Antarctic Ice Sheet during the Last Glacial Maximum and its subsequent retreat history: a review. Quat. Sci. Rev. 21, 49-70.

Anderson, J.B., Simkins, L.M., Bart, P.J., De Santis, L., Halberstadt, A.R.W., Olivo, E., Greenwood, S.L., 2019. Seismic and geomorphic records of Antarctic Ice Sheet evolution in the Ross Sea controlling factors in its behavior. Geol. Soc. London. Spec. Publ. 475, 223-240, doi:10.1144/SP475.5.

Armand, L.K., Crosta, X., Romero, O., Pichon, J.J., 2005. The biogeography of major diatom taxa in Southern Ocean sediments: 1. Sea ice related species. Palaeogeogr. Palaeoclimatol. Palaeoecol. 223, 93-126.

Arrigo, K.R., van Dijken, G.L., 2004. Annual changes in sea-ice, chlorophyll a, and primary production in the Ross Sea, Antarctica. Deep-Sea Res. II 51, 117-138.

Asioli, A., Langone, L., 1997. Relationship between recent planktonic foraminifera and water mass properties in the western Ross Sea (Antarctica). Geogr. Fis. Dinam. Quat. 20, 193-198.

Bak, Y.-S., Yoo, K.-C., Yoon, H.I., Lee, J.-D., Yun, H., 2007. Diatom evidence for Holocene paleoclimatic change in the South Scotia Sea, West Antarctica. Geosci. J. 11, 11-22.

Bart, P.J., Sjunneskog, C., Chow, J.M., 2011. Piston-core based biostratigraphic constraints on Pleistocene oscillations of the West Antarctic Ice Sheet in western Ross Sea between North

KOPRI 극지연구소

Basin and AND-1B drill site. Mar. Geol. 289, 86-99, doi:10.1016/j.margeo.2011.09.005.

Berger, W.H., 1970. Biogenous deep-sea sediments: fractionation by deep-sea circulation. Geol. Soc. Am. Bull. 81, 1385-1402.

Bintanja, R., van de Wal, R.S.W., Oerlemans, J., 2005. Modelled atmospheric temperatures and global sea levels over the past million years. Nature 437, 125-128.

Bonaccorsi, R., Melis, R., Persistence of living planktonic foraminifera (Neogloboquadrina pachyderma) in Antarctic sea-ice inferred from a study of a sediment core (Ross Sea continental margin), 2001. In: Chela-Flores, J., Owen, T., Raulin, F. (Eds.), First steps in the orgin of life in the Universe. Springer, Dordrecht, 255-260.

Ceccarori, L., Frank, M., Frignani, M., Langone, L., Ravaioli, M., Mangini, A., 1998. Late Quaternary fluctuations of biogenic component fluxes on the continental slope of the Ross Sea, Antarctica. J. Mar. Syst. 17, 515-525.

Chase, Z., Kohfeld, K.E., Matsumoto, K., 2015. Controls on biogenic silica burial in the Southern Ocean. Global Biogeochm. Cycles 29, 1599-1616, doi:10.1002/2015GB005186.

Christ, A.J., Talaia-Murray, M., Elking, N., Domack, E.W., Leventer, A., Lavoie, C., Brachfeld, S., Yoo, K.-C., Gilbert, R., Jeong, S.-M., Petrushak, S., Wellner, J., the LARISSA Group, 2015. Late Holocene glacial advance and ice shelf growth in Barilari Bay, Graham Land, west Antarctic Peninsula. Geol. Soc. Am. Bull. 127, 297-315, doi:10.1130/B31035.1.

Clark, P.U., Dyke, A.S., Shakun, J.D., Carlson, A.E., Clark, J., Wohlfarth, B., Mitrovica, J.X., Hostetler, S.W., McCabe, A.M., 2009. The Last Glacial Maximum. Science 325, 710-714, doi:10.1126/science.1172873.

Collier, R., Dymond, J., Honjo, S., Manganini, S., Francois, R., Dunbar, R., 2000. The vertical flux of biogenic and lithogenic material in the Ross Sea: moored sediment trap observations 1996-1998. Deep-Sea Res. II 47, 3491-3520.

Crosta, X., Romero, O., Armand, L.K., Pichon, J.J., 2005. The biogeography of major diatom taxa in Southern Ocean sediments: 2. Open ocean related species. Palaeogeogr. Palaeoclimatol. Palaeoecol. 223, 66-92.

Cunningham, W.L., Leventer, A., Andrews, J.T., Jennings, A.E., Licht, K.L., 1999. Late Pleistocene-

Holocene marine conditions in the Ross Sea, Antarctica: evidence from the diatom record. The Holocene 9, 129-139.

DeMaster, D.J., 1981. The supply and accumulation of silica in the marine environment. Geochim. Cosmochim. Acta 5, 1715-1732.

Diekmann, G.S., Spindler, M., Lange, M.A., Ackley, S.F., Eicken, H., 1991. Antarctic sea ice:

a habitat for the foraminifer Neogloboquadrina pachyderma. J. Foramin. Res. 21, 182-189.

Dinniman, M.S., Klinck, J.M., Smith Jr., W.O., 2011. A model study of Circumpolar Deep Water on the West Antarctic Peninsula and Ross Sea continental shelves. Deep-Sea Res. II 58, 1508-1523.

Domack, E.W., 1992. Modern carbon-14 ages and reservoir corrections for the Antarctic Peninsula and Gerlache Strait area. Antarctic Journal of the United States 27, 63-64.

Domack, E.W., Leventer, A., Dunbar, R., Taylor, F., Brachfeld, S., Sjunneskog, C., Cowan, E., Daniels, J.W., Escutia, C., Evans, A., Eyles, N., Guyodo, Y., Ioio, M., Iwai, M., Kyte, F., Lauer, C., Maldonado, A., Morez, T., Osterman, L., Pudsey, C., Schuffert, J., Vigar, K., Weinheimer, A., Williams, T., Winter, D., Wolf-Welling, T.C.W., 2001. Chronology of the Palmer Deep site, Antarctic Peninsula: A Holocene palaeoenvironmental reference for the circum-Antarctic. The Holocene 11, 1-9, doi:10.1191/095968301673881493.

Domack, E.W., Jacobson, E.A., Shipp, S., Anderson, J.B., 1999. Late Pleistocene-Holocene retreat of the West Antarctic Ice-Sheet system in the Ross Sea: Part 2-Sedimentologic and stratigraphic signature. Geol. Soc. Am. Bull. 111, 1517-1536.

Elderfield, H., Ferretti, P., Greaves, M., Crowhurst, S., McCave I.N., Hodell, D., Piotrowski, A.M., 2012. Evolution of ocean temperature and ice volume through the mid-Pleistocene climate transition. Science 337, 704-709.

Elverhoi, A., Roaldset, E., 1983. Glaciomarine sediments and suspended particulate matter, Weddell Sea shelf, Antarctica. Polar Res. 1, 1-21.

Folk, R.L., Ward, W.C., 1957. Brazos River bar [Texax]; a study in the significance of grain size parameters. J. Sediment. Res. 27, 3-26.

Frank, T.D., James, N.P., Bone, Y., Malcolm, I., Bobak, L.E., 2014. Late Quaternary carbonate deposition at the bottom of the world. Sediment. Geol. 305, 1-16, doi:10.1016/j.sedgeo.2014.02.008.

Gordon, A.L., 2009. Bottom water formation. In: Steele, J.H., Thorpe, S.A., Turekian, K.K. (Eds.), Ocean currents. Associated Press, 263-269.

Halberstadt, A.R.W., Simkins, L.M., Greenwood, S.L., Anderson, J.B., 2016. Past ice-sheet behavior: retreat scenarios and changing controls in the Ross Sea, Antarctica. The Cryosphere 10, 1003-1020, doi:10.5194/tc-10-1003-2016.

Hillenbrand, C.D., Kuhn, G., Frederichs, T., 2009. Record of a Mid-Pleistocene depositional anomaly in West Antartic Continental margin sediments: an indicator for ice-sheet collapse?. Quat. Sci. Rev. 28, 1147-1159.

Hillenbrand, C.D., Larter, R.D., Dowdeswell, J.A., Ehrmann, W., Cofaigh, C.Ó., Benetti, S., Graham, A.G.C., Grobe, H., 2010. The sedimentary legacy of a palaeo-ice stream on

the shelf of the southern Bellingshausen Sea: Clues to West Antarctic glacial history during the Late Quaternary. Quat. Sci. Rev. 29, 2741-2763.

Hodell, D.A., Venz-Curtis, K.A., 2006. Late Neogene history of deepwater ventilation in the Southern Ocean. Geochem. Geophys. Geosyst. 7, Q09001, doi:10.1029/2005GC001211.

Jacobs, S.S., Jenkins, A., Giulivi, C.F., Dutrieux, P., 2011. Stronger ocean circulation and increased melting under Pine Island Glacier ice shelf. Nat. Geosci. 4, 519-523, doi:10.1038/ngeo1188.

Jouzel, J., Masson-Delmotte, V., Cattani, O., Dreyfus, G., Falourd, S., Hoffmann, G., Minster, B., Nouet, J., Barnoloa, J.M., Chappellaz, J., Fischer, H., Gallet, J.C., Johnsen, S., Leuenberger, M., Loulergue, L., Luethi, D., Oerter, H., Parrenin, F., Raisbeck, G., Raynaud, D., Schilt, A., Schwander, J., Selmo, E., Souchez, R., Spahni, R., Stauffer, B., Steffensen, J.P., Stenni, B., Stocker, T.F., Tison, J.L., Werner, M., Wolff, E.W., 2007. Orbital and millennial Antarctic climate variability over the past 800,000 years. Science 317, 793-796.

Kellogg, T.B., Kellogg, D.E., 1988. Antarctic cryogenic sediments: Biotic and inorganic facies of ice shelf and marine-based ice sheet environments. Palaeogeogr. Palaeoclimatol. Palaeoecol. 67, 51-74.

Kennett, J.P., 1968. The fauna of the Ross Sea: part 6: ecology and distribution of foraminifera. Dept. Sci. Ind. Res. Bull. 186, 1-47.

Kim, S. ,Yoo, K.C., Lee, J.I., Khim, B.K., Bak, Y.S., Lee, M.K., Lee, J., Domack, E.W., Christ, A.J., Yoon, H.I., 2018. Holocene paleoceanography of Bigo Bay, west Antarctic Peninsula: Connections between surface water productivity and nutrient utilization and its implication for surface-deep water mass exchange. Quat. Sci. Rev. 192, 59-70, doi:10.1016/j.quascirev.2018.05.028.

Lamb, A.L., Wilson, G.P., Leng, M.J., 2006. A review of coastal palaeoclimate and relative sea-level reconstructions using δ13C and C/N ratios in organic material. Earth Sci. Rev. 75, 29-57.

Leventer, A., 1991. Sediment trap diatom assemblages from the northern Antarctic Peninsula region. Deep Sea Res. 38, 1127-1143.

Leventer, A., Domack, E.W., Ishman, S.E., Brachfeld, S., McClennen, C.E., Manley, P.L., 1996. Productivity cycles of 200-300 years in the Antarctic Peninsula region: Understanding likages among the sun, atmosphere, oceans, sea ice, and biota. Geol. So. Am. Bull. 108, 1626-1644, doi:10.1130/0016-7606(1996)108<1626:PCOYIT>2.3.CO;2.

Leventer, A., Domack, E.W., Barkoukis, A., McAndrews, B., Murray, J., 2002. Laminations from the Palmer Deep: A diatom-based interpretation. Paleoceanography 17, 8002,

doi:10.1029/2001PA000624.

Leventer, A., Dunbar, R.B., 1988, Recent diatom record of McMurdo Sound, Antarctica: Implications for the history of sea-ice extent: Paleoceanography 3, 259-274.

Licht, K.J., Jennings, A.E., Andrews, J.T., Williams, K.M., 1996, Chronology of late Wisconsin ice retreat from the western Ross Sea, Antarctica. Geology 24, 223-226.

Licht, K.J., Dunbar, N.W., Andrews, J.T., Jennings, A.E., 1999. Distinguishing subglacial till and glacial marine diamictons in the western Ross Sea, Antarctica: Implications for a last glacial maximum grounding line. GSA Bulletin 111, 91-103.

Lisiecki, L.E., Raymo, M.E., 2005. A Pliocene-Pleistocene stack of 57 globally distributed benthic δ18O records. Paleoceanography 20, PA1003, doi:1029/2004PA001071.

Lüthi, D., Le Floch, M., Bereiter, B., Blunier, T., Barnola, J.M., Siegenthaler, U., Raynaud, D., Jouzel, J., Fischer, H., Kawamura, K., Stocker, T.F., 2008. High-resolution carbon dioxide concentration record 650,000-800,000 years before present. Nature 453, 379-382.

McGlannan, A.J., Bart, P.J., Chow, J.M., DeCesare, M., 2017. On the influence of post-LGM ice shelf loss and grounding zone sedimentation on West Antarctic ice sheet stability. Mar. Geol. 392, 151- 169, doi:10.1016/j.margeo.2017.08.005.

McKay, R., Browne, G., Carter, L., Cowan, E., Dunbar, G., Krissek, L., Naish, T., Powell, R., Reed, J., Talarico, F., Wilch, T., 2009. The stratigraphic signature of the late Cenozoic Antarctic Ice Sheets in the Ross Embayment. GSA Bulletin 121, 1537-1561, doi:10.1130/B26540.1.

McKay, R.M., De Santis, L., Kulhanek, D.K., and the Expedition 374 Scientists, 2019. Ross Sea West Antarctic Ice Sheet History. Proceedings of the International Ocean Discovery Program, 374: College Station, TX (International Ocean Discovery Program), doi:10.14379/iodp.proc.374.2019.

McKay, R.M., Dunbar, G.B., Naish, T.R., Barrett, P.J., Carter, L., Harper, M., 2008. Retreat history of the Ross Ice Sheet (Shelf) since the Last Glacial Maximum from deep-basin sediment cores around Ross Island. Palaeogeogr. Palaeoclimatol. Palaeoecol. 260, 245-261, doi:10.1016/j.palaeo.2007.08.015.

McKay, R., Golledge, N.R., Maas, S., Naish, T., Levy, R., Dunbar, G., Kuhn, G., 2016. Antarctic marine ice-sheet retreat in the Ross Sea during the early Holocene. Geology 44, 7-10, doi:10.1130/G37315.1.

McKay, R., Naish, T., Carter, L., Riesselman, C., Dunbar, R., Sjunneskog, C., Winter, D., Saniorgi, F., Warren, C., Pagani, M., Schouten, S., Willmott, V., Levy, R., DeConto, R., Powell, R.D., 2012. Antarctic and Southern Ocean influences on Late Pliocene global cooling. Proc. Natl. Acad. Sci. 109, 6423- 6428, doi:10.1073/pnas.1112248109.

KOPRI 극지연구소

Mortlock, R.A., Froelich, P.N., 1989. A simple method for the rapid determination of opal in pelagic marine sediments. Deep-Sea Res. 36, 1415-1426.

Naish, T., Powell, R., Levy, R., Wilson, G., Scherer, R., Talarico, F., Krissek, L., Niessen, F., Pompilio, M., Wilson, T., Carter, L., DeConto, R., Huybers, P., McKay, R., Pollard, D., Ross, J., Winter, D., Barrett, P., Browne, G., Cody, R., Cowan, E., Crampton, J., Dunbar, G., Dunbar, N., Florindo, F., Gebhardt, C., Graham, I., Hannah, M., Hansaraj, D., Harwood, D., Helling, D., Henrys, S., Hinnov, L., Kuhn, G., Kyle, P., Läufer, A., Maffioli, P., Magens, D., Mandernack, K., McIntosh, W., Millan, C., Morin, R., Ohneiser, C., Paulsen, T., Persico, D., Raine, I., Reed, J., Riesselman, C., Sagnotti, L., Schmitt, D., Sjunneskog, C., Strong, P., Taviani, M., Vogel, S., Wilch, T., Williams, T., 2009. Obliquity-paced Pliocene West Antarctic ice sheet oscillations. Nature 458, 322-328, doi:10.1038/nature07867.

NSIDC, 1998. Distributed active archive center. NSIDC. http://www-nsidc.colorado.edu/NSIDC/CATALOG/ENTRIES/nsi-0056.html.

Orsi, A.H., Wiederwohl, C.L., 2009. A recount of Ross Sea waters. Deep-Sea Res. II 56, 778-795.

Paillard, D., Laeyrie, L., Yiou, P., 1996. Macintosh Program Performs Time-series Analysis, vol. 77. EOS Transactions American Geiophysical Union, Washington D.C., p. 379.

Pritchard, H.D., Ligtenberg, S.R.M., Fricker, H.A., Vaughan, D.G., Broeke, M.R. van den, Padman, L.,

2012. Antarctic ice sheet loss driven by basal melting of ice shelves. Nature 484, 502-505, doi:10.1038/nature10968.

Prothro, L.O., Simkins, L.M., Majewski, W., Anderson, J.B., 2018. Glacial retreat patterns and processes determined from integrated sedimentology and geomorphology records. Mar. Geol. 395, 104-119, doi:10.1016/j.margeo.2017.09.012.

Quaia, T., Cespuglio, G., 2000. Stable isotopes records from the western Ross Sea continental slope (Antarctica): Considerations on Carbonate Preservation, Terra Antarctica Reports 4, 199-210.

Reimer, P.J., Bard, E., Bayliss, A., Beck, J.W., Blackwell, P.G., Ramsey, C.B., Buck, C.E., Cheng, H., Edwards, R.L., Friedrich, M., Grootes, P.M., Guilderson, T.P., Haflidason, H., Hajdas, I., Hatté, C., Heaton, T.J., Hoffmann, D.L., Hogg, A.G., Hughen, K.A., Kaiser, K.F., Kromer, B., Manning, S.W., Niu, M., Reimer, R.W., Richards, D.A., Scott, E.M., Southon, J.R., Staff, R.A., Turney, C.S.M., van der Plicht, J., 2013. IntCal13 and Marine13 Radiocarbon age calibration curves 0-50,000 years cal BP. Radiocarbon 55, 1869-1887.

Robinson, R.S., Brzezinski, M.A., Beucher, C.P., Horn, M.G.S., Bedsole, P., 2014. The changing roles of iron and vertical mixing in regulatng nitrogen and silicon cycling in

KOPRI 극지연구소

the Southern Ocean over the last glacial cycle. Paleoceanograhpy 29, 1179-1195, doi:10.1002/2014PA002686.

Scherer, R.P., 1994. A new method for the determination of absolute abundance of diatoms and other silt-sized sedimentary particles. J. Paleolimn. 12, 171-180.

Siddall, M., Hönisch, B., WaelBroeck, C., Huybers, P., 2010. Changes in deep Pacific temperature during the mid-Pleistocene Transition and Quaternary. Quat. Sci. Rev. 29, 170-181.

Simkins, L.M., Anderson, J.B., Greenwood, S.L., Gonnermann, H.M., Prothro, L.O., Halberstadt, A.R.W., Strearns, L.A., Pollard, D., DeConto, R.M., 2017. Anatomy of a meltwater drainage system beneath the ancestral East Antarctic ice sheet. Nat. Geosci. 10, 691-697, doi:10.1038/NGEO3012.

Sjunneskog, C., Taylor, F., 2002. Postglacial marine diatom record of the Palmer Deep, Antarctic Peninsula (ODP Leg 178, Site 1098) 1. Total diatom abundance. Paleoceanography 17, 10.1029/2000PA000563.

Smith, W., Sedwick, P., Arrigo, K., Ainley, D., Orsi, A., 2012. The Ross Sea in a sea of change. Oceanography 25, 90-103, doi:10.5670/oceanog.2012.80.

Sprenk, D., Weber, M.E., Kuhn, G., Rosén, P., Frank, M., Molina-Kescher, M., Liebetrau, V., Röhling,

H.G., 2013. Southern Ocean bioproductivity during the last glacial cycle- new detection menthod and decadal-scale insight from the Scotia Sea. Geol. Soc. London Spec. Publ. 381, 245-261, doi:10.1144/SP381.17.

Sprindler, M., Dieckman, G.S., 1986. Distribution and abundance of the planktonic foraminifer Neogloboquadrina pachyderma in sea ice of the Weddell Sea (Antarctica). Polar Biol. 5, 185-191.

Stockwell, D.A., 1991. Distribution of Chaetoceros resting spores in the Quaternary sediments from Leg 119. In: Barron, J., Larsen, B., et al., (Eds.), Proc. ODP, Sci. Res., College Station, TX (Ocean Drilling Program) 119, 599-610.

Stuiver, M., Reimer, P.J., 1993. Extended 14C database and revised CALIB radiocarbon calibration program. Radiocarbon 35, 215-230.

Taviani, M., Reid, D.E., Anderson, J.B., 1993. Skeletal and isotopic composition and paleoclimatic significance of late Pleistocene carbonates, Ross Sea, Antarctica. J. Sediment. Res. 63, 84-90.

The RAISED Consortium, Bentley, M.J., Cofaigh, C.Ó., Anderson, J.B., Conway, H., Davies, B., Graham, A.G.C., Hillenbrand, C.-D., Hodgson, D.A., Jamieson, S.S.R., Larter, R.D., Mackintosh, A., Smith, J.A., Verleyen, E., Ackert, R.P., Bart, P.J., Berg, S., Brunstein, D., Canals, M., Colhoun, E.A., Crosta, X., Dickens, W.A., Domack, E., Dowdeswell, J.A., Dunbar, R., Ehrmann, W., Evans, J., Favier, V., Fink, D., Fogwill,

KOPRI 극지연구소

C.J., Glasser, N.F., Gohl, K., Golledge, N.R., Goodwin, I., Gore, D.B., Greenwood, S.L., Hall, B.L., Hall, K., Hedding, D.W., Hein, A.S., Hocking, E.P., Jakobsson, M., Johnson, J.S., Jomelli, V., Jones, R.S., Klages, J.P., Kristoffersen, Y., Kuhn, G., Leventer, A., Licht, K., Lilly, K., Lindow, J., Livingstone, S.J., Massé, G., McGlone, M.S., McKay, R.M., Melles, M., Miura, H., Mulvaney, R., Nel, W., Nitsche, F.O., O'Brien, P.E., Post, A.L., Roberts, S.J., Saunders, K.M., Selkirk, P.M., Simms, A.R., Spiegel, C., Stolldorf, T.D., Sugden, D.E., van der Putten, N., van Ommen, T., Verfaillie, D., Vyverman, W., Wagner, B., White, D.A., Witus, A.E., Zwartz, D., 2014. A community-based geological reconstruction of Antarctic Ice Sheet deglaciation since the Last Glacial Maximum. Quat. Sci. Rev. 100, 1-9, doi:10.1016/j.quascirev.2014.06.025.

Thompson, A.F., Stewart, A.L., Spence, P., Heywood, K.J., 2018. The Antarctic Slope Current in a changing climate. Rev. Geophys. 56, 741-770, doi:10.1029/2018RG000624.

Wu, L., Wang, R., Xiao, W., Ge, S., Chen, Z., Krijgsman, W., 2017. Productivity-climate coupling recorded in Pleistocene sediemnts off Prydz Bay (East Antarctica). Palaeogeogr. Palaeoclimatol. Palaeoecol. 485, 260-270, doi:10.1016/j.palaeo.2017.06.018.

Yabuki, T., Suga, T., Hanawa, K., Matsuoka, K., Kiwada, H., Watanabe, T., 2006. Possible source of the Antarctic bottom water in the Prydz Bay region. J. Oceanogr. 62, 649-655, doi:10.1007/s10872- 006-0083-1.

Yoon, H.I., Yoo, K.C., Bak, Y.S., Lee, Y.I., Lee, J.I., 2009. Core-based reconstruction of paleoenvironmental conditions in the southern Drake Passage (West Antarctica) over the last 150 ka. Geo-Mar. Lett. 29, 309-320, doi:10.1007/s00367-009-0144-8.

KOPRI 극지연구소

Table 1. Radiocarbon dates from RS15-GC40 and RS15-GC41. The calibration program CALIB 7.1 (Stuiver and Reimer, 1993; Reimer et al., 2013) was used to convert the 14C ages to calendar ages (σ 2) with a reservoir correction of 1300 years (△R = 900 years). BF: benthic foraminifer and PF: planktonic foraminifer.

Depth (cm)	Analyzed material	Lab code	^{14}C age (yr BP)	Error (yr)	δ^{18}O (‰)	cal. yr BP (min)	cal. yr BP (max)	Calendar age (yr BP)
RS15-GC40								
3	BF + PF	Rafter-40933/1	17,432	±79	–	19,212	19,685	19,460
5	PF	Beta-489,452	21,790	±70	+4.7	24,360	24,978	24,642
30	PF	Beta-489,453	43,290	±620	+4.4	44,228	46,462	45,329
100	BF + PF	Rafter-40933/2	Back-ground					
RS15-GC41								
23	BF + PF	Rafter-40933/3	17,791	±86	–	19,620	20,125	19,887
25	PF	Beta-489,454	18,760	±60	+5.1	20,850	21,317	21,073

KOPRI
극지연구소

Table 2. Tie points obtained by whole round measured MS graphical correlations between RS15-GC40 and RS15-GC41 and tie points obtained by graphical correlations of RS15-GC41 whole round measured MS and LR-04 (Lisiecki and Raymo, 2005).

RS15-GC40 MS to RS15-GC41 MS		RS15-GC41 MS to LR-04	
RS15-GC40 (cm)	RS15-GC41 (cm)	RS15-GC41 (cm)	LR-04 (ka)
85	91	91	126
224	227	241	222
		283	237
		387	326
		490	403

KOPRI
극지연구소

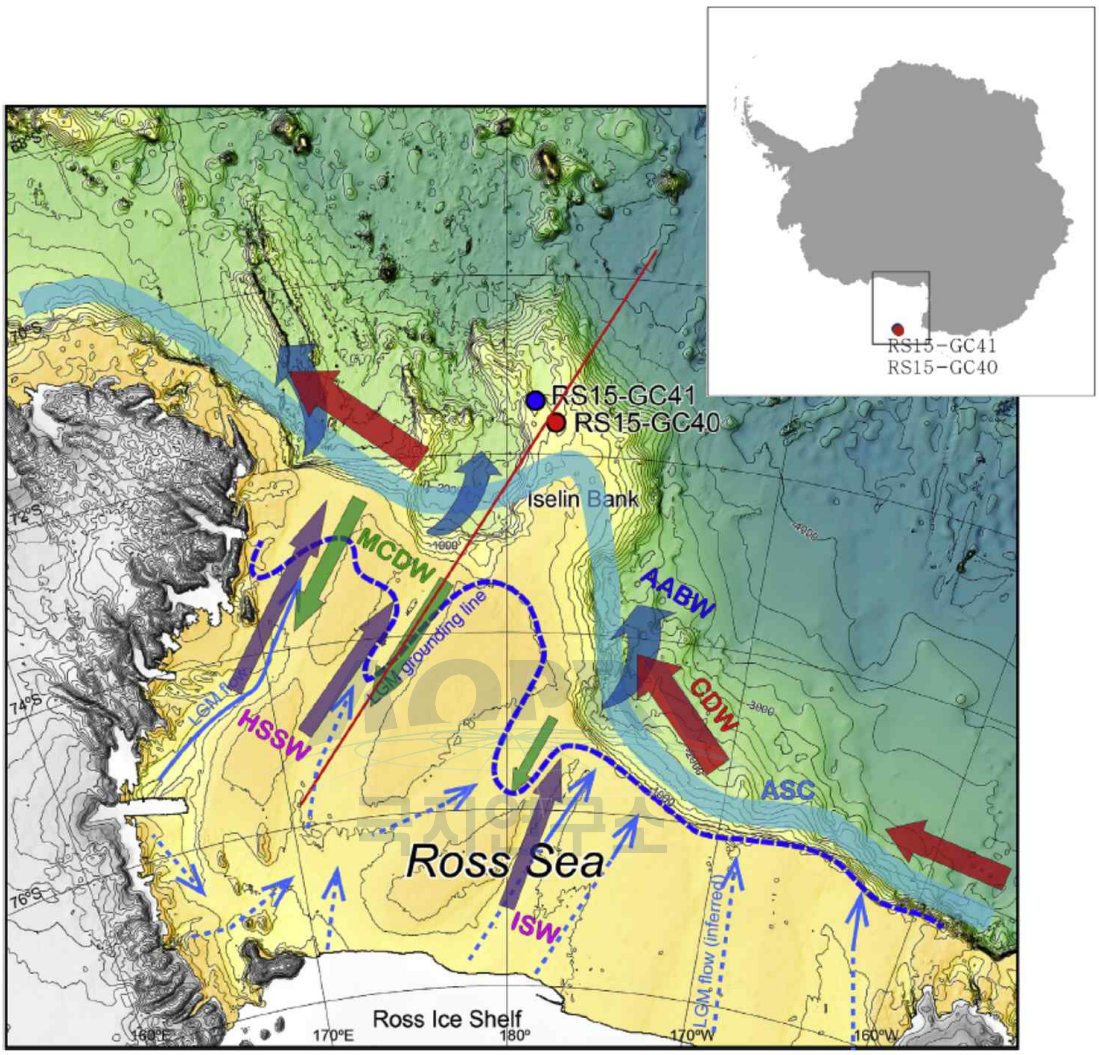


Figure 1. Regional map of the Ross Sea showing core locations of RS15-GC40 and RS15-GC41. Last Glacial Maximum (LGM) grounding line (blue dashed) and LGM ice flow directions (sky blue arrows) are modified from Anderson et al. (2002). Antarctic Slope Current (ASC), Antarctic Bottom Water (AABW), Circumpolar Deep Water (CDW), Modified CDW (MCDW), High Salinity Shelf Water (HSSW), and Ice Shelf Water (ISW) are modified from Smith et al. (2012). The red line is the axis for schematic model Figure 6.

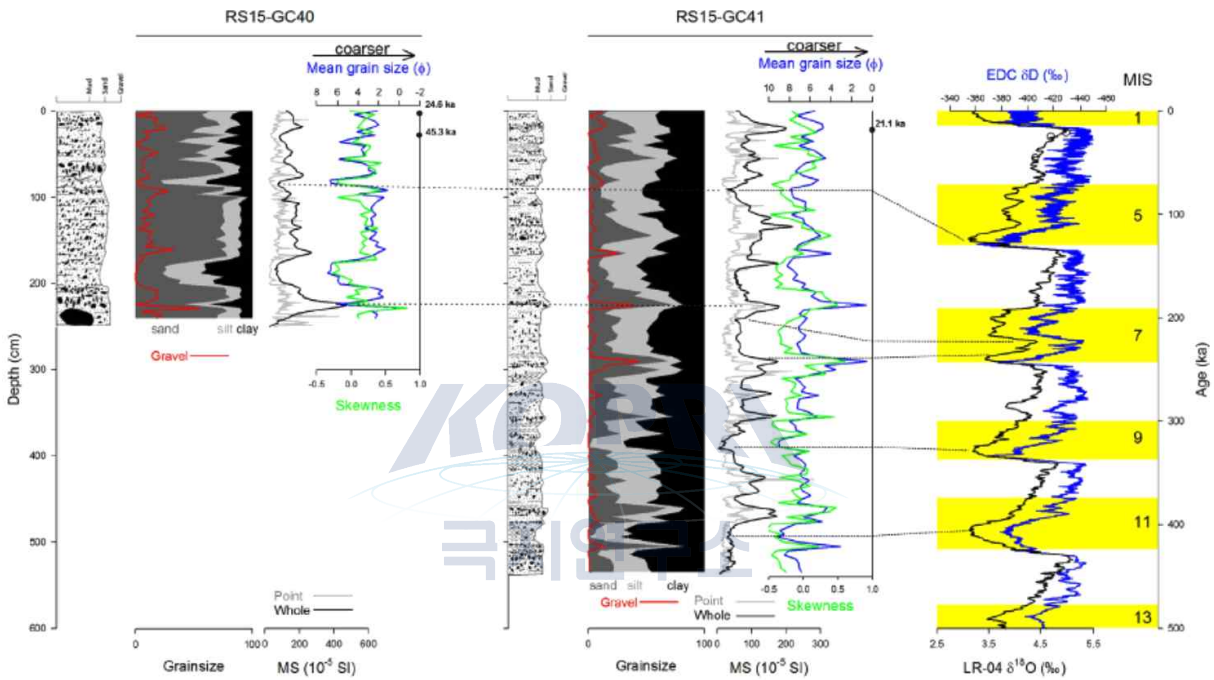


Figure 2. Graphical correlations of MS values between RS15-GC40 and RS15-GC41 and graphical correlations of MS values of RS15-GC41 with LR-04 $\delta^{18}O$ (Lisiecki and Raymo, 2005) and EDC δ D and dust record (Jouzel et al., 2007). Interglacial periods are marked by yellow box with marine isotope stage (MIS) numbers. Lithofacies, skewness, mean grain size, and grain size, normalized to sand/silt/clay total, of two cores are plotted together. Black closed circles are foraminifer AMS 14C dates and their $\delta^{18}O$ values (open circles) are plotted together with LR-04 $\delta^{18}O$.

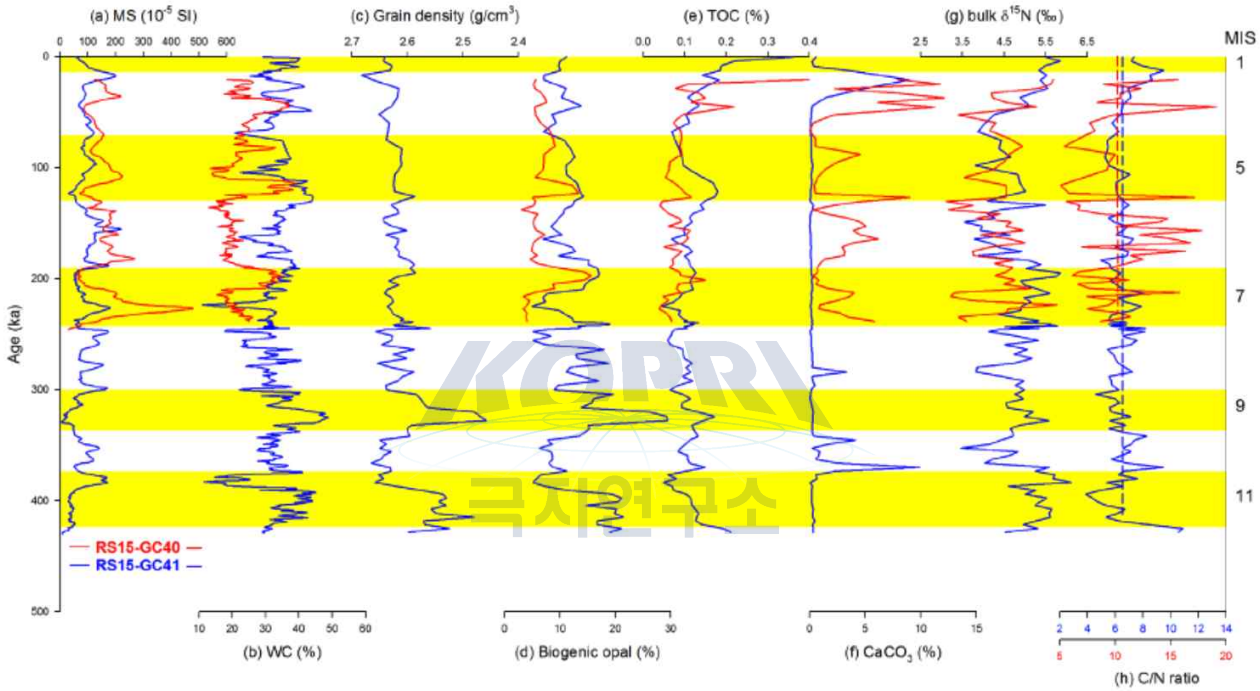
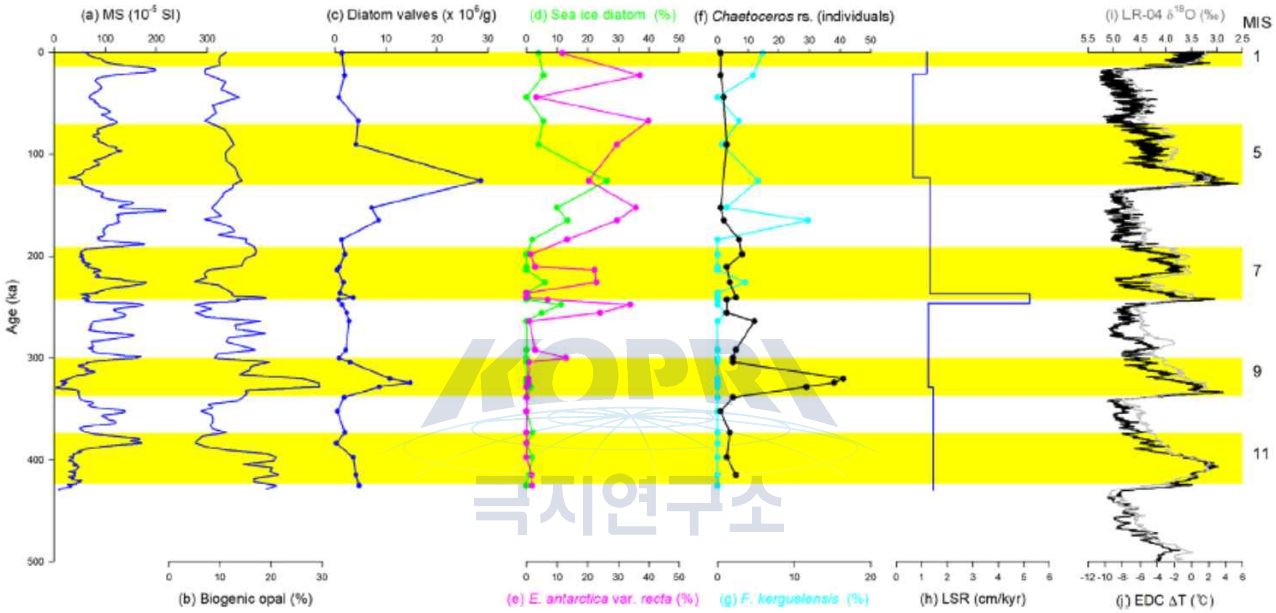


Figure 3. Downcore profiles of (a) MS, (b) WC, (c) grain density, (d) biogenic opal concentration, (e) TOC concentration, (f) $CaCO_3$ concentration, (g) bulk $\delta^{15}N$, and (h) C/N ratio of RS15-GC40 (red) and RS15-GC41 (blue). Interglacial periods are marked by yellow box with marine isotope stage (MIS) numbers. Dashed vertical lines are mean C/N value for each core.



Figue 4. Downcore profiles of (a) MS, (b) biogenic opal concentration, (c) total diatom valve, relative abundance of (d) sea ice diatoms, (e) E. antarctica var. recta, and (f) F. kerguelensis, (g) Chaetoceros resting spores, and (h) LSR of RS15-GC41 with (i) LR-04 δ^{18}O (gray, Lisiecki and Raymo, 2005), and (j) ΔT of EDC ice core (black, Jouzel et al., 2007). Interglacial periods are marked by yellow box with marine isotope stage (MIS) numbers.

KOPRI 극지연구소

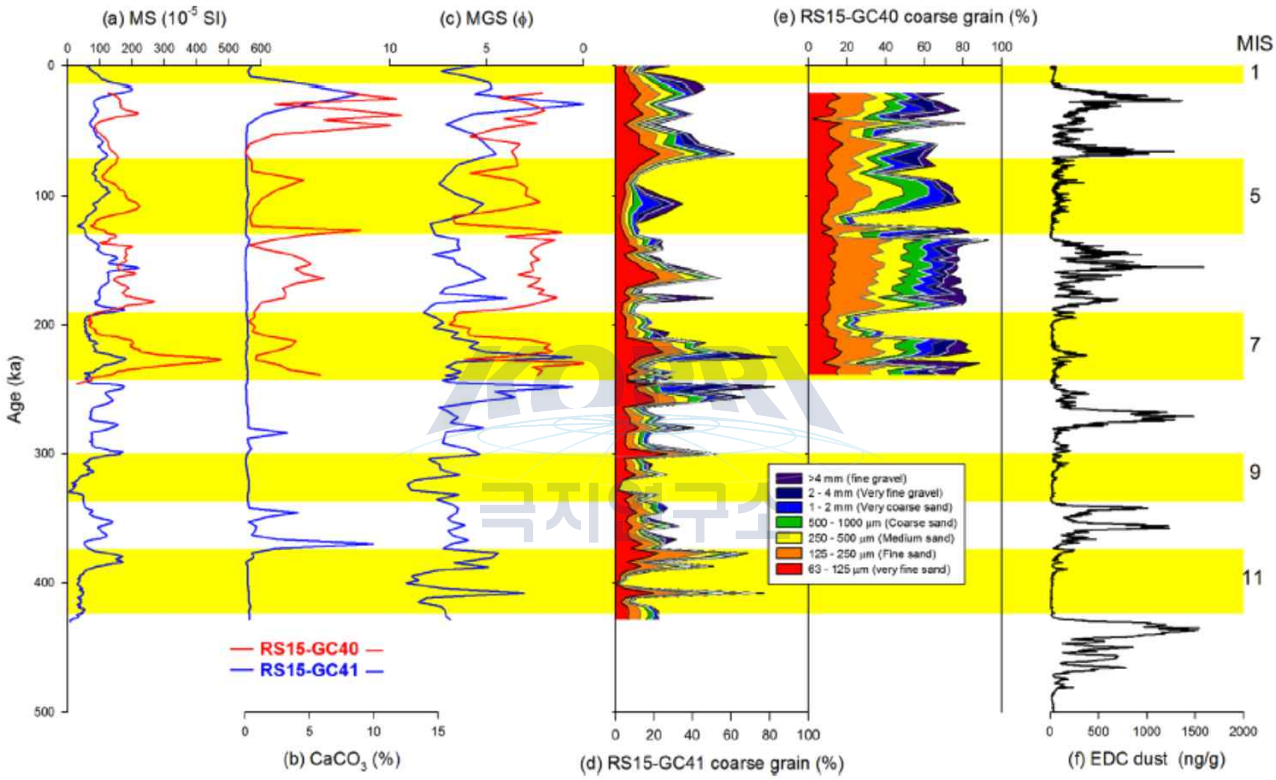


Figure 5. Downcore profiles of (a) MS, (b) $CaCO_3$ concentration, and (c) MGS of RS15-GC40 (red) and RS15-GC41 (blue), (d) composition of coarse grains (>63 µm) of RS15-GC41 and (e) RS15-GC40 with (f) EDC ice core dust record (black, Jouzel et al., 2007)

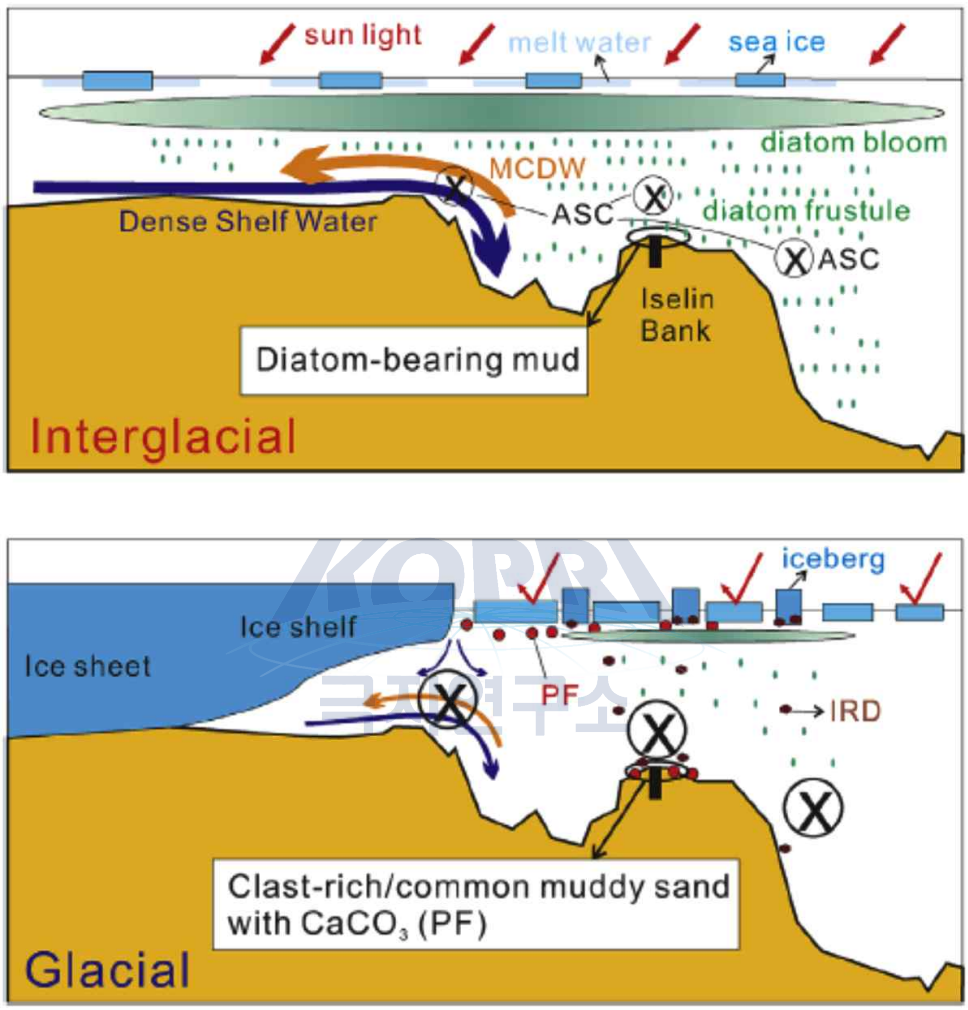


Figure 6. Schematic models of the glacial periods and interglacial periods in the Iselin Bank region over the last 400 kyrs. The transect is shown in Figure 1 as red line. Modified Circumpolar Deep Water (MCDW), Antarctic Slope Current (ASC), ice rafted debris (IRD), and planktonic foraminifer (PF).

제 23 장

Glacial-interglacial changes in oceanic conditions and depositional process in the continental rise in response to ice sheet (shelf) variation in Bellingshausen Sea, Antarctica[16)]

Sunghan Kim[a,*], Young-Suk Bak[b], Joseph G. Prebble[c], Myung-Il Kang[a], Sookwan Kim[d], Jinku Park[a], Min Kyung Lee[a], Jae Il Lee[a], Kyu-Cheul Yoo[a], Heung Soo Moon[a]

[a]Korea Polar Research Institute, Incheon, 21990, South Korea
[b]Department of Earth and Environmental Sciences, Jeonbuk National University, Jeonju, 54896, South Korea
[c]Department of Surface Geosciences, GNS Science, Lower Hutt, New Zealand
[d]Korea Institute of Ocean Science and Technology, Busan 49111, Republic of Korea

KOPRI 극지연구소

Abstract: Antarctic continental margin sediments are eroded from the shelf and transported to the slope/rise in association with changing ice sheet configuration. Understanding the dynamics of this transport pathway is important for utilizing distal deep-sea sedimentary archives to determine past changes in the Antarctic ice sheet. However, these connections are poorly understood. Here we present multi-proxy records of two sediment cores (BS17-GC01 and BS17-GC02) from the Bellingshausen Sea continental rise, to explore relationships between depositional regime and ice sheet dynamics. Two cores show depositional/sedimentological variations on glacial-interglacial scales. Biogenic sediments were deposited during MIS 1, 5, and 7 under open ocean conditions. Glacial to deglacial sediments were laminated as a result of varying intensity of bottom currents. Terrestrially derived sediments are inferred to be transported from shelf both as grounded ice advanced during glacial expansion, and as ice retreated during deglacial periods. Sediment color shifted to brown after deglacial periods with high Mn/Ti and occurrence of bioturbation, indicating increasing bottom water oxygenation in the study area. Since surface water

16) 이 연구 결과는 다음의 논문으로 출판되었음: Jung, J. et al. (2021). "Glacial-interglacial changes in oceanic conditions and depositional process in the continental rise in response to ice sheet (shelf) variation in Bellingshausen Sea, Antarctica" Frontiers in Marine Science 10: 1183516.

production started to increase from deglacial periods, we infer increased bottom water oxygenation in this setting is due to ventilation (i.e., Antarctic Bottom Water (AABW) formation), implying that AABW formation was increased during interglacial periods from deglacial period whereas was decreased during glacial periods. Thus, sedimentary/depositional changes in BS17-GC01 and BS17-GC02 are closely linked to ice sheet dynamics during the late Quaternary.

1. Introduction

The stability of the West Antarctic Ice Sheet (WAIS) is strongly influenced by variability of the surrounding ocean (Golledge et al., 2012; Pritchard et al., 2012; Deconto and Pollard, 2016). The spatial and temporal pattern of ice sheet advance/retreat across the continental shelf is largely a function of ocean water mass exchange along the glacial front. On glacial/interglacial timescales, this water mass exchange is influenced by the geomorphology (e.g., Dinniman et al., 2011; Lavoie et al., 2015), which is in turn influenced by tectonic process, glacier dynamics, bottom currents, and sediment input. However, sedimentary deposits that could be used to reconstruct glacial dynamics on glacial/interglacial timescales are fragmentary and cryptic in this setting. Although the Antarctic continental shelf contains a valuable record of deglacial to recent ice dynamics (e.g., De Santis et al., 1995; Domack et al., 1999), the advance of erosional ice sheets to the shelf break during the Last Glacial Maximum (LGM) (Anderson et al., 2002; Ó Cofaigh et al., 2014; The RAISED et al., 2014) means that LGM and older archives are rare on the continental shelf. For the most part, LGM and older sediments have been eroded and transported to the upper slope and continental rise (e.g., Anderson, 1999; Dowdeswell et al., 2002, 2008; Noormets et al., 2009). It is these deep-sea archives we must interpret, to understand ice dynamics during the LGM and older times.

It is normally recognized that dense shelf water formation, occurred by brine rejection in association with high sea ice formation in Antarctic coastal polynyas, is related to the formation of Antarctic Bottom Water (AABW), which is the densest water mass (Tamura et al., 2008). As a result, AABW is characterized by high oxygen concentration (Gordon, 2009). It is reported that AABW formation restarted or intensified at the end of glacial periods, that is deglacial periods, when grounded ice began to retreat on the shelf (Wu et al., 2018; Jimmez-Espejo et al., 2020). Since the production of AABW is related to shelf cavities (Wu et al., 2018; Jimmez-Espejo et al., 2020), these deep-sea archives will provide information on bottom water redox condition variations on glacial-interglacial time scale.

In this study, we use two sedimentary records from the continental rise of the Bellingshausen Sea, to infer changes in oceanographic conditions and sediment depositional process, in response to ice sheet variation on the Bellingshausen Sea continental shelf. To do this, we analyze lithology, physical properties (magnetic susceptibility (MS), grain density, and color reflectance), geochemical proxies (CaCO3, total organic carbon (TOC), biogenic opal concentrations, and C/N ratio), paleontological records (diatoms and palynomorphs), manganese/titanium (Mn/Ti) ratio, zirconium/rubidium (Zr/Rb) ratio, and grain size records with grains >1 mm.

2. Depositional Setting

In the Bellingshausen Sea, a wide sediment fan is formed directly seaward of the shelf break (Fig. 1), reflecting the large amount of sediment that has been transported from the shelf to slope and rise areas by this pathway (Dowdeswell et al., 2008). Because of intermittent and erosional sediment input (i.e., gravity flows), the sample sites on the fan are not an ideal archive infer paleoenvironmental changes associated with the neighboring ice sheet. Moreover, application of environmental proxies from this upper- to middle-slope depositional environment is hampered by the coarse sediment originating from the ice margin during glacial periods (e.g., Dowdeswell et al., 2008 and references therein). Because drift sediments are well developed from the western Antarctic Peninsula to Bellingshausen Sea sector of the Antarcitic margin (Rebesco et al., 2002; Hillenbrand et al., 2008a), previous studies have focused on the influence of bottom currents on this region and depositional environment, with a particular emphasis on interpreting cores collected from close to the shelf break (Pudsey and Camerlenghi, 1998; Lucchi et al., 2002; Lucchi and Rebesco, 2007; Hillenbrand et al., 2021).

Along western Antarctic Peninsula to Bellingshausen Sea sector of the Antarcitic margin, sedimentation during glacial periods includes, (faintly) laminated sediments with less biogenic components, deposited by a combination of contourite, meltwater plumite, and distal turbidite mechanisms (Hillenbrand et al., 2021 and references therein). The northern extent of these glacial facies is not yet established, due to lack of distal, deep water core records from the Bellingshausen Sea.

Surface sediments of the nearby sea, Amundsen Sea, shows a regional variability; most notably difference between east and west (Hillenbrand et al., 2003). To date, most research effort has been on the area east of the Peter I. Island (e.g., Pudsey and Camerlenghi, 1998, Lucchi et al., 2002; Hillenbrand et al., 2003, 2009, 2021). Understanding the accumulation of sedimentary records from the west, which are likely to represent a

different mode of deposition given the distinct surficial sediments, is necessary to obtain a complete picture of paleoceanographic evolution of the Bellingshausen Sea region during the late Quaternary.

3. Materials and Methods

Two gravity cores were collected from the continental rise of the Bellingshausen Sea by IBR/V Araon during the ANA07D cruise in 2017; 217 cm-long BS17-GC01 (67°22.8947′ S, 96°23.2464′ W, 4627 m water depth) and 846 cm-long BS17-GC02 (68°09.4940′ S, 94°34.7988′ W, 4361 m water depth) (Fig. 1). The two cores were stored cold before being opened, described, and sub-sampled at the Korea Polar Research Institute (KOPRI). Core photos and chemical elements were measured by ITRAX core scanner at KOPRI. X-radiographs were taken from 8 cm x 30 cm x 1 cm slabs at KOPRI. Physical properties, geochemical proxies, and grain size analysis were performed at KOPRI. Analysis of diatom assemblages was performed at Jeonbuk National University and palynology analysis was performed at GNS Science. All data for BS17-GC01 and BS17-GC02 are in supplementary table 1 and 2, respectively.

KOPRI
극지연구소

3.1. Physical properties (Magnetic Susceptibility, color reflectance, and grain density)

The Magnetic Susceptibility (MS) for BS17-GC01 and BS17-GC02 was measured at 1 cm-intervals on split half core sections using a Bartington MS-2B susceptibility meter. The MS values for BS17-GC01 was reported in Kim et al. (2022a). Color reflectances a* and b*, which reflect the balance between red (+) and green (-) and yellow (+) and blue (-), respectively, were measured at 1 cm intervals on split half core sections of two cores by spectrophotometry. The grain density was measured at 10 cm intervals for BS17-GC02 and 4 cm intervals for BS17-GC01 using a gas pycnometer (AccuPyc II 1340). All physical properties were measured at KOPRI.

3.2. Geochemical proxies (biogenic opal, TOC, and CaCO3 concentrations)

All geochemical proxies for BS17-GC01 and BS17-GC02 were measured at 2 cm intervals on 1 cm thick sub-samples at KOPRI. Biogenic silica concentration was measured using a Continuous Flow Analyzer (SKALAR SANplus Analyzer) with wet-alkaline extraction method modified from DeMaster (1981) following the method of Kim et al. (2018a). Biogenic opal concentration was calculated by multiplying biogenic silica

concentration by 2.4 (Mortlock and Froelich, 1989). The relative error of biogenic silica concentration in sediment samples is less than 1%. Total inorganic carbon (TIC) concentration was measured using UIC CO2 coulometer (Model CM5240). CaCO3 concentration was calculated by multiplying TIC concentration by 8.333. The relative standard deviation for CaCO3 concentration is ±1%. Total carbon (TC) and total nitrogen (TN) concentrations were measured by an Organic Elemental Analyzer (FLASH 2000 NC Analyzer) with an analytical precision less than ±0.1% and ±0.16%, respectively. TOC concentration was calculated by the difference between TC and TIC. C/N ratio was calculated as TOC/TN.

3.3. Diatom assemblage analysis

Fifty samples were analyzed at 10 cm intervals for brown units and 50 cm intervals for gray units for BS17-GC02 and twenty-two samples were analyzed at 10 cm intervals for BS17-GC01. Due to the predominant occurrence of Fragilariopsis kerguelensis, in the intervals of high biogenic opal concentration, up to 200 diatom specimens were counted. The other intervals had extremely low diatom abundances due to poor preservation, 200 microscope fields of view were observed and counted. The sample preparation and diatom counting methods followed Bak et al. (2018). The quantitative analysis of the diatom slides followed the procedures described in Scherer (1994). Absolute abundance was calculated using the following equation: abundance = ((A × B)/(C × D))/E, where A is the number of specimens counted, B is the area of the settling chamber, C is the number of microscope fields of view, D is the area of the field of view, and E is the sample mass.

3.4. Palynology analysis

Because both cores have brown-gray color alterations and BS17-GC02 has more color cycles, only core BS17-GC02 was examined for palynology. 13 samples were selected from dark brown, brown, and gray units. Samples were dried and weighed. Cold 10% HCl was added to the dried sample to remove carbonates, followed by 24 hours in cold 52% HF and a second cold wash in 10% HCl. Samples were placed in an ultrasonic bath for up to a minute, sieved through a 6 µm mesh to remove small particulate material, and mounted on glass slides in glycerine jelly. A single lycopodium tablet (batch 1061) was introduced during processing to determine absolute palynomorph abundance. Palynology was performed at the GNS Science palynology laboratory.

All counts were completed on a light microscope at 400x magnification. For this study, 100 palynomorph specimens were counted for each sample where possible. The

entire slide was scanned for samples in which palynomorphs were rare.

3.5. Grain size analysis and count of grains >1 mm

After removing biogenic components (organic matter, biogenic silica, CaCO3) from bulk sediments using 34% H2O2, 2N NaOH, and 10% HCl, respectively, grain size was analyzed at 8 cm intervals for BS17-GC02 and at 4 cm intervals for BS17-GC01. Grain size was analyzed using a laser diffraction instrument (Mastersizer 3000, Malvern) at KOPRI. The classification of sediments follows that of Folk and Ward (1957).

X-radiographs of center slices (1 cm thick x 8 cm width x 30 cm length) removed from each core section. Then, grains >1 mm in diameter were manually counted every 1 cm on the X-radiograph images.

3.6. Mn/Ti and Zr/Rb ratios

The distribution of chemical elements for both cores was determined non-destructively using an ITRAX core scanner at KOPRI. Following the procedure of Croudace et al. (2006), we analyzed at 5 mm intervals with a 3 kW Mo X-ray tube under 30 kV and 30 mA with a dwell time of 5 seconds. In this study, we focus on Mn, Ti, Zr, and Rb elemental XRF peak area intensities measured in total counts per second (CPS). The elemental data are presented as Mn/Ti and Zr/Rb ratios to account for changes in water content or physical properties.

4. Chronology

4.1. BS17-GC02

Previous studies of sediment accumulation in the Western Antarctic Peninsula region have aligned high MS intervals containing low biological production with glacial periods and assigned low MS intervals containing high biological production to interglacial periods (e.g., Pudsey and Camerlenghi, 1998; Pudsey, 2000; Hillenbrand et al., 2009, 2021). BS17-GC02 showed a similar lithologic pattern to previous cores collected from the western Antarctic Peninsula (e.g., Pudsey and Camerlenghi, 1998; Pudsey, 2000; Lucchi et al., 2002; Hillenbrand et al., 2009). Recently, Hilllenbrand et al. (2021) established age models for cores from the study area by a combination of correlating δ18O data of planktonic foraminifera with LR04 (Lisiecki and Raymo, 2005), Marine Tephra B (MIS 5/6 boundary at

~130 ka; Hillenbrand et al., 2008b), and accelerator mass spectrometry (AMS) 14C dates. This chronological result was consistent with previous chronological frames. Thus, we apply the chronological scheme in Hillenbrand et al. (2021) for the BS17-GC02 age model. A bioturbated biogenic interval at core top (0 – 35 cm) likely corresponds to interglacial MIS 1, the next biogenic interval (348 – 398 cm) likely corresponds to interglacial MIS 5, and the deeper biogenic interval (660 – 698 cm) likely corresponds to interglacial MIS 7. We infer the intervening intervals correspond to the glacial periods MIS 2 – 4, 6, and 8. However, as it is acknowledged in Hillenbrand et al. (2021), it is not established that the biogenic interval spans the entire MIS 5 and MIS 7 intervals, (or represent only MIS 5e MIS 7e, respectively). We also acknowledge that there is some uncertainty in MIS boundaries in this study due to gradational/bioturbated contacts.

AMS 14C dates were obtained using planktonic foraminifera, Neogloboquadrina pachyderma (sin.), at 354 cm and 372 cm (Kim et al., 2022b). The two radiocarbon ages were calibrated using CALIB 7.1 (Stuiver and Reimer, 1993) with the MARINE13 dataset (Reimer et al., 2013) using a constant marine reservoir effect of 1300 years, consistent with previous Southern Ocean and Western Antarctic Peninsula studies (e.g., Domack et al., 2001; Pugh et al., 2009; Kilfeather et al., 2011; Xiao et al., 2016). The calibrated ages were 20.6 ka at 354 cm and 37.5 ka at 372 cm. These carbon dates are inconsistent with the chronological scheme described above, which assigns the interval 354 – 372 cm to interglacial MIS 5. Although planktonic foraminifera 14C dates have been previously reported from cores collected from the western Antarctic Peninsula region, (Hillenbrand et al., 2021), we note our dates are the first reported from the first sub-surface CaCO3 interval. As a result, we have limited opportunity to assess the reliability and lateral reproducibility of the two AMS 14C dates we report. Thus, in this study, we follow the established regional chronology by ignoring the two AMS 14C dates for BS17-GC02 we obtained, but note that further investigation of the regional-scale chronological scheme of the western Antarctic Peninsula may be warranted, along with further investigation using radiometric dating approaches (Pudsey and Camerlenghi, 1998; Lucchi et al., 2002; Lucchi and Rebesco, 2007; Hillenbrand et al., 2021).

4.2. BS17-GC01

The correlation between MS values and the European Project for Ice Coring in Antarctica (EPICA) Dronning Maud Land (EDML) ice core dust record (Fischer et al., 2007) has been used for age establishment of Scotia Sea sediment cores, although there has been debate about the causal mechanisms that isochronously connect the two settings (e.g., Pugh et al., 2009; Weber et al., 2012; Xiao et al., 2016; Kim et al., 2018b; Shin et al., 2020). Kim

et al. (2022a) established an age model for BS17-GC01 by correlating MS values to EDML ice core dust record. In that scheme, the biogenic interval at the upper part of the core (0 – 35 cm) corresponded to MIS 1, the 35 – 217 cm interval corresponded to MIS 2 – 4; 35 – 78 cm for MIS 2, 78 – 189 cm for MIS 3, and 189 – 217 cm for MIS 4.

5. Results

5.1. Lithology and physical properties

5.1.1. BS17-GC02

BS17-GC02 sediments alternated between decimeter-scale bioturbated diatom-bearing mud with foraminifera (interglacial MIS 1, 5, and 7), and meter-scale laminated mud inferred to be of terrestrial origin (MIS 2 – 4, 6, and 8). The biogenic intervals were composed of dark brown diatom-bearing mud, overlain by gray mud with foraminifera. These intervals are characterized by decreasing biogenic opal concentration up-section, with a gradual/bioturbated contact (Fig. 2). The laminated intervals can be divided into two units; a gray unit, overlain by a brown unit (Fig. 2). We infer gray intervals correspond to glacial periods and brown intervals were likely deposited during periods of ice retreat (i.e., deglacial period) (Fig. 2).

MS values at BS17-GC02 show fluctuating values from 20 to 1500 10-5 SI (Fig. 2a). MS values were constantly low (<100 10-5 SI) during interglacial MIS 1, 5, and 7. In contrast, MS values were high and variable during MIS 2 – 4, 6, and 8 (Fig. 2a). In spite of color difference between the brown and gray units, there was no significant difference in MS values during MIS 2 – 4, 6, and 8 (Fig. 2a).

Grain density (g/cm3) of BS17-GC02 ranges mostly from 2.4 to 2.7 (Fig. 3e). Grain density values were noticeably low during interglacial MIS 1, 5, and 7 (Fig. 3e).

Color reflectance (a* and b* values) of BS17-GC02 was high in the brown intervals inferred to have been deposited under deglacial to interglacial conditions, and low in the gray intervals inferred to have been deposited under glacial conditions (Fig. 2b and c). Maximum a* and b* values were found in the dark brown intervals (interglacial MIS 1, 5, and 7) (Fig. 2). Mn/Ti ratios showed increased values from deglacial to interglacial periods (Fig. 2i). However, Mn/Ti ratios from interglacial MIS 1, 5, and 7 were not higher than those observed during deglacial periods (Fig. 2i).

5.1.2. BS17-GC01

KOPRI 극지연구소

BS17-GC01 showed alternating deposition between bioturbated (diatom-bearing) mud (corresponding to MIS 1 and 3) and faintly laminated/structureless sandy mud (corresponding to MIS 2 and 4) (Fig. 4). The brown units are composed of bioturbated mud overlying intermittently laminated mud. In contrast to BS17-GC02, diatom frustules were found during MIS 1 only (Fig. 4). The gray units are composed of structureless sandy mud, overlying faintly laminated mud (Fig. 4).

MS values from BS17-GC01 were also constantly low (<100 10-5 SI) during interglacial MIS 1 and MIS 3 (Fig. 4a), but were high during MIS 2 and 4.

Grain density (g/cm3) of BS17-GC01 ranges mostly from 2.6 to 2.7 (Fig. 5f). Grain density showed relatively low values during MIS 1 and 3 (Fig. 5f).

Color reflectance (a* and b* values) from BS17-GC01 showed high values in brown intervals (inferred to be deposited during deglacial to interglacial periods) and low values in gray intervals inferred to represent deposition under glacial conditions (Fig. 4b and c). Maximum a* and b* values were recorded at the upper part of of brown intervals (Fig. 4b and c). Mn/Ti ratios showed increased values during MIS 1 and 3, relative to sediment deposited during MIS 2 and 4 time (Fig. 4i).

KOPRI 극지연구소

5.2. Geochemical measurements (biogenic opal, TOC, CaCO3, and C/N ratio)

5.2.1. BS17-GC02

In BS17-GC02, biogenic opal concentrations showed high values (15–20%) during interglacial MIS 1, 5, and 7, and low values (<10%) during MIS 2–4, 6, and 8 (Fig. 2d). TOC values were high, though variable, (0.3%) in the gray laminated glacial intervals (Fig. 2f). TOC concentrations showed minimum values during deglacial periods, and increased during interglacial MIS 1, 5, and 7 (Fig. 2f). In general, C/N ratios co-varied with TOC; high during glacial MIS 2–4, 6, and 8, low/moderate during deglacial periods, and low/increasing during interglacial MIS 1, 5, and 7 (Fig. 2g). CaCO3 concentrations were generally very low (~0%), but increased CaCO3 concentrations were observed occurred right above biogenic opal peaks of interglacial MIS 5 and 7 (Fig. 2h).

5.2.2. BS17-GC01

In BS17-GC01, elevated concentrations of biogenic opal were observed in sediments deposited during interglacial MIS 1 (10–12%) and MIS 3 (8–10%), whereas low concentrations (<5%) were observed during MIS 2 and 4 (Fig. 4d). TOC concentrations were

generally lower than BS17-GC02 (<0.2%). Except for a brief peak (0.2%) in MIS 4, TOC concentrations were relatively increased during MIS 1 and 3, compared to MIS 2 and 4 (Fig. 4f). C/N ratios were lower during MIS 1 and 3, than MIS 2 and 4 (Fig. 4g). CaCO3 was generally absent in the core, but a trace amount (0.6 – 0.8%) was observed in sediments deposited during MIS 2 (Fig. 4h).

5.3. Diatom and palynology record

5.3.1. BS17-GC02

Twenty-four diatom species belonging to 10 genera were identified in BS17-GC02. Diatoms were abundant (46 – 243 105 valves/g) during interglacial MIS 1, 5, and 7, and were absent in other lithologies (Fig. 3h). Fragilariopsis kerguelensis, an open ocean species (Crosta et al., 2005; Xiao et al., 2016), dominated the assemblages (85 – 95%) (Fig. 3i). Other minor species were found together with F. kerguelensis during interglacial MIS 1, 5, and 7 and were absent in the other intervals (Table S2).

Palynomorphs concentrations of BS17-GC02 are very low (<165 palynomorphs/g sediment) in all 13 samples examined (Fig. 3g). Although the palynomorph abundance was extremely low (~10 specimens/g) in the dark brown units, these samples contained Impagidinium pallidum. This is one of the few forms of dinoflagellate cyst observed in modern high southern latitudes core top samples, and is inferred to be in situ (Esper and Zonneveld, 2007; Prebble et al., 2013). Intervals with a palynomorph concentration of >45 palynomorphs/g contains a mixture of dinoflagellate cyst and pollen forms characteristic of pre-Quaternary Antarctic Sediments of Eocene-Miocene age (Truswell, 1983; Askin, 2000; Askin and Raine, 2000). These dinoflagellate cysts include Hystrichosphaeridium spp., Enneadocysta, Operculodinium spp., and Spinidinium spp., while pollen includes various types of Nothofagidites, Podocarpidites spp., trilete, and monolete spores (Table S2).

5.3.2. BS17-GC01

Eighteen diatom species belonging to 12 genera were identified in BS17-GC01. Diatoms were abundant (112 – 202 x105/g) during MIS 1, and were very rare to absent during MIS 2 – 4 (Fig. 5h). During MIS 3, biogenic opal concentration was relatively high. In contrast, diatoms samples from sediments of MIS 3 were barren. F. kerguelensis was dominant (83 – 100%) in most samples were diatoms were present (Fig. 5i). At 59 cm, the relative abundance of F. kerguelensis was reduced to 55%. In that sample, Dactyliosolen antarcticus (22%), Eucampia antarctica sp. (11%), and Paralia sulcata (11%) were more

common (Fig. 5i, Table S1).

5.4. Grain size analysis and grains >1 mm

5.4.1. BS17-GC02

Sediments of BS17-GC02 are dominated by mud fraction (Fig. 3a), with silt fraction higher than clay fraction (Fig. 3a). Laminated intervals are characterized by a marked increase in mean grain size (MGS), driven by an increase in silt fraction. The MGS was generally less than 20 μm (Fig. 3b). In addition, sortable silt (SS: 10 – 63 μm) MGS showed a consistent variation pattern with MGS (Fig. 3b).

Grains >1 mm are found throughout BS17-GC02 (Fig. 3f), and occur more frequently during deglacial periods, with highest frequency during interglacial MIS 1, 5, and 7 (Fig. 3).

5.4.2. BS17-GC01

The mud fraction is dominant (>95%) during MIS 1 and 3, whereas sand content sharply increased (up to 40%) during MIS 2 and 4 (Fig. 5a). As a result, MGS increased during MIS 2 and 4. SS MGS also showed consistent pattern with MGS variation (Fig. 5b).

Interestingly, grains >1 mm were found during MIS 1 and 3, but not found during MIS 2 and 4 (Fig. 5g).

6. Discussion

6.1. Glacial periods

6.1.1. Deep-water site BS17-GC02 ice covered and likely anoxic during glacials

During glacial periods gray laminated mud was deposited at BS17-GC02. This mud was characterized by fluctuating MS values, low a* and b* values, low biogenic opal concentration, high but fluctuating TOC concentration, high C/N ratios, low CaCO3 concentration, low Mn/Ti, fluctuating MGS, high grain density, dispersed grains >1 mm, increased total palynomorphs represented by reworked species, and an absence of diatoms (Figs. 2 and 3). These characteristics are very similar to sediments deposited on the western Antarctic Peninsula continental slope/rise during glacial periods (Pudsey and Camerlenghi,

1998; Lucchi et al., 2002; Lucchi and Rebesco, 2007; Hillenbrand et al., 2021). In the western Antarctic Peninsula region, laminated sediments, with reduced biogenic component deposited during glacial periods have previously been interpreted as being deposited by a combination of contourite, meltwater plumite, and distal turbidites (Hillenbrand et al., 2021 and references therein). We infer broadly similar deposition mechanisms for BS17-GC02, although since this site is located further north (~300 km from shelf break) than other previously reported cores on the drift, we infer influence from meltwater plumite to be low.

Sortable Silt MGS has previously been used as a proxy for bottom current speed in a range of deep water settings (e.g., McCave and Hall, 2006; McCave et al., 2017; Wu et al., 2018; McCave and Andrews, 2019; Hillenbrand et al., 2021). Since SS MGS and percentage of sortable silt in mud generally covaries in the core ($r > 0.5$) (Fig. 3d), we follow the approach of previous authors in this region and apply SS MGS as a proxy for bottom current speed at BS17-GC02 (McCave and Andrews, 2019, Hillenbrand et al., 2021). Recently, modified sediment grain size distributions free of IRD influence to recalculate SS MGS have been introduced to sediments including IRDs in the polar regions (Stevenard et al., 2023). The ln(Zr/Rb) ratio is considered and is used as a grain-size proxy free of sandy IRD influence in Antarctic sediment cores (Wu et al., 2020; Stevenard et al., 2023). Since ln(Zr/Rb) ratio of BS17-GC01 showed a good consistence with SS MGS (Fig. 5), we did not recalculate SS MGS free of IRD influence in this study. SS MGS data showed a mean value of 19 μm with standard deviation of 4 μm, indicating a relatively small glacial-interglacial changes in bottom-current velocity (Fig. 3b). This is consistent with previous study results (Pudsey and Camerlenghi, 1998; Vautravers et al., 2013; Hillenbrand et al., 2021).

TOC concentrations at BS17-GC02 increased during glacial periods (Fig. 2f). Hillenbrand et al. (2021) reported increased refractory TOC during glacial periods in the glacial sediments in the western Antarctic Peninsula. C/N ratios are indicative of the degree of marine vs terrestrial organic matter because marine organic matter has lower C/N ratios than those of terrestrial organic matter (Lamb et al., 2006 and references therein). Despite the lack of extant terrestrial vegetation and unique soils on present day Antarctica, this relationship has also been used to infer changes in organic matter source on glacial-interglacial time scales in the Ross Sea and the Scotia Sea, where analysis of sediment cores showed high C/N ratios during glacial periods (Kim et al., 2020a, 2020b; Ha et al., 2022). In addition, high C/N ratios are found in subglacial to proximal depositional environments in the Antarctic sediments (Smith et al., 2019). Thus, high C/N ratios in laminated gray mud at BS17-GC02 suggest that the high TOC concentration is related to the reworked TOC from shelf regions during advance of grounded ice. Palynomorph assemblages also support down slope reworking (Fig. 3g). MS values are

commonly observed to correlate to proxies of terrestrial input in the Antarctic sediment cores, often showing high values during glacial periods (Leventer et al., 1996; Pudsey and Camerlenghi, 1998; Hillenbrand and Cortese, 2006; Hillenbrand et al., 2009, 2021; Kim et al., 2020a, 2020b). We infer this relationship is also likely to hold in the present setting, and interpret intervals of increased and fluctuating MS values to indicate terrestrial sediment input from the shelf region (Fig. 2a).

In the modern Southern Ocean south of the Polar Front, biogenic opal production is controlled by sea ice (Chase et al., 2015). During glacial periods, a northward expansion of both summer and winter sea ice coverage around the Antarctic margin has been proposed (Gersonde et al., 2005), along with northward migration of oceanic fronts (Kemp et al., 2010; Manoj and Thamban, 2015; Roberts et al., 2017). The sedimentary signature of these glacial sediments is terrigenous laminated/stratified mud with rare IRD, and a low proportion of biogenic components (biogenic opal and CaCO3) (Hillenbrand et al., 2021). We infer the low biological productivity of surface waters during glacial periods in our study area is likely related to extended sea ice conditions coinciding with northward front migration. Lucchi and Rebesco (2007) and Hillenbrand et al. (2021) also proposed that perennial sea ice condition in the south of BS17-GC02 during glacial periods.

Normalized Mn/Ti ratios in marine sediments have been used as an indicator of relative bottom water oxygenation in deep ocean settings (e.g., Jaccard et al., 2016; Wagner and Hendy 2017; Wu et al., 2018). Mn/Ti was constantly low during glacial periods, consistent with low oxygen conditions (Fig. 2i). Although Hillenbrand et al. (2021) proposed progressively decreasing bottom water oxygenation in glacial-aged sediment cores on the drift off the western Antarctic Peninsula, they inferred conditions remained oxic throughout. We acknowledge that Mn/Ti is uncalibrated, and because other redox sensitive elements were not measured in this study and by Hillenbrand et al. (2021), it is difficult to be confident about the exact oxygenation state of the bottom water during glacial periods. However, we note that in our cores, laminations deposited during glacial periods were well preserved without bioturbation, suggesting that the bottom water oxygen may have been too low to support benthic organisms. We infer that bottom water oxygen concentration was low during glacial periods in our study area (dysoxic to anoxic), consistent with conclusions of other workers from around the Antarctic continent supporting ceased/decreased AABW formation (e.g., Jaccard and Galbraith, 2012; Galbraith and Jaccard, 2015; Jaccard et al., 2016; Wagner and Hendy, 2017; Wu et al., 2018). Bottom water oxygenation is related to ventilation and export production (Kim et al., 2011, 2017; Jaccard and Galbraith, 2012; Galbraith and Jaccard, 2015; Jaccard et al., 2016; Wagner and Hendy, 2017; Wu et al., 2018). Although increased TOC is refractory, the relatively high TOC concentration has potential to draw down bottom water oxygen in the study area. The

KOPRI 극지연구소

decomposition of the elevated TOC input may additionally draw down dissolved oxygen concentration of the bottom water during glacial periods. Thus, the dysoxic to anoxic bottom water condition was ascribed to ceased/decreased oxygen-rich AABW formation and additional decomposition of elevated organic matter during glacial periods.

A schematic of the inferred depositional environments during the interglacial phase is shown in Figure 7a.

6.1.2. Glacial deposition at BS17-GC01

There is a brown interval, corresponding to MIS 3, at BS17-GC01. Mn/Ti ratio showed high values in both brown intervals (MIS 1 and 3) (Fig. 4i). We infer these ratio values are consistent with oxic bottom water condition at BS17-GC01 site during MIS 3, coinciding with increased opal concentrations during this time. However, no diatoms or other bio-siliceous fragments were observed. However, due to the presence of black colored volcanic sand sized grains we infer the origin of the opal is volcanic. Volcanic grains are vitric in BS17-GC01 (Fig. S1). This means they likely have low MS values and implies that rapid formation. As a result, they tend to be extracted by we-alkaline method. In addition, Zulaikah and Nurlaily (2018) reported volcanic ash has lower MS values than classic sand and/or silt. High C/N ratios also indicate that reworked sediments are dominant.

During MIS 2, diatom production was low, but the assemblage was dominated by F. kerguelensis (Fig. 5h and i), with occurrences of Eucampia antarctica sp., an indicator BS17-GC01 probably covered by seasonal, but not perennial, sea ice during that time (Crosta et al., 2005; Xiao et al., 2016) (Table S1). Increased gravelly IRDs (grains >1 mm) were observed only during MIS 3 which is relatively warmer climate during the last glacial period MIS 2 and MIS 4 (Fig. 5g). The absence of gravelly IRDs at BS17-GC01 indicates that gravelly IRDs were probably limited to BS17-GC02 site during MIS 2 and 4.

SS MGS showed increased values up to 40 μm during MIS 2 and 4 (Fig. 5b). This indicates that the bottom current intensified during MIS 2 and 4 at distal continental rise site. That is, bottom current speed was higher at BS17-GC01 than that at BS17-GC02 during MIS 2 and 4. ln(Zr/Rb) data are largely in agreement with SS MGS data, supporting stronger bottom current at BS17-GC01 site.

In both the Scotia and Bellingshausen Seas, the increased MS values during glacial periods are related to sand- to coarse silt-sized grains (16 – 250 μm) having high MS values, implying that MS could be used to infer IRD transport in this setting (Kim et al., 2018b, 2020b, 2022a; Shin et al., 2020). Kim et al. (2020b) proposed that different source regions between glacial and deglacial/interglacial periods could result in different IRD with different characteristics deposited at the sites. Kim et al. (2022a) proposed that sand- to

coarse silt-sized grains, entrapped into grounded ice while advancing, were mainly deposited on the continental shelf during ice shelf development during deglacial to interglacial periods by sub ice shelf melting. In contrast, icebergs during glacial periods still contains the sand- to coarse silt-sized grains and were drifted into the deep basin. We infer that IRD was delivered to BS17-GC01 throughout the last glacial period, but the size characteristics if the IRD was unique during MIS 3. However, it was reported that very fine sands can be sorted by bottom current in the Drake Passage where (Wu et al., 2021). Nonetheless, sand sized grains are difficult to be transported from source areas considering the directions of currents and sinking rate of sand grains. SS MGS values during MIS 2 and 4 are ~40 μm (Fig. 5b), which is similar to those reported in the Drake Passage (Wu et al., 2021). Thus, possibility of sorting sand sized grains by bottom current cannot be ruled out.

A schematic of the inferred depositional environments during the glaciation phase is shown in Figure 7a.

6.2. Deglacial periods

6.2.1. BS17-GC02

During deglacial periods, brown laminated mud was deposited at BS17-GC02. This mud was characterized by fluctuating MS values, high a* and b* values, low/decreased C/N ratios, high Mn/Ti, fluctuating MGS, high grain density, and disperse grains >1 mm. Biological characteristics of the interval included low biogenic opal, TOC, CaCO3, an absence of diatoms, and increased total palynomorphs represented by reworked species (Figs. 2 and 3). These characteristics are similar to those observed in other deglacial settings (Hillenbrand et al., 2021).

The overall sedimentary characteristics between glacial and deglacial periods in this setting are quite similar (Hillenbrand et al., 2021; this study). Thus, deglacial brown laminated mud at BS17-GC02 is considered mainly contourites as well. However, we infer that the down-slope sediment transportation mechanism is different between glacial and deglacial periods. Down-slope sediment transportation occurred by the advance of grounded ice across the shelf during glacial periods (Hillenbrand et al., 2021), but occurred by sediment-rich subglacial melt water out as grounded ice retreats across the shelf during deglacial periods.

Other outstanding difference between the two periods are sediment color and elemental composition; gray with low Mn/Ti during glacial periods vs brown with high Mn/Ti during deglacial periods (Fig. 2i). Elevated Mn has been widely reported from the

Southern Ocean during deglacial periods, and attributed to high-oxygen conditions (Jaccard and Galbraith, 2012; Galbraith and Jaccard, 2015; Jaccard et al., 2016; Wagner and Hendy, 2017; Wu et al., 2018): we infer the increased Mn/Ti rations during deglacials at BS17-GC02 arises from increased bottom water oxygenation. This is consistent with observations of rapidly increasing bottom-water oxygen oxygenation during glacial termination at other sites along the western Antarctic Peninsula (Hillenbrand et al., 2021) and in Prydz Bay (Wu et al., 2018).

We are intrigued by the constantly low TOC concentrations (Fig. 2f). It has previously been suggested that TOC minima in these settings could imply low (1–2 cm/kyr) sedimentation rates or minimum input of refractory organic material (Hillenbrand et al., 2021). A few deci-meter to meter scale deposits during deglacial periods implies that high sedimentation rates although we cannot define the glacial-deglacial-interglacial boundary precisely in this study. The thickness of glacial terminations of previously reported cores also showed similar sedimentation (Hillenbrand et al., 2021). In the Scotia Sea surface diatom production started to increase from deglacial periods with sea ice retreat (Sprenk et al., 2013; Xiao et al., 2016; Kim et al., 2020b). As sea ice is the main controlling factor for surface diatom production in the Southern Ocean (Chase et al., 2015), surface diatom production should have increased during deglacial periods with sea ice decrease although the signal of increased production is not clear in sediments. This is supported by C/N ratios. The last deglacial period showed TOC minima with low to moderate C/N ratios indicating some sediment input from the shelf region (Fig. 2f and g). However, the two previous deglacial intervals showed low C/N ratios indicating that organic carbon relatively more originates from surface water by biological production. However, decomposition of non-refractory organic matter under oxic bottom water conditions can draw down TOC concentration (Hillenbrand et al., 2021). This likely results in low TOC concentrations in the sediment. Thus, TOC minima with low to moderate C/N ratios indicates increased proportion of marine organic matter and increased decomposition of the organic matter under oxic bottom water conditions during deglacial periods. Co-occurrence of bioturbation and laminated mud during deglacial periods suggests depositional alternation between lamination as a combination of distal turbidite and contourite leaving high sedimentation and bioturbated hemipelagic deposition leaving low sedimentation. This seems to be related to discontinuous retreat of ice sheet/shelf on the shelf.

A schematic of the inferred depositional environments during the interglacial phase is shown in Figure 7b.

6.2.2. BS17-GC01

The faintly laminated, bioturbated brown interval at BS17-GC01 is considered to represent deposition during the last deglacial period (Fig. 4). MS values sharply decreased into the last deglacial, accompanied by an increase in biogenic opal concentration (Fig. 4a and d). We infer this represents an increase in diatom production, while the assemblage contains increasing frequency of the (mainly) open water species F. kerguelensis (Fig. 5h). Although C/N ratios of BS17-GC02 showed moderate values, those of BS17-GC01 showed low values (Figs. 2g and 4g). This means that BS17-GC01 site became open ocean condition earlier than BS17-GC02, as expected. The long distance of BS17-GC01 from the shelf break can additionally result in less terrestrial influence than BS17-GC02. Mn/Ti started to increase with a* and b* increases, indicating oxygenated bottom water condition at BS17-GC01 site (Fig. 4b, c, and i).

A schematic of the inferred depositional environments during the deglaciation phase is shown in Figure 7b.

6.3. Interglacial periods

6.3.1. Interglacial periods from site BS17-GC02

During interglacial periods, dark brown to gray biogenic bearing mud is deposited at BS17-GC02. It is characterized by minimum of MS values, high a* and b* values, increased biogenic opal concentration, increasing TOC concentration, increasing C/N ratios (but still low), increased CaCO3 concentration (right after biogenic opal), high Mn/Ti, fluctuating MGS, low grain density, abundant grains >1 mm, decreased total palynomorphs represented by modern like species, and increased diatoms consisting mainly of F. kerguelenesis (Figs. 2 and 3). These characteristics are similar to those of peak to moderate (late) interglacial periods in the western Antarctic Peninsula (Hillenbrand et al., 2021).

As previous studies in the Amundsen and Bellingshausen Seas reported increased surface diatom productivity during interglacial periods (Hillenbrand et al., 2009, 2021), biogenic opal concentration showed its maxima within dark brown intervals, indicated by the maxima of a* and b* (Fig. 2b and c). TOC concentration increased but C/N ratio was still low, implying that export production increase is related to increased surface water diatom production (Fig. 2f and g). Total diatom valves also significantly increased during interglacial periods (Fig. 2i). The dominant species is F. kerguelensis, an open ocean species indicating Antarctic Circumpolar Current influence (Zielinski and Gersonde, 1997; Abelmann et al., 2006; Xiao et al., 2016). In addition, total palynomorph, composed of reworked species, is significantly reduced but few species living modern like open ocean conditions was observed (Fig. 3g). MS values were constantly low and grain density decreased,

implying less terrestrial input and increased biogenic component under open ocean conditions during interglacial periods.

Occurrence of grains >1 mm was focused on the interglacial periods implying that gravelly IRD input likely increased during interglacial periods in the Bellingshausen Sea (Fig. 3f). Mn/Ti ratio was also elevated, but not higher than those during deglacial periods despite its darker brown color (Fig. 2i). Although TOC concentrations were similar to those observed during glacial periods, interglacial sediments are characterized by brown color, bioturbation, and high Mn/Ti (Fig. 2i). These characteristics suggest bottom water at BS17-GC02 remained oxygenated during interglacial periods. We conclude that the main factor to control bottom water oxygenation in this setting is bottom water formation, not surface production, which draws down dissolved oxygen by decomposition, in the Bellingshausen Sea. An increase in CaCO3 concentration, mainly composed of planktonic foraminifera N. pachyderma, overlies biogenic opal maxima at BS17-GC02 during MIS 5 and 7 coincident with change of sediment color changed into gray across a gradual bioturbated boundary (Fig. 2). However, neither CaCO3 peak nor gray colored sediment were observed in MIS 1. This suggests that increased CaCO3 intervals may include also the early part of glacial periods. This is consistent with previous reports that high biogenic intervals correspond to glacial to early part of glacial periods (Hillenbrand et al., 2021).

A schematic of the inferred depositional environments during the interglacial phase is shown in Figure 7c.

KOPRI 극지연구소

6.3.2. Interglacial periods from site BS17-GC01

Although biogenic opal concentration maxima occurred in peak interglacial periods of BS17-GC01, marked by dark brown intervals corresponding maximum of a* and b*, dark brown intervals were not observed in the core (Fig. 4). Biogenic opal concentration showed high values and total diatom valves, consisting of mainly F. kerguelensis (~90%), were outstandingly high, indicating increased surface diatom production under open ocean conditions (Figs. 4d, 5h, and 5i). Grain density showed decreased values, also supporting increased biological composition at BS17-GC01. Biogenic opal and TOC concentration at BS17-GC01 was lower than BS17-GC02. This is consistent with lower grain density values at BS17-GC02 than those at BS17-GC01 (Figs. 3e and 5f). CaCO3 concentrations of BS17-GC01 and BS17-GC02 during MIS 1 were very low although those of BS17-GC02 during MIS 5 and 7 were relatively high (Figs. 2h and 4h). Since core top CaCO3 concentration increase was found from some cores not all, indicating some local effect (Hillenbrand et al., 2021).

Decreased SS MGS values and ln(Zr/Rb) during MIS 1 indicates that bottom current was intensified during MIS 2 and 4 at BS17-GC01 site. The last glacial-Holocene

Antarctic Circumpolar Current flow speed differences in the Drake Passages showed different pattern according to its latitude (McCave et al., 2014). In addition, glacial-interglacial frontal migration in the Southern Ocean was reported (Kemp et al., 2010; Manoj and Thamban, 2015; Roberts et al., 2017). Thus, the bottom water intensity change on glacial-interglacial scale at the study site is also considered to be related to glacial-interglacial frontal migration. As McCave et al. (2014) and Kim et al. (2020b) reported increased SS MGS from the south of the Polar Front close to slope/rise boundary, BS17-GC01 record might reflect intensified southwestward flowing bottom current influence.

A schematic of the inferred depositional environments during the interglacial phase is shown in Figure 7c.

7. Conclusions

In this study, we documented glacial-interglacial succession from two sediment cores from the Bellingshausen Sea continental rise to understand glacial-interglacial changes in oceanographic conditions and depositional process in response to ice sheet dynamics. The followings are the main conclusions:

1. Surface diatom production started to increase from deglacial periods as ice sheet/shelf retreated, reaching a maximum during interglacials MIS 1, 5, and 7. In MIS 5 and MIS 7, the maxima of diatom productivity was overlain by a CaCO3 peak (but not in MIS 1). Low diatom production is thought to be related to the influence of extensive sea ice. Low MS values also indicate that input of terrestrial material was lowest during MIS 1, 5, and 7. However, frequent occurrence of IRD grains indicate active ice shelf calving on the shelf during interglacial periods.
2. Terrestrially-derived, laminated mud was dominant during glacial and deglacial periods. During glacial periods, gray laminated mud was observed, with increased refractory TOC, low Mn/Ti, and lacking bioturbation, implying dysoxic bottom water conditions. In contrast, we infer, brown laminated mud with increased Mn/Ti and intermittent bioturbation observed in sediments deposited during deglacial periods, implies oxic bottom water conditions.
3. Increased bottom water oxygenation endured during interglacial periods until surface diatom production increased. Thus, we infer the main factor controlling bottom water oxygenation in this setting is the degree of AABW formation; increased during interglacial and decreased during glacial periods.
4. A strong correlation between SS MGS and %SS imply that SS at two cores can be used as a proxy for bottom current intensity, despite IRD influence. Laminated mud during

glacial to deglacial periods is likely a result of varying bottom current intensity.

KOPRI
극지연구소

벨링스하우젠해에서의 빙상 빙하기 간빙기 변화에 따른 해양환경 변화와 퇴적 작용 변화[17)]

Sunghan Kim[a,*], Young-Suk Bak[b], Joseph G. Prebble[c], Myung-Il Kang[a], Sookwan Kim[d], Jinku Park[a], Min Kyung Lee[a], Jae Il Lee[a], Kyu-Cheul Yoo[a], Heung Soo Moon[a]

[a]Korea Polar Research Institute, Incheon, 21990, South Korea
[b]Department of Earth and Environmental Sciences, Jeonbuk National University, Jeonju, 54896, South Korea
[c]Department of Surface Geosciences, GNS Science, Lower Hutt, New Zealand
[d]Korea Institute of Ocean Science and Technology, Busan 49111, Republic of Korea

요약: 남극 대륙 주변부 퇴적물은 빙상의 구성 변화와 연관되어 대륙붕에서 침식된 뒤 사면 및 해저 융기로 수송된다. 이러한 수송 경로의 동역학을 이해하는 것은 원거리 심해 퇴적 기록을 활용하여 과거 남극 빙상의 변화를 규명하는 데 매우 중요하다. 그러나 이러한 연결 관계는 아직 충분히 이해되지 못하고 있다. 본 연구에서는 벨링스하우젠해 대륙 융기에서 채취된 두 개의 퇴적 코어(BS17-GC01, BS17-GC02)에 대한 다중 지표 기록을 제시하여, 퇴적 체계와 빙상 동역학 간의 관계를 탐구하였다. 두 코어는 빙기-간빙기 규모에서 퇴적학적 및 퇴적물 특성 변화를 보인다. 생물기원 퇴적물은 해양동위원소단계 1, 5, 7 동안 개방 해양 조건에서 퇴적되었다. 빙기에서 융빙기로 전이되는 시기의 퇴적물은 저층 해류 강도의 변화에 의해 층리 구조가 발달하였다. 육상 기원 퇴적물은 빙기 동안 접지빙이 확장하면서 대륙붕으로부터 수송되었을 뿐 아니라, 융빙기 동안 빙상이 후퇴하는 과정에서도 운반된 것으로 해석된다. 퇴적물 색은 융빙기 이후 갈색으로 변화하였으며, 높은 Mn/Ti 비율과 생물교란의 출현은 연구 지역에서 저층수 산소화가 증가했음을 시사한다. 표층 생산성은 융빙기부터 증가하기 시작하였으므로, 이 지역에서의 저층수 산소화 증가는 환기 작용, 즉 남극저층수 형성과 관련된 것으로 추정된다. 이는 융빙기 이후 간빙기 동안 남극저층수 형성이 증가한 반면, 빙기 동안에는 감소했음을 의미한다. 따라서 BS17-GC01과 BS17-GC02에서 나타나는 퇴적 및 퇴적환경 변화는 후기 제4기 동안의 빙상 동역학과 밀접하게 연관되어 있다.

17) 이 연구 결과는 다음의 논문으로 출판되었음: Jung, J. et al. (2021). "Glacial-interglacial changes in oceanic conditions and depositional process in the continental rise in response to ice sheet (shelf) variation in Bellingshausen Sea, Antarctica" Frontiers in Marine Science 10: 1183516.

References

Abelmann, A., Gersonde, R., Cortese, G., Kuhn, G. and Smetacek, V. (2006). Extensive phytoplankton blooms in the Atlantic sector of the glacial Southern Ocean. Paleoceanography 21, PA1013. doi:10.1029/2005PA001199.

Anderson, J. B. (1999). Antarctic Marine Geology. Cambridge University Press, Cambridge.

Anderson, J. B., Shipp, S. S., Lowe, A. L., Wellner, J. S. and Mosola, A. B. (2002). The Antarctic Ice Sheet during the Last Glacial Maximum and its subsequent retreat history: a review. Quat. Sci. Rev. 21, 49–70.

Askin, R. A. (2000). Spores and pollen from the McMurdo Sound erratics, Antarctica. Antarct. Res. Ser. 76, 161–181.

Askin, R. A. and Raine, J. I. (2000). Oligocene and Early Miocene terrestrial palynology of the Cape Roberts Drillhole CRP-2/2A, Victoria Land Basin, Antarctica. Terra Antarctica 7, 493–501.

Bak, Y.-S., Yoo, K.-C., Lee, J. I. and Yoon, H. I. (2018). Glacial-interglacial records from sediments in Powell Basin, Antarctica. Antarct. Sci. 30, 371–378.

Chase, Z., Kohfeld, K. E. and Matsumoto, K. (2015). Controls on biogenic silica burial in the Southern Ocean. Global Biogeochm. Cycles 29, 1599–1616. doi:10.1002/2015GB005186.

Crosta, X., Romero, O., Armand, L. K. and Pichon, J. J. (2005). The biogeography of major diatom taxa in Southern Ocean sediments: 2. Open ocean related species. Palaeogeogr. Palaeoclimatol. Palaeoecol. 223, 66–92.

Croudace, I. W., Rindby, A. and Rothwell, R. G. (2006). ITRAX: description and evaluation of a new multi-function X-ray core scanner. Geological Society, London, Special Publicatios 267, 51–63.

DeConto, R. M. and Pollard, D. (2016). Contribution of Antarctica to past and future sea level rise. Nature 531, 591–597. doi:10.1038/nature17145.

DeMaster, D. J. (1981). The supply and accumulation of silica in the marine environment. Geochim. Cosmochim. Acta 5, 1715–1732.

De Santis, L., Anderson, J. B., Brancolini, G. and Zayatz, I. (1995). Seismic Record of Late Oligocene Through Miocene Glaciation on the Central and Eastern Continental Shelf of the Ross Sea. In: Cooper, A. K., Barker, P. F. and Brancolini, G. (Eds.), Geology and Seismic Stratigraphy of the Antarctic Margin. American Geophysical Union Antarctic Research Series 68. pp. 235–260.

Dinniman, M. S., Klinck, J. M. and Smith Jr., W. O. (2011). A model study of Circumpolar Deep Water on the West Antarctic Peninsula and Ross Sea continental shelves.

KOPRI 극지연구소

Deep-Sea Res. II 58, 1508–1523. doi:10.1016/j.dsr2.2010.11.013.

Domack, E. W., Jacobson, E. A., Shipp, S. and Anderson, J. B. (1999). Late Pleistocene–Holocene retreat of the West Antarctic Ice-Sheet system in the Ross Sea: Part 2—Sedimentologic and stratigraphic signature. GSA Bull. 111, 1517–1536.

Domack, E. W., Leventer, A., Dunbar, R., Taylor, F., Brachfeld, S., Sjunneskog, C., Cowan, E., Daniels, J. W., Escutia, C., Evans, A., Eyles, N., Guyodo, Y., Ioio, M., Iwai, M., Kyte, F., Lauer, C., Maldonado, A., Morez, T., Osterman, L., Pudsey, C., Schuffert, J., Vigar, K., Weinheimer, A., Williams, T., Winter, D. and Wolf-Welling, T. C. W. (2001). Chronology of the Palmer Deep site, Antarctic Peninsula: A Holocene palaeoenvironmental reference for the circum-Antarctic. The Holocene 11, 1–9. doi:10.1191/095968301673881493.

Dowdeswell, J. A., Ó Cofaigh, C., Taylor, J., Kenyon, N. H., Mienert, J. and Wilken, M. (2002). On the architecture of high-latitude continental margins: the influence of ice-sheet and sea-ice processes in the Polar North Atlantic. In: Dowdeswell, J. A. and Ó Cofaigh, C. (Eds.), Glacier-Influenced Sedimentation on High-Latitude Continental Margins. Geological Society, Special Publication 203. pp. 33–54 London.

Dowdeswell, J. A., Ó Cofaigh, C., Noormets, R., Larter, R. D., Hillenbrand, C.-D., Benetti, S., Evans, J. and Pudsey, C. J. (2008). A major trough-mouth fan on the continental margin of the Bellingshausen Sea, West Antarctica: The Belgica Fan. Mar. Geol. 252, 129–140.

Esper, O. and Zonneveld, K. A. F. (2007). The potential of organic-walled dinoflagellate cysts for the reconstruction of past sea-surface conditions in the Southern Ocean. Mar. Micropaleontol. 65, 185–212.

Fischer, H., Fundel, F., Ruth, U., Twarloh, B., Wegner, A., Udisti, R., Becagli, S., Castellano, E., Morganti, A., Severi, M., Wolff, E., Littot, G., Röthlisberger, R., Mulvaney, R., Hutterli, M. A., Kaufmann, P., Federer, U., Lambert, F., Bigler, M., Hansson, M., Jonsell, U., De Angelis, M., Boutron, C., Siggaard-Andersen, M.-L., Steffensen, J. P., Barbante, C., Gaspari, V., Gabrielli, P. and Wagenbach, D. (2007). Reconstruction of millennial changes in dust emission, transport and regional sea ice coverage using the deep EPICA ice cores from the Atlantic and Indian Ocean sector of Antarctica. Earth Planet. Sci. Lett. 260, 340–354.

Folk, R. L. and Ward, W. C. (1957). Brazos River bar [Texax]; a study in the significance of grain size parameters. J. Sediment. Res. 27, 3–26.

Galbraith, E. D. and Jaccard, S. L. (2015). Deglacial weakening of the oceanic soft tissue pump: Global constraints from sedimentary nitrogen isotopes and oxygenation proxies. Quat. Sci. Rev. 109, 38–48. doi:10.1016/j.quascirev.2014.11.012.

Gersonde, R., Crosta, X., Abelmann, A. and Armand, L. (2005). Sea-surface temperature and

KOPRI 극지연구소

sea ice distribution of the Southern Ocean at the EPILOG Last Glacial Maximum – a circum-Antarctic view based on siliceous microfossil records. Quat. Sci. Rev. 24, 869–896.

Golledge, N. R., Fogwill, C. J., Mackintosh, A. N. and Buckley, K. M. (2012). Dynamics of the last glacial maximum Antarctic ice sheet and its response to ocean forcing. Proc. Natl. Acad. Sci. doi:10.1073/pnas.1205385109.

Gordon, A. L. (2009). Bottom water formation. In: Steele, J. H., Thorpe, S. A. and Turekian, K. K. (Eds.), Ocean Currents. Associated Press, 263–269.

Ha, S., Colizza, E., Torricella, F., Langone, L., Giglio, F., Kuhn, G., Macrì, P. and Khim, B.-K. (2022). Glaciomarine sediment deposition on the continental slope and rise of the central Ross Sea since the Last Glacial Maximum. Mar. Geol. 445, 106752. doi:10.1016/j.margeo.2022.106752.

Hillenbrand, C.-D., Camerlenghi, A., Cowan, E. A., Hernández-Molina, F. J., Lucchi, R. G., Rebesco, M. and Uenzelmann-Neben, G. (2008a). The present and past bottom-current flow regime around the sediment drifts on the continental rise west of the Antarctic Peninsula. Mar. Geol. 255, 55–63.

Hillenbrand, C.-D., Crowhurst, S. J., Williams, M., Hodell, D. A., McCave, I. N., Ehrmann, W., Xuan, C., Piotrowski, A. M., Hernández-Molina, F. J., Graham, A. G. C., Grobe, H., Williams, T. J., Horrocks, J. R., Allen, C. S. and Larter, R. D. (2021). New insights from multi-proxy data from the West Antarctic continental rise: Implications for dating and interpreting Late Quaternary paleoenvironmental records. Quat. Sci. Rev. 257, 106842. doi:10.1016/j.quascirev.2021.106842.

Hillenbrand, C.-D. and Cortese, G. (2006). Polar stratification: a critical view from the Southern Ocean. Palaeogeogr. Palaeoclimatol. Palaeoecol. 242, 240–252.

Hillenbrand, C.-D., Grobe, H., Diekmann, B., Kuhn, G. and Fütterer, D. J. (2003). Distribution of clay minerals and proxies for productivity in surface sediments of the Bellingshausen and Amundsen seas (West Antarctica) – Relation to modern environmental conditions. Mar. Geol. 193, 253–271.

Hillenbrand, C.-D., Kuhn, G. and Frederichs, T. (2009). Record of a Mid-Pleistocene depositional anomaly in West Antarctic continental margin sediments: an indicator for ice-sheet collapse? Quat. Sci. Rev. 28, 1147–1159.

Hillenbrand, C.-D., Moreton, S. G., Caburlotto, A., Pudsey, C. J., Lucchi, R. G., Smellie, J. L., Benetti, S., Grobe, H., Hunt, J. B. and Larter, R. D. (2008b). Volcanic time-markers for Marine Isotopic Stages 6 and 5 in Southern Ocean sediments and Antarctic ice cores: implications for tephra correlations between palaeoclimatic records. Quat. Sci. Rev. 27, 518–540.

Jaccard, S. L. and Galbraith, E. D. (2012). Large climate-driven changes of oceanic oxygen

concentrations during the last deglaciation. Nat. Geosci. 5, 151–156. doi:10.1038/ngeo1352.

Jaccard, S. L., Galbraith, E. D., Martínez-García, A. and Anderson, R. F. (2016). Covariation of deep Southern Ocean oxygenation and atmospheric CO2 through the last ice age. Nature 530, 207–210. doi:10.1038/nature16514.

Jimenez-Espejo, F. J., Presti, M., Kuhn, G., McKay, R., Crosta, X., Escutia, C., Lucchi, R. G., Tolotti, R., Yoshimura, T., Huertas, M. O., Macrì, P., Carburlotto, A. and De Santis, L. (2020). Late Pleistocene oceanographic and depositional variations along the Wilkes Land margin (East Antarctica) reconstructed with geochemical proxies in deep-sea sediments. Glob. Planet. Change 184, 103045. doi:10.1016/j.gloplacha.2019.103045.

Kemp, A. E. S., Grigorov, I., Pearce, R. B. and Naveira Garabato, A. C. (2010). Migration of the Antarctic Polar Front through the mid-Pleistocene transition: evidence and climatic implications. Quat. Sci. Rev. 29, 1993–2009.

Kilfeather A. A., Ó Cofaigh, C., Lloyd, J. M., Dowdeswell, J. A., Xu, S. and Moreton, S. G. (2011). Ice-stream retreat and ice-shelf history in Marguerite Trough, Antarctic Peninsula: Sedimentological and foraminiferal signatures. Geol. Soc. Am. Bull. 123, 997–1015. http://doi:10.1130/B30282.1.

Kim, S., Khim, B.-K., Uchida, M., Itaki, T. and Tada, R. (2011). Millennial-scale paleoceanographic events and implication for the intermediate-water ventilation in the northern slope area of the Bering Sea during the last 71 kyrs. Global. Planet. Change 79, 89–98. doi:10.1016/j.gloplacha.2011.08.004.

Kim, S., Khim, B.-K., Ikehara, K., Itaki, T., Shibahara, A. and Yamamoto, M. (2017). Millennial-scale changes of surface and bottom water conditions in the northwestern Pacific during the last deglaciation. Glob. Planet. Change 154, 33–43. doi:10.1016/j.gloplacha.2017.04.009.

Kim, S., Lee, J. I., McKay, R. M., Yoo, K. C., Bak, Y. S., Lee, M. K., Roh, Y. H., Yoon, H. I., Moon, H. S. and Hyun, C. U. (2020a). Late Pleistocene paleoceanographic changes in the Ross Sea – Glacial-interglacial variations in paleoproductivity, nutrient utilization, and deep-water formation. Quat. Sci. Rev. 239, 106356. doi:10.1016/j.quascirev.2020.106356.

Kim, S., Lee, M. K., Shin, J. Y., Yoo, K. C., Lee, J. I., Kang, M. I., Moon, H. S. and Prebble, J. G. (2022a). Variation in magnetic susceptibility in the Bellingshausen Sea continental rise since the last glacial period and implications for terrigenous material input mechanisms. Palaeogeogr. Palaeoclimatol. Palaeoecol. 594, 110948. doi:10.1016/j.palaeo.2022.110948.

Kim, S., McKay, R. M., Lee, J. I., Yoo, K. C., Lee, M. K. and Moon, H. S. (2022b).

Bioturbation supplying young carbon into West Antarctic continental margin sediment. Palaeogeogr. Palaeoclimatol. Palaeoecol.

Kim, S., Yoo, K. C., Lee, J. I., Roh, Y. H., Bak, Y. S., Um, I. K., Lee, M. K. and Yoon, H. I. (2020b). Paleoceanographic changes in the Southern Ocean off Elephant Island since the last glacial period: Links between surface water productivity, nutrient utilization, bottom water currents, and ice-rafted debris. Quat. Sci. Rev. 249, 106563. doi:10.1016/j.quascirev.2020.106563.

Kim, S., Yoo, K. C., Lee, J. I., Khim, B. K., Bak, Y. S., Lee, M. K., Lee, J., Domack, E. W., Christ, A. J. and Yoon, H. I. (2018a). Holocene paleoceanography of Bigo Bay, west Antarctic Peninsula: Connections between surface water productivity and nutrient utilization and its implication for surface-deep water mass exchange. Quat. Sci. Rev. 192, 59–70. doi:10.1016/j.quascirev.2018.05.028.

Kim, S., Yoo, K. C., Lee, J. I., Lee, M. K., Kim, K. and Yoon, H. I. (2018b). Relationship between magnetic susceptibility and sediment grain size since the last glacial period in the Southern Ocean off the northern Antarctic Peninsula – Linkages between the cryosphere and atmospheric circulation. Palaeogeogr. Palaeoclimatol. Palaeoecol. 505, 359–370. doi:10.1016/j.palaeo.2018.06.016.

Lamb, A. L., Wilson, G. P. and Leng, M. J. (2006). A review of coastal palaeoclimate and relative sea-level reconstructions using δ13C and C/N ratios in organic material. Earth Sci. Rev. 75, 29–57.

Lavoie, C., Domack, E. W., Pettit, E. C., Scambos, T. A., Larter, R. D., Schenke, H.-W., Yoo, K. C., Gutt, J., Wellner, J., Canals, M., Anderson, J. B. and Amblas, D. (2015). Configuration of the Northern Antarctic Peninsula Ice Sheet at LGM based on a new synthesis of seabed imagery. The Cryosphere 9, 613–629. doi:10.5194/tc-9-613-2015.

Leventer, A., Domack, E. W., Ishman, S. E., Brachfeld, S., McClennen, C. E. and Manley, P. (1996). Productivity cycles of 200–300 years in the Antarctic Peninsula region: understanding linkages among the sun, atmosphere, oceans, sea ice, and biota. Geol. Soc. Am. Bull. 108, 1626–1644. doi:10.1130/0016-7606(1996)108<1626:PCOYIT>2.3.CO;2.

Lisiecki, L. E. and Raymo, M. E. (2005). A Pliocene-Pleistocene stack of 57 globally distributed benthic δ18O records. Paleoceanography 20, PA1003. doi:1029/2004PA001071.

Lucchi, R. G. and Rebesco, M. (2007). Glacial contourites on the Antarctic Peninsula margin: insight for palaeoenvironmental and palaeoclimatic conditions. In: Viana, A.R., Rebesco, M., (Eds.), Economic and Palaeoceanographic Significance of Contourite Deposits. Geological Society, Special Publications, 276. pp. 111–127 London.

KOPRI 극지연구소

Lucchi, R. G., Rebesco, M., Camerlenghi, A., Busetti, M., Tomadin, L., Villa, G., Persico, D., Morigi, C., Bonci, M. C. and Giorgetti, G. (2002). Mid-late Pleistocene glacimarine sedimentary processes of a high-latitude, deep-sea sediment drift (Antarctic Peninsula Pacific margin). Mar. Geol. 189, 343–370.

Manoj, M. C. and Thamban, M. (2015). Shifting frontal regimes and its influence on bioproductivity variations during the Late Quaternary in the Indian sector of Southern Ocean. Deep-Sea Res. II 118, 261–274. doi:10.1016/j.dsr2.2015.03.011.

McCave, I. N. and Andrews, J. T. (2019). Distinguishing current effects in sediments delivered to the ocean by ice. I. Principles, methods and examples. Quat. Sci. Rev. 212, 92–107. doi:10.1016/j.quascirev.2019.03.031.

McCave, I. N., Crowhurst, S. J., Kuhn, G., Hillenbrand, C.-D. And Meredith, M. P. (2014). Minimal change in Antarctic Circumpolar Current flow speed between the last glacial and Holocene. Nat. Geosci. 7. doi:10.1038/NGEO2037.

McCave, I. N. and Hall, I. R. (2006). Size sorting in marine muds: processes, pitfalls and prospects for palaeoflow-speed proxies. Geochem. Geophys. Geosyst. 7, Q10N05. doi:10.1029/2006GC001284.

McCave, I. N., Thornalley, D. J. R. and Hall, I. R. (2017). Relation of sortable silt grain size to deep-sea current speeds: calibration of the 'Mud Current Meter'. Deep-Sea Res. Part I 127, 1–12.

Mortlock, R. A. and Froelich, P. N. (1989). A simple method for the rapid determination of opal in pelagic marine sediments. Deep-Sea Res. 36, 1415–1426.

Noormets, R., Dowdeswell, J. A., Larter, R. D., Ó Cofaigh, C. and Evans, J. (2009). Morphology of the upper continental slope in the Bellingshausen and Amundsen Seas – Implications for sedimentary processes at the shelf edge of West Antarctica. Mar. Geol. 258, 100–114. doi:10.1016/j.margeo.2008.11.011.

Ó Cofaigh, C., Davies, B. J., Livingstone, S. J., Smith, J. A., Johnson, J. S., Hocking E. P., Hodgson, D. A., Anderson, J. B., Bentley, M. J., Canals, M., Domack, E., Dowdeswell, J. A., Evans, J., Glasser, N. F., Hillenbrand, C.-D., Larter, R. D., Roberts, S. J. and Simms, A. R. (2014). Reconstruction of ice-sheet changes in the Antarctic Peninsula since the Last Glacial Maximum. Quat. Sci. Rev. 100, 87–110. doi:10.1016/j.quascirev.2014.06.023.

Prebble, J. G., Crouch, E. M., Carter, L., Cortese, G., Bostock, H. and Neil, H. (2013). An expanded modern dinoflagellate cyst dataset for the Southwest Pacific and Southern Hemisphere with environmental associations. Mar. Micropaleontol. 101, 33–48.

Pritchard, H. D., Ligtenberg, S. R. M., Fricker, H. A., Vaughan, D. G., Broeke, M. R. and van den, Padman, L. (2012). Antarctic ice sheet loss driven by basal melting of ice shelves. Nature 484, 502–505. doi:10.1038/nature10968.

KOPRI 극지연구소

Pudsey, C. J. (2000). Sedimentation on the continental rise west of the Antarctic Peninsula over the last three glacial cycles. Mar. Geol. 167, 313–338.

Pudsey, C. J. and Camerlenghi, A. (1998). Glacial-interglacial deposition on a sediment drift on the Pacific margin of the Antarctic Peninsula. Antarct. Sci. 10, 286–308.

Pugh, R. S., MaCave, I. N., Hillenbrand, C.-D. and Kuhn, G. (2009). Circum-Antarctic age modeling of quaternary marine cores under the Antarctic circumpolar current: ice core dust-magnetic correlation. Earth Planet. Sci. Lett. 284, 113–123.

Rebesco, M., Pudsey, C., Canals, M., Camerlenghi, A., Barker, P., Estrada, F. and Giorgetti, A. (2002). Sediment drift and deep-sea channel systems, Antarctic Peninsula Pacific Margin. In: Stow, D. A. V., Pudsy, C. J., Howe, J. A., Faugères. J. C. and Viana, A. R. (Eds.), Deep-water Contourite Systmes: Modern Drifts and Ancient Series, Seismic and Sedimentary Characteristics. Geological Society, London, Memoirs 22, pp. 353–371.

Reimer, P. J., Bard, E., Bayliss, A., Beck, J. W., Blackwell, P. G., Ramsey, C. B., Buck, C. E., Cheng, H., Edwards, R. L., Friedrich, M., Grootes, P. M., Guilderson, T. P., Haflidason, H., Hajdas, I., Hatté, C., Heaton, T. J., Hoffmann, D. L., Hogg, A. G., Hughen, K. A., Kaiser, K. F., Kromer, B., Manning, S. W., Niu, M., Reimer, R. W., Richards, D. A., Scott, E. M., Southon, J. R., Staff, R. A., Turney, C. S. M. and van der Plicht, J. (2013). IntCal13 and Marine13 Radiocarbon age calibration curves 0-50,000 years cal BP. Radiocarbon 55, 1869–1887.

Roberts, J., McCave, I. N., McClymont, E. L., Kender, S., Hillenbrand, C. D., Matano, R., Hodell, D. A. and Peck, V. L. (2017). Earth Planet. Sci. Lett. 474, 397–408. doi:10.1016/j.epsl.2017.07.004.

Scherer, R. P. (1994). A new method for the determination of absolute abundance of diatoms and other silt-sized sedimentary particles. J. Paleolimnol. 12, 171–180.

Shin, J. Y., Kim, S., Zhao, X., Yoo, K. C., Yu, Y., Lee, J. I., Lee, M. K. and Yoon, H. I. (2020). Particle-size dependent magnetic properties of Scotia Sea sediments since the Last Glacial Maximum: Glacial ice-sheet discharge controlling magnetic proxeis. Palaeogeogr. Palaeoclimatol. Palaeoecol. 557, 109906. doi:10.1016/j.palaeo.2020.109906.

Smith, J. A., Graham, A. G. C., Post, A. L., Hillenbrand, C.-D., Bart, P. J. and Powell, R. D. (2019). The marine geological imprint of Antarctic ice shelves. Nat. Commun. 10, 5635. doi:10.1038/s41467-019-1349605.

Sprenk, D., Weber, M. E., Kuhn, G., Rosén, P., Frank, M., Molina-Kescher, M., Liebetrau, V. and Röhling, H. G. (2013). Southern Ocean bioproductivity during the last glacial cycle—new detection method and decadal-scale insight from the Scotia Sea. Geol. Soc. London. Spec. Publ. 381, 245–261. doi:10.1144/SP381.17.

Stevenard, N., Govin, A., Kissel, C. and Toer, A. (2023). Correction of the IRD influence for

paleo-current flow speed reconstructions in hemipelagic sediments. Paleoceanography and Paleoclimatology 38, e2022PA004500. doi:10.1029/2022PA004500.

Stuiver, M. and Reimer, P. J. (1993). Extended 14C data base and revised CALIB 3.0 14C age calibration program. Radiocarbon 35, 215–230.

Tamura, T., Ohshima, K. I. and Nihashi, S. (2008). Mapping of sea ice production for Antarctic coastal polynyas. Geophys. Res. Lett. 35, L07606, doi:10.1029/2007/GL032903.

The RAISED Consortium, Bentley, M. J., Ó Cofaigh, C., Anderson, J. B., Conway, H., Davies, B., Graham, A. G. C., Hillenbrand, C.-D., Hodgson, D. A., Jamieson, S. S. R., Larter, R. D., Mackintosh, A., Smith, J. A., Verleyen, E., Ackert, R. P., Bart, P. J., Berg, S., Brunstein, D., Canals, M., Colhoun, E. A., Crosta, X., Dickens, W. A., Domack, E., Dowdeswell, J. A., Dunbar, R., Ehrmann, W., Evans, J., Favier, V., Fink, D., Fogwill, C. J., Glasser, N. F., Gohl, K., Golledge, N. R., Goodwin, I., Gore, D. B., Greenwood, S. L., Hall, B. L., Hall, K., Hedding, D. W., Hein, A. S., Hocking, E. P., Jakobsson, M., Johnson, J. S., Jomelli, V., Jones, R. S., Klages, J. P., Kristoffersen, Y., Kuhn, G., Leventer, A., Licht, K., Lilly, K., Lindow, J., Livingstone, S. J., Massé, G., McGlone, M. S., McKay, R. M., Melles, M., Miura, H., Mulvaney, R., Nel, W., Nitsche, F. O., O'Brien, P. E., Post, A. L., Roberts, S. J., Saunders, K. M., Selkirk, P. M., Simms, A. R., Spiegel, C., Stolldorf, T. D., Sugden, D. E., van der Putten, N., van Ommen, T., Verfaillie, D., Vyverman, W., Wagner, B., White, D. A., Witus, A. E. and Zwartz, D. (2014). A community-based geological reconstruction of Antarctic Ice Sheet deglaciation since the Last Glacial Maximum. Quat. Sci. Rev. 100, 1–9. doi:10.1016/j.quascirev.2014.06.025.

Truswell, E. M. (1983). Recycled Cretaceous and Tertiary pollen and spores in Antarctic marine sediments: A catalogue. Palaeontogr. Abt. B. 186, 121–174.

Vautravers. M. J., Hodell, D. A., Channell, J. E. T., Hillenbrand, C.-D., Hall, M., Smith, J. A. and Larter, R. D. (2013). Palaeoenvironmental records from the West Antarctic Peninsula drift sediments over the last 75 ka. In: Hambrey, M. J., Barker, P. F., Barrett, P. J., Bowman, V., Davies, B., Smellie, J. L. and Tranter, M. (Eds.), Antarctic Palaeoenvironmnets and Earth-Surface Processes, 318, Geol. Soc. London Special Publ. pp. 263–276. doi:10.1144/SP381.12.

Wagner, M. and Hendy, I. L. (2017). Trace metal evidence for a poorly ventilated glacial Southern Ocean. Quat. Sci. Rev. 170, 109–120. doi:10.1016/j.quascirev.2017.06.014.

Weber, M. E., Kuhn, G., Sprenk, D., Rolf, C., Ohlwein, C. and Ricken, W. (2012). Dust transport from Patagonia to Antarctica—a new stratigraphic approach from the Scotia Sea and its implications for the last glacial cycle. Quat. Sci. Rev. 36, 177–

188.

Wu, L., Wang, R., Xiao, W., Krijgsman, W., Li, Q., Ge, S. and Ma, T. (2018). Late Quaternary deep stratification-climate coupling in the Southern Ocean: implications for changes in abyssal carbon storage. Geochem. Geophys. Geosyst. 19. doi:10.1002/2017GC007250.

Wu, L., Wilson, D. J., Wang, R., Yin, X., Chen, Z., Xiao, W. and Huang, M. (2020). Evaluating Zr/Rb ratio from XRF scanning as an indicator of grain-size variations of glaciomarine sediments in the Southern Ocean. Geochem. Geophys. Geosyst. 21, e2020GC009350. doi:10.1029/2020GC009350.

Wu, S., Lembke-Jene, L., Lamy, F., Arz, H. W., Nowaczyk, N., Xiao, W., Zhang, X., Hass, H. C., Titschack, J., Zheng, X., Liu, J., Dumm, L., Diekmann, B., Nünberg, D., Tiedemann, R. and Kuhn, G. (2021). Orbital- and millennial-scale Antarctic Circumpolar Current variability in Drake Passage over the past 140,000 years. Nat. Commun. 12:3948. doi:10.1038/s41467-021-24264-9.

Xiao, W., Frederichs, T., Gersonde, R., Kuhn, G., Esper, O., Zhang, X., 2016. Constraining the dating of late quaternary marine sediment records from the Scotia Sea (Southern Ocean). Quat. Geochronol. 31, 97–118. http://doi.org/10.1016/j.quageo.2015. 11.003.

Zielinski, U., Gersonde, R., 1997. Diatom distribution in Southern Ocean surface sediments (Atlantic sector): implications for paleoenvironmental reconstructions. Palaeogeogr. Palaeoclimatol. Palaeoecol. 129, 213–250.

Zulaikah, S. and Nurlaily, I. P. (2018). Magnetic domain distribution analysis of volcanic material from the 2017 eruptions of Mount Agung, Indonesia. J. Phys. Conf. Ser. 1093, 012029. doi:10.1088/1742-6596/1093/1/012029.

KOPRI 극지연구소

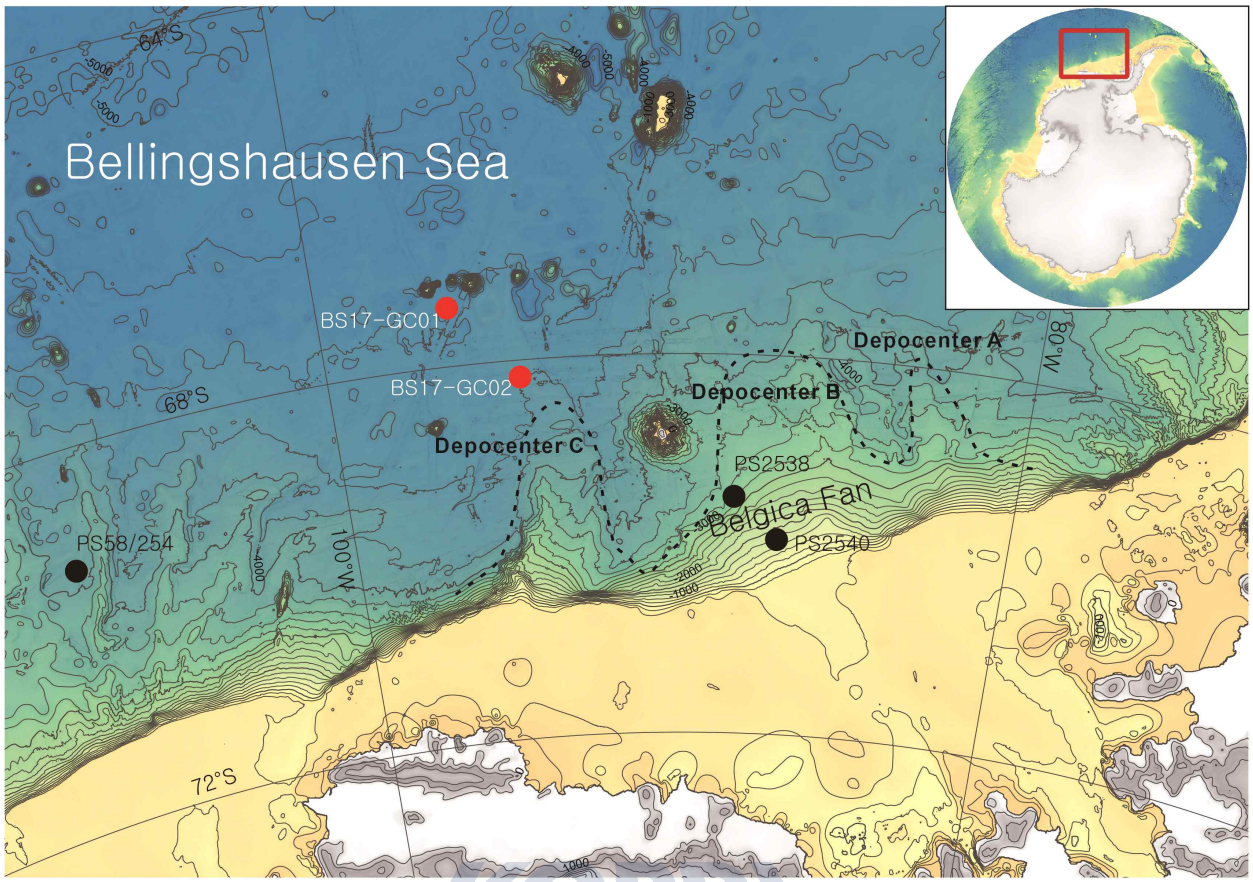


Figure #. Location map of the study area in the Bellingshausen Sea continental margin, West Antarctica, with core locations for BS17-GC01 and BS17-GC02 (red circles) and previously reported cores (black circles). Dashed lines indicate sediment depocenters from Scheuer et al. (2006).

KOPRI 극지연구소

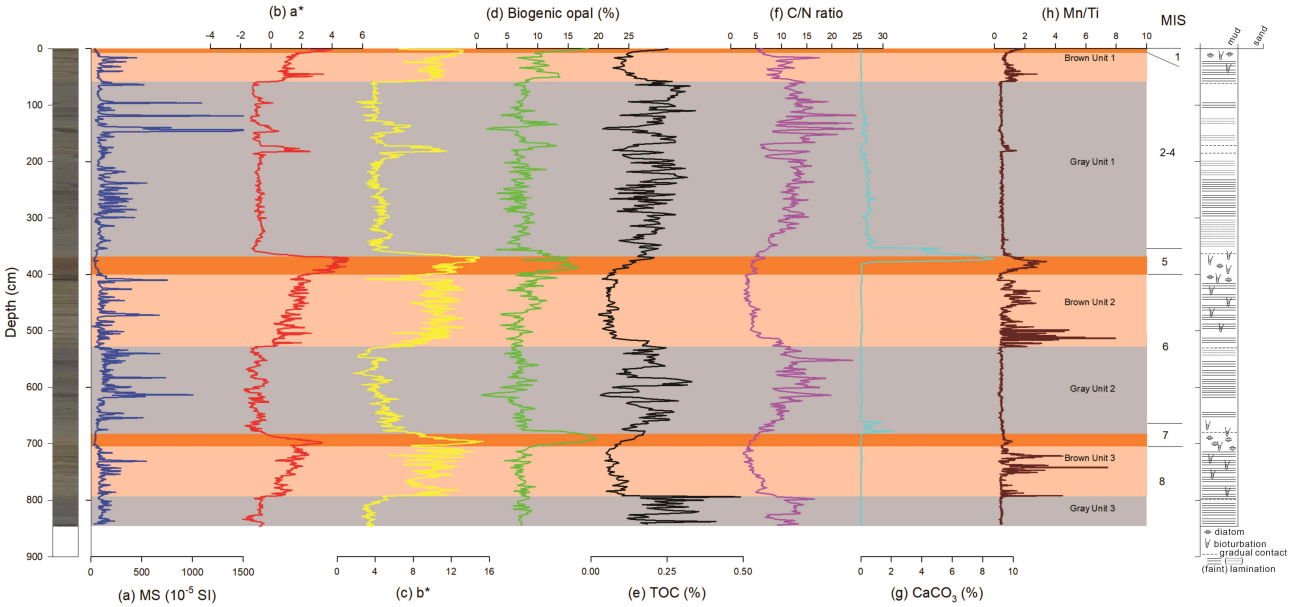


Figure #. Downcore variations of (a) MS, (b) a*, (c) b*, (d) biogenic opal concentration, (e) diatom valves, (f) TOC concentration, (g) C/N ratio, (h) CaCO3 concentration, (i) Mn/Ti ratio of BS17-GC02. Core photo image and lithologic log are shown on the left and right, respectively. MIS: Marine Isotope Stage.

KOPRI
극지연구소

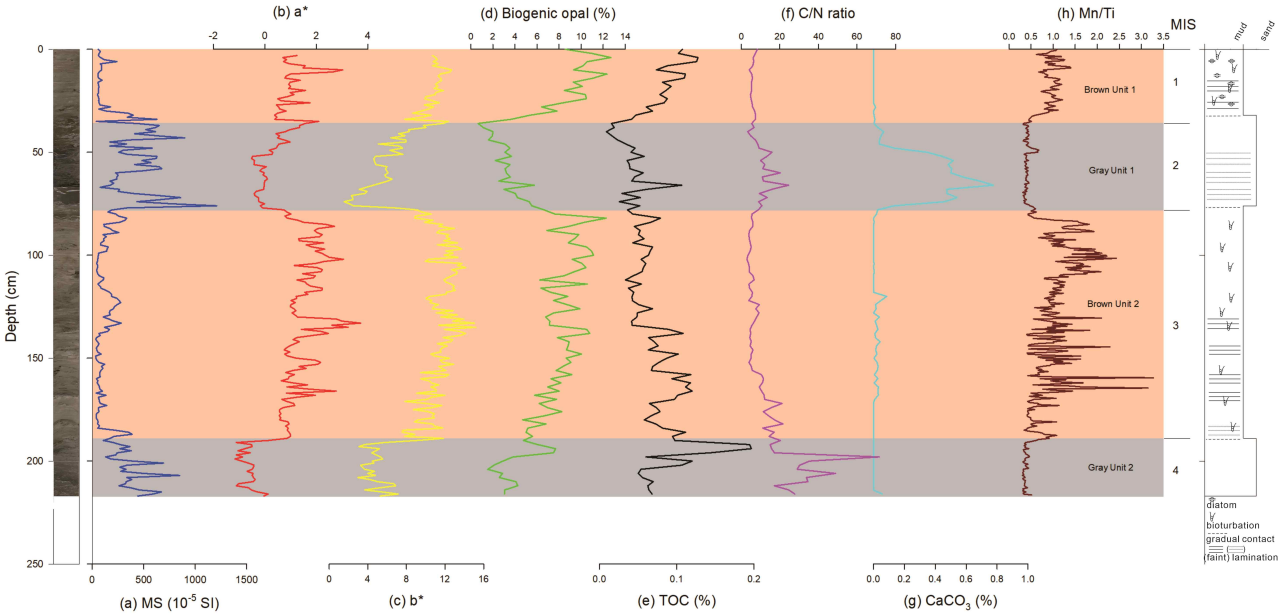


Figure #. Downcore variations of (a) fraction of sand (white), silt (dark green), and clay (green), (b) MGS of bulk sediment (black) and SS (red), (c) SS% in mud fraction, (d) 7 point-running correlation between SS MGS and SS%, (e) grain density, (f) grains >1 mm, (g) total palynomorphs, (h) total diatom valves, and (i) relative abundance of F. kerguelensis of BS17-GC02. Lithologic log is shown on the left. MIS: Marine Isotope Stage.

KOPRI
극지연구소

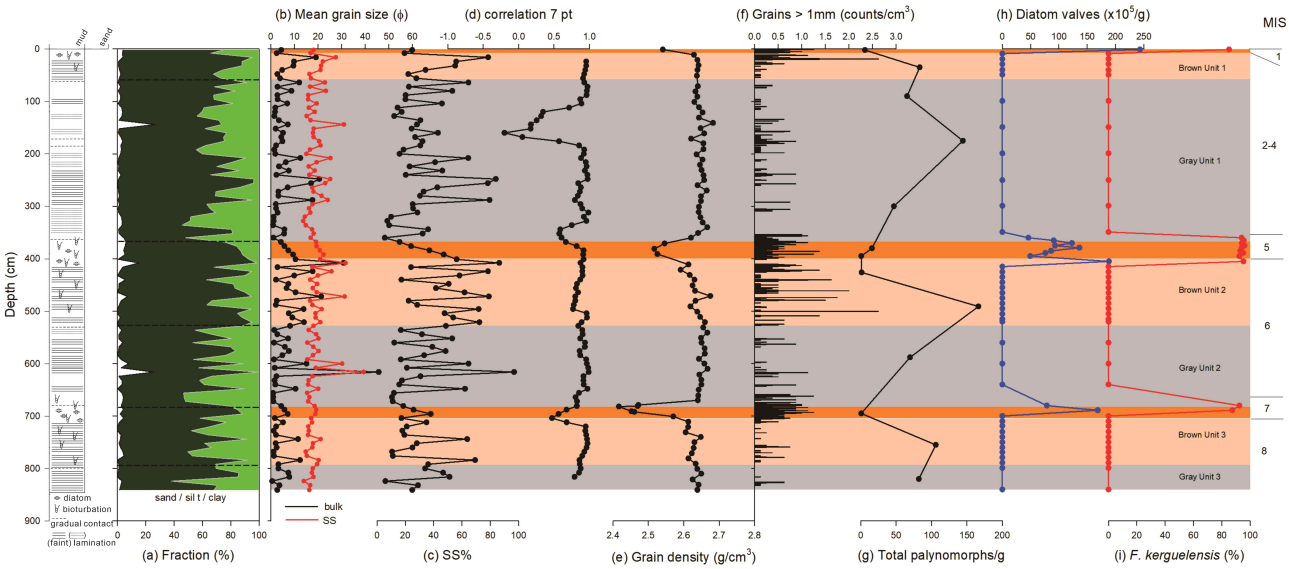


Figure #. Downcore variations of (a) MS (Kim et al., 2022a), (b) a*, (c) b*, (d) biogenic opal concentration, (e) diatom valves, (f) TOC concentration, (g) C/N ratio, (h) CaCO3 concentration, (i) Mn/Ti ratio of BS17-GC01. Core photo image and lithologic log are shown on the left and right, respectively. MIS: Marine Isotope Stage.

KOPRI
극지연구소

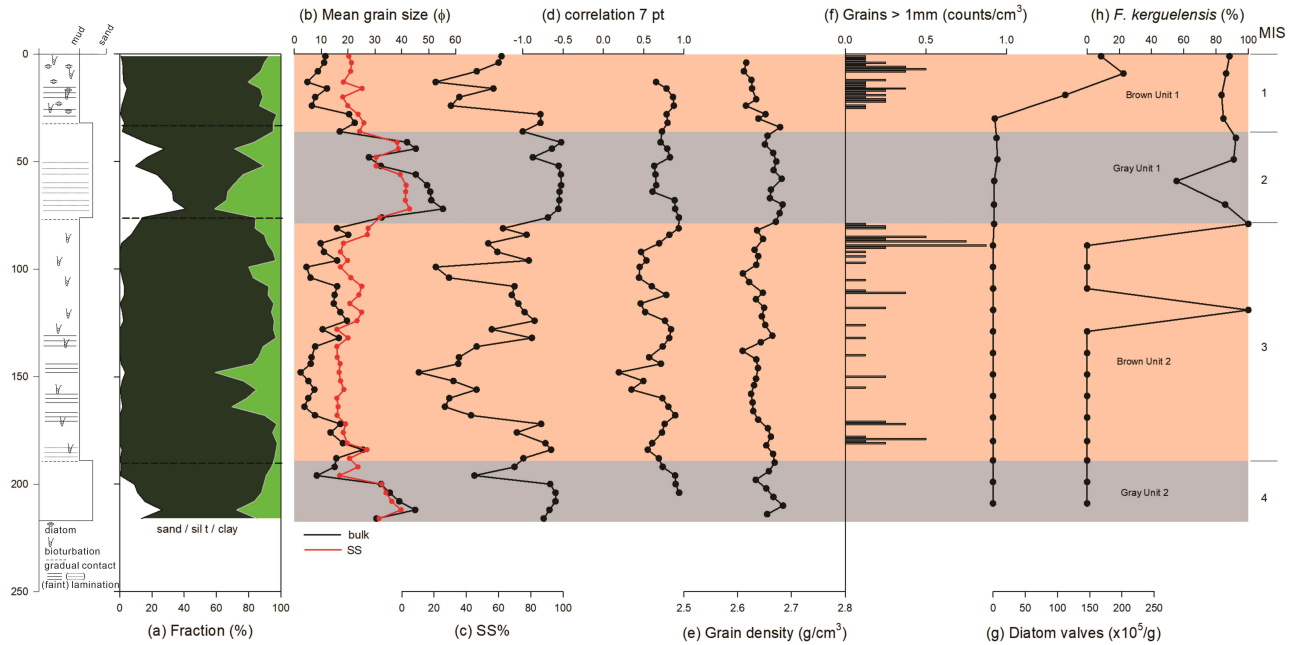


Figure #. Downcore variations of (a) fraction of sand (white), silt (dark green), and clay (green), (b) MGS of bulk sediment (black) and SS (red), (c) SS% in mud fraction, (d) 7 point-running correlation between SS MGS and SS%, (e) ln(Zr/Rb), (f) grain density, (g) grains >1 mm, (h) total diatom valves, and (i) relative abundance of F. kerguelensis of BS17-GC01. Lithologic log is shown on the left. MIS: Marine Isotope Stage.

KOPRI 극지연구소

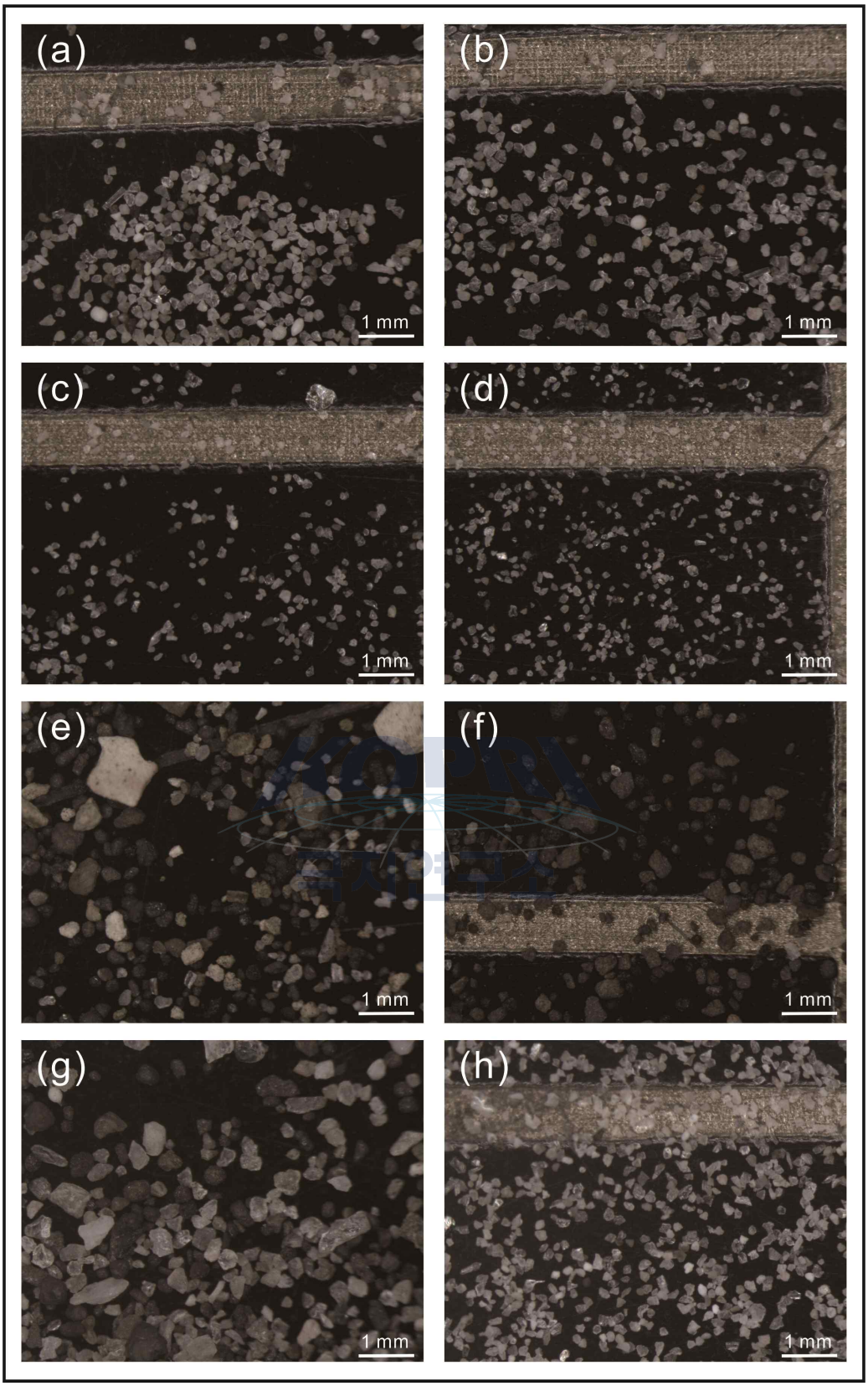


Figure #. Microscopic photos of grains >63 μm of BS17-GC01 at (a) 0 cm, (b) 20 cm, (c) 50 cm, (d) 70 cm, (e) 110 cm, (f) 140 cm, (g) 170 cm, and 200 cm. 0 cm and 20 cm belong to MIS 1, 50 cm and 70 cm belong to MIS 2, 110 cm, 140 cm, and 170 cm belong to MIS 3, and 200 cm belongs to MIS 4.

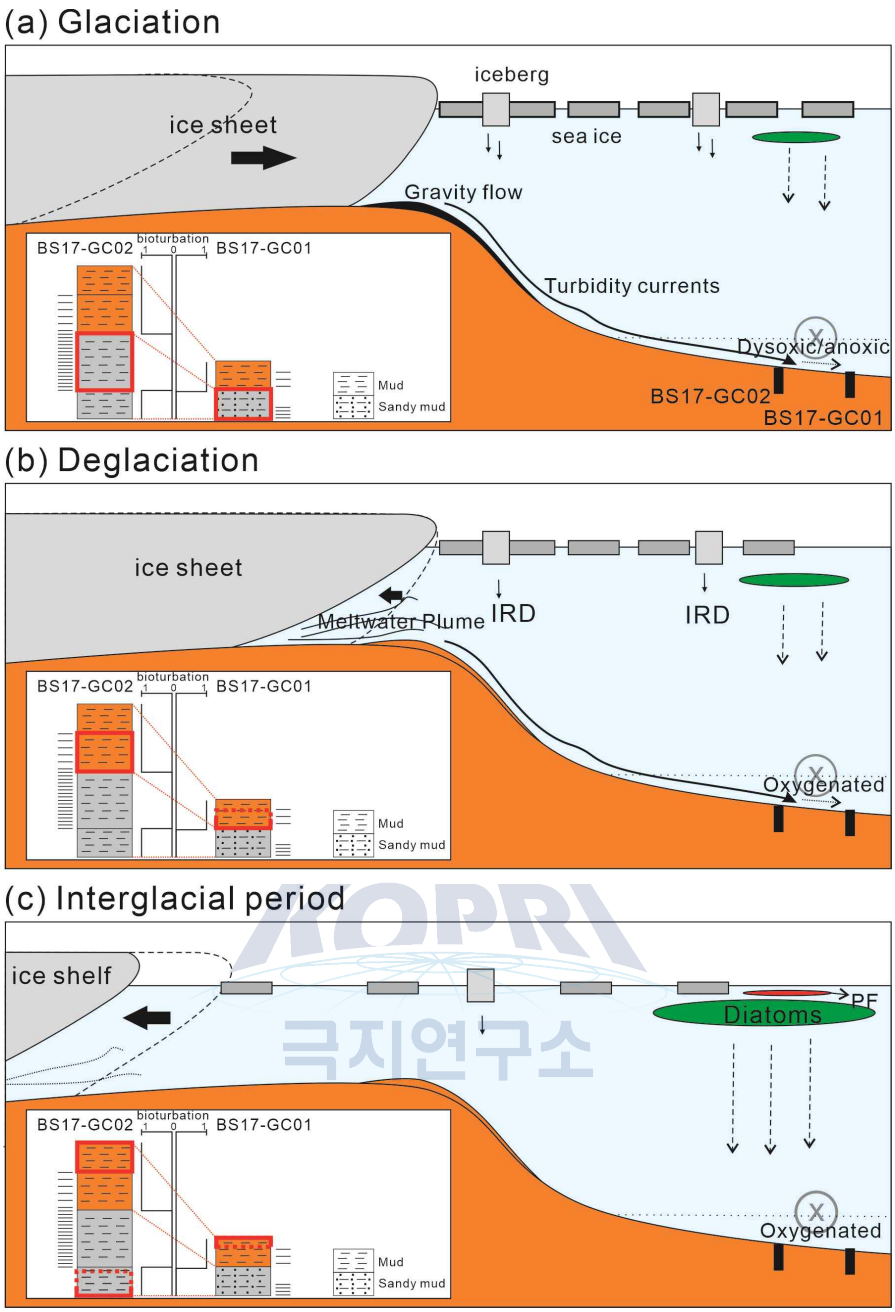


Figure #. Schematic depositional models of (a) glaciation phase, (b) deglaciation phase, and fully retreated phase (late/warm interglacial period) in the Bellingshausen Sea continental rise. PF: planktonic foraminifers and IRD: ice rafted debris.

KOPRI
극지연구소

제 24 장

Bioturbation supplying young carbon into West Antarctic continental margin sediment[18)]

Sunghan Kim[a,b],*, Robert M. McKayc, Jae Il Lee[a], Kyu-Cheul Yoo[a], Min Kyung Lee[a], Heung Soo Moon[a]

[a]Korea Polar Research Institute, [b]University of Science and Technology (UST), [c]Victoria University of Wellington

ABSTRACT: Accelerator Mass Spectrometry (AMS) 14C dating is a widely applied method for establishing high-precision chronologies used to underpin late Quaternary paleoclimatic studies. Feedbacks associated with Antarctic Ice Sheets (AIS) and Southern Ocean variance are thought to have played a critical role in regulating past global climate changes since the Last Glacial Maximum. However, determining the exact role of the AIS and Southern Ocean in these changes has proven difficult because of the sparse occurrence of biogenic carbonate suitable for AMS 14C dating in Antarctica. Consequently, AMS 14C dating is often measured on acid insoluble organic matter (AIOM) from bulk sediment samples, which are often biased towards ages that are older than the depositional age, due to pervasive reworking of old carbon. In this scenario, ages can still potentially provide maximum deposition ages, but such interpretations need to be assessed carefully. Here, we document AIOM and foraminifer AMS 14C dates at the same depth intervals from Antarctic continental margin cores, and we find AIOM AMS 14C dates can range between 2000 to 16,000 years younger than those of foraminifera samples. The younger AIOM 14C dates were found in bioturbated sedimentary facies, which often have extremely low sedimentation rates in Antarctica. In cores with low sedimentation rates, the down sediment contribution of organic carbon from macro-benthos can be quite significant in the sediment column with low organic carbon concentration. After considering possibilities of contamination, foraminifer reworking, and remineralization of secondary carbonate to explain this offset, we conclude that bioturbation plays an important role in the Antarctic carbon cycle as a young carbon supplier to depth into the sediment column. This has clear implications for using condensed sedimentary sections to date post-LGM records in Antarctica. These bioturbation processes also have implications for novel

18) 이 연구 결과는 다음의 논문으로 출판되었음: Kim, S. et al. (2022). "Bioturbation supplying young carbon into West Antarctic continental margin sediment." Palaeogeography, Palaeoclimatology, Palaeoecology 602: 111161.

radiocarbon dating methods that have recently been developed to overcome sediment reworking processes and more accurately constrain timing of past AIS retreat, including ramped pyrolysis and compound specific isotopes methods.

1. Introduction

Past variations in the extent of the marine-based Antarctic Ice Sheets (AIS) are believed to have resulted in some of the largest feedbacks in the Earth system over past ice age cycles, regulating changes in planetary albedo, sea level, and Southern Hemisphere wind fields and overturning oceanic circulation, as well as carbon cycling associated with Southern Ocean primary productivity. Consequently, constraining the timing of marine-based ice sheet retreat in Antarctica since the Last Glacial Maximum is critical in order to gain a more complete understanding of the climate/oceanographic changes that led to, or resulted from past ice sheet variations. However, constraining a reliable and robust chronology of past marine ice sheet retreat from marine embayments on the continental shelves, where the majority of past AIS variance occurred has been problematic This is due to a general lack of carbonate, such as foraminifers or shell fragments, in most Antarctic sedimentary settings due to corrosive water masses (Kennett, 1968; Anderson, 1975; The RAISED Consortium et al., 2014). As a result, many studies use acid insoluble organic matter (AIOM) for age dating of Antarctic continental margin sediments (e.g., Licht et al., 1998; Domack et al., 1999a, 1999b; McKay et al., 2008; Hillenbrand et al., 2010; Xiao et al., 2016; Kim et al., 2018b, 2018c). In these studies, the majority of core top ages were often older than the local reservoir age (e.g., Licht et al., 1996; Andrews et al., 1999; Domack et al., 1999b; Hillenbrand et al., 2010; Xiao et al., 2016; Kim et al., 2018c), interpreted to be the consequence of reworking of old carbon that is incorporated into the sediment syn-depositionally (Gordon and Harkness, 1992; Hillenbrand et al., 2010).

Recently, to overcome or to minimize the old carbon influence on 14C dating of AIOM, the Ramped PyrOx method has been developed to measure discrete populations of carbon based on their thermal stability, which is inferred to be a function of the age of that carbon (Rosenheim et al., 2008). Comparison of Ramped PyrOx ages from Antarctic Peninsula Holocene sediment cores revealed relatively younger ages, which in some (but not all) settings are similar to foraminifer 14C ages, and are consequently thought to be more reliable than AIOM ages derived in settings where organic carbon input is high (Subt et al., 2016; Venturelli et al., 2020). Other studies have employed the measurement of 14C in the humic acid fraction, or from compound specific isotopes, and the results in those studies also revealed younger ages than that from the residue fraction (Xiao et al., 2016; Yokoyama et

al., 2016; Prothro et al., 2020). Although AIOM dates younger than carbonate 14C dates have previously reported from some Ross Sea sediment cores, the implications of post-depositional reworking of carbon into the sediment column for the development of radiocarbon chronologies are largely overlooked (e.g., Licht et al., 1996; Domack et al., 1999b; Licht and Andrews, 2002; McKay et al., 2008). Consequently, identifying the sedimentary processes that lead to such an offset may have implications for determining sedimentary materials using for radiocarbon dating, including using the novel methods discussed above. As the cost of accelerator mass spectrometry (AMS) 14C dating is expensive and carbonate AMS 14C dates are viewed as more robust, 14C dating from AIOM is often not measured in the intervals where there are suitable carbonate materials to date.

In this study, we report AIOM and foraminifer AMS 14C dates from paired samples within 8 cores from along the West Antarctic margin (Fig. 1). We aim to identify if there is a consistent pattern of offset between AIOM 14C dates and foraminiferal dates, and use characteristics of sedimentary facies to identify the mechanism that could account for the transport of young carbon into the sediment column on the Antarctic continental margin, and how these processes could be identified to assist in developing more robust and consistent chronologies of glacial retreat patterns.

KOPRI
극지연구소

2. Materials and methods

Sediment cores RS15-GC40, RS15-LC42, RS15-GC67, RS15-GC107 and RS15-LC108 were collected were collected from the continental shelf to continental rise of the Ross Sea, by R/V Araon in 2015 (Cruises ANA05B and ANA06A). In addition, sediment cores BS17-GC02 and BS17- GC07 collected from the continental rise and shelf of the Bellingshausen Sea by R/V Araon in 2017 (cruise ANA07D), while GC04-G03 collected from the Powell Basin by Yuzhmorgeologiya (2004/2005 KARP Cruise) were also studied.

Box cores AMRS20-BC03, AM20-BC08, AM20-BC09, AM20-BC12 were collected from the continental shelf and slope from the Ross Sea to Amundsen Sea by R/V Araon in 2020 (cruise ANA10B). Box cores BS17-BC08, BS17-BC12 and a multi core BS17-M09 was collected from the Bellingshausen Sea continental shelf by R/V Araon in 2017 (cruise ANA07D). A box core AP18- BC08 was collected from the eastern Bransfield Basin by R/V Araon in 2018 (cruise ANA08D). All core locations and water depths are shown in Figure 1, with additional details given in Table 1.

The cores were stored cold before being opened, described, and sub-sampled at the Korea Polar Research Institute (KOPRI), where core photos were taken by ITRAX, and X-radiographs taken from 8 cm x 30 cm x 1 cm slabs. Sediment surface images of the box

cores were taken, as well as a vertical image of BS17-MC09. Bioturbation intensity was visually inspected from observations of the x-radiograhps, using scales used in McKay et al. (2019). To determine bioturbation semi- quantitatively, the Droser and Bottjer (1986) ichnofabric index (0-4), modified by Savrda et al. (2001), was used:

0 = no apparent bioturbation (≤10%)
1 = slight bioturbation (>10-30%)
2 = moderate bioturbation (>30-60%)
3 = heavy bioturbation (>60-90%)
4 = complete bioturbation (>90%)

2.1. Radiocarbon dating

In order to compare radiocarbon dates obtained from foraminifer and AIOM at the same depths, only intervals which have enough foraminifers for age dating were analyzed, with a total of 11 paired samples using AIOM and foraminifer radiocarbon dating across the eight cores studied (Table 2). Since the dominant biogenic carbonate component in all cores were the planktonic foraminifera (PF) Neogloboquadrina pachyderma (sin.), PF was used to measure 14C dates in most samples. However, benthic foraminifers (BF) were found in RS15-GC67, thus radiocarbon dating using BF Globocassidulina biora was additionally conducted in that core. All AMS 14C dates were measured at Beta Analytic, USA.

3. Result

3.1. Dating

Some PF AMS 14C dates are previously reported; RS15-GC40 5 cm (Kim et al., 2020), BS17- GC02 354 and 372 cm, and GC04-G03 272 cm (Kim et al., 2018c). AIOM AMS 14C dates mostly range from ~13,000 to ~24,000 yr BP with exceptions of 5810 yr BP at 2 cm in BS17-GC07 and 36,410 yr BP at 272 cm in GC04-G03 (Fig. 2a, Table 2). In contrast, PF AMS 14C dates range from ~16,500 to ~34,500 yr BP, except for 2920 yr BP at 2 cm in BS17-GC07 (Fig. 2a, Table 2). BF AMS 14C dates at 50 and 95 cm in RS15-GC67 were generally similar to PF AMS 14C dates with slightly older ages (Fig. 2a, Table 2). Positive ΔAgeAIOM-F (AIOM minus foraminifer AMS 14C dates) values were found at 10 cm in RS15-LC42, 354 cm in BS17-GC02, 2 cm in BS17-GC07, and 272 cm in GC04-G03, with a range from 860 to 5660 years (Fig. 2). A positive ΔAgeAIOM-F is attributed to the well-document input of reworked carbon incorporated into the sediment

syn−depositionally on the Antarctic margin (Andrews et al. 1999). This is confirmed in samples with a positive ΔAgeAIOM−F by higher percent modern carbon (PMC) of foraminifer (PMCforam) samples than AIOM (PMCAIOM) samples (Fig. 2b, Table 2). However, the bias of AIOM ages towards an older− than−depositional age is not uniform, as numerous samples demonstrate significantly negative ΔAgeAIOM−F values. This is consistent with the PMCAIOM being higher than PMCforam (Fig. 2b, Table 2). Such negative values were observed in RS15−GC40 (5 cm), RS15−GC67 (50, 81, and 95 cm), RS15−GC107 (14 cm), RS15−LC108 (18 cm), and BS17−GC02 (372 cm), with a range from − 1980 to −16,040 years (Fig. 2).

3.2. Core images and x−radiographs

Bioturbation is observed over ranges of a few centimetres to a few decimetres from RS15−GC40, RS15−GC67, RS15−LC42, RS15−GC107, RS15−LC108, BS17−GC02, BS17−GC07, and GC04−G03 (Fig. 3). Dated intervals with relatively low bioturbation (no bioturbation to moderate bioturbation from McKay et al. (2019)) were observed at RS15−LC42 10 cm, BS17−GC02 354 cm, BS17−GC07 2 cm, and GC04−G03 272 cm (Fig. 3).

Cemented worm tubes are commonly observed in surface sediments of box cores from Antarctic Peninsula to the Ross Sea (Fig. 4). The x−radiographs of box cores, where the core tope sediment is well preserved, show the bioturbated intervals can reach a few decimetres as well (Fig. 5e).

4. Discussion

4.1 Negative ΔAgeAIOM−F and potential causes

It has been widely reported that AIOM 14C ages are often older than foraminifer 14C ages, and that AIOM 14C age of core top sediment is older than the local reservoir age, due to the presence of reworked carbon. This effect is often corrected for by subtracting the core top age from dates below the surface, on the assumption of a constant rate of old carbon supply during deposition (Gordon and Harkness, 1992; Andrews et al., 1999; McKay et al., 2008; Hillenbrand et al., 2010; Subt et al., 2016; Prothro et al., 2020). However, such assumptions are dependent on a stable sedimentary environment, which is unlikely during glacial transitional phases, and where there are shifts in sedimentary facies that are indicative of baseline shifts in sediment supply (Licht et al., 1998; Anderson et al., 2014). The presence

of negative ΔAgeAIOM−F in the West Antarctic continental margin from the Antarctic Peninsula to the Ross Sea needs to be explained, and has implications for the depositional age for samples at depth. The negative ΔAgeAIOM−F does not seem to be related to specific location or water depth. To distinguish the cause and the meaning of negative ΔAgeAIOM−F, we discuss the possibilities of 1) contamination of AIOM 14C dating samples by modern young carbon; 2) reworking of foraminifers; and 3) re−mineralization of secondary carbonate on foraminifers; and 4) the down core reworking of AIOM14C by bioturbation.

The possibility of contamination of AIOM 14C dating samples by modern young carbon is very low. Firstly, two samples showed positive ΔAgeAIOM−F values (RS15−LC42 at 10 cm and BS17− GC02 at 354 cm), but they were directly sampled alongside other samples from RS15−GC40, RS15− GC107, RS15−LC108, and BS17−GC02 (Table 2). In addition, the δ13C values of organic matter in this study are −25.7 to −23.5□ which is similar to those reported by previous studies from the West Antarctic continental margin including the Ross and Bellingshausen Seas (e.g., Domack et al., 1999b; McKay et al., 2008; Hillenbrand et al., 2010; Kim et al., 2018c).

Downcore reworking of foraminifers i.e., by bioturbators and/or iceberg mixing could cause negative ΔAgeAIOM−F. However, if the foraminifers were reworked from somewhere else, foraminifers and surrounding sediments are likely to be transported together, largely by glacigenic or mass flow processes (Arndt et al. 2017). Negative ΔAgeAIOM−F values have previously been reported from the Ross Sea shelf region, and it was proposed that BF were reworked on account of reversely ordered BF AMS 14C dates (Licht and Andrews, 2002). However, both AIOM and PF/BF foraminifer AMS 14C dates at RS15−GC67 showed a chronological order, indicating they are probably not reworked. Where we have dated PF and BF in paired samples from core RS−GC67, they show consistent ages (Fig. 2). If foraminifera were substantially reworked by glacigenic or mass flow processes, it would be highly unlikely that distinct populations of PF and BF would record near identical ages that are also older than the AIOM ages. This interpretation is supported by evidence presented by Prothro et al. (2020) who showed that glacially reworked diamicts in core NBP1502A KC48 (74.473S, 173.511E, 539 m depth) contained paired PF and BF dates that had distinctly different ages (~5 kyr difference), while these were also 5−10 kyr younger than AIOM ages from the same depth. In addition, many intervals with negative ΔAgeAIOM−F values are found in the bioturbated, diatom−rich intervals, where there is no evidence of mass flow processes or glacial reworking that is commonly associated with interpretations of foraminiferal reworking in the Antarctica (Arndt et al., 2017; Prothro et al., 2020; Majewski et al., 2020), indicating in situ deposition within a marine setting (Fig. 3). This lack of physical reworking by mass flow or glacial processes is also supported by well−preserved foraminiferal tests in the sediment (Fig. 6). In addition, we note that RS15−GC40 is not located in zone where debris

flow resulting from grounded ice expansion would be expected, as it is located on top of the Iselin Bank, and glacigenic debris flow would be focused around this feature, and contourite drifts deposited on the margins and on top of it (c.f., the Hallet Ridge in Kim et al., 2018a). McKay et al. (2019) also show similar diamict deposits at Site U1523, which formed as sheeted sediment drifts on the flank on the Iselin Bank.

The negative ΔAgeAIOM−F could be derived by re−mineralization of the carbonate ion in the pore water with old ages on the deposited foraminifers. However, as mentioned earlier, the preservation status of both planktonic and benthic foraminifers was generally good (Fig. 6). Authigenic carbonate formation often results in brown−colored foraminiferal tests (Cook et al., 2011; Asahi et al., 2016), but such tests were not found in any cores. Authigenic or secondary carbonate formation often occurs in high $CaCO_3$ concentration intervals (e.g., Lim et al., 2009; Clemens et al., 2016) and is often related to methane seepage (e.g., Lim et al., 2009). No evidence for methane seepage has been found from any study site so far. In addition, microscopic observation of RS15−GC107 at 14 cm, which has the highest $CaCO_3$ concentration (~25%), revealed that authigenic carbonate is insignificant. Indeed, Energy Dispersive Spectroscopy analysis confirmed no secondary $CaCO_3$ precipitation within the aperture of PF in sediment cores from the Ross Sea including RS15−LC42 and RS15−LC108 (Albot, 2016).

These combined lines of evidence suggest the foraminifer AMS 14C dating results are reliable indicators of the depositional age of the sediment. Consequently, the negative Δ AgeAIOM−F values in the West Antarctic continental margin need to be explained. Negative ΔAgeAIOM−F values were found in moderately to heavily bioturbated (RS15−GC107 14 cm, RS15−LC108 18 cm, RS15−GC67 50, 81, and 95 cm, and BS17−GC02 372 cm) and slightly to moderately bioturbated intervals (RS15−GC40 5 cm) (Fig. 3). However, positive Δ AgeAIOM−F values are found in slightly bioturbated intervals, directly underlying beds with sharp basal contacts that are not bioturbated (RS15−LC42 10 cm, RS17−GC02 354 cm, and GC04−G03 272 cm) (Fig. 3). According to Kim et al. (2020) and Ohneiser et al. (2019), coarse intervals in RS15−GC40 and RS15−LC42 result from IRD input and winnowing, and RS15−GC67 shows relatively well−preserved planktonic foraminifera with some degree of dissolution and well−preserved benthic foraminifera in these coarse intervals with other well−preserved biogenic carbonates. RS15−GC40 and RS15−GC67 show low sedimentation rates (SRs), thus bioturbation likely occurs under oxic bottom water conditions. Box cores collected from along the West Antarctic margin show common worm tubes within poorly sorted, clast−rich diatomaceous sediments (Fig. 4), but bioturbation in the clast−rich coarse intervals is less distinctive on the x−radiographs of corresponding gravity core top sediments in spite of these benthic organisms (Fig. 5). Thus, we infer that bioturbation is likely pervasive in these intervals but distinct burrows are obscured by the clast−rich nature of the

KOPRI 극지연구소

facies (Fig. 3).

4.2. Young carbon injection by bioturbation

Although there are many different styles of bioturbation, cemented tubes and worms are commonly observed in the Antarctic continental margin surface sediment from Antarctic Peninsula to the Ross Sea (Fig. 4). The x−radiographs of box cores, having cemented tubes and worms on the seafloor, show how their bioturbation is mixing the surface sediment (Fig. 5). The box core x−radiographs are similar to those of age measured intervals (Figs. 4 and 5). Thus, we postulate that bioturbation in the Antarctic sediments is mainly caused by burrowing/tube worms. However, we cannot rule out a possibility that other bioturbators could likely produce similar observations.

The x−radiograph of pervasively bioturbated intervals shows the potential for individual burrows to vertically mix the sediment column by several centimetres (RS15−GC107 (14 cm), RS15−LC108 (18 cm), and BS17−GC02 (372 cm)) (Fig. 3). Indeed, it is reported that bioturbation depth on mixing is the order of ~5−15 cm in the Scotia Sea and Weddell Sea, Antarctica (Diaz, 2004). Living organisms exchange carbon with their environment by photosynthesis or grazing (Bowman, 1990). Because the main source of food for benthos is sinking detritus, 14C ages of living worms and organic parts in their tubes are thought to have younger ages than ambient sedimentary organic matter. Relatively slow circulation and mixing within the oceans lead to significant geographic variations at the ocean surface and depth variations in marine reservoir effect (Ascough et al., 2005). Benthos living different water depths may have different reservoir effect, but the difference is thought to be less significant due to their main source of food which has similar marine reservoir effect to PF. 500−1800−year difference of reservoir age was reported during the Holocene from lakes and oceans (Geyh et al., 1998; Zhou et al., 2009; Hua et al., 2020). Thus, temporal variation in local reservoir age should be considered. However, there is no information on temporal variation in local reservoir age in the study area and ΔAgeAIOM−F values are greater than a few thousands. Thus, we consider the reservoir related issue is not important in this study.

Thus, alongside vertical mixing of the sediment itself via burrowing, their excretion or a part or whole of their dead body has the potential to supply significant amounts of younger organic carbon in the sub−surface sediments. Consequently, where there is more severe bioturbation intensity, there will be more transport of young carbon into the sediment column. While such processes may have minimal impact in many depositional settings, the SRs on the Antarctic continental shelf are extremely low, with many post−LGM sedimentary records used to date glacial retreat being usually significantly less than 1 m (Anderson et al., 2014). Recent post−glacial chronologies dating the onset of open marine conditions using a

suite of cores include examples from highly−condensed, bioturbated intervals that are between 20−50 cm thick, but deposited over the mid− to Late Holocene (c.f., Domack et al., 1999; Yokoyama et al., 2016; Prothro et al., 2020). Consequently, while the amount of young carbon introduced by bioturbation processes might be small, if the bioturbation depth of mixing is of the order of ~5−15 cm (Diaz, 2004; Carvalho et al., 2011; Soltwedel et al., 2019), and there are extremely low SRs, this process will have a significant influence on the 14C age of the sediment − as evidenced by negative ΔAgeAIOM−F values. Although SRs in glacial marine settings may be highly variable on short time scale, continuous occurrence of bioturbation processes indicates that the short time scale variability is less significant on benthic organisms.

It is important to understand the relationship between bioturbation intensity and degree of young carbon input to estimate the young carbon effect on the sediment age. However, bioturbation intensity is difficult to be quantified due to its subjective characteristic. Young carbon influence is not homogeneous neither vertically nor horizontally in the sediment. In addition, the amount of young carbon input is also likely variable through time. These points may act as a limit to understand the relationship between bioturbation intensity and degree of young carbon input. Thus, we currently concluded that negative ΔAgeAIOM−F values are attributed to bioturbation without currently being able to statistical quantify between bioturbation intensity and degree of young carbon input.

KOPRI
극지연구소

4.3. Implications

While we have only investigated AIOM dates in this study, this process is likely to influence all components of organic matter in the bulk sediment column, including those ages derived from compound specific isotopes or humic acids (Xiao et al., 2016; Yokoyama et al., 2016; Prothro et al., 2020). Our results do not rule out the use of AIOM or compound specific age constraints in post glacial retreat sequences in Antarctica, but highlights the need for the influence of bioturbation to be assessed, and when vetting the accuracy of these age constraints, a higher weighting should be applied to cores where the post−glacial sediment is several metres thick (i.e. higher SRs), or where the sediment column is clearly laminated as a primary open marine deposit. In such sediments this process is likely to be less of an influence, as evidenced in previous comparisons of carbonate and AIOM dates where the post LGM sediment is ~2 m thick and is organic−rich (c.f. core NBP1502A KC48 in Prothro et al., 2020). Consequently, if ages from highly−condensed bioturbated sedimentary sections are included in regional compilations, they may result in age estimates that are anomalously young and difficult to reconcile with ages from longer (or non− bioturbated) cores and on−land records of retreat via cosmogenic nuclide studies or raised beaches.

While bioturbation could also influence ages derived by Ramped PyrOx, the underlying principle of this method is that it "unmixes" different population of carbon based on thermal stabilities, and by inference age (Rosenheim et al., 2008). Therefore, it is feasible that this method could potentially overcome some of the uncertainties associated with dating highly-condensed bioturbated intervals on the Antarctic continental margin. However, such condensed intervals will still lack accuracy in dating the exact timing of glacial retreat, and it may be difficult to completely distinguish syn-depositional carbon from younger and older carbon populations supplied by bioturbation and reworking, respectively.

The complications of bioturbation in determining ages of deposition is further highlighted by Barker et al. (2007), who reported that up to 2200 years of planktonic foraminifer AMS 14C age difference could be found between different species and between intact and fragmented specimens from the sedimentary bioturbated zone. However, in our study, only well-preserved single species, N. pachyderma (sin.) or G. biora, were picked for age dating and ΔAgeAIOM-F is greater than 2000 years. Consequently, the effects of mixing foraminifera downcore are thought to be secondary to the influence of bioturbation transporting and depositing young organic matter (i.e., their excretion or a part or whole of their dead body) downcore.

Previously, the role of bioturbation in the sediment was considered as mixing near surface sediments and consequently homogenizing the sediment (Peng and Broecker, 1984), resulting in older ages of carbonate in the mixed sediment (Nozaki et al., 1977; Berger and Johnson, 1978). Nonetheless, we found that the bioturbated intervals in the Antarctic continental margin have a great potential for young carbon injection into the sediment in association with bioturbation creating heterogeneous sediment and carbonate populations. Since this young carbon affects AIOM AMS 14C dates, caution is needed to use AIOM 14C dates in for highly condensed bioturbated facies in future studies on the Antarctic margin, which may provide anomalously younger ages of retreat, including those using novel compound specific and Ramped PyrOx methods.

KOPRI 극지연구소

서남극 대륙 주변부 퇴적물로 젊은 탄소를 공급하는 생교란

김성한[a,b],*, Robert M. McKay[c], 이재일[a], 유규철[a], 이민경[a], 문흥수[a]

[a]극지연구소, [b]과학기술연합대학원대학교, [c]Victoria University of Wellington

요약: 질량가속기 탄소연대 측정법은 제 4기 후기 고기후 연구에서 고정밀 연대 결과를 설정하는 방법으로 널리 사용되고 있다. 남극빙상과 남빙양과 관련된 되먹임의 변동은 지난 마지막 최대 빙하기 이후 과거 지구 기후 변화를 조절하는 중요한 인자로 생각되어져 왔다. 그러나 남극빙상 과 남빙양의 정확안 역할을 규명하는데는 연대 측정에 사용되는 생물 탄산염의 부재로 인한 어려 움이 있었다. 결과적으로 질량가속 탄소연대 측정은 유공충이 아닌 벌크 퇴적물 시료에서 산에 녹지 않는 유기물에서 측정되었다. 유기물 연대 결과는 오래된 탄소의 영향으로 보통 퇴적연대 보다 오래되었다고 측정되는 경향이 있다. 하지만, 여전히 연대는 최대 퇴적 연대을 제시할 수는 있지만, 이러한 해석에는 많은 주의를 요한다. 여기서 우리는 남극 대륙주변부 코어에서 같은 깊 이에서 산에 녹지 않는 유기물과 유공충의 연대 결과를 보고하였다. 그리고 우리는 2000−16000 년 정도 산에 녹지 않는 유기물의 연대가 유공충의 연대에 비해 더 젊게 나타났다. 이러한 젊은 산에 녹지 않는 유기물의 연대는 생교란이 나타나는 퇴적상에서 나타났다. 이는 퇴적률이 낮다는 것을 의미한다. 낮은 퇴적률을 가지는 코어들에서 저서생물에 의한 퇴적물 아래로의 유기물 유입 은 연대 결과에 큰 영향을 미칠 수 있다. 오염, 유공충의 재동, 2차 탄산염 광물 결정화 등을 고려 한 후, 우리는 생교란이 새로운 탄소를 퇴적물로 공급할 수 있는 중요한 역할을 한다는 것을 밝 혔다. 이 연구 결과는 현재 개발된 새로운 연대 측정법들에 대해서 새로운 의미를 제시한다.

참고 문헌

Albot, O.B., 2016. Pleistocene cyclostratigraphy on the continental rise and abyssal plain of the western Ross Sea, Antarctica. PhD thesis, Victoria University of Wellington.

Anderson, J.B., 1975. Factors controlling CaCO3 dissolution in the Weddell Sea from foraminiferal distribution patterns. Mar. Geol. 19, 315-332.

Anderson, J.B., Conway, H., Bart, P.J., Witus, A.E., Greenwood, S.L., McKay, R.M., et al., 2014. Ross Sea paleo-ice sheet drainage and deglacial history during and since the LGM. Quat. Sci. Rev. 100, 31-54.

Andrews, J.T., Domack, E.W., Cunningham, W.L., Leventer, A., Licht, K.J., Timothy, A.J., DeMaster, D.J., Jennings, A.E., 1999. Problems and possible solutions concerning radiocarbon dating of surface marine sediments, Ross Sea, Antarctica. Quat. Res. 52, 206-216.

Arndt, J.E., Hillenbrand, C.-D., Grobe, H., Kuhn, G., Wacker, L., 2017. Evidence for a dynamic grounding line in outer Filchner Trough, Antarctica, until the early Holocene. Geology 45, 1035- 1038, doi:10.1130/G39398.1.

Asahi, H., Kender, S., Ikehara, M., Sakamoto, T., Takahashi, K., Ravelo, A.C., Alvarez Zarikian, C.A., Khim, B.K., Leng, M.J., 2016. Orbital-scale benthic foraminiferal oxygen isotope stratigraphy at the northern Bering Sea slope Site U1343 (IODP Expedition 323) and its Pleistocene paleoceanographic significance. Deep-Sea Res. II 125-126, 66-83, doi:10.1016/j.dsr2.2014.01.004.

Ascough, P., Cook, G., Dugmore, A., 2005. Methodological approaches to determining the marine radiocarbon reservoir effect. Prog. Phys. Geogr. 29, 532-547.

Barker,S., Broecker, W., Clark, E., Hajdas, I., 2007. Radiocarbon age offsets of foraminifera resulting from differential dissolution and fragmentation within the sedimentary bioturbated zone. Paleoceanography 22, PA2205, doi:10.1029/2006PA001354.

Berger, W.H., Johnson, R.F., 1978. On the thickness and the 14C age of the mixed layer in deep-sea carbonates. Earth Planet. Sci. Lett. 41, 223-227.

Bowman, S., 1990. Radiocarbon dating (Interpreting the past). University of California Press, pp. 64.

Carvalho, F.P., Oliveira, J.M., Soares, A.M.M., 2011. Sediment accumulation and bioturbation rates in the deep Northeast Atlantic determined by radiometric techniques. ICES J. Mar. Sci. 68, 427-435, doi:10.1093/icesjms/fsr005.

Clemens, S.C., Kuhnt, W., LeVay, L.J., Anand, P., Ando, T., Bartol, M., Bolton, C.T., Ding, X., Gariboldi, K., Giosan, L., Hathorne, E.C., Huang, Y., Jaiswal, P., Kim, S., Kirkpatrick, J.B., Littler, K., Marino, G., Martinez, P., Naik, D., Peketi, A., Phillips,

KOPRI 극지연구소

S.C., Robinson, M.M., Romero, O.E., Sagar, N., Taladay, K.B., Taylor, S.N., Thirumalai, K., Uramoto, G., Usui, Y., Wang, J., Yamamoto, M., Zhou, L., 2016. Site U1443. In: Clemens, S.C., Kuhnt, W., LeVay, L.J., the Expedition 353 Scientists, (Eds.), Indian Monsoon Rainfall. Proc. IODP 353, College Station, TX, doi:10.14379/iodp.proc.353.103.2016.

Cook, M.S., Keigwin, L.D., Birgel, D., Hinrichs, K.U., 2011. Repeated pulses of vertical methane flux recorded in glacial sediments from the southeast Bering Sea. Paleoceanography 26, PA2210, doi:10.1029/2010PA001993.

Diaz, R.J., 2004. Biological and physical processes structuring deep-sea surface sediments in the Scotia and Weddell Seas, Antarctica. Deep-Sea Res. II 51, 1515-1532.

Domack, E.W., Jacobson, E.A., Shipp, S.S., Anderson, J.B., 1999a. Late Pleistocene-Holocene retreat of the West Antarctic Ice-Sheet system in the Ross Sea: Part 2-Sedimentologic and stratigraphic signature. GSA Bull. 111, 1517-1536.

Domack, E.W., Taviani, M., Rodriguez, A., 1999b. Recent sediment remolding on a deep shelf, Ross Sea: implications for radiocarbon dating of Antarctic marine sediments. Quat. Sci. Rev. 18, 1445- 1451.

Droser, M.L., Bottjer, D.J., 1986. A semiquantitative field classification of ichnofabric. J. Sediment. Res. 56, 558-559.

Geyh, M.A., Schotterer, U., Grosjean, M., 1998. Temporal changes of the 14C reservoir effect in lakes. Radiocarbon 40, 921-931.

Gordon, J.E. Harkness, D.D., 1992. Magnitude and geographic variation of the radiocarbon content in Antarctic marine life: Implications for reservoir corrections in radiocarbon dating. Quat. Sci. Rev. 11, 697-708.

Heaton, T.J., Köhler, P., Butzin, M., Bard, E., Reimer, R.W., Austin, W.E.N., Ramsey, C.B., Grootes, P.M., Hughen, K.A., Kromer, B., Reimer, P.J., Adkins, J., Burke, A., Cook, M.S., Olsen, J., Skinner, L., 2020. MARINE20 - The marine radiocarbon age calibration curve (0-55,000 cal BP). Radiocarbon 62, 779-820.

Hillenbrand, C.D., Larter, R.D., Dowdeswell, J.A., Ehrmann, W., Cofaigh, C.Ó., Benetti, S., Graham, A.G.C., Grobe, H., 2010. The sedimentary legacy of a palaeo-ice stream on the shelf of the southern Bellingshausen Sea: Clues to West Antarctic glacial history during the Late Quaternary. Quat. Sci. Rev. 29, 2741-2763.

Hua, Q., Ulm, S., Yu, K., Clark, T.R., Nothdurft, L.D., Leonard, N.D., Pandolfi, J.M., Jacobsen, G.E., Zhao, J., 2020. Temporal variability in the Holocene marine radiocarbon reservoir effect for the Tropical and South Pacific. Quat. Sci. Rev. 249, 106613.

Kennett, J.P., 1968. The fauna of the Ross Sea: part 6: ecology and distribution of foraminifera. Dept. Sci. Ind. Res. Bull. 186, 1-47.

KOPRI 극지연구소

Kim, S., Lee, J.I., McKay, R.M., Yoo, K.C., Bak, Y.S., Lee, M.K., Roh, Y.H., Yoon, H.I., Moon, H.S., Hyun, C.U., 2020. Late Pleistocene paleoceanographic changes in the Ross Sea – Glacial–interglacial variations in paleoproductivity, nutrient utilization, and deep–water formation. Quat. Sci. Rev. 239, 106356, doi:10.1016/j.quascirev.2020.106356.

Kim, S., De Santis, L., Hong, J.K, Cottlerle, D., Petronio, L., Colizza, E., Kim, Y.G., Kang, S.G., Kim, H.J., Kim, S., Wardell, N., Geletti, R., Bergamasco, A., McKay, R., Jin, Y.K., Kang, S.H., 2018a. Seismic stratigraphy of the Central Basin in northwestern Ross Sea slope and rise, Antarctica: Clues to the late Cenozoic ice–sheet dynamics and bottom–current activity. Mar. Geol. 395, 363–379, doi:10.1016/j.margeo.2017.10.013.

Kim, S., Yoo, K.C., Lee, J.I., Khim, B.K., Bak, Y.S., Lee, M.K., Lee, J., Domack, E.W., Christ, A.J., Yoon, H.I., 2018b. Holocene paleoceanography of Bigo Bay, west Antarctic Peninsula: Connections between surface water productivity and nutrient utilization and its implication for surface–deep water mass exchange. Quat. Sci. Rev. 192, 59–70, doi:10.1016/j.quascirev.2018.05.028.

Kim, S., Yoo, K.C., Lee, J.I., Lee, M.K., Kim, K., Yoon, H.I., 2018c. Relationship between magnetic susceptibility and sediment grain size since the last glacial period in the Southern Ocean off the northern Antarctic Peninsula – Linkages between the cryosphere and atmospheric circulation. Palaeogeogr. Palaeoclimatol. Palaeoecol. 505, 359–370, doi:10.1016/j.palaeo.2018.06.016.

Licht, K.J., Andrews, J.T., 2002. The 14C record of late Pleistocene ice advance and retreat in the central Ross Sea, Antarctica. Arctic, Antarctic, and Alpine Research 34, 324–333.

Licht, K.J., Cunningham, W.L., Andrews, J.T., Domack, E.W., Jennings, A.E., 1998. Establishing chronologies from acid–insoluble organic 14C dates on Antarctic (Ross Sea) and Arctic (North Atlantic) marine sediments. Polar Res. 17, 203–216.

Licht, K.J., Jennings, A.E., Andrews, J.T., Williams, K.M., 1996. Chronology of late Wisconsin ice retreat from the western Ross Sea, Antarctica. Geology 24, 223–226.

Lim, D., Choi, J., Xu, Z., Kim, M., Choi, D., Jung, H., Lee, P., 2009. Methane–derived authigenic carbonates from the Ulleung basin sediments, East Sea of Korea. Continental Shelf Research 29, 1588–1596, doi:10.1016/j.csr.2009.04.013.

Majewski, W., Prothro, L.O., Simkins, L.M., Demianiuk, E.J., Anderson, J.B., 2020. Foraminiferal patterns in deglacial sediment in the western Ross Sea, Antarctica: Life near grounding lines. Paleoceanogr. Paleocl. 35, e2019PA003716, doi:10.1029/2019PA003716.

McKay, R.M., Dunbar, G.B., Naish, T.R., Barrett, P.J., Carter, L., Harper, M., 2008. Retreat history of the Ross Ice Sheet (shelf) since the Last Glacial Maximum from

KOPRI 극지연구소

deep-basin sediment cores around Ross Island. Palaeogeogr. Palaeoclimatol. Palaeoecol. 260, 245-261, doi:10.1016/j.palaeo.2007.08.015.

McKay, R.M., De Santis, L., Kulhanek, D.K., the Expedition 374 Scientists, 2019. Ross Sea West Antarctic Ice Sheet History. Proceedings of the International Ocean Discovery Program 374, College Station, TX (International Ocean Discovery Program), doi:10.14379/iodp.proc.374.2019.

Nozaki, Y., Cochran, J.K., Turekian, K.K., Keller, G., 1977. Radiocarbon and 210Pb distribution in submersible-taken deep-sea cores from project FAMOUS. Earth Plant. Sci. Lett. 34, 167-173.

Ohneiser, C., Yoo, K.C., Albot, O,B., Cortese, G., Riesselman, C., Lee, J.I., McKay, R., Bollen, M. ,Lee, M.K., Moon, H.S., Kim, S., Beltran, C., Levy, R., Wilson, G.S., 2019. Magneto-biostratigraphic age models for Pleistocene sedimentary records from the Ross Sea. Glob. Planet. Change 176, 36-49.

Peng, T.H., Broecker, W.S., 1984. The impacts of bioturbation on the age difference between benthic and planktonic foraminifera in deep-sea sediments. Nucl. Instrum. Methods Phys. Res., Sect. B, 233, 346-352.

Prothro, L., Majewski, W., Yokoyama, Y., Simkins, L., Anderson, J., Yamane, M., et al., 2020. Timing and pathways of East Antarctic Ice Sheet retreat. Quat. Sci. Rev. 230, 106116.

Rosenheim, B.E., Day, M.B., Domack, E., Schrum, H., Benthien, A., Hayes, J.M., 2008. Antarctic sediment chronology by programmed-temperature pyrolysis: Methology and data treatment. Geochem. Geophys. Geosyst. 9, Q04005, doi:10.1029/2007GC001816.

Savrda, C.E., Krawinkel, H., McCarthy, F.M.G., McHugh, C.M.G., Olson, H.C., Mountain, G., 2001. Ichnofabrics of a Pleistocene slope succession, New Jersey, margin: relations to climate and sea-

level dynamics. Palaeogeogr. Palaeoclimatol. Palaeoecol. 171, 41-61, doi:10.1016/S0031-0182(01)00266-8.

Soltwedel, T., Hasemann, C., Vedenin, A., Bergmann, M., Taylor, J., Krauß, F., 2019. Bioturbation rates in the deep Fram Strait: Results from in situ experiments at the arctic LTER observatory HAUSGARTEN. J. Exp. Mar. Biol. 511, 1-9, doi:10.1016/j.jembe.2018.11.001.

Stuiver, M., Reimer, P.J., 1993. Extended 14C database and revised CALIB radiocarbon calibration program. Radiocarbon 35, 215-230.

Subt, C., Fangman, K.A., Wellner, J.S., Rosenheim, B.E., 2016. Sediment chronology in Antarctic deglacial sediments: Reconciling organic carbon 14C ages to carbonate 14C ages using Ramped PyrOx. The Holocene 26, 265-273, doi:10.1177/0959683615608688.

KOPRI 극지연구소

The RAISED Consortium, Bentley, M.J., Cofaigh, C.Ó., Anderson, J.B., Conway, H., Davies, B., et al., 2014. A community-based geological reconstruction of Antarctic Ice Sheet deglaciation since the Last Glacial Maximum. Quat. Sci. Rev. 100, 1-9, doi:10.1016/j.quascirev.2014.06.025.

Venturelli, R.A., Siegfried, M.R., Roush, K.A., Li, W., Burneet, J., Zook, R., Fricker, H.A., Priscu, J.C., Leventer, A., Rosenheim, B.E., 2020. Mid-Holocene grounding line retreat and readvance at Whillans Ice Stream, West Antarctica. Geophys. Res. Lett. 47, e2020GL088476, doi:10.1029/2020GL088476.

Xiao, W., Frederichs, T., Gersonde, R., Kuhn, G., Esper, O., Zhang, X., 2016. Constraining the dating of late Quaternary marine sediment records from the Scotia Sea (Southern Ocean). Quat. Geochronol. 31, 97-118, doi.org/10.1016/j.quageo.2015.11.003.

Yokoyama, Y., Anderson, J.B., Yamane, M., Simkins, L.M., Miyairi, Y., Yamazaki, T., et al., 2016. Widespread collapse of the Ross Ice Shelf during the late Holocene. Proc. Natl. Acad. Sci. U.S.A. 113, 2354-2359, doi:10.1073/pnas.1516908113.

Zhou, A., Chen, F., Wang, Z., Yang, M., Qiang, M., Zhang, J. Temporal change of radiocarbon reservoir effect in Sugan Lake, northwest China during the late Holocene. Radiocarbon 51, 529- 535.

KOPRI
극지연구소

Table 1. Information on sediment cores used in this stduy. ^{14}C: AMS 14C measured, X: x-radiographs, and PI: photo images of sediment.

Core	Location and water depth	^{14}C	X	PI	region
RS15-GC107	68°04.0741′S, 178°37.9066′W, 3050 m deep	v	v	v	
RS15-LC108	67°29.6139′S, 178°45.1185′W, 3690 m deep	v	v	v	Ross Sea slope/rise
RS15-LC42	71°49.3969′S, 178°34.7602′E, 2084 m deep	v	v	v	
AMRS20-BC04	76°03.1359′S, 156°26.7317′W, 3219 m deep		v	v	
RS15-GC40	71°37.0044′S, 178°17.4630′W, 1083 m deep	v	v	v	Ross Sea outer shelf
RS15-GC67	73°05.1869′S, 170°52.7400′E, 567 m deep	v	v	v	Ross Sea shelf
AMRS20-BC03	75°09.7062′S, 179°05.8579′W, 544 m deep		v	v	
AM20-BC08	73°46.0990′S, 127°54.8069′W, 725 m deep		v	v	
AM20-BC09	74°10.3588′S, 129°06.7084′W, 872 m deep		v	v	Amundsen Sea shelf
AM20-BC12	73°56.0184′S, 127°47.9195′W, 790 m deep		v	v	
BS17-GC02	68°09.4940′S, 94°34.7988′W, 4361 m deep	v	v	v	Bellingshausen Sea rise
BS17-GC07	71°52.0190′S, 85°20.9170′W, 502 m deep	v	v	v	
BS17-BC08	73°38.9265′S, 81°21.0207′W, 671 m deep		v	v	Bellingshausen Sea shelf
BS17-MC09	73°40.8372′S, 81°18.9309′W, 630 m deep			v	
BS17-BC12	72°26.9860′S, 73°33.2001′W, 560 m deep		v	v	
AP18-BC18	62°07.4960′S, 56°07.8605′W, 1324 m deep		v	v	Bransfield Eastern Basin
GC04-G03	61°19′S, 49°48′W, 2907 m deep	v	v	v	Powell Basin

KOPRI
극지연구소

Table 2. Conventional ^{14}C ages used in this study. AIOM: acid insoluble organic matter, PF: planktonic foraminifera (Neogloboquadrina pachyderma sin.), BF: benthic foraminifera (Globocassidulina biora), PMC: percent modern carbon, SR: sedimentation rate, BI: bioturbation intensity (0: no biotrubation, 1: slight bioturbation, 2: moderate biotrubation, 3: heavy bioturbation, and 4:complete bioturbation), RS: Ross Sea, BS: Bellingshausen Sea, and PB: Powell Basin, d13C values are provided only for AIOM samples.

Core (depth)	Lab code	^{14}C age (yr BP)	PMC (pMC)	$\delta^{13}C$ (‰)	Material	SR (cm/kyr)	BI	Region	Reference
RS15-GC40 (5 cm)	Beta521623	13,080 ± 50	19.6 ± 0.1	−24.2	AIOM	0.39	1–2	RS outer shelf	This study
	Beta489452	21,790 ± 70	6.6 ± 0.1	-	PF				Kim et al. (2020)
RS15-GC67 (50 cm)	Beta447356	15,160 ± 40	15.1 ± 0.1	−24.5	AIOM	2.78	2–3		This study
	Beta451756	17,140 ± 50	11.8 ± 0.1		PF				
	Beta447365	17,970 ± 70	10.7 ± 0.1		BF				
RS15-GC67 (81 cm)	Beta451752	16,090 ± 50	13.5 ± 0.1	−24.3	AIOM	9.05	2–3	RS shelf	This study
	Beta447367	20,920 ± 90	7.4 ± 0.1	-	BF				
RS15-GC67 (95 cm)	Beta451753	17,820 ± 60	10.9 ± 0.1	−24.4	AIOM	1.02	2–3		This study
	Beta451758	33,860 ± 260	1.5 ± 0.1	-	PF				
	Beta447368	34,090 ± 260	1.4 ± 0.1	-	BF				
RS15-LC42 (10 cm)	Beta521626	17,360 ± 60	11.5 ± 0.1	−23.9	AIOM	–	0–1	RS slope/rise	This study
	Beta489455	16,500 ± 40	12.8 ± 0.1	-	PF				
RS15-GC107 (14 cm)	Beta521625	16,720 ± 60	12.5 ± 0.1	−23.9	AIOM	0.42	3	RS rise	This study
	Beta489457	30,520 ± 140	2.2 ± 0.1	-	PF				
RS15-LC108 (18 cm)	Beta521624	17,740 ± 60	11.0 ± 0.1	−23.5	AIOM	0.67	3		This study
	Beta489458	24,340 ± 80	4.8 ± 0.1	-	PF				
BS17-GC02 (354 cm)	Beta508166	24,020 ± 80	5.0 ± 0.1	−24.7	AIOM	–	0–1	BS rise	This study
	Beta489460	18,360 ± 50	10.2 ± 0.1	-	PF				
BS17-GC02 (372 cm)	Beta508167	22,890 ± 90	5.8 ± 0.1	−25.7	AIOM	1.03	2–3		This study
	Beta489459	34,580 ± 220	1.4 ± 0.1	-	PF				
BS17-GC07 (2 cm)	Beta564901	5810 ± 30	48.5 ± 0.1	−23.4	AIOM	–	2	BS shelf	This study
	Beta568908	2920 ± 30	69.5 ± 0.1	-	PF				
GC04-G03 (272 cm)	Beta564899	36,410 ± 290	1.1 ± 0.1	−23.5	AIOM	–	1	PB	This study
	Beta447376	26,240 ± 110	3.8 ± 0.1	-	PF				Kim et al. (2018a)

KOPRI 극지연구소



Figure 1. West Antarctic continental margin with core locations. Red dots are sites for 14C dating (see Table 2). Black dots are sites for box and multi core sediment surface images in Figures 4 and 5.

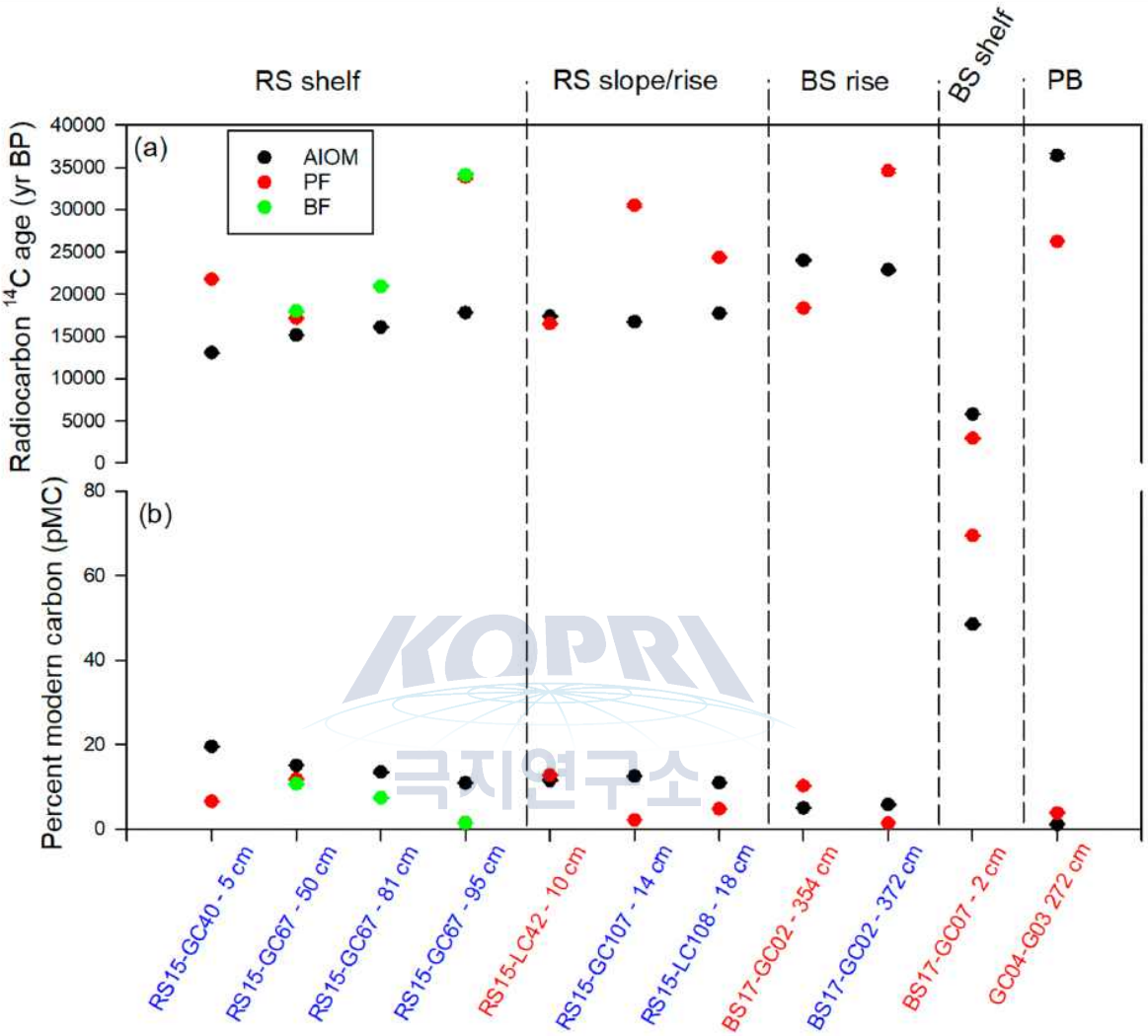


Figure 2. (a) Accelerated Mass Spectrometry (AMS) 14C dates and (b) percent modern carbon of acid insoluble organic matter (AIOM: black) with planktonic (PF: red) and/or benthic foraminifers (BF: green) for 8 cores from the West Antarctic continental margin. RS: Ross Sea, BS: Bellingshausen Sea, and PB: Powell Basin in the Antarctic Peninsula. Negative and positive ΔAgeAIOM−F values are marked by blue and red color, respectively.

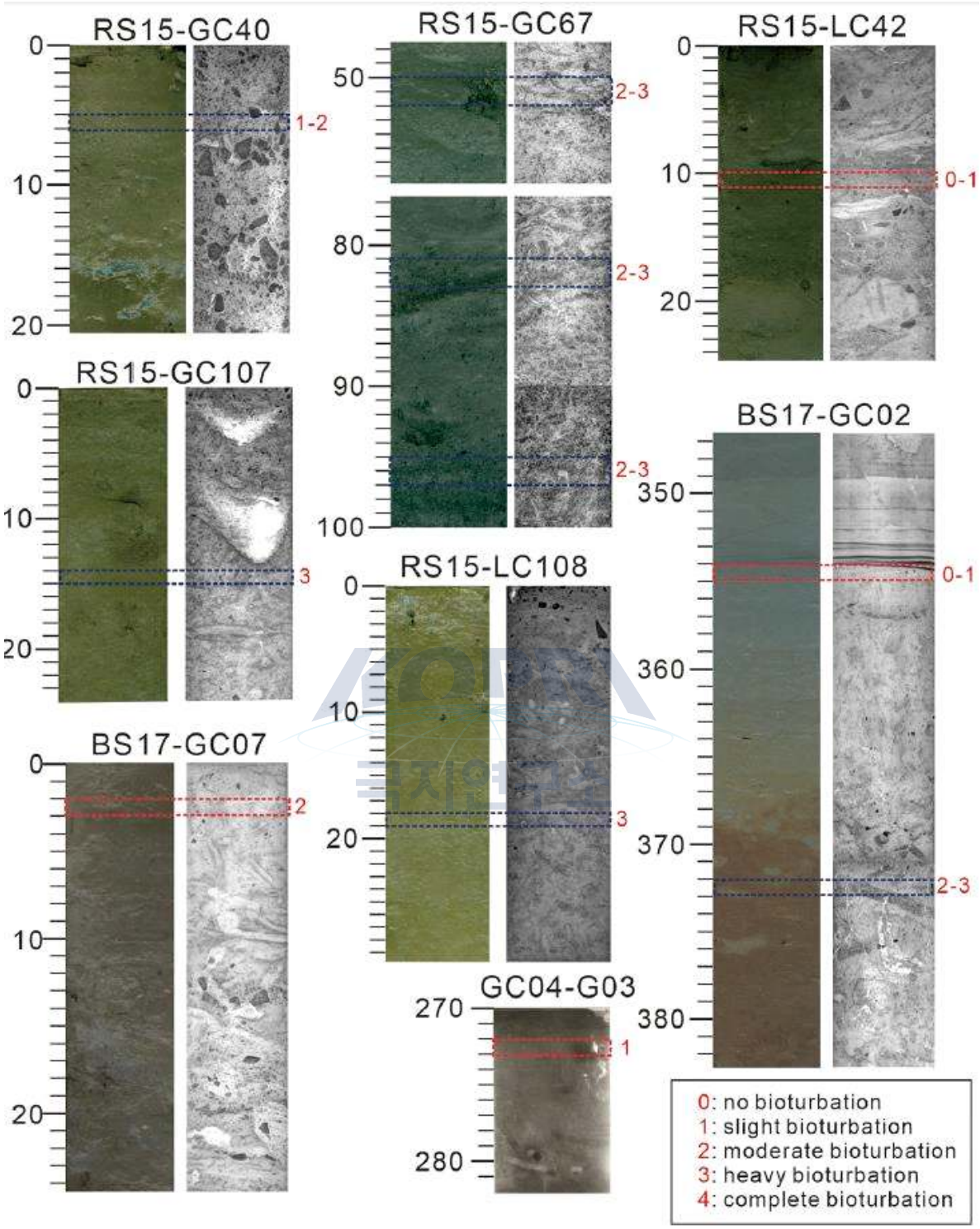


Figure 3. Core image and x-radiographs including AMS 14C dating intervals of all cores. AMS 14C dating intervals are marked by dashed rectangles (blue color for negative ΔAgeAIOM-F values and red color for positive ΔAgeAIOM-F values). Red numbers indicate bioturbation scales modified from Droser and Bottjer (1986) and Savrda et al. (2001).



Figure 4. Box core surface sediment images from 40 cm by 50 cm box-core can with tube worms and their organic matter cemented tubes pointed by red arrows; (a) AMRS20-BC03, (b) AMRS20-BC04, (c) AM20-BC08, (d) AM20-BC09, (e) AM20-BC12, (g) BS17-BC08, and BS17-BC12. (f) vertical distribution of organic matter cemented tubes of AM20-BC12 and (i) in situ organic matter cemented tubes in multi core top sediment of BS17-MC09.

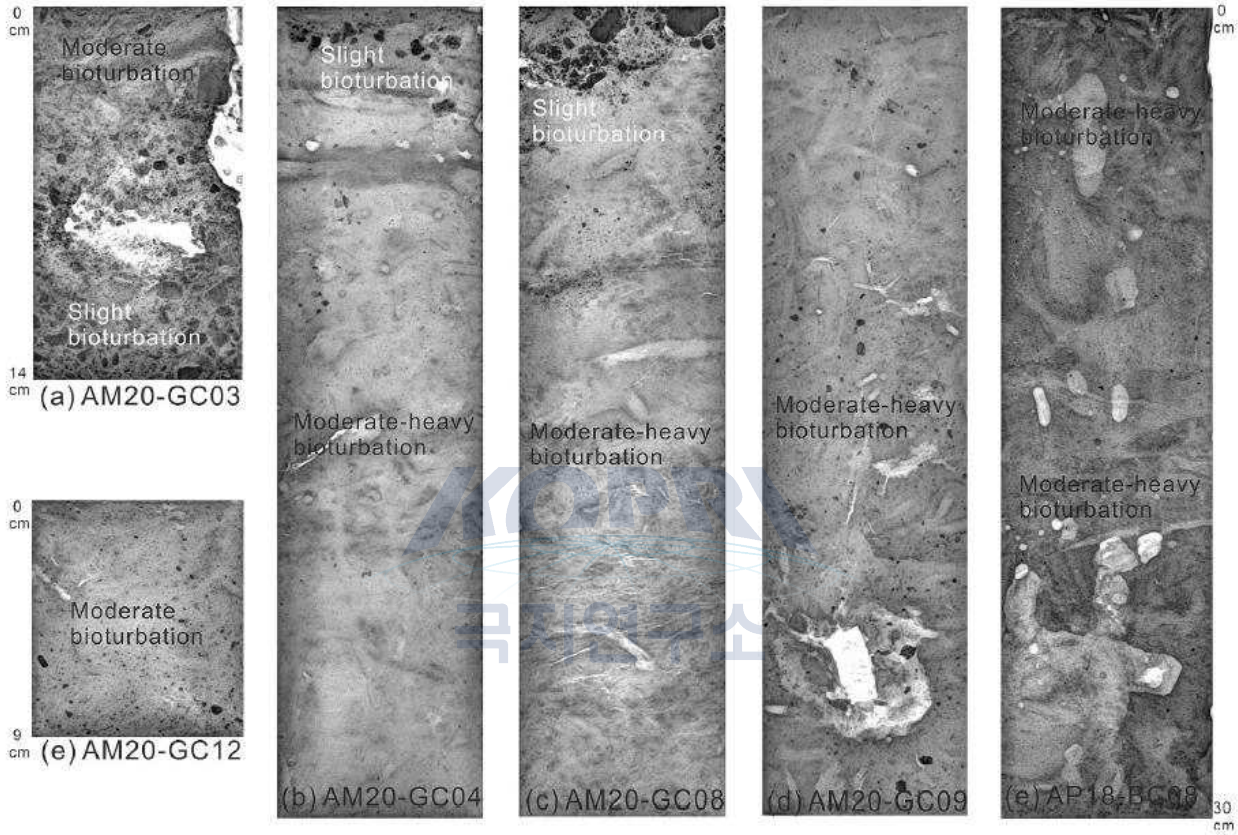


Figure 5. X-radiographs of core top sediments for (a) AMRS20-GC03, (b) AMRS20-GC04, (c) AM20-GC08, (d) AM20-GC09, (e) AM20-GC12, and (f) AP18-BC08. Bioturbation scales are modified from Droser and Bottjer (1986) and Savrda et al. (2001). Coordinates of gravity cores are identical to those of box cores.

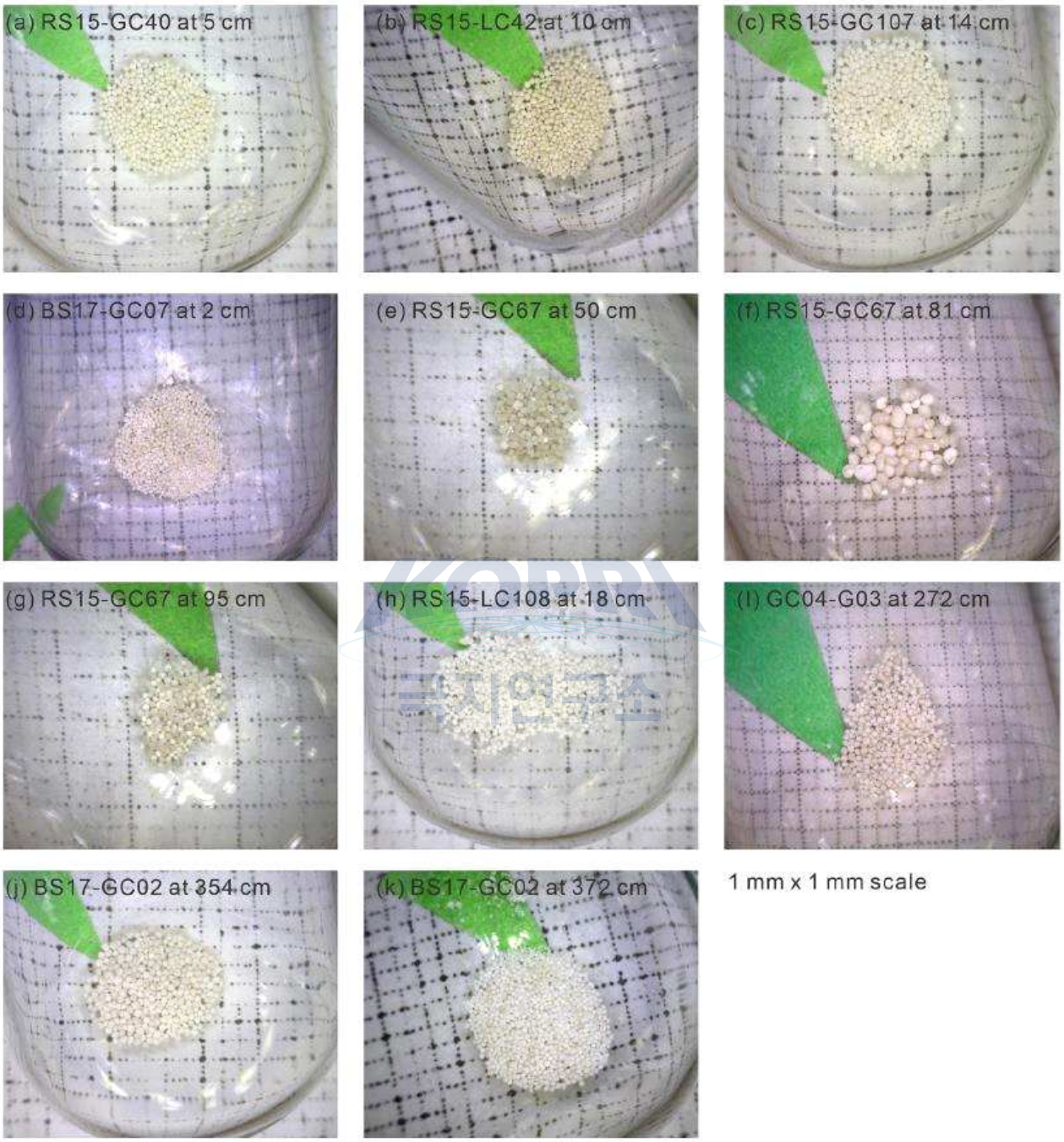


Figure 6. Images of picked foraminifera before age dating. Images were provided by Beta Beta Analytic, USA.

제 25 장

Variation in magnetic susceptibility in the Bellingshausen Sea continental rise since the last glacial period and implications for terrigenous material input mechanisms[19)]

Sunghan Kim[a,b,*], Min Kyung Lee[a], Ji Young Shin[c], Kyu-Cheul Yoo[a], Jae Il Lee[a], Myung-Il Kang[a], Heung Soo Moon[a], Joseph G. Prebble[d]

[a]Korea Polar Research Institute, [b]Department of Polar Sciences, University of Science and Technology (UST), [c]Peking University, [d]GNS Science

Abstract: Magnetic susceptibility (MS) is routinely used as a proxy for terrigenous material input to Antarctic continental margin sediments. Variations in terrigenous input on glacial-interglacial timescales in this setting are related to a range of environmental changes; including to the cryosphere, atmosphere, and hydrosphere. However, the exact environmental factors and depositional processes that control MS values in sedimentary cores from the Antarctic continental margin remains unresolved. Here, we explore in detail sedimentary physical characteristics and MS values of core BS17-GC01 collected from Bellingshausen Sea continental rise, to understand how depositional process have varied during the late Quaternary. We found that input of terrigenous material increased markedly during Marine Isotope Stages (MIS) 2 and 4, compared to deposition during the adjacent interstadial and Holocene times. Variation in the bulk MS values were associated with changes in grain size. Size specific massnormalized MS measurements show the fine fraction (<16 μm) has the highest MS values, followed by the coarse silt fraction (16-63 μm). However, because coarse silt is the predominant grain size, the increased bulk MS during MIS 2 and 4 are mainly driven by changes in this fraction. We propose that the coarse silt with high bulk MS values observed in glacial sediments were transported to the site as iceberg rafted debris, originating from the Bellingshausen Sea shelf region. In contrast, grains >1 mm – a commonly applied proxy for glacial transport in this setting – were observed during MIS 1 and 3 only. We conclude these contrasting signatures of iceberg rafted debris in this Bellingshausen Sea core arise from changes in the to the erosive dynamics of the adjacent ice shelf and continental

KOPRI 극지연구소

19) 이 연구 결과는 다음의 논문으로 출판되었음: Kim, S. et al. (2022). "Variation in magnetic susceptibility in the Bellingshausen Sea continental rise since the last glacial period and implications for terrigenous material input mechanisms." Palaeogeography, Palaeoclimatology, Palaeoecology 594: 110948.

shelf on glacial/interglacial timescales.

1. Introduction

Variation of the Antarctic Ice Sheet (AIS) is associated with change in the adjacent oceans, including surface water production, circulation, and terrigenous sediment input, transport mechanisms, and transport pathways (Diekmann, 2007; Hillenbrand et al., 2009, 2021; Sprenk et al., 2013; Kim et al., 2020a). Because the West Antarctic Ice Sheet (WAIS) is a marine-based ice sheet, it is likely to respond relatively quickly to changing climate and ocean conditions, with rates of change greatest in the Bellingshausen Sea and Amundsen Sea regions (Paolo et al., 2015; Cook et al., 2016; Garbe et al., 2020). To understand past WAIS variability on glacial-interglacial timescales, it is necessary to study deep-ocean sedimentary records from the continental rise, as the continental shelves contain only sedimentary records deposited since the last deglaciation.

Deep ocean sediments of the western Antarctic Peninsula region are characterized by grey laminated mud, with depositional features attributable to a combination of turbidites, contourites, and plumites observed (Hillenbrand et al., 2021). These sedimentary features are commonly found in sediment cores collected from sediment depocenters which receive sediments from shelf area by gravitational processes (Dowdeswell et al., 2008).. Understanding the environmental settings that give rise to these sedimentary features, along with the complementary processes that transport sediment to the deep sea such as ice rafting, aeolian transport, gravity flow, and currents, are key to gaining insights of past ice sheet variation.

Three key tools used to interpret depositional change in this setting are grain size, bulk Magnetic susceptibility (MS), and size specific MS. Magnetic susceptibility records from Antarctic sediment cores have been interpreted by many workers to indicate relative abundance terrigenous material input (e.g., Leventer et al., 1996; Ceccarori et al., 1998; Diekmann et al., 2000; Hillenbrand et al., 2009; Yoon et al., 2009; Sprenk et al., 2013). For example, variation of MS values from Southern Ocean cores off the northern Antarctic Peninsula and Scotia Sea, showed strong correlations with the European Project for Ice Coring in Antarctica (EPICA) Dronning Maud Land (EDML) ice core dust record (Fischer et al., 2007), showing high values during glacial periods and low values during interglacial periods (Diekmann et al., 2000; Pugh et al., 2009; Weber et al., 2012; Xiao et al., 2016; Kim et al., 2018a, 2020a). While the exact mechanism for the strong correlations between MS values in sediment cores and ice core dust record is unclear (Diekmann et al., 2000; Pugh et al., 2009; Weber et al., 2012; Xiao et al., 2016; Kim et al., 2018a, 2020a), Kim et al. (2018a) reported that the bulk MS values are related to grain size and that the sediments ranging from coarse

KOPRI 극지연구소

silt to fine sand which have high MS are the main driver of the increased MS values during glacial periods.

In this study, we compare grain size, including grains >1 mm, with bulk MS and size- specific MS measurements of a sediment core from the Bellingshausen Sea continental rise to 1) reconstruct terrigenous input variation, 2) define the sedimentary size fraction that has the greatest influence on variation of bulk MS, and thus 3) unravel the sediment transport mechanisms to this site since the last glacial period in response to ice sheet variation.

2. Material and methods

One gravity core was collected from the continental rise of the Bellingshausen Sea by IBR/V Araon during the ANA07D cruise in 2017; 217 cm-long BS17-GC01 (67°22.8947′S, 96°23.2464′W, 4467 m water depth; Fig. 1). BS17-GC01 is located in the abyssal plain. The core site is located north of sediment depocenter C (Scheuer et al., 2006), indicating that hemi-pelagic deposition might be dominant. The core was stored cold before being opened, described, and sub-sampled at the Korea Polar Research Institute (KOPRI), where core photos were taken by ITRAX, X-radiographs were taken from 8 cm x 30 cm x 1 cm slabs, and MS measurements and grain size analysis were performed.

KOPRI 극지연구소

2.1. Physical properties (magnetic susceptibility and grain density)

The volume MS of BS17-GC01 were measured at 1 cm intervals on split half-core sections using a Bartington MS2E point sensor in SI unit at KOPRI. For size-specific MS measurements, bulk sediments of 4-6 g were collected at 22 selected depths and biogenic components were removed by H2O2, HCl, and NaOH solution. The chemical treatment was performed with the same procedure in Shin et al. (2020), who showed that magnetic signals of fine particles (e.g., non-interacting single-domain magnetite) were preserved by this treatment. For particle-size separation, >63 μm (sand-sized) fraction was sieved by wet sieving, and then the residual sediment solution was separated into 16-63 μm (coarse silt-sized) grains and <16 μm (fine-sized) fractions by settling, following Stokes' law. In detail, after a 3-minute sonication, the sample solution was well mixed in a 250 ml beaker. After 135 seconds, upper 4 cm supernatant was extracted and repeated until supernatant became clear. Then, particles <16 μm were gathered by centrifugation at 4000 rpm for 20 min. After weighing dry mass, each size fraction was packed in a 10 cm3 sample container and subjected to MS measurements at low frequency (470 Hz) using a Bartington MS2B

sensor. Of a total 66 sized samples, MS values of 15 sand-sized samples were not measured as the sample mass was too low (<0.05 g) to obtain an accurate measurement. Mass-normalized MS (10-6 m3/kg) was calculated using sample mass and volume, after correction for the background MS values of diamagnetic materials in the sample container. Then, mass-weighted MS was calculated by multiplying the mass-normalized MS by the mass proportion of each size fraction. As bulk MS can be described as the sum of mass-weighted MS of each size fraction, the percentage contribution of size-specific MS to bulk one was calculated as follows:

Contribution to bulk MS (%) = mass-weighted MS / bulk MS (i.e., sum of mass-weighted MS of each size fraction) / 100

The grain density was measured on bulk sediment at 4 cm intervals for BS17-GC01 using a gas pycnometer (AccuPyc II 1340).

2.2. Grain size analysis and count of grains >1 mm

After removing the organic matter and biogenic silica from the bulk sediments using 10% H_2O_2 and 2N NaOH, respectively, grain size was analyzed at 10 cm intervals for BS17-GC01. Coarser fractions (>63 μm) were weighted at 1-phi intervals using sieves, while finer fractions (<63 μm) were analyzed using a Micrometrics SediGraph III 5120 at KOPRI. The classification of sediments follows that of Folk and Ward (1957).

X-radiographs were captured of center slices (1 cm thick x 8 cm width x 30 cm length) removed from each core section. Grains >1 mm in diameter were manually counted every 1 cm on the X-radiographs and the counts were divided by 8 cm3 to obtain counts/cm^3.

2.3. Radiocarbon dating

Four accelerator mass spectrometry (AMS) 14C dates were measured at Beta Analytic, USA (Table 1). Because of the lack of foraminifers or calcareous shell fragments in the sediments, all AMS 14C dating was conducted on acid insoluble organic matter (AIOM). This AIOM AMS 14C dating has been commonly used to date sediment ages of Antarctic sediments characterized by poor carbonate preservation in many studies from Ross Sea, Bellingshausen Sea, and Scotia Sea (Licht et al., 1996; Domack et al., 1999, 2001; McKay et al., 2008; Hillenbrand et al., 2010; Kim et al., 2020a).

3. Age model

Previous studies in this depositional setting have inferred intervals of high MS and low biological production to be deposited during glacial periods, and intervals of low MS intervals and high biological production to record interglacial deposition (Pudsey and Camerlenghi, 1998; Hillenbrand et al., 2009, 2021; Shin et al., 2020). The correlation between MS values and the EDML ice core dust record has been used for age establishment of Scotia Sea sediment cores (Weber et al., 2012; Xiao et al., 2016; Kim et al., 2018a). Although there has been debate about the causal mechanisms that isochronously connect the two settings (Pudsey, 2000; Pugh et al., 2009; Weber et al., 2012; Xiao et al., 2016; Kim et al., 2018a), high MS peaks in the Scotia Sea sediments were matched with high non-sea salt Ca2+ concentration, indicative of dust input (Lambert et al., 2011) in the EDML ice core (Fischer et al., 2007). The age model established for that core using sediment MS-ice core dust record matching was supported by humic acid 14C dates, geomagnetic excursion records, and ash layer ages (Xiao et al., 2016). In this study, we observed a similar pattern of MS variation to that in Scotia Sea cores, so have applied a graphical correlation between the MS and EDML ice core dust record to establish an age model (Pudsey, 2000; Pugh et al., 2009; Weber et al., 2012; Xiao et al., 2016; Kim et al., 2018a), based on the EDML ice core dust record (Fischer et al., 2007, Fig. 2). Although we acknowledge that the distance between the Bellingshausen and Scotia Seas is considerable, we conclude that this approach is justified as the depositional settings are sufficiently similar. In addition, Kim et al. (2018a) reported a strong linkage between atmospheric circulation and cryosphere changes suggesting that assumption is valid for initial tests in our study area. We hope that future studies will identify other corroborating evidence from this area, such as tephra layers, that will support this chronology. The AnalySeries software was used to produce graphical correlations (Paillard et al., 1996). Six tie points were constrained for the age model for BS17-GC01 (Table 2, Fig. 2). Based on six tie points, the linear correlation coefficient (r) was calculated as 0.76 between EDML dust and BS17-GC01 MS values.

The core-top 14C age of BS17-GC01 was 11,140 yr BP, which is too old compared to previously reported local reservoir ages (Berkman and Forman, 1996; Domack, 1992; Gordon and Harkness, 1992; Harden et al., 1992) or core top ^{14}C ages in the Antarctica (Hillenbrand et al., 2010; Xiao et al., 2016). Although core top loss cannot be quantified due to the lack of a box core from this site, some core top loss during core recovery in this deep ocean setting cannot be discounted. However, we observed oxygenated sediment at the top of our core, indicating core top loss was likely not significant. Thus, we assumed that the core top is of Recent age. However, this decision has no relevance to the current study, where we focus on glacial-interglacial comparison. To account for reworked carbon, we treat all radiocarbon ages as maximum ages. We calibrated 14C dates after correcting core top age

following Lee et al. (2010) with an assumption of similar old carbon influence with depths using Calib 8.2 with Marine20 (Stuiver and Reimer, 1993; Heaton et al., 2020) (Table 1). However, δ13C of organic matter at 34 cm (−27□) is different from the others (−24.8±0.3□) (Table 1). We therefore did not use the age from 34 cm in this age model (Fig. 3). The age model below 186 cm was inferred by linear extrapolation beyond two tie points at 141 cm and 186 cm. Based on this linear extrapolation, the age of the bottom of the core (217 cm) was inferred to be ~69 ka (Fig. 3).

4. Results

According to the age model, BS17−GC01 likely covers over the last ~70 kyr with sedimentation rates of ~3 cm/kyr.

The bulk MS values of BS17−GC01 alternated between low values (<100 10−5 SI) from 0 to 31 cm (0 to 15.5 ka) and 76 to 182 cm (31.5 to 62 ka), and high values (up to 1200 10−5 SI) from 31 to 76 cm (15.5 to 31.5 ka) and 182 to 217 cm (62 to 69 ka) (Fig. 4). Grains >1 mm were found only in high bulk MS intervals (Fig. 4). Low bulk MS intervals are characterized by brownish diatom bearing (0−31 cm) to diatom−poor (76−182 cm) bioturbated mud with some intercalated fine laminated layers in the lower interval (Fig. 4). In contrast, the high bulk MS intervals are characterized by grayish massive and structureless silt. Faint laminae occurred in the lower part of 31−77 cm interval (Fig. 4).

Grain density ranged from 2.6 to 2.7, showing relatively high density associated with the high bulk MS intervals and low density in low bulk MS intervals (Fig. 4). The mean grain size variation pattern also resembles that of the MS values and the grain density (Fig. 4). The silt fraction was predominant (range 30−98 mass %, average ~79%) and followed by the clay fraction (range 0.4−70 mass %, average ~20%). An interval of relatively high bulk MS was observed between 114 to 138 cm (41.6 to 52.3 ka), also associated with an increase of grain density and the mean grain size.

The mass−normalized MS of the fine silt and clay (<16 μm) and coarse silt sized fractions (16−63 μm) showed increased values with bulk MS increases from 31 to 76 cm (15.5 to 31.5 ka) and 182 to 217 cm (62 to 69 ka) and decreased values from 0 to 31 cm (0 to 15.5 ka) and 76 to 182 cm (31.5 to 62 ka) (Fig. 5). Although the mass−normalized MS of sand fraction (>63 μm) was not calculated from all samples due to limited sample mass, it was higher from 0 to 31 cm (0 to 15.5 ka) than from 31 to 76 cm (15.5 to 31.5

ka) (Fig. 5). This indicates that the MS variation pattern of sand was different from those of fine silt and clay (<16 μm) and coarse silt sized fractions (16–63 μm). The coarse silt size fraction was predominant throughout the core and increased 90% especially in high bulk MS intervals (Fig. 5). According to mass-weighted MS values, MS values of the coarse silt sized fraction are almost ten times higher than those of fine (<16 μm) and sand sized fractions (>63 μm) (Fig. 5). In the high bulk MS intervals, the coarse silt sized fraction contributes 80% of the bulk MS value (Fig. 5).

5. Discussion

5.1. Terrigenous material input variation since the last glacial period

Magnetic mineral assemblages can provide information on sediment provenance and transport processes (Robinson, 1986; Stoner and Andrews, 1999; Brachfeld et al., 2002, 2009; Kissel et al., 2003). Previous studies have interpreted down-core MS variability to reflect changes in the relative proportion of terrigenous and biogenic sediment in a core from the continental shelf of the West Antarctic Peninsula; high for more terrigenous sediment input and low for more biogenic sediment input (Leventer et al., 1996; Brachfeld and Banerjee, 2000; Brachfeld et al., 2002). Similar negative correlations between biogenic abundance and MS values have also been observed from the western Antarctic continental margin (Ceccarori et al., 1998; Hillenbrand et al., 2009; Yoon et al., 2009; Sprenk et al., 2013). We apply these observations to our interpretation of core BS17-GC01, and use MS variation of BS17-GC01 as an indicator for changes in terrigenous material input to the Bellingshausen Sea continental rise.

The MS values of BS17-GC01 were distinctly elevated during MIS 2 and 4 and also increased at 41.6–52.3 ka with EDMS dust elevation, indicating increased MS values during cold periods (Fig. 2). This is consistent with previous results showing high MS values during glacial periods in the western Antarctic continental margin and northern Antarctic Peninsula (Ceccarori et al., 1998; Diekmann et al., 2000; Hillenbrand et al., 2009; Allen et al., 2010; Xiao et al., 2016; Kim et al., 2018a, 2020a, 2020b) or high MS values during cold periods in the western Antarctic continental shelves (Leventer et al., 1996; Lee et al., 2012; Kim et al., 2018b). We extend these observations to the Bellingshausen Sea, where we conclude that terrigenous material input to the continental rise also increased during cold/glacial periods in that sector too over the last 70 ka. Terrigenous components have higher density than biogenic components. Thus, the co-variation of the MS values and the grain density record also support terrigenous material increases during cold/glacial periods (Fig. 4).

5.2. The key size fraction for MS variation since the last glacial period

An understanding of the sedimentary size fraction that controls MS values at a site is key to interpret understand terrigenous material transport based. There have been a range of correlations observed, and environmental interpretations proposed, for MS susceptibility measurements made on Antarctic sedimentary cores. From the Western Antarctic Peninsula, higher MS values coincided with increased flux of fine-grained terrigenous material at a site in Barilari Bay (Reilly et al., 2016). In the Scotia Sea, eolian-borne dust was proposed as the source of MS increase (Pugh et al., 2009; Weber et al., 2012). However, in the Palmer Deep of the Western Antarctic Peninsula, Brachfeld and Banerjee (2000) and Brachfeld et al. (2002) suggested that increased MS values reflect greater flux of iceberg rafted debris (IRD) during the LGM and the Early Holocene, while high MS values during cold periods in Southern Ocean cores west of the Antarctic Peninsula were related to the grain size changes (Kim et al., 2018a, 2020a). A correlation between elevated MS values and increased grain size during cold/glacial periods was also reported from Ross Sea cores (Kim et al., 2020b). In the present study, mean grain size co-varied with the MS values at this Bellingshausen Sea continental rise site (Fig. 4). In contrast to Brachfeld and Banerjee (2000), who reported increased MS values coincided with greater flux of IRD in a core from Palmer Deep, our study of core BS17-GC01 found grains >1 mm (inferred to be transported as IRD), were observed only during MIS 1 and 3. Grains >1 mm coincided with low bulk MS values and were found in fine sediments (Fig. 4). Since more than 95 mass % sediments were mud in BS17-GC01, changes in mean grain size were related to changes in the proportion of silt and clay (Fig. 4). This suggests that silt fraction is responsible for high bulk MS values in BS17-GC01.

Kim et al. (2018a) showed that down-core variation in bulk MS values were related to variation of sediment grain size between coarse silt to fine sand. They separated bulk sediments into three size fractions; sand-fraction (>63 μm), coarse silt-fraction (16-63 μm), and fine fraction (<16 μm). We followed their scheme in this study. The mass-normalized MS of sand fraction ranged from 0.23 to 1.39 10-6m3/kg, showing high values during MIS 1 (Fig. 5). In contrast, the MS values of the coarse silt fraction ranged from 1.3 to 4.1 10-6m3/kg, showing relatively high values during MIS 2 and 4 (Fig. 5). Finally, the mass-normalized MS of the fine fraction ranged from 0.7 to 6.6 10-6m3/kg, showing a co-variation pattern with the bulk MS values (Fig. 5). However, because the proportional contribution of each size fraction changes down core, the mass-weighted values of each fraction should also be considered. Mass-weighted MS values of the coarse silt fraction showed a similar variation pattern to the bulk MS values (Fig. 5). In contrast, mass-weighted MS values of fine fraction differ from the bulk MS values; the contribution of fine fraction

increased up to 30–40% in low bulk MS intervals during MIS 1 and 3 (Fig. 5). In summary, the bulk MS values are mainly controlled by coarse silt size fraction, in particular high bulk MS intervals (where MS values >80%) (Fig. 5).

5.3. An IRD transport mechanism for fine grained sediments with high MS values to the Bellingshausen Sea continental rise

We expect terrigenous materials to be transported to Southern Ocean sediment cores by various mechanisms such as: IRD, surface and/or bottom currents, gravity flow, volcanic eruptions, and eolian dust (Diekmann et al., 2000; Lucchi et al., 2002; Nielsen et al., 2007; Pugh et al., 2009; Weber et al., 2012; Xiao et al., 2016; Kim et al., 2018a, 2020a; Hillenbrand et al., 2021). These mechanisms differ in their tendency to transport and concentrate terrigenous materials of various grain sizes, such that grain-size distribution data can be helpful to infer transport mechanism. In this section, we examine the possibility of each transport mechanism in turn, and conclude the most likely transport mechanism for fine grained sediments with high MS values to the Bellingshausen Sea continental rise is as IRD.

In the Scotia sea, it was proposed that high MS intervals were caused by eolian dust, based on co-variation of sediment MS values and ice core dust records (Pugh et al., 2009; Weber et al., 2012). However, analysis of the mass-normalized MS data in our study indicates intervals of high MS are not caused by wind transported dust. Based on mass-weighted MS values, the coarse silt is responsible for the bulk MS variation in BS17-GC01. The fine fraction, which is thought to include dust, has high mass-weighted MS values during MIS 4, but are more or less similar from MIS 1 to MIS 3 (Fig. 5). In addition, the contribution of fine fraction to the bulk MS values of BS17-GC01 were low (<20%) in the high bulk MS intervals (Fig. 5). This indicates that the sediments with high MS values in the Bellingshausen Sea continental rise were not likely to have been transported by wind.

In the Atlantic sector of the Southern Ocean, Nielsen et al. (2007) concluded that MS variation was controlled by volcanic tephra, inferring that coarse-grained volcanic tephra was first deposited on sea ice and multi-year ice then rafted to the Atlantic sector of the Southern Ocean. If the MS in BS17-GC01 was controlled by volcanic materials, it would require volcanic activity in the Bellingshausen Sea region to be correlated with climate change (Fig. 2). However, the volcanic events are likely sporadic rather than climate-associated. In addition, we infer temporal correlation of volcanic activity between the Atlantic sector of the Southern Ocean and the West Antarctic Peninsula region is unlikely. MS values of Scotia Sea cores showed a similar variation pattern to ice core dust records, but volcanic activity associated MS peaks were episodic (Xiao et al., 2016; Kim et al., 2018a). In addition, the same tephra layers were not found in cores from the continental margin of Bellingshausen Sea

and Amundsen Sea (Hillenbrand et al., 2008b), implying that volcanic influence is not ubiquitous. Thus, we conclude the MS variations we observe are not related to volcanism.

Gray laminated mud is widely deposited in the continental slope to upper rise, in association with bottom current and down-slope turbidity currents during glacial periods (Lucchi et al., 2002; Lucchi and Rebesco, 2007; Hillenbrand et al., 2008a, 2021). Although sediments from BS17-GC01 deposited during early MIS 2 are faintly laminated, they are in general massive/structureless during most of MIS 2 and MIS 4, (Fig. 4). Even if bottom currents and/or turbidity currents influenced depositional process in the study area, we consider this unlikely to be a significant and consistent factor. Instead, we interpret a hemi-pelagic depositional setting in BS17-GC01, due to the virtual absence of lamination typical of contourites (Lucchi and Rebesco, 2007). During glacial periods, oceanographic fronts migrated northward with ice sheet advance (Gersonde et al., 2005). The resulting moat that developed north of BS17-GC17 (Fig. 1) means contourite deposition in this site during glacial periods is unlikely. Although coarse (silt-sized) sediments can be transported as plumite under glacier advanced conditions, it is likely the continental rise is located too far from the glacial source for plumites to reach (Lucchi et al., 2002).

The possibility of dissolution of magnetic grains also needs to be considered. Magnetic grains are dissolved by iron-reducing bacteria under low oxygen conditions (Canfield and Berner, 1987; Kostka and Nealson, 1995; Grimley and Arruda, 2007). However, absent- to poor- bioturbation and grayish sediment color of MIS 2 and 4 suggest relatively oxygenated conditions compared to MIS 1 and 3 sediments, which are characterized by bioturbation and brownish sediment. Even if there is some dissolution of magnetic minerals in association with redox condition changes in the study site, we conclude this is unlikely to have made a significant contribution to the MS variation in BS17-GC01.

In modern times, the surface current on the Antarctic continental shelves are the westward-flowing Antarctic Coastal Currents (Orsi et al., 1995; Whitworth et al., 1998). The Antarctic Slope Current also flows westward along the Antarctic continental shelf (Jacobs, 1991). Stronger bottom currents were reported in the south Scotia Sea during glacial periods (Kim et al., 2020a) along with northward migration of oceanic fronts in the oceans around Antarctica (Gersonde et al., 2005). The Antarctic Coastal Currents were likely absent or insignificant due to absence of a continental shelf during glacial periods. In spite of changes in current strength and location, the overarching pattern of Antarctic Slope Current is expected similar to the modern. Thus, it is unlikely to play a significant role in the transport sediments from the shelf to the deep-basin.

Secondary processes of sediment focusing also need to be considered because high MS intervals are composed of ~95% silt in BS17-GC01 (Fig. 5). The sedimentation rates during MIS 2 and 4 are higher than those during MIS 1 and 3 in BS17-GC01, although still

relatively low (<5 cm/kyr) (Fig. 3). However, higher sedimentation rates were not observed from high MS intervals in Scotia Sea sediment cores (e.g., Weber et al., 2012; Xiao et al., 2016). Even if there were influence of secondary, sediment-focusing, processes in the study area, the consistent temporal variation we observed in the MS values leads us to conclude they are unlikely to have been a significant contributor to high MS values.

Because concentration of grains >1 mm does not correlate with the bulk MS values in BS17-GC01, it is tempting to conclude that icebergs were not the dominant transport mechanism of high MS fine-grained sediments to the site. However, we believe that the mineralogy of the coarse sand grains makes IRD the most plausible mechanism. Fine-grained IRD has been proposed in other settings: coarse silt to fine sand size sediment a Southern Ocean core off the northern Antarctic Peninsula were inferred to have been transported as IRD (Kim et al., 2018a; Shin et al., 2020), and Jonkers et al. (2015) reported sediment carried by icebergs in Kongsfjorden was dominated by coarse silt. Although the characteristics of icebergs in Kongsfjorden may not be representative in the Antarctic setting, in the absence of direct observations of sediment load of Antarctic ice bergs, we have assumed similarity. Of all the transport pathways considered, we suggest ice-rafting is the most compelling mechanism to produce the sedimentary structures and physical properties we observe in core BS17-GC01 during both glacials and interglacials.

KOPRI 극지연구소

5.4. If IRD transport is consistent, source areas and erosion histories vary

In the previous section, we concluded that the dominant transport pathway of sediment to site BS17-GC01 under both interglacial and glacial conditions was as IRD. Here, we propose that the contrasting sedimentary signatures we observed on glacial/interglacial timescales is likely due variation of source areas and erosion histories, rather than changes in transport mechanism.

This is consistent with Kim et al. (2020a), who observed differing sedimentary characteristics between deglacial and interglacial periods, (including a coarse fraction; i.e., grains > 1mm) and glacial periods (only coarse silt to fine sand fraction). They inferred ice-rafting as the dominant mode of transport throughout, and attributed the sedimentary changes to differences of source regions. We infer the same process in this study.

We infer the source of the coarse silt with high MS values are most likely from the continent and/or re-worked shelf sediments. Sediments with high MS values are commonly found in diamicton facies on the Antarctic continental shelf (Hillenbrand et al., 2005, 2010; Christ et al., 2015). Observations of modern grounding line settings show glacigenic debris consisting of diamicton or clast-rich mud, with basal crevasses and a debris-rich layer up to 20 m-thick (Powell et al., 1996). Kim et al. (2018b) reported increased MS values during the

Neoglacial period under more glacial influence in West Antarctic inner shelf region. During glacial periods, these basal debris – probably with high MS values – are transported to the shelf break by advancing ice feeding debris-rich icebergs. In contrast, during deglacial to interglacial periods, icebergs are more often calved from ice shelves, which tends to leave the ice sheet basal debris on the shelf. This may be related to why under open ocean conditions >1mm IRD grains and low MS values are observed in the Antarctic continental shelf (e.g., Domack et al., 2001; Hillenbrand et al., 2005; McKay et al., 2008; Kim et al., 2018b).

The sedimentary source regions for core BS17-GC01 are most likely Bellingshausen Sea shelf region, and the changes in MS values with time likely to be corresponding to changes in source area. However, our understanding of controlling factors for MS values, and underlying geology of Antarctic continental shelves, including Bellingshausen Sea, is poor. Thus, the detailed source regions for the high MS glacial sediments should be investigated in the future. Although grains larger than coarse sand are variable in IRD in icebergs in Kongsfjorden, most sediments are composed of smaller than fine sand grains (Jonkers et al., 2015). However, lack of the coarse grains during glacial periods in also needs further investigation.

In general, only larger grains (i.e., >1 mm) are considered sedimentary evidence of IRD (Diekmann, 2007; Weber et al., 2012; Xiao et a., 2016; Kim et al., 2018a), although mud and very fine sand are the dominant sedimentary load of icebergs (Jonkers et al., 2015). Our study considers the possibility that ice rafting could also be a significant mechanism to transport only relatively fine-grained sediment to the deep ocean in some situations. If this is true, the absence of IRD does not always indicate an absence of icebergs.

6. Conclusions

We documented grain size frequency of grains >1 mm, along with bulk and size specific mass-normalized MS of a sediment core from the Bellingshausen Sea continental rise to 1) reconstructing variability of terrigenous input, 2) define the main sedimentary size fraction that drives MS value variation, and 3) interpret the sediment transport mechanisms since the last glacial period in response to ice sheet variation.

Bulk MS values, indicative of terrigenous material input, markedly increased during MIS 2 and 4 in the Bellingshausen Sea continental rise. The bulk MS values co-varied with mean grain size and particularly related to coarse silt fraction. Although the mass-normalized MS of fine and coarse silt fraction was high during MIS 2 and 4, mass-weighted calculation indicates that the coarse silt fraction is responsible for increased bulk MS values during MIS 2 and 4. Mass-normalized MS values of each fraction varied through time, indicating changes

in source region accompanying with transport mechanism changes rather than just coarse silt/fine fraction ratio changes. The high bulk MS values during glacial periods are ascribed to coarse silt-sized terrigenous material input as IRD. The contrasting sedimentary record between glacial and glacial times in the Bellingshausen Sea continental rise is thought to be associated with changing source area, rather than changes in transport mechanisms.

KOPRI
극지연구소

지난 마지막 빙하기 이후 남극 벨링스하우젠해 대륙대에서의 대자율 변동과 육성기원 물질 유입 기작에 관한 의의

김성한[a,b], 이민경[a], 신지영[c], 유규철[a], 이재일[a], 강명일[a], 문흥수[a], Joseph G. Prebble[d]

[a]Korea Polar Research Institute, [b]Department of Polar Sciences, University of Science and Technology (UST), [c]Peking University, [d]GNS Science

요약: 대자율은 남극 대륙주변부로 들어오는 육성기원 물질을 나타내는 프록시로 흔히 사용된다. 육성기원 물질의 유입의 빙하기-간빙기 규모 변동은 빙권, 대기권, 수권의 변화를 포함한 다양한 환경적 변화와 관련된다. 그러나 남극대륙주변부에서 퇴적물 코어의 대자율 값을 조절하는 정확한 환경적 요인과 퇴적 작용에 대해서는 아직 풀리지 않았다. 여기서 우리는 벨링스하우젠해 대륙대에서 획득된 BS17-GC01의 자세한 퇴적 물리학적 특성과 대자율 값을 제 4기 후기 동안 어떻게 퇴적 과정이 변했는지를 이해하기 위해 자세히 살펴보았다. 우리는 육성기원 물찔의 유입이 Marien Iotope Stage (MIS) 2와 4에서 간빙기인 홀로세와 MIS 3 시기 대비 현저하게 증가하는 것을 발견하였다. 벌크 대자율 값의 변동은 퇴적물의 입도 변화와 관련이 있었다. 입도에 따른 구간별로 대자율 값을 측정하였더니, <16 μm의 구간에서 가장 높은 대자율 값을 가지며, 16-63 μm 구간이 그 뒤를 이었다. 하지만, 조립한 실트질이 가장 우세한 입도 분포를 보이기 때문에 MIS 2와 4 동안 증가하는 대자율 값은 16-63 μm 구간에 입자에 의해서 조절되는 것으로 생각된다. 우리는 빙하기 구간에서 발견되는 높은 대자율 값을 가지는 이 조립한 실트가 빙하쇄설성퇴적물의 형태로 빙산에 의해서 벨링스하우젠해 인근의 대륙에서 부터 운반되어져 왔다고 제안하였다. 대조적으로, 흔히 빙하쇄설성 퇴적물로 간주되는 >1 mm 입자들은 MIS 1과 3 시기 동안에만 발견되었다. 우리는 이러한 빙하기-간빙기에 따른 빙하쇄설성퇴적물의 대조되는 양상이 벨링스하우젠해 코어에서 나타나는 것이 빙하기/간빙기 시기 동안 빙붕/빙상의 대륙붕에서의 침식 양상의 변화와 관련이 있는 것으로 결론지었다.

참고 문헌

Allen, C.S., Oakes-Fretwell, L., Anderson, J.B., Hodgson, A., 2010. A record of Holocene glacial and oceanographic variability in Neny Fjord, Antarctic Peninsula. The Holocene 20, 551-564.

Berkman, P.A., Forman, S.L., 1996. Pre-bomb radiocarbon and the reservoir correction for calcareous marine species int he Southern Ocean. Geophys. Res. Lett. 23, 363-366.

Brachfeld, S.A., Banerjee, S.K., 2000. Rock-magnetic carriers of century-scale susceptibility cycles in glacial- marine sediments from the Palmer Deep, Antarctic Peninsula. Earth Planet. Sci. Lett. 176, 443-445.

Brachfeld, S., Banerjee, S.K., Guyodo, Y., Acton, G.D., 2002. A 13,200 year history of century to millennial scale paleoenvironmental change magnetically recorded in the Palmer Deep, western Antarctic Peninsula. Earth Planet. Sci. Lett. 194, 311-326.

Brachfeld, S., Barletta, F., St-Onge, G., Darby, D., Ortiz, J.D., 2009. Impact of diagenesis on the environmental magnetic record from a Holocene sedimentary sequence from the Chukchi-Alaskan margin, Arctic Ocean. Glob. Planet. Change 68, 100-114.

Canfield, D.E., Berner, R.A., 1987. Dissolution and pyritization of magnetite in anoxic marine sediments. Geochim. Cosmochim. Ac. 51, 645-659.

Ceccarori, L., Frank, M., Frignani, M., Langone, L., Ravaioli, M., Mangini, A., 1998. Late Quaternary fluctuations of biogenic component fluxes on the continental slope of the Ross Sea, Antarctica. J. Mar. Syst. 17, 515- 525.

Christ, A.J., Talaia-Murray, M., Elking, N., Domack, E.W., Leventer, A., Lavoie, C., Brachfeld, S., Yoo, K.-C., Gilbert, R., Jeong, S.-M., Petrushak, S., Wellner, J., the LARISSA Group, 2015. Late Holocene glacial advance and ice shelf growth in Barilari Bay, Graham Land, west Antarctic Peninsula. Geol. Soc. Am. Bull. 127, 297-315.

Cook, A.J., Holland, P.R., Meredith, M.P., Murray, T., Luckman, A., Vaughan, D.G., 2016. Ocean forcing of glacier retreat in the western Antarctic Peninsula. Science 353, 283-286.

Diekmann, B., Kuhn, G., Rachold, V., Abelmann, A., Brathauer, U., Fütterer, D.K., Gersonde, R., Grobe, H., 2000. Terrigenous sediment supply in the Scotia Sea (Southern Ocean): response to Late Quaternary ice dynamics in Patagonia and on the Antarctic Peninsula. Palaeogeogr. Palaeoclimatol. Palaeoecol. 162, 357-387.

Diekmann, B., 2007. Sedimentary patterns in the late Quaternary Southern Ocean. Deep-Sea Res. II 54, 2350- 2366.

Domack, E.W., 1992. Modern carbon-14 ages and reservoir corrections for the Antarctic

KOPRI 극지연구소

Peninsula and Gerlache Strait area. Antarctic Journal of the United States 27, 63–64.

Domack, E.W., Jacobson, E.A., Shipp, S., Anderson, J.B., 1999. Late Pleistocene–Holocene retreat of the West Antarctic Ice–Sheet system in the Ross Sea: Part 2––sedimentologic and stratigraphic signature. GSA Bulletin 111, 1517–1536.

Domack, E., Leventer, A., Dunbar, R., Taylor, F., Brachfeld, S., Sjunneskog, C., ODP Leg 178 Scientific Party, 2001. Chronology of the Palmer Deep site, Antarctic Peninsula: a Holocene palaeoenvironmental reference for the circum–Antarctic. The Holocene 11, 1–9.

Fischer, H., Fundel, F., Ruth, U., Twarloh, B., Wegner, A., Udisti, R., Becagli, S., Castellano, E., Morganti, A., Severi, M., Wolff, E., Littot, G., Röthlisberger, R., Mulvaney, R., Hutterli, M.A., Kaufmann, P., Federer, U., Lambert,

F., Bigler, M., Hansson, M., Jonsell, U., De Angelis, M., Boutron, C., Siggaard–Andersen, M.–L., Steffensen, J.P., Barbante, C., Gaspari, V., Gabrielli, P., Wagenbach, D., 2007. Reconstruction of millennial changes in dust emission, transport and regional sea ice coverage using the deep EPICA ice cores from the Atlantic and Indian Ocean sector of Antarctica. Earth Planet. Sci. Lett. 260, 340–354.

Folk, R.L., Ward, W.C., 1957. Brazos River bar [Texas], a study in the significance of grain size parameters. J. Sediment. Res. 27(1), 3–26.

Garbe, J., Albrecht, T., Levermann, A., Donges, J.F., Winkelmann, R., 2020. The hysteresis of the Antarctic Ice Sheet. Nature 585, 538–544, doi:10.1038/s41586–020–2727–5.

Gersonde, R., Crosta, X., Abelmann, A., Armand, L., 2005. Sea–surface temperature and sea ice distribution of the Southern Ocean at the EPILOG Last Glacial Maximum––a circum–Antarctic view based on siliceous microfossil records. Quat. Sci. Rev. 24, 869–896.

Gordon, J.E., Harkness, D.D., 1992. Magnitude and geographic variation of the radiocarbon content in Antarctic marine life: implications for reservoir correction in radiocarbon dating. Quat. Sci. Rev. 11, 697–708.

Grimley, D.A., Arruda, N.K., 2007. Observations of magnetite dissolution in poorly drained soils. Soil Sci. 172, 968–982.

Harden, S.L., DeMaster, D.J., Nittrouer, C.A., 1992. Developing sediment geochronologies for high–latitude continental shelf deposits: A radiochemical approach. Mar. Geol. 130, 69–97.

Heaton, T.J., Köhler, P., Butzin, M., Bard, E., Reimer, R.W., Austin, W.E.N., Ramsey, C.B., Grootes, P.M., Hughen, K.A., Kromer, B., Reimer, P.J., Adkins, J., Burke, A., Cook, M.S., Olsen, J., Skinner, L., 2020. MARINE20 – The marine radiocarbon age calibration curve (0–55,000 cal BP). Radiocarbon 62, 779–820.

Hillenbrand, C.–D., Baesler, A., Grobe, H., 2005. The sedimentary record of the last

glaciation in the western Bellingshausen Sea (West Antarctica): Implications for the interpretation of diamictons in a polar–marine setting. Mar. Geol. 216, 191–204.

Hillenbrand, C.–D., Camerlenghi, A., Cowan, E.A., Hernández–Molina, F.J., Lucchi, R.G., Rebesco, M., Uenzelmann– Neben, G., 2008a. The present and past bottom–current flow regime around the sediment drifts on the continental rise west of the Antarctic Peninsula. Mar. Geol. 255, 55–63.

Hillenbrand, C.D., Crowhurst, S.J., Williams, M., Hodell, D.A., McCave, I.N., Ehrmann, W., Xuan, C., Piotrowski, A.M., Hernández–Molina, F.J., Graham, A.G.C., Grobe, H., Williams, T.J., Horrocks, J.R., Allen, C.S., Larter, R.D., 2021. New insights from multi–proxy data from the West Antarctic continental rise: implications for dating and interpreting late Quaternary paleoenvironmental records. Quat. Sci. Rev. 257, 106842.

Hillenbrand, C.–D., Kuhn, G., Frederichs, T., 2009. Record of a Mid–Pleistocene depositional anomaly in West Antarctic continental margin sediments: an indicator for ice–sheet collapse? Quat. Sci. Rev. 28, 1147– 1159.

Hillenbrand, C.–D., Larter, R.D., Dowdeswell, J.A., Ehrmann, W., Cofaigh, C.Ó., Benetti, S., Graham, A.G.C., Grobe, H., 2010. The sedimentary legacy of a palaeo–ice stream on the shelf of the southern Bellingshausen Sea: Clues to West Antarctic glacial history during the Late Quaternary. Quat. Sci. Rev. 29, 2741–2763.

Hillenbrand, C.–D., Moreton, S.G., Caburlotto, A., Pudsey, C.J., Lucchi, R.G., Smellie, J.L., Benetti, S., Grobe, H., Hunt, J.B., Larter, R.D., 2008b. Volcanic time–markers for Marine Isotopic Stages 6 and 5 in Southern Ocean sediments and Antarctic ice cores: implications for tephra correlations between palaeoclimatic records. Quat. Sci. Rev. 27, 518–540.

Jacobs, S.S., 1991. On the nature and significance of the Antarctic slope front. Mar. Chem. 35, 9–24.

Jonkers, L., Barker, S., Hall, I.R., Prins, M.A., 2015. Correcting for the influence of ice–rafted detritus on grain size– based paleocurrent speed estimates. Paleoceanography 30, 1347–1357.

Kim, S., Lee, J.I., McKay, R.M., Yoo, K.C., Bak, Y.S., Lee, M.K., Roh, Y.H., Yoon, H.I., Moon, H.S., Hyun, C.U., 2020b. Late Pleistocene paleoceanographic changes in the Ross Sea – Glacial–interglacial variations in paleoproductivity, nutrient utilization, and deep–water formation. Quat. Sci. Rev. 239, 106356.

Kim, S., Yoo, K.C., Lee, J.I., Khim, B.K., Bak, Y.S., Lee, M.K., Lee, J., Domack, E.W., Christ, A.J., Yoon, H.I., 2018b. Holocene paleoceanography of Bigo Bay, west Antarctic Peninsula: Connections between surface water productivity and nutrient utilization and its implication for surface–deep water mass exchange. Quat. Sci. Rev.

192, 59-70.

Kim, S., Yoo, K.C., Lee, J.I., Lee, M.K., Kim, K., Yoon, H.I., 2018a. Relationship between magnetic susceptibility and sediment grain size since the last glacial period in the Southern Ocean off the northern Antarctic Peninsula - Linkages between the cryosphere and atmospheric circulation. Palaeogeogr. Palaeoclimatol. Palaeoecol. 505, 359-370.

Kim, S., Yoo, K.C., Lee, J.I., Roh, Y.H., Bak, Y.S., Um, I.K., Lee, M.K., Yoon, H.I., 2020a. Paleoceanographic changes in the Southern Ocean off Elephant Island since the last glacial period: Links between surface water productivity, nutrient utilization, bottom water currents, and ice-rafted debris. Quat. Sci. Rev. 249, 106563.

Kissel, C., Laj, C., Clemens, S., Solheid, P., 2003. Magnetic signature of environmental changes in the last 1.2 Myr at ODP Site 1146, South China Sea. Mar. Geol. 201, 119-132.

Kostka, J.E., Nealson, K.H., 1995. Dissolution and reduction of magnetite by bacteria. Environ. Sci. Technol. 29, 2535-2540.

Lambert, F., Bigler, M., Steffensen, J.P., Hutterli, M., Fischer, H., 2011. The calcium-dust relationship in high- resolution data from Dome C, Antarctica. Clim. Past 7, 1113-1137.

Lee, J.I., Yoon, H.I., Yoo, K.-C., Lim, H.S., Lee, Y.I., Kim, D., Bak, Y.S., Itaki, T., 2012. Late Quaternary glacial- interglacial variations in sediment supply in the southern Drake Passage. Quat. Res. 78, 119-129.

Leventer, A., Domack, E., Barkoukis, A., McAndrews, B., Murray, J., 2002. Laminations from the Palmer Deep: A diatom-based interpretation. Paleoceanography 17, 8002.

Leventer, A., Domack, E.W., Ishman, S.E., Brachfeld, S., McClennen, C.E., Manley, P., 2015. Productivity cycles of 200-300 years in the Antarctic Peninsula region: Understanding linkages among the sun, atmosphere, oceans, sea ice, and biota. GSA Bulletin 108, 1626-1644.

Licht, K.J., Jennings, A.E., Andrews, J.T., Williams, K.M., 1996. Chronology of late Wisconsin ice retreat from the western Ross Sea, Antarctica. Geology 24, 223-226.

Lucchi, R.G., Rebesco, M., Camerlenghi, A., Busetti, M., Tomadin, L., Villa, G., Persico, D., Morigi, C., Bonci, M.C., Giorgetti, G., 2002. Mid-late Pleistocene glacimarine sedimentary processes of a high-latitude, deep-sea sediment drift (Antarctic Peninsula Pacific margin). Mar. Geol. 189, 343-370.

Lucchi, R.G., Rebesco, M., 2007. Glacial contourites on the Antarctic Peninsula margin: insight for palaeoenvironmental and palaeoclimatic conditions. In: Viana A.R., Rebesco, M., (Eds.), Economic and Palaeoceanographic Significance of Contourite Deposits. Geological Society, Special Publications:

KOPRI 극지연구소

London, 276, pp. 111–127.

McKay, R.M., Dunbar, G.B., Naish, T.R., Barrett, P.J., Carter, L., Harper, M., 2008. Retreat history of the Ross Sea Ice Sheet (Shelf) since the Last Glacial Maximum from deep–basin sediment cores around Ross Island. Palaeogeogr. Palaeoclimatol. Palaeoecol. 260, 245–261.

Nielsen, S.H.H., Hodell, D.A., Kamenov, G., Guilderson, T., Perfit, M.R., 2007. Origin and significance of ice–rafted detritus in the Atlantic sector of the Southern Ocean. Geochem. Geophy. Geosy. 8, 1–23.

Orsi, A.H., Whitworth, T., Nowlini Jr., W. D., 1995. On the meridional extent and fronts of the Antarctic circumpolar current. Deep–Sea Res. I 42(5), 641–673.

Paillard, D., Laeyrie, L., Yiou, P., 1996. Macintosh Program Performs Time–series Analysis. EOS Transactions American Geiophysical Union 77, 379.

Paolo, F.S., Fricker, H.A., Padman, L., 2015. Volume loss from Antarctic ice shelves is accelerating. Science 348, 327–331.

Powell, R.D., Dawber, M., McInnes, J.N., 1996. Observations of the grounding–line area at a floating glacier terminus. Annals of Glaciology 22, 217–223.

Pudsey, C.J., 2000. Sedimentation on the continental rise west of the Antarctic Peninsula over the last three glacial cycles. Mar. Geol. 167, 313–338.

Pudsey, C.J., Camerlenghi, A., 1998. Glacial–interglacial deposition on a sediment drift on the Pacific margin of the Antarctic Peninsula. Antarct. Sci. 10, 286–308.

Pugh, R.S., McCave, I.N., Hillenbrand, C.–D., Kuhn, G., 2009. Circum–Antarctic age modeling of quaternary marine cores under the Antarctic circumpolar current: ice core dust–magnetic correlation. Earth Planet. Sci. Lett. 284, 113–123.

Reilly, B.T., Natter, C., Brachfeld, S.A., 2016. Holocene glacial activity in Barilari Bay, west Antarctic Peninsula, tracked by magnetic mineral assemblages: Linking ice, ocean, and atmosphere. Geochem. Geophy. Geosyst. 17, 4553–4565.

Robinson, S.G., 1986. The late Pleistocene palaeoclimatic record of North Atlantic deep–sea sediments revealed by mineral–magnetic measurements. Phys. Earth Planet. Inter. 42, 22–47.

Scheuer, C., Gohl, K., Larter, R.D., Rebesco, M., Udintsev, G., 2006. Variability in Cenozoic sedimentation along the continental rise of the Bellingshausen Sea, West Antarctica. Mar. Geol. 227, 279–298.

Shin, J.Y., Kim, S., Zhao, X., Yoo, K.C., Yu, Y., Lee, J.I., Lee, M.K., Yoon, H.I., 2020. Particle–size dependent magnetic properties of Scotia Sea sediments since the Last Glacial Maximum: Glacial ice–sheet discharge controlling magnetic proxies. Palaeogeogr. Palaeoclimatol. Palaeoecol. 557, 109906.

Sprenk, D., Weber, M.E., Kuhn, G., Rosén, P., Frank, M., Molina–Kescher, M., Liebetrau,

V., Röhling, H.G., 2013. Southern Ocean bioproductivity during the last glacial cycle-new detection method and decadal-scale insight from the Scotia Sea. Geol. Soc. London. Spec. Publ. 381, 245-261.

Stoner, J.S., Andrews, J.T., 1999. The North Atlantic as a Quaternary magnetic archive. In: Maher, B., Thompson, R., (Eds.), Quaternary Climates, Environments and Magnetism. Cambridge University Press, Cambridge, pp. 49-80.

Stuiver, M., Reimer, P.J., 1993. Extended 14C database and revised CALIB radiocarbon calibration program. Radiocarbon 35, 215-230.

Thompson, A.F., Speer, K.G., Chretien, M.S., 2020. Genesis of the Antarctic Slope Current in West Antarctica. Geophys. Res. Lett. 47, e2020GL087802.

Weber, M.E., Kuhn, G., Sprenk, D., Rolf, C., Ohlwein, C., Ricken, W., 2012. Dust transport from Patagonia to Antarctica-a new stratigraphic approach from the Scotia Sea and its implications for the last glacial cycle. Quat. Sci. Rev. 36, 177-188.

Whitworth, T., Orsi, A.H., Kim, S.J., Nowlin,W.D., Locarnini, R.A., 1998. Water masses and mixing near the Antarctic slope front. Ocean Ice Atmos. Interact. A. T. Antarct. Cont. Margin 75, 1-27.

Xiao, W., Frederichs, T., Gersonde, R., Kuhn, G., Esper, O., Zhang, X., 2016. Constraining the dating of late quaternary marine sediment records from the Scotia Sea (Southern Ocean). Quat. Geochronol. 31, 97- 118.

Yoon, H.I., Yoo, K.C., Bak, Y.S., Lee, Y.I., Lee, J.I., 2009. Core-based reconstruction of paleoenvironmental conditions int he southern Drake Passage (West Antarctica) over the last 150 ka. Geo-Mar. Lett. 29, 309- 320.

KOPRI 극지연구소

Table 1. Radiocarbon dates from core BS17-GC01. AIOM: acid insoluble organic matter

Depth (cm)	Analyzed material	Lab code	^{14}C age (yr BP)	Corrected and calibrated age (cal. yr BP) with age range	δ^{13}C (‰)
0	AIOM	Beta-508,160	11,140 ± 40	0	−25.2
12	AIOM	Beta-508,161	16,000 ± 50	5589 (5410–5778)	−24.5
24	AIOM	Beta-508,162	17,840 ± 60	7538 (7375–7700)	−24.8
[a]34	AIOM	Beta-510,060	19,370 ± 60	9275 (9063–9459)	−27

KOPRI 극지연구소

Table 2. Tie points obtained by graphical correlations of BS17-GC01 MS values and EDML ice core nssCa^{2+} record (Fischer et al., 2007).

BS17-GC01 MS to EDML ice core nssCa^{2+}	
BS17-GC01 (cm)	EDML (ka)
35	17.6
47	23.6
67	29.5
107	38.45
141	53.6
186	62.8

KOPRI
극지연구소

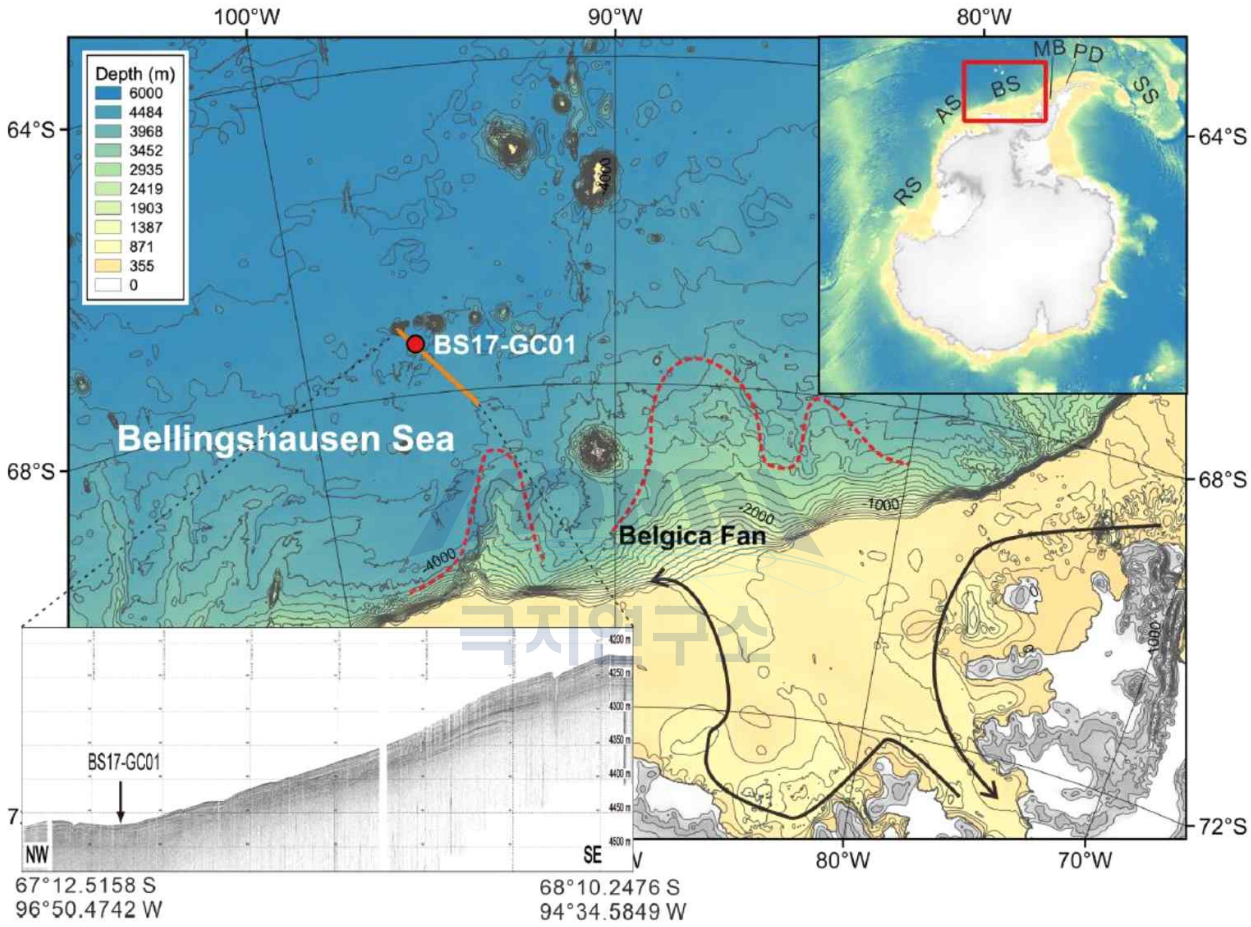


Figure 1. Study area and location of core BS17-GC01 . Orange line indicates sub-bottom profile survey line. Black arrows indicate surface flow modified from Thompson et al. (2020). Red dashed lines indicate sediment depocenter, modified from Scheuer et al. (2006). RS: Ross Sea, As: Amundsen Sea, BS: Bellingshausen Sea, MB: Marguerite Bay, PD: Palmer Deep, SS: and Scotia Sea.

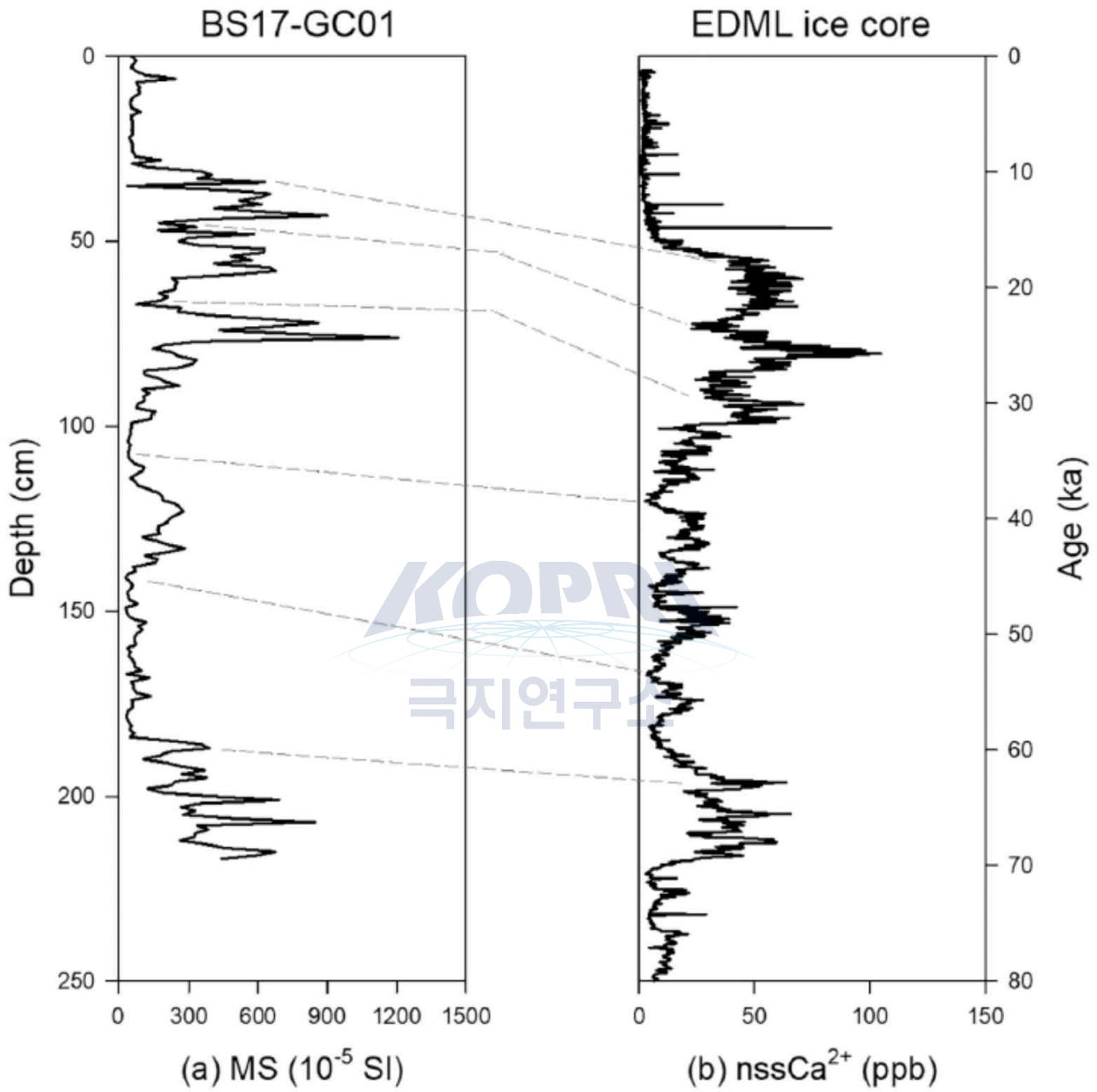


Figure 2. Graphical correlations between (a) the bulk MS of BS17-GC01 and (b) EDML ice core dust record (Fischer et al., 2007). Six tie points were applied (Table 2).

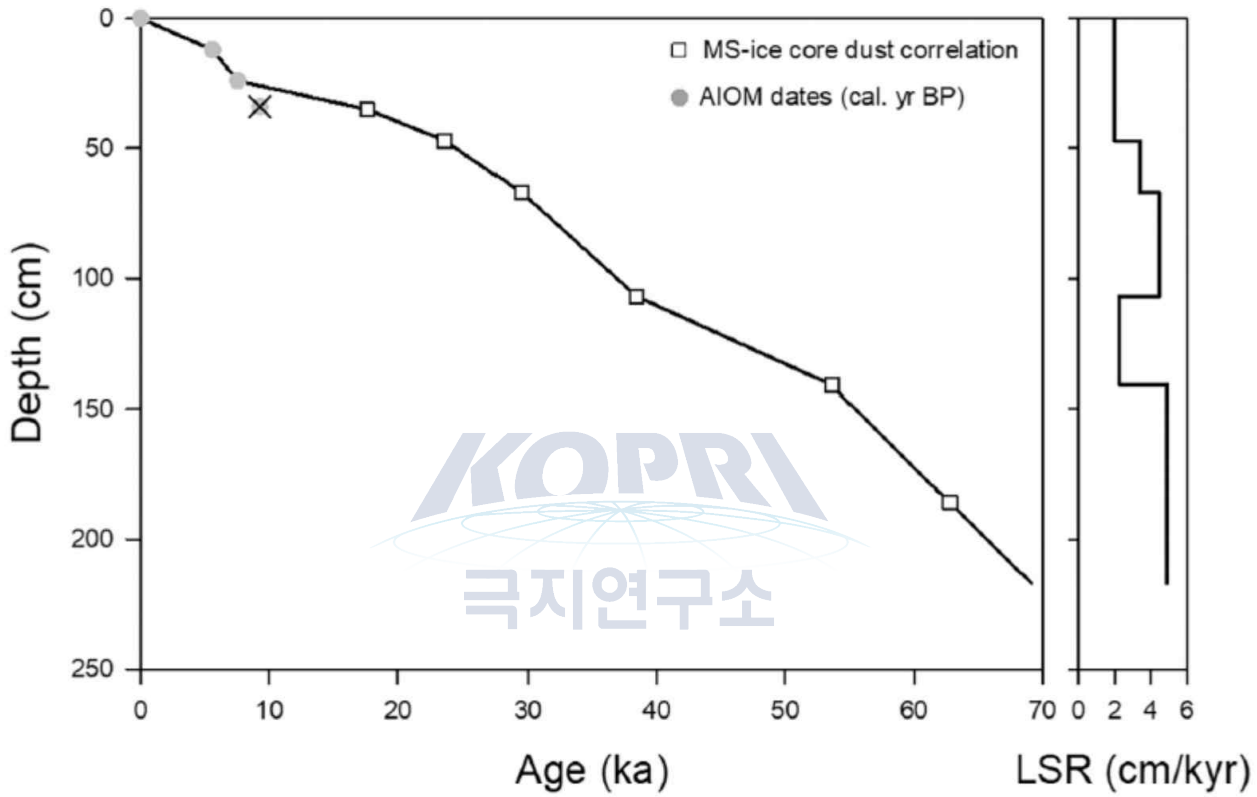


Figure 3. An age-depth model for BS17-GC01 including radiocarbon chronology (gray circles) and tie points based on MS of BS17-GC01 and EDML ice core dust record (Fischer et al., 2007, open squares) with linear sedimentation rate. X mark indicates an age point excluded in the age model.

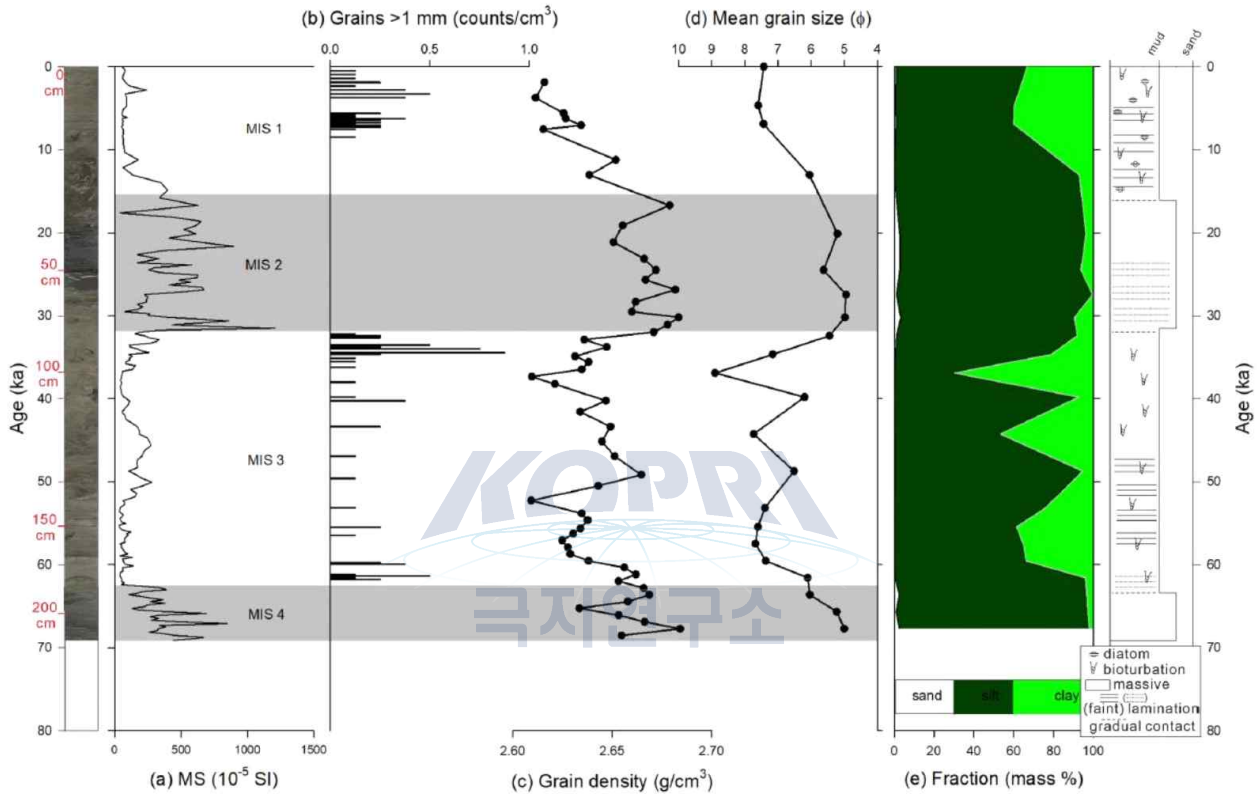


Figure 4. Downcore profiles of (a) the bulk MS, (b) grains >1 mm, (c) grain density, (d) mean grain size, and (e) fractional proportion of sand, silt, and clay with core photo (left) and lithologic column (right) of BS17-GC01. High MS intervals are marked as gray boxes. Photo image and lithologic column are adjusted to age-scale according to age tie points. Red tics and numbers indicate core depths.

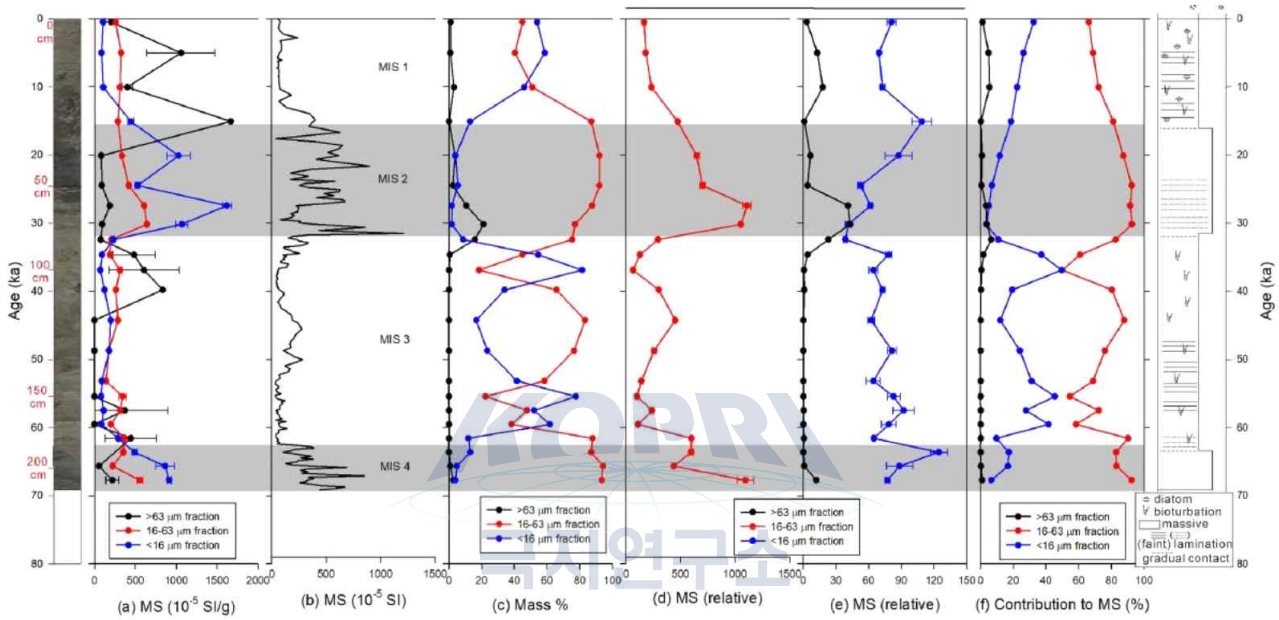


Figure 5. Downcore profiles of (a) mass-normalized MS of sand (black), coarse silt (red), and fine fraction (blue), (b) the bulk MS, (c) fractional mass weight percentages, (d) mass-weighted MS of coarse silt (red), (e) mass-weighted MS of sand (black) and fine fraction (blue), (f) fractional contribution to the bulk MS values of BS17-GC01 with core photo (left) and lithologic column (right) of BS17-GC01. High bulk MS intervals are marked as gray boxes. Photo image and lithologic column are adjusted to age-scale according to age tie points.

제 26 장

Petrology and quartz grain microtextures of marine shoreline sands from the Punta Arenas area, southernmost Chile and King George Island, Antarctica and implications for their depositional history[20)]

HyeJeong Kim[1], A Chim Lee[1], Yong Il Lee[1], Min Kyung Lee[2]

[1]School of Earth and Environmental Sciences, Seoul National University, Seoul 08826, Korea, [2]Division of Glacial Environment Research, Korea Polar Research Institute, Incheon 21990, Korea

ABSTRACT: Modal composition and quartz microtextures were analyzed to investigate the provenance tectonic setting and transport mechanism in shoreline sediments from the Punta Arenas (PA) area in the southernmost part of Chile and King George Island (KGI), West Antarctica. In the sediments from both areas, volcanic rock fragments were the predominant framework grain, and a significant amount of quartz was also found in the PA area. The provenance tectonic setting of the PA area was a recycled orogen, and that of the KGI area was a magmatic arc. Quartz grains exhibited subangular shape, medium to high relief, and mainly mechanical microtextures, which were induced by high shear stress (>80%) and high-energy percussion (<20%). The shoreline sands of the two areas did not differ significantly in the distribution of frequency of microtextures of glacial and aqueous origins, so it is interpreted that the sand sediments from both areas had similar glacial and aqueous transport histories. The percussion microstructures, which occurred in less than 20% of the sands in both areas, may be due to the relatively short residence time in the energetic aqueous conditions. The presence of weathered quartz grains fractured by glaciers indicates that they had undergone significant weathering in the preceeding warm periods. The presence of high count of pre-weathered microtextures suggests that many grains travel into glacial stream carrying the pre-weathering microfeatures, which can be recognized in the sedimentary record.

20) 이 연구 결과는 다음의 논문으로 출판되었음: Kim, H. et al. (2023). "Petrology and quartz grain microtextures of marine shoreline sands from the Punta Arenas area, southernmost Chile and King George Island, Antarctica and implications for their depositional history." Episodes 46: 47-62.

1. Introduction

Clastic sediments contain information on the tectonic, climatic, and magmatic history of continents. Among the factors controlling petrological characteristics of clastic sediments, the tectonic setting and lithology of the source rocks are the most important controls affecting the composition of sand sediments (i.e., Johnsson and Basu, 1993). Petrographic analysis is a standard method for studying provenance (e.g., Dickinson and Suczek, 1979; Ingersoll and Suczek, 1979). Surface microtextures on quartz grains provide an insight into the sedimentary history of clastic sediments. The subject of sand grain surface microtextures to sedimentology using scanning electron microscopy (SEM) was first introduced by Krinsley and Doornkamp (1973) and since then many following researchers applied this technique to interpret the specific transport agents and/or depositional environments (Margolis and Krinsley, 1974; Mahaney, 2002; Vos et al., 2014 amongst others). In particular, the analysis of quartz grain surface textures is a powerful tool in distinguishing between sand grains originating from a glacial depositional environment and sand grains affected by subaqueous sedimentary processes (Strand et al., 2003). Two processes dominate in the glacial environments: they are crushing (fracturing) and abrasion (grinding or attrition) (Iverson, 1990; Iverson et al., 1996; Mahaney, 1995, 2002; Hart, 2006; Rose and Hart, 2008; Benn and Evans, 2010; Cowan et al., 2014; Vos et al., 2014). Large conchoidal fractures, subparallel linear fractures, arcuate steps, crescentic gouges, angularity, and high relief are particularly diagnostic glacial microtextures (Margolis and Krinsley, 1974; Williams and Morgan, 1993; Mahaney and Kalm, 1995). Transport via saltation and traction in subaqueous environments produces quartz surface textures resulting from grain to grain collision of which V-shaped and irregular impact pits are diagnostic (Manker and Ponder, 1978; Georgiev and Stoffers, 1980; Linde and Mycielska-Dowgallo, 1980; Manickam and Barbaroux, 1987; Williams and Thomas, 1989; Mahaney, 2002; Vos et al., 2014). However, the degree to which quartz grains in tills are fractured and abraded is in large part due to ice thickness, distance of transport, and/ or ice dynamics (Mahaney et al., 1988; Mahaney, 1995; Molén, 2014). Increasing ice thickness and transport distance may result in increasing extent of subparallel fracture surfaces (both linear and conchoidal forms), particle relief and edge sharpness, arc-shaped steps, crescentic gouges, and deep grooves (Mahaney, 1995). In this study, petrographic and SEM analyses of quartz grains from marine shoreline sands in the Punta Arenas (PA) area in the southernmost part of Chile and in the Barton and Weaver peninsulas, King George Island (KGI), West Antarctica were carried out to examine variations in sand composition and surface texture of quartz grains. While sediment composition of the Barton and Weaver peninsulas, KGI has been studied by Choi et al. (2003) and Lee et al. (2019), that of the PA area has not been studied

before. The tectonic setting of the southern part of the Southern Andes is different from that of the middle–northern parts of the Southern Andes and is characterized by three orogenic and magmatic cycles: (i) Late Cretaceous compressional deformation, in association with the closure of the backarc basin, (ii) Paleogene collision of the Farallón–Aluk seismic ocean ridge, and (iii) Miocene subduction of the Chile seismic ridge beneath South America (Ghiglione et al., 2016). Using the composition of sediment derived from the southern part of the Southern Andes, we investigated the tectonic setting of the provenance. And in this study, we first report the results of the microtextures on quartz grain surfaces in shoreline sediments of the two areas to (1) characterize the frequency and variations of microtextures, (2) interpret the major depositional environment and transport mechanism of these sediments, and (3) detect any preservation of the previous history and the modification in the current littoral environments. If microtextural arrangements of different generations are observed, a grain history of successive sedimentary cycles can be established by elucidating their cross–cutting relations. Studies of grain modification by glaciation and weathering are scarce in Antarctica and the southern tip of South America, with the exception of one study done on the lacustrine sediments in the Fildes Peninsula on King George Island (Hernández et al., 2018). Thus, this study adds to that inventory.

KOPRI
극지연구소

2. Study Areas

Thiry–seven coastal–zone samples were collected from the western shoreline of the Strait of Magellan in the PA area, southernmost Chile (Fig. 1A) and the shorelines of the Barton and Weaver Peninsulas, KGI, West Antarctica (Fig. 2). These shoreline sediments are generally coarse–grained, especially those in KGI, West Antarctica, and are generally composed of gravel–sized clasts. Shorelines with sandy sediments have a limited distribution between coastal gravels or in areas protected by coastal gravels. The fact that the shoreline sediments of KGI are mostly composed of gravels indicates that the studied coastal zones are under strong wave energy influenced by strong winds (Choi et al., 2003). Most of the shoreline sediments selected for this study were transported from glacial areas by glaciers flowing from the inland ice sheet. It is deduced that following deglaciation, a strong parallel uplift of the mean sea level was produced with initially transgressive effects. Isostatic rebound that probably occurred rather late compared to postglacial transgression, is superimposed with very complex and articulate phenomena. After first experiencing the transgressive effects of the strong parallel rise in the mean sea level after deglaciation, these sediments may have experienced the effects of isostatic rebound which probably occurred later compared to the post–glacial transgression.

2.1. The Punta Arenas Area, S Chile

The studied PA area shore sites (Fig. 1C) are located along the eastern coast of the Brunswick Peninsula, southernmost Chile, facing the Strait of Magellan between 53°01'−53°34'S and 70°49'− 70°57'W. The Brunswick Peninsula is located in the east of the southern part of the Patagonian Andes, which represents the southern Andes south of latitude around 45칸. The southern Patagonian Andes are characterized by thick sequences of Mesozoic marine sediments and extensive areas of Tertiary 'back−arc' basaltic rocks (Rabassa and Clapperton, 1990). The Southern Andes record the closing of a back−arc oceanic basin, and almost no volcanic arc activity (Ramos, 1999). The southern Patagonian Andes is overlain by the Patagonian Ice Sheet, extending north−south for 360 km and the area between 51−55° and 68−73° was occupied by five major piedmont outlet glaciers of the Patagonian Ice Sheet (Fig. 1B) (Darvill et al., 2017). The PA area was occupied by the Magellan glacial lobe and the maximum thickness of the Patagonian Ice Sheet from which the Magellan lobe drained during the Last Glacial Maximum was more than 1,000 m (Hulton et al., 2002). Maximum transport distance to the PA area from the hypothesized ice divide is estimated to be around 100 km (cf., Darvill et al., 2017). Darvill et al. (2017) presented various glacial landform assemblages in the southernmost Patagonian Plain formed by five glacial lobes, indicative of typical behavior of active temperate glaciers displaying warm−based ice actively re−advancing during overall retreat of the ice margin. The Magellan lobe advanced during the last glacial cycle, and during the Last Glacial Maximum the Magellan lobe readvanced fast with possible surge−like ice flow (Darvill et al., 2017). The Magellan lobe may have been undergoing rapid retreat by at least 14−15 ka. The geology of the Brunswick Peninsula is characterized by thick sedimentary successions with a general SE strike, exposing the different units with decreasing age towards the NE (Otero et al., 2012) (Fig. 1B). Narrow Paleozoic metamorphic rocks are distributed along the southwestern margin of the peninsula, followed to the northeast by a belt of Upper Jurassic quartz−porphyric effusive rocks and a belt of Upper Jurassic to Lower Cretaceous marine sedimentary rocks in that order (Katz, 1963). Then, Lower to Upper Cretaceous marine sedimentary rocks are distributed in most of the peninsula and Paleogene marine to continental sedimentary rocks are distributed in the northern part of the peninsula including Punta Arenas and its vicinity.

The southernmost region of South America has been undergoing a post−glacial uplift since the beginning of the Holocene. About 50 km south of Punta Arenas, the Puerto del Hambre area was located more than 100 km behind the limit of the last glaciation. The glacier here melted as early as 15.8 ka and the area underwent a post−glacial isostatic uplift during and after deglaciation since about 13 ka, slightly earlier than the regional post−glacial uplift (Porter et al., 1984). The southernmost region of South America has experienced

maximum submergence by the middle Holocene (~5 ka) and the coastlines along the Strait of Magellan emerged recently (Porter et al., 1984). Winds in the PA area are strong (7 m s−1 on average) and almost unidirectional. Winds blow from the west 60% of the time, and from the northwest and southwest for another 20% of the time (Medeiros and Kjerfve, 1988). Strong winds, reaching speeds of 27 m s−1, are common during the winter and spring when cold Antarctic air masses push northward (ENAP, 1974 cited in Medeiros and Kjerfve, 1988).

2.2. King George Island, W Antarctica

KGI is the largest island in the South Shetland Islands, off the northernmost tip of the Antarctic Peninsula (Fig. 2A) and is located in the center of the archipelago. The South Shetland Islands belong to part of magmatic arcs (Scotia Arc), which is closely linked to the formation of the Antarctic Peninsula (Smellie et al., 1984). KGI has an area of 1,150 km2 and the Collins Ice Cap (Fig. 2B) centered on the island during Last Glacial Maximum. The Marian Cove Glacier, one of outlet glaciers of the Collins Ice Cap, traversed the Barton and Weaver peninsulas. Both peninsulas are located at the southwestern end of KGI (Fig. 2B) and are separated by a small tributary fjord, Marian Cove, which has a length of ca. 3.5 km, a width of ca. 1.5 km, and a maximum depth of 120 m. The Weaver Peninsula is located to the northwest of Marian Cove and the Barton Peninsula is located to the southeast of the cove (Fig. 2C). The outlet of the cove is Maxwell Bay, the main fjord formed during the last glacial maximum (Simms et al., 2011). Flow to Maxwell Bay via Marian Cove was mainly by a fast−flowing, strongly convergent outlet glacier, the Marian Cove Glacier. The maximum transport distance of the Marian Cove Glacier to the current coastlines of the two peninsulas from the divide of the Collins Ice Cap was ~6 km. At present the maximum ice thickness of the Collins Ice Cap on King George Island is 357 m just north of the divide (Simões et al., 1999). The ice−free areas of the Barton and Weaver peninsulas have a gentle topography with a central plain. The altitude and size of the ice−free area of the Weaver Peninsula are lower and smaller, respectively, than those of the Barton Peninsula. The morphology of the ice−free areas of both peninsulas is predominantly characterized by a glacial landscape, with steep cliffs along the coast and a rather smooth, hilly interior. During the Last Glacial Maximum, KGI was covered by a large ice cap and the Barton and Weaver peninsulas became progressively ice free since the Last Glacial Maximum (Chang et al., 2003). Based on cosmogenic 36Cl age−dating, Seong et al. (2009) reported that the exposure age of the highest areas on the Barton Peninsula was 15.5 ± 2.5 ka, which represents the timing of the beginning of deglaciation, consistent with the timing of deglaciation in Maxwell Bay at around 17 ka (Yoon et al., 1997). Maxwell Bay gradually became open ocean conditions since 9.1 ka by retreat of persistent ice cover, possibly an ice shelf (Simms et al., 2011). The deglaciation

of Marian Cove occurred after 1300 14C yr B.P. (Yoon et al., 1997). KGI is undergoing an isostatic uplift after the removal of the ice sheet (Barsh and Mäusbacher, 1986). The current coastline of KGI was submerged during the Holocene and the modern rates of uplift for KGI are ca. 3 mm y−1 (Bentley et al., 2005). The Barton Peninsula has the ice−free area 5 times larger than the Weaver Peninsula. The geology of the ice−free areas in the Weaver and Barton peninsulas is somewhat different (Fig. 2C). The Barton and Weaver peninsulas are composed of three lithologies: volcaniclastics (the Sejong Formation), calc−alkaline volcanic rocks, and the intrusive rocks (Lee et al., 2001). The Sejong Formation forms the lowest stratigraphic unit in both peninsulas and is of Eocene in age. The Sejong Formation is composed of subaerial volcaniclastic sediments such as agglomerate, tuff breccia, and lapilli tuff (Yoo et al., 2001). In the Barton Peninsula it is distributed in the southwestern and southern parts forming cliffs close to the coastline, whereas in the Weaver Peninsula the Sejong Formation is distributed in most of the ice−free area. Mafic to intermediate volcanic rocks of Eocene in age (Jwa et al., 1992; Willan and Armstrong, 2002) overlie the Sejong Formation and are most widely distributed in the Barton Peninsula, but in the Weaver Peninsula they are narrowly present only in the southwestern and northern parts. Most of these lava flows are basaltic andesite containing plagioclase phenocrysts or plagioclase and pyroxene phenocrysts and are associated with some massive andesites. Two fairly thick lapilli tuffs are intercalated in the lava flows in the eastern part of the Barton Peninsula. In the central northwestern part of the Barton Peninsula, there are very small mass of fine−crystalline diorite and relatively large stock of medium−crystalline granodiorite. The whole−rock 40Ar/39Ar age of the diorite is 48.4 ± 0.5 Ma (Early Eocene; Kim et al., 2000) and the K−Ar ages of two biotite crystals isolated from the granodiorite are 41.9 ± 0.9 Ma and 41.2 ± 0.9 Ma (Lee et al., 1996). The volcanic rocks surrounding the granodiorite in the Barton Peninsula were mostly altered extensively by hydrothermal fluids and in some parts they were altered multiple times. This hydrothermal alteration is interpreted as a consequence of shallow hydrothermal processes associated with the intrusion of granodiorite (Hwang and Lee, 1998). The hydrothermal alteration zone in direct contact with the granodiorite is dominated by chloritization of amphiboles and albitization, but sericitization of feldspars occurs as distance increases, and kaolinitization of sericite becomes more dominant at a further distance (Hur et al., 2001). KGI has a cold oceanic climate. Current climatic data for the study area recorded at the King Sejong Station for 9 years (1988−1996) show an average annual temperature of −1.8캜, relative humidity of 89%, precipitation of 437.6 mm, and wind velocity of 7.9 m s−1, with major directions of northwest and southwest (Lee et al., 1997).

3. Methods and Materials

Marine shoreline samples were collected along the western coast of the Strait of Magellan near Punta Arenas, S Chile (Fig. 1C) and on the coasts of the Weaver and Barton peninsulas, KGI (Fig. 2C). A total of 37 sand samples (5 samples from the PA area, 26 samples from the Barton Peninsula, and 6 samples from the Weaver Peninsula) were observed using a polarizing microscope after making thin sections. 32 sand samples from the Barton and Weaver peninsulas analyzed in a study by Lee et al. (2019) were also used in this study. Each sample was examined for modal composition using quartz, feldspar, rock fragment, and accessory grains by counting at least 200 points. A total of 10 representative samples (five samples from each sample collection area) were selected for detailed SEM microtextural analysis of quartz grain surfaces. Bulk sand samples were washed with tap water and more than 30 quartz grains from each sample were handpicked under the binocular microscope. Selected quartz grains were immersed into non-diluted H2O2 for 15 minutes in order to remove organic matter following the method of Lewis and Armstrong (1994). Then, the grains were immersed into 5 wt.% Calgon for 12 hours to remove clay and adhering particles. Afterwards, they were washed with distilled water and dried in a 50℃ oven. Carbon coating was done after spreading quartz grains on a slide glass. Using a SEM (JEOL JSM-5400), 14-23 quartz grains per sample were randomly observed. The atlas of Mahaney (2002) was used to identify microtextures and we generally adopted a classification scheme of microtextures following the criteria proposed by Vos et al. (2014). Microtextures were classified into three groups: mechanical, chemical, and mixed mechanical and chemical origin. The frequency of the occurrence of single microtextures was then calculated by counting the number of times a microtexture was identified on the grains in each sample. Histograms of microtextural frequency were used for initial examination of the raw data following methods outlined in Mahaney (2002), Immonen (2014), and Vos et al. (2014).

4. Results

4.1. Sand Composition

The components of sand grains were categorized into nine types: monocrystalline quartz, polycrystalline quartz, single feldspar, feldspar aggregate, plutonic rock fragment, metamorphic rock fragment, fresh and altered volcanic rock fragment, and accessory minerals (Fig. 3). The modal composition of the studied sand grains is listed in Table 1. The average quartz-feldspar-rock fragment ratio (QFR) of sand samples from the PA area was Q36.7F7.4R55.9 and belonged to the litharenite clan with one sample of the feldspathic

litharenite clan (Fig. 4A). The most dominant framework grain was rock fragment, and among rock fragments, volcanic rock fragment was predominant, especially altered volcanic rock fragment (the average ratio of altered volcanic rock fragment to fresh volcanic rock fragment is 6), followed by minor subequal amount of plutonic and metamorphic rock fragments. The second dominant framework grain was quartz, and polycrystalline quartz grains were more abundant than monocrystalline quartz grains except for sample PA2506. Feldspar constituted average 7.4% of framework grains. The studied shoreline sand samples plotted in recycled orogen field in a tectonic environment-discriminating QtFL diagram of Dickinson (1985) (Fig. 4B). The most dominant sand grain from shorelines of the Weaver and Barton peninsulas, KGI was volcanic rock fragment, constituting 85% and 93% of framework grains, respectively. Like volcanic rock fragments in sands of the PA area, altered volcanic rock fragment dominated over fresh volcanic rock fragment with an average ratio of 3. The next dominant framework grain was plutonic rock fragment, constituting 21% and 22% of the framework grains of the Weaver and Barton peninsulas, respectively. Quartz and feldspar occurred very rarely. The average QFR ratio of the shoreline sands of the Weaver Peninsula was Q4.4F11.0R84.6 and that of the Barton Peninsula is Q2.0F5.2R92.9 (Fig. 4A). The observed framework composition of sands from this study was almost consistent with that of Lee et al. (2019). In a tectonic environment-discriminating QtFL diagram of Dickinson (1985), the studied shoreline sand samples of the two peninsulas plotted in magmatic- arc field (Fig. 4B).

KOPRI 극지연구소

4.2. Quartz Microtextures

The size of the observed quartz grains was mostly coarse- to very coarse-grained, with an average grain size ranging between 746 μm (PA2506) and 1278 μm (28-1). Quartz grains were fresh and had little modification, but a considerable amount of fractured preweathered grains were also observed. The results of SEM microtextural analysis are presented in full in Table 2. Microtextural percentages reported in this study referred to the number of grains exhibiting a particular microtexture. Examples of the variety of microtextures at each sampling area are displayed in Figs. 5 and 6. Data on microtextural frequency are displayed in frequency occurrence plots (Fig. 7) and the average frequencies of microtextures of the two sample suites are shown in Fig. 8.

4.3. Mechanical Microtextures

The quartz grains studied under SEM exhibited textures that originated predominantly from mechanical actions. Within the population of shoreline sands of both areas, the

dominant shapes were subangular (av. 92.5% and 82.7% in the PA and KGI areas, respectively; Figs. 5 and 6) with minor angular outlines. Angular quartz grains were slightly more abundant in the KGI samples (av. 16.0%) than in the PA samples (av. 3.5%). Quartz grains with rounded outline are observed very rarely except one sample in the KGI area (04-03). Conchoidal fractures, especially medium fractures (av. 66.0% and 53% in the PA and KGI areas, respectively) followed by large fractures, were the most frequently observed mechanical microfracture in shoreline quartz grains in both areas. Similarly, arcuate and straight steps associated with conchoidal fractures were observed relatively in high frequency (Fig. 7). Straight steps were more abundantly found in the KGI sands (av. 62.7%) than in the PA area sands (av. 41.2%). The frequency of parallel striations (av. 38% and range = 28-67% in the PA area and av. 55% and range = 40-60% in the KGI area), graded arcs (crescentic gouges; av. 31%, range = 20-39% in the PA area and av. 39%, range = 7-73% in the KGI area), and straight/curved grooves and scratches (av. 40%, range = 13-57% in the PA area and av. 52%, range = 33-80% in the KGI area) (Figs. 5 and 6) were also commonly observed microtextures in sands of both areas. In the PA area samples, V-shaped percussion cracks occurred on 80% of the grains (av. 29%, range = 21-73%), and crescentic percussion cracks (av. 21%, range = 7-40%) occurred on all grains. Similarly, V-shaped percussion cracks (av. 25%, range = 7-67%) and crescentic percussion cracks (av. 31%, range = 13-53%) were observed in the KGI samples. About 40 percent of the observed grains showed some edge abrasion (rounding) (Fig. 5). Also, edge rounding textures occurred on some grains in the PA sands (av. 38%, range = 26-67%), but more abundantly in the KGI samples (av. 51%, range = 40-73%).

4.4. Mechanical and/or Chemical Microtextures

The microtextures such as elonglated depression, chattermarks, and adhering particles are grouped as of mechanical/chemical origin (Table 2). The frequency of distribution of mechanical/chemical features between the two shoreline areas is not generally different from each other, except that chattermarks are more sparsely distributed in the PA area samples (av. 2.7%) than in the KGI sands (13.3%). All sand grains are of medium to high relief (Fig. 7; av. 45.8% and 46.1%, respectively, in the PA area and av. 30.7% and 61.3%, respectively, in the KGI area). Adhering particles are common (>50%) in the sand grain surfaces of the two areas (Fig. 7).

4.5. Chemical Microtextures

Chemical features identified are solution pits, solution crevasses, and rare silica

globules (Fig. 7). These chemical microtexures are formed by chemical dissolution and precipitation, however, their frequency is relatively very low (Fig. 7). In addition to these fresh microtextures, some grains contain preweathered textures (Figs. 5 and 6).

5. Discussion

5.1. Provenance

The sands of the PA area had a higher proportion of quartz grains and a higher proportion of quartz to feldspar than those of the Weaver and Barton peninsulas, KGI (Fig. 3A). Together with the abundant polycrystalline quartz and volcanic rock fragment content, this suggests that the former sands were derived primarily from Paleozoic metamorphic and Jurassic volcanic rocks of the Southern Andes. On the other hand, volcanic rocks were the main source rocks of the studied shoreline sand samples of the Weaver and Barton peninsulas, KGI. Plutonic rock was the second important source rock. The results of tectonic setting analysis for source terrains in the two regions were consistent with the current geologic setting of each area. Based on the sand modal composition and geochemical data, Lee et al. (2019) interpreted that the source rocks and provenance tectonic setting of the Barton and Weaver peninsulas, KGI as volcanic and plutonic rocks formed in a magmatic arc setting. The results of this study support this interpretation. However, since the sand composition of shorelines of the Barton and Weaver peninsulas differs from the proportion of distributed bedrock exposed in the ice-free areas of the two peninsulas, the sediment may have been sourced from bedrock distributed in the glacial drainage basin now covered by the Marian Cove Glacier. The quartz grains studied for microtexture in the PA area came from the Southern Andes and in situ Mesozoic sedimentary and metamorphic rocks, whereas quartz grains in the KGI shorelines was mainly from Eocene granodiorite exposures in the ice-free areas of the Barton Peninsula and plutonic rocks beneath the ice cover of the Barton and Weaver peninsulas.

5.2. Transport Processes

Generally, the surface textures of detrital quartz grains present in the sediments are formed due to the processes involving transportation and deposition. The shoreline dataset displays a variety of transport-induced microtextures. Grains have experienced both glacial transport under sustained shear stress and subaqueous transport with saltation and traction. These two transport styles produce different microtextures. However, the large number of grain characteristics in Figure 7 makes it difficult to compare the sample suites, but the two

sample suites from KGI and the PA areas show broadly similar results. The microtextures were sorted into one of three groups following the proposal of Sweet and Brannan (2016). The three genetic groupings are (1) sustained-shear- stress microtextures, (2) percussion microtextures, and (3) polygenetic microtextures based on inferred fracturing processes, reflecting transport styles. Sustained-shear-stress microtextures form through a grain stylus at grain-to-grain contact along existing shear planes in viscous media, such as ice or debris flows and include straight/curved grooves and scratches, crescentic gouges, and parallel striation (Figs. 5B, C, D and 6B, E, F) (Mahaney, 2002; Sweet and Brannan, 2016). As the sustained-shear-stress microtextures have been commonly reported from grains entrained in glacial environments (Mahaney, 2002), the observed sustained-shear-stress microtextures are interpreted as a product of subglacial grinding. Sand grains of the KGI area showed higher frequency of parallel striations than those in the PA area (Fig. 8), which may reflect shorter distance of transport and faster rate of deposition in the former than in the latter (e.g., Damiani et al., 2006). The triangular faceted form (Fig. 5D) resulted from bedrock detachment or from grain-to-bedrock stress (Krinsley and Doornkamp, 1973; Mahaney, 2002; Rose and Hart, 2008). The most recognizable glacial features and microtextures caused by sustained-shear-stress fracturing are angular outlines, high reliefs, conchoidal fractures, subparallel linear fractures, steps and crescentic gouges, all of which were formed as a result of subglacial till deformation underneath glaciers at least ca. 500 m in thickness (Mahaney et al., 1996). The moderate frequency of these fracture and abrasion microtextures in the studied shoreline sands suggests that the thickness of the glaciers that produced these microtextures was thicker than or close to the threshold thickness. This interpretation is supported by the maximum thickness of the Patagonian Ice Sheet (>1,000 km; Hulton et al., 2002) from which the Magellan glacial lobe drained to the PA area, and the present maximum ice thickness of the Collins Ice Cap (357 m just north of the divide; Simões et al., 1999) from which the Marian Cove Glacier drained to the Weaver and Barton peninsulas, KGI. Percussion microtextures include randomly oriented V-shaped percussion cracks, crescentic percussion cracks, and edge rounding, resulting from grain-on-grain impact in low viscous media such as water or air during transport via saltation and traction (Margolis, 1968; Krinsley and Donahue, 1968; Campbell and Thompson, 1991; Mahaney and Kalm, 2000; Mahaney, 2002; Mahaney and Dohm, 2011; Vos et al., 2014). In this study,

The percussion microtextures are interpreted to reflect saltation transport in the high-energy littoral zones rather than eolian transport due to coarse grain size. They were likely produced in the current shoreline environments, mostly after post-glacial uplift. In littoral zones, the breaking of waves and the oscillatory movement of waves are the dominant sediment transport mechanism. The studied shoreline samples exhibit largely fresh surfaces, while dissolution features are sparsely present. About 38-51% of the observed grains show

some edge abrasion (rounding) and about 25–29% of grains show V-shaped percussion cracks (Figs. 5B, F and 6B, C), both as a result of water transport. We interpret that V-shaped percussion cracks developed atop sustained-shear-stress microtextures that formed during earlier glacial transport. V-shaped percussion cracks are not necessarily formed by marine processes, but are very likely meltwater induced, and could even be formed within or below basal ice. There may be some water transport underneath glaciers and the high frequency of fracture and abrasion microtextures suggestive of stick-slip processes (Barcilon and MacAyeal, 1993) indicates that these microtextures may have developed under high cryostatic pressure during grain- tograin, grain-to-clast, and grain-to-bed interactions in the subglacial environments (Tison et al., 1993; Mahaney, 1995). The wet-based glaciers of the Patagonian Ice Sheet during the last glacial period (Darvill et al., 2017) would involve large volume of subglacial water allowing grain-to-grain contact during transport, which suggests that some percussion microtextures in the sands of the PA area may have formed during subglacial transport. Polygenetic microtextures include conchoidal fractures, arcuate steps, straight steps, and flat cleavage surfaces (fracture face) and have been observed in a variety of depositional systems under different styles and transport media (e.g., Mahaney, 2002). Considering possible transport processes for the studied shoreline sand suites, the polygenetic microtextures are interpreted to reflect glacial stress (Mahaney and Kalm, 2000; Mahaney, 2002) and aqueous saltation (Mahaney and Kalm, 2000; Mahaney and Dohm, 2011; Armstrong-Altrin and Natalhy-Pineda, 2014). Conchoidal fractures on littoral grains are more uniform in size and generally smaller than 10 μm (Krinsley and Donahue, 1968). Conchoidal fractures >10 μm in size were observed more frequently on the studied sands and thus between the two glacial stress origin is more likely. Conchoidal fractures along with arcuate and straight steps are produced due to the pressure generated due to a massive impact (Margolis and Krinsley, 1974; Mahaney, 2002; Immonen et al., 2014; Vos et al., 2014). According to Higgs (1979) and Mahaney (2002), the size and frequency of conchoidal fractures are a reflection of the vibrational energy released during grain-to-grain collisions. Typical glacially crushed grains display large-scale fractures and abrasion (Molén, 2014). Between the curved conchoidal fractures, meandering ridges (Fig. 6B) traversing across the grain surface in a form of intersection line were observed (i.e., Krinsley and Donahue, 1968). The impact producing the radial fracture pattern (Fig. 5F) could result from stickslip movement in a glacier or from water transport in a high-energy stream (Mahaney, 2002). The relation between stick slip and V-shaped percussion cracks could be built up a bit by relating friction from stick slip releasing water to lead to grain-grain collisions. Upturned plates formed by shattering of quartz grains during high collision (Fig. 5E) were also formed in the glacial environments (Krinsley et al., 1976). These three groups of microtextures are plotted on pie diagrams for semiquantitative comparison of the studied samples (Fig. 9). On

KOPRI 극지연구소

these pie diagrams, the two sample suites are not different from each other with a ratio between percussion and sustained−shear−stress microtextures of ~1.3. Percussion microtextures must reflect aqueous saltation and traction from the littoral zone plus any subglacial fluvial transport. A ratio of 1.3 between sustained shear microtextures and percussion microtextures in both sample suites still indicates that there is a difference between the two microtextures, reflecting the more abundance of glacially modified microtextures than subaqueously modified microtextures. This observation suggests that microtextures formed during the sustained shearing processes can leave their traces on sand grains for a longer time and thus can be recognized in the sedimentary record.

5.3. Preweathered Grains

Quartz grains in glacial sediments may also bear microfeatures resulting from weathering that occurred prior to glacial entrainment. Several preweathered grains show some weathered surfaces in juxtaposition to fresh glacial crushing microtextures (Figs. 5E, F, and 6B). Chemical textures may well develop on grain surfaces long exposed prior to their release, while these textures may be absent or poorly developed on adjacent surfaces where attachment to the source rock excluded or limited weathering. Due to overprinted fresh glacially crushed microtextures, it is difficult to judge that both sample suites show nonuniform weathering of the grains' surfaces, but considerable percent of the observed sand grains showed characteristic of grains released from their source rock by chemical processes (i.e., Krinsley and Doornkamp, 1973). The fractured preweathered quartz grains (Fig. 10) accounted for an average of 27% (range = 7−47%) of all observed grains in the PA area, while they were observed with an average of 59% (range = 33−100%) of all examined grains in the KGI area. The higher occurrence frequency of fractured preweathered quartz grains in the shoreline sands of KGI than in the shoreline sands of the PA area is thought to be due to the shorter transport distance compared to the latter. The presence of preweathered quartz grains indicates that sand grains were subjected to significant weathering before being released from bedrock and entrained by glaciers, perhaps in the preceding interglacial. In contrast to the weathered grains of the PA area, which have a multicyclic origin, the presence of preweathered quartz grains observed on KGI suggests that the Antarctic Peninsula region experienced a fairly warm interglacial paleoclimatic conditions. Alternatively, the history of warm weathering can be traced further back to the pre−Quaternary. Hernández et al. (2018), who studied the lacustrine sediments of Profound Lake, located on the Fildes Peninsula on the southwestern tip of King George Island, posited a much longer period of weathering back into the Paleogene. Later subaqueous percussion transport in the glacial meltwater and littoral zone modified glacially induced microtextures resulting from grain−tograin impact processes.

6. Conclusions

The average quartz−feldspar−rock fragment ratio (QFR) of sand samples from the PA area and the Weaver and Barton peninsulas, KGI was Q36.7F7.44R55.9 and Q2.4F6.3R91.3, respectively, and belonged to the litharenite clan. The dominant framework grain in both areas was (altered) volcanic rock fragment. The provenance tectonic setting of the sand samples studied at the PA area and at KGI was a recycled orogen and a magmatic arc, respectively. Quartz grains studied under SEM exhibited textures primarily resulting from mechanical actions. Within the shoreline sand populations of both areas, quartz grains were characterized by a dominant subangular shape and medium to high relief. Among the mechanical microtextures, polygenetic microtextures (av. 57−59%), including conchoidal fractures, arcuate steps, straight steps, and flat cleavage surfaces, were dominant over sustained− shear−stress (av. 23−24%; straight/curved grooves and scratches, crescentic gouges, and parallel striation) and percussion (av. 18%; V−shaped percussion cracks, crescentic percussion cracks, and edge rounding) microtextures. The sustained−shear−stress microtextures were generated by subglacial grinding and the percussion microtextures were generated by saltation transport in present−day high−energetic littoral zones. Considering the relatively large fracture characteristics, the polygenetic microtextures are interpreted as likely reflecting glacial stress. There was little difference in the frequency of microtextures of glacial and subaqueous origins in the studied shoreline sands of the two studied areas with different ice thickness and transport distances. The results of this study suggest that in both areas, possibly ice thickness and transport distance exceeded the thresholds for the development of the glacial microtextures (~500 m thick and ~4 km long; Mahaney, 1995). Glacial signals have now survived overprinting in marine shoreline environments, probably due to their relatively short residence time in high−energy littoral environments. The presence of weathered quartz grains fractured by glaciers indicates that the sand grains were subjected to significant weathering before being released from bedrock and entrained by glaciers, possibly in the preceeding interglacials and/or older warm periods. This study provided a case study to interpret grain history by observing the cross−cutting relations of microtextures to grain modifications generated during successive sedimentary cycles in the northern Antarctic and southern sub−Antarctic zones. Preweathered grains were released from bedrock and were modified by glacial stress while transported in the glacial stream, and during this process, they were modified through grain−grain collisions in meltwater or in the basal ice. After that, the grains may also have undergone modification in the littoral zone by grain−grain collisions.

KOPRI 극지연구소

칠레 푼타 아레나스와 남극 킹조지 섬 해빈 모래의 광물 조성 및 석영 입자의 미세구조를 통한 퇴적사 연구

김혜정[1], 이아침[1], 이용일[1], 이민경[2]

[1]서울대학교 지구환경과학부, [2]한국해양과학기술원 부설 극지연구소

요약: 칠레 최남단의 푼타 아레나스와 서남극의 킹조지 섬의 해안 퇴적물의 광물 조성과 석영입자의 미세구조를 분석하여 기원지의 지구조 환경과 이동 기작을 조사하였다. 이 두 지역의 퇴적물은 주로 화산암편으로 구성되어 있고 푼타 아레나스 퇴적물의 경우 석영도 상당량 포함되어 있다. 푼타 아레나스 지역과 킹조지섬 퇴적물 기원지의 지구조 환경은 재순환된 조산대와 마그마 기원 화산호이다. 석영 입자들은 아원마상 형태이며, 중간에서 높은 정도의 양각을 나타내고, 높은 전단응력 (>80%) 과 고에너지 타격 (<20%) 에 의해 기계적으로 생성된 미세구조를 가지고 있다. 두 지역의 해안선에서 채취한 모래들은 빙하 혹은 물 기원의 미세구조의 빈도에 있어서는 큰 차이를 보이지 않으며, 따라서 두 지역의 모래 모두 빙하와 물에 의해 해안선까지 이동된 점은 유사하다고 볼 수 있다. 타격에 의한 미세구조는 두 지역의 모래에서 20% 미만으로 나타나는데, 에너지가 강한 물에 의해 이동되었던 시간이 상대적으로 짧았기 때문인 것으로 생각된다. 빙하에 의해 쪼개지기 전 입자들이 이미 풍화를 거쳤는데 이는 이 입자들이 빙하에 운반되기 전 앞선 따뜻한 시기 동안 상당한 풍화를 받았음을 지시한다. 이미 풍화를 받은 미세 구조들이 많이 관찰되는 것은 풍화에 의해 이미 미세구조가 생성된 입자들이 빙하의 흐름에 의해 운반되었음을 시사하며, 이는 퇴적물 기록에서 확인할 수 있다.

참고 문헌

Armstrong-Altrin, J.S., and Natalhy-Pineda, O., 2014. Microtextures of detrital sand grains from the Tecolutla, Nautla, and Veracruz beaches, western Gulf of Mexico: implications for depositional environment and paleoclimate. Arabian Journal of Geosciences, v. 7, pp. 4321-4333.

Armstrong-Altrin, J.S., and Natalhy-Pineda, O., 2014, Microtextures of detrital sand grains from the Tecolutla, Nautla, and Veracruz beaches, western Gulf of Mexico: implications for depositional environment and paleoclimate. Arabian Journal of Geosciences, v. 7, pp. 4321-4333.

Barcilon, V., and MacAyeal, D.R., 1993, Steady flow of a viscous ice stream across a no slip/free transition at the bed. Journal of Glaciology, v. 39, pp. 167-185.

Barsh, D., and Mäusbacher, R., 1986, New data on the relief development of the South Shetland Islands, Antarctica. Interdisciplinary Science Reviews, v. 11, pp. 211-219.

Benn, D.I., and Evans, D.J.A., 2010, Glaciers and Glaciation. Hodder Education, London, 802 p.

Bentley, M.J., Hodgson, D.A., Smith, J.A. and Cox, N.J., 2005, Relative sea level curves for the South Shetland Islands and Marguerite Bay, Antarctic Peninsula. Quatenary Science Reviews, v. 24, pp. 1203-1216.

Campbell, S., and Thompson, I.C., 1991, The palaeoenvironmental history of Late Pleistocene deposits at Moel Tryfan, North Wales: evidence from Scanning Electron Microscopy (SEM). Proceedings of the Geologists' Association, v. 102, pp. 123-134.

Chang, S.-K., Lee, J.I., Choi, M.Y., and Hur, S.D., 2003, Geology around the King Sejong Station, King George Island off the Antarctic Peninsula. Journal of the Geological Society of Korea, v. 39, pp. 271-286 (in Korean with English abstract).

Choi, T.J., Lee, Y.I., and Yoon, H.I., 2003, Characteristics of beach sands, King George Island, West Antarctica. Journal of the Geological Society of Korea, v. 39, pp. 391-402 (in Korean).

Cowan, E.A., Chistoffersen, P., Powell, R.D., and Talarico, F.M., 2014, Dynamics of the late Plio- Pleistocene West Antarctic Ice Sheet documented in subglacial diamictites, AND-1B drill core. Global and Planetary Change, v. 119, pp. 56-70.

Damiani, D., Giorgetti, G., and Turbanti, I.M., 2006, Clay mineral fluctuations and surface textural analysis of quartz grains in Pliocene-Quaternary marine sediments from Wilkes Land continental rise (East-Antarctica): paleoenvironmental significance. Marine Geology, v. 226, pp. 281-295.

Darvill, C.M., Stokes, C.R., Bentley, M.J., Evans, D.J.A., and Lovell, H., 2017, Dynamics of

KOPRI 극지연구소

former ice lobes of the southern Patagonian Ice Sheet based on a glacial landsystems approach. Journal of Quaternary Science, v. 32, pp. 857−876.

Dickinson, W.R., 1985, Interpreting provenance relations from detrital modes of sandstones. In: Zuffa, G.G. (Ed.), Provenance of Arenites. D. Reidel, Boston, pp. 333−361.

Dickinson, W.R., and Suczek, C.A., 1979, Plate tectonics and sandstone composition. American Association of Petroleum Geologists Bulletin, v. 63, pp. 2164−2182.

Folk, R.L., 1974, Petrology of Sedimentary Rocks. Hemphill Publishing Company, Texas, 182 p.

Georgiev, V.M., and Stoffers, P., 1980, Surface textures of quartz grains from Late Pleistocene to Holocene sediments of the Persian Gulf/Gulf of Oman − An application of the scanning electron microscope. Marine Geology, v. 36, pp. 85−96.

Ghiglione, M.C., Ramos, V.A., Cuitiño, J., and Barberón, V., 2016, Growth of the Southern Patagonian Andes (46−53oS) and their relation to subduction processes. In: Folguera, A., Naipauer, M., Sagripanti, L., Ghiglione, M.C., Orts, D.L, and Giambiagi, L. (Eds.), Growth of the Southern Andes. Springer Earth System Sciences, pp. 201−240.

Hart, J.K., 2006, Athabasca Glacier, Canada − a field example of subglacial ice and till erosion? Earth Surface Processes and Landforms, v. 31, pp. 65−80.

Higgs, R., 1979, Quartz−grain surface features of Mesozoic−Cenozoic sands from the Labrador and western Greenland continental margins. Journal of Sedimentary Petrology, v. 49, pp. 599−610.

Hernández, A.C., Bastias, J., Matus, D. and Mahaney, W.C., 2018, Provenance, transport and diagenesis of sediment in polar areas: a case study in Profound Lake, King George Island, Antarctica. Polar Research, 37, 1490619.

Hulton, N.R.J., Purves, R.S., McCulloch, R.D., Sugden, D.E., and Bentley, M.J., 2002, The Last Glacial Maximum and deglaciation in southern South America. Quaternary Science Reviews, v. 21, pp. 233−241.

Hur, S.D., Lee, J.I., Hwang, J., and Choe, M.Y., 2001, K−Ar age and geochemistry of hydrothermal alteration in the Barton Peninsula, King George Island, Antarctica. Ocean and Polar Research, v. 23, pp. 11−21.

Hwang, J., and Lee, J.I., 1998, Hydrothermal alteration and mineralization in the granodioritic stock of the Barton Peninsula, King George Island, Antarctica. Economic and Environmental Geology, v. 31, pp. 171−183.

Immonen, N., Strand, K., Huusko, A., and Lunkka, J.P., 2014, Imprint of late Pleistocene continental processes visible in ice−rafted grains from the central Arctic Ocean. Quaternary Science Reviews, v. 92, pp. 133−139.

Ingersoll, R.V., and Suczek, C.A., 1979, Petrology and provenance of Neogene sand from Nicobar and Bengal fans. DSDP sites 211 and 218. Journal of Sedimentary Petrology,

KOPRI 극지연구소

v. 49, pp. 1217−1228.

Iverson, N.R., 1990, Laboratory simulations of glacial abrasion: comparison with theory. Journal of Glaciology, v. 36, pp. 304−314.

Iverson, N.R., Hooyer, T.S., and Hooke, R.LeB., 1996, A laboratory study of sediment deformation: stress heterogeneity and grain−size evolution. Annals of Glaciology, v. 22, pp. 167−175.

Johnsson, M.J., and Basu, A. (Eds.), 1993, Processes Controlling the Composition of Clastic Sediments. Geological Society of America, Special Paper 284, 342 p.

Jwa, Y.−J., Park, B.−K., and Kim, Y., 1992, Geochronology and geochemistry of the igneous rocks from Barton and Weaver peninsulas, King George Island: A review. In: Yoshida, Y., Kaminuma, K., and Shiraishi, K., (Eds.), Recent Progress in Antarctic Earth Science. Terra Scientific Publishing Company, Tokyo, pp. 439−442.

Katz, H.R., 1963, Revision of Cretaceous stratigraphy in Patagonian cordillera of Ultima Esperanza, Magallanes Province, Chile. American Association of Petroleum Geologists Bulletin, v. 47, pp. 506−524.

Kim, H., Lee, J.I., Chose, M.Y., Cho, M., Zheng, X., Sang, H., and Qiu, J., 2000, Geochronologic evidence for early cretaceous volcanic activity on Barton Peninsula, King George Island, Antarctica. Polar Research, v. 19, pp. 251−260.

Krinsley, D.H., and Donahue, J., 1968, Environmental interpretation of sand grain surface textures by electron microscopy. Geological Society of America Bulletin, v. 79, pp. 743−748.

Krinsley, D.H., and Doornkamp, J.C., 1973, Atlas of Sand Grain Surface Textures. Cambridge University Press, Cambridge, 256 p.

Krinsley, D.H., Friend, P.F., and Klimentidis, R., 1976, Eolian transport textures on the surfaces of sand grains of Early Triassic age. Geological Society of America Bulletin, v. 87, pp. 130−132.

Lee, B.Y., Won Y., and Oh. S.N., 1997, Meteorological characteristics at King Sejong Station, Antarctica (1988 −1996). Korea Ocean Research and Development Institute, Ansan, Report BSPE 97604−00−1020−7, pp. 571−599.

Lee, J.I., Hur, S.D., Yoo, C.M., Yeo, J.P., Kim, H., Hwang, J., Choe, M.Y., Nam, S.H., Kim, Y., Park, B.−K., Zheng, X., and López−Martínez, J., 2001, Explanatory text of the geological map of Barton and Weaver Peninsulas, King George Island, Antarctica (1:10,000). Korea Ocean Research and Development Institute, Ansan, 28 p.

Lee, J.I., Hwang, J., Kim, H., Kang, C.Y., Lee, M.J., and Nagao, K., 1996, Subvolcanic zoned granitic pluton in the Barton and Weaver peninsulas, King George Island, Antarctica. Proceedings National Institute of Polar Research Symposium on Antarctic Geoscience, 9, pp. 76−90.

KOPRI 극지연구소

Lee, Y.I., Choi, T., and Lim, H.S., 2019, Petrological and geochemical compositions of beach sands of the Barton and Weaver peninsulas of King George Island, West Antarctica: implications for provenance and depositional history. Episodes, v. 42, pp. 149－164.

Lewis, C.A., and Armstong, G.A., 1994, An evaluation of different methods of preparation of quartz grains for study of their surface features by scanning electron microscopy. Acta Microscopica, v. 3, pp. 99－105.

Linde, K., and Mycielska－Dowgallo, E., 1980, Some experimentally produced microtextures on grain surfaces of quartz sand. Geografiska Annaler, v. 62A, pp. 171－184.

Mahaney, W.C., 1995, Pleistocene and Holocene glacier thickness, transport histories and dynamics inferred from SEM microtextures on quartz particles. Boreas, v. 24, pp. 293－304.

Mahaney, W.C., 2002, Atlas of Sand Grain Surface Textures and Applications. Oxford University Press, Oxford, U.K., 237 p.

Mahaney, W.C., and Dohm, J.M., 2011, The 2011 Japanese 9.0 magnitude earthquake: test of a kinetic energy wave model using coastal configuration and offshore gradient of Earth and beyond. Sedimentary Geology, v. 239, pp. 80－86.

Mahaney, W.C., and Kalm, V., 1995, Scanning electron microscopy of Pleistocene tills in Estonia. Boreas, v. 24, pp. 13－29.

Mahaney, W.C., and Kalm, V., 2000, Comparative SEM study of oriented till blocks, glacial grains and Devonian sands in Estonia and Latvia. Boreas, v. 29, pp. 35－51.

Mahaney, W.C., Claridge, G., and Campbell, I., 1996, Microtextures on quartz grains in tills from Antarctica. Palaeogeography, Palaeoclimatology, Palaeoecology, v. 121, pp. 89－103.

Mahaney, W.C., Vortisch, W., and Julig, P., 1988, Relative differences between glacially crushed quartz transported by mountain and continental ice－some examples from North America and East Africa. American Journal of Science, v. 288, pp. 810－826.

Manickam, S., and Barbaroux, L., 1987, Variations in the surface texture of suspended quartz grains in the Loire river: An SEM study. Sedimentology, v. 34, pp. 495－510.

Manker, J.P., and Ponder, R.D., 1978, Quartz grain surface features from fluvial environments of northeastern Georgia. Journal of Sedimentary Petrology, v. 48, pp. 1227－1232.

Margolis, S., 1968, Electron microscopy of chemical solution and mechanical abrasion features on quartz sand grains. Sedimentary Geology, v. 2, pp. 243－256.

Margolis, S., Krinsley, D., 1974, Process of formation and environmental occurrence of microfeatures on detrital quartz grains. American Journal of Science, v. 274, pp. 449－464.

Medeiros, C., and Kjerfve, B., 1988, Tidal characteristics of the Strait of Magellan. Continental Shelf Research, v. 8, pp. 947－960.

KOPRI 극지연구소

Molén, M.O., 2014, A simple method to classify diamicts by scanning electron microscope from surface microtextures. Sedimentology, v. 61, pp. 2020−2041.

Otero, R.A., Torres, T., Le Roux, J.P., Hervé, F., Fanning, C.M.,; Yury−Y衰ez, R.E., and Rubilar−Rogers, D.A., 2012, Late Eocene age proposal for the Loreto Formation (Brunswick Peninsula, southernmost Chile), based on fossil cartilaginous fishes, paleobotany and radiometric evidence. Andean Geology, v. 39, pp. 180−200.

Porter, S.C., Stuiver, M., and Heusser, C.J., 1984, Holocene sea−level changes along the Strait of Magallan and Beagle Channel, southernmost South America. Quaternary Research, v. 22, pp. 59−67.

Rabassa, J., and Clapperton, C.M., 1990, Quaternary glaciations of the southern Andes. Quaternary Science Reviews, v. 9, pp. 153−174.

Ramos, V.A., 1999, Plate tectonic setting of the Andean Cordillera. Episodes, v. 22, pp. 183−190. Rose, K.C., and Hart, J.K., 2008, Subglacial comminution in the deforming bed: Inferences from SEM analysis. Sedimentary Geology, v. 203, pp. 87−97.

Seong, Y.B., Owen, L.A., Lim, H.S., Yoon, H.I., Kim, Y., Lee, Y.I., and Caffee, M.W., 2009, Rate of late Quaternary ice−cap thinning on King George Island, South Shetland Islands, West Antarctica defined by cosmogenic 36Cl surface exposure dating. Boreas, v. 38, pp. 207−213.

Simms, A.R., Milliken, K.T., Anderson, J.B., and Wellner, J.S., 2011, The marine record of deglaciation of the South Shetland Islands, Antarctica since the Last Glacial Maximum. Quaternary Science Reviews, v. 30, pp. 1583−1601.

Simões, J.C., Bremer, U.F., Aquino, F.E., and Ferron, F.A., 1999, Morphology and variations of glacial drainage basins in the King George Island ice field, Antarctica. Annals of Glaciology, v. 29, pp. 220−224.

Smalley, I.J., 1966, The properties of glacial loess and the formation of loess deposits. Journal of Sedimentary Petrology, v. 36, pp. 669−676.

Smellie, J.L., Pankhurst, R.J., Thomson, M.R.A., and Davies, R.E.S., 1984, The geology of the South Shetland Islands: VI. Stratigraphy, Geochemistry and Evolution. British Antarctic Survey, Science Report 87, 85 p.

Strand, K., Passchier, S., and Näsi, J., 2003, Implications of quartz grain microtextures for onset Eocene/Oligocene glaciation in Prydz Bay, ODP Site 1166, Antarctica. Palaeogeography, Palaeoclimatology, Palaeoecology, v. 198, pp. 101−111.

Sweet, D.E., and Brannan, D.K., 2016, Proportion of glacially to fluvially induced quartz grain microtextures along the Chitina River, SE Alaska, U.S.A. Journal of Sedimentary Research, v. 86, pp. 749−761.

Tison, J.−L., Petit, J.−R., Barnola, J.−M., and Mahaney, W.C., 1993, Debris entrainment at the ice− bedrock interface in sub−freezing temperature conditions (Terre Adélie,

KOPRI 극지연구소

Antarctica). Journal of Glaciology, 39, 303−315.

Tulaczyk, S., Kamb, B., Scherer, R.P., and Engelhardt, H.F., 1998, Sedimentary processes at the base of a west Antarctic ice stream: constraints from textural and compositional properties of subglacial debris. Journal of Sedimentary Research, v. 68, pp. 487−496.

Vos, K., Vandenberghe, N., and Elsen, J., 2014, Surface textural analysis of quartz grains by scanning electron microscopy (SEM): From sample preparation to environmental interpretation. Earth−Science Reviews, v. 128, pp. 93−104.

Willan, R.C.R., and Armstrong, D.C., 2002, Successive geothermal, volcanic−hydrothermal and contact−metasomatic events in Cenozoic volcanic−arc basalts, South Shetland Islands, Antarctica. Geological Magazine, v. 139, pp. 209−231.

Williams, A.T., and Morgan, P., 1993, Scanning electron microscope evidence for offshore−onshore sand transport at Fire Island, New York, USA. Sedimentology, v. 40, pp. 63−77.

Williams, A.T., and Thomas, M.C., 1989, Analysis of barrier island surface sediments by scanning electron microscopy. Marine Geology, v. 86, pp. 101−118.

Yoo, C.M., Choe, M.Y., Jo, H.R., Kim, Y., and Kim, K.H., 2001, Volcaniclastic sedimentation of the Sejong Formation (Late Paleocene−Eocene), Barton Peninsula, King George Island, Antarctica. Ocean and Polar Research, v. 23, pp. 97−107.

Yoon, H.I., Han, M.W., Park, B.K., Oh, J.K., and Chang, S.K., 1997, Glaciomarine sedimentation and paleo−lacial setting of Maxwell Bay and its tributary embayment, Marian Cove, South Shetland Islands, Antarctica. Marine Geology, v. 140, pp. 265−282.

KOPRI 극지연구소

Table 1. Modal composition (%) of coastal shoreline sands from the Punta Arenas area, S Chile and Weaver and Barton peninsulas, King George Island, W Antarctica.

Sample	Quartz		Feldspar		Rock fragment				Accessory minerals			Total	Q[d]	F[d]	R[d]
	single	polycryst.	single	aggregate	plutonic	metamorp.	volca(F)[b]	volca(A)[c]	pyroxene	biotite	chlorite				
Punta Arenas area, S Chile															
PA2503*	8.8	24.4	3.2	0.7	10.1	0.0	8.0	43.8	0.4	0.7	0.0	100	33.5	3.9	62.5
PA2504*	4.1	15.6	2.2	0.8	8.3	12.9	7.2	46.9	1.0	1.0	0.2	100	20.1	3.1	76.8
PA2505*	17.2	27.9	5.6	0.0	0.0	3.1	9.0	34.6	1.0	1.7	0.0	100	46.3	5.7	47.9
PA2506*	37.8	9.6	15.9	0.8	0.0	3.2	2.0	24.3	1.2	4.4	0.8	100	50.6	17.8	31.5
PA2507*	6.4	25.2	4.8	1.6	5.2	7.6	15.2	30.4	3.2	0.4	0.0	100	32.8	6.6	60.6
			6.3		4.7	5.4							36.7	7.4	55.9
King George Island, W Antarctica															
Weaver Peninsula															
04-01[a]	0.5	5.0	2.0	9.0	8.0	0.0	55.5	19.5	0.5	0.0	0.0	100	5.5	11.1	83.4
04-02	0.0	7.5	3.0	7.5	4.0	0.0	51.0	27.0	0.0	0.0	0.0	100	7.5	10.5	82.0
04-03[a]	1.0	8.0	7.5	11.0	11.0	0.0	30.0	28.0	3.0	0.5	0.0	100	9.3	19.2	71.5
04-17	0.9	0.5	9.5	3.2	21.4	0.0	25.5	36.8	2.3	0.0	0.0	100	1.4	13.0	85.6
04-18	0.0	1.6	1.6	9.2	40.8	0.4	40.8	37.2	1.2	0.0	0.0	100	1.2	8.2	90.6
04-19	0.0	1.5	0.0	4.0	40.1	0.0	18.3	36.1	0.0	0.0	0.0	100	1.5	4.0	94.5
Barton Peninsula					20.9										
30-20[a]	0.3	8.8	0.3	5.0	3.5	0.0	52.7	29.3	0.0	0.0	0.0	100	9.1	5.3	85.6
30-22	10.8	0.0	3.6	3.2	37.2	0.0	4.0	40.8	0.0	0.4	0.0	100	10.8	6.8	82.3
30-24	2.0	1.5	0.5	1.5	58.5	0.0	26.0	10.0	0.0	0.0	0.0	100	3.5	2.0	94.5
30-26	1.9	1.3	1.3	4.4	60.6	0.0	3.1	27.5	0.0	0.0	0.0	100	3.2	5.7	91.1
31-34	0.0	0.0	0.5	10.5	27.0	0.0	9.0	47.5	2.5	3.0	0.0	100	0.0	11.6	88.4
31-32	4.4	0.0	6.0	13.2	28.4	0.0	14.0	32.8	0.8	0.4	0.0	100	4.5	19.4	76.1
31-29	0.0	0.0	2.8	11.9	17.0	0.0	28.4	39.9	0.0	0.0	0.0	100	0.0	14.7	85.3
31-29-1	0.5	0.0	0.5	1.0	42.0	0.0	34.0	22.0	0.0	0.0	0.0	100	0.5	1.5	98.0
31-25	1.0	0.0	3.5	18.5	23.5	0.0	12.5	39.0	0.5	1.5	0.0	100	1.0	22.4	76.5
31-28[a]	1.5	2.5	4.5	14.5	13.5	2.0	33.0	28.0	0.5	0.0	0.0	100	4.0	19.1	76.9
31-26	0.0	0.0	0.0	0.0	41.0	0.0	38.5	20.5	0.0	0.0	0.0	100	0.0	0.0	100.0
28-02	0.0	0.0	1.0	0.0	27.0	0.0	19.6	52.5	0.0	0.0	0.0	100	0.0	1.0	99.0
28-07	0.0	0.5	0.0	0.0	26.4	0.0	15.0	58.2	0.0	0.0	0.0	100	0.5	0.0	99.5
28-06	0.0	0.0	0.5	0.0	11.4	0.0	42.1	46.0	0.0	0.0	0.0	100	0.0	0.5	99.5
29-17	0.0	0.0	1.5	0.0	18.0	0.0	26.0	54.5	0.0	0.0	0.0	100	0.0	1.5	98.5
29-16	0.0	0.0	0.0	0.5	19.4	0.0	32.5	47.6	0.0	0.0	0.0	100	0.0	0.5	99.5
29-15	0.0	1.0	0.0	0.5	18.7	0.0	37.8	42.1	0.0	0.0	0.0	100	1.0	0.5	98.5
29-14	0.0	0.0	0.0	0.5	15.8	0.0	53.5	30.2	0.0	0.0	0.0	100	0.0	0.5	99.5
29-13	0.5	0.0	0.5	0.5	12.5	0.0	39.4	46.6	0.0	0.0	0.0	100	0.5	1.0	98.5
28-01[a]	0.0	6.3	0.6	5.0	15.0	0.0	33.1	40.0	0.0	0.0	0.0	100	6.3	5.6	88.1
29-12	0.5	0.5	2.4	0.0	30.1	0.0	32.0	34.5	0.0	0.0	0.0	100	1.0	2.4	96.6
29-11	0.0	0.0	0.0	0.0	18.5	0.0	29.3	52.2	0.0	0.0	0.0	100	0.0	0.0	100.0
29-10	0.0	0.0	1.5	0.5	3.4	0.0	29.1	65.5	0.0	0.0	0.0	100	0.0	2.0	98.0
29-08	1.5	2.5	1.5	0.5	14.2	0.0	12.7	67.2	0.0	0.0	0.0	100	4.0	2.0	94.0
29-05	0.4	0.0	0.0	6.0	1.6	0.0	23.2	68.8	0.0	0.0	0.0	100	0.4	6.0	93.6
29-06	0.0	0.5	2.0	0.5	6.9	0.5	11.8	77.8	0.0	0.0	0.0	100	0.5	2.5	97.0

[a]Samples used for quartz microtexture observation.
[b]Volca(F) represents fresh volcanic rock fragment.
[c]Volca(A) represents altered volcanic rock fragment.
[d]Q–quartz; F–feldspar; R–rock fragment.

KOPRI 극지연구소

Table 2. Microtextures of quatz grains from the Punta Arenas area, S Chile and Weaver and Barton peninsulas, King George Island, W Antarctica (classification after Vos et al. (2014).

mechanism	microtextures	Punta Arenas area					King George Island					genesis[*]
							Weaver Peninsula		Barton Peninsula			
		PA2503	PA2504	PA2505	PA2506	PA2507	04-01	04-03	30-20	31-28	28-01	
mechanical	1. angular outline	4.3	0	0	6.7	6.7	20	13.3	13.3	26.7	6.7	
	2. subangular outline	82.6	100	100	93.3	86.7	80	73.3	86.7	73.3	100	
	3. rounded outline	13	0	0	0	0	0	20	6.7	0	6.7	
	4. small conchoidal fractures (<10 µm	13	7.1	13.3	0	33.3	33.3	33.3	13.3	26.7	13.3	polygentic
	5. medium conchoidal fractures (<10(	52.2	64.3	60	66.7	86.7	60	53.3	33.3	66.7	53.3	polygentic
	6. large conchoidal fractures (>100 µr	30.4	64.3	53.3	46.7	33.3	40	40	46.7	73.3	26.7	polygentic
	7. arcuate steps	60.7	78.6	53.3	46.7	66.7	46.7	53.3	60	73.3	60	polygentic
	8. straight steps	34.8	64.3	26.7	26.7	53.3	46.7	80	60	80	46.7	polygentic
	9. meandering ridges	0	7.1	0	0	0	20	20	13.3	13.3	6.7	
	10. flat cleavage surface (abrasion surfa	30.4	7.1	6.7	20	26.7	80	26.7	53.3	33.3	33.3	polygentic
	11. graded arcs (crescentic gouges)	39.1	21.4	20	40	33.3	53.3	6.7	6.7	73.3	53.3	sustained shear stres
	12. v-shaped percussion cracks	21.7	21.4	26.7	0	73.3	13.3	13.3	26.7	66.7	6.7	percussion
	13. straight/curved grooves and scratch	39.1	57.1	40	13.3	53.3	80	46.7	33.3	60	40	sustained shear stres
	14. upturned plates	39.1	42.8	26.7	33.3	33.3	46.7	6.7	33.3	53.3	73.3	polygentic
	15. crescentic percussion cracks	26.1	7.1	13.3	20	40	20	53.3	13.3	26.7	40	percussion
	16. bulbous edges	0	0	0	0	0	0	0	0	0	0	percussion
	17. abrasion fatigue	0	14.3	13.3	0	40	40	6.7	6.7	0	13.3	
	18. parallel striations	30.4	28.6	66.7	26.7	40	60	53.3	60	60	40	sustained shear stres
	19. imbricated grinding features	0	0	0	0	0	0	0	0	0	0	
chemical	20. oriented etch pits	0	0	0	6.7	0	0	0	0	0	0	
	21. solution pits	13	0	0	66.7	0	6.7	0	0	6.7	6.7	
	22. solution crevasses	0	0	0	20	6.7	6.7	0	0	0	0	
	23. scaling	0	0	0	0	0	0	0	0	0	0	
	24. silica globules	4.3	0	0	20	0	0	0	0	0	0	
	25. silica flowers	0	0	0	6.7	0	0	0	0	0	0	
	26. silica pellicle	0	0	0	0	0	0	0	0	0	0	
	27. crystalline overgrowths	0	0	0	0	0	0	0	0	0	0	
mechanical/ chemical	28. low relief	0	0	0	0	0	0	0	0	0	0	
	29. medium relief	87	28.6	33.3	20	60	20	33.3	20	53.3	26.7	
	30. high relief	13	78.6	60	73.3	4	80	53.3	60	46.7	66.7	
	31. elongated depressions	13	0	0	60	0	6.7	6.7	13.3	6.7	6.7	
	32. chattermarks	0	7.1	0	0	6.7	6.7	13.3	6.7	13.3	26.7	
	33. adhering particles	39.1	71.4	20	60	86.7	93.3	66.7	46.7	80	20	
	34. arcuate/circular polygonal cracks	0	0	0	0	0	0	0	0	0	0	

[*]After Sweet and Brannan (2016).

KOPRI 극지연구소

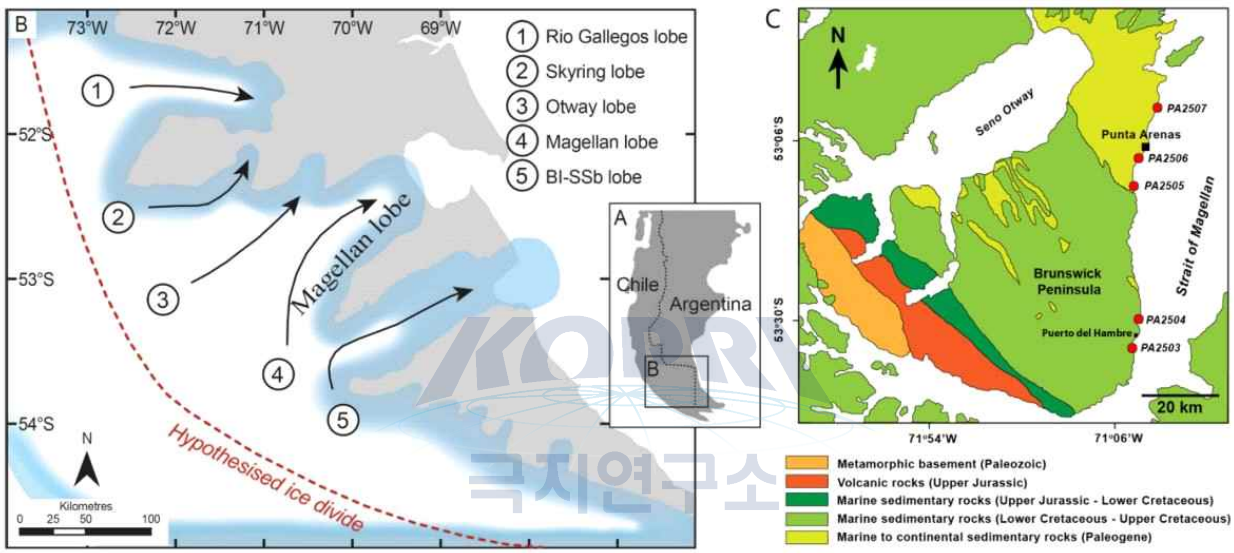


Fig. 1. (A) Location of southern South America. (B) Stylized representation of the southernmost part of the former Patagonian Ice Sheet, highlighting the five former glacial lobes in southern South America (after Darvill et al., 2017). (C) Sampling sites and geological maps of the Punta Arenas area, southernmost Chile.

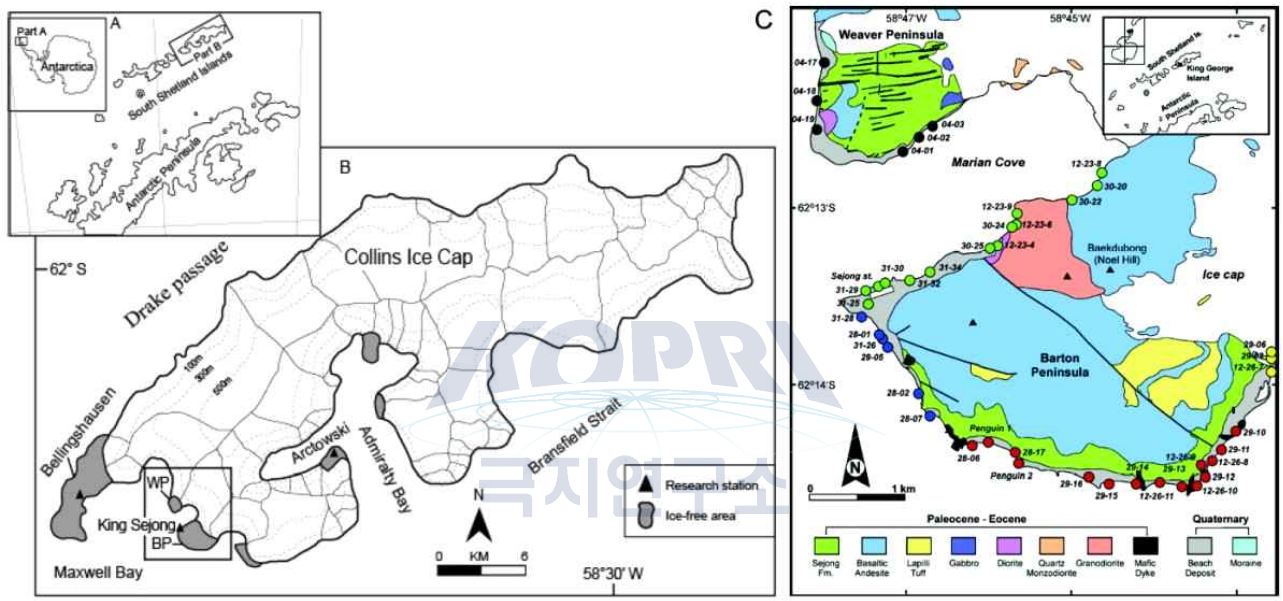


Fig. 2. (A) Location of the South Shetland Islands in Antarctica. (B) The Collins Ice Cap centered on King George Island and its glacial drainage-basin divides (after Seong et al., 2009). (C) Sampling sites and geological maps of the Barton and Weaver peninsulas, King George Island, West Antarctica (modified after Lee et al., 2019).

KOPRI 극지연구소

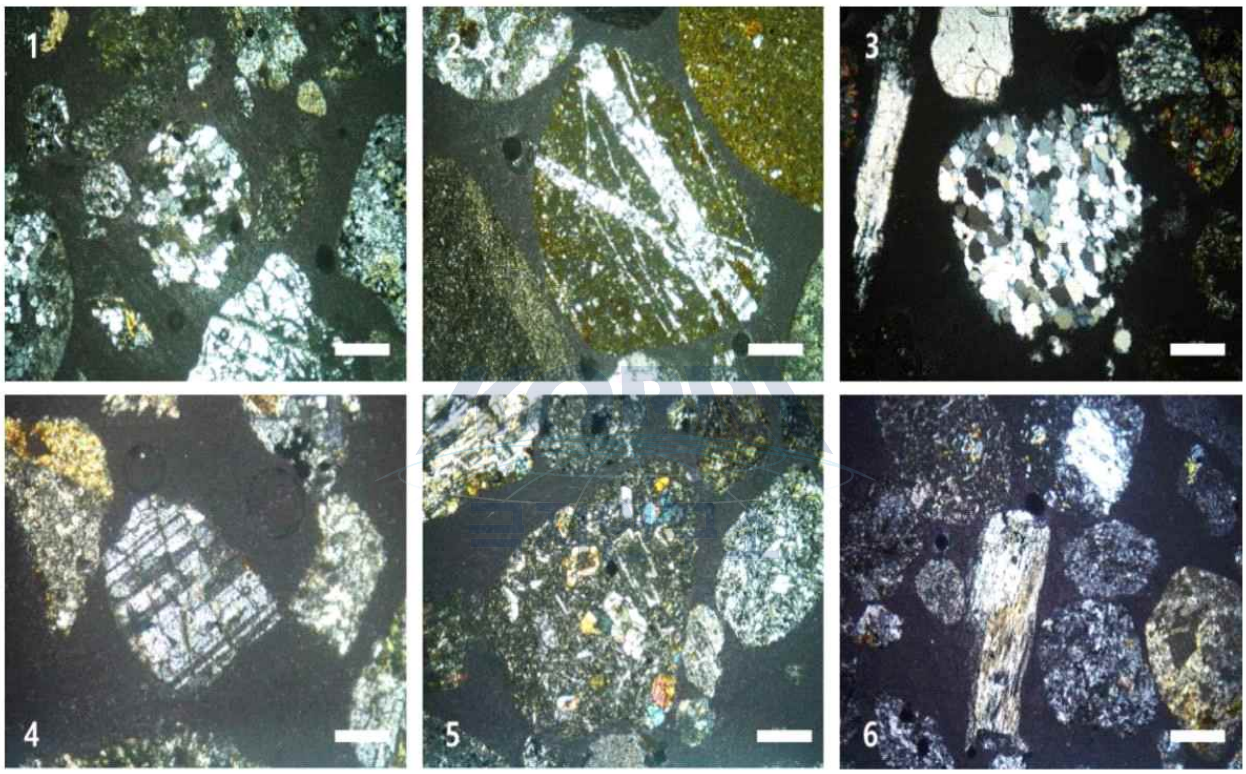


Fig. 3. Examples of sand grain photomicrograph. 1. Plutonic rock fragment, 2. Altered volcanic rock fragment, 3. Polycrystalline quartz, 4. Feldspar (plagioclase), 5. Fresh volcanic rock fragment, and 6. Accessory mineral (center). Scale bar is 0.5 mm long.

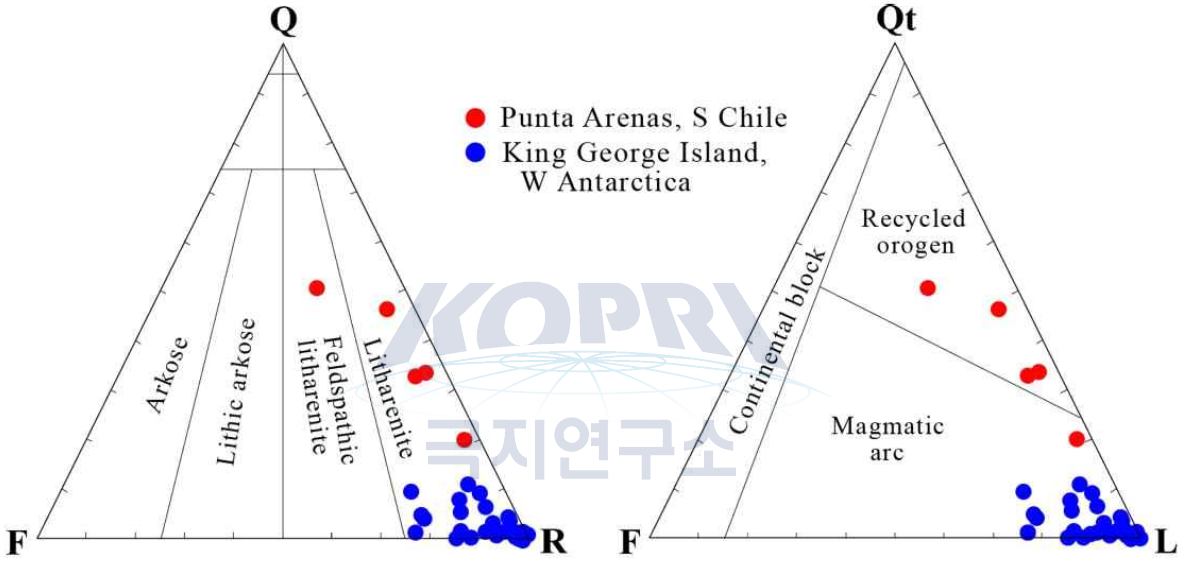


Fig. 4. (A) Sandstone classification (after Folk, 1974) and (B) clast source terrane (after Dickinson, 1985) of the sand samples from the PA area, southernmost Chile and the Barton and Weaver peninsulas, KGI, West Antarctica. The studied sand samples were classified as lithic arenite with one sample from the PA area as feldspathic litharenite.

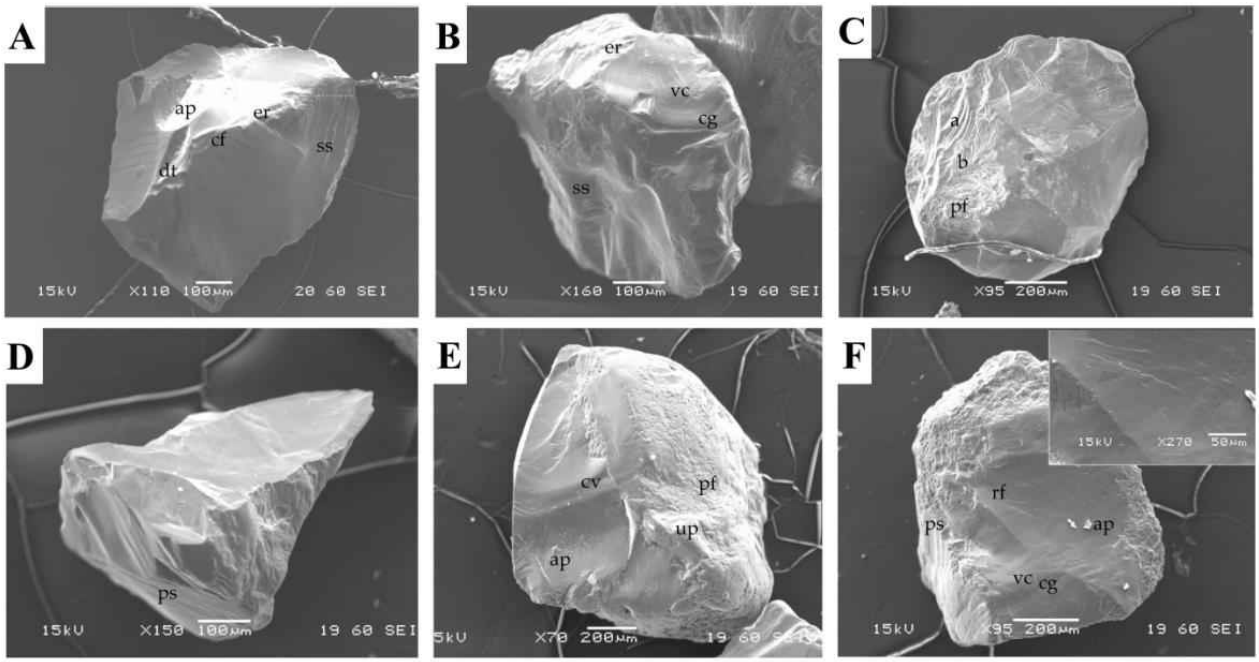


Fig. 5. Selected SEM micrographs of grains from the PA area, S Chile showing typical morphological and mechanical textures. Most of the grains in this figure record multiple microtextures that are labeled. A) Angular grain showing high relief, straight steps (ss), conchoidal fracture (cf), edge rounding (abrasion; er), deep trough (dt) and adhesion particles (ap) on PA2505-4-2 sand grain. B) Subangular grain showing medium relief on PA2506-6-1 sand grain. Curved grooves (cg) across grain surface and later modified by V-shaped percussion cracks (vc). Depth of groove approaches 10 µm. Straight steps (ss; subparallel linear fractures). Many of the edges demonstrate rounding (er). C) Surface showing numerous conchoidal fracture planes with arcuate (a) and straight (b) steps, demonstrating numerous locations on grain edges where a block has broken off, and preweathered microfeatures (pf) on PA2504-3 sand grain. D) A well-fractured angular grain (PA2506-13) showing a 'hand-axe' form represented by large conchoidal fractures (e.g., [12]) and parallel striations (ps). E) A preweathered grain (PA2507-16) that is abraded without much fracturing effects. Upturned plate (up), curved groove (cv) across grain surface, and adhesion particles (ap). The fresh grain shows preweathered features (pf) on its upper right part and fracturing and abrasion on the left flank. The inset shows the enlarged view of the left central part of the grain. V-shaped percussion cracks are observed on the surface where faint radial fracture was generated. F) Faint radial fracture (rf) developed on a preweathered grain (PA2507-11). Also observed are parallel striations (ps), adhering particles (ap), curved groove (cg), and V-shaped percussion cracks (vc) on radial fracture plane. Adhering particles may result from glacial grinding processes (Smalley, 1966).

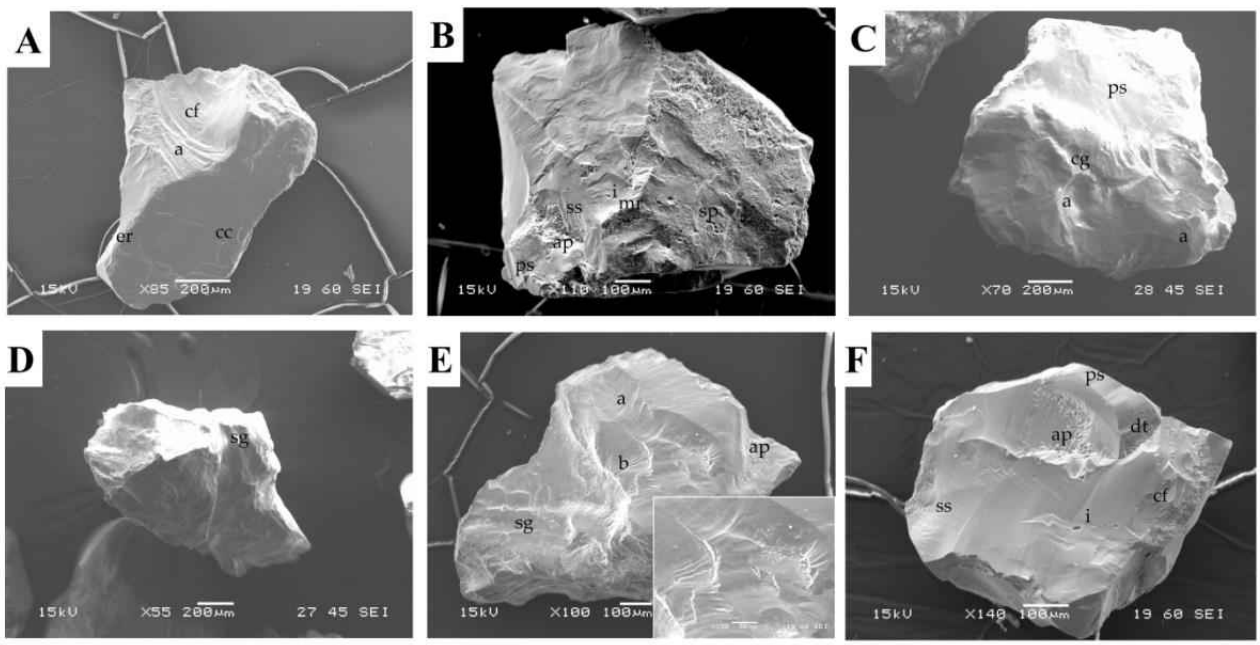


Fig. 6. Selected SEM micrographs of grains from KGI, South Shetland Islands, W Antarctica showing typical morphological and mechanical textures. Most of the grains in this figure record multiple microtextures that are labeled. A) Subangular outline, low relief, conchoidal fracture (cf), arcuate steps (a), crescentic percussion cracks (cc) on 31−28−2 sand grain. Many of the edges demonstrate rounding (er). B) Subangular outline, medium relief, parallel striation (ps), solution pits (sp), straight steps (ss), adhering particles (ap), and meandering ridge (mr) on 31−28−10 sand grain. Remnants of inclusions (i) are present on the fracture plane. Preweathered surface cut by surfaces with arcuate steps and straight steps showing a multiple history for this grain. Meandering ridge traverses across the grain surface. C) Subangular outline, medium relief, severely abraded and fractured quartz, parallel striations (ps), conchoidal fracture (a; arcuate step), and a curved groove (cg) across grain surface on 28−1−7 sand grain. D) Angular grain showing high relief and subparallel straight grooves (sg; deep troughs) on 28−1−16 sand grain. E) A multitude of abraded surfaces with faint vestiges of fractures along with sharp edges and subdued relief on 31−28−6 sand grain, similar in kind to grains reported from the West Antarctic Ice Sheet by Tulaczyk et al. (1998). Conchoidal fractures forming arcuate (a) and straight (b) steps, straight grooves (sg), and adhesion particles (ap) are also shown. The inset shows the enlarged view of the center of the grain. After arcuate and straight steps were generated by glacial stress, V−shaped percussion cracks were generated. F) Angular outline, medium relief, conchoidal fractures (cf), adhesion particles (ap), parallel striation (ps), and deep trough (dt) on 31−28−14 sand grain. Note the straight steps (ss) and the presence of lined−up, nm−scale pits (arrows), which are interpreted as the remnants of a fluid inclusion (i) trail.

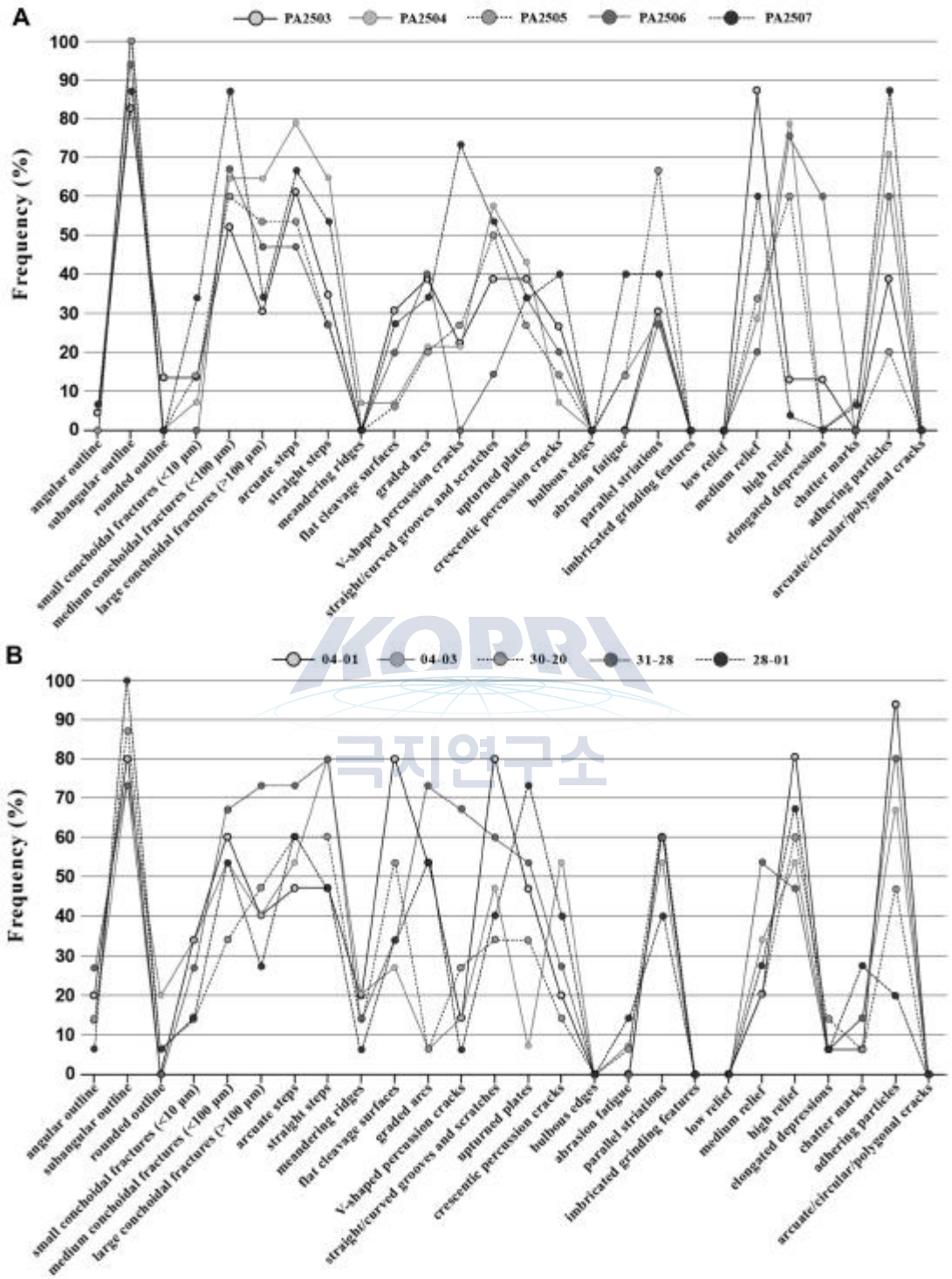


Fig. 7. Occurrence frequency of microtextures of quartz grains from (A) the PA area, southern Chile and (B) KGI, West Antarctica.

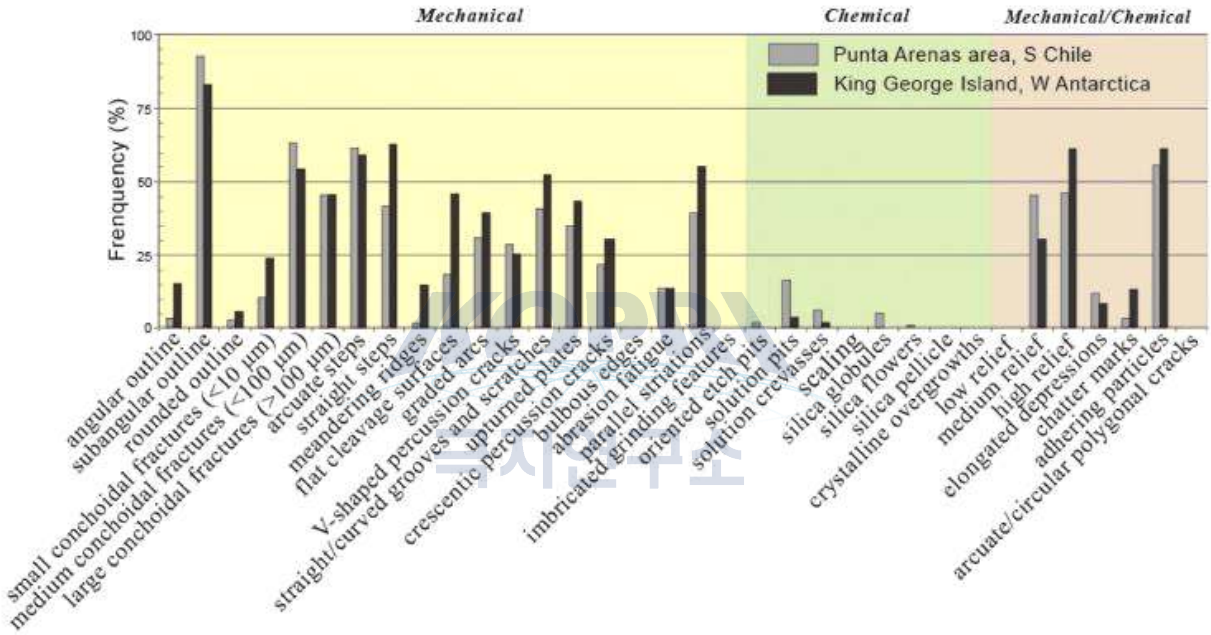


Fig. 8. Average frequency distribution of quartz grains occurring with specific microtextures in samples of the PA area, southern Chile and KGI, West Antarctica. The microtexturescorrespond to those listed in Table 2.



KOPRI
극지연구소

Fig. 9. Pie diagrams illustrating the relative abundances of sustained shear stress, percussion, and polygenetic fractures of shoreline sand samples from the PA area, S Chile (A) and KGI, W Antarctica (B). Sustained-shear-stress fracture includes curved and straight grooves, deep troughs, graded arcs, and parallel striation. Percussion fracture includes randomly oriented V-shaped cracks and crescentic percussion cracks. Polygenetic fracture includes conchoidal fractures, arcuate and straight steps, flat cleavage surface, and upturned plate. Note that the proportion of mechanically produced microtextures by specific transport processes in the shoreline sands of the two high latitude regions is similar.

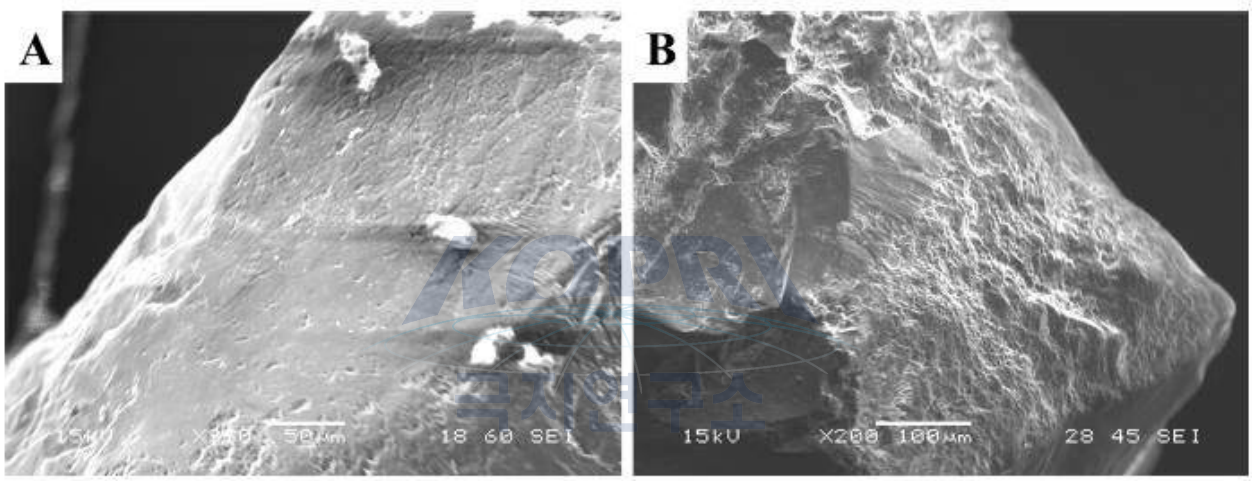


Fig. 10. SEM micrographs showing preweathered grain modification by glacial stress. A) Preweathered grain surface was modified by glacial abrasion, followed by generation of V-shaped percussion cracks (PA-2507-4-1). B) Arcuate steps, parallel steps, and flat surface developed on preweathered grain (04-01-11-1).

제 27 장

A Comparison of Methods for Identifying and Quantifying Ice Rafted Debris on the Antarctic Margin[21)]

Robert McKay[1], Olga Albot[1], Gavin B. Dunbar[1], Jae Il Lee[2] , Min Kyung Lee[2], Kyu-Cheul Yoo[2], Sunghan Kim[2], Nikita Turton[1,3], Denise Kulhanek[4], Molly Patterson[5], and Richard Levy[1,3]

[1]Antarctic Research Centre, Victoria University of Wellington, [2]Korea Polar Research Institute, [3]GNS Science, [4]Christian-Albrechts-Universität zu Kiel, [5]Binghamton University

ABSTRACT: Quantification of ice rafted debris (IRD) abundances in deep-sea records is often used as a key proxy for identifying links between ice sheet instability and the oceanic overturning circulation. There currently exist multiple methods to determine IRD content in deep-sea sediment cores. The preference for a given method is often determined by the accessibility to core material and destructive nature of some methods. While many studies have discussed the caveats between linking IRD to ice sheet dynamics, the uncertainties relating to the methodological approaches are often not considered in the interpretation or comparisons between different IRD datasets, particularly in the Antarctic. To address this, we compare three independent methodologies of obtaining IRD abundances and also discuss how different approaches will affect determinations of mass accumulation rates (MARs). The three methodologies we examine include: counting clasts >2 mm in x-radiographs; the sieved weight percentage of the medium-to-coarse sand fraction (250 μm-2 mm); and volumetric estimates of the >125 μm sand fraction using laser diffraction particle size analysis. The x-radiograph and sieve methods produced comparable results, while the laser particle size analysis, although showing comparable long-term signals at most locations, in general has lower correlation to the other two methods and therefore a higher potential to obtain a noisy signal. We discuss the caveats associated with all methods, and emphasize that a combination of multiple methods should ideally be employed when assessing if a core is suitable for IRD study, and if sand or gravel fractions are accurately reflecting contents of IRD.

1. Introduction

21) 이 연구 결과는 다음의 논문으로 출판되었음: McKay, R. et al. (2022). "A Comparison of Methods for Identifying and Quantifying Ice Rafted Debris on the Antarctic Margin." Paleoceanography and Paleoclimatology 37: e2021PA004404.

Records of the flux of ice rafted debris (IRD) to the seafloor over time have provided fundamental insights into the past behavior of marine-terminating polar ice sheets. Debate about the exact relationship between IRD content of seafloor sediment and ice sheet dynamics is ongoing. Several reasons for this debate exist. First, studies are highly variable in defining the size fraction that is used for determining IRD and measuring it (Andrews, 2000; Conolly & Ewing, 1965; Diekmann et al., 2003; Passchier, 2011; Patterson et al., 2014; Ruddiman, 1977), potentially leading to different results from different researchers. Second, IRD could conceivably reflect (a) a change in the flux of icebergs across the study site, (b) a change in the mass of debris carried by icebergs, (c) a change in the melt rate of icebergs across the study site, or (d) some combination of all three (Cook et al., 2014; Hillenbrand et al., 2009; Starr et al., 2021; Williams et al., 2010). Despite these caveats, it is clear from geological archives that IRD commonly displays a coherent relationship with other proxies indicating that underlying climatic drivers explain many IRD records. There have recently been a large number of studies reconstructing IRD abundance (e.g., Hillenbrand et al., 2009; Kanfoush et al., 2002, 2000; Ó Cofaigh et al., 2001) or IRD flux in the Southern Ocean and Antarctic margin (Carter et al., 2002; Diekmann, 2007; Diekmann et al., 2003; Grobe & Mackensen, 1992; Hillenbrand et al., 2002; Ó Cofaigh et al., 2001; Passchier, 2011; Patterson et al., 2014; Starr et al., 2021; Weber et al., 2014). It is important to note that many IRD studies commonly utilize different methods for measuring its abundance in the sediment matrix. All of these methods quantify the measurement of coarse grain sizes (with various size fraction cut offs) that provide a proxy measure for the total IRD content in a sample, which in reality comprises all grain sizes, but it is difficult to isolate the IRD fraction at finer grain sizes (e.g., in the mud fraction). However, depending on the depositional setting and processes, some of the coarse size fractions used for IRD proxies may capture grains that are not ice rafted, or lack statistical significance when measuring the abundance of "outsized" grains in a grain size distribution. In this paper, we conduct a comparison of three commonly used methods to determine IRD abundance to assess if different signals in the resultant datasets can be explained by the use of different laboratory approaches.

1.1. Paleooceanographic Significance of IRD

The presence of outsized sand and gravel clasts in deep-sea muds recovered from high latitudes is commonly interpreted to represent the flux of melting icebergs calving off marine-terminating glaciers, and thus reflects changes in the mass balance of ice sheets (Jansen et al., 2000; Kanfoush et al., 2000). The significance of such records was recognized in north Atlantic sediments, where prominent layers of concentrated IRD with a Laurentian

provenance, termed Heinrich layers, were identified in sediment cores (Andrews & Voelker, 2018; Bond et al., 1992; Dowdeswell et al., 1999; Heinrich, 1988; Hemming, 2004). The leading hypothesis for the genesis of these layers is that they reflect ice shelf collapses from subsurface oceanic warming, resulting in a surge of the marine margins of the Laurentide Ice Sheet which released large quantities of debris-rich icebergs into the north Atlantic (Flückiger et al., 2006; Hulbe et al., 2004; Li & Piper, 2015; Marcott et al., 2011). Because the Antarctic Ice Sheets (as a total average) lose ~50% of their mass by iceberg calving from outlet glaciers and ice streams (Depoorter et al., 2013), it is proposed IRD records that lie in the primary iceberg pathways on the Antarctic continental margin are a reliable proxy of shifting ice sheet dynamics (Hillenbrand et al., 2009; Passchier, 2011; Patterson et al., 2014; Weber et al., 2014; Williams et al., 2010). However, mass loss by iceberg calving on individual ice shelves can vary between 10% and 90%, with the remainder taken up by basal melt, which could result in regional differences of IRD abundances and the relationship to ice dynamics (Depoorter et al., 2013). Iceberg calving from thinning ice shelves in negative mass balance is also dominated by more frequent calving events, and this process is distinct from the more periodic processes of isolated tabular icebergs that break up from ice shelves in neutral or positive mass balance regimes (Liu et al., 2015). Consequently, it is proposed by many of the above studies that an enhanced signal of IRD should be present in the deep ocean proximal to Antarctica during large deglaciation events.

The frequency characteristics of such IRD pulses from Prydz Bay and the Adélie Land continental margin of Antarctica throughout the Miocene, Pliocene, and Pleistocene are consistent with pacing by changes in Earth's orbital geometry (i.e., Milankovitch cycles), which suggests that the volume of Antarctica's ice sheet also fluctuate on this timescale (Escutia et al., 2003; Hansen et al., 2015; Lucchi et al., 2002; Passchier, 2011; Patterson et al., 2014; Williams & Handwerger, 2005; Williams et al., 2010). Millennial-scale pulses of IRD to the Scotia Sea during the last deglaciation (20-9 kyr) are also interpreted to represent episodes of Antarctic marine ice sheet instability on sub-orbital timescales, indicating that IRD peaks and fluxes in this setting represent major deglaciation events and have the potential to provide high-resolution archives of dynamic ice sheet discharge leading into interglacial periods (Diekmann et al., 2003; Ehrmann & Grobe, 1991; Hepp et al., 2006; Hillenbrand & Fütterer, 2001; Weber et al., 2014).

1.2. Physical Controls on IRD Deposition

The interpretation and significance of IRD is likely to vary in different regions, as the debris content of icebergs is determined by numerous factors. Glaciers and ice streams in warmer glacial thermal regimes produce and carry abundant sand and silt-sized grains by

means of glacial erosion of primary bedrock (Evans & Pudsey, 2002). However, in West Antarctica, dynamic ice streams override and rework pre-existing muddy tills and glacimarine muds/diamictites that have accumulated in Late Cenozoic sedimentary basins that are several kilometers thick. In this case, sand and gravel eroded directly from bedrock may be relatively less abundant than for sites bordering East Antarctica, although recycling of clasts from older glacial diamictites is likely to occur (McKay et al., 2019; Tulaczyk et al., 1998). Additionally, the base of large ice shelves, such as the Ross Ice Shelf, are commonly debris free, and large iceberg calving events from such ice shelves may deliver little IRD to the ocean (Anderson, 1999).

Glacier speed and calving rate both further influence iceberg production and size (Bassis et al., 2017), while other controls such as coastal morphology, sea ice extent, sea surface temperatures (SSTs) and current directions exert a strong influence on iceberg survival, residence time, and the spatial distribution of icebergs (Gilbert, 1990; Jansen et al., 2000; Starr et al., 2021; Teitler et al., 2010; Figure 1). In addition, IRD abundance in the depositional record may also reflect regional processes controlled by the ice sheet response to glacial-interglacial environmental variability, such as current winnowing and changes in sedimentation rates, rather than regional-scale episodes of increased/decreased iceberg calving (McCave & Andrews, 2019; Ó Cofaigh & Dowdeswell, 2001).

KOPRI 극지연구소

1.3. Issues With the Interpretation of IRD Records

Given the number of complicated controls on IRD deposition outlined above, there is long standing debate regarding what IRD flux represents in terms of ice sheet stability and the methodology used to derive IRD records. Clark and Pisias (2000) propose that only greatly enhanced fluxes of IRD from the Antarctic ice sheets deposited over a large area can be unambiguously interpreted in terms of changes in dynamic ice sheet discharge. This assertion is dependent on a number of assumptions, including whether or not: (a) IRD is delivered through fallout from icebergs rather than sea ice, because sea-ice transport of IRD in the Antarctic is (at present) restricted to coastal settings (Chewings et al., 2014); (b) an increase in IRD is representative of an increased iceberg flux as opposed to a greater amount of debris incorporated at the base of the ice sheet from which icebergs are calved off or changes in iceberg melt rates; and (c) the amount of IRD is similar in all icebergs, and thus, whether or not there is a correlation between IRD concentration and iceberg flux (Clark & Pisias, 2000). Consequently, the IRD flux to the seafloor is dependent on the number and size of icebergs passing over the site, the proximity to the calving glaciers, the type and size of the glacier it has calved from, drift paths relating to ocean currents changing through time, and the variability of sea ice and SSTs. All of these factors vary greatly with local climatic,

oceanographic and glacial regimes, which can be assessed via comparisons to multiproxy datasets and modeling studies (Cook et al., 2014; Gilbert, 1990; Golledge et al., 2014; Powell & Domack, 2002; Starr et al., 2021).

We do not attempt to address these complex issues regarding the relationship between ice dynamics and IRD flux in this paper, other than to note that site-specific considerations must clearly be accounted for when interpreting and applying a methodology to these records. We also note a multiproxy approach can at least constrain some of the environmental variables thought to control IRD flux, but clearly our understanding would benefit from more comprehensive observations of modern processes.

1.4. Criterion for Defining IRD in Antarctic Margin Sediments

In recent studies of ice proximal environments on the continental rise to abyssal plain in Antarctica, a range of grain sizes have commonly been used to define the IRD fraction including, but not restricted to, 125 μm–2 mm, 250 μm–2 mm, or >2 mm. These ranges are determined on the basis that the settling velocity of such material is too high for it to be transported over long distances by processes other than ice rafting. However, downslope mass transport processes must still be considered for sites proximal to the Antarctic margin (Cowan et al., 2020; Kanfoush et al., 2000; Murphy et al., 2002; Patterson et al., 2014; St. John & Krissek, 1999; Weber et al., 2014).

In the Antarctic, transport of sediment by sea ice in coastal regions is generally restricted to the 63–150 μm fraction, that is, a size fraction that can readily be blown on to sea ice by wind, with most sand-size sediment restricted to coastal fast ice <5 km offshore (Chewings et al., 2014). Similarly, resuspension by traction currents is generally restricted to the <63 μm fraction (Andrews, 2000) but could be higher in regions with extreme bottom current speeds (Lamy et al., 2015; McCave & Andrews, 2019). Grain shape and surface texture have been used to identify sediment transport via these different processes, with sub-angular to angular clasts containing a high abundance of fractures and striations/gouges used as indicators of an iceberg-rafted, rather than sea ice-rafted, origin (St. John et al., 2015). However, this alone does not confirm that a grain is rafted by either an iceberg or sea ice to the site, as a glacial erosion signature is likely to be pervasive on the Antarctic continental margin as this is the predominant mechanism for physical weathering of sediment. Similarly, well-rounded grain shapes have been used in some settings to distinguish grains that have been potentially wind-blown onto sea ice and subsequently transported offshore (Passchier et al., 2021). However, such rounding could also be inherited from non-glacial strata that have been eroded and deposited within sub-glacially deposited diamictites. For example, subglacially deposited diamictites in the AND-1B drill core from the Ross Sea

continental shelf have clasts contents that comprise up to 15% of rounded quartz with preserved chemical overgrowths derived from the Devonian Beacon Supergroup fluvial deposits, with little alteration of the original grain shape (Talarico et al., 2012). Assessment of volcanic tephra grains in the coarse fraction can help assess if primary ashfall onto the ocean surface, or drifting sea ice can account for delivery of coarse grains into the deep ocean, although distinguishing ice rafted versus primary volcanic ashfall can be difficult in regions dominated by active volcanics (Nielsen et al., 2007). Moreover, re- deposition via any of the above processes is likely to be rapid and include grains where the original subglacial grain shape/surface textures are likely to remain preserved.

2. Methods of Determining IRD Flux

An issue that is often overlooked in interpreting and comparing IRD records is that a number of different methods are employed to categorize and quantify the IRD content in sediment cores (Andrews, 2000). The most frequently used methods in the Antarctic region include: (a) counting particles in the 150 μm–2 mm size fraction under the microscope where particles categorized as IRD are quartz, feldspars, mafic minerals, and metamorphic lithic fragments (Kanfoush et al., 2000; Murphy et al., 2002); (b) measuring the weight percentages of the 250 μm–2 mm size fraction and then visually checking by microscope whether the grains are non-biogenic, volcanic, or diagenetic in origin and correcting for these by numerical or physical removal (Cowan et al., 2008; Patterson et al., 2014; St. John & Krissek, 1999); (c) visually counting lithogenic particles (either >1 or >2 mm) from the x-radiographs of the sediment core, either by scans on the half/whole cores or subsampled by slabs/uchannels, and binning these into discrete intervals to determine a number of grains per volume of sediment (Cowan et al., 2008; Grobe, 1987; Weber et al., 2014); and (d) Laser Particle Sizer Analysis (LPSA) of the size-frequency distribution and determination of the relative volume percentage of the 125 μm–2 mm fraction (Hansen et al., 2015; Passchier, 2011).

We do not comprehensively cross compare all published methods in this paper and have chosen methods to compare that rely on either a volumetric, weight or counting approach, but similar caveats and issues should be considered and investigated for other methods not examined here. Each of the methods we investigate utilizes one of these approaches, and has previously been applied to sediment cores from the continental margin of the Antarctic, and as noted earlier, inferred through the use of multiproxy approaches to identify changes in ice sheet dynamics.

Although grains of all sizes can be carried by icebergs, the lower size limit of 125 or

250 μm used to identify unambiguous IRD is often assumed to eliminate the finer material transported by sea ice, bottom currents, wind or turbidity/gravity currents. However, the abundance, and spatial and temporal patterns of IRD estimates can vary depending on the grain size fraction being measured, and therefore site−specific considerations are needed (Andrews, 2000). It is even more critical to assess the relevance of these size limits in determining an ice rafted origin for sediment when working on a continental margin, as medium sand and coarser grains can be transported to the deep ocean via density currents or mass flow processes, while high energy currents can act to resuspend sediment. Additionally, diagenetic and biogenic material can also contribute to this size fraction and needs to be accounted for in any calculations of IRD. Comparison of modern drift pathways of large icebergs (>5 km 2) indicate that in Antarctica, iceberg concentrations are highest over the continental rise region (Figure 1). Even under scenarios of greatly reduced ice sheet volume, the current system responsible for this drift pattern is unlikely to have changed direction or location due to bathymetric and geostrophic considerations (DeConto et al., 2007). All of the sites utilized in this paper lie just to the north of the eastward flowing pathway of the Antarctic Slope Current, from which smaller icebergs are transported northward via eddies and gyres (Rackow et al., 2017; Tournadre et al., 2016). It is argued that because this current and associated eddies and gyres focuses icebergs, it holds the most potential to obtain records of past changes in ice dynamics (Passchier, 2011; Patterson et al., 2014; Weber et al., 2014; Williams et al., 2010), but this depositional setting is also complicated by other continental margin sedimentary processes (Donda et al., 2007; King et al., 2022). Site−specific considerations must therefore be taken into account, via development of a full depositional model using complementary datasets, including seismic survey data, sedimentary facies analysis, and geochemical data.

All methods of determining IRD have advantages and uncertainties (Table 1). For example, LPSA is a rapid and simple method, and has major advantages over other grain size methods, such as SediGraph or coulter counter, in that it can quickly measure the entire frequency distribution of grain size in the mud to sand fraction (0−2 mm). All methods that use samples from sediment cores are limited by the availability of sample, due to the small core diameters, and pressures from other sampling requirements. The consequence of this is that the minimum sample volume/mass required significantly increases with the maximum grain size that is to be captured accurately (Kowalenko & Babuin, 2013; Rawle, 2015). In addition to sample availability, the LPSA method is also limited by the analytical method. First, the sample mass required to obtain obscuration values suitable to accurately measure a given size range greatly varies, with sand−rich samples requiring more sediment than mud−rich sediment. Consequently, in mud−rich sediments that are common in glacial settings the LPSA is often limited to using sample sizes of 0.1−1 g of sediment, but a greater volume of

sediment is required to capture the sand fraction more precisely in these systems (~1–2 g for medium sands). This issue led Kowalenko and Babuin (2013) to conclude that laser diffraction methods were not well suited to sample where the entire distribution range from clay to sands needs to be measured precisely. The exact mass of sediment required varies between instruments and the dispersion module, which controls the volume of water and thus the concentration of the sediment circulating in the analyzer. However, a key point here is that the mass of sediment analyzed is controlled by the need to obtain a correct obscuration value on the instrument, rather than sample availability itself.

An additional consideration is that the LPSA measurement is derived from a volume percentage calculation from a small total sample volume, and volume percentage can only be converted to weight via assumptions of grain shape, density and optical properties (Blott & Pye, 2006). Blott and Pye (2006) also note issues with LPSA software modelling of sand distributions that use assumptions of log–normal distributions. IRD is unlikely to have such a distribution, and is more likely to approximate a uniform distribution, although this is source lithology dependent. Modelling normal distributions is most problematic in highly skewed, truncated or bimodal samples (Blott & Pye, 2006), and such samples are pervasive in glaciated settings.

Given the above issues, a caveat exists as to whether the number of medium–sand and coarser particles present in a sample is a good representation of their actual abundance in sediment in any of the methods we examine. This problem can be illustrated by a simple example of two grains in a measurement having a diameter of 125 and 1,250 μm, using lower end member values for total sample size. The larger of these grains has 1,000 times the volume of the smaller grain. Assuming a density of quartz (2.65 g/cm 3), the 1,250 μm grain has a mass of 0.0027 g, and for a bulk sample weight of 0.15 g used in the LPSA measurement this single grain could represent up to 1.8% of the total. This caveat also exists for sieving methods, as the presence or absence of a few coarse sand grains can therefore make a large difference to the estimated weight percentage of IRD in small bulk samples. In sieving, to obtain 1.8% of this size fraction from 5 g of sediment would require >30 grains of a 1,250 μm diameter, although a single 2 mm grain could represent up to 0.88% in a 5 g sieve sample (and 7.4% in a 0.15 g LPSA sample).

So although the above examples show that both methods do have issues with statistical significance due to sample availability, a key difference is that sieving is not analytically limited to having a prescribed sample size in the same way as the LPSA method, which is dependent on obscuration value for the analysis (Kowalenko & Babuin, 2013). While not completely overcoming these statistical issues (particularly at the upper size limits of 1–2 mm), in most studies a greater sample mass should be measured (10–20 g) in sieving than the example given above. In reality, in all of these methods there would be sand grains of a

range of values between 125 μm and 2 mm. These hypothetical scenarios only serve to highlight the relative difference in the statistical significance when measuring sand grains from small sample volumes in LPSA, relative to those of sieving. For example, a single 1062.5 μm grain (midpoint of the LSPA measurement range) would give a 0.18% value in a 0.9 g of LPSA sample (upper mass value measured on the LPSA in this study), whereas in sieving, a 1,125 μm grain (midpoint of sieve method) would be only 0.02% in a 10 g sample, a preferable lower limit of sieving in this study.

The above examples do not downplay that issues with statistical significance in the sieve and x− radiograph counting methods also exist, and limited sample volume is also likely to impact the reproducibility of the abundance of the >250 μm fraction. However, the above scenario highlights uncertainties that are potentially (but not always) an order of magnitude larger using the LPSA method, with the potential that this could create a noisier signal. To assess the relative impact of this, we conduct reproducibility experiments for both the LPSA and sieving methods, as well as the x−radiograph counting method (see Section 3.3).

In addition, all methods require the assessment of whether a grain in the designated IRD size fraction is authigenic, biogenic or volcanic in origin (Table 1). On its own, the LPSA method cannot reliably distinguish between such grains, and therefore this method requires confidence that dissolution of these biogenic components in both the fine and coarse fraction has been successfully conducted prior to analysis (see Section 3), and no diagenetic, volcanic or eolian particles are present. In sieve−based methods, the abundance of authigenic and biogenic material only needs to be removed from the coarse fraction (as IRD MAR and abundance is measured relative to the entire sediment population), and its presence and confirmation of successful removal can be readily assessed by microscope examination. Like the LPSA method, the sieve−based methods may also require independent analysis of the fine grain fraction, or assessment of the core face or x− radiographs to identify sediment facies, to understand the context in which the >250 μm fraction was deposited. That is, to determine whether processes such as gravity flows, wind−blown grains, or winnowing could enhance the abundance of the >250 μm size fraction independent of the flux of IRD.

Visually counting grains on x−radiographs or under the microscope, is potentially subject to operator−induced uncertainties through misidentification of IRD but has considerable advantages over other methods as it can measure the larger−outsized clasts. X−radiographs also have the substantial advantage in that they allow for continuous data to be produced downcore, in contrast to the discrete sampling required for sieve and LPSA methods (Grobe, 1987). It also readily allows for the identification of sedimentary structures that could indicate traction currents and sediment winnowing that would otherwise result in an overestimate of IRD content. Traditionally, the optimal method for creating x−radiograph images involves obtaining 1 cm thick slabs of the sediment core face (cf. Weber et al., 2014),

or opportunistic scanning of U−channel samples (cf., Cowan et al., 2008), as images obtained from a point source on half and whole round core often severely distort spatial measurements as the angle of the path x−rays take through the core will be highly variable, that is, a parallax effect (Croudace et al., 2006). This can result in difficulty in compiling a single composite image of a core derived from multiple x−ray measurements and can result in either the duplication, or deletion of objects near the edges of each image used to create the composite image (Figure 2). Finally, as this method commonly examines either a >1 or >2 mm fraction, the size being determined by that which can be reliably distinguished on x−radiograph images. Reliably picking these grains is dependent on the quality of the image and contrast in density of the grains relative to the background lithology. In addition, similar to the sample availability issues for sieving and LPSA, some cores may also lack statistical significance in cores where IRD abundance of >2 mm grains is relatively low. Therefore, this approach is more suitable to regions of intense iceberg rafting (Grobe, 1987; Weber et al., 2014).

Slab−based/U−channel sampling or line scan imaging largely overcomes the distortions inherent in imaging whole round cores with point−source x−rays. However, slab sampling is a (partially) destructive method, and where archive cores have already been sampled this is not an option. Nevertheless, these slabs/U−channels can subsequently be resampled for further analysis of the IRD or sediment (Cowan et al., 2008). Access to computed tomography (CT)−scan imaging is becoming increasingly accessible, and overcomes this obstacle (particularly on archive core halves) − but this is a computationally and financially expensive method, and not always logistically practical over hundreds of meters of drill core, or on legacy cores that have already been sampled. Finally, because this method commonly measures the gravel fraction (>2 mm), and some sediment cores, especially piston cores, have a narrow diameter (e.g., 66 mm for a standard Integrated Ocean Drilling

Program cores (IODP) piston core), larger grains are not going to be sampled (e.g., cobbles) and will either be pushed out of the way by the advanced piston corer (potentially resulting in significant coring disturbance), or result in incomplete recovery.

3. Materials and Methods

3.1. Core Sampling and Description

To conduct the comparisons of the three IRD abundance methods, two sediment gravity cores (11 cm diameter) RS15−LC42 and RS15−LC48 were obtained by the Korea Polar Research Institute (KOPRI) Icebreaker R/V Araon in 2014/15 (Figure 1) from contourite

drifts in 2,084 and 3,167 m water depth, respectively, in the Western Ross Sea. The cores were split, and visual core descriptions were undertaken aided by x-radiograph imaging (Jung et al., 2019; Ohneiser et al., 2019) and verified by quantitative grain size analysis using LPSA. For x-radiograph analysis, a 1-cm-thick, 8 × 30-cm slab was removed from the center of each split core section, placed within plastic plates and x- rayed. Discrete samples for sieve and LPSA were then collected from cores RS15-LC42 and RS15- LC48. RS15-LC48 was sampled approximately every 20 cm (total of 74 samples), and RS15-LC42 was sampled approximately every 10 cm (total of 121 samples). Each homogenized sample was subsampled for the sieve and LPSA analyses, and consequently each analysis for these methods is from identical depths. We intentionally selected cores for our IRD comparison study that are not ideal due to turbidite deposition and/or winnowing. However, because these processes are pervasive on the Antarctic continental margin records, we consider the chosen records to be the representative of a range of records used in IRD studies previously, and therefore relevant to defining the appropriate size-range cut-off and methods used to distinguish IRD. Consequently, the results presented in this study should not be used as records to define ice dynamics, unless further investigation of influences affecting concentration of the relevant size fraction is carried out. For broader assessment of the significance of different Antarctic continental margin depositional settings, we assess the differences in results from CT-scan x-radiographs, LPSA and sieving methods at two sites where IRD records have been previously published using either sieve or LPSA to assess reproducibility between methods in these settings. These settings include a levee setting at Integrated Ocean Drilling Program (IODP) Site U1361 (water depth 3,465 m) offshore from Adélie Land, where overbank spill from canyon-focused cascading water flows and turbidity currents, is separated by prolonged periods of hemipelagic and pelagic sedimentation, suspended sediment deposition from contour currents, and ice-rafting processes (Escutia et al., 2011; Patterson et al., 2014). At this site, it has previously been noted downslope currents are too weak to extensively winnow the fine fraction, and while coarse sand grains and clasts (>2 mm) are absent in sand laminae (Patterson et al., 2014; Wilson et al., 2018). We also sampled a continental rise contourite drift obtained by Ocean Drilling Program (ODP) Site 1165 offshore from Prydz Bay (water depth 3,537 m; Figure 1), which is characterized by mudstones with thin silt laminae influenced by contour currents, interbedded with bioturbated diatom rich muds deposited via hemipelagic processes (O'Brien et al., 2001; Passchier, 2011.). All depths used in this study used the IODP CSF-B depth scale (in meters below seafloor; mbsf), which corrects for core recovery exceeding 100% due to expansion (Escutia et al., 2011).

3.2. IRD Counting From X-Radiographs

For the RS15-LC42 and RS15-LC48 cores, lithogenic grains >2 mm in diameter were identified visually in x-radiographs from 1-cm thick slabs with an 8 cm width. The stratigraphic depth and a- axis length of each grain was recorded using a custom-made script in MatlabTM, and the number of grains >2 mm was then binned in 2 cm depth increments downcore, which results in a determination of number grains/16 cm 3 (Figure 2). Correlation of the counts provided by the two users is r = 0.961 and r = 0.927 for cores RS15-LC42 and RS15-LC48, respectively.

For the ODP 1165 and IODP 1361 cores, grains >2 mm along their a-axis were measured from a 1 cm thick "composite slice" of stacked CT scan images obtained from the archive half of each core using HOROS open source software and binned into 2 cm intervals. ODP and IODP piston cores have a diameter of 6.6 cm, which results in a determination of number grains/13.2 cm 3. However, in these cores, the two separate counts were conducted on composite slices that were offset by 5 mm (parallel to the core face) to assess reproducibility from slabs taken from different images within the CT-scan stack. Although the slabs are overlapping and ideally would have been offset by 1 cm, the round nature of the core meant a larger offset resulted in significant differences of the volume being measured. Correlation of the counts from these offset "slabs" provided by the two different users are r = 0.696 and r = 0.814 for cores IODP Site U1361 and ODP Site 1165, respectively. Where counts were different by more than four grains, these images were cross checked by each user, and in all cases verified to be real; for example, due to the presence of pebble nests/concentrations, or one large grain in one image containing multiple smaller grains in the other slab image.

These methodologies are broadly consistent with previous ship-based investigations of Antarctic continental margin sediments, with the abundance of material >2 mm considered an indicator of the content of IRD (Grobe, 1987). Two clast counts of the same x-radiographs for RS15- LC42 and RS15-LC48 were made by different operators to assess the influence of subjectivity (Figure 3). Subjectivity can arise from overlapping grains, or lower density grains occurring on a background of intense burrowing or lithological complexity (e.g., lenses of fine sand). An important point for obtaining reproducible results with this approach is that all operators are working with the same criterion for defining IRD. Without standardization of criteria it is inevitable that independent laboratory groups will generate different results depending on how they are trained to identify IRD. This "training" aspect will also influence automatic algorithm-based or machine-learning counting methods, which ideally have to be fine-tuned for any given site to account for different lithofacies, IRD grain density, overlapping grains, and core/x-radiograph quality. In this paper, the final IRD count data is an average of the two IRD count runs made by the two independent operators (Figure 3).

3.3. Sieve Analysis

Approximately 10−15 cm 3 of dry sample (oven dried at 50℃ for 24 hr) were initially weighed (~10−20 g) and then wet sieved at 250 μm. The >250 μm fraction was then dry sieved at 250 μm− 2 mm and weighed. Each sample was then visually checked under a stereo microscope for biogenic components (biogenic silica, CaCO3), and authigenic minerals. Removal of the biogenic component can potentially be determined by visual estimates through counting methods, but this adds a qualitative aspect to the IRD abundance calculation, when subtracting the biogenic percentages determined (Kanfoush et al., 2002; Murphy et al., 2002). This is because these estimates are volume− based, but the IRD abundance is weight−based, and as biogenic grains are composed of opal/ carbonate and are highly porous/hollow, they are often orders of magnitudes less dense than lithogenic grains, so a volume−based estimate will not be proportional to weight−based estimates (Murphy et al., 2002). In order to maintain consistency in the weight−based estimates via sieving, we physically/chemically treated the >250 μm fraction.

To remove foraminifera, the samples were treated with ~20 mL of 10% hydrochloric acid (HCl) for approximately 2 hr to dissolve CaCO3. Biogenic silica was removed from the coarse fraction by adding ~20 mL of 1M sodium hydroxide (NaOH) for a 72−hr period. The samples were heated in a water bath to 70℃ and occasionally stirred (Lewis & McConchie, 1994). The washed samples were then dried, and final weights recorded. On reobservation, it was clear that large robust radiolaria tests survived the 1M NaOH treatment. These were subsequently removed by crushing the dry >250 μm fraction with very gentle finger pressure between two pieces of paper and then re−sieved. This method successfully crushed the fragile radiolaria with no destruction of the lithological fraction.

Consequently, this may provide a much more rapid and more appropriate alternative (or pretreatment) to chemical dissolution of biogenic silica in the >250 μm fraction. However, it should be checked there are no fragile lithologies within the IRD fraction that could also be removed with this method. This is easily assessed through visual examination of the <250 μm fraction after sieving.

3.3.1. Reproducibility of Sieve Analyses

We also conducted reproducibility experiments on 25 samples from ODP Site 1165, with a volume of 10 cm 3 for each replicate sample (Figure 5g). The results show very high reproducibility with an R−value of 0.95. Although the residual plot (the difference between two independent analyses of the same samples) shows that there is greater variance at weight percentages above 6% (values range between 6% and 10%), no other systematic biases exist

in this distribution indicating good reproducibility is obtained by this method at this site. The greater variance at weight percentages above 6% suggest some statistical significance issues result from the presence of higher numbers of very coarse sands (>1 mm) in a relatively small sample size.

3.4. Laser Particle Size Analysis

3.4.1. Pretreatment and Analytical Procedure

Although some LPSA measurements are analytically limited to measuring 0.15−0.9 g of sediment in the mud−rich sediments of this study, prior to analysis we pre−treated 2 g of bulk sample to avoid biasing samples to minorlithological components (e.g., sand lenses or laminae). Processing of this amount of sample also readily allows for reproducibility experiments to be conducted. Biogenic carbonate was removed with 10% HCl for approximately two hours, and organic matter was subsequently removed by adding ~20 mL of 27% hydrogen peroxide (H2O2) to the bulk samples for a 72−hr period, heating them in a water bath at 70캯 (Lewis & McConchie, 1994), and then washed/centrifuged three times in 18MΩ water to remove the remaining H2O2 and reaction product. Visual examination of smear slides of the RS15−LC42 and RS15LC−48 samples reveals <20% biogenic silica content. Biogenic silica was removed by adding ~20 mL of 1M sodium hydroxide (NaOH) for a 72−hr period in a 70캯 water bath and occasionally stirring the samples (Lewis & McConchie, 1994). Smear slides were assessed to determine if biogenic silica dissolution was complete. The samples were washed in 18MΩ water and centrifuged at 4,700 ppm three times, and the supernatant was decanted and replaced with fresh 18 MΩ water following each of the treatments.

Prior to analysis the samples were subsampled (~0.15−0.9 g dependent on the mud content) to obtain an optimal laser obscuration (6%−14%) for the Beckman Coulter LS 13 320, with an aqueous liquid module (which circulates the sediment within a water volume of 1.25 L). The cone− and− quartering−method of dry, processed sediment was used for the subsampling (Lewis & McConchie, 1994). This technique involves mixing and evenly dividing the sample into smaller quantities, which ensures representative subsampling for the entire range of grain sizes. The subsamples were then dispersed in ~50 mL of 0.5 g/L sodium hexametaphosphate and agitated in a beaker placed in an ultrasonic bath for a minimum of 20 min. The samples were then immediately analyzed on the LPSA for 60 s, with no use of an ultrasonic probe, which could potentially damage sand grains.

The laser was re−aligned, and the background was measured before every sample, and the detector offset was measured every 30 min. The resulting measurements were converted to

grain size using the QuartzNatural.rf780d optical model, which assumes all material has a refractive index of quartz suspended in water. Glass bead informal standards (250, 68, and 24 μm modal sizes) were run at the beginning and end of every day to check the instrument was operating correctly.

3.4.2. Assessment of Biogenic Silica Removal

Biogenic silica measurements confirm smear slide observations that the biogenic silica content ranges between 10% and 17% by volume in these samples. Numerous samples in the sieve analysis indicated robust radiolarians >250 μm in size survived NaOH digestion and required physical removal by gentle crushing. However, weightbased estimates of coarse fractions are less likely to be biased by low abundances of sand-sized diatoms and radiolarians, as they have a very low density and weight compared to terrigenous grains. This is because diatom frustules and radiolaria tests are hollow compared to a grain of quartz and are composed of highly porous biosiliceous material. These can be readily examined and removed in sieve-based methods. Due to these large density differences, moderate amounts of radiolarians/diatoms will have minimal influences on the weight of the coarse fraction, but despite this we still recommend that sieve-based methods physically/chemically remove biogenic particles, rather than estimating the weight difference via volumetric based assessment from microscope counting. However, as the underlying measurements in LPSA are volume-based, even small amounts of biogenic silica could significantly impact measurements. Thus, successful removal from all size fractions should be carefully assessed when undertaking LPSA measurements.

Three samples from RS15-LC48 were analyzed in triplicate to assess the extent of opal dissolution with different concentrations of NaOH. The first set of subsamples was an untreated control sample; the second set of subsamples was treated with ~20 mL of 0.2 M NaOH solution (cf. Passchier, 2011); the third set with 1M NaOH (cf. Patterson et al., 2014). This concentration is a more aggressive treatment and was expected to more efficiently remove biogenic silica, but may also have the potential to damage some clay minerals (Carroll & Starkey, 1971; Müller & Schneider, 1993) which we discuss below.

Smear slides of each sample were examined under a microscope after treatment. All samples treated with 0.2 M NaOH contained common siliceous sponge spicule fragments and partially dissolved diatoms (Figure 4). Smear slides of the 1M NaOH treatment showed almost complete dissolution of biogenic silica with rare instances of wispy "spines" and diatom fragments. Scanning Electron Microscope (SEM) images also show only rare fragments of diatoms observed in the 1M NaOH treated samples, but with whole diatoms still present in the 0.2 M NaOH treated samples (Figure 4).

The concentration of NaOH used to digest biogenic silica has a large effect on the grain size frequency curves (Figure 4). Two of the samples treated with 0.2 M NaOH solution have a similar grain-size frequency distributions to that of 1M NaOH treatment, suggesting complete dissolution where the biogenic silica content in the bulk samples is relatively low (Figure 4). However, the results of sample 217-219 cmbsf indicate that more aggressive treatment was needed to completely remove biogenic silica from this sample (Figure 4). We also emphasize that the percentage of biogenic silica in the bulk sample alone may not be a reliable estimate for the strength of treatment required as some genera of diatoms and radiolaria are more susceptible to dissolution than others (Ryves et al., 2001). In our samples, the majority of biogenic silica dissolved with 0.2 and 1M NaOH treatment occurred in the fine-grained (<63 μm) fraction, which is consistent with the grain size distribution of biogenic silica particles in Antarctic margin sediments (Pudsey, 2002; Warner & Domack, 2002). The similarity of the 0.2 and 1.0 M results in the two samples with low observed biogenic silica (Figure 4) also indicate that for our samples the increased strength of 1M relative to 0.2 M NaOH treatment is not causing additional damage to clay minerals in these samples. However, there remains the possibility that clay minerals susceptible to NaOH leaching may completely have been dissolved at 0.2 M NaOH leaching, and thus this could add additional error when comparing %IRD relative to the total sediment population using the LPSA method relative to other methods.

We note there is a fining of grain size in the clay fraction between the NaOH-treated and untreated samples for all samples we treated. While this could result from breakdown of clay minerals or biogenic opal to a finer grain size, we view this as unlikely because the distributions are consistent between 0.2 and 1 M NaOH treatments. If biogenic opal or susceptible clay minerals were still present after 0.2 M NaOH treatment, additional breakdown/ dissolution would be expected in all samples with the stronger 1M treatment, but only the sample RS15-LC48, 217-219 cm showed this (Figure 4). Consequently, we propose the more likely cause of this fining is that smoothing procedures in LPSA software are designed to model log-normal distributions around specific modes (Blott & Pye, 2006). The dissolution of biogenic opal in the silt fraction results in a lower mode at that size range, and a broader-shaped distribution would be expected if that mode was muted after dissolution (see Section 3.4.3 for more details on these software considerations).

A final caveat here is that sand-sized biogenic silica may be more resilient to dissolution and is less likely to be observed on smear slides – a result that we also observed in the sieving procedure where radiolaria survived a 1M NaOH treatment. Therefore, periodic sieving of treated subsamples should be conducted in biogenic-rich sediments to assess if biogenic silica is present in samples otherwise to be analyzed by LPSA. Such radiolaria may account for the single outlier peak in the coarse sand fraction for the 1M NaOH experiment

in RS15-LC48 217-219 cm. However, in this particular sample such peaks are not seen in the untreated or the 0.2 M treated samples, and therefore this could represent a single-sand grain of 450 μm diameter in that one sub-sample.

3.4.3. Reproducibility Test of Laser Particle Size Analyzer in IRD-Bearing Sediment

To determine the reproducibility of the LPSA to characterize medium to coarse sand fraction in mud-rich samples, 18 repeat samples for RS15-42 and 16 repeat samples for RS15-48 were run, where each sample was subsampled into three aliquots (from dry samples) and analyzed in the LPSA after biogenic and organic treatment had been completed. Samples with material >125 μm (e.g., potential IRD) in size (Figures 5a and 5b) showed lower reproducibility. Samples with no >125 μm grains all showed good reproducibility (Figures 5c and 5d), suggesting poor sample homogeneity across subsamples is the main cause of poor reproducibility. Reproducibility of the <63 μm fraction was good in all samples (Figure 5), indicating that the low number of out-sized sand grains in mud-rich sediment on the LPSA is the cause of the poor reproducibility in the >125 μm fraction. Sample 10-12 cm in RS15-LC42 displayed high IRD values in sieve and x-radiograph analyses, but highly variable IRD values in the LPSA 125 μm-2 mm method. While Samples 1 and 2 have high 125 μm-2 mm values (7.7% and 11%, respectively), most of this size range in the LPSA data is on the shoulder of a well sorted sand mode at 110 μm, with no values >250 μm. However, Sample 3 in the replicate tests, shows two modes in the IRD fraction, at ~500 and 1000 μm, which likely represent outlier IRD grains. These outliers appear to have significantly affected the entire distribution of the <250 μm fraction (e.g., note widening of the distribution around the 110 μm mode). This is likely a function of the problems associated with the LPSA software models assuming a log-normal distribution (Blott & Pye, 2006), when the real sediment populations in glacial settings do not contain such a distribution, with potentially single occurrences of outlier grains in the coarse sand fraction being overestimated.

3.5. Statistical Tests

We use bivariate cross plots with linear fit regression models to assess relationships between the different methods and reproducibility. For LPSA and sieve data, each discrete sample was from identical depths (see Section 3.1), while for the x-radiograph data we re-binned the raw count data so that that bin edges matched the top and bottom depths of the discrete LPSA/sieve samples (Figure 6). Pearson pairwise linear correlation coefficients (R-values) are used to quantify goodness of fit. However, R-values should not be used in isolation, as R-values can be strongly influenced by outliers. This influence is evident in plots

of residual values against the linear fit model, which is a measure of the distance of a given data point from its predicted value based on the linear fit model. More confidence can be placed on correlation when high R−values coincide with a residual plot that forms a relatively random distribution of points above and below the 0−line value of residuals, with minimal outliers.

Linear regression lines are also calculated, and regression lines where the intercept passes closer to the origin are interpreted to demonstrate a better consistency between methods. This is because each method has different size ranges, and therefore assessment of the distance that regression lines intercept from the origin provides a measure of whether one method (and size cut−off) is less sensitive to the measuring of potential IRD than the other method; for example, the LPSA versus x−radiograph cross plots for RS15−LC42 and RS15−LC48 indicate the LPSA measurements more regularly show a complete absence of 125 μm−2 mm grains, where x−radiographs indicate >2 mm grains are present. Such a relationship results in the regression line intercepting above zero on the x−radiograph count axis and that the x−radiograph count is more sensitive at measuring IRD in these cores (Figure 7). This is also identifiable in the residual plot by a wide scatter of residual values at the intercept value on the fitted values axis. Such relationships provide insights into whether further investigation of the grain size distributions is required to determine if an over−estimate is picking up non−IRD (e.g., turbidite sands), or if the under−estimate is not sensitive enough to record IRD in a statistically significant manner (e.g., a small sample volume).

KOPRI 극지연구소

4. Comparison of the IRD Methods

The three published analytical methods compared in this study to determine the "coarse− grained" content for cores RS15−LC42 and RS15−LC48 all utilize different grain size limits to determine the IRD component. In this section, the apparent differences in IRD content attributable to using different size limits between these methods are quantified by comparing downcore variation between 125 μm and 2 mm (volume % using LPSA), 250 μm−2 mm (weight % by sieving) and >2 mm (clast counts in x−radiograph images) estimates.

4.1. RS15−LC42 Comparison of X−Radiograph, Sieve, and LPSA Methods

A qualitative visual assessment of RS15−LC42 shows a good comparison between all three methods in most sections of the core, but some sections show large discrepancies (Figure 6). For example, between 400 and 453 cmbsf and 720 and 760 cmbsf, the LPSA method is less consistent in registering higher values in the 125 μm−2 mm fraction than the more persistent elevated values evident in the sieve (250 μm−2 mm) and x−radiograph data (>2 mm; Figure 6). A linear regression model was applied to the cross plot of the various methods (Figure 7).

The strongest correlation coefficient value occurs in the sieve and LPSA regression (R−value = 0.758). However, the cross plot and residual plot also demonstrate there are some biases in this correlation, with a large number of LPSA >125 μm measurements yielding 0% when the sieve method contains up to 11% by weight in this size class (Figure 7), but low sieve values more generally correspond to low LPSA values. This indicates the LPSA more commonly underestimates the IRD fraction (as defined by the >125 μm fraction) at this site when compared to the sieve data IRD fraction (as defined by the >250 μm fraction). A near identical bias is observed in the comparison of LPSA versus x−radiograph counts (Figure 7), but some relatively high LPSA values also correspond to 0 values in x−radiograph counts. However, in general the LPSA versus x−radiograph method comparison also demonstrates a good correlation, but is lower (R−value = 0.527) than the LPSA versus sieve. The correlation of sieve versus x−radiograph data has an R−value of 0.677, while the residual plots demonstrate less bias in distributions, but the x−radiograph method may slightly underestimate IRD content because 0 values can correspond to sieve weights up to ~3%. Despite these biases, these results indicate the LPSA, sieve and x−radiograph methods are relatively consistent in identifying IRD grains at this site.

For some samples, the LPSA data indicate IRD presence, whereas the sieving analysis does not. However, grain size frequency distribution curves demonstrate the samples are mostly sandy silt, with some samples showing a well−sorted sand mode between ~63 and 100 μm. The coarse shoulder of this mode passes into the 125 μm fraction in numerous samples, but at sizes above 250 μm there is an irregular distribution of coarser particles (Figure 6).

4.2. RS15−LC48 Comparison of X−Radiograph, Sieve, and LPSA Methods

The qualitative visual assessment of RS15−LC48 size data also shows a reasonable comparison between all three methods but with intervals where there are large discrepancies. The LPSA method shows two anomalously high data points between 550 and 580 cmbsf, as well as an under−sensitivity to recording grains between 125 μm and 2 mm (e.g., 499−535 cmbsf), compared to the other two methods and their respective size fractions (Figure 6). The R−value of 0.175 demonstrates minimal correlation between the x−radiograph and LPSA methods and is also lower for the LPSA versus sieve comparison (R = 0.417) than for site RS15−LC42 (Figure 7). Residual plots for both of the cross plot comparisons to LPSA measurements show distinctly biased distributions caused by the LPSA 125 μm − 2 mm measurements consistently showing 0% values when the sieve and x−radiograph methods for estimating IRD (250 μm and 2 mm) indicate higher values (Figure 7).

Both cross comparisons with the LPSA indicate that the regression line intercept is

offset from the origin, further suggesting the LPSA is less sensitive to measuring potential IRD at this site, when compared to the sieve and x-radiograph methods. The sieve versus x-radiograph correlation at RS15-LC48 has the highest R-value of 0.608 with a gradient that passes close to the origin. The residual plots demonstrate less clear biases in the distributions, with an even distribution of residuals across a range of fitted values. This indicates the sieve and x-radiograph methods demonstrate a more reliable consistency in identifying potential IRD grains (as defined by various differences in size factions) at site RS15-LC48 than the LPSA.

As for RS-LC42, the LPSA data indicate IRD presence in some samples, whereas the sieving data indicate absence of IRD. Grain size frequency distribution curves for RS15-LC48 demonstrate the samples are mostly sandy silt, with some samples showing a well-sorted sand mode between ~63 and 100 μm. The shoulder of this mode passes into the 125 μm fraction, but this influence is greatly reduced when compared to RS15-LC42 distributions. At sizes above ~250 μm, there is an irregular distribution of coarse grained particles that is more consistent with a coarse tail distribution of IRD (Figure 6).

4.3. IODP Site U1361 Comparison of X-Radiograph, Sieve, and LPSA Methods

We analyzed sieve and LPSA data, as well as x-radiograph images from CT scans in the 130 to 146 mbsf interval of U1361 (Figure 8), which is stratigraphically below that studied by Patterson et al. (2014), but the range of facies and depositional processes appear similar (Escutia et al., 2011). Facies assemblages at IODP Site U1361 consist of finely laminated muds, massive and bioturbated muds, and are interpreted as representing deposition by non-erosive spill-over of low density turbidity currents or cascading water masses, as well as hemipelagic and bottom current influenced deposition (Escutia et al., 2011). The non-erosive, and gradual depositional nature of these spill-over deposits, alongside a relatively consistent sedimentation rate has allowed previous studies to use the IRD records at this site to infer past shifts in ice sheet dynamics (Patterson et al., 2014). Our datasets indicate a poor visual comparison between the sieve (250 μm-2 mm) and the LPSA (125 μm-2 mm) values (Figure 8). One sample was extremely high in all measurements (at 142.46 mbsf), and when included in the correlation analyses produced a high correlation value. However, when this one point is excluded (alongside a short 55 cm long interval that was u-channeled; Figure 8), the sieve versus LPSA correlations have an R-value of 0.3343, with a large number of LPSA measurements having 0 values when the sieving shows up to ~1.3%wt, and vice versa some high LPSA value coincide with low sieve values (Figure 8c). The grain size frequency distribution curves indicate samples contain well sorted sands with modes displaying shoulders that cross into the 125- 250 μm fraction. This is inconsistent with the "coarse tail"

distribution shown in the frequency curves from RS15-LC42 and RS15-LC48 (Figures 6 and 8b), and is more consistent with sand laminae deposition from an overbank levee turbidite (Strachan et al., 2016). The grain size frequency distribution also indicates most of the U1361 samples have a small, but persistent well sorted sand mode between 125 and 250 μm, with very few samples containing grains exceeding 250 μm in size. Such a mode is potentially more consistent with turbidite or other non-IRD origin. The LPSA data indicates that the shoulder of the well-sorted sand mode does extend marginally into >250 μm fraction, which could add a small amount of noise to the IRD estimates when using 250 μm as the lower limit cut-off in sieving. However, previous works have shown that the LPSA modeling assumption of a log-normal distribution is not always valid at these size ranges, and sieve data can show a more skewed distribution that do not extend as broadly into these coarser grain sizes (Blott & Pye, 2006). Consequently, while these LPSA software modeling artifacts will by default affect the LPSA estimates, they may not affect the sieve-based estimates. For samples where the influence of these shoulders is ambiguous in sieve data, visual or quantitative estimates of sorting in the coarse fraction could be used to assess if a non-IRD grain size populations is influencing the >250 μm fraction.

The CT-scan x-radiograph counts also showed the lowest reproducibly in the cores used in our study (Figure 3). As these counts were from profile "slices" taken at different (but overlapping) depths in the core face, and count numbers per 2 cm bin were often less than 2 grains, this suggests there may be a statistical significance issue with the small volume of sediment being measured in these 1 cm slabs, in combination with the relatively low concentration of IRD in this core example. With CT-scans, this issue could be potentially overcome by measuring a thicker composite slab through the entire core volume, which may result in overlapping grains being counted (particularly in automated methods), but in cores with low abundances, these could be visually assessed via secondary analysis of the 3D CT-scan images. The x-radiograph versus sieve method correlations are the strongest in the set of comparison ($r = 0.4476$), which is also apparent in visual examination of the datasets (Figure 8a). This statistical significance issue is evident in many x-radiograph count values being 0 when sieve estimates are sensitive to recording grains, alongside the different CT-scan composite slabs showing lower correlation ($r = 0.696$; Figure 3). The LPSA versus x-radiograph method correlation is the weakest ($r = 0.2163$).

4.4. ODP Site 1165 Comparison of X-Radiograph, Sieve, and LPSA Methods

Similar to U1361, we investigated sieve and LPSA data alongside CT-scan x-radiograph images at this site. We analyzed the 20 to 36 mbsf interval of ODP Site 1165 by sieving grains over 250 μm in diameter, for samples as close to the same depths for the

LPSA measurements presented by Passchier (2011) as remaining sample availability would allow. Despite a slight offset in some
samples, our datasets still indicate a very good visual correlation between our x-radiograph (>2 mm) and sieve (250 μm-2 mm) data, and the LPSA (125 μm-2 mm) results presented by Passchier (2011) (Figure 9). This is demonstrated by an R-value of 0.7 for sieve versus LPSA measurement. Compared to the other sites studied by us, the LPSA 125 μm-2 mm shows better consistency with the other methods in measuring coarse grained particles. Although there are still numerous samples that show 0% when sieving >250 μm gave values up to 2%, this bias is more subdued in the residual plot when compared to the other sites investigated in this study (Figure 9).

The CT-scan x-radiograph counts were binned to the same depths as LPSA and sieve samples, respectively, and also showed the higher reproducibly in this core compared to U1361. We interpret the higher correlation here in the CT-scan data to be the consequence of the higher gravel content resulting in this size fraction having higher statistically significance, which is also displayed by the higher correlation between the two counts for the CT-scan images (Figure 3). The x-radiograph versus sieve methods have a good correlation ($r = 0.515$), which is also apparent in visual examination of the datasets (Figure 9). The LPSA versus x-radiograph methods show the weakest correlation ($r = 0.385$). Despite these correlation values, the qualitative visual comparison appears strong between all three datasets, albeit with an increased sensitivity to measuring the coarse fraction between 125 μm and 2 mm when compared to the x-radiograph counts of grains >2 mm. This increased sensitivity is evidenced by the slope of the linear regression in the cross plot (Figure 9b). The residual and cross plots show less systematic biases when compared to the other sites in this study.

5. Discussion

5.1. Implications of Methodology on Estimating IRD Percentages

The results of this study indicate higher correlations between IRD percentage determined by sieve analysis (250 μm-2 mm) and visual clast counts using x-radiograph analysis (>2 mm). Although good correlations can also be clearly identified with the LPSA data and the other two methods in many cases, it generally displays a weaker relationship to the x-radiograph method (Figures 7-9). The grain size frequency distribution curves (Figures 6 and 8) show that the >125 μm fraction is potentially capturing the coarse-grained shoulder of well-defined modes in sandy silts and silty sands in the samples we analyzed. As discussed earlier, this well-defined mode is more consistent with turbidite silt/sand beds noted in the

visual descriptions of the U1361 core (Escutia et al., 2011). Although this fraction is undoubtebly capturing an IRD component, it is apparent that at such levee sites on the Adélie Land margin and contourite drifts in the Ross Sea, the >125 μm LPSA method may be overestimating the IRD component of sediments by incorporating part of a size mode likely deposited or concentrated by other processes. Consequently, although it may capture a significant IRD signal, it is also likely to result in a noisier signal.

Examining these distributions, the >250 μm fraction as measured by the LPSA instead could potentially reduce the spurious peaks associated with the shoulder of the sandy silts and silty sand modes. However, another key feature of the LPSA comparisons to the other two methods is that it also fails to regularly detect any sediment in this size fraction, whereas both sieve and X-radiograph analysis consistently show measurable amounts (Figures 6, 8 and 9). Our tests on LPSA measurements demonstrates high reproducibility in the mud to fine-sand fraction, but lower reproducibility for the >125 μm fraction due to the sample sizes being measured, and consequently raising the grain size threshold to 250 μm is not likely to resolve this issue.

The larger sample size of 10-15 cm 3 of dry sample (10-20 g) used for dry sieving appears to show that the 250 μm-2 mm grain size fraction at site 1165 (Figures 5g and 5h) has good statistical significance ($r = 0.95$), alongside better correlation to the x-radiograph data ($r = 0.45$, 0.51, 0.61, and 0.68) for cores IODP U1361, ODP site 1165, RS15-LC48, and RS15-LC42, respectively. The issue of subjectivity in x-radiograph counting could account for some of the differences with the sieving method, but also clast counts on x-radiographs may include low density "mud pellets" and diagenetic particles, that are either disaggregated or discarded in visual observations by the sieving method. Despite this caveat, in all of our studied sites there is consistency between sieve and x-radiograph methods, but less consistency between x-radiograph and LPSA methods. This suggests the sieve and x-radiograph methods have a higher signal-to-noise ratio than the LPSA method when attempting to quantify a size fraction that could be interpreted as IRD, although site- specific aspects regarding IRD concentrations and statistical significance of the 250 μm-2 mm and >2 mm fraction should also be considered in any assessment of these size fractions representing IRD. Additionally, defining if these coarse fractions are indeed ice rafted is a separate, but equally important consideration, and can only really be assessed in tandem with visual examination of the coarse fraction (i.e., volcanic, eolian, and biogenic origins) alongside assessment of the full grain size frequency distributions via LPSA analysis. In a continental margin setting there remains the possibility that any of the above methods could also record downslope processes, and the fine fraction and sedimentary descriptions/interpretation should be used to rule out mass flow and winnowing processes that could result in IRD being overestimated at any given core site. Geophysical datasets, such as seismic profiles and

multibeam bathymetry are also useful tools to assess the broad-scale sedimentary processes that could potentially deliver or rework coarse-grained material to any given site, and whether such processes have to be considered at a finer resolution by the core sedimentology. While our study is not explicitly defending whether the particular grain size fractions we examine indeed represent IRD, the datasets we present provide indicators that 125 μm may not always be suitable as a lower cut-off size limit for IRD in all depositional settings on the Antarctic margin. Almost all of the sites we examine with LPSA measurement display grain size frequency distributions that contain well-sorted coarse silt to fine sand modes, with shoulders of these modes passing into the >125 μm fraction. These are likely to be due to either the presence of bottom currents transporting fine sands in the bed load (e.g., RS15-LC42 and RS15-LC48), or due to delivery of sands via turbidity currents (e.g., IODP Site U1361; Figure 8). The strong visual comparison of the results from ODP Site 1165, and lack of systematic biases in the cross plots, indicate the contourite drifts at that site may be suitable for assigning a lower cut-off limit of 125 μm (e.g., Passchier, 2011). However, a key advantage of the CT-scan dataset is that it provides a far higher resolution dataset than either the sieve or LPSA methods (Figure 9). Assessment of the full frequency distribution range would be a useful tool, alongside measures of sorting (cf. Passchier, 2011; McCave & Andrews, 2019), to verify whether the LPSA is indeed a reliable assessment of the IRD content, but also to provide improved confidence that post-depositional winnowing is not concentrating IRD.

KOPRI 극지연구소

5.2. IRD Mass Accumulation Rates Versus Lag Deposits

All of the above methods also need to consider winnowing processes that may act to concentrate IRD. The sorting parameter [spread of the sizes around the mean (Folk & Ward, 1957)] of the terrigenous component using LPSA analyses has been used as evidence that winnowing process have resulted in concentration of coarser grained particles (Passchier, 2011; Patterson et al., 2014). It is assumed that if a peak in the IRD MAR coincides with a well-sorted terrigenous sand fraction, then these peaks may be caused by winnowing of fine-grained material due to high-energy bottom currents. For this assumption to hold, a comparison of the source sediment and the resultant sediment deposit must be made in order to identify the sedimentary transport process (e.g., winnowing), and thus, it is not possible to identify the depositional environment from a single parameter derived from the grain-size frequency distribution. This problem is exaggerated in glaciated margin settings, where grain size populations are commonly multimodal. These modes result from a range of sediment delivery processes, via gravity/traction currents, glacimarine outwash, hemipelagic settling, and ice rafting. Therefore, winnowing of muds with minor sands/gravels could result in a sediment

with a more even distribution of mud/sand and gravel and is therefore more poorly sorted than it was prior to winnowing.

Consequently, a more prudent approach to assess if the original IRD MAR is preserved in a stratigraphic section is to use a range of parameters determined from the grain-size frequency distribution, including mean grain size, skewness and sorting, alongside sedimentary structures of the deposit to assess for evidence of winnowing (McCave & Andrews, 2019; Rebesco et al., 2014). The presence of cross-laminae and scour features in silt and sandy silt beds in both RS15-LC42 and RS15-LC48 indicates that current velocities reached at least 23 cms $^{-1}$ that is required for movement of silt (McCave & Hall, 2006). However, while current-induced erosion has had some influence at both RS15 sites, sorting is consistently poor at both sites and shows no clear relationship to IRD content, suggesting that for most of the core there is no current influence on IRD content, but more careful attention is clearly warranted for specific intervals. We do not address this issue further in this paper, as the influence of bottom currents and distinguishing these from primary IRD deposition has been recently reviewed for glacial settings in detail by McCave and Andrews (2019), who recommend running correlation coefficients of fine fraction sorting versus IRD to more rigorously define downcore changes in this relationship.

KOPRI 극지연구소

6. Determining IRD Mass Accumulation Rates: Implications of Using Different Methodologies

Raw IRD abundance fractions are a critical component of determining IRD MAR, but the grain size cut-off values for determining IRD differ between methods, and as a result, the absolute abundances of IRD MAR calculated will also vary, making intercomparisons between methods problematic. However, the differences between methods also have significant implications for the calculations used to determine IRD MAR. All IRD MAR calculation methods require determination of Dry Bulk Density (DBD) and Linear Sedimentation Rates (LSR), and these are effectively uniform between methods. DBD values are often measured in much lower resolution than the IRD sample spacings, and thus DBD values are required to be interpolated to the IRD sample spacing, usually using the nearest neighbor approach (e.g., Patterson et al., 2014; St. John & Krissek, 1999). This may not be appropriate in cores where there is large amount lithological variation; although regression- based methods of the low resolution DBD data to linescan datasets (GRAPE Density; XRF) and facies distribution in a core could also be used to improve resolution. Similarly, LSRs are also dependent on resolution of the age model, and this can result in large artifacts when determining MARs and is likely to be the largest influence on uncertainties in IRD MARs. For example, short

duration magnetic reversals could amplify any sharp pulses in sedimentation that might otherwise be missed in longer duration polarity intervals, where the time averaging is longer and short phases with high sedimentation are muted by long periods with low background sedimentation rates. Consequently, caution should be exercised in interpretation of large pulses or baseline shifts of IRD MAR that coincide with paleomagnetic boundaries, as well as comparing IRD MAR curves between different sites that have age models of different resolution – as well as shifts in the quality of an age model down core. Again, a facies-based approach could help with identifying where sedimentation rates are likely to occur within polarity zones.

The above caveats exist for all determinations of MAR (including those of non-IRD variables), but the difference in methods in determining IRD MAR have some stand-alone considerations – in particular corrections for the presence of biogenic material. Consequently, we focus on the uncertainties in IRD MAR calculation that will result from using different methodological procedures. The sieve method captures the 250 μm-2 mm coarse sand percent and this can easily be visually checked for biogenic/diagenetic/volcanic ash content to determine the percent IRD within the 250 μm-2 mm fraction (St. John & Krissek, 1999). Consequently, the following equation:

1. IRD MAR = IRD × CS250 μm-2 mm × DBD × LSR

where the IRD MAR is in g/cm 2/kyr, CS250 μm-2 mm is the proportion of the 250 μm-2 mm grain-size fraction in respect to the bulk sediment (on a weight basis), DBD is in g/cm 3, and LSR is the interval average LSR in cm/kyr. In this method IRD is visually estimated and corrected for (used as a decimal fractional value in the above equation). Thus, this is only a qualitative estimate of the weight percent, which is compounded further by the biogenic material such as diatoms or radiolarians having a significantly lower density (i.e., they are porous and hollow) than detrital or authigenic grains.

In the sieve-based method of Patterson et al. (2014), and our study, biogenic silica and foraminifera were chemically treated from the 250 μm to 2 mm sand fraction only, which removes the potentially qualitative aspect of counting biogenic particles as a volumetric component and converting these to a weight estimate (see methods). Subsequent to chemical treatment, each sample was visually reexamined under a binocular microscope to check for fresh volcanic ash, clay aggregates, and

diagenetic minerals. These can either be visually corrected for, or a more conservative approach is to discard the samples. This allows for a simple modification of equation one.

2. IRD MAR = CSTerr250 μm-2 mm × DBD × LSR

where CS%Terr250 μm-2 mm is the proportion of the 250 μm-2 mm grain size fraction

weight in respect to the bulk sediment (on a weight basis), which is left after treatment to remove biogenic material. To determine the %>125 μm using the LPSA method, the entire bulk sediment is treated with 10% HCl, 27% H2O2 and 1M NaOH solution to remove biogenic particles and organic matter prior to measurement. This is an important distinction from the sieve method particle size range that only removes biogenic material from the >250 μm fraction. As NaOH treatment is suggested to have the potential to dissolve fine clays, an independent method for determining opal in the bulk sediment is often used. In this method, IRD MAR is calculated according to the methodology of Passchier (2011) with the following equation:

3. IRD MAR = CS125 μm−2 mm × TERR × DBD × LSR

Aside from the lower cut−off of 125 μm to calculate CS, and that it is based on volume percentage, the TERR is the terrigenous fraction calculated by subtraction of the %CaCO3 and %Biogenic silica from the bulk sediment fraction (i.e., the entire grain size distribution) as a weight percentage. The %CaCO3 and %Biogenic silica datasets are commonly at lower resolutions than grain size measurements and require interpolation between values or use regression−based methods (Passchier, 2011), introducing their own uncertainties, which are not propagated into the above calculation. While such uncertainties will be consistent within a given methodology, the use of different methodological approaches make comparison of IRD MAR between sites problematic. Another key uncertainty in this method is the assumption that %CS125μm−2 mm does not require correction for other non−IRD fraction. We discuss the possibility of other processes influencing this size fraction above, but volcanic ash, diagenetic minerals and other non−IRD particles could be present, and independent methods will be required to determine if these are present in a sediment population (Passchier et al., 2021). It could be argued this is also the case for x−radiograph based methods, although the 2 mm cut−off for defining an IRD grain means visual examination of the core face is likely to be sufficient for a trained operator to identify diagenetic grains and particles delivered by volcanic eruptive processes.

7. Conclusions

An assessment of the IRD content in several cores from the Antarctic margin was undertaken using the following three methodologies: (a) sieve analysis (250 μm−2 mm) providing IRD contents in weight percentage, (b) LPSA volume estimates of the 125 μm−2 mm fraction; and (c) visual counts of clasts exceeding 2 mm in size identified in x−radiographs. The sieve analysis and x−radiograph clast counts show a moderate−to−strong

correlation. The LPSA analysis and x- radiograph clast counts also display good correlations in some settings, but are in general weaker. The lower correlation values between IRD content determined by LPSA and other methods in most of the studied sites, suggests the LPSA method is less precise and less accurate with respect to measuring its respective size fraction used to determine IRD. We suspect that the primary reason for this is the very small sample size (~0.15-0.9 g) that is required for the correct obscuration of the laser particle sizer for samples of these lithologies. A consequence of the small sample size is that the coarse "tail" of the grain size distribution of a poorly sorted sandy mud may potentially be represented by relatively few grains. Further complicating this method is that the lower cut-off of 125 μm may also sample material that is not ice rafted in origin (e.g., turbidite sands).

The higher correlation of sieve-based estimates and X-radiograph counts for IRD appears to be a less noisy representation of the IRD component than the LPSA >125 μm method in the samples we examined from Antarctic continental margin sediments. However, this does not rule out the use of LPSA data in defining an IRD population in a sample, indeed in some settings such as ODP Site 1165 it correlated well. For all methods, we argue that careful assessment of the various caveats regarding sample processing and analysis, and depositional processes need to be conducted. While we suggest LPSA is a noisier signal, x-radiograph and sieve methods also suffer from potential statistical significance issues in some settings.

Regardless of the method used, careful assessment of grain size frequency distributions and parameters, in combination with robust sedimentary descriptions of structures and visual examination of the coarse fraction must be used before a selected size fraction can be deemed as ice rafted. The exact size fraction used to define IRD will vary depending on depositional setting, and due diligence must be conducted in each study location. Assessment of sedimentary structures or grain size frequency data that indicate sediment winnowing or delivery of coarse material (e.g., fine sand and greater) by non-ice rafting should be mandatory before designating sand particles as IRD. In addition, although the use of a single statistical parameter to assess the influence of deep- water seabed erosion on continental margin sedimentary sequences may be valid in some situations, it should be used with caution in sediments with multimodal grain size populations-sediments that are pervasive in glaciated margins. Our study highlights the importance of assessing methodological impacts on IRD abundance within different depositional settings on the Antarctic margin, and provides guidance for glaciated margin sediments to assess if outsized particles in a grain size population are likely to be ice rafted in origin.

KOPRI 극지연구소

남극 대륙경계부에서 빙하운반역의 동정과 수량화의 방법 비교

Robert McKay[1], Olga Albot[1], Gavin B. Dunbar[1], 이재일[2], 이민경[2], 유규철[2], 김성한[2], Nikita Turton[1,3], Denise Kulhanek[4], Molly Patterson[5], and Richard Levy[1,3]

[1]Victoria University of Wellington, [2]극지연구소, [3]GNS Science, [4]Institut für Geowissenschaften, Christian-Albrechts-Universität zu Kiel, [5]Binghamton University

요약: 심해 기록 빙하운반역 양의 정량화는 종종 빙상 불안정성과 해양 전복 순환 사이의 연결을 식별하기 위한 주요 프록시로 사용된다. 현재 심해 퇴적물 코어에서 IRD 함량을 결정하는 여러 가지 방법이 있다. 주어진 방법에 대한 선호도는 종종 코어 시료 자료에 대한 접근성과 어떤 방법의 파괴적인 특성에 따라 결정된다. 많은 연구가 빙하운반역과 빙상 역학을 연결할 때의 주의 사항에 대해 논의했지만 방법론적 접근과 관련된 불확실성은 특히 남극의 경우 빙하운반역 데이터 세트 간의 해석 또는 비교에서 고려되지 않는 경우가 많다. 이를 해결하기 위해 이 연구에서는 빙하운반역의 양을 계산하는 세 가지 독립적인 방법론을 비교하고 서로 다른 접근 방식이 질량 축적률 결정에 어떤 영향을 미치는지 논의한다. 여기서 다루는 세 가지 방법론은 다음과 같다: x-선 사진에서 2mm 이상의 입자를 세는 것; 체질하여 중립질~조립질 모래 (250μm- 2mm)의 중량 백분율을 구하는 ; 레이저 회절 입자 분석기를 이용하여 125 μm 보다 큰 모래의 부피를 추정하는 것. x-선 사진 및 체질 방법은 비슷한 결과를 나타내는 반면, 레이저 입자 크기 분석은 대부분의 위치에서 비슷한 장기적 신호를 보여주지만 일반적으로 다른 두 방법과 상관 관계가 낮기 때문에 신뢰할 수 없는 신호를 얻을 가능성이 더 높다. 모든 방법과 관련된 주의 사항에 대해 논의한 결과 코어가 IRD 연구에 적합한지, 모래 또는 자갈 함량이 빙하운반역 함량을 정확하게 반영하는지 평가하기 위해서 이상적으로 여러 방법의 조합을 사용해야 한다.

참고 문헌

Amante, C., & Eakins, B. W. (2009). ETOPO1 Global Relief Model converted to PanMap layer format [Data set]. NOAA-National Geophysical Data Center.

Anderson, J. B. (1999). Antarctic marine geology. UK: Cambridge University Press.

Andrews, J. (2000). Icebergs and iceberg rafted detritus (IRD) in the North Atlantic: Facts and assumptions. Oceanography, 13(3), 100-108.

Andrews, J. T., & Voelker, A. H. L. (2018). "Heinrich events" (& sediments): A history of terminology and recommendations for future usage. Quaternary Science Reviews, 187, 31-40.

Bassis, J. N., Petersen, S. V., & MacCathles, L. (2017). Heinrich events triggered by ocean forcing and modulated by isostatic adjustment. Nature, 542(7641), 332-334.

Blott, S. J., & Pye, K. (2006). Particle size distribution analysis of sand-sized particles by laser diffraction: An experimental investigation of instrument sensitivity and the effects of particle shape. Sedimentology, 53(3), 671-685.

Bond, G., Heinrich, H., Broecker, W., Labeyrie, L., McManus, J., Andrews, J., et al. (1992). Evidence for massive discharges of icebergs into the North Atlantic ocean during the last glacial period. Nature, 360(6401), 245-249.

Carroll, D., & Starkey, H. C. (1971). Reactivity of clay minerals with acids and alkalies. Clays and Clay Minerals, 19(5), 321333.

Carter, L., Neil, H. L., & Northcote, L. (2002). Late Quaternary ice-rafting events in the SW Pacific Ocean, off eastern New Zealand. Marine Geology, 191(1-2), 19-35.

Chewings, J. M., Atkins, C. B., Dunbar, G. B., & Golledge, N. R. (2014). Aeolian sediment transport and deposition in a modern high-latitude glacial marine environment. Sedimentology, 61(6), 1535-1557

Clark, P. U., & Pisias, N. G. (2000). Interpreting iceberg deposits in the deep sea. Science, 290(5489), 51-52. Conolly, J. R., & Ewing, M. (1965). Ice-rafted detritus as a climatic indicator in Antarctic deep-sea cores. Science, 150(3705), 1822-1824

Cook, C. P., Hill, D. J., van de Flierdt, T., Williams, T., Hemming, S. R., Dolan, A. M., et al. (2014). Sea surface temperature control on the distribution of far-traveled Southern Ocean ice-rafted detritus during the Pliocene. Paleoceanography, 29(6), 2014PA002625.

Cowan, E. A., Hillenbrand, C.-D., Hassler, L. E., & Ake, M. T. (2008). Coarse-grained terrigenous sediment deposition on continental rise drifts: A record of Plio-Pleistocene glaciation on the Antarctic Peninsula. Palaeogeography, Palaeoclimatology, Palaeoecology, 265(3), 275-291.

KOPRI 극지연구소

Cowan, E. A., Zellers, S. D., Müller, J., Walczak, M. H., Worthington, L. L., Caissie, B. E., et al. (2020). Sediment controls dynamic behavior of a Cordilleran Ice Stream at the last glacial maximum. Nature Communications, 11(1), 1826.

Croudace, I. W., Rindby, A., & Rothwell, R. G. (2006). Itrax: Description and evaluation of a new multi− function X−radiograph core scanner. Geological Society, London, Special Publications, 267(1), 51−63.

DeConto, R., Pollard, D., & Harwood, D. (2007). Sea ice feedback and Cenozoic evolution of Antarctic climate and ice sheets. Paleoceanography, 22, PA3214.

Depoorter, M. A., Bamber, J. L., Griggs, J. A., Lenaerts, J. T. M., Ligtenberg, S. R. M., van den Broeke, M. R., & Moholdt, G. (2013). Calving fluxes and basal melt rates of Antarctic ice shelves. Nature, 502, 89−92.

Diekmann, B. (2007). Sedimentary patterns in the late Quaternary Southern Ocean. Deep Sea Research Part II: Topical Studies in Oceanography, 54(21), 2350−2366.

Diekmann, B., Fütterer, D. K., Grobe, H., Hillenbrand, C. D., Kuhn, G., Michels, K., et al. (2003). Terrigenous sediment supply in the polar to temperate South Atlantic: Land−ocean links of environmental changes during the late quaternary. In G.Wefer, S.Mulitza, & V.Ratmeyer (Eds.), The South Atlantic in the late Quaternary: Reconstruction of material budgets and current systems (pp. 375−399). Berlin, Heidelberg: Springer.

Donda, F., Brancolini, G., O'Brien, P. E., De Santis, L., & Escutia, C. (2007). Sedimentary processes in the Wilkes Land margin: A record of the Cenozoic East Antarctic Ice Sheet evolution. Journal of the Geological Society, 164(1), 243−256.

Dowdeswell, J. A., Elverhøi, A., Andrews, J. T., & Hebbeln, D. (1999). Asynchronous deposition of ice− rafted layers in the Nordic seas and north Atlantic Ocean. Nature, 400(6742), 348−351.

Ehrmann, W. U., & Grobe, H. (1991). Cyclic sedimentation at sites 745 and 746. Proceedings of the Ocean Program, Scientific Results, ODP, Kerguelen Plateau−Prydz Bay, 119, 225−237.

Escutia, C., Brinkhuis, H., & Klaus, A. (2011). Proceedings of the Ocean Drilling Program, Expedition 318, Wilkes Land Glacial History. Retrieved from http://publications.iodp.org/proceedings/318/318title.html

Escutia, C., Warnke, D., Acton, G. D., Barcena, A., Burckle, L., Canals, M., & Frazee, C. S. (2003). Sediment distribution and sedimentary processes across the Antarctic Wilkes Land margin during the Quaternary. Deep Sea Research Part II: Topical Studies in Oceanography, 50(8−9), 1481−1508.

Evans, J., & Pudsey, C. J. (2002). Sedimentation associated with Antarctic Peninsula ice shelves: Implications for palaeoenvironmental reconstructions of glacimarine sediments.

KOPRI 극지연구소

Journal of the Geological Society, 159(3), 233-237.

Flückiger, J., Knutti, R., & White, J. W. C. (2006). Oceanic processes as potential trigger and amplifying mechanisms for Heinrich events. Paleoceanography, 21(2).

Folk, R. L., & Ward, W. C. (1957). Brazos River bar [Texas]; a study in the significance of grain size parameters. Journal of Sedimentary Research, 27(1), 3-26.

Gilbert, R. (1990). Rafting in glacimarine environments. Geological Society, London, Special Publications, 53(1), 105-120.

Golledge, N. R., Menviel, L., Carter, L., Fogwill, C. J., England, M. H., Cortese, G., & Levy, R. H. (2014). Antarctic contribution to meltwater pulse 1A from reduced Southern Ocean overturning. Nature Communications, 5.

Grobe, H. (1987). A simple method for the determination of ice-rafted debris in sediment cores. Polarforschung, 57, 123-126.

Grobe, H., & Mackensen, A. (1992). Late Quaternary climatic cycles as recorded in sediments from the Antarctic continental margin. Antarctic Research Series - American Geophysical Union, 56, 349-376.

Hansen, M. A., Passchier, S., Khim, B.-K., Song, B., & Williams, T. (2015). Threshold behavior of a marine-based sector of the East Antarctic Ice Sheet in response to early Pliocene ocean warming. Paleoceanography, 30(6), 2014PA002704.

Heinrich, H. (1988). Origin and consequences of cyclic ice rafting in the Northeast Atlantic Ocean during the past 130,000 years. Quaternary Research, 29(2), 142-152.

Hemming, S. R. (2004). Heinrich events: Massive late Pleistocene detritus layers of the North Atlantic and their global climate imprint. Reviews of Geophysics, 42(1).

Hepp, D. A., Mörz, T., & Grützner, J. (2006). Pliocene glacial cyclicity in a deep-sea sediment drift (Antarctic Peninsula Pacific Margin). Palaeogeography, Palaeoclimatology, Palaeoecology, 231(1-2), 181-198.

Hillenbrand, C.-D., & Fütterer, D. (2001). Neogene to Quaternary deposition of opal on the continental rise west of the Antarctic Peninsula, ODP Leg 178, Sites 1095, 1096, and 1101. In P. F.Barker, A.Camerlenghi, G. D.Acton, & A. T. S.Ramsay (Eds.), Proceedings of the Ocean Drilling Program Science Results (Vol. 1, p. 178).

Hillenbrand, C.-D., Fütterer, D., Grobe, H., & Frederichs, T. (2002). No evidence for a Pleistocene collapse of the West Antarctic Ice Sheet from continental margin sediments recovered in the Amundsen Sea. Geo-Marine Letters, 22(2), 51-59.

Hillenbrand, C.-D., Kuhn, G., & Frederichs, T. (2009). Record of a Mid-Pleistocene depositional anomaly in West Antarctic continental margin sediments: An indicator for ice-sheet collapse?Quaternary Science Reviews, 28(13-14), 1147-1159.

Hulbe, C. L., MacAyeal, D. R., Denton, G. H., Kleman, J., & Lowell, T. V. (2004). Catastrophic ice shelf breakup as the source of Heinrich event icebergs.

Paleoceanography, 19(1).

Jansen, E., Fronval, T., Rack, F., & Channell, J. E. T. (2000). Pliocene–Pleistocene ice rafting history and cyclicity in the Nordic Seas during the last 3.5 Myr. Paleoceanography, 15(6), 709–721.

Jung, J., Park, Y., Lee, K., Hong, J.–P., Lee, J., Yoo, K., et al. (2019). Clay Mineralogical characteristics and origin of sediments deposited during the Pleistocene in the Ross Sea, Antarctica. Journal of the Mineralogical Society of korea, 32(3), 163–172.

Kanfoush, S. L., Hodell, D. A., Charles, C. D., Guilderson, T. P., Mortyn, P. G., & Ninnemann, U. S. (2000). Millennial–scale instability of the Antarctic ice sheet during the last glaciation. Science, 288(5472), 1815–1819.

Kanfoush, S. L., Hodell, D. A., Charles, C. D., Janecek, T. R., & Rack, F. R. (2002). Comparison of ice– rafted debris and physical properties in ODP Site 1094 (South Atlantic) with the Vostok ice

core over the last four climatic cycles. Palaeogeography, Palaeoclimatology, Palaeoecology, 182(3), 329–349.

King, M. V., Gales, J. A., Laberg, J. S., McKay, R. M., De Santis, L., Kulhanek, D. K., et al. (2022). Pleistocene depositional environments and links to cryosphere–ocean interactions on the eastern Ross Sea continental slope, Antarctica (IODP Hole U1525A). Marine Geology, 443, 106674.

Kowalenko, C. G., & Babuin, D. (2013). Inherent factors limiting the use of laser diffraction for determining particle size distributions of soil and related samples. Geoderma, 193–194, 22–28.

Lamy, F., Arz, H. W., Kilian, R., Lange, C. B., Lembke–Jene, L., Wengler, M., et al. (2015). Glacial reduction and millennial–scale variations in Drake Passage throughflow. Proceedings of the National Academy of Sciences, 112(44), 13496–13501. pnas.1509203112

Lewis, D. W., & McConchie, D. (1994). Practical sedimentology (2nd Ed.), New York: Chapman and Hall. Retrieved from https://trove.nla.gov.au/version/44779937

Li, G., & Piper, D. J. W. (2015). The influence of meltwater on the Labrador current in Heinrich event 1 and the Younger Dryas. Quaternary Science Reviews, 107, 129–137.

Liu, Y., Moore, J. C., Cheng, X., Gladstone, R. M., Bassis, J. N., Liu, H., et al. (2015). Ocean–driven thinning enhances iceberg calving and retreat of Antarctic ice shelves. Proceedings of the National Academy of Sciences, 112(11), 3263–3268.

Lucchi, R. G., Rebesco, M., Camerlenghi, A., Busetti, M., Tomadin, L., Villa, G., et al. (2002). Mid–late Pleistocene glacimarine sedimentary processes of a high–latitude, deep–sea sediment drift (Antarctic Peninsula Pacific margin). Marine Geology, 189(3–4), 343–370.

KOPRI 극지연구소

Marcott, S. A., Clark, P. U., Padman, L., Klinkhammer, G. P., Springer, S. R., Liu, Z., et al. (2011). Ice− shelf collapse from subsurface warming as a trigger for Heinrich events. Proceedings of the National Academy of Sciences, 108(33), 13415−13419.

McCave, I. N., & Andrews, J. T. (2019). Distinguishing current effects in sediments delivered to the ocean by ice. I. Principles, methods and examples. Quaternary Science Reviews, 212, 92−107.

McCave, I. N., & Hall, I. R. (2006). Size sorting in marine muds: Processes, pitfalls, and prospects for paleoflow−speed proxies. Geochemistry, Geophysics, Geosystems, 7(10). McKay, R. M., Albot, O. B., Dunbar, G. B., Lee, J. I., Lee, M. K., Yoo, K.−C., et al. (2020). Ice rafted debris proxies for

sediment cores RS15−LC42, RS15−LC48, IODP Site 318−U1361 and ODP Site 118−1165. [Dataset]. PANGAEA. https://doi.org/10.1594/PANGAEA.920653dataset

McKay, R. M., De Santis, L., Kulhanek, D. K., & IODP Expedition 374 Science Team. (2019). Proceedings of the International Ocean Discovery Program, 374.

Müller, P. J., & Schneider, R. (1993). An automated leaching method for the determination of opal in sediments and particulate matter. Deep Sea Research Part I: Oceanographic Research Papers, 40(3), 425−444.

Murphy, L., Warnke, D. A., Andersson, C., Channell, J., & Stoner, J. (2002). History of ice rafting at South Atlantic ODP site 177−1092 during the Gauss and late Gilbert Chrons. Palaeogeography, Palaeoclimatology, Palaeoecology, 182(3−4), 183−196.

Nielsen, S. H. H., Hodell, D. A., Kamenov, G., Guilderson, T., & Perfit, M. R. (2007). Origin and significance of ice−rafted detritus in the Atlantic sector of the Southern Ocean. Geochemistry, Geophysics, Geosystems, 8(12), Q12005.

O'Brien, P.E., Cooper, A.K., Richter, C., & the Shipboard Scientific Party. (2001). Proceedings of the Ocean Drilling Program, Initial Reports (Vol. 188). College Station, TX (Ocean Drilling Program).

Ó Cofaigh, C., & Dowdeswell, J. A. (2001). Laminated sediments in glacimarine environments: Diagnostic criteria for their interpretation. Quaternary Science Reviews, 20(13), 1411−1436.

Ó Cofaigh, C., Dowdeswell, J. A., & Pudsey, C. J. (2001). Late Quaternary iceberg rafting along the Antarctic Peninsula continental rise and in the Weddell and Scotia seas. Quaternary Research, 56(3), 308−321.

Ohneiser, C., Yoo, K.−C., Albot, O. B., Cortese, G., Riesselman, C., Lee, J. I., et al. (2019). Magneto− biostratigraphic age models for Pleistocene sedimentary records from the Ross Sea. Global and Planetary Change, 176, 36−49.

Passchier, S. (2011). Linkages between East Antarctic ice sheet extent and Southern Ocean temperatures based on a Pliocene high−resolution record of ice−rafted debris off

Prydz Bay, East Antarctica. Paleoceanography, 26, 13 PP.

Passchier, S., Hansen, M. A., & Rosenberg, J. (2021). Quartz grain microtextures illuminate Pliocene periglacial sand fluxes on the Antarctic continental margin. The Depositional Record, 7(3), 564– 581.

Patterson, M. O., McKay, R., Naish, T., Escutia, C., Jimenez-Espejo, F. J., Raymo, M. E., et al. (2014). Orbital forcing of the east Antarctic ice sheet during the Pliocene and early Pleistocene. Nature Geoscience, 7(11), 841–847.

Powell, R., & Domack, G. W. (2002). 12–modern glaciomarine environments. In J.Menzies (Ed.), Modern and past glacial environments (pp. 361–389). Oxford: Butterworth–Heinemann.

Pudsey, C. J. (2002). Neogene record of Antarctic Peninsula glaciation in continental rise sediments: ODP Leg 178, site 1095. Proceedings of the Ocean Drilling Program: Scientific Results, 178, 1– 25.

Rackow, T., Wesche, C., Timmermann, R., Hellmer, H. H., Juricke, S., & Jung, T. (2017). A simulation of small to giant Antarctic iceberg evolution: Differential impact on climatology estimates. Journal of Geophysical Research: Oceans, 122, 3170–3190.

Rawle, A. F. (2015). Representative sampling – another Cinderella of particle size analysis. Procedia Engineering, 102, 1707–1713.

Rebesco, M. (2003). Data report: Numerical evaluation of diffuse spectral reflectance data and correlation with core photos, ODP Site 1165, Wild Drift, Cooperation Sea, Antarctica. In A. K.Cooper, P. E.O'Brien, & C.Richter (Eds.), Proceedings of the Ocean Drilling Program: Scientific Results (Vol. 188).

Rebesco, M., Hernández-Molina, F. J., Van Rooij, D., & Wåhlin, A. (2014). Contourites and associated sediments controlled by deep–water circulation processes: State–of–the–art and future considerations. Marine Geology, 352, 111–154.

Ruddiman, W. F. (1977). Late Quaternary deposition of ice–rafted sand in the subpolar North Atlantic (lat 40° to 65갾). GSA Bulletin, 88(12), 1813–1827.

Ryves, D. B., Juggins, S., Fritz, S. C., & Battarbee, R. W. (2001). Experimental diatom dissolution and the quantification of microfossil preservation in sediments. Palaeogeography, Palaeoclimatology, Palaeoecology, 172(1), 99–113.

St John, K., & Krissek, L. A. (1999). Regional patterns of Pleistocene ice–rafted debris flux in the North Pacific. Paleoceanography, 14(5), 653–662.

St John, K., Passchier, S., TantillO, B., Darby, D., & Kearns, L. (2015). Microfeatures of modern sea– ice–rafted sediment and implications for paleo–sea–ice reconstructions. Annals of Glaciology, 56(69), 83–93.

Starr, A., Hall, I. R., Barker, S., Rackow, T., Zhang, X., Hemming, S. R., et al. (2021). Antarctic icebergs reorganize ocean circulation during Pleistocene glacials. Nature,

589(7841), 236-241.

Strachan, L. J., Bostock, H. C., Barnes, P. M., Neil, H. L., & Gosling, M. (2016). Non-cohesive silt turbidity current flow processes; insights from proximal sandy-silt and silty-sand turbidites, Fiordland, New Zealand. Sedimentary Geology, 342, 118-132.

Stuart, K. M., & Long, D. G. (2011). Tracking large tabular icebergs using the SeaWinds Ku-band microwave scatterometer. Deep Sea Research Part II: Topical Studies in Oceanography, 58(11), 1285-1300.

Talarico, F. M., McKay, R. M., Powell, R. D., Sandroni, S., & Naish, T. (2012). Late Cenozoic oscillations of Antarctic ice sheets revealed by provenance of basement clasts and grain detrital modes in ANDRILL core AND-1B. Global and Planetary Change, 96(97), 23-40.

Teitler, L., Warnke, D. A., Venz, K. A., Hodell, D. A., Becquey, S., Gersonde, R., & Teitler, W. (2010). Determination of Antarctic Ice Sheet stability over the last ~500 ka through a study of iceberg- rafted debris. Paleoceanography, 25(1).

Tournadre, J., Bouhier, N., Girard-Ardhuin, F., & Rémy, F. (2016). Antarctic icebergs distributions 1992-2014. Journal of Geophysical Research: Oceans, 121(1), 327-349.

Tulaczyk, S., Kamb, B., Scherer, R. P., & Engelhardt, H. F. (1998). Sedimentary processes at the base of a West Antarctic ice stream; constraints from textural and compositional properties of subglacial debris. Journal of Sedimentary Research, 68(3), 487-496.

Warner, N. R., & Domack, E. W. (2002). Millennial- to decadal-scale paleoenvironmental change during the Holocene in the Palmer Deep, Antarctica, as recorded by particle size analysis. Paleoceanography, 17, PAL-5.

Weber, M. E., Clark, P. U., Kuhn, G., Timmermann, A., Sprenk, D., Gladstone, R., et al. (2014). Millennial-scale variability in Antarctic ice-sheet discharge during the last deglaciation. Nature, 510(7503), 134-138.

Williams, T., & Handwerger, D. (2005). A high-resolution record of early Miocene Antarctic glacial history from ODP Site 1165, Prydz Bay. Paleoceanography, 20(2), PA2017.

Williams, T., van de Flierdt, T., Hemming, S. R., Chung, E., Roy, M., & Goldstein, S. L. (2010). Evidence for iceberg armadas from East Antarctica in the Southern Ocean during the late Miocene and early Pliocene. Earth and Planetary Science Letters, 290(3-4), 351-361.

Wilson, D. J., Bertram, R. A., Needham, E. F., Flierdtvan de, T., Welsh, K. J., McKay, R. M., et al. (2018). Ice loss from the East Antarctic Ice Sheet during late Pleistocene interglacials. Nature, 561, 383-386.

KOPRI 극지연구소

Table 1. Summary of IRD Methods Examined in This Study, Alongside Benefits, and Caveats for Each Method as Discussed in the Main Text

Method	Size range measured	Type of measurement	Comments
Laser Particle Sizer Analysis	125 μm–2 mm	Volume	Analytical restrictions for sample masses (~<1 g) in mud-rich samples reduces statistical significance of coarse sand fraction.
			Requires effective dissolution of biogenic opal/carbonate, and other non-IRD components from all size fractions prior to measurement. To determine Mass Accumulation Rates, these components have to be quantified using other estimates.
			Measures entire size fraction, and frequency distribution curves can be used to assess if >125 μm fraction is distinct from other sediment populations (e.g., well-sorted sands).
			Relatively rapid method, although chemical dissolution methods of entire sediment population can be time consuming.
Sieve	250 μm–2 mm	Weight	Sample availability from core material is generally 10–20 g (but could be larger if needed), and statistical significance of coarse sand fraction will reduce with sample size.
			Requires removal of biogenic opal/carbonate, and other non-IRD components from 250 μm to 2 mm fraction prior to weighing. No subsequent corrections are required for the IRD component of the Mass Accumulation Rates calculation.
			Only measures <250 μm and 250 μm–2 mm fractions, and requires additional frequency distribution analysis (esp., LPSA) to confirm if 250 μm–2 mm fraction is distinct from non-IRD populations.
			Relatively rapid method. Chemical dissolution/ physical removal of biogenic material only required on 250 μm–2 mm fraction (e.g. centrifuging is not required), but requires supporting LPSA and processing time (see above).
X-radiograph count	>2 mm	Count	Statistical significance is dependent on concentration/ size of IRD in core, and the core diameter.
			Correction for biogenic opal is not required, as this is generally less than 2 mm, while large biogenic carbonate particles are unlikely to be counted as IRD.
			Other non-IRD components (ash, diagenetic minerals) could be potentially counted as IRD.
			No subsequent corrections are required for the IRD component of the Mass Accumulation Rates calculation. Some user-based subjectively in identifying IRD, and size cut-off used is dependent on image quality, grain density, and contrast with background sediment. These will vary from core to core, as well as across facies variations within a core.
			X-radiograph images can be used to assess for winnowing, or other deposition processes that could account for >2 mm grains in the core.
			Rapid, potentially non-destructive method, but requires consistent training and cross validation between two (or more) users.

KOPRI 극지연구소

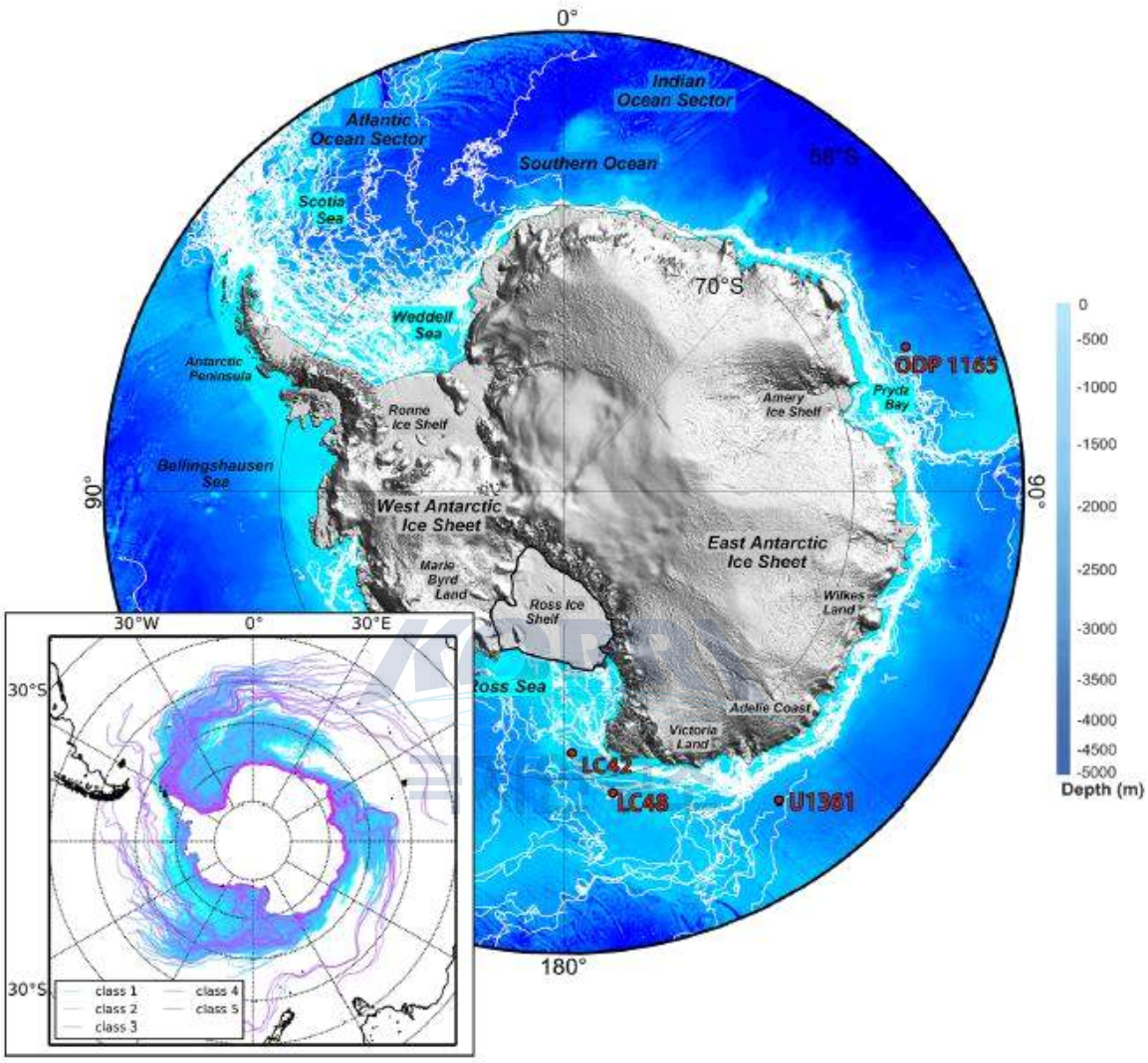


Figure 1. Map of the Antarctic continent and offshore bathymetry showing sites in this study. White lines around the Antarctic continent depict modern iceberg (>5 km 2) tracks between 1999 and 2009 (Stuart & Long, 2011). Topography and bathymetry derived from the ETOPO1 global relief model (Amante & Eakins, 2009). Insert: 12 years simulation of modeled trajectories of small (class 1 = <1 km 2 surface area) to large (class 5 = >1,000 km 2 surface area) icebergs (from: Rackow et al., 2017).

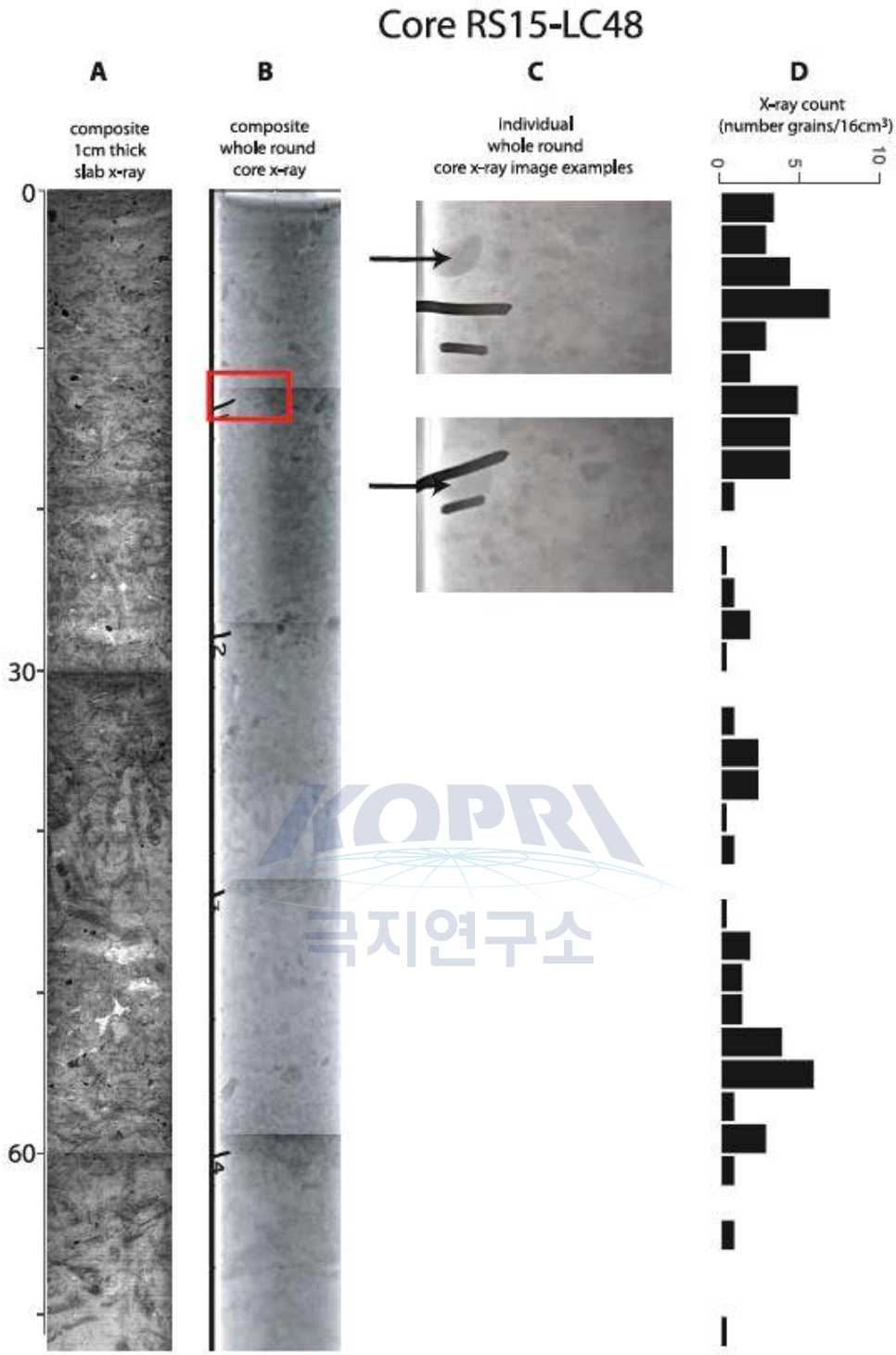


Figure 2. Representative example of X-radiograph images and counting results from RS15-LC48. (a) Composite image of separate 30 cm long x-radiograph of a 1-cm thick slab; (b) Composite X-radiograph from the whole round core. Reference markers (labeled 1-5) were placed every 15 cm on the core liner. These markers remained constant, while the core was moved relative to the x-ray source to obtain each image collected. (c) Zoom of separate images taken from whole round core (red box in b), with black arrows showing distortion of the image and apparent movement of a clast relative to the reference marker. (d) Counts of clasts >2 mm along the a-axis, as measured on the 1-cm x-radiograph "slab" images, binned into 2 cm intervals.

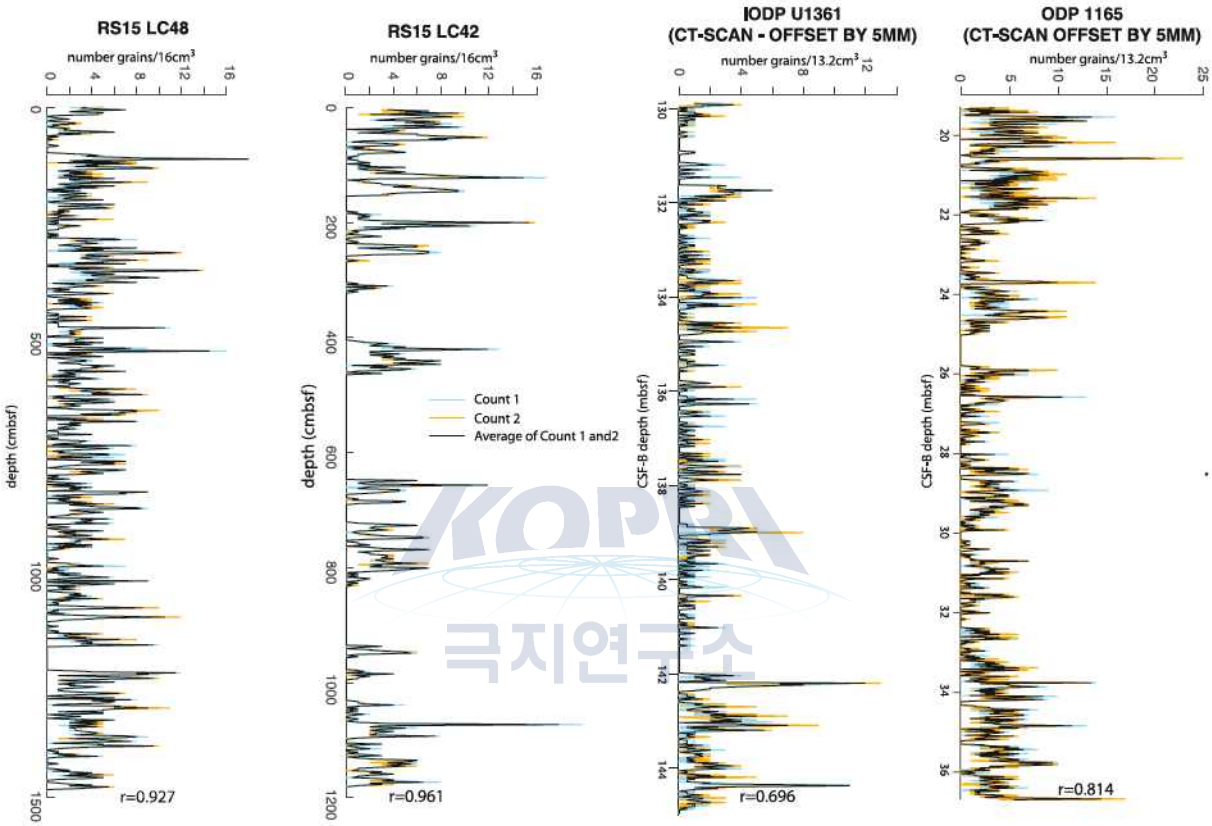


Figure 3. X-radiograph (x-ray) counts from cores RS15-LC48 and RS15-LC42, and CT-scan counts from ODP site 1165 and IODP site U1361. Count 1 (blue) and 2 (orange) were undertaken by two separate users, and the average value is shown (black). For cores RS15-LC48 and RS15- LC42, although there are minor differences in absolute values between users, the signals are consistent and correlation values are high. For cores ODP Site 1165 and IODP Site 1361, the correlation values and visual comparisons are likely lower because the images measured were different between users, that is, counts were from 1-cm thick composite slabs from CT-scans offset by 5 mm within the core face.

KOPRI 극지연구소

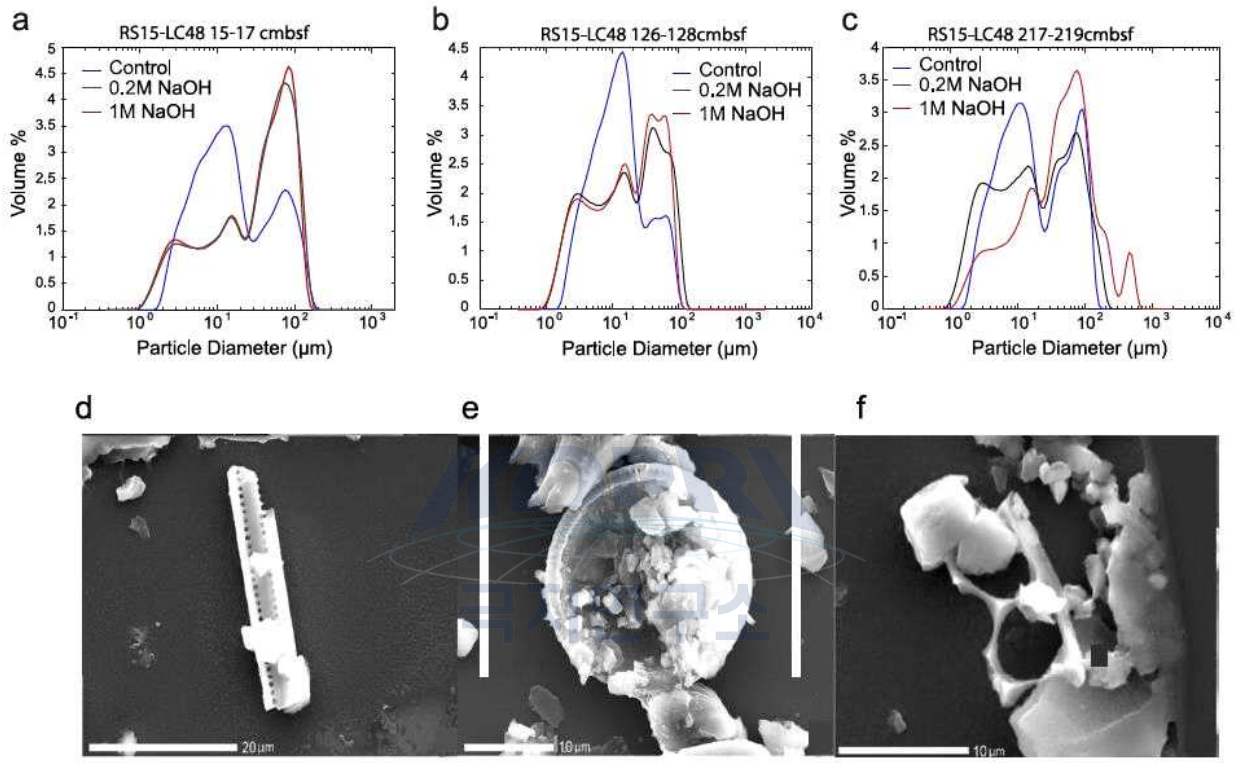


Figure 4. (a)−(c) Grain size frequency curves for three representative samples from core RS15−LC48 that were subsampled three times. Each subsample was treated with 0.2 M NaOH and 1M NaOH solutions, and a control with no NaOH treatment. (d) and (e) SEM images of diatom content in RS15−LC48 after 0.2 M NaOH treatment. (f) SEM images of diatom content in RS15− LC48 after 1M NaOH treatment.

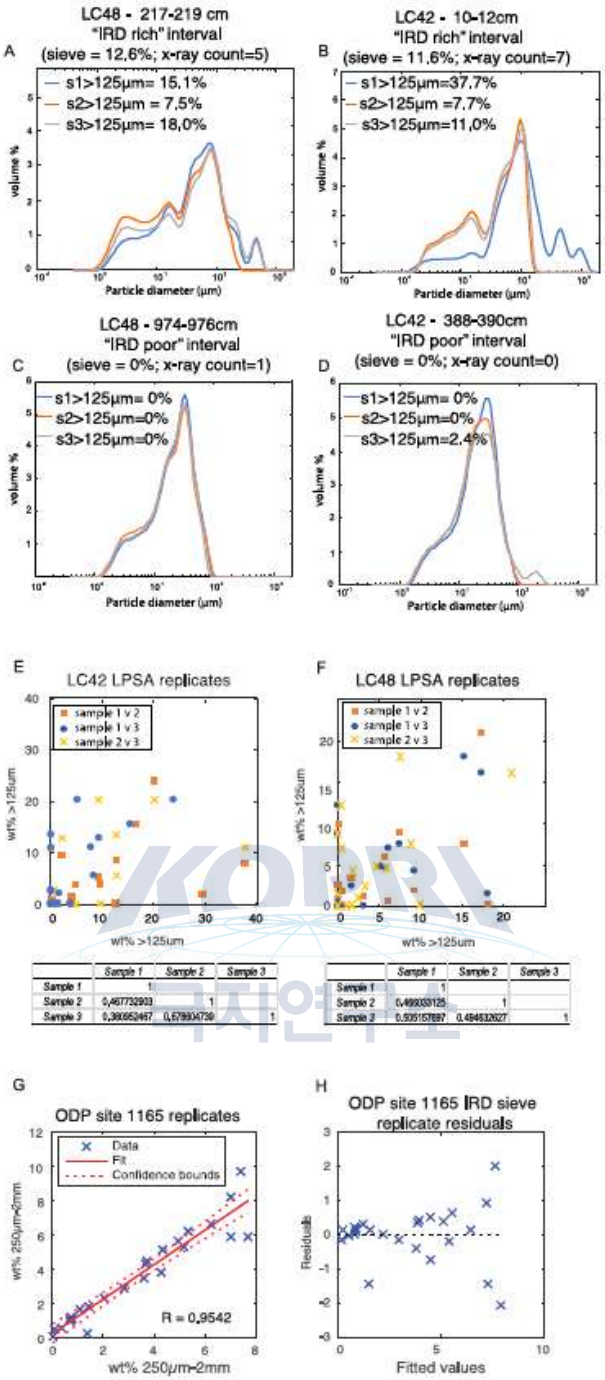


Figure 5. (a)−(d) Representative examples of repeat measurements on separate subsamples (replicate samples) using the Laser Particle sizer in cores RS15−LC42 and RS15−LC48. Note the lower reproducibility in the coarse fraction (>125 µm) in samples described as "IRD−rich," as identified in other counting methods. Good reproducibility is shown in the fine fraction (<125 µm) for both IRD−rich and IRD−poor samples. (e) Cross plot of replicate sample runs for RS15− LC42 >125 µm LPSA measurements, with Pearson pairwise linear correlation coefficients (R values) matrix below. (f) Cross plot of replicate sample runs for RS15−LC48 > 125 µm LPSA measurements, with Pearson pairwise linear correlation coefficients matrix (R values) below. (g) Cross plot of results of replicate sieving analyses (>250 µm) of samples from ODP Site 1165, with linear regression model and 95% confidence bounds. Each replicate comprised ~10 cm 3 volume. (h) Plot of residuals versus fitted values from the linear regression model for the replicate sample runs from ODP Site 1165.

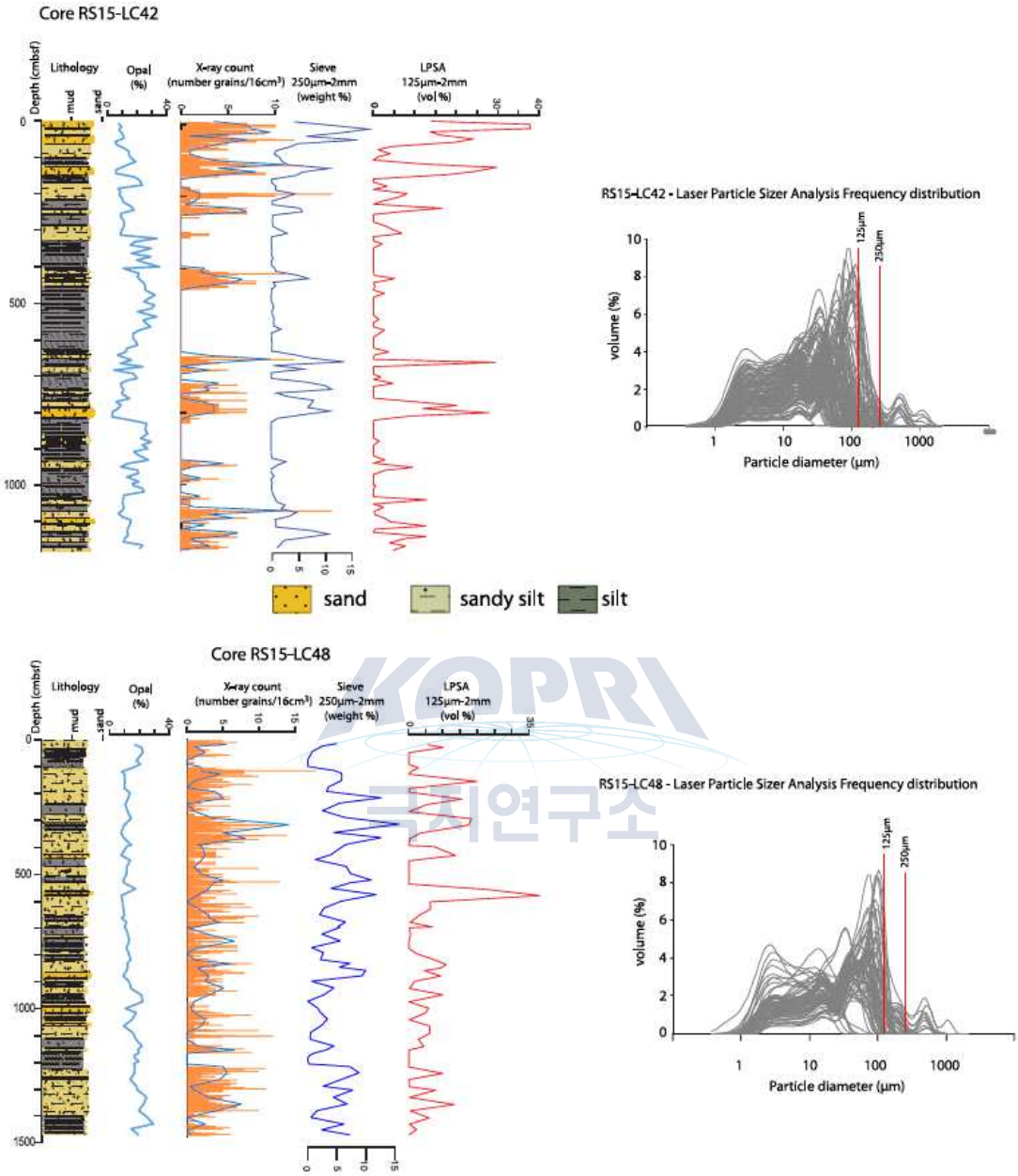


Figure 6. Lithological columns (after Ohneiser et al., 2019), biogenic opal %, coarse fraction grain size analysis, and LPSA grain size measurements from cores RS15-LC42 (top row) and RS15-LC48 (bottom row). Grain size analysis shows number of clasts (>2 mm) counted on x-radiographs (x-ray count), percentages of the terrigenous fraction 250 µm-2 mm obtained by sieving, and volume percentages of the biogenic-free fraction 125 µm-2 mm as determined by LPSA. The x-radiograph (x-ray) counts are shown as binned values as number of grains over a 2 cm core depth interval (orange bars), and values interpolated to the same depths as the sieve and LPSA values (gray lines).

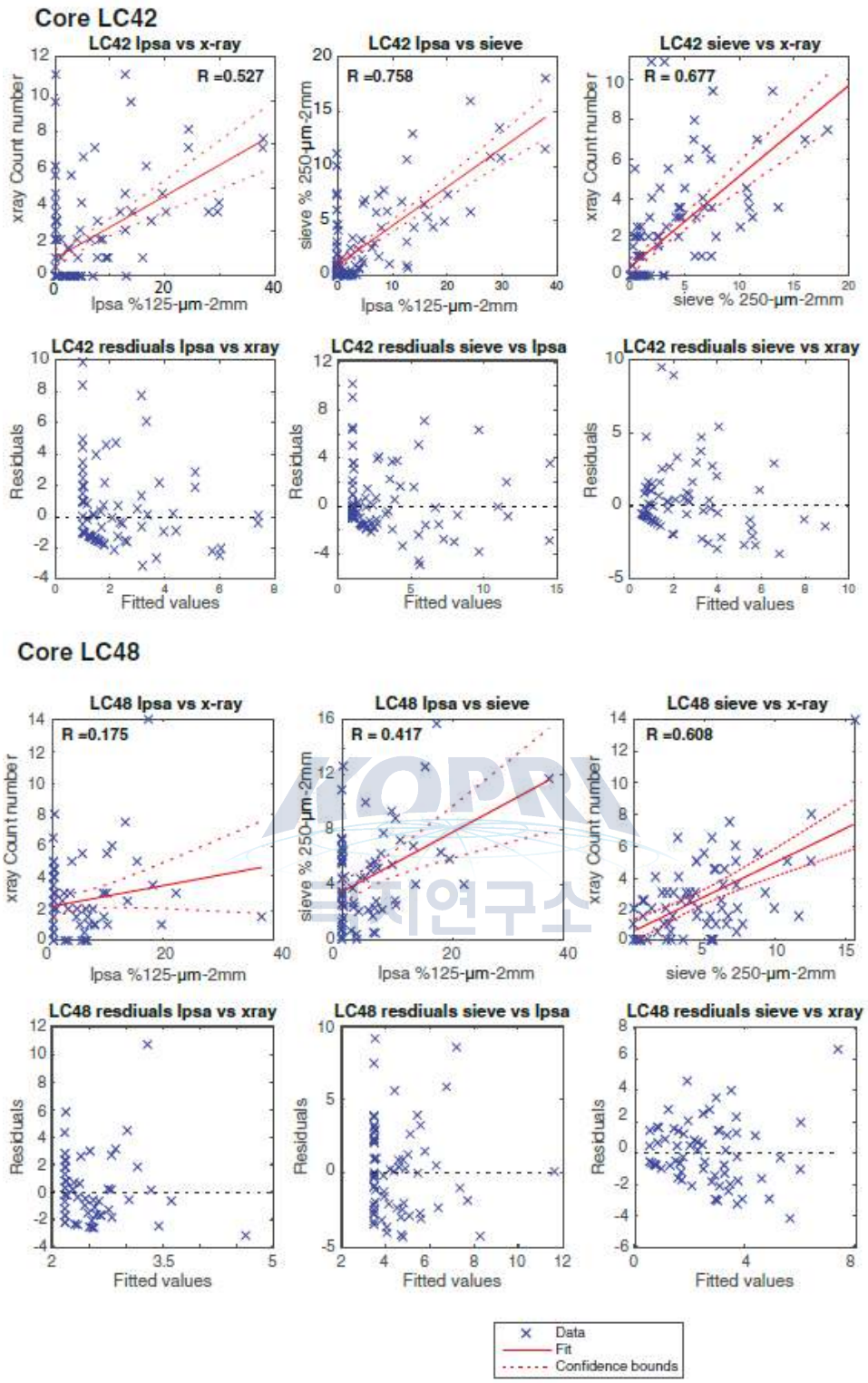


Figure 7. (Top row) Cross plots of x-radiograph (x-ray count) clast values, sieve-based weights of 250 µm-2 mm, and 125 µm-2 mm LPSA analysis for RS15-LC42, with linear regression model and 95% confidence bounds. (Second row) Plot of residuals vs. fitted values from the linear regression model for cross plots shown in top row. (Third row) Cross plots of x-radiograph (x- ray) count values, sieve-based weights of 250 µm-2 mm, and 125 µm-2 mm LPSA analysis for RS15-LC48, with linear regression model and 95% confidence bounds. (Bottom row) Plot of residuals vs. fitted values from the linear regression model for cross plots shown in third row.

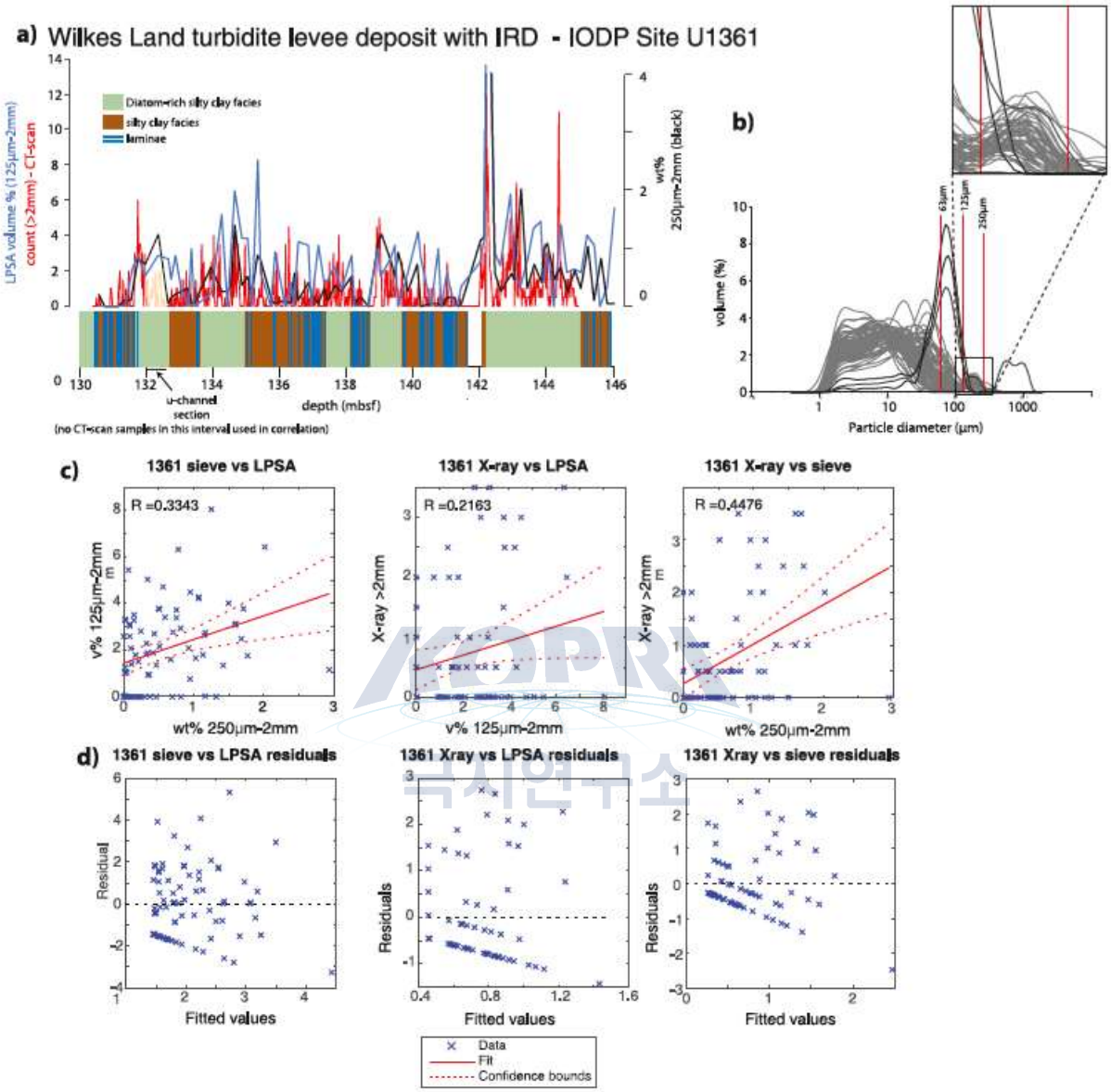


Figure 8. (a) Downcore comparison of coarse fraction content measurements from sieve (>250 µm), LPSA methods (>63 and 125 µm) and x-radiograph (x-ray) methods at IODP Site 1361, an levee setting on the lower continental rise offshore from Adélie Land (Escutia et al., 2011); Lithological column follows lithofacies classification scheme of Patterson et al. (2014), with laminae mapped to depth from core photos, and adjusted to the CSF-B depth scale to correct for core expansion. (b) Grain size frequency distributions of the LPSA measurements shown in panel (a); (c) Cross plot of sieved-based measurements of >250 µm weight percentages and LPSA >125 µm percentages, with linear regression model and 95% confidence bounds. (d) Plot of residuals vs. fitted values from the linear regression model for plot in panel (c).

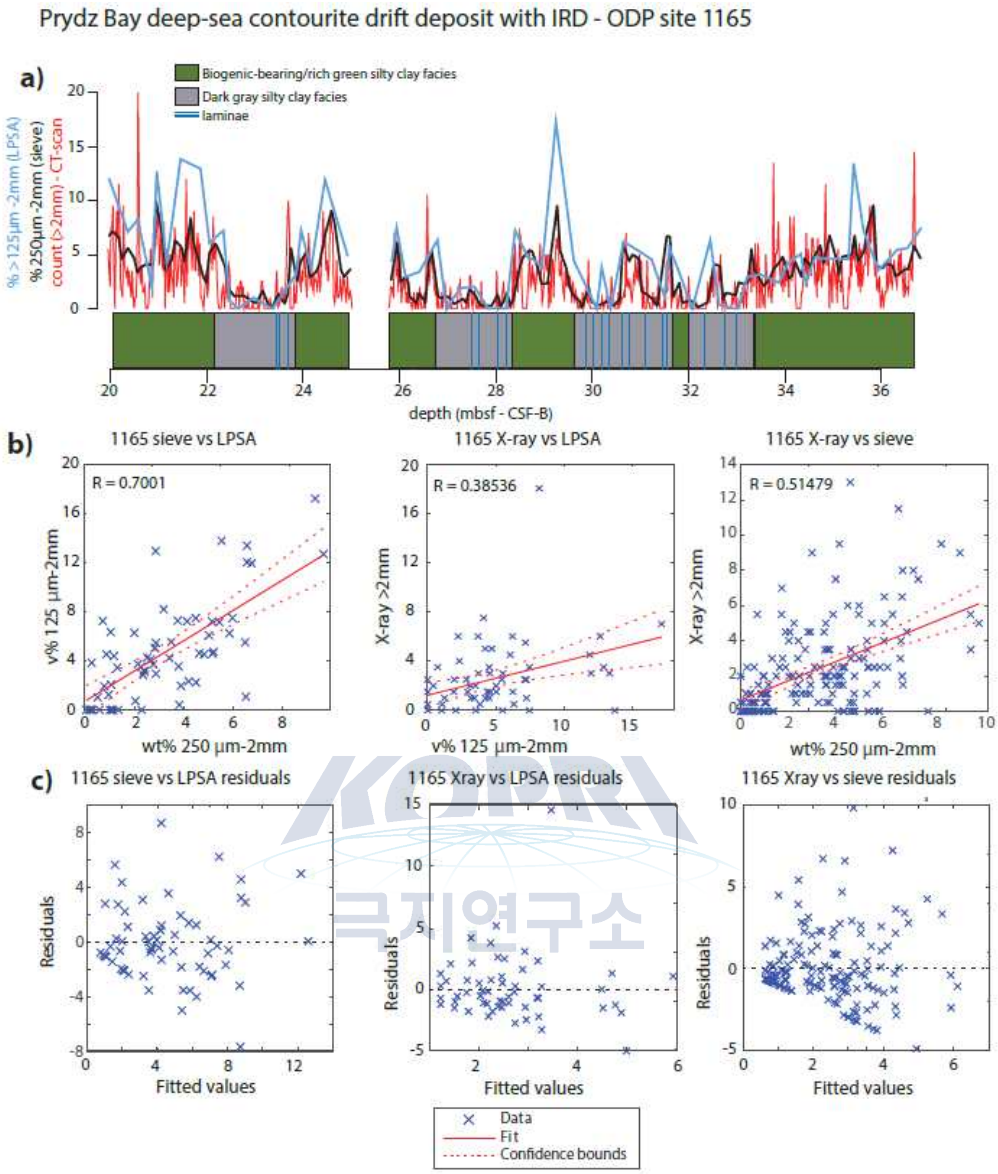


Figure 9. (a) Downcore comparison of measurements for coarse grain size fractions from sieve (>250 μm), LPSA methods (>125 μm from Passchier, 2011) and x-radiograph (x-ray) methods at ODP Site 1165, a mixed turbidite levee and contourite drift deposit on the continental rise offshore from Prydz Bay (O'Brien et al., 2001); Lithological column is based on color reflectance data interpretations of lithofacies (Rebesco, 2003), observations of bioturbation and laminae occurrence in CT-scan photos, and are adjusted to the CSF-B depth-scale to correct for core expansion. (b) Cross plot of sieve-based measurements of >250 μm weight percentages and LPSA >125 μm percentages at ODP Site 1165, with linear regression model and 95% confidence bounds. (c) Plot of residuals versus fitted values from the linear regression model for plot in panel (b).

KOPRI 극지연구소

제 28 장

^{10}Be 동위원소 분석을 통한 고환경 연구

이현희

한국해양과학기술원 부설 극지연구소

초록: 우주선유발 동위원소(Cosmogenic Nuclides)는 우주에서 유입되는 강력한 우주방사선이 지구의 구성물질과 핵반응을 일으키며 만들어내는 동위원소들로, 노출된 암석의 표면에서 만들어지는 'in-situ' 성분과 'meteoric/authigenic' 성분을 이용해 다양한 환경 변화를 복원하는 연구를 할 수 있다. 암석의 노출연대측정(in-situ)은 빙하의 후퇴나 두께 감소에 의한 노출 시기를 밝혀낼 수 있으며, 해양퇴적물(meteoric)에서의 농도 변화는 빙붕이나 해빙과 같은 빙권 변화를 추적할 수 있다. 동남극 빙상의 Hollingsworth 빙하는 MIS 2의 LGM 이후 점차 두께가 감소하였으며, LGM 이전에 더 두꺼운 빙하가 존재하여 LLGM이 나타났음을 발견하였다. 또한, 홀로세 후기에 걸쳐 하류의 David 빙하의 소모 시기가 상반되어 나타나, 빙하 소모의 원인이 다른 것을 밝혀내었다. 로스 빙붕이 후퇴하여 개방되어 있는 로스해의 표층퇴적물이 지역별로 다른 농도의 meteoric 10Be 농도가 나타났으며, 이에 영향을 미치는 인자로 해빙의 지속성을 분석하였다. 폴리나의 강력한 바람으로 해빙이 제거되는 지역에 높은 농도가 나타났으며, 운반된 해빙이 집적되어 소멸하는 대륙붕 외곽 지역에서도 높은 농도가 나타났다. 차후 남극 해양에서의 해빙 및 해양 퇴적 환경을 추적하는 연구에 활용될 지시자로서 기대가 된다.

1. 육상의 빙하 변화 연구

1.1. 개요 및 육상 고빙하 퇴적물/기반암 시료 채취

연구지역은 이전 연구의 남극 로스해 테라노바 베이의 3개의 분출빙하(Campbell, Priestley, David)와 달리 David 빙하의 상류 노출지역(Ricker Hills)이다. 빙하 후퇴 이후 지형면이 노출된 시기를 밝혀내기 위해 우주선유발 동위원소를 이용한 노출연대 측정을 위한 암석 시료를 채취하였다(그림 1). 시료는 모두 빙하에 의해 운반되어 온 erratic cobble로, 석영이 대부분으로 이루어진 사암/역암이다. 시료 채취와 현장 조사는 2016-2017년 장보고과학기지의 하계연구활동에 의해 이루어졌으며, 총 11개의 시료 채취와 빙하에 의해 형성된 빙하지형의 조사, 인근 퇴적암 조사를 통해 이루어졌다(그림 2).

1.2. 우주선유발 동위원소 in-situ 10Be 측정

채취한 시료는 모두 250~710 μm의 sand size로 분쇄하였다. 희석된 질산과 불산을 이용

해 대기중에서 유입될 수 있는 meteoric 10Be을 제거하고 석영이 아닌 불순물을 모두 제거하였다. 질량가속기(Accelerator Mass Spectrometry)를 이용한 저준위 동위원소비 측정을 위해 guide isotope 9Be을 일정량 주입하였다. 순수 석영 시료를 강한 불산에 녹인 후 이온교환수지(ion exchange column)을 이용해 양이온을 최대한 제거하여 순도 높은 Be을 수집하였다. 암모니아를 이용해 수화물로 만든 후, 고온에서 산화시켜 BeO의 형태로 수집되었다.

BeO는 AMS에서 Cs을 이용한 이온화와 스퍼터링을 위해 전도체인 Nb과 혼합되어 타겟으로 제작되었다. AMS를 이용해 Be의 동위원소인 9Be의 양이 전류를 측정하는 패러데이 컵에서, 10Be의 양이 가스 이온화 챔버에서 카운팅 되었으며, 두 동위원소의 비인 10Be/9Be로 결과가 측정되었다. 주입된 guide isotope 9Be의 양을 이용해 10Be의 실제 양을 계산하여 노출연대로 환산되었다.

1.3. 결과

총 11개의 시료는 노출지역을 뒤덮고 있던 빙하의 상류와 하류 각각 2개의 면으로 그룹이 되었다(그림 2). 가장 높은 곳인 1249.5 m와 1182.4 m에서 12.3 ~ 1.2 ka의 연대가 나왔으며, 반대쪽 사면의 하류 지역은 22.1 ~ 0.8 ka의 연대가 나왔다. 현재 Hollingsworth 빙하가 후퇴하며 남겨진 가장 최근의 lateral moarine은 약 2.0 ~ 1.2 ka 사이의 시기에 집중적으로 만들어져 당시 굉장히 빠른 후퇴가 일어났음을 알 수 있다(그림 3).

1.4. 논의

1.4.1. 빙하 거동 변화 복원

KOPRI 극지연구소

상류와 하류의 사면에서 얻어진 노출연대를 통해 빙하의 표면 경사를 시기적으로 제한할 수 있었다. 상류 사면의 12.3 ka와 2.3 ka 지점에 존재했던 빙하의 말단면은 하류 사면의 22.1 ka 지점과 0.8 ka 지점 사이에 연결되어 있어야 한다. 이러한 방식을 이용해 빙하의 표면 경사는 5.4 ~ 8.5° 사이로 제한이 되었고, 이를 이용해 가장 높은 연대인 22.1 ka 당시의 빙하 두께를 복원을 하였다(그림 4). 또한 기후적 요건을 고려할 경우 한랭한 빙기에 빙하의 두께 변화가 온난한 간빙기에 비해 낮았을 것을 고려하면, 빙하의 표면 경사는 5.4 ~ 6.8° 사이로 더 제한되었다.

빙하의 표면 경사를 토대로 최대 고도를 복원할 경우 노출연대의 가장 오래된 연대는 22.1 ka로 최종빙기의 중반에 약 1315.4 m의 고도까지 두꺼워졌을 것으로 보인다. 또한 MIS (Marine Isotope Stage) 2의 초반인 약 29 ka까지 확장할 경우 최대 1361.8 m의 고도까지 빙하게 덮이는 것을 알 수 있다. 하지만 이 모든 경우를 고려하여도 상류의 가장 높은 봉우리인 Benson Knob의 상부 평탄 빙하지형면에 도달하지 못한다(그림 5). 이를 통해 Hollingsworth 빙하는 일반적으로 알려져 있는 MIS 2의 Last Glacial Maximum(LGM)에 가장 두꺼웠던 것이 아닌, 그 이전의 시기에 더 두꺼운 빙하가 존재하였을 것으로 예상된다. 특히 테라노바베이로 흘러드는 분출빙하들 역시 MIS 4에 더 두꺼운 빙하가 존재하였음을 증명하였고, 종합적으로 Local Last Glacial Maximum (LLGM)이 동남극빙상 전반에 걸쳐 나타났음을 밝혀내었다.

1.4.2. 기후적 함의 해석

노출연대측정 결과와 빙하의 두께 변화를 시간당 감소율로 계산할 경우 온난한 간빙기인

MIS 1 중반시기 까지도 변화가 매우 낮음을 볼 수 있다(그림 6). 특히 하류의 분출빙하들이 홀로세 중기인 약 6 ka에 빠른 붕괴를 보였음에도 불구하고 상류의 Hollingsworth 빙하는 거의 변화율의 변동이 나타나지 않았다. 반면 약 2.3 ka에 굉장히 급격하고 빠른 빙하의 소모가 나타났음을 알 수 있다. 이는 로스빙붕의 붕괴로 인해 불안정해진 하류의 David 빙하가 6 ka에 빠르게 소모되었으나, 수분의 공급이 원활해지며 적설량이 증가함으로써 상류의 빙하는 오히려 소모에 변동이 적었던 것으로 해석할 수 있다(그림 6C). 반대로 대기 중 CO2의 농도가 높아지고 바다표범의 군집이 많아지는 온난해지는 시기에 상류의 Hollingsworth 빙하가 빠르게 소모되어 분출빙하와 다르게 기후의 영향에 직접적으로 영향을 받았음을 밝혀내었다.

2. 해양의 해빙 변화 연구

2.1. 개요 및 해양퇴적물 시료 채취

연구지역은 남극 로스해와 웨델해에의 표층시료를 이용하였으며 2013, 2015년의 하계연구항차에서 아라온호를 이용해 채취된 시료이다(그림 7). 이전의 연구는 대기에서 생성되어 해양퇴적물에 집적된 meteoric 10Be의 농도차를 이용하여 빙붕의 거동 변화 복원 연구에 주로 활용되었다. 해수면에서 얼어붙으며 형성되는 해빙은 빙붕에 비해 시간적, 공간적으로 더 일시적이고 얇지만, 마찬가지로 대기에서 침전되는 동위원소의 유입을 막아주고 훨씬 더 넓은 지역에서 연구에 활용을 할 수 있다는 장점이 있다. 또한 해빙의 변화를 추적하는 지시자로서 최초로 보고되는 연구로서 앞으로의 활용성이 매우 기대된다.

KOPRI 극지연구소

2.2. 우주선유발 동위원소 meteoric 10Be 측정

채취한 시료는 광물 내에 축적된 in-situ 성분의 유입을 막기 위해 분쇄하지 않은 형태로 사용하였다. 점토 입자 크기의 퇴적물을 450°에서 산화시켜 유기물을 제거한 후 약한 염산하이드록실아민-아세트산 혼합물에 끓여 흡착된 성분만을 우려내었다. guide isotope인 9Be을 일정량 주입한 후 이온교환수지(ion exchange column)을 이용해 양이온을 최대한 제거하여 순도 높은 Be을 수집하였다. 암모니아를 이용해 수화물로 만든 후, 고온에서 산화시켜 BeO의 형태로 수집되었다.

BeO는 AMS에서 Cs을 이용한 이온화와 스퍼터링을 위해 전도체인 Nb과 혼합되어 타겟으로 제작되었다. AMS를 이용해 Be의 동위원소인 9Be의 양이 전류를 측정하는 패러데이 컵에서, 10Be의 양이 가스 이온화 챔버에서 카운팅 되었으며, 두 동위원소의 비인 10Be/9Be로 결과가 측정되었다. 주입된 guide isotope 9Be의 양을 이용해 10Be의 실제 양을 계산하여 노출연대로 환산되었다.

2.3. 결과

총 13개의 시료는 매우 큰 편차를 보였으나 지역적으로 일정한 특징들을 반영하고 있다(그림 8). 가장 최근에 무너진 라르센 빙붕에서는 가장 높은 9Be과 가장 낮은 10Be의 농도가 나타나며 상대적으로 10Be/9Be의 비가 매우 낮게 나왔다. 남빙양의 경우 과거와 현재 모두 빙붕의 영향을 전혀 받지 않아 10Be과 10Be/9Be 모두 가장 높게 나왔다.

2.4. 논의

2.4.1. 빙붕 거동 변화 복원

빙붕의 영향을 최근 수십년 전까지 받았던 웨델해의 라르센 빙붕은 다른 해양에 비해 10Be의 농도가 낮게 감지되었다(그림 8). 특히, 최근에서야 빙붕의 일부가 떨어져 나간 라르센 C 빙붕의 전면부에서는 가장 낮은 10Be 농도가 감지되었고, 특히 빙하로부터 쏟아진 물질이 공급되며 높은 농도의 육상기원 9Be이 감지되었다. 동위원소의 비는 다른 해양 지역에 비해 극단적으로 낮은 10Be/9Be 값을 보이며 빙붕의 거동 변화가 퇴적의 가장 큰 방해물임을 밝혀내었다.

2.4.2. 해빙 변화 추적

로스해는 홀로세 중기에 빠른 로스빙붕의 후퇴로 현재와 유사한 범위까지 빙붕이 후퇴하였다. 표층에 집적된 근래의 동위원소의 농도를 분석한 결과, 해류의 흐름보다는 해빙의 영향이 시기적으로나 공간적으로 다른 것이 주 원인임을 밝혀내었다(그림 9).

서로스해의 높은 10Be/9Be 비율과 동로스해의 10Be 농도는 해빙의 높은 농집도와 높은 상관관계를 보였으며, 상대적으로 개방되어 있는 중앙로스해는 동위원소의 농도가 낮게 나타났다. 또한 높은 농집도의 해빙은 대기기원 10Be의 집적을 방해할뿐만 아니라, 결빙 기간 중에 대기 중에서 공급되는 양을 해빙의 표면에 보관하고 있다가 소멸되는 장소에 높은 농도로 집적된 동위원소를 침전시키는 것을 확인하였다. 이는 로스빙붕과 테라노바베이에서 강력하게 불어오는 폴리나로 인해 이동이 이루어짐을 확인하였다.

해빙의 거동과 지속성에 의한 10Be 변화 연구는 처음 보고되는 것으로서, 해당 연구 방법을 해양퇴적물의 깊이에 따라서도 분석하여 해빙 변화 연구에 계속 활용될 수 있을 것으로 기대된다.

Paleoenvironmental Research on ^{10}Be isotope analysis

Hyun Hee Rhee

Korea Polar Research Institute

Abstract: Cosmogenic Nuclides are isotopes produced by strong cosmic radiation entering from space and causing nuclear reactions with constituents of the Earth. 'In-situ' components are produced on the exposed rock surfaces, and 'meteoric/authigenic' components can restore various environmental changes. Surface exposure dating (in-situ) can reveal the timing of exposure due to glacial retreat or lowering, and concentration changes in marine sediments (meteoric) can track cryosphere changes such as ice shelves and sea ice. The Hollingsworth Glacier in the East Antarctic Ice Sheet gradually decreased in thickness after the LGM during MIS 2, and it was found that thicker glacier existed before the LGM, suggesting that LLGM occurred. In addition, the timing of lowering of the downstream David glacier appeared to be contradictory throughout the late Holocene, revealing that the cause of glacier consumption was different. Different concentrations of meteoric 10Be were found in surface sediments of the Ross Sea where the Ross Ice Shelf was retreated and opened, and the persistence of sea ice was analyzed as a factor influencing this. High concentrations appeared in areas where sea ice was removed by strong winds (Polyna), and high concentrations were also found in areas outside the continental shelf where transported and accumulated sea ice and disappeared. It is expected that it will be used as an indicator to be used in future studies tracking sea ice and marine sedimentary environments in the Antarctic Ocean.

KOPRI 극지연구소

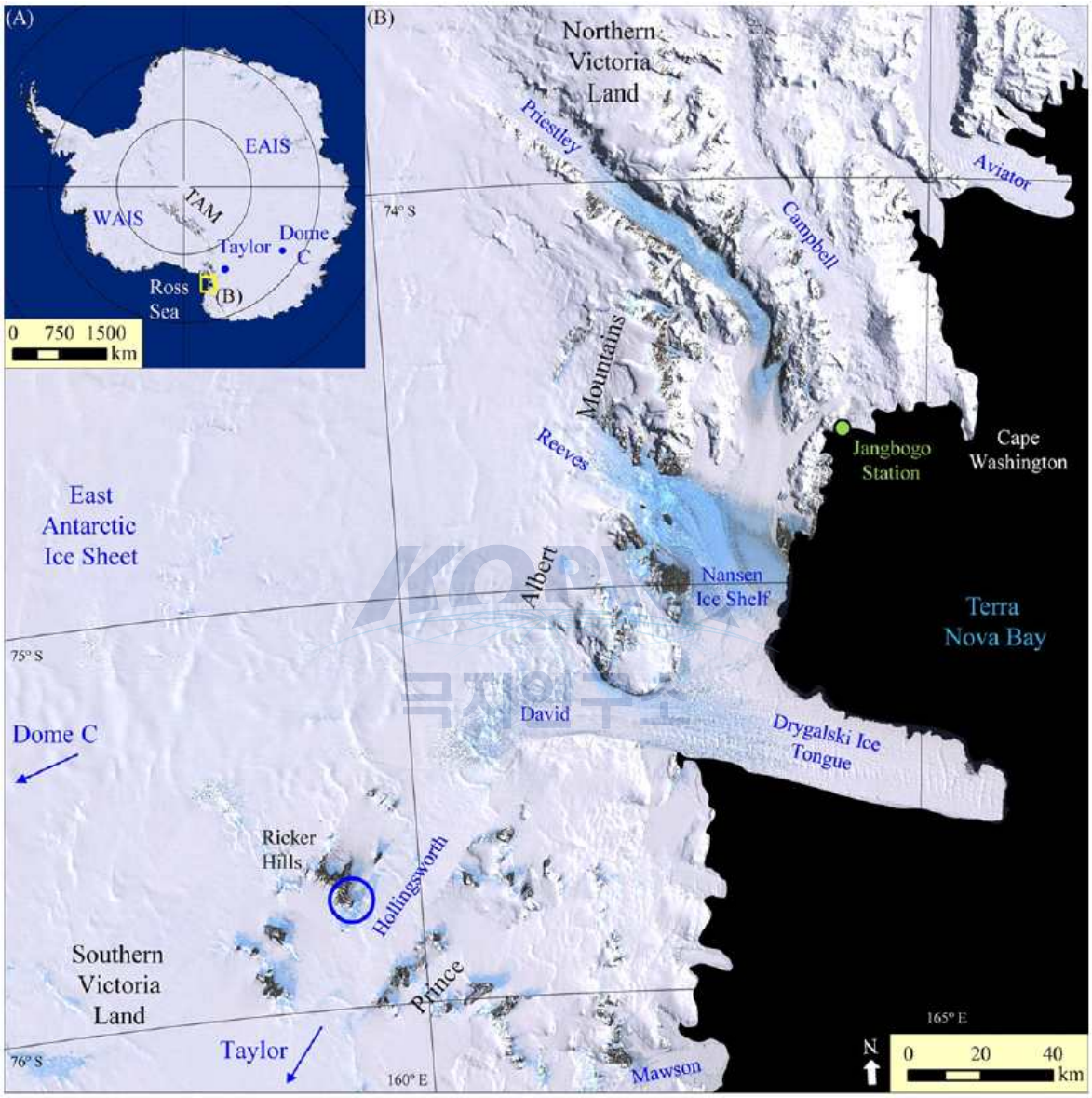


그림 1. 연구지역 인근의 Landsat Mosaic 위성지도. Hollingsworth 빙하는 David 빙하의 남쪽 상류 지역으로, 현재는 노출된 Ricker Hills와 Benson Knob 봉우리를 과거에 덮고 있었다.

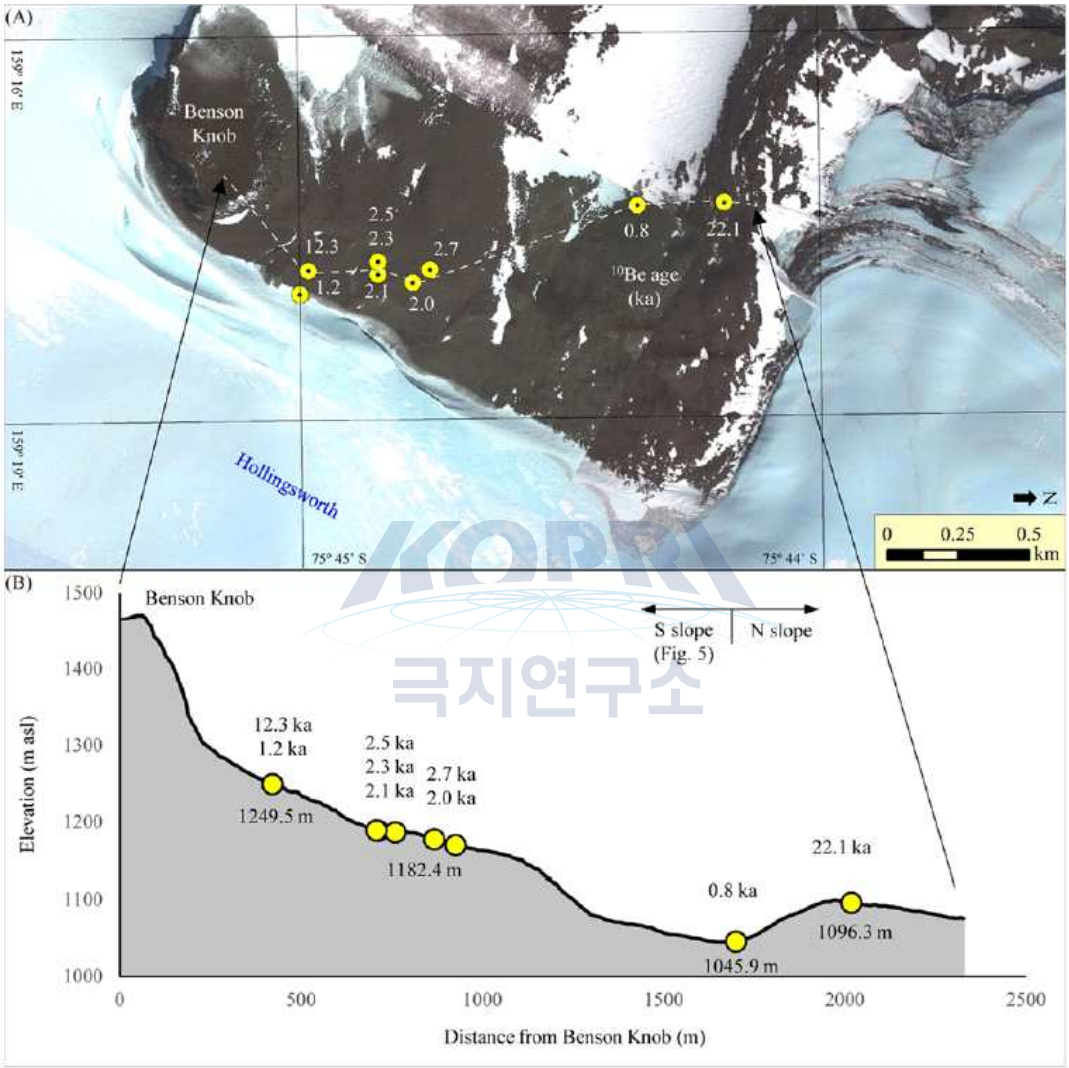


그림 2. 연구지역인 Ricker Hills 노출지역의 위성지도와 지형면의 고도 프로파일 상 표현한 노출연대 측정 결과.

KOPRI 극지연구소

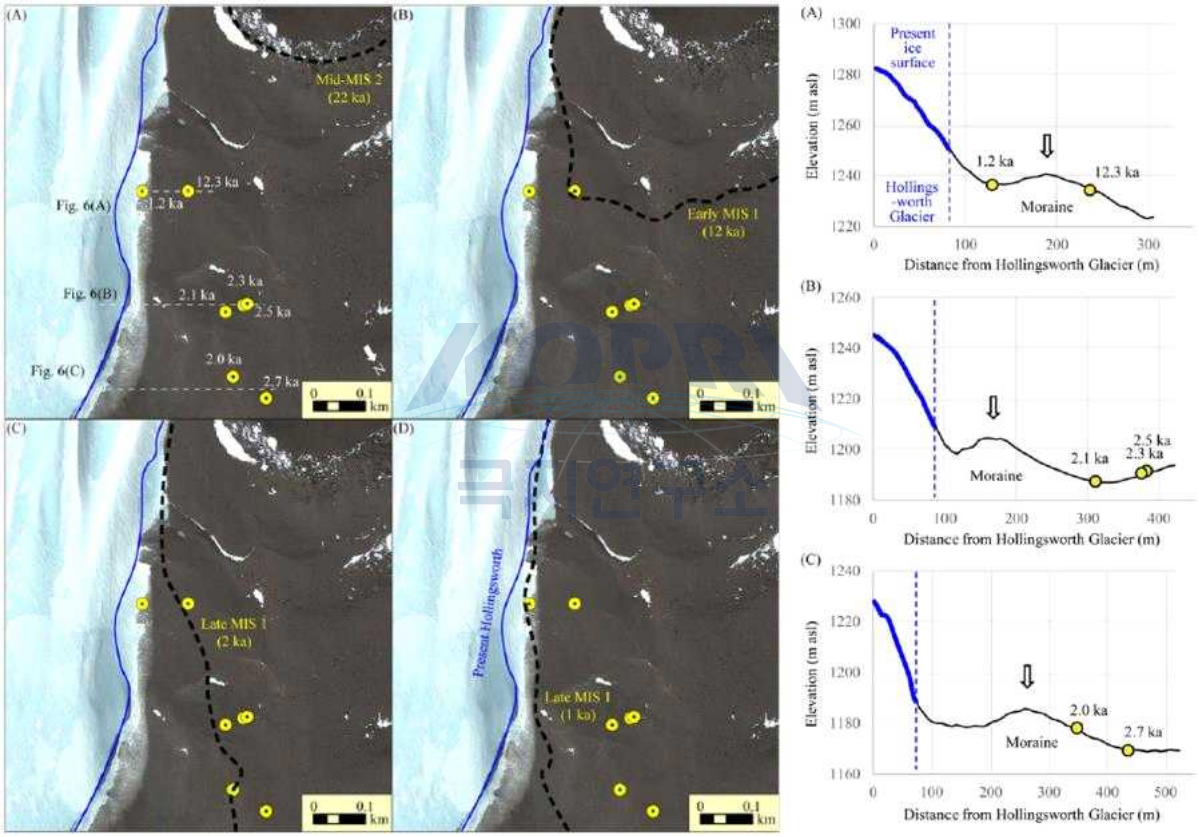


그림 3. 노출연대 측정 결과와 모레인의 연대 한정 방식.

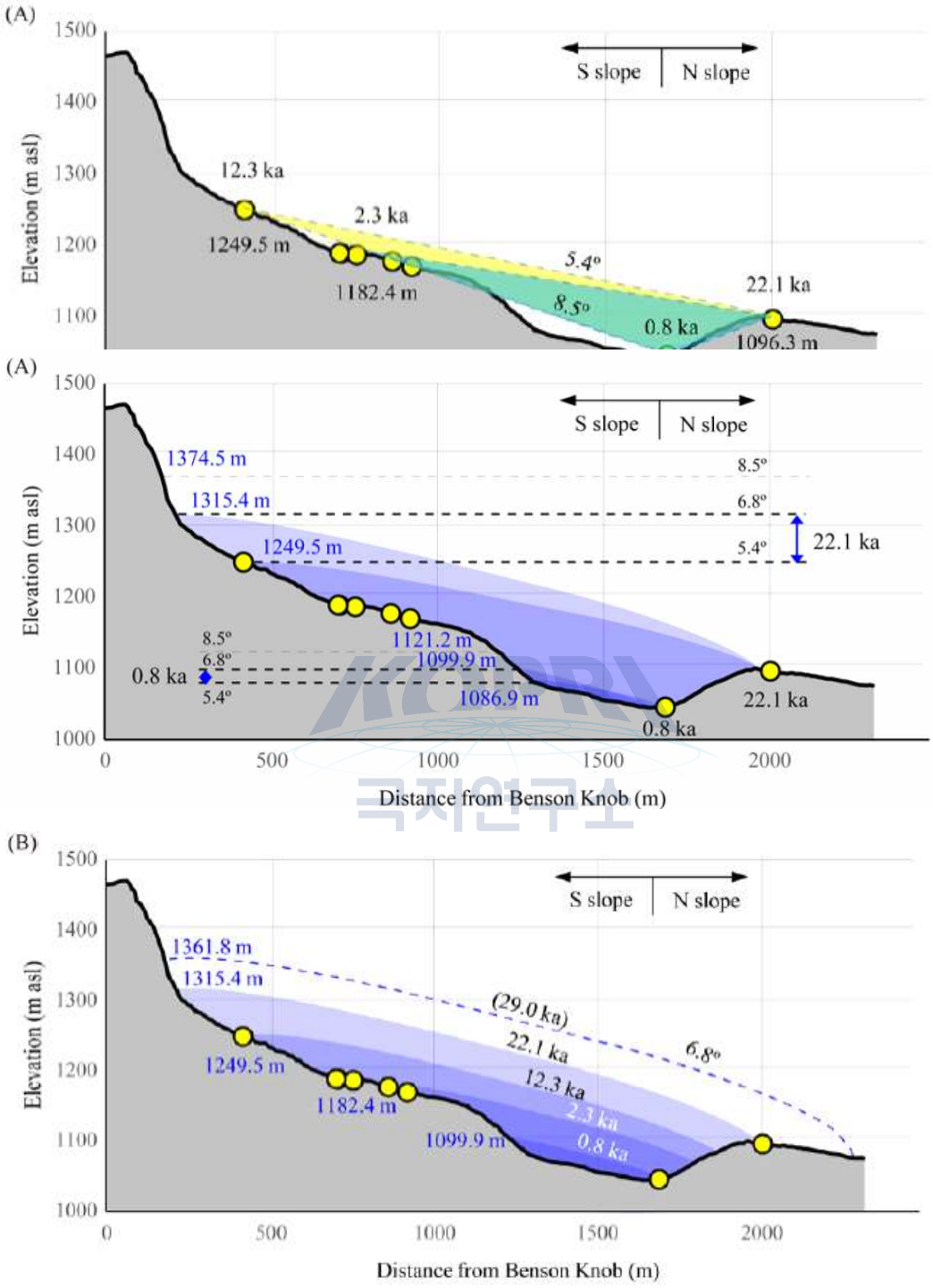


그림 4. 상류/하류 사면의 노출연대 측정 결과를 종합한 빙하의 경사/두께 한정 방식.

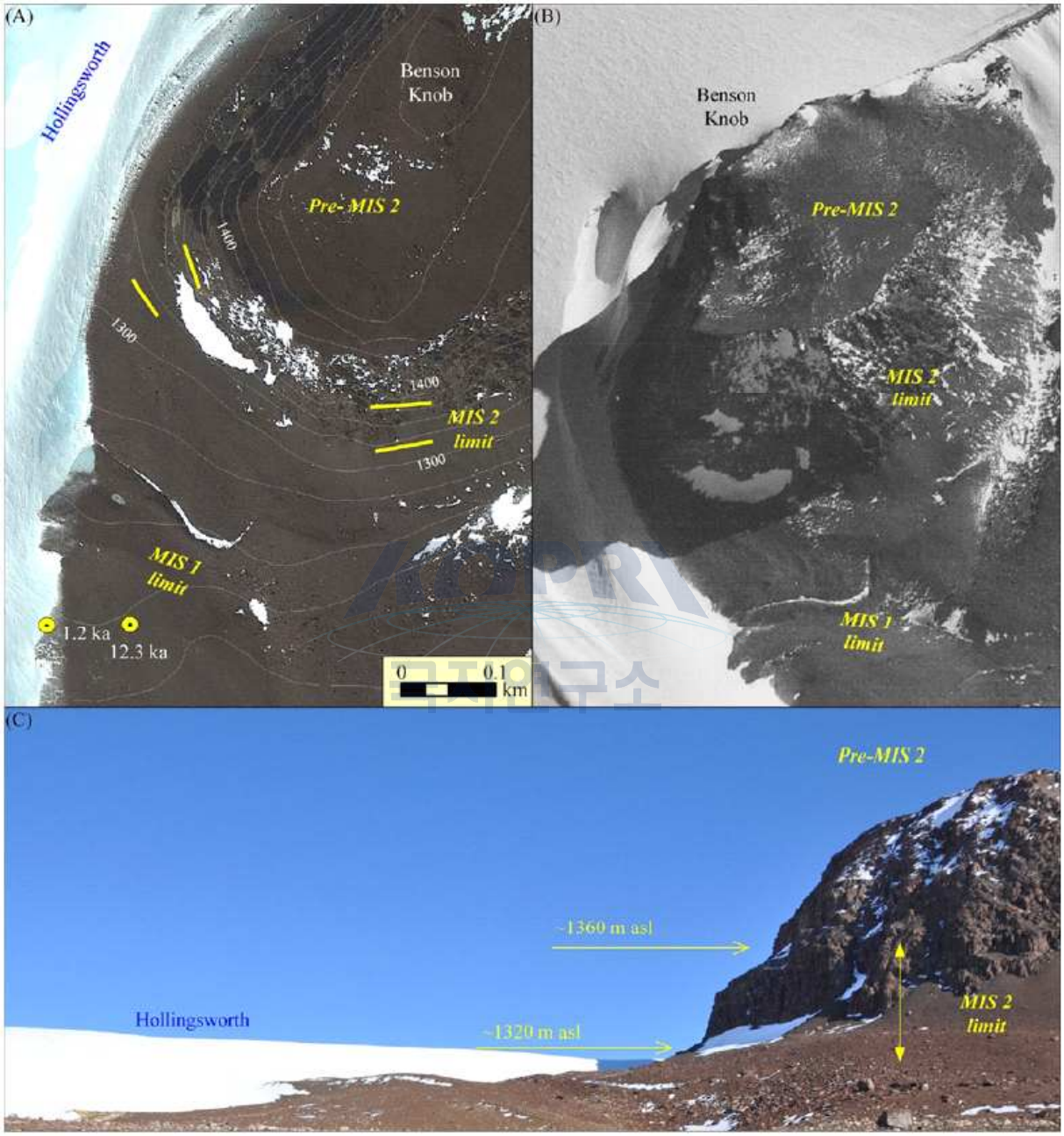


그림 5. MIS 2가 아닌 그 이전의 시기에 더 두꺼운 빙하가 형성되었으며 당시의 trimline으로 추정되는 단차가 보인다.

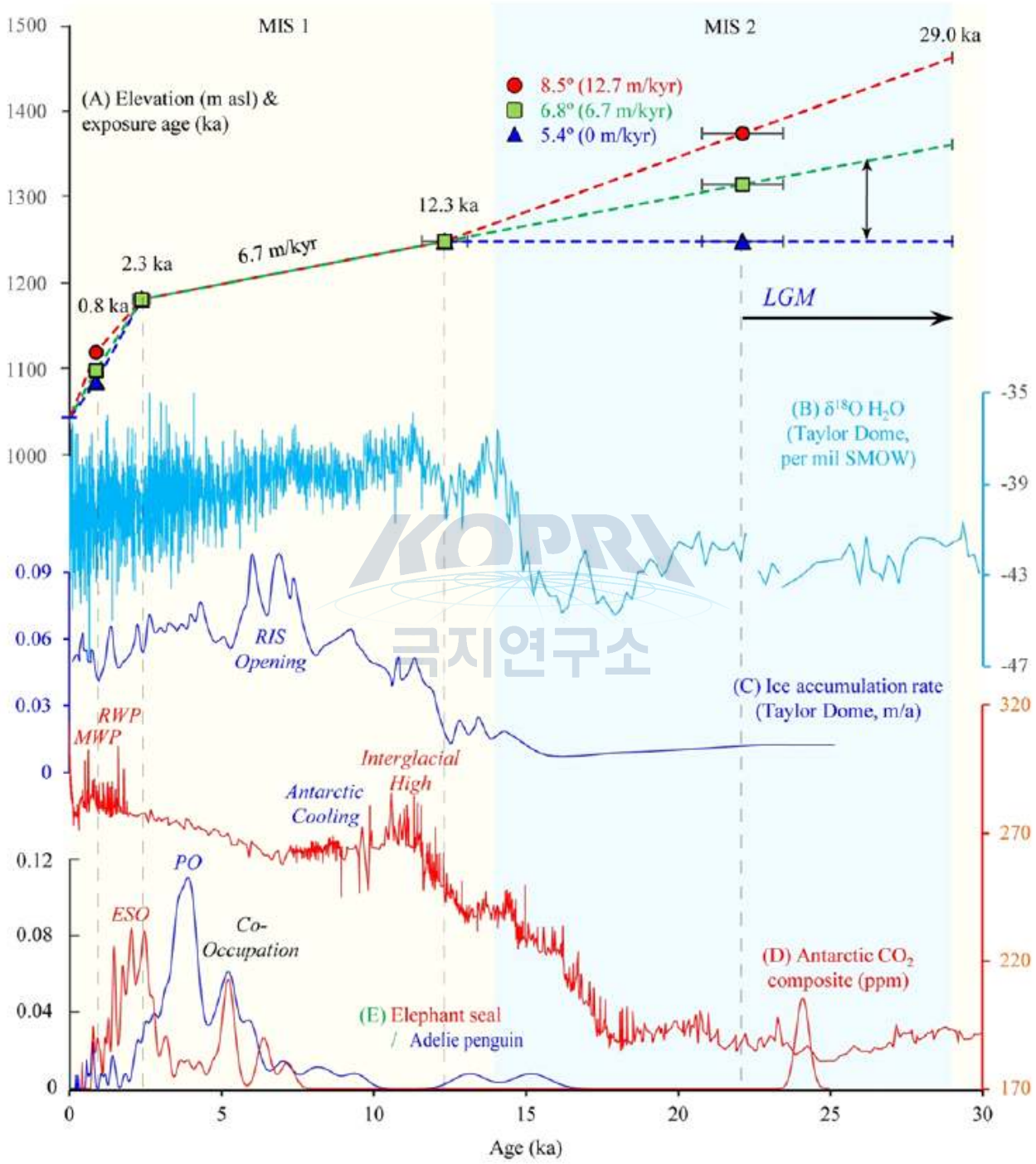


그림 6. 약 3만년전으로부터의 남극 기후 변화와 빙하 거동, 생명체 군집 변화의 비교.

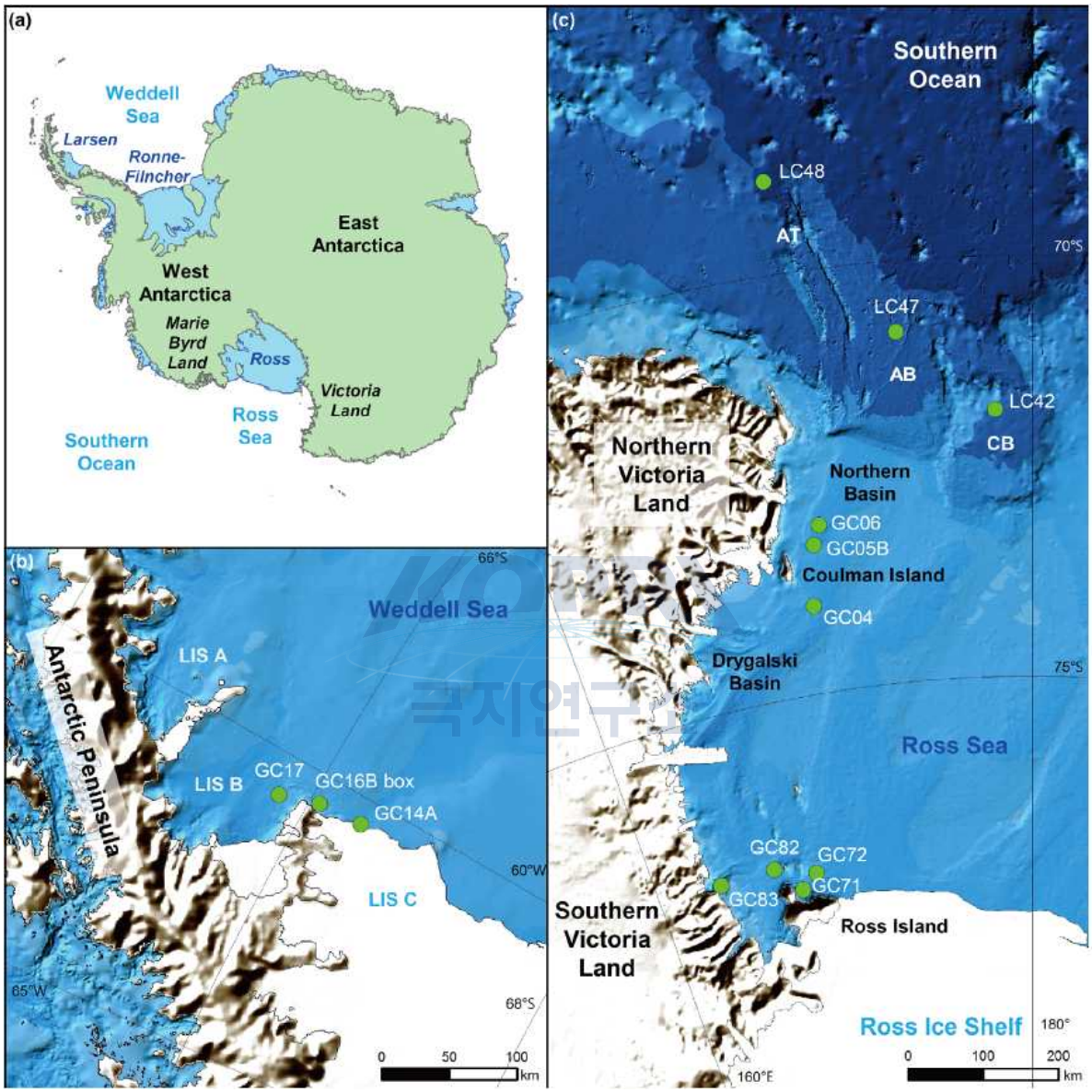


그림 7. 해양퇴적물 표층시료의 획득 지역을 표시한 지도.

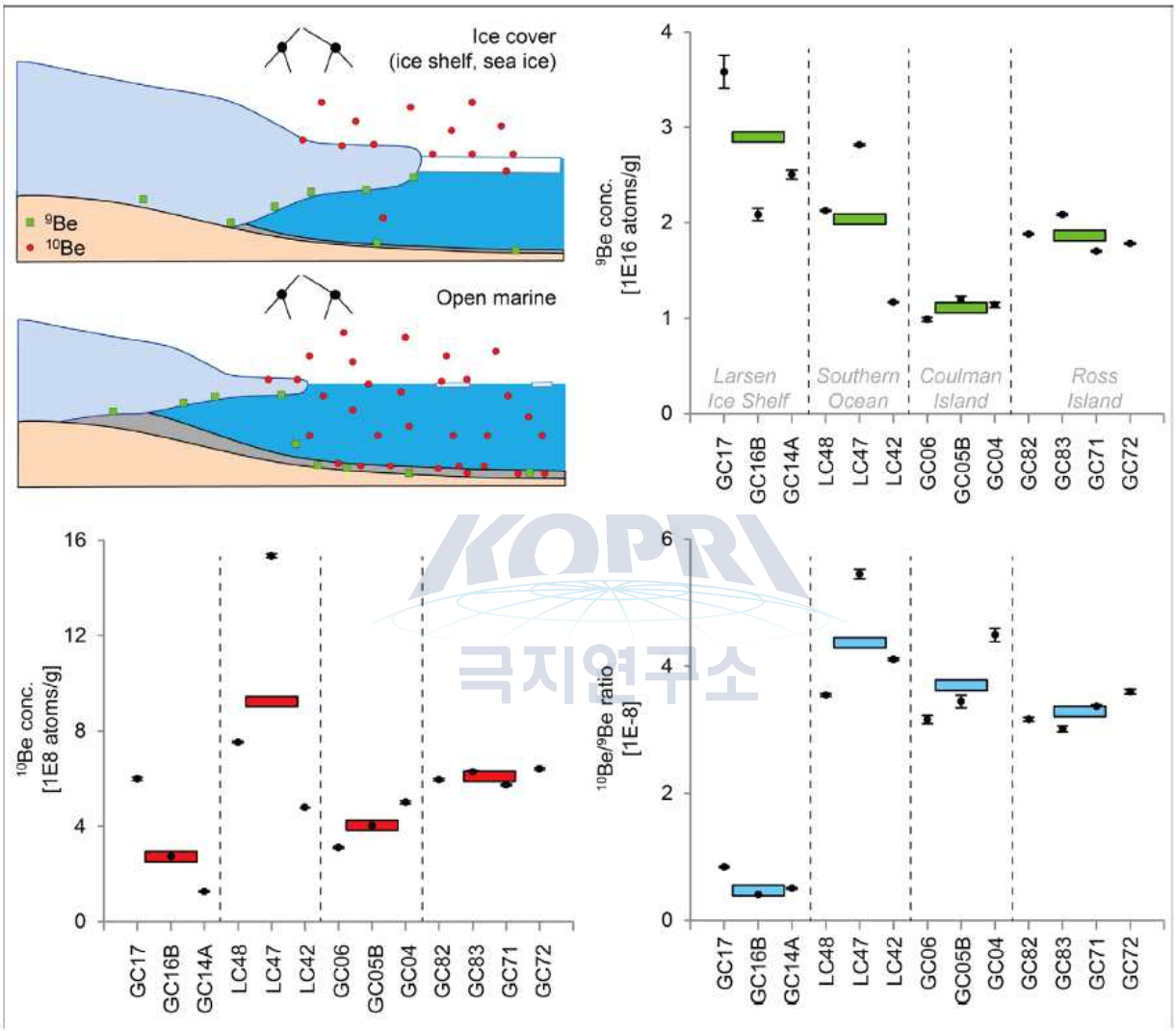


그림 8. 해양퇴적물 표층시료에 나타나는 10Be 농도 결과와 차이의 원리.

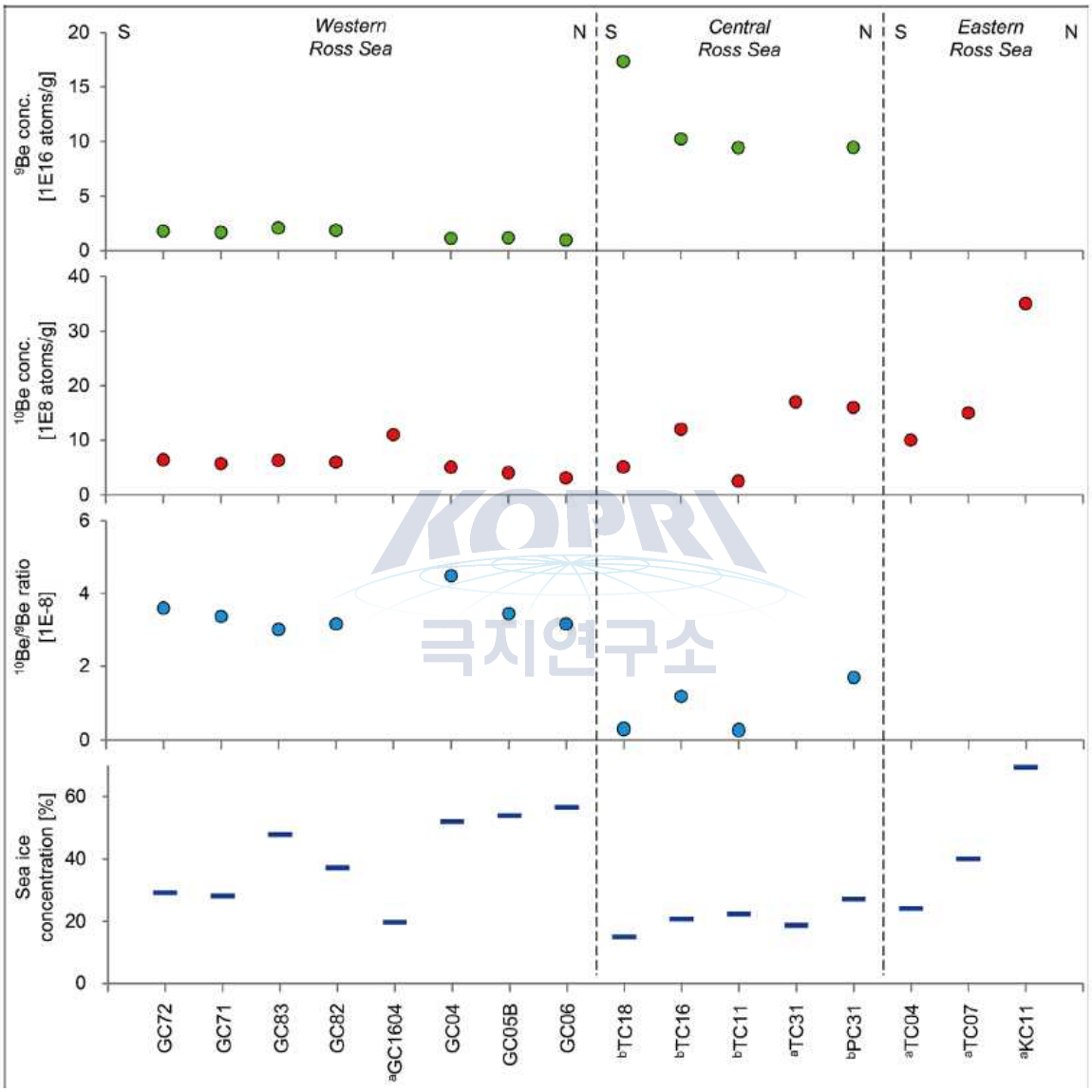


그림 9. 해양퇴적물 표층시료에 나타나는 10Be 농도 결과와 차이의 원리.

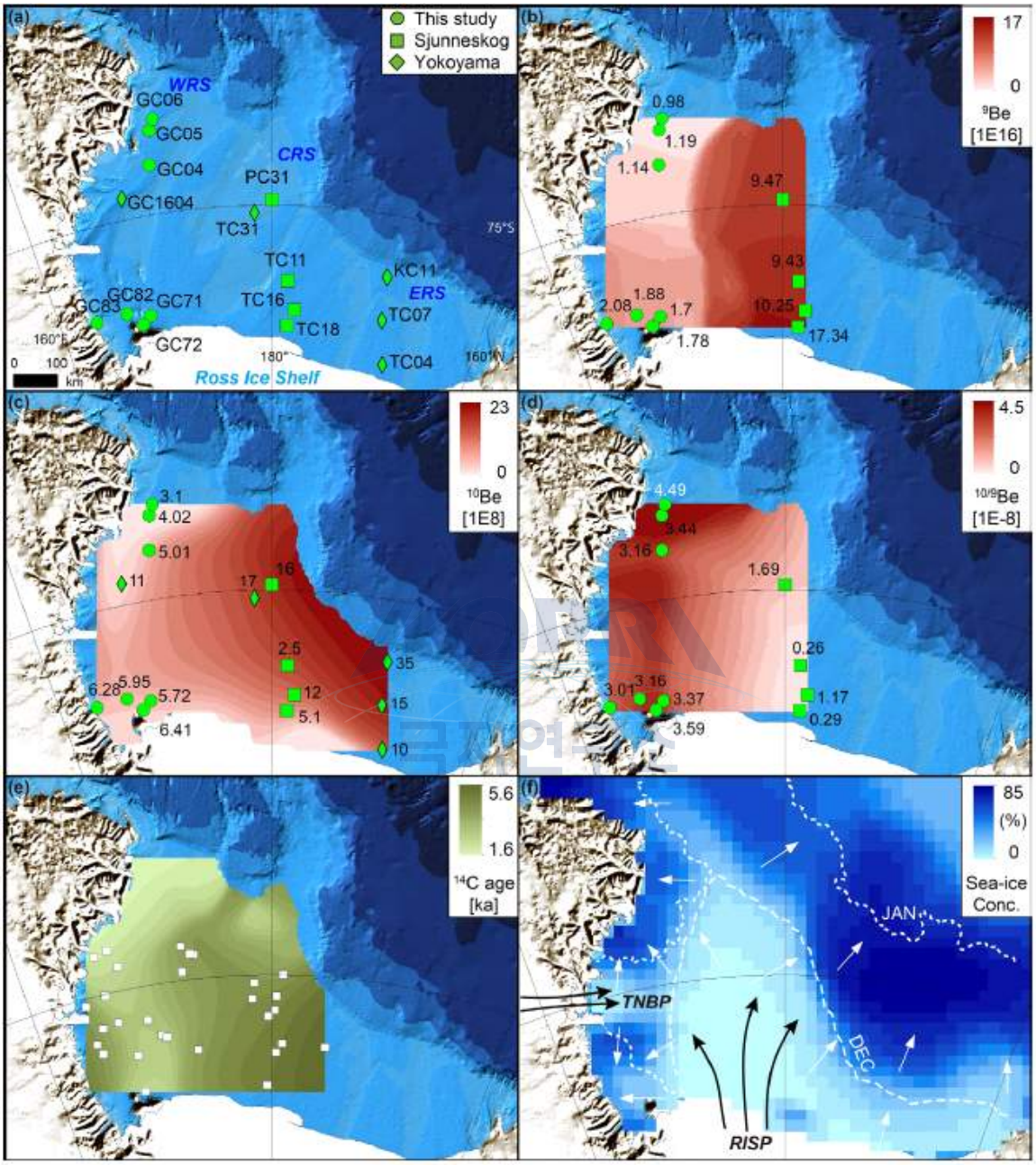


그림 10. 해양퇴적물 표층시료에 나타나는 10Be 농도 결과와 차이의 원리.

제 29 장

Fallacy of paleoproductivity signals by the recycled biogenic components: case study in the Central Basin of the northwestern Ross Sea[22)]

Boo-Keun Khim[1], Sunghan Kim[2], Min Kyung Lee[2], Young Kwan Sohn[3], Jae Il Lee[2] and Kyu Cheul Yoo[2]

[1]Department of Oceanography and Marine Research Institute, BK21 School of Earth and Environmental Systems, Pusan National University, Busan, Korea.
[2]Division of Glacial & Earth Sciences, Korea Polar Research Institute, Incheon, Korea.
[3]Department of Geology, Gyeongsang National University, Jinju, Korea.

KOPRI 극지연구소

Abstract: Core LC42, retrieved from the Central Basin of the northwestern Ross Sea, contains three distinct sediment facies (IRD (ice-rafted debris)-poor bioturbated sandy mud, IRD-rich massive sandy mud, and laminated mud) that are interleaved with each other and deposited over the last 1 Ma. The biogenic components (biogenic opal, total organic carbon, and total nitrogen) of the laminated mud layers are consistently higher than the other two facies throughout the core. Based on the depositional succession of sediment facies and IRD-related depositional processes in the Antarctic continental margin, the laminated mud layers without IRD have been deposited during the glacial periods, but the enhanced paleoproductivity in terms of biogenic components during the mud deposition is unexpected. Backscattered electron imagery substantiates distinctly different componentry of the alternating light and dark laminae in the laminated mud. In particular, the light laminae contain scattered diatom fragments and eroded sand-sized lumps of fossil-bearing mud, whereas the dark laminae are clayey and diatomaceous. Both laminae thus are characterized by the high biogenic components, but they are interpreted to have been principally recycled from older deposits because diatom fragments are mostly reworked and old and their archives are poorly preserved. During the glacial periods, these laminated

22) 이 연구 결과는 다음의 논문으로 출판되었음: Khim. et al. (2024). "Fallacy of paleoproductivity signals by the recycled biogenic components: case study in the Central Basin of the northwestern Ross Sea" Geoscience Letters 11: 50.

muds were deposited downward by milky plumes of meltwater discharged underneath the advancing glaciers that scoured the earlier deposited and semi-consolidated diatom-rich sediments. Our study thus highlights that the recycling of biogenic particles should be precautious to avoid the fallacy of paleoclimatic interpretation in formulating climate-productivity models in the Antarctic continental margin.

1. Introduction

Antarctic cryosphere and hydrosphere are vulnerable to the impact of orbital-scale climate change in terms of ice sheet activity (Prothro et al. 2020). As a consequence, contrasting sediments as exemplified by an interglacial open marine deposit and a glacial diamicton have been deposited on the Antarctic continental shelves during the warm and cold conditions, respectively, in association with the advance or retreat of ice sheet (Anderson et al. 1984; Domack et al. 1999; Domack and Powell 2018). On the other hand, in the Antarctic continental margin where the ice sheet was not grounded, the amount of ice-rafted debris (IRD) has been proposed as a key to distinguish interglacial and deglacial (IRD-rich) sediments from glacial (IRD-poor or absent) sediments (Anderson et al. 1979; Anderson 1999; Khim et al. 2017; Smith et al. 2019; Hillenbrand et al. 2021; Bollen et al. 2022).

The Ross Sea continental shelf is known for being a biological 'hot spot' in the Southern Ocean, connecting the biogenic silica production in the water column to the current pattern of biosiliceous sediment accumulation (Ledford-Hoffman et al. 1986; Dunbar et al. 1989; Langone et al. 1998). In the Ross Sea, during the glacial periods, the biological productivity was limited in most continental shelves due to the advancing ice sheet (Frignani et al. 1998; McKay et al. 2008), and it was also reduced in the distal continental margin, mainly due to the wider expansion of seasonal or permanent sea ice coverage and limited nutrient availability (Ceccaroni et al. 1998; Cunningham et al. 1999). This confirms the coupling between climate and productivity (i.e., high productivity during warm interglacial), as verified from the numerous sedimentary records in the Ross Sea continental margin (Tolotti et al. 2013; Kim et al. 2020; Hartman et al. 2021; Li et al. 2022) as well as in the other Antarctic continental margin (Frank et al. 1995; Wu et al. 2017; Hillenbrand et al. 2021; Lu et al. 2022).

Recently, a core RS15-LC42 (hereafter LC42) was collected near the eastern flank of the Hallett Ridge in the Central Basin of the northwestern Ross Sea (Fig. 1). Khim et al. (2024) conducted the microscopic examination of the laminated mud layers in LC42, explaining that these laminated muds contain the components recycled by the transportation

and redeposition of reworked sediments from the older deposits. In this study, we performed multi-analyses of the biogenic components (biogenic opal, total organic carbon [TOC], and total nitrogen [TN]) in this core and found out their extraordinary results, which contradicts climate-productivity model based on glaciomarine sediment deposition. Our novel finding suggests that the recycled biogenic particles of the laminated mud layers in LC42 are an important example against the climate-productivity model, warning that overly simplistic glaciomarine sedimentation should be precautious for the reliable paleoenvironmental interpretations in the Antarctic continental margin.

2. Materials and Methods

The Central Basin is a deep semi-closed tectonic depression forming the slope basin located at the mouth of the JOIDES Basin in the northwestern Ross Sea (Fig. 1). During the austral summer of 2015, an 11.75-m-long core LC42 was collected from the northwestern moat (71°49.40′S, 178°34.76′E, 2084 m water depth) in the Central Basin using jumbo gravity coring system aboard I/B Araon. Optical images of LC42 were captured using ITRAX core scanner, and X-ray radiographic images were taken on 1-cm-thick sediment slabs using X-ray inspection equipment (SOFTEX W-100W) at Korea Polar Research Institute (KOPRI). X-ray images were digitized to obtain the gray scale (0 ~ 255) of sediment brightness.

KOPRI 극지연구소

Total carbon (TC), total nitrogen (TN), and biogenic opal contents were measured at 5 cm intervals at KOPRI. Because of such low-resolution sampling, the dark and light lamina cannot be separated during the analysis. TC and TN content was determined using an organic elemental analyzer (FLASH, 2000 NC Analyzer) with an analytical precision of less than ± 0.1%. Total inorganic carbon (TIC) content was measured using UIC CO2 coulometer (Model CM5240) with an analytical precision of less than ± 0.1%. Total organic carbon (TOC) content was calculated as the difference between TC and TIC content. Biogenic silica (SiBIO) concentration was measured using a continuous flow analyzer (SKALAR SANplus Analyzer) and the wet-alkaline extraction method modified from DeMaster (1981). Biogenic opal content was calculated by multiplying SiBIO concentration by 2.4 (Mortlock and Froelich 1989). The relative analytical error of SiBIO concentration is less than 1%.

Grain size analysis was performed on the selected three horizons that represent the major sediment lithology. Organic matter was removed from the bulk sediments using 10% H2O2. Coarser fractions (> 63 mm) were weighed at 1 phi interval using sieves, while finer fractions (< 63 mm) were analyzed using a Micromeritics Sedigraph III 5120 at KOPRI.

To examine the componentry of laminated sediments, polished sections were prepared using a fluid displacive resin embedding technique modified from Pike and Kemp (1996). These sections were examined using scanning electron microscope (SEM) (× 100-10000) with backscattered electron imagery (BSEI) of JEOL (JZA8530F PLUS) Field-Emission Electron Probe Micro-Analyzer at Gyeongsang National University (Korea).

3. Results and Discussion

Sediment lithology, age, and glaciomarine deposition of LC42

Based on visual observations and examinations, the sediments of LC42 were divided into three facies: (1) IRD-poor bioturbated sandy mud, (2) IRD-rich massive sandy mud, and (3) laminated mud (Fig. 2, Supplement Fig. S1). This classification was confirmed by the grain size distribution (Fig. 2). In particular, the coarse-grained particles are absent in the laminated mud. Despite the repetition of these three sediment facies throughout the core, their vertical succession does not show cyclic pattern. It is worth noting that the uppermost part of the core is occupied by IRD-poor bioturbated sandy mud and IRD-rich massive sandy mud, which overlie the laminated mud (Fig. 2, Supplement Fig. S1). LC42 preserves eight intervals of laminated sediments with varying thicknesses (10 cm to about 2 m) throughout the core. The laminated sediments are devoid of IRD and bioturbation. The laminations consist of alternating relatively thicker light laminae and relatively thinner dark laminae (Fig. 2 and Supplement Fig. S1). Khim et al. (2024) carried out the microscopic observation and backscattered electron imagery examination of these laminated muds, and reported that the light laminae consists of mostly terrigenous angular to subangular silt-sized particles with diatom fragments and eroded fossil-bearing sand-sized lumps and the dark laminae are composed of biogenic clays with very tiny pieces of fossils.

Ohneiser et al. (2019) reported the preliminary magneto-biostratigraphy of LC42 that contains the first appearance datum (0.57-0.65 Ma) of Thalassiosira antarctica and the Matuyama-Brunhes boundary (0.781 Ma). Later, Bollen et al. (2022) confirmed that LC42 spans the last 1.34 Ma, based on a new magnetobiostratigraphic age model (Fig. 3). This implies that, if the glaciomarine sedimentation was continuous, there must be at least 10 orbital-scale (i.e., eccentricity) interglacial and glacial cycles during the deposition of LC42. Nonetheless, determining the precise age of each sediment facies and correlating with the interglacial-glacial cycles have proven challenging, despite the speculative correlation (Fig. 3) by Bollen et al. (2022). Thus, we cannot differentiate the interglacial and glacial cycles as well as the sedimentation rate change.

Based on the glaciomarine depositional processes in the Antarctic continental margins (Anderson 1999; Domack and Powell 2018), IRD deposition increased during the warm period by more active calving and floating ice, whereas the lack of IRD seems to be due to the wide development of sea ice during the glacial period. Based on the temporal succession of sediment facies at the uppermost of core and application to the glaciomarine sedimentation, IRD-poor bioturbated sandy mud and IRD-rich massive mud might have been deposited during the interglacial and deglacial periods, whereas the laminated mud may represent glacial sediments without IRD (Anderson et al. 1979; Anderson 1999; Khim et al. 2017; Domack and Powell 2018). Recently, Bollen et al. (2022) reported the hypothesized schematic depositional conditions for three sediment facies in LC42. IRD-rich deposit was influenced by a combination of enhanced glacial calving during the glacial retreat and export of shelf water during interglacial and weak glacial periods. In contrast, IRD-poor deposit and laminated sediments were formed due to glacial scouring to induce slope failures and turbidity currents as well as transport of shelf sediments by meltwater pulses, depending on the partial or full glacial advance.

Paleoproductivity change in terms of biogenic components in LC42

TOC, TN, and biogenic opal contents of glaciomarine sediments serve as an indicator of surface water productivity in the Ross Sea, although their preservation potentials are different, depending on diverse environmental factors (e.g., Langone et al. 1998). For example, Bahr et al. (2014) reported the XRD scanning geochemical data of contourites in the Gulf of Cadiz, and suggested that the bromine (Br) record represents TOC content in response to the climate signals. Th results indicate that the geochemical information was infl ed by the bottom water activity rather than the surface water properties, despite the millennial timescale. Downcore variation of TOC, TN, and biogenic opal contents of LC42 exhibits remarkable characteristics throughout the core (Fig. 3). All biogenic contents of laminated mud are consistently higher compared to other two sediment facies. Despite the low-resolution sampling interval (5 cm), variations of these components are more common within the laminated mud layer. In particular, variation of these three properties shows a clearly parallel pattern in laminated mud layer throughout the core (Fig. 3).

The linear relationship between TOC and TN contents provides evidence of their typical marine origin (Fig. 4a). The strong positive relationship between TOC and biogenic opal contents further supports the interdependence of these components. Their relationship in LC42 shows that the biogenic opal content during the interglacial period is similar to that of the Holocene surface sediments (Fig. 4b and c) and that the variation range of TOC

and biogenic opal contents in LC42 is not much different between the interglacial and glacial periods (Fig. 4b). High TOC and biogenic opal contents of laminated mud layers are characteristic, because they were formed during the glacial periods. On the other hand, high C/N ratios of laminated mud layers result from the different degradation between TOC and TN, which reflects that the organic matters of laminated mud layers experienced the differential degradation before the deposition. Such high C/N ratios of laminated mud layers are different from those of diamicton and calving ice that contain the terrestrial organic matters in the Ross Sea (Smith et al. 2019). Based on the climate-productivity model, high productivity occurred during the interglacial periods, which was verified by the higher deposition of TOC and biogenic opal content during the warm conditions in the Ross Sea as shown in cores ANTA91-8 (Ceccaroni et al. 1998) and RS15-GC41 (Kim et al. 2020) (Fig. 4c). In LC42, thus, it can be simply interpreted that the deposition of the laminated mud reflects a higher productivity condition, representing the warm interglacial periods. However, it contradicts the interpretation by the glaciomarine depositional processes as described in the previous section.

In general, the paleoproductivity increased from the glacial periods to the deglacial-to-interglacial periods in the Antarctic continental margin including the Ross Sea (Frank et al. 1995; Ceccaroni et al. 1998; Frignani et al. 1998; Cunningham et al. 1999; McKay et al. 2008; Tolotti et al. 2013; Wu et al. 2017; Kim et al. 2020; Hartman et al. 2021; Li et al. 2022; Lu et al. 2022). Such increase can be attributed to the reduction of sea ice coverage, which promoted the light availability for photosynthesis, and to more nutrient supply by the current system such as the Antarctic Slope Current. In the Ross Sea continental margin, similar to other Antarctic continental margins, interglacial sediments are characterized by high biogenic components, compared to glacial sediments (Cunningham et al. 1999; Tolotti et al. 2013; Kim et al. 2020; Hartman et al. 2021; Li et al. 2022). Hence, considering the depositional evolution by the temporal succession of sediment lithology in LC42, the high content of biogenic components in the laminated mud layers is unusual.

False paleoproductivity signal by recycled biogenic components in LC42

The laminated terrigenous muds, which are lack of biogenic components, have been reported in the continental slope and rise of the Antarctic continental margins and are thought to be the products of contour currents during the glacial periods (e.g., Venuti et al. 2011). On the other hand, the laminated biosiliceous muds show circum-Antarctic distribution in the inner shelf basins and troughs of the Antarctic continental shelves (e.g., Leventer et al. 2006; Tesi et al. 2020). In particular, varved couplets, representing seasonality, of diatomaceous lamina reflect extremely high primary productivity in the

calving bays of the Antarctic ice sheet during the deglaciation (Stickley et al. 2005). However, the laminated mud layers in LC42 are not typical of both types of laminated muds in the Antarctic continental margin.

BSEI verifies that the light and dark laminae are millimeterto submillimeter-thick and composed mainly of silty and clayey particles, respectively (Fig. 5a, e, i). In this laminated mud layer, due to the low-resolution sampling interval, the fluctuation of biogenic components (TOC and biogenic opal) depends on the sampling horizons of light or dark laminae (Figs. 3 and 5). The coarse-grained light lamina consists of very fine sandto silt-sized angular to subangular quartz and feldspar grains, and contains considerable amounts of sandto silt-sized biogenic fragments and sand-sized lumps of coagulated very small diatom fragments and clay particles (Fig. 5b, f, j and k). In contrast, the fine-grained dark lamina consists of sparsely scattered silt-sized particles of terrigenous or biogenic origin in a diatomaceous clayey matrix (Fig. 5a and l). Nonetheless, high biogenic components of these laminae in the laminated mud are attributed to the tiny fragments of diatom and clay-sized powder with eroded diatom-rich lumps or chips (Fig. 5b, c, f, g and j). Although some diatom archives are preserved (Fig. 5h), it is clearly discernible that most diatoms are tiny fragments, clay-sized powders, and semi-consolidated pieces, which were principally recycled (Fig. 5c, f, g and j). In addition, Bollen et al. (2022) reported that diatom species in the laminated mud layers are mostly old (Pliocene to Miocene) and reworked. Thus, high TOC, TN, and biogenic opal contents of the laminated mud layers in LC42 were not related to the enhanced biological productivity in the surface water of the Central Basin at the time of mud deposition.

During the Last Glacial Maximum, the ice sheet did not advance to the shelf edge in the central and western Ross Sea (e.g., Lee et al. 2017). The glacial activity near the grounding line of ice sheet have influenced the depositional condition in the Central Basin of the northwestern Ross Sea. The gravity flow or mass flow including slope failure and turbidity currents occurred frequently at the front of grounding line (e.g., Anderson et al. 1984; Domack and Powell 2018). The preservation of laminated mud layers in the Central Basin seem spatially limited, because the same kind of sediment facies has not been reported yet. The laminated muds were deposited due to the continuous supply of a milky plume generated by meltwater underneath the advancing glacier. This milky plume contained the eroded lumps of semi-consolidated diatom-rich fossiliferous sediments. Following the glacial pumping, the lamination may have been formed by the density-based segregation of grain size and selective settling during the continuous flow. Khim et al. (2024) observed pinch-and-swelling and low-angle inclined lamination from the light laminae with possible internal truncation surfaces and particle imbrication, which suggests that the mud deposition might have occurred by dilute density currents (Mulder et al.

2003; Tripsanas and Piper 2008). These density currents could have been fed by subglacial meltwater discharges or buoyant suspensions associated with mass wasting processes, such as slide/slump or slope failure and debris flows including turbidity currents, near the grounding lines (Bollen et al. 2022). In addition, framboidal pyrites observed in the laminated muds evidenced that the dissolved oxygen concentration was low during the deposition or postdeposition (Fig. 5d). In the similar way, the deglacial and glacial sediments in the continental slope and rise of the Ross Sea are characterized by higher levels of biogenic components than the Holocene sediments (Khim et al. 2021; Ha et al. 2022), which were interpreted to be due to the glacial supply of reworked diatom-rich shelf sediments (Fig. 4d). Our finding thus confirms that the degree of paleoproductivity should be judged cautiously by considering the recycling of biogenic particles to avoid a wrong or overly simplistic interpretation based on the current climate-productivity model in the Antarctic continental margin.

4. Conclusions

Glaciomarine sediments around the Antarctic continental margin provided important paleoceanographic and paleoclimatic information in association of ice sheet dynamics. The climate-productivity model in the Antarctic continental margin defines the coupling of climate change and biological productivity, i.e., high productivity during the warm interglacial and vice versa. In the Ross Sea continental margin, the glacial productivity was reduced due to the wider expansion of seasonal or permanent sea ice coverage and limited nutrient availability. Core LC42 from the Central Basin contains a series of laminated mud layer that were characterized by high biogenic components, compared to the IRD-poor bioturbated sandy mud and IRD-rich massive mud layers, although the laminated mud deposition might have occurred during the glacial periods. Such unexpected contrast was solved by BSEI observation that most biogenic components of the laminated muds were recycled from older deposits, containing old and reworked diatom fragments, eroded sand-sized lumps of fossil-bearing mud, and diatomaceous clayey particles. In situ paleoproductivity information seems difficult to obtain in terms of conventional biogenic proxies in the case of the laminated mud deposition in the Central Basin. Finally, reworking of older biogenic components in the Antarctic depositional system should have been considered, avoiding the misinterpretation of the paleoclimate and paleoenvironment.

KOPRI 극지연구소

중앙 분지 북서 로스해에서의 사례 연구: 재순환된 생물기원 성분에 의한 고생산성 신호의 오류

Boo-Keun Khim[1], Sunghan Kim[2], Min Kyung Lee[2], Young Kwan Sohn[3], Jae Il Lee[2] and Kyu Cheul Yoo[2]

[1]Department of Oceanography and Marine Research Institute, BK21 School of Earth and Environmental Systems, Pusan National University, Busan, Korea.
[2]Division of Glacial & Earth Sciences, Korea Polar Research Institute, Incheon, Korea.
[3]Department of Geology, Gyeongsang National University, Jinju, Korea.

요약: 북서부 로스해 중앙 분지에서 채취된 LC42 코어는 지난 100만 년 동안 서로 교호하며 퇴적된 세 가지 뚜렷한 퇴적상(IRD(빙하 기원 부유 쇄설물)가 적은 생물교란 사질 이질, IRD가 풍부한 괴상 사질 이질, 층리질 이질)을 포함한다. 코어 전 구간에 걸쳐 층리질 이질층의 생물기원 성분(생물기원 오팔, 총유기탄소, 총질소)은 다른 두 퇴적상보다 일관되게 높게 나타난다. 남극 대륙 주변부에서의 퇴적상 천이와 IRD 관련 퇴적 과정을 바탕으로 해석할 때, IRD가 없는 층리질 이질층은 빙기 동안 퇴적된 것으로 판단된다. 그러나 이질 퇴적 동안 생물기원 성분 증가로 나타나는 고생산성의 증가는 예상 밖의 결과이다. 후방산란전자 영상은 층리질 이질을 구성하는 밝은 층리와 어두운 층리가 구성 성분에서 뚜렷한 차이를 보임을 보여준다. 특히 밝은 층리는 산재된 규조류 파편과 화석을 포함한 이질이 침식되어 형성된 모래 크기 덩어리를 포함하는 반면, 어두운 층리는 점토질이며 규조류가 풍부하다. 따라서 두 층리 모두 생물기원 성분이 높다는 특징을 보이지만, 규조류 파편이 대부분 재동된 오래된 것이고 그 보존 상태가 불량하다는 점에서, 이들 성분은 주로 고기 퇴적물로부터 재순환된 것으로 해석된다. 빙기 동안 이러한 층리질 이질은 전진하는 빙하 하부에서 방출된 탁한 용융수 플룸에 의해 하향 퇴적되었으며, 이 과정에서 이전에 퇴적되어 반고결된 규조류 풍부 퇴적물이 침식되었다. 따라서 본 연구는 남극 대륙 주변부에서 기후-생산성 모델을 수립할 때 고기후 해석의 오류를 피하기 위해 생물기원 입자의 재순환 가능성을 신중히 고려해야 함을 강조한다.

References

Anderson JB (1999) Antarctic marine geology. Cambridge University Press, Cambridge

Anderson JB, Kurtz DD, Weaver FM (1979) Sedimentation on the Antarctic continental slope. In: Doyle LJ, Pilkey O (eds) Geology of continental slopes. SEPM, Tulsa

Anderson JB, Brake CF, Myers NC (1984) Sedimentation on the Ross sea continental shelf, Antarctica. Mar Geol 57:295-333

Bahr A, Jimenez-Espejo FJ, Kolasinac N, Grunert P, Hernandez-Molina FJ, Rohl U, Voelker AHL, Escutia C, Stow DAV, Hodell D, Alvarez-Zarikian CA (2014) Deciphering bottom current velocity and paleoclimate signals from contourite deposits in the Gulf of Cadiz during the last 140 kyr: an inorganic geochemical approach. Geochem Geophys Geosyst 15:3145-3160

Bollen M, Riesselman CR, Ohneiser C, Albot O, McKay R, Lee MK, Yoo KC, Kim S, Lee JI, Levy R (2022) Pleistocene oceanographic variability in the Ross Sea: a multiproxy approach to age model development and paleoenvironmental analyses. Global Planet Ch 216:103901. https://doi.org/10.1016/j. glopalcha.2022.103901

Ceccaroni L, Frank M, Frignani M, Langone L, Ravaioli M, Mangini A (1998) Late Quaternary fluctuations of biogenic component fluxes on the continental slope of the Ross Sea, Antarctica. J Mar Syst 17:515-525

Cunningham WL, Leventer A, Andrews JT, Jennings AE, Licht KJ (1999) Late Pleistocene-Holocene marine conditions in the ross sea, Antarctica: evidence from the diatom record. The Holocene 9:129-139

DeMaster DJ (1981) The supply and accumulation of silica in the marine environment. Geochim Cosmochim Acta 45:1715-1732

Domack EW, Powell R (2018) Chapter 7 Modern glaciomarine environments and sediments: an Antarctic perspective. In: Menzies J, van der Meer J (eds) Past glacial environments. Elsevier, Amsterdam

Domack EW, Jacobson EA, Shipp S, Anderson JB (1999) Late Pleistocene-Holocene retreat of the West Antarctic Ice-Sheet system in the ross sea: part 2-sedimentologic and stratigraphic signature. Geol Soc Am Bull 111:1517-1536

Dunbar RB, Leventer A, Stockton WL (1989) Biogenic sedimentation in McMurdo sound, Antarctica. Mar Geol 85:155-179

Frank M, Eisenhauer A, Bonn WJ, Walter P, Grobe H, Kubik PW, Dittrich-Hannen B, Mangini A (1995) Sediment redistribution versus paleoproductivity change: Weddell Sea margin sediment stratigraphy and biogenic particle flux of the last 250,000 years deduced from 230Thex, 10Be and biogenic barium profiles. Earth Planet Sci Lett 136:559-573

Frignani M, Giglio F, Langone L, Ravaioli M, Mangini A (1998) Late Pleistocene-Holocene sedimentary fluxes of organic carbon and biogenic silica in the northwestern Ross Sea, Antarctica. Annals Glaciol 27:697-703

Ha S, Colizza E, Torricella F, Langone L, Giglio F, Kuhn G, Macri P, Khim BK (2022)

KOPRI 극지연구소

Glaciomarine sediment deposition on the continental slope and rise of the central Ross Sea since the Last Glacial Maximum. Mar Geol 445:106752

Hartman JD, Sangiorgi F, Barcena MA, Tateo F, Giglio F, Albertazzi S, Jtrincardi F, Bijl PK, Langone L, Asioli A (2021) Sea-ice, primary productivity and ocean temperatures at the Antarctic marginal zone during late Pleistocene. Quat Sci Rev 266:107069

Hillenbrand CD, Crowhurst SJ, Williams M, Hodell DA, McCave IN, Ehrmann W, Xuan C, Piotrowski AM, Hernendez-Molina FJ, Graham AGC, Grobe H, Williams TJ, Horrocks JR, Allen CS, Larter RD (2021) New insights from multi-proxy data from the West Antarctic continental rise: Implications for dating and interpreting Late Quaternary palaeoenvironmental records. Quat Sci Rev 257:106842

Khim BK, Song B, Cho HG, William T, Escutia C (2017) Late Neogene sediment properties in the Wilkes Land continental rise (IODP Exp. 318 Hole U1359A) East Antarctica. Geosci J 21:21-32

Khim BK, Colizza E, Lee JI, Giglio F, Ha S, Bak YS (2021) Biological productivity and glaciomarine sedimentation in the central basin of the northwestern Ross sea. Polar Sci 28:100682

Khim BK, Sohn YK, Lee MK, Kim S, Lee JI, Yoo KC (2024) Pleistocene glaciomarine laminated muds in the Central Basin of the northwestern Ross Sea and their paleoceanographic records. Terra Nova 36:37-44. https://doi. org/10.1111/ter.12688

Kim S, Lee JI, McKay RM, Yoo KC, Bak YS, Lee MK, Roh YH, Yoon HI, Moon HS, Hyun CU (2020) Late Pleistocene paleoceanographic changes in the Ross Sea-Glacial-interglacial variations in paleoproductivity, nutrient utilization, and deep-water formation. Quat Sci Rev 239:106356

Langone L, Frignani M, Labbrozzi L, Ravaioli M (1998) Present-day biosiliceous sedimentation in the northwestern Ross Sea, Antarctica. J Mar Syst 17:459-470

Ledford-Hoffman PA, DeMaster DJ, Nittrouer CA (1986) Biogenicsilica accumulation in the Ross Sea and the importance of Antarctic continental shelf deposits in the marine silica budget. Geochim Cosmochim Acta 50:2099-2110

Lee JI, McKay RM, Golledge NR, Yoon HI, Yoo KC, Kim HJ, Hong JK (2017) Wide-spread persistence of expanded East Antarctic glaciers in the southwest Ross Sea during the last deglaciation. Geology 45:403-406

Leventer A, Domack E, Dunbar R, Pike J, Stickley C, Maddison E, Brachfeld S, Manley P, McClennen C (2006) Marine sediment record from the East Antarctic margin reveals dynamics of ice sheet recession. Geol Soc Am Today 16:4-10

Li G, Bu R, Yi L, Hu B, Li Y, Ji Y, Li Y, Wang L (2022) Geochronology and paleoenvironmental changes of Late Pleistocene sediments in the ross sea Antarctica. Front Earth Sci 10:863336

Lisiecki LE, Raymo ME (2005) A Pliocene-Pleistocene stack of 57 globally distributed benthic δ 18O records. Paleoceanography 20:1

Lu L, Zheng X, Chen Z, Yan W, Wu S, Zheng L-W, Wang X, Chen Y, Kao S (2022)

One-to-one coupling between Southern Ocean productivity and Antarctica climate. Geophys Res Lett. https://doi.org/10.1029/2022GL098761

McKay RM, Dunbar GB, Naish TR, Barrett PJ, Carter L, Harper M (2008) Retreat history of the ross ice sheet (Shelf) since the last glacial maximum from deep-basin sediment cores around ross Island. Palaeogeogr Palaeoclimatol Palaeoecol 260:245-261

Mortlock RA, Froelich PN (1989) A simple method for the rapid determination of opal in pelagic marine sediments. Deep Sea Res 36:1415-1426

Mulder T, Syvitski JPM, Migeon S, Faugere JC, Savoye B (2003) Marine hyperpycnal flows: initiation, behavior and related deposits. Rev Mar Petrol Geol 20:861-882

Ogg JG (2020) Chapter 5 Geomagnetic polarity time scale. Geologic time scale. Elsevier, Amsterdam

Ohneiser C, Yoo KC, Albot OB, Cortese G, Riesselman C, Lee JI, McKay R, Bollen M, Lee MK, Moon HS, Kim S, Beltran C, Levy R, Wilson G (2019) Magneto-biostratigraphic age models for Pleistocene sedimentary records from the Ross Sea. Global Planet Ch 176:36-49

Pike J, Kemp AES (1996) Preparation and analysis techniques for studies of laminated sediments. Palaeoclimatology and Palaeoceanography from laminated sediments. Geol Soc London Spec Publ. https://doi.org/10. 1144/GSL.SP.1996.116.01.05

Prothro LO, Majewski W, Yokoyama Y, Simkins LM, Anderson JB, Yamane M, Miyairi Y, Ohkouchi N (2020) Timing and pathways of east Antarctic ice sheet retreat. Quat Sci Rev 230:106166

Smith JA, Graham AGC, Post AL, Hillenbrand CD, Bart PJ, Powell RD (2019) The marine geological imprint of Antarctic ice shelves. Nat Comm 10:5635

Stickley CE, Pike J, Leventer A, Dunbar R, Domack EW, Brachfeld S, Manley P, McClennan C (2005) Deglacial ocean and climate seasonality in laminated diatom sediments, Mac. Robertson Shelf Antarctica. Palaeogeogr Palaeoclimatol Palaeoecol 227:290-310

Sutter J, Fischer H, Grosfeld K, Karlsson NB, Kleiner T, Van Liefferinge B, Eisen O (2019) Modelling the Antarctic Ice Sheet across the mid-Pleistocene transition implications for Oldest Ice. Cryosphere 13:2023-2041

Tesi T, Belt ST, Gariboldi K, Muschitiello F, Smik L, Finocchiaro F, Giglio F, Colizza E, Gazzurra G, Giordano P, Morigi C, Capotondi L, Nogarotto A, Koseoglu D, Di Roberto A, Gallerani A, Langone L (2020) Resolving sea ice dynamics in the north-western Ross Sea during the last 26 ka: from seasonal to millennial timescales. Quat Sci Rev. https://doi.org/10.1016/j.quascirev. 2020.106299

Tolotti R, Salvi C, Salvi G, Bonci MC (2013) Late Quaternary climate variability as recorded by micropalaeontological diatom data and geochemical data in the western Ross Sea, Antarctica. Ant Sci 25:804-820

Tripsanas EK, Piper DJW (2008) Late quaternary stratigraphy and sedimentology of orphan basin: implications for meltwater dispersal in the southern Labrador sea. Palaeogeogr Palaeoclimatol Palaeoecol 260:521-539

Venuti A, Florindo F, Caburlotto A, Hounslow MW, Hillenbrand CD, Strada E, Talarico FM, Cavallo A (2011) Late Quaternary sediments from deep-sea sediment drifts on the Antarctic peninsula pacific margin: climatic control on provenance of minerals. J Geophys Res (Solid Earth) 116:B06104. https://doi.org/10.1029/2010JB007952

Wu L, Wang R, Xia W, Ge S, Chen Z, Krijgsman W (2017) Productivity-climate coupling recorded in Pleistocene sediments off Prydz Bay (East Antarctica). Palaeogeogr Palaeoclimatol Palaeoecol 485:260-270

KOPRI
극지연구소

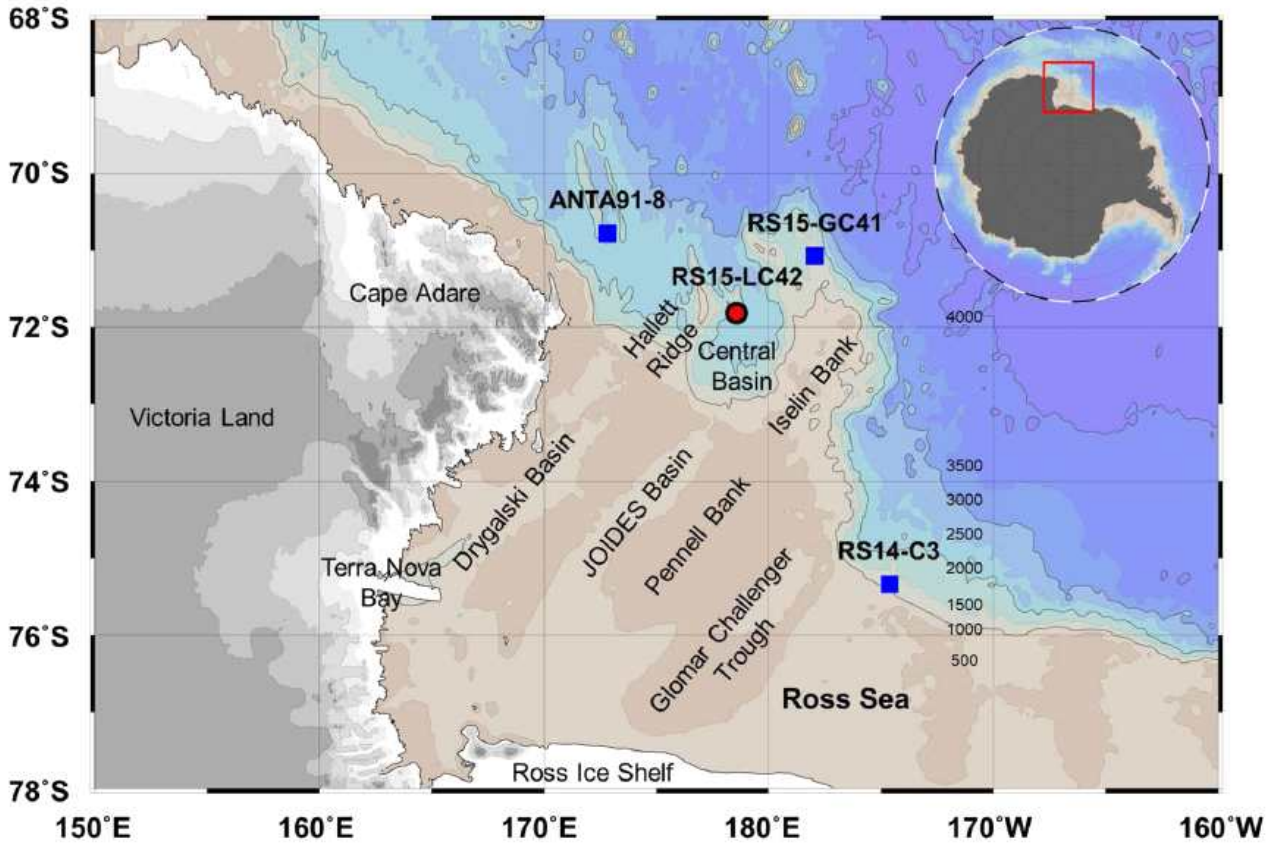


Figure #. Bathymetric map showing the geomorphologies in the Ross Sea with the location of core RS15-LC42 (this study) and other studied cores ANTA91-8 (Ceccaroni et al. 1998), RS15-GC41 (Kim et al. 2020), and RS14-C3 (Ha et al. 2022

KOPRI
극지연구소

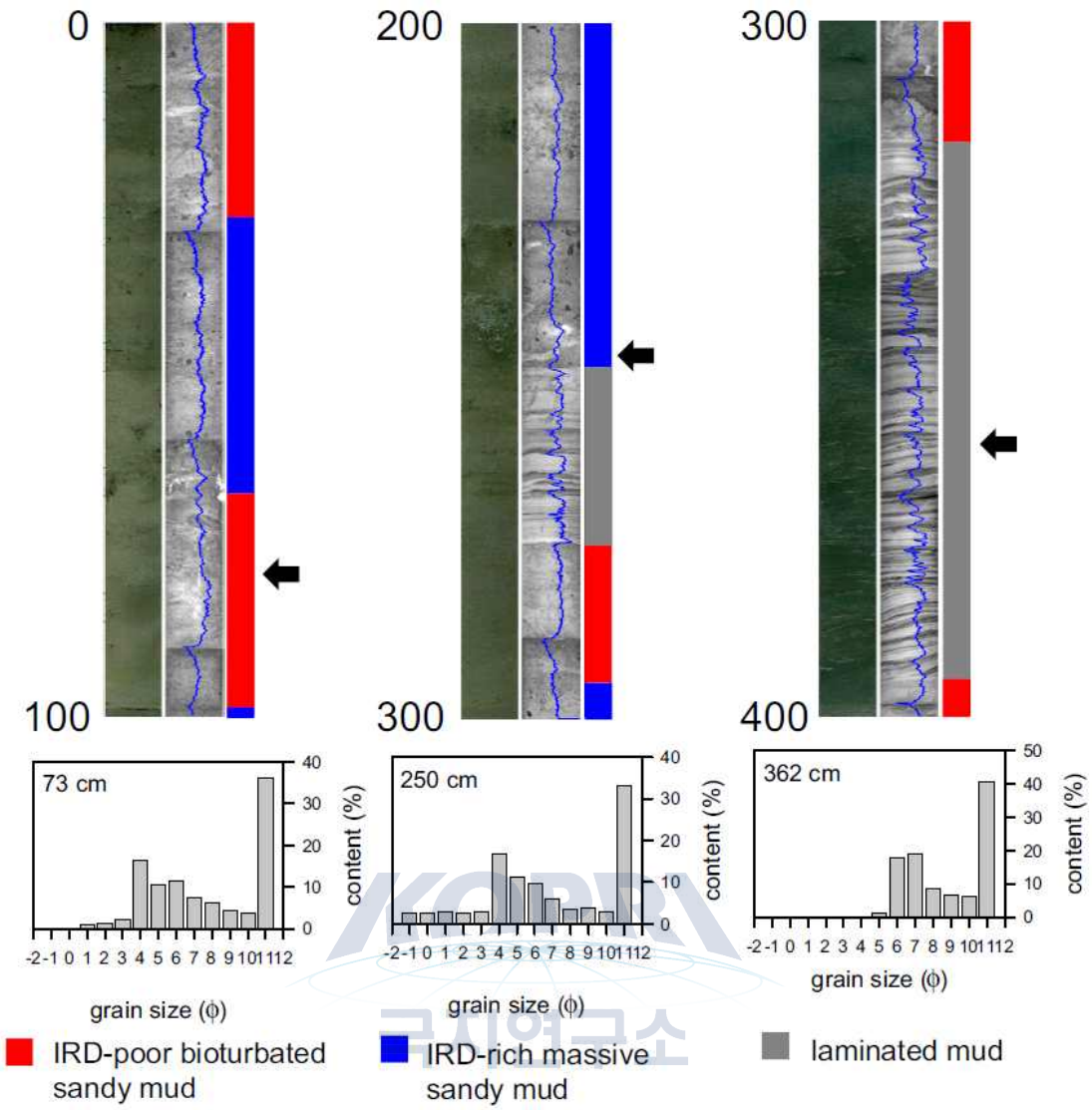


Figure #. Selected core photos and X-ray photographs of core LC42, consisting of three major lithologic facies (IRD-poor bioturbated sandy mud, IRD-rich massive mud, laminated mud). Three sediment facies were distinguished by the grain size distribution of horizon marked by the black arrow. Blue line on the X-ray photograph shows the gray scale to delineate the laminations

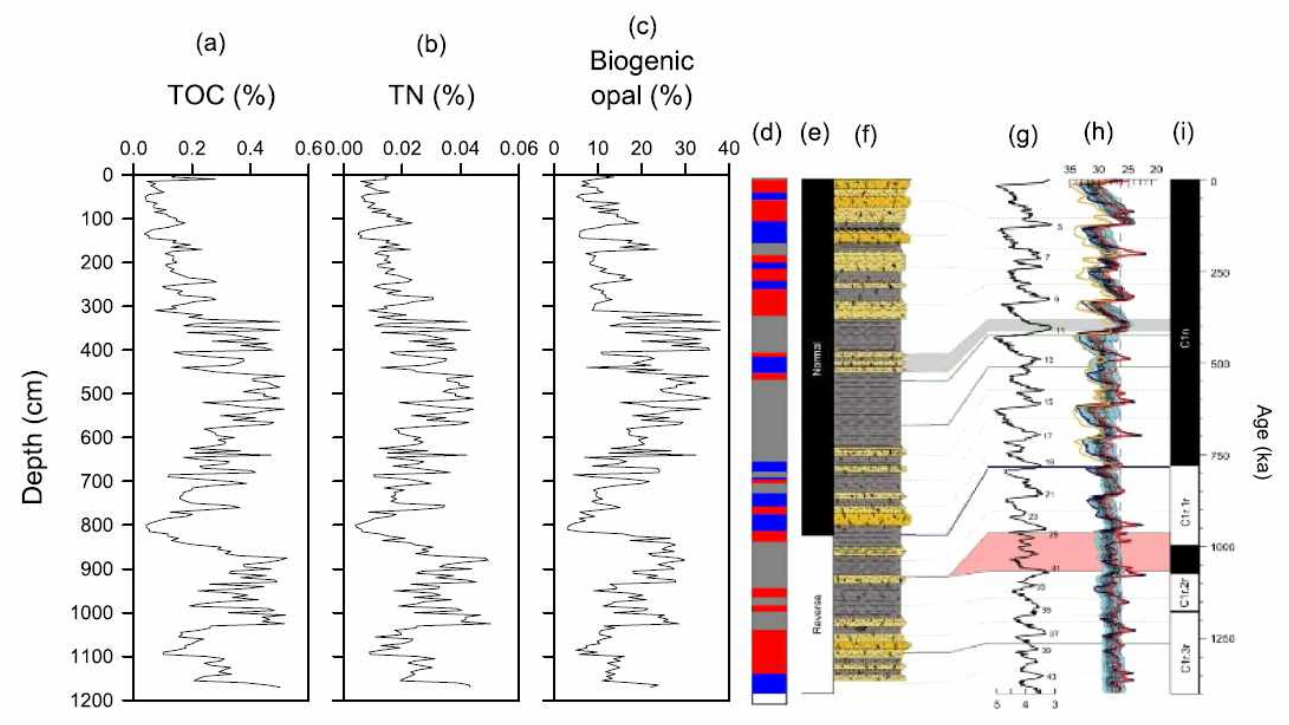


Figure #. a-c Downcore variation of TOC, TN, and biogenic opal content; d schematic summary of sediment facies; e geomagnetic polarity (after Bollen et al. 2022); f sediment lithology (after Ohneiser et al. 2019); g the global benthic foraminifera δ18O stack (Lisiecki and Raymo 2005); h modeled Antarctic ice volume (Sutter et al. 2019); and i the global polarity timescale (Ogg 2020). The grey shaded area aligns the gravel peak from 4.0 to 4.5 mbsf to MIS 11 for reference and the red shaded area shows the missing time period over the interpreted hiatus at ~ 9.34 mbsf (Bollen et al. 2022)

KOPRI 극지연구소

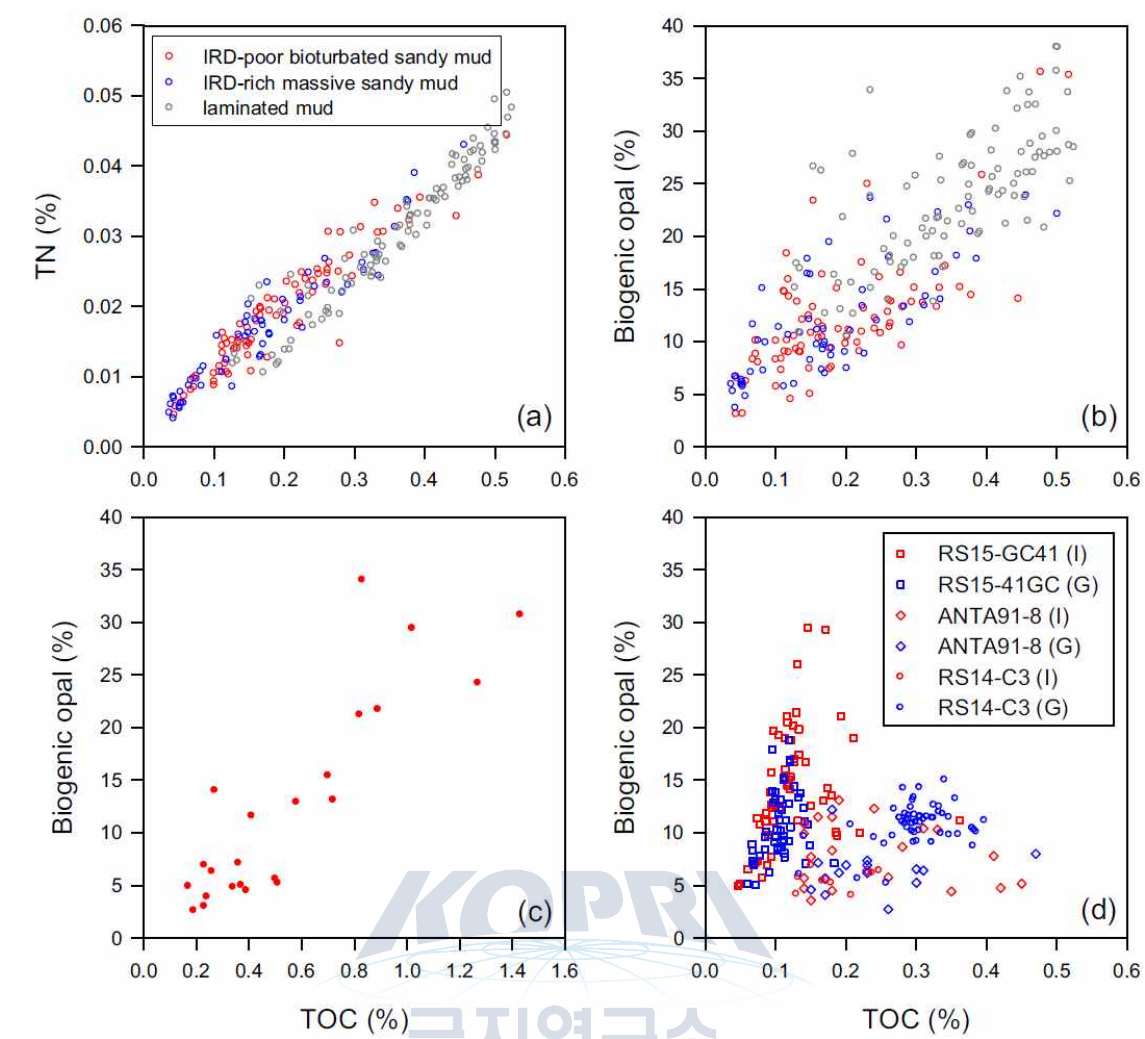


Figure #. a Correlation between TOC and TN contents of each lithology in LC42. b Correlation between TOC and biogenic opal contents of each lithology in LC42. c Correlation between TOC and biogenic opal contents of surface sediments (Langone et al. 1998). d Correlation between TOC and biogenic opal contents of cores RS15-GC41 (Kim et al. 2020), ANTA91-8 (Ceccaroniet al. 1998), and RS14-C3 (Ha et al. 2022) between the interglacial and glacial periods

KOPRI 극지연구소

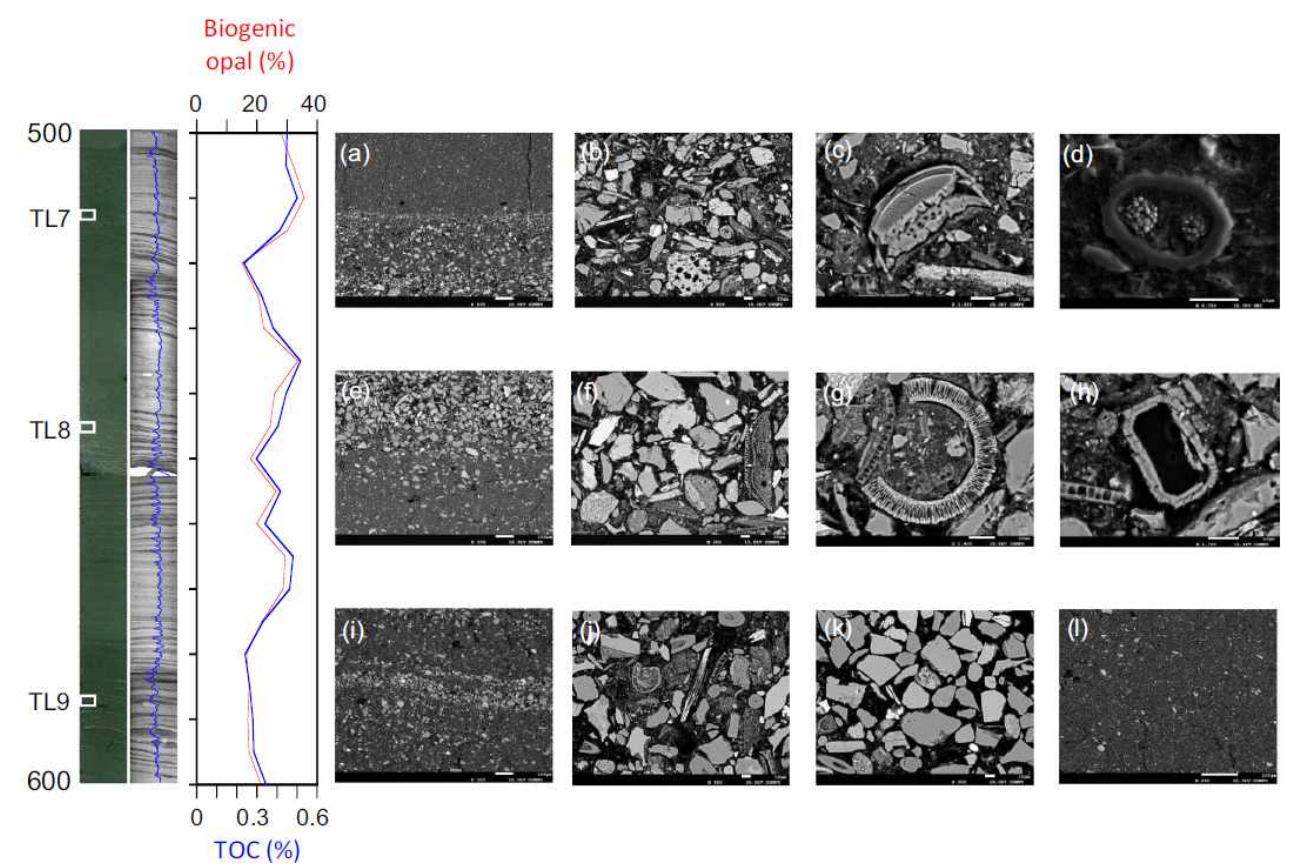


Figure #. Core photo, X-ray photograph, and downcore variation of biogenic opal and TOC contents between 500 and 600 cm of LC42, representing the laminated mud layer, with three positions of polished sections (TL7, TL8, and TL9). Blue line on the X-ray photograph shows the gray scale to delineate the laminations. BSEI of polished sections (a to d from TL7, e to h from TL8, and i to l from TL9): a alternations of light and dark laminae with sharp boundary, scale bar: 100 um (× 100); b coarse-grained componentry of fragmented diatoms, scale bar: 10 um (× 500); c fragmented diatom, scale bar: 10 um (× 1300); d framboidal pyrite, scale bar: 100 um (× 2700); e alternations of light and dark laminae with gradual boundary, scale bar: 100 um (× 100); f coarse-grained componentry of semi-consolidated eroded lump contained diatom fragments, scale bar: 10 um (× 500); g semi-consolidated diatom fragments infilled in the biogenic fossil, scale bar: 10 um (× 1400); h archive diatom, scale bar: 10 um (× 1700); i alternations of submillimeter-thick, light and dark laminae, scale bar: 100 um (× 100); j coarse-grained componentry of semi-consolidated eroded lump contained diatom fragments, scale bar: 10 um (× 500); k angular to subangular silt-sized grains, scale bar: 10 um (× 500); l diatomaceous clayey matrix with very fine silt particles, scale bar: 100 um (× 200). More BSEI of polished sections of LC42 refers to Khim et al. (2024)

제 30 장

Controls on spatial heterogeneity in dinoflagellate cyst distribution in recent sediments off West Antarctica[23)]

So-Young Kim[a,*], Taewook Park[a], Fabienne Marret[b*], Kyu-Cheul Yoo[a], Jeong-Hoon Kim[a], Lorena Rebolledo[c], Jung-Ok Choi[a], Hyoung Sul La[a], Sun-Yong Ha[a], Heung Soo Moon[a]

[a]Korea Polar Research Institute, [b]University of Liverpool, [c]Instituto Antárctico Chileno

Abstract: Here we present the study of 48 new dinoflagellate cyst assemblages from the west Antarctic shelf sediments on a wide longitudinal scale, with a greater representation of ice-proximal sites, and provide a comprehensive overview of their distributional patterns and multiple environmental forcing factors. We find a strong spatial heterogeneity in the dinoflagellate cyst distribution patterns; 1) the northern Antarctic Peninsula region is dominated by *Islandinium*? *minutum*, *Selenopemphix antarctica* and *Brigantedinium* spp. in association with meltwater-induced stratification and high diatom productivity, 2) the Bellingshausen-Amundsen Seas is dominated by *Gymnodinium microreticulatum* and *Selenopemphix* sp. 1, under influences of strong offshore winds, unstable water column and *Phaeocystis* blooms in austral summer, and 3) the Ross Sea shows an extreme contrast - the east-central region under vigorous vertical mixing and high *Phaeocystis* production is dominated by *Selenopemphix* sp. 1, while the western side with high sea-ice concentration and sea-ice derived meltwater stratification is dominated by *Polarella glacialis* cysts together with *Nucicla umbiliphora*, *I.*? *minutum* and *Cryodinium meridianum*. The robust along-shelf separations of the dinoflagellate cyst species compositions highlight melt-related hydrodynamic-meteorological coupling processes around maritime Antarctica that control physico-biological properties and overall microplankton communities therein. As the ice-shelf disintegration and sea-ice loss continue, there will be a fundamental reconfiguration of microplankton production and their community structures in a future Antarctic Ocean with greater open-water areas. This study highlights the potential of dinoflagellate cysts to monitor changes in

23) 이 연구 결과는 다음의 논문으로 출판되었음: Kim, S.Y. et al. (2026). "Controls on spatial heterogeneity in dinoflagellate cyst distribution in recent sediments off West Antarctica." Marine Pollution Bulletin 222: 118631.

hydrographic conditions and plankton communities in these sensitive polar marine ecosystems.

1. Introduction

Antarctica is considered one of Earth's last great frontiers because of its remote location and frozen, harsh environments. Encircled by polar oceans and the southern westerly wind belt that obstruct warming air, the isolated continent has long been considered a climate wildcard that does not directly respond to contemporary global mean temperature rise (e.g., Parkinson and Cavalieri, 2012; Hahn et al., 2020). However, recent observations report a significant warming in Antarctica at almost twice the rate of other regions of the world during the last decades (Dalaiden et al., 2022; Casado et al., 2023). This phenomenon, known as polar amplification, has been observed in the Arctic (Bekryaev et al., 2010; Rantanen et al., 2022), linked to rising temperatures and rapid sea-ice loss (Gille, 2002; Shi et al., 2021; Purich and Doddridge, 2023). Likewise, detectable shifts in physical, chemical and biological components of the Antarctic Ocean at regional and continental scales track a sign this region may have entered a "new regime" of losing ice coverage (Purich and Doddridge, 2023; Swadling et al., 2023). Emerging impacts of the current Antarctic climate state are ascertained and closely monitored by rapid melt of ice sheet/shelves and sea-ice changes in the west Antarctic sector (e.g., Cook and Vaughan, 2010; Rignot et al., 2013; Massom et al., 2018). Because ice-ocean interactions drive hydrodynamic processes and biogeochemical cycles in the Antarctic Ocean, being a key component in its marine ecosystems, such changes will likely have far-reaching ramifications for west Antarctic marine biotas and their community structures (Henley et al., 2020; Pinkerton et al., 2021).

Marine microplankton populations form the basis of Antarctic marine food chains and play a major role in the biological carbon pump and the global carbon budget (Sherr and Sherr, 2007; Arrigo et al., 2008; Falkowski, 2012). They are sensitive to surface oceanographic conditions and their growth is strongly tied to a complex interplay of hydrographic properties (i.e., sea-ice dynamics, meltwater input, water column structure and its stability), as well as light intensity (Goffart et al., 2000; Park et al., 2017; Costa et al., 2020). As the aforementioned warming of atmosphere and sea-ice loss continues, biomass and composition of microplankton communities in the west Antarctic seas will likely face critical changes. In its Arctic counterpart, widespread transitions in the marine microplankton dynamics and other elements of community structure led by ongoing changes in their hydrographic regime have already been reported (e.g., Ardyna et al.,

2014; Lewis et al., 2020; Jung et al., 2021; Kim et al., 2023). Nonetheless, information on overall biogeography and ecological characteristics of microplankton communities inhabiting the Antarctic Ocean is still generally scarce, fragmented and restricted to specific locations.

Dinoflagellates are eukaryotic unicellular organisms and play a crucial role in ocean primary production and food web dynamics (e.g., Taylor et al., 2008; G´omez, 2012; Bravo and Figueroa, 2014). In the Antarctic seas, they form one of the major microplankton groups after diatoms and the prymnesiophyte *Phaeocystis* (Kopczy´nska et al., 2007; Sherr and Sherr, 2007). Occurring as both primary and secondary producers, about 20 % of the dinoflagellate species go through a cyst stage by forming a protective biopolymer wall around the dormant dinoflagellate, which enables them to sink to ocean floor and become fossilized in sediments (e.g., Bravo and Figueroa, 2014). Studies of global and regional distributions of cysts in recent sediments in various oceans and seas have demonstrated strong relationships with sea-surface conditions (temperature, salinity, nutrients and sea-ice cover duration), enabling to establish the biogeographical and ecological preferences of cyst-forming dinoflagellate taxa (cf. Marret and Zonneveld, 2003; Marret et al., 2020; de Vernal et al., 2020and references therein). However, the southern polar region is still a data-sparse region, due to logistical difficulties and the previous notion of the Antarctic seas being a 'barren place' of dinoflagellate cyst production (e.g., McMinn, 1995). With the improvement of field work logistics and continued scientific interest, investigations on sea-surface waters, sea-floor sediments and sediment traps have documented the occurrences of dinoflagellates and their cysts within this region, prompting further investigation for new discoveries (e.g., Harland and Pudsey, 1999; Hartman et al., 2018; Esper and Zonneveld, 2007). Noteworthy is a recent compilation of dinoflagellate cyst data from the Southern Ocean, which revealed clear species-specific differences in their oceanographic affinities (Thöle et al., 2023). However still, some geographic areas remain unknown, particularly most of the west Antarctic continental margin in close proximity to ice-covered environments.

Here we present new dinoflagellate cyst data from the Pacific sector of Antarctic marginal seas on a wide longitudinal scale, from the northern Antarctic Peninsula to the Ross Sea, mostly representing ice- proximal locations. With the ongoing warming in Antarctica, physical and biogeochemical processes in these regions are currently undergoing substantial change, and responses of dinoflagellate populations to such forcings are still unknown. The principal goals of this study were: (1) to document sedimentary dinoflagellate cyst distributions in this almost unexplored ice-proximal region; (2) to examine their biogeographical traits related with prevailing oceanographic conditions; and (3) to explore key biotic-abiotic factors and their interactions that shape spatial patterns

of dinoflagellate cyst distributions.

2. Study area

The study area includes much of the west Antarctic continental shelves, stretching along the northern Antarctic Peninsula, the Bellingshausen Sea, the Amundsen Sea and the Ross Sea (~47°W to 163°E) (Fig. 1). To the north, the Antarctic Circumpolar Current (ACC) flows eastward around Antarctica, isolating cold southern polar waters from warm subtropical waters. Owing to fracture zones in the Pacific-Antarctic Ridge, it flows southward in the Pacific sector of the Southern Ocean and enables the Circumpolar Deep Water (CDW), branches of the ACC, to be positioned more south than in other regions of Antarctica. The warm, saline CDW moves further south and intrudes onto the west Antarctic continental shelves via submarine glacial troughs, transferring heat underneath floating ice-shelf and causing its basal melt (Nakayama et al., 2018; Park et al., 2024). Such oceanographic features are also strongly linked to dynamics of the West Antarctic Ice Sheet (WAIS) - an area of 2.25 ×106 km2 containing over 3.6×106 km^3 of ice (Lythe et al., 2001) - which has been losing mass at an accelerating rate in recent decades due to basal melting of ice shelves driven by enhanced on-shelf intrusions of warm CDW (Rignot et al., 2013; Park et al., 2024). During austral summer, polynyas (i.e., open water areas surrounded by sea-ice) occur in the coastal region through oceanic currents or cold, dry katabatic winds that blow northward from the continental interior and push the newly produced sea-ice away (Bromwich et al., 1998; Tamura et al., 2008). This unique oceanographic feature has received much attention recently, because it often promotes high levels of phytoplankton production during spring and summer compared to surrounding ice-covered waters (Arrigo and van Dijken, 2003; Arrigo et al., 2008).

The above hydrographic properties are strongly regulated by large- scale changes in atmospheric and oceanic circulations. The Southern Hemisphere westerly winds (SWW), a strong, zonally symmetric wind belt that encircles the Antarctic continent, modulate the strength of the ACC. For instance, the ACC is getting stronger when the ACC contracts poleward during a positive phase of the Southern Annular Mode (SAM) - the major mode of southern high latitude atmospheric circulation variability - enhancing onshore intrusions of warm CDW (Thompson and Solomon, 2002; Toggweiler and Russell, 2008; Park et al., 2024). The ACC is also closely linked with the Weddell Gyre and Ross Gyre - large cyclonic ocean circulations located east of the Antarctic Peninsula and north of the Ross Sea, respectively. These gyre systems dynamically interact with the

surface circulation of Antarctic continental marginal seas (Neme et al., 2021; Prend et al., 2024).

3. Materials and methods

3.1. Sample collection and laboratory treatments

A total of 48 sediment cores were collected using a box corer during several research cruises of the R/V ARAON (2010–2021), with the exception of samples 8–10 (the R/V Polarstern) and samples 1, 3, 6 and 7 (the R/V Yuzhmorgeologiya). The sampling locations are distributed from 59 to 78°S and from 47°W to 163°E, within water depths of 270–4141 m along the west Antarctic continental shelf seas including the northern Antarctic Peninsula, the Bellingshausen Sea, the Amundsen Sea and the Ross Sea (Table 1; Fig. 1a). The uppermost sediment layers (~1 cm) of the box cores (stored in a core repository (4 °C) at the Korea Polar Research Institute) were subsampled and processed, following the standard palynological preparation procedure described in de Vernal et al. (2010). Approximately 10–30 g of wet sediment per sample were oven–dried at 60 °C for 24 h, and weighted. For the calculation of dinoflagellate cyst concentrations, one *Lycopodium clavatum* spore tablet of batch #1031 (X =20,848 per tablet, σ =±1546, University of Lund) was added to each sample, and they were treated with 20 mL of 10 % hydrochloric acid (HCl) at room temperature for the removal of calcium carbonate. After 20 min, the samples were rinsed with distilled water, and treated with 20 mL of 40 % hydrofluoric acid (HF) at room temperature for 20 min to remove silicates. After repeating the HCl and HF steps for 2–3 times, the residues were treated with HF and left overnight. The final residues were treated with HCl for 20 min and washed with distilled water to neutralize the pH. Finally, samples were sieved using a 10–μm pore–sized mesh and the residue was preserved in a 10–mL vessel with two to three drops of phenol added. A droplet of homogenized residue from each sample was mounted on a microscope slide using glycerin jelly, and sealed with paraffin wax.

3.2. Cyst identification

Dinoflagellate cysts were counted with a Leica research microscope (DM2500LED) at 400 × and 1000 × magnification. Dinoflagellate cysts were observed in all samples, and a minimum count of 300 cyst per sample was attempted based on the

recommendation of Mertens et al. (2009)although not all samples yielded enough cysts to achieve this goal – for 21 samples, counts did not exceed 300. Six samples containing fewer than 100 cysts (samples 4, 18, 19, 25, 28 and 46; supplementary data Table S1) were excluded from further data analysis and interpretation. An average of 1182 dinoflagellate cysts (min 2, max 12,488) were counted from each sample. Dinoflagellate cysts were identified according to published morphological descriptions (Marret and de Vernal, 1997; Pie´nkowski et al., 2013; Hartman et al., 2018, 2019). Species of the genus *Brigantedinium*, which often did not allow clear observation of the archeopyle due to the orientation or folding of the cyst, were grouped as *Brigantedinium* spp. without further identification. Small (17–28 μm) microreticulate spherical cysts of pale brownish color with a chasmic archeopyle were identified as *Gymnodinium microreticulatum* based on the description and illustration in Ribeiro et al. (2012)and Hartman et al. (2018). We tentatively assigned the species of *Islandinium* to *Islandinium*? *minutum* due to the high morphological similarity with specimens observed in Pie´nkowski et al. (2013)and described in Head et al. (2001)and Potvin et al. (2018). Importantly, we distinguished *Selenopemphix antarctica* – a pale brown cyst with a circular outline that is extremely apically–antapically compressed (diameter: 52–68 μm) – and *Selenopemphix* sp. 1 characterized by much larger body diameter (82–98 μm) with a rigid sulcus and a distinct conical apical complex (Marret and de Vernal, 1997; Esper and Zonneveld, 2007; Hartman et al., 2018). A particular note is for the cysts of *Polarella glacialis*, which have been often overlooked in previous palynological studies due to unsuitable sample preparation techniques (e.g., a coarser–than–10 μm mesh size, warm acid treatment, acetolysis) that could result in the loss of these small–sized cysts (12–17 μm long and 8–15 μm wide) (Harðard´ottir et al., 2024). Here, the use of room– temperature acids and 10 μm mesh pore size allowed to include this species in the dinocyst assemblage composition analysis. Other palynomorphs such as organic linings of foraminifera and cysts and lorica of ciliates were also present in the palynological slides but were not analyzed.

Dinoflagellate cyst concentrations are expressed as concentrations of dinoflagellate cysts per weight of dry sediment and calculated as follows (Benninghoff, 1962):

$$c \text{ (dinoflagellate cysts g}^{-1} \text{ dry sediment)} = \frac{gc \times Lt \times t}{Lc \times w}$$

where c is the concentration =number of dinoflagellate cysts per gram of dry sediment, gc is the number of counted dinoflagellate cysts, Lt is the number of *Lycopodium* spores/tablet, t is the number of tablets added to the sample, Lc is the number of counted *Lycopodium* spores, and w is the weight of dried sediment (g) for each sample.

3.3. Environmental conditions

Long-term climatologically averaged datasets of austral summer chlorophyll-*a* (Chl-*a*) and sea-ice concentration over the entire Southern Ocean were utilized to provide essential baseline information for the study region. Monthly climatological mean surface Chl-*a* concentrations for the austral summer months of December and January (2003-2019) were obtained from MODIS-AQUA Ocean Color data, with a spatial resolution of 9 km (Fig. 1b). Daily sea-ice concentration data during the months of January and February were compiled for the period from 1998 to 2016 at a resolution of 25 km per pixel (Fig. 1c), provided by the National Snow and Ice Data Center (NSIDC) (Nimbus-7 SMMR and DMSP SSM/I-SSMIS Passive Microwave Data; http://nsidc.org). Sea- surface temperature and salinity were extracted for each site from the World Ocean Atlas 2018 (Garcia et al., 2019) for the four seasons (January-February-March (JFM), April-May-June (AMJ), July-August- September (JAS), October-November-December (OND)).

To gain insights into key environmental factors influencing marine microplankton assemblage structures on the Ross Sea shelf, Chl-*a* and sea-ice concentration datasets at a 4 km spatial resolution, along with wind data at 10 m height above the sea surface - derived from the monthly average of daily-mean datasets produced by the European Centre for Medium-Range Weather Forecasts (ECMWF) Reanalysis 5 (ERA5) and calculated using vector average method (Grange, 2014) - were obtained for the months of December from 2011 to 2020. This was particularly done to study the impacts of winds on regional ocean dynamics and microplankton distributions in the Ross Sea, especially in December with maximum summer biomass and productivity (e.g., Kaufman et al., 2017; Arrigo et al., 2000; D'Sa et al., 2021; Smith Jr. et al., 2003; Smith Jr., 2022; Portela et al., 2025).

3.4. Statistical analysis

Ordination techniques were used on 42 dinoflagellate cyst assemblages to detect possible relationship between cyst distribution and environmental conditions. We excluded six samples where counts were below 100 (samples 4, 18, 19, 25, 28 and 46). The software e-Primer was used to carry out a non-metric dimensional scaling (NMDS) and principal component analysis (PCA). NMDS was performed on square-root transformed percentages of cyst assemblages. NMDS techniques are appropriate for biotic parameters while principal component analysis is usually the preferred method for abiotic parameters (Clarke and Gorley, 2015). Normalized values of environmental conditions were used for

the PCA.

4. Results

Fifteen dinoflagellate cyst taxa were identified from the 48 study sites (Table 2; supplementary data Table S1). Dinoflagellate cysts were observed in all sediment samples, and species richness at any single sample ranged between two (site 18) and 12 (site 6), with an average of seven taxa per site (Table 1). Total dinoflagellate cyst concentrations at each sampling site are shown in Table 1. The concentrations per gram dry weight of sediment sample ranged from three to 145,159 cysts/g (5,133 cysts/g on average). In general, higher concentrations were observed at locations around the northern Antarctic Peninsula (sites 1-10) and the Ross Sea (sites 33-48). Samples from the Bellingshausen Sea and the Amundsen Sea have relatively lower concentrations. Overall, dinoflagellate cyst assemblages were dominated by cysts of *P. glacialis*, *I.? minutum*, *Selenopemphix* sp. 1 and *Nucicla umbiliphora*. Other taxa that have relatively high abundance include *G. microreticulatum*, *S. antarctica*, *Cryodinium meridianum* and *Brigantedinium* spp. (Table 2). The autrotrophic species (with the exception of cysts of *P. glacialis*) occur in very low abundance, with *Impagidinium pallidum* being the most represented.

To illustrate spatial changes in the dinoflagellate cyst distributions, the samples are grouped into three geographic sectors along the west Antarctic shelves: the northern Antarctic Peninsula (sites 1-10; sector A), the Bellingshausen-Amundsen (sites 11-32; sector B) and the Ross Sea (sites 33-48; sector C) (see Fig. 1a). Based on species relative abundance and the NMDS analysis, three distinct cyst assemblages were identified (Figs. 3 and 5A) and can be partially matched against geographical sectors. Assemblages from the northern Antarctic Peninsula (sector A) were characterized by the highest species diversity (max. 12 taxa) and a large dominance of *I.? minutum* (up to 97 %), as previously reported by Pie´nkowski et al. (2013). To a lesser extent, the assemblages were also dominated by *S. antarctica* (up to 55 %) and *Brigantedinium* spp. (up to 58 %). The Bellingshausen Sea and Amundsen Sea (sector B) assemblages were mostly composed of *Selenopemphix* sp. 1 (up to 81 %) and *G. microreticulatum* (up to 65 %). In contrast, the Ross Sea assemblages (sector C) were characterized by an overwhelming dominance of *P. glacialis* cysts (up to 98 %), followed by *Selenopemphix* sp. 1 (up to 95 %). Four taxa (*P. glacialis* cysts, *Selenopemphix* sp. 1, *N. umbiliphora* and *C. meridianum*) tend to be exclusively restricted to the Ross Sea sector, being highly concentrated at sites close to the westernmost Ross Sea coastal area (Figs. 3 and 4;

supplementary data Table S1).

The NMDS (Fig. 5a) clearly identifies three assemblages that can be linked to the three sectors (except for site 45). The multivariate analysis (Fig. 5c) suggests that all sites from sector A except site 5 are related to open ocean conditions without the presence of sea-ice cover. The PCA highlights three different groupings of environmental conditions, with axis 1 and axis 2 explaining 37.4 % and 28.7 % of the variation respectively. Some sites of sectors A and C seem to be under the influence of SSS mostly, whereas sites from sectors A and B could be related to Chl-*a* and sites from sectors B and C related to SST and sea-ice % (Fig. 5c).

Ordination of the taxa show a clear division between autotrophic and heterotrophic species, with the exception of cysts of *P. glacialis* and *I. pallidum* (Fig. 5b). In our study, we have characterized *G. microreticulatum* as a mixotrophic taxon based on the literature (Gómez and Panisse, 2020) and interestingly, it is located within the group of heterotrophic species. We note that, over the last decade, large efforts have been made to restructure the traditional classification of planktonic protist communities according to their nutritional modes (i.e., phytoplankton and microzooplankton) by introducing mixotrophy (photoautotrophy plus phagoheterotrophy) as a third trophic state (e.g., Mitra et al., 2016, 2023; Flynn et al., 2019). As yet, such new categorization is still a challenge because the trophic diversity within many microplankton communities is not clearly established and intensive experimental work as well as expert knowledge are required to determine mixotrophs (Schneider et al., 2020; Costa et al., 2022).

5. Discussion

5.1. General features in the dinoflagellate cyst assemblages

Marine environments close to the Antarctic continent have long been considered to be absent of extant dinoflagellate cysts (e.g., McMinn, 1995) and modern biogeography of dinoflagellate cyst species in the region is hampered by a general lack of data and prior attention. Despite these issues, significant distributions of dinoflagellate cysts in recent sediment around Antarctica have been previously reported (e.g., Marret and de Vernal, 1997; Pie´nkowski et al., 2013; Hartman et al., 2018). More recently, the Southern Hemisphere dinoflagellate cyst data compiled by Th¨ole et al. (2023) further extended our knowledge on the dinoflagellate cyst assemblage structures and distributions in the Antarctic Ocean. Our new dataset shows substantial sedimentary concentrations of dinoflagellate cysts within the west Antarctic ice-shelf environments, southwards of 60°

S, mostly in ice-proximal locations. Notwithstanding the limited data available, the dinoflagellate cyst abundance and assemblage compositions observed in the present study are concordant with previously published investigations. For instance, in the northern Antarctic Peninsula region, the dominant taxon (*I.? minutum*) and its concentration (0-5403 cysts/g, 1180 cysts/g on average) (Figs. 3 and 4) bear resemblance to those reported by Pie´nkowski et al. (2013) and Th¨ole et al. (2023) with maximum values of 9096 cysts/g and 4556 cysts/g, respectively. Th¨ole et al. (2023) also found similar taxon compositions in the Ross Sea surface sediments dominated by *P. glacialis*, *I.? minutum*, *N. umbiliphora* and *Selenopemphix* species. In addition, significant occurrences of bi-polar species (*I.? minutum*, *I. pallidum* and cyst of *P. glacialis*) and Antarctic endemic species (*S. antarctica*, *C. meridianum* and *N. umbiliphora*) are in line with the previous investigation of Marret et al. (2020). We speculate that similar morphological traits with unknown motile affinities between *S. antarctica* and *Selenopemphix* sp. 1 (Fig. 2c, j) may suggest phenotypic variation within a single taxon, possibly resulting from rapidly changing temperature environments (e.g., Chen et al., 2011; Tang et al., 2021). However, our data cannot provide conclusive evidence and this issue requires further investigation.

Overall, our data reported here show generally high dinoflagellate cyst concentrations in the Antarctic settings that are comparable to those reported from its Arctic counterpart, where concentrations fluctuating from a few hundreds to several thousands of cysts per gram (e.g., Radi et al., 2001; Grøsfjeld et al., 2009; Allan et al., 2020; Kim et al., 2023). Although information on sedimentation rates in the study area is rare and often uncertain, existing sedimentation data from some Antarctic continental shelf sediments suggest that the surface sediments may cover a Late Holocene to modern age (Th¨ole et al., 2023). There are also reports of 210Pb-based age estimations made in these regions - for instance, the western Bransfield Strait at the northwestern edge of the Antarctic Peninsula (0.06-0.15 cm/yr; Masqu´e et al., 2002), the northwestern Ross Sea (0.02-0.12 cm/yr; Langone et al., 1998) and the Amundsen Sea polynya (0.09 cm/yr; Kim et al., 2021). Thus, it can be speculated that our surface sediments may cover about 10-50 years of sediment accumulation.

Importantly, most dinoflagellate cysts behave like silt particles in the water column and could be transported over long distances by water currents before their settling down to the sea floor (Dale, 1996; Nooteboom et al., 2019, 2022). This raises a question whether our dinoflagellate cyst data represent cyst production from the surface water directly overlying the study sites, or if they mostly comprise allochthonous cysts that were formed elsewhere (i.e., lower latitude regions) and latitudinally transported towards Antarctica. In the Southern Ocean, however, meridional transport is generally

weak and its influence on sinking trajectory of particle materials is negligible, particularly in the ice-proximal locations due to the absence of strong currents (Th¨ole et al., 2023). Therefore, we infer that the dinoflagellate cyst assemblages herein are likely to reflect the populations in the overlying surface waters, rather than significant latitudinal transport processes, inferring a number of environmental factors that foster high levels of dinoflagellate production in the study region. It should be noted that there is uncertainty associated with reworking and redeposition of bottom sediments by specific mechanisms, such as advection of warm circumpolar deep waters flowing towards the west Antarctic ice shelves (Seidenstein et al., 2024; Lanham et al., 2025) and subglacial sediment-rich meltwater runoff from distributed drainage systems (Hawkings et al., 2014). Therefore, different topographic configurations of the shelves as well as region-specific depositional environments and taphonomic processes may have affected the dinoflagellate cyst signals at varying degrees, but this issue requires further investigation.

The Southern Ocean is generally defined as the largest high-nutrient low-chlorophyll region, due to light and iron (Fe) co-limitation on phytoplankton growth and primary productivity (Sunda and Huntsman, 1997; Boyd et al., 2007). In contrast, ice-proximal Antarctic coasts show high Chl-*a* concentrations (e.g., Behera et al., 2020; Pinkerton et al., 2021) (see also Fig. 1b), paired with intense phytoplankton bloom development during austral spring and summer (Arrigo and van Dijken, 2003; Arrigo et al., 2008). This phenomenon is primarily attributed to several effects combined- notably, the development of coastal polynyas during austral spring and summer driven by offshore katabatic winds and/or the on-shelf intrusion of warm CDW (Vaughan, 2008; Jenkins et al., 2010; Wåhlin et al., 2010), providing essential habitats and light intensity for phytoplankton communities therein. In recent decades, the effects of climate warming not only cause extension of ice-free areas and consequent enhanced irradiation along the coastlines, but also strengthen the CDW inflow and significant basal melting of the ice shelves, releasing additional glacial/ice sheet-derived iron (Fe) for photosynthetic microplankton blooms in the shelf waters (Sedwick et al., 2000; Tian et al., 2023). This notion gains further support from the mean summer Chl-*a* concentration and the satellite-derived sea-ice concentration data that show averaged locations of open ocean conditions, concurrent with high primary production, along the west Antarctic coasts (Fig. 1b,c).

5.2. Spatial heterogeneity along the west Antarctic shelves

As previously described, surface sediments from the west Antarctic seas show generally high dinoflagellate cyst concentrations at the shallow-shelf ice-proximal locations subject to a longer open-water season with sufficient nutrient supply, which

may create favorable conditions for overall phytoplankton production. A clear along-shelf pattern in terms of assemblage compositions and cyst abundances divides the study area into three spatial domains. Sector A at the northernmost tip of the Antarctic Peninsula shows a relatively higher taxon diversity (15 species), when compared to other sectors that are more strongly confined to polar, sea-ice influenced environments (Table 1; Fig. 3). Also, sporadic occurrences of cosmopolitan taxa with large environmental tolerances (e.g., *Dalella chathamensis*, *N. labyrinthus* and *I. sphaericum*) reflect comparatively more prevalent open-ocean conditions in this region with a relatively wide salinity and temperature range (Marret and Zonneveld, 2003). As those reported from the previous investigation (e.g., Marret and de Vernal, 1997; Marret and Zonneveld, 2003; Pie´nkowski et al., 2013) and sediment traps (Harland and Pudsey, 1999), we observed high concentrations of *S. antarctica*, *I.? minutum* and *I. pallidum* - the typical Southern Ocean taxa associated with cold water and polar environments - together with the cosmopolitan taxa *Brigantedinium* spp. Such co-occurrences of cosmopolitan and polar ocean taxa may infer overall large environmental variations over this region. These features are in line with pronounced atmospheric warming (Steig et al., 2009; Thompson and Solomon, 2002; Bozkurt et al., 2018) and ocean surface waters (Meredith and King, 2005; Couto et al., 2017) along the Antarctic Peninsula over the past century, resulting in glacier retreat (Cook et al., 2005; Vaughan, 2006), collapses of ice shelves (Cook and Vaughan, 2010; Rignot et al., 2013) and sea-ice loss (Stammerjohn et al., 2008). Such changes expended open water domains with a high degree of seasonality in sea-surface environments (Smith and Stammerjohn, 2001; Stammerjohn et al., 2008), which would have created more favorable conditions for cosmopolitan dinoflagellate cyst taxa. A particular note is for the predominance of *I.? minutum* (~5400 cysts/g) that corresponds to studies previously reported from the Prince Gustav Channel (~9000 cysts/g; Pie´nkowski et al., 2013) and the northern tip of the Antarctic Peninsula (~4500 cysts/g; Th¨ole et al., 2023). This perhaps may involve a lateral transport from the Weddell Sea to sector A along the Iceberg Alley - a major pathway for the WAIS-derived icebergs that drift northward via the Weddell gyre circulation (Weber et al., 2021; Th¨ole et al., 2023). Despite this issue, there is little doubt that the high concentration of *I.? minutum* in this area is the result from in-situ production, especially when considering its co-dominance with other heterotrophic taxa (*S. antarctica* and *Brigantedinium* spp.) that are known to be important grazers of bloom-forming diatoms (Sherr and Sherr, 2007). Indeed, coastal waters of the northern Antarctic Peninsula show an extensive austral summer bloom of diatoms (e.g., Prézelin et al., 2004; Mendes et al., 2012; Costa et al., 2020), supplying an ample food source for the heterotrophic dinoflagellates to grow. It seems that the development of a stratified water column associated with increased

meltwater inputs, as well as an ample supply of nutrients and light (Venables et al., 2013; Seyitmuhammedov et al., 2022), was the main driver of large diatom biomass in this region (Arrigo et al., 1999; Prézelin et al., 2004; Höfer et al., 2019).

We found a strong contrast in the dinoflagellate cyst compositions and taxon diversity between sector A and B. A reduced taxon diversity and a disappearance of cosmopolitan taxa in sector B can be ascribed to more oceanographically, climatically isolated polar environments when compared to sector A, as previously described. A particular note is for a sharp decrease in *I.? minutum*, *S. antarctica* and *Brigantedinium* spp. concentrations accompanied by a dominance of *Selenopemphix* sp. 1 and *G. microreticulatum* (Figs. 3 and 4). While Antarctic coastal marine phytoplankton populations are primarily occupied by both diatoms and *Phaeocystis* (Alderkamp et al., 2012; Smith Jr. et al., 2014; Mangoni et al., 2017), the Bellingshausen and Amundsen seas of sector B are typically dominated by *Phaeocystis* during austral summer (e.g., Boyd et al., 1995; Bode et al., 2002; Delmont et al., 2014). This indicates a distinctive hydrographic property that may act as an environmental barrier – that is, whereas sector A is becoming free of grounded ice due to rapidly increasing temperature (e.g., Milliken et al., 2009; Michalchuk et al., 2009; Minzoni et al., 2015), sector B is surrounded by the WAIS and ice shelves that facilitate katabatic winds blowing seaward and cooling the surface ocean (Bromwich et al., 1998; Tamura et al., 2008; Fig. 1a). According to observational studies, hydrodynamic processes associated with glacial meltwater and strong katabatic wind surges in sector B severely deteriorate water column stability and also deepen upper mixed layers (Hellmer, 2004; Bintanja et al., 2013; Bronselaer et al., 2018; Price et al., 2008; Jourdain et al., 2017; Silvano et al., 2018; Bett et al., 2020), consequently triggering the exclusive *Phaeocystis* growth (Arrigo et al., 1999, 2010; Goffart et al., 2000). In addition, for brown-walled species, effects of post-depositional degradation are possible due to their susceptibility to oxygenized conditions (Zonneveld et al., 2001). As yet, this notion remains speculative until further data on various factors affecting such species-selective oxidative degradation (e.g., local changes in sedimentation rates and oxygen exposure time after cysts were buried to surface sediments) becomes available.

The general prevalence of *Selenopemphix* sp. 1 and *G. microreticulatum* in sector B is likely to reflect their ecological and habitat preferences that is well-suited to thrive in a *Phaeocystis*-dominated environment (Fig. 6). Tentatively, we hypothesize that the large occurrence of *Selenopemphix* sp. 1 (Figs. 3, 4d and 6), a brown protoperidinioid dinoflagellate cyst that is generally assumed to be heterotrophic (Brenner and Biebow, 2001; Ellegaard et al., 2013), may be linked to its feeding strategy favorably grazing on *Phaeocystis* rather than diatoms. Indeed, there are finds of extraordinary

Phaeocystis-bloom events that seem to serve as an important food resource for its predators (Alderkamp et al., 2012; Lee et al., 2022), including dinoflagellates (Tang et al., 2001; Nejstgaard et al., 2007; Grattepanche et al., 2011; Swalethorp et al., 2019). More intriguingly is the high occurrence of *G. microreticulatum*, a taxon that has recently been related to mixotrophism in the literature (G´omez and Panisse, 2020) and seems here to be prevalent within heterotrophic species (Fig. 5b). However, such ecophysiological and nutritional processes are beyond the scope of this study and our data cannot provide conclusive evidence regarding the controls on their preferential distribution. Further in-depth observational and bio-incubation studies are needed to explore potential interactions between these microplankton groups and mechanisms operating their community structures and distributions over this region.

In sector C, an interesting contrast in the dinoflagellate cyst distributions was observed between the east-central and western Ross Sea regions. While the south-central Ross Sea samples (sites 33-38) are strongly dominated by *Selenopemphix* sp. 1, the westernmost coastal locations (sites 39-48) show a prevalence of cysts of *P. glacialis* accompanied by some heterotrophic taxa such as *N. umbiliphora*, *I.*? *minutum* and *C. meridianum* (Figs. 3 and 4). The assemblage composition in the east-central Ross Sea has some communality with sector B, dominated by *Selenopemphix* sp. 1, possibly indicating weak environmental gradients between the two regions. Towards the western Ross Sea, we observed a remarkable shift in the cyst assemblage composition - from a *Selenopemphix* sp. 1-dominated to a *P. glacialis* cyst-dominated community (Figs. 3 and 4d,e). The cyst of *P. glacialis*, a bipolar sea-ice taxon occurring in both Arctic and Antarctic circumpolar regions (Montresor et al., 2003; Marret et al., 2020), has been often ignored in previous dinoflagellate cyst studies due to sample preparation protocols and/or preservation issue (Heikkil¨a et al., 2014; Th¨ole et al., 2023 and references therein). As the 48 samples under study were uniformly processed using the same method, the dominance of *P. glacialis* cysts in the western Ross Sea (sites 39-48) is likely to be a result of its preferential occurrence in this sector. Why then is there such sharp contrast in the dinoflagellate cyst assemblage compositions between the east-central and western Ross Sea regions?

5.3. Environmental forcing factors separating dinoflagellate cyst distributions in the Ross Sea

The Ross Sea, one of the regions with the largest primary productivity in the Southern Ocean, is characterized by massive phytoplankton blooms during austral spring and summer seasons and can be divided into two distinct regions: 1) the central Ross Sea polynya area with a high degree of *Phaeocystis* production, and 2) the western

boundary of the Ross Sea, including Terra Nova Bay and Victoria Land coast, with an intense diatom-dominated ice-edge bloom (e.g., Mangoni et al., 2017; Goffart et al., 2000; Misic et al., 2024). We find that this spatial disparity of the two phytoplankton group blooms in the Ross Sea clearly overlaps with the aforementioned dinoflagellate cyst distribution patterns (Fig. 7a). Satellite-derived imagery of Chl-*a* (mg/m3) distribution during austral summer clearly shows how the east-central Ross Sea stands out by its high primary production (Fig. 7b), primarily caused by *Phaeocystis* blooms (e.g., Goffart et al., 2000; Misic et al., 2024) as a consequence of deteriorated water column stability and a large ice-free area facilitated by strong katabatic winds (Arrigo and van Dijken, 2003, 2004; Mangoni et al., 2017; Fig. 7c). As suggested in the previous section, the observed predominance of *Selenopemphix* sp. 1 in the east-central Ross Sea sediments (Fig. 7a) seems to well conform to the physical and biological conditions favored by *Phaeocystis* populations.

In contrast, the elevated Chl-*a* concentrations along the western margin of the Ross Sea is driven by diatom blooms (Fig. 7b; Arrigo and van Dijken, 2004; Mangoni et al., 2017; Misic et al., 2024), with a dominance of the pennate diatom *Fragilariopsis* spp. (e.g., Smith Jr. and Nelson, 1985; Goffart et al., 2000). This is primarily ascribed to a strong water column stratification, favored by diatoms that have physiological superiority in photoprotection processes and high tolerance to photoinhibition under excessive light conditions (Mills et al., 2010; Alderkamp et al., 2012). The strong stratification during the summer is possible, because of a substantial melting of sea-ice that has been advected from further east and piled up into a sizable volume along the shelf margin (Fig. 7c; Arrigo and van Dijken, 2004). Such intense diatom blooms, typically occurring within the ice-edge off the coast of Victoria Land, corroborate well our dinoflagellate cyst data for the western Ross Sea samples (sites 39-48) - the disappearance of *Selenopemphix* sp. 1 in concert with robust occurrences of some heterotrophic dinoflagellate cysts (i.e., *I.? minutum*, *N. umbiliphora* and *C. meridianum*) that seem to preferentially consume diatoms (Figs. 3, 4 and 7a). Also noteworthy is an overwhelming concentration of autotrophic and sympagic *P. glacialis* cysts in the western Ross Sea sites with heavy sea-ice concentrations that seemingly provided a tailored habitat for this taxon (Harðard´ottir et al., 2024) (Fig. 7a, c). Given that this species typically inhabits brine channels within sea-ice and underlying waters (Thomson et al., 2006; Montresor et al., 1999, 2003), its bloom initiation is likely to occur much earlier than the diatom bloom, at a time when sea-ice is still intensely accumulated in the region. It should be noted that the dominance of *P. glacialis* cysts may also be related to other environmental factors and ecophysiological processes at the sites such as nutrient levels, brine channel structure and phenotypic plasticity of this species (Heikkil¨a et al., 2014;

Rengefors et al., 2015; Zheng et al., 2012; Harðard´ottir et al., 2024) and thus, further in-depth investigations with in-situ or culture experiments are needed to explain the underlying mechanism of the observed phenomena. Taken all together, the Ross Sea's dinoflagellate cyst distributions are closely linked to their different trophic strategies. Especially, the heterotrophic dinoflagellate herbivory may be analogous to photoautotrophic microplankton community structures shaped by hydrodynamic properties - i.e., sea-ice distribution and its integrity, as well as water column stability intermingling with meteorological forcing.

5.4. Further implications

Notwithstanding the general scarcity of dinoflagellate cysts in the Antarctic Ocean sediments reported previously, our study reveals considerable concentrations of dinoflagellate cysts along the ice- proximal west Antarctic shelf sediments, indicating substantial motile dinoflagellate populations in the upper water. We speculate that such patterns will only intensify in the coming decades, because a continuously reducing sea-ice extent and a sufficient Fe supply from melting glacial ice will enhance irradiation and fertilization for phytoplankton blooms (Sedwick et al., 2000; Alderkamp et al., 2012; Park et al., 2017), promoting heterotrophic dinoflagellate production. This study also highlights complex physico-biological coupling processes under warming climate and its consequences for the marine microplankton community structure along the western Antarctic continental shelves as illustrated in Fig. 8. In the northern Antarctic Peninsula with the highest surface air temperature warming rate over West Antarctica, a large amount of glacial meltwater results in highly stratified surface waters in austral summer, fostering diatom blooms and heterotrophic dinoflagellate populations (mainly, *I.? minutum*, *S. antarctica* and *Brigantedinium* spp.) that graze on them (Fig. 8a). The sector B encompassing the Bellingshausen-Amundsen seas stands out by offshore winds that create large open water areas (polynyas) and well-mixed water column conditions, under which *Selenopemphix* sp. 1 and *G. microreticulatum* feeding on *Phaeocystis* populations can dominate (Fig. 8b). In sector C, the east-central Ross Sea polynya, i.e., a region under strong katabatic wind activities that generate weak water column stratification and *Phaeocystis* blooms, the assemblages are dominated by *Selenopemphix* sp. 1, while on the western side ice-inhabiting *P. glacialis* cysts and diatom- grazing dinoflagellate cysts dominate, presumably due to heavy sea-ice conditions and subsequent meltwater-stratified surface waters that foster diatom blooms (Fig. 8c). We carefully speculate that such along-shelf separation of the dinoflagellate cyst assemblage distribution will have significant alterations in a future Antarctic Ocean. That said,

ongoing Antarctic ice-shelf disintegration and sea-ice loss may trigger widespread modifications of melt-driven hydrodynamic processes, which will adjust overall microplankton biomass and community structures as well as interactions between predators and preys. This notion aligns with important cryospheric and biological consequences from the base of the marine food chain reported in the Arctic having less sea-ice cover (e.g., Frainer et al., 2017; Jung et al., 2021; Kim et al., 2023). All this information combined depicts the necessity for further in-depth investigations on microplankton production and mechanisms operating their community structures in these sensitive polar marine environments. Further, the unique assemblage structure of dinoflagellate cyst distributions identified in this study highlights their strong potentials as a proxy for monitoring changes in hydrographic conditions and microplankton communities in the Antarctic marine ecosystems.

KOPRI
극지연구소

서남극 주변 해양 표층퇴적물의 와편모조류 시스트 공간 분포 특성에 영향을 미치는 주요 환경요인

김소영[a,*], 박태욱[a], Fabienne Marret[b*], 유규철[a], 김정훈[a], Lorena Rebolledo[c], 최정옥[a], 나형술[a], 하선용[a], 문흥수[a]

[a]극지연구소, [b]University of Liverpool, [c]Instituto Antárctico Chileno

요약: 본 연구에서는 넓은 경도 범위의 서남극 대륙붕 내 빙하 인접 해역에서 채집한 표층퇴적물에서 새롭게 관찰된 48개의 와편모조류 시스트 군집을 분석하고, 그 분포 양상 및 주요 환경 조절 요인들을 종합적으로 제시하였다. 연구 결과, 와편모조류 시스트 분포는 다음과 같은 뚜렷한 공간적 이질성을 보였다; 1) 남극반도 북부 지역은 융빙수에 의한 성층화 및 높은 규조 생산성으로 인해 *Islandinium*? *minutum*, *Selenopemphix antarctica*, *Brigantedinium* spp.가 우점하였다, 2) 벨링스하우젠-아문젠해는 강한 연안 외향풍, 불안정한 수층 구조, *Phaeocystis* 대번성의 영향으로 *Gymnodinium microreticulatum*과 *Selenopemphix* sp. 1이 우점하였다, 3) 로스해는 극명한 대비를 보이는데, 동부-중앙 지역은 강한 연직 혼합과 높은 *Phaeocystis* 생산 환경 아래 *Selenopemphix* sp. 1이 우점하는 반면, 높은 해빙 농도와 해빙 기원 융빙수에 의한 성층화가 나타나는 서부 지역에서는 *Polarella glacialis* 시스트가 *Nucicla umbiliphora*, *I.*? *minutum*, *Cryodinium meridianum*과 함께 우점하였다. 서남극 대륙붕을 따라 뚜렷하게 나타나는 와편모조류 시스트 종 조성의 차이는 남극해 주변의 융빙 작용에 따른 수리-기상학적 상호작용이 물리·생물학적 특성 및 해양 미세플랑크톤 군집 구조를 조절하고 있음을 의미한다. 현재 남극에서 빙붕 붕괴와 해빙 감소 현상이 지속됨에 따라, 향후 남극해에서는 개방 수역(open-water area)의 확장과 함께 해양 플랑크톤 생산과 군집 구조에 큰 재편이 일어날 수 있음을 지시한다. 본 연구는 와편모조류 시스트가 극지 해양생태계의 수문 환경 및 플랑크톤 군집 변화의 모니터링 지표로 활용될 수 있음을 의미한다.

참고 문헌

Alderkamp, A.C., Kulk, G., Buma, A.G.J., Visser, R.J.W., van Dijken, G.L., Mills, M.M., Arrigo, K.R., 2012. The effect of iron limitation on the photophysiology of *Phaeocystis antarctica* (Prymnesiophyceae) and *Fragilariopsis cylindrus* (Bacillariophyceae) under dynamic irradiance. J. Phycol. 48 (1), 45-59.

Allan, E., de Vernal, A., Krawczyk, D., Moros, M., Radi, T., Rochon, A., Seidenkrantz, M. S., Zaragosi, S., 2020. Distribution of dinocyst assemblages in surface sediment samples from the West Greenland margin. Mar. Micropaleontol. 159, 101818.

Ardyna, M., Babin, M., Gosselin, M., Devred, E., Rainville, L., Tremblay, J.-É., 2014. Recent Arctic Ocean sea ice loss triggers novel fall phytoplankton blooms. Geophys. Res. Lett. 41 (17), 6207-6212. https://doi.org/10.1002/2014GL061047.

Arrigo, K.R., van Dijken, G.L., 2003. Phytoplankton dynamics within 37 Antarctic coastal polynya systems. J. Geophys. Res. 108, C83271.

Arrigo, K.R., van Dijken, G.L., 2004. Annual changes in sea-ice, chlorophyll a, and primary production in the Ross Sea, Antarctica. Deep Sea Res. Part II Top. Stud. Oceanogr. 51 (1-3), 117-138.

Arrigo, K.R., Robinson, D.H., Worthen, D.L., Dunbar, R.B., DiTullio, G.R., van Woert, M., Lizotte, M.P., 1999. Phytoplankton community structure and the drawdown of nutrients and CO2 in the Southern Ocean. Science 283, 365-367.

Arrigo, K.R., Ditullio, G.R., Dunbar, R.B., Robinson, D.H., VanWoert, M., Worthen, D.L., Lizotte, M.P., 2000. Phytoplankton taxonomic variability in nutrient utilization and primary production in the Ross Sea in the Ross Sea. J. Geophys. Res. 105 (C4), 8827-8846. https://doi.org/10.1029/1998JC000289.

Arrigo, K.R., van Dijken, G.L., Long, M., 2008. Coastal Southern Ocean: a strong anthropogenic CO2 sink. Geophys. Res. Lett. 35, L21602.

Arrigo, K.R., Mills, M.M., Kropuenske, L.R., van Dijken, G.L., Alderkamp, A.C., Robinson, D.H., 2010. Photophysiology in two major Southern Ocean phytoplankton taxa: Photosynthesis and growth of *Phaeocystis antarctica* and *Fragilariopsis cylindrus* under different irradiance levels. Integr. Comp. Biol. 50 (6), 950-966.

Behera, N., Swain, D., Sil, S., 2020. Effect of Antarctic sea ice on chlorophyll concentration in the Southern Ocean. Deep Sea Res. Part II Top. Stud. Oceanogr. 178, 104853.

Bekryaev, R.V., Polyakov, I.V., Alexeev, V.A., 2010. Role of polar amplification in long-term surface air temperature variations and modern Arctic warming. J. Climate 23, 3888-3906.

KOPRI 극지연구소

Benninghoff, W.S., 1962. Calculation of pollen and spores density in sediments by addition of exotic pollen in known quantities. Pollen Spores 6, 332-333.

Bett, D.T., Holland, P.R., Naveira Garabato, A.C., Jenkins, A., Dutrieux, P., Kimura, S., Fleming, A., 2020. The impact of the Amundsen Sea freshwater balance on ocean melting of the West Antarctic Ice Sheet. J. Geophys. Res. Oceans 125, e2020JC016305.

Bintanja, R., van Oldenborgh, G.J., Drijfhout, S.S., Wouters, B., Katsman, C.A., 2013. Important role for ocean warming and increased ice-shelf melt in Antarctic sea-ice expansion. Nat. Geosci. 6 (5), 376-379. https://doi.org/10.1038/ngeo1767.

Bode, A., Castro, C.G., Doval, M.D., Varela, M., 2002. New and regenerated production and ammonium regeneration in the western Bransfield Strait region (Antarctica) during phytoplankton bloom conditions in summer. Deep-Sea Res. Part II 49, 787-804.

Boyd, P.W., Robinson, C., Savidge, G., Williams, P.J.L., 1995. Water column and sea-ice primary production during austral spring in the Bellingshausen Sea. J. Plankton Res. 42 (4-5), 1177-1200.

Boyd, P.W., Jickells, T., Law, C.S., Blain, S., Boyle, E.A., Buesseler, K.O., Coale, K.H., Cullen, J.J., de Baar, H.J.W., Follows, M., Harvey, M., Lancelot, C., Levasseur, M., Owens, N.P.J., Pollard, R., Rivkin, R.B., Sarmiento, J., Schoemann, V., Smetacek, V., Takeda, S., Tsuda, A., Turner, S., Watson, A.J., 2007. Mesoscale iron enrichment experiments 1993-2005: synthesis and future directions. Science 315, 612-617.

Bozkurt, D., Rondanelli, R., Marin, J.C., Garreaud, R., 2018. Foehn event triggered by an atmospheric river underlies record-setting temperature along continental Antarctica. J. Geophys. Res. Atmos. 123, 3871-3892.

Bravo, I., Figueroa, R.I., 2014. Towards an ecological understanding of dinoflagellate cyst functions. Microorganisms 2, 11-32.

Brenner, W., Biebow, N., 2001. Missing autofluorescence of recent and fossil dinoflagellate cysts — an indicator of heterotrophy? Neues Jb. Geol. Pal¨antol. Abh. 219, 229-240.

Bromwich, D., Liu, Z., Rogers, A.N., Van Woert, M.L., 1998. Winter atmospheric forcing of the Ross Sea polynya. In: Jacobs, S.S., Weiss, R.F. (Eds.), Ocean, ice, and atmosphere: interactions at the Antarctic continental margin. American Geophysical Union, Washington, DC, pp. 101-133.

Bronselaer, B., Winton, M., Griffies, S.M., Hurlin, W.J., Rodgers, K.B., Sergienko, O.V., Stouffer, R.J., Russell, J.L., 2018. Change in future climate due to Antarctic meltwater. Nature 564 (7734), 53-58.

KOPRI 극지연구소

Casado, M., H´ebert, R., Faranda, D., Landais, A., 2023. The quandary of detecting the signature of climate change in Antarctica. Nat. Clim. Chang. 13, 1082-1088.

Chen, B., Irwin, A.J., Finkel, Z.V., 2011. Biogeographic distribution of diversity and size-structure of organic-walled dinoflagellate cysts. Mar. Ecol. Prog. Ser. 425, 35-45.

Clarke, K.R., Gorley, R.N., 2015. PRIMER v7: User Manual/Tutorial. PRIMER-E, Plymouth.

Cook, A.J., Vaughan, D.G., 2010. Overview of areal changes of the ice shelves on the Antarctic Peninsula over the past 50 years. Cryosphere 4, 77-98.

Cook, A.J., Fox, A.J., Vaughan, D.G., Ferrigno, J.G., 2005. Retreating glacier fronts on the Antarctic Peninsula over the past half-century. Science 308 (5721), 541-544.

Costa, M.R.A., Sarmento, H., Becker, V., Bagatini, I.L., Unrein, F., 2022. Phytoplankton phagotrophy across nutrients and light gradients using different measurement techniques. J. Plankton Res. 44 (4), 507-520.

Costa, R.R., Mendes, C.R.B., Tavano, V.M., Dotto, T.S., Kerr, R., Monteiro, T., Odebrecht, C., Secchi, E.R., 2020. Dynamics of an intense diatom bloom in the Northern Antarctic Peninsula, February 2016. Limnol. Oceanogr. 65 (9), 2056-2075.

Couto, N., Martinson, D.G., Kohut, J., Schofield, O., 2017. Distribution of upper circumpolar deep water on the warming continental shelf of the West Antarctic Peninsula. J. Geophys. Res. Oceans 122, 5306-5315. https://doi.org/10.1002/2017JC012840.

Dalaiden, Q., Schurer, A.P., Kirchmeier-Young, M.C., Goosse, H., Hegerl, G.C., 2022. West Antarctic surface climate changes since the mid-20th century driven by anthropogenic forcing. Geophys. Res. Lett. 49, e2022GL099543.

Dale, B., 1996. Dinoflagellate cyst ecology: Modelling and geological applications. In: Jansonius, J., McGregor, D.C. (Eds.), Palynology: Principles and Applications. American Association of Stratigraphic Palynologists Foundation, College Station, Texas, pp. 1249-1275.

Delmont, T.O., Hammar, K.M., Ducklow, H.W., Yager, P.L., Post, A.F., 2014. *Phaeocystis antarctica* blooms strongly influence bacterial community structures in the Amundsen Sea polynya. Front. Microbiol. 5, 646.

D'Sa, E.J., Kim, H.-C., Ha, S.-Y., Joshi, I., 2021. Ross Sea dissolved organic matter optical properties during an austral summer: biophysical influences. Front. Mar. Sci. 8, 749096.

Ellegaard, M., Figueroa, R.L., Versteegh, G.J.M., 2013. Dinoflagellate life cycles, strategy and diversity: key foci for future research. In: Lewis, J.M., Marret, F., Bradley, L.R. (Eds.), Biological and Geological Perspectives of Dinoflagellates. The

KOPRI 극지연구소

Micropalaeontological Society, Special Publications, London, pp. 249-261.

Esper, O., Zonneveld, K.A.F., 2007. The potential of organic-walled dinoflagellate cysts for the reconstruction of past sea-surface conditions in the Southern Ocean. Mar. Micropaleontol. 65, 185-212.

Falkowski, P., 2012. The power of plankton. Nature 483, 17-20.

Flynn, K.J., Mitra, A., Anestis, K., Anschütz, A.A., Calbet, A., Ferreira, G.D., Gypens, N., Hansen, P.J., John, U., Martin, J.L., Mansour, J.S., Maselli, M., Medi´c, N., Norlin, A., Not, F., Pitta, P., Romano, F., Saiz, E., Schneider, L.K., Stolte, W., Traboni, C., 2019. Mixotrophic protists and a new paradigm for marine ecology: where does plankton research go now? J. Plankton Res. 41 (4), 375-391.

Frainer, A., Primicerio, R., Kortsch, S., Aune, M., Dolgov, A.V., Fossheim, M., Aschan, M. M., 2017. Climate-driven changes in functional biogeography of Arctic marine fish communities. Proc. Natl. Acad. Sci. U. S. A. 114 (46), 12202-12207.

Garcia, H.E., Boyer, T.P., Baranova, O.K., Locarnini, R.A., Mishonov, A.V., Grodsky, A., Paver, C.R., Weathers, K.W., Smolyar, I.V., Reagan, J. R., Seidov, D., Zweng, M.M., 2019. World Ocean Atlas 2018: Product Documentation. Mishonov, A., Technical Editor.

Gille, S.T., 2002. Warming of the Southern Ocean since the 1950s. Science 295, 1275-1277.

Goffart, A., Catalano, G., Hecq, J.H., 2000. Factors controlling the distribution of diatoms and *Phaeocystis* in the Ross Sea. J. Mar. Syst. 27, 161-175.

G´omez, F., 2012. A quantitative review of the lifestyle, habitat and trophic diversity of dinoflagellates (Dinoflagellata, Alveolata). Syst. Biodivers. 10 (3), 267-275.

G´omez, F., Panisse, C., 2020. Chapter 1: Diversity and classification of dinoflagellates. In: Subba Rao, D.V. (Ed.), Dinoflagellates: Classification, Evolution, Physiology and Ecological Significance. Nova Science Publishers.

Grange, S.K., 2014. Technical note: averaging wind speeds and directions, p. 12. https://doi.org/10.13140/RG.2.1.3349.2006.

Grattepanche, J.-D., Vincent, D., Breton, E., Christaki, U., 2011. Microzooplankton herbivory during the diatom-*Phaeocystis* spring succession in the eastern English Channel. J. Exp. Mar. Biol. Ecol. 404, 87-97.

Grøsfjeld, K., Harland, R., Howe, J., 2009. Dinoflagellate cyst assemblages inshore and offshore Svalbard reflecting their modern hydrography and climate. Nor. J. Geol. 89, 121-134.

Hahn, L.C., Armour, K.C., Battisti, D.S., Donohoe, A., Pauling, A.G., Bitz, C.M., 2020. Antarctic elevation drives hemispheric asymmetry in polar lapse rate climatology and feedback. Geophys. Res. Lett. 47, e2020GL088965.

KOPRI 극지연구소

Harðard´ottir, S., Haile, J.S., Ray, J.L., Limoges, A., Van Nieuwenhove, N., Lalande, C., Grondin, P.−L., Jackson, R., Skaar, K.S., Heikkil¨a, M., Berge, J., Lundholm, N., Mass´e, G., Rysgaard, S., Seidenkrantz, M.−S., De Schepper, S., Lorenzen, E.D., Lovejoy, C., Ribeiro, S., 2024. Millennial−scale variations in Arctic sea ice are recorded in sedimentary ancient DNA of the microalga *Polarella glacialis*. Commun. Earth Environ. 5, 25. https://doi.org/10.1038/s43247−023−01179−5.

Harland, R., Pudsey, C.J., 1999. Dinoflagellate cysts from sediment traps deployed in the Bellingshausen, Weddell and Scotia seas, Antarctica. Mar. Micropaleontol. 37, 77-99.

Hartman, J.D., Bijl, P.K., Sangiorgi, F., 2018. A review of the ecological affinities of marine organic microfossils from a Holocene record offshore of Ad´elie Land (East Antarctica). J. Micropalaeontol. 37, 445-497.

Hartman, J.D., Sangiorgi, F., Bijl, P.K., Versteegh, G.J.M., 2019. *Nucicla umbiliphora* gen. et sp. nov.: a Quaternary peridinioid dinoflagellate cyst from the Antarctic margin. Palynology 43 (1), 94-103.

Hawkings, J.R., Wadham, J.L., Tranter, M., Raiswell, R., Benning, L.G., Statham, P.J., Tedstone, A., Nienow, P., Lee, K., Telling, J., 2014. Ice sheets as a significant source of highly reactive nanoparticulate iron to the oceans. Nat. Commun. 5 (1), 3929.

Head, M.J., Harland, R., Matthiessen, J., 2001. Cold marine indicators of the late Quaternary: the new dinoflagellate cyst genus *Islandinium* and related morphotypes. J. Quat. Sci. 16, 681-698.

Heikkil¨a, M., Pospelova, V., Hochheim, K.P., Kuzyk, Z.Z.A., Stern, G.A., Barber, D.G., 2014. Surface sediment dinoflagellate cysts from the Hudson Bay system and their relation to freshwater and nutrient cycling. Mar. Micropaleontol. 106, 79-109.

Hellmer, H.H., 2004. Impact of Antarctic ice shelf basal melting on sea ice and deep ocean properties. Geophys. Res. Lett. 31, L10307.

Henley, S.F., Cavan, E.L., Fawcett, S.E., Kerr, R., Monteiro, T., Sherrell, R.M., Bowie, A. R., Boyd, P.W., Barnes, D.K., Schloss, I.R., Marshall, T., Flynn, R., Smith, S., 2020. Changing biogeochemistry of the Southern Ocean and its ecosystem implications. Front. Mar. Sci. 7, 581.

H¨ofer, J., Giesecke, R., Hopwood, M.J., Carrera, V., Alarc´on, E., Gonz´alez, H.E., 2019. The role of water column stability and wind mixing in the production/export dynamics of two bays in the Western Antarctic Peninsula. Prog. Oceanogr. 174, 105-116.

Jenkins, A., Dutrieux, P., Jacobs, S.S., McPhail, S.D., Perrett, J.R., Webb, A.T., White, D.,

KOPRI 극지연구소

2010. Observations beneath Pine Island Glacier in West Antarctica and implications for its retreat. Nat. Geosci. 3, 468-472.

Jourdain, N.C., Mathiot, P., Merino, N., Durand, G., Sommer, J.L., Spence, P., Dutrieux, P., Madec, G., 2017. Ocean circulation and sea-ice thinning induced by melting ice shelves in the A mundsen Sea. J. Geophys. Res. Oceans 122, 2550-2573.

Jung, J., Cho, K.-H., Park, T., Yoshizawa, E., Lee, Y., Yang, E.J., Gal, J.-K., Ha, S.-Y., Kim, S., Kang, S.-H., Grebmeier, J.M., 2021. Atlantic-origin cold saline water intrusion and shoaling of the nutricline in the Pacific Arctic. Geophys. Res. Lett. 48, e2020GL090907.

Kaufman, D.E., Friedrichs, M.A.M., Smith Jr., W.O., Hofmann, E.E., Dinniman, M.S., Hemmings, J.C.P., 2017. Climate change impacts on Southern Ross Sea phytoplankton composition, productivity, and export. J. Geophys. Res. Oceans 122, 2339-2359.

Kim, S.Y., Lim, D., Rebolledo, L., Park, T., Esper, O., Munoz, P., La, H.S., Kim, T.W., Lee, S.H., 2021. A 350-year multiproxy record of climate-driven environmental shifts in the Amundsen Sea Polynya, Antarctica. Glob. Planet. Change 205, 103589.

Kim, S.Y., Park, T., Marret, F., Potvin, ´E., Cho, K.H., Jung, J., Lee, Y., La, H.S., Ha, S.Y., Kim, S.K., Kang, S.H., Yang, E.J., Nam, S.I., Hong, J.K., 2023. Strong regionalism in dinoflagellate cysts in recent sediments from the Chukchi-East Siberian Sea, Arctic Ocean. Prog. Oceanogr. 211, 102970.

Kopczy´nska, E.E., Savoye, N., Dehairs, F., Cardinal, D., Elskens, M., 2007. Spring phytoplankton assemblages in the Southern Ocean between Australia and Antarctica. Polar Biol. 31, 77-88.

Langone, L., Frignani, M., Labbrozzi, L., Ravaioli, M., 1998. Present-day biosiliceous sedimentation in the NW Ross Sea (Antartica). J. Mar. Syst. 17, 459-470.

Lanham, J., Mazloff, M., Naveira Garabato, A.C., Siegert, M., Mashayek, A., 2025. Seasonal regimes of warm circumpolar deep water intrusion toward Antarctic ice shelves. Commun. Earth Environ. 6 (1), 168.

Lee, Y., Park, J., Jung, J., Kim, T.W., 2022. Unprecedented differences in phytoplankton community structures in the Amundsen Sea Polynyas, West Antarctica. Environ. Res. Lett. 17 (11), 114022.

Lewis, K.M., van Dijken, G.L., Arrigo, K.R., 2020. Changes in phytoplankton concentration now drive increased Arctic Ocean primary production. Science 369, 198-202.

Lythe, M., Vaughan, D.G., The BEDMAP Consortium, 2001. BEDMAP: a new ice thickness and subglacial topographic model of Antarctica. J. Geophys. Res. 106, 11335-11352.

Mangoni, O., Saggiomo, V., Bolinesi, F., Margiotta, F., Budillon, G., Cotroneo, Y., Misic, C., Rivaro, P., Saggiomo, M., 2017. Phytoplankton blooms during austral summer in the Ross Sea, Antarctica: driving factors and trophic implications. PLoS ONE 12 (4), e0176033.

Marret, F., de Vernal, A., 1997. Dinoflagellate cyst distribution in surface sediments of the southern Indian Ocean. Mar. Micropaleontol. 29 (3-4), 367-392.

Marret, F., Zonneveld, K.A.F., 2003. Atlas of modern organic-walled dinoflagellate cyst distribution. Rev. Palaeobot. Palynol. 125 (1-2), 1-200.

Marret, F., Bradley, L., de Vernal, A., Hardy, W., Kim, S.Y., Mudie, P., Penaud, A., Pospelova, V., Price, A.M., Radi, T., Rochon, A., 2020. From bi-polar to regional distribution of modern dinoflagellate cysts, an overview of their biogeography. Mar. Micropaleontol. 159, 101753.

Masqu´e, P., Isla, E., Sanchez-Cabeza, J.A., Palanques, A., Bruach, J.M., Puig, P., Guill´en, J., 2002. Sediment accumulation rates and carbon fluxes to bottom sediments at the Western Bransfield Strait (Antarctica). Deep Sea Res. Part II Top. Stud. Oceanogr. 49 (4-5), 921-933.

Massom, R.A., Scambos, T.A., Bennetts, L.G., Reid, P., Squire, V.A., Stammerjohn, S.E., 2018. Antarctic ice shelf disintegration triggered by sea ice loss and ocean swell. Nature 558, 383-389.

McMinn, A., 1995. Why are there no post-Paleogene dinoflagellate cysts in the Southern Ocean. Micropaleontology 41, 383-386.

Mendes, C.R.B., de Souza, M.S., Garcia, V.M.T., Leal, M.C., Brotas, V., Garcia, C.A.E., 2012. Dynamics of phytoplankton communities during late summer around the tip of the Antarctic Peninsula. Deep Sea Res. Part I Oceanogr. Res. Pap. 65, 1.

Meredith, M.P., King, J.C., 2005. Rapid climate change in the ocean west of the Antarctic Peninsula during the second half of the 20th century. Geophys. Res. Lett. 32, L19604.

Mertens, K.N., Verhoeven, K., Verleye, T., Louwye, S., Amorim, A., Ribeiro, S., Deaf, A.S., Harding, I.C., De Schepper, S., Gonz´alez, C., Kodrans-Nsiah, M., de Vernal, A., Henry, M., Radi, T., Dybkjaer, K., Poulsen, N.E., Feist-urkhardt, S., Chitolie, J., Heilmann-Clausen, C., Londeix, L., Turon, J.-L., Marret, F., Matthiessen, J., McCarthy, F.M.G., Prasad, V., Pospelova, V., Hughes, J.E.K., Riding, J.B., Rochon, A., Sangiorgi, F., Welters, N., Sinclair, N., Thun, C., Soliman, A., Van Nieuwenhove, N., Vink, A., Young, M., 2009. Determining the absolute abundance of dinoflagellate cysts in recent marine sediments: the *Lycopodium* marker-grain method put to the test. Rev. Palaeobot. Palynol. 157 (3-4), 238-252.

Michalchuk, B., Anderson, J.B., Wellner, J.S., Manley, P.L., Bohaty, S., Majewski, W.,

KOPRI 극지연구소

2009. Holocene climate and glacial history of the northeastern Antarctic Peninsula: the marine sedimentary record from a long SHALDRIL core. Quat. Sci. Rev. 28, 3049-3065.

Milliken, K.T., Anderson, J.B., Wellner, J.S., Bohaty, S., Manley, P., 2009. High-resolution Holocene climate record from Maxwell Bay, South Shetland Islands, Antarctica. Geol. Soc. Am. Bull. 121, 1711-1725.

Mills, M.M., Kropuenske, L.R., van Dijken, G.L., Alderkamp, A.C., Berg, G.M., Robinson, D.H., Welschmeyer, N.A., Arrigo, K.R., 2010. Photophysiology in two major Southern Ocean phytoplankton taxa: photosynthesis and growth of *Phaeocystis antarctica* (Prymnesiophyceae) and *Fragilariopsis cylindrus* (Bacillariophyceae) under simulated mixed layer irradiance. J. Phycol. 46, 1114-1127.

Minzoni, R., Anderson, J.B., Fernandez, R., Wellner, J.S., 2015. Marine record of Holocene climate, ocean, and cryosphere interactions: Herbert Sound, James Ross Island. Antarctica. Quat. Sci. Rev. 129, 239-259.

Misic, C., Bolinesi, F., Castellano, M., Olivari, E., Povero, P., Fusco, G., Saggiomo, M., Mangoni, O., 2024. Factors driving the bioavailability of particulate organic matter in the Ross Sea (Antarctica) during summer. Hydrobiologia 851, 2657-2679.

Mitra, A., Flynn, K.J., Tillmann, U., Raven, J.A., Caron, D., Stoecker, D.K., Not, F., Hansen, P.J., Hallegraeff, G., Sanders, R., Wilken, S., McManus, G., Johnson, M., Pitta, P., Våge, S., Berge, T., Calbet, A., Thingstad, F., Jeong, H.J., Burkholder, J., Glibert, P.M., Gran´eli, E., Lundgren, V., 2016. Defining planktonic protist functional groups on mechanisms for energy and nutrient acquisition: incorporation of diverse mixotrophic strategies. Protist 167 (2), 106-120.

Mitra, A., Caron, D.A., Faure, E., Flynn, K.J., Leles, S.G., Hansen, P.J., McManus, G.B., Not, F., do Rosario Gomes, H., Santoferrara, L.F., Stoecker, D.K., Tillmann, U., 2023. The Mixoplankton Database (MDB): Diversity of photo-phago-trophic plankton in form, function, and distribution across the global ocean. J. Eukaryot. Microbiol. 70 (4), e12972.

Montresor, M., Procaccini, G., Stoecker, D.K., 1999. *Polarella glacialis*, Gen. Nov., sp. Nov. (Dinophyceae): Suessiaceae are still alive! J. Phycol. 35, 186-197.

Montresor, M., Lovejoy, C., Orsini, L., Procaccini, G., Roy, S., 2003. Bipolar distribution of the cyst-forming dinoflagellate *Polarella glacialis*. Polar Biol. 26 (3), 186-194.

Nakayama, Y., Menemenlis, D., Zhang, H., Schodlok, M., Rignot, E., 2018. Origin of Circumpolar Deep Water intruding onto the Amundsen and Bellingshausen Sea continental shelves. Nat. Commun. 9, 3403.

Nejstgaard, J.C., Tang, K.W., Steinke, M., Dutz, J., Koski, M., Antajan, E., Long, J.D., 2007. Zooplankton grazing on Phaeocystis: a quantitative review and future

challenges. Biogeochemistry 83, 147-172.

Neme, J., England, M.H., Hogg, A.M., 2021. Seasonal and interannual variability of the Weddell Gyre from a high-resolution global ocean-sea ice simulation during 1958-2018. J. Geophys. Res. Oceans 126, e2021JC017662.

Nooteboom, P.D., Bijl, P.K., van Sebille, E., von der Heydt, A.S., Dijkstra, H.A., 2019. Transport bias by ocean currents in sedimentary microplankton assemblages: implications for paleoceanographic reconstructions. Paleoceanogr. Paleoclimatol. 34, 1178-1194.

Nooteboom, P.D., Bijl, P.K., Kehl, C., van Sebille, E., Ziegler, M., von der Heydt, A., Dijkstra, H.A., 2022. Sedimentary microplankton distributions are shaped by oceanographically connected areas. Earth Syst. Dyn. 13 (1), 357-371.

Park, J., Kuzminov, F.I., Bailleul, B., Yang, E.J., Lee, S., Falkowski, P.G., Gorbunov, M.Y., 2017. Light availability rather than Fe controls the magnitude of massive phytoplankton bloom in the Amundsen Sea polynyas, Antarctica. Limnol. Oceanogr. 62, 2260-2276.

Park, T., Nakayama, Y., Nam, S., 2024. Amundsen Sea circulation controls bottom upwelling and Antarctic Pine Island and Thwaites ice shelf melting. Nat. Commun. 15 (1), 2946.

Parkinson, C.L., Cavalieri, D.J., 2012. Antarctic sea ice variability and trends, 1979-2010. The Cryosphere 6, 871-880.

Pie´nkowski, A.J., Marret, F., Scourse, J.D., Thomas, D.N., 2013. Organic-walled microfossils from the North-West Weddell Sea, Antarctica: records from surface sediments after the collapse of the Larsen-A and Prince Gustav Channel ice shelves. Antarct. Sci. 25, 565-574.

Pinkerton, M.H., Boyd, P.W., Deppeler, S., Hayward, A., H¨ofer, J., Moreau, S., 2021. Evidence for the impact of climate change on primary producers in the Southern Ocean. Front. Ecol. Evol. 9, 592027.

Portela, E., Meyer, M.G., Heywood, K.J., Smith Jr., W.O., 2025. Unprecedented summer phytoplankton bloom in the Ross Sea. Geophys. Res. Lett. 52, e2024GL111264.

Potvin, E., Kim, S.Y., Yang, E.J., Head, M.J., Kim, H.C., Nam, S.I., Yim, J.H., Kang, S.H., 2018. *Islandinium minutum* subsp *barbatum* subsp nov (Dinoflagellata), a new organic-walled dinoflagellate cyst from the Western Arctic: morphology, phylogenetic position based on SSU rDNA and LSU rDNA, and distribution. J. Eukaryot. Microbiol. 65, 750-772.

Prend, C.J., MacGilchrist, G.A., Manucharyan, G.E., Pang, R.Q., Moorman, R., Thompson, A.F., Griffies, S.M., Mazloff, M.R., Talley, L.D., Gille, S.T., 2024. Ross gyre variability modulates oceanic heat supply toward the West Antarctic continental

KOPRI 극지연구소

shelf. Commun. Earth Environ. 5, 47.

Pr´ezelin, B.B., Hofmann, E.E., Moline, M., Klinck, J.M., 2004. Physical forcing of phytoplankton community structure and primary production in continental shelf waters of the Western Antarctic Peninsula. J. Mar. Res. 62, 419-460.

Price, M.R., Heywood, K.J., Nicholls, K.W., 2008. Ice−shelf_ocean interactions at Fimbul Ice Shelf, Antarctica from oxygen isotope ratio measurements. Ocean Sci. 4, 89-98.

Purich, A., Doddridge, E.W., 2023. Record low Antarctic sea ice coverage indicates a new sea ice state. Commun. Earth Environ. 4 (1), 1-9. https://doi.org/10.1038/s43247− 023−00961−9.

Radi, T., de Vernal, A., Peyron, O., 2001. Relationships between dinocyst assemblages in surface sediments and hydrographic conditions in the Bering and Chukchi seas. J. Quat. Sci. 16, 667-680.

Rantanen, M., Karpechko, A.Y., Lipponen, A., Nordling, K., Hyv¨arinen, O., Ruosteenoja, K., Vihma, T., Laaksonen, A., 2022. The Arctic has warmed nearly four times faster than the globe since 1979. Commun. Earth Environ. 3 (1), 168.

Rengefors, K., Logares, R., Laybourn−Parry, J., Gast, R.J., 2015. Evidence of concurrent local adaptation and high phenotypic plasticity in a polar microeukaryote. Environ. Microbiol. 17, 1510-1519.

Ribeiro, S., Amorim, A., Andersen, T.J., Abrantes, F., Ellegaard, M., 2012. Reconstructing the history of an invasion: the toxic phytoplankton species *Gymnodinium catenatum* in the Northeast Atlantic. Biol. Invasions 14 (5), 969-985. https://doi.org/10.1007/ s10530−011−0132−6.

Rignot, E., Jacobs, S., Mouginot, J., Scheuchl, B.L., 2013. Ice−shelf melting around Antarctica. Science 341, 266-270. https://doi.org/10.1126/science.1235798.

Rintoul, S.R., Hughes, C.W., Olbers, D., 2001. Chapter 4.6 The antarctic circumpolar current system. In: Siedler, G., Church, J., Gould, J. (Eds.), International Geophysics, 77. Academic Press, pp. 271-302.

Schneider, L.K., Anestis, K., Mansour, J., Anschütz, A.A., Gypens, N., Hansen, P.J., John, U., Klemm, K., Martin, J.L., Medic, N., Not, F., Stolte, W., 2020. A dataset on trophic modes of aquatic protists. Biodivers. Data J. 8, e56648.

Sedwick, P.N., Ditullio, R., Mackey, D.J., 2000. Iron and manganese in the Ross Sea, Antarctica: seasonal iron limitation in Antarctic shelf waters. J. Geophys. Res. 105, 11321-11336.

Seidenstein, J.L., Leckie, R.M., McKay, R., De Santis, L., Harwood, D., Scientists, I.E. 374, 2024. Pliocene-Pleistocene warm−water incursions and water mass changes on the Ross Sea continental shelf (Antarctica) based on foraminifera from IODP

expedition 374. J. Micropalaeontol. 43 (2), 211-238.

Seyitmuhammedov, K., Stirling, C.H., Reid, M.R., van Hale, R., Laan, P., Arrigo, K.R., van Dijken, G., Alderkamp, A.-C., Middag, R., 2022. The distribution of Fe across the shelf of the Western Antarctic Peninsula at the start of the phytoplankton growing season. Mar. Chem. 238, 104066.

Sherr, E., Sherr, B., 2007. Heterotrophic dinoflagellates: a significant component of microzooplankton biomass and major grazers of diatoms in the sea. Mar. Ecol. Prog. Ser. 352, 187-197.

Shi, J.R., Talley, L.D., Xie, S.-P., Peng, Q., Liu, W., 2021. Ocean warming and accelerating Southern Ocean zonal flow. Nat. Clim. Chang. 11, 1090-1097.

Silvano, A., Rintoul, S.R., P˜nna-Molino, B., Hobbs, W.R., van Wijk, E., Aoki, S., Tamura, T., Williams, G.D., 2018. Freshening by glacial meltwater enhances melting of ice shelves and reduces formation of Antarctic Bottom Water. Sci. Adv. 4, eaap9467.

Smith, J.A., Graham, A.G.C., Post, A.L., Hillenbrand, C.D., Bart, P.J., Powell, R.D., 2019. The marine geological imprint of Antarctic ice shelves. Nat. Commun. 10, 5635.

Smith Jr., W.O., 2022. Primary productivity measurements in the Ross Sea, Antarctica: a regional synthesis. Earth Syst. Sci. Data 14, 2737-2747.

Smith Jr., W.O., Nelson, D.M., 1985. Phytoplankton bloom produced by a receding ice edge in the Ross Sea: spatial coherence with the density field. Science 227, 163-166.

Smith Jr., W.O., Dinniman, M.S., Klinck, J.M., Hofmann, E., 2003. Biogeochemical climatologies in the Ross Sea, Antarctica: seasonal patterns of nutrients and biomass. Deep Sea Res. Part II 50 (22-26), 3083-3101. https://doi.org/10.1016/j.dsr2.2003.07.010.

Smith Jr., W.O., Ainley, D.G., Arrigo, K.R., Dinniman, M.S., 2014. The oceanography and ecology of the Ross Sea. Annu. Rev. Mar. Sci. 6, 469-487.

Smith, R.C., Stammerjohn, S.E., 2001. Variations of surface air temperature and sea ice extent in the western Antarctic Peninsula (WAP) region. Ann. Glaciol. 33, 493-500.

Stammerjohn, S.E., Martinson, D.G., Smith, R.C., Iannuzzi, R.A., 2008. Sea ice in the western Antarctic Peninsula region: spatio-temporal variability from ecological and climate change perspectives. Deep Sea Res. Part II Top. Stud. Oceanogr. 55 (18-19), 2041-2058.

Steig, E.J., Schneider, D., Rutherford, S.D., Mann, M.E., Comiso, J.C., Shindell, D.T., 2009. Warming of the Antarctic ice-sheet surface since the 1957 International Geophysical Year. Nature 457, 459-462.

Sunda, W.G., Huntsman, S.A., 1997. Interrelated influence of iron, light and cell size on

KOPRI 극지연구소

marine phytoplankton growth. Nature 390, 389-392. https://doi.org/10.1038/37093.

Swadling, K.M., Constable, A.J., Fraser, A.D., Massom, R.A., Borup, M.D., Ghigliotti, L., Granata, A., Guglielmo, L., Johnston, N.M., Kawaguchi, S., Kennedy, F., Kiko, R., Koubbi, P., Makabe, R., Martin, A., McMinn, A., Moteki, M., Pakhomov, E.A., Peeken, I., Reimer, J., Reid, P., Ryan, K.G., Vacchi, M., Virtue, P., Weldrick, C.K., Wongpan, P., Wotherspoon, S.J., 2023. Biological responses to change in Antarctic sea ice habitats. Front. Ecol. Evol. 10, 1073823.

Swalethorp, R., Dinasquet, J., Logares, R., Bertilsson, S., Kjellerup, S., Krabberød, A.K., Council, S.R., 2019. Microzooplankton distribution in the Amundsen Sea Polynya (Antarctica) during an extensive *Phaeocystis antarctica* bloom. Prog. Oceanogr. 170, 1.

Tamura, T., Ohshima, K.I., Nihashi, S., 2008. Mapping of sea ice production for Antarctic coastal polynyas. Geophys. Res. Lett. 35 (7), L07606.

Tang, K.W., Jakobsen, H.H., Visser, A.W., 2001. *Phaeocystis globosa* (Prymnesiophyceae) and the planktonic food web: feeding, growth, and trophic interactions among grazers. Limnol. Oceanogr. 46, 1860-1870.

Tang, Y.Z., Gu, H., Wang, Z., Liu, D., Wang, Y., Lu, D., Hu, Z., Deng, Y., Shang, L., Qi, Y., 2021. Exploration of resting cysts (stages) and their relevance for possibly HABs- causing species in China. Harmful Algae 107, 102050.

Taylor, F.J.R., Hoppenrath, M., Saldarriaga, J.F., 2008. Dinoflagellate diversity and distribution. Biodivers. Conserv. 17, 407-418.

Th¨ole, L.M., Nooteboom, P.D., Hou, S., Wang, R., Nie, S., Michel, E., Sauermilch, I., Marret, F., Sangiorgi, F., Bijl, P.K., 2023. An expanded database of Southern Hemisphere surface sediment dinoflagellate cyst assemblages and their oceanographic affinities. J. Micropalaeontol. 42, 35-56.

Thompson, D.W.J., Solomon, S., 2002. Interpretation of recent Southern Hemisphere climate change. Science 296 (5569), 895-899.

Thomson, P.G., McMinn, A., Kiessling, I., Watson, M., Goldsworthy, P.M., 2006. Composition and succession of dinoflagellates and chrysophytes in the upper fast ice of Davis Station, East Antarctica. Polar Biol. 29, 337-345.

Tian, H.A., van Manen, M., Bunnell, Z.B., Jung, J., Lee, S.H., Kim, T.W., Reichart, G., Conway, T.M., Middag, R., 2023. Biogeochemistry of iron in coastal Antarctica: isotopic insights for external sources and biological uptake in the Amundsen Sea polynyas. Geochim. Cosmochim. Acta 363, 51.

Toggweiler, J.R., Russell, J., 2008. Ocean circulation in a warming climate. Nature 451 (7176), 286-288.

Vaughan, D.G., 2006. Recent trends in melting conditions on the Antarctic Peninsula and their implications for ice-sheet mass balance and sea level. Arct. Antarct. Alp. Res. 38 (1), 147-152.

Vaughan, D.G., 2008. West Antarctic Ice Sheet collapse - the fall and rise of a paradigm. Clim. Change. 91, 65-79.

Venables, H.J., Clarke, A., Meredith, M.P., 2013. Wintertime controls on summer stratification and productivity at the western Antarctic Peninsula. Limnol. Oceanogr. 58 (3), 1035-1047.

de Vernal, A., Henry, M., Bilodeau, G., 2010. Micropaleontological preparation techniques and analyses. In: Les Cahiers du GEOTOP, Third edition 3. Universite du Quebec a Montreal, Montreal, p. 31.

de Vernal, A., Radi, T., Zaragosi, S., Van Nieuwenhove, N., Rochon, A., Allan, E., De Schepper, S., Eynaud, F., Head, M.J., Limoges, A., Londeix, L., Marret, F., Matthiessen, J., Penaud, A., Pospelova, V., Price, A., Richerol, T., 2020. Distribution of common modern dinoflagellate cyst taxa in surface sediments of the Northern Hemisphere in relation to environmental parameters: the new n=1968 database. Mar. Micropaleontol. 159, 101796.

Wåhlin, A.K., Yuan, X., Björk, G., Nohr, C., 2010. Inflow of warm circumpolar deep water in the Central Amundsen Shelf. J. Phys. Oceanogr. 40, 1427-1434.

Weber, M.E., Raymo, M.E., Peck, V.L., Williams, T., 2021. IODP Expedition 382 Scientists Iceberg Alley and Subantarctic Ice and Ocean Dynamics Proceedings of the International Ocean Discovery Program, 382: College Station, TX (International Ocean Discovery Program).

Zheng, S.X., Wang, G.Z., Lin, S.J., 2012. Heat shock effects and population survival in the polar dinoflagellate *Polarella glacialis*. J. Exp. Mar. Biol. Ecol. 438, 100-108.

Zonneveld, K.A.F., Versteegh, G.J.M., de Lange, G.J., 2001. Paleoproductivity and post-depositional aerobic organic matter decay reflected by dinoflagellate cysts assemblages of the Eastern Mediterranean S1 sapropel. Mar. Geol. 172, 181-195.

KOPRI 극지연구소

Table 1. Sediment sampling site number, geographical coordinates, water depth, total dinoflagellate cyst concentrations, counted cysts and number of taxa for each analyzed sample. Sampling sites with low cyst counts (〈100) are indicated by an asterisk (*).

Sector	Site No.	Cruise	Year	Gear	Latitude	Longitude	Water depth (m)	Total dinoflagellate cyst concentrations (cysts/g)	Cyst sum	Number of taxa
A	1	*Yuzhmorgeologiya* Expedition	2008	Box corer	-62.031	-56.221	2210	5661	1795	9
	2	*Araon* Expedition	2010	Box corer	-62.191	-57.315	1420	442	268	8
	3	*Yuzhmorgeologiya* Expedition	2008	Box corer	-60.229	-58.864	3630	297	437	10
	4*	*Araon* Expedition	2013	Box corer	-65.752	-64.471	443	64	92	5
	5	*Araon* Expedition	2013	Box corer	-64.702	-63.015	345	1020	410	7
	6	*Yuzhmorgeologiya* Expedition	2002	Box corer	-59.814	-49.229	4141	870	980	12
	7	*Yuzhmorgeologiya* Expedition	2002	Box corer	-60.381	-47.005	786	650	412	8
	8	*Polarstern* Expedition	2016	Box corer	-61.830	-55.647	2624	3406	551	6
	9	*Polarstern* Expedition	2016	Box corer	-63.757	-60.442	633	1539	220	4
	10	*Polarstern* Expedition	2016	Box corer	-63.233	-61.344	1283	1436	206	8
B	11	*Araon* Expedition	2017	Box corer	-71.214	-87.983	444	229	177	8
	12	*Araon* Expedition	2017	Box corer	-71.460	-87.201	510	321	360	6
	13	*Araon* Expedition	2017	Box corer	-71.867	-85.349	502	383	386	7
	14	*Araon* Expedition	2017	Box corer	-73.649	-81.350	671	1276	977	8
	15	*Araon* Expedition	2017	Box corer	-72.209	-73.943	625	983	745	8
	16	*Araon* Expedition	2017	Box corer	-72.450	-73.553	560	840	596	8
	17	*Araon* Expedition	2017	Box corer	-71.495	-77.279	612	94	112	5
	18*	*Araon* Expedition	2017	Box corer	-70.860	-79.699	631	3	2	2
	19*	*Araon* Expedition	2016	Box corer	-72.084	-118.884	745	22	28	4
	20	*Araon* Expedition	2016	Box corer	-73.040	-115.725	710	336	247	6
	21	*Araon* Expedition	2016	Box corer	-74.172	-112.530	788	203	147	5
	22	*Araon* Expedition	2016	Box corer	-73.819	-113.045	1036	247	110	4
	23	*Araon* Expedition	2016	Box corer	-73.500	-112.000	420	130	101	4
	24	*Araon* Expedition	2016	Box corer	-73.500	-116.500	374	211	167	7
	25*	*Araon* Expedition	2016	Box corer	-74.080	-115.725	1064	122	56	2
	26	*Araon* Expedition	2016	Box corer	-74.867	-102.080	945	287	153	5
	27	*Araon* Expedition	2016	Box corer	-74.141	-128.204	568	60	139	5
	28*	*Araon* Expedition	2016	Box corer	-72.994	-126.974	270	9	20	4
	29	*Araon* Expedition	2016	Box corer	-73.682	-123.579	580	733	644	8
	30	*Araon* Expedition	2016	Box corer	-73.280	-114.950	827	1199	370	4
	31	*Araon* Expedition	2016	Box corer	-72.431	-116.339	537	138	198	6
	32	*Araon* Expedition	2016	Box corer	-73.764	-128.303	711	185	130	8
C	33	*Araon* Expedition	2021	Box corer	-77.711	-161.853	408	306	311	7
	34	*Araon* Expedition	2021	Box corer	-77.974	-173.557	525	242	266	5
	35	*Araon* Expedition	2021	Box corer	-77.697	-179.201	644	665	589	5
	36	*Araon* Expedition	2021	Box corer	-76.633	-179.200	619	649	426	5
	37	*Araon* Expedition	2021	Box corer	-75.567	-179.199	555	696	779	7
	38	*Araon* Expedition	2021	Box corer	-77.010	171.000	745	1389	1038	6
	39	*Araon* Expedition	2014	Box corer	-76.845	163.844	720	23871	3593	7
	40	*Araon* Expedition	2021	Box corer	-74.751	165.107	692	19033	5463	7
	41	*Araon* Expedition	2021	Box corer	-75.349	164.682	660	16065	12488	8
	42	*Araon* Expedition	2014	Box corer	-75.948	163.000	930	145159	10552	7
	43	*Araon* Expedition	2012	Box corer	-75.089	165.057	1165	5267	2583	8
	44	*Araon* Expedition	2015	Box corer	-75.204	164.276	1081	3505	1246	7
	45	*Araon* Expedition	2015	Box corer	-74.914	164.520	543	1553	1543	7
	46*	*Araon* Expedition	2015	Box corer	-75.002	163.725	669	46	23	7
	47	*Araon* Expedition	2018	Box corer	-72.723	171.574	567	574	832	7
	48	*Araon* Expedition	2015	Box corer	-72.076	170.456	575	3949	3766	7

Table 2. List of dinoflagellate cyst taxa identified in the investigated sediments, trophic type (H=Heterotrophs; P=Phototrophs; M=Mixotrophs), relative abundance of cyst species (%) and cyst concentrations (cysts/g).

Taxon name (code)	Motile affinity	Trophic mode	Percentage range (%)	Concentration range (cysts/g)
Brigantediniumspp. (Bspp)	*Protoperidiniumspp.*	H	0–58.3	0–507
Cryodinium meridianum (Cmer)	Unknown	H	0–7.3	0–289
Cyst of *Polarella glacialis*(Pgla)	*Polarella glacialis*	P	0–98.7	0–140,647
Dalella chathamense(Dcha)	Unknown	P	0–3.4	0–14
Impagidinium aculeatum(Iacu)	Unknown	P	0–0.1	0–1
Impagidinium pallidum(Ipal)	Unknown	P	0–50.0	0–53
Impagidinium sphaericum(Isph)	Unknown	P	0–10.1	0–30
Impagidinium spp. (Ispp)	Unknown	P	0–0.5	0–1
Islandinium ?minutum(Imin)	*Islandinium ?minutum*	H	0–96.7	0–5403
Gymnodinium microreticulatum (Gmic)	*Gymnodinium microreticulatum*	M	0–64.8	0–426
Nematosphaeropsis labyrinthus(Nlab)	Unknown	P	0–3.9	0–12
Nucicla umbiliphora(Numb)	Unknown	H	0–39.1	0–1947
Selenopemphix antarctica(Sant)	Unknown	H	0–54.9	0–787
*Selenopemphix*sp. 1 sensu Esper and Zonneveld (2007) (Ssp1)	Unknown	H	0–98.2	0–1444
*Spiniferites*spp. (Sspp)	Unknown	P	0–4.4	0–2

KOPRI
극지연구소

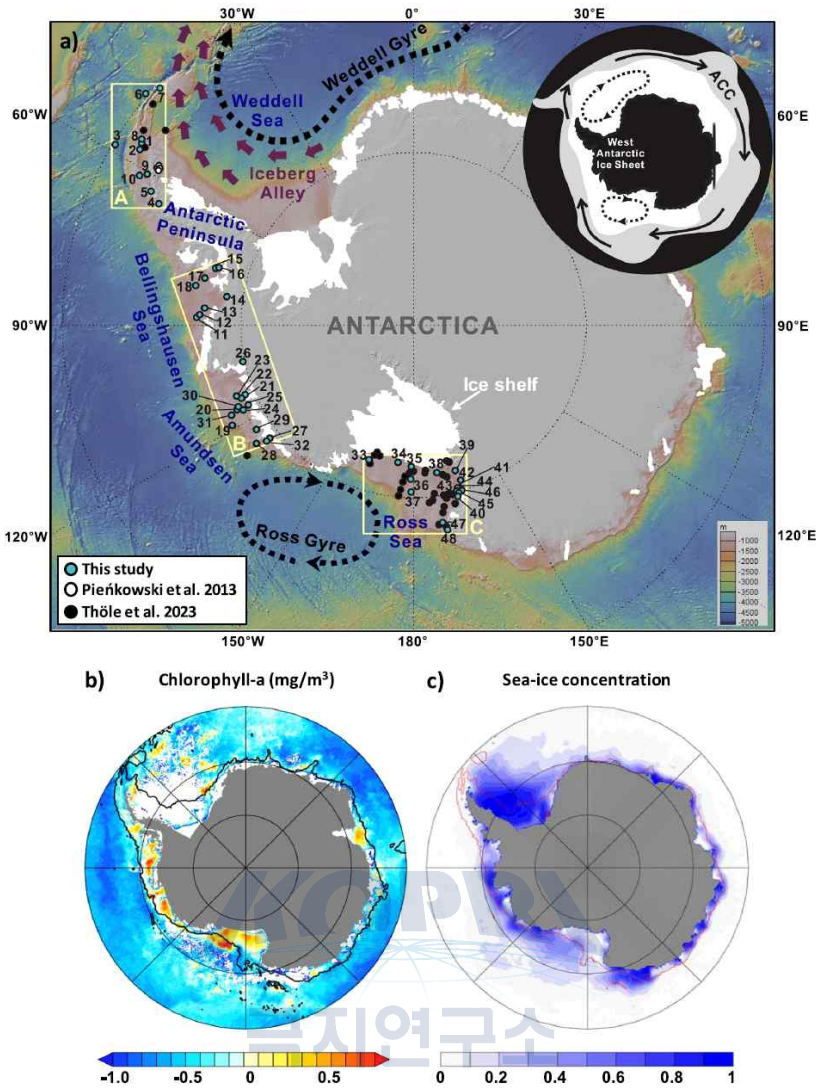


Figure 1. Map of the study area illustrating locations of sampling sites and main oceanographic features. (a) Surface sediment samples used in our study are indicated by their numbers (blue dots; details in Table 1). Previously published sites are white (Pie´nkowski et al., 2013) and black (Th¨ole et al., 2023) dots. Arrows indicate major ocean current patterns (dashed black line = Weddell/Ross gyres and purple = Iceberg Alley): the upper right map visualizes approximate locations of Weddell & Ross gyres and the Antarctic Circumpolar Current (ACC) flows eastward around Antarctica (after Rintoul et al., 2001). White areas represent ice shelves (after Smith et al., 2019). (b) Mean logarithmic chlorophyll−*a* concentration (mg/m3) derived from MODIS−AQUA Ocean Color data during the austral summers (2003–2019). (c) Mean satellite−observed sea−ice concentrations during the austral summers (1998–2016), provided by the National Snow and Ice Data Center (NSIDC) (Nimbus−7 SMMR and DMSP SSM/I−SSMIS Passive Microwave Data; http://nsidc.org). Geographic locations are divided into three major regions: the northern Antarctic Peninsula (sites 1–10; sector A), the Bellingshausen–Amundsen Seas (sites 11–32; sector B) and the Ross Sea (sites 33–48; sector C). (For interpretation of the references to color in this figure legend, the reader is referred to the web version of this article.)

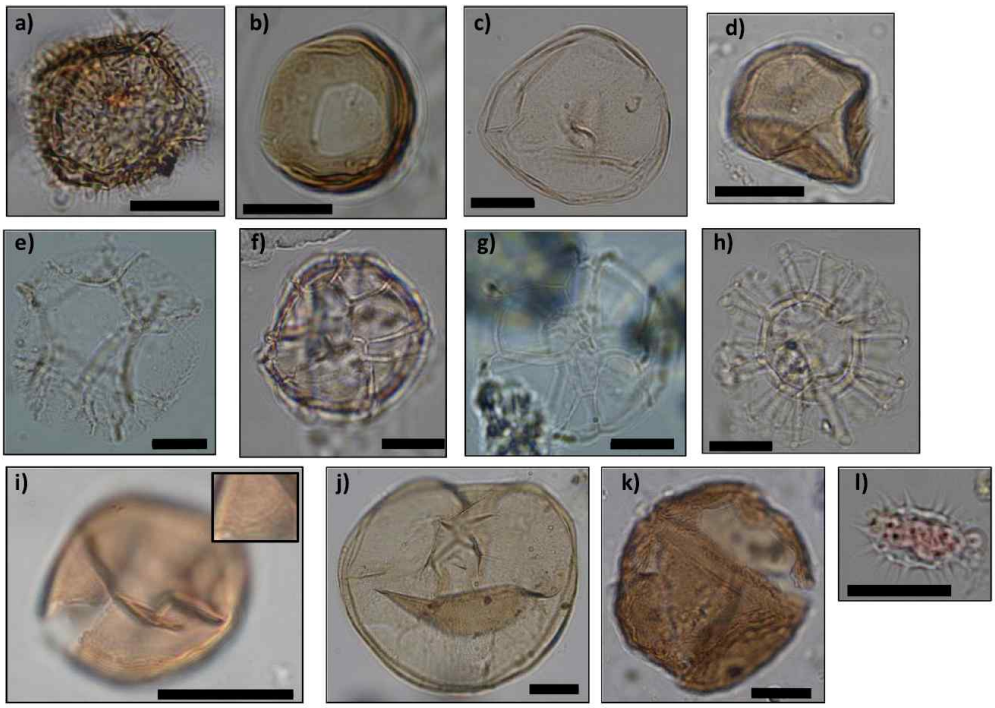


Figure 2. Photomicrographs of selected dinoflagellate cysts collected in surface sediments from the west Antarctic shelves (Scale bars = 20 μm). (a) *Islandinium*? *minutum*. (b) *Brigantedinium simplex*. (c) *Selenopemphix antarctica*. (d) *Cryodinium meridianum*. (e) *Impagidinium pallidum*. (f) *Impagidinium sphaericum*. (g) *Dalella chathamense*. h) *Nematosphaeropsis labyrinthus*. i) *Gymnodinium microreticulatum*, with a chasmic archaeopyle and microreticulate pattern (inset box). j) *Selenopemphix* sp. 1. k) *Nucicla umbiliphora*. l) Cyst of *Polarella glacialis*.

KOPRI 극지연구소

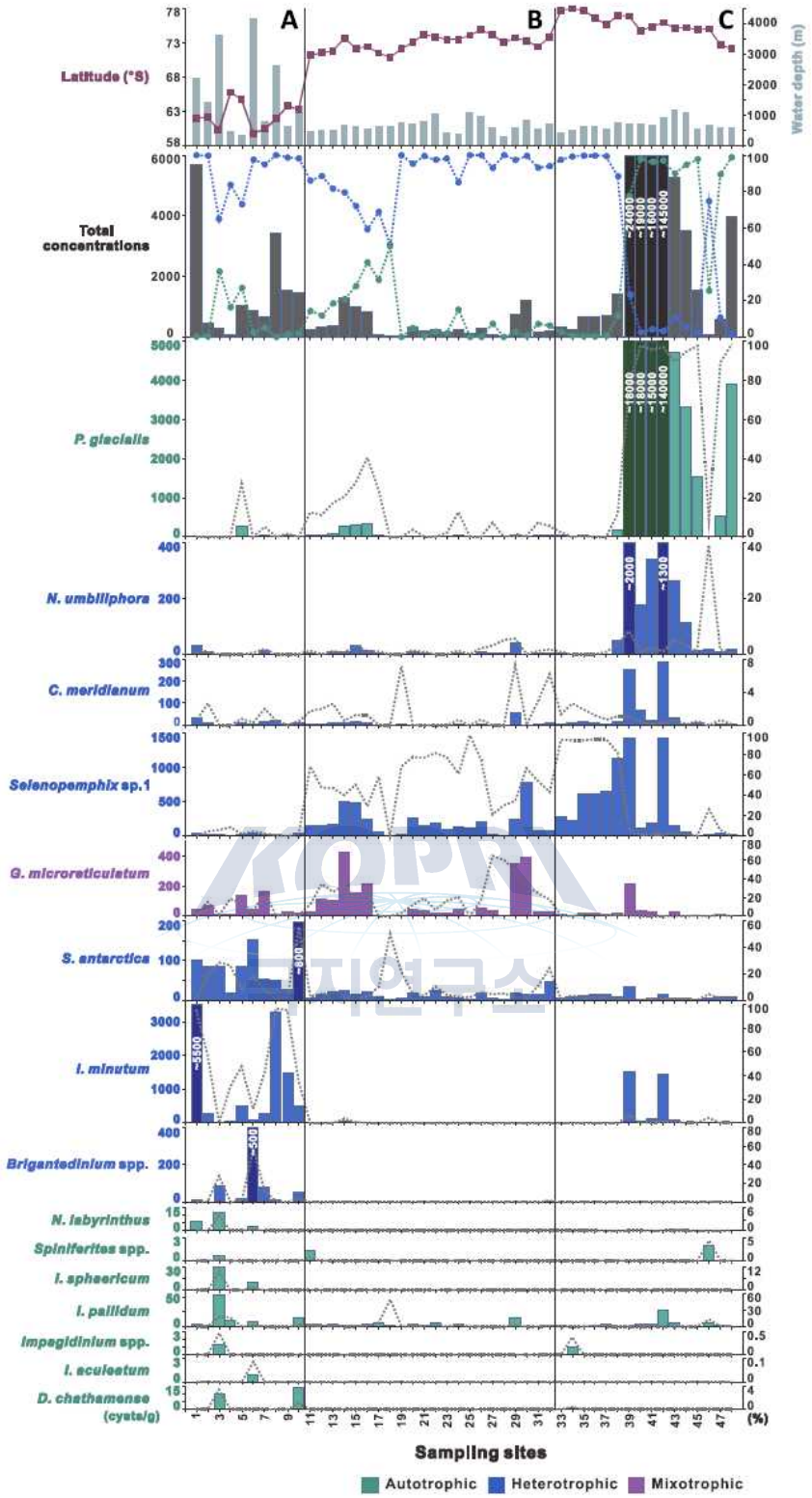


Figure 3. Total cyst concentrations (cysts/g; bar) and relative abundances of dinoflagellate cyst taxa (%; dotted line) in surface sediment samples (autotrophic taxa = green, heterotrophic taxa = blue, mixotrophic taxa = purple). Spatial domains of sectors A (sites 1-10), B (sites 11-32) and C (sites 33-48) are denoted on the top of the diagram. Six samples with low cyst counts (<100) are indicated by an asterisk (*). (For interpretation of the references to color in this figure legend, the reader is referred to the web version of this article.)

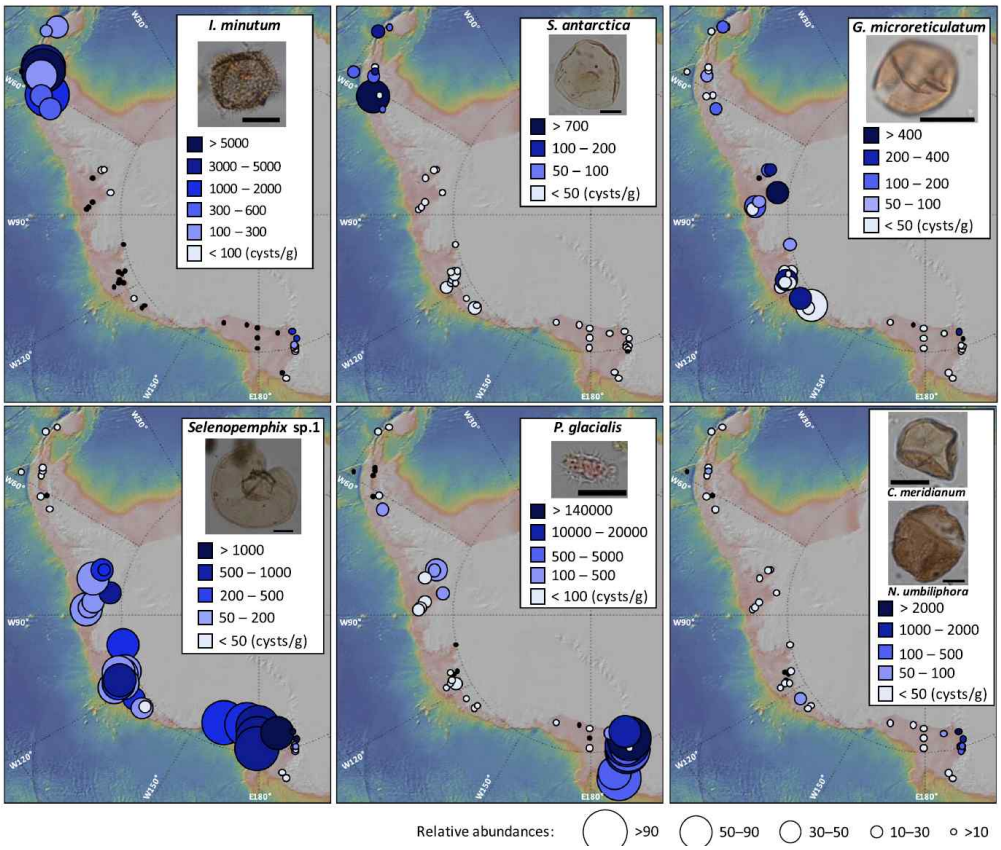


Figure 4. Distributions of key dinoflagellate cyst taxa, expressed as percentages and concentrations (cysts/g). (a) *Islandinium*? *minutum*. (b) *Selenopemphix antarctica*. (c) *Gymnodinium microreticulatum*. (d) *Selenopemphix* sp. 1. (e) Cyst of *Polarella glacialis*. (f) *Cryodinium meridianum* and *Nucicla umbiliphora*.

KOPRI 극지연구소

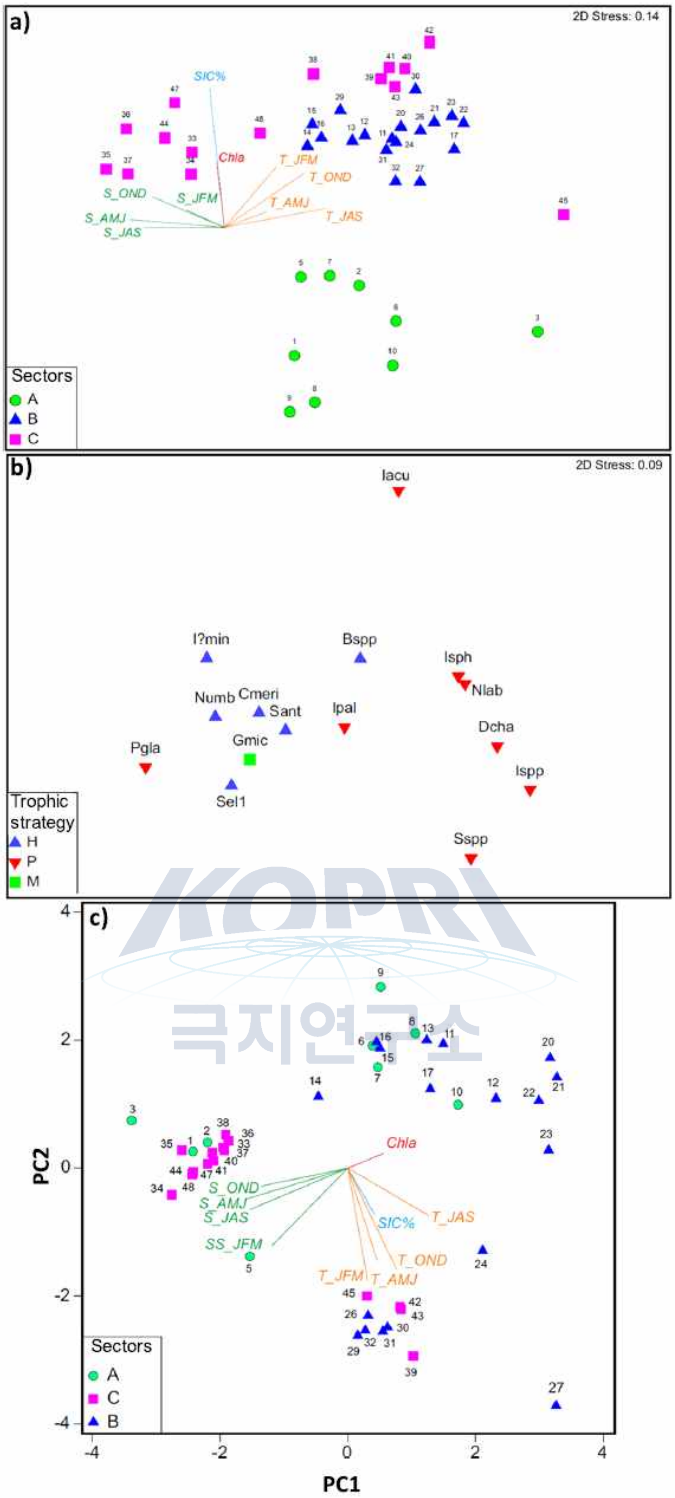


Figure 5. Ordination analysis performed on dinoflagellate cyst assemblages and environmental conditions. (a) Non-metric multi-dimensional scaling (NMDS) on 42 dinoflagellate cyst assemblages (percentages were square-root transformed; Bray-Curtis similarity) with environmental vectors (see Table 2 for codes). (b) NMDS plot for the dinocyst taxa with trophic status. (c) Principal Component analysis on normalized environmental conditions. PC1 and PC2 explain 37.4 % and 28.7 % of the variance respectively.

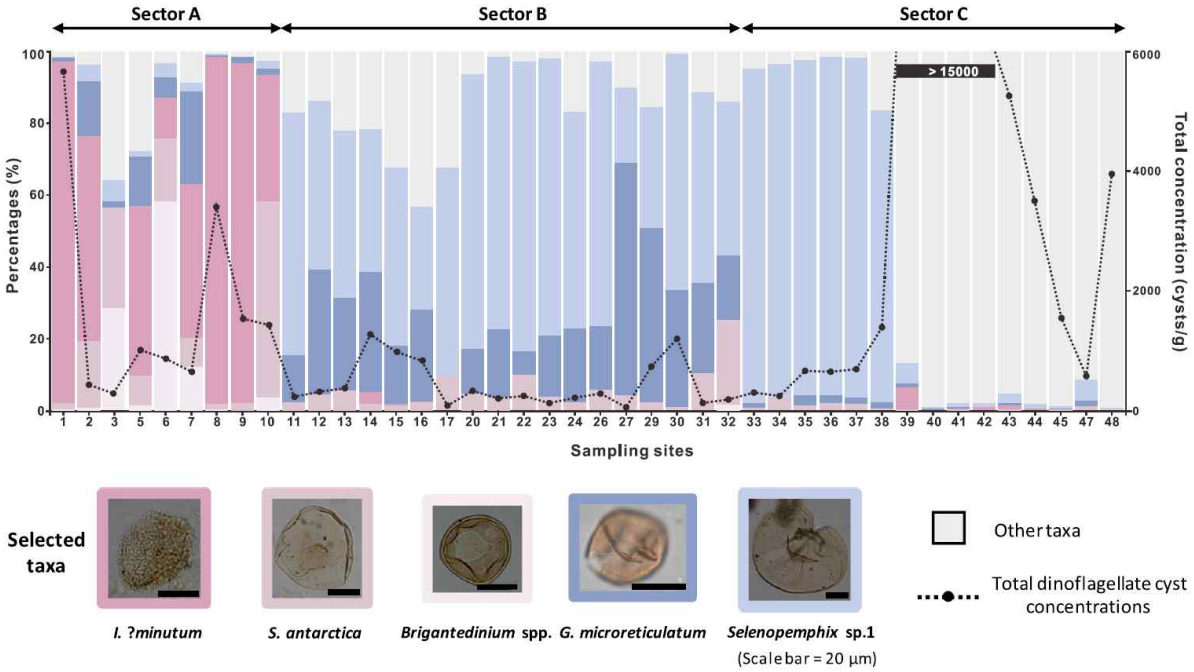


Figure 6. Stacked bar plot showing the relative abundance of five selected dinoflagellate cyst taxa in each sediment sample collected in the study area. The 'others' category contains all the other taxa. Sampling sites are grouped by sectors and arranged from east to west (left to right).

KOPRI
극지연구소

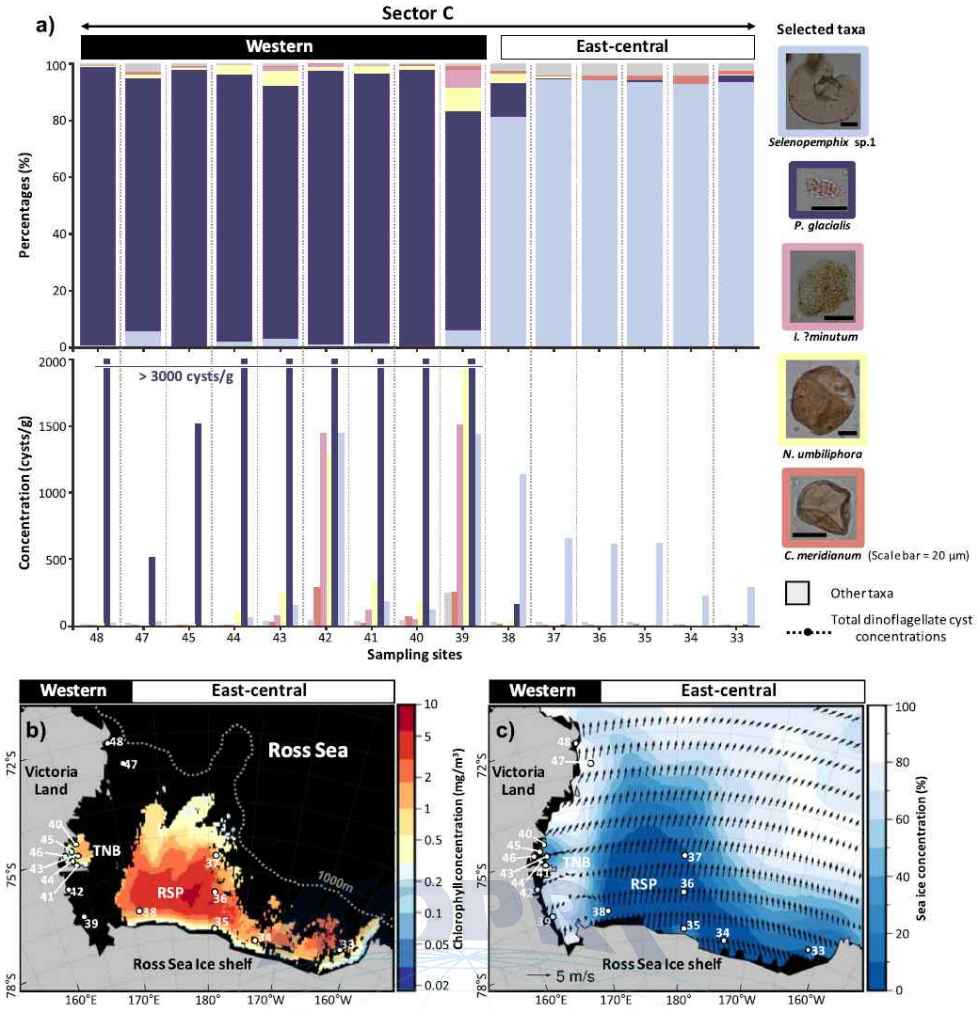


Figure 7. Summary diagram of selected dinoflagellate cyst taxa and climatology of the Ross Sea in austral summer. (a) Relative abundances (%; upper chart) and concentrations (cysts/g; lower chart) of the main dinoflagellate cysts in the Ross Sea samples. The 'others' category contains all the other taxa. (b, c) A composite image of satellite-derived logarithmic chlorophyll-*a* concentrations (mg/m3) and sea-ice concentration (%) overlaid on wind vectors (m/s) for the months of December from 2011 to 2020. TNB = Terra Nova Bay. RSP = Ross Sea Polynya.

극지연구소

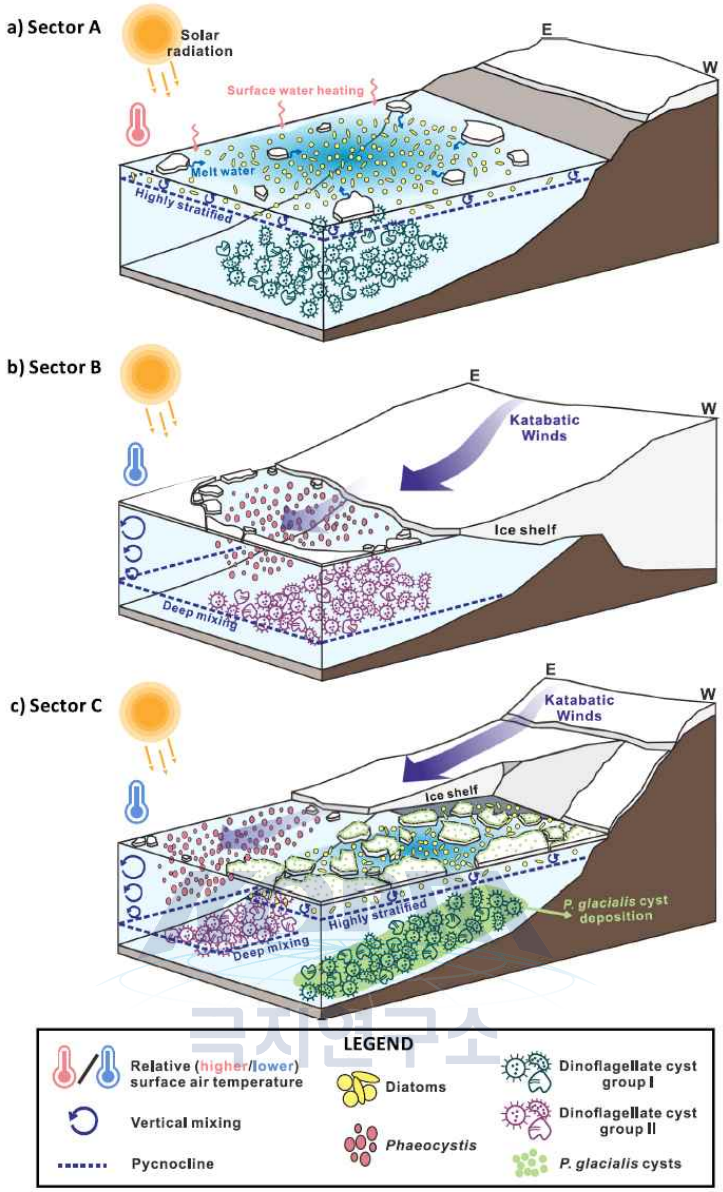


Figure 8. Conceptual overview of mechanisms causing regional disparities in dinoflagellate cyst species compositions between the northern Antarctic Peninsula (sector A), the Bellingshausen-Amundsen seas (sector B) and the Ross Sea (sector C) under the current Arctic warming trend. (a) Sector A is characterized by a large amount of glacial meltwater due to higher surface air temperature that results in highly stratified surface waters in austral summer, favored by diatoms and dinoflagellate (Group I) populations. (b) Sector B illustrates strong offshore winds that create large open water areas (polynyas) along with an unstable, well-mixed water column, promoting *Phaeocystis* and dinoflagellate (Group II) growths. (c) Schematic representation of the east-central Ross Sea polynya region dominated by dinoflagellate (Group II) in association with a weak water column stratification under strong katabatic wind activities, and the western Ross Sea dominated by ice-associated *P. glacialis* cysts and the diatom-grazing dinoflagellate cysts resulting from heavy sea-ice conditions before the diatom growth season and subsequent meltwaterstratified surface waters for diatom blooms. Dinoflagellate group I = *I.? minutum*, *S. antarctica*, *Brigantedinium* spp., *N. umbiliphora* and *C. meridianum*. Dinoflagellate group II = *Selenopemphix* sp. 1 and *G. microreticulatum*.

제 31 장

Pleistocene oceanographic variability in the Ross Sea: A multiproxy approach to age model development and paleoenvironmental analyses[24)]

Michael Bollen[a,b,*], Christina R. Riesselman[a], Christian Ohneiser[a], Olga Albot[c], Robert McKay[d], Min Kyung Lee[e], Kyu-Cheul Yoo[e], Sunghan Kim[e], Jae Il Lee[e], Richard Levy[f]

[a]University of Otago, [b]University of Lausanne, [c]Victoria University of Wellington, [d]Korea Polar Research Institute, [e]GNS Science

ABSTRACT: Understanding how ocean circulation has varied around Antarctica in the past is vital because significant volumes of ice are grounded below sea level, and therefore ice sheet variations are strongly coupled with oceanographic variability at the continental shelf margin. This study investigates the 11.75 m sediment core RS15-LC42, retrieved from the Central Basin of the Ross Sea. A magneto-biostratigraphic age model was constructed from a magnetic reversal stratigraphy, diatom biostratigraphy, and the relative paleointensity of the geomagnetic field. The core spans the last 1.34 Myr with a mean sedimentation rate of 0.88 cm/kyr, providing insights into paleoceanographic variability in the Ross Sea throughout the Pleistocene. Winnowed deposits enriched in iceberg rafted debris were formed due to a combination of enhanced glacial calving during glacial retreats, and export of Dense Shelf Water during interglacial and weak glacial periods when the ice-sheet was not grounded in the outer Joides Trough. During periods where the ice sheet grounded on the outer Ross Sea continental shelf, laminated sediments rich in reworked diatoms are interpreted to have formed due to glacial scouring and transport of shelf sediments to the mouth of the Joides Trough, where slope failures and meltwater pulses remobilized this material downslope to the Central Basin. Dense shelf water formation is inferred to be most intense during interglacial periods, with reduced export from the Joides Trough during ice sheet advances. The study does not find any evidence for prolonged ice-sheet grounding in the outer Ross Sea since ~0.3 Ma, however, we conclude that the grounding line reached the outer shelf frequently between 0.3 and 1.2 Ma, supporting higher Antarctic ice volumes during glacial periods in this interval.

KOPRI 극지연구소

24) 이 연구 결과는 다음의 논문으로 출판되었음: Bollen, M. et al. (2022). "Pleistocene oceanographic variability in the Ross Sea: A multiproxy approach to age model development and paleoenvironmental analyses." Global and Planetary Change 216: 103901.

1. Introduction

Numerous fundamental questions remain regarding the Ross Sea and the Southern Ocean, especially concerning the stability of the Ross Ice Shelf (RIS) and greater West Antarctic Ice Sheet (WAIS). As much of the WAIS is grounded below sea level, it is highly susceptible to changes in ocean heat flux, which in turn trigger marine ice sheet instability processes that relate to the over- deepened morphology of West Antarctica's continental shelf margins (Golledge et al., 2012; Pollard and DeConto, 2009; Thomas and Bentley, 1978). The RIS is one of the main outflows from the WAIS, and it acts to buttress the continental ice sheet upstream (Dupont and Alley, 2005; Mercer, 1968; Thomas, 1979; Weertman, 1974). The Southern Ocean is currently warming and freshening, with export rates of cold and saline Antarctic Bottom Water (AABW) reported to be decreasing as a result (Gille, 2002; Menezes et al., 2017; Meredith et al., 2014; Purkey and Johnson, 2010; Williams et al., 2016). In addition, the intrusion of warm water onto the continental shelf has been directly recorded in many areas around the Antarctic margin, including the Ross Sea, Amundsen Sea, and Antarctic Peninsula regions (Castagno et al., 2017; Hillenbrand et al., 2017; Morrison et al., 2020; Smith et al., 1999; Wåhlin et al., 2010). The delivery of warm Circumpolar Deep Water (CDW) to the glacial face is understood to drive increased melt rates, leading to ice shelf retreat and collapse (Dinniman et al., 2011; Pritchard et al., 2012). Instrumental and observational records of the Antarctic oceanographic system only extend back a few decades, limiting our ability to understand how our current observations compare with the naturally variable system. Through paleoceanographic reconstructions from sediment records in the Ross Sea, it is possible to determine how the oceanography of the region has changed through time with respect to past variations in WAIS extent.

Paleoenvironmental studies based on sediment cores must have a robust chronological framework, enabling inferred environmental events to be placed accurately into the global context. Age constraints are frequently derived from biostratigraphic markers, magnetic reversals, and radioisotope dating. Biostratigraphic markers can be sparse in Pleistocene sediments from the Southern Ocean and there are only two geomagnetic reversals over the last million years, which makes the construction of precise age models difficult. In this study, we use relative paleointensity (RPI) dating to generate a high-resolution continuous age model for core RS15-LC42.

The assumption underlying RPI dating is that the strength of the detrital remnant magnetisation (DRM) is a linear function of ambient magnetic field strength during deposition under stable geological conditions (King et al., 1983; Tauxe, 1993). DRM refers to the

alignment of magnetic grains after they have settled to the sediment–water interface and undergone compaction. The natural remnant magnetisation (NRM) throughout the core reflects a combination of the initial DRM and any post–depositional remnant magnetic overprints (Tauxe, 1993), along with any viscous magnetization acquired during coring and sample handling. While the NRM generally reflects ambient field strength during deposition, it is also controlled by the type and concentration of magnetic material present (Tauxe, 1993). Therefore, normalisation of NRM is undertaken to reduce these non–field related variations. The appropriate normalising parameter is a matter for debate, and it may vary between core records according to the influence of the expected non–field factors. Common normalisers of NRM are the lab induced magnetizations; anhysteric remnant magnetization (ARM), isothermal remnant magnetization (IRM), and magnetic susceptibility (MS) (Tauxe, 1993).

Once a downcore estimate of RPI is determined, this record of normalized remanence is compared and aligned to globally stacked records of magnetic field strength to create a continuous high–resolution age model (Channell et al., 2009). The RPI reference stack used in this study is the PISO–1500, which was created by matching RPI estimates from globally distributed sedimentary paleo–records with benthic foraminifera oxygen isotopes (Channell et al., 2009). PISO–1500 is therefore tied to the geomagnetic polarity timescale (GPTS) through magnetic reversals, and oxygen isotope stratigraphy (Channell et al., 2009). Global data stacking averages the effects of local non– dipolar field factors, producing a globally applicable record of magnetic field strength through time. Published global reference stacks for the Pleistocene include PISO–1500 (0–1.5 Ma; Channell et al., 2009), SINT–2000 and PADM2M (0–2.0 Ma; Valet et al., 2005; Ziegler et al., 2011), and EPAPIS– 3 Ma (0.8–3.0 Ma; Yamazaki and Oda, 2005).

The advantage of RPI dating is that geomagnetic field variations are globally synchronous and independent of Earth surface processes, therefore when environmentally affected variations in magnetic mineral assemblage and concentration can be successfully normalised, it is possible to generate an age model that is neither biased by environmental influences, nor reliant on the interpretations of proxy data (King et al., 1983; Tauxe, 1993). The disconnection between chronometry and paleoenvironmental interpretation enables us to study the absolute timing of events indicated by paleoenvironmental proxies, rather than dating the core by tuning such proxy records based on the assumption that their variations align synchronously with global climate variations or expected regional events. Consequently, the use of RPI dating has grown substantially over the past 30 years. The technique has been applied to an array of sedimentary records ranging from high–resolution Holocene cores from the Antarctic Peninsula (Willmott et al., 2006), to deep time records from the equatorial Pacific that extend back into the Eocene (Channell and Lanci, 2014; Ohneiser et al., 2013; Yamamoto et al., 2014). Global stacks of geomagnetic intensity provide the framework for

RPI correlation, and are tied to the GPTS by magnetic reversals, oxygen isotope stratigraphy (Channell et al., 2009), K/Ar (Laj et al., 2000), 14C, and beryllium dating (Guyodo and Valet, 1996, 1999). RPI dating has been successfully applied to generate age models for Pleistocene sedimentary records and from around the Antarctic margin and wider Southern Ocean (Brachfeld et al., 2003; Channell et al., 2000; Li et al., 2022; Macrì et al., 2005, 2006, 2010; Sagnotti et al., 2001; Stoner et al., 2002).

Recently published studies from the Central Basin and wider Ross Sea have shed some light on oceanographic and sedimentological processes at the shelf break and slope. Modelling completed by Morrison et al. (2020) found that CDW inflow was concentrated in cold water regions where dense shelf water (DSW) forms. Export plumes of DSW from the continental shelf lower the sea surface height at the shelf break, tilting the pycnocline landward and resulting in a net CDW transport onto the shelf (Morrison et al., 2020). In the model, DSW plumes originating from the Joides Trough into the Central Basin flow down the western side of the trough deflected under the effects of Coriolis. Average plume thicknesses range between 300 and 600 m with velocities averaging from 0.4 to 0.6 ms−1, while extreme export events exceed 1 ms−1 (Morrison et al., 2020). In this model, on−shelf CDW transport is predominantly confined to the central and eastern sides of the troughs. Complimentary geophysical and sedimentological evidence suggests that the export plumes observed in the modern austral summer are sufficiently strong to mobilise mud and sandy mud at the slope break and transport it downslope (Gales et al., 2021). Interglacial deposition on the continental shelf and slope is dominated by these lithologies, transported through iceberg rafting; pelagic, hemipelagic, and crossslope currents; and biogenic deposition (Gales et al., 2021; Kim et al., 2018). Glaciogenic deposition on the shelf is characterised by increased clay and gravel contributions with low sand content, a composition that requires higher shear stress to erode and transport than is currently observed during DSW export events (Gales et al., 2021). In contrast, subglacial meltwater pulses during glacial intervals are strong enough to erode these glacially derived sediments and scour erosive channels in the upper continental slope (Gales et al., 2021). The upper slope sediments are often rich in biogenic sediment, especially with respect to diatomaceous material deposited during preceding interglacial intervals with sustained open−ocean conditions (Khim et al., 2021; Tolotti et al., 2013). Ice sheet scouring during glacial advances mobilises, reworks and transports this sediment to the shelf break, enabling further transport offshore by slope failures, meltwater pulses, and DSW plumes (Gales et al., 2021; Khim et al., 2021; Tolotti et al., 2013).

Here, we present an investigation into the sediment core RS15−LC42, which was collected onboard the RV Araon by the Korea Polar Research Institute (KOPRI) during the ANA05B cruise. The 11.75 m long core was collected from 71° 49.40′ S, 178° 34.76′ E in 2084 m water depth (Fig. 1). The core site is in the Central Basin, located on the continental

rise to the west of the Iselin Bank, immediately downslope from the terminus of the Joides Trough. The Joides Trough is a known outflow pathway for DSW, a cold saline component that mixes with overlying water masses to form AABW (Morrison et al., 2020; Orsi and Wiederwohl, 2009; Smith Jr et al., 2012). The Joides Trough is also a conduit for the intermittent intrusion of CDW from the Central Basin up onto the continental shelf (Morrison et al., 2020; Smith Jr et al., 2012). This CDW is entrained from the Antarctic Circumpolar Current (ACC) into the Ross Sea Gyre (RSG), flowing west along the continental slope (Smith Jr et al., 2012). This study focuses on understanding Pleistocene variations in bottom water export from the Ross Sea via the Joides Trough, and associated environmental drivers. To achieve this, we first employ RPI dating to revise the age model for RS15-LC42 presented by Ohneiser et al. (2019). We then present diatom micropaleontology and gravel clast abundance records to provide insight into the sedimentary and oceanographic processes in the Central Basin.

2. Methods

2.1. Sedimentology

RS15-LC42 was split at KOPRI. Cores were described from core face visual description, quantitative grain size analysis (Mckay et al., 2022a) and using x-radiographs to identify sedimentary structures. We used the lithological classification scheme developed for ANDRILL (Krissek et al., 2007).

The sedimentology of RS15-LC42 is divided into three units (Ohneiser et al., 2019). Unit 1 (0 m-1.55 m) is sandy diamict (e.g. gravelly muddy sand), with fine-to-medium sand beds interbedded with silt layers. The basal contact of these sand and diamict beds are mostly gradational, although where sharp wavy contacts exist these are also bioturbated. Unit 2 (1.55 m-3.15 m) consists of muddy diamict (e.g. gravelly muddy sand) interbedded with laminated and bioturbated silt. Unit 3 (3.15 m-11.75 m) consists of dm- to m-scale beds of laminated silt that generally lack gravel, interstratified with dm-scale beds of sandy silt, bioturbated silts and gravelly muddy sand beds. In all units, laminated silt intervals consist of parallel laminae and planar cross bedding, with sharp upper and lower contacts, however, they vary in bed thickness and coarse clast abundance. A generalised sedimentological description of RS15-LC42 is provided in Supplementary Fig. S1.

The analysis of gravel abundance in the core followed the method of McKay et al., 2022a, slabs 1 cm deep, 8 cm wide, and 30 cm long were sampled for the length of the core. Each slab was sealed into an acrylic case and then imaged and X-rayed. The resulting

X-ray slab scans were analysed for clasts greater than approximately 2 mm in diameter, the occurrences of which were then summed into 2 cm depth bins. The method is consistent with previous ship-based investigations of Antarctic continental margin sediments, with the abundance of material >2 mm considered a reliable indicator of iceberg rafted debris (IRD) (Grobe, 1987; Weber et al., 2014). Repeat counts were completed by two independent operators then averaged to determine the final IRD count presented here. The gravel count data independently produced by the two counters were strongly correlated (R2 value of 0.82).

2.2. Diatom biostratigraphy and micropaleontology

Thirty-five samples were taken between 2 cm and 1165 cm depth. Duplicate diatom slides were prepared from 45 mg of dry sediment per sample, using the method of Warnock and Scherer (2015a). Slides were mounted with Norland Optical Adhesive #61 (refractive index 1.56) and observed using an Olympus BH2 optical microscope under 630× magnification. Diatom valves with uniquely recognisable characteristics preserved were identified and recorded, notably the centre and margin of centric diatoms, and the apices of pennate diatoms. Due to extensive fragmentation, it was determined that quantitative counts would be heavily biased by the variable robustness of each species' silicate structure (e.g., Scherer et al., 2004; Warnock and Scherer, 2015b), skewing population data in favour of the most physically robust taxa. As an alternative method, presence/absence data were recorded, reducing preservation-state bias.

Quantitative counts were completed for absolute diatom abundance (ADA) and incorporated all partial and whole valves observed in the sample. Fragmented centric valves were counted as one if the middle was preserved, while pennate taxa were counted as one half for each apex. ADA was calculated following the method of Warnock and Scherer (2015a), counting the total number of valves in at least 30 fields of view per sample.
The first and last appearance datums (FAD; LAD) for diatom taxa were obtained from the biostratigraphic framework of IODP Expedition 374 to the Ross Sea (McKay et al., 2019). For taxa not represented in this framework, we used the constrained optimisation (CONOP) models of Crampton et al. (2016), and Cody et al. (2008). The biostratigraphic framework including FADs and LADs of each diatom taxon is presented in Supplementary Table S1.

The influence of reworking was identified based on the cooccurrence of Miocene, Pliocene and Pleistocene taxa. A reworking index was generated to resolve signatures of regional sediment reworking, conservatively based on the diversity of diatom taxa with LADs ≥2.58 Ma (≥Pliocene). The taxa selected as reworking indicator species are presented in Table 1.

2.3. Paleomagnetism

U-channel samples were collected from core RS15-LC42 at KOPRI and shipped to the Otago Paleomagnetic Research Facility (OPRF) at the University of Otago. Magnetic moment measurements of u-channels were made at the 150 nT magnetically shielded room at the Otago paleomagnetic Research Facility (OPRF) using a 2G Enterprises DC 760.5, pass-through superconducting rock magnetometer. U-channels were demagnetised at 5 mT increments in fields between 5 mT and 50 mT, then at 60 mT, 70 mT, 80 mT and at 100 mT using the inline AF demagnetisation coils. After AF demagnetisation, an ARM was imparted using a DC bias field of 39.79 A/m (0.05 mT) in alternating fields of 100 mT using the slowest possible tray speed of 8 cm/s. Magnetic susceptibility was measured with an inline Bartington magnetic susceptibility loop on the split core face (Ohneiser et al., 2019).

A magneto-biostratigraphic age model was published for RS15-LC42 by Ohneiser et al. (2019). A magnetic reversal from reverse to normal polarity occurs at 8.26 mbsf ±0.03 tm, interpreted as the Brunhes- Matuyama reversal (B-M reversal; C1n-C1r.1r) at 0.781 Ma (Hilgen et al., 2012). A linear age model from the sediment-water interface to the B-M reversal was supported by the first occurrence of Thalassiosira antarctica (FAD 0.57-0.65 Ma) between 5.40 and 5.64 mbsf, with an average sedimentation rate of 1.06 cm/kyr (Ohneiser et al., 2019). That study also found that the dominant carriers of NRM in RS15-LC42 are low coercivity magnetic minerals, including magnetite and maghemite.

Sixty samples were taken from the u-channels for magnetic mineralogy analyses at ~20 cm intervals. Hysteresis loops and isothermal remnant magnetisation (IRM) curves were generated using a Princeton Measurements Corporation vibrating sample magnetometer (VSM, MicroMag 2900). Fragments were attached directly to the VSM sample rod for analysis and varied in dry mass from 0.02 to 0.16 g with a mean mass of 0.064 g. Hysteresis was measured with a maximum field of ±500 mT, a variable field increment, and averaging time of 1 s. IRM was completed with a maximum field of ±1 T, field increment of 13 μT, and averaging time of 1 s. In samples with low absolute magnetic concentrations <15 mAm2/kg, noise in the fitted hysteresis loops resulted in anomalously high coercivity calculations. Coercivity data were cleaned with a magnetic saturation threshold applied at 15 mAm2/kg, below which all coercivity measurements were removed. The S-ratio for describing magnetic hardness was determined by normalising IRM at 300 mT by that obtained at 1000 mT (Evans and Heller, 2003). Thermomagnetic curves from six samples were measured using an AGICO MFK-1CS Kappa-bridge, where samples were heated to ~710 ◦C in air with the magnetic susceptibility of the sediments measured concurrently.

Sections with poor demagnetisation behavior were removed from the record, for example from 2.25 to 2.55 mbsf. Ohneiser et al. (2019) identified intervals of poor

demagnetization behavior at all sites in their study (including this one) which they suggested was linked to core recovery, post cruise core handling, or sampling. Filtering parameters for acceptable data quality were defined by the Maximum Angular Deviation (MAD) of characteristic remnant magnetization (< 15°), RPI slope R-value (> 0.9), and demagnetisation behaviour.

2.4. Age model construction

A magneto-biostratigraphically constrained linear age model for RS15-LC42 was previously constructed using the first occurrences of diatom taxa and magnetic reversal stratigraphy (Ohneiser et al., 2019). Here, we improve on that model by aligning peaks and troughs in the relative paleointensity record of RS15-LC42 to the PISO-1500 global stack of magnetic field intensity (Channell et al., 2009). The RPI estimate of RS15-LC42 was determined by normalising NRM by ARM to reduce the effect of changes in magnetic concentration (Channell et al., 2014, 2016; Tauxe, 1993). As RPI records are generally non-coherent over timescales shorter than a few thousand years (Tauxe, 1993), a 10 kyr moving average was applied to PISO-1500.

ARM, RPI, and PISO-1500 were analysed for spectral coherence using the wavelet coherence (WTC) function in the "biwavelet" package for 'R' to ensure their suitability for reliable RPI based age modelling (Gouhier et al., 2018). The WTC resembles a localised correlation coefficient in the time-frequency space throughout the records. As such, it enables the observation of spectral relationships which do not covary in a predictable linear fashion. The WTC used the morlet wavelet coherence method, with 1000 Monte Carlo randomisations. The RS15-LC42 RPI record was aligned to the 10 kyr moving average of the PISO-1500 stack using the 'Match' protocol, following the methods of Lisiecki and Lisiecki (2002) and Channell et al. (2009). The Match protocol utilises dynamic programming to objectively find the optimal fit between two datasets (Lisiecki and Lisiecki, 2002). To obtain the best results from "Match", the RPI record and PISO-1500 stack were standardised by calculating the series mean, subtracting it from each point, and dividing by the standard deviation of the respective data set. This produced records of the RS15-LC42 RPI estimate and the PISO-1500 stack which each had a mean of zero and a standard deviation of one. Tie points were initially determined at the surface (0.05 mbsf, 5 ka), and the B-M magnetic reversal (8.26 mbsf, 781 ka). The previous age model for RS15-LC42 (Ohneiser et al., 2019), which assumed a linear sedimentation rate from present to the B-M reversal, indicated that the Jamarillo sub-chron should be present. However this interval is not preserved in the core. Therefore, a hiatus was hypothesized to span the Jamarillo subchron (9.34 mbsf, 960-1070 ka), with the timing constrained by sedimentological and paleomagnetological evidence, and

fine−tuned using the Match protocol. The record alignment was first evaluated visually to ensure an acceptable match, with a further three tie points added visually during the Match protocol. The final fit quality between the aligned records was statistically evaluated using the 'biwavelet' R package, where WTC between the NRM/ARM RPI Estimate and PISO−1500 was analysed with the parameters described prior.

3. Results

3.1. Paleomagnetism

NRM varies from 3.00 × 10−4 to 5.91 × 10−2 A/m, while ARM varies from 4.27 × 10−3 to 1.87 × 10−1 A/m. NRM and ARM generally vary in phase, with peaks around 2.1 mbsf and 7.4 mbsf. Magnetic susceptibility ranges from 8 to 237 S.I. x 10−5. Neither NRM nor ARM display a predictable relationship with the lithology when compared to sand, clay and silt content respectively.

Hysteresis and IRM analyses determined the coercivity of RS15−LC42 is low throughout the core, with Hc ranging from 8 mT to 15 mT, and Hcr values between 26 and 43 mT (Fig. 2). Saturation magnetization (Ms) varies from 2.2 to 139.4 mAm2/kg. The upper 2.5 m of the core display Hcr values varying around 40 mT, with samples from 2.5 mbsf to 11.75 mbsf displaying values averaging around 30 mT. The S−ratio of samples above 2.5 mbsf varied with a minimum of 1.02, while deeper samples fluctuated around 1.01. The elevated Hcr and S−ratio of samples in the uppermost ~2.5 m of the core indicates a minor contribution of a higher coercivity mineral that is not preserved below ~2.5 mbsf. A distinct change in sediment colour is observed at 2.58 mbsf, changing from green/brown (above) to green (below).

Thermomagnetic analyses revealed a dominant Curie temperature of ~580 ◦C in all samples (Fig. 3a). Samples at 0.60 mbsf and 1.40 mbsf also display a distinctive decrease in magnetic susceptibility from ~300−450 ◦C, with total demagnetisation not occurring until ~650 ◦C. In the sample from 5.20 mbsf, the Curie temperature was not reached at 700 ◦C, possibly indicating the presence of hematite in the sample. Ohneiser et al. (2015) identified numerous sources of hematite in Transantarctic Mountain lithologies with significant concentrations in Skelton Group and Beacon Supergroup rocks, therefore this isolated sample may contain IRD from these source rocks. Analysing magnetic hysteresis data in a Day Plot indicates that the dominant magnetic carrier is single domain grainsize magnetite throughout all samples (n = 46), except for one outlier (Fig. 3b; Dunlop, 2002).

3.2. Age model

NRM was normalised by ARM to generate the RPI estimate. Fig. 4a displays a low WTC between the normaliser (ARM) and the RPI estimate of RS15−LC42. The newly revised age model is presented in Fig. 5, with the standardised output of the Match protocol displayed in Fig. 5a. A strong WTC between the aligned RPI estimate and PISO−1500 is observed in >20 kyr periods (Fig. 4b). Between the core−top and the B−M between the RPI estimate of RS15−LC42 and the PISO−1500 global stack. Below the B−M magnetic reversal (0.781 Ma) at 8.26 m, all significant peaks and troughs also align, except for a hiatus spanning the C1r.1n Jamarillo chron from 0.96 Ma to 1.07 Ma, suggested to occur at ~9.34 mbsf. This proposed hiatus aligns with a sharp facies change between laminated silts and massive gravel−rich sediments and could be interpreted to result from a high energy period resulting in erosion of surficial sediments. The presence of normal faults in the interval also indicates that the hiatus could be the result of local slumping. The modelled core bottom age estimate is 1.344 Ma. The sedimentation rate across the model varies from 0 cm kyr−1 to 2.6 cm kyr−1, with a mean rate of 0.88 cm kyr−1.

3.3. Diatom micropaleontology

Absolute diatom abundance varies from 1.48 × 106 v gdm−1 to 6.67 × 107 v gdm−1 throughout the core (Fig. 6). Coarse−grained sandy intervals are characterised by low ADA (<5 × 106 v gdm□ 1), while finegrained silty intervals generally display ADA >2 × 107 v gdm−1. The diatom assemblages in RS15−LC42 are separated into two distinct groups, defined by the diversity of reworking indicator species present in each sample (Fig. 6). Reworking is inferred from the presence of multiple early− Pliocene and Miocene taxa, while the co−occurrence of T. antarctica throughout the upper 5.40 m of RS15−LC42 constrains the age of deposition to <0.65 Ma.

The first diatom regime is characterised by a low reworked diatom diversity observed in samples from the surface to 3.00 mbsf, from 7.50 to 8.25 mbsf, and from 10.50 to 11.00 mbsf. These intervals all have a similar lithology, characterised by medium−fine sands interbedded with muddy laminae. 17 of 18 the samples in these intervals have either zero or one Pliocene or Miocene taxa present, while the remaining sample (1.40 mbsf) has only two. The second diatom regime occurs throughout the remainder of the core, where reworked diatoms are more diverse. In this regime, between two and six reworked indicator taxa are present in each sample. The lithology of these samples is fine−grained laminated silts and sandy silts. Complete diatom assemblage observations are presented in Supplementary Table S1.

3.4. Gravel abundance

Gravel counts vary from zero to 15 clasts / 2 cm bin, with the highest abundance in coarse- grained intervals above 2.5 mbsf (Fig. 6). Other peaks in gravel abundance are observed in intervals from 4.0 to 4.5 mbsf, 6.5 to 8.2 mbsf, and from 10.0 to 11.7 mbsf. Gravel is largely absent from laminated intervals throughout the core.

4. Discussion

4.1. Application of relative paleointensity dating on variable lithologies

There have been multiple criteria suggested for the reliable application of RPI dating to marine sediment records. These criteria include; 1) magnetite of reasonably homogenous concentration and grainsize as the dominant carrier of magnetic remanence, 2) characteristic remnant magnetisation vectors should accurately record expected magnetic field variations and geocentric axial dipole (GAD) field orientation, 3) the normalisation is preferably tested by different methods, all bearing similar results, 4) RPI estimates should be non-coherent with bulk rock magnetic parameters, and 5) RPI records from a region should agree within a common timescale (Tauxe, 1993). Here, we will address these conditions as they apply to RS15-LC42.

The dominant magnetic carrier throughout RS15-LC42 is interpreted to be pseudo-single domain magnetite at all depths. This mineralogy is inferred from the low coercivity throughout the core, supported by thermomagnetic heating curves which all display a sharp decrease in susceptibility at the curie temperature of ~580 ◦C (Fig. 3a). Thermomagnetic and hysteresis analyses provide evidence for a minor mineralogical change at ~2.5 mbsf, with the presence of a higher coercivity mineral above this point that is not observed in deeper samples. We are unable to pinpoint where this change occurs using the mineralogical dataset due to the sampling resolution in this interval. Core images display a sharp colour change at 2.58 mbsf, with orange-green above and green below. The colour contact is interpreted as the Fe-redox boundary, where the sediment changes from an oxidative regime above to a reducing regime below. At the boundary, maghemite present above 2.58 mbsf is reduced to magnetite (Lyle, 1983; Yamazaki and Ikehara, 2012; Yamazaki and Solheid, 2011). We suggest that the outer skin of magnetite grains have oxidised to maghemite above the Fe-redox boundary, increasing coercivity and magnetic hardness as a result. Surficial maghemite alteration on magnetite grains can also account for the small

KORI 극지연구소

increase and subsequent decrease in magnetic susceptibility seen while heating samples from 300 ∘C to 450 ∘C during thermomagnetic analyses (Gehring et al., 2009; Yamazaki and Ikehara, 2012; Yamazaki and Solheid, 2011). A recent study has determined that grainsurface oxidation of magnetite to maghemite above the Fe−redox boundary appears to have an insignificant effect on RPI as a dating tool (Yamazaki and Solheid, 2011), thus satisfying the mineralogical conditions for reliable RPI estimations.

Both ARM and NRM vary over two orders of magnitude throughout RS15−LC42, indicating that variations in magnetic concentration have a large impact on the NRM, resulting in a nonlinear relationship between ambient field strength and NRM. NRM was normalised by ARM to reduce the effect of magnetic concentration variability on NRM intensity. Normalisation by MS returned similar trends in downcore RPI estimates, satisfying the normalisation criteria. A poor WTC between ARM and the RPI estimate is observed in Fig. 4a. As ARM is not coherent with our RPI estimate, we reject the hypothesis that concentration variability drives the observed changes in the RPI estimate. Thus, concentration variability is determined to be within reasonable bounds for accurate chronometry. Fig. 4b displays a strong coherence between the aligned RPI record and the PISO−1500 global RPI stack, indicating that the RPI estimate accurately reflects changes in global magnetic field intensity over the past 1.34 Ma.

The detrital remanence in the core is an excellent recorder of the magnetic field, with observed inclinations agreeing well with the expected GAD at the sample site (−80.7∘ normal polarity / +80.7∘ reversed polarity; Ohneiser et al., 2019). As the sediment accurately reflects the ambient magnetic orientation during deposition, it supports the RPI estimate as an accurate record of relative magnetic field strength.

The significant concentration variability and subtly variable magnetic mineralogy in RS15− LC42 provide grounds for RPI−based age modelling to be treated with caution. However, a strong coherence between the aligned RPI estimate and the PISO−1500 global RPI stack, supported by magnetic reversal stratigraphy and diatom biostratigraphy, indicates that the dating technique and resulting age model is robust in this instance. The technique improved the existing linear age model with three tie points into a dynamic continuous age model. As indicated here, RPI dating should be seriously considered as a dating method from sediment cores on the Antarctic margin, even when the variability in sedimentology and magnetic mineralogy demands a cautious approach. This method may be especially useful to complement age models for Pleistocene records where biostratigraphic first occurrences and magnetic reversals are sparse, with the potential to assist the chronometry of high−resolution Holocene records.

4.2. Sedimentological Interpretations

The presented age model of RS15-LC42 indicates that the core has a continuous record of sedimentation preserved from 1.34 Ma to the present, with an average sedimentation rate of 0.88 cm/kyr. While preliminary sedimentological observations defined numerous sharp contacts at facies boundaries these are generally bioturbated. Most major facies lower contacts are gradational and bioturbated. These gradational and bioturbated facies associations, combined with parallel and planar cross bedded laminae, are highly consistent with sandy contourite models (Rebesco et al., 2014), superimposed with deposition of ice rafted debris. None of the sedimentary structures or facies associations indicate deposition by turbidity currents or direct subglacial deposition, which would result in substantial erosion and subsequent substantial time gaps in the age model. The site location on the continental rise in 2084 m water is unlikely to have ever been overridden by depths (McKay et al., 2022b). Furthermore, earlier seismic studies over the site indicated that the sediment forms a sheeted drift morphology with internal sediment waves, further emphasizing deposition as a contourite system deposited on a submarine bank (Kim et al., 2018). There is one exception to this interpretation of a lack of substantial age gaps, where a sharp facies dislocation is observed from laminated muds to gravel-rich bioturbated sediments at 9.34 mbsf. Normal faults indicative of slumping are observed near this facies change which is not seen elsewhere in the core, supporting the presence of a hiatus at this depth. The proposed hiatus extends across the Jamarillo sub-chron from MIS 31 to 25. MIS 31 is understood to be the last known collapse of the WAIS in the Ross Sea sector, interpreted from sedimentological observations of the ANDRILL project (McKay et al., 2012; Naish et al., 2009). While it is possible that oceanographic conditions during MIS 31 and 25 increased bottom current velocities to form this hiatus, we do not have sufficient evidence from the region to isolate this as the cause.

A study of sedimentology and diatom biostratigraphy provides insight into the state of glaciation in the Ross Sea and WAIS and corresponding changes in regional physical oceanography. The sediment record spans a few key climatic events, including 1) the Mid-Pleistocene Transition (MPT) where glacial cyclicity shifted from ~100 kyr to ~41 kyr, occurring between 1.25 and 0.70 Ma (Raymo et al., 2006), 2) an increase in interglacial amplitude from MIS 11 until the present, where interglacial temperatures are reported to be generally 1.5-2 ◦C warmer than those interglacials prior (Masson-Delmotte et al., 2010), and 3) numerous warm interglacial periods which may have resulted in the partial or complete retreats of marine-based ice sheets in West Antarctica. RS15-LC42 is well situated to resolve oceanographic variability of the Ross Sea across these events, especially concerning bottom water export from the Joides Trough, and CDW inflow to the continental shelf.

Gravel clasts are most abundant in coarse-grained intervals where ADA and reworking diversity is lowest. Gravel-rich intervals (GRI) could either be attributed to an

increase in clast delivery from melting icebergs, current winnowing removing fine-grained sediments and increasing the proportion of gravel clasts, or a combination of both (Drewry and Cooper, 1981; Stow et al., 2002). The removal of fine material concentrates the remaining coarse-grained sediments left behind, creating a protective 'lag' and preventing further erosion from taking place (Drewry and Cooper, 1981). This process prevents large erosional unconformities from forming and results in a continuous, though sporadically compressed, sediment record (Drewry and Cooper, 1981). In light of this evidence, GRI are interpreted to result from IRD delivery concentrated by bottom currents sufficiently strong to erode fine silts and muds.

By contrast, intervals with low gravel abundances are interpreted to form during periods of reduced glacial calving and slow bottom current velocities. The proximity of grounded ice sheets to the shelf break during full glacial periods resulted in the subglacial scouring and delivery of continental shelf sediments to the outer shelf, where meltwater plumes, slope instabilities, and bottom currents further acted to erode and subsequently transport reworked sediments downslope into the Central Basin in dense plumes (Gales et al., 2021; Morrison et al., 2020). It is proposed that the fringing ice shelves, in combination with enhanced frontal melting, could have also reduced the delivery of IRD offshore during glacial maxima.

Applying the revised age model, GRI frequently align with warm interglacial periods, as inferred from the benthic foraminifera δ18O stacks, near and far-field paleoclimate studies, and ice

sheet modelling (Fig. 6). One such example is the GRI from 4.0 to 4.5 mbsf that coincides with MIS 11. It has been proposed that either a partial or complete collapse of marine-based sectors of the WAIS occurred during MIS 11 at ~0.4 Ma (Hillenbrand et al., 2009; Raymo and Mitrovica, 2012; Scherer et al., 1998). The age model indicates that GRI were also formed episodically during MIS 1- 7, 15, 17-19, and before the MPT from MIS 35 to 41, with numerous small gravel-rich horizons dispersed throughout the rest of the core. The timing of these events supports the sedimentation model of GRI formation during interglacial periods in the Ross Sea, with the greater glacial calving resulting in increased delivery of IRD to the Central Basin.

Marine isotope stages are defined by the global stack of benthic foraminifera δ18O, interpreted to represent global ice volume as more 16O is locked in the ice caps during glacial periods resulting in a concentration increase of 18O in the ocean (Lisiecki and Raymo, 2005). As the state of glaciation may not always be globally synchronous (Raymo et al., 2006), this metric may not accurately resolve ice volume changes local to the Ross Sea region or wider WAIS. As such, we do not necessarily expect every 'interglacial' MIS to result in the local formation of iceberg armadas or increased bottom water formation and export in the

Ross Sea and wider Antarctic.

Specific gravel depositing episodes are less distinct since 0.3 Ma, with a significant concentration of IRD present throughout the uppermost ~2.5 m of RS15-LC42. The relatively coarse grain size prevalent through this interval suggests that deposition occurred in a relatively high energy environment, reducing the settlement of fine-grained silts and concentrating IRD. This evidence suggests that there was a significant change in glacial dynamics in the Ross Sea at 0.3 Ma, with similar conditions observed from MIS 17-19, and MIS 35-41. Evidence from the core and benthic foraminiferal records indicates that between 0.4 and 0.8 Ma, the Antarctic ice volume during glacial periods was larger than those since (Lisiecki and Raymo, 2005; Masson-Delmotte et al., 2010), while interglacial temperatures are suggested to have warmed by 1-2 ◦C since 0.4 Ma also. The abundance of gravel clasts, coupled with the rare presence of reworked diatomaceous sediment and coarser grainsize since 0.3 Ma, indicates that IRD was readily delivered to the core site, while the delivery of continental shelf sediment either ceased or reduced significantly.

There are a few notable silty laminated intervals with low evidence of reworking preserved in the upper 2.5 mbsf, all of which align with elevated δ18O values indicating ice sheet growth and colder conditions. The absence of reworking above 2.5 mbsf in RS15-LC42 indicates that these glacial advances may not have extended to the shelf break, preventing shelf sediments from being transported offshore. Paired with a decrease in dense water formation on the shelf, bottom current velocities in the Central Basin would likely decrease, enabling the formation of these laminated beds under weak cross-slope currents. We interpret this data as evidence that the ice sheet has not grounded at the continental shelf break in the outer Joides Trough since MIS 10. We infer that the provenance of sediment since 0.3 Ma has consisted of primary sediments from IRD and biological productivity, deposited under the effects of sustained bottom currents forming interbedded drift deposits, with laminated silt intervals formed during glacial periods where reduced bottom water export occured from the shelf. While the sedimentary hiatus at ~9.34 mbsf aligns with MIS 31, the erosional surface could be related to slope failures, bottom current erosion, or any number of episodic events. There is insufficient data to conclude that the hiatus is a result of sustained environmental changes.

4.3. Reworking provenance

The prevalence of reworked diatom taxa in laminated intervals throughout RS15-LC42 is a key feature of the sediment record. A low diversity of reworked diatom taxa are present in the uppermost ~3 m, with a substantially more diverse range of reworked Pliocene and Miocene taxa in almost all samples observed below this depth. The emplacement

of reworked taxa in the Central Basin is proposed to result from glacial advances acting to erode, entrain, and transport Pliocene and Miocene sediments to the continental shelf break. At the shelf break, the reworked sediment was exposed to subsequent remobilisation by basal meltwater plumes, DSW export plumes from the Joides Trough, and slope failures. Through these mechanisms, sediment was under the action of sustained bottom currents (Chow and Bart, 2003; Gordon et al., 2009; Muench et al., 2009). Cores from the International Ocean Discovery Program Expedition 374 to the Ross Sea also found evidence for substantial diatom reworking in sediments of Pleistocene age (McKay et al., 2018). These cores were obtained from the continental shelf and slope to the east of the Iselin Bank, with sites U1523 –U1525 located in comparable depositional environments to RS15–LC42. Torricella et al. (2021) presented a sedimentation model for the Central Basin from the LGM to present, based on a similar study of the sedimentology and micropaleontology of box core samples. The authors suggested a sedimentation model where glaciogenic silt sediments are delivered to the outer shelf by the Ross Ice Sheet, maintained in suspension as they travelled to the shelf break and downslope, then entrained in a westward flowing contour current before its subsequent settlement in drift deposits. Multiple other studies have also documented diatom reworking in LGM glaciogenic tills in the Ross Sea, including Kellogg and Kellogg (1981), and Sjunneskog and Scherer (2005). Our study finds limited evidence to support the deposition of shelf–derived reworked sediments during interglacial periods, potentially due to the winnowing effect of the DSW export currents – however, the general model of sedimentation is in strong agreement during glacial intervals.

The widespread reworking of Pliocene and Miocene taxa into Pleistocene sediments across the entire Ross Sea region supports the hypothesis that reworking is driven by ice advances over the whole continental shelf of the Ross Sea. During interglacial periods or glacial intervals where the ice sheet does not extend to the outer shelf, the delivery pathway is interrupted as shelf sediments are unable to be transported to the shelf break for remobilisation. This mechanism explains the notable absence of reworked diatomaceous material in sediments deposited since 0.3 Ma and other interglacially derived GRI, indicating that the ice sheet has not grounded in the outer Joides Trough since MIS 10, nor was it grounded during MIS 18 or 34.

This proposed mechanism of reworked diatom provenance is supported by past research carried out on the continental shelf of the Ross Sea. Deep Sea Drilling Project Leg 28, Site 273 was drilled on the continental shelf between the Drygalski and Joides Troughs in 491 m water depth (McCollum, 1975). It was observed in this core that a significant portion of the stratigraphic section post–Miocene was likely truncated as a result of glacial erosion across the continental shelf (McCollum, 1975). Extensive glacial scouring is further supported by geophysical seismic surveys carried out on the continental shelf across the Ross Sea and

Joides Trough (Alonso et al., 1992; Bart et al., 2011; Chow and Bart, 2003; Bart and De Santis, 2012; De Santis et al., 1995). The seismic profiles, age-correlated to the DSDP Site 273 cores, confirmed that northward dipping Miocene and Pliocene sediments have been significantly truncated by past grounded ice advances onto the inner continental shelf of the Ross Sea (Alonso et al., 1992; Chow and Bart, 2003). Bart et al. (2011) report that seismic stratigraphic sequences indicated that glacial advances to the continental shelf-break have occurred at least ten times over the past 2 Ma, with evidence for at least two advances in the past 0.7 Ma – although these advances could have truncated evidence of earlier and more frequent advances.

4.4. Paleo-deposition model of continental slope sedimentation and links to ice volume and oceanographic variance

4.4.1. Elevated IRD content and winnowing by bottom currents: Ice-sheet margin shoreward of continental shelf break during glacial maxima (0 to 0.3 Ma; and 1.2 to 1.4 Ma)

Recent modelling and observations focused on the Ross Sea reported that the export pathway of DSW plumes is directed down the western flank of the Central Basin under Coriolis, while CDW is upwelled on the eastern side to maintain mass balance on the shelf. The site of RS15- LC42 is likely under the direct influence of DSW export plumes, therefore preserving a history of bottom water export intensity, and by inference consequent CDW upwelling in the Ross Sea sector of the Southern Ocean (Morrison et al., 2020). We expect that in RS15-LC42, periods of active DSW export from the Joides Trough will be represented by coarse-grained lithologies resulting from fine winnowing at the seafloor, with an associated increase in IRD concentration.

Past research has reported that Antarctic ice volume during glacial periods has decreased from MIS 10, and the WAIS likely has not grounded in the outer Ross Sea since this time. In RS15- LC42 from 0.3 Ma until the present, and before the MPT initiation at 1.2 Ma, there is limited evidence of regional-scale sediment reworking (see Section 4.4.2), coupled with low ADA, and a high concentration of gravel clasts. A similar set of characteristics are observed during interglacials, and 'mild' glacial intervals for a ~ 50 kyr period around MIS 19 (7.6 to 8.0 mbsf), from MIS 15 to MIS 17, and during MIS 11. This evidence supports that IRD was readily delivered to the continental shelf as a result of glacial calving, concentrated by winnowing from strong bottom currents (Fig. 7). The absence of reworked diatomaceous material indicates that the ice-sheet did not ground on the outer continental shelf in the Joides Trough region of the Ross Sea during these times, and that

relatively warm oceanic conditions prevailed during the proposed 'mild' glacial periods.

Previous studies of sedimentology from the inner shelf at AND-1B have also suggested reduced Antarctic ice volumes during late Pleistocene interglacials since MIS 11, compared to those between ~0.4 and 1.1 Ma (McKay et al., 2012). These interpretations are consistent with the depositional regimes here observed, with reduced ice volumes on the continental shelf that enabled the development of ice-front polynyas, allowing the formation and resultant frequent export of DSW through troughs from the continental shelf, while the calving of icebergs readily supplied IRD to the region. DSW export plumes have been measured with current speeds >1.5 ms-1 in modern times (Gordon et al., 2004, 2009), with modelled velocities of dense plumes reaching 1 ms-1, and thicknesses on the order of hundreds of meters (Morrison et al., 2020). Gales et al. (2021) reported that while these currents are sufficient to prevent channels from infilling on the upper slope, they are unlikely to cause further erosion or channelisation. As such, any sediments entrained in DSW plumes during warm intervals are likely to originate from recent primary sedimentation, explaining the notable absence of reworking signatures in sediments deposited during warm interglacial periods. We conclude that DSW plumes are the dominant factor controlling sedimentation during interglacial and 'mild' glacial periods where the ice sheet did not advance to the outer shelf (Fig. 7a, b). We suggest that energetic plumes maintained a bottom current velocity sufficient to winnow fine-grained sediments and concentrate IRD into gravel lags, however, they were not strong enough to erode the gravel clasts and create a complete hiatus.

4.4.2. Regional reworking signatures, with low energy deposition: Ice-sheet grounded on the outer shelf during glacial maxima (0.3 to 1.2 Ma)

The sustained presence of reworked diatoms in fine-grained laminated sediments from 0.3 to 1.2 Ma indicates that diatomaceous material was readily transported from the continental shelf into the Central Basin during glacial periods across this interval. We suggest that sediments were scoured by an ice sheet grounded in the outer shelf, transporting sediments to the shelf break where energetic meltwater plumes, density-driven currents, and slope failures eroded and transported it downslope from the Joides Trough (Fig. 7c). The deposition of reworked laminated silts in the Central Basin requires two key conditions; 1) sufficiently high-energy erosive events on the continental shelf to erode and entrain reworked sediments into density-driven plumes, and 2) sustained bottom currents to transport the shelf-derived fine sediments downslope to the Central Basin, with eventual deposition under low current speeds at the core site. Numerous models of continental margin sedimentation processes have been proposed from around the Antarctic (Grobe and Mackensen, 1992; Holder et al., 2020; Kim et al., 2020; Lucchi et al., 2002; Pudsey, 2000). Laminated silty

drift deposits are formed by the lateral spill out of low-density turbidity currents (Lucchi et al., 2002), where fine-grained sediments are entrained in the turbulent flow and overtop the levees, becoming entrained in westward flowing cross-slope currents before settlement in drift deposits behind topographic highs. This is our favoured sedimentological model during full glacial periods, maintaining a strong agreement with the observed sedimentological and micropaleontological evidence.

While the erosion of reworked sediments is also possible by DSW export plumes, the reduction in salinity of the surface waters due to enhanced glacial meltwater input, combined with the absence of a subglacial cavity to accumulate DSW before episodically pulsing over the shelf break, leads us to hypothesize that any bottom water export was too significantly reduced in both net volume and flow intensity during glacial maxima to drive the required sediment remobilisation. The combination of a fringing ice shelf and frontal melting at the shelf break caused a reduction in the calving of debris-rich icebergs, with an ensuing reduction in the regional deposition of IRD. Gales et al. (2021) reported that subglacially sourced, sediment-laden meltwater plumes can incise erosive channels on the upper continental slope in the Ross Sea. It is also plausible therefore that any fine shelf-derived sediments eroded by these buoyant plumes could be transported offshore in upper ocean currents, resulting in pelagic sedimentation in the abyssal ocean. If buoyant plumes were the main mechanism for the distribution and sedimentation of reworked diatomaceous material, we would expect to see evidence for reworking throughout the entirety of the core, as it would be less reliant on the proximity of the grounding line to the shelf break. Other possible factors influencing glacial deposition in the Central Basin include; 1) a decrease in DSW export volume resulting in a more confined export pathway which did not coincide with the core site, and 2) a reduction in the density of exported DSW causing the plume to equilibrate at a shallower depth, and subsequently either reducing bottom current velocities or entirely preventing them from reaching the abyssal depths of the Central Basin.

Modern DSW is formed in ice-front and coastal polynyas, with the cold saline brine sinking and accumulating on grounded-ice free areas of the continental shelf. During Quaternary full glacial periods when the ice sheet extended to the outer shelf, the proximity of the ice-front to warm modified CDW is proposed to increase melt rates and freshen the surface waters, potentially at a rate sufficient to negate brine rejection during sea-ice formation and prevent DSW formation (Amblas and Dowdeswell, 2018). Amblas and Dowdeswell (2018) suggest that any DSW exported during glacial periods may be primarily formed in open-ocean polynya settings that are sustained by the upwelling of warm deep water. As such, any export would be less channelized and unlikely to form energetic plumes sufficient to winnow the sediments. Our interpretation is supported by prior studies that reported during partial ice sheet advances across the continental shelf, DSW may have been

formed in coastal and ice front polynyas akin to modern conditions (Amblas and Dowdeswell, 2018; Hillenbrand et al., 2017; Klages et al., 2017).

Warm interglacial periods from 0.3 to 1.2 Ma (MIS 11, 15, 17–19, 31) are identified by the presence of bioturbated coarse sediments with abundant IRD and low reworking, interpreted to form due to a mixture of increased iceberg calving, and a coupled escalation in oxygenated bottom water export. Findings from RS15–LC42 indicate that from the beginning of the MPT (1.2 Ma) until ~0.3 Ma, the WAIS regularly extended to and grounded on the outer shelf of the Ross Sea during glacial intervals. This stimulated the erosion and transport of reworked fine sediments from the continental shelf offshore, entrained in density–driven currents from slope failures, DSW plumes, and turbidity currents initiated by meltwater plumes. Deposition occurred in the Central Basin behind topographic highs as a drift deposit (Kim et al., 2018), under the effects of a weak sustained cross–slope current associated with either weak bottom water export or the west–flowing landward limb of the Ross Sea Gyre.

4.4.3. Implications for Ross Sea glacial history

Near and far–field studies on the Pleistocene history of the WAIS in the Ross Sea have proposed numerous likely collapse events during MIS 5e, 7, 11, 13–15, 25, and 31, although evidence for complete marine–based ice–sheet loss in the West Antarctic remains equivocal (Hillenbrand et al., 2009; McKay et al., 2012; Pollard and DeConto, 2009; Scherer et al., 2008). Super–interglacial periods have been modelled to occur at MIS 17, 25 and 31, with these time periods coinciding with the loss of much of the marine–based WAIS (Naish et al., 2009; Pollard and DeConto, 2009). MIS 31 has arguably the strongest case for a significant collapse of marine–based ice sheets in the Antarctic, with multiple lines of evidence suggesting a mean global temperature 4–5 ◦C warmer than the present, with Ross Sea surface temperatures 3–5 ◦C warmer than present (DeConto et al., 2012; McKay et al., 2012; Naish et al., 2009; Scherer et al., 2008; Beltran et al., 2020). The IRD rich intervals in RS15–LC42 indicate an increase in the dynamic discharge of debris –rich icebergs from Transantarctic outlet glaciers, suggesting that the retreat of the marine–based ice sheet was more extensive during MIS 5, 7, 11, 15, 17–19, and 35–41 than other interglacial periods preserved in our record. The enhanced delivery of glacially remobilized sediments that formed laminated muddy intervals indicates that ice sheet regularly extended to the outer shelf during glacial intervals between 0.3 and 1.2 Ma. The sedimentological and biostratigraphic variability within RS15–LC42 provides a window into the glacial and oceanographic history of the Ross Ice Shelf and the Ross Sea respectively. There are still notable knowledge gaps concerning the potential changes in the depositional environment and sedimentary provenance throughout the core to elucidate the paleoenvironmental history of the Central Basin. Further studies of the

KOPRI 극지연구소

geochemistry and provenance of the IRD, and the clay mineralogy and their associated neodymium isotopic signatures from RS15−LC42 are currently underway at KOPRI to shed light on these unknowns.

5. Conclusions

Paleoceanographic studies in the Antarctic rely on strong and accurate chronostratigraphic frameworks. In the Southern Ocean, the low frequency of biostratigraphic FADs and LADs and magnetic reversals throughout the Pleistocene, coupled with low sedimentation rates, often makes the generation of robust high−resolution age models difficult. Here, we enhanced the published age model for RS15−LC42 using relative paleointensity dating to create a high resolution and statistically robust dynamic age model. The age model revealed that gravel−rich intervals represent IRD deposits, formed due to the intensification of iceberg calving during interglacial and mild glacial periods, coupled with enhanced bottom water velocities due to DSW export. When the ice shelf was grounded on the outer shelf during glacial periods, it scoured and transported glaciogenic and interglacial sediments to the shelf break, where slope failures and meltwater pulses remobilized and transported reworked sediments downslope in turbidity currents. Fine sediments were retained in suspension in cross slope currents and deposited in a continuous drift deposit at the site of RS15− LC42. We suggest that DSW export is most vigorous during interglacial periods, with a significant reduction in channelized export as the ice sheet extends to the shelf break. Our study suggests that glacial periods have warmed since MIS 10, and finds that it is unlikely that the ice−sheet grounded in the outer Joides Trough during the most recent 0.3 Ma, however, it appears to have regularly grounded near the shelf break during glacial periods between 0.3 and 1.2 Ma. More work is required to determine how these conditions impact oceanographic variability in the region, and how it may relate to the glacial stability of marine−based glaciers in the Ross Sea region. Supplementary data to this article can be found online at https://doi.org/10.1016/j.gloplacha.2022.103901.

KOPRI 극지연구소

플라이스토세 동안 로스해의 해양 변동성: 여러 프록시 데이터 비교를 통한 연대 설정 및 과거 환경 분석

Michael Bollena,[b,*], Christina R. Riesselman[a], Christian Ohneisera, Olga Albot[c], Robert McKay[c], 이민경[d], 유규철[d], 김성한[d], 이재일d, Richard Levy[e]

[a]University of Otago, [b]University of Lausanne, [c]Victoria University of Wellington, [d]극지연구소, [e]GNS Science

요약: 과거 남극대륙 주변의 해수 순환이 어떻게 변화했는지를 이해하는 것은 중요하다. 왜냐하 면 상당량의 빙하가 해수 아래에 위치하고 있는데, 빙상 변화와 대륙붕 경계부에서의 해양의 변 동성이 밀접한 관계를 갖고 있기 때문이다. 이 연구에서는 로스해 중앙 분지에서 채취한 RS15- LC42 코어 퇴적물 (길이 11.75 m) 을 조사하였다. 지자기의 역전, 지구 자기장의 상대적 세기와 규조종의 출현 연대를 통해 연대 모델을 수립하였다. 이 코어 퇴적물은 약 134만년 동안의 기록 을 보존하고 있고, 평균 퇴적률은 0.88cm/1000년 이며, 플라이스토세 동안 로스해의 고해양 변동 성에 대한 정보를 담고 있다. 빙하에 의해 운반된 입자가 많으며 체질된 퇴적물은 빙하가 후퇴한 시기 빙하의 쪼개짐이 심해지고 간빙기 혹은 약한 빙하기 동안 빙상이 Joides Trough 바깥쪽 해 저면에 닿아있지 않을 때 Dense Shelf Water가 유입되면서 형성되었다. 로스해 바깥쪽 대륙붕에 빙상 하부가 닿아있던 동안에는 재동되어 쌓인 규조류가 포함된 엽리구조를 나타내는 퇴적물이 쌓였는데, 이 퇴적물은 빙하가 지나가면서 대륙붕에 있던 퇴적물을 Joides Trough 입구까지 끌고 갔던 것이 경사면에서 빙하용융수에 의해 재동되어 중앙분지에 다시 퇴적된 것으로 해석된다. Dense Shelf Water의 형성은 간빙기 동안 가장 활발한 것으로 추정되므로, 빙상이 전진하는 동안 에는 Joides Trough 주변에서 Dense Shelf Water의 흐름이 감소되었을 것이다. 이 연구 결과에 의 하면 30만년 이후 현재까지 로스해 대륙붕 경계부에서 빙상이 전진한 증거는 없으며, 30만년과 120만년 사이에는 빙상의 하부와 대륙붕 경계면이 빈번하게 접촉한 것으로 추정된다. 그러므로 이 시기 동안의 빙하기에는 남극의 빙하 부피가 현재보다 더 컸다고 볼 수 있다.

참고 문헌

Alonso, B., Anderson, J.B., Díaz, J.I., Bartek, L.R., 1992. Pliocene-pleistocene seismic stratigraphy of the Ross Sea: evidence for multiple ice sheet grounding episodes. Antarctic Research Series 93-103.

Amblas, D., Dowdeswell, J.A., 2018. Physiographic influences on dense shelf-water cascading down the Antarctic continental slope. Earth Sci. Rev. 185, 887-900. Bart, P.J., De Santis, L., 2012. Glacial intensification during the Neogene: a review of seismic stratigraphic evidence from the Ross Sea, Antarctica, continental shelf. Oceanography 25 (3), 166-183.

Bart, P.J., Sjunneskog, C., Chow, J.M., 2011. Piston-core based biostratigraphic constraints on Pleistocene oscillations of the West Antarctic Ice Sheet in western Ross Sea between North Basin and AND-1B drill site. Mar. Geol. 289 (1-4), 86-99.

Beltran, C., Golledge, N.R., Ohneiser, C., Kowalewski, D.E., Sicre, M.A., Hageman, K.J., Smith, R., Wilson, G.S., Maini′e, F., 2020. Southern Ocean temperature records and ice-sheet models demonstrate rapid Antarctic ice sheet retreat under low atmospheric CO2 during Marine Isotope Stage 31. Quat. Sci. Rev. 228, 106069.

Brachfeld, S., Domack, E., Kissel, C., Laj, C., Leventer, A., Ishman, S., Gilbert, R., Camerlenghi, A., Eglinton, L.B., 2003. Holocene history of the Larsen - a Ice Shelf constrained by geomagnetic paleointensity dating. Geology 31 (9), 749-752.

Castagno, P., Falco, P., Dinniman, M.S., Spezie, G., Budillon, G., 2017. Temporal variability of the Circumpolar Deep Water inflow onto the Ross Sea continental shelf. J. Mar. Syst. 166, 37-49.

Channell, J.E.T., Lanci, L., 2014. Oligocene-Miocene relative (geomagnetic) paleointensity correlated from the equatorial Pacific (IODP Site U1334 and ODP Site 1218) to the South Atlantic (ODP Site 1090). Earth Planet. Sci. Lett. 387, 77-88.

Channell, J.E.T., Stoner, J.S., Hodell, D.A., Charles, C.D., 2000. Geomagnetic paleointensity for the last 100 kyr from the sub-antarctic South Atlantic: a tool for inter-hemispheric correlation. Earth Planet. Sci. Lett. 175 (1-2), 145-160.

Channell, J.E.T., Xuan, C., Hodell, D.A., 2009. Stacking paleointensity and oxygen isotope data for the last 1.5 Myr (PISO-1500). Earth Planet. Sci. Lett. 283 (1-4), 14-23.

Channell, J.E.T., Wright, J.D., Mazaud, A., Stoner, J.S., 2014. Age through tandem correlation of Quaternary relative paleointensity (RPI) and oxygen isotope data at IODP Site U1306 (Eirik Drift, SW Greenland). Quat. Sci. Rev. 88, 135-146.

Channell, J.E.T., Hodell, D.A., Curtis, J.H., 2016. Relative paleointensity (RPI) and oxygen isotope stratigraphy at IODP Site U1308: North Atlantic RPI stack for 1.2-2.2 Ma

KOPRI 극지연구소

(NARPI-2200) and age of the Olduvai Subchron. Quat. Sci. Rev. 131, 1-19.

Chow, J.M., Bart, P.J., 2003. West Antarctic Ice Sheet grounding events on the Ross Sea outer continental shelf during the middle Miocene. Palaeogeogr. Palaeoclimatol. Palaeoecol. 198 (1- 2), 169-186.

Cody, R.D., Levy, R.H., Harwood, D.M., Sadler, P.M., 2008. Thinking outside the zone: high-resolution quantitative diatom biochronology for the Antarctic Neogene. Palaeogeogr. Palaeoclimatol. Palaeoecol. 260, 92-121.

Crampton, J.S., Cody, R.D., Levy, R., Harwood, D., McKay, R., Naish, T.R., 2016. Southern Ocean phytoplankton turnover in response to stepwise Antarctic cooling over the past 15 million years. Proc. Natl. Acad. Sci. 113 (25), 6868-6873.

Day, R., Fuller, M., Schmidt, V.A., 1977. Hysteresis properties of titanomagnetites: Grainsize and compositional dependence. Phys. Earth Planet. Inter. 13 (4), 260-267.

De Boer, B., Lourens, L.J., Van De Wal, R.S., 2014. Persistent 400,000-year variability of Antarctic ice volume and the carbon cycle is revealed throughout the Plio-Pleistocene. Nat. Commun. 5 (1), 1-8.

De Santis, L., Anderson, J.B., Brancolini, G., Zayatz, I., 1995. Seismic record of late Oligocene through Miocene glaciation on the central and eastern continental shelf of the Ross Sea. Geology and Seismic Stratigraphy of the Antarctic Margin 68, 235-260.

DeConto, R.M., Pollard, D., Kowalewski, D., 2012. Reprint of: Modeling Antarctic ice sheet and climate variations during Marine Isotope Stage 31. Glob. Planet. Chang. 96, 181-188.

Dinniman, M.S., Klinck, J.M., Smith Jr., W.O., 2011. A model study of Circumpolar Deep Water on the West Antarctic Peninsula and Ross Sea continental shelves. Deep-Sea Res. II Top. Stud. Oceanogr. 58 (13-16), 1508-1523.

Drewry, D.J., Cooper, A.P.R., 1981. Processes and models of Antarctic glaciomarine sedimentation. Ann. Glaciol. 2, 117-122.

Dunlop, D.J., 2002. Theory and application of the Day plot (Mrs/Ms versus Hcr/Hc) 1. Theoretical curves and tests using titanomagnetite data. Journal of Geophysical Research: Solid Earth 107 (B3), EPM-4.

Dupont, T.K., Alley, R.B., 2005. Assessment of the importance of ice-shelf buttressing to ice-sheet flow. Geophys. Res. Lett. 32 (4). Evans, M., Heller, F., 2003. Environmental Magnetism: Principles and Applications of Enviromagnetics, 86, p. Elsevier.

Fenner, J., Schrader, H.J., Wienigk, H., 1976. Diatom phytoplankton studies in the southern Pacific Ocean, composition and correlation to the Antarctic Convergence and its paleoecological significance. Initial Reports of the Deep Sea Drilling Project 35, 757-813.

KOPRI 극지연구소

Gales, J., Rebesco, M., De Santis, L., Bergamasco, A., Colleoni, F., Kim, S., Accettella, D., Kovacevic, V., Liu, Y., Olivo, E., Colizza, E., Florindo-Lopez, C., Zgur, F., McKay, R., 2021. Role of dense shelf water in the development of Antarctic submarine canyon morphology. Geomorphology 372, 107453.

Gehring, A.U., Fischer, H., Louvel, M., Kunze, K., Weidler, P.G., 2009. High temperature stability of natural maghemite: a magnetic and spectroscopic study. Geophys. J. Int. 179 (3), 1361-1371.

Gille, S.T., 2002. Warming of the Southern Ocean since the 1950s. Science 295 (5558), 1275-1277.

Golledge, N.R., Fogwill, C.J., Mackintosh, A.N., Buckley, K.M., 2012. Dynamics of the last glacial maximum Antarctic ice-sheet and its response to ocean forcing. Proc. Natl. Acad. Sci. 109 (40), 16052-16056.

Gordon, A.L., Zambianchi, E., Orsi, A., Visbeck, M., Giulivi, C.F., Whitworth, T., Spezie, G., 2004. Energetic plumes over the western Ross Sea continental slope. Geophys. Res. Lett. 31 (21).

Gordon, A.L., Orsi, A.H., Muench, R., Huber, B.A., Zambianchi, E., Visbck, M., 2009. Western Ross Sea continental slope gravity currents. Deep-Sea Res. II Top. Stud. Oceanogr. 56 (13-14), 796-817.

Gouhier, T.C., Grinsted, A., Simko, V., 2018. R package biwavelet: Conduct Univariate and Bivariate Wavelet Analyses (Version 0.20.17). Available from.

Grobe, H., 1987. A simple method for the determination of ice-rafted debris in sediment cores. Polarforschung 57 (3), 123-126.

Grobe, H., Mackensen, A., 1992. Late Quaternary climatic cycles as recorded in sediments from the Antarctic continental margin. The Antarctic paleoenvironment: a perspective on Global Change. Antarctic Research Series 56, 349-376.

Guyodo, Y., Valet, J.P., 1996. Relative variations in geomagnetic intensity from sedimentary records: the past 200 thousand years. Earth Planet. Sci. Lett. 143, 23-36.

Guyodo, Y., Valet, J.P., 1999. Global changes in intensity of the Earth's magnetic field during the last 800 kyr. Nature 399, 249-252.

Hilgen, F.J., Lourens, L.J., Van Dam, J.A., Beu, A.G., Boyes, A.F., Cooper, R.A., Krijgsman, W., Ogg, J.G., Piller, W.E., Wilson, D.S., 2012. The Neogene period. In: The Geologic Time Scale. Elsevier, pp. 923-978.

Hillenbrand, C.D., Kuhn, G., Frederichs, T., 2009. Record of a Mid-Pleistocene depositional anomaly in West Antarctic continental margin sediments: an indicator for ice-sheet collapse? Quat. Sci. Rev. 28 (13-14), 1147-1159.

Hillenbrand, C.D., Smith, J.A., Hodell, D.A., Greaves, M., Poole, C.R., Kender, S., Williams, M., Andersen, T.J., Jernas, P.E., Elderfield, H., Klages, J.P., Roberts, S.J., Gohl, K.,

Larter, R.D., Kuhn, G., 2017. West Antarctic Ice Sheet retreat driven by Holocene warm water incursions. Nature 547 (7661), 43–48.

Holder, L., Duffy, M., Opdyke, B., Leventer, A., Post, A., O'Brien, P., Armand, L.K., 2020. Controls since the mid–Pleistocene transition on sedimentation and primary productivity downslope of Totten Glacier, East Antarctica. Paleoceanography and Paleoclimatology 35, e2020PA003981.

Kellogg, T.B., Kellogg, D.E., 1981. Pleistocene sediments beneath the Ross Ice Shelf. Nature 293 (5828), 130–133.

Khim, B.K., Colizza, E., Lee, J.I., Giglio, F., Ha, S., Bak, Y.S., 2021. Biological productivity and glaciomarine sedimentation in the Central Basin of the northwestern Ross Sea since the last glacial maximum. Polar Science 100682.

Kim, S., De Santis, L., Hong, J.K., Cottlerle, D., Petronio, L., Colizza, E., Kim, Y.G., Kang, S.G., Kim, H.J., Kim, S., Wardell, N., Geletti, R., Bergamasco, A., McKay, R., Jin, Y.K., Kang, S.H., 2018. Seismic stratigraphy of the Central Basin in northwestern Ross Sea slope and rise, Antarctica: clues to the late Cenozoic ice–sheet dynamics and bottom–current activity. Mar. Geol. 395 (June 2017), 363–379.

Kim, S., Lee, J.I., McKay, R.M., Yoo, K.C., Bak, Y.S., Lee, M.K., Roh, Y.H., Yoon, H.I., Moon, H.S., Hyun, C.U., 2020. Late pleistocene paleoceanographic changes in the Ross Sea – glacial–interglacial variations in paleoproductivity, nutrient utilization, and deep–water formation. Quat. Sci. Rev. 239, 106356.

King, J., Banerjee, S.K., Marvin, J., 1983. A new rock–magnetic approach for selecting sediments for geomagnetic paleointensity studies: application to paleointensity for the last 4000 years. J. Geophys. Res. 88, 5911–5921.

Klages, J.P., Kuhn, G., Hillenbrand, C.D., Smith, J.A., Graham, A.G., Nitsche, F.O., Frederichs, T., Jernas, P.E., Gohl, K., Wacker, L., 2017. Limited grounding–line advance onto the West Antarctic continental shelf in the easternmost Amundsen Sea Embayment during the last glacial period. PLoS One 12 (7), e0181593.

Krissek, L., Browne, G., Carter, L., Cowan, E.A., Dunbar, G., McKay, R., Naish, T., Powell, R.D., Reed, J., Wilch, T., 2007. ANDRILL–MIS Science Team. Sedimentology and Stratigraphy of the AND–1B Core, ANDRILL McMurdo Ice Shelf Project, Antarctica. ANDRILL Research and Publications. Terra Antartica 14 (3), 185–222.

Laj, C., Kissel, K., Mazaud, A., Channel, J.E.T., Beer, J., 2000. North Atlantic palaeointensity stack since 75ka (NAPIS–75) and the duration of the Laschamp event. Transactions of The Royal Society A; Mathematical Physical and Engineering Sciences 358 (1768), 1009–1025.

Li, G., Bu, R., Yi, L., Hu, B., Li, Y., Ji, Y., Wang, L., 2022. Geochronology and Paleoenvironmental changes of late Pleistocene sediments in the Ross Sea, Antarctica.

Frontiers in Earth Science 10, 863336.

Lisiecki, L.E., Lisiecki, P.A., 2002. The application of dynamic programming to the correlation of paleoclimate records. Paleoceanography 17 (D4), 1049.

Lisiecki, L.E., Raymo, M.E., 2005. A Pliocene–Pleistocene stack of 57 globally distributed benthic δ18O records. Paleoceanography 20 (1).

Lucchi, R.G., Rebesco, M., Camerlenghi, A., Busetti, M., Tomadin, L., Villa, G., Persico, D., Morigi, C., Bonci, M.C., Giorgetti, G., 2002. Mid–late Pleistocene glacimarine sedimentary processes of a high–latitude, deep–sea sediment drift (Antarctic Peninsula Pacific margin). Mar. Geol. 189 (3– 4), 343–370.

Lyle, M., 1983. The brown–green color transition in marine sediments: a marker of the Fe (III)–Fe (II) redox boundary 1. Limnol. Oceanogr. 28 (5), 1026–1033.

Macrì, P., Sagnotti, L., Dinar`es–Turell, J., Caburlotto, A., 2005. A composite record of late Pleistocene relative geomagnetic paleointensity from the Wilkes Land Basin (Antarctica). Phys. Earth Planet. Inter. 151 (3–4), 223–242.

Macrì, P., Sagnotti, L., Lucchi, R.G., Rebesco, M., 2006. A stacked record of relative geomagnetic paleointensity for the past 270 kyr from the western continental rise of the Antarctic Peninsula. Earth Planet. Sci. Lett. 252 (1–2), 162–179.

Macrì, P., Sagnotti, L., Dinar`es–Turell, J., Caburlotto, A., 2010. Relative geomagnetic paleointensity of the Brunhes Chron and the Matuyama–Brunhes precursor as recorded in sediment core from Wilkes Land Basin (Antarctica). Phys. Earth Planet. Inter. 179 (1–2), 72–86.

Masson–Delmotte, V., Stenni, B., Pol, K., Braconnot, P., Cattani, O., Falourd, S., Kageyama, M., Jouzel, J., Landais, A., Minster, B., Barnola, J.M., Chappellaz, J., Krinner, G., Johnsen, S., R¨othlisberger, R., Hansen, J., Mikolajewicz, U., Otto–Bliesner, B., 2010. EPICA Dome C record of glacial and interglacial intensities. Quat. Sci. Rev. 29 (1–2), 113–128.

McCollum, D.W., 1975. Diatom stratigraphy of the Southern Ocean. In: Texas A & M University, Ocean Drilling Program, College Station, TX, United States.

McKay, R., Naish, T., Powell, R., Barrett, P., Scherer, R., Talarico, F., Kyle, P., Monien, D., Kuhn, G., Jackolski, C., Williams, T., 2012. Pleistocene variability of Antarctic Ice Sheet extent in the Ross Embayment. Quat. Sci. Rev. 34, 93–112.

McKay, R.M., De Santis, L., Kulhanek, D.K., Ash, J.L., Beny, F., Browne, I.M., Cortese, G., Cordeiro de Sousa, I.M., Dodd, J.P., Esper, O.M., Gales, J.A., Harwood, D.M., Ishino, S., Keisling, B.A., Kim, S., Laberg, J.S., Leckie, R.M., Müller, J., Patterson, M. O., Romans, B.W., Romero, O.E., Sangiorgi, F., Seki, O., Shevenell, A.E., Singh, S.M., Sugisaki, S.T., van de Flierdt, T., van Peer, T.E., Xiao, W., Xiong, Z., 2019. Expedition 374 methods. In: McKay, R.M., De Santis, L., Kulhanek, D.K. (Eds.), and

KOPRI 극지연구소

the Expedition 374 Scientists, Ross Sea West Antarctic Ice Sheet History. Proceedings ofthe International Ocean Discovery Program, 374: College Station, TX (International Ocean Discovery Program.

McKay, R.M., De Santis, L., Kulhanek, D.K., Expedition 374 Scientists, 2018. Expedition 374 Preliminary Report: Ross Sea West Antarctic Ice Sheet History. International Ocean Discovery Program 374.

McKay, R.M., Albot, O., Dunbar, G.B., Lee, J. Il, Lee, M.K., Yoo, K., Kim, S., Turton, N., Kulhanek, D., Patterson, M., Levy, R., 2022a. A comparison of methods for identifying and quantifying ice rafted debris on the Antarctic margin. Paleoceanography and Paleoclimatology 37 (4).

McKay, R.M., Escutia, C., De Santis, L., Donda, F., Duncan, B., Gohl, K., Gulick, S., Hern′andez-Molina, J., Hillenbrand, C.-D., Hochmuth, K., Kim, S., Kuhn, G., Larter, R., Leitchenkov, G., Levy, H., Naish, R., O'Brien, P., P′erez, L., Shevenell, E., Williams, T., 2022b. Cenozoic history of Antarctic glaciation and climate from onshore and offshore studies. In: Antarctic Climate Evolution. Elsevier, pp. 41-164.

Menezes, V.V., Macdonald, A.M., Schatzman, C., 2017. Accelerated freshening of Antarctic Bottom Water over the last decade in the Southern Indian Ocean. Science Advances 3 (1).

Mercer, J.H., 1968. Antarctic Ice and Sangamon Sea level, pp. 217-225. Meredith, M.P., Jullion, L., Brown, P.J., Naveira Garabato, A.C., Couldrey, M.P., 2014. Dense waters of the Weddell and Scotia Seas: recent changes in properties and circulation. Philos. Trans. R. Soc. A Math. Phys. Eng. Sci. 372 (2019), 20130041.

Morrison, A.K., Hogg, A.M., England, M.H., Spence, P., 2020. Warm Circumpolar Deep Water transport toward Antarctica driven by local dense water export in canyons. Science Advances 6 (18), eaav2516.

Muench, R.D., Wåhlin, A.K.,¨Ozg¨okmen, T.M., Hallberg, R., Padman, L., 2009. Impacts of bottom corrugations on a dense Antarctic outflow: NW Ross Sea. Geophys. Res. Lett. 36 (23).

Naish, T., Powell, R., Levy, R., Wilson, G.S., Scherer, R.P., Talarico, F., Krissek, L.A., Niessen, F., Pompilio, M., Wilson, T., Carter, L., DeConto, R., Huybers, P., McKay, R., Pollard, D., Ross, J., Winter, D., Barrett, P., Browne, G., Williams, T., 2009. Obliquity-paced Pliocene West Antarctic ice sheet oscillations. Nature 458 (7236), 322-328.

Ogg, J.G., 2020. Geomagnetic Polarity Time Scale. Geologic Time Scale, 2020, pp. 159-192.

Ohneiser, C., Acton, G., Channell, J.E., Wilson, G.S., Yamamoto, Y., Yamazaki, T., 2013. A middle Miocene relative paleointensity record from the Equatorial Pacific. Earth Planet. Sci. Lett. 374, 227-238.

KOPRI 극지연구소

Ohneiser, C., Wilson, G.S., Cox, S., 2015. Characterisation of magnetic minerals from southern Victoria Land, Antarctica. N. Z. J. Geol. Geophys. 58, 52–65.

Ohneiser, C., Yoo, K.C., Albot, O.B., Cortese, G., Riesselman, C., Lee, J.I., McKay, R., Bollen, M., Lee, M.K., Moon, H.S., Kim, S., Beltran, C., Levy, R., Wilson, G.S., 2019. Magneto–biostratigraphic age models for Pleistocene sedimentary records from the Ross Sea. Glob. Planet. Chang. 176, 36– 49.

Orsi, A.H., Wiederwohl, C.L., 2009. A recount of Ross Sea waters. Deep–Sea Res. II Top. Stud. Oceanogr. 56 (13–14), 778–795.

Pollard, D., DeConto, R.M., 2009. Modelling West Antarctic ice sheet growth and collapse through the past five million years. Nature 458 (7236), 329–332.

Pritchard, H., Ligtenberg, S.R., Fricker, H.A., Vaughan, D.G., van den Broeke, M.R., Padman, L., 2012. Antarctic ice–sheet loss driven by basal melting of ice shelves. Nature 484 (7395), 502–505.

Pudsey, C.J., 2000. Sedimentation on the continental rise west of the Antarctic Peninsula over the last three glacial cycles. Mar. Geol. 167 (3–4), 313–338.

Purkey, S.G., Johnson, G.C., 2010. Warming of global abyssal and deep Southern Ocean waters between the 1990s and 2000s: contributions to global heat and sea level rise budgets. J. Clim. 23 (23), 6336–6351.

Raymo, M.E., Mitrovica, J.X., 2012. Collapse of polar ice sheets during the stage 11 interglacial. Nature 483 (7390), 453.

Raymo, M.E., Lisiecki, L.E., Nisancioglu, K.H., 2006. Plio–Pleistocene ice volume, Antarctic climate, and the global δ18O record. Science 313 (5786), 492–495.

Rebesco, M., Hern´andez–Molina, F.J., Van Rooij, D., Wåhlin, A., 2014. Contourites and associated sediments controlled by deep–water circulation processes: state–of–the–art and future considerations. Mar. Geol. 352, 111–154.

Romero, O.E., Armand, L.K., Crosta, X., Pichon, J.J., 2005. The biogeography of major diatom taxa in Southern Ocean surface sediments: 3. Tropical/Subtropical species. Palaeogeogr. Palaeoclimatol. Palaeoecol. 223 (1–2), 93–126.

Sagnotti, L., Macrı´, P., Camerlenghi, A., Rebesco, M., 2001. Environmental magnetism of Antarctic Late Pleistocene sediments and interhemispheric correlation of climatic events. Earth Planet. Sci. Lett. 192 (1), 65–80.

Scherer, R.P., Aldahan, A., Tulaczyk, S., Possnert, G., Engelhardt, H., Kamb, B., 1998. Pleistocene collapse of the West Antarctic ice sheet. Science 281 (5373), 82–85.

Scherer, R.P., Sjunneskog, C.M., Iverson, N.R., Hooyer, T.S., 2004. Assessing subglacial processes from diatom fragmentation patterns. Geology 32 (7), 557–560.

Scherer, R.P., Bohaty, S.M., Dunbar, R.B., Esper, O., Flores, J.A., Gersonde, R., Harwood, D.M., Roberts, A.P., Taviani, M., 2008. Antarctic records of precession–paced

KOPRI 극지연구소

insolation-driven warming during early Pleistocene Marine Isotope Stage 31. Geophys. Res. Lett. 35 (3).

Sjunneskog, C., Scherer, R.P., 2005. Mixed diatom assemblages in glacigenic sediment from the central Ross Sea, Antarctica. Palaeogeogr. Palaeoclimatol. Palaeoecol. 218 (3-4), 287-300.

Smith Jr., W.O., Sedwick, P.N., Arrigo, K.R., Ainley, D.G., Orsi, A.H., 2012. The Ross Sea in a sea of change. Oceanography 25 (3), 90-103. Smith, D.A., Hofmann, E.E., Klinck, J.M., Lascara, C.M., 1999. Hydrography and circulation of the west Antarctic Peninsula continental shelf. Deep-Sea Res. I Oceanogr. Res. Pap. 46 (6), 925-949.

Stoner, J.S., Laj, C., Channell, J.E.T., Kissel, C., 2002. South Atlantic and North Atlantic geomagnetic paleointensity stacks (0-80 ka): implications for inter-hemispheric correlation. Quat. Sci. Rev. 21 (2002), 1141-1151.

Stow, D., Pudsey, C., Howe, J., Faugeres, J.C., Viana, A., 2002. Deep-Water Contourite Systems. Geological Society of London.

Sutter, J., Fischer, H., Grosfeld, K., Karlsson, N.B., Kleiner, T., Van Liefferinge, B., Eisen, O., 2019. Modelling the Antarctic Ice Sheet across the mid-Pleistocene transition - implications for Oldest Ice. Cryosphere 13 (7), 2023-2041.

Tauxe, L., 1993. Sedimentary records of relative paleointensity of the geomagnetic field: theory and practice. Rev. Geophys. 31 (3), 319-354.

Thomas, R.H., 1979. The dynamics of marine ice sheets. J. Glaciol. 24 (90), 167-177.

Thomas, R.H., Bentley, C.R., 1978. A model for Holocene retreat of the West Antarctic ice sheet. Quat. Res. 10 (2), 150-170.

Tigchelaar, M., Timmermann, A., Pollard, D., Friedrich, T., Heinemann, M., 2018. Local insolation changes enhance Antarctic interglacials: insights from an 800,000-year ice sheet simulation with transient climate forcing. Earth Planet. Sci. Lett. 495, 69-78.

Tolotti, R., Salvi, C., Salvi, G., Bonci, M.C., 2013. Late Quaternary climate variability as recorded by micropalaeontological diatom data and geochemical data in the western Ross Sea, Antarctica. Antarctic Science 25 (6), 804.

Torricella, F., Melis, R., Malinverno, E., Fontolan, G., Bussi, M., Capotondi, L., Del Carlo, P., Di Roberto, A., Geniram, A., Kuhn, G., Khim, B.K., Morigi, C., Scateni, B., Colizza, E., 2021. Environmental and oceanographic conditions at the continental margin of the central basin, Northwestern Ross Sea (Antarctica) since the last glacial maximum. Geosciences 11 (4), 155.

Valet, J.P., Meynadier, L., Guyodo, Y., 2005. Geomagnetic dipole strength and reversal rate over the past two million years. Nature 7043, 802-805.

Wåhlin, A.K., Yuan, X., Bj¨ork, G., Nohr, C., 2010. Inflow of warm Circumpolar Deep Water in the central Amundsen shelf. J. Phys. Oceanogr. 40 (6), 1427-1434.

KOPRI 극지연구소

Warnock, J.P., Scherer, R.P., 2015a. A revised method for determining the absolute abundance of diatoms. J. Paleolimnol. 53 (1), 157–163.

Warnock, J.P., Scherer, R.P., 2015b. Diatom species abundance and morphologically–based dissolution proxies in coastal Southern Ocean assemblages. Cont. Shelf Res. 102, 1–8.

Weber, M., Clark, P., Kuhn, G., Timmermann, A., Sprenk, D., Gladstone, R., Chikamoto, M., 2014. Millennial–scale variability in Antarctic ice–sheet discharge during the last deglaciation. Nature 510 (7503), 134–138.

Weertman, J., 1974. Stability of the junction of an ice sheet and an ice shelf. J. Glaciol. 13 (67), 3– 11.

Williams, G.D., Herraiz–Borreguero, L., Roquet, F., Tamura, T., Ohshima, K.I., Fukamachi, Y., Fraser, A.D., Gao, L., Chen, H., McMahon, C.R., Harcourt, R., Hindell, M., 2016. The suppression of Antarctic bottom water formation by melting ice shelves in Prydz Bay. Nat. Commun. 7 (1), 12577.

Willmott, V., Domack, E.W., Canals, M., Brachfeld, S., 2006. A high resolution relative paleointensity record from the Gerlache–Boyd paleo–ice stream region, northern Antarctic Peninsula. Quat. Res. 66 (1), 1–11.

Yamamoto, Y., Yamazaki, T., Acton, G.D., Richter, C., Guidry, E.P., Ohneiser, C., 2014. Palaeomagnetic study of IODP Sites U1331 and U1332 in the equatorial Pacific–extending relative
geomagnetic palaeointensity observations through the Oligocene and into the Eocene. Geophys. J. Int. 196 (2), 694–711.

Yamazaki, T., Ikehara, M., 2012. Origin of magnetic mineral concentration variation in the Southern Ocean. Paleoceanography 27 (2).

Yamazaki, T., Oda, H., 2005. A geomagnetic paleointensity stack between 0.8 and 3.0 Ma from equatorial Pacific sediment cores. Geochem. Geophys. Geosyst. 6 (11).

Yamazaki, T., Solheid, P., 2011. Maghemite–to–magnetite reduction across the Fe–redox boundary in a sediment core from the Ontong–Java Plateau: influence on relative palaeointensity estimation and environmental magnetic application. Geophys. J. Int. 185 (3), 1243–1254.

Ziegler, L.B., Constable, C.G., Johnson, C.L., Tauxe, L., 2011. PADM2M: a penalized maximum likelihood model of the 0–2 Ma palaeomagnetic axial dipole moment. Geophys. J. Int. 184 (3), 1069–1089.

KOPRI 극지연구소

Table 1. Reworking indicator diatom taxa from RS15−LC42. The last appearance datums (LAD) of all taxa are Pliocene or earlier. The first and last appearance datums, FAD and LAD respectively, are reported in Ma. The data source is primarily the IODP Expedition 374 Ross Sea expedition biostratigraphic framework. For taxa not included in this framework, FAD and LAD are reported from CRS2 (Crampton et al., 2016, CONOP Model S2), CRS3 (Crampton et al., 2016, CONOP Model S3), and C08 (Cody et al., 2008). LAD(*) datums are associated with datums that indicate the timing of exclusion from polar regions, as determined by the Crampton et al. (2016) CONOP models. However these taxa remain extant in tropical and subtropical settings (Fenner et al., 1976; Romero et al., 2005).

Taxon	LAD (Ma)	FAD (Ma)	Source
Actinoptychus senarius (Ehrenberg) Ehrenberg	12.28*	17.27	CRS3
Coscinodiscus apiculatus Schmidt et al.	3.78	6.34	C08
Coscinodiscus radiatus Ehrenberg	5.30*	10.14	CRS2
Coscinodiscus rhombicus Castracane	17.62	28.45	CRS3
Denticulopsis delicata Yangasawa and Akiba	4.33	13.70	CRS3
Denticulopsis hustedtii (Simonsen and Kanaya) Simonsen	Late Middle Miocene		EXP374
Denticulopsis lauta (Bailey) Simonsen	13.00	15.70	EXP374
Denticulopsis maccollumi Simonsen	14.30	16.70	EXP374
Denticulopsis spp.	Early Pliocene	Early Miocene	EXP374
Fragilariopsis arcula (Gersonde) Gersonde et Bárcena	4.50	8.50	EXP374
Fragilariopsis aurica (Gersonde) Gersonde et Bárcena	4.20	8.40	EXP374
Fragilariopsis praecurta (Gersonde) Gersonde et Bárcena	4.20	11.00	EXP374
Nitzschia denticuloides Schrader	11.70	13.50	EXP374
Thalassiosira gersondei Barron in Baldauf & Barron, 1991	9.00	10.30	EXP374
Thalassiosira oliverana var. *sparsa* Harwood and Maruyama	4.90	8.60	EXP374

KOPRI 극지연구소

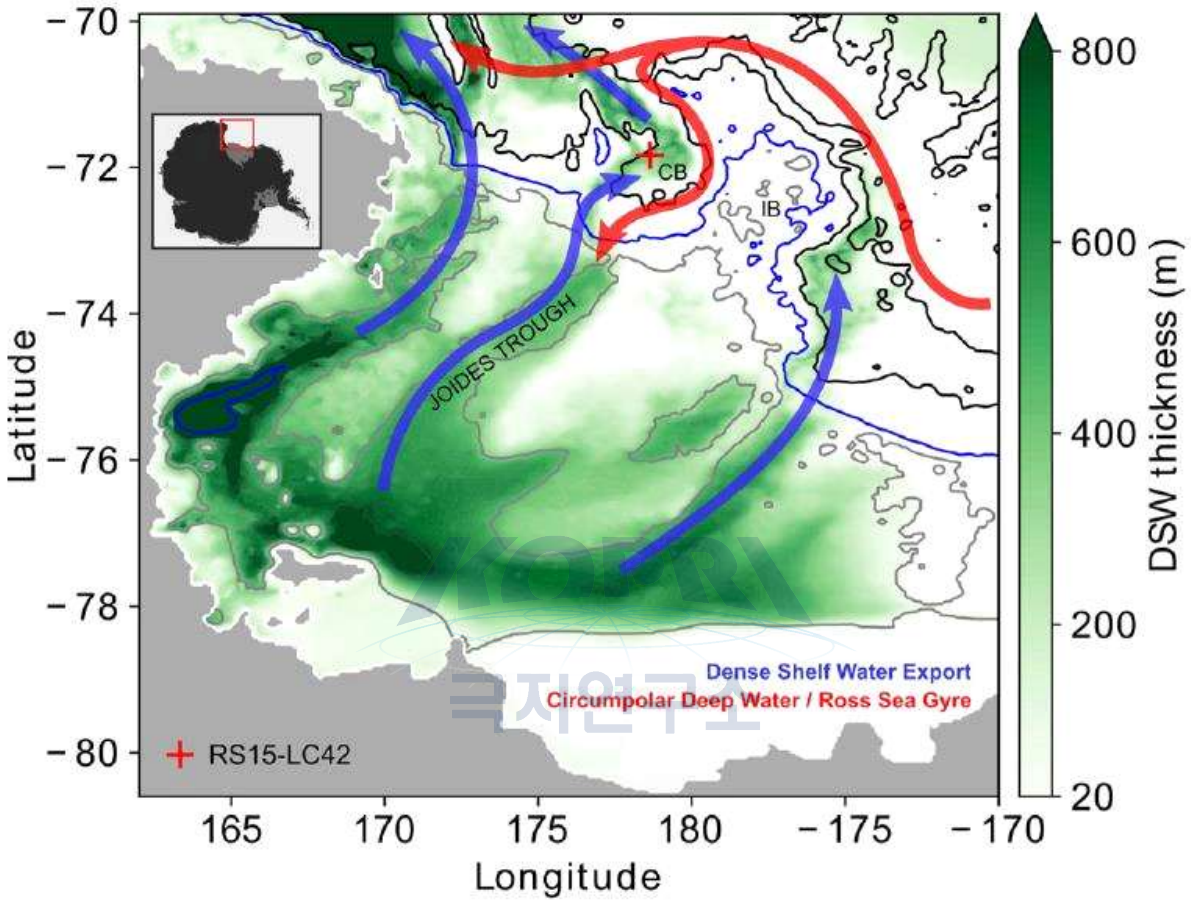


Figure 1. Location map displaying the location of RS15-LC42 in the Central Basin (CB). The red box in the inset map displays the map location relative to Antarctica. The site is located downslope from the terminus of the Joides Trough on the continental slope in the Ross Sea. Red and blue arrows display generalised current pathways associated with circumpolar deep water (CDW) and dense shelf water (DSW) respectively. Green shading displays modelled DSW plume thickness under modern conditions, showing that energetic bottom water export plumes are active at the study location, and likely drive sedimentological variability within the core. Figure modified from Morrison et al., 2020. (For interpretation of the references to colour in this figure legend, the reader is referred to the web version of this article.)

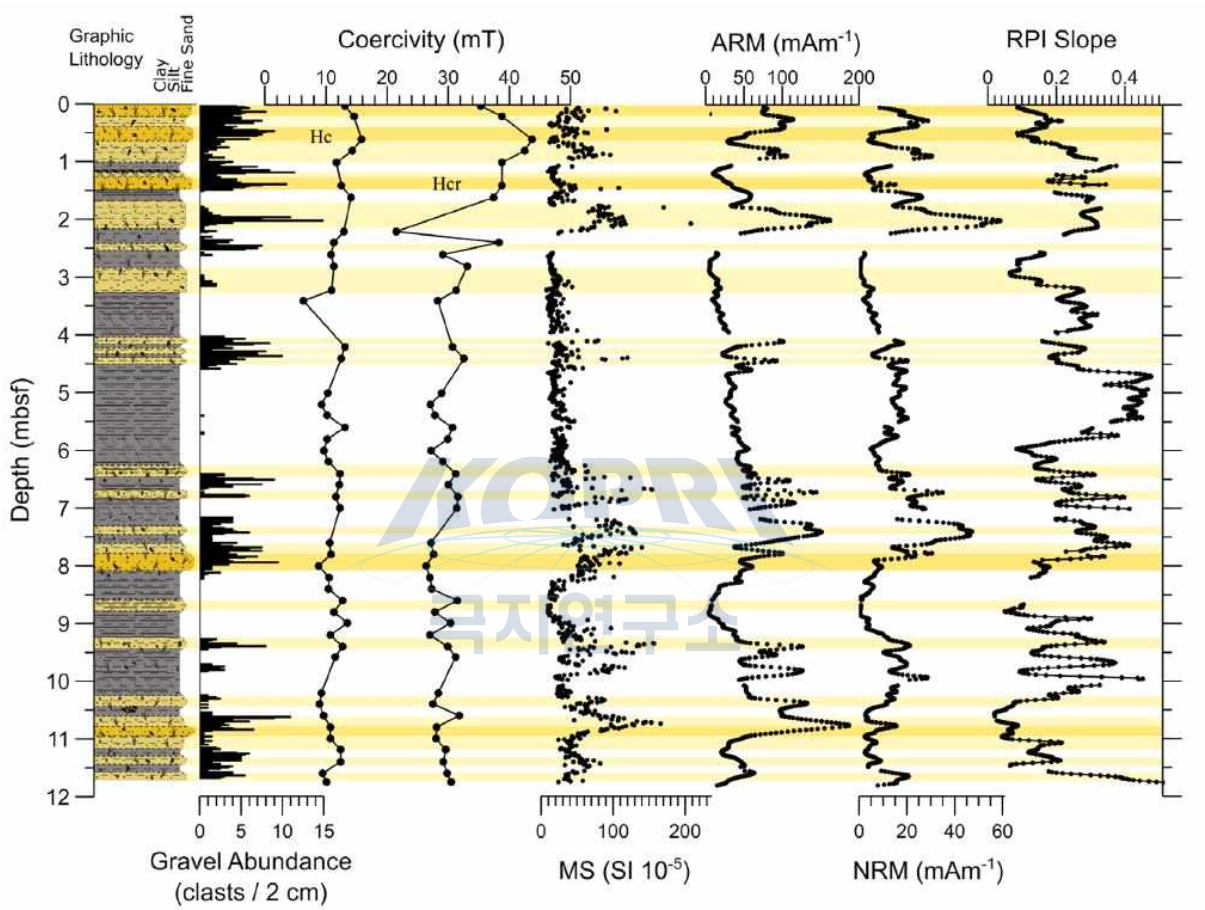


Figure 2. RS15-LC42 downcore (a) lithology, (b) gravel clast abundance, (c) Hc and Hcr coercivity, (d) S-ratio measure of magnetic hardness, (e) saturation magnetization (Ms), (f) magnetic susceptibility (MS), (g) ARM, (h) NRM, and (i) RPI Slope (10-40 mT).

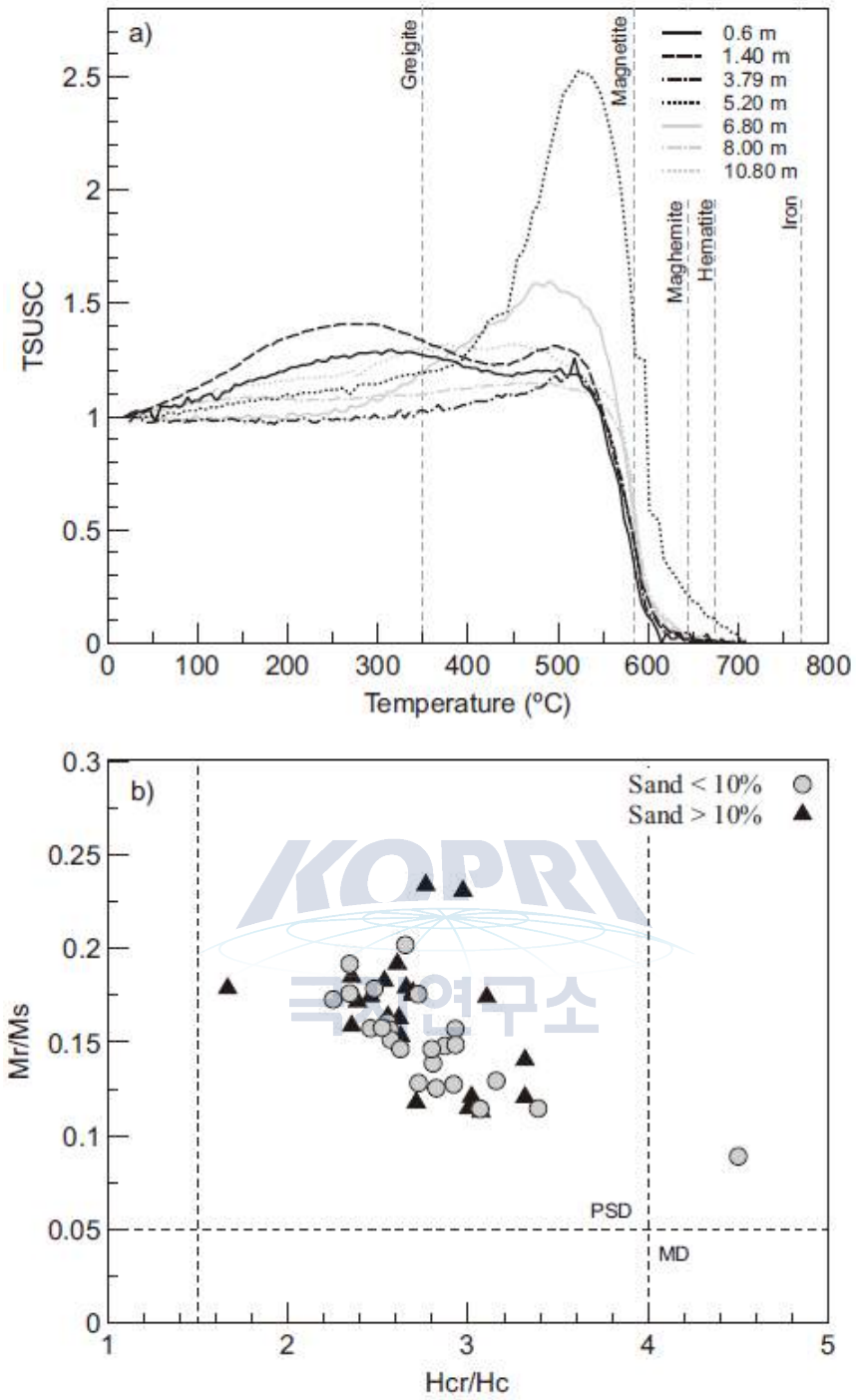


Figure 3. a) Thermomagnetic heating curves of six samples from RS15-LC42 measured in an AGICO Kappabridge. Dashed lines display distinctive Curie temperatures for commonly deposited iron oxide minerals (magnetite, maghemite, hematite) and a product of sulphide reduction in the sediment (greigite). b) Day plot of hysteresis parameters, indicative of magnetic grainsize (Day et al., 1977). Magnetic grainsize domains are separated by dashed lines, with PSD and MD representing pseudo-single domain and multi-domain grain sizes respectively. Data is classed by grainsize according to the proportion of sand in the sample (grainsize <4 Ø).

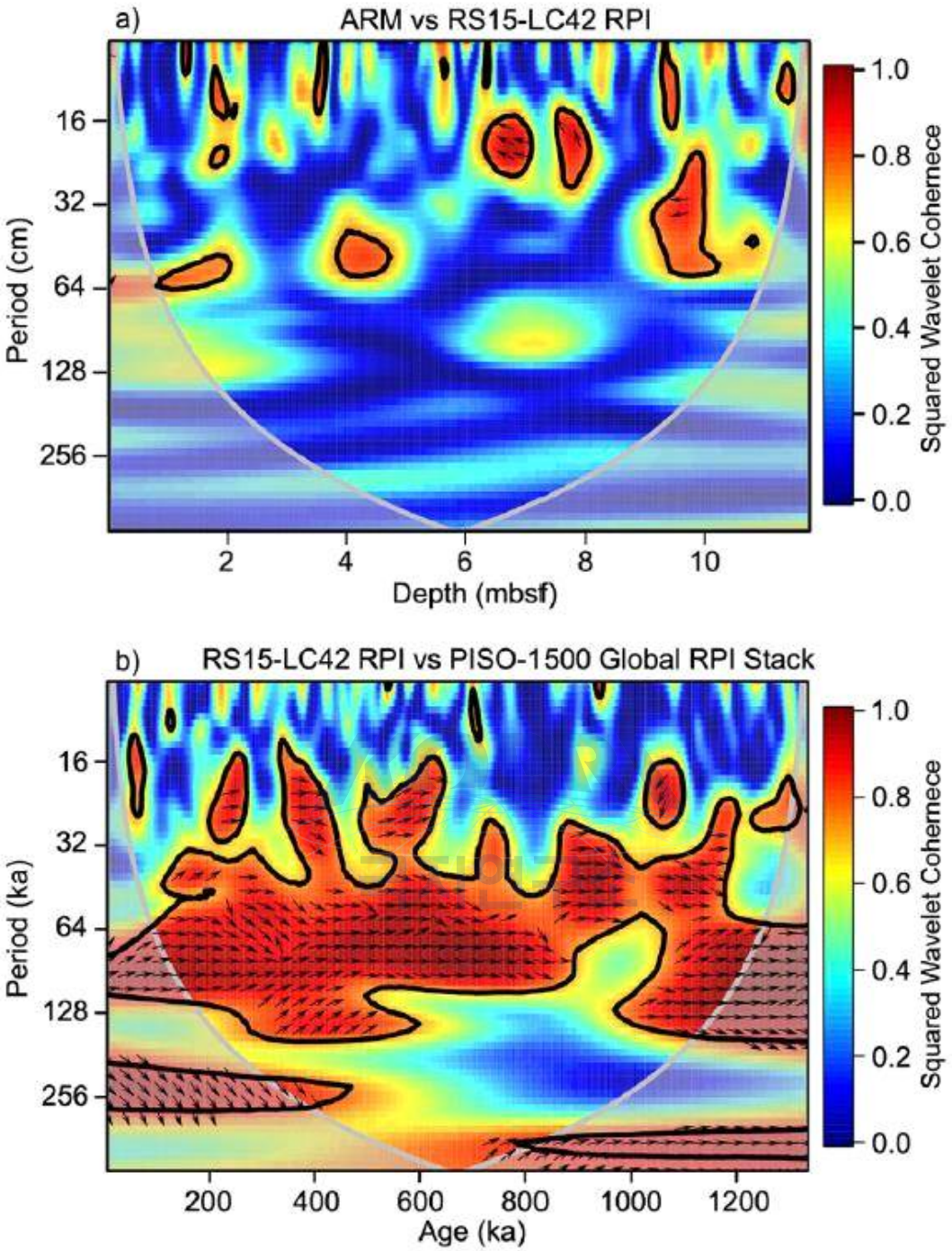


Figure 4. Wavelet coherence plots of a) the ARM and RPI Slope of RS15-LC42, and b) the aligned RPI estimate and 10 kyr moving average of the PISO-1500 global RPI stack. Wavelet coherence was computed using the 'biwavelet' package in R, computing 1000 iterations. The thick black contour marks the 5% significance level of coherency against red noise. Grey curved lines mark the limits of the cone of influence, where edge effects make analyses unreliable. Phase relationships are indicated by arrows, with in-phase arrows pointing right, anti-phase pointing left, and instances where the RPI signal leads the PISO signal by arrows oriented pointing down. (For interpretation of the references to colour in this figure legend, the reader is referred to the web version of this article.)

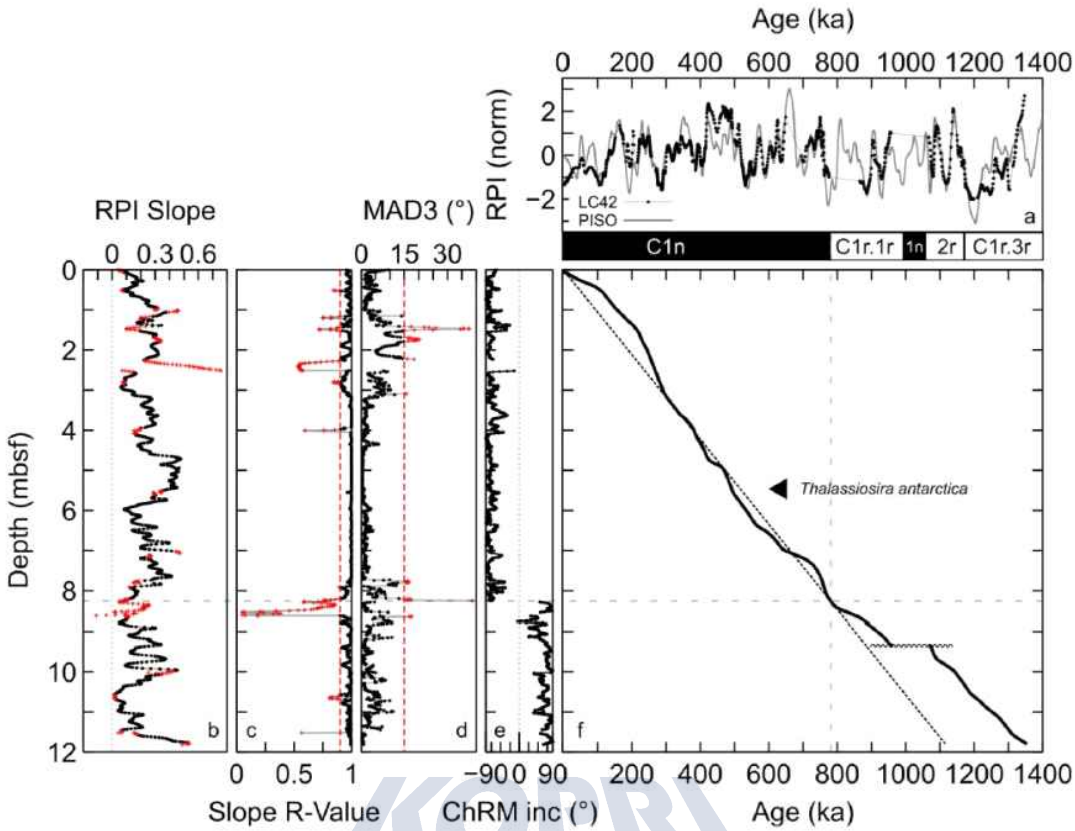


Figure 5. (a) The aligned RPI slope record from RS15−LC42 and the PISO−1500 10 kyr moving average, both standardised to a mean of 0 and SD of 1. The Geomagnetic Polarity Time Series is appended below, with normal polarity chrons displayed in black, and reverse polarity chrons displayed in white. (b) Downcore plot of the RPI slope from RS15−LC42. Black points indicate the data which was used for the Match protocol, with red crosses showing data that was excluded according to acceptable thresholds in R−Value, maximum angular deviation (MAD), and demagnetization behavior. (c) RPI slope R−value, displaying the correlation coefficient between NRM and ARM at AF strengths between 0 and 40 mT. A threshold of 0.9 was defined, with the corresponding RPI slope data of all points below this threshold being excluded from the RPI−PISO match procedure. (d) The MAD of principal component analysis (PCA). Red crosses indicate data above an acceptable data threshold of 15◦ (red dashed line), with all data above this value excluded from the RPI−PISO match procedure. (e) The Characteristic Remnant Magnetisation (ChRM) inclination of PCA, which aligns with the expected inclination of 80.7◦ reversed polarity, and − 80.7◦ normal polarity. (f) The newly revised age model (solid black line) compared to the existing age model of Ohneiser et al., 2019 (dashed black line). The black triangle displays the FO of Thalassiosira antarctica between 5.40 and 5.64 mbsf at 0.65 Ma. The undulating line at 9.34 mbsf marks the interpreted hiatus spanning the C1r.1n Jamarillo subchron, with the light grey dashed lines linking the fundamental initial age control of 0.781 Ma at 8.26 mbsf, defined by the Bruhnes−Maruyama magnetic reversal. (For interpretation of the references to colour in this figure legend, the reader is referred to the web version of this article.)

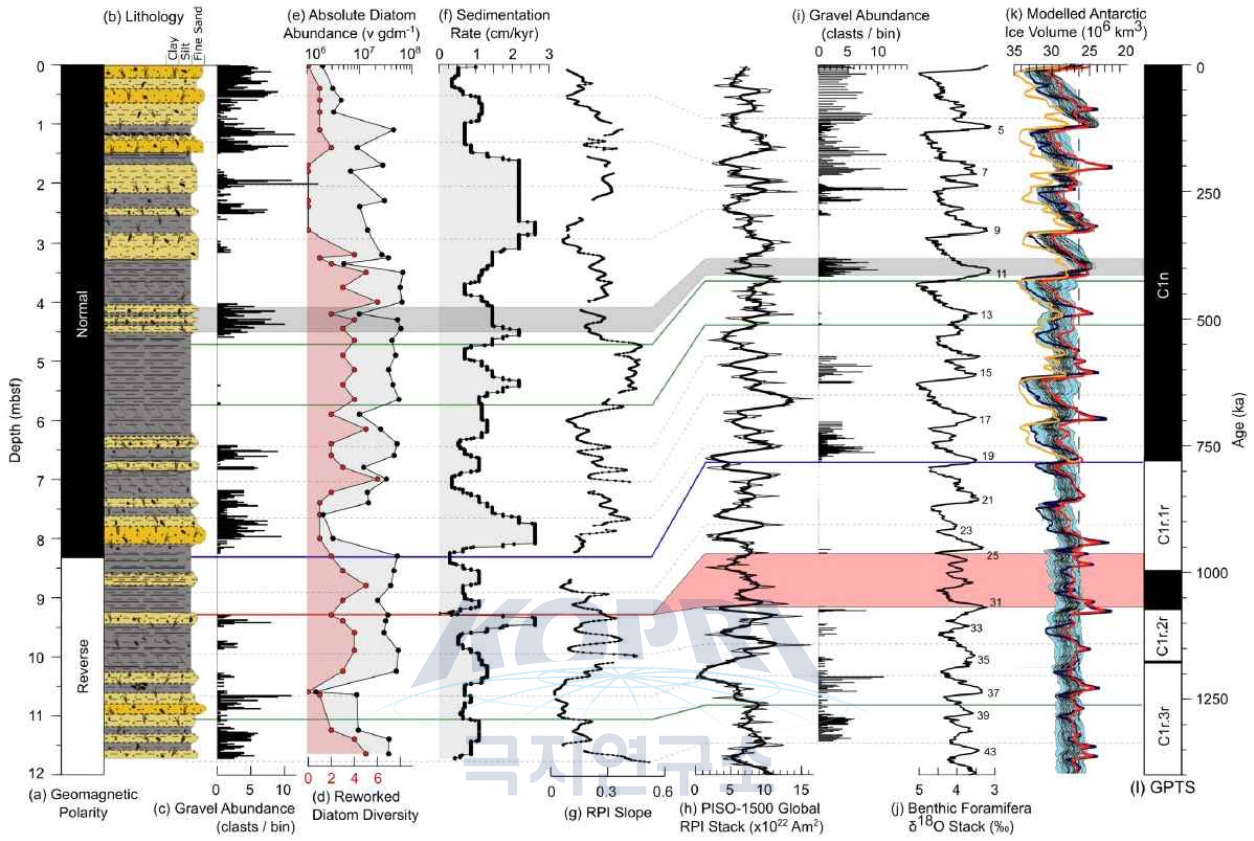


Figure 6. Panels (a–g) plot against core depth in meters below seafloor, displaying downcore records of (a) geomagnetic polarity, (b) lithology, (c) gravel abundance, (d) reworked diatom diversity (red), (e) absolute diatom abundance (black) (ADA) of samples from RS15–LC42. (f) Displays the modelled sedimentation rate according to RPI age modelling. The (g) RPI Slope record is aligned by the grey dashed lines to corresponding points on the (h) PISO–1500 global RPI stack (Channell et al., 2009). The blue line indicates the B–M Magnetic reversal tie point, while green lines display other tie points manually picked after the initial Match protocol to fine– tune the records. Panels (i–l) plot against the age axis, where (i) displays gravel abundance data, (j) shows the global benthic foraminifera δ18O stack (Lisiecki and Raymo, 2005), k) presents modelled Antarctic ice volume (Figure adapted from Sutter et al., 2019; blue shading = model ensemble from Sutter et al., 2019; black line = Pollard and DeConto, 2009; red line = De Boer et al., 2014, yellow line = Tigchelaar et al., 2018), and (l) plotting the global polarity timescale (Ogg, 2020). The grey shaded area aligns the gravel peak from 4.0 to 4.5 mbsf to MIS 11 for reference. The red shaded area shows the missing timeperiod over the interpreted hiatus at ~9.34 mbsf. (For interpretation of the references to colour in this figure legend, the reader is referred to the web version of this article.)

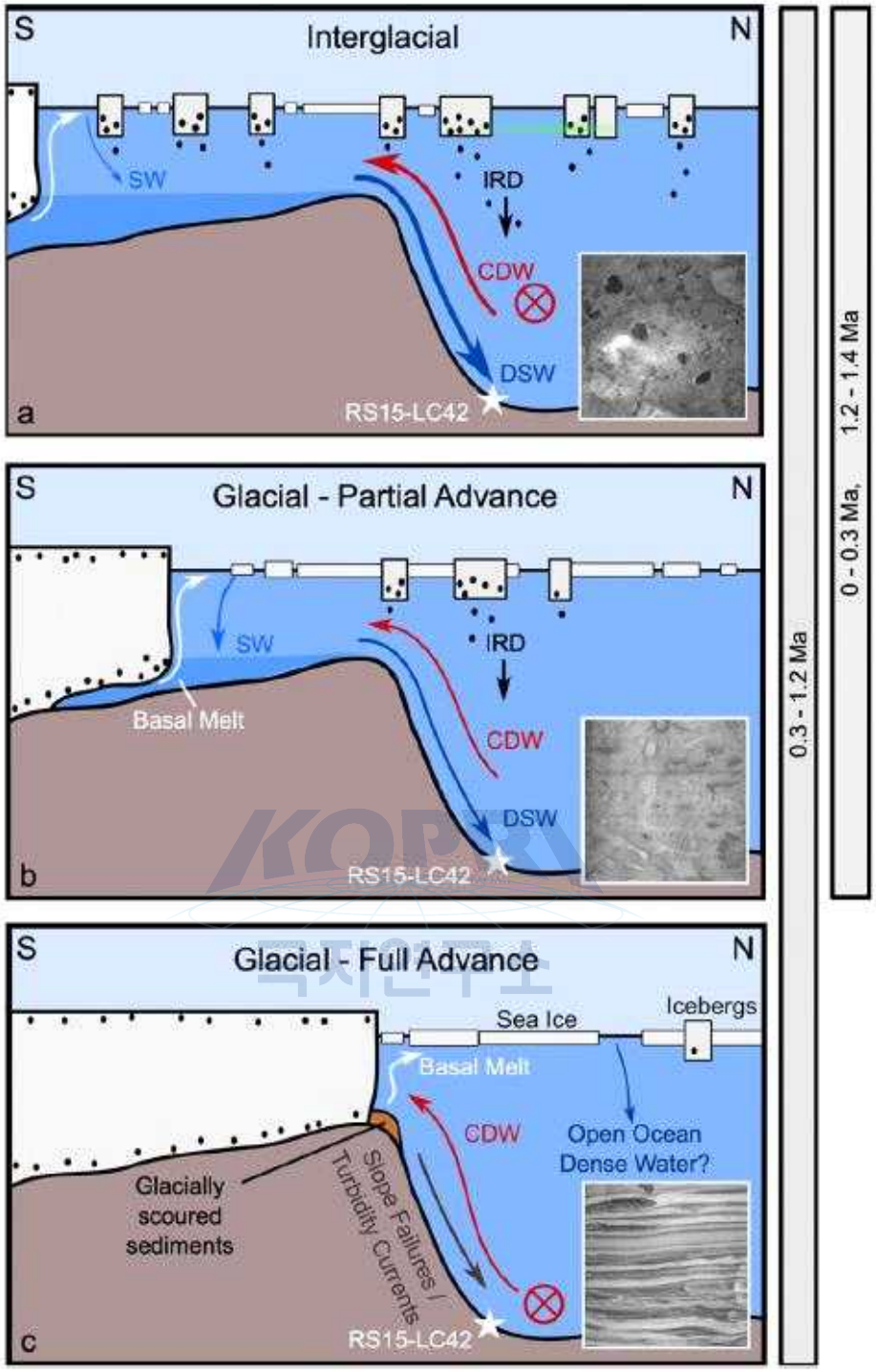


Figure 7. (Top row) Cross plots of x-radiograph (x-ray count) clast values, sieve-based weights of 250 μm-2 mm, and 125 μm-2 mm LPSA analysis for RS15-LC42, with linear regression model and 95% confidence bounds. (Second row) Plot of residuals vs. fitted values from the linear regression model for cross plots shown in top row. (Third row) Cross plots of x-radiograph (x- ray) count values, sieve-based weights of 250 μm-2 mm, and 125 μm-2 mm LPSA analysis for RS15-LC48, with linear regression model and 95% confidence bounds. (Bottom row) Plot of residuals vs. fitted values from the linear regression model for cross plots shown in third row.

제 32 장

남극 로스해 대륙대 퇴적물의 대자율 이방성 연구: 고수류 변화 복원에 대한 적용 가능성 평가[25)]

신지영[1], 이민경[2], 강명일[2], 주영지[1]

[1]국립부경대학교
[2]한국해양과학기술원 부설 극지연구소

요약: 남극 대륙주변부 퇴적물은 기후에 따른 빙하 환경 및 해양 순환 변화의 영향을 받아 고유의 퇴적 특성을 기록한다. 본 연구에서는 로스해 대륙대에서 해류 변동성과 관련된 고환경 복원을 위하여 퇴적상, 입도분포 및 대자율 이방성(Anisotropy of magnetic susceptibility, AMS) 분석을 수행하였다. 퇴적상은 빙운쇄설물이 풍부한 다이아믹트와 조립질 입자가 거의 없는 엽층리 실트로 구분된다. 엽층리 실트 퇴적상에는 파형의 경계부 및 사엽층리가 잘 발달되어 있으며, 이는 지속적인 저층 해류의 영향을 지시한다. 다이아믹트 퇴적상은 생물 교란 구조가 빈번하고 퇴적구조가 뚜렷하지 않지만, 저층 해류의 키질작용에 의한 박층의 역질/사질층이 종종 관찰된다. AMS 분석 결과, 이방성 정도(P')는 퇴적상 및 입도 변화와 연관성을 보이지 않으며, 이는 교란 등에 의한 자성입자의 2차적인 배열의 결과로 판단된다. 따라서 P'의 변동성은 본 연구에서 해류 세기의 직접적인 지시자로 적용하기 어렵다. 그러나 이방성 타원체는 엽층리 실트 및 역질/사질층이 협재된 다이아믹트 구간에서 강화된 편원구조(oblate) 특성을 보이며, 이는 로스해 주변의 지형류에 의한 등수심 퇴적체 형성 모델과 일치한다. 이러한 결과는 자성입자의 배열을 반영하는 자기 이방성 조직이 로스해 저층 해류 순환에 따라 엽층리 형성 및 키질 작용과 같은 퇴적 기작의 변화를 민감하게 반영할 수 있음을 시사하며, 향후 다양한 극지 환경에서의 AMS 연구 및 퇴적 지시자를 이용한 종합적 해석의 필요성을 강조한다.

1. 서론

남극 대륙 주변의 해양 순환은 빙상 하부로 열을 운반함으로써 빙상의 불안정성을 유발하여 전지구 열염순환과 해수면 변화에 중요한 영향을 미친다(Joughin and Alley, 2011; Golledge et al., 2012). 특히 남극종단산맥(Transantarctic Mountains) 서쪽의 서남극(West Antarctica) 지역은 빙상의 대부분이 해수면 아래에 잠겨 있어 동남극에 비해 기후 변화에 더욱 민감하게 반응한다(Hughes, 1973). 서남극과 동남극의 경계에 위치한 로스해(Ross Sea)는 빙붕(ice shelf) 과 대륙붕이 넓게 발달한 지역으로(그림 1), 빙상의 성장과 후퇴에 따라 많은 양의 남극저층수(Antarctic Bottom Water)를 형성하여 전지구 해양 순환과 기후 조절 체계에 중추적인 역할을 한다(Orsi et al., 2002; Orsi and Wiederwohl, 2009). 이러한 독특한 지리·해양학적 조건으로 인해 로스해는 과거, 현재, 미래의 기후 변화를 이해하기 위한 주요 연구 지역으로 알려져 있다(e.g., Jacobs et al., 2002; Anderson et al., 2014; Schmidtko et al., 2014; McKay et

25) 이 연구 결과는 다음의 논문으로 출판되었음: 신지영 외 (2024). "남극 로스해 대륙대 퇴적물의 대자율 이방성 연구: 고수류 변화 복원에 대한 적용 가능성 평가." 지질학회지 60권 제4호, pp. 349-360.

al., 2019). 로스해 대륙주변부의 퇴적작용은 주로 빙상의 전진과 후퇴에 따라 다양한 표층, 사면, 심층 해류의 상호작용에 의해 조절되며, 빙하쇄설류, 저탁류, 등수심 퇴적체 등 고유의 퇴적 기록을 형성한다 (Pudsey, 2000; Lucchi et al., 2002; Lucchi and Rebesco, 2007). 빙상의 전진 및 후퇴에 직접적인 영향을 받는 로스해 대륙붕에서는 많은 고기후·고해양 연구가 이루어졌으나, 대륙대 퇴적물은 비교적 지속적인 퇴적 기록을 통해 심해 순환에 대한 정보를 제공할 수 있는 장점이 있음에도 연구결과가 부족한 실정이다. 로스해에서 수행된 이전의 퇴적·지구물리학적 연구는 대륙사면-대륙대의 퇴적 지형 및 구조를 기반으로 마이오세 이후 강화된 저층 해류(bottom current)의 장기 진화를 밝혔다(De Santis et al., 1999; McKay et al., 2019; Conte et al., 2021). 하지만 이러한 퇴적 구조가 항상 뚜렷하게 식별되는 것은 아니며, 남극해 퇴적물의 특성상 유공충 등 생물 기원 탄산염 입자를 이용한 상세한 연대층서 정립의 어려움으로 인해 플라이스토세 동안의 로스해 해류 순환에 대한 정보는 여전히 제한적이다. 선행 연구에 따르면, 플라이스토세 동안 로스해 대륙붕에 접지된 빙상은 기후 전이기(climate transition)에 따라 진화하여, 중기 플라이스토세 전이기(Mid-Pleistocene Transition, MPT; ~700-1,200 ka)에 걸쳐 그 범위가 확장되고 중기 브룬스 전이기(Mid-Brunhes Transition, MBT; ~400-600 ka) 이후 감소한 것으로 추정된다 (McKay et al., 2012). 이러한 빙상의 진화는 로스해 해류 체계 또한 기후 전이기에 따라 변화하였을 가능성을 나타낸다(e.g., Albot, 2016; Bollen et al., 2022). 대자율(magnetic susceptibility)은 외부 자기장에 비례하는 시료의 자화 능력을 나타내며, 대자율 이방성(Anisotropy of Magnetic Susceptibility, AMS)은 측정방향에 따라 달라지는 대자율 값에 기반하여 입자의 통계적인 배열상태를 빠르게 추정할 수 있는 지구물리학적 분석 방법이다(Ellwood and Ledbetter, 1979; Doh, 1991; Tarling and Hrouda, 1993; Son et al., 2000). 이러한 원리를 기반으로 해성 퇴적층의 대자율 이방성 분석은 퇴적물 입자의 배열을 제어하는 고수류 방향 및 세기를 재구성하는 데 성공적으로 적용되었다(e.g., Joseph et al., 1998, 2002; Parés et al., 2007; Ohneiser and Wilson, 2018). 그러나 남극 대륙주변부와 같은 고위도 지역에서는 지구자기장의 수평 성분이 작아 고지자기 편각 (paleomagnetic declination)의 정확도가 낮기 때문에 퇴적물 시추코어에 기록된 자북(paleomagnetic north) 방향을 결정하기 어렵고, 이 때문에 편각을 이용한 입자 배열 방향 보정 및 고수류 방향 복원은 제한적이다. 또한 극지의 역동적인 퇴적환경, 즉 빙상의 전진 및 후퇴에 따른 다양한 퇴적 작용으로 인한 측정·해석상의 어려움 때문에 남극해 퇴적물에서 대자율 이방성을 적용한 연구는 거의 없다. 본 연구에서는 지난 ~70만년 동안 형성된 남극 로스해 대륙대 퇴적물에서 퇴적상, 입도분포 및 대자율 이방성 분석에 기반한 종합적인 정보를 바탕으로 해류 순환과 관련된 과거 퇴적환경을 추정한다. 또한, 일반적으로 저층 해류 세기 지시자로 이용되는 분급성 실트(sortable silt)와 대자율 이방성 결과의 비교를 통하여 저층 해류 변동성 지시자로서 자기 이방성 조직(magnetic fabric)의 적용 가능성을 평가하고자 한다.

2. 연구시료 및 방법

2.1. 연구지역 및 시료

연구시료는 극지연구소의 2014/2015 남극 탐사(ANA05B) 동안 로스해 서부 대륙대(68° 53.9289'S, 171° 09.8914'E)에 서 회수한 퇴적물 중력코어 RS15-LC48(수심 3,167 m; 길이 1,472 cm)을 이용하였다. 연구 정점은 남극저층수의 주요 유출 경로 중 하나인 Adare Trough의 약 100 km 북쪽에 위치하며(Orsi and Wiederwohl, 2009; Morrison et al.,2020), 저층수 상층에는 고온, 고염의 두꺼운 순환심층수(Circumpolar Deep Water)층이 존재한다(Orsi and Wiederwohl, 2009). 남극사면류(Antarctic Slope

Current)는 대륙사면을 따라 서향하는 지형류(geostrophic current)이며, 로스환류 (Ross Gyre)의 남쪽 경계와 상호작용한다(Whitworth et al., 1985). 대륙붕에서는 해빙 형성과 염분 방출로 인해 고염대륙붕수(High Salinity Shelf Water)가 생성되며, 고염대륙 붕수가 순환심층수와 혼합되어 로스해 남극저층수 의 기원이 되는 고밀도 대륙붕수(Dense Shelf Water)가 심층으로 유출된다(Orsi et al., 1999; Gordon et al., 2009). 이렇게 로스해에서 형성된 남극저층수는 지형을 따라 서쪽으로 확산되어 전지구 심해에 산소를 공급한다(Jacobs, 2004; Orsi et al., 1999). 연구 코어 RS15-LC48의 U-channel 시료를 이용한 고지자기 결과에 의하면(Ohneiser et al., 2019), 해당 코어의 최하부는 약 250만 년 전에 해당하며 마지막 지자기 역전 기록인 브룬스-마쓰야마 경계(78만년 전)는 약 430 cm 깊이 에서 확인된다(평균 퇴적율 약 0.55 cm/kyr). 본 연구에서는 대자율 이방성 분석을 위하여 코어의 최상부 약 340 cm 구간에서 플라스틱 큐브(7 cm3)를 이용하여 거의 연속적으로 총 152개의 부시료를 채취하였다. 부시료 채취 과정에서 각각의 큐브는 표시된 화살표가 코어 상부 방향을 가리키도록 하여 퇴적물 표면에 부드럽게 밀어 넣었다(그림 2).

2.2. 대자율 이방성 측정

본 연구를 위하여 코어 RS15-LC48의 큐브 시료를 대상으로 한국지질자원연구원이 보유한 Agico MFK1-A Kappabridge의 시료 자동회전・측정 장치를 이용하여 대자율 이방성을 측정하였다. 또한 해당 코어의 부피 대자율(κ)은 코어 스캐닝을 통해 측정되었으며 Ohneiser et al. (2019) 에 의하여 보고된 바 있다. 각 시료에 대해 3차원 대자율 이방성 타원체(AMS ellipsoid)는 서로 수직인 최대(K1), 중간(K2), 최소(K3) 대자율 값을 주축으로 하여 정의된다(Tarling and Hrouda, 1993). 평균 부피 대자율(Km)은 Km = (K1 + K2 + K3)/3으로 계산되며, κ와 유사한 경향성을 비교할 수 있다. 이방성 타원체는 퇴적물의 자기조직(sediment magnetic fabric)을 평가하기 위해 활용되며, 세 주축을 기반으로 계산된 매개변수는 다음과 같다(Jelinek, 1981; Hrouda, 1982): 자기선구조(L) = K1/K2, 자기 엽리구조(F) = K2/K3, 이방성변수(P') = exp{2[(1 − m)2 + (2 − m)2 + (3 − m)2]}1／2, 형태변수(T) = [2(2 − 3) / (1 − 3)] − 1 (여기서 1 = ln K1, 2 = ln K2, 3 = ln K3, m = (1 + 2 + 3)/3을 나타냄). P'는 이방성의 정도를 나타내며, 값이 클수록 입자의 정렬이 강해지는 것을 의미하는 고수류 세기의 지표로 사용된다(e.g., Joseph et al., 1998, 2002; Parés et al., 2007). T는 타원체의 형태를 편원형태(Oblate; 0<T≤1) 또는 편장형태(Prolate; −1≤T<0)로 정의한다. 이방성 타원체를 도식화하기 위해 세 주축을 하반구에 투영하였다. 투영망의 좌표계는 시료 좌표계를 따른다. 코어 절단면은 x축에 수직이며, 퇴적물 표면으로 큐브 시료를 밀어 넣는 방향은 -x축 방향이다(그림 2).

2.3. 퇴적상 관찰 및 퇴적물 입도 분석

코어 RS15-LC48의 퇴적상 관찰 결과 및 퇴적물 슬랩(두께 1 cm, 폭 8 cm, 길이 30 cm)에 대한 X-선 사진은 Ohneiser et al. (2019)과 Jung et al. (2019)에서 보고되었다. 본 연구에서는 이전 연구 결과들을 바탕으로 코어 최상부 350 cm 구간에 대해 상세한 퇴적상 관찰을 수행하였다. 또한 X-선 사진으로부터 평균 2 cm 깊이 간격으로 계수된 조립한 빙운쇄설물(>2 mm)의 개수는 McKay et al. (2022)에서 제공된 자료를 이용하였다.

입도 분석을 위해 8 cm 깊이 간격으로 채취된 퇴적물 부시료를 동결 건조한 후, McKay et al. (2022)가 제안한 방법을 따라 과산화수소, 염산 및 수산화나트륨 처리를 통해 생물기원 성분을 제거하였

다. 2 mm의 체를 사용하여 조립한 입자를 분리하였다. 이후 극지연구소의 레이저 입도분석기(Malvern Mastersizer 3000)를 사용하여 2 mm 이하의 사질-이질 퇴적물을 대상으로 입도 분포를 측정하였으며, 입도변수는 Folk and Ward (1957)를 따라 계산되었다. 분급성 실트 구간(10-63 μm)의 평균 입도(SS)는 해양퇴적물에서 저층 해류의 속도 지시자로 사용되며, 극지 환경에서도 종종 적용된다(McCave et al., 1995; McCave and Andrews, 2019). 그러나 빙운쇄설물 함량이 높은 극지 퇴적물의 경우 값의 계산은 분급이 불량한 조립질 입자들에 상당한 영향을 받을 수 있기 때문에, Paterson and Heslop (2015)과 Stevenard et al. (2023)의 Matlab 소프트웨어를 이용하여 빙운쇄설물의 영향을 보정한 SS IRD_free 값을 계산하였다.

3. 결 과

3.1. 퇴적상 및 입도분포 특성

코어 RS15-LC48에는 주로 역 및 모래 입자가 풍부한 조립질의 다이아믹트 퇴적상과 조립질 입자가 없거나 드물게 산출하는 엽층리 실트 퇴적상이 교호한다(Ohneiser et al., 2019). 연구 구간(<350 cm)의 실트층에는 대체로 mm 규모의 평행(plana-) 및 사엽층리(cross lamination)가 인지된다(그림 3a). 특히, 70-102 cm 및 270-286 cm에서 엽층리 및 파형(wavy)의 경계부가 잘 발달하며, 상부 및 하부의 경계면이 명확하고 생물교란 구조가 드물다(그림 3a, 4a, 4b). 한편, 모래 입자가 풍부한 다이아믹트에서는 일반적으로 퇴적구조가 뚜렷하지 않고 생교란작용의 흔적이 관찰되지만, 때때로 생물교란이 적은 사질 및 역질층(sand-/gravel-rich layer) 또한 나타난다(예: 280-310 cm) (그림 3a, 3b, 4). 퇴적물의 입도분포는 다이아믹트 구간에서 높은 모래 함량을, 엽층리 실트 구간에서 높은 세립질 및 조립질 실트 함량을 보인다(그림 3c). 모래 함량 변화는 빙운쇄설물 함량 변화와도 유사한 경향성을 보여(그림 3d), 많은 조립질 입자가 빙운쇄설물의 형태로 유입되었음을 의미한다. 분급성 실트의 평균 입도 및 함량(SS%)은 전체 퇴적물의 평균 입도 및 모래 함량과 유사한 경향을 보인다(그림 3e-3g). 값과 분급성 실트의 분율(SS%)간의 상관계수(correlation coefficient;r)는 상부 350 cm 구간에서 0.21으로 낮아, 선행연구의 결과를 고려할 때 해류에 의한 분급작용의 결과(well current-sorted; r>0.5)로 보기 어렵다(McCave and Andrews, 2019). 반면 값과 모래(>63 μm) 함량간의 상관계수는 0.81로 높은 값을 보이는데, 이는 값이 모래 입자 유입에 주된 역할을 한 빙운쇄설물 함량의 영향을 받았음을 의미할 수 있다(e.g., McCave and Andrews, 2019).

연구시료의 입도 자료에서 빙운쇄설물의 영향을 보정하기 위하여 다수의 end-member (EM)를 사용하여 성분을 분리하는 방법(Stevenard et al., 2023)을 적용하였다. 총 6개의 EM을 이용하여 주성분분석을 수행한 후, EM1-3을 이용하여 SSIRD_free를 계산하였다(Supplementary 그림 1). 빙운쇄설물 영향을 보정한, SS IRD_free와 SS%IRD_free의 상관계수는 0.87로, 보정 전과 비교하여 크게 증가한 값을 보인다. 코어 깊이에 따른 SS IRD_free값은 전반적으로 엽층리 실트구간 내에서 낮지만(예: ~75 cm, ~105 cm, ~275-280 cm), 사엽층리가 발달한 ~80-100 cm 구간에서는 비교적 높게 나타난다(그림 3h).

3.2. 자기특성

대자율은 일반적으로 퇴적물 내 자성광물의 함량에 비례하며, 대륙주변부에서는 주로 육상기원 퇴적물의 기원지, 운반기작 등 환경 조건에 따른 암석학적 특성 변화를 반영한다. 코어 RS15-LC48의 대

자율(χ) 값은 전반적으로 다이아믹트층에서 높고 엽층리 실트에서 낮게 나타나 퇴적물 입도 변화와 연관성을 보인다(Ohneiser et al., 2019). 연구 시료(<350 cm)에서도 마찬가지로 대자율값의 변화는 빙운쇄설물 및 모래 함량과 유사한 경향을 보이며, 이는 조립질 입자가 비교적 풍부한 자성광물을 포함하는 것을 의미한다(그림 3c, 3d, 3i).

연구 시료의 평균대자율(Km) 값은 약 95.0 × 10-5 SI와 291 × 10-5 SI 사이의 비교적 높은 값을 보이며, 이는 자철석, 마그헤마이트와 같은 페리자성광물(ferrimagnetic minerals)이 퇴적물의 대자율에 주로 영향을 미친다는 것을 지시한다(Tarling and Hrouda, 1993). Ohneiser et al. (2019)는 코어 RS15-LC48에 대한 암석자기 특성 분석을 통해 ~580℃ 의 큐리온도를 갖는 자철석이 주요 자성광물이며, 자성광물의 자기구역상태(magnetic domain state)가 위단자기구역(pseudo single domain)에 해당함을 확인하였다. 대자율 이방성 분석 측면에서, 이러한 자기특성은 단자기구역(single domain) 자성광물의 자화특성에 의해 이방성 타원체의 축이 뒤바뀌는 역자기조직(inverse magnetic fabric) 효과를 배제할 수 있게 한다(Rochette et al., 1992).

코어 깊이에 따른 이방성 정도(P') 값은 <20 cm, 60-105 cm, 130-160 cm, 270-340 cm 구간에서 비교적 크게 변동하며(1.004-1.048), 이들은 ~1.01 정도의 낮고 안정적인 P' 값을 보이는 구간과 교호한다(그림 3k). 본 연구에서는 이를 편의상 각각 높은/낮은 이방성 구간이라고 정의한다. 이러한 P' 값의 변동은 자기 선구조 L보다는 엽리구조 F와 상관관계를 보이고, 퇴적상과 규칙적인 연관성은 뚜렷하지 않다(그림 3j, 3k). 자기조직 특성은 L과 F의 상관관계를 도식화하는 Flinn diagram (Flinn, 1962) 및 P'-T diagram (Jelínek, 1981)에서 잘 나타난다: 높은 이방성 구간은 비교적 높은 F 값과 양의 T 값으로 인해 편원형 구조 영역에 해당하는 반면, 낮은 이방성 구간은 T 값이 다양하게 분포하여 무작위한 모양을 나타낸다(그림 5a, 5b). 연구시료의 P'-T 관계를 Joseph et al. (1998)이 경험적으로 분류한 퇴적환경과 비교할 때, 낮은 이방성 구간은 원양/반원양 환경에 해당하는 반면, 높은 이방성 구간은 대부분 드리프트(drift) 퇴적체 영역과 일치한다(그림 5b).

본 연구에서는 고위도 연구지역 시료의 특성상 고지자기 편각의 불확실성이 높아(Ohneiser et al., 2019) 이방성 타원체의 배열 방향을 지리적으로 복원하지는 못하였으나, 투영망에 도시된 주축의 분포를 이용하여 자기조직과 입자배열 상태를 확인하였다. 연구 시료는 전반적으로 수직방향의 K3 축과 수평면에서 K1 및 K2 축의 거들(girdle) 분포를 보여주며(그림 5c), 이는 일반적으로 수평면에 퇴적된 1차 퇴적 조직을 반영한다(Hrouda, 1982). 높은 이방성 구간은 K3 축이 비교적 군집되어 나타나 이방성 증가와 일치하는 반면(그림 5d), 낮은 이방성 구간은 특히 K2 및 K3축이 크게 분산되어 있음을 보여준다(그림 5e).

4. 토 의

4.1. 퇴적상과 퇴적환경 변화

코어 RS15-LC48에서 반복하여 관찰되는 엽층리와 점이적인 경계 하부의 생교란작용의 흔적은 남극 대륙주변부에서 빙하기-간빙기 퇴적환경 변화에 따라 발달하는 등수심 퇴적체 모델과 유사하다(Rebesco et al., 2014). 연구 구간(<350 cm) 내 사질 다이아믹트의 희미하거나 부재한 엽층리와 광범위한 생물교란구조는 저탁류가 발생하는 높은 에너지의 퇴적환경에서 형성된 것으로 보기 어렵다(Busetti et al., 2003; Rebesco et al., 2014). 그러나 이 구간에서는 역질층(gravel-rich layer)이 종종 발견되며(그림 3, 4), 다량의 빙운쇄설물 유입과 저층 해류에 의한 세립질 입자의 침식을 수반한 키질 작용(erosional

winnowing)에 의한 것으로 해석된다(Stow and Piper, 1984; Howe et al., 2001; Bollen et al., 2022). 이는 퇴적환경 내 세립한 이질/실트질 입자를 제거할 수 있는 강도의 해류의 영향이 있었음을 의미하지만, 그 수준은 침식에 의한 부정합면이 아닌 연속적인 퇴적기록을 형성하는 정도였을 것으로 보인다(e.g., Drewry and Cooper, 1981).

70-102 cm 구간의 엽층리 실트에서 잘 발달된 사엽층리, 파형의 명확한 하부 경계 및 생물교란의 감소는 지속적인 저층 해류의 영향으로 해석된다(그림 3, 4). 이 구간에서 모래 함량이 적은 것은 저층 해류의 속도가 높지 않음을 의미하지만, 분급성 실트의 평균 입도(SS IRD_free) 증가는 저층 해류의 속도가 이들을 운반하기에는 충분하였음(>23 cm/s)을 시사한다(그림 3h; McCave and Hall, 2006). 한편, 270-286 cm 구간의 엽층리 실트에서는 세립질 실트가 우세하여 비교적 저에너지의 퇴적 환경이었을 것으로 추론된다(그림 3h). 두 구간의 엽층리 실트에서 빙운쇄설물이 거의 없는 것은 대륙붕에 접지한 빙상(grounded ice sheet)이 연구지역 부근까지 전진하여 빙상 붕괴가 감소했거나, 혹은 빙상이 멀리 후퇴하여 연구지역까지 도달한 빙운쇄설물이 감소한 것으로 해석할 수 있다(McKay et al., 2012; Albot, 2016).

코어 RS15-LC48에 대한 고지자기 연대가 ~430 cm 깊이에서 약 78만년 전임을 고려할 때, 연구구간(최상부 350 cm)는 최대 70만년 전후로부터의 퇴적 환경을 반영할 것으로 추정할 수 있다. 선행 연구에서, 해당 시기 동안 로스해 중앙분지 대륙대에 생물교란구조의 빈도가 높은 다이아믹트와 엽층리 실트가 교호하는 유사한 퇴적상이 나타나며, 엽층리 실트에서 재동된 규조류의 높은 종다양성이 확인되었다(Bollen et al., 2022). Bollen et al. (2022)이 제시한 퇴적환경 모델에 따르면, 빙하기 동안에는 접지된 빙상이 최대로 전진했을 때 빙상 저면에서 유출되는 융빙수, 사면붕괴, 또는 융빙수에 의한 저밀도 저탁류 등에 의해 대륙사면으로 공급된 세립질 퇴적물이 대륙대 주변의 등수심류에 의해 엽층리를 형성하고, 빙상이 후퇴하면서 강화된 고밀도 대륙붕수 유출에 의해 조립질 입자가 주를 이루는 희미한 엽층리가 발달한 퇴적상이 형성되는 반면, 빙상이 완전히 후퇴한 간빙기 동안에는 엽층리가 나타나지 않고 풍부한 빙운쇄설물과 생교란작용의 증거가 특징적으로 나타난다. 본 연구 지역의 경우에도, 추후 상세한 연대모델이 보강되어야 하나, 퇴적상의 유사성을 고려할 때 해당 모델에 의해 해류 체계 및 퇴적작용이 조절되었을 가능성이 높다고 판단된다.

4.2. 퇴적환경 변화와 자기 이방성

연구 지역의 퇴적 모델에서 모래가 풍부한 조립질 퇴적층은 빈번한 고밀도 대륙붕수 유출에 의한 비교적 강한 에너지의 퇴적 환경에서 형성된 것으로 설명한다(Bollen et al., 2022). 본 연구시료의 경우, 해류 세기 지시자로 사용된 SS IRD_free는 퇴적상에 따라 뚜렷한 변화를 보이지는 않으나, 다음과 같은 근거로 다이아믹트에 비해 엽층리 실트가 저에너지의 퇴적 환경에서 형성되었을 것으로 추론한다: 1) 고에너지 환경을 지시하는 모래 함량이 엽층리 실트 구간에서 낮은 것(그림 3c); 2) SS IRD_free의 가장 낮은 값이 엽층리 실트 구간에서 나타나는 것(~75 cm, ~105 cm, ~275-280 cm; 그림 3h). 따라서 연구지역에 형성된 엽층리 실트는 지형류 또는 상대적으로 미약한 고밀도 대륙붕수 유출과 같은 저에너지의 저층 해류에 의한 퇴적작용을 반영하는 것으로 해석된다. 그러나 전반적으로 일정한 SS IRD_free 변화는 해류 체계 변화에 의한 해류 속도 차이(혹은 그에 의한 기록)가 연구지역에서 뚜렷하지 않았을 가능성을 시사한다. 또한 상부 약 80-100 cm 구간의 실트질 엽층에서 높은 SS IRD_free를 고려하면(그림 3h), 시기별로 빙하 환경 조건에 따라 등수심 퇴적체를 형성하는 퇴적물 가용성 및 해류 세기에 차이가 있었을 가능성 또한 존재한다.

일반적으로 해류 속도 증가에 의한 자성입자 배열 강화는 퇴적물 입도 증가를 수반하지만 (Ledbetter and Ellwood, 1980), 본 연구시료의 자기 이방성 정도(P’) 변화는 퇴적상 및 입자크기와 연관성을 보이지 않는다(그림 3e, 3k). P’ 변동과 관련된 입자 배열은 이방성 타원체의 투영을 통해 보다 상세히 이해할 수 있다(그림 5). 높은 이방성 구간에서 관찰되는 K3 축의 군집과 K1 축의 +X 방향으로의 경사는 인편구조(imbrication)의 발달을 지시하며(그림 5d), 강화된 편원구조 및 드리프트 퇴적체의 특징과 잘 일치한다 (Knight and Walker, 1988; Tauxe et al., 1998). 한편, 낮은 이방성 구간에서는 K3 축이 수직 축에서 크게 벗어나 있으며(그림 5e), 일반적으로 무작위한 K2와 K3축의 평면 분포를 특징으로 하는 원양성 퇴적환경의 자기조직과 일치하지 않는데 이는 1차 퇴적 구조의 교란을 나타낸다. 자기 이방성 결과는 시료 채취 과정의 오염에 민감하기 때문에 결과 해석 이전에 다음과 같은 요인이 고려되어야 한다. 첫째, 선상에서의 퇴적물 코어 채취/회수 과정은 코어 내 퇴적층에 변형을 야기하여 층리의 수직적인 혼합(mingling), 뒤틀림(distortion), 상향 아치구조(upward-arching beds) 등을 형성할 수 있다 (Snowball et al., 2019; Yang et al., 2019). 둘째, 코어 절개 시 코어 라이너가 이완되거나 절개면 퇴적물을 긁어내는 과정으로 인해 K1 축이 코어 절개면과 평행하게 정렬될 수 있다(Copons et al., 1997; Aubourg and Oufi, 1999; Shimono et al., 2014; Snowball et al., 2019). 셋째, 코어 절개 및 큐브 시료 채취 과정에서 적용된 압축응력(좌표계에서 x축 방향)은 K1 혹은 K3 축 분포가 x축을 따라 확장되도록 할 수 있다(Gravenor et al., 1984; Copons et al., 1997; Xuan et al., 2012; Yang et al., 2019). 본 연구시료의 경우, X-선 사진과 이방성 타원체로부터 코어 퇴적물 및 절개면이 교란되지 않았음을 확인할 수 있다. 그러나 K1 축이 x축 방향을 가리키는 것을 고려할 때 큐브 시료 채취 과정에서 응력에 의한 일부 이방성 타원 체의 오염을 완전히 배제할 수는 없다. 이러한 오염은 특히 빙운쇄설물이 다량 포함된 일부 시료에서 심각하게 작용할 가능성이 있다. 시료 채취에 의한 오염 외에도, 낮은 이방성 구간에서 K3와 K2 축이 거들(girdle)을 형성하는 것은 해당 방향(K2-K3)으로의 grain rolling 현상으로 해석될 수 있으며(Tarling and Hrouda, 1993; Tauxe et al., 1998), 이는 rolling에 요구되는 충분한 세기의 해류(e.g., 고밀도 대륙붕수 유출)가 존재했음을 시사한다. 따라서 낮은 이방성 구간은 낮은 해류 속도보다는 2차 자기조직에 의한 교란을 반영하는 것으로 해석된다.

일부 시료의 오염 가능성에도 불구하고, 편원구조의 자기 이방성 구간(높은 이방성 구간)은 엽층리 실트층과 얇은 역질/사질층이 산출하는 구간과 잘 일치한다(그림 3). 따라서 본 연구시료에서 관찰되는 자기 이방성 변화는 입자크기 변화와 관계없이 저층 해류에 의한 퇴적 기작의 변화, 즉 엽층리 형성 및 키질 작용과 관련된 자성입자 배열의 편원구조 강화를 반영하는 것으로 판단된다. 이러한 등수심 퇴적체의 형성은 기후 변화에 따른 로스해 해류 체계 변화를 반영하며, 한랭한 기간 동안 고밀도 대륙붕수가 약화되고 대륙대 하부에서 로스해 주변을 서쪽 방향으로 흐르는 지형류(로스환류/순환심층수)가 저층 해류로서 연구지역의 퇴적작용에 주요한 영향을 미친 것으로 해석된다(Lucchi et al., 2002; Lucchi and Rebesco, 2007; Kim et al., 2018; Bollen et al., 2022). 연구 시료는 약 70만년 동안 여러 번의 빙하기와 간빙기를 포함할 것으로 추정되지만, 퇴적상에서 각 빙하기-간빙기 주기를 뚜렷하게 식별하기 어렵다 (그림 3a). 그럼에도 불구하고, 로스해 빙상이 기후 전이기에 따라 진화한 것을 고려할 때, 연구 시료의 하부(>~240 cm)에서 관찰되는 엽층리, 자갈층 및 자기 편원구조(그림 3a, 3h, 3k)는 MPT 이후 확장된 로스해 빙상(~800 ka; McKay et al., 2012)과 함께 연구지역에 발달한 지형류의 영향으로 추정된다. 이후 다이아믹트층의 발달(<~240 cm)은 MBT 이후 로스해 대륙붕에 접지된 빙상의 후퇴(~300- 400 ka; McKay et al., 2012; Bollen et al., 2022)와 연관지을 수 있으며, 상부(>~150 cm)에서 나타나는 엽층리, 자갈층 및 자기 편원구조는 플라이스토세 후기 빙하기 동안 연구지역에 지형류가 영향을 미쳤음을 시사한다(그림 3a, 3h, 3k). 이러한 해석은 상세한 연대모델 정립과 다양한 퇴적 지시자를 활용한 추가 연구를

통해 검증되어야 한다.

결과적으로, 본 연구시료에서 자기 이방성 정도(P')의 변동성은 2차 퇴적 자기조직 혹은 일부 잠재적인 시료채취 과정에서의 오염에 의해 해류 속도의 직접적인 지시자로 적용되기 어려운 것으로 판단된다. 그러나 퇴적상 및 퇴적 조직과 자기조직의 전반적인 연관성을 고려할 때, 이방성은 해류 변화에 따른 입자배열 및 퇴적 기작의 변화를 민감하게 반영하여 퇴적환경에 대한 정보를 빠르게 제공할 가능성이 있다. 따라서 이러한 가능성을 확인하기 위해서 향후 다양한 극지역 퇴적물에 대한 자기 이방성 분석을 시도할 필요성이 있으며, 다중 고환경 지시자 분석에 근거하여 보다 종합적인 해석이 요구된다.

5. 결 론

본 연구에서는 퇴적상, 입도분포 및 대자율 이방성 분석 결과를 종합하여 로스해 대륙대에서의 저층 해류 변동성을 조사하였으며, 다음과 같은 결론을 도출하였다.

1) 퇴적상은 풍부한 빙운쇄설물, 생물교란구조 및 모래 함량으로 특징지어지는 다이아믹트와 조립질 입자 및 생물교란구조가 매우 드문 엽층리 실트로 구분된다.

2) 엽층리 실트에 발달된 사엽층리와 파형의 경계부는 지속적인 저층 해류의 영향을 지시하며, 대륙사면으로 공급된 세립질 퇴적물과 로스해 주변을 흐르는 지속적인 지형류에 의해서 형성된 것으로 해석된다.

3) 다이아믹트는 고밀도 대륙붕수 유출과 관련된 높은 에너지의 해류 환경으로 해석되며, 분급성 실트의 함량과 입자크기는 엽층리 실트 내에서 낮은 값을 보여 다이아믹트에 비해 비교적 낮은 에너지의 해류(지형류)의 영향을 지시한다.

4) 자기 이방성 정도(P')는 퇴적상 및 입자크기 변화와 뚜렷한 연관성이 없으며 낮은 이방성 구간은 2차 자기조직에 의한 교란을 반영하는 것으로 판단된다. 반면, 높은 이방성 구간은 강화된 자기 편원구조를 보이며 실트 엽층 및 자갈층 구간에서 저층 해류의 영향을 지시한다. 이러한 결과는 자기 이방성 조직이 로스해 해류 순환에 따른 퇴적 기작의 변화를 민감하게 반영할 가능성을 시사한다.

KOPRI 극지연구소

References

Albot, O.B., 2016, Pleistocene cyclostratigraphy on the continental rise and abyssal plain of the western Ross Sea, Antarctica. MS thesis, Victoria University, Wellington, New Zealand, 171.

Anderson, J.B., Conway, H., Bart, P.J., Witus, A.E., Greenwood, S.L., McKay, R.M., Hall, B.L., Ackert, R.P., Licht, K., Jakobsson, M. and Stone, J.O., 2014, Ross Sea paleo-ice sheet drainage and deglacial history during and since the LGM. Quaternary Science Reviews, 100, 31-54.

Aubourg, C. and Oufi, O., 1999, 11. Coring-induced magnetic fabric in piston cores from the Western Mediterranean. Proceedings of the Ocean Drilling Program, 161, Scientific Results. https://doi.org/10.2973/odp.proc.sr.161.255.1999.

Bollen, M., Riesselman, C.R., Ohneiser, C., Albot, O., McKay, R., Lee, M.K., Yoo, K.-C., Kim, S., Lee, J.I. and Levy, R., 2022, Pleistocene oceanographic variability in the Ross Sea: A multiproxy approach to age model development and paleoenvironmental analyses. Global Planet Change, 216, 103901.

Busetti, M., Caburlotto, A., Armand, L., Damiani, D., Giorgetti, G., Lucchi, R.G., Quilty, P.G. and Villa, G., 2003, Plio-Quaternary sedimentation on the Wilkes land continental rise: preliminary results. Deep Sea Research Part II: Topical Studies in Oceanography, 50, 1529-1562.

Conte, R., Rebesco, M., Santis, L.D., Colleoni, F., Bensi, M., Bergamasco, A., Kovacevic, V., Gales, J., Zgur, F., Accettella, D., Steur, L.D., Ursella, L., McKay, R., Kim, S., Lucchi, R.G. and the IODP Expedition 374 Scientists, 2021, Bottom current control on sediment deposition between the Iselin Bank and the Hillary Canyon (Antarctica) since the late Miocene: An integrated seismic-oceanographic approach. Deep Sea Research Part I: Oceanographic Research Papers, 176, 103606. https://doi.org/10.1016/j.dsr.2021.103606.

Copons, R., Parés, J.M., Dinarès-Turell, J. and Bordonau, J., 1997, Sampling induced AMS in soft sediments: A case study in Holocene (glaciolacustrine rhythmites from Lake Barrancs (central Pyrenees, Spain). Physics and Chemistry of the Earth, 22, 137-141.

De Santis, L., Prato, S., Brancolini, G., Lovo, M. and Torelli, L., 1999, The Eastern Ross Sea continental shelf during the Cenozoic: implications for the West Antarctic ice sheet development. Global Planet Change, 23, 173-196.

Doh, S.J., 1991, Anisotropy of Magnetic Susceptibility and Its Geological Applications. Economic and Environmental Geology, 24, 71-79 (in Korean with English abstract).

Dotto, T.S., Naveira Garabato, A., Bacon, S., Tsamados, M., Holland, P.R., Hooley, J., Frajka-Williams, E., Ridout, A. and Meredith, M.P., 2018, Variability of the Ross Gyre, Southern Ocean: Drivers and responses revealed by satellite altimetry. Geophysical Research Letters, 45, 6195-6204.

Drewry, D.J. and Cooper, A.P.R., 1981, Processes and models of Antarctic glaciomarine sedimentation. Annals of Glaciology, 2, 117-122.

Ellwood, B.B. and Ledbetter, M.T., 1979, Paleocurrent indicators in deep-sea sediment. Science, 203, 1335-1337.

Flinn, D., 1962, On folding during three-dimensional progressive deformation. Quarterly Journal of the Geological Society, 118, 385-428.

Folk, R.L. and Ward, W.C., 1957, A study in the significance of grain size parameters. Journal Sedimentary Petrology, 27, 3-27.

Golledge, N.R., Fogwill, C.J., Mackintosh, A.N. and Buckley, K.M., 2012, Dynamics of the last glacial maximum Antarctic ice-sheet and its response to ocean forcing. Proceedings of the National Academy of Sciences, 109, 16052-16056.

Gordon, A.L., Orsi, A.H., Muench, R., Huber, B.A., Zambianchi, E. and Visbeck, M., 2009, Western Ross Sea continental slope gravity currents. Deep Sea Research Part II: Topical Studies in Oceanography, 56, 796-817.

Gravenor, C.P., Symons, D.T.A. and Coyle, D.A., 1984, Errors in the anisotropy of magnetic susceptibility and magnetic remanence of unconsolidated sediments produced by sampling methods. Geophysical Research Letters, 11, 836-839.

Howe, J.A., Stoker, M.S. and Woolfe, K.J., 2001, Deep-marine seabed erosion and gravel lags in the northwestern Rockall Trough, North Atlantic Ocean. Journal of the Geological Society, 158, 427-438.

Hrouda, F., 1982, Magnetic anisotropy of rocks and its application in geology and geophysics. Geophysical Surveys, 5, 37-82.

Hughes, T., 1973, Is the West Antarctic ice sheet dis-integrating? Journal of Geophysical Research, 78, 7884-7910.

Jacobs, S.S., 2004, Bottom water production and its links with the thermohaline circulation. Antarctic Science, 16, 427-437.

Jacobs, S.S., Giulivi, C.F. and Mele, P.A., 2002, Freshening of the Ross Sea during the late 20th century. Science, 297, 386-389.

Jelínek, V., 1981, Characterization of the magnetic fabric of rocks. Tectonophysics, 79, T63-T67.

Joseph, L.H., Rea, D.K. and Van der Pluijm, B.A., 1998, Use of grain size and magnetic fabric analyses to distinguish among depositional environments. Paleoceanography, 13, 491-501.

Joseph, L.H., Rea, D.K., Van der Pluijm, B.A. and Gleason, J.D., 2002, Antarctic environmental variability since the late Miocene: ODP Site 745, the East Kerguelen sediment drift. Earth and Planetary Science Letters, 201, 127-142.

Joughin, I. and Alley, R.B., 2011, Stability of the West Antarctic ice sheet in a warming world. Nature Geoscience, 4, 506-513.

Jung, J., Park, Y., Lee, K., Hong, J., Lee, J., Yoo, K., Lee, M. and Kim, J., 2019, Clay Mineralogical Characteristics and Origin of Sediments Deposited during the Pleistocene in the Ross Sea, Antarctica. Journal of Mineralogical Society of Korea, 32, 163-172 (in Korean with English abstract).

Kim, S., De Santis, L., Hong, J.K., Cottlerle, D., Petronio, L., Colizza, E., Kim, Y.-G., Kang, S.-G., Kim, H.J., Kim, S., Wardell, N., Geletti, R., Bergamasco, A., McKay, R., Jin, Y.K. and Kang, S.-H., 2018, Seismic stratigraphy of the Central Basin in northwestern Ross Sea slope and rise, Antarctica: Clues to the late Cenozoic ice-sheet dynamics and bottom-current activity. Marine Geology, 395, 363-379.

KOPRI 극지연구소

Knight, M.D. and Walker, G.P.L., 1988, Magma flow directions in dikes of the Koolau Complex, Oahu, determined from magnetic fabric studies. Journal of Geophysical Research: Solid Earth, 93, 4301-4319.

Ledbetter, M.T. and Ellwood, B.B., 1980, Spatial and temporal changes in bottom-water velocity and direction from analysis of particle size and alignment in deep-sea sediment. Marine Geology, 38, 245-261.

Lucchi, R.G. and Rebesco, M., 2007, Glacial contourites on the Antarctic Peninsula margin: insight for palaeoenvironmental and palaeoclimatic conditions. Geological Society, London, Special Publications, 276, 111-127.

Lucchi, R.G., Rebesco, M., Camerlenghi, A., Busetti, M., Tomadin, L., Villa, G., Persico, D., Morigi, C., Bonci, M.C. and Giorgetti, G., 2002, Mid-late Pleistocene glacimarine sedimentary processes of a high-latitude, deep-sea sediment drift (Antarctic Peninsula Pacific margin). Marine Geology, 189, 343-370.

McCave, I.N. and Andrews, J.T., 2019, Distinguishing current effects in sediments delivered to the ocean by ice. I. Principles, methods and examples. Quaternary Science Reviews, 212, 92-107.

McCave, I.N. and Hall, I.R., 2006, Size sorting in marine muds: Processes, pitfalls, and prospects for paleoflow-speed proxies. Geochemistry, Geophysics, Geosystems, 7, Q10N05.

McCave, I.N., Manighetti, B. and Robinson, S.G., 1995, Sortable silt and fine sediment size/composition slicing: parameters for palaeocurrent speed and palaeoceanography. Paleoceanography and Paleoclimatology, 10, 593-610.

McKay, R.M., De Santis, L. and Kulhanek, D.K., 2017, Expedition 374 scientific prospectus: Ross Sea West Antarctic Ice Sheet history. International Ocean Discovery Program, 374.

McKay, R.M., De Santis, L. and Kulhanek, D.K., 2019, Ross Sea West Antarctic Ice Sheet History. Proceedings of the International Ocean Discovery Program, 374.

McKay, R., Naish, T., Powell, R., Barrett, P., Scherer, R., Talarico, F., Kyle, P., Monien, D., Kuhn, G., Jackolski, C. and Williams, T., 2012, Pleistocene variability of Antarctic Ice Sheet extent in the Ross Embayment. Quaternary Science Reviews, 34, 93-112.

McKay, R., Albot, O., Dunbar, G.B., Lee, J.I., Lee, M.K., Yoo, K., Kim, S., Turton, N., Kulhanek, D., Patterson, M. and Levy, R., 2022, A comparison of methods for identifying and quantifying ice rafted debris on the Antarctic margin. Paleoceanography and Paleoclimatology, 37, e2021PA004404.

Morrison, A.K., Hogg, A.McC., England, M.H. and Spence, P., 2020, Warm Circumpolar Deep Water transport toward Antarctica driven by local dense water export in canyons. Science advances, 6, eaav2516.

Ohneiser, C. and Wilson, G.S., 2018, Eccentricity-paced Southern Hemisphere glacial-interglacial cyclicity preceding the middle Miocene climatic transition. Paleoceanography and Paleoclimatology, 33, 795-806.

Ohneiser, C., Yoo, K.-C., Albot, O.B., Cortese, G., Riesselman, C., Lee, J.I., McKay, R., Bollen, M., Lee, M.K., Moon, H.S., Kim, S., Beltran, C., Levy, R. and Wilson, G.S., 2019, Magnetobiostratigraphic age models for Pleistocene sedimentary records from the Ross Sea. Global Planet Change, 176,

36-49.

Orsi, A.H., Johnson, G.C. and Bullister, J.L., 1999, Circulation, mixing, and production of Antarctic Bottom Water. Progress in Oceanography, 43, 55-109.

Orsi, A.H., Smethie, W.M. and Bullister, J.L., 2002, On the total input of Antarctic waters to the deep ocean: A preliminary estimate from chlorofluorocarbon measurements. Journal of Geophysical Research: Oceans, 107, 31-1.

Orsi, A.H. and Wiederwohl, C.L., 2009, A recount of Ross Sea waters. Deep Sea Research Part II: Topical Studies in Oceanography, 56, 778-795.

Parés, J.M., Hassold, N.J.C., Rea, D.K. and van der Pluijm, B.A., 2007, Paleocurrent directions from paleomagnetic reorientation of magnetic fabrics in deep-sea sediments at the Antarctic Peninsula Pacific margin (ODP Sites 1095, 1101). Marine Geology, 242, 261-269.

Paterson, G.A. and Heslop, D., 2015, New methods for unmixing sediment grain size data. Geochemistry, Geophysics, Geosystems, 16, 4494-4506.

Pudsey, C.J., 2000, Sedimentation on the continental rise west of the Antarctic Peninsula over the last three glacial cycles. Marine Geology, 167, 313-338.

Rebesco, M., Hernández-Molina, F.J., Rooij, D.V. and Wåhlin, A., 2014, Contourites and associated sediments controlled by deep-water circulation processes: State-of-the-art and future considerations. Marine Geology, 352, 111-154.

Richter, C., Acton, G., Endris, C. and Radsted, M., 2007, Handbook for shipboard paleomagnetists. Ocean Drilling Program Technical Notes.

Rochette, P., Jackson, M. and Aubourg, C., 1992, Rock magnetism and the interpretation of anisotropy of magnetic susceptibility. Reviews of Geophysics, 30, 209-226.

Schmidtko, S., Heywood, K.J., Thompson, A.F. and Aoki, S., 2014, Multidecadal warming of Antarctic waters. Science, 346, 1227-1231.

Shimono, T., Yamazaki, T. and Inoue, S., 2014, Influence of sampling on magnetic susceptibility anisotropy of soft sediments: comparison between gravity and piston cores. Earth, Planets and Space, 66, 1-8.

Snowball, I., Almqvist, B., Lougheed, B.C., Wiers, S., Obrochta, S. and Herrero-Bervera, E., 2019, Coring induced sediment fabrics at IODP Expedition 347 Sites M0061 and M0062 identified by anisotropy of magnetic susceptibility (AMS): criteria for accepting palaeomagnetic data. Geophysical Journal International, 217, 1089-1107.

Son, M., Kim, I.S., Lee, D., Lee, J.-D., Kim, J.S. and Paik, I.S., 2000, Geological characteristics in the eastern part of the Ulsan Fault area, Korea: Structural geology and anisotropy of magnetic susceptibility (AMS) in the Tertiary Miocene Waup Basin. Journal of the Geological Society of Korea, 36, 195-216 (in Korean with English abstract).

Stevenard, N., Govin, A., Kissel, C. and Van Toer, A., 2023, Correction of the IRD influence for paleo-current flow speed reconstructions in hemipelagic sediments. Paleoceanography and Paleoclimatology, 38, e2022PA004500.

Stow, D.A.V. and Piper, D.J.W., 1984, Deep-water fine-grained sediments: facies models. Geological Society, London, Special Publications, 15, 611-646.

KOPRI 극지연구소

Tarling, D.H. and Hrouda, F. (Eds.), 1993, The magnetic anisotropy of rocks. United Kingdom: Chapman and Hall. Tauxe, L., Gee, J.S. and Staudigel, H., 1998, Flow directions in dikes from anisotropy of magnetic susceptibility data: The bootstrap way. Journal of Geophysical Research: Solid Earth, 103, 17775-17790.

Whitworth III, T., Orsi, A.H., Kim, S.J., Nowlin Jr, W.D. and Locarnini, R.A., 1985, Water masses and mixing near the Antarctic Slope Front. Ocean, ice, and atmosphere: interactions at the Antarctic continental margin, 75, 1-27.

Xuan, C., Channell, J.E.T., Polyak, L. and Darby, D.A, 2012, Paleomagnetism of Quaternary sediments from Lomonosov Ridge and Yermak Plateau: implications for age models in the Arctic Ocean. Quaternary Science Reviews, 32, 48-63.

Yang, T., Zhao, X., Petronotis, K., Dekkers, M.J. and Xu, H., 2019, Anisotropy of magnetic susceptibility (AMS) of sediments from Holes U1480E and U1480H, IODP Expedition 362: sedimentary or artificial origin and implications for paleomagnetic studies. Geochemistry, Geophysics, Geosystems, 20, 5192-5215.

KOPRI
극지연구소

Anisotropy of magnetic susceptibility of sediments in the Ross Sea continental rise, Antarctica: Evaluation of paleocurrent variability reconstruction

Ji Young Shin[1], Min Kyung Lee[2], Myung-Il Kang[2], Young Ji Joo[1]

[1]Pukyong National University
[2]Korea Polar Research Institute

요약: The Antarctic continental margins exhibit unique sedimentary characteristics influenced by climatic changes in glacial environments and oceanic circulation. This study aims to trace the variability of bottom current and associated paleoenvironmental conditions in the Ross Sea continental rise through comprehensive interpretation of sedimentary facies, grain size distribution, and anisotropy of magnetic susceptibility (AMS). The sedimentary facies of the studied core are divided into two, diamictite with abundant ice-rafted debris (IRD) and laminated silt lacking IRD. Silty sediments with well-developed wavy contact and cross laminae indicate the influence of sustained bottom currents. The diamictite layers display faint or absent sedimentary structures and abundant bioturbation, but occasionally contain gravel and sand-rich layers formed by bottom-current winnowing. AMS results show that the degree of magnetic anisotropy (P') has no consistent relationship with sedimentary facies and grain size variations, probably due to disturbances from secondary magnetic fabrics, and is not regarded as a direct proxy for current intensity. However, enhanced oblate fabrics align with the laminated silts and gravel-rich layers, contourite deposition by geostrophic currents flowing around the Ross Sea. These results imply that magnetic fabrics may sensitively reflect sedimentary processes that vary with bottom current systems in the Ross Sea (e.g., lamination and winnowing), highlighting the need for future magnetic studies in various polar environmental settings.

KOPRI 극지연구소

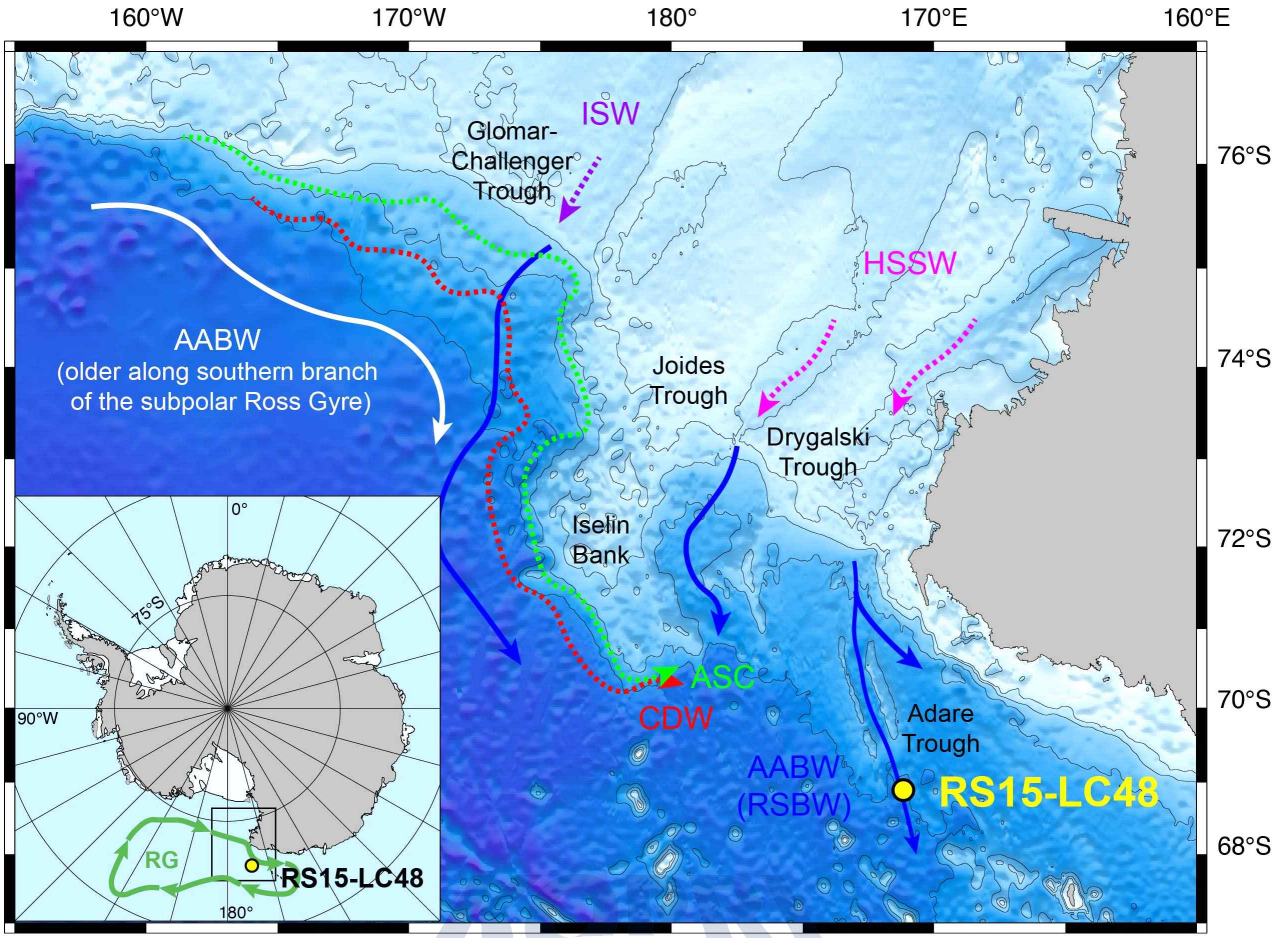


Figure 1. Map of the Ross Sea continental margin and location of the studied core RS15-LC48 (modified from McKay et al., 2017). The principal water masses are illustrated by arrows. ISW (purple): Ice Shelf Water formed by Ross ice shelf melting; HSSW (pink): High Salinity Shelf Water produced on the continental shelf; CDW (red): Circumpolar Antarctic Deep Water; ASC (green): Antarctic Slope Current; AABW (blue and white): Antarctic Bottom Water; RSBW: Ross Sea Bottom Water which is a newly formed AABW from mixture of HSSW and CDW. In the inset: Ross Sea Gyre (RG) modified from Dotto et al. (2018) and the study area (black rectangle).

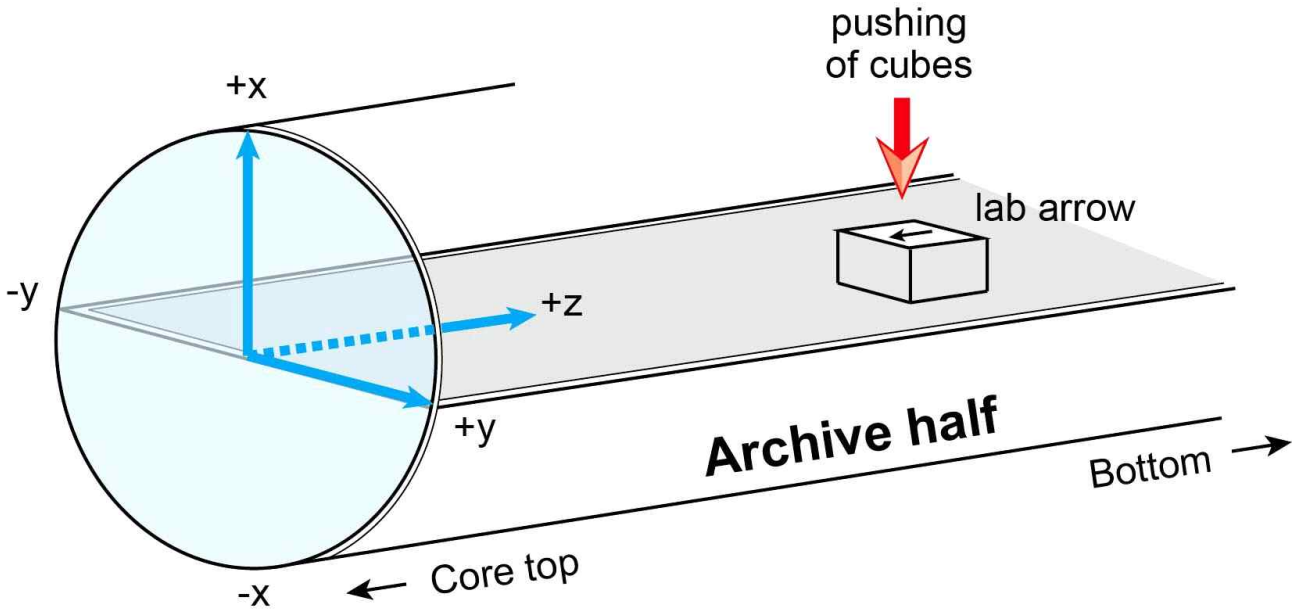


Figure 2. Sampling scheme and sample coordinate system used in this study (after Richter et al., 2007).

KOPRI
극지연구소

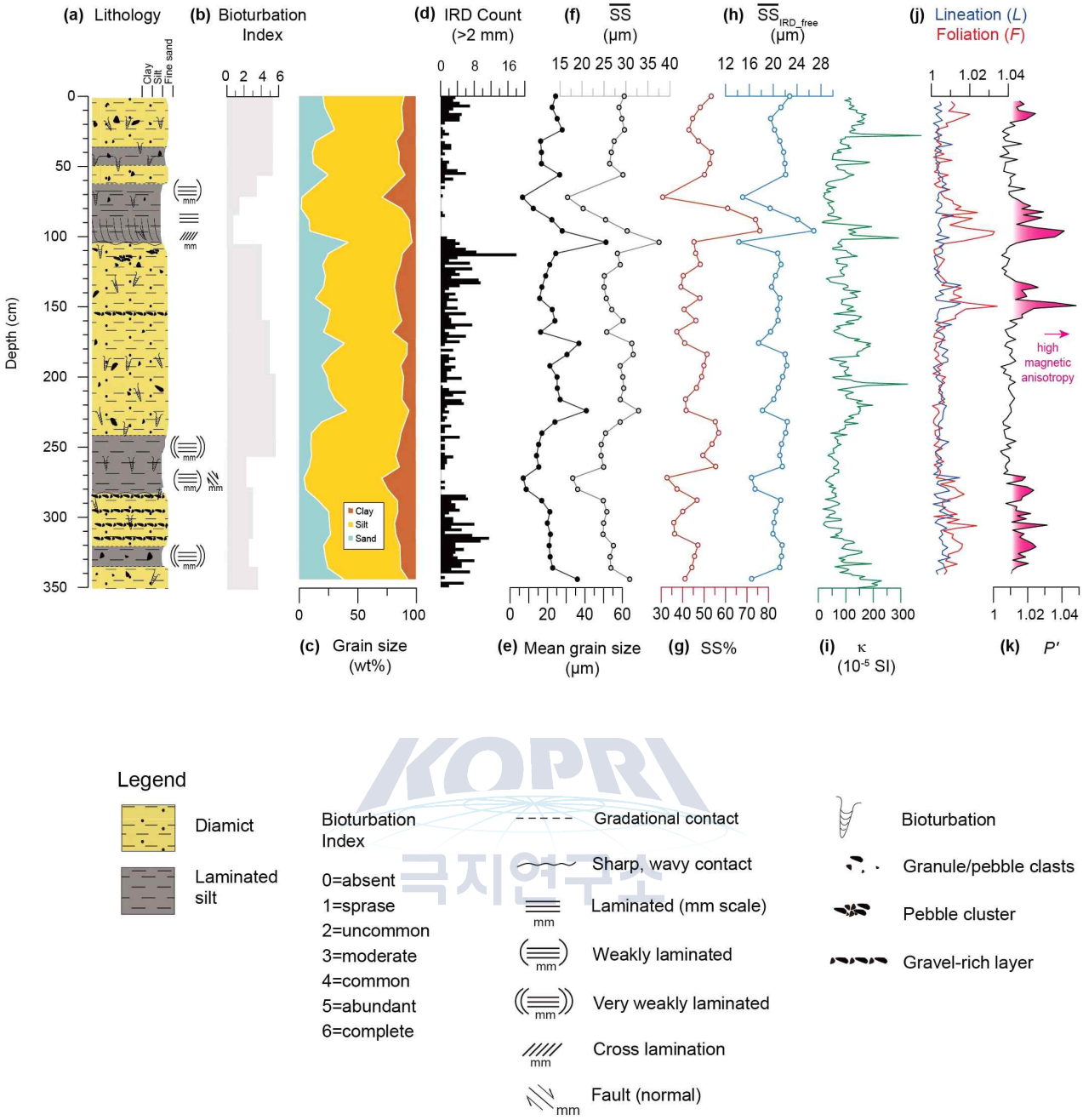
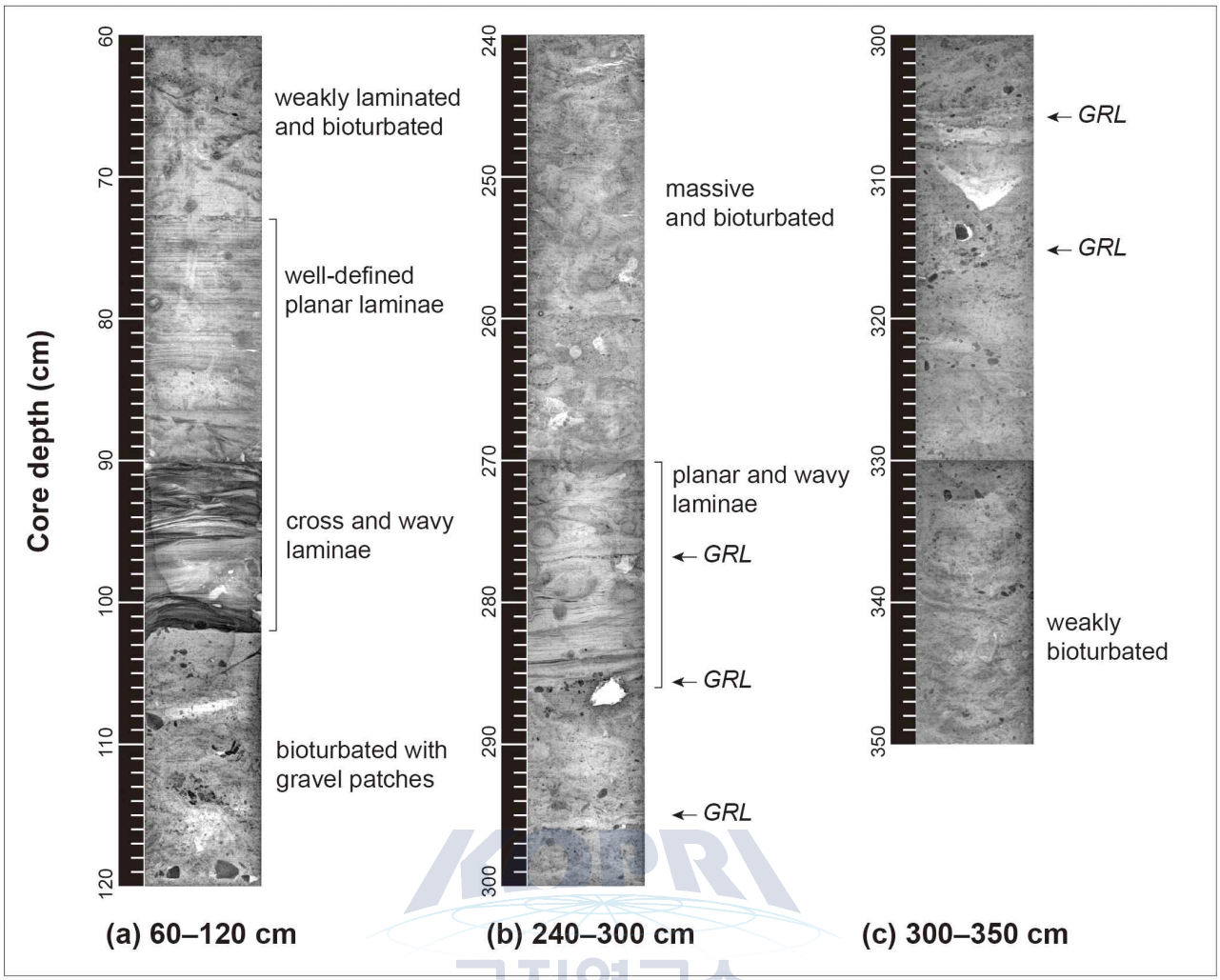


Figure 3. Stratigraphic variations in lithology, grain size and magnetic anisotropy data of core RS15-LC48 (top 350 cm). (a) Lithologic description (modified after Ohneiser et al., 2019), (b) bioturbation index (Albot, 2016), (c) ice-rafted debris (IRD) >2 mm count (McKay et al., 2022), (d) contents of sand (>63 μm), silt (4-63 μm) and clay (>4 μm), (e) mean grain size, (f) mean grain size of sortable silt, (g) content of sortable silt, (h) mean grain size of sortable silt after IRD correction, (i) κ, magnetic susceptibility (Ohneiser et al., 2019), (j) magnetic lineation L and magnetic foliation F, and (k) the corrected degree of anisotropy (P'). Shaded layers represent laminated silts.

KOPRI 극지연구소



KOPRI
극지연구소

Figure 4. X-ray images of core sections showing characteristics of sedimentary structures and texture. (a) 60-120 cm, (b) 240-300 cm, and (c) 300-350 cm. Gravel-rich layers (GRLs) are marked by arrows.

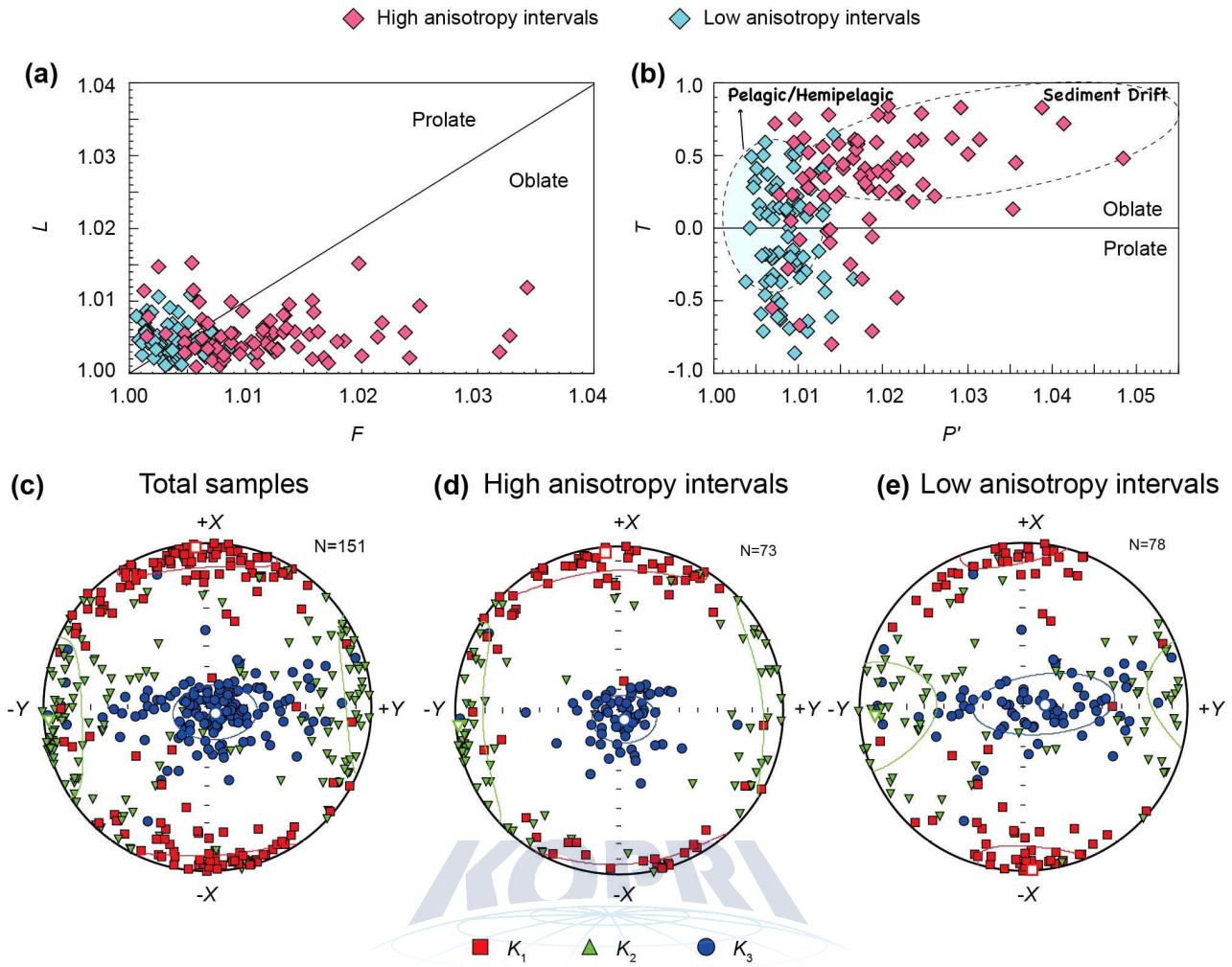
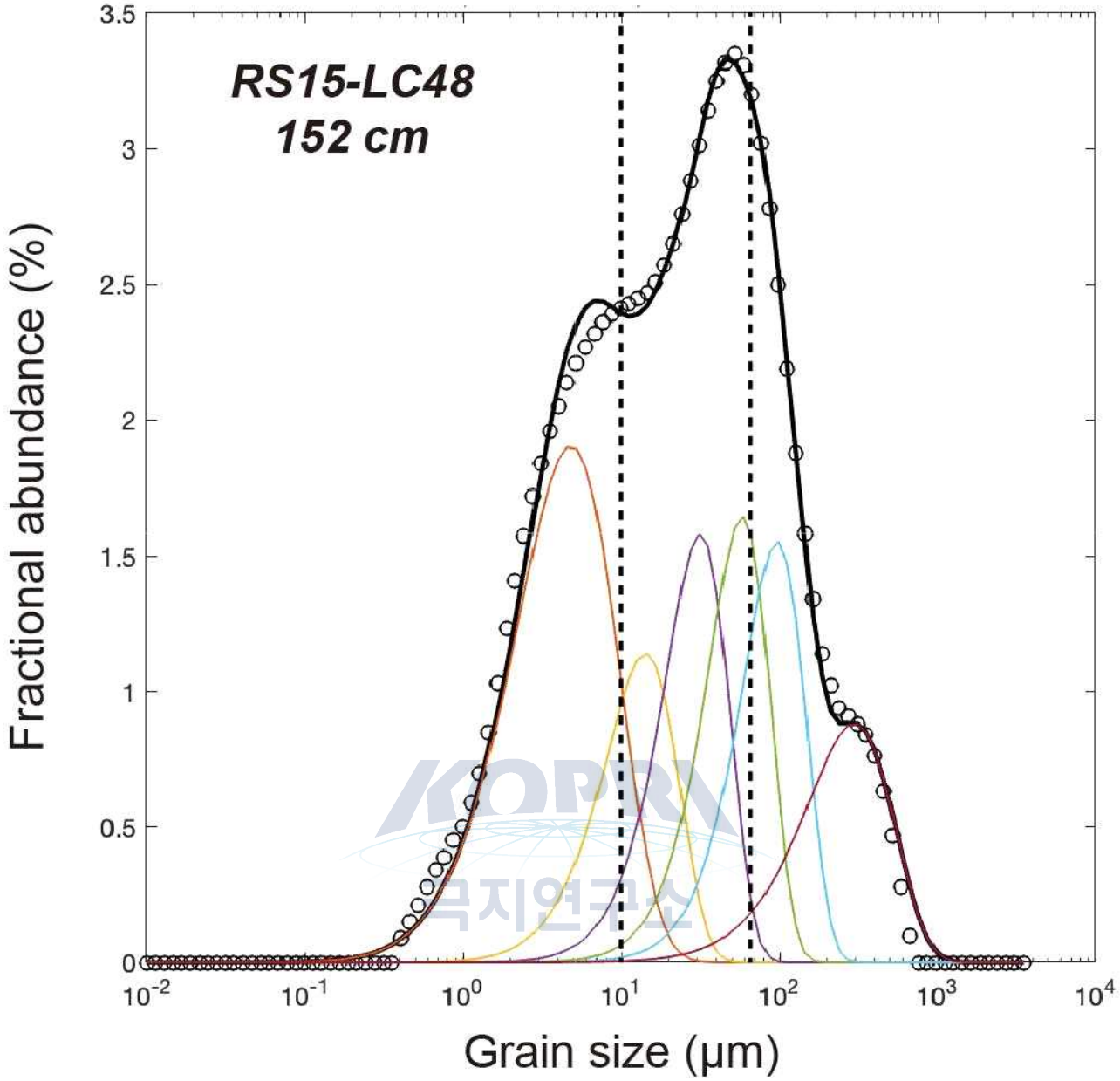


Figure 5. Bivariate plots of AMS parameters and lower hemisphere projections of the three principal AMS axes. (a) Lineation L versus foliation F plotted in a Flinn diagram (Flinn, 1962), (b) The corrected anisotropy degree P' versus the shape parameter T plotted on a Jelínek (1981) plot. Shaded areas in the Jelínek plot represent empirical relationships between magnetic fabric and typical depositional mechanisms determined by Joseph et al. (1998). Projections of the K1 (red), K2 (green), and K3 (blue) axes for (c) the total studied samples, (d) high anisotropy intervals, and (e) low anisotropy intervals. The mean directions of the principal axes are presented as open symbols together with their 95% confidence ellipses.

KOPRI
극지연구소



Supplementary Figure 1. Representative grain size distribution and its unmixing result for IRD-corrected sortable silt calculation. Six End-Members (EMs) are defined in the order of increasing grain size (EM 1-6). EM 1-3 were used as the current-sorted EM group in this study (e.g., Stevenard et al., 2023). Vertical dashed lines indicate the sortable silt range (10-63 μm).

제 33 장

Elemental composition of smectite minerals in continental rise sediments from the Amundsen Sea, West Antarctica, as a tool to identify detrital input from various sources throughout late Quaternary glacial–interglacial cycles[26)]

Young Kyu Park[a], Claus-Dieter Hillenbrand[b], Werner Ehrmann[c], Hanbeom Park[a], Julia S. Wellner[d], Jennifer R. Horrocks[e], Jinwook Kim[a,*]

[a]Department of Earth System Sciences, Yonsei University, Seoul, Republic of Korea; [b]British Antarctic Survey, Cambridge, United Kingdom; [c]Institute for Geophysics and Geology, University of Leipzig, Germany; [d]Department of Earth and Atmospheric Sciences, University of Houston, Houston, TX, USA; [e]Department of Geography, Durham University, Durham, United Kingdom

Abstract: Detrital smectite is a ubiquitous clay mineral in marine sediments and has a variable total Fe, Al, and Mg composition depending on the source, i.e., bedrock or unconsolidated sedimentary strata, the smectite is derived from. Analyses of elemental composition of smectite minerals in marine sediments can help to differentiate the smectite sources and, thus, sediment provenance, with potentially far-reaching paleo-environmental implications. In this study, we investigated the smectite compositions of modern-latest Holocene seafloor surface sediments deposited offshore from the Amundsen Sea drainage sector, where the West Antarctic Ice Sheet is currently unstable and losing mass due to ocean-forced melting, to detect and understand the variabilities of their elemental composition and geographical distribution. The smectite composition in continental rise sediments was compared to that of potential source areas on the Amundsen Sea continental shelf and in the sub-Antarctic South Pacific basin. Furthermore, we analyzed the smectite composition of sediments in continental rise cores deposited during the last glacial and last interglacial periods to reconstruct source variations over glacial-interglacial cycles. In particular, high contents of Al-Fe-rich smectite indicate that the glacial sediments had been supplied from the coastal region around Pine

26) 이 연구 결과는 다음의 논문으로 출판되었음: Park, Y. et al. (2024). "Elemental composition of smectite minerals in continental rise sediments from the Amundsen Sea, West Antarctica, as a tool to identify detrital input from various sources throughout late Quaternary glacial-interglacial cycles" Chemical Geology 657: 122116.

Island Bay by the cross-shelf advance of the West Antarctic Ice Sheet during the last glacial period. This clearly contrasts with the smectite minerals in rise sediments deposited during the present and the last interglacial periods that are composed of two distinct smectite types (Mg-rich and Al-rich, respectively), indicating their supply from multiple sources. During interglacials, Mg-rich smectite is probably transported by Circumpolar Deep Water from the sub-Antarctic South Pacific basin to the continental rise, while Al-rich smectite is supplied as part of ice rafted debris and by marine currents from the coasts around the Amundsen Sea embayment. Our research demonstrates that analysis of the elemental composition of smectite minerals on the Amundsen Sea continental margin provides a valuable tool to trace variations in sources for detrital sediment components and their pathways throughout glacial-interglacial cycles.

1. Introduction

The West Antarctic Ice Sheet (WAIS) is a largely marine-based ice sheet, and has undergone significant thinning and retreat in its Amundsen Sea drainage sector over the last four decades (e.g. Rignot et al., 2019; Smith et al., 2020). It has been suggested that current deglaciation of this sector may culminate in future WAIS collapse in response to continued global warming, which could contribute up to ca. 3-4 m to global sea-level rise (DeConto and Pollard, 2016; Vaughan, 2008). The current mass loss in the Amundsen Sea sector is associated with the upwelling of relatively warm Circumpolar Deep Water (CDW) that intrudes to the inner shelf, causing increased basal melting of ice shelves there and reducing the buttressing effect of these ice shelves for grounded glaciers feeding into them (e.g. Jacobs et al., 2012; Jenkins et al., 2016; Pritchard et al., 2012). These findings that were largely obtained by remote sensing over the last few decades suggest potential WAIS instability, which has been corroborated by ice-sheet model runs (e.g. DeConto and Pollard, 2016). However, to fully comprehend the dynamical behavior of the WAIS, the model simulations need to be complemented with and validated by the long-term ice-sheet record archived in continental margin sediments deposited offshore from the WAIS. Particularly, sedimentary sequences from the Antarctic continental rise can provide valuable high resolution records of ice sheet dynamics and paleo-environmental changes (e.g. Escutia et al., 2009; Hillenbrand and Ehrmann, 2005) because in contrast to sediment records from the shelf and slope erosion by glacial-overriding or reworking by gravitational processes usually do not occur there. Detrital components of marine sediments on the continental rise supplied from the nearby continental shelf or surrounding ocean areas, can be used to reconstruct environmental changes over a wide region. For example, the terrigenous detritus can give clues about

delivery of glacigenic debris by the ice sheet, hemipelagic sediment input by the eastward flowing Antarctic Circumpolar Current (ACC, Fig. 1), and/or supply of suspended particles by regional bottom currents (Hillenbrand et al., 2021; Lucchi et al., 2002; Lucchi and Rebesco, 2007).

An effective strategy for reconstructing past ice sheet dynamics and transport of glacigenic detritus is to investigate sediment provenance using the mineralogical and geochemical characteristics of marine sediments deposited at the periphery of the ice sheet (Cook et al., 2013; Hillenbrand et al., 2003; Licht and Hemming, 2017; Williams et al., 2010; Wilson et al., 2018). For example, depositional processes and transport pathways of terrigenous detritus at present and in the past have been inferred from the spatial and temporal variations in the relative proportions of clay minerals on the continental rise and in the deep sea and their comparison with those of potential source rocks and shelf sediments in nearby coastal areas (Biscaye, 1965; Hillenbrand and Ehrmann, 2001; Hillenbrand et al., 2009a; Hillenbrand et al., 2009b; Hillenbrand et al., 2010; Jung et al., 2019; Pandarinath, 2009; Park et al., 2019; Petschick et al., 1996). Along the West Antarctic continental margin the sources of clay mineral assemblages deposited on the rise have been traced to their potential sources on the Antarctic continent by mapping of distinct clay mineral provinces on the shelf, i.e., a "smectite province" around the South Shetland Islands (northwestern Antarctic Peninsula), a "chlorite province" along the western Antarctic Peninsula coast, an "illite province" offshore from Ellsworth Land, and a "kaolinite province" on the Amundsen Sea shelf (Ehrmann et al., 2011; Hillenbrand and Ehrmann, 2001; Hillenbrand et al., 2003). However, in seafloor surface sediments from the Amundsen Sea continental rise, unusually high smectite contents had been observed that were too high to be explained by smectite supply from nearby shelf sediments only (Ehrmann et al., 2011). Several possibilities were proposed to explain these relatively high smectite contents on the rise: 1) supply from the volcanic Peter I. Island by a westward flowing bottom current; 2) eastward supply in bottom water originating from the Ross Sea region by the ACC; or 3) southward supply of smectite-rich clay from the sub-Antarctic South Pacific basin by a deep-water current (Ehrmann et al., 2011; Hillenbrand et al., 2003). However, none of these hypotheses could be confirmed or refuted by analyzing the clay mineral assemblages alone, even though such studies demonstrated that the smectite contents were also increased in pre-Holocene interglacial sediments on the eastern Amundsen Sea continental rise (Hillenbrand et al., 2009b; Horrocks, 2018).

Thus, smectite minerals in Amundsen Sea sediments may play a critical role for reconstructing provenance and paleo-environmental changes. The term "smectite" is often referred as a group name to swelling 2:1 layered clay-sized phyllosilicates with water molecules and various cations in the interlayer (Weaver and Pollard, 1973). For example,

depending on variation in the octahedral cations, nontronite (Fe-rich), saponite (Mg-rich), and montmorillonite-beidellite (Al-rich) can be distinguished (Velde, 1995; Weaver and Pollard, 1973). Smectites in deep-sea sediments can be of detrital origin or originate from authigenic processes (Chamley, 1994; Deconinck and Chamley, 1995; McKinley et al., 1999). Detrital smectites can be derived from the continent as a product of chemical weathering of volcanic or igneous rocks under warm, semi-arid climate conditions (Chamley, 1989; Righi and Meunier, 1995), or as a product of physical weathering and glacial reworking of hydrothermally altered volcanic bedrock and tephra under (sub-)polar conditions (Jeong et al., 2004). Smectites can also be derived from sediments or metamorphic rocks (Drief and Nieto, 2000). The smectite composition (dioctahedral or trioctahedral smectite) usually depends on the mineral or chemical composition of the weathered source bedrock and sedimentary strata (McKinley et al., 1999). Authigenic smectites can form by the hydrothermal alteration of volcanic glass or volcanic rocks (Chamley, 1989). These authigenic smectites are typically Fe-rich (nontronite) or Mg-rich (saponite) (Hillier, 1995). Distinguishing the different types of smectite may therefore allow to determine transport pathways of sedimentary particles from continental and oceanic sources. Recently, analysis of smectite minerals in late Quaternary marine sediments from the southern Drake Passage and Bellingshausen Sea has been used to reconstruct transport pathways of sedimentary detritus from its West Antarctic sources (Park et al., 2019).

In this study, the elemental compositions of smectite minerals in seafloor surface sediments from the Amundsen Sea continental rise were analyzed by transmission electron microscopy (TEM) and compared with the compositions of smectite minerals in seafloor surface sediments from potential source areas, i.e., the Amundsen Sea continental shelf and the sub-Antarctic South Pacific basin. In addition, sources of smectites in continental rise sediments deposited during the last glacial period and the last interglacial period were investigated to reconstruct glacial-interglacial changes in sediment transport. The results suggest that elemental composition of smectites can be utilized as a new, powerful tool to trace sediment provenance, and improve our understanding of provenance changes in the paleo-record and its relation to past variations in WAIS extent and drainage.

2. Materials and Methods

2.1. Samples

Six seafloor surface sediment samples (0-1 cmbsf depth of BC27 and BC36; 0-3 cmbsf depth of BC480, BC488, BC495 and BC502 [cmbsf: centimeters below seafloor]) recovered with box corers from the Amundsen Sea, including three shelf, one slope, one rise and one

abyssal sample, were analyzed for this study. Core BC480 comes from Pine Island Bay, BC488 from the upper continental slope, BC495 from the continental rise, BC502 from the sub-Antarctic South Pacific basin, BC27 from the Pine Island Glacier front, and BC36 from the Thwaites Glacier front (Fig. 1, Table 1). Our strategy for sample site selection took into account the following two considerations: First, Pine Island Glacier (PIG) and Thwaites Glacier (TG) are by far the largest glacial systems draining ice – and, thus, presumably glacigenic debris – into the Amundsen Sea. Second, previously published results of clay mineral investigations as well as neodymium and strontium isotope analyses on the fine-grained fractions of seafloor surface sediments in the region had revealed that the provenance fingerprints of detritus supplied by PIG and TG are progressively modified along the detritus transport pathway northwards across the shelf by admixture of detritus delivered by ice draining the eastern coastline of the Amundsen Sea embayment and glaciers draining into the Amundsen Sea to the west of TG (Ehrmann et al., 2011; Simoes Pereira et al., 2018; Simoes Pereira et al., 2020).

Seafloor surface sediments at sites BC488 and BC495 are composed of brownish foraminiferal mud, at site BC480 of brownish mud, and at site BC502 of diatomaceous ooze. Based on sedimentation rates derived from existing age models for various cores from the continental shelf and rise of the eastern Amundsen Sea and the sub-Antarctic South Pacific basin (Clark et al., 2024; Esper and Gersonde, 2014; Hillenbrand et al., 2009b; Hillenbrand et al., 2013; Horrocks, 2018; Kirshner et al., 2012), the seafloor surface sediments have a modern to late Holocene age.

In addition, two down-core samples from piston core PC494, which was – together with nearby box core BC495 – recovered from a sediment drift on the continental rise, were analyzed for this study. A glacial sample was obtained from laminated to stratified terrigenous mud at a core depth of 199–202 cmbsf deposited during Marine Isotope Stage (MIS) 2–4 (14–57 ka) and an interglacial sample was obtained from foraminifera bearing-mud at 496–498 cmbsf depth deposited during MIS 5e (116–130 ka) (Horrocks, 2018). For comparison, another sample from sediments deposited during MIS 5e was analyzed from International Ocean Discovery Program (IODP) Expedition 379 Site U1533 (Fig. 1), which had been drilled on the same sediment drift (Gohl et al., 2021). The sample was taken from 54 to 55 cm depth in core section U1533A 1H-1, which corresponds to a subseafloor depth of 2.50 m.

2.2. Sample preparation

Sample preparation for X-ray diffraction (XRD) analysis followed the methods described by Jackson (1969). The sediment samples were treated with hydrogen peroxide (30% H2O2, 9.79 M) to disperse the particles by removing the organic matter. In addition, the

sediment samples were treated with 1 N NaOAc (pH 5) to remove carbonate (Jackson, 1969). The clay fraction <2㎛ was then collected through centrifugation at 1000 rpm for 2 min. Air-dried clay samples, prepared by the filter-peel method using a 0.45-㎛ membrane filter paper, were placed on a slide glass for the diffractometer measurements (Moore and Reynolds Jr, 1989), and then the mounts were solvated overnight with ethylene glycol in a desiccator to measure an ethylene-glycolated clay sample.

Sediment samples were also impregnated with LR White resin followed by the structural water exchange procedure (Kim et al., 1995) to measure the petrophysical properties of smectite using transmission electron microscopy (TEM). This method allows to prevent the collapse of the smectite layer to 10 Å identical to mica when subjected to the high-energy electron beam during TEM operation, and thus to distinguish smectite layers by measuring layer spacing (Kim et al., 1995). The impregnated samples were cut into 120-nm thick sections using a diamond knife ultramicrotome (ULTRACUT UCT, Leica, installed at Eulji University, Seongnam, Korea) and then placed on a holey carbon TEM grid (Kim et al., 1995; Yang et al., 2016).

2.3. X-ray diffractometry

The XRD profiles of the air-dried and glycolated clay samples were recorded in the range 2°-40° 2Θ and 2°-30° 2Θ, respectively, with a scanning speed of 1.5°/min at a step size of 0.02° using a Rigaku MiniFlex II diffractometer at Yonsei University, Seoul (Korea), with a CuKα radiation source at 30 kV and 15 mA. The receiving and divergence slit sizes were 0.3 mm and 1.25°, respectively. The Crystallographica Search-Match program (version 2.0.3.1) was used to identify the major clay minerals and semi-quantitative analysis of clay minerals were performed by comparing the basal reflections for the glycolated and air-dried XRD profiles (method in the Appendix A). For the glycolated sample, clay minerals were identified by 17 Å peak for smectite, 10 Å peak for mica, and 7 Å peak for chlorite and kaolinite. Kaolinite and chlorite were differentiated by resolving the (002) kaolinite peak and (004) chlorite peak at 3.57 and 3.54 Å, respectively (Biscaye, 1964; Ehrmann et al., 2011). Semi-quantification of R0 mica/smectite mixed layer in the glycolated samples was confirmed by Sybilla method (Drits and Sakharov, 1976; McCarty et al., 2009). R1 mica/smectite mixed layer was confirmed by the appearance of peaks at 9.84° and 15.74° 2Θ (Kim et al., 2019; Park et al., 2024).

2.4. Transmission Electron Microscopy (TEM)

A JEOL JEM-F200 transmission electron microscope fitted with an energy-dispersive X-ray spectrometer (EDS) at Yonsei University was operated at a voltage of 200 kV to

acquire the physico-chemical properties of smectite. K-factors for EDS analysis can be obtained by the transformation of intensity ratio to concentrations of real standards (Cliff and Lorimer, 1975). Theoretically calculated standard can generate error of chemical quantification compared to the directly determined in the used equipment with standard materials (Conconi et al., 2023). However, the difference between calculated factor and real factor of major elements in smectite are not dramatics (Conconi et al., 2023), not greatly affecting to the final quality of the structural formula of smectite. In addition, all smectite analyses were performed with the same equipment, so the same errors affected all analyses, and comparisons are not affected by these errors. Hundreds of bright-field lattice fringe images with corresponding selected-area electron diffraction (SAED) patterns and EDS for smectite clay minerals were recorded; they were analyzed using the DigitalMicrograph TM software (Version 3.22. 1461. 0, Gatan Inc., Pleasanton, CA, USA).

2.4.1. Determining elemental composition of smectite and visualization in a ternary diagram

The quantification of structural composition of smectite was calculated based on 10 oxygen atoms and 2 hydroxyl groups (Christidis et al., 2023; Marshall, 1935). In total, we analyzed ~240 smectite packets from all sediment samples (at least 10 packets per sample). Because of limitation of TEM-EDS quantification, the distribution of Al between tetrahedral and octahedral position and possibility of interlayer Mg could be affected by the intrinsic errors. Therefore, the overall proportions of the Al-Mg-Fe instead of the octahedral cation in smectite minerals from each sediment samples are compared. The composition ratio of total Al-Mg-Fe of individual smectite minerals from each surface sediment sample characterizing a potential source area (i.e., samples BC480, BC488, BC27, BC36 and BC502) are summarily shown as a compositional field for each sample in the ternary diagram, whereas the Al-Mg-Fe ratios of individual smectite minerals from the sediment samples of cores PC494, BC495 and U1533 are plotted as individual data points in the same ternary diagram (Appendix A; Table A.2-10 and Appendix B). Furthermore, the similarity between the total Al, Mg, and Fe compositions of smectites from each sediment sample was evaluated using the *Kolmogorov-Smirnov (K-S) method* (Stuart and Ord, 1999). The K-S statistical test is a nonparametric test expressing the cumulative distributions of data which are compared both visually and by cumulative frequencies. The maximum absolute difference between the two cumulative distribution functions (D-statistic) determines the similarity, with a smaller D-statistic value indicating stronger similarity (Appendix A; Table A.11).

3. Results

3.1. Clay mineral composition

Major components of the clay fraction <2㎛ of the sediment samples (BC495, PC494, BC480, BC488, BC502, BC27, and BC36) are the clay minerals smectite (Sme, 17Å, glycolated), Mica (Mca, 10Å), chlorite (Chl, 14 and 7Å) and kaolinite (Kln, 7Å), which were identified in XRD profiles for the air-dried and ethylene-glycolated samples (Fig. 2). Non-clay minerals, such as quartz (Qz), plagioclase (Pl), and pyroxene (Px) were also identified in all clay samples. Kaolinite and chlorite were differentiated by resolving the (002) kaolinite peak and (004) chlorite peak at 3.57 and 3.54 Å, respectively (Fig. 2). The proportion of clay minerals from continental shelf (BC480, BC27, and BC36) sediment are high mica contents (28-67%), while sediment (BC502) from South Pacific Basin reveals a relatively high content of smectite (49%) and low content of kaolinite (5%). Furthermore, it is noticeable that clay mineral contents in BC495 (smectite (22%), mica (45%) and kaolinite (14%)) and in MIS 5 in PC494 (smectite (31%), mica (43%) and kaolinite (9%)) are clearly contrast with those in MIS 2-4 in PC494 (smectite (16%), mica (54%), and kaolinite (19%)) (Appendix A; Table A.1). The appearance of R1 mica/smectite mixed layers is not measured (XRD peak at 9.84° and 15.74° 2Θ) for the samples (Fig. 2), except BC36 showing minor content of R0 mica/smectite mixed layer (~6 wt%) confirmed by Sybilla method (Appendix A; Table A.1) resulting in the relatively intense smectite peak (17Å) after glycolation.

KOPRI 극지연구소

3.2. Results of Transmission Electron Microscopy (TEM) analysis

3.2.1. Identification of smectite minerals and semi-quantification of their composition by energy-dispersive X-ray spectrometry (EDS)

Representative TEM micrographs of clay packets show layer spacings ranging from 1.1 to 1.3 nm and layer terminations on the lattice fringe images that correspond to a diffuse d001 = 1.09-1.17 nm of SAED patterns (insets in Fig. 3a), typical for smectite. The aforementioned inset diffuse SAED patterns indicate that the smectite layers have a turbostratically disordered structure due to the variations in elemental composition, layer periodicity, and layer terminations. Structural elemental compositions of the smectites revealed by TEM-EDS (Fig. 3b) show a lower Al/Si ratio (~0.4), K (~0.2) and variations in octahedral cations (Fe, Al, Mg) (Table 2, and Appendix A; Table A.2-10). Representative EDS spectra of the smectite minerals from cores BC495, PC494 (MIS 5e) and BC502 show a higher intensity of Mg compared to smectite minerals in the other sediment samples. The average structural formula of smectites from all surface sediment samples are summarized in Table 3.

3.2.2. Al-Fe-Mg compositions of smectites

The compositional Al-Fe-Mg fields defined by the composition of the smectite minerals from potential modern sediment sources, such as PIG (BC27), TG (BC36), Pine Island Bay (BC480), the eastern Amundsen Sea embayment slope (BC488), and the sub-Antarctic South Pacific basin (BC502), are given in Appendix A. Tables A.2, A.3, A.7, A.8, A.9 and visualized in the ternary diagram of Fig. 4, where also the smectite compositions of modern-late Holocene (BC495) as well as last glacial and last interglacial (both PC494) sediment samples from the continental rise are plotted. The smectites from the continental shelf and slope (BC27, BC36, BC480 and BC488) have on average high Al contents (58%; full range 23-91%), intermediate Fe contents (29%; full range 7-64%) and low Mg contents (13%; full range 2-27%) (Appendix B). The smectites from the sub-Antarctic South Pacific basin (BC502) reveal on average intermediate Mg (31%; full range 16-55%), Fe (39%; full range 17-55%) and Al contents (30%; full range 8-67%). Smectites in modern-late Holocene sediments from continental rise site BC495 are on average characterized by high Al contents (52%; full range 23-90%) and intermediate Fe (28%; full range 3-48%) and Mg contents (20%; full range 7-47%). This composition differs from that of smectite minerals deposited at nearby rise site PC494 during MIS 2-4, which have on average comparable Fe contents (25%; full range 14-39%), but higher Al (62%; full range 46-76%), and lower Mg contents (13%; full range 10-21%). The smectite minerals in the MIS 5e sediments of continental rise cores PC494 and U1533 have on average intermediate Al (45%; full range 17-72%), Fe (38%; full range 12-59%) and Mg contents (20%; full range 11-36%) (Appendix B). In general, the Al, Mg and Fe contents in smectites of interglacial sediments from the Amundsen Sea continental rise show a relatively large compositional variability.

3.3. K-S tests of smectite compositions

The Al-Mg-Fe compositions of smectites in the interglacial and glacial sediments from rise sites PC494 and BC495 were statistically compared with those of smectites from potential source areas on the Amundsen Sea shelf and in the sub-Antarctic South Pacific basin using cumulative distribution functions (Fig. 5) and D-statistics (Appendix A; Table A.11). The cumulative distributions of Al, Mg, and Fe in smectites from the glacial sample from core PC494 are visually similar to those of smectites in modern-late Holocene sediments from the Amundsen Sea continental shelf and slope. This similarity is also evident from the D-statistics of Al (0.3), Mg (0.3) and Fe (0.3). The cumulative distributions of Al, Fe and Mg composition in smectites from the interglacial samples at rise sites PC494 and U1533 (MIS 5e) as well as BC495 (modern-late Holocene) have intermediate values between those of smectites on the

continental shelf and slope and in the sub-Antarctic South Pacific basin. Similarity of elemental compositions between interglacial smectites from rise sites BC495 [Al (0.64), Mg (0.47) and Fe (0.60)] and PC494 and U1533 (MIS 5e) [Al (0.48), Mg (0.56) and Fe (0.27)] and modern-late Holocene smectites from site BC502 was calculated in D-statistics (Appendix A; Table A.11).

4. Discussion

4.1. Geographical variability in elemental composition of smectite

The clay mineral assemblages in core BC495 and PC494 (MIS 5e) in continental rise exhibit significantly higher smectite contents than MIS 2-4 in PC494 (Appendix A; Table A.1). It is necessary to distinguish various types of smectite likely to be transported from multi-provenance (Park et al., 2019) on the Amundsen Sea continental rise. The elemental compositions of smectites from the potential source areas on the Amundsen Sea shelf and slope (BC27, BC36, BC480, BC488) and the sub-Antarctic South Pacific basin (BC502) define two groups: 1) Al-rich smectites (neatly dioctahedral smectite) with intermediate Fe contents in samples from the former area and 2) additional presence of Mg-rich smectites (minor component of trioctahedral smectite and/or montmorillonite component) in the sample from the latter area (Fig. 4, Table 2 and Appendix B). Smectites in the sediments samples in this study are in general dioctahedral smectite, however sums of octahedral cations higher than 2 (Appendix A; Table A.2-10), likely due to the interlayer Mg or mixing with minor content of trioctahedral smectites. Hence, when sum of the octahedral cation is too high and the interlayer charge is too low as noted interlayer Mg must be present in Table A.2-10 in Appendix A (Elert et al., 2018; Garcia-Romero et al., 2021; Sanchez-Roa et al., 2018).

Al-Fe rich smectites in sample BC27 recovered in front of PIG are probably supplied with detritus derived from pre-Oligocene sediments that contain weathering products of altered Jurassic granites and Paleozoic-Mesozoic granitoids underlying the PIG drainage basin (Simoes Pereira et al., 2018; Simoes Pereira et al., 2020). These acidic and intermediate igneous rocks are mainly composed of quartz, plagioclase and alkali feldspar. Of that, plagioclase and alkali feldspar can produce dioctahedral smectites as weathering products (Aoudjit et al., 1995). The presence of pre-Oligocene sedimentary strata is indicated by the relatively high content of kaolinite, which is a typical weathering product of (sub-)tropical climate conditions, both in sample BC27 and in other sediment samples close to the PIG grounding line (Ehrmann et al., 2011; Simoes Pereira et al., 2020). Some additional relatively Fe-rich smectite may come from weathering products of Fe-rich minerals (i.e. biotite and

pyroxene), which are typical components of mafic-rich basaltic rocks or volcaniclastics (Chang et al., 1986; Hillier, 1995). Basaltic rocks of Miocene to recent age are widespread in the hinterland of the Amundsen Sea embayment (e.g. LeMasurier, 2013; Simoes Pereira et al., 2018), with the presence of hyaloclastic deposits at volcanic centers documenting that some eruptions occurred in contact with ice (e.g. LeMasurier, 2002), which may have produced smectite.

Abundant Al-rich and Fe-rich smectites in sample BC36 recovered in front of TG are likely supplied with detritus originating from subglacial mafic volcanic rocks (de Vries et al., 2018) and biotite-bearing granitoids, as also suggested by Sr and Nd isotope data (Simoes Pereira et al., 2020). Again, these smectites are highly likely to be eroded from sedimentary strata containing detritus derived from these igneous rocks (Drief and Nieto, 2000), because the kaolinite contents in sample BC36 and other samples taken in front of TG are even higher than in samples close to PIG (Ehrmann et al., 2011; Simoes Pereira et al., 2020). Minor contents of R0 mica/smectite mixed layer supported detrital sediment could be also derived from diagenetic sediments (Nieto et al., 1996). Even though there are hardly any outcrops within the TG and PIG catchments, which makes it difficult to accurately interpret the geological sources for the smectites, our findings together with previously published data (Ehrmann et al., 2011; Simoes Pereira et al., 2018; Simoes Pereira et al., 2020) point to recycling and mixing of detritus during subglacial erosion and transport.

Sample BC480 from Pine Island Bay indicates supply of some additional Al-rich smectite minerals, which may reflect delivery of detritus derived from the east coast of Pine Island Bay (Canisteo Peninsula) and/or eroded by glaciers feeding into the Crosson Ice Shelf directly to the east of TG (Simoes Pereira et al., 2020), and from sedimentary strata, such as the Cretaceous to early Neogene sediments cropping out at/near the seabed on the southern Amundsen Sea embayment shelf (Gohl et al., 2017; Klages et al., 2020; Nieto et al., 1996).

Notably, the Mg contents of smectites in the shelf samples never exceed 27%, whereas the smectites in sample BC502 from the sub-Antarctic South Pacific basin have Mg contents up to 55%. These Mg-rich smectites probably result from the submarine alteration of volcanic glass or oceanic crust basalt, including ferro-magnesian minerals in hydrothermal environments (Garcia-Romero et al., 2005; Hillier, 1995; McKinley et al., 1999; Mcmurtry and Yeh, 1981). Such processes have been reported from the sub-Antarctic South Pacific basin (Hollister and Worstell, 1976).

Smectite minerals in the Amundsen Sea continental rise samples PC494 and BC495 are, as in other Neogene and Quaternary Antarctic continental rise sediments (e.g. Escutia et al., 2009; Hillenbrand and Ehrmann, 2005), probably mainly of detrital origin but may also include authigenic smectites formed in the sub-Antarctic Pacific basin. High K contents in interlayer of smectite (higher than Ca), also supported that those smectite, are mainly detrital

smectites in marine environments (Drief and Nieto, 2000). Smectites in the glacial sediments at site PC494 have high Al- and low Mg-contents, comparable to smectites in the modern-late Holocene sediments from the Amundsen Sea continental shelf (Fig. 4). In contrast, the smectite assemblages in the interglacial rise sediments (MIS 1 [0-14 ka] in BC495 and MIS 5e in PC494 and U1533) include, besides Al and Fe enriched smectite minerals, additionally Mg enriched smectites (Fig. 4 and Table 2). In this respect, the smectites deposited on the Amundsen Sea continental rise during interglacial periods, especially the smectites in core BC495, show some similarity to smectites from site BC502 in the sub-Antarctic South Pacific basin (Fig. 4). In addition, the most frequent of smectites in continental shelf are predominantly beidellites, but some smectites in BC495 and BC502 recognized by Si near 4 atoms per formula unit and high Mg contents are closely corresponding to montmorillonite (or intermediate cases). (Weaver and Pollard, 1973). This finding suggests that during interglacials minor quantities of trioctahedral Mg-rich smectites and/or montmorillonite components (Mg-rich) are advected southwards from the sub-Antarctic South Pacific Basin towards the Amundsen Sea continental margin by bottom and deep waters, such as CDW. The cumulative distribution functions (Fig. 5) and D-statistics (Appendix A; Table A.11) confirm the similarity of smectite elemental compositions in the interglacial continental rise samples with those in BC502.

However, the Mg contents in smectites from the MIS 5e samples of cores PC494 and U1533 are generally lower (≤36%) than in smectites from the nearby surface sediment sample BC495 (≤47%), and the MIS 5e smectites also contain less Al (<72%) but more Fe (≤ 59%) than the smectites in the surface sediment sample (Al ≤90%, Fe ≤48%; Appendix B). These differences in Al, Mg and Fe contents between late-Holocene and MIS 5e smectites from the Amundsen Sea continental rise could be due to different environmental conditions between the modern and the last interglacial. For example, less Al-rich smectite might have been supplied to the deep Amundsen Sea from the Antarctic continent during MIS 5e, when the WAIS is assumed to have been much more retreated than today (e.g., DeConto and Pollard, 2016; Dutton et al., 2015; Lau et al., in press). Alternatively, bottom water advection to the Amundsen Sea continental rise during MIS 5e could have been different from MIS 1. All studied rise sites are today located within the eastward flowing ACC (Gohl et al., 2021; Horrocks, 2018). Grain-size proxy data from a sediment core in Drake Passage have shown that ACC flow speed was not only consistently higher during interglacials than during glacials throughout the last 1.3 Myr, but also that ACC current speed was higher during MIS 5e than during MIS 1 (Toyos et al., 2020). This may indicate that during the last interglacial period more fine-grained detrital particles originating from the Ross Sea sector, including smectites with a different Al-Mg-Fe composition, were advected eastward to the Amundsen Sea continental rise than during the present interglacial.

4.2. Sediment transport to the Amundsen Sea continental rise throughout a glacial-interglacial cycle

Based on the possible sources of smectite in the Amundsen Sea sector of West Antarctica and the sub-Antarctic South Pacific basin identified in this study and previously reported temporal changes in clay mineral assemblages on the Amundsen Sea continental rise (Hillenbrand et al., 2002; Hillenbrand et al., 2009b; Horrocks, 2018), the following transport and depositional model for glacial-interglacial cycles is suggested (Fig. 6).

During a glacial period, the grounding line of the WAIS advanced across the Amundsen Sea shelf to or at least close to the shelf edge (cf. Gohl et al., 2013; Larter et al., 2014). This ice advance was focused in paleo-ice streams that emanated from the mouths of major modern ice streams, such as PIG and TG (Larter et al., 2014), from where the potential source samples for this study were selected. Moreover, annual sea ice cover over the continental slope and rise lasted much longer during glacial periods than during interglacial periods and was possibly even perennial during glacial maxima (Bostock et al., 2013; Konfirst et al., 2012). During the glacial maxima the merged Pine Island-Thwaites paleo-ice stream accumulated large volumes of eroded glacigenic debris at the shelf break. This material was subsequently transported down the continental slope by gravitational processes, such as slumps and debris flows, and further down to the continental rise by turbidity currents, with bottom currents redistributing the fine-grained particles and accumulating them as sediment drifts (Dowdeswell et al., 2006; Hillenbrand et al., 2009b; Horrocks, 2018; Uenzelmann-Neben and Gohl, 2012) (Fig. 6). As for other parts of the West Antarctic margin, meltwater plumes may also have contributed to the deposition on the continental rise during times of maximum ice-sheet extent (Lucchi and Rebesco, 2007; Pudsey, 2000). This proposed depositional model is consistent with the previously reported increase of kaolinite in the glacial sediments on the Amundsen Sea rise (Hillenbrand et al., 2002; Hillenbrand et al., 2009b; Horrocks, 2018) and the dominance of Al-rich and Mg-poor smectites in the MIS 2-4 sediments at site PC494 reported here. The Al-Fe-Mg composition of smectites deposited on the continental rise during the last glacial period generally matches that of smectites characterizing the modern-late Holocene sediments on the continental shelf (BC488, BC480, BC27, and BC36). Conversely, there is no evidence for the contribution of any Mg-rich smectites from the sub-Antarctic South Pacific basin to the sediment deposition on the rise during glacials (Fig. 4), suggesting an only weak advection of deep and bottom waters, including CDW, towards the West Antarctic margin.

At the beginning of an interglacial period, the sedimentary processes on the Amundsen Sea continental rise were mainly controlled by the retreat of the WAIS from the outer shelf. The grounding line of the WAIS started to retreat towards today's coastline of

the Amundsen Sea embayment (cf. Larter et al., 2014), and the long-lasting annual sea ice cover over the continental slope and rise gave way to longer open-marine conditions throughout the year (Bostock et al., 2013). With progressive grounded ice retreat the smectite contents on the rise, like in the modern-late Holocene sediments at site BC495 and the MIS 5e sediments at site PC494, increased in response to reduced offshore supply of kaolinite enriched detritus (Hillenbrand et al., 2009b; Horrocks, 2018). During interglacial periods terrigenous detritus was transported from West Antarctica to the continental rise mainly as iceberg rafted debris (IRD), which comprises material of all grain sizes, with the icebergs drifting within surface currents associated with the Antarctic Coastal Current and the ACC (Lucchi et al., 2002). This is also documented by the predominance of Al rich smectites with intermediate Fe contents in the interglacial sediment samples from cores BC495, PC494 and U1533 (Fig. 4). In contrast, aeolian supply of detritus to the West Antarctic continental rise was negligible during interglacial periods because the terrigenous component of the interglacial sediments is dominated by detritus derived from West Antarctica rather than dust derived from South America or Australia (e.g., Wengler et al., 2019).

In addition to the Antarctica-derived detritus, the presence of Mg-enriched smectites in the interglacial sediments at rise sites BC495, PC494 and U1533 indicates supply of fine-grained particles from the sub-Antarctic South Pacific basin (Fig. 4). These Mg-rich smectites were current-transported to the continental rise within deep and bottom waters, such as CDW, that probably flowed eastward within the ACC before being advected southward towards the Antarctic continental margin (Fig. 1). Both sediment core data from the Amundsen Sea shelf and ice-sheet models had previously indicated that intensified CDW advection towards the West Antarctic margin played a crucial role in forcing WAIS retreat from the outer shelf during past deglaciations (Hillenbrand et al., 2017; Pollard and DeConto, 2009).

5. Conclusions

Glacial-interglacial provenance changes of sediments from the Amundsen Sea continental rise were investigated by comparing the elemental composition of smectite clay minerals with those of potential sources areas. Al-Fe rich smectite (dioctahedral smectite dominant) in glacial sediment are mainly originated with detritus derived from weathering products of igneous rock or sedimentary material. Conversely, with progressive grounded ice retreat, the presence of Mg-rich smectite (montmorillonites and/or some trioctahedral smectites) could be supplied by the current-transportation, such as CDW, that advected southward towards the Antarctic continental margin. The observed glacial-interglacial changes

in smectite composition can be explained by varying contributions from smectite sources located under the Amundsen Sea drainage sector of the WAIS and on the Amundsen Sea continental shelf on one hand and the sub-Antarctic South Pacific basin on the other hand. The new results help to develop and refine a sediment transport and depositional model for the Amundsen Sea continental margin throughout late Quaternary glacial-interglacial cycles in relation to paleo-environmental changes, especially past WAIS dynamics.

KOPRI
극지연구소

서남극 아문젠해 대륙사면 퇴적물 내 스멕타이트 광물의 원소 조성을 활용한 제4기 빙기-간빙기 주기 동안 쇄설성 물질의 기원지 규명 연구

Young Kyu Park[a], Claus-Dieter Hillenbrand[b], Werner Ehrmann[c], Hanbeom Park[a], Julia S. Wellner[d], Jennifer R. Horrocks[e], Jinwook Kim[a]

[a]Department of Earth System Sciences, Yonsei University, Seoul, Republic of Korea; [b]British Antarctic Survey, Cambridge, United Kingdom; [c]Institute for Geophysics and Geology, University of Leipzig, Germany; [d]Department of Earth and Atmospheric Sciences, University of Houston, Houston, TX, USA; [e]Department of Geography, Durham University, Durham, United Kingdom

요약: 쇄설성 스멕타이트는 해양 퇴적물에 보편적으로 존재하는 점토광물로, 기원지(예: 기반암 또는 미고결 퇴적층)에 따라 Fe, Al, Mg 조성이 다양하게 나타난다. 따라서 해양 퇴적물 내 스멕타이트의 원소 조성을 분석하면 스멕타이트의 기원을 구분하고 퇴적물 기원지를 추적할 수 있으며, 이는 고환경 해석을 제공할 수 있다. 본 연구에서는 현재 급격한 빙상 용융을 겪고 있는 서남극 빙상의 아문젠해 전면 해역에서, 최후기 홀로세의 표층 퇴적물에 포함된 스멕타이트 원소 조성의 변동성과 지리적 분포를 규명하기 위해 스멕타이트 조성을 조사하였다. 또한 대륙사면 퇴적물 내 스멕타이트 조성을 아문젠해 대륙붕의 잠재적 기원지 및 아남극 남태평양 분지의 잠재적 기원지와 비교하였다. 더 나아가 최후 빙하기와 최후 간빙기에 대륙사면에 퇴적된 코어 퇴적물의 스멕타이트 조성을 분석하여, 빙하기-간빙기 주기 동안 기원지 변화를 복원하였다. 특히 Al-Fe 스멕타이트의 높은 함량은 최후 빙하기 동안 서남극 빙상이 대륙붕을 가로질러 전진하면서 파인섬 만 주변 연안 지역에서 공급된 물질이 빙기 퇴적물에 우세했음을 시사한다. 이는 현생 및 최후 간빙기에 퇴적된 대륙사면 퇴적물에서 서로 구별되는 두 유형의 스멕타이트 (Mg과 Al)가 나타나며, 다중 기원지로부터의 공급을 지시하는 것과 뚜렷이 대조된다. 간빙기에는 Mg 스멕타이트가 아남극 남태평양 분지에서 환남극 심층수 (CDW)에 의해 대륙사면으로 수송되었을 가능성이 높으며, Al 스멕타이트는 빙산 운반 퇴적물의 일부로서 및 아문젠해 주변 연안에서 해류에 의해 공급된 것으로 해석된다. 본 연구는 아문젠해 대륙 주변부에서 스멕타이트 원소 조성 분석이 빙기-간빙기 주기 동안 쇄설성 퇴적물 성분의 기원과 수송 경로의 변동을 추적하는 데 유효한 도구임을 보여준다.

References

Aoudjit, H., Robert, M., Elsass, F., Curmi, P., 1995. Detailed study of smectite genesis in granitic saprolites by analytical electron microsopy. Clay Minerals, 30(2): 135-147.

Biscaye, P.E., 1964. Distinction between kaolinite and chlorite in recent sediments by X-ray diffraction. American Mineralogist: Journal of Earth and Planetary Materials, 49(9-10): 1281-1289.

Biscaye, P.E., 1965. Mineralogy and sedimentation of recent deep-sea clay in the Atlantic Ocean and adjacent seas and oceans. Geological Society of America Bulletin, 76(7): 803-832.

Bostock, H.C., Barrows, T.T., Carter, L., Chase, Z., Cortese, G., Dunbar, G.B., Ellwood, M., Hayward, B., Howard, W., Neil, H., 2013. A review of the Australian–New Zealand sector of the Southern Ocean over the last 30 ka (Aus-INTIMATE project). Quaternary Science Reviews, 74: 35-57.

Chamley, H., 1989. Clay formation through weathering. In: Chamley, H. (Ed.), Clay sedimentology. Springer Berlin, Heidelberg, pp. 21-50.

Chamley, H., 1994. Clay mineral diagenesis. NATO ASI SERIES C MATHEMATICAL AND PHYSICAL SCIENCES, 453: 161-161.

Chang, H.K., Mackenzie, F.T., Schoonmaker, J., 1986. Comparisons between the diagenesis of dioctahedral and trioctahedral smectite, Brazilian offshore basins. Clays and Clay Minerals, 34: 407-423.

Christidis, G., Chryssikos, G., Derkowski, A., Dohrmann, R., Eberl, D., Joussein, E., Kaufhold, S., 2023. Methods for Determination of the Layer Charge of Smectites: A Critical Assessment of Existing Approaches. Clays and Clay Minerals, 71: 1-29.

Clark, R., Wellner, J., Hillenbrand, C., Totten, R., Smith, J., Simkins, L., Larter, R., Hogan, K., Graha, A., Nitsche, F., Synchronous retreat of Thwaites and Pine Island glaciers in response to external forcings in the 580 pre-satellite era. P. Natl. Acad. Sci. USA.

Cliff, G., Lorimer, G.W., 1975. The quantitative analysis of thin specimens. Journal of Microscopy, 103(2): 203-207.

Conconi, R., Ventruti, G., Nieto, F., Capitani, G., 2023. TEM-EDS microanalysis: Comparison among the standardless, Cliff & Lorimer and absorption correction quantification methods. Ultramicroscopy, 254: 113845.

Cook, C.P., Van De Flierdt, T., Williams, T., Hemming, S.R., Iwai, M., Kobayashi, M.,

KORDI 극지연구소

Jimenez-Espejo, F.J., Escutia, C., González, J.J., Khim, B.-K., 2013. Dynamic behaviour of the East Antarctic ice sheet during Pliocene warmth. Nature Geoscience, 6(9): 765-769.

de Vries, M.v.W., Bingham, R.G., Hein, A.S., 2018. A new volcanic province: an inventory of subglacial volcanoes in West Antarctica. Geological Society, London, Special Publications, 461(1): 231-248.

Deconinck, J., Chamley, H., 1995. Diversity of smectite origins in Late Cretaceous sediments: example of chalks from northern France. Clay minerals, 30(4): 365-379.

DeConto, R.M., Pollard, D., 2016. Contribution of Antarctica to past and future sea-level rise. Nature, 531(7596): 591-597.

Dorschel, B., Hehemann, L., Viquerat, S., Warnke, F., Dreutter, S., Tenberge, Y.S., Accettella, D., An, L., Barrios, F., Bazhenova, E., 2022. The international bathymetric chart of the southern ocean version 2. Scientific data, 9(1): 275.

Dowdeswell, J.A., Evans, J., O'Cofaigh, C., Anderson, J.B., 2006. Morphology and sedimentary processes on the continental slope off Pine Island Bay, Amundsen Sea, West Antarctica. Geological Society of America Bulletin, 118(5-6): 606-619.

Drief, A., Nieto, F., 2000. Chemical composition of smectites formed in clastic sediments. Implications for the smectite-illite transformation. Clay Minerals, 35(4): 665-678.

Drits, V., Sakharov, B., 1976. X-ray structural analysis of mixed-layer minerals. Transactions of the Academy of Sciences USSR, 295: 1-252.

Dutton, A., Carlson, A.E., Long, A.J., Milne, G.A., Clark, P.U., DeConto, R., Horton, B.P., Rahmstorf, S., Raymo, M.E., 2015. Sea-level rise due to polar ice-sheet mass loss during past warm periods. Science, 349(6244).

Ehrmann, W., Hillenbrand, C.D., Smith, J.A., Graham, A.G.C., Kuhn, G., Larter, R.D., 2011. Provenance changes between recent and glacial-time sediments in the Amundsen Sea embayment, West Antarctica: clay mineral assemblage evidence. Antarctic Science, 23(5): 471-486.

Elert, K., Azañón, J.M., Nieto, F., 2018. Smectite formation upon lime stabilization of expansive marls. Applied Clay Science, 158: 29-36.

Escutia, C., Bárcena, M., Lucchi, R., Romero, O., Ballegeer, A., Gonzalez, J., Harwood, D., 2009. Circum-Antarctic warming events between 4 and 3.5 Ma recorded in marine sediments from the Prydz Bay (ODP Leg 188) and the Antarctic Peninsula (ODP Leg 178) margins. Global and Planetary Change, 69(3): 170-184.

KOPRI 극지연구소

Esper, O., Gersonde, R., 2014. New tools for the reconstruction of Pleistocene Antarctic sea ice. Palaeogeography, Palaeoclimatology, Palaeoecology, 399: 260-283.

García-Romero, E., Vegas, J., Baldonedo, J., Marfil, R., 2005. Clay minerals as alteration products in basaltic volcaniclastic deposits of La Palma (Canary Islands, Spain). Sedimentary Geology, 174(3-4): 237-253.

García-Romero, E., Lorenzo, A., García-Vicente, A., Morales, J., García-Rivas, J., Suárez, M., 2021. On the structural formula of smectites: a review and new data on the influence of exchangeable cations. Journal of applied crystallography, 54(1): 251-262.

Gohl, K., Uenzelmann-Neben, G., Larter, R.D., Hillenbrand, C.-D., Hochmuth, K., Kalberg, T., Weigelt, E., Davy, B., Kuhn, G., Nitsche, F.O., 2013. Seismic stratigraphic record of the Amundsen Sea Embayment shelf from pre-glacial to recent times: Evidence for a dynamic West Antarctic ice sheet. Marine Geology, 344: 115-131.

Gohl, K., Freudenthal, T., Hillenbrand, C.D., Klages, J., Larter, R., Bickert, T., Bohaty, S., Ehrmann, W., Esper, O., Frederichs, T., 2017. MeBo70 seabed drilling on a polar continental shelf: Operational report and lessons from drilling in the Amundsen Sea Embayment of West Antarctica. Geochemistry, Geophysics, Geosystems, 18(11): 4235-4250.

Gohl, K., Wellner, J., Klaus, A., 2021. Amundsen Sea West Antarctic Ice Sheet History. Proceedings of the International Ocean Discovery Program, 379.

Hillenbrand, C.D., Ehrmann, W., 2001. Distribution of clay minerals in drift sediments on the continental rise west of the Antarctic Peninsula, ODP Leg 178, Sites 1095 and 1096, Barker, PF, Camerlenghi, A., Acton, GD, and Ramsay, ATS (Eds.), Proc. ODP, Sci. Results, 178 [Online]. Available from World Wide Web: http://www-odp.tamu.edu/publications/178_SR/VOLUME/CHAPTERS/SR178_08.PDF.

Hillenbrand, C.D., Fütterer, D.K., Grobe, H., Frederichs, T., 2002. No evidence for a Pleistocene collapse of the West Antarctic Ice Sheet from continental margin sediments recovered in the Amundsen Sea. Geo-Marine Letters, 22: 51-59.

Hillenbrand, C.D., Grobe, H., Diekmann, B., Kuhn, G., Futterer, D.K., 2003. Distribution of clay minerals and proxies for productivity in surface sediments of the Bellingshausen and Amundsen seas (West Antarctica) - Relation to modern environmental conditions. Marine Geology, 193(3-4): 253-271.

Hillenbrand, C.D., Ehrmann, W., 2005. Late Neogene to Quaternary environmental changes in the Antarctic Peninsula region: evidence from drift sediments. Global and Planetary

KOPRI 극지연구소

Change, 45(1-3): 165-191.

Hillenbrand, C.D., Ehrmann, W., Larter, R.D., Benetti, S., Dowdeswell, J.A., Cofaigh, C.O., Graham, A.G.C., Grobe, H., 2009a. Clay mineral provenance of sediments in the southern Bellingshausen Sea reveals drainage changes of the West Antarctic Ice Sheet during the Late Quaternary. Marine Geology, 265(1-2): 1-18.

Hillenbrand, C.D., Kuhn, G., Frederichs, T., 2009b. Record of a Mid-Pleistocene depositional anomaly in West Antarctic continental margin sediments: an indicator for ice-sheet collapse? Quaternary Science Reviews, 28(13-14): 1147-1159.

Hillenbrand, C.D., Larter, R.D., Dowdeswell, J.A., Ehrmann, W., Cofaigh, C.O., Benetti, S., Graham, A.G.C., Grobe, H., 2010. The sedimentary legacy of a palaeo-ice stream on the shelf of the southern Bellingshausen Sea: Clues to West Antarctic glacial history during the Late Quaternary. Quaternary Science Reviews, 29(19-20): 2741-2763.

Hillenbrand, C.D., Kuhn, G., Smith, J.A., Gohl, K., Graham, A.G., Larter, R.D., Klages, J.P., Downey, R., Moreton, S.G., Forwick, M., 2013. Grounding-line retreat of the west Antarctic ice sheet from inner Pine island Bay. Geology, 41(1): 35-38.

Hillenbrand, C.D., Smith, J.A., Hodell, D.A., Greaves, M., Poole, C.R., Kender, S., Williams, M., Andersen, T.J., Jernas, P.E., Elderfield, H., Klages, J.P., Roberts, S.J., Gohl, K., Larter, R.D., Kuhn, G., 2017. West Antarctic Ice Sheet retreat driven by Holocene warm water incursions. Nature, 547(7661): 43-48.

Hillenbrand, C.D., Crowhurst, S., Williams, M., Hodell, D., McCave, I., Ehrmann, W., Xuan, C., Piotrowski, A., Hernández-Molina, F., Graham, A., 2021. New insights from multi-proxy data from the West Antarctic continental rise: Implications for dating and interpreting Late Quaternary palaeoenvironmental records. Quaternary Science Reviews, 257: 106842.

Hillier, S., 1995. Erosion, sedimentation and sedimentary origin of clays. In: Velde, B. (Ed.), Origin and Mineralogy of Clays: Clays and the Environment. Springer, Berlin, Heidelberg, pp. 162-219.

Hollister, C.D., Worstell, P., 1976. Initial Reports of the Deep Sea Drilling Project, Vol. 35: Covering Leg 35 of the Cruises of the Drilling Vessel "Glomar Challenger", Callao, Peru, to Ushuaia, Argentina, February-March 1974. U.S. Government Printing Office.

Horrocks, J., 2018. The formation and Late Quaternary palaeoenvironmental history of sediment mounds in the Amundsen Sea, West Antarctica. PhD Thesis, Department of Geography, Durham University.

KOPRI 극지연구소

Jackson, M.L., 1969. Soil Chemical Analysis: Advanced Course. (Edition 2). Madison, Wisconsin.

Jacobs, S., Jenkins, A., Hellmer, H., Giulivi, C., Nitsche, F., Huber, B., Guerrero, R., 2012. The Amundsen Sea and the Antarctic ice sheet. Oceanography, 25(3): 154-163.

Jenkins, A., Dutrieux, P., Jacobs, S., Steig, E.J., Gudmundsson, G.H., Smith, J., Heywood, K.J., 2016. Decadal ocean forcing and Antarctic ice sheet response: Lessons from the Amundsen Sea. Oceanography, 29(4): 106-117.

Jeong, G.Y., Yoon, H.I., Lee, S.Y., 2004. Chemistry and microstructures of clay particles in smectite-rich shelf sediments, South Shetland Islands, Antarctica. Marine Geology, 209(1-4): 19-30.

Jung, J., Yoo, K.C., Lee, K.H., Park, Y.K., Lee, J.I., Kim, J., 2019. Clay Mineralogical Characteristics of Sediments Deposited during the Late Quaternary in the Larsen Ice Shelf B Embayment, Antarctica. Minerals, 9(3): 153.

Kim, J., Dong, H., Yang, K., Park, H., Elliott, W.C., Spivack, A., Koo, T.-h., Kim, G., Morono, Y., Henkel, S., 2019. Naturally occurring, microbially induced smectite-to-illite reaction. Geology, 47(6): 535-539.

Kim, J.W., Peacor, D.R., Tessier, D., Elsass, F., 1995. A Technique for Maintaining Texture and Permanent Expansion of Smectite Interlayers for Tem Observations. Clays and Clay Minerals, 43(1): 51-57.

Kirshner, A.E., Anderson, J.B., Jakobsson, M., O'Regan, M., Majewski, W., Nitsche, F.O., 2012. Post-LGM deglaciation in Pine island Bay, west Antarctica. Quaternary Science Reviews, 38: 11-26.

Klages, J.P., Salzmann, U., Bickert, T., Hillenbrand, C.-D., Gohl, K., Kuhn, G., Bohaty, S.M., Titschack, J., Müller, J., Frederichs, T., 2020. Temperate rainforests near the South Pole during peak Cretaceous warmth. Nature, 580(7801): 81-86.

Konfirst, M.A., Scherer, R.P., Hillenbrand, C.D., Kuhn, G., 2012. A marine diatom record from the Amundsen - Sea Insights into oceanographic and climatic response to the Mid-Pleistocene Transition in the West Antarctic sector of the Southern Ocean. Marine Micropaleontology, 92-93: 40-51.

Larter, R.D., Anderson, J.B., Graham, A.G.C., Gohl, K., Hillenbrand, C.D., Jakobsson, M., Johnson, J.S., Kuhn, G., Nitsche, F.O., Smith, J.A., Witus, A.E., Bentley, M.J., Dowdeswell, J.A., Ehrmann, W., Klages, J.P., Lindow, J., Cofaigh, C.O., Spiegel, C., 2014. Reconstruction of changes in the Amundsen Sea and Bellingshausen Sea sector of the West Antarctic Ice Sheet since the Last Glacial Maximum. Quaternary Science

KOPRI 극지연구소

Reviews, 100: 55-86.

Lau, S.C., Wilson, N.G., Golledge, N.R., Naish, T.R., Watts, P.C., Silva, C.N., Cooke, I.R., Allcock, A.L., Mark, F.C., Linse, K., in press. Genomic evidence for West Antarctic Ice Sheet collapse during the Last Interglacial Period. bioRxiv, https://doi.org/10.1101/2023.01.29.525778.

LeMasurier, W., 2002. Architecture and evolution of hydrovolcanic deltas in Marie Byrd Land, Antarctica. In: J. L. Smellie, M.G.C. (Ed.), Volcano-Ice Interaction on Earth and Mars. Geological Society of London Special Publications, London, pp. 115-148.

LeMasurier, W., 2013. Shield volcanoes of Marie Byrd Land, West Antarctic rift: oceanic island similarities, continental signature, and tectonic controls. Bulletin of Volcanology, 75: 1-18.

Licht, K.J., Hemming, S.R., 2017. Analysis of Antarctic glacigenic sediment provenance through geochemical and petrologic applications. Quaternary Science Reviews, 164: 1-24.

Lucchi, R.G., Rebesco, M., Camerlenghi, A., Busetti, M., Tomadin, L., Villa, G., Persico, D., Morigi, C., Bonci, M.C., Giorgetti, G., 2002. Mid-late Pleistocene glacimarine sedimentary processes of a high-latitude, deep-sea sediment drift (Antarctic Peninsula Pacific margin). Marine Geology, 189(3-4): 343-370.

Lucchi, R.G., Rebesco, M., 2007. Glacial contourites on the Antarctic Peninsula margin: insight for palaeoenvironmental and palaeoclimatic conditions. Geological Society, London, Special Publications, 276(1): 111-127.

Marshall, C., 1935. Layer lattices and the base-exchange clays. Zeitschrift für Kristallographie-Crystalline Materials, 91(1-6): 433-449.

McCarty, D.K., Sakharov, B.A., Drits, V.A., 2009. New insights into smectite illitization: A zoned K-bentonite revisited. American Mineralogist, 94(11-12): 1653-1671.

McKinley, J., Worden, R., Ruffell, A., 1999. Smectite in sandstones: a review of the controls on occurrence and behaviour during diagenesis. In: Richard H. Worden, S.M. (Ed.), Clay mineral cements in sandstones. International Association of Sedimentologists, Blackwell Publishing, pp. 109-128.

Mcmurtry, G.M., Yeh, H.W., 1981. Hydrothermal Clay Mineral Formation of East Pacific Rise and Bauer Basin Sediments. Chemical Geology, 32(3-4): 189-205.

Moore, D.M., Reynolds Jr, R.C., 1989. X-ray Diffraction and the Identification and Analysis of Clay Minerals. Oxford University Press (OUP).

Nieto, F., Ortega-Huertas, M., Peacor, D., Arostegui, J., 1996. Evolution of illite/smectite from

early diagenesis through incipient metamorphism in sediments of the Basque-Cantabrian Basin. Clays and Clay Minerals, 44: 304-323.

Pandarinath, K., 2009. Clay minerals in SW Indian continental shelf sediment cores as indicators of provenance and palaeomonsoonal conditions: a statistical approach. International Geology Review, 51(2): 145-165.

Park, H., Yang, K., Koo, T.-h., Kang, I., Yamamoto, Y., Kim, J., 2024. Physico-chemical properties of illite in the organic matter (OM)-rich claystone of Nankai Trough contrast with coeval OM-poor claystone: IODP Expedition 348. Applied Clay Science, 250: 107267.

Park, Y.K., Lee, J.I., Jung, J., Hillenbrand, C.D., Yoo, K.C., Kim, J., 2019. Elemental Compositions of Smectites Reveal Detailed Sediment Provenance Changes during Glacial and Interglacial Periods: The Southern Drake Passage and Bellingshausen Sea, Antarctica. Minerals, 9(5): 322.

Petschick, R., Kuhn, G., Gingele, F., 1996. Clay mineral distribution in surface sediments of the South Atlantic: Sources, transport, and relation to oceanography. Marine Geology, 130(3-4): 203-229.

Pollard, D., DeConto, R.M., 2009. Modelling West Antarctic ice sheet growth and collapse through the past five million years. Nature, 458(7236): 329-U89.

Pritchard, H., Ligtenberg, S.R., Fricker, H.A., Vaughan, D.G., van den Broeke, M.R., Padman, L., 2012. Antarctic ice-sheet loss driven by basal melting of ice shelves. Nature, 484(7395): 502-505.

Pudsey, C.J., 2000. Sedimentation on the continental rise west of the Antarctic Peninsula over the last three glacial cycles. Marine Geology, 167(3-4): 313-338.

Righi, D., Meunier, A., 1995. Origin of clays by rock weathering and soil formation. In: Velde, B. (Ed.), Origin and mineralogy of clays: clays and the environment. Springer, Berlin, Heidelberg, pp. 43-161.

Rignot, E., Mouginot, J., Scheuchl, B., Van Den Broeke, M., Van Wessem, M.J., Morlighem, M., 2019. Four decades of Antarctic Ice Sheet mass balance from 1979-2017. Proceedings of the National Academy of Sciences, 116(4): 1095-1103.

Sánchez-Roa, C., Bauluz, B., Nieto, F., Abad, I., Jimenéz-Millán, J., Faulkner, D., 2018. Micro-and nano-scale study of deformation induced mineral transformations in Mg-phyllosilicate-rich fault gouges from the Galera Fault Zone (Betic Cordillera, SE Spain). American Mineralogist, 103(10): 1604-1621.

Simões Pereira, P., van de Flierdt, T., Hemming, S.R., Hammond, S.J., Kuhn, G., Brachfeld, S., Doherty, C., Hillenbrand, C.D., 2018. Geochemical fingerprints of glacially eroded bedrock from West Antarctica: Detrital thermochronology, radiogenic isotope systematics and trace element geochemistry in Late Holocene glacial-marine sediments. Earth-Science Reviews, 182: 204-232.

Simões Pereira, P., van de Flierdt, T., Hemming, S.R., Frederichs, T., Hammond, S.J., Brachfeld, S., Doherty, C., Kuhn, G., Smith, J.A., Klages, J.P., Hillenbrand, C.D., 2020. The geochemical and mineralogical fingerprint of West Antarctica's weak underbelly: Pine Island and Thwaites glaciers. Chemical Geology, 550: 119649.

Smith, B., Fricker, H.A., Gardner, A.S., Medley, B., Nilsson, J., Paolo, F.S., Holschuh, N., Adusumilli, S., Brunt, K., Csatho, B., 2020. Pervasive ice sheet mass loss reflects competing ocean and atmosphere processes. Science, 368(6496): 1239-1242.

Stuart, A., Ord, K., 1999. S. Arnold Kendall' s Advanced Theory of Statistics Vol. 2A, Classical Inference and the Linear Model. Arnold Publishers.

Totten, R.L., Majewski, W., Anderson, J.B., Yokoyama, Y., Fernandez, R., Jakobsson, M., 2017. Oceanographic influences on the stability of the Cosgrove Ice Shelf, Antarctica. The Holocene, 27(11): 1645-1658.

Toyos, M.H., Lamy, F., Lange, C.B., Lembke-Jene, L., Saavedra-Pellitero, M., Esper, O., Arz, H.W., 2020. Antarctic Circumpolar Current Dynamics at the Pacific Entrance to the Drake Passage Over the Past 1.3 Million Years. Paleoceanography and Paleoclimatology, 35(7): e2019PA003773.

Uenzelmann-Neben, G., Gohl, K., 2012. Amundsen Sea sediment drifts: archives of modifications in oceanographic and climatic conditions. Marine Geology, 299: 51-62.

Vaughan, D.G., 2008. West Antarctic Ice Sheet collapse - the fall and rise of a paradigm. Climatic Change, 91(1-2): 65-79.

Velde, B., 1995. Composition and mineralogy of clay minerals. In: Velde, B. (Ed.), Origin and mineralogy of clays: clays and the environment. Springer, Berlin, Heidelberg, pp. 8-42.

Weaver, C., Pollard, L., 1973. Developments in Sedimentology, vol. 15, The Chemistry of Clay Minerals. Elsevier Sci., New York.

Wengler, M., Lamy, F., Struve, T., Borunda, A., Böning, P., Geibert, W., Kuhn, G., Pahnke, K., Roberts, J., Tiedemann, R., 2019. A geochemical approach to reconstruct modern dust fluxes and sources to the South Pacific. Geochimica et Cosmochimica Acta, 264: 205-223.

KOPRI 극지연구소

Williams, T., van de Flierdt, T., Hemming, S.R., Chung, E., Roy, M., Goldstein, S.L., 2010. Evidence for iceberg armadas from East Antarctica in the Southern Ocean during the late Miocene and early Pliocene. Earth and Planetary Science Letters, 290(3-4): 351-361.

Wilson, D.J., Bertram, R.A., Needham, E.F., van de Flierdt, T., Welsh, K.J., McKay, R.M., Mazumder, A., Riesselman, C.R., Jimenez-Espejo, F.J., Escutia, C., 2018. Ice loss from the East Antarctic Ice Sheet during late Pleistocene interglacials. Nature, 561(7723): 383-386.

Yang, K., Kim, J.W., Kogure, T., Dong, H.L., Baik, H., Hoppie, B., Harris, R., 2016. Smectite, illite, and early diagenesis in South Pacific Gyre subseafloor sediment. Applied Clay Science, 134: 34-43.

KOPRI
극지연구소

Table 1. Sediment core information in this area. BC = box core; PC = piston core.

Core	Sample depth (cm)	**Age**	**Location**	**Sediment description**
BC480	0-3	Modern-late Holocene	Amundsen Sea, inner continental shelf (Pine Island Bay)	Brownish mud
BC488	0-3	Modern-late Holocene	Amundsen Sea, upper continental slope	Brownish foraminiferal mud
PC494	199-202	MIS 2-4	Amundsen Sea, drift crest on continental rise	Laminated to stratified terrigenous mud
PC494	496-498	MIS 5e	Amundsen Sea, drift crest on continental rise	Foraminifera bearing mud
BC495	0-3	Modern-late Holocene	Amundsen Sea, drift crest on continental rise (very close to site PC494)	Brownish foraminiferal mud
BC502	0-3	Modern-late Holocene	Sub-Antarctic South Pacific basin	Brownish diatomaceous ooze
BC27	0-1	Modern-late Holocene	Amundsen Sea, inner continental shelf (Pine Island Glacier front)	Olive-brown mud with traces of diatoms
BC36	0-1	Modern-late Holocene	Amundsen Sea, inner continental shelf (Thwaites Glacier front)	Olive-brown sandy mud with traces of diatoms
U1533A 1H-1	54-55	MIS 5e	Amundsen Sea, drift flank on continental rise	Brown bioturbated diatomaceous ooze

극지연구소

Table 2. Compositional range of elemental composition of smectites from each investigated sample (calculated with O = 10 and OH = 2) obtained by TEM-EDS (Appendix A; Table A. 2-10)

Sample	Tetrahedral sheet		Octahedral sheet					Interlayer			Number of smectites analyzed
	Si	Al(4)	Al(6)	Mg	Fe	Ti	Mn	K	Ca	Na	
BC495	3.23-3.99	0.01-0.77	0.39-1.81	0.14-1.1	0.07-1.25	0-0.13	0-0.05	0.01-0.36	0.01-0.13	0-0.2	53
PC494 (MIS 2-4)	3.39-3.94	0.06-0.61	0.83-1.55	0.21-0.62	0.3-0.9	0-0.05	0-0.03	0.01-0.47	0-0.03	0	10
PC494 (MIS 5e)	3.12-3.99	0.01-0.88	0.07-1.4	0.23-0.73	0.39-1.7	0-0.12	0-0.25	0-0.34	0.06-0.39	0-0.25	63
BC480	3.22-3.99	0.01-0.78	0.54-1.82	0.04-0.5	0.15-1.27	0-0.06	0	0.01-0.37	0.01-0.05	0	10
BC488	3.44-3.93	0.07-0.56	0.29-1.5	0.1-0.65	0.34-1.48	0-0.07	0	0-0.37	0.04-0.25	0	21
BC27	2.99-3.91	0.09-1.01	0.18-1.43	0.19-0.82	0.36-1.81	0-0.1	0-0.03	0.04-0.44	0.01-0.04	0	18
BC36	3.3-3.98	0.02-0.7	0.54-1.5	0.13-0.67	0.35-1.37	0-0.07	0-0.06	0-0.2	0-0.08	0-0.23	36
BC502	3.45-3.98	0.02-0.55	0.12-1.33	0.33-1.39	0.37-1.4	0.01-0.09	0-0.03	0-0.3	0.01-0.04	0	21
U1533	3.22-3.94	0.06-0.78	0.12-1.4	0.26-0.89	0.29-1.5	0-0.08	0-0.05	0-0.29	0-0.06	0-0.25	17

KORA 극지연구소

Table 3. Average structural formula of smectites from each investigated sample (calculated with O = 10 and OH = 2) obtained by TEM-EDS.

Sample	Average structural formula
BC495	$(Ca_{0.04}K_{0.13}Na_{0.04})(Al_{0.97}Mg_{0.5}Fe_{0.68}Ti_{0.02}Mn_{0.01})(Si_{3.72}Al_{0.28})O_{10}(OH)_2$
PC494 (MIS 2-4)	$(Ca_{0.01}K_{0.2})(Al_{1.17}Mg_{0.33}Fe_{0.61}Ti_{0.01}Mn_{0.01})(Si_{3.71}Al_{0.29})O_{10}(OH)_2$
PC494 (MIS 5e)	$(Ca_{0.14}K_{0.08}Na_{0.03})(Al_{0.74}Mg_{0.47}Fe_{0.86}Ti_{0.03}Mn_{0.03})(Si_{3.69}Al_{0.31})O_{10}(OH)_2$
BC480	$(Ca_{0.02}K_{0.15})(Al_{1.12}Mg_{0.31}Fe_{0.68}Ti_{0.02})(Si_{3.71}Al_{0.29})O_{10}(OH)_2$
BC488	$(Ca_{0.12}K_{0.1}Na_{0.02})(Al_{1.01}Mg_{0.32}Fe_{0.74}Ti_{0.01}Mn_{0.01})(Si_{3.72}Al_{0.28})O_{10}(OH)_2$
BC27	$(Ca_{0.02}K_{0.18})(Al_{1.02}Mg_{0.39}Fe_{0.76}Ti_{0.02}Mn_{0.01})(Si_{3.53}Al_{0.47})O_{10}(OH)_2$
BC36	$(Ca_{0.03}K_{0.08}Na_{0.03})(Al_{1.12}Mg_{0.3}Fe_{0.71}Ti_{0.01}Mn_{0.01})(Si_{3.67}Al_{0.33})O_{10}(OH)_2$
BC502	$(Ca_{0.02}K_{0.09})(Al_{0.55}Mg_{0.75}Fe_{0.92}Ti_{0.02}Mn_{0.01})(Si_{3.83}Al_{0.17})O_{10}(OH)_2$
U1533	$(Ca_{0.02}K_{0.08}Na_{0.12})(Al_{0.8}Mg_{0.52}Fe_{0.86}Ti_{0.02}Mn_{0.01})(Si_{3.64}Al_{0.36})O_{10}(OH)_2$

KOPRI
극지연구소

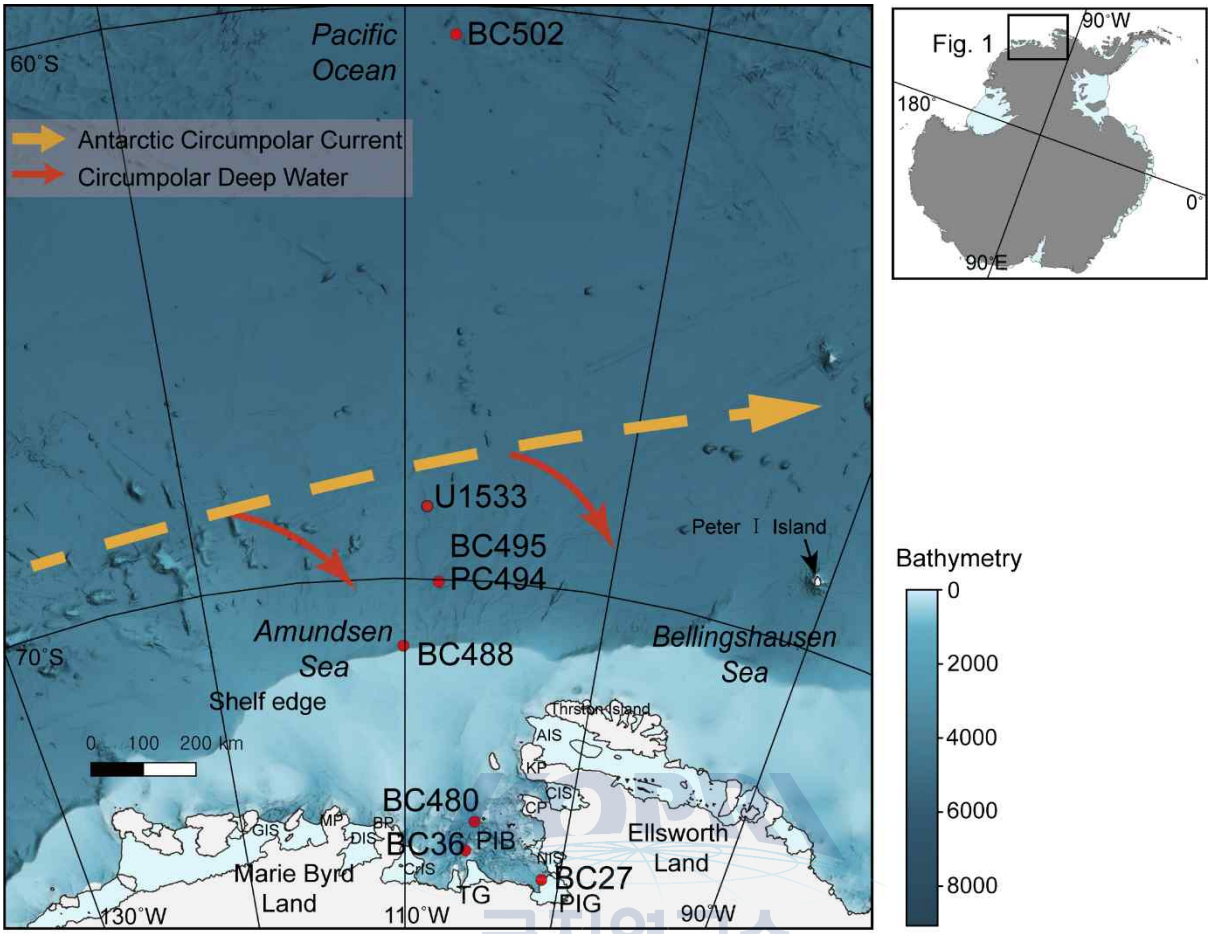


Figure 1 Location of core samples, BC27 (Pine Island Glacier front), BC36 (Thwaites Glacier), BC480, and BC488 on the Amundsen Sea shelf and slope, BC495/PC494 and U1533 on the Amundsen Sea continental rise and sample BC502 in the sub-Antarctic South Pacific basin. Schematic ocean circulation modified from Totten et al. (2017). Bathymetry obtained from Dorschel et al. (2022). AIS = Abbot Ice Shelf, BP = Bear Peninsula, CIS = Cosgrove Ice Shelf, CP = Canisteo Peninsula, CrIS = Crosson Ice Shelf, DIS = Dotson Ice Shelf, GIS = Getz Ice Shelf, KP = King Peninsula, MP = Martin Peninsula, NIS = Northern Ice Shelf, PIB = Pine Island Bay, PIG = Pine Island Glacier, TG = Thwaites Glacier.

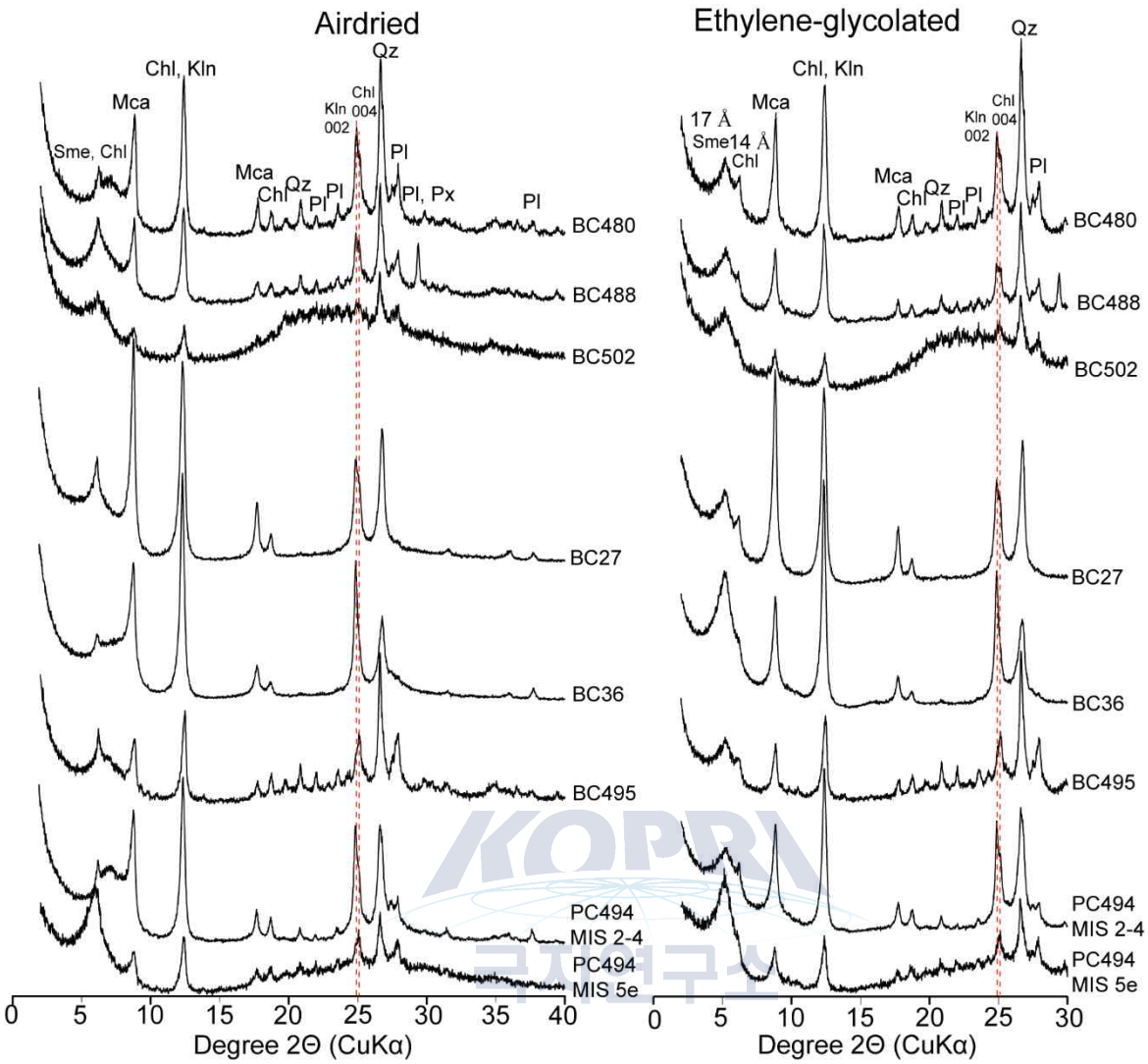


Figure 2 X-ray diffraction (XRD) patterns of air-dried and ethylene-glycolated clay (<2 μm) samples from seafloor surface sediments collected at sites BC480, BC488, BC495, BC502, BC27 and BC36, and from MIS 2-4 (last glacial period) and MIS 5e (last interglacial) sediments from site PC494 on the continental rise. There is a clear separation of chlorite (14 Å) and smectite (17 Å) after glycolation. Kaolinite was identified by a separation of kaolinite (002) peak at 24.9° 2θ and chlorite (004) peak at 25.1-25.2° 2θ (red dotted line). Sme: smectite, Chl: chlorite, Kln: kaolinite, Mca: mica, Pl: plagioclase, Qz: quartz, and Px: pyroxene.

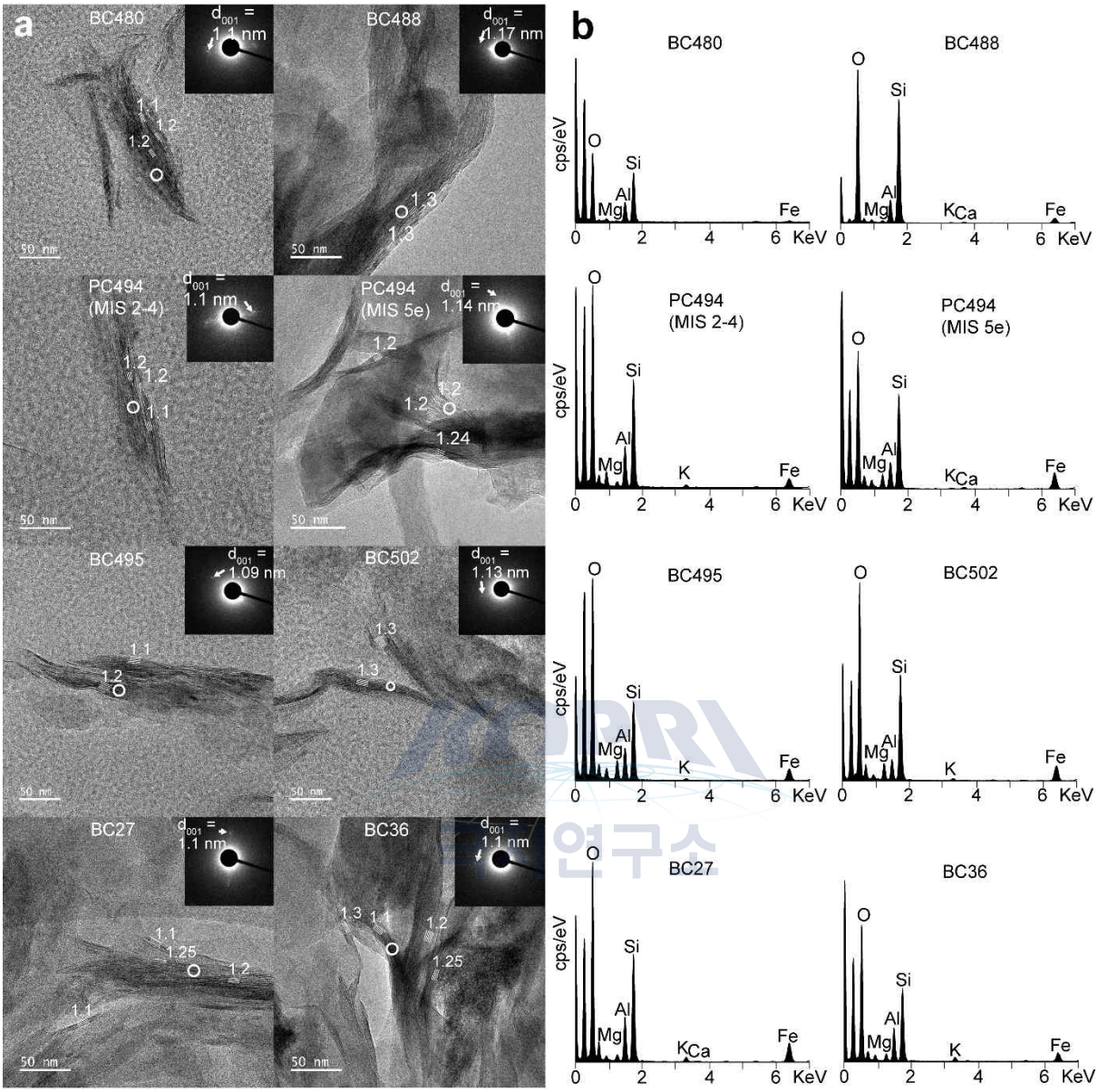


Figure 3 Representative TEM micrographs of lattice fringes in smectites and corresponding selected-area electron diffraction (SAED) pattern (d_{001}=1.09-1.17nm) from (a) BC480, BC488, PC494 (MIS2-4), PC494 (MIS5e), BC495, BC502, BC27, and BC36. (b) Representative EDS spectra of smectite in each sample showing compositional variations reflecting supply from different sources (white circle).

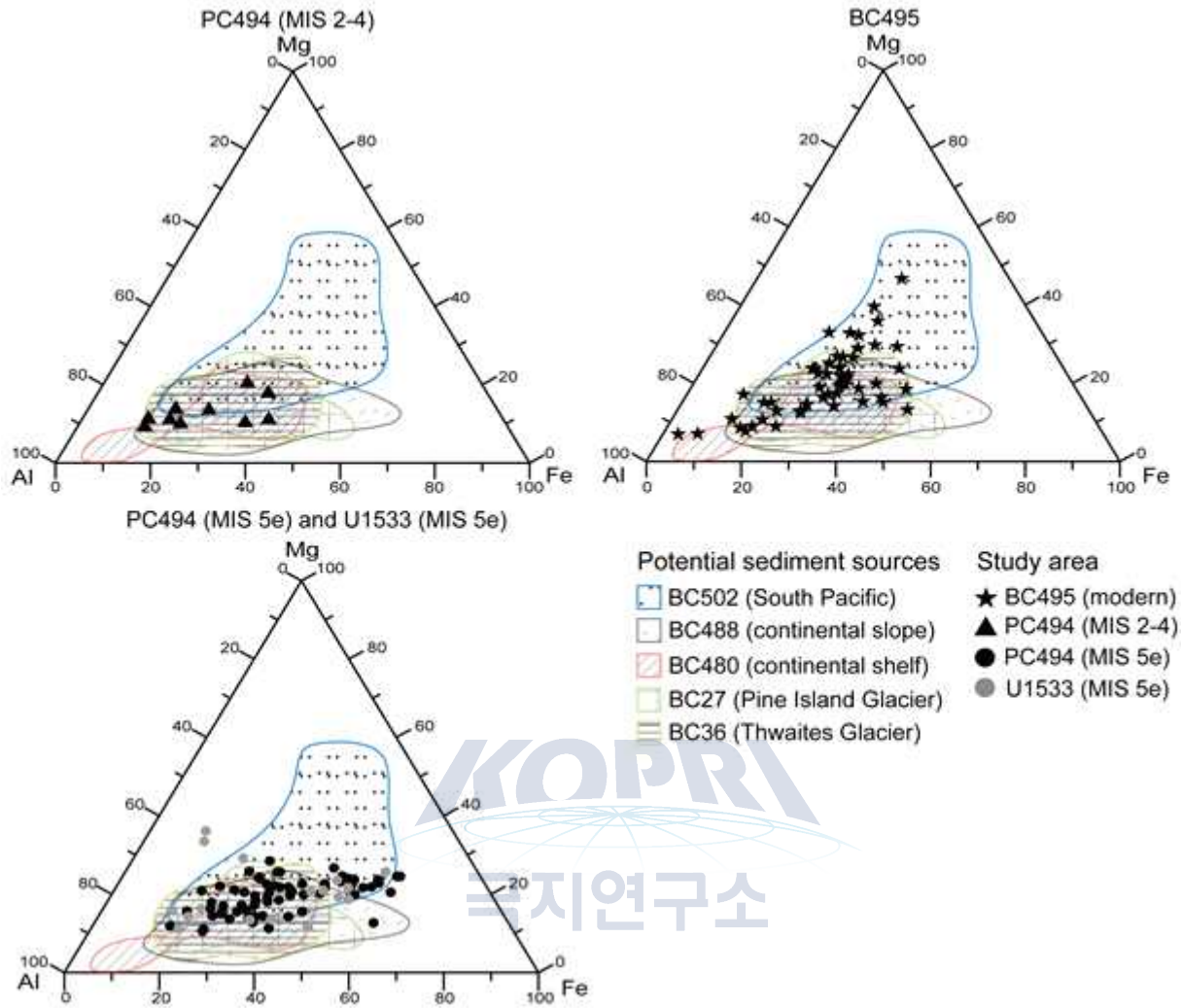


Figure 4 Total Al-Fe-Mg compositions of the smectite minerals for samples BC495, PC494 and U1533 (Amundsen Sea continental rise) plotted in ternary diagrams (stars: BC495, triangles: PC494 MIS 2-4, black circles: PC494 MIS 5e, gray circles: U1533 MIS 5e). Compositional fields shown for potential sediment source samples encircle all Al-Fe-Mg compositions of individual smectite minerals analyzed for each source sample: BC502 (sub-Antarctic South Pacific basin), BC480 (Pine Island Bay), BC488 (Amundsen Sea continental slope), BC27 (Pine Island Glacier front), and BC36 (Thwaites Glacier front).

KOPRI 극지연구소

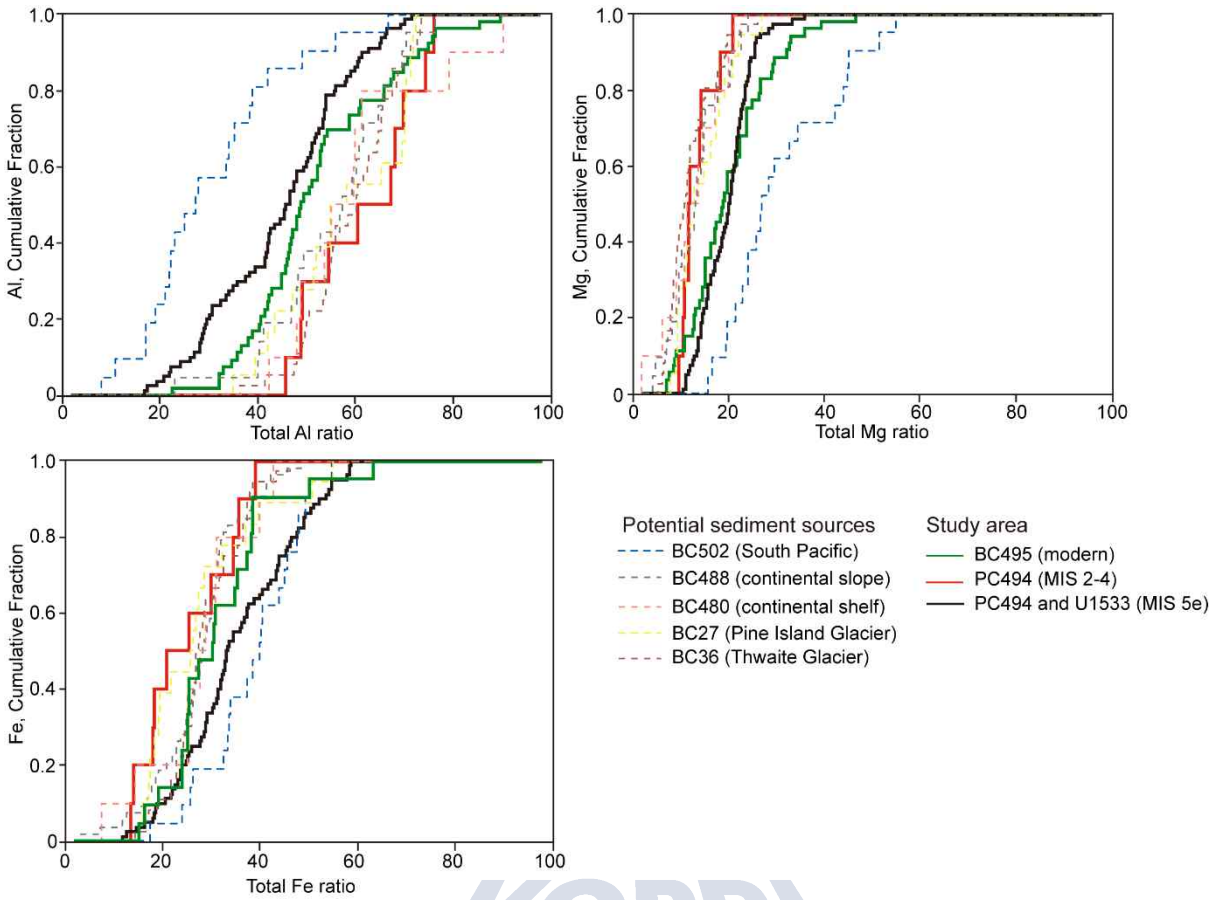


Figure 5 Kolmogorov-Smirnov distributions of total Al, Mg, and Fe ratio in the smectites in samples from continental rise sites BC495 (green solid line) and PC494 (MIS 2-4: red solid line) and PC494 and U1533 (MIS 5e: black solid line) in comparison to those from potential source areas on the Amundsen Sea shelf and slope (BC480: pink dotted line; BC36: brown dotted line; BC488: grey dotted line; BC27: yellow dotted line) and in the sub-Antarctic South Pacific basin (BC502: blue dotted line).

KORDI 극지연구소

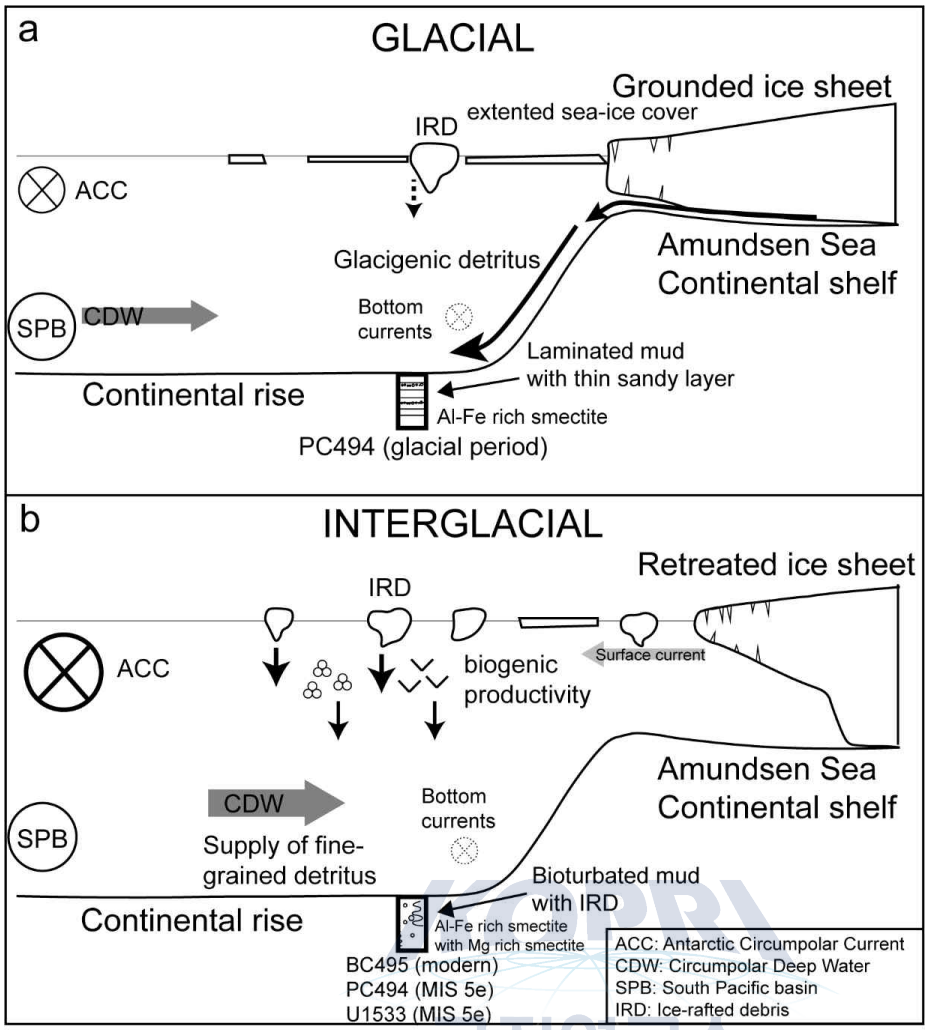


Figure 6 Cartoon showing possible transport routes of fine-grained detritus and associated paleo-environmental conditions at the continental margin of the Amundsen Sea throughout a late Quaternary glacial-interglacial cycle. (a) During glacial periods, the main source of sediment deposited on the continental rise is supply of glacigenic detritus, including Al-rich smectites, from the Amundsen Sea shelf transported by gravitational down-slope processes, including turbidity currents, and meltwater plumes. (b) During interglacials, the terrigenous components deposited on the rise consist of detritus, including Al-rich smectites delivered by iceberg rafting from the Amundsen Sea coast, but also of fine-grained detritus, including Mg rich smectites, originating from the sub-Antarctic South Pacific basin and advected by deep and bottom waters, such as CDW, towards the Amundsen Sea continental margin. Eastward ACC flow was stronger during interglacial periods than during glacial times (Toyos et al., 2020).

제 34 장

Pleistocene glaciomarine laminated muds in the Central Basin of the northwestern Ross Sea and their palaeoceanographic records[27)]

Boo-Keun Khim[1], Young Kwan Sohn[2], Min Kyung Lee[3], Sunghan Kim[3], Jae Il Lee[3], Kyu Cheul Yoo[3]

[1]Department of Oceanography and Marine Research Institute, Pusan National University, Busan, Korea

[2]Department of Geology, Gyeongsang National University, Jinju, Korea

[3]Division of Glacial Environment Research, Korea Polar Research Institute, Incheon, Korea

Abstract: Glaciomarine laminated muds around the Antarctic continental margin are important in the marine geological record related to ice sheet dynamics. Microscopic observation and backscattered electron imagery of Pleistocene laminated muds in the Central Basin (Ross Sea) reveal that the light laminae comprise terrigenous angular to subangular silt-sized particles, scattered diatom fragments, and eroded sand-sized lumps of fossil-bearing mud. In contrast, the dark laminae are clayey and biogenic with very tiny pieces of fossils. These laminated muds are interpreted to have been deposited by subglacial meltwater plumes underneath the advancing glaciers that torn off the earlier-deposited and semi-consolidated diatom-rich sediments. Thus, most biogenic components of these laminated muds were recycled from older deposits, indicating that they are not related to enhanced biological production during the mud deposition. Our study suggests that the recycling of biogenic particles should be considered when interpreting the palaeoclimatic and palaeoceanographic implications of Antarctic environmental system.

1. Introduction

27) 이 연구 결과는 다음의 논문으로 출판되었음: Khim, et al. (2023). "Pleistocene glaciomarine laminated muds in the Central Basin of the northwestern Ross Sea and their palaeoceanographic records" Terra Nova, 36: 37-44.

The Antarctic Ice Sheet (AIS) has played a crucial role in affecting the environmental conditions related to the sediment depositional system in the Southern Ocean. Colleoni et al. (2018) reviewed the responses of the Antarctic environmental system to the changes in ice sheet basal hydrology, continental margin evolution, and ocean circulation through the complicated processes across the ice-bed-ocean interfaces of the AIS. In particular, the Antarctic ice shelves are the terminus of the AIS glaciers that responds sensitively to the ice-sheet dynamics around the Antarctic continental margin (Smith et al., 2019). In this context, the marine geological signatures of glacial-interglacial cycles have been well recognized from the studies of the Antarctic continental margin related to the presence, absence, and collapse of ice shelves (Domack & Powell, 2018).

Studies of the depositional processes of glaciomarine sediments in the Antarctic marine settings have offered important clues to understanding the diverse interplay among the ice sheet, ice shelf, and ocean within the Antarctic depositional systems. In the Antarctic continental margins, two general types of glaciomarine laminated sediments have been reported: laminated terrigenous muds and laminated biosiliceous muds. The former generally occurs in the continental slope and rise and is thought to be the product of contour currents (e.g., Anderson, 1999). The glacial sediments in the Pacific margin of the Antarctic Peninsula consist of this type of muds (Lucchi & Rebesco, 2007; Pudsey, 2000; Venuti et al., 2011). In addition, Domack (1990) reported a rhythmically laminated sequence of silt and clay in the Antarctic continental shelf, including fjord and bay. The production of these muds was attributed to the basal melting processes and tidal flushing at the grounding zone within the subglacial system. On the other hand, laminated biosiliceous muds, consisting dominantly of biosiliceous (diatom) component, shows a circum-Antarctic distribution in the inner shelf basins and troughs (Alley et al., 2018; Leventer et al., 2006; Maddison et al., 2012; Stickley et al., 2005). Extremely thick laminated diatom-rich sediment sequences can accumulate because the troughs and enclosed basins act as natural sediment traps. These diatom-rich laminated sediments are known to record the palaeoenvironmental and palaeoceanographic conditions at seasonal to interannual timescales. In particular, varved couplets of diatomaceous lamina can form in regions of extremely high primary productivity in the calving bays of the Antarctic ice sheet during the deglaciation (e.g., Leventer et al., 2006).

Ohneiser et al. (2019) reported the glaciomarine laminated muds in the Central Basin at the upper continental slope of the northwestern Ross Sea. In this study, we reveal, based on the macroto microscopic observations of sediment texture, componentry, and structure, that the type of these laminated muds is different and previously undocumented. We attempt to interpret the depositional processes and conditions during the formation of Pleistocene laminated muds and discuss their palaeoclimatic implications to shed light on

the interplay between the ocean and the ice sheet.

2. Materials and Methods

The Central Basin is located at the mouth of the JOIDES Basin in the northwestern Ross Sea (Figure 1), forming a deep semi-closed tectonic depression surrounded by different morphological features, including continental slope, intra-slope basin, ponded basin, basin floor, and topographic highs (Kim et al., 2018). An 11.75 mlong core RS15-LC42 (hereafter LC42) was collected in the northwestern moat (71°49.40′ S, 178°34.76′ E, 2084 m water depth; Figure 1) between the small contour-parallel mounds near the right flank of the Hallett Ridge in the Central Basin using jumbo gravity coring system during the cruise of R/V Araon in the austral summer of 2015. Optical images of LC42 were obtained using an ITRAX core scanner and X-ray images were taken on 1-cmthick sediment slabs using X-ray inspection equipment (SOFTEX W-100 W). Twenty thin and polished sections from eight intervals of laminated sediments of LC42 (Figure 2) were prepared using a fluid displacive resin embedding technique modified from Pike and Kemp (1996). These sections were examined using a Nikon polarizing microscope (×100-1000) and scanning electron microscope (SEM) (×100-10,000) with backscattered electron imagery (BSEI) of JEOL (JZA-8530F PLUS) Field-Emission Electron Probe MicroAnalyser. The age, grain size, and diatom assemblage of LC42 were reported in the previous studies (Albot, 2016; Bollen, 2019; Ohneiser et al., 2019).

3. Results

LC42 consists of mostly gravelly sandy mud with interbeds of fineto-medium sand, bioturbated silts, and clast-free laminated mud. The sediment facies of LC42 can be divided into (1) IRD (ice-rafted debris)-poor bioturbated sandy mud, (2) IRD-rich massive sandy mud, and (3) laminated mud without IRD (Figure 2). These facies are arranged without any obvious order or cyclicity. Eight laminated mud intervals are identified with variable thicknesses (10 cm to about 2 m) and generally sharp boundaries with the other facies. Throughout the core, laminations are very similar and devoid of IRD and bioturbation, and consist of alternating relatively thinner light laminae and thicker dark laminae, which are mostly plane-parallel, locally pinchand-swelling, and low-angle inclined.

Microscopic observation of thin sections clarifies that the light and dark laminae are millimetreto submillimetre-thick and composed mainly of silty and clayey particles, respectively (Figure 3). The contacts between these laminae are either sharp or transitional

and planar to undulatory. SEM examination reveals more clearly that the fine-grained lamina consists of sparsely scattered silt-sized particles of terrigenous or biogenic origin in a clayey matrix (Figure 4). In contrast, the coarse-grained lamina is composed dominantly of very fine sandto silt-sized angular to subangular quartz and feldspar grains, commonly without mud matrix (Figure 4), and contains considerable amounts of sandto silt-sized biogenic fragments and sand-sized lumps of coagulated very small diatom fragments and clay particles (Figure 5). In addition, framboidal pyrites are observed in all laminated mud layers (Figure 6). All these features are observed equivalently and repeatedly in the eight laminated mud layers of LC42 (Appendix S1).

4. Discussion

The glaciomarine laminated muds of LC42 seem unexpected in terms of depositional age, although Ohneiser et al. (2019) reported the magneto-biostratigraphic age. The first appearance of Thalasssiosira antarctica (a first appearance datum [FAD] age of 0.57-0.65 Ma; Cody et al., 2008) between 5.40 and 5.64 m may be unreliable due to co-occurrence with a diverse reworked Miocene and early Pliocene flora. They correlated the normal to reversed polarity change at 8.26 m ± 0.03 m with the Matuyama-Brunhes boundary (0.781 Ma) within Marine Isotope Stage 19 during the interglacial period (Hilgen et al., 2012). In addition, the occurrence of Fragilariopsis kerguelensis (a FAD of ~2.3 Ma; Cody et al., 2008) at 11.65 m may provide a maximum limiting constraint on the basal age. Thus, despite the uncertainty, we assume that the formation of LC42 has continued more than ~1 Ma during which the orbital-scale (~100 ka) glacial-interglacial cycles were repeated at least 10 times. As the currently reported geological period of laminated mud deposition in the Antarctic continental margin is limited mainly to the Holocene to the last glacial period (Alley et al., 2018; Maddison et al., 2012; Stickley et al., 2005), the laminated muds of LC42 can provide new information on the glaciomarine sedimentation over a much longer geological time.

Because the estimated ages of LC42 may be unreliable, the exact depositional ages of individual laminated mud intervals are difficult to date. Nevertheless, deposition of the eight laminated mud intervals, despite the variable thicknesses (10 cm to about 2 m), must have occurred during more than 1 Ma under the conditions of the repeated advance and retreat of ice sheet in the Ross Sea. At the top of the core, the IRD-poor bioturbated sandy mud and IRD-rich massive sandy mud overlies the first laminated mud (Figure 2). It can be regarded as indirect evidence that the deposition of the laminated mud is not related to the warm conditions during the deposition of the IRD-poor bioturbated sandy mud and

IRD-rich massive sandy mud, suggesting the IRD-free laminated mud deposition might have occurred in the cold periods.

The advance and retreat of the Ross Ice Sheet between the glacial and interglacial periods were recorded in the sedimentary sequences in the continental shelf areas (Smith et al., 2019). In general, IRD deposition increased during the warm period by increased calving and floating ice. During the Last Glacial Maximum, the Ross Ice Sheet did not advance to the shelf edge in the central and western Ross Sea (Anderson et al., 2014; Hall et al., 2013; Lee et al., 2017). During the glacial periods, the grounding line was located near the shelf edge of the northwestern Ross Sea, where the glacial activity of ice sheet had a greater influence on the depositional condition in the continental slope and rise (Anderson et al., 2014). In addition, meltwater-derived debris flows occur frequently to cause mass transport towards the continental slope proximal to the grounding lines (Anderson, 1999). Fine-grained sediments might be transported farther away from the ice-shelf zone, and glacial marine muds with well-sorted and very fine sand are deposited by basal debris settling. Other glacial fine-grained laminated sediments are deposited as contourites in the drift areas of the deep continental margin by the intensified activity of the bottom current (Sprenk et al., 2014).

Depositional conditions which result in an absence of IRD usually require a sub-ice shelf environment far from the calving line in cold ocean conditions, favouring the deposition of laminated muds lacking in basal debris from melt-out. The absence of IRD and bioturbation in the laminated muds of LC42 suggests that the mud deposition occurred in the glacial periods. These laminated muds were deposited by the continuous supply of milky meltwater plumes generated underneath the advancing glacier that contained the eroded lumps of semi-consolidated diatom-rich fossiliferous sediments. After the glacial pumping of meltwater plumes, the density-based segregation of grain size and selective settling during the continuous flow may have facilitated the formation of laminated muds. The pinch-andswelling and low-angle inclined lamination of the light laminae with possible internal truncation surfaces and imbrication of particles (Figure 5) suggests the mud deposition from dilute density currents. The density currents might have been fed either from the waxing and waning subglacial meltwater discharges or from buoyant suspensions associated with mass wasting processes (slide/slump and debris flows) near the grounding lines (Mulder et al., 2003; Tripsanas & Piper, 2008).

The formation of laminated sediment sequence requires two fundamental conditions: the compositional (clastic, chemical, and/or biogenic) changes of the sediments and the preservation of sediment lamination without bioturbation (e.g., Kemp, 1996). The laminated muds of LC42 are distinguishable from the laminated terrigenous muds and laminated biosiliceous muds, in terms of the particle compositions (Figures 3 and 4). Typical

laminated terrigenous muds consist of different-sized detrital particles and laminated biosiliceous muds alternate the detrital particles and biogenic remains (e.g., Alley et al., 2018; Maddison et al., 2012; Venuti et al., 2011). On the other hand, the lamination of LC42 is characterized by the alternations of light and dark laminae that are composed of particles from diverse origins. Albot (2016) reported that the detrital particles in the laminated muds of LC42 show bimodal (silt and clay, corresponding to the light and dark laminae) grain size distribution. However, the particle composition in these laminae is unusual in that the coarse-grained light lamina contains sand-sized biogenic fragments and eroded lumps or chips of semi-consolidated diatom-rich sediments that might be deposited much earlier in addition to mostly very fine sandto silt-sized angular to subangular siliciclastic particles (Figures 5 and 6). In contrast, the clayey particles of the dark lamina are dominantly composed of biogenic powders of ground fossils with very fine siltsized biogenic fragments. Bollen (2019) reported the abundant old (Pliocene to Miocene) diatom species (e.g., Coscinodiscus rhombicus, Denticulopsis hustedtii, Fragilariopsis arcula, and Thalassiosira oliverana) from these laminated mud layers, although some archives of young diatom fossils were observed (Figure 6). Thus, a significant portion of the sedimentary particles in the laminated muds was derived from older diatom-rich sediments that were eroded and transported by ice sheet advance to the Central Basin. In addition, framboidal pyrites in the laminated mud layers indicate the low oxygen concentration of bottom water inhibiting the biological activity and preserving sediment lamination without bioturbation in the depositional environment (Figure 6).

The Antarctic continental margin is generally characterized by decreased productivity during the glacial periods, depending on the light and nutrient availability (e.g., Bonn et al., 1998). Such coupling between productivity and climate has been well observed from the sedimentary records in the Antarctic continental shelf (e.g., Frignani et al., 1998). The glacial productivity was also reduced in the Antarctic continental slope and rise due to much wider expansion of seasonal or permanent sea ice coverage (e.g., Wu et al., 2017). On the other hand, it was found recently that the deglacial and glacial sediments of the Ross Sea continental slope and rise are characterized by higher levels of biogenic components than the Holocene sediments, which were interpreted to be due to the glacial supply of reworked diatom-rich shelf sediments (Ha et al., 2022; Khim et al., 2021). Under this situation, the application of a simplistic productivity-climate model to LC42 would lead to a wrong interpretation that the fossiliferous laminated muds represent enhanced productivity during warm climate conditions. However, such high biogenic components of the laminated mud result from the abundant supply of either tiny fragmented and congregated diatoms or even the clay-sized diatomaceous powders finely ground by advancing glaciers also during the cold glacial period. In particular, these diatoms are

distinguished in that they are mostly old and reworked (Bollen, 2019), and are not related to diatom production in the surface water of the Central Basin at the time of laminated mud deposition. Thus, the laminated muds of LC42 present insightful evidence on the Pleistocene palaeoclimate in the Central Basin.

5. Conclusions

The light and dark laminated muds of core LC42 from the Central Basin are characterized by distinctly different componentry, distinguishable from typical laminated terrigenous muds or biosiliceous muds and glacial contourites in the Antarctic continental margin. Terrigenous silt-sized particles, scattered diatom fragments, and eroded sand-sized lumps of fossil-bearing mud are dominant in the light lamina, whereas biogenic clayey particles are enriched in the dark laminae. However, because most biogenic components of the laminated muds were recycled from older deposits, in situ palaeoproductivity information during the mud deposition seems difficult to obtain in terms of conventional biogenic proxies in the case of the Central Basin. Finally, reworking of older biogenic components in the Antarctic depositional system should have been considered, avoiding the misinterpretation of the palaeoclimate and palaeoenvironment.

KOPRI
극지연구소

플라이스토세 로스해 북서부 중앙 분지의 빙해양 엽층 니질퇴적물의 고해양 기록

Boo-Keun Khim[1], Young Kwan Sohn[2], Min Kyung Lee[3], Sunghan Kim[3], Jae Il Lee[3], Kyu Cheul Yoo[3]

[1]Department of Oceanography and Marine Research Institute, Pusan National University, Busan, Korea

[2]Department of Geology, Gyeongsang National University, Jinju, Korea

[3]Division of Glacial Environment Research, Korea Polar Research Institute, Incheon, Korea

요약: 남극 대륙 주변의 빙하해성 층리질 이질 퇴적물은 빙상 역학과 관련된 해양지질 기록에서 중요한 의미를 지닌다. 로스해 중앙 분지에 분포하는 플라이스토세 층리질 이질 퇴적물에 대한 현미경 관찰과 후방산란전자 영상 분석 결과, 밝은 층리는 각진 내지 아각진 형태의 육상 기원 실트 크기 입자, 산재된 규조류 파편, 그리고 화석을 포함한 이질 퇴적물이 침식되어 형성된 모래 크기의 이질 덩어리로 구성되어 있음을 보여준다. 반면, 어두운 층리는 점토질이며 생물기원 성분이 우세하고, 매우 미세한 화석 파편을 포함한다. 이러한 층리질 이질 퇴적물은 전진하는 빙하 하부에서 형성된 빙저 용융수 플룸에 의해 퇴적된 것으로 해석되며, 이 과정에서 이전에 퇴적되어 반고결된 규조류 풍부 퇴적물이 뜯겨 나와 재작용되었을 것으로 판단된다. 따라서 이 층리질 이질 퇴적물에 포함된 대부분의 생물기원 성분은 오래된 퇴적물로부터 재순환된 것이며, 이질 퇴적 당시의 생물 생산성 증가와 직접적으로 연관된 것은 아니다. 본 연구는 남극 환경 시스템의 고기후 및 고해양학적 의미를 해석할 때 생물기원 입자의 재순환 과정을 반드시 고려해야 함을 시사한다.

References

Albot, O. B. (2016). Pleistocene cyclostratigraphy on the continental rise and abyssal plain of the western Ross Sea, Antarctica. MS Thesis, Victoria University, Wellington, New Zealand, 171.

Alley, K., Patacca, K., Pike, J., Dunbar, R., & Leventer, A. (2018). Iceberg Alley, East Antarctic margin: Continuously laminated diatomaceous sediments from the late Holocene. Marine Micropaleontology, 140, 56-68.

Anderson, J. B. (1999). Antarctic marine geology (p. 289). Cambridge University Press.

Anderson, J. B., Conway, H., Bart, P. J., Witus, A. E., Greenwood, S. L., McKay, R. B., Hall, B. L., Ackert, R. P., Licht, K., Jakobsson, M., & Stone, J. O. (2014). Ross Sea paleo-ice sheet drainage and deglacial history during and since the LGM. Quaternary Science Reviews, 100, 31-54.

Bollen, M. (2019). The response of marine diatoms to environmental drivers in the Ross Sea, and applications as a paleoceanographic proxy. MS Thesis, University of Otago, New Zealand, 61.

Bonn, W. J., Gingele, F. X., Grobe, H., Mackensen, A., & Futterer, D. K. (1998). Palaeoproductivity at the Antarctic continental margin: Opal and barium records for the last 400 ka. Palaeogeography, Palaeoclimatology, Palaeoecology, 129, 195-211.

Cody, R. D., Levy, R. H., Harwood, D. M., & Sadler, P. M. (2008). Thinking outside the zone: High-resolution quantitative diatom biochronology for the Antarctic Neogene. Palaeogeography, Palaeoclimatology, Palaeoecology, 260, 92-121.

Colleoni, F., De Santis, L., Siddoway, C. S., Bergamasco, A., Golledge, N. R., Lohmann, G., Passchier, S., & Siegert, M. J. (2018). Spatiotemporal variability of processes across Antarctic ice-bed-ocean interfaces. Nature Communications, 9, 2289. https://doi.org/10.1038/ s41467-018-04583-0

Domack, E. W. (1990). Laminated terrigenous sediments from the Antarctic peninsula: The role of subglacial and marine processes. In J. A. Dowdeswell & J. D. Scourse (Eds.), Glaciomarine environments: Processes and sediments (pp. 91-103). Geological Society of London, Special Publication 53.

Domack, E. W., & Powell, R. (2018). Chapter 7 Modern glaciomarine environments and sediments: An Antarctic perspective. In J. Menzies & J. van der Meer (Eds.), Past glacial environments (pp. 181-272). Elsevier.

Frignani, M., Giglio, F., Langone, L., Ravaioli, M., & Mangini, A. (1998). Late Pleistocene-Holocene sedimentary fluxes of organic carbon and biogenic silica in the northwestern Ross Sea, Antarctica. Annals of Glaciology, 27, 697-703.

KOPRI 극지연구소

Ha, S., Colizza, E., Torricella, F., Langone, L., Giglio, F., Kuhn, G., Macri, P., & Khim, B. K. (2022). Glaciomarine sediment deposition on the continental slope and rise of the Central Ross Sea since the last glacial maximum. Marine Geology, 445, 106752.

Halberstadt, A. R. W., Simkins, L. M., Greenwood, S. L., & Anderson, J. B. (2016). Past ice-sheet behaviour: Retreat scenarios and changing controls in the Ross Sea, Antarctica. The Cryosphere, 10, 1003-1020.

Hall, B. L., Denton, G. H., Stone, J. O., & Conway, H. (2013). History of the grounded ice sheet in the Ross Sea sector of Antarctica during the last glacial maximum and the last termination. In M. J. Hambrey, P. F. Barker, P. J. Barrett, V. Bowman, B. Davies, J. L. Smellie, & M. Tranter (Eds.), Antarctic Paleoenvironments and earth-surface processes (pp. 167-181). Geological Society of London, Special Publication 381.

Hilgen, F. J., Lourens, L. J., Van Dam, J. A., Beu, A. G., Boyes, A. F., Cooper, R. A., Krijgsman, W., Ogg, J. G., Piller, W. E., & Wilson, D. S. (2012). The Neogene period. In F. M. Gradstein, J. G. Ogg, M. Schmidtz, & G. Ogg (Eds.), The geologic time scale (pp. 923-978). Elsevier.

Kemp, A. E. S. (1996). Palaeoclimatology and Palaeoceanography from laminated sediments (p. 258). Geological Society of London, Special Publication 116.

Khim, B. K., Colizza, E., Lee, J. I., Giglio, F., Ha, S., & Bak, Y. S. (2021). Biological productivity and glaciomarine sedimentation in the Central Basin of the northwestern Ross Sea. Polar Science, 28, 100682.

Kim, S., De Santis, L., Hong, J. K., Cottlerle, D., Petronio, L., Colizza, E., Kim, Y. G., Kang, S. G., Kim, H. J., Kim, S., Wardell, N., Geletti, R., Bergamasco, A., McKay, R., Jin, Y. K., & Kang, S. H. (2018). Seismic stratigraphy of the Central Basin in northwestern Ross Sea slope and rise, Antarctica: Clues to the late Cenozoic ice-sheet dynamics and bottom-current activity. Marine Geology, 395, 363-379.

Lee, J. I., McKay, R. M., Golledge, N. R., Yoon, H. I., Yoo, K. C., Kim, H. J., & Hong, J. K. (2017). Widespread persistence of expanded East Antarctic glaciers in the Southwest Ross Sea during the last deglaciation. Geology, 45, 403-406.

Leventer, A., Domack, E., Dunbar, R., Pike, J., Stickley, C., Maddison, E., Brachfeld, S., Manley, P., & McClennen, C. (2006). Marine sediment record from the East Antarctic margin reveals dynamics of ice sheet recession. Geological Society of America Today, 16, 4-10.

Lucchi, R. G., & Rebesco, M. (2007). Glacial contourites on the Antarctic peninsula margin: Insight for palaeoenvironmental and palaeoclimatic conditions. In A. R. Viana & M. Rebesco (Eds.), Economic and Palaeoceanographic significance of Contourite deposits (pp. 111-127). Geological Society of London, Special Publication 276.

Maddison, E. J., Pike, J., & Dunber, R. (2012). Seasonally laminated diatom-rich sediments from Dumont d'Urville trough, East Antarctic margin: LateHolocene Neoglacial Sea-ice conditions. The Holocene, 22, 857-875.

Mulder, T., Syvitski, J. P. M., Migeon, S., Faugere, J. C., & Savoye, B. (2003). Marine hyperpycnal flows: Initiation, behavior and related deposits. A review. Marine Petroleum and Geology, 20, 861-882.

Ohneiser, C., Yoo, K. C., Albot, O. B., Cortese, G., Riesselman, C., Lee, J. I., McKay, R., Bollen, M., Lee, M. K., Moon, H. S., Kim, S., Beltran, C., Levy, R., & Wilson, G. (2019). Magneto-biostratigraphic age models for Pleistocene sedimentary records from the Ross Sea. Global and Planetary Change, 176, 36-49.

Pike, J., & Kemp, A. E. S. (1996). Preparation and analysis techniques for studies of laminated sediments. In A. S. E. Kemp (Ed.), Palaeoclimatology and Palaeoceanography from laminated sediments (pp. 37-48). Geological Society of London, Special Publication 116.

Pudsey, C. J. (2000). Sedimentation on the continental rise west of the Antarctic peninsula over the last three glacial cycles. Marie Geology, 167, 313-338.

Smith, J. A., Graham, A. G. C., Post, A. L., Hillenbrand, C. D., Bart, P. J., & Powell, R. D. (2019). The marine geological imprint of Antarctic ice shelves. Nature Communications, 10, 5635. https://doi.org/10. 1038/s41467-019-13496-5

Sprenk, D., Weber, M. E., Kuhn, G., Wennrich, V., Hartmann, T., & Seelos, K. (2014). Seasonal changes in glacial polynya activity inferred from Weddell Sea varves. Climate of the Past, 10, 1239-1251.

Stickley, C. E., Pike, J., Leventer, A., Dunbar, R., Domack, E. W., Brachfeld, S., Manley, P., & McClennan, C. (2005). Deglacial Ocean and climate seasonality in laminated diatom sediments, mac. Robertson shelf, Antarctica. Palaeogeography, Palaeoclimatology, Palaeoecology, 227, 290-310.

Tripsanas, E. K., & Piper, D. J. W. (2008). Late quaternary stratigraphy and sedimentology of Orphan Basin: Implications for meltwater dispersal in the southern Labrador Sea. Palaeogeography, Palaeoclimatology, Palaeoecology, 260, 521-539.

Venuti, A., Florindo, F., Caburlotto, A., Hounslow, M. W., Hillenbrand, C. D., Strada, E., Talarico, F. M., & Cavallo, A. (2011). Late quaternary sediments from deep-sea sediment drifts on the Antarctic peninsula Pacific margin: Climatic control on provenance of minerals. Journal of Geophysical Research (Solid Earth), 116, B06104. https:// doi.org/10.1029/2010JB007952

Wu, L., Wang, R., Xia, W., Ge, S., Chen, Z., & Krijgsman, W. (2017). Productivity-climate coupling recorded in Pleistocene sediments off Prydz Bay (East Antarctica). Palaeogeography, Palaeoclimatology, Palaeoecology, 485, 260-270.

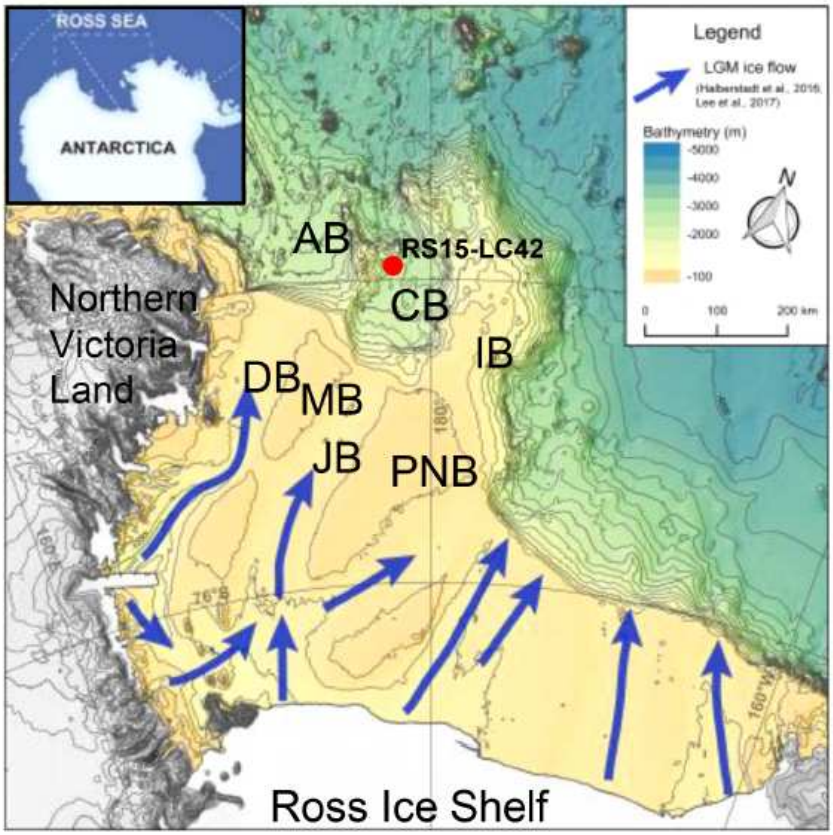


Figure #. Bathymetric map of the Ross Sea (modified from Kim et al., 2018) with the location of core RS15-LC42. Blue arrows represent the likely LGM ice flows along the main glacial troughs on the continental shelf. AB, Adare Basin; CB, Central Basin; DB, Drygalski Basin; IB, Iselin Bank; JB, Joides Basin; MB, Mawson Bank; PNB, Pennell Bank.

KOPRI 극지연구소

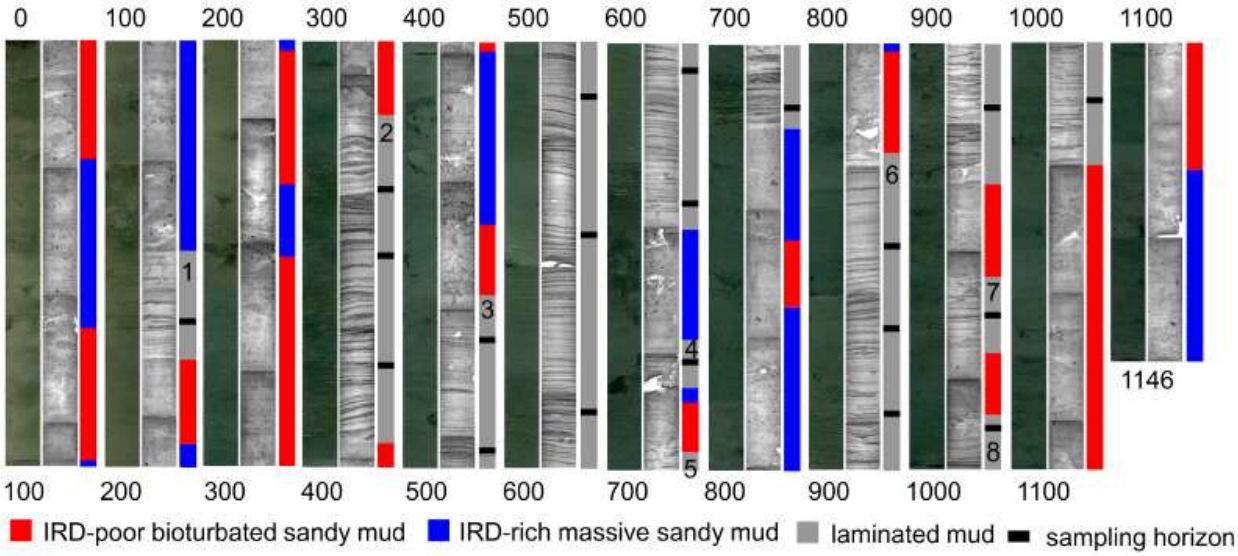


Figure #. Core photos and X-ray photographs of core LC42, consisting of three major lithological facies (IRD-poor bioturbated sandy mud, IRD-rich massive sandy mud, laminated mud). Sample horizons for the thin and polished sections are indicated. Refer to Appendix S1 for the positions of the thin and polished sections.

KOPRI
극지연구소

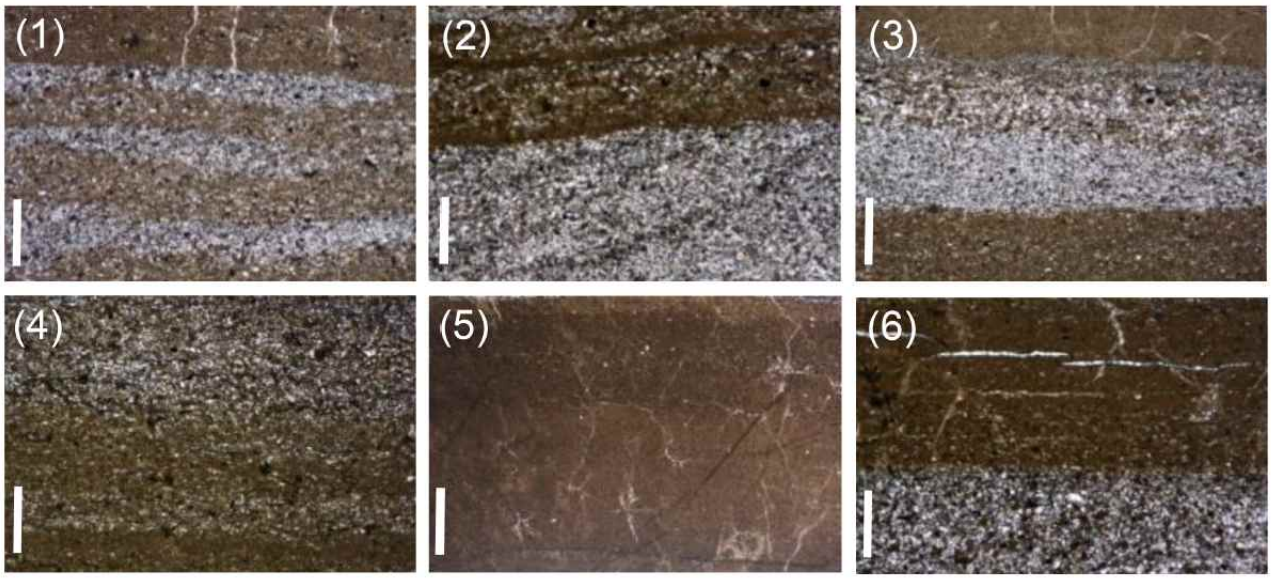


Figure #. Selected photomicrographs of thin sections of core LC42. (1) Alternations of submillimetre-thick, light and dark laminae (TL2), (2) very thin dark and light laminae with a sharp truncated boundary (TL4), (3) a light lamina, showing internal grain size variations, with sharp upper and lower boundaries to the dark lamina (TL5), (4) a dark and light lamina with gradational boundary (TL7), (5) an internally massive, dark clay lamina (TL12), (6) a light and dark lamina with relatively sharp boundary (TL13). Scale bar is 0.5 mm long. Refer to Appendix S1 for thin lamination (TL) numbers and their positions. More photomicrographs of thin sections are compiled in Appendix S1. [Colour figure can be viewed at wileyonlinelibrary.com]

KOPRI
극지연구소

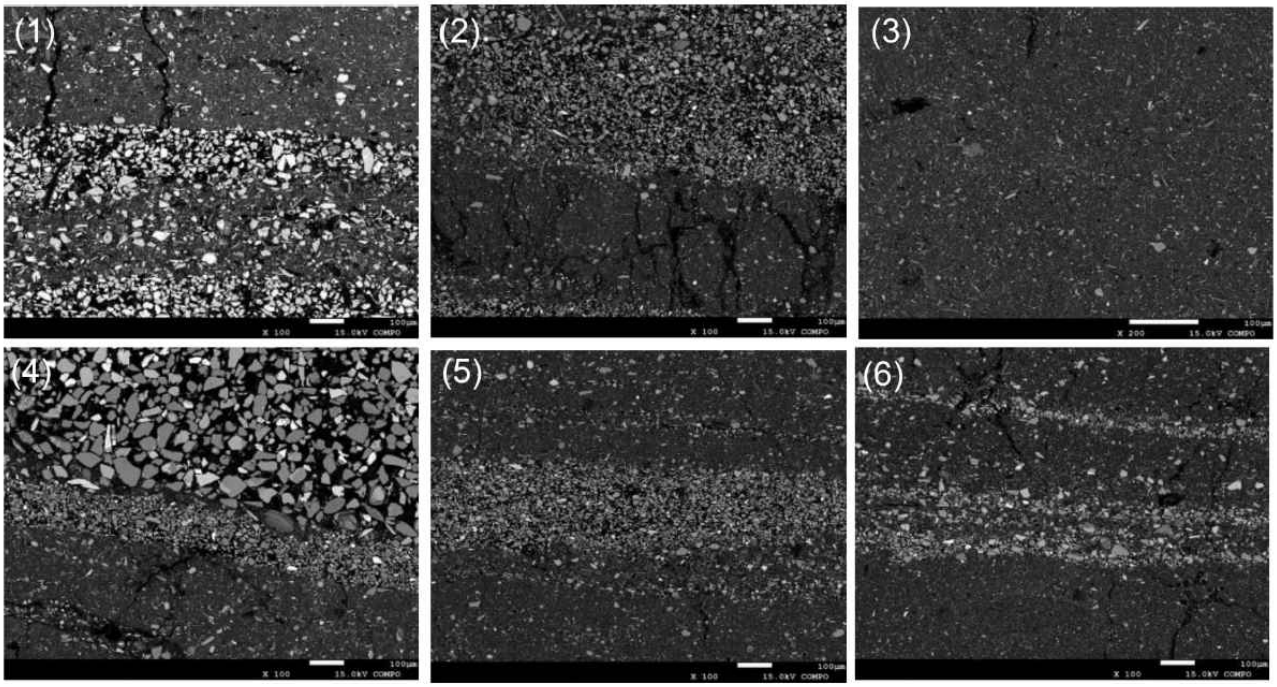


Figure #. Selected BSEI of polished sections of core LC42, representing the dark and light lamina. (1) A dark lamina intercalated with light laminae (TL2, ×100), (2) typical dark and light lamina (TL10, ×100), (3) massive clay-rich dark lamina (TL12, ×200), (4) multiple layering of laminae with different grain sizes (TL13, ×100). Note the openwork texture of the coarse lamina: (5) a very thin light lamina with diffuse upper and lower boundaries (TL17, ×100), (6) very thin light laminae within dark lamina (TL19, ×100). Scale bar is 100 μm long. Refer to Appendix S1 for thin lamination (TL) numbers and their positions. More BSEI of polished sections are compiled in Appendix S1.

KOPRI 극지연구소

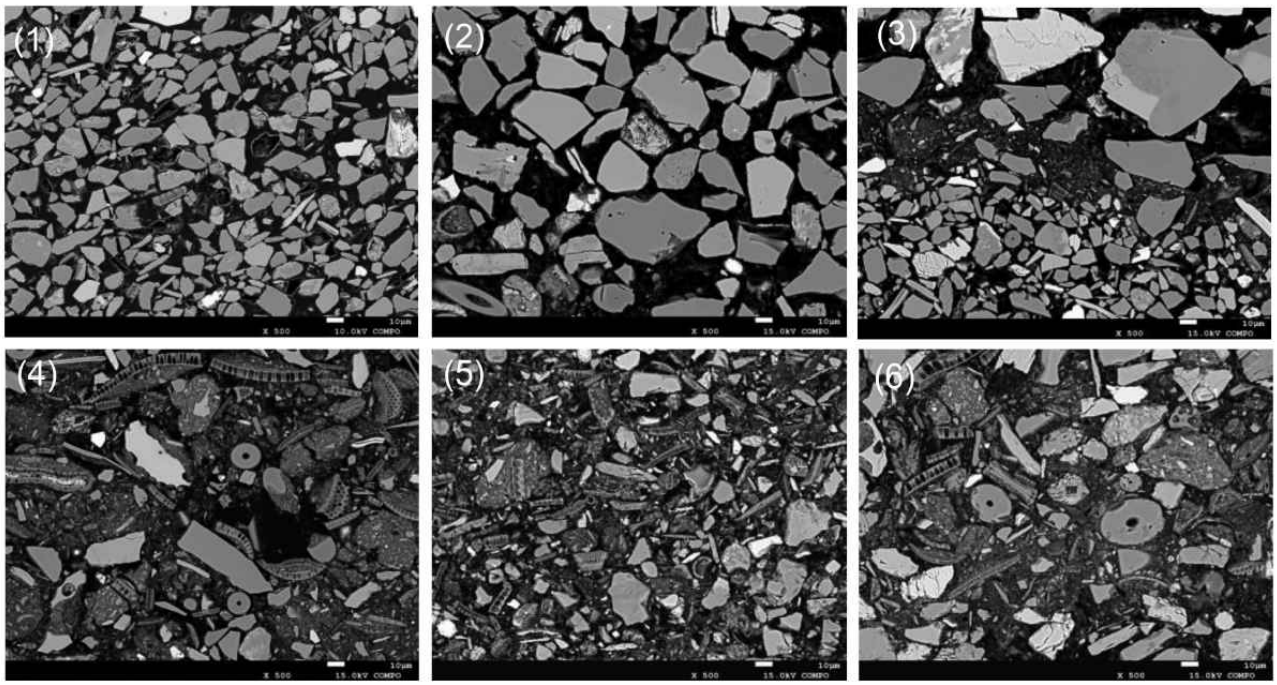


Figure #. Selected close-up BSEI of polished sections of core LC42 showing the components of light lamina. (1) Close-up of fine silt-sized particles (TL1, ×500), (2) close-up of coarse silt-sized particles (TL9, ×500), (3) inverse grading-like boundary between the fine silt-sized particles overlain by the very fine sand-sized particles (TL13, ×500), (4-6) close-up of mixed terrigenous and biogenic sediment lumps or aggregates containing tiny biogenic fragments (4: TL4, 5: TL7, 6: TL8, ×500). Scale bar is 10 μm long. Refer to Appendix S1 for thin lamination (TL) numbers and their positions. More close-up BSEI of polished sections are compiled in Appendix S1.

KOPRI
극지연구소

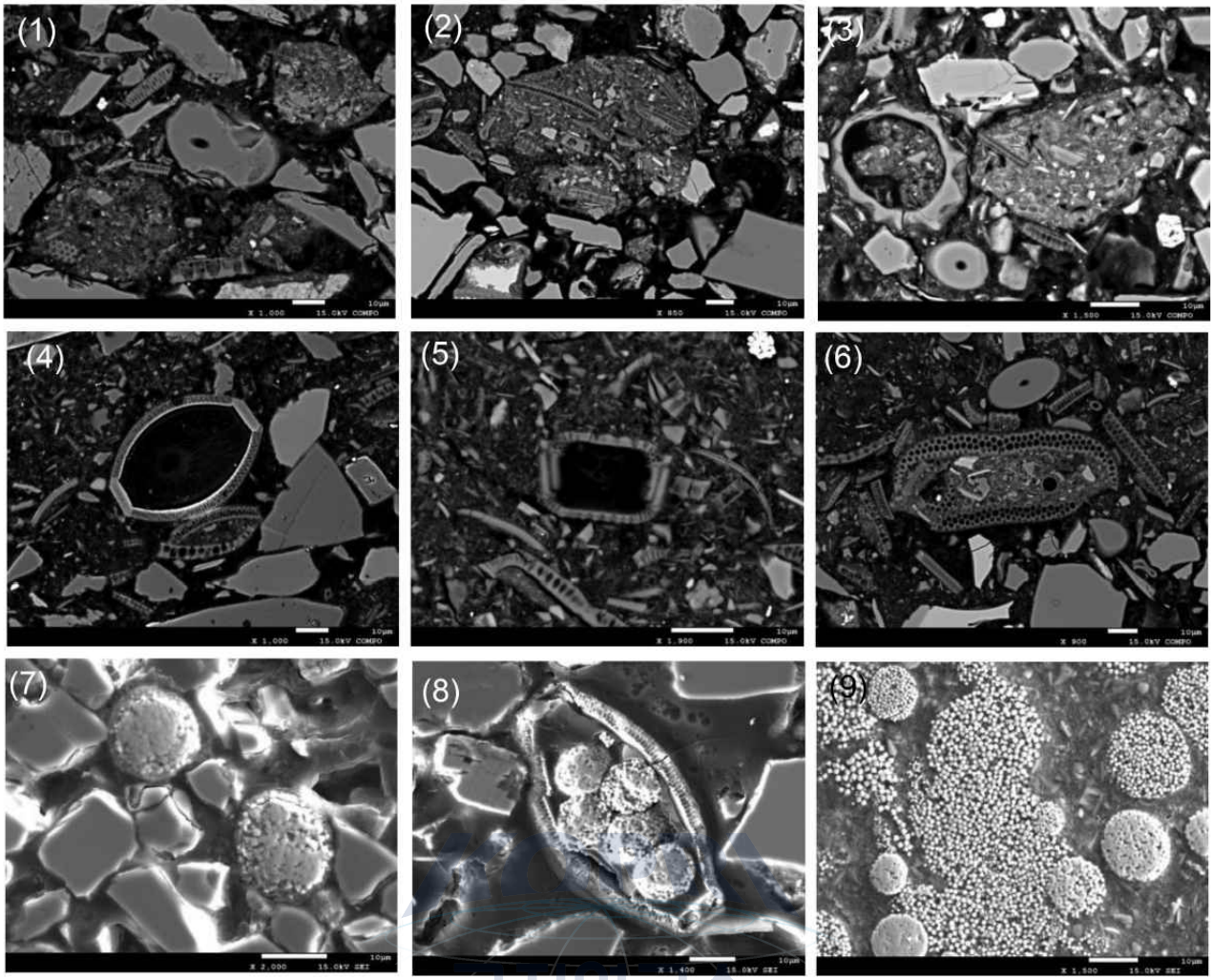


Figure #. Selected close-up BSEI of mixed terrigenous and biogenic sediment lumps or aggregates (1: TL5, ×1000, 2: TL11, ×850, 3: TL16, ×1500), archived unidentified diatom fossils and fragments (4: TL2, ×1000, 5: TL2, ×1900, 6: TL4, ×900), and framboidal pyrite patches (7: TL18, ×2000, 8: TL13, ×1400, 9: TL20, ×1500). Scale bar is 10 μm long. Refer to Appendix S1 for thin lamination (TL) numbers and their positions. More close-up BSEI of polished sections are compiled in Appendix S1.

제 35 장

Glacial-interglacial environmental changes in the Drake Passage over the past 600 kyrs[28)]

Sunghan Kim[a,b,*], Jae Il Lee[a], Kyu-Cheul Yoo[a], Min Kyung Lee[a], Young-Suk Bak[c], Myung-Il Kang[a], Sookwan Kim[d], Jinku Park[a]

[a]Korea Polar Research Institute, Incheon 21990, Republic of Korea
[b]Department of Polar Sciences, University of Science and Technology (UST), Incheon 21990, Republic of Korea
[c]Department of Earth and Environmental Sciences, Jeonbuk National University, Jeonju, 54896, Republic of Korea
[d]Korea Institute of Ocean Science and Technology, Busan 49111, Republic of Korea

KOPRI 극지연구소

Abstract: Oceanographic conditions in the Southern Ocean are closely related to the oceanic frontal system. Glacial-interglacial changes in cryosphere influence variations in oceanic fronts in the Southern Ocean and vice versa, causing changes in surface water productivity, nutrient utilization, bottom water chemistry, and/or bottom current intensity. Here, we documented geochemical, nitrogen isotope, and grain size records over the last 600 kyrs from the Drake Passage with previously published data to compare between glacial and interglacial oceanic conditions from surface to bottom. Biogenic opal (diatom) and export productions were high during interglacial periods and low during glacial periods. Surface water production was dominated by open ocean species during both glacial and interglacial periods without a clear glacial-interglacial change in sea ice species. After Marine Isotope Stage (MIS) 9, interglacial biogenic opal and diatom abundance increased distinctively with decreased terrestrial influence. Nutrient utilization increased (decreased) during interglacial (glacial) periods with increased (decreased) surface water production, particularly after MIS 9. This indicates that surface water production was regulated by light availability in association with sea ice duration/extent. According to good correlation between sortable silt mean grain size (SS MGS) and %sortable silt, SS MGS can be used for bottom current

28) 이 연구 결과는 다음의 논문으로 출판되었음: Kim, S. et al. (2023). "Glacial-interglacial environmental changes in the Drake Passage over the past 600 kyrs" Palaeogeography Palaeoclimatology, Palaeoecology 631: 111835.

intensity indicator in this study; increased (decreased) bottom current during glacial (interglacial) periods. Increased glacial bottom current is likely related to southwestward flowing bottom current. Interglacial bottom current intensity became also significantly weakened after MIS 9. However, outstanding interglacial warmth in the Drake Passage occurred from MIS 9, not following the global trend to occur after MIS 11. This implies that more studies from the Southern Ocean in response to the Mid-Brunhes Event are required in the future.

1. Introduction

The earth's climate has experienced ~100 kyr glacial-interglacial changes over the last 800 kyrs (Imbrie et al., 1993; Clark et al., 2006). According to ice core δD-derived temperature (Jouzel et al., 2007), atmospheric CO2 (EPICA-community-members, 2004; Lüthi et al., 2008), and global benthic oxygen isotope stack (LR04, Lisiecki and Raymo, 2005), interglacial periods became warmer from Marine Isotope Stage (MIS) 11/12 than those before. This climatic event is called Mid-Brunhes Event (MBE, Jansen et al., 1986) or Mid-Brunhes Transition (MBT, Yin, 2013). Glacial-interglacial oceanic frontal variations in the Southern Ocean were reported (e.g., Gersonde et al., 2005; Kemp et al., 2010; Manoj and Thamban, 2015; Roberts et al., 2017). However, there were not many sediment cores recovering sedimentary records beyond MIS 11 in the Antarctic continental margins, limiting climatic/oceanographic comparison in the Southern Ocean between pre- and post-MBE. As Barth et al. (2018) reported that changes in carbon cycle, ice sheets, and monsoon strength occurred during MIS 13 or MIS 14, although their relationship with the MBE is unclear. Thus, it needs to be verified whether the Antarctic Ocean follows global climate variation pattern.

Oceanographic fronts developed in the Southern Ocean are merging in the Drake Passage (Fig. 1). The climatic sensitivity in the Drake Passage was proposed by previous results of nearby sediment cores from the south Scotia Sea, based on Holocene surface productivity variation (Kim et al., 2020a). This indicates that subtle climate changes are recorded in Drake Passage sediments. Kim et al. (2020a) reported that paleoceanographic changes including surface production and nutrient utilization and cryosphere changes including sea ice and ice sheet/shelf are strongly coupled, based on multi-proxy records from the Last Glacial Maximum (LGM). Lamy et al. (2015) and Toyos et al. (2020) reported that glacial-interglacial Antarctic Circumpolar Current (ACC), which is an important factor for controlling oceanographic conditions in the Drake Passage. Wu et al. (2021) also reconstructed ACC changes during the last 140 kyrs. Wang et al. (2017) showed different

glacial-interglacial variation pattern of coral δ15N between Subantarctic zone and Antarctic zone in the Drake Passage. However, there's a caveat that there are no comprehensive studies dealing with surface and bottom oceanographic changes together. Thus, multi-proxy sedimentary records from the Antarctic zone in the Drake Passage is necessary to understand glacial-interglacial Drake Passage climatic system.

Diatoms are the dominant phytoplankton in the Southern Ocean (DeMaster, 2002). Diatom assemblage changes can indicate surface oceanographic conditions (e.g., Gersonde et al., 2005; Sjunneskog and Winter, 2012; Leventer et al., 2015; Kim et al., 2018a). During sinking and burial diatom dissolution occurs (Archer, 1993; Ragueneau et al., 2000), consequently fragmented frustules are preserved in the sediment especially under poor preservation places. However, surface diatom productivity studies have been poorly conducted, although some diatom assemblage studies were conducted (e.g., Bak et al., 2010a). According to Chase et al. (2015), in the areas south of the Polar Front (PF) sea ice duration acts as a main controller, whereas in places north of the PF nutrient availability controls surface diatom production. Thus, biogenic opal concentration, representative of diatom production (Kienast et al., 2002), can be used to reconstruct surface paleoceanographic condition changes together with diatom assemblage data and nutrient utilization, providing the linkage between surface production and nutrient utilization, which has not been reported from the Drake Passage.

In this study, we reconstruct oceanographic conditions in both surface and bottom over the last 600 kyrs using multi-proxies including biogenic opal, total organic carbon (TOC) and total nitrogen (TN), and nitrogen isotope of organic matter, grain size, and sortable silt (SS: 10 – 63 μm) with previously published data to understand the orbital-scale paleoceanographic variations and to compare between pre- and post-MBE paleoceanographic conditions in the Drake Passage.

2. Study area

The Drake Passage is under the influence of the clockwise-flowing ACC, the largest ocean current in the world (Orsi et al., 1995). The largest ACC volume transport in the Drake Passage is observed across the PF (Whitworth et al., 1982; Orsi et al., 1995). As a result, a strong eastward flow occupies from the surface to deep water, but south of the PF (~59°S) westward counter currents are dominated (Fig. 1). Westward flowing along-slope current and its counter-currents show seasonal variations: stronger during austral winter and weaker during austral summer (Fig. 1). Weddell Sea Deep Water and Warm Deep Water from the Weddell Sea flows anti-clockwise along the slope and upper rise (Fig. 1,

Hernández-Molina et al., 2006). Shelf surface water circulation in the western Antarctic Peninsula shows a small size clockwise gyre (Fig. 1, Hofmann et al., 1996).

Chase et al. (2015) showed increasing sea ice duration and nutrients toward the Antarctic continent from the PF. Both silicates and nitrates are abundant in the shelf region (Fig. 1). The highest opal burial occurred in the PF and decreased both northward and southward with increasing distance from the PF. The study site is located at the northern margin of winter sea ice and summer sea ice is limited in the shelf region (Fig. 1).

The southern Drake Passage is proximal to South Shetland Islands (SSI) and the northern Antarctic Peninsula, which are mainly composed of Mesozoic and Cenozoic subduction-associated volcanic and plutonic rocks (Thomson and Pankhurst, 1983; Machado et al., 2005a, 2005b). ℳNd of surface sediments showed high values around West Antarctic Peninsula margin including SSI (-3.3 ~ 1.5), whereas low values in the Weddell Sea region (-6.5 ~ -9.8) (Fig. 1, Lee et al., 2012 and references therein). This supports those sediments from Antarctic Peninsula and SSI are volcanic origins.

3. Materials and Methods

A gravity core GC05-DP02 (61°02.7096′S, 62°38.3859′W, 3503 m deep, 595 cm long) was collected from the Drake Passage off the South Shetland Islands by R/V Yuzhmorgeologiya (Fig. 1).

All geochemical proxies for GC05-DP02 were measured at 2 cm intervals on 1 cm thick sub-samples at the Korea Polar Research Institute (KOPRI). Biogenic silica concentration was measured using a Continuous Flow Analyzer (SKALAR SANplus Analyzer) with a wet-alkaline extraction method modified from DeMaster (1981) following the method of Kim et al. (2018b). Biogenic opal concentration was calculated by multiplying biogenic silica concentration by 2.4 (Mortlock and Froelich, 1989). The relative error of biogenic silica concentration in sediment samples is less than 1%. Total inorganic carbon (TIC) concentration was measured using UIC CO2 coulometer (Model CM5240). CaCO3 concentration was calculated by multiplying TIC concentration by 8.333. The relative standard deviation for CaCO3 concentration is ±1%. Total carbon (TC) concentration was measured by an Organic Elemental Analyzer (FLASH 2000 NC Analyzer) with an analytical precision of less than ±0.1%. TOC concentration was calculated by the difference between TC and TIC. C/N ratios were calculated by TOC/TN.

Nitrogen isotopes were measured at 2 cm intervals using an EA‐IRMS (Europa Scientific RoboPrep-CN elemental analyzer & Europa Scientific 20-20 mass spectrometer) at Iso-Analytical Ltd., UK. Inorganic nitrogen was reported in high latitudes (Schubert and

KOPRI 극지연구소

Calvert, 2001). Kim et al. (2020a) showed no significant differences between bulk nitrogen isotope (δ15N) and nitrogen isotope of acid treated samples (δ15Nacid) in Scotia Sea cores. Thus, δ15Nacid was measured after HCl treatment in this study.

After removing all biogenic components (biogenic opal, organic matter, and CaCO3) from the bulk sediments using sodium hydroxide, hydrogen peroxide, and hydrochloric acid, respectively, the grain size was analyzed at 10 cm intervals using a laser diffraction particle analyzer (Malvern Mastersizer 3000). The mean grain size (MGS) of SS of GC05-DP02 was calculated following McCave and Andrews (2019).

Diatom assemblage analysis was previously conducted by Bak et al. (2010a).

4. Age determination

The chronology of GC05-DP02 was constrained by Lee et al. (2012). We generally followed their age scheme. The age model is based on three accelerator mass spectrometry 14C dates of planktonic foraminifera in the upper part of core GC05-DP02 and last occurrence datums of diatom Hemidiscus karstenii (180–190 cm) and radiolarian Stylatractus universus Hays at 440 cm (Lee et al., 2012). We acknowledge that there is some chronological uncertainty whether the interglacial interval corresponds to the whole interglacial stage or peak interglacial periods only (e.g., MIS 5 vs 5e or MIS 7 vs 7e), as GC05-DP02 records do not seem to reflect millennial-scale variation.

5. Results

Biogenic opal concentration varies from 5% during glacial periods to 7–15% during interglacial periods (Fig. 2). Interglacial biogenic opal concentration became higher after MIS 9 (10–15%) than those before (~7%). Variations in TOC and TN resemble that of biogenic opal concentration, ranging from 0.1% during glacial periods to 0.15–0.3% during interglacial periods and from ~0.02% during glacial periods to 0.03–0.04% during interglacial periods, respectively. Although TOC and TN were relatively lower during MIS 7 compared to MIS 1, 5, and 9, they also became generally higher after MIS 9 (Fig. 2). Biogenic opal, TOC, and TN all were anti-correlated with magnetic susceptibility.

CaCO3 concentration was very low in general, except for two glacial periods; 15% during MIS 2–4 and 3% during MIS 6 (Fig. 2). The main constituent of CaCO3 is planktonic foraminifera. C/N ratios were generally low <8, except for 10–12 during MIS 2–4 (Fig. 2).

δ15Nacid values vary from 2‰ to 5.5‰ and the glacial-interglacial difference is not

as clear as other proxies mentioned above (Fig. 2). Variation amplitudes are small before MIS 10, but became larger after MIS 10 showing relatively higher δ15Nacid values during MIS 5, 7, and 9 (Fig. 2).

SS MGS varies from 17 μm to 25 μm showing high values during glacial periods and low values during interglacial periods (Fig. 3). Interglacial SS MGS distinctly decreased from ~20 um before to ~17 um after MIS 9 (Fig. 3). SS MGS variation was in parallel with SS percentage from mud (%SS) (Fig. 3). Sand fraction increased during glacial periods with increases in MGS (Fig. 3).

6. Discussion

6.1 Glacial-interglacial surface oceanographic condition changes

Biogenic opal concentration shows a good negative correlation with MS values (r=0.62) (Fig. 4). Because MS values are indicative of terrestrial input (e.g., Ceccarori et al., 1998; Diekmann et al., 2000; Hillenbrand et al., 2009; Yoon et al., 2009; Sprenk et al., 2013; Kim et al., 2018b), the negative correlations were reported from Antarctic continental margin cores indicating that diatom production increased under open ocean conditions with less terrestrial influence and vice versa. Biogenic opal concentration also showed good correlations with TOC concentration (r=0.66) and total diatom abundance (r=0.59) (Fig. 4). This suggests that biogenic opal concentration well reflects surface diatom production and control export production in the Drake Passage. GC05-DP02 is located north of the winter sea ice margin today (Fig. 1) in the south of the PF. Chase et al. (2015) reported that sea ice duration is the main controlling factor for biogenic opal production and burial in the south of the PF. Diatom assemblage and biogenic opal concentration of cores in the Scotia Sea also showed that diatom productions are controlled by sea ice (e.g., Xiao et al., 2016; Kim et al., 2020a).

It was reported expanded sea ice in the SO during glacial periods (e.g., Gersonde et al., 2005; Xiao et al., 2016; Kim et al., 2020a) and expanded ice sheet/shelf in the Antarctic Peninsula (Anderson et al., 2002; Ó Cofaigh et al., 2014; The RAISED et al., 2014). Thus, sea ice coverage and duration in the study site likely increased during glacial periods with ice sheet/shelf advance. As a result, diatom production decreased (increased) during glacial (interglacial) periods under more (less) sea ice influence. Biogenic opal concentration and diatom total valve support this inference (Fig. 5).

Diatom data of GC05-DP02 were previously reported in Bak et al. (2010a) and downcore variation of major species are shown in Figure S1. Diatom species, Fragilariopsis

kerguelensis, Thalassiosira lentiginosa, Thalassionema nizschioides, Hemidiscus karstenii, and Dactyliosolen antarcticus are abundant under open ocean condition and/or more ACC influence (Crosta et al., 2005). Thus, we grouped them as open ocean species in this study. In contrast, Actinocyclus actinochilus, Fragilariopsis curta, F. cylndrus, F. ritscheri, F. separanda, Thalassiosira antarctica are reported to be related to sea ice (Armand et al., 2005). Thus, we grouped them as sea ice species in this study. However, since F. curta and F. cylindrus were rare in GC05-DP02 (Bak et al., 2010a). In the Scotia Sea, Eucampia antarctica showed glacial-interglacial variation; high during glacial periods (Xiao et al., 2016; Kim et al., 2020a). Open ocean species are generally abundant during interglacial periods (Fig. 5, Bak et al., 2010a). However, their relative abundance increased during MIS 10 and 12 (Fig. 5). On the other hand, sea ice diatoms or E. antarctica generally do not show clear glacial-interglacial variations, except for abundant E. antarctica during MIS 12 (Fig. 5). Interglacial total diatom abundance significantly increased after MIS 9 compared to previous interglacial periods (Fig. 5).

In Scotia Sea sediments, diatom assemblage shows a general glacial-interglacial variation; high F. kerguelensis during interglacial vs high E. antarctica during glacial periods (Bak et al., 2010b; Xiao et al., 2016). However, a sediment core from the Scotia Sea showed high relative abundance of F. kerguelensis during some glacial periods with low biogenic opal concentration (Xiao et al., 2016). Thus, diatom production is likely dominated by open ocean species both during interglacial and glacial periods in the Antarctic Zone of the Drake Passage and Scotia Sea. GC05-DP02 site is located at the margin of modern winter sea ice (Fig. 1). In addition, Hemming et al. (2007) reported that northward frontal migration was small during glacial periods. Thus, the influence of sea ice during glacial periods in the study area may have been slightly increased, allowing F. kerguelensis as the dominant species even during glacial periods. Less clear glacial-interglacial variation in sea ice species of GC05-DP02 also supports less distinct glacial-interglacial sea ice condition in the Drake Passage over the last 600 kyrs (Fig. 5). However, low biogenic opal and TOC concentrations and low diatom abundance suggest diatom preservations are poor, which is supported by diatom observation results (Bak et al., 2010a). Thus, less distinctive glacial-interglacial pattern in sea ice diatom could be derived from poor preservation even under increased sea ice influence conditions. One clear thing is that low biogenic opal concentration, diatom abundance, and TOC concentration during glacial periods indicates suppressed surface water production. Considering the modern core location at the margin of winter sea ice, sea ice influence (i.e., duration and/or extent) must have increased at GC05-DP02 during glacial periods.

δ15Nacid values, indicative of nitrate utilization in the surface water (Francois et al., 1992; Altabet and Francois, 1994), showed increased values during MIS 5, 7, and 9 (Fig. 2).

In the Polar Front of the Ross Sea sector, Studer et al. (2015) reported that increased nutrient utilization with decreased production during glacial periods indicate Antarctic water stratification during glacial periods. Glacial stratification of Antarctic Ocean was once proposed previously (e.g., Robinson and Sigman, 2008). However, the relationship between δ15Nacid values and surface water production provides important information on whether the controlling factor for surface water production is light-limiting or nutrient-limiting (e.g., Kim et al., 2020a). Synchronous variation patterns of surface production and nitrate utilization from MIS 10 to MIS 2 are found in GC05-DP02; high during interglacial and low during glacial periods (Fig. 2), although their statistical correlations are low. This indicates that surface diatom production at GC05-DP02 is controlled by light-limiting. Thus, high nitrate utilization during interglacial periods was caused by increased diatom production under less sea ice influence, whereas low nitrate utilization during glacial periods is likely caused by suppressed diatom production under more sea ice influence, which limits light penetration, in the Drake Passage. That is, sea ice extent/duration controlled glacial-interglacial variation of light availability.

Because the C/N ratio can be used for organic matter origin (Lamb et al., 2006), high C/N ratios are found under the increased terrestrial influence in the Antarctica (e.g., Smith et al., 2019; Kim et al., 2020a, 2020b). However, except for the last glacial period, MIS 2–4, C/N ratios were lower than 8 regardless of glacial-interglacial cycles (Fig. 2). This means that organic material deposited in GC05-DP02 originated from surface biological production. This suggests that even during glacial periods surface production was controlling export production despite decreased production.

6.2 Glacial-interglacial bottom oceanographic condition changes

SS MGS is used as an indicator of bottom current intensity (e.g., McCave et al., 2014, 2017; Jonkers et al., 2015; Wu et al., 2018, 2021; McCave and Andrews, 2019). In places with iceberg rafted debris (IRD) deposition, however, caution is required to use SS as a bottom current indicator, because IRD particles include a substantial amount of mud. Jonkers et al. (2015) and Wu et al. (2018) used grain size distribution after removing the IRD signal. Recently, McCave and Andrews (2019) reported that if %SS and SS MGS have a strong correlation, the SS MGS can be used for reconstruction of bottom current intensity regardless of IRD influence.

SS MGS and SS% of GC05-DP02 showed a parallel variation having a strong correlation (r=0.89) (Figs. 3 and 4). This indicates that fine sediments are thought to be well current-sorted, thus implying that SS MGS can be used for bottom current intensity of the study site despite IRD input in GC05-DP02. Wu et al. (2020) reported that Zr/Rb can be

used for bottom current intensity indicator in the Antarctic continental margins. Wu et al. (2021) showed a similar variation pattern between mean grain sizes of 10–63 μm and 10–125 μm and Zr/Rb ratio in the Drake Passage. High SS MGS occurred during glacial and low SS MGS occurred during interglacial periods (Fig. 3). This means that the bottom current intensity at study site was stronger during glacial periods than that of interglacial periods. However, Toyos et al. (2020) reported increased (decreased) SS MGS during the Holocene (LGM) in the Subantarctic Drake Passage. Wu et al. (2021) also reported increased bottom current during interglacial periods in the Subantarctic Drake Passage. This indicates that glacial-interglacial bottom current variation pattern is different between north and south of the Polar Front in the Drake Passage. According to SS MGS comparison between the Holocene and the LGM in the Scotia Sea, bottom current was stronger in the north of PF during the LGM whereas was stronger during the Holocene in the south of PF, and this is related to the glacial-interglacial latitudinal migration of ACC (McCave et al., 2014). Thus, strengthened bottom current during glacial periods is not thought to be related to the ACC at GC05-DP02 site because of its position located in the south of PF.

Sediment drifts are well developed on the western slope and rise of the Antarctic Peninsula (Barker et al., 2002; Rebesco et al., 2002; Hillenbrand et al., 2008; 2021). Gray laminated mud was found during glacial periods from cores in the drift. Southwestward flow bottom currents are responsible for the development of drift sediment (Pudsey and Camerlenghi, 1998; Lucchi et al., 2002; Lucchi and Rebesco, 2007; Hillenbrand et al., 2021). Little has been known about the southwestward flowing bottom current flowing along the West Antarctic Peninsula. Increased SS MGS during glacial periods were reported from south of PF close to southern boundary of ACC; Southern Ocean off Elephant Island (Kim et al. 2020a) and from the eastern Scotia Sea (McCave et al., 2014), which are close to the southern boundary of ACC. Thus, the increased bottom current intensity during glacial periods is likely related to the southwestward flowing bottom current. According to modern 30 years observation (Fetterer et al., 2017), GC05-DP02 is influenced by the southwestward flowing counter-current which becomes stronger during winter (Fig. 1). Likewise, during glacial periods the counter current was likely stronger due to northward migration of oceanic fronts and stronger wind. Wind-driven Antarctic Slope Current became stronger during winter (Fig. 1) and reported stronger during glacial periods in the Ross Sea (Kim et al. 2020b). As Huang et al. (2020) reported that Antarctic Bottom Water formation from the Weddell Sea decreased during glacial periods, increased bottom current intensity at the GC05-DP02 site is likely not related to Weddell Sea-derived bottom/deep water mass. Thus, our results show southwestern-ward bottom current was strengthened and even in north of southern ACC in the Drake Passage during glacial periods.

$CaCO_3$ is poorly preserved in the Antarctic continental margin (e.g., Anderson,

1975). CaCO3 varies from 20% during MIS 2 and 4 to 60% during MIS 1 and 5 in DP00-02 (60°59.8′S, 65°21.4′W, 2710 m deep) corrected from the Drake Passage (Bae et al., 2003). On the other hand, GC05-DP02, located in ~800 m deeper water depth than DP00-02, showed absence of CaCO3 during interglacial periods and 15% during MIS 2–4 and 3% during MIS 6 (Fig. 2). Since both GC05-DP02 (~61°S) and DP00-02 (~61°S) are located south of PF, the different CaCO3 variation pattern is most likely related to water depth difference to influence preservation. This indicates that CaCO3 preservation of deep-water in the Drake Passage is very poor during interglacial periods and it became better during MIS 2–4 and 6 because CaCO3 was absent during other glacial periods in GC05-DP02 (Fig. 2).

Increased Ca/Al ratios during MIS 2–4 and 6 with occurrence of foraminifera were observed from Prydz Bay (Wu et al., 2017). Increased CaCO3 during MIS 2–4 and 6 were also found in cores from the Cosmonaut Sea (Bonn et al., 1998). However, why during MIS 2–4 and 6 glacial periods only a better CaCO3 preservation remained difficult to explain. Although the increased CaCO3 could be due to input of reworked shells from the shelf in association with advanced ice sheet during glacial periods, the dominant component is planktonic foraminifera and shell fragments were not observed. Anderson et al. (1975) reported that cold, saline shelf water production in the southwestern Weddell Sea continental shelf is undersaturated with respect to CaCO3. This water is mixed into Antarctic Bottom Water (Seabrooke et al., 1971). Because Antarctic Bottom Water formation from the Weddell Sea decreased during MIS 2 and 6 but increased during MIS 1 and 5 (Huang et al., 2020), CaCO3 variation pattern in GC05-DP02 is likely related to Weddell Sea-derived bottom water such as WSDW influencing our site. Nonetheless, according to core locations and/or water depths, different variation patterns occur in the Antarctic continental margin (Bonn et al., 1998; Bae et al., 2003; Rickaby et al., 2010; Wu et al., 2017; this study). Thus, more thorough study is necessary to understand glacial-interglacial carbonate system in the Antarctic Ocean in the future.

6.4 Climatic shift after MIS 9, not MIS 11

Antarctic ice core showed δD-derived temperature (Jouzel et al., 2007) and atmospheric CO2 (EPICA-community-members, 2004; Lüthi et al., 2008) increased after MIS 11 (Fig. 6). In addition, interglacial global ice volume also reduced after MIS 11 (Fig, 6d, Lisiecki and Raymo, 2005). Further retreat of grounding line since MIS 11 was reported from the Wilkes Land (Wilson et al. 2018). Based on SS MGS records from the Southern Ocean Atlantic sector, southward migrations of the PF, sub-Antarctic Front, and southern boundary of the ACC were reported during post-MBE interglacial periods (Kemp et al., 2010; Saavedra-Pellitero et al., 2017). Coinciding with this change, Circumpolar Deep Water

upwelling in the south of the PF became stronger (Kemp et al., 2010) and high coccolithophore production occurs by changes in sea surface temperature and nutrient regimes (Saavedra-Pellitero et al., 2017). However, significant changes occurred after MIS 9 in GC05-DP02 (Fig. 6). Increased interglacial diatom production and export production together with decreased terrestrial influence after MIS 9 in GC05-DP02 are likely related to the southward migration of oceanic fronts. After MIS 9, nitrate utilization showed clearer glacial-interglacial variations. The interglacial bottom current at the study site became significantly weakened after MIS 9. The study site is under the influence of southwestward flowing counter bottom current in modern days (Fig. 1). This current became stronger during winter, thus southward migration of ACC and other oceanographic fronts mostly restricted the counter current after MIS 9. Interglacial MS values also became significantly lower after MIS 9 implying decreased terrestrial influence (Fig. 2). As a result, interglacial %sand decreased after MIS 9 with fine grain (<10 μm) increase (Fig. 3). Parts of MIS 11 record may have been eroded by bottom current. However, it was weak during interglacial periods and observed was no sign of erosion or unconformities in GC05-DP02. Sedimentation rates showed high during interglacial and low during glacial periods (Fig. #). Thus, high sedimentation rate during MIS 11 also support no loss of MIS 11 record. Thus, we conclude distinct changes occurred from MIS 9 not MIS 11 at the study site. The characteristics of interglacial periods after MIS 9 compared to those before MIS 9 at GC05-DP02 are shown in Table 1.

However, why interglacial oceanographic condition changed after MIS 9 in GC05-DP02 is not clear, not following the global trend. Holden et al. (2011) reported early interglacial optima are apparent during MIS 1, 5, 7, 9, and 19 over the last 800 kyrs. Interglacial biogenic opal concentration increase occurred earlier in Amundsen Sea after MIS 15 (Hillenbrand et al., 2009). Interglacial biogenic opal concentration increase occurred after MIS 9 in Prydz Bay (Wu et al., 2017) and Cosmonaut Sea (Bonn et al., 1998) in the East Antarctica. Barth et al. (2018) also reported changes in carbon cycle, ice sheets, and monsoon strength occurred during MIS 13 or 14. The spatial/temporal difference of onset of interglacial warmth in the Antarctica can be due to different oceanographic response to the MBE among regions. Therefore, to understand paleoceanographic changes in response to MBE in the Antarctica, more records are needed from various locations in the future.

7. Conclusions

The geochemical, nitrogen isotope, and SS records with previously reported data from core GC05-DP02 provided insight on orbital-scale oceanographic changes in the Drake

Passage including surface conditions (i.e., surface production and nutrient utilization) and bottom conditions (i.e., bottom current intensity and carbonate preservation) during 600 kyrs. The surface diatom and export production increased during interglacial periods with increased nitrate utilization, resulting in increased sedimentation rates, whereas glacial periods showed the opposite pattern. During glacial periods bottom current intensity increased due to strengthened counter bottom current with northward frontal migration. After MIS 9 interglacial period, surface water production distinctively increased and bottom current intensity distinctively decreased in the Drake Passage compared to previous interglacial periods due to southward migration of oceanic fronts under warmer climates. Nutrient utilization increased during interglacial periods, particularly after MIS 9. Decreased nutrient utilization during glacial periods may be related to more influence of sea ice.

Preservation of CaCO3 in the Drake Passage (~3000 m deep) is very poor over the last 600 kyrs in general, except for MIS 2–4 and 6 when AABW formation from Weddell Sea regions likely decreased.

KOPRI
극지연구소

드레이크 해협의 지난 600,000년 동안 빙하기-간빙기 환경 변화[29)]

Sunghan Kim[a,b,*], Jae Il Lee[a], Kyu-Cheul Yoo[a], Min Kyung Lee[a], Young-Suk Bak[c], Myung-Il Kang[a], Sookwan Kim[d], Jinku Park[a]

[a]Korea Polar Research Institute, Incheon 21990, Republic of Korea
[b]Department of Polar Sciences, University of Science and Technology (UST), Incheon 21990, Republic of Korea
[c]Department of Earth and Environmental Sciences, Jeonbuk National University, Jeonju, 54896, Republic of Korea
[d]Korea Institute of Ocean Science and Technology, Busan 49111, Republic of Korea

요약: 남빙양의 해양학적 조건은 해양 전선 시스템과 밀접하게 연관되어 있다. 빙기-간빙기 동안 빙권의 변화는 남빙양 전선의 변동을 유발하며, 반대로 전선 변화 역시 빙권에 영향을 미쳐 표층 생산성, 영양염 이용, 저층수 화학, 그리고 저층 해류 강도의 변화를 초래한다. 본 연구에서는 드레이크 해협에서 지난 60만 년 동안의 지구화학 자료, 질소 동위원소 기록, 입도 기록을 기존 발표 자료와 함께 종합하여 빙기와 간빙기의 표층부터 저층까지의 해양 조건을 비교하였다. 생물기원 오팔과 수출 생산은 간빙기에 높고 빙기에는 낮게 나타났다. 표층 생산은 빙기와 간빙기 모두에서 개방 해양 종이 우세하였으며, 해빙 종에서는 뚜렷한 빙기-간빙기 변화가 관찰되지 않았다. 해양동위원소단계 9 이후에는 육상 기원의 영향이 감소하는 동시에 간빙기 생물기원 오팔과 규조 풍부도가 현저히 증가하였다. 영양염 이용은 간빙기에는 증가하고 빙기에는 감소하였으며, 이는 특히 해양동위원소단계 9 이후 표층 생산 증가와 함께 더욱 뚜렷하게 나타났다. 이러한 결과는 표층 생산성이 해빙 지속 기간 및 분포 범위와 연관된 광량에 의해 조절되었음을 시사한다. 또한 평균 입도와 sortable silt 비율 간의 높은 상관관계에 근거하여, 평균 입도는 본 연구에서 저층 해류 강도의 지표로 활용될 수 있으며, 저층 해류는 빙기 동안 강화되고 간빙기 동안 약화되는 경향을 보였다. 빙기 저층 해류의 증가는 남서 방향으로 흐르는 저층류와 관련될 가능성이 크다. 한편 간빙기 저층 해류 강도는 해양동위원소단계 9 이후에도 유의미하게 약화되었다. 그러나 드레이크 해협에서의 두드러진 간빙기 온난은 전 지구적으로 해양동위원소단계 11 이후 나타나는 경향과 달리 해양동위원소단계 9부터 시작되었으며, 이는 중기 브룬헤스 사건에 대한 남빙양의 반응을 이해하기 위해 향후 추가 연구가 필요함을 의미한다.

29) 이 연구 결과는 다음의 논문으로 출판되었음: Kim, S. et al. (2023). "Glacial-interglacial environmental changes in the Drake Passage over the past 600 kyrs" Palaeogeography Palaeoclimatology, Palaeoecology 631: 111835.

References

Altabet, M.A., Francois, R., 1994. Sedimentary nitrogen isotopic ratio as a recorder for surface ocean nitrate utilization. Global Biogeochemical Cycles 8, 103-116.

Anderson J.B., 1975. Factors controlling CaCO3 dissolution in the Weddell Sea from foraminiferal distribution patterns. Marine Geology 19, 315-332.

Anderson, J.B., Shipp, S.S., Lowe, A.L., Wellner, J.S., Mosola, A.B., 2002. The Antarctic Ice Sheet during the Last Glacial Maximum and its subsequent retreat history: a review. Quaternary Science Reviews 21, 49-70.

Archer, D.E., 1993. What controls opal preservation in tropical deep-sea sediments? Paleoceanography, 8, 7-21.

Armand, L.K., Crosta, X., Romero, O., Pichon, J.J., 2005. The biogeography of major diatom taxa in Southern Ocean sediments: 1. Sea ice related species. Palaeogeography, Palaeoclimatology, Palaeoecology 223, 93-126.

Bae, S.H., Yoon, H.I., Park, B.-K., Kim, Y., 2003. Late Quaternary stable isotope record and meltwater discharge anomaly events to the south of the Antarctic Polar Front, Drake Passage. Geo-Marine Letters 23, 110-116.

Bak, Y.S., Lee, J.I., Yoon, H.I., Lee, J.D., Lee, S.J., 2010a. Diatom research from the Drake Passage core sediment (GC05-DP02), Antarctica. Journal of the Geological Society of Korea 46, 553-560 (in Korean with English abstract).

Bak, Y.S., Lee, J.D., Yoon, H.I., Yoo, K.C., Lee, S.J., 2010b. Holocene paleoclimate change in the area around Elephant Island, Antarctica: evidence from the diatom record. Journal of the Geological Society of Korea 46, 111-117 (in Korean with English abstract).

Barker, P.F., Camerlenghi, A., 2002. Glacial history of the Antarctic Peninsula from Pacific margin sediments. In: Barker, P.F., Camerlenghi, A., Acton, G.D., Ramsay, A.T.S. (Eds.), Proc. ODP, Sci. Results 178 [Online], http://www-odp.tamu.edu/publications/178_SR/synth/synth.htm>.

Barth, A.M., Clark, P.U., Bill, N.S., He, F., Pisias, G., 2018. Climate evolution across the Mid-Brunhes Transition. Climate of the Past 14, 2071-2087, doi:10.5194/cp-14-2071-2018.

Behringer, D.W., Xue, Y., 2004. Evaluation of the global ocean data assimilation system at NCEP: The Pacific Ocean. Eighth Symposium on Integrated Observing and Assimilation Systems for Atmosphere, Oceans, and Land Surface. AMS 84th Annual Meeting, Washington State Convention and Trade Center, Seattle, Washington, pp. 11-15.

Bonn, W.J., Gingele, F.X., Grobe, H., Mackensen, A., Fütterer, D.K., 1998. Palaeoproductivity at the Antarctic continental margin: opal and barium records for the last 400 ka. Palaeogeography, Palaeoclimatology, Palaeoecology 139, 195-211.

Ceccarori, L., Frank, M., Frignani, M., Langone, L., Ravaioli, M., Mangini, A., 1998. Late Quaternary fluctuations of biogenic component fluxes on the continental slope of the

Ross Sea, Antarctica. Journal of Marine Systems 17, 515-525.

Chase, Z., Kohfeld, K.E., Matsumoto, K., 2015. Controls on biogenic silica burial in the Southern Ocean. Global Biogeochmical Cycles 29, 1599-1616, doi:10.1002/2015GB005186.

Clark, P.U., Archer, D., Pollard, D., Blum, J.D., Rial, J.A., Brovkin, V., Mix, A.C., Pisias, N.G., Roy, M., 2006. The middle Pleistocene transition: characteristics, mechanisms, and implications for long-term changes in atmospheric pCO2. Quaternary Science Reviews 25, 3150-3184.

Crosta, X., Romero, O., Armand, L.K., Pichon, J.J., 2005. The biogeography of major diatom taxa in Southern Ocean sediments: 2. Open ocean related species. Palaeogeography, Palaeoclimatology, Palaeoecology 223, 66-92.

DeMaster, D.J., 1981. The supply and accumulation of silica in the marine environment. Geochimica et Cosmochimica Acta 5, 1715-1732.

DeMaster, D.J., 2002. The accumulation and cycling of biogenic silica in the Southern Ocean: Revisiting the marine silica budget. Deep-Sea Research Part II 49, 3155-3167.

Diekmann, B., Kuhn, G., Rachold, V., Abelmann, A., Brathauer, U., Fütterer, D.K., Gersonde, R., Grobe, H., 2000. Terrigenous sediment supply in the Scotia Sea (Southern Ocean): response to Late Quaternary ice dynamics in Patagonia and on the Antarctic Peninsula. Palaeogeography, Palaeoclimatology, Palaeoecology 162, 357-387.

EPICA-community-members, 2004. Eight glacial cycles from an Antarctic ice core. Nature 429, 623-628.

Fetterer, F., Knowles, K., Meier, W.N., Savoie, M., Windnagel, A.K., 2017. Sea Ice Index, Version 3 [data set]. Boulder, Colorado USA. National Snow and Ice Data Center. https://doi.org/10.7265/N5K072F8.

Fischer, H., Fundel, F., Ruth, U., Twarloh, B., Wegner, A., Udisti, R., Becagli, S., Castellano, E., Morganti, A., Severi, M., Wolff, E., Littot, G., Röthlisberger, R., Mulvaney, R., Hutterli, M.A., Kaufmann, P., Federer, U., Lambert, F., Bigler, M., Hansson, M., Jonsell, U., De Angelis, M., Boutron, C., Siggaard-Andersen, M.-L., Steffensen, J.P., Barbante, C., Gaspari, V., Gabrielli, P., Wagenbach, D., 2007. Reconstruction of millennial changes in dust emission, transport and regional sea ice coverage using the deep EPICA ice cores from the Atlantic and Indian Ocean sector of Antarctica. Earth and Planetary Science Letters 260, 340-354.

Francois, R., Altabet, M.A., Burckle, L.H., 1992. Glacial-interglacial changes in surface nitrate utilization in the Indian sector of the Southern Ocean as recorded by sediment δ15N. Paleoceanography 7, 589-606.

Gersonde, R., Crosta, X., Abelmann, A., Armand, L., 2005. Sea-surface temperature and sea ice distribution of the Southern Ocean at the EPILOG Last Glacial Maximum-a circum-Antarctic view based on siliceous microfossil records. Quaternary Science Reviews 24, 869-896.

Hemming, S.R., van de Flierdt, T., Goldstein, S.L., Franzese, A.M., Roy, M., Gastineau, G.,

Landrot, G., 2007. Strontium isotope tracing of terrigenous sediment dispersal in the Antarctic Circumpolar Current: Implications for constraining frontal positions. Geochemistry Geophysics Geosystems 8, Q06N13, doi:10.1029/2006GC001441.

Hernández-Molina, F.J., Larter, R.D., Rebesco, M., Maldonado, A., 2006. Miocene reversal of bottom water flow along the Pacific Margin of the Antarctic Peninsula: stratigraphic evidence from a contourite sedimentary tail. Marine Geology 228, 93-116.

Hillenbrand, C.-D., Camerlenghi, A., Cowan, E.A., Hernández-Molina, F.J., Lucchi, R.G., Rebesco, M., Uenzelmann-Neben, G., 2008a. The present and past bottom-current flow regime around the sediment drifts on the continental rise west of the Antarctic Peninsula. Marine Geology 255, 55-63.

Hillenbrand, C.D., Kuhn, G., Frederichs, T., 2009. Record of a Mid-Pleistocene depositional anomaly in West Antartic Continental margin sediments: an indicator for ice-sheet collapse?. Quaternary Science Reviews 28, 1147-1159.

Hillenbrand, C.D., Crowhurst, S.J., Williams, M., Hodell, D.A., McCave, I.N., Ehrmann, W., Xuan, C., Piotrowski, A.M., Hernández-Molina, F.J., Graham, A.G.C., Grobe, H., Williams, T.J., Horrocks, J.R., Allen, C.S., Larter, R.D., 2021. New insights from multi-proxy data from the West Antarctic continental rise: implications for dating and interpreting late Quaternary paleoenvironmental records. Quaternary Science Reviews 257, 106842.

Hofmann, E.E., Klinck, J.M., Lascara, C.M., Smith, D.A., 1996. Water mass distribution and circulation west of the Antarctic Peninsula and including Bransfield Strait. In: Ross, R.M., Hofmann, E.E., Quentin, L.B. (Eds.), Foundations for ecological research west of the Antarctic Peninsula. Antarctic Research Series 70. American Geophysical Union, Washington, D.C., pp. 61-80.

Holden, P.B., Edwards, N.R., Wolff, E.W., Valdes, P.J., Singarayer, J.S., 2011. The Mid-Brunhes Event and West Antarctic Ice Sheet Stability. Journal of Quaternary Science 26, 474-477.

Huang, H., Gutjahr, M., Eisenhauer, A., Kuhn, G., 2020. No detectable Weddell Sea Antarctic Bottom Water export during the Last and Penultimate Glacial Maximum. Nature Communications 11, 424, doi:10.1038/s41467-020-14302-3.

Imbrie, J., Berger, A., Boyle, E.A., Clemens, S.C., Duffy, A., Howard, W.R., Kukla, G., Kutzbach, J., Martinson, D.G., McIntyre, A., Mix, A.C., Molfino, B., Morley, J.J., Peterson, L.C., Pisias, N.G., Prell, W.L., Raymo, M.E., Shackleton, N.J., Toggweiler, J.R., 1993. On the structure and origin of major glaciation cycles 2. The 100 000-year cycle. Paleoceanography 8, 699-735.

Jansen, J.H.F., Kuijpers, A., Troelstra, S.R., 1986. A Mid-Brunhes Climatic Event: Long-Term Changes in Global Atmosphere and Ocean Circulation. Science 232, 619-622.

Jonkers, L., Barker, S., Hall, I.R., Prins, M.A., 2015. Correcting for the influence of ice-rafted detritus on grain size-based paleocurrent speed estimates. Paleoceanography 30, 1347-1357, doi:10.1002/2015PA002830.

Jouzel, J., Masson-Delmotte, V., Cattani, O., Dreyfus, G., Falourd, S., Hoffmann, G., Minster, B., Nouet, J., Barnoloa, J.M., Chappellaz, J., Fischer, H., Gallet, J.C., Johnsen, S., Leuenberger, M., Loulergue, L., Luethi, D., Oerter, H., Parrenin, F., Raisbeck, G., Raynaud, D., Schilt, A., Schwander, J., Selmo, E., Souchez, R., Spahni, R., Stauffer, B., Steffensen, J.P., Stenni, B., Stocker, T.F., Tison, J.L., Werner, M., Wolff, E.W., 2007. Orbital and millennial Antarctic climate variability over the past 800,000 years. Science 317, 793-796.

Kemp, A.E.S., Grigorov, I., Pearce, R.B., Naveira Garabato, A.C., 2010. Migration of the Antarctic Polar Front through the mid-Pleistocene transition: evidence and climatic implications. Quaternary Science Reviews 29, 1993-2009.

Kienast, S.S., Calvert, S.E., Pedersen, T.F., 2002. Nitrogen isotope and productivity variations along the northeast Pacific margin over the last 120 kyr: Surface and subsurface paleoceanography. Paleoceanography 17, 1055, doi:10.1029/2001PA000650.

Kim, S., Lee, J.I., McKay, R.M., Yoo, K.C., Bak, Y.S., Lee, M.K., Roh, Y.H., Yoon, H.I., Moon, H.S., Hyun, C.U., 2020a. Late Pleistocene paleoceanographic changes in the Ross Sea - Glacial-interglacial variations in paleoproductivity, nutrient utilization, and deep-water formation. Quaternary Science Reviews 239, 106356.

Kim, S. ,Yoo, K.C., Lee, J.I., Khim, B.K., Bak, Y.S., Lee, M.K., Lee, J., Domack, E.W., Christ, A.J., Yoon, H.I., 2018a. Holocene paleoceanography of Bigo Bay, west Antarctic Peninsula: Connections between surface water productivity and nutrient utilization and its implication for surface-deep water mass exchange. Quaternary Science Reviews 192, 59-70, doi:10.1016/j.quascirev.2018.05.028.

Kim, S., Yoo, K.C., Lee, J.I., Lee, M.K., Kim, K., Yoon, H.I., 2018b. Relationship between magnetic susceptibility and sediment grain size since the last glacial period in the Southern Ocean off the northern Antarctic Peninsula - Linkages between the cryosphere and atmospheric circulation. Palaeogeogr. Palaeoclimatol. Palaeoecol. 505, 359-370.

Kim, S., Yoo, K.C., Lee, J.I., Roh, Y.H., Bak, Y.S., Um, I.K., Lee, M.K., Yoon, H.I., 2020b. Paleoceanographic changes in the Southern Ocean off Elephant Island since the last glacial period: Links between surface water productivity, nutrient utilization, bottom water currents, and ice-rafted debris. Quaternary Science Reviews 249, 106563.

Lamb, A.L., Wilson, G.P., Leng, M.J., 2006. A review of coastal palaeoclimate and relative sea-level reconstructions using δ13C and C/N ratios in organic material. Earth-Science Reviews 75, 29-57.

Lamy, F., Arz, H.W., Kilian, R., Lange, C.B., Lembke-Jene, L., Wengler, M., Kaiser, J., Baeza-Urrea, O., Hall, I.R., Harada, N., Tiedemann, R., 2015. Glacial reduction and millennial-scale variations in Drake Passage throughflow. Proceedings of the National Academy of Sciences 112, 13,496-13,501, doi:10.1073/pnas.1509203112.

Lee, J.I., Yoon, H.I., Yoo, K.C., Lim, H.S., Lee, Y.I., Kim, D., Bak, Y.S., Itaki, T., 2012. Late Quaternary glacial-interglacial variations in sediment supply in the southern Drake

Passage. Quaternary Research 78, 119-129.

Leventer, A., Domack, E.W., Ishman, S.E., Brachfeld, S., McClennen, C.E., Manley, P., 2015. Productivity cycles of 200-300 years in the Antarctic Peninsula region: Understanding linkages among the sun, atmosphere, oceans, sea ice, and biota. Geological Society of America Bulletin 108, 1626-1644.

Lisiecki, L.E., Raymo, M.E., 2005. A Pliocene-Pleistocene stack of 57 globally distributed benthic δ18O records. Paleoceanography 20, PA1003, doi:1029/2004PA001071.

Lucchi, R.G., Rebesco, M., 2007. Glacial contourites on the Antarctic Peninsula margin: insight for palaeoenvironmental and palaeoclimatic conditions. In: Viana, A.R., Rebesco, M. (Eds.), Economic and Palaeoceanographic Significance of Contourite Deposits. Geological Society, London, Special Publications 276, 111-127.

Lucchi, R.G., Rebesco, M., Camerlenghi, A., Busetti, M., Tomadin, L., Villa, G., Persico, D., Morigi, C., Bonci, M.C., Giorgetti, G., 2002. Mid-late Pleistocene glacimarine sedimentary processes of a high-latitude, deep-sea sediment drift (Antarctic Peninsula Pacific margin). Marine Geology 189, 343-370.

Lüthi, D., Le Floch, M., Bereiter, B., Blunier, T., Barnola, J.M., Siegenthaler, U., Raynaud, D., Jouzel, J., Fischer, H., Kawamura, K., Stocker, T.F., 2008. High-resolution carbon dioxide concentration record 650,000-800,000 years before present. Nature 453, 379-382.

Machado, A., Chemale Jr., F., Conceição, R.V., Kawaskita, K., Morata, D., Oteíza, O., Van Schmus, W.R., 2005a. Modeling of subduction components in the Genesis of the Meso-Cenozoic igneous rocks from the South Shetland Arc, Antarctica. Lithos 82, 435-453.

Machado, A., Lima, E.F., Chemale Jr., F., Morata, D., Oteiza, O., Almeida, D.P.M., Figueiredo, A.M.G., Alexandre, F.M., Urrutia, J.L., 2005b. Geochemistry constraints of Mesozoic-Cenozoic calc-alkaline magmatism in the South Shetland arc, Antarctica. Journal of South American Earth Sciences 18, 407-425.

Manoj, M.C., Thamban, M., 2015. Shifting frontal regimes and its influence on bioproductivity variations during the Late Quaternary in the Indian sector of Southern Ocean. Deep-Sea Research Part II 118, 261-274, doi:10.1016/j.dsr2.2015.03.011.

McCave, I.N., Thornalley, D.J.R., Hall, I.R., 2017. Relation of sortable silt grain size to deep-sea current speeds: calibration of the 'Mud Current Meter'. Deep-Sea Research Part I 127, 1-12.

McCave, I.N., Andrews, J.T., 2019. Distinguishing current effects in sediments delivered to the ocean by ice, I. Principles, methods and examples. Quaternary Science Reviews 212, 92-107, doi:10.1016/j.quascirev.2019.03.031.

McCave, I.N., Crowhurst, S.J., Kuhn, G., Hillenbrand, C.-D., Meredith, M.P., 2014. Minimal change in Antarctic Circumpolar Current flow speed between the last glacial and Holocene. Nature Geoscience 7, 113-116, doi: 10.1038/ngeo2037.

Mortlock, R.A., Froelich, P.N., 1989. A simple method for the rapid determination of opal in

KOPRI 극지연구소

pelagic marine sediments. Deep-Sea Research 36, 1415-1426.

Ó Cofaigh, C., Davies, B.J., Livingstone, S.J., Smith, J.A., Johnson, J.S., Hocking, E.P., Hodgson, D.A., Anderson, J.B., Bentley, M.J., Canals, M., Domack, E., Dowdeswell, J.A., Evans, J., Glasser, N.F., Hillenbrand, C.D., Larter, R.D., Roberts, S.J., Simms, A.R., 2014. Quaternary Research 100, 87-110.

Orsi, A.H., Whitworth, T., Nowlini Jr., W. D., 1995. On the meridional extent and fronts of the Antarctic circumpolar current. Deep Sea Research Part I 42(5), 641-673.

Pudsey, C.J., Camerlenghi, A., 1998. Glacial-interglacial deposition on a sediment drift on the Pacific margin of the Antarctic Peninsula. Antarctic Science 10, 286-308.

Ragueneau, O., Tréguer, P., Leynaert, A., Anderson, R.F., Brzezinski, M.A., DeMaster, D.J., Dugdale, R.C., Dymond, J., Fischer, G., Francois, R., Heinze, C., Maier-Reimer, E., Martin-Jézéquel, V., Quéquiner, B., 2000. A review of the Si cycle in the modern ocean: Recent progress and missing gaps in the application of biogenic opal as a paleoproductivity proxy. Earth Planetary Science Letters 26, 317-365.

Rebesco, M., Pudsey, C.J., Canals, M., Camerlenghi, A., Barker, P.F., Estrada, F., Giorgetti, A., 2002. Sediment drift and deep-sea channel systems, Antarctic Peninsula Pacific margin. In: Stow, D.A.V., Pudsey, C.J., Howe, J., Faugères, J.C., Viana, A. (eds) Deep-water contourite systems: Modern Drifts and Ancient Series, Seismic and Sedimentary Characteristics. Geological Society, London, Memoirs, 22, 353-371.

Rickaby, R.E.M., Elderfield, H., Roberts, N., Hillenbrand, C.D., Mackensen, A., 2010. Evidence for elevated alkalinity in the glacial Southern Ocean. Paleoceanography 25, PA1209, doi:10.1029/2009PA001762.

Roberts, J., McCave, I.N., McClymont, E.L., Kender, S., Hillenbrand, C.D., Matano, R., Hodell, D.A., Peck, V.L., 2017. Earth Planetary Science Letters 474, 397-408, doi:10.1016/j.epsl.2017.07.004.

Robinson, R.S., Sigman, D.M., 2008. Nitrogen isotopic evidence for a poleward decrease in surface nitrate within the ice age Antarctic. Quaternary Science Reviews 27, 1076-1090.

Saavedra-Pellitero, M., Baumann, K.H., Ullermann, J., Lamy, F., 2017. Marine Isotope Stage 11 in the Pacific sector of the Southern Ocean: a coccolithophore perspective. Quaternary Science Reviews 158, 1-14, doi:10.1016/j.quascirev.2016.12.020.

Schubert, C.J., Calvert, S.E., 2001. Nitrogen and carbon isotopic composition of marine and terrestrial organic matter in Arctic Ocean sediments: implications for nutrient utilization and organic matter composition. Deep-Sea Research Part I 48, 789-810.

Seabrooke, J.M., Hufford, G.L., Elder, R.B., 1971. Formation of Antarctic Bottom Water in the Weddell Sea. Journal of Geophysical Research 76, 2164-2178.

Sjunneskog, C., Winter, D., 2012. A diatom record of late Pliocene cooling from the Ross Sea continental shelf, AND-1B, Antarctica. Global and Planetary Change 96-97, 87-96, doi:10.1016/j.gloplacha.2012.01.013.

Smith, J.A., Graham, A.G.C., Post, A.L., Hillenbrand, C.D., Bart, P.J., Powell, R.D., 2019. The

KOPRI 극지연구소

marine geological imprint of Antarctic ice shelves. Nature Communications 10, 5635, doi:10.1038/s41467-019-13496-5.

Sprenk, D., Weber, M.E., Kuhn, G., Rosén, P., Frank, M., Molina-Kescher, M., Liebetrau, V., Röhling, H.G., 2013. Southern Ocean bioproductivity during the last glacial cycle- new detection menthod and decadal-scale insight from the Scotia Sea. Geological Society, London, Special publications 381, 245-261, doi:10.1144/SP381.17.

Studer, A.S., Sigman, D.M., Martínez-Garcia, A., Benz, V., Winckler, G., Kuhn, G., Esper, O., Lamy, F., Jaccard, S.L., Wacker, L., Oleynik, S., Gersonde, R., Haug, G.H., 2015. Antarctic Zone nutrient conditions during the last two glacial cycles. Paleoceanography 30, 845-862, doi:10.1002/2014PA002745.

The RAISED Consortium, Bentley, M.J., Cofaigh, C.Ó., Anderson, J.B., Conway, H., Davies, B., Graham, A.G.C., Hillenbrand, C.-D., Hodgson, D.A., Jamieson, S.S.R., Larter, R.D., Mackintosh, A., Smith, J.A., Verleyen, E., Ackert, R.P., Bart, P.J., Berg, S., Brunstein, D., Canals, M., Colhoun, E.A., Crosta, X., Dickens, W.A., Domack, E., Dowdeswell, J.A., Dunbar, R., Ehrmann, W., Evans, J., Favier, V., Fink, D., Fogwill, C.J., Glasser, N.F., Gohl, K., Golledge, N.R., Goodwin, I., Gore, D.B., Greenwood, S.L., Hall, B.L., Hall, K., Hedding, D.W., Hein, A.S., Hocking, E.P., Jakobsson, M., Johnson, J.S., Jomelli, V., Jones, R.S., Klages, J.P., Kristoffersen, Y., Kuhn, G., Leventer, A., Licht, K., Lilly, K., Lindow, J., Livingstone, S.J., Massé, G., McGlone, M.S., McKay, R.M., Melles, M., Miura, H., Mulvaney, R., Nel, W., Nitsche, F.O., O'Brien, P.E., Post, A.L., Roberts, S.J., Saunders, K.M., Selkirk, P.M., Simms, A.R., Spiegel, C., Stolldorf, T.D., Sugden, D.E., van der Putten, N., van Ommen, T., Verfaillie, D., Vyverman, W., Wagner, B., White, D.A., Witus, A.E., Zwartz, D., 2014. A community-based geological reconstruction of Antarctic Ice Sheet deglaciation since the Last Glacial Maximum. Quaternary Science Reviews 100, 1-9, doi:10.1016/j.quascirev.2014.06.025.

Thomson, M.R.A., Pankhurst, R.J., 1983. Age of post-Gondwanan calc-alkaline volcanism in the Antarctic Peninsula region. In: Oliver, R.L., James, P.R., Jago, J.B. (Eds.), Antarctic Earth Science. Australian Academy of Science, Canberra, pp. 328-333.

Toyos, M.H., Lamy, F., Lange, C.B., Lembke-Jene, L., Saavedraa-Pellitero, M., Esper, O., Arz, H.W., 2020. Antarctic circumpolar current dynamics at the Pacific entrance to the Drake Passage over the past 1.3 million years. Paleoceanography and Paleoclimatology 35, e2019PA003773, doi:10.1029/2019PA003773.

Wang, X.T,. Sigman, D.M,. Prokopenko, M.G., Adkins, J.F., Robinson, L.F., Hines, S.K., Chai, J., Studer, A.S, Martínez-Garcia, A., Chen, T., Haug, G.H., 2017. Deep-sea coral evidence for lower Southern Ocean surface nitrate concentrations during the last ice age. Proceedings of the National Academy of Sciences 114, 3352-3357, doi:10.1073/pnas.1615718114.

Whitworth III, T., Nowlin Jr., W.D., Worley, S.J., 1982. The net transport of the Antarctic Circumpolar Current through Drake Passage. Journal of Physical Oceanography 12, 960-971.

Wu, L., Wang, R., Xiao, W., Ge, S., Chen, Z., Krijgsman, W., 2017. Productivity-climate coupling recorded in Pleistocene sediemnts off Prydz Bay (East Antarctica). Palaeogeography, Palaeoclimatology, Palaeoecology 485, 260-270, doi:10.1016/j.palaeo.2017.06.018.

Wu, L., Wang, R., Xiao, W., Krijgsman, W., Li, Q., Ge, S., Ma, T., 2018. Late Quaternary deep stratification-climate coupling in the Southern Ocean: implications for changes in abyssal carbon storage. Geochemistry Geophysics Geosystems 19, doi:10.1002/2017GC007250.

Wu, L., Wilson, D.J., Wang, R., Yin, X., Chen, Z., Xiao, W., Huang, M., 2020. Evaluating Zr/Rb ratio from XRF scanning as an indicator of grain size variations of glaciomarine sediments in the Southern Ocean. Geochemistry Geophysics Geosystems 21, e2020GC009350, doi:10.1029/2020GC009350.

Wu, S., Kuhn, G., Diekmann, B., Lembke-Jene, L., Tiedemann, R., Zheng, X., Ehrhardt, S., Arz, H.W., Lamy, F., 2019. Surface sediment characteristics related to provenance and ocean circulation in the Drake Passage sector of the Southern Ocean. Deep-Sea Research Part I 154, 103135, doi:10.1016/j.dsr.2019.103135.

Wu, S., Lembke-Jene, L., Lamy, F., Arz, H.W., Nowaczyk, N., Xiao, W., Zhang, X., Hass, H.C., Titschack, J,. Zheng, X., Liu, J., Dumm, L., Diekmann, B., Nürnberg, D., Tiedemann, R., Kuhn, G., 2021. Orbital- and millennial-scale Antarctic Circumpolar Current variability in Drake Passage over the past 140,000 years. Nature Communications 12, 3948, doi:10.1038/s41467-021-24264-9.

Xiao, W., Frederichs, T., Gersonde, R., Kuhn, G., Esper, O., Zhang, X., 2016. Constraining the dating of late Quaternary marine sediment records from the Scotia Sea (Southern Ocean). Quaternary Geochronology 31, 97-118, doi:10.1016/j.quageo.2015.11.003.

Yin, Q., 2013. Insolation-induced mid-Brunhes transition in Southern Ocean ventilation and deep-ocean temperature. Nature 494, 222-225.

Yoon, H.I., Yoo, K.C., Bak, Y.S., Lee, Y.I., Lee, J.I., 2009. Core-based reconstruction of paleoenvironmental conditions in the southern Drake Passage (West Antarctica) over the last 150 ka. Geo-Marine Letters. 29, 309-320, doi:10.1007/s00367-009-0144-8.

KOPRI 극지연구소

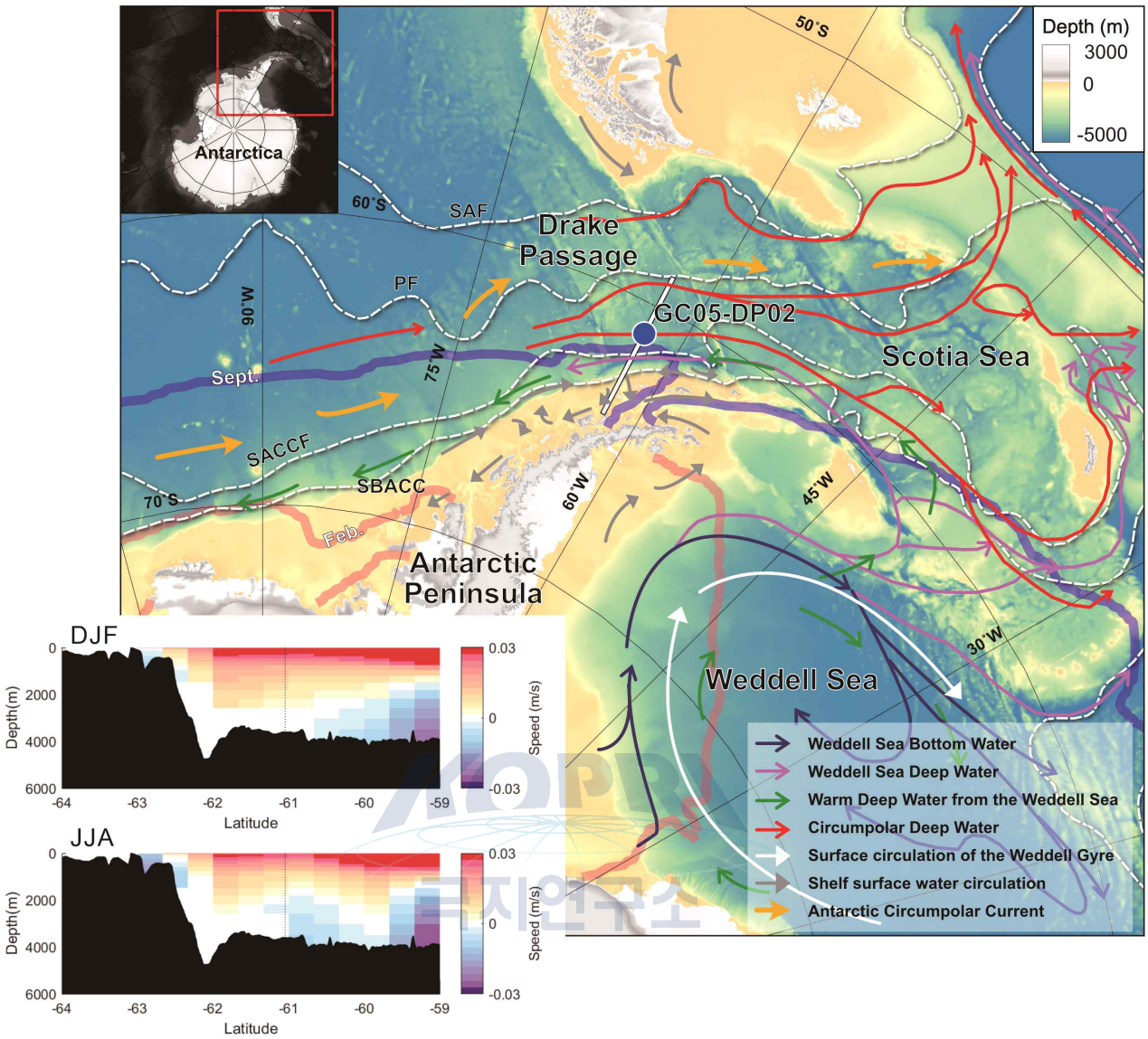


Figure #. Sediment core location and the oceanographic setting of the study area. Locations of the southern boundary of the Antarctic Circumpolar Current (SBACC), Southern Antarctic Circumpolar Current Front (SACCF), Polar Front (PF), and Subantarctic Front (SAF) are from Orsi et al. (1995). Shallow and deep water circulation paths are from Hernández-Molina et al. (2006). Shelf water circulation on the Antarctic Peninsula is from Hofmann et al. (1996). The latitude-vertical cross-sections (from 59 oS to 64oS) of the seasonal mean zonal currents (m s−1) at the longitudinal location of GC05-DP02 (62o38.3859'W) during (a) austral summer (December to February: DJF) and (b) austral winter (June to August: JJA) for 1980-2021. The positive/negative is eastward/westward. The 42-years zonal current data were obtained from the NCEP/Global Ocean Data Assimilation System (GODAS; Behringer and Xue, 2004). GODAS is based on the GFDL MOM.v3 model and is available at 1/3° latitude × 1° longitude resolution on 40 vertical levels with 10-m resolution in the upper 200 m. The bathymetric data were provided by the general bathymetric chart of the ocean and have a spatial resolution of approximately 30 arc seconds. These digital bathymetry data have higher accuracy with acoustic in situ measurements and satellite-based gravity data. Monthly median sea ice extents for the period 1981-2010 is from Fetterer et al. (2017).

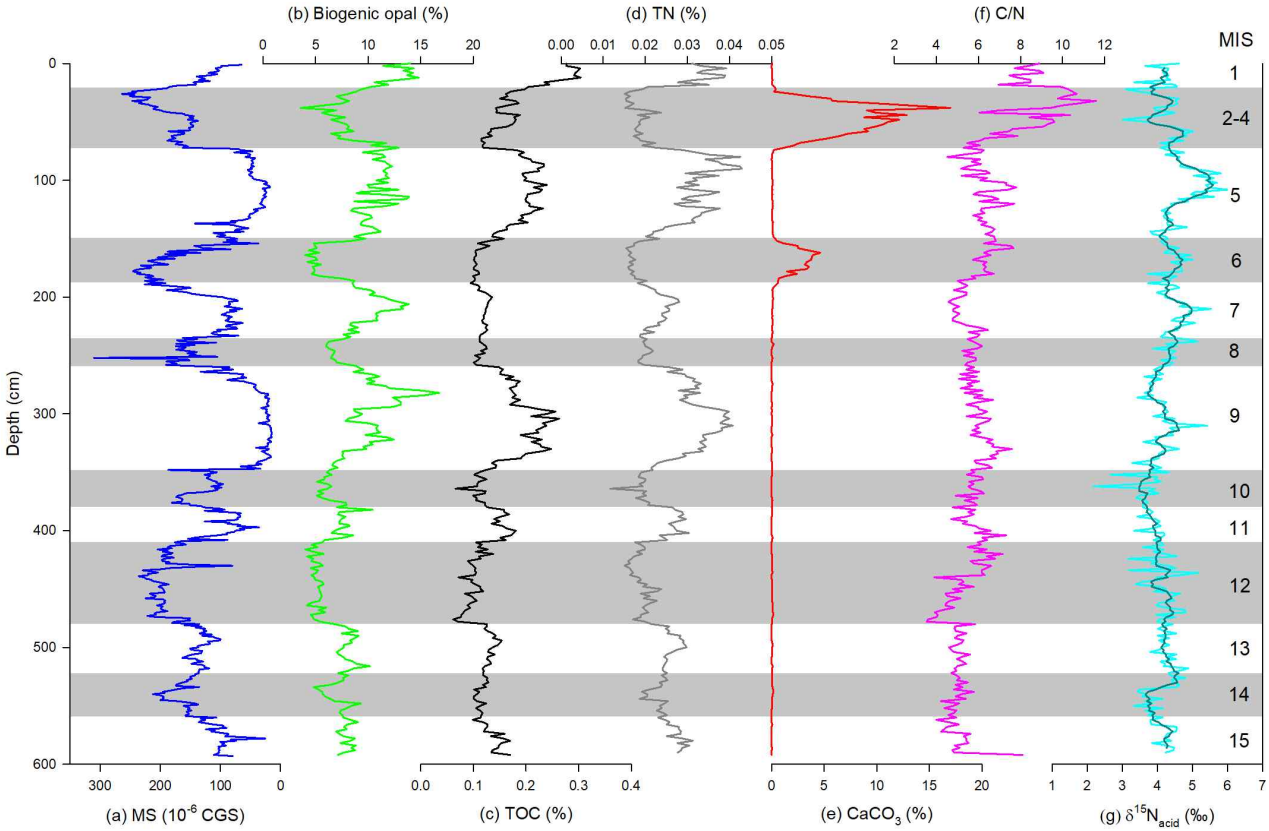


Figure #. Downcore profiles of (a) the MS (blue, Lee et al., 2012), (b) biogenic opal concentration (green), (c) TOC concentration (black), (d) TN concentration (gray), (e) CaCO3 concentration (red), (f) C/N ratio (purple), and (g) δ15Nacid (cyan) with 5-point running average values (dark cyan) of GC05-DP02. Gray boxes indicate glacial periods. MIS are marked on the right.

KOPRI 극지연구소

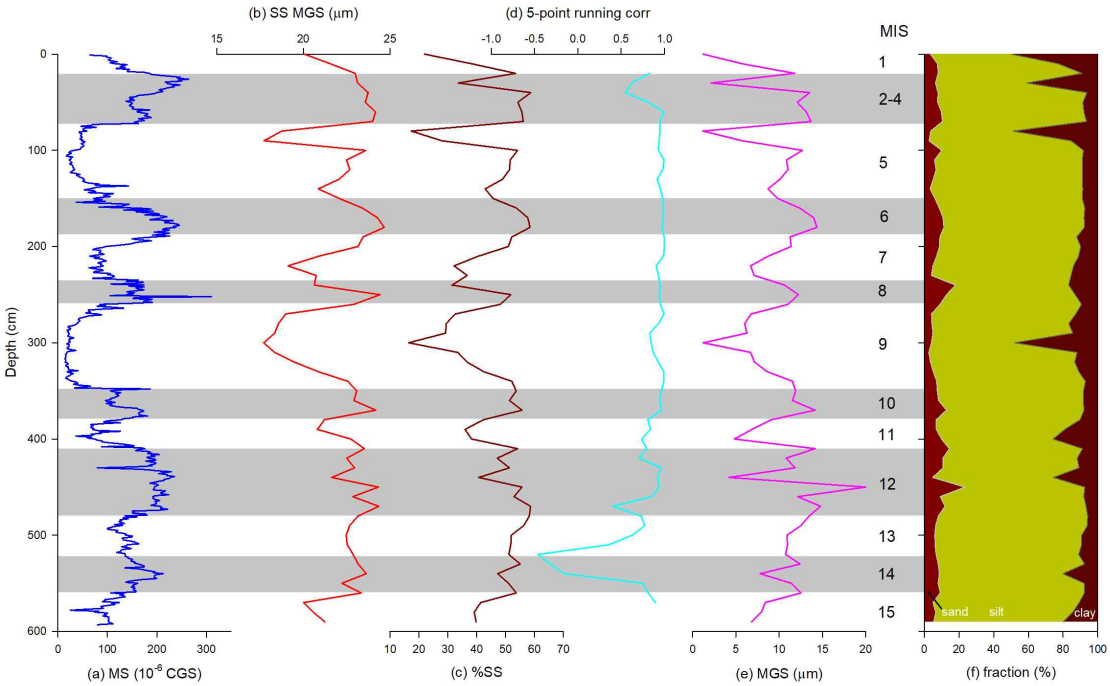


Figure #. Downcore profiles of (a) the MS (blue, Lee et al., 2012), (b) SS MGS (red), (c) %SS (dark red), (d) 5-point running correlation between SS MGS and %SS, (e) MGS (purple), and (f) fraction of sand, silt, and clay of GC05-DP02. Gray boxes indicate glacial periods. MIS are marked on the right.

KOPRI
극지연구소

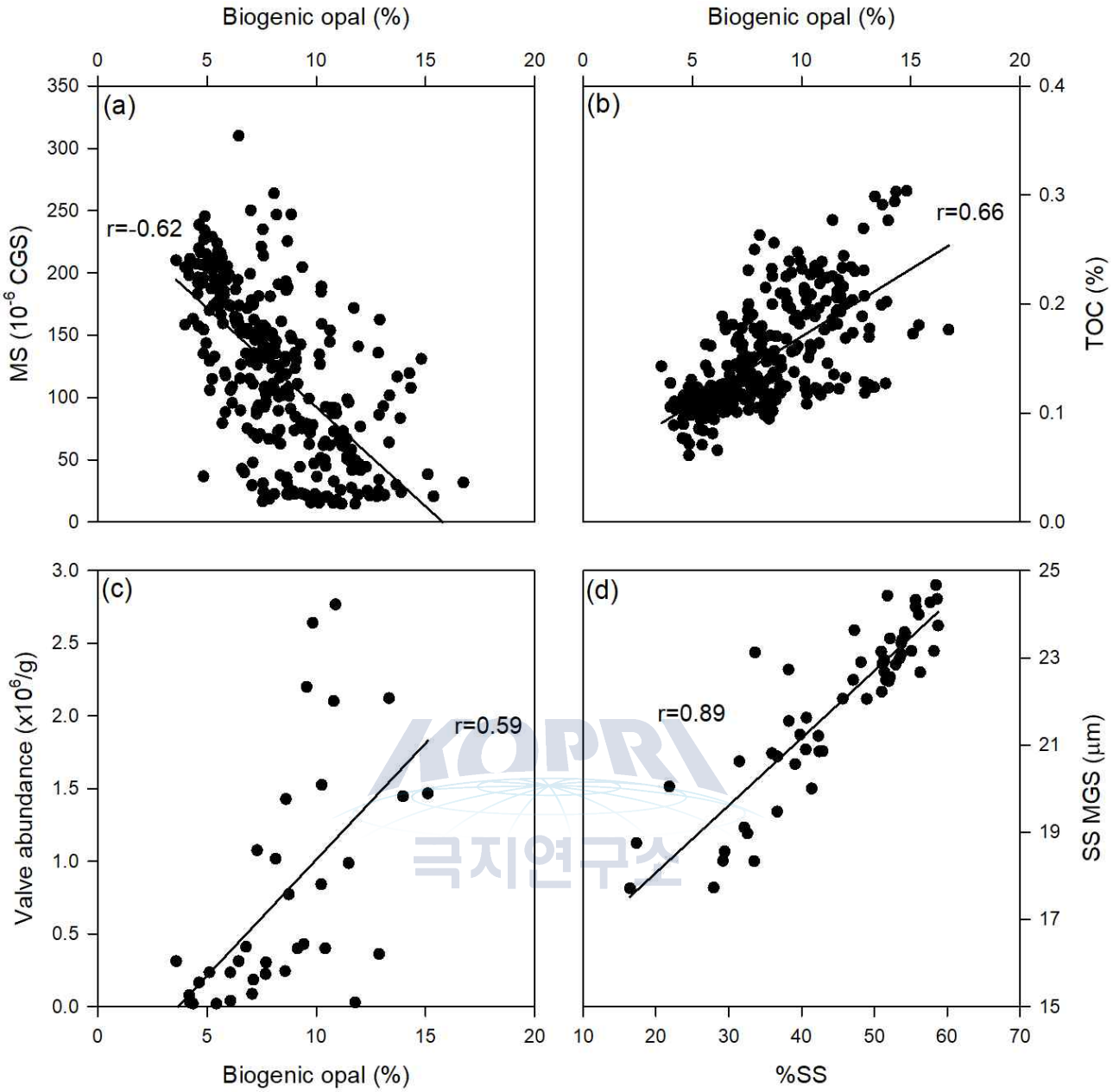


Figure #. Cross plots of biogenic opal concentration with (a) MS (r= -0.62, Lee et al., 2012), (b) TOC concentration (r=0.66), and (c) diatom total valve (r=0.59, Bak et al., 2010a), and of %SS and SS MGS (r-0.89) at GC05-DP02.

KOPRI 극지연구소

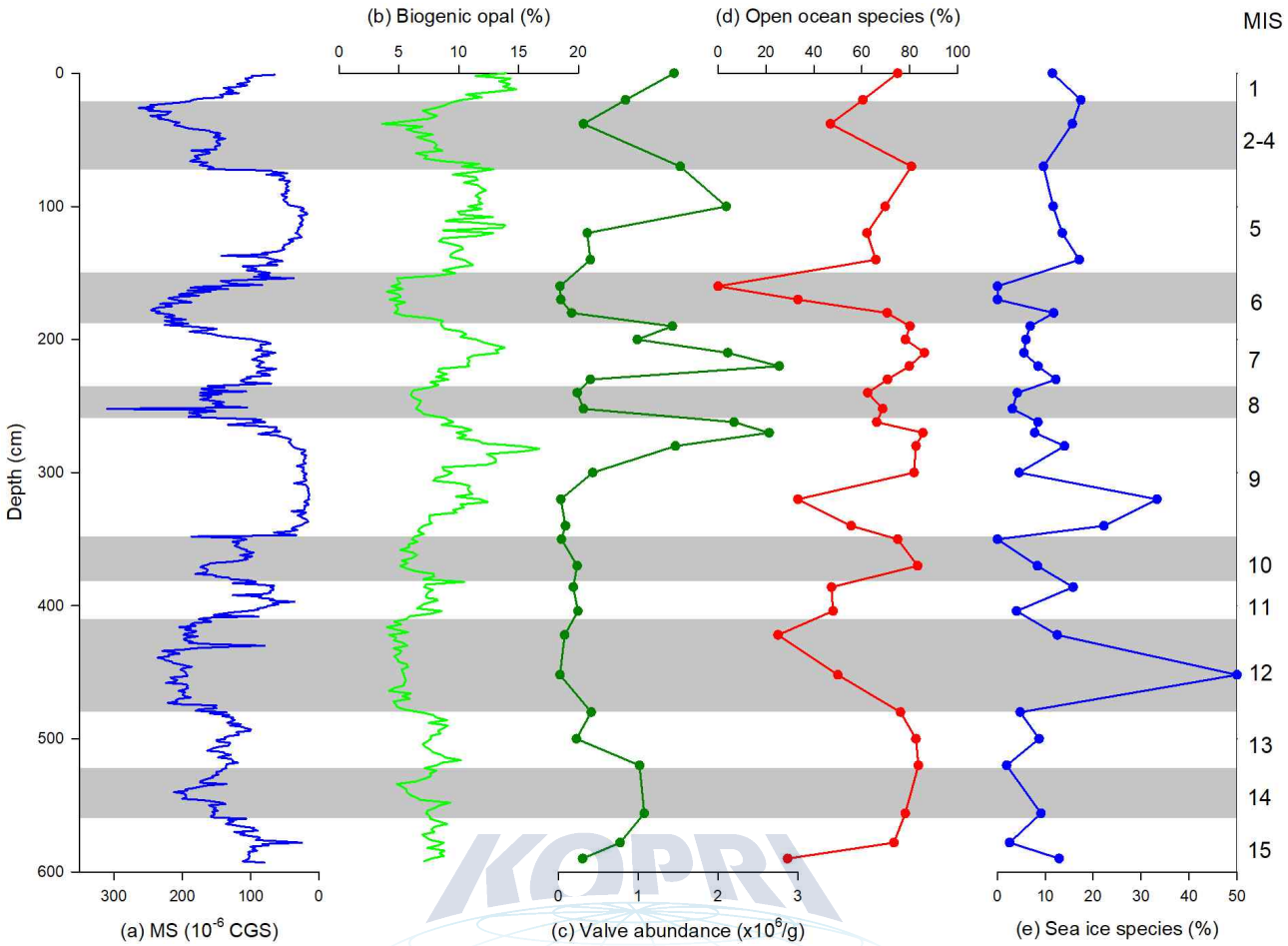


Figure #. Downcore profiles of (a) the MS (blue, Lee et al., 2012), (b) biogenic opal concentration (green), (c) diatom total valve (dark green), and relative abundances of (d) open ocean species (red), (e) sea ice species (cyan), and (f) E. antarctica (black). Diatom data are from Bak et al. (2010a). Gray boxes indicate glacial periods. MIS are marked on the right.

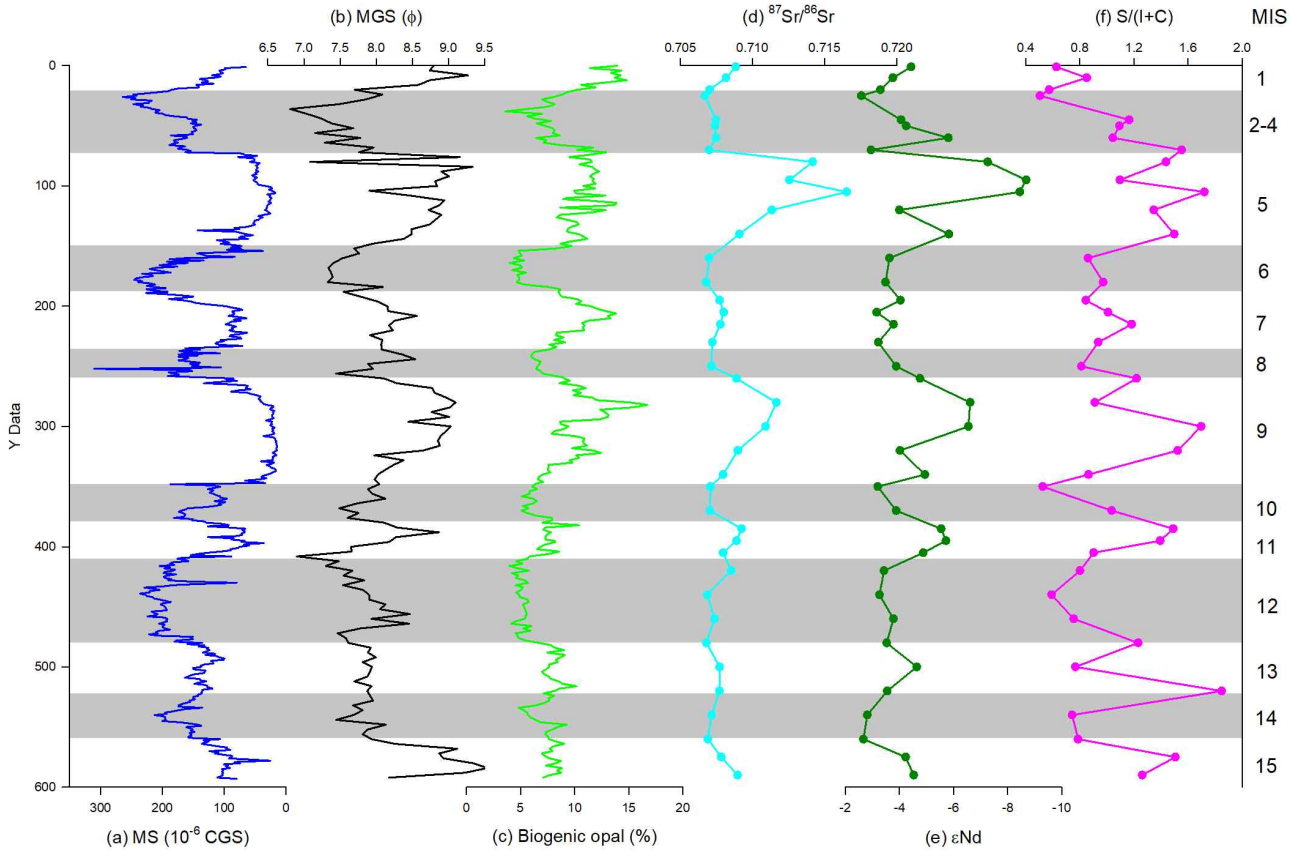


Figure #. Downcore profiles of (a) biogenic opal (green), (b) MS (blue, Lee et al., 2012), (c) SS MGS (red) of GC05-DP02, which show the interglacial warmth at MIS 9/10 boundary, comparing with (d) LR-04 benthic foraminifera oxygen isotope stack (Lisiecki and Raymo, 2005), (e) EDC δD (Jouzel et al., 2007), and (f) atmospheric CO2 concentration (EPICA-community-members, 2004), which show the interglacial warmth at MIS 11/12 boundary.

제 36 장

Mid-to-late Pleistocene Depositional Environments at the Ross Sea Continental margin: Implications for Antarctic Ice Sheet Dynamics[30)]

Chinmay Dash[1], Yeong Bae Seong[1], Ajay Kumar Singh[2], Min Kyung Lee[3], Jae Il Lee[3], Kyu-Cheul Yoo[3], Hyun Hee Rhee[4], Byung Yong Yu[5]

[1]Department of Geography Education, Korea University, Seoul, Republic of Korea
[2]Independent Researcher, Samastipur, Bihar, India
[3]Division of Glacial Environment Research, Korea Polar Research Institute, Incheon, Republic of Korea
[4]Department of Environment Education, Kongju National University, Chungnam, Republic of Korea
[5]AMS Laboratory, Korea Institute of Science and Technology, Seoul, Republic of Korea
A

KOPRI 극지연구소

Abstract: This study investigates a sediment core (RS15-LC47) from the Ross Sea continental rise to reconstruct ice sheet dynamics and paleodepositional environments over the past 800 ka. We employed a multi-proxy approach in this study, integrating whole-core magnetic susceptibility (MS), total organic carbon (TOC), calcium carbonate ($CaCO_3$), biogenic silica, sedimentological features, and the isotopic ratio of authigenic beryllium ((10Be/9Be)reac). The interval between 750 and 550 ka represents an intensified glacial phase characterized by expanded ice sheets, strengthened bottom currents, and reduced marine productivity. The dominance of contourite deposits interspersed with slumped sediments suggests that the sediment deposition occurred under highly dynamic and unstable conditions driven by intensified bottom currents. The presence of poorly sorted sediments and millimetre-scale faults further indicates gravity flow deposition, likely triggered by ice-sheet advances. Low (10Be/9Be)reac ratios in this interval suggest limited scavenging in open marine settings, likely due to reduced sediment transit time to the coring site as advancing ice sheets extended toward the shelf edge. Although TOC values are highest in this interval, a high total organic carbon/nitrogen (TOC/TN) ratio and low excess Barium (Baex) suggest increased terrestrial input from the advancing ice sheets and a reduced marine productivity under intense glacial conditions in the Ross Sea. Following the Mid-Pleistocene Transition (MPT), between 550 and

30) 이 연구 결과는 다음의 논문으로 출판되었음: Dash et al. (2025). "Mid-to-late Pleistocene Depositional Environments at the Ross Sea Continental margin: Implications for Antarctic Ice Sheet Dynamics." Palaeogeography, Palaeoclimatology, Palaeoecology 680: 113355.

250 ka, MS values remained consistently low, while (10Be/9Be)reac ratios were notably elevated, indicating relatively warmer conditions with diminished glacial influence. The TOC/TN ratios during this interval resemble those observed in the euphotic layer of the Ross Sea, with relatively higher Baex and TOC suggesting enhanced marine productivity under relatively warmer conditions between 550 and 250 ka. During the late Pleistocene (>250 ka), the depositional environment became increasingly influenced by glacial-interglacial cycles, with warmer interglacials driving enhanced productivity. During this interval, coarser grain sizes point to stronger bottom currents, while the sharp rise in (10Be/9Be)reac ratios indicates interglacial conditions associated with ice sheet retreat. The longer sediment transit from the subglacial zone to the depositional site during these warmer periods enhanced scavenging of Be isotopes in open marine settings, resulting in elevated (10Be/9Be)reac values. A positive correlation between OpalMAR, TOC%, and (10Be/9Be)reac during interglacials reflects a direct link between increased marine productivity and warmer climatic phases. Our findings emphasize how ice-sheet expansion and retreat control the depositional processes in the region.

1. Introduction

The Ross Sea contributes about 40 % of the total Antarctic Bottom Water (AABW) volume (Orsi et al., 2002) and is the primary drainage outlet of grounded ice from both eastern and western Antarctica (Anderson et al., 2014). Recent geological investigations underscore the significance of comprehending past interactions between the ocean and ice sheets in the Ross Sea sector (Nishimura et al., 1998; Jacobs et al., 2002; Chow and Bart, 2003; Bart and Owolana, 2012; McKay et al., 2012; Halberstadt et al., 2016; Anderson et al., 2019; McKay et al., 2019; Silvano et al., 2020), particularly in light of the retreating West Antarctic Ice Sheet (WAIS) (Pattyn and Morlighem, 2020). The ANDRILL 1-B core revealed 28 glacial-interglacial cycles between 5 and 1 Ma, with several hiatuses in sediment record; probably representing periods of glacial erosion (Naish et al., 2009). Ohneiser et al. (2023) demonstrated that the WAIS's advance and retreat cycles in the Ross Embayment were primarily paced by 41,000-year obliquity cycles, and that this obliquity-driven pacing persisted until the mid-Brunhes transition (430 ka). Although the evidence for the disintegration of WAIS remains uncertain during the past 1 Ma, glacial-interglacial cyclicity recorded in the AND-1B sediment core suggests episodic changes from floating to grounded state of Ross Ice shelf. Such changes seem to have been occurring in tandem with orbital cyclicity (McKay et al., 2012). Furthermore, the Ross Sea sector experienced drastic oceanographic changes during- and after- Mid-Pleistocene Transition (MPT), significantly affecting sedimentation across the continental margin. For instance, Konfirst et al. (2012) suggested the expansion of the Ross Gyre prior to MIS 16 in response to the deepening of the Amundsen Sea low, which transported the ice-proximal deposits to the outer sea (Wang et al., 2022). Nevertheless, most research in this sector of Antarctica regarding the ice sheet variation is restricted to the last

few hundred thousand years because of harsh conditions and challenges in establishing chronological records from sedimentary deposits. Consequently, there is a notable scarcity of continuous paleoenvironmental records in this part of the Antarctic continental margin. Most of the analyzed sediment cores in the Ross Sea are from the continental shelf region, where glacial overriding disrupts the continuity of the stratigraphic record. Hence, exploring sediment records from the continental slope and rise could offer a continuous paleoenvironmental record.

We investigated a sediment core (RS15-LC47) retrieved from the Ross Sea continental rise to comprehend the regional paleoceanographic changes since the mid-Pleistocene (Fig. 1). We employed whole core magnetic susceptibility (MS), total organic carbon (TOC), TOC to nitrogen ratio (C/N), calcium carbonate (CaCO3), biogenic silica, sedimentological characteristics and Beryllium (Be) isotopes in reactive phases (10Bereac, 9Bereac, and 10Bereac/9Bereac) to decipher the paleodepositional environment. MS of sediment samples is a key paleoenvironmental proxy in Antarctica, reflecting past climatic and sedimentary processes (Sagnotti et al., 2001). Variations in MS indicate changes in sediment provenance, glacial dynamics, and oceanographic changes, linked to ice sheet fluctuations and climate shifts (Robinson et al., 1995; Bollen et al., 2022; Kim et al., 2022). Ohneiser et al. (2019) analyzed sediment cores from the Ross Sea and found that those located near the continental margin contained lower-coercivity magnetic minerals compared to cores from the deeper waters. Glacial sediments typically have higher MS values than interglacial sediments due to coarser grains transported by grounded ice and icebergs. However, the benthic δ18O stack (LR04: Lisiecki and Raymo, 2005) does not strongly correlate with MS in Ross Sea cores (Ohneiser et al., 2019), likely due to asynchronous global glaciation (Raymo et al., 2006). TOC in Antarctic sediments reflects changes in the productivity, nutrient supply, and oxygen levels. Low TOC indicates reduced productivity or greater oxidation, while high TOC suggests enhanced preservation under low-oxygen conditions. Ice shelf advance during the glacial periods limits productivity, lowering TOC, whereas the interglacial retreats boost open-ocean productivity, increasing TOC deposition. C/N distinguishes oceanic and terrigenous source of organic matter (Sarmiento, 2006; Li et al., 2016). The presence and quantity of calcareous plankton, such as foraminifera and coccolithophores, which react to changes in ocean temperature, acidity, and carbonate saturation state, can be inferred from $CaCO_3$ concentrations. Similar to this, biogenic silica—which is mostly generated by diatoms—is a measure of siliceous productivity and is intimately related to oceanic frontal systems and nutrient cycling (DeMaster et al., 1992). Furthermore, sedimentological characteristics that indicate transport mechanisms, bottom current strength, and ice rafted debris (IRD) deposition include grain size distribution and depositional structures.

Although sedimentological and organic geochemical proxies have widely been used to reconstruct depositional environments in the Southern Ocean, the use of beryllium isotopes (10Be and 9Be) in Antarctic marine studies remains sparse. Recent research has shown that the (10Be/9Be)reac ratio offers valuable insights into glaciomarine processes, particularly in

tracking ice sheet dynamics (e.g., Sjunneskog et al., 2007; Valletta et al., 2018). This ratio has emerged as a reliable proxy for identifying glacial retreat and differentiating between depositional settings such as subglacial, sub-ice shelf, and open marine environments (Sjunneskog et al., 2007; Behrens et al., 2022; Sproson et al., 2024). For instance, Behrens et al., 2019, Behrens et al., 2022 used (10Be/9Be)reac ratios in the Antarctic margin sediments to track meltwater discharge, showing a close correspondence between high (10Be/9Be)reac ratios and open-marine conditions. Similarly, Sproson et al. (2024) demonstrated that downcore (10Be/9Be)reac variations from the Chilean margin captured near-synchronous expansions and retreats of the Patagonian Ice Sheet with the Northern Hemisphere glaciation. White et al. (2019) mapped (10Be/9Be)reac distributions beneath modern ice shelves, linking them to circulation regimes and basal meltwater influence. Together, these studies establish (10Be/9Be)reac as a robust tracer of past glacial dynamics, capable of revealing changes in ice-sheet proximity, sediment provenance, and marine-terrestrial mixing over the glacial-interglacial timescales. In this study, we aim to further explore this approach by combining (10Be/9Be)reac ratios with sedimentological, magnetic, and organic geochemical proxies to reconstruct paleoenvironmental conditions and ice-sheet behaviour along the Antarctic continental margin.

2. Ross Sea water masses and oceanography

Nestled within the Antarctic region, the Ross Sea showcases a dynamic blend of oceanographic conditions and circulation patterns, influenced by both climatic phenomena and physiography. It boasts the largest continental shelf region compared to other sectors of Antarctica, maintaining its depth due to isostatic adjustments relative to the mass of the continental ice cap. Renowned as one of the world's most active cyclogenetic regions, the Ross Sea experiences frequent and robust storm systems. Its distinctive physiography gives rise to potent katabatic winds streaming from the land over the ocean, notably originating from the Transantarctic Mountains and the Victoria Land coast, often resulting in the formation of coastal polynyas like the Terra Nova Bay polynya.

The circulation patterns within the Ross Sea continental shelf are intricate, driven by the interplay of water masses, surface winds, and regional topography (Orsi and Wiederwohl, 2009; Smith Jr et al., 2012). Oceanographic conditions are shaped by the influx of water masses (Fig. 1), particularly the Circumpolar Deep Water (CDW) drawn from the Antarctic Circumpolar Current. The CDW, carried poleward by the cyclonic Ross Gyre and flanked by Antarctic Surface Water (AASW) and Antarctic Bottom Water (AABW), plays a pivotal role in heat and salt budgets, as well as the regional sea-ice cycle and basal melt rate of the Ross Ice Shelf (Dinniman et al., 2011; Jacobs et al., 1970). However, the mechanisms governing the on-shelf transport of CDW remain uncertain, with proposed mechanisms including flow inertia, onshore advecting eddies, and atmospherically forced exchange. The swift diapycnal mixing of cold and low-salinity Antarctic Surface Water (AASW) with the warmer and saltier

Circumpolar Deep Water (CDW) significantly modifies the properties of the latter as it traverses the Antarctic Slope Front (ASF), giving rise to a water mass commonly known as Modified Circumpolar Deep Water (MCDW) further south. A notable portion of the High Salinity Shelf Water (HSSW) and Low Salinity Shelf Water (LSSW) drains into the deeper cavity beneath the Ross Ice Shelf, contributing to bottom water formation. The volume and salinity of Antarctic Bottom Water are intricately linked to the annual volume of sea ice produced and exported from the continental shelf. Coastal upwelling, in harmony with large-scale density currents and prevailing offshore winds, further shapes circulation patterns, particularly in proximity to the continental shelf break.

3. Materials and Methods

A gravity core, RS15-LC47 (70°50′45.33"S, 175° 4'11.34"E) (Fig. 1) was collected from the Ross Sea's lower continental rise during the Austral Summer 2015 by Korea Polar Research Institute (KOPRI) IBR/Araon cruise at a water depth of 2417 m. The core is located about 148 km South of Cape Adre, from a channel levee complex bounded by Scott and Wilson Canyons. The physical parameters and organic geochemical proxies were measured at KOPRI as per the procedure described in Kim et al., 2018a, Kim et al., 2018b, Kim et al., 2020. The core was split at KOPRI and visually described using the ANDRILL-based lithological classification scheme (Krissek et al., 2007). X-radiographs were used to identify sedimentary structures, and lithological units were defined based on consistent features observed in the lithostratigraphy. The mass accumulation rate (MAR) was estimated by multiplying Linear Sedimentation Rates (LSR) with dry bulk density. Paleoproductivity was estimated, by multiplying the sediment biogenic components with the MAR (Dymond et al., 1992). Multielement analysis (Ba, Al, Ti, and U) was performed using Inductively Coupled Plasma Mass Spectrometry (ICPMS) at the Korea Basic Science Institute (KBSI), Ochang, Korea.
Details of the materials and methods are described below:

3.1. Chronology

Dating sediments in the Southern Ocean presents significant challenges due to the limited presence of organic matter required for radiocarbon (14C) dating and the absence of a well-established continuous oxygen isotope stratigraphy, which further complicates chronological assignments. However, Relative Paleointensity (RPI) dating has emerged as a valuable method in this region, as it relies on globally synchronous geomagnetic secular variations, making it independent of local environmental conditions. Ohneiser et al. (2019) developed magneto-biostratigraphic age models for sediment cores from the Ross Sea, including RS15-LC47 (the core analyzed in this study), by integrating diatom records and geomagnetic reversal data. In their study, the Brunhes-Matuyama (B-M) reversal (773 ka) was identified at a depth of 1165 cm for the RS15-LC47 sediment core. To refine the chronological

framework, we correlated MS values of RS15-LC47 (this study; Fig. 2b) with those of a nearby core, RS15-LC42 (Bollen et al., 2022, Fig. 1), which was previously dated using an RPI-based chronology. We focused our study until the B-M reversal (773 ka), as it is the only well-established magneto-biostratigraphic age marker for the RS15-LC47 sediment core. MS values were used for correlation, as they are strongly linked to glacial-interglacial cyclicity in Antarctic marginal environments (Kim et al., 2020, Kim et al., 2022). We correlated MS values measured at 1 cm intervals for the RS15LC47 sediment core (this study) with that of the RS15LC42 sediment core (Bollen et al., 2022) using QAnalySeries software (Kotov and Pälike, 2018).

The similarity in MS trends between the two cores provided a reliable basis for correlation (Fig. 2b and c). Data preprocessing steps included normalization, outlier removal, and detrending. Peaks and trends in MS values were then aligned between the two cores, enabling the transfer of the age model from the RPI-dated RS15-LC42 core to the undated RS15-LC47 core. Since both cores are located in close proximity, they were likely influenced by similar climatic and geomagnetic conditions. This is evident in the similarity of their MS trends (Fig. 2c), which exhibit comparable temporal fluctuations in magnetic properties. For our study, we relied on two primary age markers: (1) the Brunhes-Matuyama (B-M) boundary (773 ka), as previously established by Ohneiser et al. (2019), and (2) a period of dampened MS values between 550 and 250 ka, consistently observed in Ross Sea sediment cores (Ohneiser et al., 2019) (Fig. 2b). We employed a comprehensive approach by utilizing 9 tie points across both cores to establish a chronological framework, and the correlation was effectively traced up to 773 ka (Fig. 2). Using these markers, we divided the core into three broad time intervals: 750–550 ka, 550–250 ka, and 250 ka to the present. Magnetic susceptibility (MS) trends from RS15-LC47 (this study) closely resemble those from RS15-LC42 (Bollen et al., 2022), where absolute age discrepancies of approximately 10–20 ka were noted between diatom biostratigraphic markers and RPI-based chronologies. A similar magnitude of age uncertainty can be expected in our core. Since our study focuses on the low-resolution depositional and climatic trends, the influence of these uncertainties on our overall interpretations would not change. Additionally, the previous study on the RS15-LC42 sediment core suggests the absence of erosional hiatuses within these timeframes, further supporting the robustness of our age model. This approach enhances confidence in interpreting long-term paleoenvironmental trends in the Southern Ocean and provides a valuable reference for future studies in this region.

3.2. Physical parameters and organic geochemical proxies

MS was measured at 1 cm intervals using a Bartington MS2B sensor. Water content percentage (WC %) was determined at 1 cm intervals by computing the difference in mass between wet sediment and the combined mass of dry sediment and salt, assuming a seawater salinity of 35 PSU (Millero et al., 2008). Dry bulk density was measured at 10 cm intervals

using the AccuPyc-II-1340 Gas-pycnometer. Grain size analysis was conducted at 10-cm intervals. Before grain size analysis, organic carbon and biogenic silica were removed through treatments with 10 % H2O2 and 2 N NaOH, respectively. The proportion of coarser fractions (> 63 μm) was determined by sieving, while finer fractions were analyzed using the Micrometrics Sedigraph III 5120. Statistical parameters for grain size (sorting, skewness, and kurtosis) were calculated following Folk and Ward (1957). Organic geochemical proxies such as Total Organic Carbon (TOC), Total Nitrogen (TN), Calcium Carbonate (CaCO3), and Biogenic Opal concentrations were measured at 5 cm intervals. Biogenic silica (SiBIO) concentrations were measured using a continuous flow analyzer (SKALAR SANplus Analyzer) and a wet-alkaline extraction method modified from DeMaster (1981). Biogenic opal concentrations were calculated by multiplying biogenic silica concentrations by 2.4, assuming the ratio (SiO2 + nH2O)/Si as 2.4, with nH2O constituting 10 % of biogenic SiO2 (Mortlock and Froelich, 1989). The relative analytical error of biogenic silica concentration in sediment samples is less than 1 %. Total inorganic carbon (TIC) concentration was measured using a UIC CO2 coulometer (Model CM5240). CaCO3 concentrations were calculated by multiplying TIC concentrations with 8.333, the ratio of CaCO3/C. The relative standard deviation for CaCO3 concentration was ±1 %. Total carbon (TC) concentration was measured using an elemental analyzer (FLASH, 2000 NC Analyzer) with an analytical precision of less than ±0.1 %. TOC concentrations were calculated as the difference between TC and TIC.

KOPRI 극지연구소

3.3. Elemental proxies for paleoproductivity

For multielement analysis using ICPMS, approximately 100 mg of air dried, homogenized, and powdered samples were digested using HF-HNO3-HCl acids and the residue was collected in 0.3 HNO3 solution. We estimated biogenic barium in sediments to determine paleoproductivity. Given that productivity is exclusively indicated by barite originating from organic sources, it is essential to consider and correct for other potential sources of barium, particularly terrigenous ones. To address this, we employed the Al normative approach for detrital correction. Using the measured total Al content and an upper crustal Ba/Al reference ratio of 0.0067 (Taylor and McLennan, 1985), the detrital fraction was estimated. The normative approach by Dymond et al. (1992) was used for the detrital correction Ba(excess) = Ba(total) - (Al x Ba/Al). Considering that bottom water conditions influence the preservation of Barium (McManus et al., 1998), we estimated authigenic Uranium in sediments to ascertain the prevailing oxic or anoxic preservation conditions. The authigenic fraction is estimated assuming a lithogenic U/Al ratio of 15 × 10−6 (McManus et al., 2005) and the Al concentration of the sediments, such that the corrected U (Ucorr) = Umeasured-[Al × U/Allithogenic].

3.4. Beryllium isotope analysis

For beryllium (Be) isotope analysis, a total of 70 samples were selected based on variations in magnetic susceptibility (MS) values. Samples were chosen from intervals corresponding to both high and low MS values, which are interpreted to represent glacial and interglacial periods, respectively (Robinson et al., 1995; Bollen et al., 2022; Kim et al., 2022; Rhee et al., 2022). For analysis, approximately 0.5 g of oven-dried and homogenized sediment were utilized. Gravel-sized grains were meticulously separated to prevent interpretation bias arising from diverse pathways and sources of particles. Following the method outlined by Wittmann et al. (2012), a stepwise leaching process was employed for the extraction of reactive phases of 10Be and 9Be (10Bereac and 9Bereac). Reactive amorphous and crystalline oxide phases were extracted using 0.5 N HCL and hydroxylamine hydrochloride (in 1 N HCL), respectively. The resulting extracts were combined, dried over a hotplate, and adjusted to a 10 ml volume. From this volume, 1 ml was utilized for the measurement of 9Bereac using ICPMS at KBSI. The remaining leachates were spiked with 1040 ppm 9Be, dried, and collected with 9 N HCL for subsequent column chromatographic analysis, following standard procedures at the Korea University Geochronology Laboratory (Jeong et al., 2018). The measurement of 10Be was conducted using a 6 MV Accelerator Mass Spectrometer (AMS) at the Korea Institute of Science and Technology (Lee et al., 2011; Rhee et al., 2017; Dash et al., 2021; Kim et al., 2024).

3.5. Spectral and wavelet analysis of MS data

Spectral analysis was conducted on the MS data, which was continuously measured at 1 cm intervals throughout the sediment core. To identify significant periodicities in the MS dataset, we utilized the REDFIT (v. 3.8) program (Schulz and Mudelsee, 2002), which is specifically designed for spectral analysis of unevenly spaced time series. The parameters were configured as follows: oversampling factor (ofac) = 2.0, segment count (n50) = 2, Welch windowing applied, and 1000 Monte Carlo simulations (Nsim = 1000) to assess statistical significance. Additionally, wavelet analysis was performed using PAST (v. 4.03) software (Hammer et al., 2001) to examine time-frequency variations in the MS data. A Morlet wavelet transform was employed, with a wavelet parameter of W0 = 6 and a scale width of 0.25. The data were zero-padded to accommodate edge effects, and the cone of influence was applied to account for reduced confidence at the boundaries.

4. Results

4.1. Magnetic susceptibility and lithostratigraphy

The downcore variation of MS values in the RS15-LC47 sediment core shows significant changes (Fig. 2). Between 750 and 550 ka, high MS values are observed without a discernible trend, whereas in the middle sections (550–250 ka), the values dampen. Beyond

250 ka, the MS values exhibit a marked increase in variability. These patterns exhibit a clear correspondence with the MS trends observed in the RS15-LC42 sediment core. The identified low MS values in the middle sections of both cores served as a marker horizon for wiggle matching (Fig. 2). Age-integrated MS values demonstrated a robust agreement between the two cores (Fig. 2c). The MS values for RS15-LC47 sediment core display a positive trend with the sand % (Fig. 3a). Although the correlation coefficient between magnetic susceptibility (MS) and sand % is weak, a positive trend is evident.

From a lithostratigraphic perspective, the core sediment is predominantly characterized by clay and silt (Fig. 2a). The granulometric analysis also indicates that silt and clay are the prevailing grain sizes (Fig. 4). A visual examination of the core reveals the consistent presence of intermediate layers composed of IRD and sandy mud throughout its length. Notably, the IRD-enriched layers are observed during the late Pleistocene period (> 250 ka) (Fig. 2a). The entire core exhibits evidence of bioturbation, except for the interval between 720 and 1040 cm corresponding to approximately 500 to 700 ka. During this interval, distinctive sedimentary structures such as parallel laminations and cross-beddings are apparent, deviating from the otherwise homogenous and structureless nature of the rest of the core (Fig. 2a). Within the mentioned depth range, ranging from 720 to 1040 cm, millimetre-scale faults are observable.

4.2. Geochemical proxies

Downcore variations in $CaCO_3$, TOC, C/N, Opal, and Ba_{ex} are presented in Fig. 4, with corresponding values provided in Supplementary Material I. The percentage variation of the biogenic components shows a similar trend with their MARs. CaCO3, TOC, and C/N, exhibit markedly higher values between 550 and 750 ka. Within this interval, CaCO3 varies from 0 to 2.3 % (Average = 0.52 %), the TOC varies from 0.06 to 0.41 % (Average = 0.27 %), and C/N varies from 5 to 18 (Average = 10.5). Although, these organic geochemical parameters show remarkably lower values after 550 ka, still significant fluctuations are observed (Fig. 4, Fig. 8). Between 550 ka and 250 ka, the TOC and C/N vary from 0.07 to 0.25 (Average = 0.16) and 3.67 to 6.47 (Average = 5.05), respectively. After 250 ka, both TOC % (Average = 0.13 %) and C/N (Average = 5) significantly reduce and show a gradual increasing trend toward the top of the core. The $CaCO_3$ concentration is highest at the bottom of the studied section, averaging 0.52 % during the 750-550 ka interval. Subsequently, it declines sharply, averaging 0.023 % between 550 and 250 ka, and 0.027 % after 250 ka. Opal % does not show much variation till 250 ka, however, it slightly increases and shows notable variation after that. After 250 ka the opal % varies from 9 to 22 %, with an average value of 16 %. Baex, a productivity proxy in the Southern Ocean, was analyzed for the 250-773 ka interval and showed significant variations (Fig. 4t). Baex is significantly lower in the 750 to 550 ka interval as compared to the rest of the period. Interestingly, although TOC is significantly higher between 750 and 550 ka, other productivity proxies like Baex and Opal are lower in this interval.

4.3. Variation of 10Bereac, 9Bereac and (10Be/9Be)reac

The Be isotope variation data are presented in Supplementary Material I, with their downcore trends illustrated in Fig. 4. The concentration of 10Bereac (in atoms/g) exhibits a range from 3.79 × 109 ± 1.15 × 107 to 5.55 × 107 ± 6.63 × 105, with an average value of 1.48 × 109 ± 5.57 × 106. On the other hand, authigenic 9Bereac varies from 1.18 × 1017 ± 1.6 × 1016 to 2.03 × 1016 ± 3.82 × 1014, with an average of 6.76 × 1016 ± 1.85 × 1015. The 10Be/9Be ratio (in atoms/g) ranges from 6.25 × 10−8 ± 1.29 × 10−9 to 1.76 × 10−9 ± 2.47 × 10−11, with an average value of 2.15 × 10−8 ± 5.95 × 10−10. The downcore variations of both (10Be/9Be) reac and 10Bereac follow a similar pattern. They exhibit an increasing trend toward the late Pleistocene, with the lowest values observed in the 550–750 ka interval. Interestingly, visual observations shows that the trends of (10Be/9Be) reac and 10Bereac shows opposite trends with MS values but align with Opal % and TOC % after 250 ka.

5. Discussion

5.1. Sediment facies association and depositional environment

Magnetic susceptibility, along with sediment lithological characterization, have been used as primary tools to interpret paleoenvironment from high latitude sediment cores (Mead et al., 1986; Diekmann et al., 2000; Pirrung et al., 2002; Brachfeld, 2006; Bollen et al., 2022). Initially, we assess the broad depositional environments of the sediments based on visual core descriptions and physical property analyses. To further refine our interpretations, we also incorporate the sedimentological parameters of the RS15-LC47 core reported by Al'bot, 2016, unpublished), which provide valuable insights into the core's depositional history and environmental context.

5.1.1. Ice sheet-proximal depositional environment (750–550 ka)

The lower segment of the studied interval (750–550 ka) displays distinct lithological characteristics than the rest of the core. It is characterized by parallel and cross laminations, along with millimetre-scale faults (Fig. 2a). The presence of laminated clay-rich layers, infrequent sandy layers, the absence of bioturbation, and poor sorting in this segment suggest an origin associated with contourite processes (McCave et al., 1980; Faugères et al., 1993; Howe et al., 1997; Koenitz et al., 2008; Faugères and Mulder, 2011; Thiéblemont et al., 2019). The well-defined and continuous laminations result from consistent bottom currents and are well-preserved due to the lack of bioturbation (Weber et al., 1994; Rodrigues et al., 2022). The presence of IRD layers within the laminated mud eliminates the possibility of a turbiditic origin (Rodrigues et al., 2022). Ohneiser et al. (2019) interpreted these thin gravel layers as lag surfaces, which suggest periods of increased current strength and winnowing. Once

formed, these surfaces likely act as protective armour, preventing further erosion of the underlying sediments. However, it's noteworthy that low-density turbidity currents can still transport ice-rafted debris to deeper oceans (Wang and Hesse, 1996). The occurrence of cross-laminated mud in this interval can be attributed to the intermittent sedimentation by turbidity currents (Lucchi et al., 2002; Rodrigues et al., 2022).

This period saw a significant expansion of the Antarctic ice sheets (McClymont et al., 2013; Sutter et al., 2019) and a northward shift of the polar front (Kemp et al., 2010). During full glaciation, the ice sheet extended to the outer continental shelf, narrowing the Antarctic Slope Current (ASC) (Conte et al., 2021). This confinement intensified the ASC by limiting energy dissipation and water exchange, which in turn regulated Circumpolar Deep Water (CDW) inflow and Ross Sea Bottom Water (RSBW) outflow. As a key oceanic boundary, the ASC separates cold, fresh shelf waters from the warmer, saltier CDW, influencing ice-ocean interactions, sea ice dynamics, and ice sheet stability. During glacial periods, ice sheet expansion and increased sea ice led to stronger brine rejection, enhancing dense shelf water formation and strengthening the ASC. This reinforced the barrier against CDW intrusions, reduced basal ice shelf melting, and promoted ice sheet stability while limiting ocean-atmosphere heat exchange, contributing to the regional cooling. In contrast, interglacial periods are marked by ice sheet retreat and reduced sea ice cover, weakening the ASC due to diminished brine rejection and less dense shelf water production. A weaker ASC allows greater CDW incursions onto the continental shelf, increasing basal ice shelf melting and accelerating ice sheet retreat.

In the Ross Sea sector, there have been multiple instances of the grounding line advancing toward the shelf break during glaciations since the MPT (McKay et al., 2012; Bollen et al., 2022). The advance of the grounding line initiates sediment gravity flows and turbid plumes, which are funnelled to the outer continental margin through the canyon networks (Fig. 5c; Larter and Barker, 1989; Lucchi et al., 2002). The presence of millimetre-scale faults observed within this interval indicates that they formed syn-depositionally due to the increased sedimentation associated with turbid plumes. These faults are interpreted as syndepositional sedimentary structures, as they displace thin laminas and are confined to a specific depth range. As the finer fractions of these flows settle, they are transported westward by the along-slope currents, highlighting the combined influence of downslope sediment gravity flows and along-slope currents in shaping channel-levee systems along the Antarctic margin during glacial periods. Such sedimentation pattern is further corroborated by the deposition of higher clay content and relatively higher MAR, and by the presence of poorly sorted sediments at the study site during this interval (Fig. 4). Additionally, the increased sedimentation rates and harsh glacial conditions likely suppressed biological activity. The elevated and irregular MS values observed during this period is consistent with sedimentation dominated by gravity flows. During full glacial periods, advancing ice sheets transported sediments toward the continental margin through basal erosion and bulldozing processes. This strengthened glacial activity mobilized coarser sediments, which were subsequently incorporated into gravity flow deposits. The presence of these coarser-grained materials led to elevated MS values, as

lithogenic fractions with larger grain sizes typically contain higher concentrations of magnetic minerals compared to finer sediments. Furthermore, the poor sorting characteristic of gravity flow deposits resulted in an irregular MS pattern. Gravity-driven sediment transport mechanisms, such as turbidity currents and debris flows, carried a heterogeneous mixture of grain sizes, leading to fluctuating concentrations of magnetic minerals within the stratigraphic sequence. This variability in grain size distribution and mineral composition is reflected in the irregular MS values observed in this section of the sediment core, providing insights into past glacial dynamics and associated sedimentary processes.

5.1.2. Partial-advancement of ice-sheet during mid-late Pleistocene (550-250 ka)

Following the MPT, MS values remained consistently low until MIS 8 (~ 250 ka) in both the cores (RS15-LC47 and RS15-LC42). Ohneiser et al. (2019) reported this anomalously low MS values in the middle of C1n in both continental marginal and deep-water sediment cores from the Ross Sea, suggesting persistent interglacial during this timeframe and probably ice sheets attained a stable configuration. Gravel counts are low in both the cores (Al'bot, 2016), and IRD-rich layers are sparse in this interval. Clast-rich sediment layers at the Antarctic marginal settings are attributed to the action of bottom currents, where winnowing of finer fractions due to robust bottom currents enhance the abundance of gravelly clasts (Drewry and Cooper, 1981; Bollen et al., 2022). Ice sheet models divide the post-MPT period into two episodes based on ice sheet extent (Sutter et al., 2019). The first part, spanning till MIS 11, is characterized by smaller glacial ice sheets and prolonged relatively warmer interglacials. We speculate subdued glacials during this timeframe due to the influence of prolonged relatively warming condition. Hesse et al., 1997, Hesse et al., 1999 suggest that sedimentation from meltwater plumes is limited to a few tens of kilometres near the coast during interglacial periods. The wider landward sloping continental shelf off the Pacific margin of the Antarctic Peninsula acts as a sediment trap during interglacials, hindering the supply of coarser sediments to the continental rise. The low percentages of sand and gravel (Fig. 4), along with a notable absence of IRD-rich layers in this interval, suggest that neither of the processes supplying coarser sediments to the outer continental margin, i.e., ice-sheet calving during interglacials or mobilization of sub-ice shelf sediments during glacials, were dominant during this time. The ice sheets probably remained relatively stable near the coastline, preventing the movement of coarser sub-glacial sediments or those resulting from ice-sheet calving to the offshore region (Fig. 5b).

Despite these overall trends, a closer look at granulometric parameters reveals two distinct sedimentation episodes within this interval: from MIS 15 to 11 and from MIS 11 to 8 (Fig. 4). Although the sand % remains relatively stable, silt and clay percentages, along with sorting, exhibit differing trends between the two episodes. The former is characterized by well-sorted sediments with a lower clay and higher silt percentage compared to the latter. While the clay percentage differs by a modest 10 % between the two phases, there is a more

substantial (~ 30 %) variation in silt percentage, along with noticeable differences in sorting. This implies that even though the gravel-sized clasts were trapped on the continental shelf when the ice sheets were proximal to the coastline, the interglacial meltwaters could still transport silt-sized sediments farther offshore. Thus, based on the granulometric analysis, we interpret two distinct and stable environmental conditions during this interval, the former being relatively warmer than the latter.

5.1.3. Increased Ice-Sheet Variability and High-Energy Depositional Conditions in the late Pleistocene (250 ka - present)

The late Pleistocene period (> 250 ka) is characterized by coarser grain size, IRD-rich layers, and high-frequency variations in MS values (Fig. 2, Fig. 4). The MS values are low during the interglacials of MIS 7, 5 and 3, suggesting sedimentation distal to ice-sheet (Fig. 5a). As reported by Al'bot (2016), the gravel counts also gradually increase after MPT, which is significant after 250 ka. The general sedimentation pattern in the Antarctic continental margin deposits indicates clast-dominated sediments during the late Pleistocene (Bollen et al., 2022). Ice sheet models and proxy records from the Antarctic continental margin indicate that, following MIS 11, interglacial temperatures increased by 1-2 ℃ in the high latitudes of the Southern Ocean and Antarctica (Masson-Delmotte et al., 2010), leading to greater ice volume variability with smaller interglacial and larger glacial ice sheets (Sutter et al., 2019). Previous sedimentological inferences from AND-1B indicate reduced Antarctic ice volumes during late Pleistocene interglacials since MIS 11, compared to periods between ~0.4 and 1.1 Ma (McKay et al., 2012).

Sporadic IRD layers appear in the upper part of the core post-250 ka, aligning with periods of elevated MS values, corresponding to the glacial intervals of the late Pleistocene (MIS 2-3, 4, 6, and 8). The prevalence of coarse grain sizes during these intervals suggests deposition occurred in high-energy environments that reduced the settling of finer particles and concentrated IRD. Notably, there is no sedimentological evidence of gravity flow deposits in the upper part of the core. Additionally, nearby sediment cores, including RS15-LC42 (Bollen et al., 2022) and RS15-GC41 (Kim et al., 2020), do not exhibit any signs of sediment reworking after 300 ka. This suggests that glacial advances may not have reached the shelf break, leading to decreased dense water formation on the shelf in the Central Basin. Recent geophysical and oceanographic data reveal that dense shelf water cascading at the Hillary Canyon in the Ross Sea reaches velocities up to 1 ms−1 (Gordon et al., 2004, Gordon et al., 2009; Morrison et al., 2020), which are sufficient to prevent gully infilling but not strong enough to cause significant erosion or gully incision at the shelf edge (Gales et al., 2021). This indicates that while these flows contribute to maintaining existing canyon morphology, they do not actively sculpt new features or significantly alter the seafloor. We propose that these energetic plumes maintained bottom current velocities sufficient to winnow fine-grained sediments and concentrate IRD into gravel lags, although not strong enough to erode gravel

clasts and create a complete hiatus.

We analyzed climatic periodicities using MS data up to 250 ka. The lower section of the core (750–550 ka) exhibits an irregular pattern due to gravity flow deposition, while the interval from 550 to 250 ka shows persistently low MS values. Given these inconsistencies, we excluded these time frames from the spectral analysis and focused only on data up to 250 ka to ensure reliable results. The spectral analysis (Fig. 6a) shows dominant peaks at 50 ka and 15.6 ka, indicating recurring cycles in MS variations. The 50 ka periodicity could correspond to the 41 ka obliquity cycle (Lisiecki and Raymo, 2005), which influences global climate patterns through variations in Earth's axial tilt. However, the deviation from the expected 41 ka cycle may result from site-specific depositional factors, such as changes in regional sedimentation dynamics, variations in sedimentation rates, or asynchronous nature of glaciation worldwide, as highlighted by Raymo et al. (2006). Similarly, the 15.6 ka periodicity might be related to the 19 ka precessional cycle (Petit et al., 1999), which is linked to changes in solar insolation affecting glacial dynamics and sediment transport. Our analysis does not reveal the 100 ka cyclicity, possibly because the 250 ka timeframe is too short to capture this pattern.

The wavelet analysis (Fig. 6b) provides a time-frequency representation of MS variations, allowing us to examine how these periodicities evolve over time. The presence of strong power at lower frequencies, particularly around 50 ka, suggests that the obliquity-related influence on sedimentation persisted across the studied interval. The high-energy zones at specific depths further confirm the influence of orbital-scale climate forcing. Additionally, the 15.6 ka periodicity appears intermittently, indicating that precessional-scale variations may have influenced MS fluctuations at certain intervals. The broadening and shifting of spectral power over time suggest that depositional conditions were not uniform, and external forcing factors such as paleoceanographic changes and glacial-interglacial dynamics might have contributed to modulating the recorded signals.

5.2. Pleistocene ice sheet dynamics inferred from Beryllium isotopes

5.2.1. Beryllium isotope inventory to Antarctic marginal marine environments

The Be isotopic record from this study is at par with that of open marine settings in the Ross Sea region (in the order of 109) (Sjunneskog et al., 2007; Yokoyama et al., 2016) and higher than that from the sub-ice shelf deposits. The measured 10Be in the Ross Sea region is two orders of magnitude higher than the hypothetical concentration during Holocene (in the order of 107, assuming an atmospheric flux rate of 5 × 105 atoms/cm2) (Valletta et al., 2018). This indicates that atmospheric deposition alone cannot explain the observed variations of 10Bereac concentrations in glacio-marine sediments, emphasizing the need to understand additional sources to explain the observed concentrations. The variability in (10Be/9Be)reac at the Antarctic continental margin is proposed to have been contributed by pulsed 10Be

delivery by basal melt (Valletta et al., 2018). An increasing trend observed in (10Be/9Be)reac during the interglacials is attributed to increased basal melt and higher scavenging rate. Nevertheless, it is acknowledged by previous researchers that atmospheric flux alone is inadequate to explain the observed (10Be/9Be)reac variations along the Antarctic continental margin (Sjunneskog et al., 2007; Valletta et al., 2018).

Authigenic phases in marine surface sediments record a composite of terrestrial and marine influences, where an initially terrestrial signal is later overprinted by a marine-derived component (Wittmann et al., 2017). Continental margin sites often exhibit lower reactive-phase 10Be/9Be ratios than adjacent open ocean areas, as observed in Baffin Bay (Simon et al., 2016), around Papua New Guinea (Ménabréaz et al., 2012, Ménabréaz et al., 2014), and in the Mediterranean (Simon et al., 2017). Beryllium isotope ratios in seawater are significantly higher than in freshwater (Von Blanckenburg et al., 2015). Sediment particles transported via rivers or subglacial systems initially scavenge beryllium in these low-ratio freshwater settings, and upon reaching the continental shelf, acquire an additional marine reactive layer, resulting in elevated (10Be/9Be)reac values (Wittmann et al., 2017). In glacial environments, isotopic variations follow a spatial gradient—low in subglacial settings, intermediate under ice shelves, and highest in open marine environments (Sproson et al., 2022, Sproson et al., 2024; White et al., 2019).

Meteoric 10Be, produced in the atmosphere and deposited via precipitation and dust, accumulates in Antarctic ice sheets at concentrations of 5–8 × 104 atoms/g (Baroni et al., 2011; Raisbeck et al., 2007), far exceeding seawater values. This isotope enters marine sediments through meltwater discharge, with open marine sites showing higher 10Bereac concentrations and (10Be/9Be)reac ratios due to efficient scavenging. In contrast, 9Be—originating from silicate weathering and subglacial erosion—is primarily transported via basal meltwater, leading to elevated fluxes near grounding lines. These contrasting transport pathways result in strong spatial gradients across Antarctic marginal seas. For instance, Prydz Bay core tops show higher (10Be/9Be)reac in open marine settings than beneath ice shelves (White et al., 2019), and Ross Sea records link post-glacial (10Be/9Be)reac increases with ice shelf retreat (Sjunneskog et al., 2007). Lakes such as Maruwan Oike and Skallen in East Antarctica further underscore this pattern, where higher 10Be/9Be ratios reflect intensified meltwater input from adjacent glaciers (Sproson et al., 2021).

5.2.2. Relative variation of 10Bereac and 9Bereac

While individual beryllium isotopes 10Bereac and 9Bereac may not independently offer reliable insights into paleoenvironmental conditions, their ratio (10Be/9Be)reac proves valuable (Valletta et al., 2018; Behrens et al., 2022). The decoupling between 10Bereac and 9Bereac becomes evident in their normalized plots, and a homogeneity would result in a 1:1 relationship. The observed trendline in the 10Be vs 9Be plot for the RS15-LC47 sediment core exhibits an overall slope less than 1, indicating an additional input of 10Be (Fig. 7). However,

the trendline exhibits variability across different sedimentation environments (Fig. 7), as discussed earlier (Section 5.1). During warmer intervals, the slope of the trendline is <1, while during colder episodes, it is >1. This variability in the 10Bereac vs 9Bereac relationship suggests additional 10Be input during the warmer interglacial periods (Valletta et al., 2018).

A sediment core record from the Chilean Margin (Sproson et al., 2024) shows a slope < 1 in the 10Be vs. 9Be plot (Fig. 7), indicating an enrichment of the 10Be-rich marine phase during interglacial periods—consistent with enhanced scavenging under open marine conditions. A comparable pattern has been observed in the surface sediments of same region (Fig. 7). Wittmann et al. (2017) reported that the (10Be/9Be)reac ratio in surface sediments of Chilean Margin reflects a two-component mixture: a marine phase (MUC samples) enriched in 10Be, and a fluvial phase (Terra samples) with lower ratios due to the release of dissolved 9Be during chemical weathering of continental rocks. The close resemblance between the trends observed in this study and those from the Chilean margin underscores that Be isotopic signatures in glaciomarine environments are primarily governed by the relative contributions of reactive Be from terrestrial and marine sources. During glacial maxima, reduced scavenging of 10Be-enriched marine phase leads to a steeper slope (>1), while interglacial periods favour enhanced scavenging resulting in a shallower slope (<1).

5.2.3. Paleoenvironmental/ paleoceanographic signal from (10Be/9Be)reac

The (10Be/9Be)reac is lowest in the 550-750 ka interval. This interval belongs to the later part of the MPT, characterized by extended glacial conditions (Fig. 5c) (Clark et al., 2006; Bol'Shakov, 2015; Daruka and Ditlevsen, 2016; Ford et al., 2016; Herbert, 2023). This period signifies a sudden reorganization of the climate system, occurring in at least two discernible stages, i.e., MIS 25-22 and MIS 22-16. The MIS 16 is conferred as the period with maximum global ice volume. Throughout the MIS 22 to MIS 16 timeframe, the climate system experienced modest interglacial conditions interspersed with progressively more severe glacial phases (Fig. 1b). Sedimentological record from AND-1B sediment core also suggest a large-scale expansion of an ice sheet in the Ross Embayment around ~0.78 Ma (McKay et al., 2012). Low (10Be/9Be)reac ratios in this interval suggest limited scavenging in open marine settings, likely due to reduced sediment transit time to the coring site as grounding lines extended toward the shelf edge (Fig. 5c).

The 10Bereac and the (10Be/9Be)reac values show a notable increase following MIS 16, particularly during MIS 14-11, indicating an extended interglacial condition. This observation aligns with the evidence of enhanced sorting and higher silt percentage during this interval. In contrast to mid-late MPT period, a there was a south-westward shift of the ASL and dominance of easterlies after MIS 16 (Hillenbrand et al., 2009). This altered scenario, with a southward shift of ASL and an increased advection of CDW toward the shelf zone could have caused instability in the Antarctic ice sheets. Although the (10Be/9Be)reac values during this interval are higher than those of the preceding phase, they remain lower than the late

Pleistocene values (>250 ka) observed in our study. This pattern may reflect a partial advance of ice sheets to the shelf edge, which likely increased sediment transit time to the continental rise in open marine settings. As a result, the scavenging of Be isotopes in open marine settings was moderately enhanced. We interpret this interval as a relatively warmer phase, characterized by its extended duration and moderately elevated (10Be/9Be)reac ratios (Fig. 5b). Previous studies on Antarctic marginal seas have also documented an extended interglacial period following the MIS 16, which researchers suggest may have contributed to the potential collapse of the WAIS. Hillenbrand et al. (2009) suggest the possibility of WAIS collapse occurring between MIS 15-13, drawing their conclusion from the analyses of productivity and lithogenic proxies in the Amundsen Sea. They propose that changes in circulation patterns after MIS 16 may have triggered this collapse, noting anomalous increases in biological productivity and lithogenic supply during the period spanning 621-478 ka. Similarly, Scherer et al. (1998) report a potential WAIS collapse during MIS 11, based on observations of increased 10Be concentration in sediments beneath the WAIS. They attribute this increase to open marine conditions following the disintegration of the ice sheet. In support of this, Hearty et al. (1999) and Kindler and Hearty (2000) present findings indicating notable deglaciation events between 570 and 390 ka. The discrepancy in proposed timing for the collapse of the WAIS may stem from chronological constraints. However, the period from MIS 16 to MIS 11 remains the most contentious timeframe for such a collapse. Although the observed (10Be/9Be)reac increase during the MIS-14-11 in our study does not provide direct evidence for WAIS collapse, it indicates a prolonged relative warm condition favourable for the ice-shelf disintegration.

The (10Be/9Be)reac increases significantly after 250 ka, showing opposite trend to the MS values (Fig. 4). It is proposed that interglacial temperatures have risen by 1-2 ℃ since 300 ka (Masson-Delmotte et al., 2010). The incursion of warm CDW onto the continental shelf during the interglacials has been extensively documented across various regions of the Antarctic margin (Howe and Pudsey, 1999; Steig et al., 2012; King et al., 2022; Yi et al., 2023; Lamy et al., 2024). This influx of warm CDW directly influences glacial dynamics by fuelling escalated melt rates and consequently triggering retreat and collapse of ice shelves. The intensified intrusion of CDW during the interglacials can be attributed to two main factors: firstly, diminished formation of dense water on the shelf in the Ross Sea, and secondly, a weakened ASC, which acts as a hydrographic barrier that typically restrains CDW intrusion. The retreat of grounding lines during the warmer conditions of late Pleistocene likely prolonged sediment transport through open marine environments, thereby contributing to an increase in the (10Be/9Be)reac ratio during this period.

5.2.4. Post-250 ka WAIS Dynamics in Response to Global climate transition

Our results from Beryllium isotopes analyses indicate that the WAIS was positioned near the continental shelf edge prior to 250 ka, as reflected by low (10Be/9Be) reac ratios.

After 250 ka, we observe a cyclical pattern of retreat and readvance of the WAIS. Higher 10Be/9Be ratios during this period suggests relatively more open marine conditions during retreats and subsequent readvances of the grounding line or ice shelves than the previous intervals. Similar climatic interpretations have been made from a nearby sediment core (RS15-LC42), where Bollen et al. (2022) used sedimentological, diatom assemblage, and micropaleontological data to infer a warmer period after ~300 ka. This change could be related to the previously reported climatic transition around 0.4 Ma, after which interglacial temperatures are generally 1.5-2 °C warmer than those before (Masson-Delmotte et al., 2010). Around 0.4 Ma, Earth's climate underwent a significant transition that marked the beginning of warmer and more variable interglacial periods. Before this point, the Pleistocene glacial-interglacial cycles were dominated by long, cold glacial phases with relatively cooler and shorter interglacials (Masson-Delmotte et al., 2010). After 0.4 Ma, however, interglacials became warmer and were associated with higher atmospheric CO_2 levels (Lisiecki and Raymo, 2005; Jouzel et al., 2007). Model simulations suggest that before this transition, changes in Earth's orbit led to strong feedbacks involving sea ice, temperature, evaporation, and salinity, which drove vigorous Antarctic bottom water formation and enhanced Southern Ocean overturning circulation (Yin, 2013). These conditions resulted in a cooler deep ocean and relatively subdued warmth during earlier interglacials. Barth et al. (2018) identified this transition around 0.4 Ma based on multiple global climate proxies, indicating increased climate variability and a significant shift in the Earth's climate system.

A key factor in this climatic shift was the changing behaviour of the WAIS. According to Holden et al. (2011), after 0.4 Ma the WAIS became less stable, potentially due to ongoing subglacial erosion that steepened the underlying bedrock and made the ice sheet more vulnerable to retreat. This destabilization of the WAIS contributed to the enhanced Antarctic warming seen during post-0.4 Ma interglacials. Earlier models failed to fully account for the magnitude of this warming until WAIS retreat was added as a feedback mechanism (Holden et al., 2010). Support for this comes from both ice sheet simulations (Pollard and DeConto, 2009) and erosion measurements beneath an Antarctic ice stream (Smith et al., 2007), which collectively suggest that a threshold in WAIS dynamics was crossed around this time, fundamentally altering its response to climate forcing.

5.3. Production and preservation of biogenic material at the Ross Sea continental margin

5.3.1. Opal in Drift Sediments of the Antarctica: Relevance to Biological Productivity or Preservation Dynamics?

The depositional environments of biogenic sedimentary components in this study are interpreted based on the trends of downcore variations (Fig. 4, Fig. 8). Despite the various dissolution processes, opal records in upper Quaternary sediments from Antarctica are interpreted as a proxy for the changes in the surface water productivity (Charles et al., 1991;

Hillenbrand and Fütterer, 2001; Grützner et al., 2005; Hillenbrand and Ehrmann, 2005; Weber et al., 2022). However, discrepancies between opal, TOC, CaCO3, and biogenic barium (Baex) records are observed for the 750-550 ka interval (Fig. 4). Discrepancies also exist between opal content and its accumulation rates (OpalMAR) during the 750-550 ka interval. Despite this, visual observation (Fig. 4) and bivariant plots (Fig. 9) shows that downcore variation of OpalMAR exhibit a positive trend with TOC and (10Be/9Be)reac after 550 ka, indicating increased surface productivity during warmer climatic intervals of late Pleistocene and vice versa. In general, OpalMAR is influenced by opal deposition and their preservation, while opal content may be additionally affected by dilution with other sedimentary components, primarily lithogenic particles in drift sediments. During the late Pleistocene at our study site, no significant discrepancies are observed between opal contents and OpalMAR, but differences are significant during the 750-550 ka interval (Fig. 4). This 750-550 ka period coinciding with notably high linear sedimentation rates (LSR), suggests that opal content in drift sediments were significantly masked by lithogenous particle dilution. The original depositional rates of siliceous particles are strongly influenced by changes in LSR, with lateral redistribution of biosiliceous particles by bottom currents further affecting OpalMAR. Bottom currents possibly acted as focusing mechanisms on the Antarctic Peninsula continental rise, enhancing the delivery of interglacial productivity signals from overlying water columns. Conversely, turbidity currents from unstable locations at the continental slope mainly resuspended lithogenic components, explaining the low opal contents in lower section of the core. Nonetheless, extensive occurrences of reworked diatoms along the Ross Sea continental margin during and after MPT (Bollen et al., 2022) suggest lateral redistribution of biosiliceous matter from the shelf to the continental rise, contributing to OpalMAR for the 750-550 ka period.

5.3.2. Variation of Total Organic Carbon

During the period spanning 750 to 550 ka, there is a noticeable spike in TOC and C/N ratio (Fig. 4). The average C/N value in this timeframe reaches 11, significantly higher than the Redfield ratio of 6.6 and exceeding the natural variability observed in the euphotic layer of both the Ross Sea (5.4-9.2; Fabiano et al., 1993) and the Amundsen Sea polynya (6.3 -9.2; Kim et al., 2018a). The C/N ratio serves as an indicator of sediment source, with higher values suggesting a dominance of terrestrial organic carbon (Sarmiento, 2006; Li et al., 2016). The increase in C/N reflects a peak in terrestrial input likely due to advancing ice sheets, which could have led to reduced marine productivity and an increase in glaciomarine influence. Additionally, the decrease in the Al normalized Barium (Baex), a proxy for productivity, during this period suggests diminished productivity (Fig. 4). Although Al in oceanic sediments may also be contributed from biogenic sources, other than terrigenous input, our data shows a high positive correlation between Al and Ti (Fig. 9c), suggesting that the Al is primarily terrigenous sourced. Biogenic barium signals are considered resistant to dissolution processes in Antarctic continental rise settings due to prevailing oxic conditions in

the sediment column (Shimmield et al., 1994; Bonn et al., 1998). The detrital corrected U record from our core (Fig. 4s) also suggests that Baex is not affected by anoxic dissolution. Based on the relationship between TOC, C/N and Baex it is hypothesized that the elevated organic carbon during this period might have originated from reworked bottom sediments during the glacial advance. In contrast, the period between 550 and 250 ka shows C/N levels within the range observed in the euphotic layer of the Ross Sea (Fig. 4, Fig. 8). Baex values are relatively higher during this interval (Fig. 4), correlating with high TOC. Therefore, the increased TOC values during this period are likely due to higher productivity in a relatively warm condition. Our findings are supported by anomalously lower magnetic susceptibility (MS) values and relatively higher (10Be/9Be)reac ratios compared to the preceding interval. After 250 ka, the TOC shows a gradual increase, along with increase in OpalMAR and (10Be/9Be)reac, suggesting a warmer climatic condition and increased productivity during the late-Pleistocene.

5.3.3. Variation in calcium carbonate and its significance for the bottom water dynamics during the mid- late Pleistocene

Diverse patterns of calcium carbonate preservation have been seen in deep-sea sediment cores from the Southern Ocean. These patterns are probably impacted by variations in the alkalinity of bottom waters (Emerson and Archer, 1990; Rickaby et al., 2010; Steiner et al., 2021). The Ross Sea exhibits limited preservation of calcium carbonate in its sediments due to high organic flux, low saturation states of overlying waters, influence of acidic CDW and the relatively minor role of benthic carbonate production (Hauck et al., 2012). High organic flux from primary production, which increases CO_2 levels during decomposition, leads to carbonate dissolution. The Ross Sea waters are also influenced by acidic, CO_2-rich Circumpolar Deep Water (CDW), further hindering preservation. Benthic carbonate production is minimal, with sediments primarily influenced by planktonic sources. Physical processes like abrasion, bioturbation, and bioerosion further degrade $CaCO_3$, resulting in overall low preservation in the sediments.

The RS15-LC47 sediment core shows anomalously high $CaCO_3$MAR, TOCMAR, and C/N ratios, along with evidence of gravity flow deposits between 750 and 550 ka. This suggests that the calcium carbonate in this interval was predominantly supplied by glacially reworked sediments derived from continental sources. Although calcium carbonate is largely absent from the 550 ka to the present interval, isolated peaks displaying an inverse relationship with TOC are observed (Fig. 8). These peaks generally correspond to the colder episodes, indicating enhanced calcium carbonate preservation during the glacial periods. The data suggest that post-550 ka, calcium carbonate preservation improved as productivity decreased, hinting at reduced corrosiveness of the water column in the Ross Sea during glacial phases. This accumulation of siliceous detritus on the seabed, which could facilitate the decay of organic matter and dissolution of calcareous foraminifera during interglacial periods (Kennett,

1968). Conversely, during glacial periods, strong bottom currents likely enhanced calcium carbonate preservation by limiting the deposition of fine materials (Taviani et al., 1993; Taviani and Claps, 1998; Frank et al., 2014). Additionally, the influx of corrosive CDW appears to decrease during glacial intervals, further supporting the preservation of calcium carbonate. However, a detailed analysis of the carbonate material is necessary to further elucidate the nature and source of the carbonates in the studied sediment core.

5.3.4. Paleoproductivity in the Ross Sea During the Past 800 ka

Paleoproductivity in the Ross Sea over the past 800 ka has been closely linked to climate-driven variations in sediment composition, organic carbon flux, and bottom water dynamics. Changes in opal content, TOC, and $CaCO_3$ reflect the complex interactions between surface water productivity, sediment preservation, and glacial-interglacial shifts in ocean circulation. During the 750–550 ka interval, high linear sedimentation rates significantly influenced biogenic proxy records. While opal content remained relatively low, peaks in TOC and C/N ratios suggest an increased terrestrial input, likely due to advancing ice sheets and glacial reworking of sediments. The concurrent decline in Baex indicates supply of reworked terrestrial organic matter rather than increased biological production. High C/N values further support the dominance of terrestrial organic matter. Additionally, anomalously high $CaCO_3$ accumulation during this period appears to be linked to glacially transported material rather than in situ carbonate productivity. A shift toward higher biological productivity is evident between 550 and 250 ka. Rising TOC values, along with increased Baex, indicate surface water conditions favoring primary productivity. This trend corresponds with persistent relatively warming conditions, as reflected in elevated (10Be/9Be)reac ratios and lower MS values. The alignment between OpalMAR and TOC during this interval suggests that opal dissolution had a lesser impact, allowing productivity signals to be better preserved. While $CaCO_3$ content remained low due to the influence of corrosive CDW, distinct peaks in glacial intervals indicate periods of reduced CDW incursion and enhanced bottom current activity, which may have limited fine sediment deposition and facilitated carbonate preservation. After 250 ka, a gradual increase in TOC, OpalMAR, and (10Be/9Be)reac ratios, along with frequent occurrences of lower MS values, reflects a transition to a warmer climate, leading to higher primary productivity. Strengthening interglacial conditions likely improved nutrient availability in the surface waters, further supporting biological activity. During glacial intervals, stronger bottom currents continued to modulate $CaCO_3$ preservation by winnowing fine sediments and reducing exposure to corrosive CDW. These interconnected trends highlight how climate variability has shaped biological productivity in the Ross Sea. Glacial periods were characterized by increased terrestrial input and sediment redistribution, while interglacial conditions favored enhanced primary productivity and better preservation of biogenic materials. The complex interactions between ocean circulation, sediment dynamics, and biogeochemical proxies highlight the sensitivity of the Ross Sea ecosystem to past climate

fluctuations.

6. Conclusions

This study provides crucial insights into paleoenvironmental changes in the Ross Sea continental margin over the past 800 ka, revealing the complex interplay between ice-sheet dynamics, ocean circulation, and sedimentary processes. Our multiproxy approach enhances our understanding of glacial-interglacial transitions and their environmental implications near the Antarctica continental margin. During the late Mid-Pleistocene Transition (750–550 ka), intensified glacial conditions led to ice-sheet advances onto the shelf, driving strong sediment redistribution through grounding-line fluctuations, meltwater pulses, and slope instability (Fig. 5c). Concurrently, a strengthened Antarctic Slope Current restricted Circumpolar Deep Water influx, reinforcing cold conditions. Following this period, a prolonged relatively warmer climatic phase persisted until MIS 8, characterized by relative ice-sheet stability, sustained open-water conditions, and enhanced nutrient availability (Fig. 5b). This phase likely contributed to the destabilization of the WAIS. The late Pleistocene was marked by pronounced glacial-interglacial variability, with alternating ice-sheet expansion and retreat shaping sedimentation patterns (Fig. 5a). Glacial periods saw extensive iceberg calving and ice-rafted debris deposition, accompanied by intensified bottom currents that reshaped the seafloor and influenced sediment transport. In contrast, interglacial periods were characterized by reduced ice-sheet extent, increased open-water conditions, and greater oceanographic influence. Ice-front polynyas, enhanced meltwater discharge, and improved nutrient availability during the interglacials likely supported transient phases of higher primary productivity. Post-MIS 11, interglacial warming resulted in larger glacial ice masses and smaller interglacial ice volumes, amplifying ice-sheet variability and influencing sedimentation and bottom-water circulation. Persistent dense shelf water cascades played a key role in maintaining canyon and trough morphology, preventing widespread sediment infill while modulating seafloor sediment distribution.

This study enhances our understanding of Antarctic ice-sheet dynamics and oceanographic processes over the past 800 ka, emphasizing the need for integrating organic geochemical parameters with sedimentological and isotopic proxies for accurate paleoenvironmental interpretations. For instance, our findings show that increased TOC at the base of the studied section resulted from sediment reworking during glacial advances rather than heightened primary productivity. Overall, we demonstrate that paleoenvironmental changes in the Ross Sea were closely tied to global climatic events, with ice-sheet fluctuations and oceanographic shifts exerting a dominant influence on sedimentation and productivity patterns. Moreover, the correlation between MS and (10Be/9Be)reac serves as a valuable proxy for tracking ice sheet advance and retreat, offering significant insights into glacial-interglacial dynamics. Future research should expand core analyses, incorporate biomarker-based reconstructions, and utilize numerical modeling to refine ice-sheet responses to past climate

KOPRI 극지연구소

fluctuations.

KOPRI
극지연구소

로스해 대륙 가장자리에서의 중기-후기 플라이스토세 퇴적 환경: 남극 빙상 역학에 대한 시사점

Chinmay Dash[1], 성영배[1], Ajay Kumar Singh[2], 이민경[3], 유규철[3], 이현희[4], 유병용[5]

[1]고려대학교, [2]Independent Researcher, Samastipur, Bihar, India, [3]극지연구소, [4]공주대학교, [5]한국과학기술연구원

요약: 본 연구는 지난 80만 년 동안의 빙상 역학과 고퇴적 환경을 복원하기 위해 로스해 대륙 사면에서 채취한 퇴적물 코어(RS15-LC47)를 분석하였다. 본 연구에서는 전코어 자기감수율, 총유기탄소, 탄산칼슘, 생물기원 실리카, 퇴적학적 특징, 그리고 자생 베릴륨의 동위원소 비율((^{10}Be/^{9}Be)$_{reac}$)을 통합한 다중 지표 분석 방법을 적용하였다. 750-550 ka 구간은 빙상이 확장되고 저층 해류가 강화되며 해양 생산성이 감소한 강화된 빙기 단계로 해석된다. 슬럼프 퇴적물이 간헐적으로 포함된 콘투라이트퇴적물이 우세하게 나타나는 점은, 강화된 저층 해류에 의해 매우 역동적이고 불안정한 조건에서 퇴적이 이루어졌음을 시사한다. 또한 분급이 불량한 퇴적물과 밀리미터 규모의 단층 구조는 빙상 전진에 의해 유발된 중력류 퇴적을 지시한다. 이 구간에서 낮은 (^{10}Be/^{9}Be)$_{reac}$ 비율은 개방 해양 환경에서의 스캐빈징이 제한적이었음을 의미하며, 이는 빙상이 대륙붕 가장자리까지 확장됨에 따라 퇴적물이 시추 지점까지 이동하는 시간이 단축되었기 때문으로 해석된다. 비록 TOC 값은 이 구간에서 가장 높게 나타나지만, 높은 TOC/TN 비율과 낮은 초과 바륨값은 로스해의 강한 빙기 조건하에서 빙상 전진에 따른 육상 기원 물질 유입 증가와 해양 생산성 감소를 시사한다. 중기 플라이스토세 전이기 이후인 550-250 ka 구간에서는 MS 값이 전반적으로 낮게 유지되는 반면, (^{10}Be/^{9}Be)$_{reac}$ 비율은 현저히 높게 나타나 상대적으로 온난하고 빙상 영향이 약화된 환경을 지시한다. 이 시기의 TOC/TN 비율은 로스해 유광층에서 관측되는 값과 유사하며, 상대적으로 높은 Baex와 TOC 값은 550-250 ka 동안 비교적 온난한 기후 조건하에서 해양 생산성이 증가했음을 보여준다. 후기 플라이스토세(>250 ka) 동안에는 퇴적 환경이 빙기-간빙기 주기에 더욱 강하게 지배되었으며, 간빙기의 온난한 조건이 생산성 증가를 유도하였다. 이 시기에는 조립질 입자의 증가는 강화된 저층 해류를 지시하며, (^{10}Be/^{9}Be)$_{reac}$ 비율의 급격한 증가는 빙상 후퇴와 연관된 간빙기 조건을 반영한다. 온난한 시기 동안 아빙하 지역에서 퇴적 지점까지의 이동 시간이 길어지면서 개방 해양 환경에서 베릴륨 동위원소의 스캐빈징이 증가하였고, 그 결과 (^{10}Be/^{9}Be)$_{reac}$ 값이 높아진 것으로 해석된다. 간빙기 동안 OpalMAR, TOC%, 그리고 (^{10}Be/^{9}Be)$_{reac}$ 간의 양의 상관관계는 해양 생산성 증가가 온난한 기후 단계와 직접적으로 연관되어 있음을 보여준다. 본 연구 결과는 빙상의 확장과 후퇴가 이 지역의 퇴적 과정과 퇴적 환경을 지배하는 핵심 요인임을 강조한다.

KOPRI 극지연구소

참고 문헌

Al'bot, O., 2016. Pleistocene Cyclostratigraphy on the Continental Rise and Abyssal Plain of the Western Ross Sea, Antarctica. Open Access. Victoria University of Wellington, Te Herenga Waka. https://doi.org/10.26686/wgtn.17061797.v1.

Anderson, J.B., Conway, H., Bart, P.J., Witus, A.E., Greenwood, S.L., McKay, R.M., Hall, B.L., Ackert, R.P., Licht, K., Jakobsson, M., Stone, J.O., 2014. Ross Sea paleo-ice sheet drainage and deglacial history during and since the LGM. Quat. Sci. Rev. 100, 31-54.

Anderson, J.B., Simkins, L.M., Bart, P.J., De Santis, L., Halberstadt, A.R.W., Olivo, E., Greenwood, S.L., 2019. Seismic and geomorphic records of Antarctic Ice Sheet evolution in the Ross Sea and controlling factors in its behaviour. Geol. Soc. Lond., Spec. Publ. 475, 223-240.

Baroni, M., Bard, E., Petit, J.R., Magand, O., Bourles, D., 2011. Volcanic and solar activity, and atmospheric circulation influences on cosmogenic 10Be fallout at Vostok and Concordia (Antarctica) over the last 60 years. Eochim. Cosmochim. Acta. 75, 7132-7145.

Bart, P.J., Owolana, B., 2012. On the duration of West Antarctic Ice Sheet grounding events in Ross Sea during the Quaternary. Quat. Sci. Rev. 47, 101-115.

Barth, A.M., Clark, P.U., Bill, N.S., He, F., Pisias, N.G., 2018. Climate evolution across the Mid-Brunhes transition. Clim. Past 14, 2071-2087.

Behrens, B., Miyairi, Y., Sproson, A.D., Yamane, M., Yokoyama, Y., 2019. Meltwater discharge during the Holocene from the Wilkes subglacial basin revealed by beryllium isotope analysis of marine sediments. J. Quat. Sci. 34, 603-608.

Behrens, B.C., Yokoyama, Y., Miyairi, Y., Sproson, A.D., Yamane, M., Jimenez-Espejo, F. J., McKay, R.M., Johnson, K.M., Escutia, C., Dunbar, R.B., 2022. Beryllium isotope variations recorded in the Ad´elie Basin, East Antarctica reflect Holocene changes in ice dynamics, productivity, and scavenging efficiency. Quat. Sci. Adv. 7, 100054.

Bollen, M., Riesselman, C.R., Ohneiser, C., Albot, O., McKay, R., Lee, M.K., Yoo, K.-C., Kim, S., Lee, J. Il, Levy, R., 2022. Pleistocene oceanographic variability in the Ross Sea: a multiproxy approach to age model development and paleoenvironmental analyses. Glob. Planet. Chang. 216, 103901.

Bol'Shakov, V.A., 2015. On the mechanism of the Middle Pleistocene transition. Stratigr. Geol. Correl. 23, 536-550.

Bonn, W.J., Gingele, F.X., Grobe, H., Mackensen, A., Fütterer, D.K., 1998. Palaeoproductivity at the Antarctic continental margin: opal and barium records for the last 400 ka. Palaeogeogr. Palaeoclimatol. Palaeoecol. 139, 195-211.

Brachfeld, S.A., 2006. High-field magnetic susceptibility (χHF) as a proxy of biogenic sedimentation along the Antarctic Peninsula. Phys. Earth Planet. Inter. 156, 274-282.

Charles, C.D., Froelich, P.N., Zibello, M.A., Mortlock, R.A., Morley, J.J., 1991. Biogenic opal in Southern Ocean sediments over the last 450,000 years: Implications for surface water

chemistry and circulation. Paleoceanography 6, 697-728.

Chow, J.M., Bart, P.J., 2003. West Antarctic Ice Sheet grounding events on the Ross Sea outer continental shelf during the middle Miocene. Palaeogeogr. Palaeoclimatol. Palaeoecol. 198, 169-186.

Clark, P.U., Archer, D., Pollard, D., Blum, J.D., Rial, J.A., Brovkin, V., Mix, A.C., Pisias, N. G., Roy, M., 2006. The middle Pleistocene transition: characteristics, mechanisms, and implications for long-term changes in atmospheric pCO2. Quat. Sci. Rev. 25, 3150-3184.

Conte, R., Rebesco, M., De Santis, L., Colleoni, F., Bensi, M., Bergamasco, A., Kovacevic, V., Gales, J., Zgur, F., Accettella, D., 2021. Bottom current control on sediment deposition between the Iselin Bank and the Hillary Canyon (Antarctica) since the late Miocene: an integrated seismic-oceanographic approach. Deep Sea Res. Part I Oceanogr. Res. Pap. 176, 103606.

Daruka, I., Ditlevsen, P.D., 2016. A conceptual model for glacial cycles and the middle Pleistocene transition. Clim. Dyn. 46, 29-40.

Dash, C., Lee, M.K., Seong, Y.B., Rhee, H.H., Lee, J. Il, Yoo, K.-C., 2021. 10Be and 10Be/9Be in glaciomarine sediments of Ross Sea, Antarctica: implications for mid-late Quaternary paleoenvironmental changes. J. Geol. Soc. Korea 57, 691-705.

DeMaster, D.J., 1981. The supply and accumulation of silica in the marine environment. Geochim. Cosmochim. Acta 45, 1715-1732.

DeMaster, D.J., Dunbar, R.B., Gordon, L.I., Leventer, A.R., Morrison, J.M., Nelson, D.M., Nittrouer, C.A., Smith, W.O., 1992. Cycling and accumulation of biogenic silica and organic matter in high-latitude environments: the Ross Sea. Oceanography 5, 146-153.

Diekmann, B., Kuhn, G., Rachold, V., Abelmann, A., Brathauer, U., Fütterer, D.K., Gersonde, R., Grobe, H., 2000. Terrigenous sediment supply in the Scotia Sea (Southern Ocean): response to late Quaternary ice dynamics in Patagonia and on the Antarctic Peninsula. Palaeogeogr. Palaeoclimatol. Palaeoecol. 162, 357-387.

Dinniman, M.S., Klinck, J.M., Smith Jr., W.O., 2011. A model study of Circumpolar Deep Water on the West Antarctic Peninsula and Ross Sea continental shelves. Deep-Sea Res. II Top. Stud. Oceanogr. 58, 1508-1523.

Drewry, D.J., Cooper, A.P.R., 1981. Processes and models of Antarctic glaciomarine sedimentation. Ann. Glaciol. 2, 117-122.

Dymond, J., Suess, E., Lyle, M., 1992. Barium in deep-sea sediment: a geochemical proxy for paleoproductivity. Paleoceanography 7, 163-181.

Emerson, S.R., Archer, D., 1990. Calcium carbonate preservation in the ocean. Philos. Trans. R. Soc. London. Ser. A, Math. Phys. Sci. 331, 29-40.

Fabiano, M., Povero, P., Danovaro, R., 1993. Distribution and composition of particulate organic matter in the Ross Sea (Antarctica). Polar Biol. 13, 525-533.

Faug`eres, J.-C., Mulder, T., 2011. Contour currents and contourite drifts. In: Developments in

sedimentology, 63. Elsevier, pp. 149-214.

Faug`eres, J.C., M´ezerais, M.L., Stow, D.A.V., 1993. Contourite drift types and their distribution in the North and South Atlantic Ocean basins. Sediment. Geol. 82, 189-203.

Folk, R.L., Ward, W.C., 1957. Brazos River bar [Texas]: a study in the significance of grain size parameters. J. Sediment. Res. 27, 3-26.

Ford, H.L., Sosdian, S.M., Rosenthal, Y., Raymo, M.E., 2016. Gradual and abrupt changes during the Mid-Pleistocene transition. Quat. Sci. Rev. 148, 222-233.

Frank, T.D., James, N.P., Bone, Y., Malcolm, I., Bobak, L.E., 2014. Late Quaternary carbonate deposition at the bottom of the world. Sediment. Geol. 305, 1-16.

Gales, J., Rebesco, M., De Santis, L., Bergamasco, A., Colleoni, F., Kim, S., Accettella, D., Kovacevic, V., Liu, Y., Olivo, E., Colizza, E., 2021. Role of dense shelf water in the development of Antarctic submarine canyon morphology. Geomorph 372, 107453.

Gordon, A.L., Zambianchi, E., Orsi, A., Visbeck, M., Giulivi, C.F., Whitworth III, T., Spezie, G., 2004. Energetic plumes over the Western Ross Sea continental slope. Geophys. Res. Lett. 31.

Gordon, A.L., Orsi, A.H., Muench, R., Huber, B.A., Zambianchi, E., Visbeck, M., 2009. Western Ross Sea continental slope gravity currents. Deep-Sea Res. II Top. Stud. Oceanogr. 56, 796-817.

Green, R.A., Menviel, L., Meissner, K.J., Crosta, X., Chandan, D., Lohmann, G., Peltier, W. R., Shi, X., Zhu, J., 2022. Evaluating seasonal sea-ice cover over the Southern Ocean at the last Glacial Maximum. Clim. Past 18, 845-862.

Grützner, J., Hillenbrand, C.-D., Rebesco, M., 2005. Terrigenous flux and biogenic silica deposition at the Antarctic continental rise during the late Miocene to early Pliocene: implications for ice sheet stability and sea ice coverage. Glob. Planet. Chang. 45, 131-149.

Halberstadt, A.R.W., Simkins, L.M., Greenwood, S.L., Anderson, J.B., 2016. Past ice-sheet behaviour: retreat scenarios and changing controls in the Ross Sea, Antarctica. Cryosphere 10, 1003-1020.

Hammer, O., Harper, D.A.T., Ryan, P.D., 2001. Palaeontological statistics software package for education and data analysis. Palaeontol. Electron. 4.

Hauck, J., Gerdes, D., Hillenbrand, C.D., Hoppema, M., Kuhn, G., Nehrke, G., V¨olker, C., Wolf-Gladrow, D.A., 2012. Distribution and mineralogy of carbonate sediments on Antarctic shelves. J. Mar. Syst. 90 (77-87), 2012.

Hearty, P.J., Kindler, P., Cheng, H., Edwards, R.L., 1999. A+20 m middle Pleistocene Sea-level highstand (Bermuda and the Bahamas) due to partial collapse of Antarctic ice. Geology 27, 375-378.

Herbert, T.D., 2023. The mid-Pleistocene climate transition. Annu. Rev. Earth Planet. Sci. 51, 389-418.

Hesse, R., Khodabakhsh, S., Klaucke, I., Ryan, W.B.F., 1997. Asymmetrical turbid

surface-plume deposition near ice-outlets of the Pleistocene Laurentide ice sheet in the Labrador Sea. Geo-Marine Lett. 17, 179-187.

Hesse, R., Klauck, I., Khodabakhsh, S., Piper, D., 1999. Continental slope sedimentation adjacent to an ice margin. III. The upper Labrador Slope. Mar. Geol. 155, 249-276.

Hillenbrand, C.-D., Ehrmann, W., 2005. Late Neogene to Quaternary environmental changes in the Antarctic Peninsula region: evidence from drift sediments. Glob. Planet. Chang. 45, 165-191.

Hillenbrand, C.-D., Fütterer, D., 2001. Neogene to Quaternary deposition of opal on the continental rise west of the Antarctic Peninsula, ODP Leg 178, Sites 1095, 1096, and 1101, in: Barker, PF, Camerlenghi, A., Acton, GD, and Ramsay, ATS (Eds.), Proc. ODP, Sci. Results, 178 [Online]. Available from World Wide Web: http://www-odp.tamu.edu/publications/178_SR/VOLUME/CHAPTERS/SR178_23. PDF, vol. 1.

Hillenbrand, C.-D., Kuhn, G., Frederichs, T., 2009. Record of a Mid-Pleistocene depositional anomaly in West Antarctic continental margin sediments: an indicator for ice-sheet collapse? Quat. Sci. Rev. 28, 1147-1159.

Holden, P.B., Edwards, N.R., Wolff, E.W., Lang, N.J., Singarayer, J.S., Valdes, P.J., Stocker, T.F., 2010. Interhemispheric coupling, the West Antarctic ice sheet and warm Antarctic interglacials. Clim. Past 6, 431-443.

Holden, P.B., Edwards, N.R., Wolff, E.W., Valdes, P.J., Singarayer, J.S., 2011. The Mid- Brunhes event and West Antarctic ice sheet stability. J. Quat. Sci. 26, 474-477.

C. Dash et al. P a l a e o g e o g r a p h y , P a l a e o c l i m a t o l o g y , P a l a e o e c o l o g y 680 (2025) 113355

KOPRI 극지연구소

Howe, J.A., Pudsey, C.J., 1999. Antarctic circumpolar deep water; a Quaternary paleoflow record from the northern Scotia Sea, South Atlantic Ocean. J. Sediment. Res. 69, 847-861.

Howe, J.A., Pudsey, C.J., Cunningham, A.P., 1997. Pliocene-Holocene contourite deposition under the Antarctic circumpolar current, western Falkland trough, South Atlantic Ocean. Mar. Geol. 138, 27-50.

Jacobs, S.S., Amos, A.F., Bruchhausen, P.M., 1970 December. Ross Sea oceanography and Antarctic bottom water formation. In: Deep Sea Research and Oceanographic Abstracts, 17. Elsevier, pp. 935-962. No. 6.

Jacobs, S.S., Giulivi, C.F., Mele, P.A., 2002. Freshening of the Ross Sea during the late 20th century. Science 297, 386-389.

Jeong, A., Lee, J.I., Seong, Y.B., Balco, G., Yoo, K.C., Yoon, H.I., Domack, E., Rhee, H.H., Yu, B.Y., 2018. Late Quaternary deglacial history across the Larsen B embayment, Antarctica. Quat. Sci. Rev. 189, 134-148.

Jouzel, J., Masson-Delmotte, V., Cattani, O., Dreyfus, G., Falourd, S., Hoffmann, G., Minster, B., Nouet, J., Barnola, J.M., Chappellaz, J., Fischer, H., 2007. Orbital and millennial Antarctic climate variability over the past 800,000 years. Science 317, 793-796.

Kemp, A.E.S., Grigorov, I., Pearce, R.B., Garabato, A.C.N., 2010. Migration of the Antarctic Polar Front through the mid-Pleistocene transition: evidence and climatic implications. Quat. Sci. Rev. 29, 1993-2009.

Kennett, J.P., 1968. Latitudinal variation in Globigerina pachyderma (Ehrenberg) in surface sediments of the Southwest Pacific Ocean. Micropaleontology 305-318.

Kim, B.K., Lee, S., Ha, S., Jung, J., Kim, T.W., Yang, E.J., Jo, N., Lim, Y.J., Park, J., Lee, S. H., 2018a. Vertical distributions of macromolecular composition of particulate organic matter in the water column of the Amundsen Sea Polynya during the summer in 2014. J. Geophys. Res. Ocean. 123, 1393-1405.

Kim, S., Yoo, K.-C., Lee, J. Il, Khim, B.-K., Bak, Y.-S., Lee, M.K., Lee, J., Domack, E.W., Christ, A.J., Yoon, H.Il., 2018b. Holocene paleoceanography of Bigo Bay, West Antarctic Peninsula: Connections between surface water productivity and nutrient utilization and its implication for surface-deep water mass exchange. Quat. Sci. Rev. 192, 59-70.

Kim, S., Lee, J. Il, McKay, R.M., Yoo, K.-C., Bak, Y.-S., Lee, M.K., Roh, Y.H., Yoon, H. Il, Moon, H.S., Hyun, C.-U., 2020. Late pleistocene paleoceanographic changes in the Ross Sea-Glacial-interglacial variations in paleoproductivity, nutrient utilization, and deep-water formation. Quat. Sci. Rev. 239, 106356.

Kim, S., Lee, M.K., Shin, J.Y., Yoo, K.C., Lee, J.I., Kang, M.I., Moon, H.S., Prebble, J.G., 2022. Variation in magnetic susceptibility in the Bellingshausen Sea continental rise since the last glacial period and implications for terrigenous material input mechanisms. Palaeogeogr. Palaeoclimatol. Palaeoecol. 594, 110948.

Kindler, P., Hearty, P.J., 2000. Elevated marine terraces from Eleuthera (Bahamas) and Bermuda: sedimentological, petrographic and geochronological evidence for important deglaciation events during the middle Pleistocene. Glob. Planet. Chang. 24, 41-58.

Kim, S., Seong, Y.B., Rhee, H.-H., Khandsuren, P., Yu, B.Y., Eliades, E., 2024. Cosmogenic 10Be research: standard reference materials and blank analysis. Journal of the Korean Earth Science Society 45 (6), 624-636. https://doi.org/10.5467/JKESS.2024.45.6.624.

King, M.V., Gales, J.A., Laberg, J.S., McKay, R.M., De Santis, L., Kulhanek, D.K., Hosegood, P.J., Morris, A., Expedition, I., 2022. Pleistocene depositional environments and links to cryosphere-ocean interactions on the eastern Ross Sea continental slope, Antarctica (IODP Hole U1525A). Mar. Geol. 443, 106674.

Koenitz, D., White, N., McCave, I.N., Hobbs, R., 2008. Internal structure of a contourite drift generated by the antarctic circumpolar current. Geochem. Geophys. Geosyst. 9.

Konfirst, M.A., Scherer, R.P., Hillenbrand, C.-D., Kuhn, G., 2012. A marine diatom record from the Amundsen Sea—Insights into oceanographic and climatic response to the Mid-Pleistocene transition in the West Antarctic sector of the Southern Ocean. Mar. Micropaleontol. 92, 40-51.

Kotov, S., P¨alike, H., 2018. QAnalySeries - a Cross-Platform Time Series Tuning and Analysis

Tool. AGU Fall meeting. https://agu.confex.com/agu/fm18/meetingapp.cgi/Paper/349843.

Krissek, L., Browne, G., Carter, L., Cowan, E.A., Dunbar, G., McKay, R., Naish, T., Powell, R.D., Reed, J., Wilch, T., 2007. ANDRILL-MIS Science Team. Sedimentology and Stratigraphy of the AND-1B Core, ANDRILL McMurdo Ice Shelf Project, Antarctica, 14. ANDRILL Research and Publications, Terra Antartica, pp. 185-222.

Lamy, F., Winckler, G., Arz, H.W., Farmer, J.R., Gottschalk, J., Lembke-Jene, L., Middleton, J.L., Van der Does, M., Tiedemann, R., Alvarez Zarikian, C., 2024. Five million years of Antarctic Circumpolar current strength variability. Nature 627, 789-796.

Larter, R.D., Barker, P.F., 1989. Seismic stratigraphy of the Antarctic Peninsula Pacific margin: a record of Pliocene-Pleistocene ice volume and paleoclimate. Geology 17, 731-734.

Lee, S.Y., Seong, Y.B., Shin, Y.K., Choi, K.H., Kang, H.C., Choi, J.H., 2011. Cosmogenic 10 be and OSL dating of fluvial strath terraces along the Osip-cheon River, Korea: tectonic implications. Geosci. J. 15, 359-378.

Li, Y., Zhang, H., Tu, C., Fu, C., Xue, Y., Luo, Y., 2016. Sources and fate of organic carbon and nitrogen from land to ocean: Identified by coupling stable isotopes with C/N ratio. Estuar. Coast. Shelf Sci. 181, 114-122.

Lisiecki, L.E., Raymo, M.E., 2005. A Pliocene-Pleistocene stack of 57 globally distributed benthic δ18O records. Paleoceanography 20.

Lucchi, R.G., Rebesco, M., Camerlenghi, A., Busetti, M., Tomadin, L., Villa, G., Persico, D., Morigi, C., Bonci, M.C., Giorgetti, G., 2002. Mid-late Pleistocene glacimarine sedimentary processes of a high-latitude, deep-sea sediment drift (Antarctic Peninsula Pacific margin). Mar. Geol. 189, 343-370.

Masson-Delmotte, V., Stenni, B., Pol, K., Braconnot, P., Cattani, O., Falourd, S., Kageyama, M., Jouzel, J., Landais, A., Minster, B., Barnola, J.M., 2010. EPICA Dome C record of glacial and interglacial intensities. Quat. Sci. Rev. 29, 113-128.

McCave, I.N., Lonsdale, P.F., Hollister, C.D., Gardner, W.D., 1980. Sediment transport over the Hatton and Gardar contourite drifts. J. Sediment. Res. 50, 1049-1062.

McClymont, E.L., Sosdian, S.M., Rosell-Mel´e, A., Rosenthal, Y., 2013. Pleistocene Sea- surface temperature evolution: early cooling, delayed glacial intensification, and implications for the mid-Pleistocene climate transition. Earth-Sci. Rev. 123, 173-193.

McKay, R., Naish, T., Powell, R., Barrett, P., Scherer, R., Talarico, F., Kyle, P., Monien, D., Kuhn, G., Jackolski, C., 2012. Pleistocene variability of Antarctic ice sheet extent in the Ross embayment. Quat. Sci. Rev. 34, 93-112.

McKay, R.M., De Santis, L., Kulhanek, D.K., 2019. Ross Sea West Antarctic Ice Sheet History. Proc. Int. Ocean Discov. Progr, p. 374.

McManus, J., Berelson, W.M., Klinkhammer, G.P., Johnson, K.S., Coale, K.H., Anderson, R.F., Kumar, N., Burdige, D.J., Hammond, D.E., Brumsack, H.J., McCorkle, D.C., 1998. Geochemistry of barium in marine sediments: Implications for its use as a

paleoproxy. Geochim. Cosmochim. Acta 62, 3453-3473.

McManus, J., Berelson, W.M., Klinkhammer, G.P., Hammond, D.E., Holm, C., 2005. Authigenic uranium: relationship to oxygen penetration depth and organic carbon rain. Geochim. Cosmochim. Acta 69, 95-108.

Mead, G.A., Tauxe, L., LaBrecque, J.L., 1986. Oligocene paleoceanography of the South Atlantic: paleoclimatic implications of sediment accumulation rates and magnetic susceptibility measurements. Paleoceanography 1, 273-284.

M´enabr´eaz, L., Bourl`es, D.L., Thouveny, N., 2012. Amplitude and timing of the Laschamp geomagnetic dipole low from the global atmospheric 10Be overproduction: Contribution of authigenic 10Be/9Be ratios in west equatorial Pacific sediments. J. Geophys. Res. Solid Earth 117 (B11).

M´enabr´eaz, L., Thouveny, N., Bourl`es, D.L., Vidal, L., 2014. The geomagnetic dipole moment variation between 250 and 800 ka BP reconstructed from the authigenic 10Be/9Be signature in West Equatorial Pacific sediments. Earth Planet. Sci. Lett. 385, 190-205.

Millero, F.J., Feistel, R., Wright, D.G., McDougall, T.J., 2008. The composition of Standard Seawater and the definition of the Reference-Composition Salinity Scale. Deep-Sea Res. I Oceanogr. Res. Pap. 55, 50-72.

Morrison, A.K., Hogg, A.M., England, M.H., Spence, P., 2020. Warm Circumpolar Deep Water transport toward Antarctica driven by local dense water export in canyons. Sci. Adv. 6, eaav2516.

Mortlock, R.A., Froelich, P.N., 1989. A simple method for the rapid determination of biogenic opal in pelagic marine sediments. Deep Sea Res. Part A. Oceanograph. Res. Pap. 36, 1415-1426.

Naish, T., Powell, R., Levy, R., Wilson, G., Scherer, R., Talarico, F., Krissek, L., Niessen, F., Pompilio, M., Wilson, T., 2009. Obliquity-paced Pliocene West Antarctic ice sheet oscillations. Nature 458, 322-328.

Nishimura, A., Nakasone, T., Hiramatsu, C., Tanahashi, M., 1998. Late Quaternary paleoenvironment of the Ross Sea continental shelf, Antarctica. Ann. Glaciol. 27, 275-280.

Ohneiser, C., Yoo, K.C., Albot, O.B., Cortese, G., Riesselman, C., Lee, J.I., McKay, R., Bollen, M., Lee, M.K., Moon, H.S., Kim, S., 2019. Magneto-biostratigraphic age models for Pleistocene sedimentary records from the Ross Sea. Glob. Planet. Chang. 176, 36-49.

Ohneiser, C., Hulbe, C.L., Beltran, C., Riesselman, C.R., Moy, C.M., Condon, D.B., Worthington, R.A., 2023. West Antarctic ice volume variability paced by obliquity until 400,000 years ago. Nat. Geosci. 16, 44-49.

Orsi, A.H., Wiederwohl, C.L., 2009. A recount of Ross Sea waters. Deep-Sea Res. II Top. Stud. Oceanogr. 56, 778-795.

Orsi, A.H., Smethie Jr., W.M., Bullister, J.L., 2002. On the total input of Antarctic waters to the deep ocean: a preliminary estimate from chlorofluorocarbon measurements. J. Geophys. Res. Ocean. 107, 31.

KOPRI 극지연구소

Pattyn, F., Morlighem, M., 2020. The uncertain future of the Antarctic Ice Sheet. Science 367, 1331-1335.

Petit, J.R., Jouzel, J., Raynaud, D., Barkov, N.I., Barnola, J.M., Basile, I., Bender, M., Chappellaz, J., Davis, M., Delaygue, G., Delmotte, M., 1999. Climate and atmospheric history of the past 420,000 years from the Vostok ice core, Antarctica. Nature 399, 429-436.

Pirrung, M., Hillenbrand, C., Diekmann, B., Fütterer, D., Grobe, H., Kuhn, G., 2002. Magnetic susceptibility and ice-rafted debris in surface sediments of the Atlantic sector of the Southern Ocean. Geo-Marine Lett. 22, 170-180.

Pollard, D., DeConto, R.M., 2009. Modelling West Antarctic ice sheet growth and collapse through the past five million years. Nature 458, 329-332.

Raisbeck, G.M., Yiou, F., Jouzel, J., Stocker, T.F., 2007. Direct north-south synchronization of abrupt climate change record in ice cores using Beryllium 10. Clim. Past 3, 541-547.

Raymo, M.E., Lisiecki, L.E., Nisancioglu, K.H., 2006. Plio-Pleistocene ice volume, Antarctic climate, and the global δ18O record. Science 313, 492-495.

Rhee, H.H., Seong, Y.B., Jeon, Y.G., Yu, B.Y., 2017. Bouldery slope landforms on Mt. Biseul, Korea, and implications for paleoclimate and slope evolution. Quat. Res. 88, 293-312.

Rhee, H.H., Seong, Y.B., Lee, M.K., Jeong, A., Dash, C., Lee, J. Il, Yoo, K.-C., Yu, B.Y., 2022. Spatial variations of authigenic beryllium isotopes in surface sediments of the Antarctic oceans: a proxy for sea ice dynamics and sedimentary environments. Geosci. J. 26, 455-467.

Rickaby, R.E.M., Elderfield, H., Roberts, N., Hillenbrand, C., Mackensen, A., 2010. Evidence for elevated alkalinity in the glacial Southern Ocean. Paleoceanography

Robinson, S.G., Maslin, M.A., McCave, I.N., 1995. Magnetic susceptibility variations in Upper Pleistocene deep-sea sediments of the NE Atlantic: Implications for ice rafting and paleocirculation at the last glacial maximum. Paleoceanography 10, 221-250.

Rodrigues, S., Hern´andez-Molina, F.J., Hillenbrand, C., Lucchi, R.G., Rodríguez-Tovar, F. J., Rebesco, M., Larter, R.D., 2022. Recognizing key sedimentary facies and their distribution in mixed turbidite-contourite depositional systems: the case of the Pacific margin of the Antarctic Peninsula. Sedimentology 69, 1953-1991.

Sagnotti, L., Macri, P., Camerlenghi, A., Rebesco, M., 2001. Environmental magnetism of Antarctic late Pleistocene sediments and interhemispheric correlation of climatic events. Earth Planet. Sci. Lett. 192, 65-80.

Sarmiento, J.L., 2006. Ocean Biogeochemical Dynamics. Princeton university press.

Scherer, R.P., Aldahan, A., Tulaczyk, S., Possnert, G., Engelhardt, H., Kamb, B., 1998. Pleistocene collapse of the West Antarctic ice sheet. Science 281, 82-85.

Schulz, M., Mudelsee, M., 2002. REDFIT: estimating red-noise spectra directly from unevenly spaced paleoclimatic time series. Comput. Geosci. 28, 421-426.

Shimmield, G., Derrick, S., Mackensen, A., Grobe, H., Pudsey, C., 1994. The history of barium, biogenic silica and organic carbon accumulation in the Weddell Sea and Antarctic Ocean over the last 150,000 years. In: Carbon Cycling in the Glacial Ocean:

Constraints on the Ocean's Role in Global Change: Quantitative Approaches in Paleoceanography, pp. 555-574.

Silvano, A., Foppert, A., Rintoul, S.R., Holland, P.R., Tamura, T., Kimura, N., Castagno, P., Falco, P., Budillon, G., Haumann, F.A., 2020. Recent recovery of Antarctic Bottom Water formation in the Ross Sea driven by climate anomalies. Nat. Geosci. 13, 780-786.

Simon, Q., Thouveny, N., Bourles, D.L., Nuttin, L., Hillaire-Marcel, C., St-Onge, G., 2016. Authigenic 10Be/9Be ratios and 10Be-fluxes (230Thxs-normalized) in central Baffin Bay sediments during the last glacial cycle: Paleoenvironmental implications. Quat. Sci. Rev. 140, 142-162.

Simon, Q., Bourl`es, D.L., Bassinot, F., Nomade, S., Marino, M., Ciaranfi, N., Girone, A., Maiorano, P., Thouveny, N., Choy, S., Dewilde, F., 2017. Authigenic 10Be/9Be ratio signature of the Matuyama-Brunhes boundary in the Montalbano Jonico marine succession. Earth Planet. Sci. Lett. 460, 255-267.

Sjunneskog, C., Scherer, R., Aldahan, A., Possnert, G., 2007. 10Be in glacial marine sediment of the Ross Sea, Antarctica, a potential tracer of depositional environment and sediment chronology. Nucl. Instruments Methods Phys. Res. Sect. B Beam Interact. with Mater. Atoms 259, 576-583.

Smith Jr., W.O., Sedwick, P.N., Arrigo, K.R., Ainley, D.G., Orsi, A.H., 2012. The Ross Sea in a sea of change. Oceanography 25, 90-103.

Smith, A.M., Murray, T., Nicholls, K.W., Makinson, K., A˜oalgeirsd´ottir, G., Behar, A.E., Vaughan, D.G., 2007. Rapid Erosion, drumlin formation, and changing hydrology beneath an Antarctic ice stream. Geology 35, 127-130.

Sproson, A.D., Takano, Y., Miyairi, Y., Aze, T., Matsuzaki, H., Ohkouchi, N., Yokoyama, Y., 2021. Beryllium isotopes in sediments from Lake Maruwan Oike and Lake Skallen, East Antarctica, reveal substantial glacial discharge during the late Holocene. Quat. Sci. Rev. 256, 106841.

Sproson, A.D., Yokoyama, Y., Miyairi, Y., Aze, T., Totten, R.L., 2022. Holocene melting of the West Antarctic Ice Sheet driven by tropical Pacific warming. Nat. Commun. 13, 2434.

Sproson, A.D., Yokoyama, Y., Miyairi, Y., Aze, T., Clementi, V.J., Riechelson, H., Bova, S. C., Rosenthal, Y., Childress, L.B., 2024. Near-synchronous Northern Hemisphere and Patagonian Ice Sheet variation over the last glacial cycle. Nat. Geosci. 17, 450-457.

Steig, E.J., Ding, Q., Battisti, D.S., Jenkins, A., 2012. Tropical forcing of Circumpolar Deep Water inflow and outlet glacier thinning in the Amundsen Sea Embayment. West Antarctica. Ann. Glaciol. 53, 19-28.

Steiner, Z., Sarkar, A., Liu, X., Berelson, W.M., Adkins, J.F., Achterberg, E.P., Sabu, P., Prakash, S., Vinaychandran, P.N., Byrne, R.H., 2021. On calcium-to-alkalinity anomalies in the North Pacific, Red Sea, Indian Ocean and Southern Ocean. Geochim. Cosmochim. Acta 303, 1-14.

Sutter, J., Fischer, H., Grosfeld, K., Karlsson, N.B., Kleiner, T., Van Liefferinge, B., Eisen, O.,

2019. Modelling the Antarctic Ice Sheet across the mid-Pleistocene transition-implications for Oldest Ice. Cryosphere 13, 2023-2041.

Taviani, M., Claps, M., 1998. Biogenic Quaternary carbonates in the CRP-1 drillhole, Victoria Land basin, Antarctica. Terra Antart. 5, 411-418.

Taviani, M., Reid, D.E., Anderson, J.B., 1993. Skeletal and isotopic composition and paleoclimatic significance of late Pleistocene carbonates, Ross Sea, Antarctica. J. Sediment. Res. 63, 84-90.

Taylor, S.R., McLennan, S.M., 1985. The Continental Crust: Its Composition and Evolution. Blackwell, Malden, Mass.

Thi´eblemont, A., Hern´andez-Molina, F.J., Miramontes, E., Raisson, F., Penven, P., 2019. Contourite depositional systems along the Mozambique channel: the interplay between bottom currents and sedimentary processes. Deep Sea Res. Part I Oceanogr. Res. Pap. 147, 79-99.

Valletta, R.D., Willenbring, J.K., Passchier, S., Elmi, C., 2018. 10Be/9Be ratios reflect Antarctic Ice Sheet freshwater discharge during Pliocene warming. Paleoceanogr. Paleoclimatol. 33, 934-944.

Von Blanckenburg, F., Bouchez, J., Ibarra, D.E., Maher, K., 2015. Stable runoff and weathering fluxes into the oceans over Quaternary climate cycles. Nat. Geosci. 8, 538-542.

Wang, D., Hesse, R., 1996. Continental slope sedimentation adjacent to an ice-margin. II. Glaciomarine depositional facies on Labrador Slope and glacial cycles. Mar. Geol. 135, 65-96.

Wang, J., Tang, Z., Wilson, D.J., Chang, F., Xiong, Z., Li, D., Li, T., 2022. Ocean-Forced Instability of the West Antarctic Ice Sheet since the Mid-Pleistocene. Geochem. Geophys. Geosyst. 23 e2022GC010470.

Weber, M.E., Bonani, G., Fütterer, K.D., 1994. Sedimentation processes within channel- ridge systems, southeastern Weddell Sea, Antarctica. Paleoceanography 9, 1027-1048.

Weber, M.E., Bailey, I., Hemming, S.R., Martos, Y.M., Reilly, B.T., Ronge, T.A., Brachfeld, S., Williams, T., Raymo, M., Belt, S.T., 2022. Antiphased dust deposition and productivity in the Antarctic Zone over 1.5 million years. Nat. Commun. 13, 2044.

White, D.A., Fink, D., Post, A.L., Simon, K., Galton-Fenzi, B., Foster, S., Fujioka, T., Jeromson, M.R., Blaxell, M., Yokoyama, Y., 2019. Beryllium isotope signatures of ice shelves and sub-ice shelf circulation. Earth Planet. Sci. Lett. 505, 86-95.

Wittmann, H., von Blanckenburg, F., Bouchez, J., Dannhaus, N., Naumann, R., Christl, M., Gaillardet, J., 2012. The dependence of meteoric 10Be concentrations on particle size in Amazon River bed sediment and the extraction of reactive 10Be/9Be ratios. Chem. Geol. 318, 126-138.

Wittmann, H., von Blanckenburg, F., Mohtadi, M., Christl, M., Bernhardt, A., 2017. The competition between coastal trace metal fluxes and oceanic mixing from the 10Be/9Be ratio: Implications for sedimentary records. Geophys. Res. Lett. 8443-8452.

Yi, L., Medina-Elizalde, M., Tan, L., Kemp, D.B., Li, Y., Kletetschka, G., Xie, Q., Yao, H., He,

KOPRI 극지연구소

H., Deng, C., 2023. Plio-Pleistocene deep-sea ventilation in the Eastern Pacific and potential linkages with Northern Hemisphere glaciation. Sci. Adv. 9, eadd1467.

Yin, Q., 2013. Insolation-induced mid-Brunhes transition in Southern Ocean ventilation and deep-ocean temperature. Nature 494, 222-225.

Yokoyama, Y., Anderson, J.B., Yamane, M., Simkins, L.M., Miyairi, Y., Yamazaki, T., Koizumi, M., Suga, H., Kusahara, K., Prothro, L., 2016. Widespread collapse of the Ross Ice Shelf during the late Holocene. Proc. Natl. Acad. Sci. 113, 2354-2359.

KOPRI
극지연구소

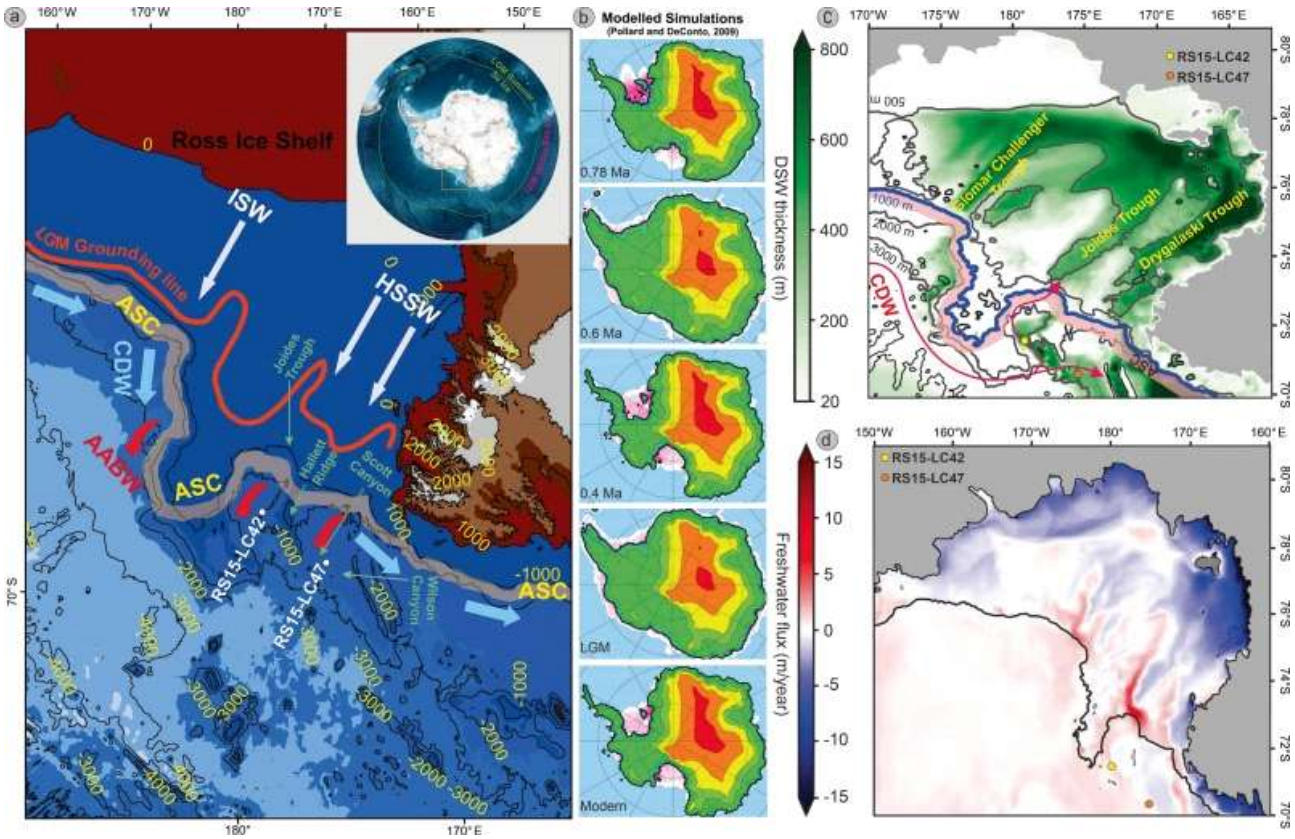


Fig. 1. (a) Regional map of the Ross Sea showing location of RS15-LC47 (this study) and RS15-LC42 (Bollen et al., 2022) sediment cores. Bathymetry and topography are based on the ETOPO1 global relief model (https://www.ngdc.noaa.gov/mgg/global/). The inset map of Antarctica shows LGM summer and winter sea ice cover (Green et al., 2022). Antarctic slope current (ASC), Antarctic bottom water (AABW), Circumpolar Deep Water (CDW), High Salinity Shelf Water (HSSW), and Ice Shelf Water (ISW) are modified from Smith Jr et al. (2012). (b) Modelled Antarctic ice volume changes since MPT (Pollard and DeConto, 2009). (c) Dense Shelf Water (DSW) thickness shown in green shades (Morrison et al., 2020), showing that energetic bottom water export plumes are active at the study location, and likely drive sedimentological variability within the core. (d) Simulated Ross Sea surface freshwater flux (Morrison et al., 2020).

KOPRI 극지연구소

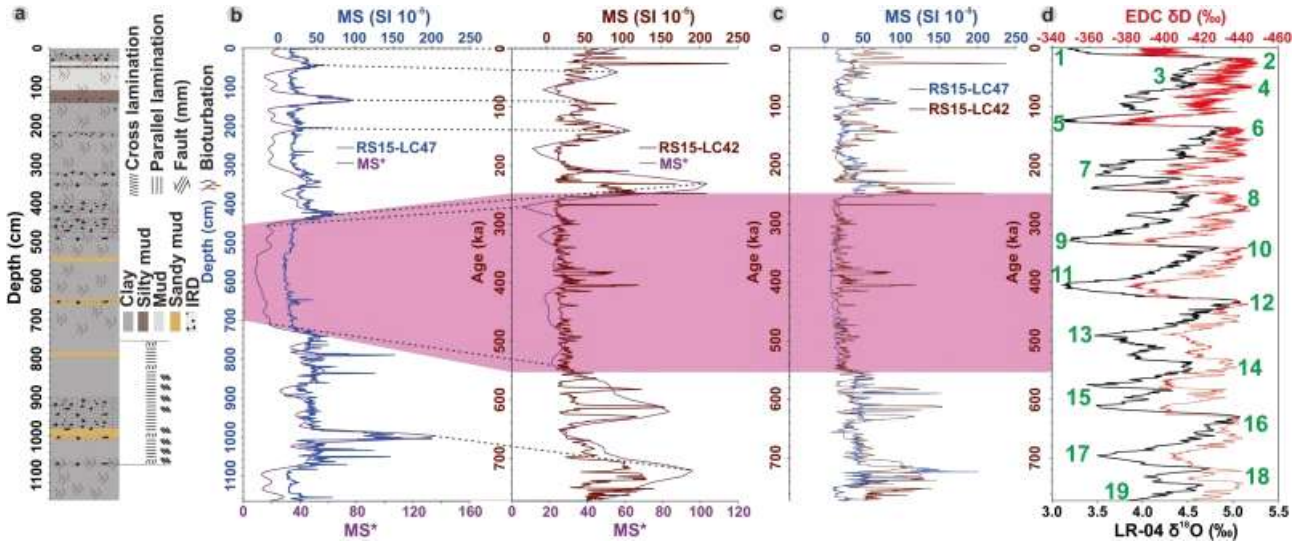


Fig. 2. (a) Lithology of the RS15-LC47 sediment core. Note: The lower segment of the studied interval (750–550 ka) displays distinct lithological characteristics than the rest of the core. It is characterized by parallel and cross laminations, along with millimetre-scale faults; (b) Wiggle matching of magnetic susceptibility (MS) values RS15-LC47 and RS15-LC42 sediment cores. Tie lines, shown as dotted lines, connect the MS values from each core, visually emphasizing the correspondence between the data sets. The anomalously low MS values in both the cores were used as marker horizons (Purple box); (c) Age-integrated MS values of RS15-LC47 and RS15-LC42 sediment cores; (d) The stacked benthic foraminiferal δ18O (LR-04 δ18O) (Lisiecki and Raymo, 2005) and EDC δD record (Jouzel et al., 2007) show marine isotope stages.

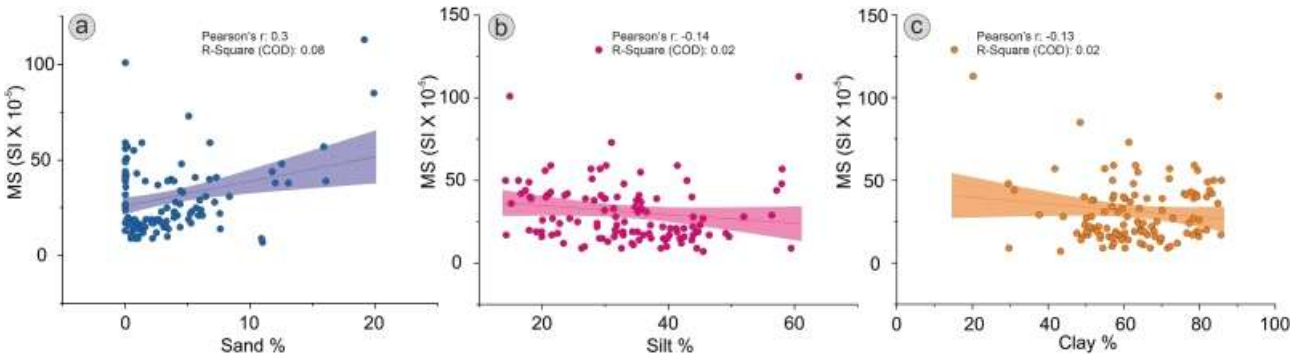


Fig. 3. Bivariate plots showing relation between different sedimentary components. (a), (b) and (c) show variation of MS values with respect to sand, silt and clay percentage, respectively.

KOPRI
극지연구소

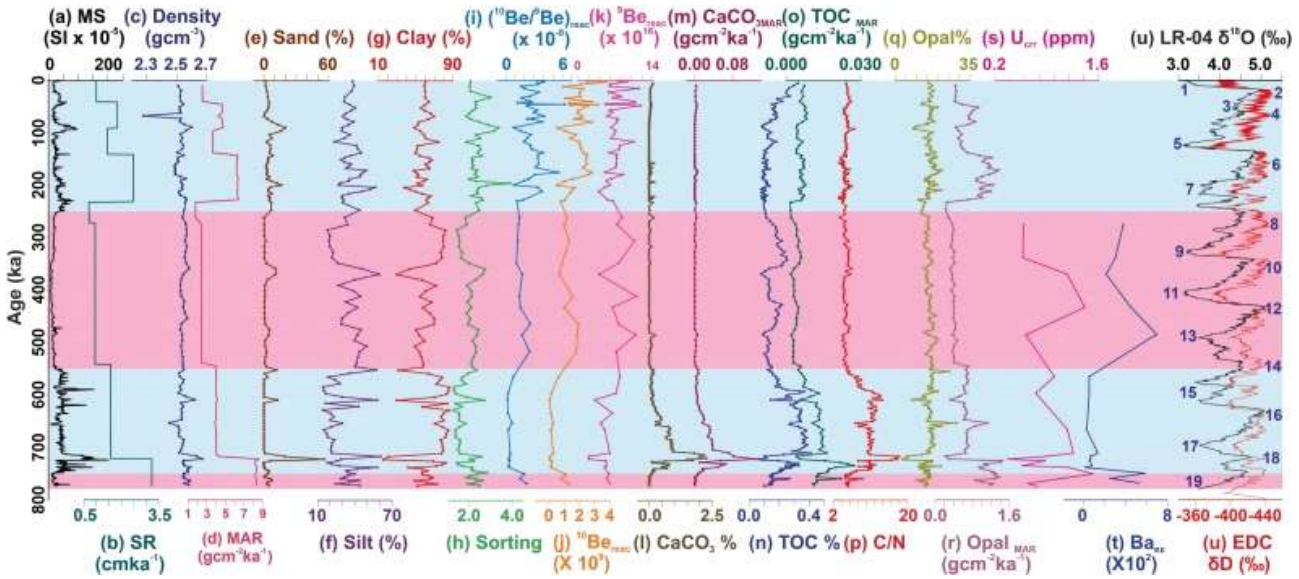


Fig. 4. Downcore variations of the different sedimentary components analyzed in this study. (I) (a) Magnetic susceptibility (MS); (b) Sedimentation rate (SR) (cm/ka); (c) Dry Bulk Density (DBD) (g/cm3); (d) Mass Accumulation Rate (MAR) (g/cm2/ka); (e) Sand %; (f) Silt %; (g) clay %; (h) Sorting; (i) (10Be/9Be)reac; (j) 10Bereac; (k) 9Bereac; (l) CaCO3%; (m) CaCO3MAR; (n) TOC %; (o) TOCMAR; (p) C/N; (q) Opal %; (r) OpalMAR; (s) Ucrr (Detrital corrected U); (t) Baex (Barium excess); (u) Stacked benthic foraminiferal δ18O (LR-04 δ18O) (Lisiecki and Raymo, 2005) and EDC δD record (Jouzel et al., 2007). The broad climatic zones based on sedimentological and geochemical analysis are represented with coloured boxes. The pink box indicates relatively warmer phases, and the light blue coloured box indicates relatively colder phases.

KOPRI 극지연구소

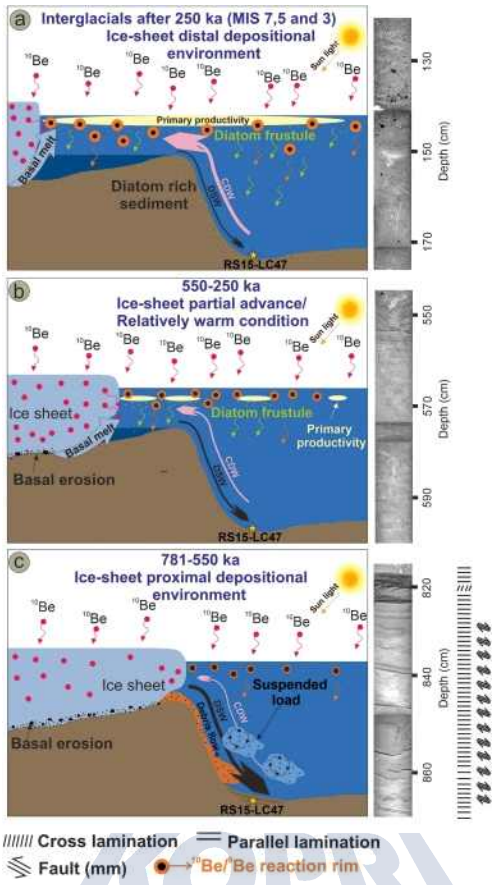


Fig. 5. Hypothesized oceanographic conditions in the Ross Sea over the past 773 ka, illustrated alongside representative X-ray images corresponding to key time intervals. Please note that the thickness of the (10Be/9Be)reac "reaction rim" conceptually represents the efficiency of Be isotope scavenging under different environmental conditions. (a) Ice-sheet distal depositional setting during the interglacial period from 250 ka to the present. This interval is characterized by a strengthened inflow of Circumpolar Deep Water (CDW). As the ice sheet retreated, sediment transit time to continental rise increased, allowing for greater accumulation of (10Be/9Be)reac in open marine conditions. Enhanced surface productivity is evident, reflecting the dominance of interglacial conditions. In contrast, Deep Shelf Water (DSW) production declines due to reduced sea-ice coverage. (b) Relatively warm interval between 550 and 250 ka with partial sea-ice advance. CDW influx remains moderately high, and sediment particles acquire moderate levels of (10Be/9Be)reac , though lower than the 250 ka-present interval due to shorter sediment transit times. Primary productivity is also moderately elevated. (c) Ice-sheet proximal depositional setting during 750-550 ka. This period is marked by intensified DSW production and reduced CDW influx. Strong DSW formation initiates gravity-driven sediment flows, redistributing shelf sediments to the outer continental margin. The (10Be/9Be)reac ratio is relatively low, indicating that when the ice sheet advanced to the shelf edge, sediment transit time in open marine settings was limited, leading to reduced scavenging of Be isotopes.

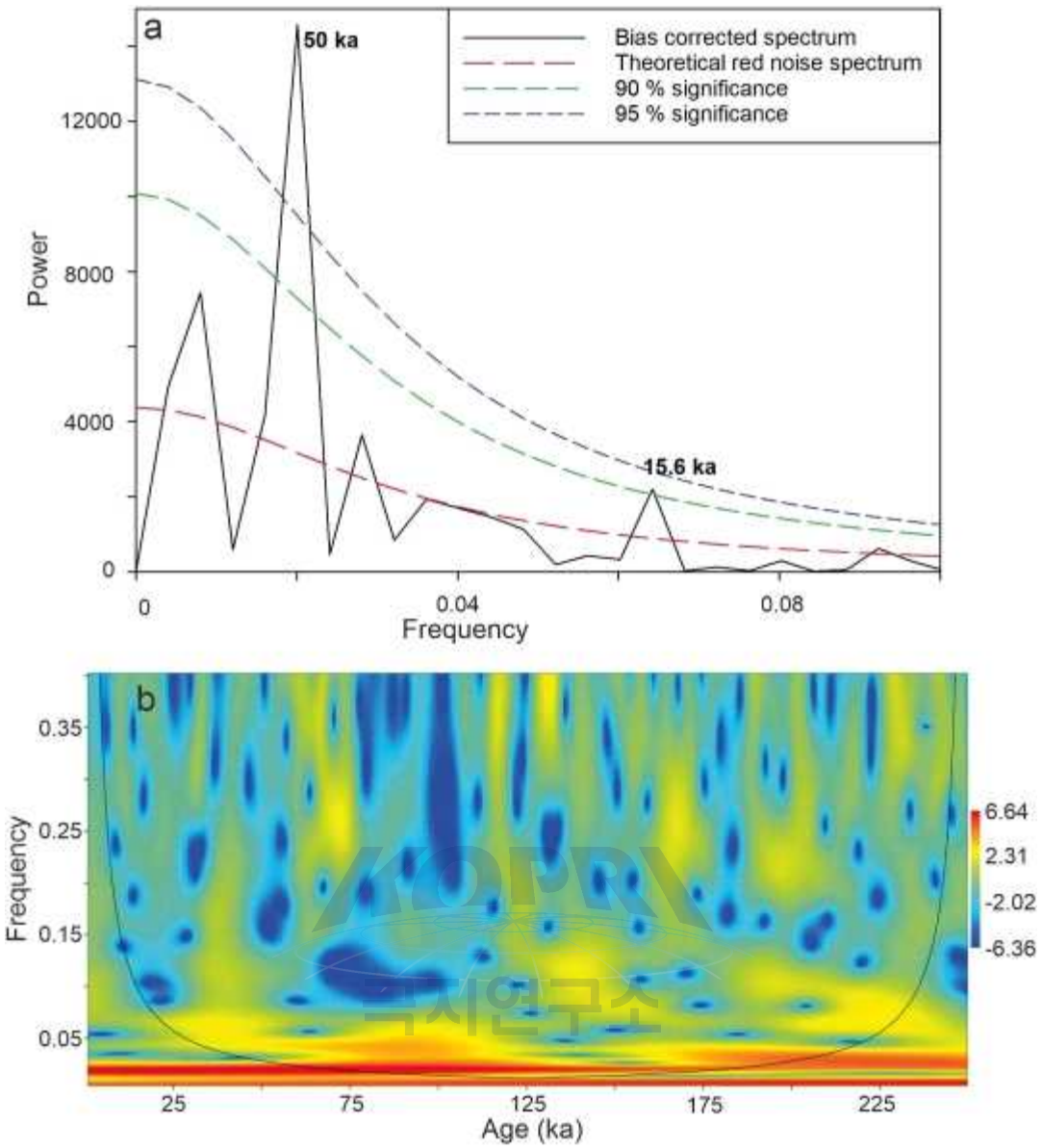


Fig. 6. Spectral and wavelet analysis of magnetic susceptibility (MS) values. (a) Power spectrum analysis showing dominant periodicities at ~50 ka and 15.6 ka. (b) Wavelet analysis illustrating the time-frequency distribution of MS variability over the past ~230 ka. The colour scale represents power intensity, with red and yellow indicating higher power and blue indicating lower power. The black contour outlines the cone of influence, beyond which edge effects may distort interpretations.

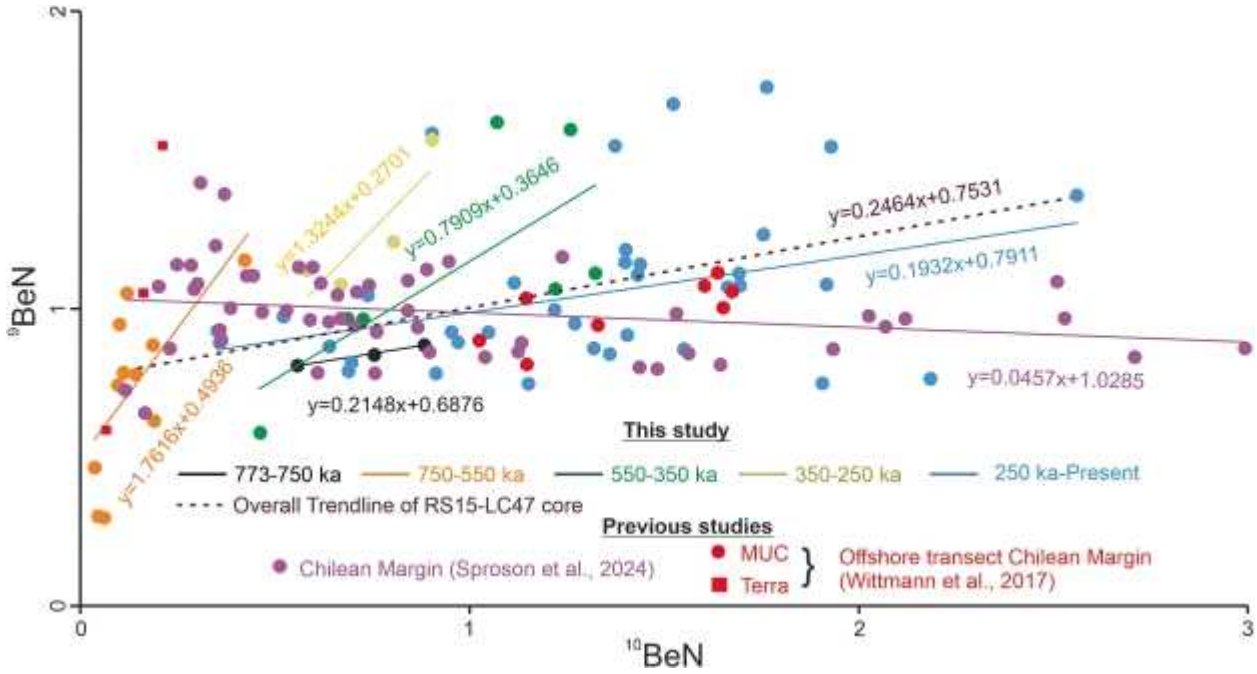


Fig. 7. Illustrates a normalized plot of 10Be versus 9Be for various timeframes as elaborated in Section 5.1. A slope greater than 1 signifies enhanced 9Be delivery resulting from basal erosion during ice-sheet advancement. Conversely, a slope less than 1 indicates augmented 10Be supply from additional sources. For comparative purposes, 10Be and 9Be data from a Chilean margin sediment core (Sproson et al., 2024) and an offshore transect (Wittmann et al., 2017) are included in the plot to evaluate their alignment with trends from this study.

KOPRI 극지연구소

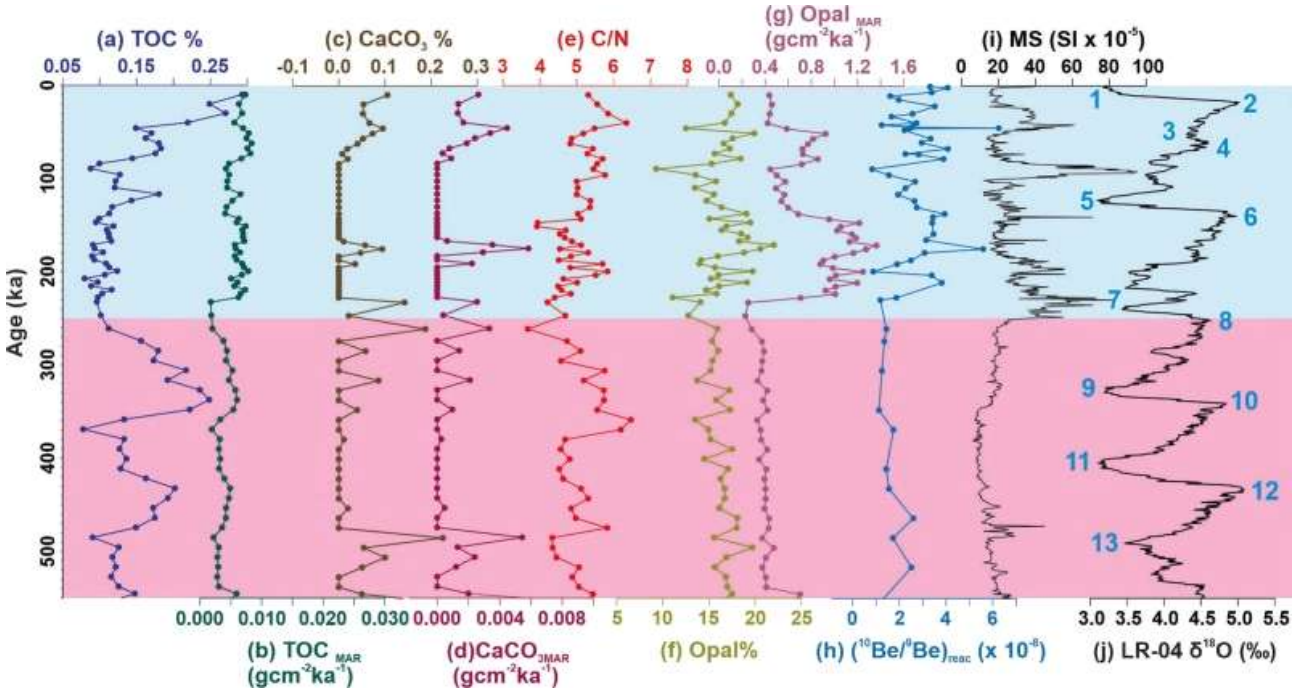


Fig. 8. Due to the elevated values of geochemical components observed within the 550–750 ka interval (as shown in Fig. 4), these parameters are plotted separately for the 550 ka to present timeframe, ensuring clearer discernment of their variations. The figure illustrates the downcore variations of: (a) TOC %; (b) TOCMAR; (c) CaCO3%; (d) CaCO3MAR; (e) C/N; (f) Opal %; (g) OpalMAR; (h) (10Be/9Be)reac; (i) MS; and (j) the stacked benthic foraminiferal δ18O (LR04 δ18O; Lisiecki and Raymo, 2005). The pink box indicates relatively warmer phase, and the light blue coloured box indicates relatively colder phase.

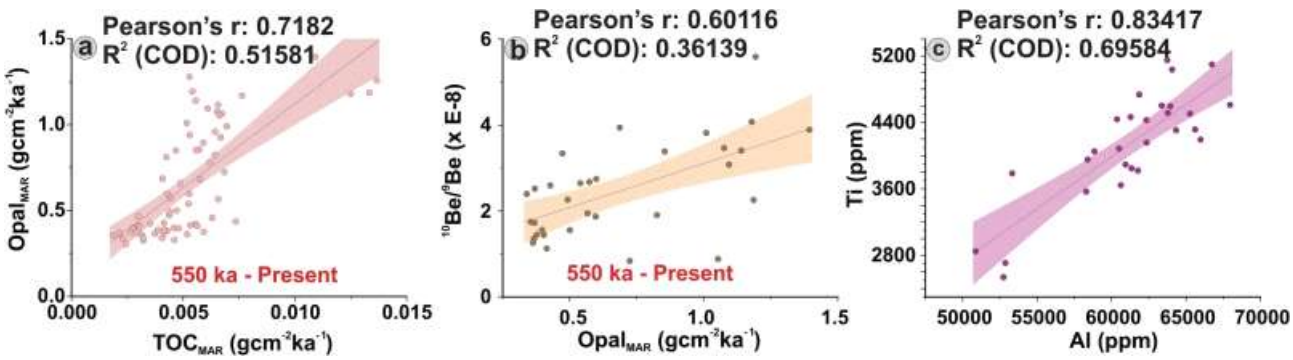


Fig. 9. Bivariate plots between (a) OpalMAR vs TOCMAR; (b) OpalMAR vs (10Be/9Be)reac; (c) Ti vs Al. Note: The bivariate plots depicting biogenic sedimentary geochemical components have been limited to 550 ka due to the anomalous increase in their concentrations beyond this point, interpreted to originate from reworked shelf sediments.

KOPRI
극지연구소

부록 별도 보고서

과거 온난화 시기의 서남극 빙상 후퇴 및 해양 순환의 공간적 변화

KOPRI
극지연구소

○ 2020-2025년 아라온 기반 탐사 요약

년 도	지 역	획득된 총 중력코어 시료
2020	아문젠해 및 로스해	12
2021	로스해 중앙 빙붕 해역	6
2022	아문젠해 닷슨 및 겟츠 A 빙붕 해역	11
2023	로스해 드라이갈스키 및 조이데스 분지	13
2024	로스해 서부 빙붕 해역	7
2025	로스해 및 동부 빙붕 해역	6

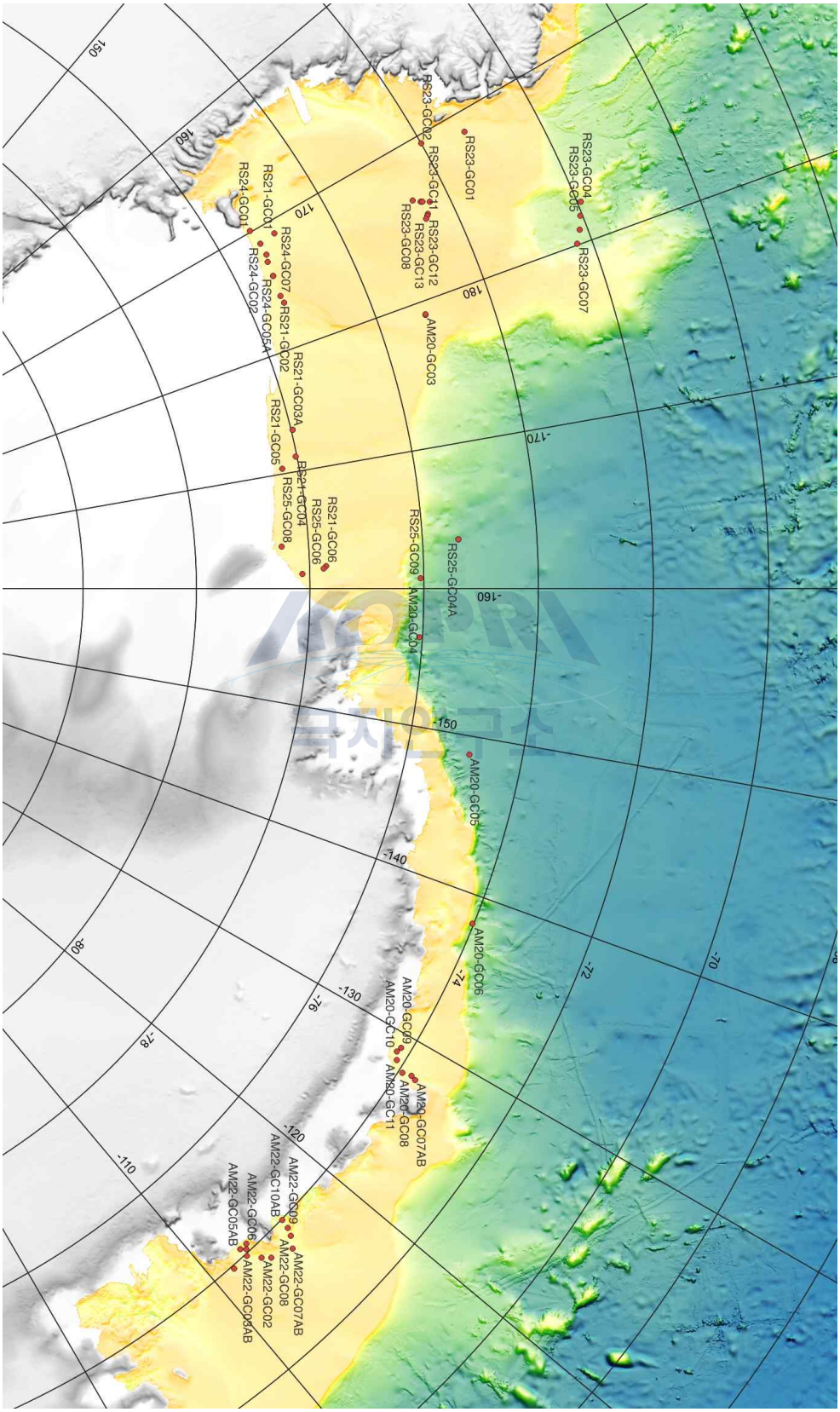
○ 사업기간 동안 획득된 중력 시추에 대한 전체 정보

Core number	Latitude	Longitude	Water depth (m)	Core recovery (cm)
AM20-GC02	75° 10.0607'S	179° 04.7460'W	547	180
AM20-GC03	75° 09.7059'S	179° 05.8327'W	544	305
AM20-GC04	76° 03.1330'S	156° 26.7917'W	3219	797
AM20-GC05	74° 55.36'S	148° 44.28'W	3746	667
AM20-GC06	74° 0.9775'S	138° 12.0505'W	2382	899
AM20-GC07AB	73° 40.4382'S	127° 49.4084'W	807	296/420
AM20-GC08	73° 46.0990'S	127° 54.8069'W	725	180
AM20-GC09	74° 10.3588' S	129° 06.7084' W	872	128
AM20-GC10	74° 12.3161' S	128° 46.8123' W	804	105
AM20-GC11	74° 07.3099' S	128° 17.1528' W	599	133
AM20-GC12AB	73° 56.0184' S	127° 47.9195' W	790	295/310
RS21-GC01	77° 00.6315'S	171° 00.0185'E	740	61
RS21-GC02	77° 23.9941'S	176° 17.9590'E	625	217
RS21-GC03A	77° 58.4119'S	173° 33.4831'W	535	288
RS21-GC03B	77° 58.4119'S	173° 33.4831'W	535	270
RS21-GC04	78° 01.5948'S	171° 15.6141'W	517	208
RS21-GC05	78° 17.3683'S	170° 27.4014'W	560	279
RS21-GC06	77° 42.6320'S	161° 51.1843'W	682	270
AM22-GC01ABC	73° 39.1502'S	113° 37.8846'W	803	277/600/600
AM22-GC02	73° 46.3271'S	113° 11.3696'W	785	342
AM22-GC03AB	73° 57.7007'S	112° 36.0902'W	921	430/446
AM22-GC04	74° 03.4465'S	112° 51.2228'W	866	710
AM22-GC05AB	74° 07.8340'S	112° 33.0079'W	975	337/296

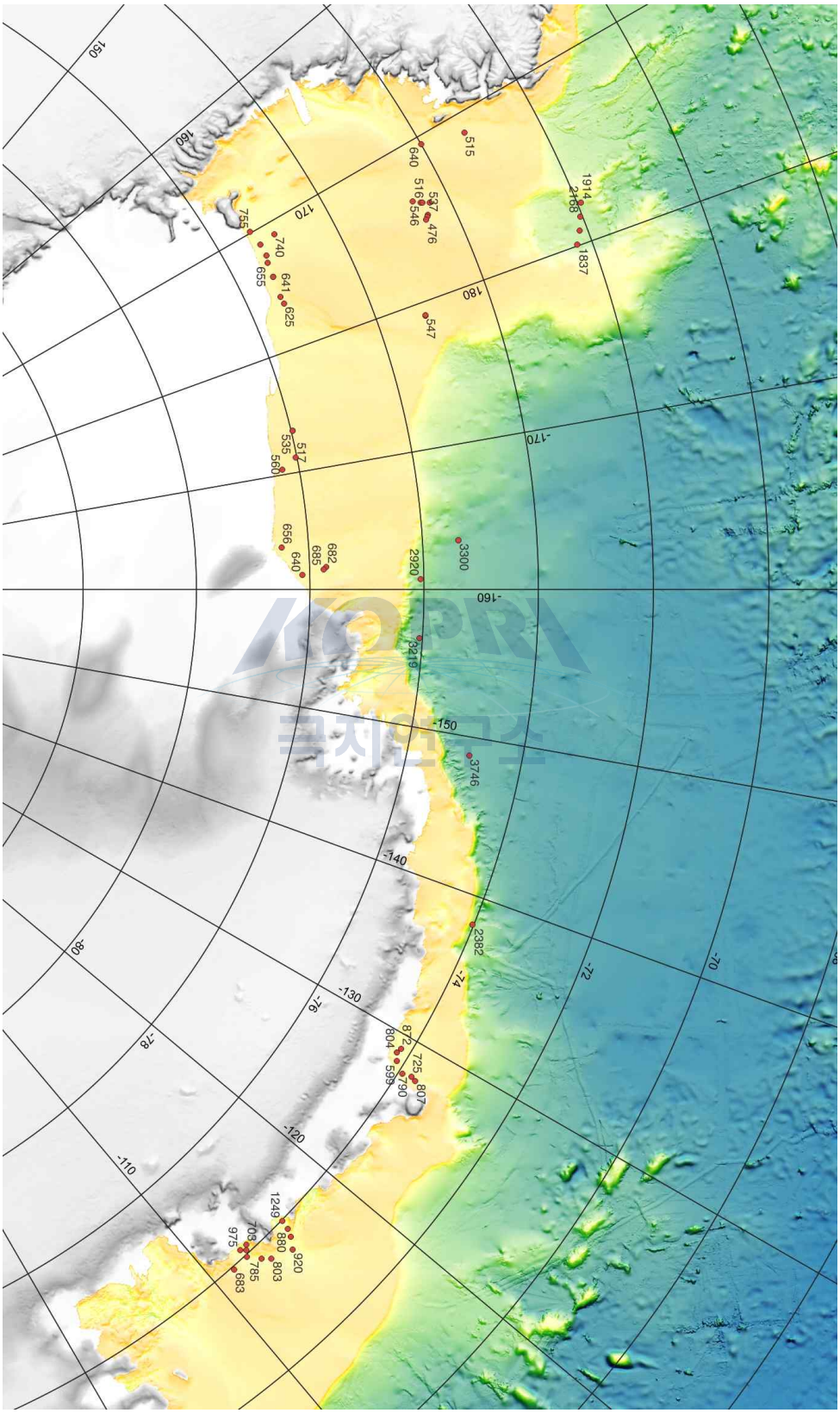
KORI 극지연구소

AM22-GC06	74° 07.4386'S	113° 05.2900'W	703	215
AM22-GC07AB	73° 30.2968'S	114° 58.1766'W	920	378/294
AM22-GC08	73° 40.8915'S	115° 27.3835'W	990	420
AM22-GC09	73° 49.1513'S	115° 40.3427'W	880	551
AM22-GC10AB	73° 58.9692'S	115° 46.1438'W	1249	440/535
AM22-GC13	73° 56.8896'S	111° 26.0451'W	683	255
RS23-GC01	73° 14.4805'S	171° 11.9843'E	515	310
RS23-GC02	73° 59.9647'S	170° 30.0713'E	640	324
RS23-GC03	74° 20.4293'S	174° 04.0968'E	576	580
RS23-GC04	71° 56.1155'S	177° 46.2063'E	1914	446
RS23-GC05	72° 02.3400'S	178° 29.3400'E	2168	243
RS23-GC06	72° 08.4628'S	179° 13.7378'E	2185	114
RS23-GC07	72° 15.2790'S	179° 54.5081'E	1837	292
RS23-GC08	74° 35.5678'S	173° 31.5171'E	516	527
RS23-GC09	74° 28.7410'S	173° 50.1901'E	546	397
RS23-GC10	74° 27.5589'S	173° 53.4003'E	570	783
RS23-GC11	74° 27.5541'S	174° 45.0622'E	537	585
RS23-GC12	74° 29.1940'S	174° 51.2201'E	532	466
RS23-GC13	74° 31.5832'S	175° 00.3799'E	476	331
RS24-GC01	77° 21.4422'S	169° 52.9158'E	755	82
RS24-GC02	77° 18.6523'S	171° 11.4645'E	813	180
RS24-GC03	77° 18.8392'S	172° 11.6210'E	691	230
RS24-GC04	77° 20.8099'S	172° 46.5450'E	655	116
RS24-GC05A	77° 22.5929'S	173° 56.3044'E	684	99
RS24-GC05B	77° 22.5929'S	173° 56.3044'E	684	99
RS24-GC07	77° 24.7021'S	175° 40.6493'E	641	200
RS25-GC04A	75° 22.0152'S	163° 25.2695'W	3300	533
RS25-GC04B	75° 22.0227'S	163° 25.2867'W	3300	500
RS25-GC06	77° 45.4167'S	161° 40.7972'W	685	272
RS25-GC07	78° 7.9040'S	161° 13.9423'W	640	250
RS25-GC08	78° 28.3389'S	163° 42.2978'W	656	270
RS25-GC09	76° 3.3653'S	160° 43.6034'W	2920	523

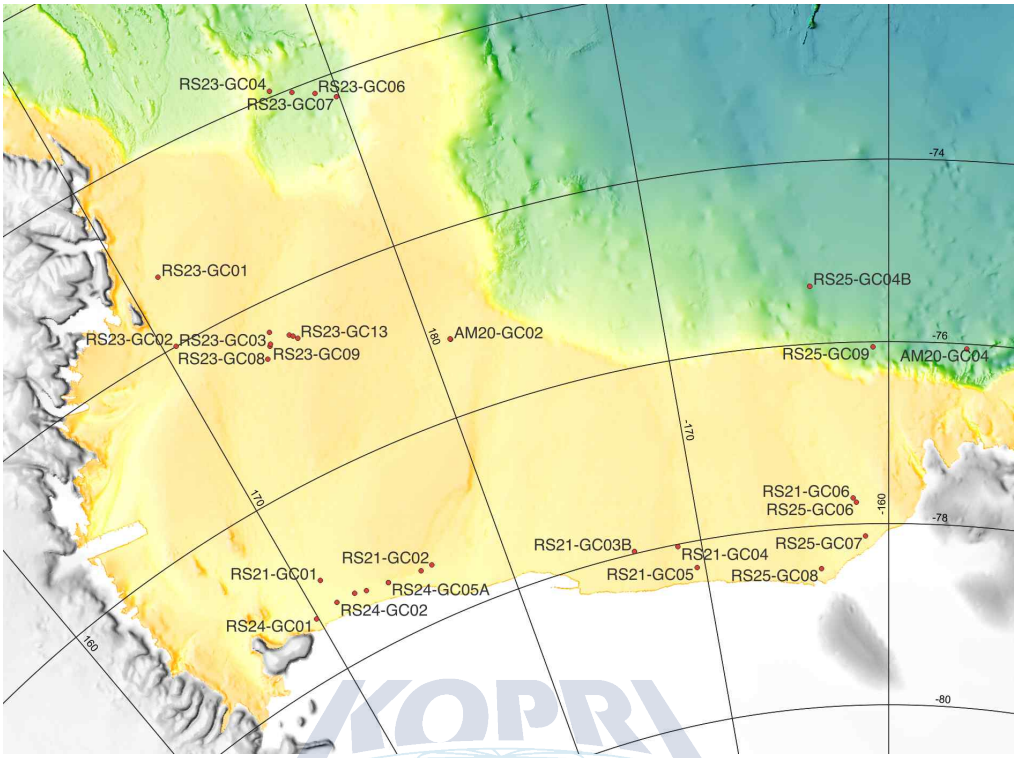
○ 사업 기간 동안 획득된 중력 시추 위치

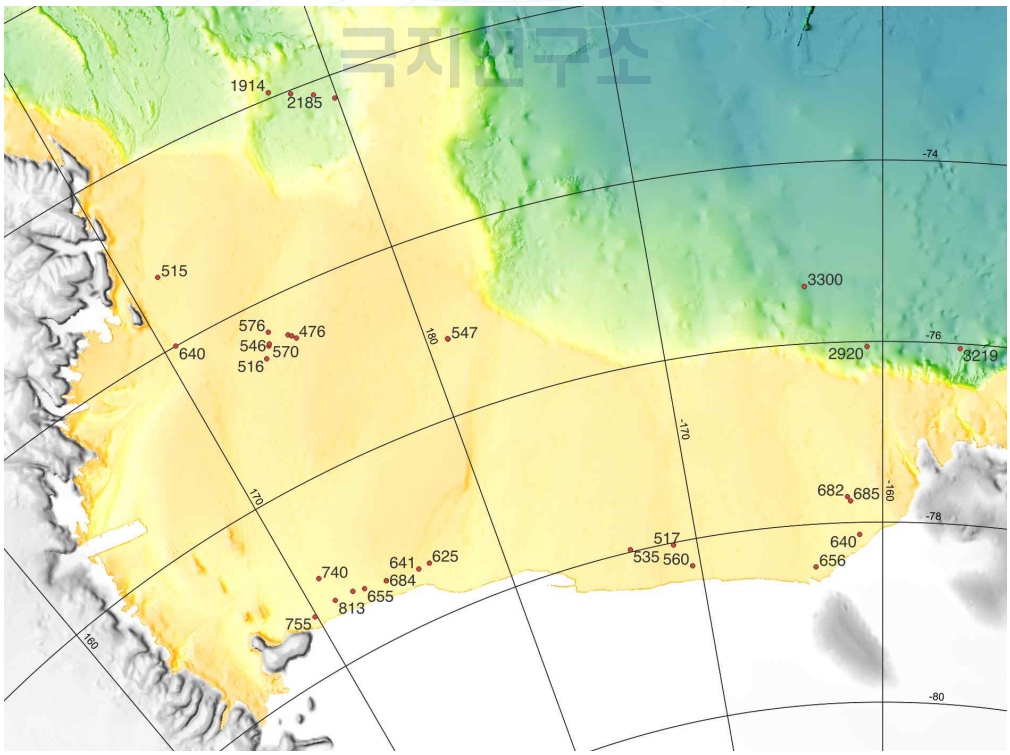


○ 사업 기간 동안 획득된 중력 시추 정점의 수심



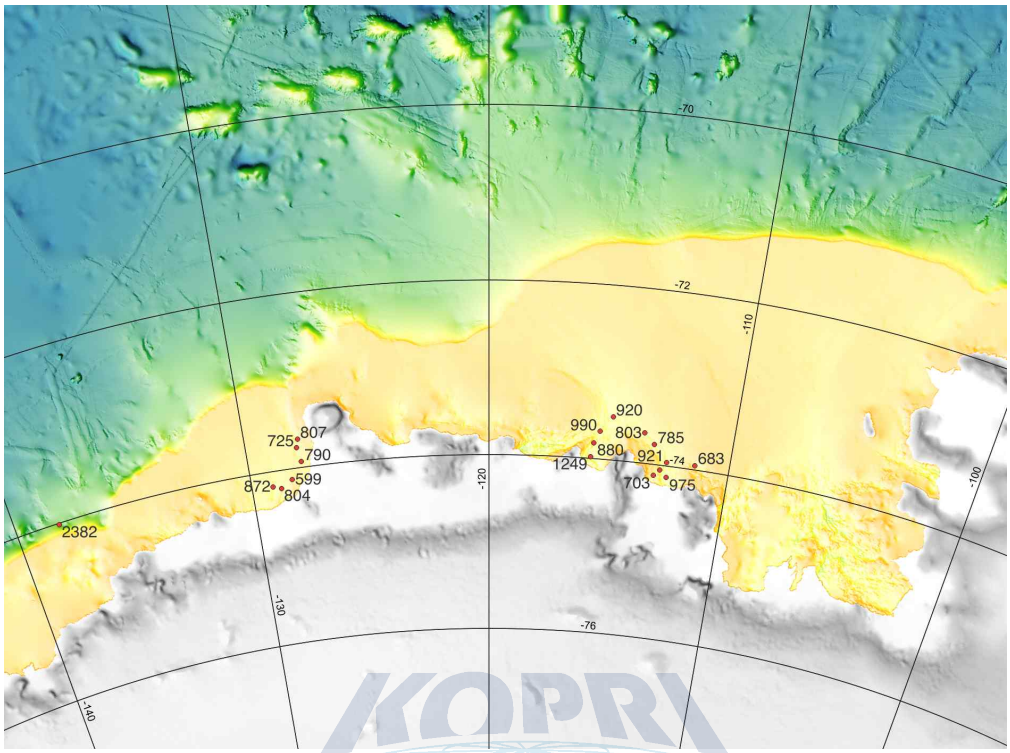
○ 연구 지역별 중력 시추 정점과 수심 (로스해)

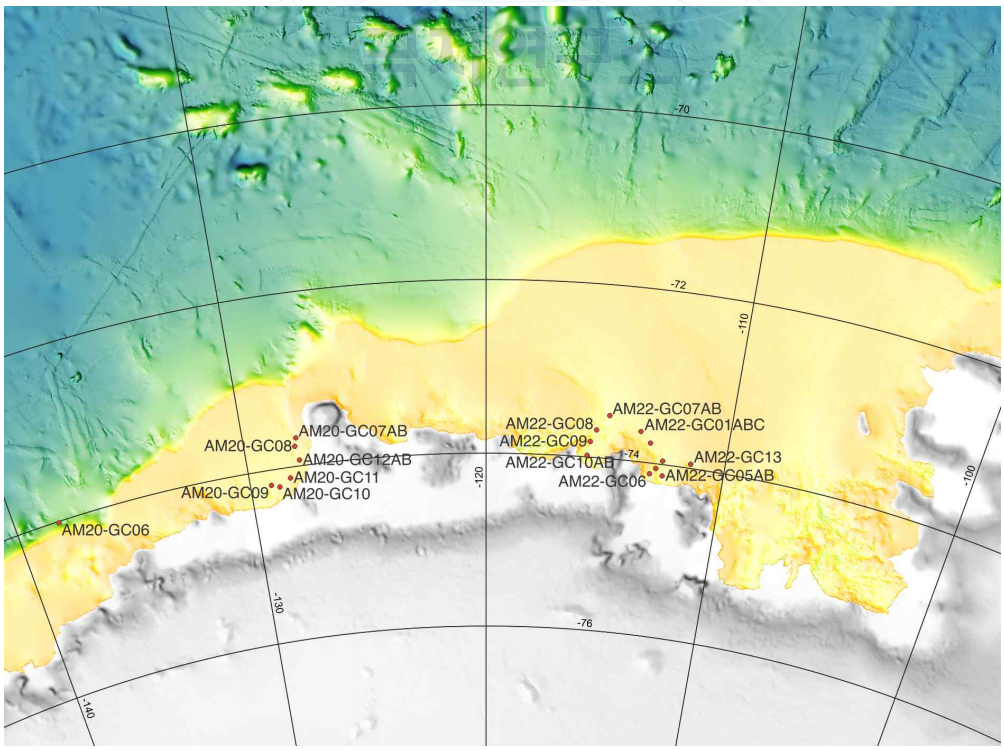




KOPRI
극지연구소

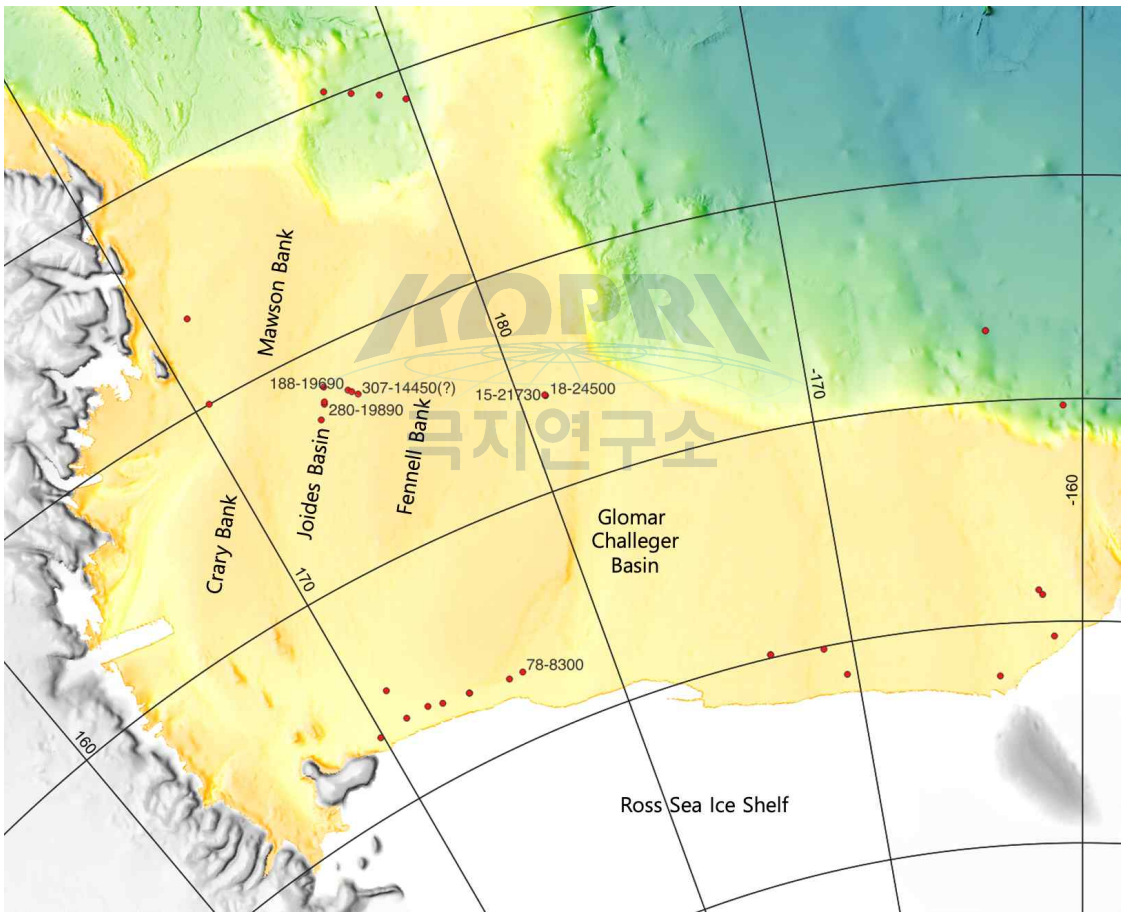
○ 연구 지역별 중력 시추 정점과 수심 (아문젠해)





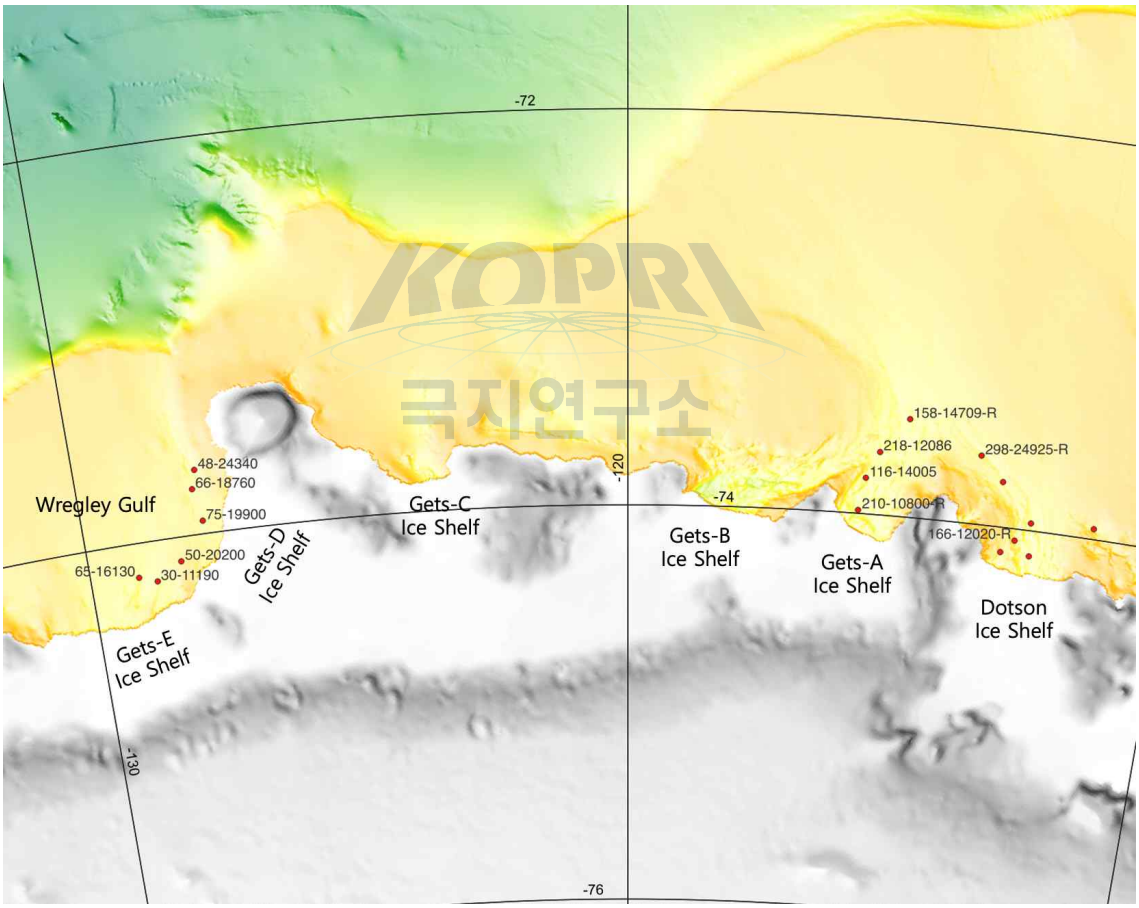
○ 연구 지역별 중력 시추 정점과 연대 추정 (로스해)

- 마지막 최대 빙하기 기준
- 라벨 표시 예시: 12-12000 (벌크 퇴적물 연대로 12 cm 12000 yrs BP, 12-12000-R은 Ramped pyrolysis 연대)
- 로스해 조이데스 중앙 분지 내 약 200 cm 깊이의 퇴적층이 홀로세 퇴적층임을 알 수 있음
- 로스 빙붕 앞 해역은 약 100 cm 깊이가 홀로세 퇴적층임



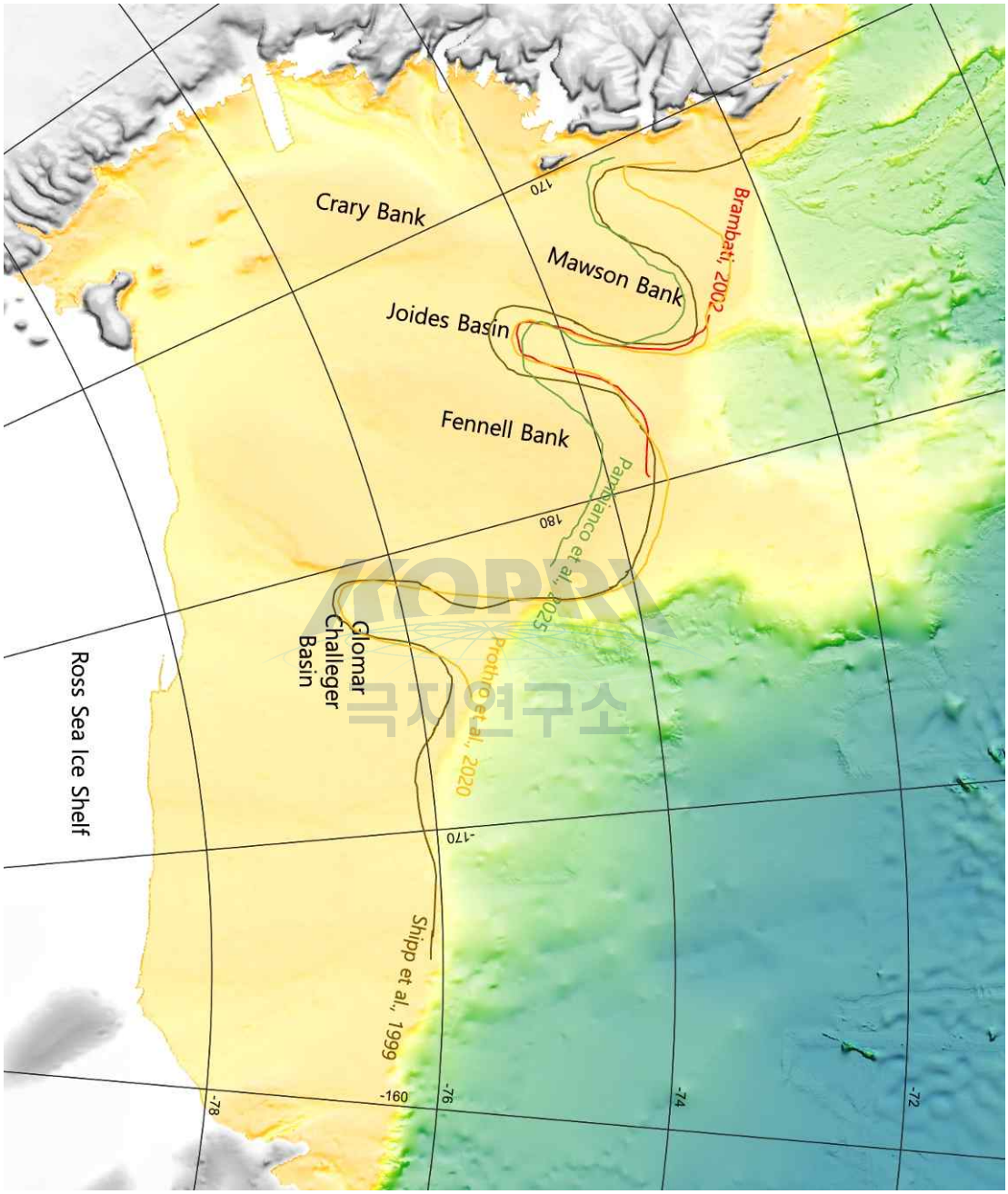
○ 연구 지역별 중력 시추 정점과 연대 추정 (아문젠해)

- 마지막 최대 빙하기 기준
- 라벨 표시 예시: 12-12000 (벌크 퇴적물 연대로 12 cm 12000 yrs BP, 12-12000-R은 Ramped pyrolysis 연대)
- 닷슨 및 겟츠-A 빙붕 앞 분지에서 약 100~200 cm 깊이가 홀로세 퇴적층임
- 겟츠-D 및 –E 빙붕 앞 분지에서 약 30 cm 이내 깊이가 홀로세 퇴적층임



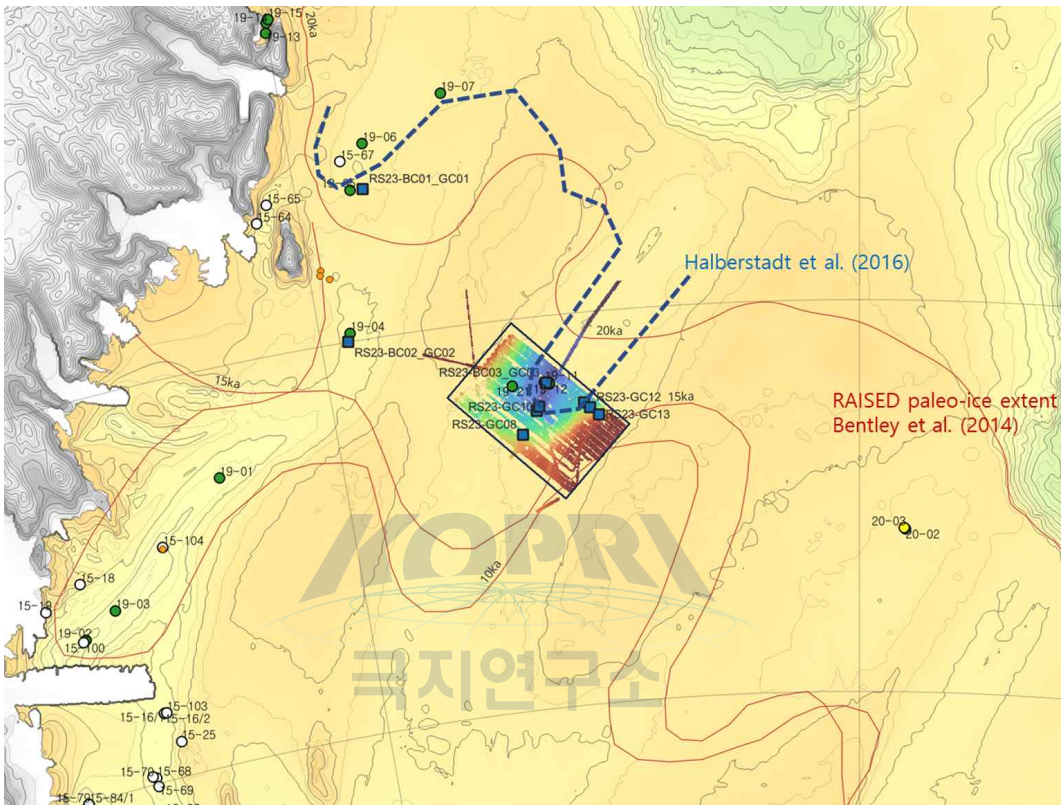
KOPRI 극지연구소

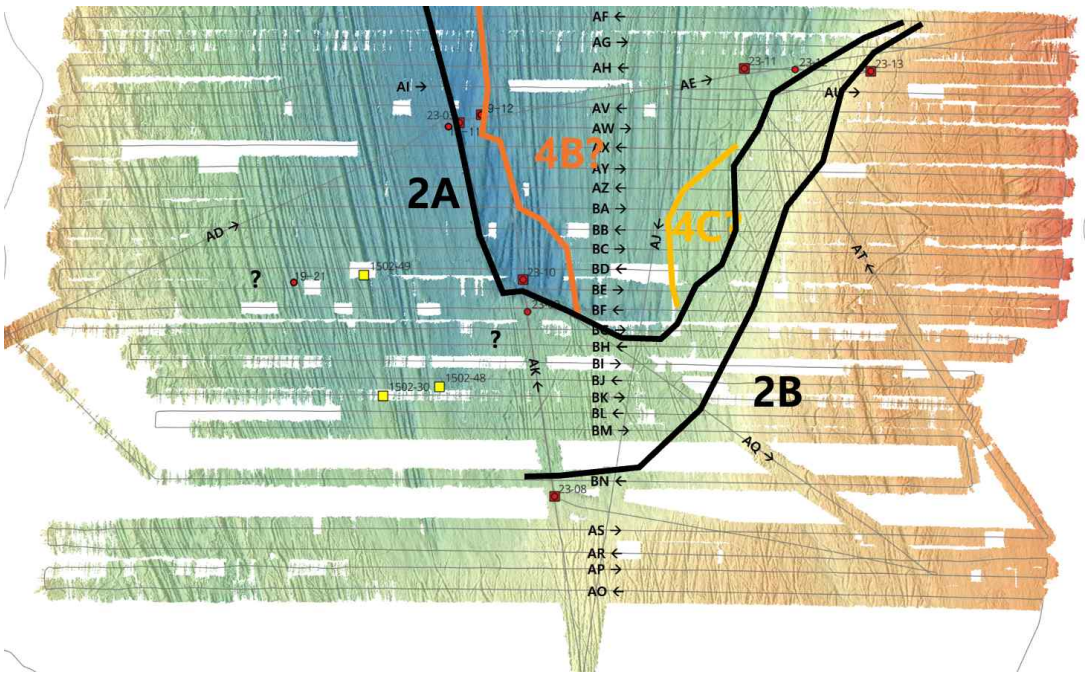
○ 마지막 최대 빙하기 동안의 로스해 빙상 확장 (기존 연구결과 중심으로)



○ 사업 기간 동안 연구 결과를 통한 마지막 최대 빙하기 동안 로스해 빙상 확장

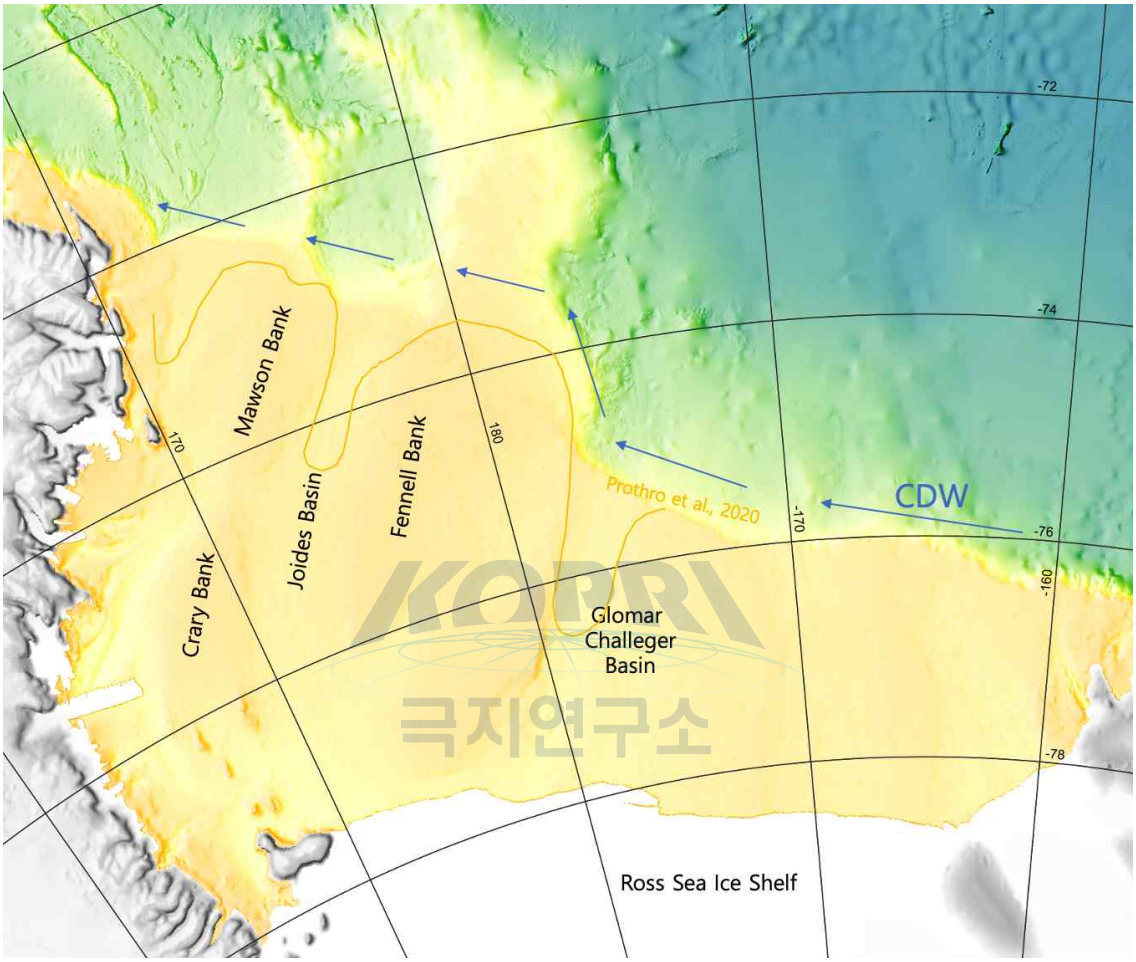
- 네모 박스: 멀티빔 자료
- 2A 라인: 마지막 최대 빙하기 빙상 해저 접지선





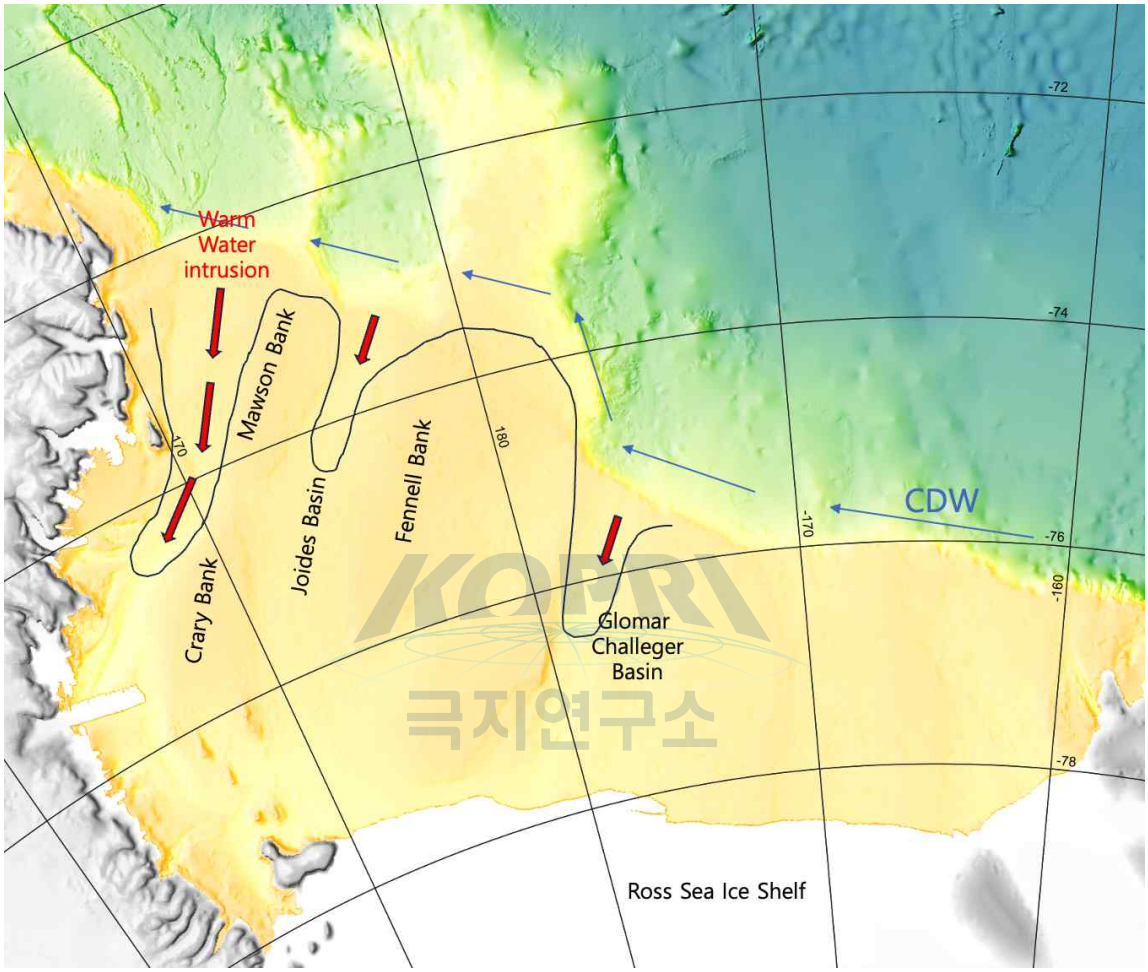
○ 마지막 최대 빙하기 이후 로스해 해양 순환의 변화

- 약 2만년 전



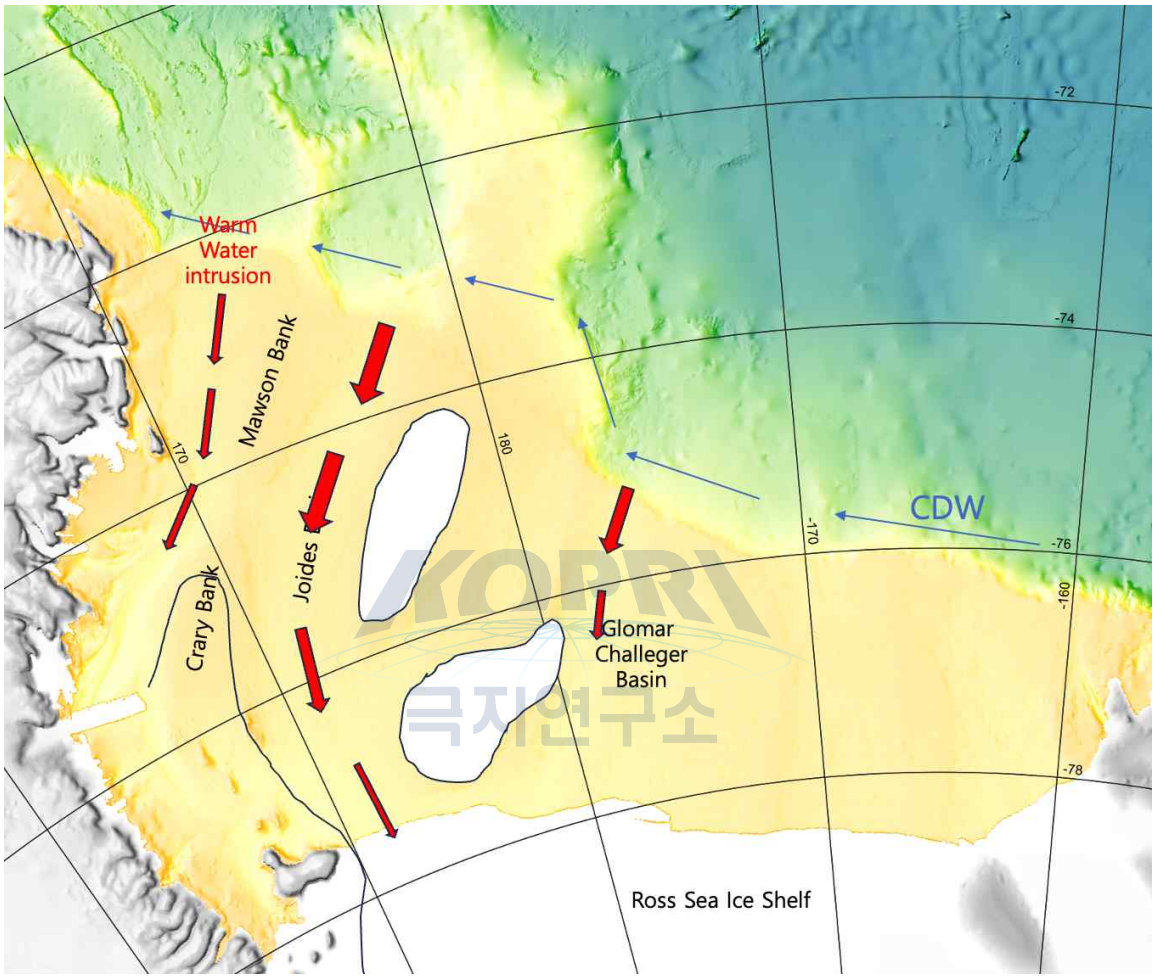
○ 마지막 최대 빙하기 이후 로스해 해양 순환의 변화

- 약 1만5천만년~1만년 전 사이



○ 마지막 최대 빙하기 이후 로스해 해양 순환의 변화

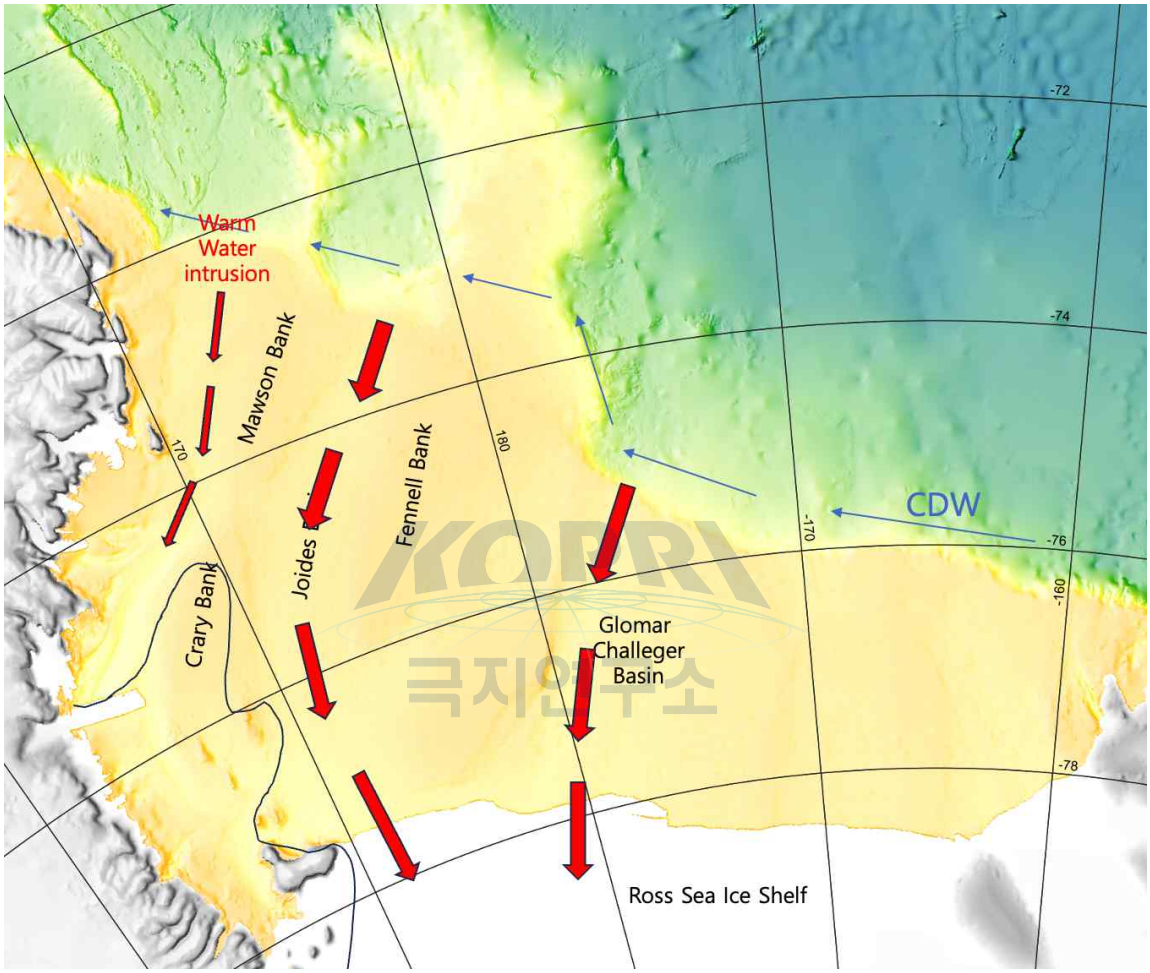
- 약 8천년 전



KOPRI
극지연구소

○ 마지막 최대 빙하기 이후 로스해 해양 순환의 변화

- 약 4천년 전



KOPRI
극지연구소

참고 문헌

Brambati A, Corradi N, Finocchiaro F, Giglio F (2002a). The position of the grounding line in the Joides Basin: an interpretation based on Sedimentological and geochemical Data. In GambleJ.A., Skinner D.N.B., Henrys S., e R. Lynch (Editors). Antarctica at the close of a Millenium. Royal Society of New Zealand Bulletin 35:365-372.

Halberstadt, A. R. W., Simkins, L. M., Greenwood, S. L., and Anderson, J. B.: Past ice-sheet behaviour: retreat scenarios and changing controls in the Ross Sea, Antarctica, The Cryosphere, 10, 1003–1020, https://doi.org/10.5194/tc-10-1003-2016, 2016.

Pambianco C., Alessio Nogarotto, Mathia Sabino, Lucilla Capotondi, et al. (2025) Past intrusion of Circumpolar Deep Water in the Ross Sea: Impacts on the ancient Ross Ice Shelf, Sci. Adv. 11, eadt7075

Prothro L. O. Majewski W. Yokoyama Y. Simkins L.M. Anderson J.B. Yamane M. et al (2020). Timing and pathways of East Antarctic ice sheet retreat. Quat. Sci. Rev.230, 106166. 10.1016/j.quascirev.2020.106166

Shipp S. S. Anderson J. Domack E. (1999). Late pleistocene–holocene retreat of the West antarctic ice-sheet system in the Ross Sea: part 1—geophysical results. Geol. Soc. Am. Bull.111, 1486–1516. 10.1130/0016-7606(1999)111<1486:lphrot>2.3.co;2

KOPRI 극지연구소

KOPRI
극지연구소

주 의

1. 이 보고서는 극지연구소에서 수행한 기본사업의 연구결과보고서입니다.

2. 이 보고서 내용을 발표할 때에는 반드시 극지연구소에서 수행한 기본사업의 연구결과임을 밝혀야 합니다.

3. 국가과학기술 기밀유지에 필요한 내용은 대외적으로 발표 또는 공개하여서는 안 됩니다.